REPORT DOCUMENTATION PAGE

AFRL-SR-AR-TR-04-

0216

1. REPORT DATE (DD-MM-YYYY) 18-07-2003	2. REPORT DATE Final Technical Report	3. DATES COVERED (From - To) 01 Jan 2003 - 31 Aug 2003

4. TITLE AND SUBTITLE
Photon Processing in Microelectronics and Photonics II
Part A: Laser Applications in Microelectronics and Optoelectronic
Manufacturing VIII

5a. CONTRACT NUMBER

5b. GRANT NUMBER
F49620-03-1-0108

5c. PROGRAM ELEMENT NUMBER

6. AUTHOR(S)
Alberto Pique
Koji Sugioka
Peter R. Herman
Jim Fieret

5d. PROJECT NUMBER

5e. TASK NUMBER

5f. WORK UNIT NUMBER

7. PERFORMING ORGANIZATION NAME(S) AND ADDRESS(ES)
Society of Photo-Optical Instrumentation Engineers (SPIE)
PO Box 10
Bellingham, WA 98227-0010

8. PERFORMING ORGANIZATION REPORT NUMBER
Volume 4977

9. SPONSORING/MONITORING AGENCY NAME(S) AND ADDRESS(ES)
Air Force Office of Scientific Research
4015 Wilson Blvd, RM 713
Arlington, VA 22203-1954

10. SPONSOR/MONITOR'S ACRONYM(S)
AFOSR/NE

11. SPONSORING/MONITORING AGENCY REPORT NUMBER

12. DISTRIBUTION AVAILABILITY STATEMENT
Approved for Public Release

20040423 014

13. SUPPLEMENTARY NOTES
ISBN 0-8194-4777-3

14. ABSTRACT
Laser processing of materials is now an established technology for micromachining, thin film synthesis, device packaging, rapid prototyping, and even nanoscale synthesis and processing of materials. The main driving force behind these developments is the seemingly limitless adaptability of lasers in providing unique materials processing solutions, manufacturing of otherwise unattainable devices and structures, and the implementation of cost-effective solutions to complex manufacturing processes. The use of lasers for manufacturing microelectronic, optoelectronic, and MEMS devises is now becoming an established enabling technology. This volume includes papers on fundamental processes, lasers and techniques, pulsed laser deposition, laser microengineering, femtosecond laser processing, laser nanoengineering, laser-engineered photonics and semiconductor structures, direct-write processing and laser microstructuring.

15. SUBJECT TERMS
Laser, photonics, microelectronics

16. SECURITY CLASSIFICATION OF:			17. LIMITATION OF ABSTRACT SAR	18. NUMBER OF PAGES 684	19a. NAME OF RESPONSIBLE PERSON Janice Gaines Walker
a. REPORT Non-classfied	b. ABSTRACT	c. THIS PAGE			19b. TELEPONE NUMBER (Include area code) (360)676-3290

Standard Form 298 (Rev. 8-98)
Prescribed by ANSI-Std Z39-18

Photon Processing in Microelectronics and Photonics II

Alberto Piqué
Koji Sugioka
Peter R. Herman
Jim Fieret
Friedrich G. Bachmann
Jan J. Dubowski
Willem Hoving
Kunihiko Washio
David B. Geohegan
Frank Träger
Kouichi Murakami
Chairs/Editors

27–30 January 2003
San Jose, California, USA

SPIE

P

PROCEEDINGS
SERIES

Volume 4977

Contents

PART A   Laser Applications in Microelectronics and Optoelectronic Manufacturing VIII

SESSION 1   FUNDAMENTAL PROCESSES

SESSION 2   LASERS AND TECHNIQUES

PART B   Laser-Based Packaging in Microelectronics and Photonics II

SESSION 14   REVIEWS AND LASER JOINING

SESSION 15   WELDING

SESSION 19   SYNTHESIS AND PHOTONICS OF NANOSCALE MATERIALS II

Conference Committees

PART A   **Laser Applications in Microelectronics and Optoelectronic Manufacturing VIII**

Conference Chairs

Alberto Piqué, Naval Research Laboratory (USA)
Koji Sugioka, RIKEN-The Institute of Physical and Chemical Research (Japan)
Peter R. Herman, University of Toronto (Canada)
Jim Fieret, Exitech Ltd. (United Kingdom)

Program Committee

David Ashkenasi, Naval Research Laboratory (USA)
Julian P. Burt, University of Wales Bangor (United Kingdom)
Paul B. Corkum, National Research Council (Canada)
Friedrich Dausinger, Universität Stuttgart (Germany)
J. Thomas Dickinson, Washington State University (USA)
Jan J. Dubowski, National Research Council (Canada)
Peter E. Dyer, University of Hull (United Kingdom)
Malcolm C. Gower, Exitech Ltd. (United Kingdom)
Constantine P. Grigoropoulos, University of California, Berkeley (USA)
Richard F. Haglund, Vanderbilt University (USA)
Henry Helvajian, The Aerospace Corporation (USA)
Adam Huang, The Aerospace Corporation (USA)
Ernst-Wolfgang Kreutz, RWTH-Aachen (Germany)
Scott A. Mathews, Potomac Photonics, Inc. (USA)
Jyotirmoy Mazumder, University of Michigan (USA)
Hiroyuki Niino, National Institute of Advanced Industrial Science (Japan)
Stefan Nolte, Friedrich-Schiller-Universität Jena (Germany)
Tatsuo Okada, Kyushu University (Japan)
Bradley R. Ringeisen, Naval Research Laboratory (USA)
Marc Talkenberg, Rheinisch-Westfälische Technische Hochschule (Germany)
James D. Talgon, Nanosphere, Inc. (USA)
Frank Träger, Universität Kassel (Germany)
Vadim P. Veiko, St. Petersburg Institute of Fine Mechanics (Russia)
Xianfan Xu, Purdue University (USA)

Session Chairs

1   Fundamental Processes
James S. Horwitz, Naval Research Laboratory (USA)

2   Lasers and Techniques
Peter R. Herman, University of Toronto (Canada)

3   Laser Microengineering I
Jim Fieret, Exitech Ltd. (United Kingdom)

4   Femtosecond Laser Processing
Koji Sugioka, RIKEN-The Institute of Physical and Chemical Research
    (Japan)

5   Laser Nanoengineering
Henry Helvajian, The Aerospace Corporation (USA)

6   Pulsed-Laser Deposition
David Ashkenasi, Laser- und Medizin-Technologie GmbH (Germany)

7   Laser Microengineering II
Michel Meunier, École Polytechnique de Montréal (Canada)

8   Laser-Engineered Photonic Structures
Hiroyuki Niino, National Institute of Advanced Industrial Science (Japan)

9   Laser Direct-Write
Gerd Esser, Bayerisches Laserzentrum GmbH (Germany)

10   Laser Microengineering III
Craig B. Arnold, Naval Research Laboratory (USA)

11   Microstructuring
Corey M. Dunsky, Electro Scientific Industries, Inc. (USA)

12   Laser-Engineered Semiconductor Structures
Alberto Piqué, Naval Research Laboratory (USA)

PART B   Laser-Based Packaging in Microelectronics and Photonics II

Conference Chairs

> **Friedrich G. Bachmann,** Rofin-Sinar Laser GmbH (Germany)
> **Jan J. Dubowski,** National Research Council (Canada)
> **Willem Hoving,** Philips Centre for Industrial Technology (Netherlands)
> **Kunihiko Washio,** NEC Corporation (Japan)

Program Committee

> **James H. Brannon,** IBM Corporation (USA)
> **J. Thomas Dickinson,** Washington State University (USA)
> **Ruediger Hack,** JDS Uniphase (USA)
> **Yongfeng Lu,** National University of Singapore (Singapore)
> **Kurt Mann,** Haas-Laser GmbH (Germany)
> **Isamu Miyamoto,** Osaka University (Japan)
> **Andreas Ostendorf,** Lazer Zentrum Hannover e.V. (Germany)
> **Manfred Rahe,** Lambda Physik AG (Germany)
> **B. Richerzhagen,** Synova SA (Switzerland)
> **Hans-Peter Schwob,** Lasag Industrial Lasers (Switzerland)
> **Xianfan Xu,** Purdue University (USA)

Session Chairs

> 14   Reviews and Laser Joining
>   **Jan J. Dubowski,** National Research Council (Canada)
>
> 15   Welding
>   **J. Thomas Dickinson,** Washington State University (USA)
>
> 16   Drilling and Cutting
>   **Willem Hoving,** Philips Centre for Industrial Technology (Netherlands)
>
> 17   Structuring
>   **Andreas Ostendorf,** Laser Zentrum Hannover e.V. (Germany)

PART C   Synthesis and Photonics of Nanoscale Materials

Conference Chairs

David B. Geohegan, Oak Ridge National Laboratory (USA)
Frank Träger, Universität Kassel (Germany)
Kouichi Murakami, University of Tsukuba (Japan)

Program Committee

Naoki Kishimoto, Naval Research Institute for Metals (Japan)
Hedi M. Mattoussi, Naval Research Laboratory (USA)
Hiroshi Yokoyama, Electrotechnical Laboratory (Japan)

Session Chairs

18   Synthesis and Photonics of Nanoscale Materials I
David B. Geohegan, Oak Ridge National Laboratory (USA)
Frank Träger, Universität Kassel (Germany)
Kouichi Murakami, University of Tsukuba (Japan)

19   Synthesis and Photonics of Nanoscale Materials II
David B. Geohegan, Oak Ridge National Laboratory (USA)
Frank Träger, Universität Kassel (Germany)
Kouichi Murakami, University of Tsukuba (Japan)

Introduction

Laser processing of materials, once largely curiosity driven, is now an established technology for micromachining, thin film synthesis, device packaging, rapid prototyping, and even nanoscale synthesis and processing of materials. The main driving force behind these developments is the seemingly limitless adaptability of lasers in providing unique material processing solutions, manufacturing of otherwise unattainable devices and structures, and the implementation of cost-effective solutions to complex manufacturing processes. The use of lasers for manufacturing microelectronic, optoelectronic, and MEMS devices is now becoming an established enabling technology; meanwhile, applications to nanotechnology are rapidly evolving.

These proceedings on Photon Processing in Microelectronics and Photonics II consist of papers presented at three conferences:

A. Laser Applications in Microelectronics and Optoelectronic Manufacturing VIII (LAMOM-VIII)
B. Laser-Based Packaging in Microelectronics and Photonics II (LPMP-II)
C. Synthesis and Photonics of Nanoscale Materials (SPNM)

These conferences were held 27–29 January (LAMOM-VIII) and 30 January (LPMP-II and SPNM) as part of LASE 2003 at Photonics West in San Jose, California, USA.

The LAMOM conference series was established in 1995 with the aim of providing a forum for discussion of both the fundamental aspects of laser materials processing and the practical applications of lasers in the manufacturing process of microelectronic, optoelectronic, and microsystem devices. The success of this conference is evident by the growing number of participants. The LAMOM conference has become a central meeting for members of the laser-materials processing community, where participants gather to share their latest findings.

LAMOM-VIII comprised 12 oral sessions plus a poster session which included papers on fundamental processes, lasers and techniques, pulsed laser deposition, laser microengineering, femtosecond laser processing, laser nanoengineering, laser-engineered photonic and semiconductor structures, direct-write processing, and laser microstructuring. Over 60 oral and poster papers including 16 invited papers were presented from the USA, Japan, Germany, Canada, the UK, Switzerland, Singapore, Russia, and Romania.

The LPMP conference series was established in 2002 in order to address the emergence of lasers as increasingly important tools for helping to overcome the limitations of conventional technologies for micropackaging applications. The aim of this conference is to bring together researchers and engineers working on all aspects of laser-based packaging of microelectronics and photonics devices. LPMP-II comprised four oral sessions on laser joining, welding, structuring, drilling,

and cutting. Over 15 papers including eight invited papers were presented from the USA, Germany, the Netherlands, Switzerland, Russia, Belgium, and the UK.

SPNM was established in order to address the many opportunities that laser-solid interactions offer for developments in the fields of nanotechnology and nanoscience. SPNM comprised two oral sessions covering the area of synthesis and photonics of nanoscale materials. Over 12 papers were presented from the USA, Canada, Japan, and Germany.

We would like to thank the members of the program committee, the invited speakers, and presenters of contributed papers, and all those who attended for their contribution to the success of LAMOM-VIII, LPMP-II, and SPNM. We also thank the SPIE technical personnel for helping in organizing this conference.

Alberto Piqué

Synergy between femtosecond science and technology

N. Bloembergen

Optical Sciences Center, University of Arizona, Tucson, AZ USA 85721

ABSTRACT

The development of lasers and of femtosecond laser pulses provides many examples, how science and technology mutually reinforce each other. A brief historical overview is presented of this synergy between curiosity-driven and goal-oriented research in this field of optics, which supports the current activity in pulsed laser-materials interactions.
Key words: Lasers, nonlinear optics, femtosecond pulses.

1. INTRODUCTION

Many scientists and engineers and some social scientists and politicians are aware of the close connection necessary for progress in science and engineering. Nevertheless a considerable separation between pure academic or ivory tower science and engineering school activities is often prevalent. I remember from my student days that an important distinction was make between "pure" and "applied" physics. The latter was obviously less pure, or even impure. Personally I have always found the interaction between academic science and industrial applications fascinating, but I remember that many of my colleagues in physics expressed surprise, when more than half a century ago, I accepted a tenured position in the Division of Engineering and Applied Physics at Harvard University, rather than join a "pure" physics department. I have had the good fortune that my major two interests in science, in magnetic resonance and in quantum opto-electronics respectively, have both been closely associated with important industrial developments. Research in magnetic resonance spectroscopy has led to major applications in chemistry and to magnetic resonance imaging (MRI), which has become a universal tool in medical diagnostics. One of the 2002 Nobel Paureates in chemistry, Kurt Wuethrich, received the award for the application of NMR in determining the structure of complex proteins. He undoubtedly considered his work as curiosity-driven science, while from the standpoint of a physicist it maybe described as a goal-oriented application of magnetic resonance spectroscopy. Similarly the development of MRI has led to new medical research and understanding. It is my expectation that eventually MRI will be honored by the award of a Nobel Prize in physiology and medicine.

The historical paradigm in optics about progress in science, made possible by advancing technology, is Galileo's telescope. He was familiar with lens grinding techniques, developed in Italy and in the Netherlands. In 1608 a Dutchman, Hans Lippershey, constructed a telescope with a magnification of three and took out a patent. Galileo improved the technology and constructed a telescope with a magnification of forty. In 1610 he published his astronomical observations in a book Siderius Nuntius. He observed four moons of Jupiter, the rings of Saturn, the phases of Venus, the mountains and valleys of the moon. He realized that his findings supported the heliocentric model of Copernicus. The Roman Catholic Church remained firmly committed to the Aristotelian geocentric model. Galileo presented a comparison between the two models in a hypothetical dialogue form, but it was clear, which model he favored. The Inquisition in Rome condemned Galileo in 1632, forced him to recant the heliocentric model and to spend the remaining years under house arrest in Tuscany. Galileo died in 1642 at the age of 78. The Vatican admitted that the Inquisition had erred only as recently as 1992.

Lens grinding technology not only opened up the field of astronomy in the seventeenth century by the development of telescopes, but also the science of microbiology by means of microscopes. Van Leeuwenhoek used a small single lens of very small focal length to obtain a magnification of more than fifty. His samples were manipulated by a fine screw in the small field of view. Van Leeuwenhoek never disclosed how he produced his lenslets, but he published his numerous observations of microscopic organisms in an extended series of letters to the Royal Society of London.

2. BACKGROUND OF LASER SCIENCE AND TECHNOLOGY

During the 19th century and the first half of the 20th century optical spectroscopy was highly developed. Powerful progress in radio-and microwave-technology before and during World War II stimulated the emergence of radiofrequency and microwave spectroscopy. These new scientific studies led in turn to new technologies of masers and lasers. Maser is an acronym standing for microwave amplification by stimulated emission of radiation. This concept was first demonstrated by J. P. Gordon, H. J. Zeiger and C. H. Townes in 1954. They used a molecular beam of ammonia molecules. With an appropriate electrode configuration the NH_3 molecules in the upper state of the inversion doublet could be separated and focused into a microwave cavity tuned to the doublet resonance, where the NH_3 molecule returned to the lower energy state of the doublet. Although this instrument was not used in practical applications, the atomic hydrogen maser based on the separation of hydrogen atoms in the upper state of the hyperfine doublet of atomic hydrogen, plays an important role as a frequency standard. The first hydrogen maser was built by D. Kleppner and N. F. Ramsey around 1960.

Further advancement proceeded not via molecular beam techniques, but through processes in condensed matter and in gaseous plasmas. Nuclear Magnetic Resonance (NMR) radio-spectroscopy and electronic paramagnetic resonance microwave spectroscopy also evolved rapidly after World War II. The phenomenon of negative absorption or amplification by stimulated emission of radiation was first demonstrated in NMR. In a two-level (spin I=1/2) system the inversion of population can be obtained in a transient fashion, during times shorter than the spin-lattice relaxation time, by three methods:
1) Adiabatic Rapid Passage
2) Instantaneous reversal of a strong external magnetic field
3) A 180° of pulse.

Following adiabatic rapid passage negative absorption was observed by F. Bloch, W. W. Hansen and M. Packard in 1946 on subsequent passage through resonance. The significance of this observation and its relationship to possible maser action remained unrecognized. R. V. Pound and E. M. Purcell achieved inversion of nuclear spin level populations in 1950 in a LiF crystal by switching the direction of external field of a millitesla in a microsecond. The absolute value of this field is larger than the internal or local magnetic field and the time interval of its directional change is shorter than the spin-spin relaxation time T_2. E. M. Purcell, R. V. Pound and N. F. Ramsey recognized the significance of population inversion and introduced the concept of negative temperature. At the relatively low radio frequency the concept of an amplifier was, however, not practical and not pursued further. The method of the so-called π-pulse, inverting the population in a two-level system, was introduced by H. Y. Carr and E. M. Purcell in 1954, based on the NMR pulse experiments, introduced by E. L. Hahn in 1950. J. Combrisson, A. Honig and C. H. Townes obtained transient maser action by using the electron spin resonance of a donor level in silicon in 1956. This did not result in a practical device.

In 1956 N. Bloembergen showed how to obtain continuous maser action by pumping and saturating a transition between two non-adjacent energy levels in a multilevel electronic spin system (S > ½). He proposed the Gd^{3+} resonance with S=7/2 in Gadolinium ethyl sulphate and maser action in this crystal was demonstrated in the same year by H. E. Scovil, G. Feher and H. Seidel. The Cr^{3+} resonances with S=3/2 in ruby were most often used in maser microwave amplifiers operating at liquid helium temperature. A noise temperature of 2° K has been achieved. These low-noise microwave amplifiers were used in the distant early warning (D E W line) radar defense in Alaska and Canada. They were also used in receivers in the Telstar and Satellite transatlantic microwave communication systems around 1960. The ruby maser was also an essential element in the parabolic microwave horn antenna, with which Penzias and Wilson discovered the 3° K microwave background radiation, the remnant of Big Bang. Microwave maser technology could not economically compete, however, with the less cumbersome technology of parametric semiconductor devices.

A. L. Schawlow and C. H. Townes proposed in 1958 the extension of these maser techniques to optical frequencies. The microwave cavity was to be replaced by a Fabry-Perot resonator. T. H. Maiman demonstrated the first operating laser in 1960. He used the same material, ruby, which was used in most masers. The optical levels of the Cr^{3+} ions were pumped by the optical radiation from a high pressure xenon discharge lamp. Laser radiation was emitted from the fluorescent R-levels at 694.3 nm. Thus, the academic investigations in microwave and optical spectroscopy spawned laser technology. The scope of this presentation does not permit to pursue the many types of lasers with a variety of pumping schemes which soon evolved. Instead the focus of the next section will be on the development of short pulse generators.

3. Development of Femtosecond Pulse Generators

At a conference in March 1961, less than one year after the realization of the first laser, R. W. Hellwarth discussed the idea of Q-switching to obtain short powerful laser pulses. He observed that "the generation of very intense and short bursts of energy by the sudden application of high regeneration feedback to a system in an excited state had been useful in several fields". He proposed to use a Kerr-cell type shutter with a reaction time of less than one nanosecond in a laser cavity. In the fall of 1961 he demonstrated Q-switching of a ruby laser, obtaining reproducible pulses of about ten nanosecond duration. In 1962 the use of a suddenly applied electric field to a Kerr cell with liquid nitrobenzene led serendipitously to the discovery of the stimulated Raman Effect. In these early years other laboratories used rapidly spinning mirrors, mounted on an air-driven turbine used in dentist drills, to obtain Q-switching. Careful mode control was not yet a priority in those early days. The Q-switched ruby laser stimulated the experimental and theoretical developments in nonlinear optics, as a novel subfield.

The next important step toward the attainment of shorter pulses was the use of a saturable dye absorber inside the laser cavity. H. W. Mockler and R. J. Collins used this technique of passive mode locking to obtain pulses of one nanosecond duration from a ruby laser. A. J. DeMaria and coworkers applied the same technique with a saturable dye in a neodymium-glass laser with a broad-band gain response. They opened up the picosecond regime by obtaining pulses shorter than one nanosecond. They refer to the technology of microwave pulse generation developed earlier by C. C. Cutler, who introduced the word "expander" for a device that has less attenuation at higher power levels. Saturable absorption is a nonlinear effect, in which the imaginary part of the index of refraction decreases with increasing intensity.

The femtosecond regime was opened up by E. P. Ippen and C. V. Shank, who used a ring laser with counter-propagating pulses with a dye gain medium and a saturable dye absorber. When the two pulses pass at the same time through a very thin jet of the absorbing dye, maximum gain is obtained. The theory of pulse formation in this case was further developed by G. H. C. New. In the femtosecond regime group velocity dispersion (GVD) produces frequency chirping. Shorter pulses can be obtained by recompressing the chirped spectrum. This can be achieved by introducing glass prism configurations inside the optical cavity, which provide different optical path lengths for different wave lengths. Thus, pulses are short as 6 fs. were obtained by R. L. Fork, et al. in 1987.

In 1991 W. Sibbett and coworkers reported spontaneous mode locking in a Ti-sapphire laser. Further experimentation and analysis revealed that incipient self-focusing occurs at high power levels. In combination with an optical aperture, this self-focusing produces a higher gain at higher power levels, as a larger fraction of the light pulse gets through the aperture. The intrinsic time constant of this dispersive Kerr effect is extremely fast, on the order of frequency detuning or of the very broad band width of the Ti-sapphire gain medium. The femtosecond Ti-sapphire lasers are much simpler to operate than the previously used dye laser systems. With compensation of chirping by GVD, H. C. Kapteyn and M. M. Murnane and coworkers have reported pulses of 4 fs. duration.

In addition to the time variation of the amplitude, or light intensity, the phase variations are also important. The combination of amplitude and phase variations leads to a complete description of the electromagnetic field during the pulse. Two experimental methods to determine the phase variations are denoted by FROG and SPIDER. These acronyms stand respectively for Frequency Resolved Optical Gating and Spectral Phase Interferometry for Direct Electric Field Reconstruction. In the FROG technique, introduced by R. Trebino and D. J. Kane, the incident pulse is split into two parts with a variable time delay. The second harmonic generated by the combination of these two pulses in a very thin nonlinear crystal platelet is analyzed spectroscopically as a function of the time delay. In the SPIDER method, introduced by C. Iaconis and I. A. Walmsley, two replicas of the input pulse with a time delay between them, are each up-converted with a longer chirped pulse obtained from the same input pulse by a dispersive delay line. The spectral interferogram of the up-converted signal has a wavelength-dependant fringe spacing. This spacing, not the spectral amplitude, is used for the reconstruction of the phase. The SPIDER method is much less demanding on the bandwidth of the up-conversion process.

These femtosecond technologies have in turn spawned new fields of science. The 1999 Nobel Prize in chemistry was awarded to A. H. Zewail for establishing the field of femtochemistry. A paradigm example is the time-resolved study of the photo-dissociation of sodium iodide molecules. A. H. Zewail and coworkers also demonstrated the time evolution of

vibrational and rotational wave packets in optically excited I_2 molecules. An early example of femtobiology is the cis-transformation of retinal, induced by light absorption. C. V. Shank et al. showed that this process, which was the first step in the perception of vision, takes place in less than 100 fs.

Materials science and solid state physics have also been advanced by femtosecond technology. Rapid electronic phase transitions have been induced in semiconductor materials on short time scales before the atoms can move significantly from their initial lattice positions. The light pulse induces a dense hot electron-hole plasma before significant energy transfer to the crystalline lattice occurs. The band-gap of Ga As, Si and Ge may decrease to zero, when more than about ten percent of the valence electrons are promoted to the conduction band. For such high degree of electronic excitation, the web of tetrahedral covalent electronic bonds unravels on a sub-picosecond time scale.

The two-photon photo-electric emission (2 PPE) has elucidated this emission process. A clean metallic crystal surface is illuminated by a femtosecond ultraviolet pulse, with a photon energy just below the work function. This pulse cannot produce photo-electric emission. It produces an electronic wave packet in front of the surface, with a small tail still inside the metal. An infrared pulse can cause emission of this highly excited wave packet. By variation of the time delay between the UV and IR pulse, the evolution of this electronic wave packet can be probed. The oscillations in the emission signal correspond to the frequency separations between the Rydberg states, describing the motion of the electron normal to the metallic surface.

The phase variation during the pulse may be optimized to preferentially obtain the generation of a particular high harmonic, e.g. the 201st harmonic, in a noble gas, or to obtain a particular chemical reaction channel of dissociation or ionization. Efforts are also under way to obtain short bursts of continuum x-rays from a localized hot dense plasma, created by a focused femtosecond pulse. Thus, the regime of sub-femtosecond or attosecond pulses is opening up.

The concentration of pulse energy in shorter pulses leads to higher peak power levels. A limitation is set by the onset of self focusing and laser-induced electric breakdown in the laser material. Consider an unfocused laser pulse of 1 cm^2 cross section with one millijoule of energy of 10 fs. duration. The power flux density is 10^8 watts/cm^2, close to the breakdown limit.

The technique of chirped pulsed amplification (CPA), introduced by D. Strickland and G. Mourou permit the attainment of higher power flux densities. The pulse is frequency-chirped and stretched in time by a set of anti-parallel gratings. This stretched pulse with lower peak intensity is amplified, and then recompressed by a matched combination grating. An increase by four or five orders of maximum intensity can thus obtained corresponding to 10^{12} or 10^{13} watts/cm^2. When this pulse is subsequently focused to an area of 10^{-8} cm^2, or the wavelength squared, power levels of 10^{20} or 10^{21} watts/cm^2 are obtainable. At about 10^{16} watts/cm^2 the light field amplitude equals the Coulomb field, responsible for the binding of a valence electron in a Bohr orbit. At 10^{18} watts/cm^2 the quiver energy of the electron due to the oscillating motion in the visible field is relativistic. The electron accelerated to about 1 Mev in a quarter of a light cycle. A new physics regime in the relativistic plasma region is attained.

Turning back to lower intensity levels, femtosecond pulses are enabling new technological applications. In medicine and surgery tissue may ablated locally without undesirable damage to surrounding tissue due to heating. The sculpting of the cornea to correct vision, the LASIK procedure, is widely applied. Femtosecond pulses are also used to drill a hole in an eye membrane, which sometimes becomes opaque following otherwise successful cataract surgery.

A train of 100 fs. femtosecond pulse, obtainable from a simple table top Ti-sapphire laser, may contain 10 nano joules per pulse, with a repetition rate of 10^4 Hertz, corresponding to an average power of one milliwatt. When such a pulse train is focused with a microscope objective just below the surface of a transparent medium to an area about 10^{-8} cm^2, a peak power flux density of 10^{13} watts/cm^2 is achievable. In the focal area a hot plasma is created for a brief time interval. Following the pulse, the medium is restored on a time scale of about 10 ps. The resolidified material contains some bound centers in excited electronic configurations, leading to a localized increase in the index of refraction. By moving a transparent sample through the focal point of the femtosecond pulse train, C. Schaffer, E. Mazur and others have demonstrated that optical wave guide structures may be written in transparent materials, such as glass, silica, quartz and sapphire. Extension to silicon and other semiconductors with infrared pulses appears possible.

The current activity in femtosecond laser-material interaction is well represented by the presentations at this conference. This historical introduction illustrates the sequences between science and technology which has made these developments possible. In my opinion, similar synergisms can be traced in most other fields of endeavor. Radical changes in technology often depend on the introduction of scientific results, which were obtained without consideration of particular applications. Novel and unforeseen combinations can lead to new technologies. Conversely, new technologies often make scientific progress possible.

Technological progress cannot always be predicted and organized from the top down. While gradual improvement can be planned, revolutionary changes require some new scientific input, almost by definition. Young investigators should be encouraged to tackle new topics without regard to short term bottom line pay-off. A strict separation of "pure" and "applied," or "curiosity-driven" and "goal-oriented" research is not helpful. The combination is more than the sum of the separate categories.

4. References

This cursory overview is based on the following seven review articles, which in turn contain a large number of references to the original research literature.

1. N. Bloembergen, "Solid State Masers" in Progress in Low Temperature Physics, Vol. III, edited by C. J. Gorter, North Holland, Amsterdam 1961, pp 396-429.

2. N. Bloembergen, "Nonlinear Optics and Spectroscopy", Rev. Mod. Phys. 54, pp 685-695, 1982.

3. N. Bloembergen, "From Nanosecond to Femtosecond Science", Rev. Mod. Phys. 71, pp 283-287, 1999.

4. N. Bloembergen, "Nonlinear Optics: Past, Present and Future", IEEE J. on Selected Topics in Quantum Electronics, 6, pp 876-880, 2000.

5. G. A. Mourou, C. P. J. Barty and M. D. Perry, "Ultrahigh-intensity Lasers", Physics Today 51, pp 22-28, Jan. 1998.

6. A. H. Zewail, "Femtochemistry", Les Prix Nobel 1999, pp 110-203, Almquist, Wiksell Int., Stockholm, 2000.

7. G. Steinmeyer, L. Gallman, F. W. Helbing and U. Keller, "Trends in Femtosecond Lasers and Spectroscopy", C. R. Acad. Sci., Paris, Série IV, pp 1389-1406, 2001.

Surface analysis by laser induced desorption time-of-flight mass spectrometry

S. D. Allen [a,b,c]*, J. M. Fu [b], Y. Surapaneni [c], A. J. Hopkins [b], P. S. Davis [a,b]

[a] Department of Chemistry and Physics, Arkansas State University,
State University, Arkansas 72467

[b] Department of Chemistry and Biochemistry, Florida State University,
Tallahassee, Florida 32306

[c] Department Electrical and Computer Engineering, FAMU/FSU
College of Engineering, Tallahassee, Florida 32310

ABSTRACT

We have built and tested a laser induced desorption (LID), electron impact ionization, time-of-flight (TOF) mass spectrometer (MS) designed to nondestructively identify and measure adsorbed contaminants on critical surfaces for the microelectronics and optics industries. The LID-TOFMS combines the capability of a TOF mass spectrometer to measure all the desorbed molecules from a single laser shot with an infrared Er:YAG laser (2.94 micron), which is not strongly absorbed by many transparent optical materials but is strongly absorbed by water, the most common adsorbed surface contaminant, to yield surface composition as a function of position on the sample. The LID-TOFMS was calibrated using an oxalic acid film on a polished stainless steel plate, which also contained adsorbed water. Contaminants on CaF_2 surfaces measured by LID-TOFMS include water and hydrocarbons. Desorbed molecules decrease with increasing irradiations at a fixed laser fluence, suggesting that the surface is being cleaned.

Keywords: laser induced desorption; time-of-flight mass spectrometer; surface analysis; contaminant

1. INTRODUCTION

Analysis of adsorbed species on surfaces is increasingly important in many technological applications.[1-3] In the electronics industry, for example, even small amount of surface contaminations can result in reduced device yield.[4] Among the many surface analytical techniques, mass spectrometry (MS) has a unique advantage in that it allows identification and quantification of all elements, isotopes, and molecular species and has become an excellent method for surface analysis.

The first step in MS surface analysis is desorption of the species from surfaces of interest, which can be achieved by several methods. Thermal desorption (TD), in which a sample is heated to drive off molecular species, is a highly developed method that has provided significant amount of information on the chemistry of adsorbate systems.[5] The limitation is that surface reactions can become competitive with desorption as the surface temperature increases and can alter the identity of molecular species before they desorb. Laser induced desorption (LID) generally uses a short pulse laser (from several hundred femtoseconds to nanoseconds), thus desorption is completed before competing surface reactions occur.[6] Typically, the peak temperature on the surface is reached within the laser pulse and the energy is confined at the surface near the point of irradiance.[7] For a 100 ns pulsed laser, the thermal diffusion length during the laser pulse is on the order of several microns on metal substrates (even less for thermal insulators and semiconductors), which is much smaller than the diameter of the laser beam (100s of microns). As a result, LID allows the surface to be probed at specific positions without modifying other areas of the sample, which is very useful in mapping the composition distribution on the surface[2,8] or monitoring adsorbate concentration at different times.[9,10] Other pulsed probe beams, such as ions, electrons, or fast atoms can also be employed for similar surface desorption analysis.[11]

In order to obtain a representative mass spectrum for a multi-component sample less selective ionization methods are required. Electron ionization (EI), the method used in this work, is useful for identifying unknown adsorbates because almost all molecules can be ionized by EI and the EI fragmentation mechanisms are well understood. Although EI has often been used in quadrupole and magnetic sector mass analyzer, its application in time-of-flight mass spectrometry (TOFMS) has not been well developed. The problem was that EI could not produce a measurable quantity of ions in the few nanoseconds, which are required for proper time of flight measurements; this can be solved by combining a pulsed extraction field[12,13] with LID. There are some reports[2,3] that laser multiphoton ionization (MPI) has been used to ionize desorbed neutrals; however, ionization yield and degree of fragmentation were sensitive not only to the wavelength used but also to the laser intensity. Single-photon ionization,[14,15] where vacuum ultraviolet (VUV) light at 118 nm (the photo energy is 10.5eV) was chosen to be just above the ionization energy of most organic molecules has also been used, but the VUV beam path must be constructed in vacuum.

TOFMS was chosen in this work because it can measure all of the desorbed molecules from a single laser shot. Compared with another mass spectrometer with this capability, the Fourier transform mass spectrometer (FTMS), TOFMS is less expensive and simpler to construct. An infrared laser of 2.94 μm with approximately a 100 ns pulse (full width at half maximum, FWHM) was interfaced with the TOFMS because it is strongly absorbed by water, the most common adsorbed surface contaminant, but not by many transparent optical materials, and can produce adsorbate maps of surface composition as a function of position on the sample with submillimeter resolution.

2. EXPERIMENTAL

The LID-EI-TOFMS instrument consists of an ultrahigh vacuum (UHV) system (Perkin-Elmer, model TNB-X), TOF-MS assembly (R.M. Jordan), X, Y, Z and Θ manipulator (Vacuum Generators, model HPT-RX) and Q-Switched Er:YAG laser (LaserSight Technologies, Inc, formerly Schwartz ElectroOptics Inc., Orlando, FL) (see Fig. 1). The sample was mounted on a holder and loaded through a sample transfer rod onto the manipulator for analysis.
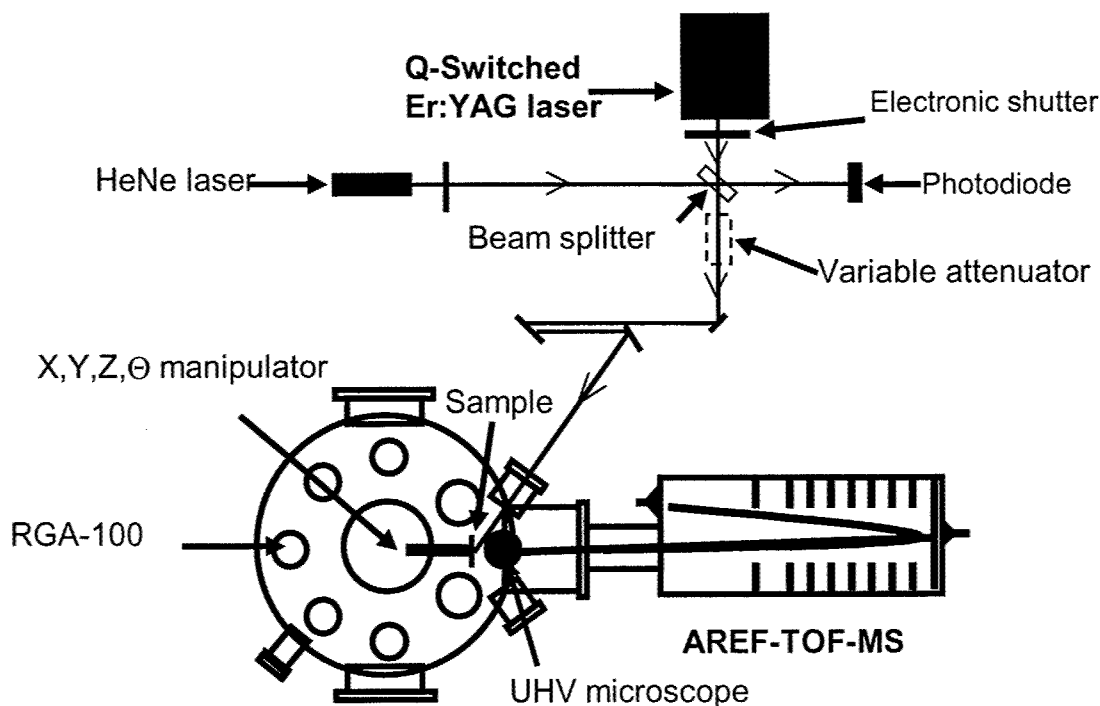
Fig. 1 Schematic drawing of the LID-EI-TOFMS system.

2.1 UHV system

The pumping system was divided into two stages, starting with a turbo pump (60 l/s) backed by a rotary vane pump (1.5 m^3/h). Once the system pressure dropped below 1×10^{-5} Torr, the ion pump (220 L/s) was turned on and the system pressure was brought to the mid 10^{-9} Torr range. A titanium sublimation pump was added to speed up the pumping process. The system was then baked at 120 °C for 30 hours. The pressure in the UHV chamber was 1×10^{-10} Torr after bake out and maintained 5×10^{-10} Torr after loading and unloading the samples repeatedly. A quadrupole mass analyzer (Stanford Research Systems, model RGA-100) was installed to monitor the background gases in the UHV system. Only H_2, H_2O, N_2 and CO_2 were detected.

2.2 TOFMS assembly

The basic design of TOFMS can be found in previous work.[15,18] Here the focus is on design of the ion source. As shown in Fig.2 (a), the sample was placed in front of and in close proximity to the repeller plate (A_1). The center of the repeller plate is open to let the laser beam pass through and has a row of fine wires (platinum 90%, iridium 10%) stretched across the opening to maintain a uniform extraction field. The acceleration plate (A_2) is partially cut at the edges to allow passage of the laser beam. The separation of the sample holder and the repeller plate provides freedom to translate the sample relative to the TOFMS and, therefore, map adsorbed species on the sample surface. The electron beam to ionize the desorbed neutral species is produced by a tungsten filament underneath the ionization region and was focused and collimated to 2 mm × 12 mm beam at the point where it intersects perpendicularly with the desorbed molecular fluence. A set of deflection plates placed between the beam source and the ionization region controls the electron beam. The electron beam is injected between the plates only when the same voltage was applied to the two deflection plates. Otherwise, the electron beam will be deflected to the plate with higher voltage and does not reach the ionization region. The electron energy, emission current and duration of the ionization beam can be adjusted separately. In the current work, the optimum parameters for ionization are found to be 60 eV, 0.5 mA and 7 μs, respectively.
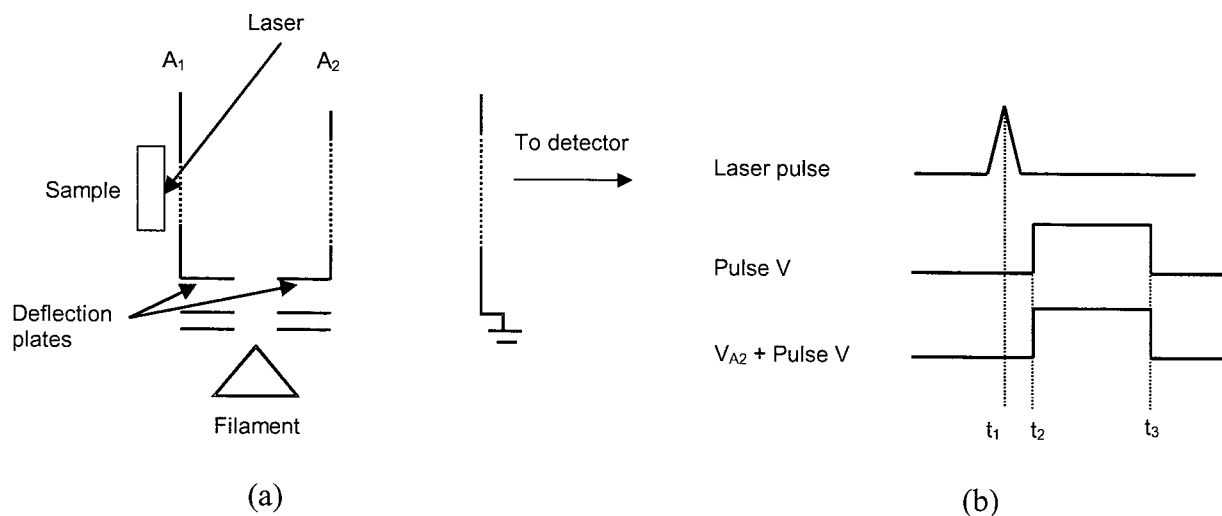
Fig. 2 (a) Configuration of the ion source. (b) Time sequence in operation of the system.

Ionization should take place in a field-free region to provide well-defined impact energy and to allow for proper space focusing.[12] In addition, a pulsed extraction field is required for proper time of flight measurements. To minimize the experimental complexity, a remote pulser, with an output voltage of (V_{A2} + Pulse V), was connected to plate A_2 to deliver a voltage pulse that can be used to extract bursts of ions and to gate or deflect the electron beam. The voltage pulse can be varied in magnitude, duration and delay time. The magnitude of the pulse voltage was set to (V_{A1} - V_{A2}), where V_{A1} and V_{A2} are 1200volts and 800volts respectively. When the pulse is turned on (at t_2 in Fig. 2 (b)), the voltage on plate A_2 equalizes to V_{A1} and remains at this voltage for the same length of time as the pulse duration. During this time, ionization occurs. After this time, i.e., at t_3 in Fig. 2 (b), the voltage on plate A_2 returns to its set value so that ions

can be extracted. The rise and fall time of the voltage pulse is less than 10 ns. In this paper, it was found that optimum signals are obtained when the delay between t_1 and t_2 are 1 μs for small molecules and 6 μs for fullerene.

2.3 Laser source

The desorption laser source was a Q-switched Er:YAG laser operated at a 2 Hz repetition rate with a laser pulse width of approximately 100 ns FWHM. The laser wavelength was 2.94 μm and the maximum output energy was 20±1 mJ/pulse. An intra-cavity aperture was installed for TEM_{00} mode operation. The angle of incidence of the desorption laser on the sample was 60° and the laser was focused on the sample by a spherical lens (f = 150 mm); the spot size was ~360 μm ($D_{1/e}$). Positioning of the laser beam on the 12 mm diameter sample was aided by a He-Ne laser collinear with the desorption laser and an ultra-high vacuum (UHV) compatible long working distance microscope. An electronic shutter was placed in the beam path to pick out single laser pulses from the low frequency Q-switched train (the time interval between two consecutive pulses was >3 s) to eliminate residual effect from the previous pulse.[19]

The timing between the firing of laser and ionization of the neutral species was synchronized to obtain optimum signal. TOFMS data was recorded at a time resolution of 10 ns by a Wavepro 940 digital oscilloscope (LeCroy).

3. CALIBRATION OF SYSTEM

The time-of-flight spectrum recorded from the oscilloscope is a spectrum of voltages vs. time. Calibration of the system is required to convert the time scale to a mass scale. The LID-EI-TOFMS was first calibrated using the main chamber background gases. The system pressure was increased and stabilized to ~10^{-8} Torr by partially closing the gate valve between the ion pump and the chamber. Averages of 50 single TOFMS scans showed consistent ion peaks of H_2, H_2O, N_2 and CO_2, as measured by the RGA-100.

Because the desorbed molecules have an initial velocity, the calibration may be slightly different for background gas and LID molecules. Therefore, calibration of the system by LID molecules was performed. Different adsorbates, such as water, oxalic acid, and fullerene on stainless steel surfaces were tested and the LID mass spectra were shown in Fig. 3. These calibration systems were also used to optimize the timing and duration of the EI extraction pulse.

Fig. 3 (a) shows a mass spectrum of clean stainless steel surface where water is the main adsorbed species. Mechanically polished 304 stainless steel was tested after being supersonically cleaned in isopropanol. The most prominent peak was the water ion H_2O^+ (m/z=18); OH^+ and O^+ (m/z=17 and 16) peaks were also from water. Other low intensity peaks, such as m/z=27, 31, 43 and 45, could be fragments from isopropanol molecules, which can be assigned to $C_2H_3^+$, CH_2OH^+, $(CH_3)_2CH^+$ and CH_3CHOH^+. The observation of a high intensity water peak is consistent with the fact that stainless steel absorbs and traps water easily. No ablation ions from stainless steel, such as Fe or Ni, were detected, indicating that the laser desorption occurred without ablating the substrate. Under the same measurement conditions and laser energy, similar water ion intensities were obtained when scanning over the surface, which suggests that water is adsorbed relatively uniformly on stainless steel after cleaning, even under UHV conditions. By measuring the water ion intensities at different delay times, the time interval between the laser pulse (t_1) and the beginning of the extraction pulse (t_3) in Fig. 2(b), the maximum velocity distribution of desorbed water can be obtained. The change of water ion intensities with delay time is shown in Fig. 4. The maximum intensity was obtained at ~6 μs, corresponding to a velocity of 1250 m/s (the travel distance between the sample surface and the center of the ionization region was 7.5 mm). The peak of the kinetic energy distribution of the desorbed water was calculated to be approximately 140 meV. This result is in general agreement with previous work by other research groups.[14,20] It also shows that the initial kinetic energy of the desorbed species is negligible compared with the total kinetic energy of ions in the TOF, which is 1000 eV in this experiment. The peak surface temperature can be estimated by equation (1),[21] if only translational cooling is considered:

$$\frac{3}{2}k_B T = \frac{1}{2}mv^2 \qquad (1)$$

where k_B is the Boltzman constant, T is the surface temperature, m is the mass of molecule and v is the velocity. The calculated surface temperature is approximately 1100K, lower than the melting point of stainless steel, 1687K.
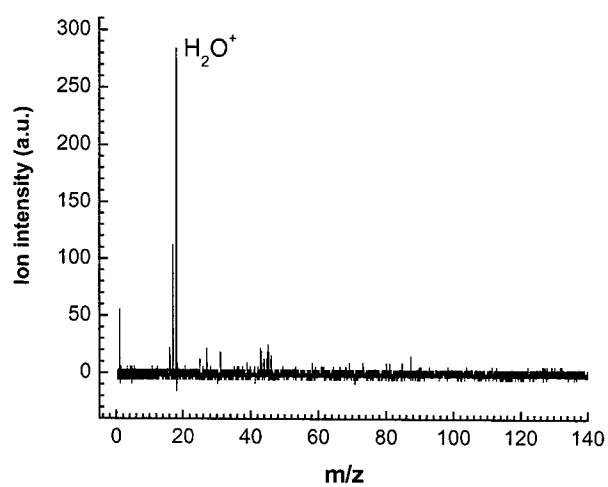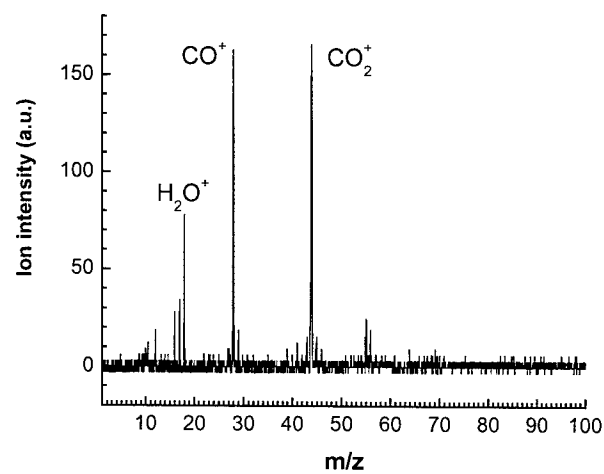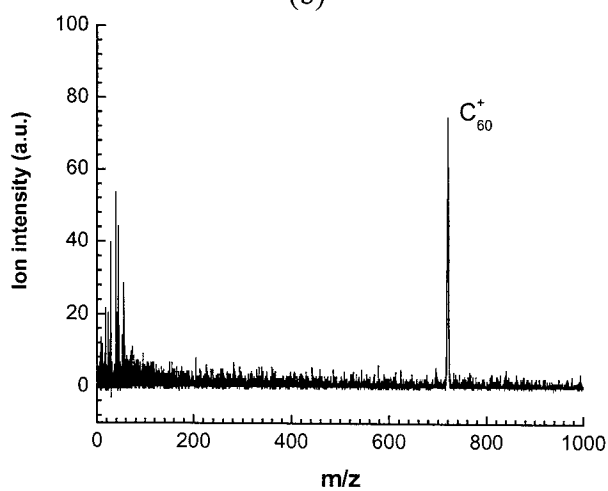
Fig. 3 Mass spectra of stainless steel surface analysis. (a) Clean stainless steel. The laser energy is 0.4 mJ. (b) Oxalic acid film on stainless steel. The laser energy is 0.4 mJ. (c) Fullerene film on stainless steel. The laser energy is 1.4 mJ.

Fig. 3 (b) shows a mass spectrum of an oxalic acid film on the polished stainless steel surface. The oxalic acid film was prepared by applying a dilute oxalic acid-isopropanol solution to the substrate. After the solvent evaporated, a visible uniform film was formed. The dominant peaks were CO^+ (m/z=28) and CO_2^+ (m/z=44). Both observed peaks are fragments; no molecular ions were detected. Water ions were also observed.

Fig. 3 (c) shows a mass spectrum of C_{60} measured by the LID-EI-TOFMS. The fullerene film was prepared by applying 36 μM C_{60}-toluene solution to the polished stainless steel surface. The laser energy for desorption was 1.4 mJ. The dominant peak consists of the molecular ions and no apparent fragments were seen. The stability is probably attributed to the many vibrational degrees of freedom of C_{60} molecular ions.[22] The peaks in the low mass region are probably from the solvent residue, i.e. hydrocarbons. This result indicates that our system has the capability of detecting a range of molecules from small (17 amu) to large (up to approximately 800 amu).
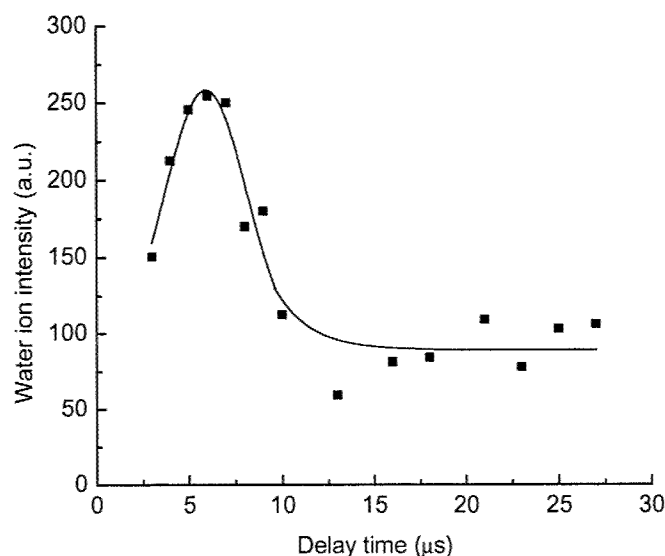
Fig. 4 Effect of delay time on water ion intensity during LID on stainless steel surface.

4. LID EXPERIMENTS ON CaF$_2$ SURFACES

The CaF$_2$ (100) samples measured in this work were obtained from St. Gobain/Bicron. They were mechanically polished and residue removal accomplished first with a soapy water rinse followed by a dry tissue wipe. The sample was then wiped clean with methanol and acetone (1:1) moistened tissue. The samples were examined under an optical microscope and no particles were seen on the surface. Prior to the LID experiments, the samples were stored in a vacuum desiccator.

It was reported[23] that surface contaminants, which were in part airborne adsorbates and in part impurities incorporated during polishing, had caused decreased transmission at DUV (deep ultra violet) wavelengths. The composition of surface contaminants was measured by LID TOFMS and the results shown in Fig. 5. Unlike water on the polished stainless steel surface, one can see that the concentration (represented by the peak value of the LID signals) and types of contaminants (represented by the mass of the ions) on the CaF$_2$ surface varied from site to site. For example, at site 1 the dominant peak is water ions H_2O^+ (m/z = 18) with only very low hydrocarbon ion peaks (m/z = 43, 44 and 45) observed. At site 2 the majority peaks are hydrocarbon ions $C_xH_y^+$ and oxygen-containing hydrocarbon ions, such as CH_2O^+ and $C_2H_4O^-$ (m/z = 30 and 44). However, it was impossible to identify the hydrocarbon composition due to the lack of molecular ions. The highest mass in spectrum (b) indicates hydrocarbon molecules containing at least 7 carbon atoms exist on CaF$_2$ surface. Water ions OH^+ and H_2O^+ (m/z = 17, 18) appeared at apparently lower concentrations than

the hydrocarbon ions at site 2. In spectrum (b), alkali ions Na^+ and K^+ were also found, which were probably from physical contact with human skin during sample handling.

A sequence of n laser pulses irradiated each site at a fixed laser fluence. As shown in Fig. 6, the ion intensity decreased with increasing number of laser pulses. The first pulse always gave the highest ion intensity. In most cases, no peak was seen after 5 pulses, suggesting that the surface contaminants were being removed and no readsorption occurred between consecutive laser pulses.
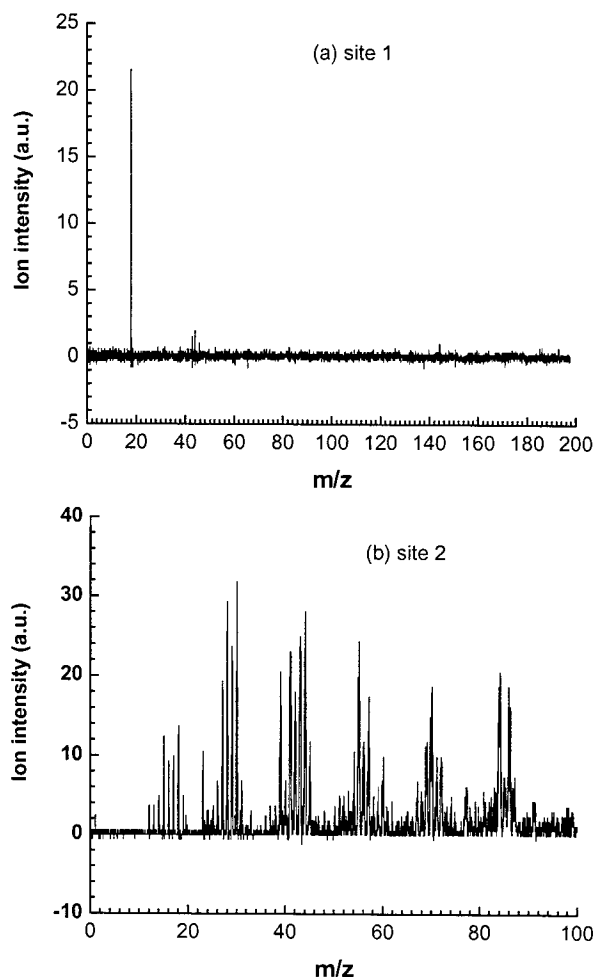
Fig. 5 Mass spectra of mechanically polished CaF_2 surface analysis. The two sites are randomly selected. The laser energy is 5.0 mJ.
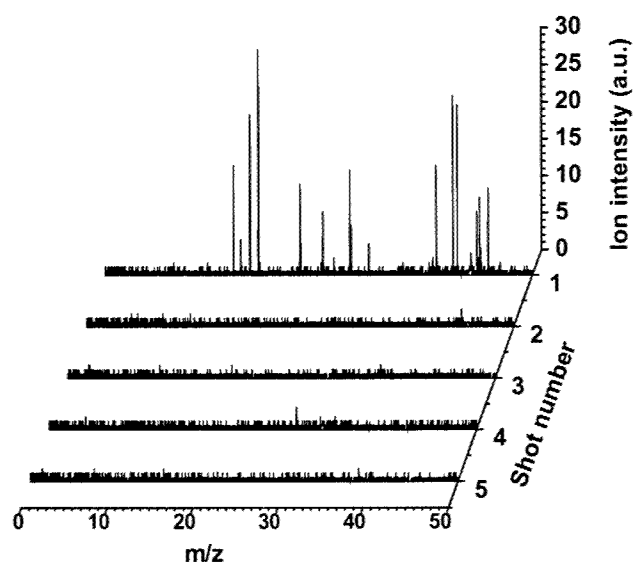
Fig. 6 LID TOF mass spectra of CaF_2 surface at different laser shots. The peak laser fluence is 5 J/cm^2. CaF_2 sample orientation is (100).

5. CONCLUSIONS

We have demonstrated that LID TOFMS is a sensitive technique for measuring adsorbed molecular and ionic species on a wide variety of surfaces. This technique can be used to identify and map surface contamination on critical surfaces such as those found in high power laser optics, ultraviolet lithography and semiconductors.

References

*Permanent address: Vice Chancellor for Research and Academic Affairs, Arkansas State University, P.O. Box 179, State University, Arkansas 72467

1. A. Benninghoven, B. Hagenhoff, and E. Niehuis, " Surface MS: probing real-world samples", *Anal. Chem.* **65**, 630A-639A(1993).
2. M.S. de Vires, D.J. Elloway, H.R. Wendt, and H.E. Hunziker, "Photoionization mass spectrometer with a microscope laser desorption source", *Rev. Sci. Instrum.* **63**, 3321-3325(1992).
3. K.R. Lykke, P. Wurz, D.H. Parker, and M.J. Pellin, "Molecular analysis by ionization of laser-desorbed neutral species", *Appl. Optics* **32**, 857-866(1993).
4. J.M. Fu, A.J. Hopkins, Y. Surapaneni, and S.D. Allen, unpublished.
5. Y.D. Kim, J. Stultz, and D.W. Goodman, "Identification of defect sites on MgO(100) surfaces", *Langmuir*, **18**, 3999-4004(2002).
6. M.S. de Vires, H.E. Hunziker, and H.R. Wendt, "Analysis of organic molecules on surfaces: laser desorption spectroscopy", in *Laser and mass spectrometry*, Edited by D.M. Lubman, p383-401(Oxford University, New York, 1990).

7. D. P. Land, D.T.S. Wang, T.-L. Tai, M.G. Sherman, J.C. Hemminger, and R.T. McIver, Jr., "Postionization of laser-desorbed neutrals for the analysis of molecular adsorbates on surfaces", in *Laser and mass spectrometry*, Edited by D.M. Lubman, p157-178(Oxford University, New York, 1990).

8. M.R. Savina and K.R. Lykke, "Chemical imaging of surfaces with laser desorption mass spectrometry", *Trends Anal. Chem.* **16**, 242-252(1997).

9. R.B. Hall, "Pulsed-laser-induced desorption studies of the kinetics of surface reactions", *J. Phys. Chem.* **91**, 1007-1015(1987).

10. A.A. Deckert, J.L. Brand, C.H. Mark, C.H. Mak, B.G. Koehler, and S.M. George, "The decomposition of methanol on Ru(100) studied using laser induced thermal desorption", *J. Chem. Phys.* **87**, 1936-1947(1987).

11. C.H. Becker and K.T. Gillen, "Surface analysis by nonresonant multiphoton ionization of desorbed or sputtered species", *Anal. Chem.* **56**, 1671-1674(1984).

12. J.E. Pollard and R.B. Cohen, "Electron-impact ionization time-of-flight mass spectrometer for molecular beams", *Rev. Sci. Instrum.* **58**, 32-37(1987).

13. J.A. Syage, "Photodissociation and metastable decay of solvated cluster ions", *J. Chem. Phys.* **92**, 1804-1810(1990).

14. C.H. Becker, L.E. Jusinski and L.M. Moro, "Infrared laser induced desorption of neutral organic compounds from frozen aqueous solution followed by single-photon ionization", *Int. J. Mass Spectrom. Ion Proc.* **95**, R1-R4(1990).

15. R.J.J.M. Steenvoorden, T.L. Weeding, P.G. Kistemaker, and J.J. Boon, "Laser desorption and laser post-ionization time-of-flight mass spectrometry", in *Methods and mechanisms for producing ions from large molecules*, edited by K.G. Standing and W. Ens, p315-323(Plenum, New York, 1991).

16. S.M. George, "Laser-induced thermal desorption", in *Investigations of surface and interfaces*-Part A, edited by B.W. Rossiter and R.C. Baetzold, Chap. 7 (John Wiley & Sons, New York, 1986).

17. J.L. Brand and S.M. George, "Effects of laser pulse characteristics and thermal desorption parameters on laser induced thermal desorption", *Surf. Sci.* **167**, 341-362(1986).

18. D.M. Lubman and R.M. Jordan, "Design for improved resolution in a time-of-flight mass spectrometer using a supersonic beam and laser ionization source", *Rev. Sci. Instrum.* **56**, 373-376(1985).

19. S. Kano, S.C. Langford, and J.T. Dickinson, "Interaction of wide band gap single crystals with 248 nm excimer laser irradiation", *J. Appl. Phys.* **89**, 2950-2957(2001).

20. J.E. Hunt, K.R. Lykke and M.J. Pellin, "Laser desorption/photoionization time-of-flight mass spectrometry of polymer additives", in *Methods and mechanisms for producing ions from large molecules*, edited by K.G. Standing and W. Ens, p309-314 (Plenum, New York, 1991).

21. P. Williams and R.W. Nelson, "On the mechanism of volatilization of large biomolecules by pulsed laser ablation of frozen aqueous solutions", in *Methods and mechanisms for producing ions from large molecules*, edited by K.G. Standing and W. Ens, p265-273 (Plenum, New York, 1991).

22. B. Winter, R. Mitzner, Ch. Kusch, E.E.B Campbell, and I.V. Hertel, "On the mechanism of C_{60} thin film laser-induced desorption", *J. Chem. Phys.* **104**, 9179-9190(1996).

23. T.M. Bloomstein, M. Rothschild, R.R. Kunz, D.E. Hardy, and R.B. Goodman, "Critical issues in 157 nm lithography", *J. Vac. Sci. Technol.* **B 16**, 3154(1998).

Dynamics study of multiwavelength excitation process
using F_2 and KrF excimer lasers

Kotaro Obata[B], Koji Sugioka[A], Takahiro Inamura[C], Hiroshi Takai[C], Koichi Toyoda[B], and Katsumi Midorikawa[A]

[1]RIKEN (The Institute of Physical and Chemical Research),
2-1 Hirosawa, Wako, Saitama 351-0198, Japan
[B]Dept. Applied Electronics, Tokyo University of Science, Yamazaki 2641, Noda, Chiba 278-8510, Japan
[C]Dept. of Electric Engineering, Tokyo Denki University, 2-2 Nishikicho, kanda, Chiyoda-ku, Tokyo 101-8457, Japan

ABSTRACT

Ablation dynamics of fused silica by multiwavelength excitation process using F_2 and KrF excimer laser has been investigated by energy analyzed mass spectrometry of ablated species. The number of Si ion generated by multiwavelength excitation process corresponds to that by single-F_2 laser ablation and to approximately 2.1 times larger than that by single-KrF excimer laser ablation. In addition, kinetic energy distribution of Si^+ ablated by multiwavelength excitation process shows almost same as that by single-F_2 laser ablation. We regard that absorption of KrF excimer laser by excited state generated by F_2 laser (excited-state absorption: ESA) causes similar electron excitation process to single-F_2 laser irradiation, resulting in enhancement of Si ion with higher kinetic energy and then in high-quality ablation.

Keywords: F_2 laser, KrF excimer laser, ablation, multiwavelength excitation process, excited-state absorption, fused silica, mass spectroscopy, dynamics.

1. Introduction

High-quality ablation of fused silica is one of the most important and attractive techniques for optoelectronic device fabrication. We have developed F_2-KrF multiwavelength excitation process, in which VUV (F_2 laser: $\lambda = 157$ nm) and UV (KrF excimer laser: $\lambda = 248$ nm) laser beams are simultaneously irradiated to the sample [1, 2]. This process achieved high-quality ablation with little thermal effect and little debris deposition as well as similarly to single-wavelength process using F_2 laser [1-7]. This process has some advantages over single-wavelength F_2 laser ablation. That is, 1) the small fluence of F_2 laser reduces the photon cost of using the high-fluence F_2 laser in the latter process, and therefore, 2) the processing area and throughput increase. Additionally, 3) since the ablation proceeds via the KrF excimer laser, the necessity for the expensive F_2 laser optics and projection system is eliminated, and a conventional excimer laser mask projection system can be utilized for micropatterning. The ablation mechanism could be attributed to excited-state absorption (ESA) [8]. Namely, electrons are first excited from the valence band to the defect levels located slightly below the

conduction band by F_2 laser, and then the electrons trapped at the defect levels are further excited over vacuum level by simultaneously irradiated KrF excimer laser. This cascade excitation process leads to bond scission in fused silica and finally causes effective ablation. However, the detailed mechanism of multiwavelength excitation process has not yet examined.

In this paper, ablation dynamics of fused silica by F_2-KrF multiwavelength excitation process is investigated for further discussion of mechanism. Observation of species ablated from fused silica by F_2-KrF multiwavelength excitation process is carried out using quadrupole mass analyzer with energy analyzer.

2. Experimental procedure

The experimental setup for ablation dynamics by F_2-KrF multiwavelength excitation process using quadrupole mass analyzer with energy analyzer is shown in Fig.1. The UV-grade fused silica (VIOSIL, thickness of 0.525 mm, Shin-Etsu Chemical Co., Ltd.) substrates were used in this experiment. Before the fused silica substrate was introduced into the chamber, ultrasonic cleaning with acetone and ethanol, followed by a DI water rinse for 5 min, was carried out. The chamber was evacuated down below 5×10^{-7} Torr. After evacuation, the fused silica substrates were simultaneously irradiated by F_2 (λ= 157 nm, τ= 20 ns) and KrF excimer (λ= 248 nm, τ= 23 ns) lasers to generate the ablated species. For coaxial irradiation of F_2 and KrF excimer laser beams, a special dichroic mirror composed by multilayers of dielectric thin film on an MgF_2 substrate was used. This mirror transmits 52 % of the F_2 laser and reflects more than 92 % of the KrF excimer laser. To detect each laser pulse at the sample surface, fluorescence from the modified fused silica was observed using a photodetector, and then the irradiation timing of each laser beam was adjusted by a digital pulse generator (Stanford DG 535). In addition, this digital pulse generator was used as trigger pulse of gate timing in quadrupole mass analyzer. In this measurement, neutral species generated by laser ablation were not ionized by additional ionization method such as electron bombardment or post laser irradiation to ablated species.
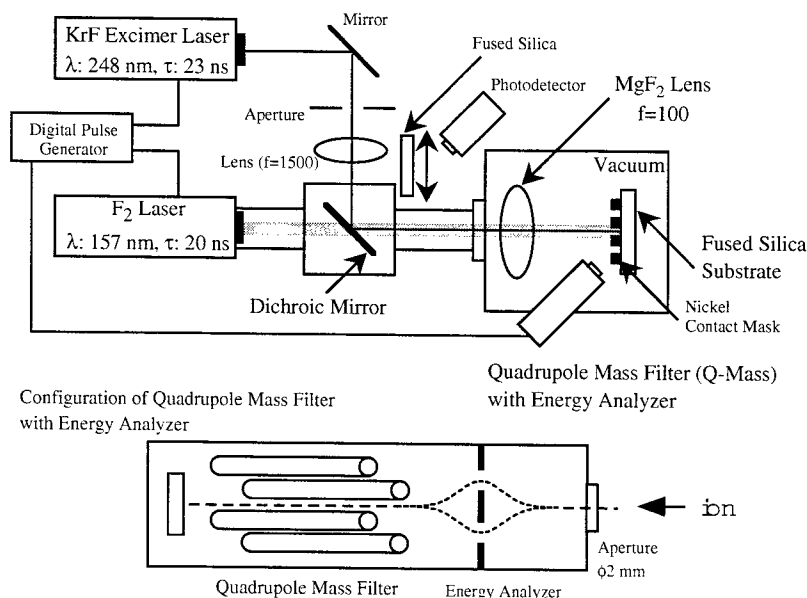
Figure 1. Experimental setup for ablation dynamics by F_2-KrF multiwavelength excitation process using quadrupole mass analyzer with energy analyzer.

3. Results and discussion

Mass spectrometry is one of the good method to examine the ablation products and has been widely used for many kinds of ablation target [9-12]. Figure 2 shows the mass-spectra of the species ablated by single-KrF excimer laser ablation (laser fluence: 2.4 J/cm^2), single-F$_2$ laser ablation (laser fluence: 1.6 J/cm^2), and F$_2$-KrF multiwavelength excitation process (laser fluence of KrF: 2.4 J/cm^2, F$_2$: 0.3 J/cm^2), respectively. Each conditions were chosen to get almost same etching rate for every irradiation method. In the case of single-F$_2$ laser ablation and F$_2$-KrF multiwavelength excitation process, the signals of mass number 28 which is attributed to silicon ion are observed and each intensity seems to be almost same. In addition, the small signals of mass number 16 which is attributed to oxygen ion are observed. On the other hand, in the spectrum of single-KrF excimer laser ablation, although the signal of silicon ion is also observed, its intensity is much smaller than that of multiwavelength excitation process and single-F$_2$ laser ablation. Additionally, the signal of oxygen ion is hardly observed.

The kinetic energy distribution of ablated ions also gives good information for investigation of ablation dynamics. From Fig. 2, all irradiation methods generated Si ion. Figure 3 shows the kinetic energy distribution of Si ions ablated at various irradiation conditions of single-KrF excimer laser ablation (a), single-F$_2$ laser ablation (b), and F$_2$-KrF multiwavelength excitation process (c), respectively. Ablated Si ions by multiwavelength excitation process show wide kinetic energy distribution up to 100 eV with strong and sharp peak at 3.5 eV, which is almost same as that by single-F$_2$ laser ablation. On the other hand, single-KrF excimer laser ablation generates only the Si ions of the sharp peak around 3.5 eV without wide kinetic energy distribution.

In order to compare the feature of the wide kinetic energy distribution of the samples used in Fig 2, the comparison of integrated signal counts (a), peak intensity (b), and range (c) of the broad spectra for F$_2$-KrF multiwavelength excitation process (laser fluence of KrF: 2.4 J/cm^2, F$_2$: 0.3 J/cm^2), single-F$_2$ laser ablation (laser fluence: 1.6 J/cm^2), and single-KrF
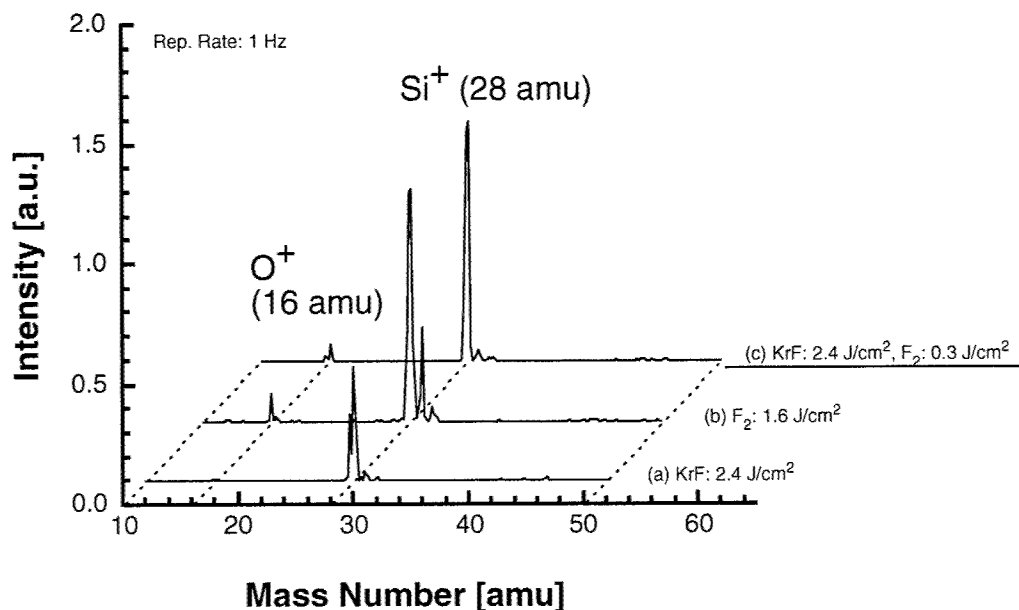
Figure 2. Mass-spectra of the species ablated at single-KrF excimer laser ablation (laser fluence: 2.4 J/cm^2), single-F$_2$ laser ablation (laser fluence: 1.6 J/cm^2), and F$_2$-KrF multiwavelength excitation process (laser fluence of KrF: 2.4 J/cm^2, F$_2$: 0.3 J/cm^2).

(a) Single-F₂ laser ablation

(b) Single-F₂ laser ablation

(c) F₂-KrF multiwavelength excitation process
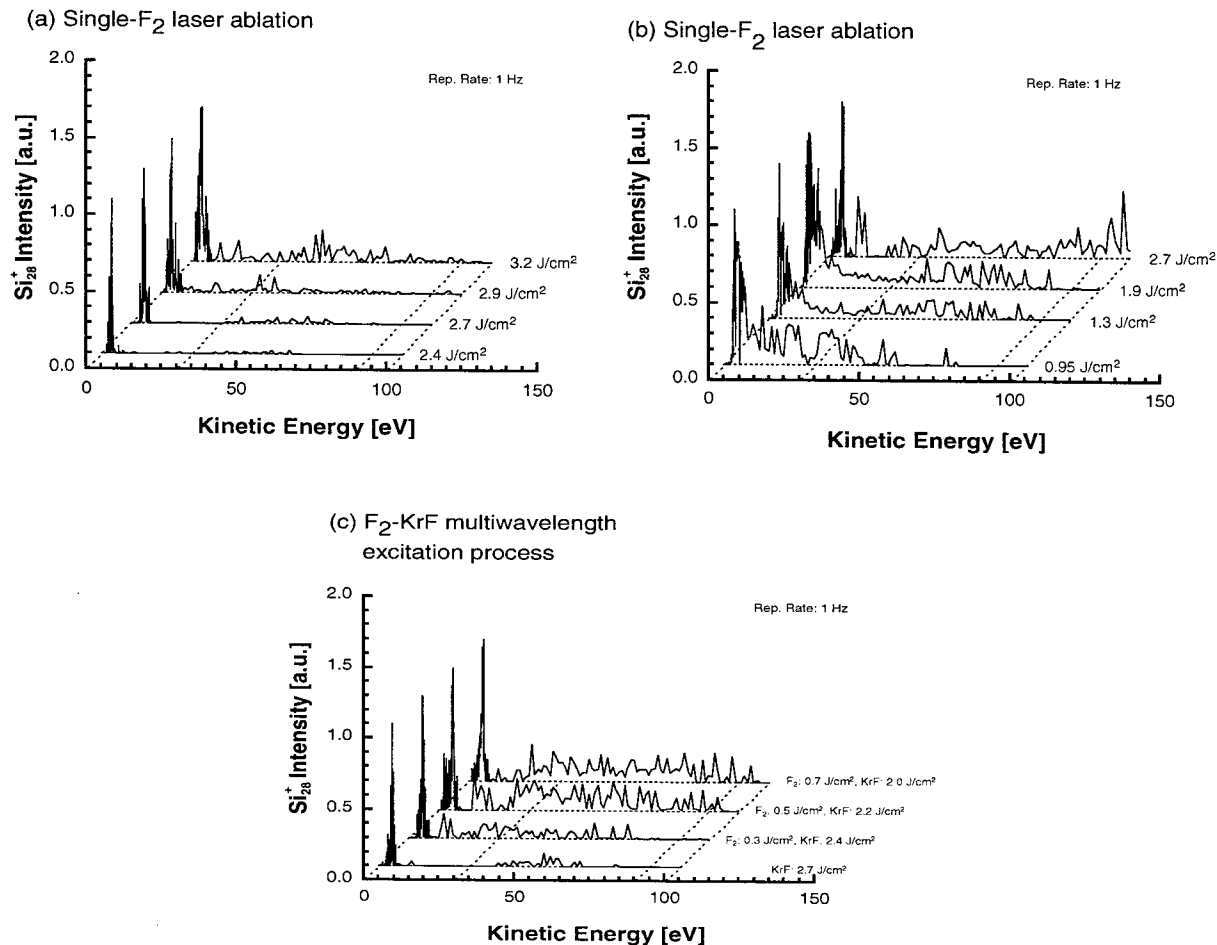
Figure 3. Kinetic energy distribution of Si ion ablated at various irradiation conditions of single-KrF excimer laser ablation (a), single-F_2 laser ablation (b), and F_2-KrF multiwavelength excitation process (c).

excimer laser ablation (laser fluence: 2.4 J/cm²) is shown in Fig 4. Laser fluence of all irradiation conditions were chosen to be almost same etching rate. The generated Si ions by each ablation method have almost same peak position around 56~60 eV in the broad spectra. In the case of multiwavelength excitation process and single-F_2 laser ablation, the range of kinetic energy distribution, peak intensity, and integrated counts seem to be almost same. On the other hand, in the case of single KrF excimer laser ablation, all parameters are much smaller compared with that by other ablation conditions.

The increase of amount of generated Si ions and kinetic energy distribution range is attributed to electron excitation in fused silica by laser irradiation. The electron excitation process in fused silica by laser irradiation can be explained by band structure of fused silica. Figure 5 shows band structure of fused silica and excitation process of electrons by single-KrF excimer laser irradiation, single F_2 laser irradiation, and F_2-KrF multiwavelength excitation process, respectively. For the case of single-KrF excimer laser, ablation takes place by multiphoton absorption, resulting in few Si ions with high-kinetic energy and then poor ablation quality. In the case of single-wavelength F_2 laser irradiation, electrons are first excited from the valence band to native defect levels, which are ascribed to impurities and defects, located slightly below the conduction band. (Direct excitation from valence band to conduction band is impossible since the band gap of
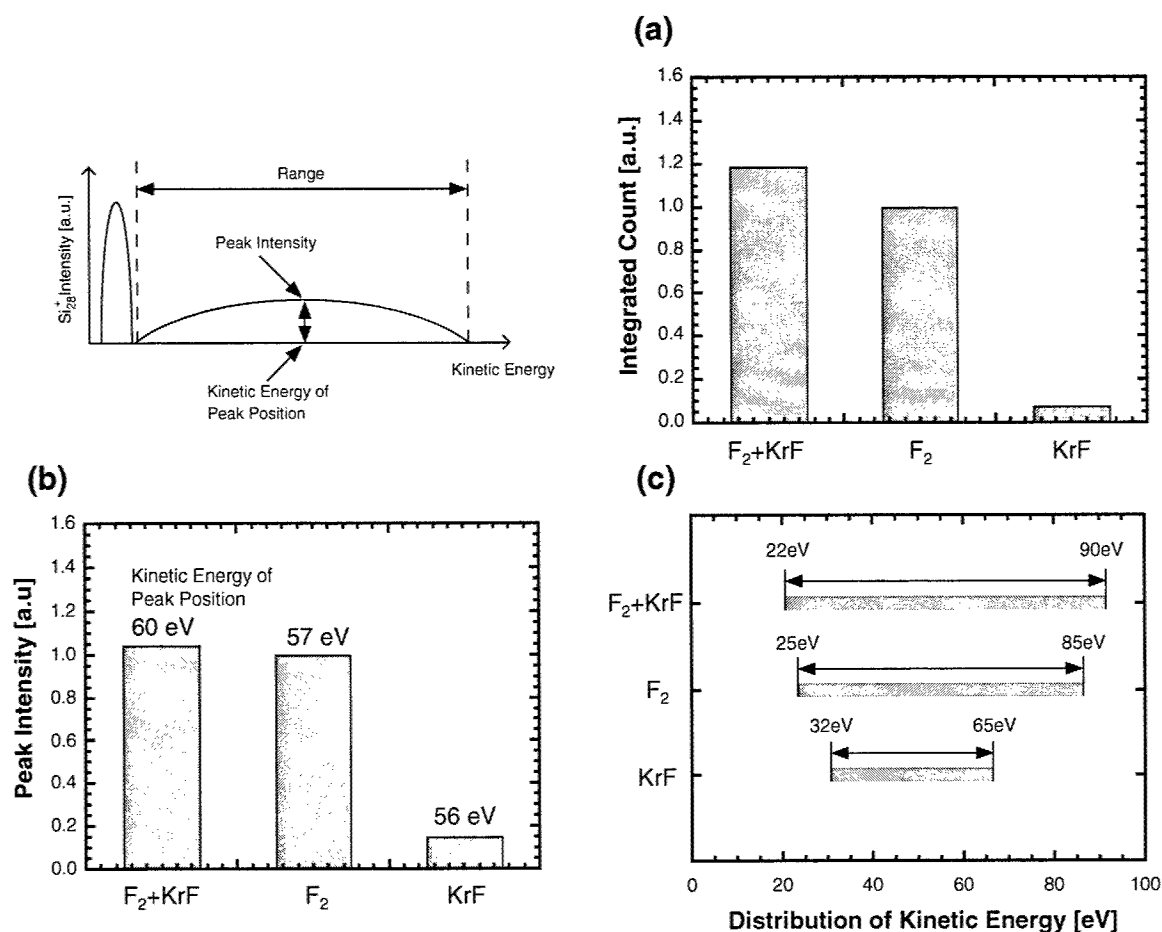
Figure 4. Comparison of integrated signal counts (a), peak intensity (b), and range (c) of wide kinetic energy distribution of the sample used in Fig. 2. (F_2-KrF multiwavelength excitation process (laser fluence of KrF: 2.4 J/cm², F_2: 0.3 J/cm²), single-F_2 laser ablation (laser fluence: 1.6 J/cm²), and single-KrF excimer laser ablation (laser fluence: 2.4 J/cm²)).
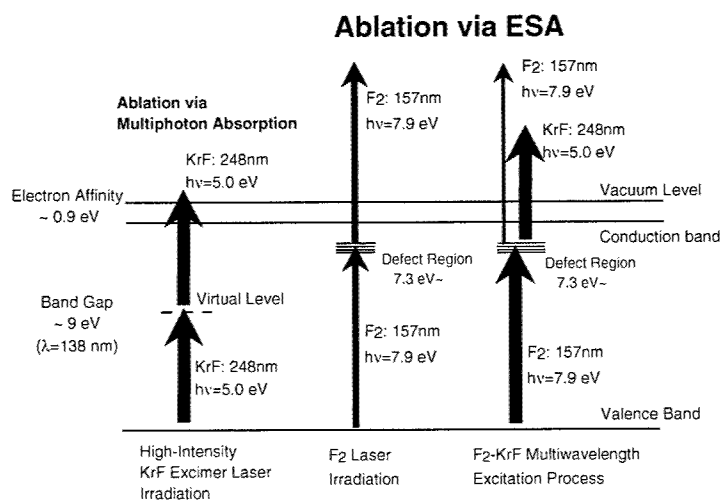
Figure 5. Band structure of fused silica.

fused silica (9.0 eV) is larger than the photon energy of F_2 laser (7.9 eV).) The excited electrons are further excited beyond the vacuum level by additional F_2 laser photons in the same pulse. Similarly, in the case of the multiwavelength excitation process, the electrons excited by F_2 laser are further excited beyond the vacuum level by simultaneously irradiated KrF excimer laser beam since sum of the electron affinity and energy difference between the conduction band and the defect level is much smaller than photon energy of KrF excimer laser. This excited-state absorption leads to similar electron excitation to the use of single-F_2 laser irradiation, resulting in generation of large amount of Si ions with larger kinetic energy. Finally, the multiwavelength excitation process as well as single-F_2 laser irradiation can achieve high-quality ablation.

4. Conclusion

Observation of species ablated from fused silica by F_2-KrF multiwavelength excitation process, single-F_2 laser ablation, and single-KrF excimer laser ablation was carried out by using quadrupole mass analyzer with energy analyzer. Si ion (mass number 28) was mainly observed for all of the above three ablation methods by mass spectrometry. F_2-KrF multiwavelength excitation process generated almost same peak intensity of Si ion as that by single-F_2 laser ablation. In addition, mass spectra of F_2-KrF multiwavelength excitation process and single-F_2 laser ablation also showed oxygen ion (mass number 16). On the other hand, mass spectrum of single KrF-excimer laser ablation sample showed much smaller Si ion peak compared with that by F_2-KrF multiwavelength excitation process and single-F_2 laser ablation and no oxygen ion peak. The ablated Si ions for multiwavelength excitation process and single-F_2 laser ablation showed broad kinetic energy distribution up to 100 eV with strong and sharp peak around 3.5 eV. This unique features of the multiwavelength excitation process were caused by the excited state absorption which induced similar electron excitation process to the single-F_2 laser irradiation. Thus, we conclude that the multiwavelength excitation process by coaxial irradiation of F_2 and KrF excimer lasers can achieve high-quality ablation compared to single-F_2 laser ablation.

References

[1] J. Zhang, K. Sugioka, T. Takahashi, K. Toyoda, and K. Midorikawa, Appl. Phys. A **71**, 23 (2000).
[2] K. Obata, K. Sugioka, T. Akane, N. Aoki, K. Toyoda, and K. Midorikawa, Appl. Phys. A **73**, 755 (2001).
[3] K. Sugioka, J. Zhang, S. Ruschin, S. Wada, H. Tashiro, and K. Toyoda, Appl. Surf. Sci. **127-129**, 843 (1998).
[4] P. R. Herman, K. P. Chen, P. Corkum, A. Naumov, S. Ng, and J. Zhang, Proc. SPIE **4088**, 345 (2000).
[5] P. R. Herman, R. S. Marjoribanks, A. Oettl, K. Chen, I. Konovalov, and S. Ness: Appl. Surf. Sci. **154-155**, 577 (2000).
[6] J. Zhang, P. R. Herman, C. Lauer, K. P. Chen, and M. Wei, Proc. SPIE **4274**, 125 (2001).
[7] K. Obata, K. Sugioka, T. Akane, N. Aoki, K. Toyoda, and K. Midorikawa, Opt. lett. **27**, 330 (2002).
[8] K. Sugioka, S. Wada, Y. Ohnuma, A. Nakamura, H. Tashiro, and K. Toyoda, Appl. Phys. Lett. **67**, 2789 (1995).
[9] F. Kokai, Y. Koga, Y. Kakudate, M. Kawaguchi, S. Fujiwara, M. Kubota, and K. Fukuda, Appl. Phys. A, **59**, 299 (1994).
[10] F. Kokai, M. Taniwaki, Y. Koga, Y. Kakudate, S. Fujiwara, K. Fukuda, M. Kawaguchi, J. Appl. Phys. **77**, 2220 (1995).
[11] D. Feldmann, J. kutzner, J. Laukemper, S. MacRobert, K. W. Welge, Appl. Phys. B, **44**, 81 (1987).
[12] S. G. Hansen, J. Appl. Phys. **68**, 1878 (1990).

Autonomous Production Cell for μm- and nm-Processing

E.W. Kreutz[*1], L. Böske[1], S. Kaierle[2], S. Mann[1], J. Ortmann[1], J. Willach[1]

[1]Lehrstuhl für Lasertechnik, Rheinisch-Westfälische Technische Hochschule Aachen
Steinbachstraße 15, 52074 Aachen, Germany
[2]Fraunhofer Institut für Lasertechnik
Steinbachstraße 15, 52074 Aachen, Germany

ABSTRACT

Shorter life time cycles of products, increasing workpiece variety and declining lot sizes demand for a closed processing chain which enables the economic production of variable products in the future. A new type of manufacturing concept for the production of the 21st century is lined out by the design of an "Autonomous Production Cell". Applied to and designed for manufacturing with laser radiation this concept shows completely new ways in comparison to former manufacturing procedures. The manufacturing processes in the Autonomous Production Cell start with a production oriented design and planning of the manufacturing procedure is including sensor controlled processing of the workpieces with integrated quality management. The quality management detects failures in the manufacturing procedure and allows back-coupling to any preceding step by means of a multistage cascaded production controller. In comparison to former concepts the user is at all times integrated into the manufacturing procedure. The user can add his own competence and creativity. At the same time he is being relieved by routine work and gets adequate help by the system in corresponding situations. The design of the components of the Autonomous Production Cell (design and planning tools, networking of sensors and actuators, user interface, etc.) has been performed as general as possible. This offers the possibility to transfer this concept with countable efforts to all the manufacturing with laser radiation such as welding, cutting, surface treatment, freeforming, rapid prototyping, etc.

Keywords: laser radiation, manufacturing, processing control, failure analysis, quality assurance

1. INTRODUCTION

The production of components in the μm- and nm-range is one of the leading technologies for the present century and is expected to have a high market potential. A large number of micro-fabrication technologies has been established over the last years. These technologies can roughly be divided into two groups: the direct processing techniques , where each single device is manufactured separately, and replication processing techniques, where a master structure is replicated into the material. While the direct methods like removal by laser radiation or laser cutting, stereolithography and photolithography have mainly been used to fabricate prototype volumes. Most of the commercial activities have been focussed on the replication methods like LIGA, hot embossing, and microinjection molding.

In addition to existing microfabrication technologies for the manufacturing of silicon-based microsystems, the increasing demand for polymer-, glass-, ceramic-, and metal-based devices requires the establishment of equivalent technologies for the microstructuring. While many micro-optical applications cannot use polymeric materials, for example, due to extremely high tolerances, it is especially the quickly growing field of microfluidic systems for the life-sciences, where polymers are the preferred materials, since they show a high compatibility to many biologically active molecules and living cells.

The advances of micro-machining with laser radiation of small pulse duration in the μs- to fs-range for the manufacturing of freeforms has been demonstrated by various authors.

---

[*] Correspondance: E-mail: kreutz@llt.rwth-aachen.de; WWW: http://www.llt.rwth-aachen.de; Phone: +49/241 8906-146
Fax: +49/241 8906-112

Shorter life time cycles of products, increasing workpiece variety and declining lot sizes demand for a closed processing chain in order to achieve economic production of variable products of high quality in the future. Therefore, the concept of a manufacturing for the production of the 21st century has been lined out by the design of an "Autonomous Production Cell" (APC) which has been demonstrated for macroprocessing of parts by laser radiation.[1]

Considerable advances in actual and future manufacturing tasks can be achieved by implementing autonomy functions into manufacturing systems. This leads to a manufacturing system which is capable of processing all manufacturing steps at a high degree of self-containment reliable and fault-free for a large period of time. To accomplish these goals an optimum user support and integration of intelligent functions into the machine control is required. An important point in this context is the combination of the different levels planning, processing, and supervision within one control loop. All relevant information to perform and control the tasks are available to the operator.

The present-day situation in manufacturing is characterized by a trend towards holistic solutions of manufacturing processes. Integration of the entire communication and information flow in the factory from the management level down to the processing level is the significant distinction to former approaches. Decreasing product life-cycles, lot sizes, enhanced product variety, and demands on the product quality intensify this evolution.

Recent manufacturing concepts were based on CIM (computer integrated manufacturing) consisting of deterministic linear steps in the task hierarchy from planning functions to highly automated workpiece processing. This development led to a "man-less factory" with the consequence of low interaction possibilities in case of faulty operations.

Actual research is focused on implementing autonomy functions in manufacturing systems leading to Autonomous Production Cells (APC). Notable characteristic of an APC is the integration of self preserving functions and the ability to define its own system boundaries. Laser radiation as a tool is particularly suitable to outline the growth of functionality. In this context the role of the user (operator) has to be redefined. The former state of the user as supporting manufacturing in the case of errors or failures will be changed in the manner that the manufacturing system supports the user in finding adequate solutions to continue the processing task. This leads to a redefinition of the user's skills, responsibility, and authority.

Outstanding characteristic of an APC is the capability to link planning functions and processing tasks to a feed-back system. The APC covers an internal stage of planning and is coupled to higher degrees of hierarchical levels. Here, the designer of APC is lined out giving some advice for its significant use for processing in the μm- and nm-range as exemplarity demonstrated for the drilling with laser radiation.

2. AUTONOMOUS PRODUCTION CELL

2.1 Concept
To obtain autonomy in a manufacturing system functions of autonomy have to be assigned to components, methods, measures, and organisation. Self-organisation means the spontaneous generation of a specific order based on a broad initial state. The complexity of the system containing numerous sensors and actuators is reduced by guidance of planning data and task specific information stored in the system control. Self-generation is only possible in particular parts of the system. An autonomous system creates its own boundary. It has own competence to initiate a feed back to the environment in the case of failures or non-fitting preparation of the task planning. Self-generation means the definition of configuration of the information processing which is necessary to perform the task given by the planning data. Sensors and actuators are initiated and adjusted. Subsets and paths of the failure analysis due to the components involved in manufacturing are established. Furthermore, task-specific instructions are generated and displayed to the user.

By means of the failure analysis mechanisms for self-preservation of the system are activated. A fault detected by a sensor or by the operator is traced along its path of emergence (by failure trees e.g.) to its source. After assigning a cause and an estimation of its relevance measures for its treatment are introduced. Failures ranging below a certain threshold of severity are compensated by the system itself by adjusting of the processing parameters onto the new conditions. Failures ranging above this threshold are treated by three ways: (1) Statistical failures concerning the

processing are compensated by adjusting the processing parameters if they range below a certain threshold of severity, (2) errors concerning the machinery require action of the operator. During repair work he is supported by the system which delivers references. This feature is expressed as task-oriented self-preservation, (3) errors caused by planning are either treated by re-planning on-site supported by the system's resources or for not executable tasks by feed back of planning data combined with information for re-planning to superior levels of planning. Failures of processing and the measures of their treatment are stored in a data bank for future applications. By this the occurrence of known errors will be prevented and the system's "knowledge" to treat failures control will be broadened.

Conception of autonomy functions to manufacturing units requests for explicit definitions of automation and autonomy. To realise autonomy functions the existence of automation functions is fundamental. If insulated production processes always work without failures simple steering is sufficient. However, the occurrence of processing failures requires a failure management with features of autonomy. This urges a permanent and application-oriented presentation of process values to the operator. Cognition lacks have to be prevented by qualified information processing. The production cell must relieve the operator and react autonomously in case of changing machine, tool, or environmental conditions. To fulfil these requirements the implementation of technological knowledge into the processing procedure is necessary. This makes the machine capable of "hitting decisions" to adapt the control sequences.

2.2 Realization
The APC handles complex processing tasks autonomously based on minimum input data (e.g. workpiece data, planning data). Ideally, the output is the finished workpiece, inserted as a half stuff. Main features of the APC are fault tolerance over a long time interval and the coupling to production steps preceding and following manufacturing (e.g. design, tool engineering). The capability of processing in small lot sizes is another significant criterion. Integration and support of the operator is of major importance because a machine cannot be autonomous by itself.

The three main functions of the APC are planning, processing, and supervision (Fig. 1).[2] First input set for planning are CAD data. These are generated on a superior level of the operational organization (e.g. design). Processing parameters are assigned to the CAD data by the planning module (Fig. 1). From the combination of all data a CNC program is generated as well as data sets for set-up of sensors and actuators are supplied to the process computer. In the first case the operator can check, and even adjust, the allocation of data and can simulate the path tracking via a visual interface.[3] Second input set of parameters is the task order supplied by commissioning. Realization is initialized by an intelligent decision-maker. Based on actual machine and processing parameters it decides if the task can be executed. Furthermore, it is able to feed back task and planning data to superior levels and to initialize a re-planning off-line in the case of severe failures occurring.
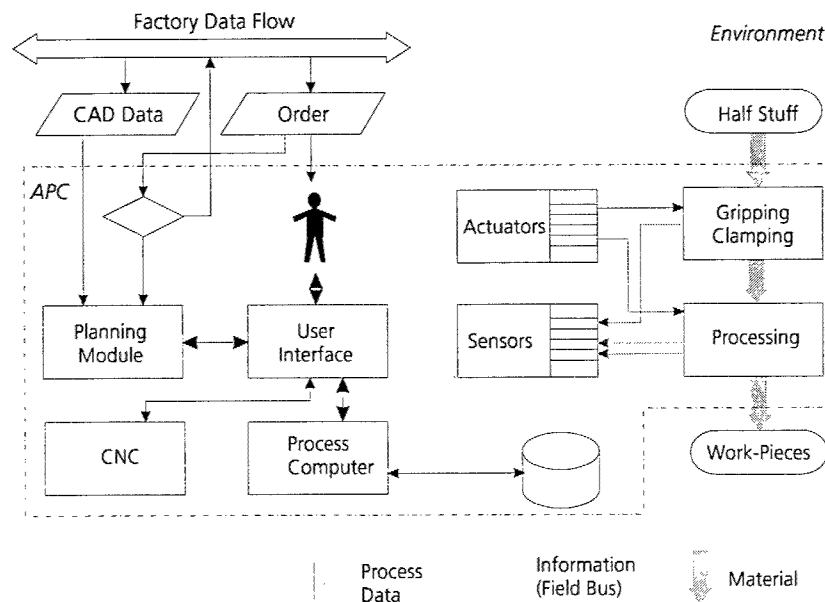
Figure 1: Scheme of the Autonomous Production Cell

Input to the processing is half-stuff, output are finished workpieces. Laser materials processing allows the extraction of characteristic signals from the process.[4] Process monitoring is made by sensors which record defined characteristics of quality. The course of the processing is influenced by actuators at distributed locations. The great bandwidth of the signals requires the standardization of data sets by intelligent network nodes. After pre-processing data are handed over to the processing computer by a field bus. The processing computer is the central element of the APC. Its functions are initializing and set-up of sensors, actuators, and robots. Furthermore, it controls manufacturing and takes on failure analysis.[5] In the case of errors the bandwidth of reactions extends from adjusting the processing parameters to re-planning of the processing within the APC. In the case of severe errors the operator is informed. During treatment the operator is supported by the process computer. If the failure cannot be treated within the human-machine system re-planning will be conducted to superior levels.

Communication between operator and machine is made via the user interface.[6] All data necessary for process steering and control is available. The operator is in the position to intervene into running manufacturing at any time. With view to laser materials processing, an example is exposed to outline the characteristics. Considering this system as self-sufficient, it can be assigned as automated system. Also creation of alerts or error messages can be obtained with automation. To identify autonomy functions, e.g. to equip the system with certain "intelligence" ,for example, the following features are essential:

- Reaching a tolerance limit, a superior system must decide, whether the processing task can be continued with adapted parameters or if it must be stopped.

- Depending on workpiece or position it must be resolved whether the processing task either can be stopped to discover the problem or has to be continued with changed parameters to avoid rejected items.

- The fault management of the superior system provides different solutions to the operator how to continue the processing task. Possible is re-planning of the task at the machine with slightly changed processing parameters or even complete stop with according notice to the planning level and useful hints for re-planing the task.

To prevent repetition of known failures kind and path of the basic error as well as all measures for its treatment are stored in a data bank. By feed-back of the data bank to failure analysis a self-learning system is defined. Continuous improvements of manufacturing and organization within the APC are ensured .

3. PLANNING

3.1 Technology Module
Laser materials processing is a high level technology, which up to now demands a time and cost intensive development of processing parameters for each specific plant and processing task. This results in a sophisticated planning procedure. In order to reduce time delays and high costs various computer aided tools are currently under development. One objective of this development is the realization of processing models which calculate the parameters used for each task. Another objective is the introduction of CA-technologies to reduce the deadlock time of a machine tool using offline planning.

Following these strategies a technology module was developed which links a CAD system and a processing model.[3] This combination offers the opportunity to plan the complete processing task offline and to create NC data sets which consider both geometrical and technological aspects. Using a processing model in a CAD/CAM system makes great demands on the calculation time. A communication interface as well as an efficient user interface are required. The communication interface handles the interaction with the technology module whereas the user interface is used to optimize the processing parameters manually. The processing model developed meets this requirements.

The technology module realized is a manufacturing oriented offline planning tool for laser materials processing. It is situated in a level between planning and processing. To interact with the environment it offers interfaces to commercially available CAD systems, to a process planning module, to the CNC control, and to a graphical user interface.
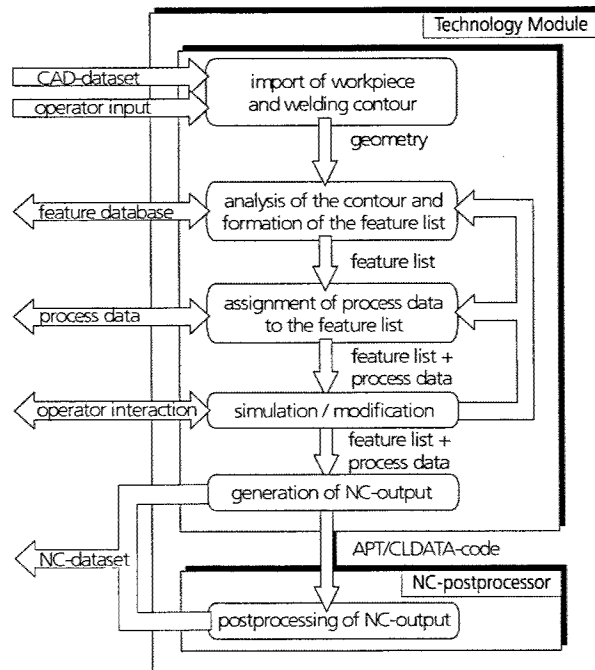
Figure 2: Block diagram of the technology module

The technology module requires CAD data sets of the workpieces to be processed as input data and an according production order.To generate the CNC code the technology module has to perform the following steps:

1. Analysis and segmentation of the processing track/volume
2. Generation of the feature list
3. Determination of the processing parameters corresponding to the features by request from the processing planning module
4. Assembling the task description
5. Simulation, collision control, kinematics control and user interactive change of the task
6. Generation of the CNC code with a CNC specific post processor.

The technology module is prepared to deliver configuration data for support of automated clamping tools. Moreover, desired values for sensors and actuators utilized during processing are generated. Due to the cascaded structure (Fig. 2) planning steps are checked periodically and are repeated with alterations in case of failures occur.

3.2 Structure

The technology module is an independent CAM system and consists of several function blocks (Fig. 2). Through the CAD interface the CAD data set of the workpieces to be processed is imported. To prepare the processing task based on the feature approach the processing sequence (track) must be set and it then is segmented into basic geometry elements (BGE). For this purpose, check points are set in adjustable equidistant intervals on the track (Fig. 3). By iteratively comparing the contour each BGE is determined. The goal is to redesign the path using BGEs by achieving a minimal offset form the original track. The more points can be incorporated in a BGE the less features will have to be generated. In general this results in a smaller volume of the generated CNC code and makes it easier to be edited.

Check points are collected until the geometrical deviation of a point exceeds a limit given by the tolerances (Fig. 3). After the complete track is redesigned by the BGEs it is analyzed and the features are generated according to the geometric constellation of the BGEs. The features are collected in a list and the auxiliary elements, parameter lists, and default processing strategies according to the features are determined. Finally, the task is represented in a sequenced list of features.
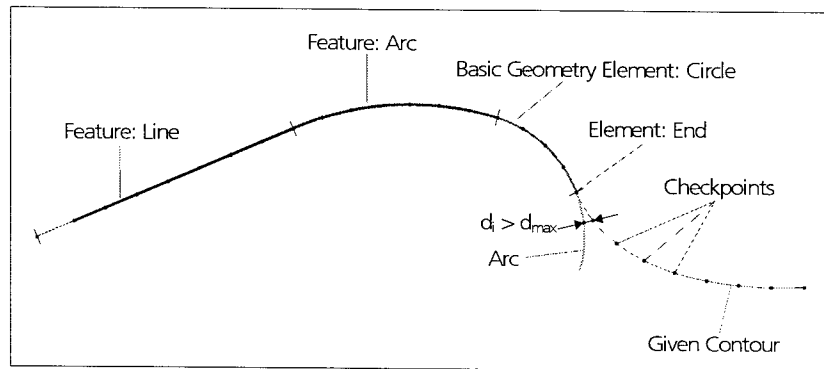
Figure 3: Segmentation of the track

Before the parameters are calculated the user has to provide the planning tool technological information and machine parameters (e.g. aperture, focal diameter, etc.) for each new combination of laser and handling system. Information necessary are material properties of the work piece. When putting in the default parameters the user is supported by a list of materials, handling systems, and laser sources. Machine parameters which can vary (e.g. beam diameter) have to be checked before starting the process planning. The processing parameters of each feature are calculated according to the default technological settings. Currently, six variable processing parameters are considered (laser power, processing speed, beam radius, focal beam radius, focal length, and focal position). The process planning module is connected to the technology module by a TCP/IP interface which manages the data transfer. By this way, the process planning module operates as a server which on request calculates the desired parameters. By this way a platform independent communication is realized which supports maximum flexibility if a component has to be changed.

After calculating the parameters the user is enabled to perform a simulation of the task and to carry out modifications in processing if desired (Fig. 3). During simulation the laser beam is moved on the track while in a separate window the actual planned processing parameters are shown. Tasks which can not be performed by the system (e.g. in case of restrictions) are determined and avoided in an early state by the possibility to change the processing strategy or to select a different one. A changed strategy is determined by a feed back to a previous block in the technology module. The reasons or restrictions which caused a failure are considered when selecting or changing the strategy. During simulation the user can change the processing parameters of the task. Effects which result from the modification are considered in the simulation as well.

As soon the result of the simulation is feasible the CNC code is generated. The list of features which describe the processing task is translated into machine codes according to DIN 66025.[7] Two variants exist. In the first case the CNC code for a specific CNC control is generated directly. This requires an adaption of the technology module to each CNC controller utilized. In the second case a machine-independent code is generated before translating intermediate code to the CNC specific file by a post processor.[8]

Due to the available interfaces the workpieces are designed in external CAD systems and then imported by the standard data exchange formats (e.g. IGES, VDAFS, STEP).[9,10] The usage of the technology module requires less training courses in comparison to complex CAD systems because of its processing oriented design.

4. APC CONTROL

4.1 Open Architecture NC-Control
In the past, the development of a control was conducted by the demands of a single machine, as a result the functionality of the control was tied and limited to the machines requirements. These device-oriented systems with proprietary hardware and software components and a tight coupling of application software, system software and hardware led to very complex and inflexible systems. Great efforts were made to maintain and further develop these products.[11]

Nowadays the control vendors and machine tool builders are confronted with more complex market requirements concerning their products based on new production technologies, the increasing rate of special purpose machines and the integration of process control into the machines. To fulfil these requirements modern approaches are based on an Open Architecture, enabling the machine tool builder and the user to adapt the control to their demands.

OSACA is the European initiative to define a vendor-neutral, open controller architecture in order to improve the competitiveness and flexibility of suppliers and users of control systems. The basic technical approach of the OSACA architecture is the hierarchical decomposition of control functionality into so-called functional units. For each of the functional units (e.g. motion control, axis control, logic control, etc.) unique interfaces are specified. This results in an interoperability, portability, scalability and reusability of applications.

The development and specification of OSACA was initiated within a European ESPRIT project.[12] Based on an analysis of requirements for a new generation of control systems the results of the project comprised the specification and implementation of an application programming interface (API) for control applications as well as an appropriate infrastructure, which is called system platform. The system platform is composed of three main components: the communication system, the reference architecture and the configuration system (Fig. 4).

Configuration System
Which AOs are running on which hardware?
How are they configured?

Reference Architecture
Which AOs are required from an NC?
Which interfaces do they have?

Communication System
How can AOs exchange data in a vendor-neutral way?
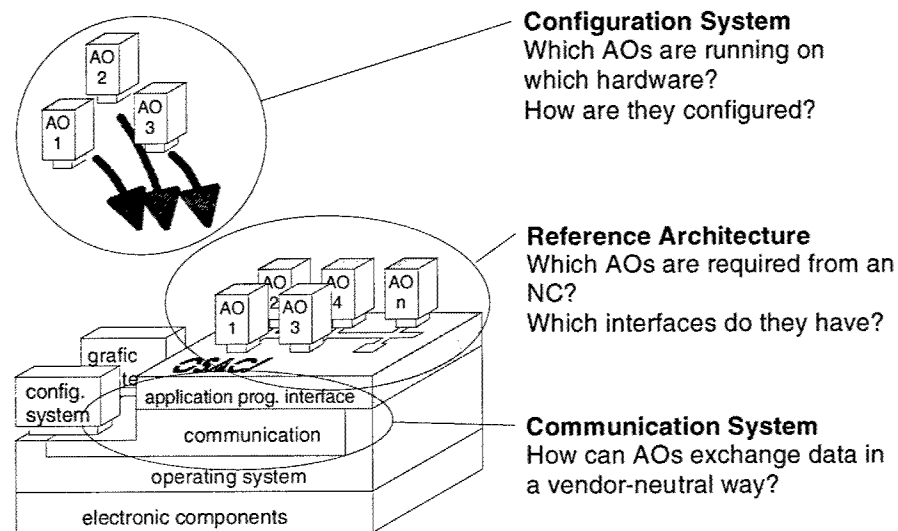
Figure 4: OSACA system platform

The communication system defines a hardware and system-software independent interface to exchange information between different application modules of a controller. The interface hides any specific details of the underlying transport system and therefore enables the combination of modules distributed on one or several processor-boards. The communication system consists mainly out of a data and a process interface. The data interface offers several variable objects that support the read and/or write access between distributed applications. The process interface consists of various processing objects that are used to describe the dynamic behavior of the applications by means of finite state machines. The state machines are described by static states, dynamic states and transitions to change the states of an application module.[11]

For an unproblematic combination of application modules from different vendors the standardization of communication interfaces is not sufficient. Moreover it is essential to define the functionality of modules and to specify their interfaces concerning the semantics and the syntax in detail. For this reason the OSACA reference architecture has been developed. By using formal templates all characteristics of the single interfaces are specified. For the data interfaces for instance the description contains among other things the unique name of the interface instance, a description of its contents, the data type, the access rights and the scaling. The description of process interfaces consists of an unambiguous name and description of its contents as well as a list of static states, dynamic states and transitions.

The requirement to assemble a control system out of building blocks leads to the demand for a dynamic configuration. In OSACA such a dynamic configuration system has been developed to enable the combination of different application modules during system start-up. This allows not only the set-up of a specific topology for a given functionality, but also the synchronisation between distributed processes.[13]

4.2 Realization of an Osaca based control

The OSACA-based control is subdivided into a non realtime and a realtime part, the communication between these parts is provided by the OSACA system platform based on the use of the TCP/IP protocol (Fig. 5). Due to the unique interfaces defined by OSACA every functional unit can run on both hardware platforms, the configuration system dynamically instantiate the modules during system start-up at the platform selected by the user.

All HMI functionality is located on the PC based part, the Microsoft Windows OS provide a consistent style of interaction. The fieldbus module for the communication with the sensor environment use the PC platform to profit by the broad spectrum of fieldbus interface cards available for the PC PCI/ISA bus. Every software module can access the received sensor data over the system platform.
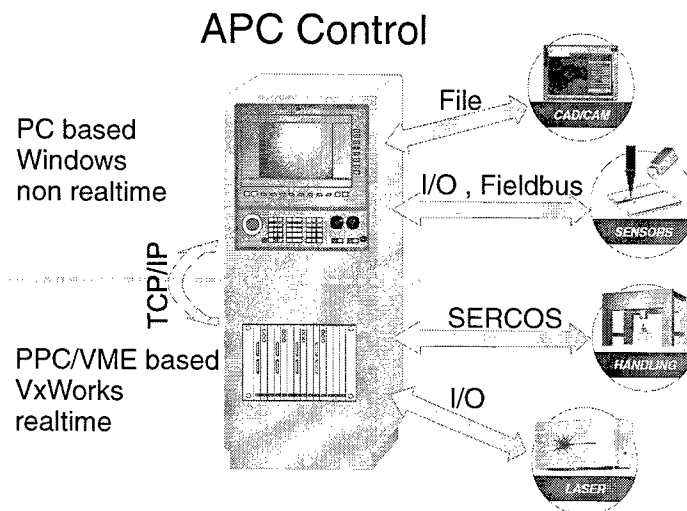
Figure 5: Control of the APC for laser materials processing

It should be kept in mind that time critical elements like control of the 5 axis handling is located in the real-time part of the system. It consists of a VME based PowerPC processor board, the VxWorks operating system, digital and analog I/O and a SERCOS interface card for the communication with the machine drives. The corresponding software architecture is illustrated in Fig. 5.

4.3 Geometry Chain

In conventional controls for 3D machining the work piece geometry is usually approximated by means of linear segments, which describe the original contour within a defined tolerance. Depending on the curvature of the contour this may lead to very short linear segments and therefore to a limitation of the feed due to the block cycle time of the CNC controller. Another limiting aspect is the lack of continuity resulting in jumps in the axes velocity profiles at the segment borders. This leads to dynamical errors in the machine motion having a reducing effect on the surface quality.

To avoid the mentioned shortcomings the OSACA-based APC-control uses splines for an analytic description of the work piece contour all the way through the geometry chain. The spline-based geometry representation offers a self-contained contour description due to the fact that any intermediate points as well as derivatives can be calculated.[3] Therefore, this representation supplies the control algorithms with optimal input data.

To fulfill the motion control tasks the geometry chain is composed of application modules for tool correction, transformation, velocity control, and interpolation (Fig. 6). The 3D tool correction and transformation are based on smooth and continuously differentiable functions. Through this best results can be achieved. The drawback of

performing a mathematically self-contained transformation is the immense computational effort that is needed. This computational effort would be an obstacle for a real-time execution of the geometric transformation. Therefore, in the APC-control an approximation is used for the spline transformation. The deviation of the generated splines from the exact trajectory can be parameterized by the user. The on-line realization of the algorithms allows the user to employ machine independent part programs and to change zero offsets for the clamping of work pieces.

It is the task of the velocity control to generate a velocity according to the spline profile. The principal aim is to achieve machining times as short as possible, which means a feed forward as high as possible within the given restrictions. The restrictions concerning the feed forward are the programmed feed as technological parameter and the dynamic limits of the drives as physical limits. In order to optimally utilize the abilities of the machine tool, the maximum velocities and accelerations have to be calculated for each axis. Because of the velocity control's position in the geometry chain behind the geometric transformation the motions of the single axis are already known. Therefore, the generation of a velocity profile for the axes of the handling system is possible.

Finally the interpolator combines the information of the distance profiles and the axes splines. It generates distinct time ticks, which depend on the interpolation cycle time. Based on a time tick, the corresponding path parameter is calculated from the distance profile. This path parameter is then inserted into the axes splines providing axes positions to be passed to the closed loop.[14]
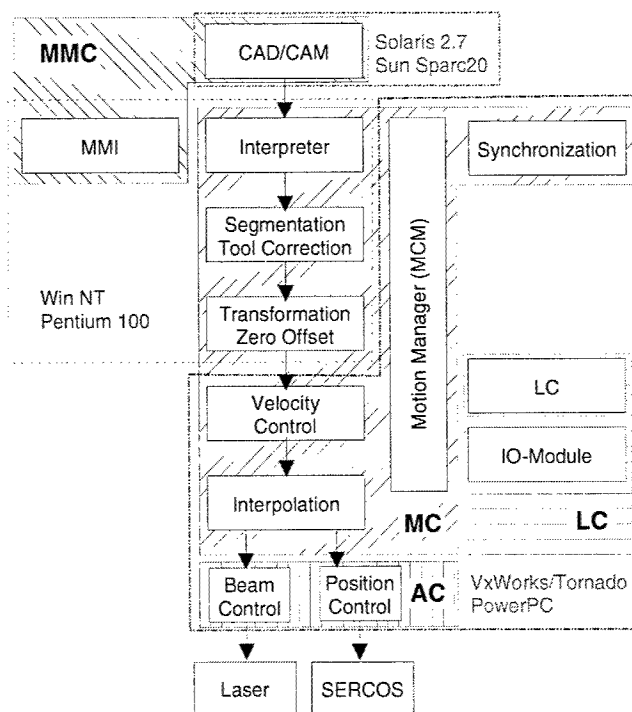
Figure 6: Structure of the OSACA-based APC Control

5. SENSOR CONTROLLED PROCESSING

The documentation and the re-feeding of the processing's results to the planning level is one of the important features of the Autonomous Production Cell. The use of these information for planning of processing strategies and technological parameters help to improve the processing quality. Several sensor systems observe the processing and deliver online information.
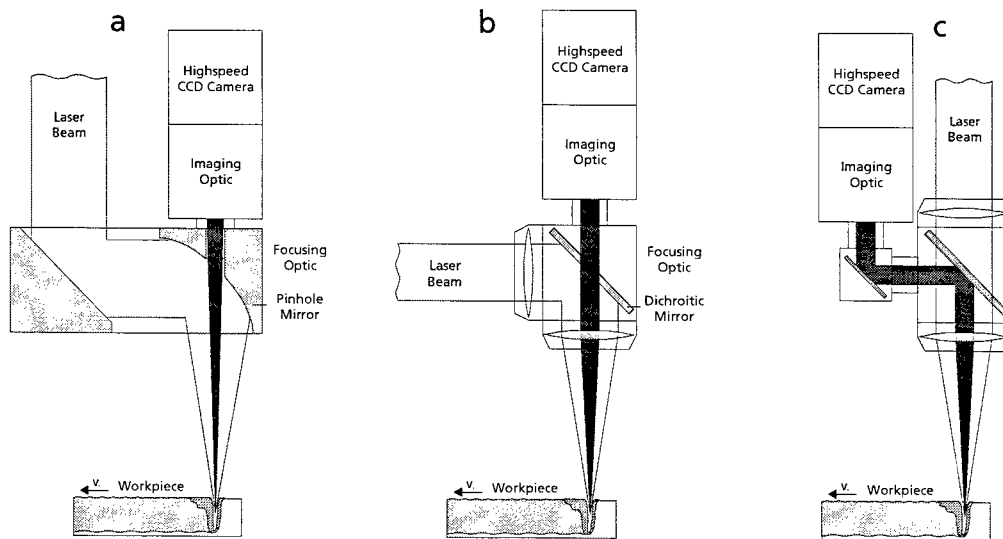
Figure 7: Setup of the coaxial process control system for CO_2 and Nd:YAG laser optics

The application of sensors and actuators in laser materials processing is useful for processing diagnosis and control in order to support the operator and to enhance the processing results. Integration of sensors and actuators primarily enhances the complexity of the system if they work in stand-alone mode. To handle the complexity each sensor/actuator has to be provided with a high degree of autonomy. A central process computer is required to collect, process, and store all data provided by the sensors and actuators. The physical connection is realized by a field bus network.[15] This allows the integration of various sensor systems for several applications.

Density-distribution of secondary radiation
at percussion drilling as a function of the pulse digit

$\Delta t = 50ms$
Framerate 2,9 Hz

Diameter 250 µm
$\lambda=1064nm$, $f_p=20Hz$, $t_p=0,25ms$, $E_p=0,25Ws$

Top view of the hole entrance
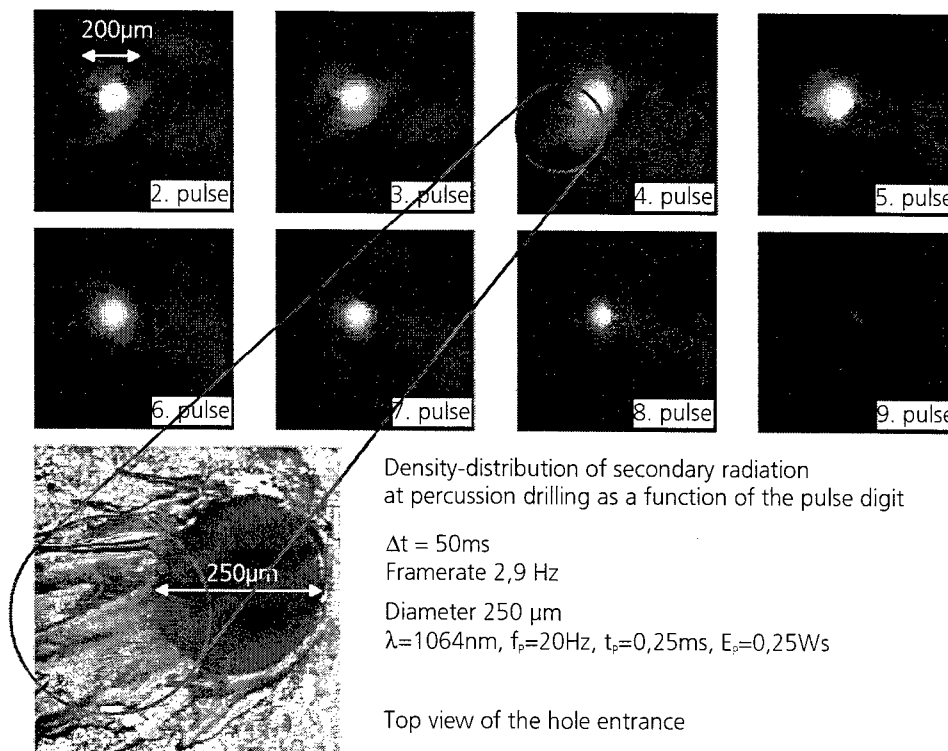
Figure 8: Coaxial Process Control at percussion drilling with Nd:YAG laser radiation

One of the sensors used is a coaxial process control system (CPC) developed by the Fraunhofer Institute for Laser Technology ILT.[16] It can be adapted for different laser processing applications.[17,18,19] The system allows the spatially resolved online inspection of the interaction zone, where the laser beam hits the workpiece surface (e.g. the keyhole during laser beam welding). It consists of a high-speed camera mounted directly at the processing head and an industrial PC for image analysis. The optical path of the camera goes coaxial with the laser beam path through the focusing optic. The design of the system allows an easy adaptation to CO_2 , Nd:YAG and diode laser optics. The camera images taken from the processing are processed online by an industrial PC.

The system's flexible design allows custom-made monitoring systems for different laser materials processing applications. In the field of microengineering, for example, the process radiation while percussion drilling of stainless steel was monitored with the coaxial process control as shown in figure 8. The first pulse triggers the camera. Beginning with the fifth pulse a decrease of the intensity of radiation can be observed with the growing number of pulses. A through boring is forming and the following pulses can not get in interaction with solid or fluid material. A correlation between the unsymmetric deposit of the melt at the surface of the material and the unsymmetric distribution of the radiation's intensity can be observed.

6. CONCLUSION

Manufacturing processes are currently in a state of change. There are growing demands on faultless production and product quality. Workpiece variety is increasing and lot sizes are decreasing. These requirements call for advanced techniques in modern production. A procedure for a reliable and flexible production planning and control structure for laser materials processing, embedded into a Autonomous Production Cell, is described. The production steps of process planning, path planning, process simulation and the operation of workpiece processing have been combined into a single autonomous operating unit. The operation is controlled by networked sensors and actuators. All collected data is stored in data banks and failure operation is reported to the appropriate planning level.

7. ACKNOWLEDGMENT

8. REFERENCES

1. N.N, Sonderforschungsbereich 368 Autonome Produktionszellen, Arbeits- und Ergebnisbericht 1994/1995/1996, Aachen 1996
2. Kaierle S, Dahmen M, Fürst B, Kittel J, Kreutz EW, Poprawe R, Autonomous Manufacturing: Planning and Control in Laser Beam Welding, Proceedings of ICALEO '96, LIA Volume 81 Laser Materials Processing, Detroit, Michigan, USA (1996) Section B, pp. 154-163
3. Kittel, J, Dahmen, M, Fürst, B, Kaierle, S, Kreutz, EW, Poprawe, R, Introduction of a CAM Feature Model for Laser Beam Welding, SPIE Proc. Vol. 3102, (1997) pp. 36-42
4. Abels, P, et al, 1995, Process Control for Laser Materials Processing, Automotive Laser Application Workshop (Detroit, MI)
5. Diekmann, A, Failure Analysis for Laser Beam Welding, Diploma thesis, Chair for Laser Technology, RWTH Aachen, Aachen, 1997
6. Kaierle, S, et al, 1996, Ergonomic User Interface Design for 3D-Laser Welding Cells, in: R.J. Koubek and W. Karwowski (eds.), Human Aspects of Advanced Manufacturing: Agility & Hybrid Automation, (IEA Press, Louisville), pp. 47 – 50
7. N.N. Programmaufbau für numerisch gesteuerte Arbeitsmaschinen (DIN 66025)", DIN Deutsches Institut für Normung e.V., Beuth Verlag, Berlin, 1974

8. N.N, "CLDATA (DIN 66215)", DIN Deutsches Institut für Normung e.V., Beuth Verlag, Berlin, 1974
9. N.N, "Format zum Austausch geometrischer Informationen (DIN 66301)", DIN Deutsches Institut für Normung e.V., Beuth Verlag, Berlin, 1986
10. N.N, "Initial Graphics Exchange Specification (IGES)", Version 5.1., U.S. Department of Commerce, National Institute of Standards and Technology, Gaithersburg (USA), 1990
11. Pritschow, G, et al, Open Control Architecture – Past, Present and Future, Annals of the CIRP Vol. 50.2/2001
12. N.N,Project Report OSACA Phase I and II, ESPRIT III EP 6379 & EP 9115, Brussels, 1996
13. N.N,OSACA Handbook, Version 1.0.1, OSACA Association, Stuttgart, 1997
14. Weck, M, Meylahn, A, Hardebusch, C, Innovative Algorithms for a Spline-Based CNC Controller, Annals of the German Academic Society for Production (WGP), no. IV, 1999
15. Kaierle, St, Abels P, Nitsch, H, Beyer, E, Sensor-/Actuator Field Bus for Control of Laser Manufacturing Systems, Proceedings of LANE'94, Maisenbach-Verlag, Bamberg, Germany (1994) p. 661-668
16. Kratzsch, C, Abels, P, Kaierle, S, Poprawe, R, Schulz, W, Online process control for laser beam materials processing, Proceedings ISATA 2000
17. Beersiek, J, Schulz, W, Verfahren und Vorrichtung zur Materialbearbeitung mit Plasma induzierender Hochenergiestrahlung, Patent DE 19741329 C 1, 1998
18. Beyer, E, Beersiek, J, Schulz, W, Nitsch, H, Verfahren und Vorrichtung zum Materialbearbeiten mit Plasma induzierender Laserstrahlung, Patent DE 4434409 C 1, 1996
19. Poprawe, A. Ehrhardt, P. Loosen, D. Petring, Advancements in welding with high-power-lasers, Proc. ICALEO'98, Section A, pp. 64-73, 1998

Novel Beam Delivery System for Microvia Drilling Using Holographic and Refractive Optics

Todd Lizotte[a] and Orest Ohar[a]

[a]NanoVia, LP, 4 Delta Drive, Londonderry, NH 03053
Phone: 603-421-0713, Fax: 603-421-0214

ABSTRACT

The research and development of the optical system described was due in part to the virtual stalemate of current microvia drilling technology within the High Density Interconnect market. The desire by industry to acquire faster processes for drilling microvias led to our research in the utilization of hybrid optical systems, where standard refractive and computer generated diffractive optics could be meshed to create a system that would out perform the current technology in the marketplace. The outcome of this work is covered in the following paper and will, at the outset, briefly cover the targeted market segment for which the beam delivery system was developed, as well as its general capabilities. The paper will cover the basic architecture and technology behind the laser optical beam delivery system, as well as the unique components that make up the assembly. Each of the optical elements within the system will be briefly described, and the CGH elements will be briefly explained, including a description of the software used. The laser beam characteristics at several points along the beam delivery will be discussed, as well as the final image formed at the target plane where the microvia is drilled. Specific performance details will be shared with regards to component efficiency, i.e. diffraction efficiency losses, as well as total system performance throughout the beam line. The final section will cover materials processing, including the remarkable process rate increases and microvia hole quality achieved.

Keywords: Microvia, Microelectronics, Hologram, Diffraction, Interconnect, Chip Package

1. INTRODUCTION

Microvia drilling is becoming a critical process in the manufacture of multi-layer substrate devices called "chip packages." Chip packaging, as it is termed, involves the manufacture of multi-layered substrates using materials to those used in making printed circuit boards. Chip packaging specifically requires a substantial amount of drilled holes called microvias, which provide electrical interconnects to the varying layers of the substrate stack (Figure 1 – Chip Package).

The Next Generation package will also continue a trend of adding more interconnect layers to the substrate. The latest Pentium IV processors use eight-layer substrates, but sources believe the Next Generation microprocessors will have substrates with 12 to 14 layers, representing a significant packaging challenge. Currently, the number of microvias exceeds 10,000 per substrate for processors and with the continued growth of silicon chip capabilities this requirement will be upwards of 40,000 to 80,000 microvias per substrate, requiring laser-drilling technology with substantial throughput capabilities.

2. TARGETED PROCESS ATTRIBUTES

The key technology of the beam delivery system is the use of a variety of optical elements ranging from simple refractive to complex computer generated holographic and diffractive designs. Each of these optics provide a specific attribute to the system and collectively provides a stable, elegant and efficient way to accomplish the task of drilling small microvia holes at greatly improved speeds.

2.1 ON-TARGET (SUBSTRATE) BEAM SHAPE

When drilling a microvia into a chip package substrate, there is a great desire, if not an absolute necessity, to have a uniform profile as the beam plunges through the dielectric material to an underlying conductor. Since many of the chip package substrates utilize thinner conductive layers, a non-uniform profile at the target plane could result in both detectable and non-detectable defects. These defects include micro fractures and adhesion failures of the conductor materials, many of which show up as shorts after plating and thermal cycling (Figure 2 – Non-Uniform Via Drilling). Beam uniformity to a level of +/-6% of energy density was found to be an acceptable level for most applications.

2.2 BEAM OUTPUT TARGET EFFICIENCY

Delivering beam energy to the target with minimal losses was of great concern; however, more emphasis was placed on maximizing the throughput of the process, rather than true optical efficiency. Inherently, most microvia drilling systems suffer from process throughput limitations caused by their mechanics, not their optics. Key bottlenecks or constraints include the performance of the galvanometers and the clear aperture of the F-Theta lens, which limits the processing area per step and repeat.

Another constraint is the speed of the motion stages that index the materials per step and repeat. Even by using more powerful lasers, the only course of action is to split the beam and create a machine with two sets of galvanometers and lenses. Unfortunately, even with this type of setup, you can only improve throughput by 50% to 80%. This is not very effective and definitely is not a solution for the future of IC chip packaging challenges.

Our goals were to first achieve standard microvia hole quality, then maximize process throughput, then optimize the beam delivery system for the greatest optical efficiency. The first efficiency target was an attempt at achieving a flat top beam profile at the target surface. Imperative to this is an understanding that, within an imaging system, the key to achieving a flat top is to produce a flat top at the mask plane and then image that aperture onto the target. After careful analysis, it was clear that there might be an easier way to achieve both the flat top and a higher level of efficiency by generating an airy disk directly from the diffractive shaping elements. In essence, we created the proper airy disk pattern as generated by edge diffraction when illuminating a fictitious aperture with a flat top profile.

It proved possible to accomplish this type of shaping by testing and adjusting the optical design; a certain degree of accuracy on the final imaged diameter of the microvia could also be achieved. However, in this scenario, for every hole size there would need to be an element change in the shaper system. This is an easy enough thing to do, but costly, and it would inject additional complexities into a production environment.

So, a simpler approach was considered: the interference of the airy disk generator illuminating an aperture was modeled. Special emphasis was placed on how it would affect the on-target diameter. As demonstrated by the results (Figures 6 through 10), the technique is capable of producing various microvia sizes while retaining its flat top profile at the target plane. With this type of technique, nearly 80% of the energy is transmitted through the shaper and the aperture at all times. As with most optical systems, the key is to reduce losses; however, in the case of microvia drilling, it is more important to retain beam quality first.

2.3 SPLITTING AND PITCH CONTROL

To increase the throughput substantially, the goal was to deliver as much energy as possible to the target plane and to ensure that the design incorporated both flexibility and control. The splitter provided the best opportunity to achieve dramatic throughput, within the capacity and mechanical constraints of a standard production.

The splitter would provide multiple beams, allowing greater utilization of a high-powered UV laser source (a 7 Watt Coherent Avia laser is used in this case). Generating more power, the 7 Watt Avia provided two increases in performance: power for splitting; and adequate pulse energy at substantially higher repetition rate (kHz). These two

increases made it possible to generate, in our case, three individual sub-beams, each capable of processing at double the standard frequency rates when processing resin coated copper films.

Next, the split beams required another level of freedom, namely pitch control. Since the three beams required a fixed pitch (separation) at the splitter, they needed to be able to be adjusted to match various on-target pitch variations. Since the goal of this beam delivery system is to process chip packaging, the pitch and grid array style of the package layout can be optimized during design. Chip and package designers often require versatility when laying out packages; the need for dynamic pitch (separation) control would be critical for meeting this need. Two methods were tested and verified and will be discussed in the next section.

3. BEAM DELIVERY ARCHITECTURE

The beam delivery system is comprised of several different modules. They are as follows (Figure 3 – Optical System Schematic):

A.   Laser Module Sub-System *(LMSS)*
B.   Wave Front Module *(WFM)*
C.   Splitter Collimator Module *(SCM)*
D.   Pitch Adjustment Module *(PAM)*
E.   High Speed Shutter Module *(HSSM)*
F.   Galvanometer Module *(GM)*

Laser Module Sub-System (LMSS) can be a multitude of lasers, wavelengths and pulse durations. The laser used in the microvia drilling platform happened to be a UV Diode Pumped Solid State Laser, manufactured by Coherent, called the Avia 7 Watt. This laser generates wavelengths of 355 nm and 266 nm, depending upon which wavelength best suits the intended material.

The ***Wave Front Module (WFM)*** is designed using diffractive beam shaping techniques, however the design used within this system actually shapes the Gaussian laser profile directly into an "airy disk" pattern, then compresses and collimates this airy disk laser beam profile. The unique feature of this type of system is that it doesn't convert the beam into a substantially uniform profile, or flat top profile, as is a common theme within the industry today.

The compressed and collimated airy disk profile output from the diffractive optics is delivered to an adjustable hybrid optic telescope where the final beam size is adjusted. Several other versions of this optical system utilize an aperture as a spatial filter or for added beam sizing. Further wavefront modification has been demonstrated by specific placement of apertures along the distance between the output of the wavefront shaper and the splitter. Combined diffraction of the airy disk profile using an aperture has led to the refinement of on-target beam sizing during imaging. These attributes are part of the pending patent.

The most important module is the ***Splitter Collimator Module (SCM)***. Based on diffractive optics, the splitter divides the incoming beam into two or more beamlets. Each of the beamlets retains the original beam shape properties. Split out at a specific fan out angle, the beamlets are captured into a collimating optic, which takes the form of a prism. Based on the fan out angle designed into the splitter, the collimating prism redirects the beams into two or more parallel beams on that fixed center-to-center pitch.

To provide as much process flexibility as possible, the beam delivery system incorporates a ***Pitch Adjustment Module (PAM)***. Two specific designs were developed for two different chip package designs used.

The first uses a duplicate prism design as was used for the collimator, however it is maneuverable along the beam access to adjust the overlap position and the final beam separation just before hitting the galvanometer's F-theta/telecentric lens system. With this design, the pitch separation between the three beams is held constant. This works very well for fixed pitch grid array applications. It also provides optimum illumination of the clear aperture of the first galvanometer mirror

by allowing all three beams to overlap each other at this location. With galvanometer mechanical speed already limiting microvia throughput, it was important to minimize these mirrors to the smallest size possible.

The second method of pitch adjustment uses three multi-axis MEMs mirrors. The use of micro mirrors allows greater flexibility as well as opportunities for dynamic pitch control of each individual beam in two (2) axes of motion.

The *High Speed Shutter Module (HSSM)* uses three small single axis galvanometers to provide a small angle offset to the beams as they leave the pitch adjustment module. These are placed into two different positions depending on the system configuration.

The *Galvanometer Module (GM)* is a standard design, but in our case two configurations were developed. One uses standard F-Theta lens for applications involving drilling of larger sized microvias and a telecentric design where microvia sizes down to 20 microns are drilled. The galvanometer scanner utilizes a standard two axes X,Y scanner unit with a patented DSP based signal converter that provided optimum signal conditioning. The digital signal conditioning increases the speed of the galvanometer set and synchronizes the galvanometers to the laser pulsing. Figure 13 shows the DSP black box and representative signals for increasing the galvanometer speed.

4. DESIGN METHODS

Our diffractive optic design utilizes both standard and custom optical design programs, such as Code V developed by Optical Research Associates and a NanoVia developed MATLAB suite. The diffractive optical designs were developed and modeled inside these different packages and then the optical coefficients were output to a mask generation and editing program developed and integrated by NanoVia utilizing an AutoCAD environment. The mask data was compiled and sent to Advanced Reproductions in Andover Massachusetts where the final chrome-on-quartz masks were produced. These masks were sent back to NanoVia for photolithography and etching steps. The final optics in wafer-form were then inspected, diced and mounted into specially designs housings at the NanoVia facility (Figure 4 – Mount). Each of the diffractive optical elements was tested independently for quality and performance, after which each were added to the assembly and tested as a complete system.

5. BEAM DELIVERY OPTICAL PERFORMANCE

The beam delivery system is divided into several modules as described earlier. The performance of the entire beam delivery is described in terms of beam characteristics and energy efficiency on a module-to-module basis, culminating in a final on-target energy density. Figure 5 – System Efficiency, shows the drop in energy as a percentage of the total input energy straight from the laser source. Figures 6 through 10 provide beam profile images and line scan intensity profile data at specific points along the beam delivery system and at the target image plane.

The beam intensity patterns were taken with a Sensor Physics CCD profilometer using a custom florescence plate design that enhanced the airy disk rings. The beam image was then computer enhanced using a MATLAB Mathworks[TM] image enhancement algorithm to emphasize the ring structure. The intensity plots were created using a high-speed linear camera that had 7 micron x 200 micron pixels in a linear array of 3000 pixels. The intensity data was transferred into a customized MATLAB Mathworks[TM] mapping file and several data smoothing and averaging algorithms to finalize the plots.

6. PROCESS RATES & QUALITY

The optical system was tested on an R&D breadboard, and the results were significant. The optical system provides 50% greater energy delivery efficiency to the target in comparison to existing systems used in the industry. It also provided greater throughput, because it delivers greater than one beam to the target.

The first generation configuration was a three (3) beam system, but now that more powerful lasers have become available, the second generation has shown the ability for five (5) beamlets or greater. In general, the optical system

breaks through the mechanical bottlenecks that exist within the current generation of one beam technology by allowing a greater number of variable and independently maneuverable beams to be directed through a single galvanometer scanner and F-Theta lens set. The ability to drill with systematically adjusted and shuttered multiple beams is just the first step towards greater throughput milestones. In its first generation configuration, throughput of grid array drilling processes can increase by 200% based on the multiple beam technique alone. With the added efficiency of the shaping and imaging technique, a further increase of 50% was shown.

The overall quality of the microvia is within the industry standard of roundness and acceptable flat top profile (Figure 14). The taper can be adjusted by varying the "energy density on target" and the smallest microvia drill size to date is approximately 25 microns. Further enhancements to galvanometer telecentric lens design and the use of hybrid diffractive imaging methods will push the capabilities of his type of design even further.

7. ILLUSTRATIONS
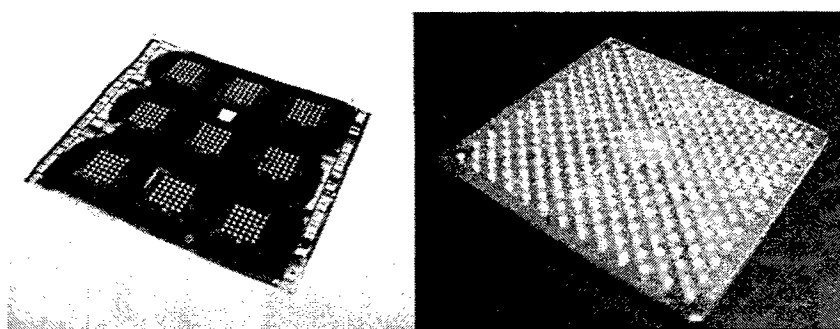
Figure 1 - Chip Packaging
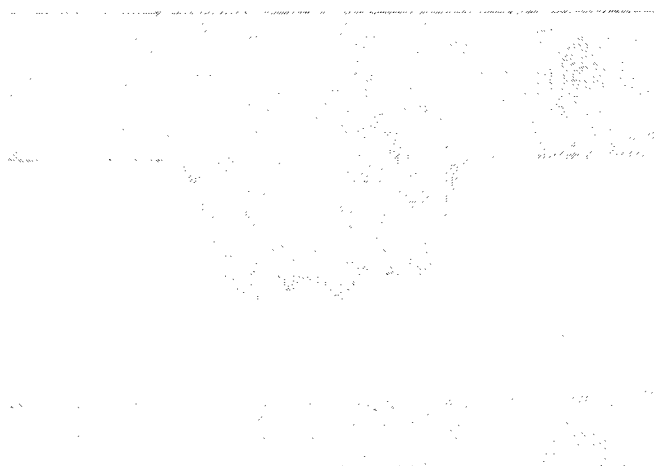
Figure 2 - Uneven Via Drilled In Polyimide
(Current problem with existing flat top shapers in the marketplace)
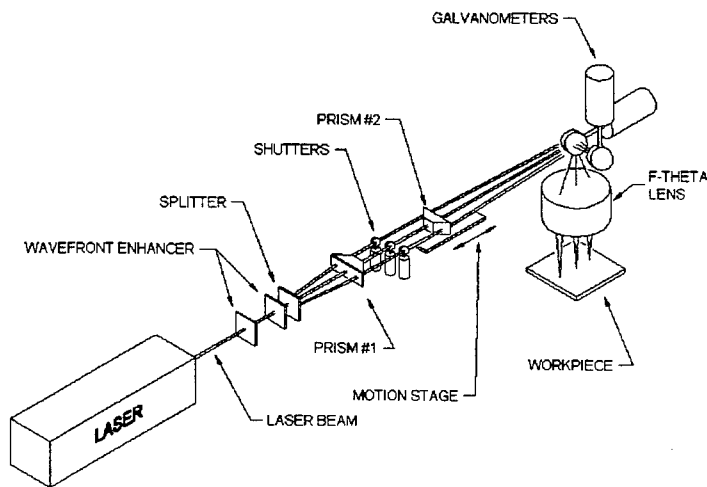
Figure 3 - Patent Optical System Schematic – First Generation
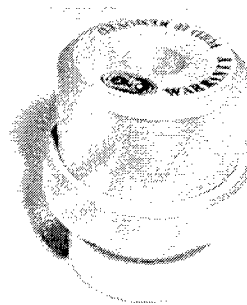
Figure 4 - Optic Mount

Modules	Measure Point	Watts	Efficiency
Laser (Avia 3 Watt)	Output	3.05	100%
Shaper	Output	2.85	93%
Splitter (3 Beam Total)	Output	2.25	74%
Collimator	Output	2.15	70%
Pitch Module	Output	2.10	67%
6 Mirrors	Output	1.95	63%
Galvanometer/Target	Total	1.84	60%

Figure 5 - System Efficiency Chart (Standard Configuration Generation #1)
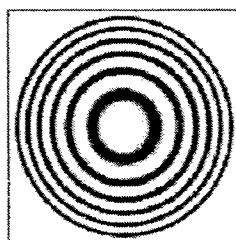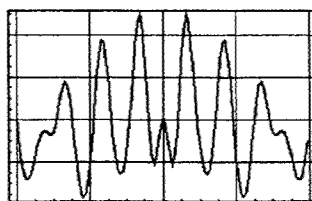
Figure 6 - Intensity & Beam (Computer Generated) Image at Aperture Before Splitter
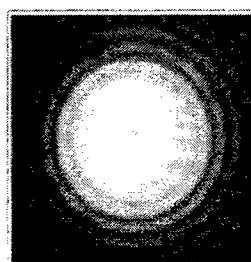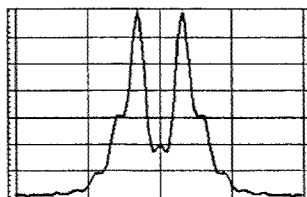
Figure 7 - Intensity & Actual Beam Image at Collimator
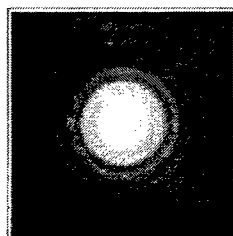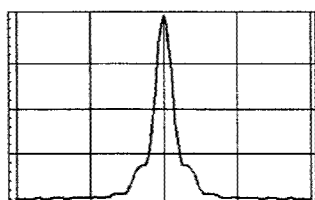
Figure 8 - Intensity & Actual Beam Image at Pitch Adjuster
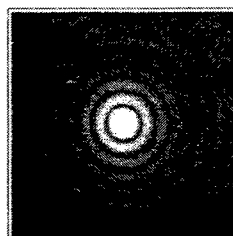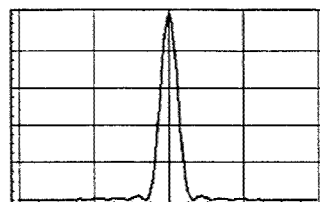
Figure 9 - Intensity & Actual Beam Image at Galvanometer Lens
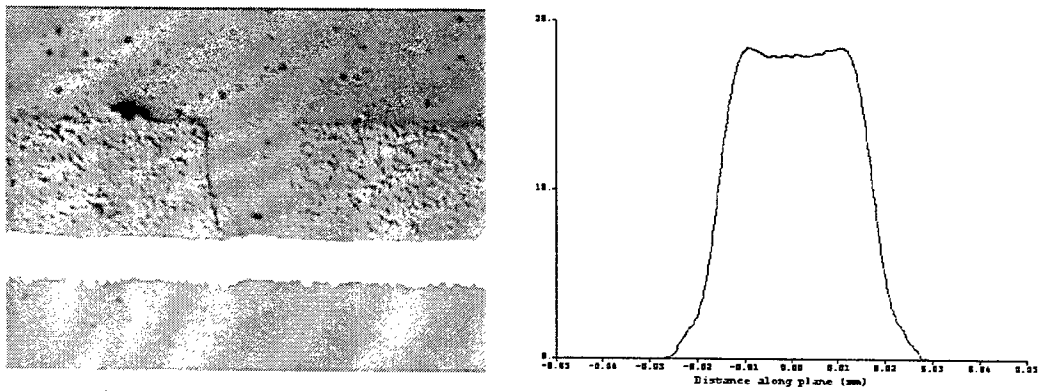
Figure 10 - Beam Profile at Target Material (Cross Section & Line Scan)
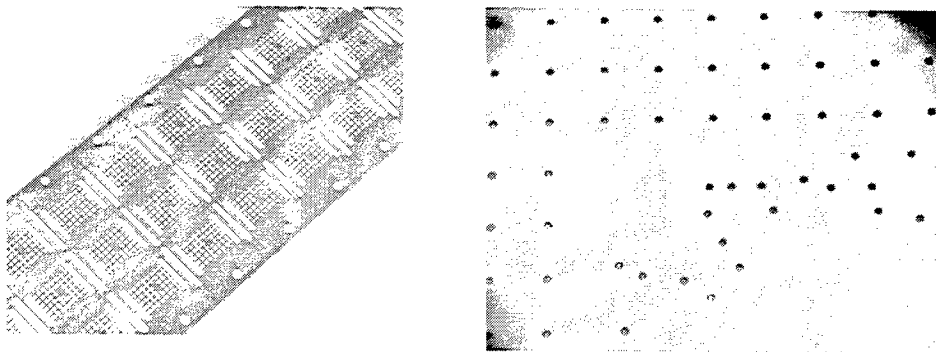
Figure 11 - Drilled Arrays on TAB & BGA Package Inner Layer
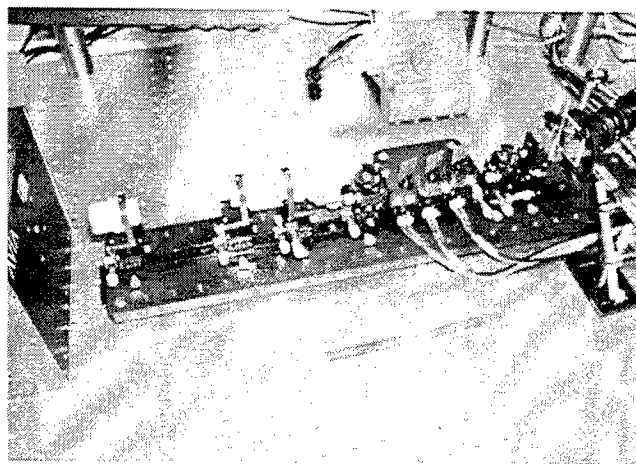
Figure 12 - Optical System Image
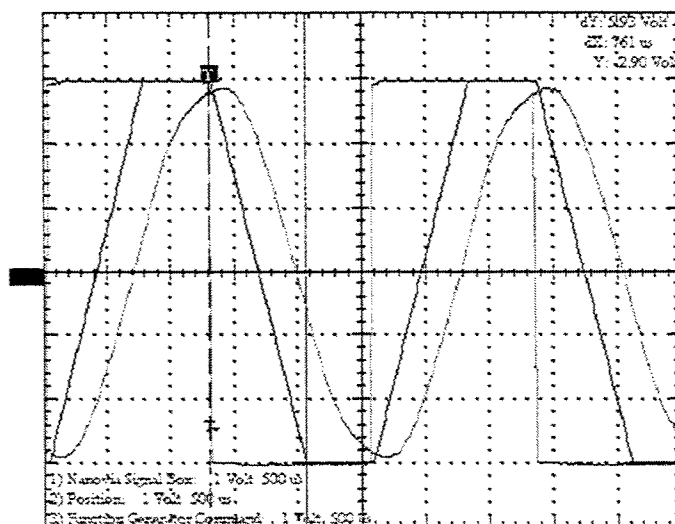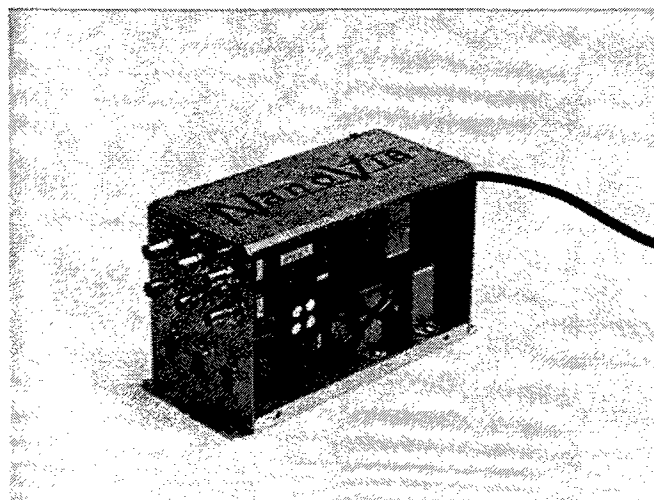
Figure 13 - DSP Black Box (Trapezoidal) & Galvanometer (Position Feedback)
and (Square Wave) Controller Signal
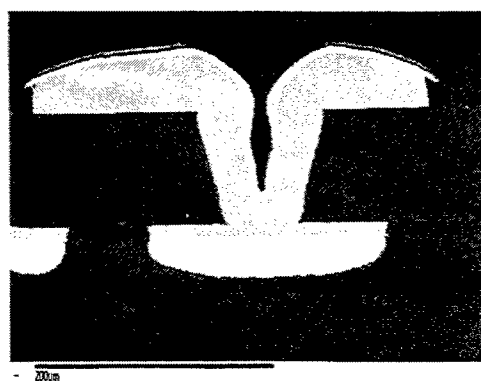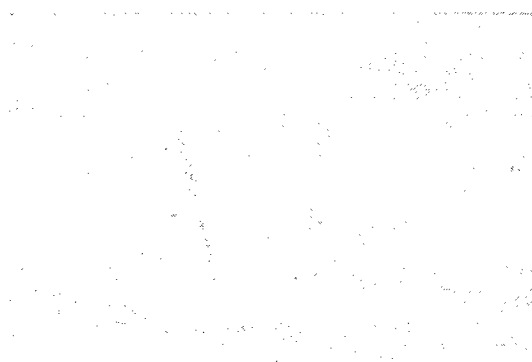
Figure 14 – 50-micron Microvia Through 50 Micron Polyimide (Drilled & Plated)

8. ACKNOWLEDGEMENTS

9. REFERENCES

1.   Schmidt, R., Wundt, K., "Fundamentals of Laser Drilling," EPC European PCB Convention, 1998.
2.   Lizotte, T., Ohar, O., O'Keefe, T. "Laser Drilling Speeds BGA Packaging," Solid State   Technology, September 1996, p. 120-128.
3.   U.S. Patent 6,420,675, assigned to NanoVia, LP.
4.   U.S. Patent 6,310,701, assigned to NanoVia, LP.
5.   U.S. Patent 6,256,121, assigned to NanoVia, LP.
6.   Lizotte, Todd, "Cleaning Laser Debris from TAB Circuits," Advanced Packaging, January 2002, p. 38-40.
7.   Lizotte, T., Ohar, O., Waters, S. Collar, "Excimer Lasers Drill Inkjet Nozzles," Laser Focus World, May 2002, Vol. 38, No. 5, p. 165-170.
8.   Nakahara, Hayao, "Microvias Come of Age," PC FAB, March 2001.
9.   Nakahara, Hayao, "Microvias and MLBs: A Drilling Pattern Forms," PC FAB, May 2000.
10.   Bergman, David, "Forming Microvias," PC FAB, March 2001.
11.   Burgess, Larry, et al., "Laser Technology," PC FAB, January 1999.
12.   U.S. Patent 5,981,880, assigned to IBM.
13.   Sumitomo Electric new release, "Sumitomo Electric has developed a new type of f-theta lens for microvia laser drilling in multilayer printed circuit boards," http://www.sei.co.jp/sn/0111/6a.html, November 2001.
14.   McCormick, Andrea, "Microvias Go Mainstream," Nikkei Electronics Asia, September 2002.
15.   Lau, J. and Pao, Y. "Reliability of BGA, CSP, Flip Chip, and Fine Pitch SMT Assemblies" McGraw-Hill Publishing, 1997.
16.   Kench, S.F. 'Rework Process for Chip Scale Components', Proceedings - Surface Mount International Conference and Exposition, San Jose, California, 1996, Vol. 1, p. 260-264.
17.   Greathouse, S. 'Critical Issues with Chip Scale Packages', Proceedings - Surface Mount International Conference and Exposition, San Jose, California, 1996, Vol.1, p. 203-215.
18.   Yasunaga, M., Baba, S., Matsuo, M., Matsushima, H., Nako, S., Tachikawa, T. 'A Lightly Dressed   LSI Chip', Proceedings IEEE Japan Int. Electronics Manufacturing Technology Symposium, 1994, p. 169-176.
19.   Baba, S., Tomit , Y., Matsuo, M., Matsushima, M., Ueda, n., Nakagawa, O. 'Molded CSP for High Pin Count' ECTC, 1996, p. 1251-1257.
20.   Bauer, C.E. 'Using Chip Scale Packages', Advanced Packaging, July/August, 1996.
21.   Black, R. and MacDonald, V. 'The Impact of CSP on the SMT Assembly Process' SMI 1996, p. 253-256.

New Fiber Lasers with Temporal Pulse Shaping of Nanosecond Pulses for "Tailoring" Flexible Laser Material Processing

Michelle L. Stock[a*], Heinrich Endert[a], and Rajesh Patel[b]

[a]IMRA America, Inc., 1044 Woodridge Ave, Ann Arbor, MI USA 48105;
[b]IMRA America Inc., 48834 Kato Road, Suite 106A, Fremont, CA USA 94538

ABSTRACT

Using an innovative approach based on Yb:fiber amplifiers and pre-shaped pulsed diode seeders, a unique laser source with tunable pulse duration and rectangular pulse shape has been developed. Based on the patented use of multimode fibers with single-mode output, the resultant system provides pulses adjustable between 4 and 20 ns duration with sharp rise times of <1.5 ns, at a repetition rate of up to 20 kHz. The output pulse energy of >15 microJoules can be maintained over the full tuning range. The high-quality output beam is coupled into a polarization-maintaining, single-mode delivery fiber for ease of integration into an application. With this "tailorable" pulse design, control of laser energy deposition in very confined laser interaction zones (by pulse shape), and of its dosage (by pulse duration) can be optimized by the user and adjusted in real-time from the laser controller in response to measured structural changes. Results of machining of materials such as Si, Cr on glass and drilling of Cu/Pl/Cu are presented, showing the unique capability of this laser and its advantageous use to ablate, structure, repair, or trim very small areas (down to sub-micron size) without damaging or influencing the underlying and/or neighboring structures.

Keywords: micromachining, microfabrication, short-pulsed lasers, fiber lasers, fiber amplifiers, nanosecond lasers

1. INTRODUCTION

In order to advance the progress of higher-speed and specialized devices, processing techniques have been a major focus of research and development in microelectronics. A popular tool in the processing of smaller and smaller devices, and in the improvement of yield in other processing techniques, is the laser. Over the years, excimer and Q-switched solid-state lasers have both been employed successfully in industrial settings. However, these lasers do not always provide the optimum laser performance, both in terms of laser parameters and in terms of laser maintenance requirements. Especially when flexibility is needed to meet changing processing goals, and size and reliability are important factors, fiber lasers are providing a new technology platform to meet the stringent needs of industrial users.

Many processing tasks can be done with microJoule-level output in the near infrared wavelength range. Fiber amplified laser systems have been demonstrated to provide microJoule-level (and even up to milliJoule) pulses at 10's of kHz to 100's of kHz with high quality spatial output and robust, compact designs.

Here we present a novel laser design for the production of specialized pulses for microfabrication applications. Using a highly efficient Yb-fiber based amplifier design, this laser produces pulse widths in the nanosecond range with special rectangular and adjustable ("tailorable") short pulse duration. These properties are obtained while maintaining the intrinsic advantages of fiber lasers in terms of high-quality output spatial mode, and robust, compact designs.

.In order to illustrate the utility of such a specialized fiber laser, examples of micromachining using this unique source of time-tailored nanosecond pulses follow. The examples include machining of Si, Cr on glass, and drilling of Cu/Pl/Cu.

*mstock@imra.com; phone 1 734 930-2560; fax 1 734 930-9957

2. FIBER AMPLIFIER TECHNOLOGY

Over the years of laser development, solid-state laser technology has emerged as a mainstay for the production of short and ultrashort pulse durations. However, even during the early days of laser research, optical fibers were identified as an attractive format for laser design[1]. Problems with production of high quality fibers held back progress during the '60's and '70's, but with the advent of interest in fiber-based telecommunications during the '80's, Erbium (Er)-doped fiber technology was improved to the point of making extremely reliable and efficient amplifiers. This provided the basis for Er-fiber based amplifiers to appear on the market in the late- 90's, and several advantages of this technology above solid-state were readily apparent, including extremely compact packaging; lack of need for water cooling; and the inherent TEM_{00} output beam.

The development of optical fiber host materials for lasers followed from that of bulk glass lasers – any dopant that could be used in standard glass could also be used in optical fiber geometry. Neodymium (Nd) and Ytterbium (Yb) fibers of high quality were produced, and in the push to develop fiber lasers with higher average powers and energies (competitive with solid-state lasers), Yb-doped fibers have been at the forefront with efficient amplification and available high power pump laser diodes. All of the record-breaking achievements in fiber-based lasers have been obtained with Yb-doped fibers[2-4] and thus Yb-doped fibers have become the basis of fiber laser products directly competitive with solid-state laser technology.

Although optical fibers have made inroads to compete with solid-state technology, for the development of pulsed fiber lasers, certain limitations must be overcome to reach higher average power and energy levels. As is true in solid-state lasers, the mode-size inside the gain material must be increased in order to extract more average power/pulse energy. However, in fibers, it is also true that the mode-size must be increased in order to avoid the onset of nonlinear effects, which can distort the pulse quality. An increase in the mode-size means an increase in the core diameter, but this leads to multimode operation. The use of large-core, multimode (MM) fiber leads to a problem – the laser output will no longer have the ideal (TEM_{00}-type) properties. We show how this has been overcome by methods developed to allow for single-mode output from multimode optical fibers.

2.1 Large-core (multimode) fiber amplifiers with single-mode output

When employing readily available and fairly standard SM fibers for amplification of short pulses, high-quality spatial output can be obtained, but the amplified power (and thus, energy) is limited, especially when temporal pulse quality must be maintained. In order to achieve amplified output powers allowing for microJoule to milliJoule level energies (necessary for most material processing and microelectronic applications) the necessary increase in core-size brings unwanted side-effects. In particular, in trying to maintain SM operation with large-core diameters, the increase in bending losses associated with such fibers provides a fundamental limit to the ultimate core size.

To avoid this limitation, it is possible to use MM fibers instead of SM fibers. This allows for higher average powers while permitting low-loss transmission without placing excessive requirements on packaging (for instance, without need for very large fiber bend radius, which places the ultimate limitation upon package size). When using MM fiber, however, it becomes much more complicated to provide for the high spatial quality output (lowest order or LP_{01} mode from fiber) necessary for efficient amplification and for high focusability. To overcome this complication, we have developed methods providing for single-mode operation of large-core, MM fibers. These methods include the use of mode-filtering and the minimization of mode-coupling, forcing diffraction-limited operation by design (for more details of innovations developed at IMRA see References 5 and 6). In order to obtain and maintain stable SM output from large core, MM fibers, the use of both processes is necessary.

There are several ways in which mode-filtering can be achieved. These include tapering the distal end of the MM fiber down to the appropriate SM core diameter or splicing a piece of SM fiber to the MM fiber. These types of physical mode-filters in the amplifier allow for stable SM output using fairly straightforward processing steps.

Mode-filtering does not guarantee that mode-coupling (the mixing of higher and lower order modes, causing power exchange and power instability) will not occur within the full length of the amplifier fiber. To maintain SM excitation (and thus, optimum amplification and stable power) mode-coupling must be managed. In principal, the main concern is

power flow between the two lowest-order fiber modes (LP_{01} and LP_{11}). Through proper fiber design, tight control of the fiber fabrication process to minimize phase matching between the two lowest-order modes, governed by the following equation:

$$\frac{2\pi}{\lambda} = \left| \beta_{LP01} - \beta_{LP11} \right|,$$

and through design of the differential modal loss/gain in the fiber (to favor amplification of the LP_{01} mode in the fiber), minimization of mode-coupling can be achieved.

The mechanism for power flow between modes in a multimode fiber is the presence of a perturbation phase-matched to the separation of the modes. Such perturbations can occur through random, microscopic "bends" due to stress, optical defects, or core diameter variations. By introducing large separation between the LP_{01} and LP_{11} modes and higher rigidity during the fiber design (affecting the core diameter and fiber geometry) and by careful control of the fabrication process, intermodal coupling can be reduced by a factor of $\sim 10^4$ times.

Further reduction of coupling out of the LP_{01} mode can be achieved by confining the amplifier dopant, favoring overlap with the LP_{01} mode, or by introducing a bend in the fiber at a radius that increases loss at the LP_{11} mode but has little or no affect on the LP_{01} mode. The impact of these methods is a drop in the intermodal coupling by at least another factor of 2-3 times. In practice, the improvement obtained in the fibers used for this work is on the order of 10^3.

So far, we have focused on the problems that are inherent to working with MM fibers for use as high-quality amplifiers. There are also benefits beyond the aforementioned improved output power / energy. A side-benefit obtained by using MM fiber is higher threshold for the onset of nonlinearities that affect amplification and pulse quality (so prevalent in SM fiber optics). However, this threshold is still within the operation range of amplifiers based on such fibers. In particular, Raman scattering must be avoided since it limits the amount of energy extraction possible.

Raman scattering steals the pulse energy from the input pulse by imparting a red-shift (generating longer wavelength) to the light. This ultimately leads to the wavelength shifting beyond the amplifier's efficient spectral amplification range, and the light becomes useless as a seed for the amplifier. Raman scattering occurs at a critical peak power that is proportional to the fiber's core area and inversely proportional to both the fiber's effective length for nonlinearity, and to the Raman gain coefficient.

By keeping in mind that the strength of nonlinear interactions is down-scalable with increased core size, decreased fiber length, and increased gain, this issue can be alleviated through appropriate fiber and sub-system design.

Considering all of the above factors, careful design of the fiber for large mode-area with good rigidity, appropriate gain profile, minimized Raman gain, and ease of mode filtering is essential to the realization of high-energy pulsed fiber amplifiers.

3. NANOSECOND, "TAILORED" PULSES BASED ON A LARGE-CORE FIBER AMPLIFIER

By understanding and applying appropriate design criteria, large core fiber amplifiers have been made and used for the production of microJoule (and greater) level output energies. The work described below focuses on systems developed with Yb-doped fiber amplifiers (YDFA) because of the high gain and availability of high power pump laser diodes and the record-breaking results obtained with such amplifiers. These robust and reliable fiber-based sources can compete on par with output energy levels from commercial solid-state laser technologies, while providing unique performance capabilities from compact, turn-key systems.

3.1 Background
The first amplified systems demonstrated using large-core YDFAs with SM output were for ultrashort pulse (femtosecond) pulses, for the development of very high peak-power sources. Such sources can be used in certain types of material processing. Use of this novel amplifier, along with chirped-pulse amplification (CPA) methods known to solid-state laser systems[6], resulted in what is known as the Fiber CPA (FCPA) laser system. The application of CPA to fiber amplifiers was pioneered at IMRA[8,5,6]. Chirped pulse amplification is a technique where the seed pulse to be

amplified is first stretched to ~ nanosecond duration, passed through the amplifier, and then "recompressed". Stretching and compression work on the basis of chromatic dispersion, introduced through either glass prisms, diffraction gratings, or in the case of the FCPA stretcher, through optical fiber. The use of the correct sign of chromatic dispersion in the chosen medium causes the faster moving spectral components of the pulse to move faster, and the slower parts to move slower (or vice versa for compressing), causing the pulse duration to lengthen in time (or shorten, in the case of compression). The FCPA fiber amplifier was developed for the amplification of pulses of up to nanosecond pulse duration, making it straightforward to utilize this amplifier for pulses from a nanosecond laser source.

3.2 "Tailored"-nanosecond pulsed system - GX Pulsar

Although there is a great deal of ongoing research and work utilizing ultrashort pulses for many types of microfabrication, the more traditional nanosecond-pulsed sources have already made inroads in industrial applications. Conventional technologies such as excimer and Q-switched solid-state lasers are heavily used, but do not always provide the optimum laser parameters for processing. By adapting the fiber amplifier developed for the FCPA, a new technology for the creation of a source of variable pulse duration and repetition rate, with special temporal properties at the microJoule level is available.

A diagram of such a laser system (the GX Pulsar) is shown in Figure 1. A directly modulated laser diode emitting at 1 um is used as the seed source, providing an input pulse energy to the amplifier of only up to a nanoJoule. This oscillator, driven by a pulse generator, provides "real-time" tunable pulse duration and tunable repetition rate. The tuning range of the pulse duration for our system was limited to 4 – 20 ns, while the repetition rate adjustment range was limited to between 10 and 20 kHz (although in principle it can provide up to 1 MHz). The laser diode has a fiber-pigtailed output, which is attached to an end-pumped large-core MM fiber amplifier module for amplification to the microJoule range. This type of amplifier has been demonstrated to provide up to 100 microJoules, but generally has ~ half of that energy in this system. The high-quality spatial output from the amplifier is shown in Figure 2.
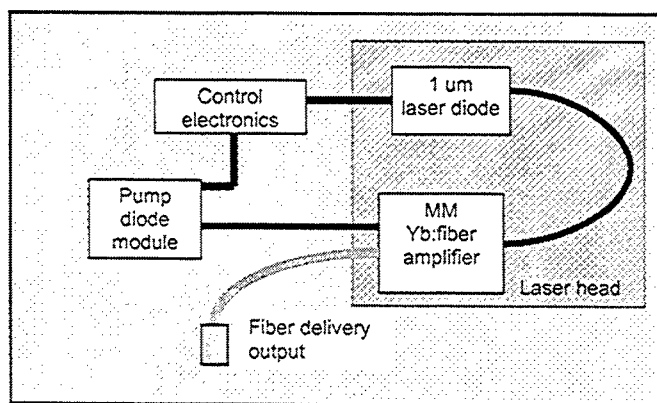
Figure 1. Schematic of GX Pulsar laser system.
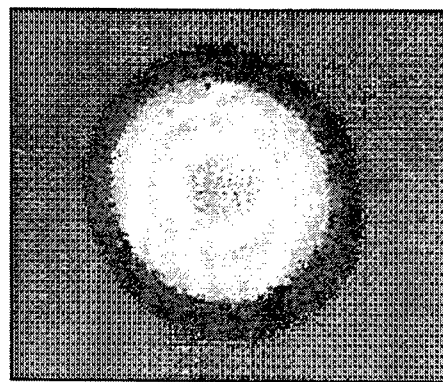
Figure 2. Output of amplifier on CCD camera.

The pump source for the MM YDFA module is a CW, fiber-coupled array of diode lasers. Because the pump source is generally a limitation to the lifetime of the full laser, using a fiber-coupled source allows easy replacement of the pump in the field. This can then extend the lifetime indefinitely, and the pump can be monitored and replaced at convenient maintenance intervals.

Another advantageous use of optical fiber in the GX Pulsar is as an aid to delivery of the laser output pulses for micromachining applications. In the MM YDFA amplifier module, the free-space output is coupled into a SM output fiber cable. The resultant output energy at 10 – 20 kHz is > 15 microJoules.

A photograph of the fully packaged GX Pulsar laser head can be found in Figure 3. The dimensions of this laser head are 18" x 6" x 5".
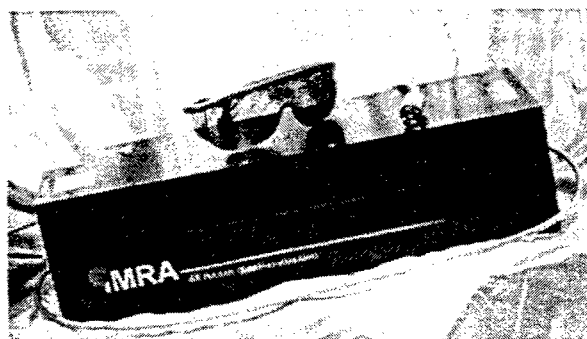
Figure 3. Photograph of GX Pulsar laser head.

The GX Pulsar provides very unique temporal output when compared to other microJoule laser sources of nanosecond pulses. The output pulses, tunable from 4 - 20 ns duration, have sharp rise- times of < 1.5 nanosecond, creating nearly rectangular pulse-shape. Also, both the temporal duration (see Figure 4) and the repetition rate are adjustable on-the-fly. On top of these unusual capabilities, over the limited range of 10 to 20 kHz, the output pulse energy can be maintained. Through a user interface on the control panel, pulse duration and repetition rate can be selected, and the pump current to the pump diode is automatically adjusted to provide constant output energy.
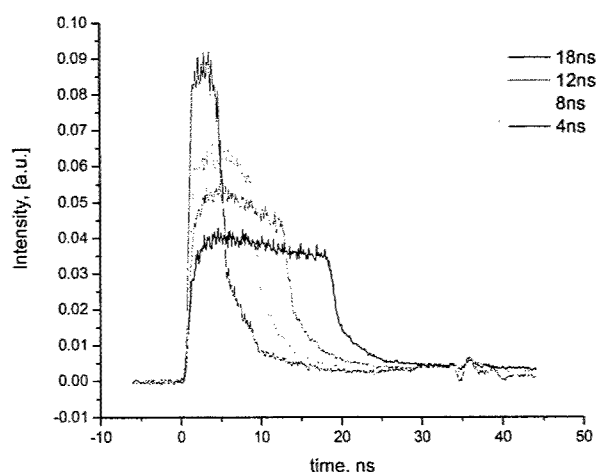
Figure 4. Output pulses showing the adjustment range and nearly-rectangular pulse shape from the GX Pulsar.

A few examples of results of the use of this one of a kind pulsed laser source relevant in potential applications are given in the following section

4. MICROMACHINING USING THE GX PULSAR LASER

As shown in the above, the GX Pulsar creates a distinctive temporal output, while maintaining high quality (and thus, highly focusable) spatial output. Its nearly-rectangular pulse shape owing to the sharp rise-time of the laser pulses is especially useful when working with thin-layer material processing. This type of micromachining capability can be useful in many application fields including semiconductor, microelectronics, medical device manufacturing, and micro marking. To show the potential of this type of nanosecond pulsed laser source, we have performed demonstrations with the GX Pulsar of micro-marking of various metals, removal of Chromium (Cr) from a quartz substrate for a Cr mask,

and fabrication of shallow small features in Si wafers. In all cases, the relatively high repetition rate and fiber delivered output are of great utility for introducing the laser output into a workstation.

4.1 Micro-marking

As miniaturization of components in various industries such as automotive, electronics, and bio-medical continues, it becomes more difficult to track them for identification, repair, or inventory purposes. One way to label such parts is to use laser micro-marking. Results of optimized micro-marking obtained on a couple of steel samples using the GX Pulsar laser are shown in Figure 5. The size of the marking features shown below is on the order of ~150 μm. Larger marking features of up to approximately 1-2 mm, visible to the naked eye, are also possible.
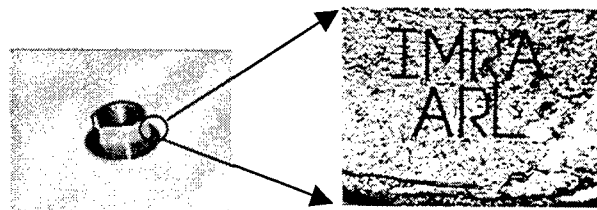
(a)
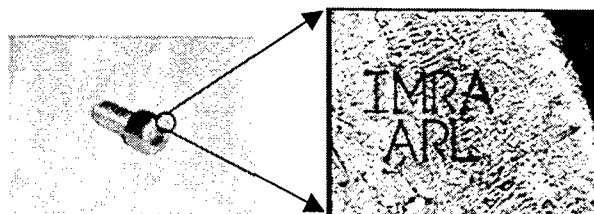
(b)

Figure 5. (a) Micro-marking on a steel nut and
(b) stainless steel cap screw

4.2 Cr mask repair

To examine the ability of the GX Pulsar for removal of thin layers of Cr without damage to the underlying quartz surface, such as is necessary for mask repair applications, a standard Cr on quartz type mask was used. Various process parameters were explored and optimized for cutting 0.8 μm Cr lines found in a test pattern. The smallest possible Cr cut obtained, about 0.2 micron, is shown in Figure 6, requiring twenty shots at 25 nJ per pulse incident on the surface.
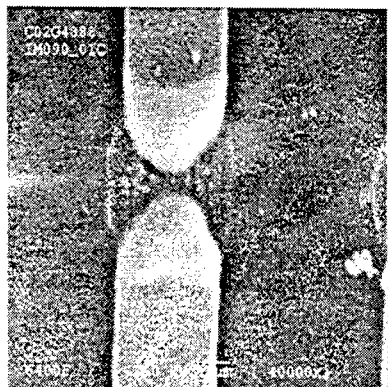
Figure 6. A ~ 0.2 micron long cut of a 0.8 micron wide Cr line on a mask.

4.3 Si wafer machining

In both the microelectronics and biomedical fields, processing of small shallow features in Si is necessary for various applications. Therefore, we tested the use of the GX Pulsar laser for such processing. The results showed that very clean cuts in Si are achievable using this type of laser. Shown below in Figure 7 are examples of very small, shallow features (with a depth of about 5 to 20 microns) created using 6 ns pulses with 10 to 20 µJ of energy per pulse at 10 kHz repetition rate. The sharp rise time of the pulses seems to provide the clean and sharp edge cuts. Even though the thermal damage is found to be nearly negligible in the lateral direction, it is possible to observe a molten "sludge" like material remaining at the bottom of the ablated features. This could be an indication that the GX Pulsar laser is not capable of deep feature ablation in Si.

(a)

(b)
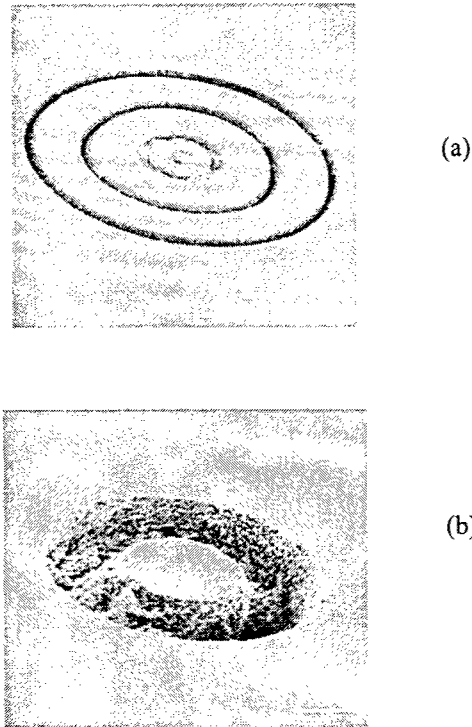
Figure 7. (a) Circular rings of ~ 20 microns widths with a depth of ~10 to 20 microns
(b) A ~ 10 to 20 microns deep doughnut feature with 20 microns pedestal in the middle.

5. CONCLUSIONS

Fiber lasers are now becoming a serious alternative to solid-state and excimer lasers in the arena of industrial material processing. In particular, we describe in this work laser systems developed based on a novel, highly efficient and modular Yb-doped fiber amplifier design. Using this innovative amplifier, we first demonstrated amplification of femtosecond pulses, but then extended it to nanosecond pulse durations. In order to achieve the needed higher energy and power output from a fiber laser (in the microJoule range and beyond) to be competitive with other laser technologies, the use of large core, multimode fiber becomes necessary. We have successfully employed such multimode fiber to attain higher energy and power, while at the same time maintaining single mode fiber quality output, essential for high quality material processing. The basis of this success is the use of physical mode filtering methods along with optimized fiber amplifier designs.

A unique nanosecond laser source made possible using this special amplifier design has been developed. The GX Pulsar provides nearly rectangular-shaped pulses with the capability to change pulse duration on demand, from 4 to 20 ns, and having a repetition rate variable between 10 to 20 kHz. Delivery of a precise dosage of energy can thus be obtained, and

can be optimized on-the-fly for different processing needs. Examples of micromachining including micro-marking of metals, Cr removal, and micromachining of Si using the GX Pulsar proves its effectiveness in applications where thin layers of material needs to be processed.

REFERENCES

1. E. Snitzer, "Proposed Fiber Cavities for Optical Masers", *J. Appl. Phys.*, **32**, 36, 1961; and E. Snitzer, "Optical Maser Action of Nd^{3+} in Barium Crown Glass", *Phys. Rev. Lett.*, **7**, 444-446, 1961.
2. V. Dominic, S. MacCormac, R. Waarts, S. Sanders, S. Bicknese, R. Dohle, E. Wolak, P. S. Yeh, and E. Zucker, "110 W Fibre Laser", *Electron. Lett.*, **35**, 1158-60, 1999.
3. J. A. Alvarez-Chavez, H. L. Ferhaus, J. Nilsson, P. W. Turner, W. A. Clarkson, D. J. Richardson, "High-energy, High-power Ytterbium-doped Q-switched Fiber Laser", *Opt. Lett.*, **25**, 37-39, 2000.
4. A. Galvanauskas and M. E. Fermann, "13-W Average Power Ultrafast Fiber Laser", *Conference on Lasers and Electro-optics (CLEO)*, paper CPD-3, 2000.
5. M. E. Fermann, A. Galvanauskas, and M. Hofer, "Ultrafast Pulse Sources Based on Multi-mode Optical Fibers", *Appl. Phys. B*, **70** [Suppl]., S13-S23, 2000.
6. A. Galvanauskas, "Mode-Scalable Fiber-Based Chirped Pulse Amplification Systems", *IEEE J. Sel. Top. In QE*, **7**, 504-517, 2001.
7. D. Strickland and G. Mourou, "Compression of Amplified Chirped Optical Pulses", *Opt. Comm.*, **56**, 219-221, 1985.
8. M. L. Stock and G. Mourou, "Chirped-pulse Amplification in an Erbium-doped Fiber Oscillator/Erbium-doped Fiber Amplifier System", Opt. Comm,, **106**, 249-252, 1993.

High Brightness Solid-State Laser Systems with Fiber Phase Conjugate Mirrors for Micro Material Processing

T. Riesbeck[*a], H.J. Eichler[a], Enrico Risse[a], A. Binder[b], D. Ashkenasi[b], G. Müller[b]

[a]TU Berlin, Optisches Institut, P1-1, Str. des 17. Juni 135, 10623 Berlin, Germany
[b]LMTB GmbH, Angewandte Lasertechnik, Schwarzschildstr. 8, 12489 Berlin, Germany

Abstract

High beam quality is one of the most important properties for micro material processing with lasers. It facilitates slight focus diameters and due to high Raleigh length even at strong focusing drilling of holes with high aspect ratio. Together with high average output powers it allows fast processes with high quality. Another important point is the wavelength of the laser radiation. Many materials e.g. diamond or silicon show no sufficient absorption at fundamental wavelength of Nd based solid-state laser sources. Frequency conversation to the second and forth harmonic allows the efficient processing of these materials. At least flexible pulse peak power and repetition rate is necessary to optimize the process. Three laser systems which fulfill these requirements are investigated. A pulsed pumped Nd:YAP System which delivers an average output power of 315 W with $M^2 = 2.6$ at the fundamental wavelength and 124 W at the second harmonic. Another pulsed pumped System based on Nd:YAG with an average output power up to 125 W with $M^2 = 2.2$ at the fundamental wavelength, 49.5 W at the second harmonic and 4.75 W at 266 nm. Due to its active Q-switch the pulse peak power of this system is variable in a wide range. Furthermore a continuously pumped amplifier arrangement with nearly diffraction limited output of 120 W average power has been achieved at 10 kHz repetition rate.

Keywords: Solid state lasers, beam quality, phase conjugation, optical fiber, frequency conversation

1. Introduction

High brightness pulsed solid-state laser sources are of great interest for application in industry and science such as high precision materials processing, visible beam generation by non-linear frequency conversion as well as plasma and X-ray production. The brightness B depends linearly on the average output power but quadratically on the beam quality $K=1/M^2$. Thus an improvement of beam quality increases the brightness considerably. In the case of materials processing, higher beam quality (lower M^2 value) leads to smaller beam waists of focused laser beams and higher intensities in the focal region. In conjunction with high average output power the required processing time decreases. The increased Rayleigh length of the laser beam results in deep and narrow cuts with high aspect ratio and low material losses.

Due to phase distortions of laser crystals, such as thermal lensing and thermally induced stress depolarization, the beam quality of conventional solid state lasers decreases rapidly with average output power. To reduce thermal loading, diode pumping can be applied resulting in improved beam quality compared to flash lamp pumped laser systems. In addition, advanced crystal geometry (e.g. slab or disk laser) can be applied to reduce the induced phase distortions [1], [2]. In any case the remaining phase distortions have to be compensated with adaptive mirrors to facilitate near diffraction limited beam quality at average output powers of several hundred Watt. Such mirrors are realized by self pumped phase conjugation based on stimulated Brillouin scattering (SBS), which are, compact and posses a fast response time without additional electronic equipment (e.g. mechanically deformed mirrors). Such SBS-mirrors can be used in oscillators and master oscillator power amplifier arrangements (MOPA). In the case of amplifier systems the beam diameter can be adapted to the amplifier. Here the phase conjugating mirror compensates phase distortions of the amplifier crystal after double or multiple passes through the amplifiers. Therefore a beam with high quality but low average power can be scaled up to the kW-range.

* thomas.riesbeck@physik.tu-berlin.de; phone +49 (30) 314-22449 ; fax: +49 (30) 314-21079,

2. Phase Conjugation By Stimulated Brillouin Scattering

Stimulated Brillouin scattering (SBS) is the major process for the realization of self pumped phase conjugating mirrors. Liquid and gaseous media of high purity as well as solid materials like glass fibers can be used with high efficiency. SBS means interaction between the incident laser beam, the reflected beam and hypersonic waves. Acoustic waves are pressure and density changes, which are correlated with a refractive index modulation. Therefore, backscattering from a sound wave can be regarded as reflection from a multi layer system, comparable to a dielectric mirror. The most important feature of SBS-mirrors is that they are self-induced and any disturbance of the incident wavefront will result in a self-adapted mirror curvature with response times in the ns range. As a result the reflected signal is phase conjugated.

Conventional Mirror   Phase Conjugate Mirror
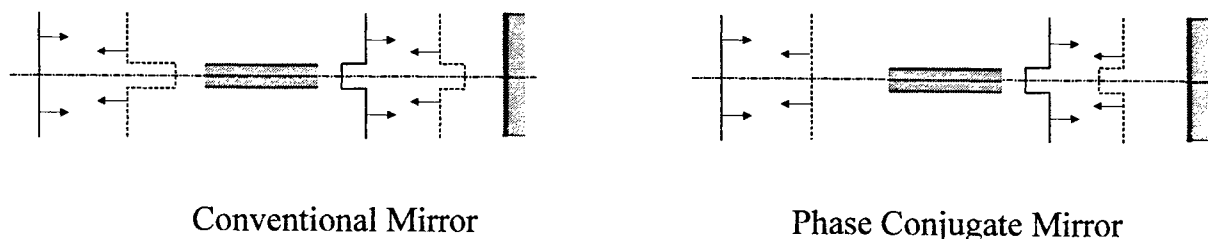
Figure 1: Reflection at a conventional and phase conjugating mirror.

To reduce the power threshold of SBS waveguide geometry can be used. The beam intensity inside the waveguide is high within a long interaction length resulting in low power thresholds. To avoid toxic liquids and gases under high pressure, multimode quartz fibers can be used. The lower Brillouin gain of quartz glass compared to suitable SBS gases and liquids can be overcome using fibers with lengths of several meters resulting in SBS thresholds down to 200 W peak power [3].

3. High Brightness Laser Systems

All setups discussed below are based on the MOPA concept, where a nearly diffraction limited master oscillator beam is increased in power within an amplifier setup After the first amplification pass the beam quality is reduced due to thermally induced phase distortions. The spatially distorted beam enters the SBS-mirror and becomes phase conjugated. As a result the reflected beam propagates along the same trajectory through the amplifier and its phase distortions. The initial beam quality of the master oscillator can be nearly reproduced if the phase distortions remain constant during the beam propagation through the amplifier arrangement. The amplified beam can be extracted with help of an optical isolation. The beam quality measurements were carried out according to the international standard "Test methods for laser beam parameters", ISO/CD 11 146.

3.1 ND:YAP MOPA System with 315 W Average Output Power

<u>Master oscillator</u>
All conditions for a suitable master oscillator can be satisfied using a flat mirror ring resonator as shown in Figure 2. The system is flash lamp pumped at a repetition rate of 100 Hz with a pumping energy of 17 Joule per shot. The pumping chamber contains an europium doped glass filter to achieve high efficiency and to protect the YALO crystal (4 mm x 79 mm) against color center formation. The uni-directional operation is realized using an external feedback mirror. The energy stability from shot to shot is about 1%. An intracavity tilted etalon with a thickness of 2 mm and a reflectivity of 73% reduces the spectral bandwidth resulting in a coherence length of approximately 30 cm. The average output power is 4.7 W in a diffraction limited beam.
For variable pulse peak powers chromium doped YAG-crystals are used as saturable absorbers to obtain passive Q-switch operation. Due to a saturation intensity of about 9 kW/cm² the oscillator emits usually a burst of pulses per flash. With an absorber length of 2 mm and a doping concentration of 0.15 at.% Cr^{4+} about 28 pulses are generated per flash lamp shot.

The single pulses show half widths between 150 ns and 170 ns (FWHM). Using different absorber lengths the number of pulses and therefore the peak power can be adjusted. For an average output power of 4.7 W the burst energy is 47 mJ at 100 Hz repetition rate. Assuming 28 pulses in one burst the single pulse energy is 1.7 mJ and the peak power about 10.6 kW.
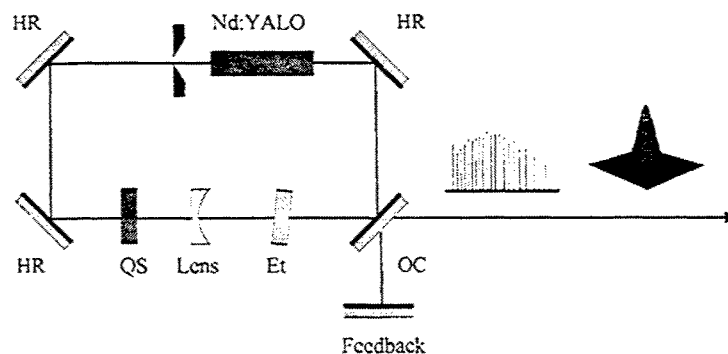
Figure 2: Nd:YALO master ring resonator with passive Q-switch. (HR: High reflective Mirror, QS: Passively Q-switch, Et: Etalon, OC: Outcoupling mirror)

Amplifier setup

With regard to the advantages of a parallel amplifier setup a solid state laser system containing four amplifiers and a master oscillator was developed (Figure 3). The system consists of a parallel arrangement of two double pass amplification stages with phase conjugating mirrors. After double pass amplification the two beams are combined again using a thin film polarizer. Optical systems between the amplifiers guarantee the variability of average pumping power without damaging optical components. Four commercially available pumping chambers from an industrial laser system are used as amplifiers in two parallel chains. The Nd:YAP rods with a diameter of 8 mm and a length of 160 mm are pumped by two flash lamps in specular cavities, with an average pumping power of 6 kW each. To achieve a high extraction efficiency the amplifiers are driven in a double pass arrangement. The oscillator beam passes an optical isolation, which prevents imperfectly polarized backtravelling parts of the beam entering the oscillator. Due to the additional components in the beam path, the power input in front of the amplifiers is reduced to 4.0 W.
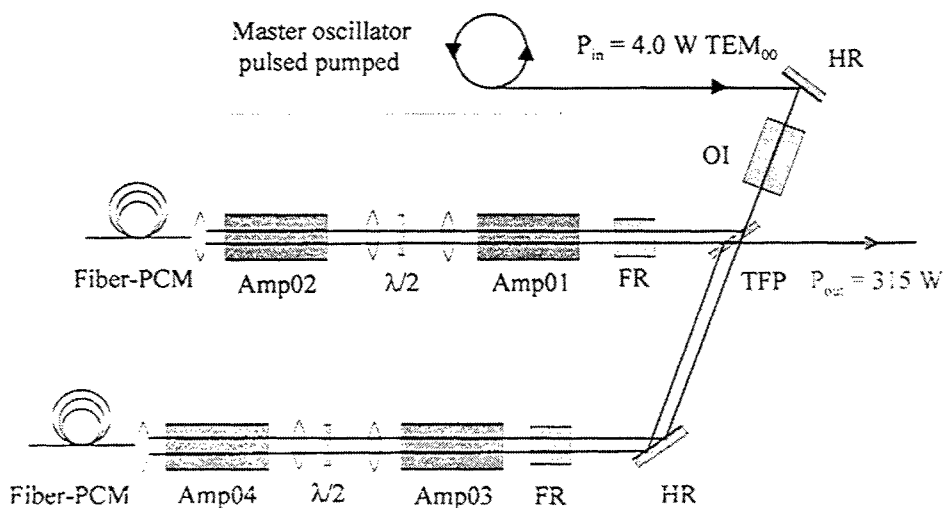
Figure 3: Setup of a four amplifier MOPA system with phase conjugating mirrors

Then the beam is splitted at the TFP in to each other perpendicular polarized parts onto the two chains. By passing a Faraday rotator the polarization plane of each beam is rotated by an angle of 45° and is then amplified by the two serial amplifier arrangements. To compensate for astigmatic thermal lenses the amplifier rods are rotated by 90° to each other and the polarization is matched again by a half wave plate. After the single pass the beam is coupled into the fiber phase conjugator. The beam is phase conjugated by a multimode silica step index fiber with a core diameter of 200 μm, a numerical aperture of 0.22, and a length of 2 m. After an additional amplifier pass the initial beam quality is almost reproduced and the beam is rotated again by an angle of 45° after passing the Faraday rotator a second time. After the two passes through the Faraday rotator the polarization plane of each beam is rotated by 90° and therefore could be extracted at the TFP. Here the amplified beams of both chains are superposed automatically due to the optical properties of the phase conjugated signal.

Applying a parallel amplifier arrangement an average output power up to 315 W is achieved at 2 kHz average repetition rate. Figure 4 shows the measured output power as a function of the oscillator power. The beam propagation factor M^2 was determined to be smaller than 2.6 for both directions in space [4].
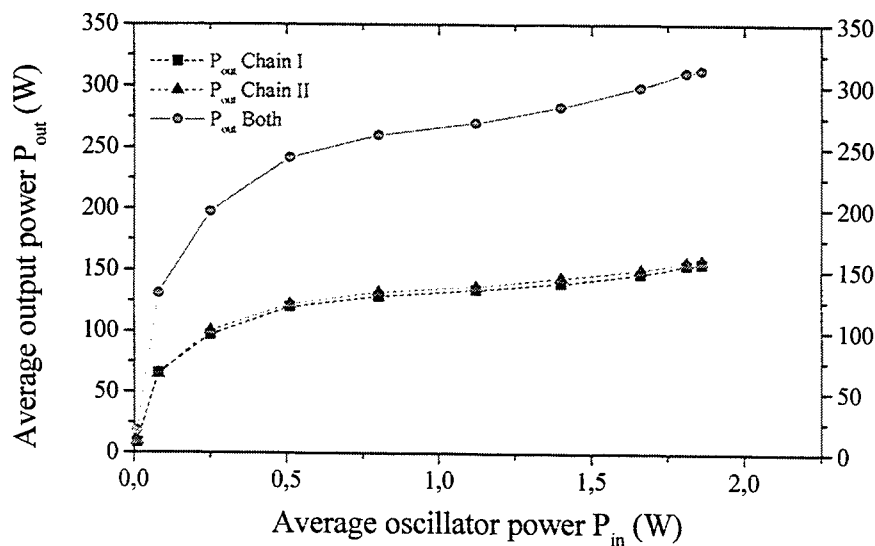
Figure 4: Measured average output power as a function of the oscillator power

Frequency conversation

For second harmonic generation (SHG) at the wavelength $\lambda = 540$ nm KTP (Potassium Titanil Phosphat) is used, a nonlinear crystal which is suited for phase matching Typ II. For forth harmonic generation BBO (β-Barium Borate) is used. In Table 1 the important properties of the used crystals are listed.

	KTP	BBO
Chemical notation	Potassium Titanil Phosphat	β-Barium-Borate
Formula	$KTiOPO_4$	$\beta\text{-}BaB_2O_4$
Phase matching	Typ-II	Typ-I
Temperature	60° C	40° C
Dimensions	6 mm x 6 mm x 15 mm	5 mm x 5 mm x 10 mm

Table 1: Important properties of the used crystals

The both crystals are cutted for a certain operating temperature at which the condition of phase matching is fulfilled. Therefore the crystals are placed in ovens to stabilize their temperature. For phase matching Typ II the second harmonic beam is generated from two perpendicular polarized parts of the fundamental beam. Due to the phase conjugation properties of the output from the laser system both superposed beam parts can be used for conversation. Therefore high average SHG output power (see figure 6) can be achieved. In figure 5 the setup for SHG is depicted. The setup for FHG is similar.
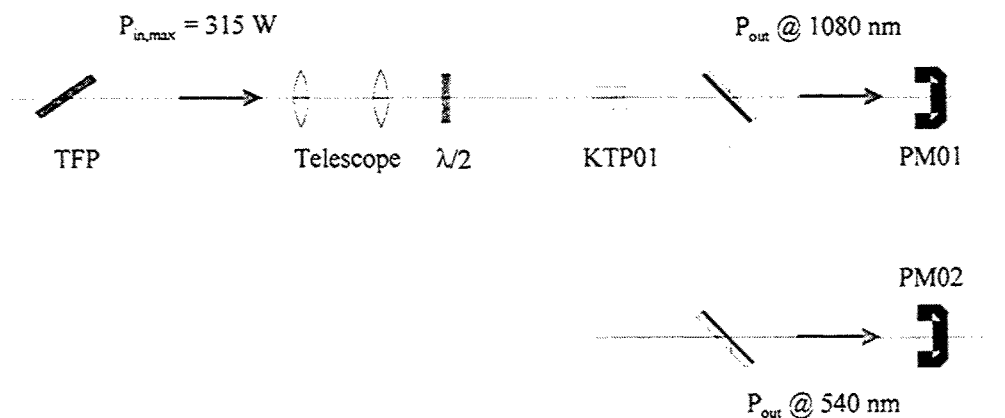
Figure 5: Setup for second harmonic generation
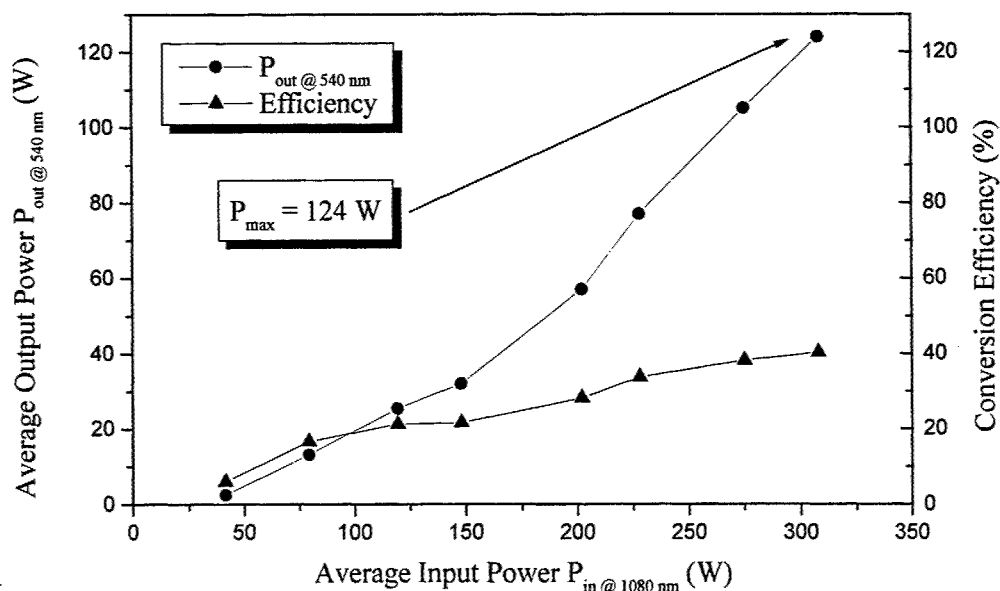
Figure 6: Measured average output power @ 540 nm as a function of the average input power

At FHG with BBO 5 W average output power @ 270 nm has been achieved. Generation of gray tracks made it impossible to obtain higher stable output.

3.2 ND:YAG MOPA System with 124 W Average Output Power

In laser media which preserve a circular state of polarization, like the cubic crystal Nd:YAG, single longitudinal mode (SLM) operation could be fulfilled in linear resonators. Spatial hole burning in linear resonators leads to low coherence length because several longitudinal modes occurring in the laser process. This problem can be solved elegantly by using a "twisted mode" design.

Master oscillator

In such a setup the active medium is positioned between two quarterwave plates and an additional polarizer is placed in the resonator, see figure 7. This causes a circular state of polarization and thus an uniform intensity distribution inside the active medium. Thus spatial hole burning doesn't occur and the resonator work in single longitudinal mode operation. The system is flash lamp pumped at a repetition rate of 100 Hz with a pump energy of 25 mJ per shot. The pumping chamber contains an europium doped glass reflector to achieve high efficiency and to protect the YAG crystal (5 mm x 140 mm) against color center formation.. The average output power is 6 W in a diffraction limited beam.

The master oscillator is optimized with respect to high temporal stability. For variable pulse peak powers an acusto optical modulator (AOM) is used, thus it is possible to generate pulses from one single pulse to 35 pulses during one pump pulse. So the average repetition rate could be varied from 100 Hz to 4 kHz. The single pulses show half widths between 27 ns (single pulse) and 120 ns (FWHM). Varying the number of pulses and thereby the pulse energy and pulse peak power make it possible to adjust the proper conditions for phase conjugation.
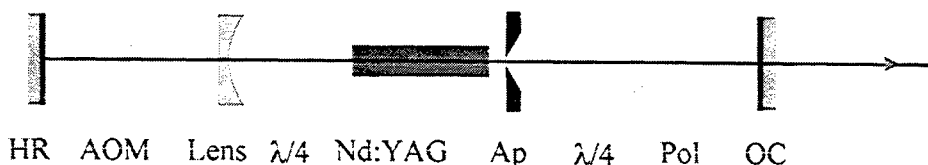
Figure 7: Linear Nd:YAG resonator in "twisted mode" operation. (HR: High reflective Mirror, AOM: Acusto optic modulator, $\lambda/4$: Quarterwave plate, AP: Aperture, Pol: Polarizer, OC: Outcoupling mirror)

Amplifier setup

The output from this master oscillator is coupled into a cascaded amplifier setup based on two amplifiers, see figure 8. Here the amplifiers consists of two Nd:YAG rods (9.5 mm x 152 mm) in the same cavities as in the system above. As mentioned above it is necessary to compensate for the birefringence occurring in Nd:YAG during strong optical pumping e. g. by a telescope together with a 90° rotator. With such a setup it is possible to keep the part of depolarised light below 4% over the whole pumping range.
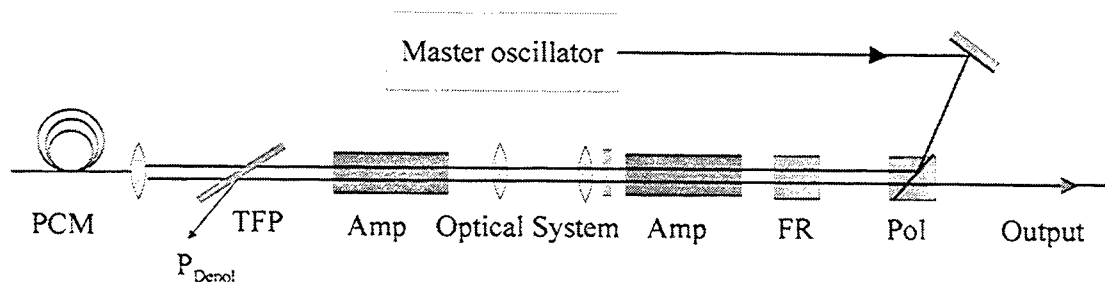
Figure 8 : Setup for a cascaded amplifier arrangement.

As a result of the better crystal qualities of YAG in comparison to YALO it is possible to operate such a MOPA system in single pass with acceptable beam quality. With the system depicted in figure 8 (without fiber PCM) we achieved an average output power of 86 W (35 burst pulses leads to an average repetition rate of 3.5 kHz) with the great advantage, that the

flexibility given by the active Q-switch can be used fully without respect of the phase conjugating conditions in the optical fiber. This is very important for material processing or high power frequency conversion. The beam quality was $M^2 < 2.4$ in both spatial directions. However it is possible to increase both average output power and beam quality by applying a fiber PCM in the single pass system (Figure 8). The output power could be increased to 124 W while the beam propagation factor M^2 was determined to be smaller than 2.2 for both directions in space. Figure 9 shows the measured output power as a function of the oscillator power.
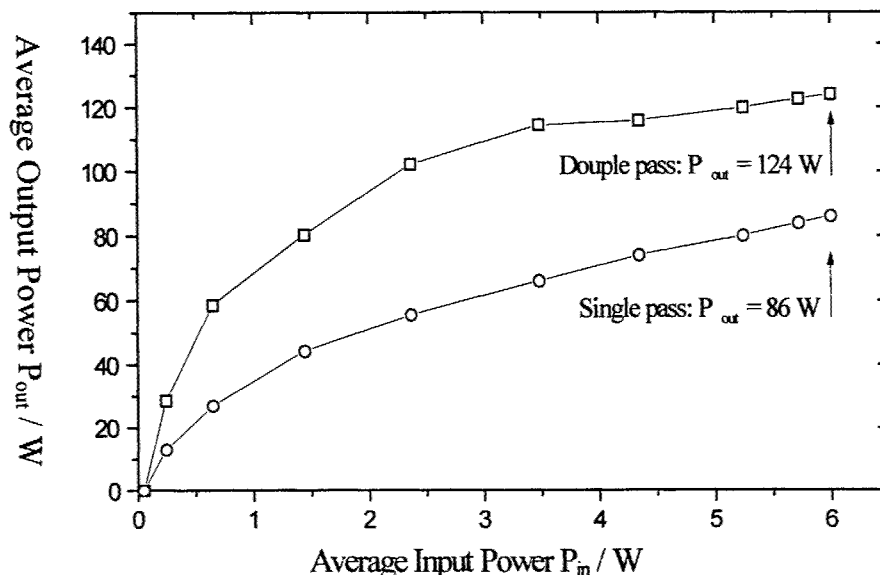
Figure 9: Measured average output power as a function of the oscillator power

Frequency conversation
The frequency conversation of this system was made in the same scheme as described in section 3.1. Crystals cutted for the fundamental wavelength of $\lambda = 1064$ nm was used with the following properties:

	KTP	BBO
Chemical notation	Potassium Titanil Phosphat	β-Barium-Borate
Formula	$KTiOPO_4$	$β-BaB_2O_4$
Phase matching	Typ-II	Typ-I
Temperature	80° C	40° C
Dimensions	5 mm x 5 mm x 20 mm	5 mm x 5 mm x 10 mm

Table 2: Important properties of the used crystals

The following output power could be achieved:

- SHG: 49.5 W @ 532 nm
- FHG: 4.75 W @ 266 nm

3.3 Continuously Pumped Nd:YAG MOPA System With Birefringence Compensation

For many applications, e. g. fast material processing cw exciting lasers with several kHz repetition rates and high brightness become of great interest. To reach high gain in amplifiers multi pass setups are necessary. Assuming a maximum average oscillator power of around 10 W and a repetition rate of 10 kHz the pulse energy cannot exceed 1 mJ. Taking a saturation energy density of 500 mJ/cm² for Nd:YAG into account, the amplifiers would operate far below their saturation fluence resulting in a small extraction efficiency. The extraction efficiency can be improved by increasing the number of amplifier passes. Therefore a four pass amplifier arrangement is applied.

Master Oscillator
The developed master oscillator is depicted in Figure 10. It consists of a diode pumping chamber, an acoustooptic modulator (AOM), an etalon, a thin-film polarizer (TFP), an output coupler and high reflectivity mirrors. The ring resonator is applied to avoid spatial hole burning. The external feedback mirror facilitates clockwise unidirectional operation. As active medium a Nd:YAG rod is used with a length of 56 mm and a diameter of 4 mm.
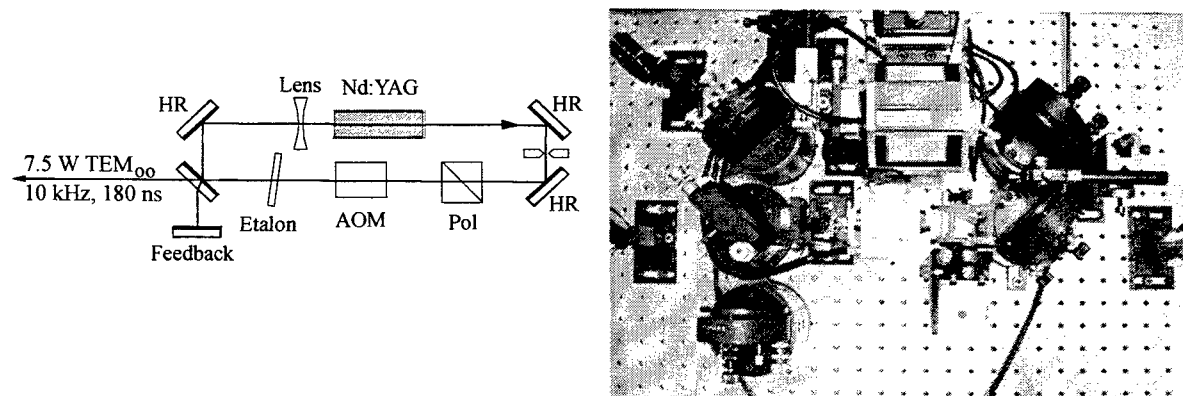
Figure 10: Scheme (left) and picture (right) of the developed cw diode pumped Nd:YAG master oscillator

A lens with a focal length of f = - 800 mm increases the fundamental mode diameter. Q-switching operation is obtained using an AOM with a repetition rate of 10 kHz and an RF driver power of 100 W. The oscillator provides an average output power of 7.5 W with a nearly diffraction limited beam quality.

Amplifier Setup
Two commercially available pumping chambers from an industrial laser system are used as amplifiers. The identical Nd:YAG rods with a diameter of 4 mm and a length of 56 mm are diode pumped. The oscillator beam passes an optical isolation and is amplified in a serial amplifier arrangement. To compensate for thermally induced stress birefringence in the active media the well known relay-imaging setup containing two lenses and a 90° quartz rotator is used. Birefringence compensation results in depolarization losses below 1.3 % after passing both amplifiers in a single pass. After the first amplification pass, the beam is collimated and reflected using a conventional curved HR-mirror.
The polarization direction is rotated by 90° passing the quarter wave plate twice. During the second pass the beam is amplified again and coupled into the fiber phase conjugator. After the double pass the depolarization losses are below 2.3 %, see Figure . The beam is phase conjugated in a multimode silica step index fiber with a core diameter of 50 μm, a numerical aperture of 0.22, and a length of 10 m. After two additional amplifier passes the initial beam quality is reproduced and the beam is extracted with help of the optical isolation. Applying the four pass scheme to the serial amplifier arrangement an average output power up to 31 W is achieved at 10 kHz repetition rate. Figure 11 shows the measured output power as a

function of the oscillator power. Applying the four pass scheme the times diffraction limit factor M^2 was determined to be smaller than 1.3 for both directions in space.
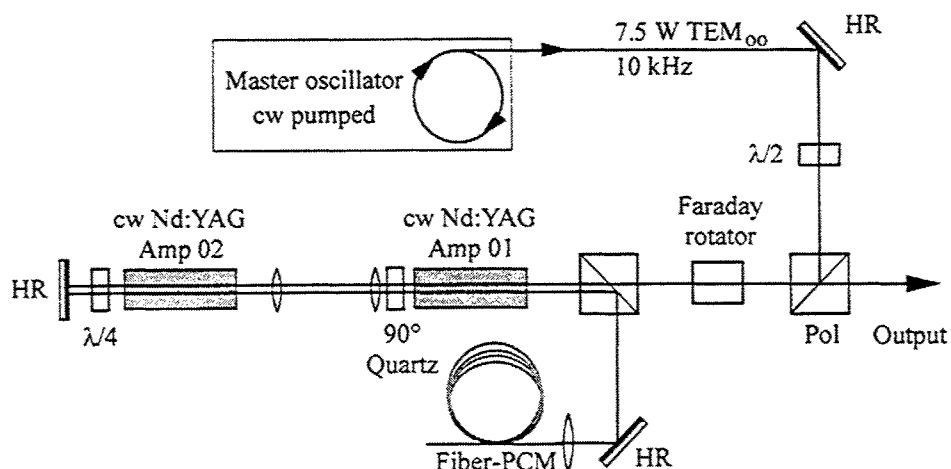
Figure 11: Continuously diode pumped MOPA system with four pass amplifier arrangement and fiber phase conjugator
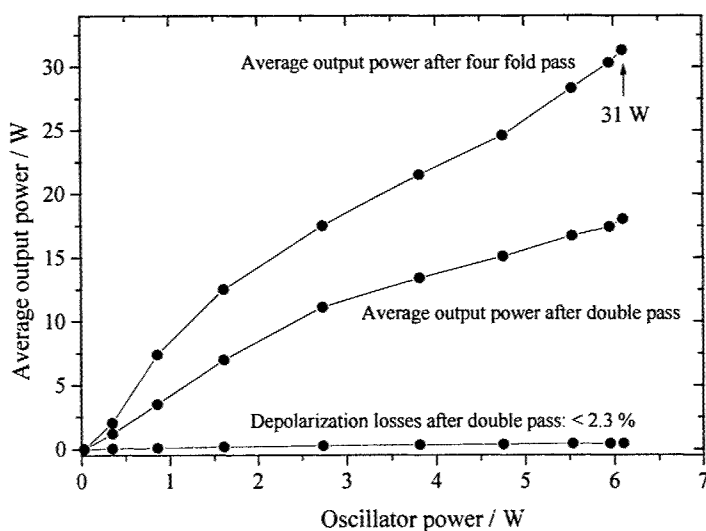
Figure 12: Measured average output power vs. oscillator power of the four pass MOPA system.

Further output power scaling possible. In addition two further pumping chambers are to be used. After double pass through the first two amplifiers the polarization of the laser beam is rotated about 90° and reflected at a Glan Laser Prism into the further two pumping chambers (Figure 13). Here the beam is amplified in the same scheme as described above in double pass. After this amplification passes the beam is coupled into the fiber phase conjugator. The beam is phase conjugated in a multimode silica step index fiber with a core diameter of 200 µm, a numerical aperture of 0.22, and a length of 5 m. After eight additional amplifier passes the beam is extracted with the help of the optical isolation. Applying this scheme an aver-

age output power up to 121 W is achieved at 10 kHz repetition rate with a nearly diffraction limited beam quality, see figure 14.
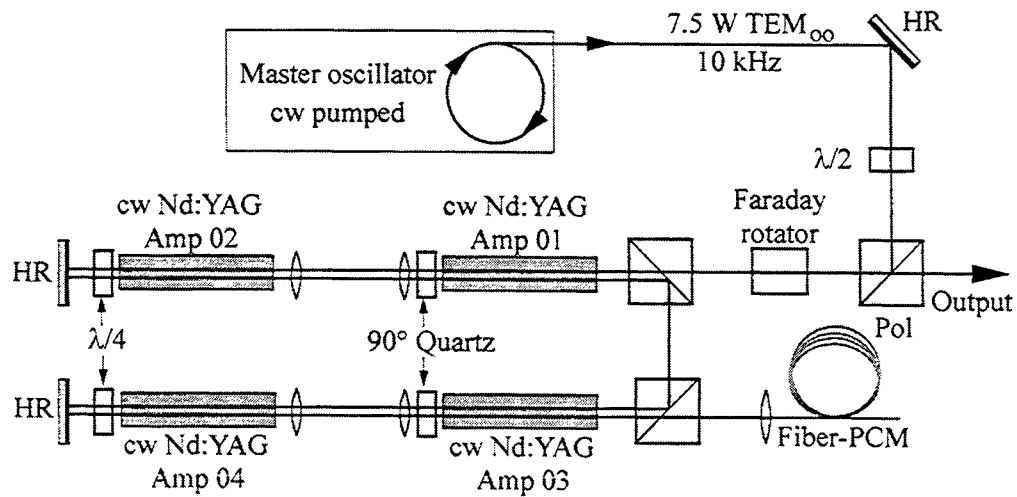
Figure 10: Setup of a MOPA system with four power amplifiers
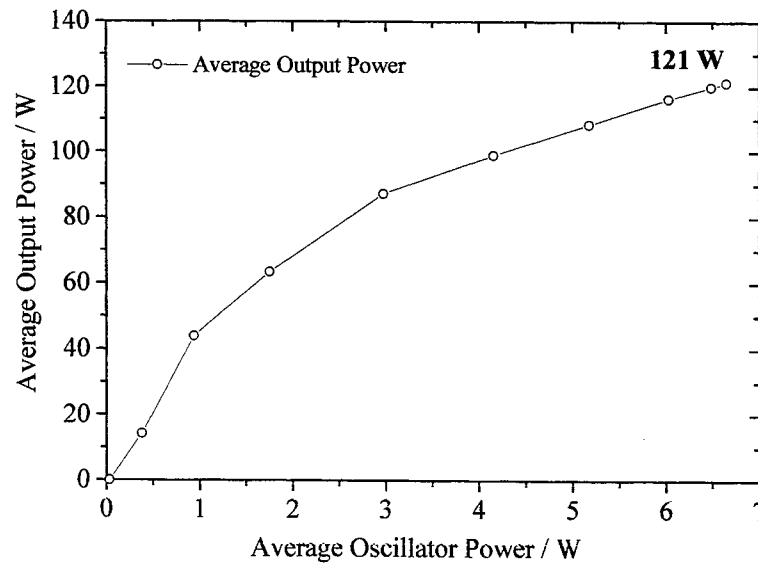
Figure 11: Output power vs. oscillator power of the MOPA system with four amplifiers

Summary

We have reported about multi kHz diode and flash lamp pumped MOPA systems with high beam quality which supply average output powers from several ten up to 315 W. Due to phase conjugation by stimulated Brillouin scattering in optical

fibers the master oscillator beam quality can be largely reproduced after double pass amplification. In parallel amplifier arrangements the average output power can be extended to several hundred Watt. Two serial amplifier chains in a parallel arrangement supply average output powers up to 315 W with high beam quality, corresponding to an M^2 value better than 2.6 for both directions in space. Due to optical systems between the amplifiers the average output power can be tuned easily by the variation of pumping power.

A further scientific and technical challenge is the extension of phase conjugation to continuous wave systems. With an advanced setup it was possible to achieve 121 W average output power in a continuously pumped system

Meet the author

Thomas Riesbeck was born in July 1961 in Schwanheim, Germany. Following 12 years employment in industry and the German Government he began started studying physics and received his diploma degree at the Optical Institut of the Technical University of Berlin (TUB) in September 1998 having completed a thesis on high power MOPA systems. After six months employment at the LMTB Berlin he started his Ph. D. at the TUB on phase conjugation for high power lasers in optical fibers.

E-Mail: thomas.riesbeck@physik.TU-Berlin.de
Phone: +49-30-314 22449
Fax: +49-30-314 21079

References

[1]   GIESEN, A.; HOLLEMANN, G.; JOHANNSEN, I.: *Diode-pumped Nd:YAG thin disc laser*. Technical Digest. CLEO '99, p.29-30, 1999.

[2]   HONEA, E.C.; BEACH, R.J.; MITCHELL, S.C.; SKIDMORE, J.A.; EMANUEL, M.A.; SUTTON, S.B.; PAYNE, S.A., AVIZONIS, P.V.; MONROE, R.S.; HARRIS, D.G.: *Dual - rod Yb:YAG laser for high-power and high-brightness applications*. OSA Trends in Optics and Photonics. Advanced Solid State Lasers. Vol.34. Proceedings p.42-7 2000.

[3]   EICHLER, H. J; MOCOFANESCU, A.; RIESBECK, TH.; RISSE, E.; BEDAU D.: *Stimulated Brillouin scattering in multimode fibers for optical phase conjugation* will be puplished in Optics Communication 2002.

[4]   RIESBECK, TH.; RISSE, E., EICHLER, H. J;: *Pulsed solid-state laser system with fiber phase conjugation and 315W average output power*, Applied Physics B (Laser and Optics) Vol 73, pp. 847-849, 2001.

New Developments in Laser Processing of Silicon Devices

Manfred Dirscherl[a], Gerd Esser[a], Stefan Kaufmann[b], Manfred Geiger[b]

[a]Bayerisches Laserzentrum (BLZ gGmbH), Konrad-Zuse-Str. 4-6, D-91052 Erlangen
[b]Chair of Manufacturing Technology, Univ. of Erlangen, Egerlandstr. 11, D-91058 Erlangen

ABSTRACT

Silicon is the standard material for the production of integrated circuits and one of the most important substrates for micro systems technology. It can be produced with an extraordinarily high purity, homogeneity and crystal perfection. Today, laser processing of silicon is becoming increasingly more interesting. This can be partly attributed to the evolution of frequency-converted solid state lasers which emit visible or ultraviolet radiation that is readily absorbed by silicon. Another reason for the growing interest in laser processing of silicon devices is that conventional technologies are approaching their limits. Especially laser cutting of thin silicon wafers as an alternative to mechanical sawing represents a very promising option for industrial applications. This paper shows current research results on laser processing of silicon. Besides laser cutting and ablation with frequency-tripled Nd:YAG lasers and Ti:Sapphire femtosecond lasers, laser welding of silicon with millisecond pulses is a focus of the presented work. When welding Si, the brittle behaviour of the material usually leads to thermally induced cracks. These cracks do typically not occur when cutting with short and ultrashort pulsed lasers. A controlled heating of the work piece can prevent cracks during welding with millisecond pulses as well. Together with laser cutting and welding, laser adjustment of silicon components by ultrashort pulse ablation of pre-stressed layer systems, which is also described in this paper, is another promising approach for high precision manufacturing of silicon micro devices.

Keywords: silicon, laser welding, laser cutting, laser adjustment

1 INTRODUCTION

SIGNIFICANCE OF SILICON

Silicon is definitely one of the most important materials in this century. Practically all integrated circuits and active electronic components are made of mono-crystalline silicon due to its outstanding semiconducting qualities. Moreover, a lot of innovative applications also exist for poly-crystalline silicon. Both, solar cells and active matrix displays for mobile computers require thin functional layers of poly-crystalline silicon.

Micro-electro-mechanical systems (MEMS) – integrated microsystems of sensors, actuators and associated electronics – represent an intensely emerging field which has just raised its first set of commercial products, such as pressure-, flow- and acceleration sensors, inkjet printer heads and micro-chemical analysis reactors. For all of these innovative applications as well as for those many others which will definitely follow due to the enormous technology push in this area, silicon as the substrate material is clearly dominating the market [1]. It is also widely assumed that this situation will not change in the near future, as the attractiveness of silicon due to its exceptional quality at low cost, its outstanding electrical, optical and mechanical properties and the possibility to directly integrate electronic circuits on the microsystem substrate cannot be offered by any alternative material.

MATERIAL PROPERTIES OF SILICON

Silicon is a semi-metallic chemical element. Its state of aggregation at ambient temperature is solid whereas its lattice structure may be mono-crystalline, poly-crystalline or amorphous. For most applications in electronics and optoelectronics the mono-crystalline structure with its extraordinary physical properties is first and foremost relevant. Silicon is a semiconductor, its conductivity can be influenced by temperature or by doping with impurity atoms. Its

outstanding physical properties – such as for example high thermal conductivity and mechanical stability – make it the ideal material for applications in microelectronics production. Silicon is not only used for active semiconductor layers but also as a substrate material. Table 1 summarizes the most important properties of silicon. It should be noted that the density of silicon differs in liquid and solid condition. The density rises during melting, i.e. the volume decreases by about 9% during phase transformation, which causes enormous thermal stress when silicon is melted, as for example when welding it (see Chapter 2).

Melting point	T_M	$= 1687$ K
Boiling point	T_B	$= 3504$ K
Density (300 K)	ρ	$= 2{,}329$ g/cm³
Density (1687 K, solid)	ρ_{solid}	$= 2{,}30$ g/cm³
Density (1687 K, liquid)	ρ_{liquid}	$= 2{,}51$ g/cm³
Thermal expansion (300 K)	α_{th}	$= 2{,}6 \times 10^{-6}$ /K
Direct band gap (300 K)	E_G	$= 3{,}4$ eV
Indirect band gap (300 K)	E_G	$= 1{,}1$ eV

Table 1: Material properties of silicon

Most important for laser processing of silicon are its optical properties, especially the absorption coefficient which is diagrammed in Figure 1 for a range of laser-relevant wavelengths. The fact, that literature knows several different data sets with partially considerable differences is already an indication that these values are highly dependent on the special. experimental conditions. Smallest dopings or slightly different surface properties can have a substantial influence on the material's optical absorption. Furthermore, this coefficient is heavily temperature-dependent as well, which makes the absorption diagram valid for the beginning of a laser pulse only and leads to many different, laser-specific descriptions of ablation mechanisms. Generally speaking, the following can be summarized:

Photons with energy much less than the direct or indirect band gap energy can directly excite lattice vibrations. Direct and indirect transitions of electrons from the valence to the conduction band are possible when the photon energy is higher than the energy of the band gap. In case of indirect absorption, phonons are absorbed or emitted during photon absorption. The third absorption process is free carrier absorption. Independent of the specific photon energy, electrons of the conduction band can be excited by absorbing photons. Then, they interact with phonons causing a rise of the lattice temperature. Due to these absorption phenomena, the photon energy and the temperature have a strong influence on the absorption coefficient.
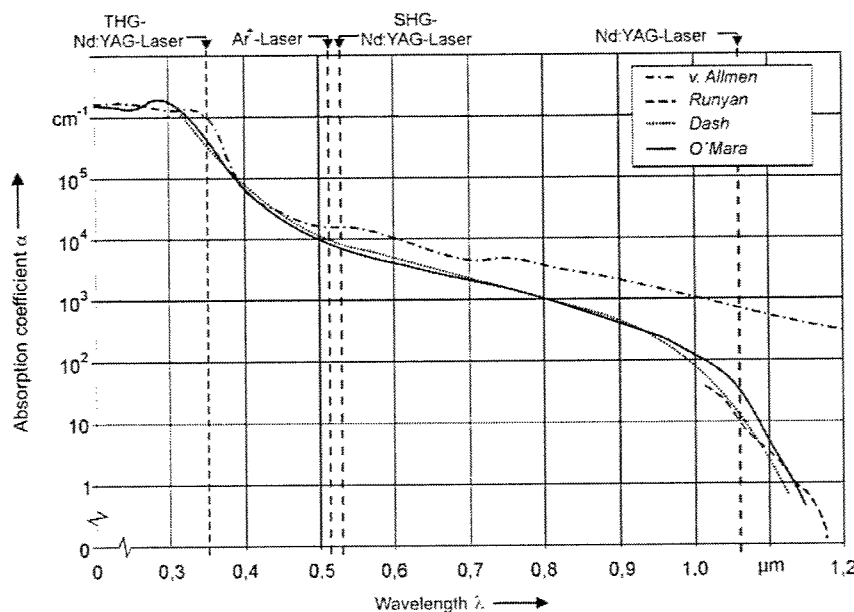
Figure 1: Absorption of Silicon in dependence of the laser wavelength

For the Nd:YAG-laser with its wavelength of 1064 nm for example, the photon energy is nearly as high as the indirect band gap of silicon. Direct transitions are not possible. As phonons are necessary for indirect absorption, and free carriers for free carrier absorption, the absorption coefficient increases with a rising temperature. At room temperature, the absorption is weak and the absorption length is higher than 500 μm. The absorption length decreases to some microns at a temperature of 800 K. Liquid silicon behaves like a metal and absorbs Nd:YAG-laser beams within some nanometers. As a result, the rise in temperature is very slow at the beginning of a laser pulse, but accelerates enormously afterwards [2].

MOTIVATION OF THIS PAPER

Whereas nowadays it is absolutely no problem to obtain raw silicon in nearly any desired crystal quality, purity, size and shape, the real challenge lies in the geometrical and chemical structuring of the material. The trend towards continued miniaturisation and integration is still proceeding and demands the development of silicon micromachining techniques capable of generating and handling structures of ever-decreasing sizes, the current state-of-the-art being around 0.25 μm. From the beginning of laser technology in the 20th century a reduction by a factor of two every seven years has been observed in the typical feature size processed by laser micromachining [3].

Although silicon is one of the most thoroughly investigated materials and modern silicon micromachining technology offers a wide range of established processes for crystal generation, sawing, etching, plating and doping, conventional methods for silicon microstructuring found in the semiconductor industry do have their limitations. Many of them can be overcome by using some of the innovative, high-accuracy laser microprocessing techniques described in this paper. Laser material processing of silicon is recently receiving more and more attention due to the availability of compact, reliable femtosecond and frequency-converted solid state lasers which emit high quality radiation in wavelengths and intensities highly suitable for silicon micromachining.

Laser processing offers mainly two key advantages over other e. g. chemically based structuring techniques. First, laser systems are much more flexible. Changes in component geometry do not require manufacturing of new tools or masks but can simply be performed by reprogramming the instruction sequence. Furthermore, one and the same laser is able to perform completely different tasks. Just by appropriate altering of laser and focus parameters, an Nd:YAG laser can be used for ablation and for welding of silicon components. Therefore, laser micromachining is a very economical alternative especially for small production quantities. Second, laser micromachining allows the generation of true 3D structures and surface profiles. By changing scanning speed or count and altering laser power, continuous or at least finely stepped relief patterns can be generated using laser ablation mechanisms. Especially this quality of laser processing will certainly be appreciated in the near future by MEMS and MOEMS applications with their ever-growing geometrical complexity.

Ablation-based laser micromachining is one of the topics of this paper, but its main intention is to present two other highly innovative, yet quite unknown laser processes for manufacturing of silicon devices: laser beam welding and laser induced micro-adjustment.

2   LASER PROCESSING OF SILICON

LASER CUTTING AND MICROMACHINING

Trends in Laser sources

Laser manufacturers are aware of the potential of laser micromachining of silicon and are focussing their effort to provide new laser sources for this field of application which overcome the drawbacks of their predecessors. Ultrashort-pulse laser ablation is widely gaining recognition because it allows – in contrast to conventional laser ablation – structuring with highest precision by minimal damage to the adjacent material [4].

In a conventional ablation process, the pulse duration is too long to prevent an interaction of the generated plasma with the laser beam and therefore additional absorption occurs. With ultrashort pulses (durations in the short ps- and fs-range) laser pulse and thermal effects like melting, evaporation and heat conduction are temporally separated [5]. The

absorbed laser energy is initially constricted to a very small volume at the material surface determined by the laser focus area and the optical penetration depth (several 10 nm for silicon e. g. for an Ti:Sapphire-based 800 nm oszillator) where extremely high temperatures occur leading to instant vaporisation. Therefore, melt formation is mostly avoided.

However, state-of-the-art femtosecond lasers based on Ti:Sapphire oscillators are too bulky, too complex to handle, too unreliable and – last but not least – too expensive for industrial application. New laser active media are therefore currently being researched which allow to be diode-pumped and therefore make the complex optical setup for pumping the Ti:Sapphire crystal obsolete. Especially interesting for material microprocessing are ytterbium-doped crystals such as Yb:BOYS ($Yb^{3+}:Sr_3Y(BO_3)_3$) or Yb:GdCOB ($Ca_4GdO(BO_3)_3$) [6]. Those crystals show excellent properties, including effective pumping with InGaAs-diodes, broad emission spectrum and – using modern, active mode-locking techniques – extremely short pulses with high peak powers.

Other current studies are concerned with advancing the performance, beam quality and efficiency of diode pumped solid state lasers. New resonator designs like slab crystals, more effective cooling and frequency conversion techniques as well as power amplification are applied to match the technological requirements of laser microprocessing.

Trends in Applications

Industrial as well as scientific researchers are currently discovering a lot of new applications and products based on the technological push created by the development of advanced solid-state and femtosecond turnkey laser systems. The basic concept of silicon laser micromachining by ablation is being rediscovered and significantly enhanced to match the new state of laser technology.

The Fraunhofer Institute for Material and Beam Technology for example is currently researching silicon drilling and area ablation by frequency-doubled Nd:YAG lasers [7]. Many other recent publications are dealing with femtosecond pulse laser micromachining of silicon [e.g. 8]. Ultra-short pulse lasers in the fs regime have proven to be applicable for high precision structuring of semiconductors as they minimise thermal and mechanical influences and therefore largely avoid thermal melting, cracks and deposits. Spectra-Physics has recently published work on a new Q-switched Nd:YVO$_4$-laser emitting in the green at 532 nm which can be ideally applied for high-speed direct laser marking of semiconductor chip directly on the wafer before dicing, as thermal damaging of the front-side circuitry is no longer a concern [9].

Laser beam cutting of sheet metal and polymers has been successfully established as an industrial, high-speed and high-accuracy processing technique already years ago. Laser beam cutting of silicon, however, has up to now never been able to really solve the inherent technological problems causing poor quality and speed as well as substantial damage to the silicon substrate. The thermal conductivity of silicon is 156 W/mK, which is about 4 times higher than that of steel, its surface is highly reflective for CO_2 and Nd:YAG lasers and the energy band gap lies at the very high level of 1.1 eV, which is ten times the photon energy of a CO_2 laser [10]. Apart from that, Silicon is very brittle and sensitive for thermal damage; it is therefore considered as a very complicated material for laser cutting. Many publications dealing with laser cutting of silicon report severe quality problems including cracks, deposition of resolified debris and the formation of burrs and recasts. Also the achievable cutting speeds could not compete with conventional methods, such as dicing with diamond saws and scribe-and-break.

New, promising results achieved with new, high-power frequency converted solid-state lasers however are receiving growing interest. Especially microcutting of ultrathin wafers has been successfully demonstrated (see Figure 2).

In order to get a deeper insight into the fundamental principles of laser beam cutting of silicon, its basic process mechanisms are currently being investigated at the BLZ. For our experiments, we are using a Coherent AVIA Laser with an
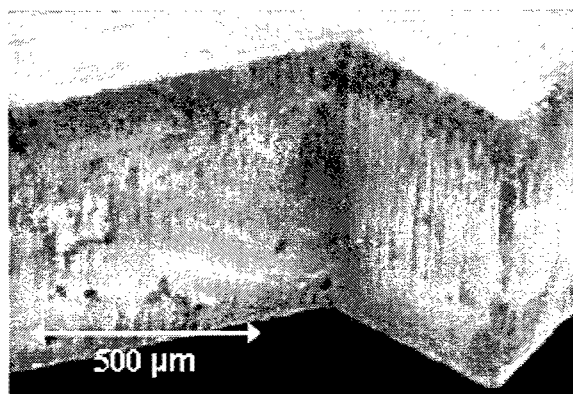
Figure 2: Microcutting of thin silicon substrates (Courtesy of Exitech, UK)

average power of 4,5 W. This diode pumped, frequency-tripled Nd:YAG Laser offers a maximum pulse power of 8200 W and pulse durations in the 20 ns regime. In the experimental setup, the laser beam, using a scanner optic with a focal length of 270 mm, is guided in lines over a 1 mm thick silicon wafer to form grooves. These marks are subsequently studied by preparing polished grinding patterns without prior cleaning or etching. This way, it is possible to reliably detect the dimensions of the heat-affected zone, micro cracks, debris and other damages to the substrate. Figure 3 shows the result of the first series of experiments, which were performed under altering focus conditions. For each groove, the silicon surface is moved 200 μm towards the scanner lens starting at a position 3 mm further than the focus (-3 mm in the diagram) and moving a total range of 6 mm. The depth of each groove and its width at the surface are measured.

Obviously, the geometry of the generated grooves highly depends on the focal offset. Only within a ±0,2 mm range of the exact focus position, the maximum groove depth can be achieved. At higher offsets, it is dramatically reduced, nearly independent of the offset's direction. Regarding the groove width, a practically reverse tendency is found. The deepest grooves are at the same time the narrowest; a small focus offset has a widening effect. If the silicon surface is positioned more than 2 mm away from the focal point, both depth and width rapidly decrease until no more effects can be observed.

This result experimentally confirms the theoretical considerations about the absorption mechanisms of silicon (see chapter 1). A small irradiated focus area results in a higher energy density which in turn leads to a higher absorption coefficient and therefore causes a superproportional rise in ablation efficiency. Further research studies will include variations in focal length and repetition rate.

Figure 3: Focus-dependent groove ablation of silicon

The experiments were performed using a scanning speed of 15 mm/s, sufficiently high to avoid thermally induced cracks. Melt formation however, cannot be completely inhibited.

LASER BEAM WELDING OF SILICON COMPONENTS

Due to its outstanding physical – especially electronic and optical – properties and the wide availability of already established micromaching processes from the domain of electronic production, silicon is considered the ideal substrate not only for integrated circuits but also for sensors, actuators and even for most complex electro-optical microsystems. Promising applications for silicon micro-welding exist in all of these technological areas. Complex sensors, for example, often consist in several silicon components, mounted on each other in multiple layers. Regarding manufacturing technology for micro-optoelectro-mechanical systems (MOEMS), joining of silicon lenses and other optical and electro-optical components made of silicon with silicon substrates represents a key task which could be performed using laser beam welding.

State-of-the-art technologies for joining silicon components are soldering, bonding and gluing. Although laser beam welding promises considerable advantages like higher flexibility, direct joining without additional filler materials, thermal stability and locally restricted thermal charge, no practical applications have been reported so far, because of one very severe drawback: The appearance of thermally induced cracks.

Figure 4: Laser welding of silicon leads to thermally induced cracks

Figure 4 shows metallographic grinding patterns of two welding spots applied to a parallel and an orthogonal joint of two silicon dices by a pulsed Nd:YAG laser. After re-solidification several small and large cracks can be observed in and around the heated area. Especially the large cracks often lead to a complete mechanical breakdown of the welding spots, the welded parts can be easily separated again. The reason for this phenomenon can be found in the brittleness of crystalline silicon. The material can hardly perform any ductile reshaping. During laser heating, the volume of heated silicon tries to stretch due to thermal expansion and later shrinks again during re-solidification. As the silicon substrate surrounding the welding spot does not relieve the resulting mechanical tensions by plastic deformation numerous cracks are initiated which can easily penetrate the brittle material for large distances [11].

Already when discussing the absorption coefficient of silicon in chapter 1, a strong temperature dependence of its physical and optical properties could be observed. The mechanical properties of silicon also vary considerably with changing temperatures. This is pointed out by Figure 5 which shows the yield stress of silicon in a temperature range from 300°C to 1100°C.
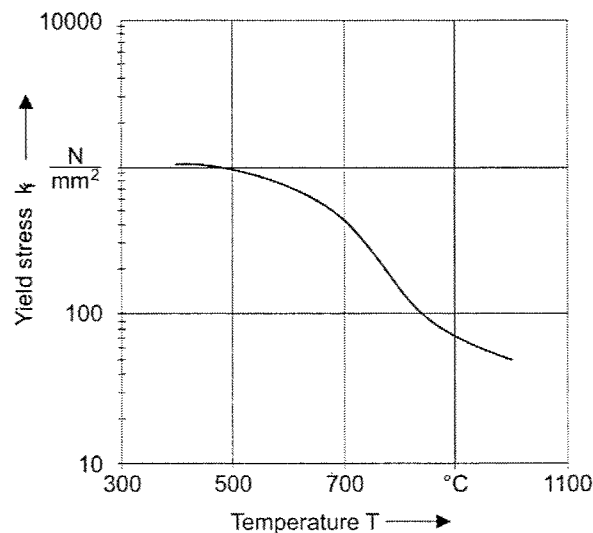
Figure 5: Yield stress of silicon

The material obviously shows a remarkably lowered yield stress already at a temperature only half as high as the melting point (1412°C) and changes its brittle properties into ductile behavior at temperatures higher than 600°C. In order to significantly reduce thermally induced stress during the welding process and in order to reach at the same time a more ductile behavior of the silicon compontens, enabling the material to relax residual stresses by plastic

deformations, a new strategy for avoiding cracks during laser welding of silicon was developed: The substrate near the welding spot is preheated by a slightly defocused cw-operated Nd:YAG Laser until a second, pulsed Nd:YAG Laser performs the actual welding in a single pulse.

In order to determine the optimum parameters (temperature and focus area for preheating, pulse length and power of the welding laser) the whole process was modeled and simulated using the FE-software "Sysworld". Thermal as well as mechanical stresses in the welding area were analyzed using the following boundary conditions:

- The geometrical setup is simplified to an axially symmetrical blind welding spot, which allows two-dimensional simulation.

- Heat dissipation is calculated for convection and thermal radiation using a temperature-dependent heat-transfer coefficient.

- The absorption of laser energy takes place only at the surface elements using the absorption properties of liquid silicon.

Figure 6 shows typical profiles of equivalent stress (v. Mises) during impact of the laser pulse (t = 1000 ms) and during cooling down using the optimum process parameters found: Preheating for 1000 ms with 150 W and a beam diameter of 2 mm [2].
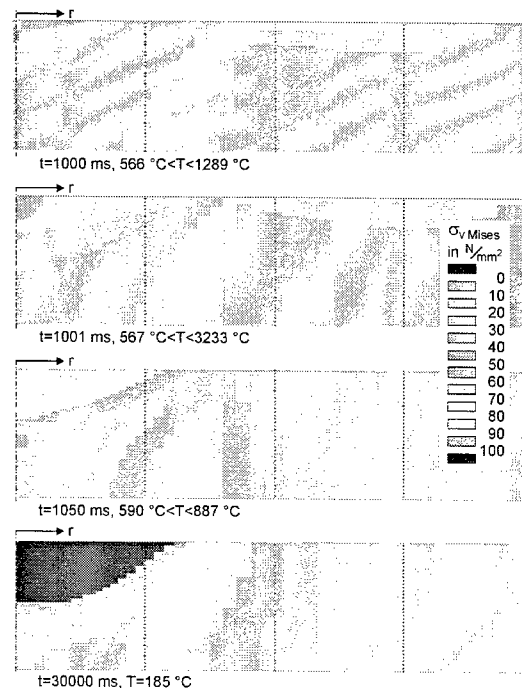
Figure 6: FEM-analysis of equivalent stress

The overall results of our simulation studies have clearly proved the assumption that preheating of the silicon components before welding significantly lowers the occurring thermally induced stress. Compared to laser beam welding without preheating, only 20-30% of the peak stress is reached. The higher warm-up temperatures are used, the lower stresses are built up in the substrate. Especially for preheating temperatures higher than 350°C a nearly linear correlation to the peak equivalent stress can be observed (see Figure 7).
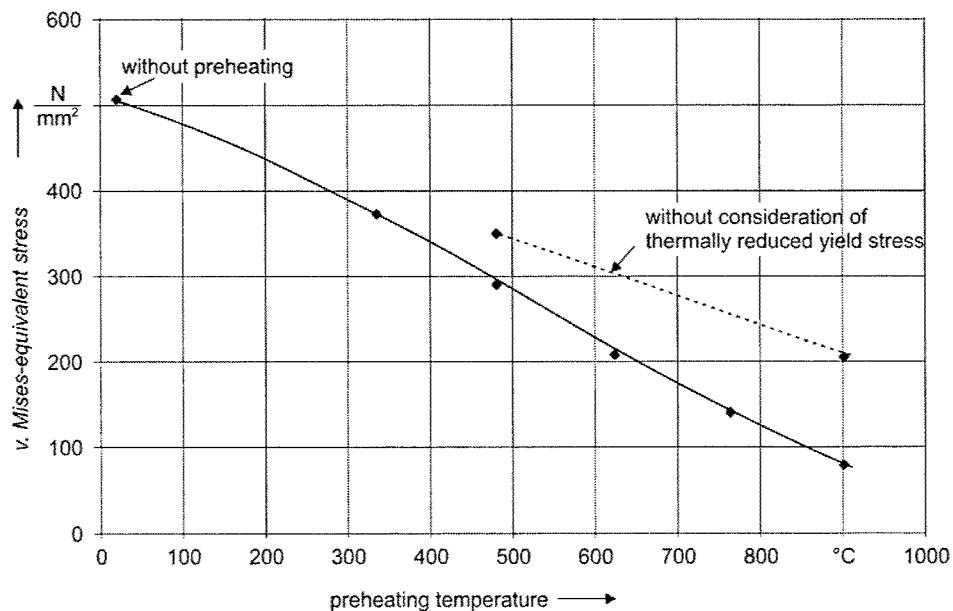
Figure 7: v. Mises equivalent stress after cooling down to T = 200°C

The simulation results presented above could be verified by experimental investigations. The defocused laser for preheating the samples was activated five seconds before the welding laser pulse and disabled two seconds later. The surface temperature of the silicon sample was measured at about T = 1200°C using a pyrometer. After cooling metallographic grinding patterns were prepared. On the left side Figure 8 shows the top view of a welded sample. The right side displays a polished micrograph section after etching. The small dots and lines in the center do not indicate cracks, but rather show the dislocations in the silicon. The borderline between the melt pool from the pulsed laser and the raw material is also visible. Due to two sequenced pulses combined with a sample movement there are two overlapping melt pools.
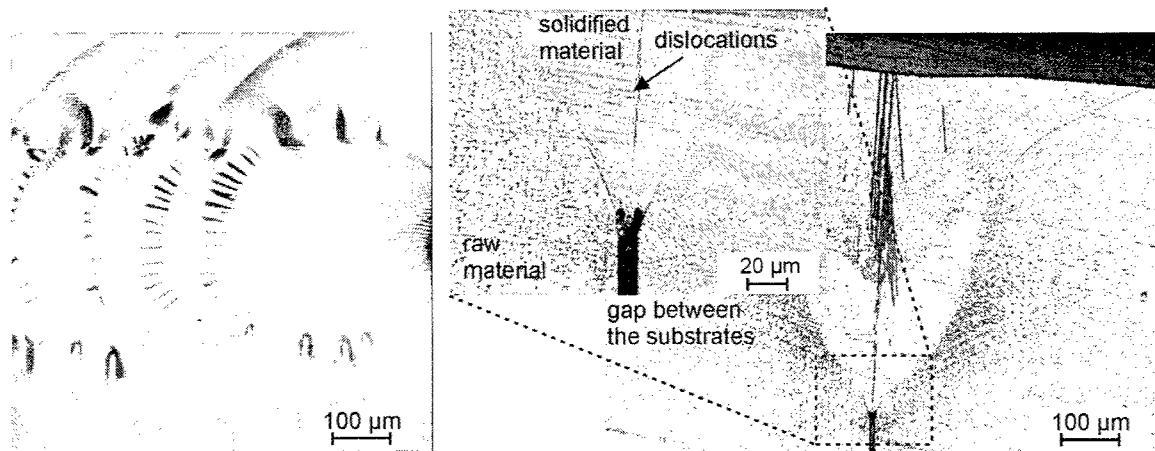
Figure 8: Crack-free laser beam welding of silicon

The experimental results demonstrate clearly, that crack-free welding of silicon is possible using a combination of a continuous wave and a pulsed Nd:YAG laser.

NON-THERMAL LASER ADJUSTMENT OF SILICON ACTUATORS

Accurate positioning of smallest optical, mechanical or electronic components represents an up-to-date key assignment in micro-manufacturing, e.g. of MEMS and MOEMS. Instead of high-precision manufacturing of each individual component and high-accuracy assembly it has turned out much cheaper and easier to perform production and mounting quick and roughly tolerated and to micro-adjust the critical components in a second step using specially designed actuators.

Laser radiation can be used to induce thermal stresses in material surfaces which lead to bending effects in thin substrates following the so called "thermal gradient mechanism (TGM)" [12]. Following this principle, laser-operated actuators as a link between the functional component and the chassis have been developed which allow contact-free positioning in several axes by irradiating specific spots for a defined time with laser pulses. This technique has already outclassed conventional actuators based on fine thread screws in many fields, as it allows complete automation in a closed-loop process. It has been successfully introduced for a number of high-precision industrial applications and is widely gaining attention. Siemens, for example is using the process to adjust contact springs of miniature relais with a yearly output of about 13 million devices [13]. Other known industrial applications include the micro-adjustment of reed-contacts and drive actuator arms holding the read/write heads for computer hard drives.

The fact, however, that the mechanism for this laser adjustment process rests upon thermal effects has been found unfavourable mainly for two reasons. First, the final bending angle is not reached until the actuator has been given a certain time to cool down. Depending on the material, this cooling can take 1-30 seconds. If – in an automatic control loop – several iterations are required until the desired position of the functional component is finally reached within the given tolerances, the process step of laser adjustment can become very time-consuming. Second, residual tensions remain in the actuator after completion of the adjustment. Near the surface, these tensions often reach the scale of the material's yield stress. This represents a certain risk, as the actuator then is more susceptible to mechanical or thermal loads. Also, the long-term position stability of an exceedingly pre-stressed material is by far less reliable than that of a system without prior exposure to high temperatures.

From these disadvantages the need to avoid heat transfer into the actuator material as much as possible can be derived. On the other hand, exactly this heat transfer is crucially needed to drive the thermal bending mechanism, which represents a contradictory demand.

To solve this problem, the BLZ together with research partners from industry and science is currently developing the new approach of NOTILA (Non-thermal Impact Laser Adjustment) [14]. It is built on a fundamentally different underlying mechanism: An initially pre-stressed mechanical system is micro-deformed by gradually relaxing its elastic tensions [see Fig. 1].
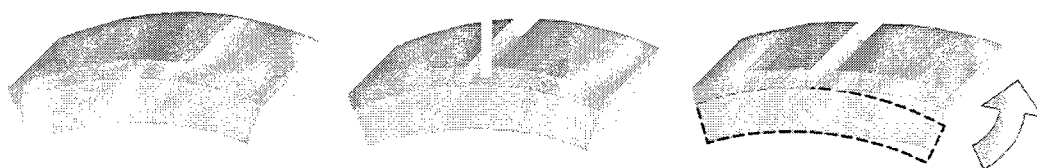
Figure 9: Basic process of laser micro-adjustment by ablation of pre-stressed layers

The pre-stressed actuator is created by coating a silicon substrate using standard chemical or physical vapour deposition (CVD or PVD) techniques which are well established in semiconductor manufacturing. In our experiments, we applied a Si_3N_4 layer of 0,31 μm thickness on rectangular pieces of a 1 mm silicon wafer. The coating process takes place at a temperature of 770°C. As the thermal expansion coefficient of silicon and silicon nitride is significantly different, a

Coating Process:

Vapor Deposition of Si₃N₄ at 770 °C

Substrate: Si-Wafer
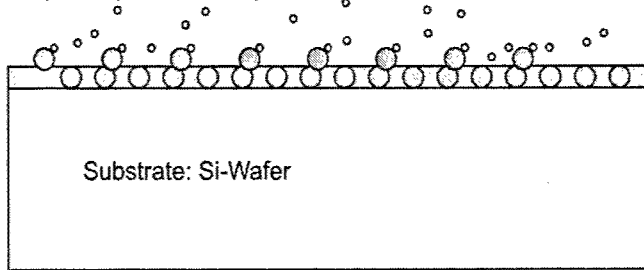
After Cooling:

Elastic residual tensions remain in the actuator

Tension

Compression
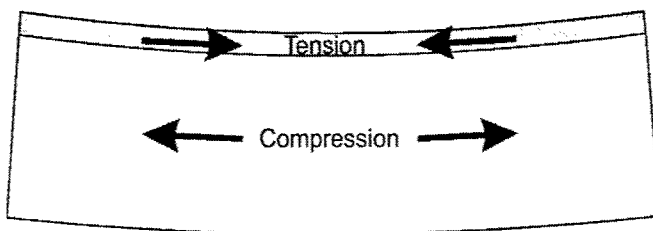
Figure 10: Formation of residual tensions by CVD-coating

tension is created when the coated material has cooled down to ambient temperature leading to a small distortion. The principle is similar to the one used for bimetal dices.

By ablation of the coating layer, as shown in Figure 9 the stress propagation can be interrupted. Evidently, the actuator instantly relaxes at this spot and bends back like an elastic spring. The amount of bending can be controlled by ablation depth, dimension of the ablated area, thickness of substrate and coating and of course by choosing different coating materials. Obviously, this mechanism is able to overcome the drawbacks of conventional, thermally induced laser micro-bending. First, the displacement occurs directly after the laser interaction, idle times for heat transfer and cooling are not required. Second, the whole mechanism relies on considerably low, elastic tensions exclusively. Undesirable effects like long-term instability are not to be expected. It is very important however, that the ablation process itself is performed applying as low heat exposure as possible. The use of short and ultra-short pulsed laser systems is essentially required.

For the first series of practical tests we used a Lambda Physik 315i-KrF Excimer-Laser. This device offers a wavelength of 248 nm, a pulse duration of 20 ns and a maximum energy per pulse of 800 mJ. The laser beam is expanded, homogenized, shaped via a mask to form a thin line and projected onto the actuator surface.

The 35 x 7 mm rectangular samples are fixed at one end and irradiated in their middle. At the other end, the small displacements Δz are measured using fiber-optical contact-free sensors, capable to resolve 0,1 μm. Figure 11 shows the experimental setup. These sensors consist of a sensor head, connected with a fiber pack to an opto-electronic converter. The signal data is processed and sent to a computer via the serial interface. As several ablation lines next to each other are created on one actuator during the experiments, the bending angle

$$\alpha = \arctan\frac{\Delta z}{L}$$

is measured and analyzed instead of the displacement Δz. The use of actuators based on silicon already considers future developments, e. g. the monolithic integration of functional, semiconductor components directly in the actuator or even the design of complex silicon microsystems containing sensors, actuators and integrated circuits on a single chip.

Fiber Pack

Adjustment Clamp

Sensor Head

Bending Edge

Actuator

Δz

L

Line-shaped laser beam

Figure 11: Experimental setup

The experimental results confirm the concept of NOTILA. Micro-adjustment by ablation of pre-stressed layers is possible. The tensile stress at the surface of the samples is reduced by the laser pulses, the underlying silicon substrate can relax and a displacement in z-direction is observed.
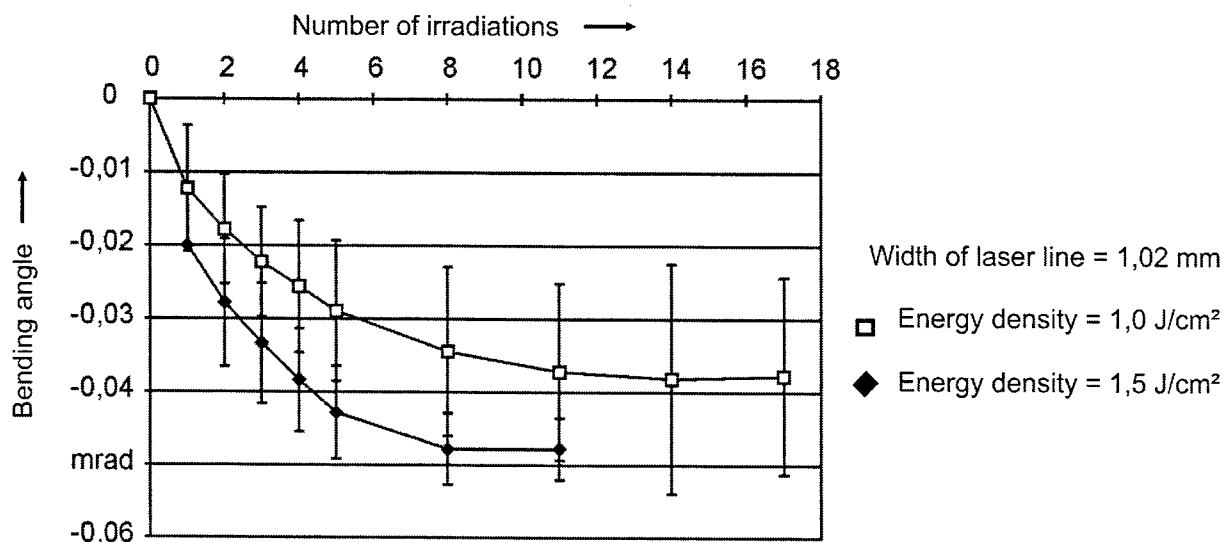
Figure 12: Bending angle for different numbers of irradiation and laser energy densities

The run of both curves detected for two different laser energy densities is clearly declining (Figure 12). After about 10 irradiations the growth of the bending angle comes to an end. The maximum achievable bending angle for the chosen width of the laser line reaches approximately 0,05 mrad, probably when the coating layer is completely removed. Microscopic analysis confirms that the coating is entirely removed without major damage to the silicon substrate. The wide tolerances indicated in the diagram are probably due to surface-near micro cracks resulting from the laser material interaction. These cracks occur irregularly and weaken the material in dependence of their depth, leading to a high scattering in the experimental results (see Figure 13).
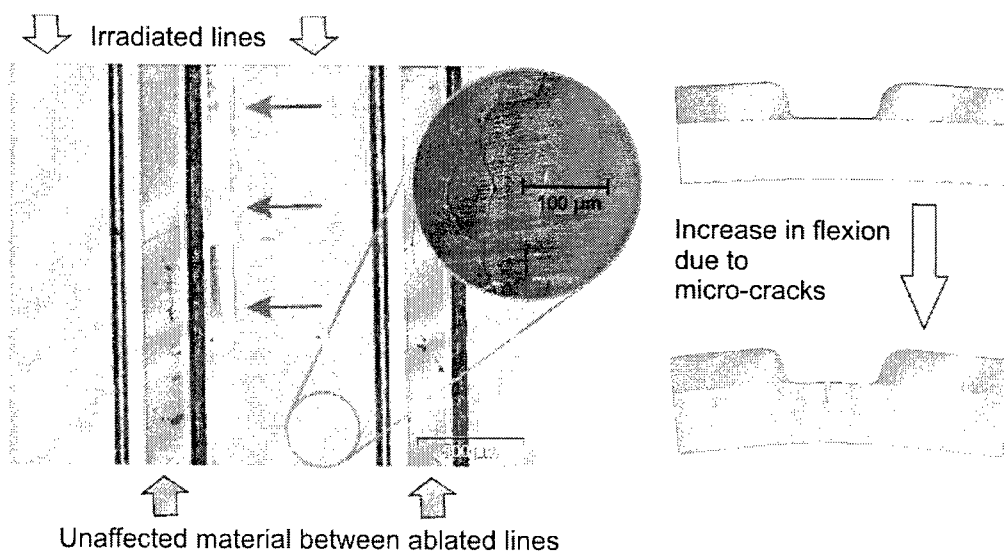
Figure 13: Formation of micro-cracks in the ablation area

It is therefore planned to perform the following studies using femtosecond lasers. Other project objectives include the variation of the coating thickness and material and the development of optimised actuators carrying several different layers. By choosing suitable coating materials with different inherent tensions, it should be possible to influence not only the increment of deformation, but also its direction.

3 CONCLUSION AND OUTLOOK

This paper has briefly reviewed a wide range of recent developments in laser processing of silicon. Furthermore three topical areas have been presented where current research activities are performed by the BLZ. Latest analytical and experimental results have been presented.

Current trends in industrial and scientific research clearly confirm that ablation-based laser micromachining of silicon has reached a new level concerning processing quality and accuracy due to the availability of recent frequency-converted diode-pumped solid-state and femtosecond lasers. Especially the emerging of diode-pumped, compact and reliable turnkey femtosecond laser sources, which can be expected within the next few years, will presumably mean a significant push for this market, especially as conventional techniques for silicon micro-structuring are reaching their limits.

By both, experimental and simulation studies the feasibility of crack-free laser beam welding of silicon could be demonstrated. Preheating of the silicon components significantly lowers thermally induced stress and allows the material to perform small, ductile deformations which compensate its mechanical tensions and avoid the formation of cracks. For practical applications it is necessary to balance the minimum required temperature for crack-free laser welding and the maximum allowed temperature concerning component damage. Further investigations in experiments and FE-calculations are necessary.

Non-thermal laser adjustment by ablation of elastically pre-stressed systems has been presented as a new concept which could be confirmed by promising experimental studies. The new underlying mechanism is able to overcome the drawbacks of laser-bending based on thermal tensions. NOTILA will be further researched; it is expected to allow significantly faster and more accurate laser adjustment than the conventional, thermal method.

However these three facets of silicon laser-processing are very interesting applications each on its own, it should be mentioned that – in combination – they represent a completely new toolkit for the manufacturing of silicon devices. For example, the design of really 3D-shaped silicon microsystems instead of simple stacks of bonded dice can be realized by applying a combination of laser welding and laser ablation techniques. The concept of silicon-based actuators allows the direct on-chip integration of position-critical components together with their micro-positioning devices without a further need for additional parts, manufacturing and assembly steps. It is widely assumed that already in the near future many very complex hybrid microsystems – e. g. for medical application as drug delivery implants – will highly benefit from flexible laser micro-manufacturing techniques.

4 REFERENCES

1. Andrew S. Holmes, „Laser fabrication and assembly processes for MEMS", Proc. SPIE Photonics West LASE 2001
2. S. Kaufmann, „Grundlegende Untersuchungen zum Nd:YAG-Laserstrahlfügen von Silizium für Komponenten der Optoelektronik". Meisenbach , Bamberg 2002
3. J. Meijer, „Laser Micromachining". In Micromachining of Engineering Materials; Mc Geough, J., Ed.; Marcel Decker, Inc.: New York, 2003; Chapter 8.
4. H. K. Tönshoff, A. Ostendorf, F. Korte, J. Serbin and T. Bauer, "Generation of periodic microstructures with femtosecond laser pulses", Proc SPIE 4426, pp. 177-179, 2002
5. C. Föhl, K. Breitling, K. Jasper, J. Radtke and F. Dausinger, "Precision drilling of metals and ceramics with short and ultrashort pulsed solid state lasers", SPIE Proc 4426, pp. 104-107, 2002
6. M. Hatcher, „Compact Sources Seek Fresh Industrial Niches" Opto & Laser Europe 12/2002, pp. 19-20

7. Udo Klotzbach, Michael Panzner, Jörg Kasper et al., „Processing of silicon by Nd:YAG-lasers with harmonics generation", Proc. Icaleo 2002

8. J. Meijer, K. Du, A. Gillner et al., „Laser Machining by Short and Ultrashort Pulses, State of the Art", Annals of the CIRP, pp. 1-20, 2002

9. M. Watts, "Giving a Green Light", Photonics Spectra 10/2001

10. G.C. Lim, Tuan Ahn Mai, David Low, Qiong Chen, "High Quality Laser Microcutting of Difficult-to-Cut Materials – Copper and Silicon Wafer", Proc. Icaleo 2002

11. M. Geiger, K. Lenfert, „Innovationen durch Laser Engineering: Berichtsband zum Zwischenkolloquium FORLAS II", Bamberg, Meisenbach, 1999

12. F. Meyer-Pittroff, G. Esser, M. Geiger, „Schnelle Laserstrahl-Mikroumformung bei geringer thermischer Belastung", in: M. Geiger, M. Fleckenstein, „Laser in der Elektronikproduktion und Feinwerktechnik LEF 2002", pp.131-146, Meisenbach, Bamberg, 2002

13. H. Hanebuth, C. Hamann, „Präzisionsmontage und –justage mit dem Laserstrahl in der Elektronikproduktion", in: M. Geiger, A. Otto, „Laser in der Elektronikproduktion und Feinwerktechnik LEF'99", pp. 141 – 155, Bamberg, Meisenbach, 1999

14. G. Eßer, A. Huber, M. Geiger, „Verfahren zur Positionsjustage lageemprindlicher Bauteile, insbesondere von Mikrobauteilen der Elektronik, Optoelektronik oder Mechanik", patent application, 2000

High-speed cutting of thin materials with a Q-switched laser in a water-jet vs. conventional laser cutting with a free running laser

Frank R. Wagner[*a], Christophe Boillat[a], Jean-Marie Buchilly[a], Akos Spiegel[**b], Nandor Vago[b],
Bernold Richerzhagen[a]

[a]Synova Inc; [b]Dept. of Atomic Physics, Budapest Univ. of Techn. and Economics

ABSTRACT

Cutting of thin material, c.f. stencils, stents and thin wafers, is an important market for laser machining. Traditionally this task is performed using flash-lamp pumped, free-running Nd:YAG lasers.

Using the water-jet guided laser technology, we experienced that the use of Q-switched lasers leads to superior results while cutting a variety of thin materials. In this technique, the laser is conducted to the work piece by total internal reflection in a thin stable water-jet, comparable to the core of an optical fiber. Utilizing this system, we obtain burr-free, slightly tapered cuts at the same speed as the classical laser cutting and without distinguishable heat affected zone. The main difference is, except the water-jet usage, the pulse duration which is approximately 400 ns instead of 20 to 200 µs in the case of free running lasers. Up to 40'000 high quality apertures per hour can be achieved in stencil mask cutting with the new system.

We will compare qualitatively the two possibilities: conventional laser cutting with free-running lasers and water-jet guided laser cutting with Q-switched lasers. The results will be discussed in terms of the different physical effects involved in the material removal upon both methods. In particular the importance of molten material expulsion by the water-jet will be pointed out and compared to the action of the assist-gas.

The mentioned effects show that the combination of short pulse laser and water-jet will be beneficial for the production of a wide range of precision parts.

Keywords: Laser cutting, Q-switched laser, free running laser, pulse length, stencils, metal foil, 1064 nm.

1. INTRODUCTION

Cutting of thin materials is often difficult or impossible with abrasive or mechanical means, due to the sensitivity of the material to forces. Cracking will appear in brittle materials like silicon, and plastic deformation appears in metals typically. For this reason namely wet chemical etching and laser cutting, as low force machining possibilities, are applied in this field.

Focusing on thin metal foil machining, the main advantage of chemical etching is the complete absence of forces and burrs. However the shape of the edges is not well adapted for some applications like solder paste stencils and the reproducibility and precision of the etching process are also minor compared to laser cutting. Classical laser cutting is not completely force free as the assist gas executes a certain pressure onto the metal foil. An important disadvantage with respect to many applications however is the build-up of burrs, usually on the backside of the foil. Also, as the material is simply molten due to the absorbed light energy and removed by the assist gas stream, a heat-affected zone (HAZ) can be distinguished close to the cutting edge. The HAZ is visible by the oxidation around the edge and it also changes the grain size of the metal[1] and thus the mechanical properties close to the edge. In spite of these disadvantages, classical laser cutting is more and more used in industrial stencil production because of the superior precision and the ever-decreasing pitch of electronic components.

The water-jet guided laser is a relatively new technique, which combines the positive aspects of conventional laser cutting and chemical etching. In the following, we will present the improvements in cut quality that are achieved using this technique and we will outline the reasons for the observed effects.

2. EXPERIMENTAL DETAILS

A sketch of the water-jet guided laser cutting system is shown in Figure 1. The used laser for thin metal foil cutting is a multimode Q-switched Nd:YAG laser (SL902, Spectron Laser Systems Ltd. (UK)). We use pure de-ionized and filtered

water at 5 to 50 MPa for the water-jet. The nozzles are made out of sapphire or diamond in order to generate a long stable portion of the water jet. The laser beam, coming from the fiber delivery of the laser, is collimated, passes a beam expander and is focused through a quartz window into the nozzle. The situation in the coupling unit is very much like in an usual fiber coupling, except the fact that the intensity distribution of the light is flat-top and not Gaussian, due to the mode mixing in the fiber delivery of the laser and the imaging properties of the setup. Once in the water jet, the light is reflected at the air-water interface due to the refractive index step (Figure 2).
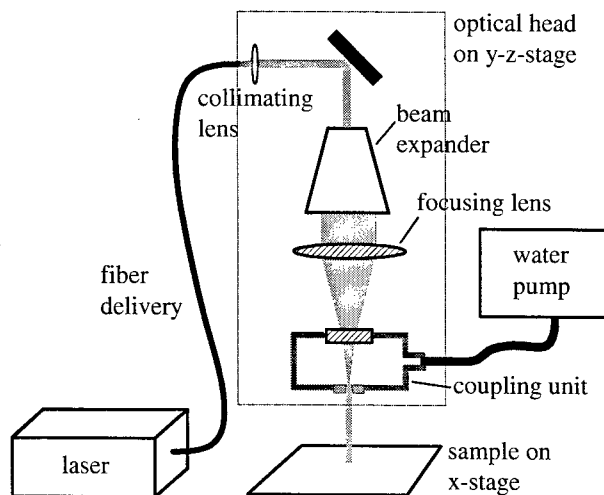
Figure 1: Schematic of the water-jet guided laser setup
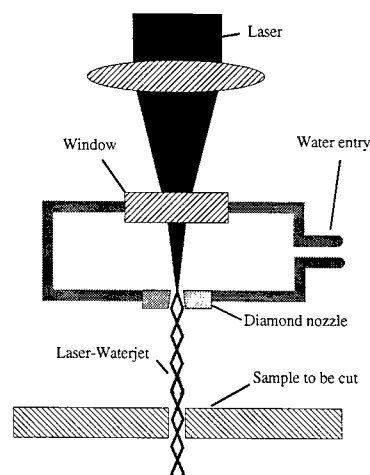
Figure 2: Detailed sketch of the coupling unit

The samples are clamped onto a motorized stage, and during the cutting process the samples are moved under the water-jet guided laser beam (laser-water-jet), or the optical head moves in the perpendicular direction. The z-variation of the stage is only necessary in order to adapt to the different working distances of differently sized nozzles at different water pressures [2] and is not used during the cutting procedure.

3. RESULTS AND DISCUSSION

Figure 3 shows comparison photographs: The upper line represents typical edges as they are obtained with a conventional (commercial) laser stencil cutting machine using a free running Nd:YAG Laser in 150 µm thick stainless steel foil. The laser parameters of the samples in Figure 3a and Figure 3b are summarized in Table 1.

Average laser power	Pulse repetition rate	Pulse length	Assist gas	Laser beam diameter
19 W	1'600 Hz	120 µs	Air, 15 bar	40 µm

Table 1: Classical laser processing parameters for 150-µm thick stainless steel foil. Optimized for quality and speed. Samples are shown in Figure 3, upper line.

More generally the pulse durations of the free running YAG lasers are limited to $\tau > 20$ µs, the pulse repetition rate is $f < 4$ kHz, and the average laser power is typically 20 W for the required beam quality (fine cutting). The above parameters are quite typical for stencil cutting in general. The pulse duration is adapted according to the thickness of the steel foil, longer pulses are used for thicker materials. See for example [3] who use 190 µs pulse duration for 200 µm thick samples.

The second line of Figure 3 shows the result of the optimized water-jet guided laser processing. The used Q-switched Nd:YAG-laser has a maximum average power of 65 W. The process parameters are summarized in Table 2. Comparing the parameters and the cutting speed of both methods, which is very similar (about 4.5 mm/s to 5 mm/s), we can state that both processes work with similar energy efficiency.

Average laser power	Pulse repetition rate	Pulse length	Water jet pressure	Laser-beam /water-jet diameter
22 W	25'000 Hz	0.4 μs	330 bar	50 μm or 75 μm

Table 2: Water jet guided laser-processing parameters for 150- μm thick stainless steel foil. Optimized for quality and speed. The average laser power value takes into account the losses in the 36 mm long water-jet due to absorption. The average power directly after the fiber delivery is 33W.
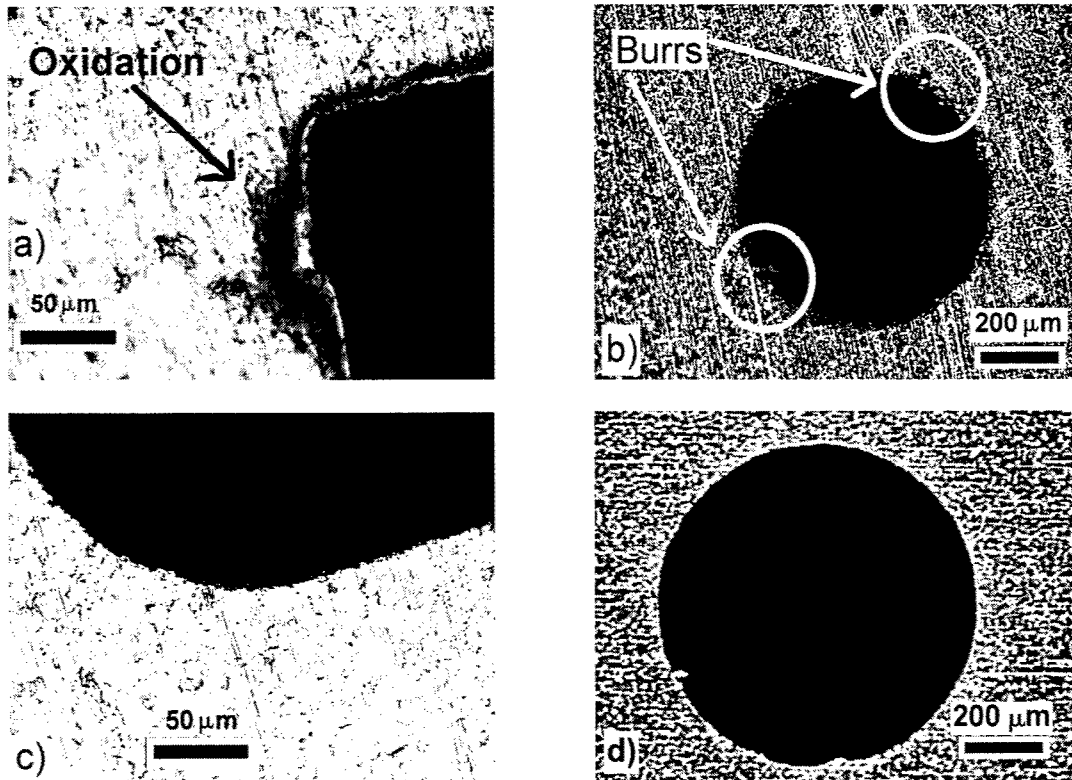
Figure 3: Optical microscope images of stencil apertures in 150 μm thick stainless steel. *Upper row:* Cut quality of a commercial conventional laser-cutting machine. a) Front side view of a corner, b) Backside view of a round aperture. *Lower row:* Cut quality achieved by the water-jet guided laser. c) Front side quality of a rounded corner. d) Backside view of a round aperture.

The width of the oxidation zone near the edge of the classical laser cut (Figure 3a) is approximately 12 μm. No oxidation is visible at the same magnification on the stencil which was cut with the water-jet guided laser (Figure 3c). The problem of burr formation, or particles on the backside of the apertures, is visible in Figure 3b for the classical laser cut. Figure 3d shows a slightly bigger hole that was produced with the water-jet guided laser, illustrating that particles and burrs can completely be avoided using this technique.

It is somewhat difficult to compare the two techniques, conventional and water-jet guided laser cutting, because of the numerous different parameters. However, concerning the oxidation zone, one important point is for sure the pulse duration of the laser.

An approximate expression to characterize the HAZ during non-ablative laser heating is given by the heat penetration length $l_{th} = 2 \cdot \sqrt{D\tau}$, where τ designates the laser pulse duration and D the thermal diffusivity of the heated material [4]. In the ablative case, i.e. during laser cutting, this expression overestimates the visible HAZ as a big part of the heat is used for the phase changes from solid to liquid, and eventually from liquid to vapor. Another part of the laser generated heat is carried away by the hot melt leaving the cutting kerf. For the sample showed in Figure 3a we obtain $l_{th} = 44$ μm, using the pulse duration given in Table 1 and $D = 4.0 \ 10^{-6}$ m^2/s (value from reference[4]).

In spite of this overestimation of the HAZ by the thermal penetration length, we may in a first step assume the square root relationship of the HAZ with respect to the laser pulse duration. Knowing the pulse lengths of 0.4 μs and 120 μs, we can estimate the HAZ of the Q-switched laser to be roughly 17 times smaller than the one caused by the free running laser used for the classical laser cutting. According to this calculation and Figure 3a, one would expect to end up with 12 μm / 17 = 0.7 μm of oxidation zone around the cut with the Q-switched laser. This is small enough to be invisible on Figure 3a and Figure 3c.

The question to address is then: *why do classical laser cutting machines do not use the favorable short Q-switch pulses?* The answer to this scientifically and economically interesting question can be found in the unwritten condition under which the small HAZ for the Q-switched lasers was derived. The above conclusion is only valid if the mechanism of material removal is the same with both lasers. This includes a variety of physical effects and their relative importance for the laser induced material removal. The most important are: (i) material related effects like phase changes and temperature dependent heat conduction; (ii) plasma related effects like plasma intensity, plasma life time, shielding efficiency etc.; and (iii) melt expulsion effects like convective cooling, melt flow velocity profile, assist gas turbulences etc.

If the delicate equilibrium of these effects is changed, the width of the HAZ may be strongly affected as illustrated in Figure 4. The image shows a cut that was produced using the same Q-switched laser as employed for the water-jet guided laser cutting and the same 150 μm thick stainless steel foil and the sample was moved at 4.5 mm/s. However, neither water-jet nor assist gas were used for the melt expulsion, and the result is an impressively larger HAZ together with redeposition on the front side and burrs on the backside.
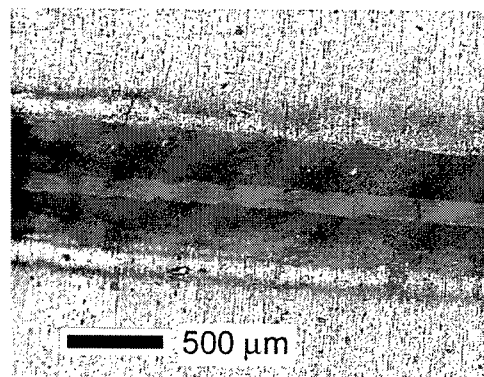
Figure 4: Optical microscope image of a laser cut with neither assist gas nor water-jet. The laser was the same Q-switched laser as used for the water-jet guided laser cutting.

This image does not prove that classical Q-switched laser cutting results in bad cut quality or large HAZ, it only illustrates the sensitivity of the cut quality to changes in the processing conditions. Optimized Q-switched laser cutting of metals often leads to important redeposition of droplets on the front side of the sample, which is difficult to remove[5]. Burr formation too is more important in the case of classical laser cutting with short pulses. As already mentioned before both effects, redeposition and burr formation, are an important disadvantage in solder paste stencil production. This is the reason why commercial stencil cutting machines, that are based on classical laser cutting, do not use Q-switched lasers in spite of the better HAZ that may be reached with these lasers.

To understand qualitatively the physical reasons we only need to consider the changes when using a Q-switched laser instead of a free-running laser: First the Q-switched pulses exhibit higher peak powers than the long pulses. This leads more easily to vapor formation, which expels small droplets of the melt against the assist gas stream. The gas stream cannot change the direction of these small and dense particles because of their relatively high momentum. Once the hot droplets touch the sample surface, they cool down and solder themselves to the surface. Secondly, the short pulse duration causes a small melt life-time. During this smaller time, the same gas jet can move the same volume of melt only over a smaller distance. If the distance that the melt can be moved by the gas jet, is smaller than the sample thickness, burr formation occurs. As it is visible in Figure 3b, even with relatively long pulses and a high assist gas pressure, some burrs/particles remain after traditional laser cutting at the backside of the sample.

Before coming to describe the situation during the water-jet guided laser process, we want to make sure to distinguish classical *cutting* and *drilling* with Q-switched lasers. The above paragraph and the mentioned disadvantages exhibited

by Q-switched lasers refer *only* to cutting applications. Q-switched lasers are in fact widely and successfully used for drilling applications (percussion drilling), where fast expulsion of the melt to the top surface is needed and small HAZ and small recast layer thickness could be obtained in blind holes.

We already saw that the gas jet and its relatively low momentum is involved in the negative effects occurring upon classical laser cutting with Q-switched lasers. In the case of water-jet guided laser cutting with Q-switched lasers, the situation is different, because a high momentum medium is used to expel the melt from the cutting kerf. If vapor is formed during water-jet guided laser cutting, the droplets cannot go against the water jet because it has similar density compared to the melt droplets, and high speed (up to 290 m/s). Thus no redeposition is observed in the water-jet guided case (Figure 3c). Similarly burr formation can completely be avoided when working close to the cutting threshold, because the melt is removed very efficiently (Figure 3d).

After stressing so much the high momentum of the used water-jet, it might be useful to mention that the high momentum is not associated to a high force on the sample as the water is directed through the cutting kerf and only touches the melt front. The gas jet on the contrary diverges directly after the nozzle and most of the gas pushes perpendicularly on the sample surface causing a high force on the sample in spite of the lower gas jet momentum.

In summary we can state that the high momentum of the water jet avoids burr formation and redeposition of droplets. In the absence of these effects it is also possible to take advantage of the small HAZ being associated with the short pulse duration. It is however impossible, for the moment, to give quantitative values for the width of the HAZ upon water-jet guided laser cutting. Too many physical processes involved in the material removal are modified by the usage of the water-jet. In the above discussion we neglected for example the changed heat conduction. It is clear that the water jet somehow cools the sample in between the laser pulses, but only a beginning to describe the heat conduction was made recently by Li *et al.*[6]. We also neglected the strongly changed plasma properties, which are subject to active research in the context of laser hardening[7].

4. CONCLUSIONS AND SUMMARY

In conclusion, cutting results of thin metal foils obtained by conventional laser cutting with a free running YAG-laser and by water-jet guided laser cutting using a Q-switched YAG-laser were compared. The cut quality is much better with the water-jet guided laser technique for similar cutting speeds and process efficiency. Namely a much smaller heat affected zone and the absence of burrs were demonstrated. Explanations for the quality differences are proposed, highlighting both, the role of the laser pulse duration and the role of the water jet momentum.

The example shows how the Q-switched laser can become a high quality cutting tool for thin materials when employed in the water-jet guided technique.

5. ACKNOWLEDGEMENTS

6. REFERENCES

1.   A. Luft, U. Franz, A. Emsermann and J. Kaspar: Appl. Phys. A, **63**, (1996), 93-101.
2.   A.M. Sterling and C.A. Sleicher: J. Fluid Mech., **68**, (1975), 477-495.
3.   G. Conti, E. Mattaini, L. Chiappetti *et al.*: Publ. Astr. Soc. Pacific, **113**, (2001), 452-462.
4.   D. Bäuerle: *"Laser processing and chemistry"* (Springer, Berlin, 1996).
5.   Personal communication: T. Sidler, Institute of Applied Optics, EPFL, Switzerland, 2002.
6.   C.-F. Li, R. Kovacevic and D. Johnson: Proc. Mech. Eng. Part B, **accepted by**, (2003).
7.   L. Berthe, R. Fabbro, P. Peyre, L. Tollier and E. Bartnicki: J Appl. Phys., **82**, (1997), 2826 - 2832.

Water Jet Guided Laser vs. Saw Dicing

Natalia Dushkina[*a], Frank R Wagner[b], Christophe Boillat[b], Jean-Marie Buchilly[b],
Bernold Richerzhagen[b]

[a]Laboratory of Laser Applications, The Gem City Engineering Co., 1425 N. Keowee St.,
Dayton, OH, USA 45404;

[b]SYNOVA SA, Parc Scientific A, Lausanne, CH 1015, Switzerland

ABSTRACT

The incessantly growing demands for higher speed of the wireless telecommunications and more compact devices require using of thin compound semiconductor wafers. The dicing is the very last process of the wafer manufacturing. At this stage the IC pattern is completely built up and the wafer has the highest value. Therefore, the goal of the singulation process is to provide the highest possible throughput. The conventional saw techniques "struggle" at their speed limits, while the conventional laser is not an appropriate dicing tool due to the strong thermal effect and big heat affected zones. The water-jet guided laser technology provides cool laser dicing since the laser is coupled in a fine stable water-jet and conducted to the work piece by means of total internal reflection like through an optical fiber, as the relatively low water pressure (10 - 30 MPa) of the tiny jet with diameter 40 - 100 μm results in a negligible force on the sample. This technology provides higher cutting speeds and burr-free kerf quality. By means of the Laser MicroJet, wafers as thin as 25 μm could be diced in streets of 50 μm width, with almost 100% wafer throughput. Here we compare the water-jet guided laser cutting with conventional techniques for dicing of thin semiconductor wafers. The results for Silicon and GaAs/Ge wafers are discussed in terms of speed, kerf quality and die fracture strength.

Keywords: Laser cutting, water jet, Q-switched Nd:YAG laser, semiconductor wafers

1. INTRODUCTION

In a drive towards higher production volumes and lower costs, the optoelectronics market is constantly pushing the semiconductor wafer production to smaller chip size using high-density packaging technologies and 8" and 12" wafers. The incessantly growing demands of the telecommunications industry for higher speed and more compact devices boosted the production of thin (less than 200 μm) compound semiconductor wafers, such as GaAs, Ge/GaAs, etc. Yield improvement is one of the key performance indicators depending strongly on the quality of the wafer post-fab processing since at that stage the wafer has the highest value. Dicing of GaAs wafers is not a trivial process, because GaAs wafers are fragile and brittle. The most commonly used dicing techniques at the moment are the saw dicing and scribe/break processes. A lot of improvements have been done recently of the saw dicing techniques in order to satisfy the high customers requirements and it is still the most widely used dicing tool for wafers with standard thickness.

Resinoid blades, the most commonly used in saw dicing, provide high-quality kerf with width of 30 μm, but they raise a lot of handling problems: they are very fragile, break easily and have very short life (<1000 cuts or one and a half wafers). Due to the blade wear, the quality is not consistent and the processing speed is low; therefore, the throughput is very slow and yield is low. The resin-bonded diamond blades also present availability and cost problems due to their complicated manufacturing process. Some of the handling and availability problems were diminished with the newly developed Disco electroplated blades, with strength being their biggest advantage over the resinoid blades. Besides the improvements, common saw methods are close to their limits and it is doubtful that these methods will meet the future demands of flexibility, high cutting speed, production rate and yield.

The scribe/break process allows for the reduction of the street size over 50% increasing the number of die per wafer. But this technique is limited to only large dies (larger than 1 mm x 1mm), the scribes are unreliable, the operation is

---

[*] ndushkina@gemcity.com; phone 1 937 221-5275; fax 1 937 221-5922; http://www.gemcity.com;

slow, and requires precise alignment. In 2001 Tyco Electronics reported a series of scribing improvements that have increased the throughput and reduced the dicing time to 35 minute/wafer, but more improvements still need to be made, especially concerning alignment and software problems.[1]

Both methods are limited to straight-line dicing and do not allow free-shape cutting or singulation of multi-project wafers. Conventional laser processing, one already well developed and approved technique for material processing, increases appreciably the flexibility and 3D-cutting possibilities, but is not appropriate for dicing of structured semiconductor wafers. The most popular IR lasers are fast and powerful, but introduce heat damages and slag, while the UV laser, gaining recently more and more popularity for their "cool" cutting, are still slow and do not provide enough output power for an efficient material processing.[2,3]

The water-jet guided laser technology combines the advantages of both laser groups: by confining a powerful Nd:YAG laser beam into a tiny water-jet, it provides fast and highly efficient "cool" laser cutting. Moreover, the employment of the Synova laser MicroJet® allows arbitrary shape cutting and multi-project wafer processing. Due to the negligible thermal effect and mechanical force-free cutting, wafers as thin as 25 µm could be diced in streets of 50 µm width, with almost 100% wafer throughput. The results for dicing of silicon (Si) and gallium arsenide (GaAs) wafers with the laser MicroJet® are presented in this paper, as well as a numerical evaluation of the cutting speed and its dependence on the material thickness and laser parameters. Also a comparison of the mechanical strength of dies cut with saw and water-jet guided laser is presented and discussed.

2. THE WATER JET GUIDED LASER TECHNOLOGY

The water jet guided laser technology was invented and developed by one of the authors (B.R.), who called it Laser MicroJet®.[4,5] In 1998, the concept was implemented in sophisticated laser cutting and dicing machines produced by Synova SA in Switzerland. The Gem City Engineering Co. (GCE) is the official distributor and representative of Synova SA for America. The Laboratory for laser applications at GCE is equipped with two Laser MicroJet® machines, which are used for demo-samples and development of Synova applications.
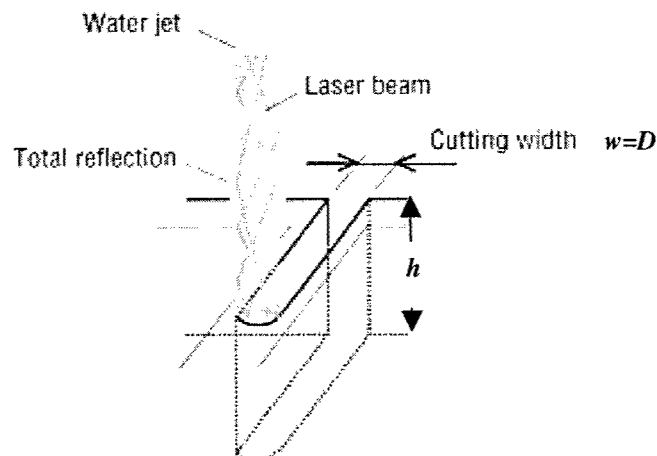
Fig. 1. The mechanism of wafer-dicing process. The water jet guides the laser beam as an optical fiber.

The water-jet guided laser technology provides low-temperature laser dicing since the laser beam is coupled in a fine, stable water-jet and conducted to the sample by means of total internal reflection (Fig. 1). Thus, the water jet can be referred to as a fluid optical waveguide of variable length. This feature allows a working distance of 2-3 inches and eliminates the problems of precise alignment and focusing on the sample of the conventional lasers. The diameter of the water jet is determined by the nozzle diameter, which might be 30, 50, 75, 100 and 150 µm. The high laminarity of the water jet provides kerf width of the same size as the water jet diameter. The relatively low pressure (10 - 30 MPa) of the tiny water jet results in a negligible force on the sample; thus, there is no mechanical stress during cutting. This is of

great importance when dicing thin and brittle GaAs wafers. The water jet itself does not cut the sample, but plays a tri-fold function in the cutting process: 1) it guides the laser beam to the sample; 2) immediately cools the interaction area, and 3) simultaneously cleans the residues from the kerf.

Synova MicroJet® machines use Nd:YAG lasers with wavelength of 1064 nm working in pulsed or Q-switch regimes (Table 1). The water jet guided laser is suited for processing of any material that absorbs at this wavelength, such as any metal, semiconductor and some ceramics, the only limitation being the thickness. Unfortunately, materials that are transparent for the Nd:YAG laser wavelength, like glass and oxide layers, cannot be processed with high quality. To broaden the range of materials that might be cut with the MicroJet®, the team of Synova is developing a new laser system using a frequency-doubled Nd:YAG laser with a wavelength of 532 nm.

Table 1. Parameters of the Synova lasers

	Pulsed Laser	Q-switched Laser
Pulse Duration	80 – 250 μs	100 – 500 ns
Pulse Frequency	1 – 1000 Hz	5-25 kHz
Energy per pulse	0.01 – 20 J	<5 mJ

3. VELOCITY CALCULATIONS

A stable laser cutting process is described theoretically by the power balance of the incoming and outgoing power contributions, i.e., the laser beam energy absorbed in the material has to be equal to the energy necessary for heating and transforming the material along the cutting process. The most general expression of the power required for a conventional laser cutting is:[6]

$$AP_L + P_r = P_{Tm} + P_m + P_v + P_l \ .$$ (1)

The terms in the left side are the absorbed laser power AP_L and the power P_r of the exothermal reaction in the case of oxidation cutting, while the terms in the right side account for: (1) heating the material from room to the melting temperature P_{Tm}, (2) the latent heat of melting P_m, (3) heating the melt to the vaporization point P_v, and (4) the latent heat of evaporation P_l. This equation gives a rough approximation of the energy required for the different processes of material transformation, and does not take into account losses, the duration of irradiation, and the energy distribution in the laser beam. A more detailed and accurate analysis, based on the energy conservation, should include also these factors.

The theoretical description of the water-jet guided laser cutting given below is based on the assumption that the cutting occurs at evaporation and the water jet removes the ablated material. Also, bearing in mind that the laser beam is confined into a water-jet undergoing multiple reflections like in an optical fiber, we assume that the distribution of the laser energy across the water-jet is constant. Another factor, simplifying the analysis, is the alternation heating and cooling effect due to the pulse working regime used in the MicroJet® cutting. During the pulse duration the laser beam is absorbed and interacts with matter as in the case of conventional laser cutting. Between the pulses, though, the water-jet instantly cleans and cools the kerf, and therefore, the accumulation of heat accumulation might be ignored and any following cycle might be considered independently from the previous one. The equation of the power balance that describes the water-jet guided laser cutting could be obtained from Eq. (1) bearing in mind the assumptions above:

$$tAP_L = \rho V[C_p(T_m - T_0) + L_m + C_p(T_v - T_m) + L_v] \quad ,$$ (2)

where A is the material absorptivity of the laser energy, P_L is the laser beam power, ρ is the mass density, V is the volume of the removed material, C_p is the heat capacity, T_m and T_v are the temperature of melting and evaporation, respectively, T_0 is the room temperature, L_m is the latent heat of fusion and L_v is the latent heat of evaporation. The total interaction time t, also taken into account, represents the time required for the cutting front to move to a distance l with speed v, thus, $t = l/v$. The mass of the removed material is $\rho V = \rho whl$, where h the material thickness, and w is the kerf

width (Fig. 1). At best working conditions, the kerf width is the same as the diameter of the water jet, which is equal to the nozzle diameter D, i.e., $w=D$. After substitution and rearrangement, Eq. (2) might be rewritten in a form giving the cutting speed:

$$v = \frac{AP_L}{Dh\rho[C_p(T_m-T_0)+L_m+C_p(T_v-T_m)+L_v]} \quad . \tag{3}$$

The main output power P_L of a pulsed laser, is the product of the pulse energy E_p and the pulse frequency f, i.e., $P_L=E_pf$. The energy per pulse is determined by multiplying the pulse output value by the pulse duration $E_p=P_p\tau$. Thus, Eq. (3) might be rewritten in a simpler form:

$$v = C\frac{E_pf}{Dh} \quad , \tag{4}$$

where

$$C = \frac{A}{\rho[C_p(T_m-T_0)+L_m+C_p(T_v-T_m)+L_v]} \tag{5}$$

is a constant for the given material. Eq. (4) gives a direct connection of the cutting speed with the laser parameters and the cutting conditions, such as nozzle diameter D and material thickness h. Higher speed might be obtained when using a smaller nozzle. Also the higher is the pulse energy and the laser frequency, the higher is the speed. For given laser parameters and a nozzle diameter, the speed decreases with increasing the thickness.
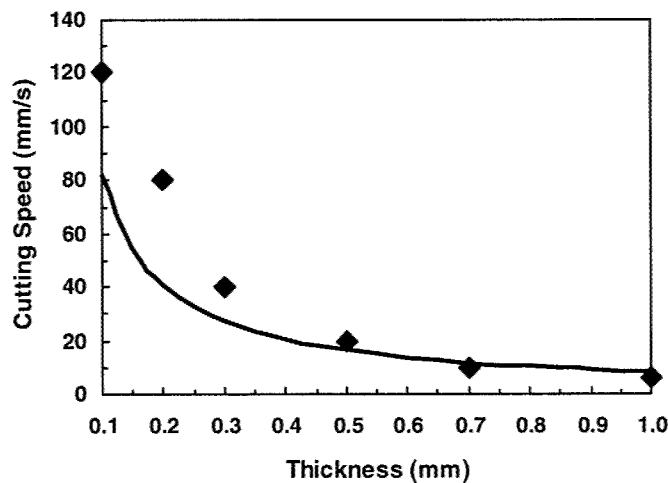
Fig. 2. Dependence of the cutting speed on the material thickness. The solid curve is calculated for silicon using Eq. (3) for a given set of laser parameters. The symbols are real values of the cutting speed obtained with different lasers.

The solid curve on Fig. 2 shows the dependence of the cutting speed on the thickness, calculated with Eq. (3) for silicon with material characteristics listed in Table 2. The values for the laser parameters are the real values of the Q-switched Nd:YAG laser (Vectormark of Haas), which was used for all demo-cuts shown in this paper: the output power in Q-switch regime is 19 W, as measured, and the laser pulse frequency and duration are given in Table 3. The curve is build for a single set of laser parameters considering a single cutting pass.

Table 2. Physical Properties of Si and GaAs

Characteristics	Si	References	GaAs	References
Absorptivity A	0.7	6	0.6	6
Mass density ρ (kg/m^3)	2330	6-9	5320	10-12
Specific heat C_p (J/kg K) at 300 K	711	8	322	8, 13
Melting temperature T_m (K)	1683	7	1511	14
Latent heat of fusion L_m (J/kg)	1.65x10^6	15	6.68x10^5	14, 16
Temperature of evaporation T_v (K)	2628	15	3000	18
Latent heat of evaporation L_v (J/kg)	10.58 x10^6	15		

Eq. (3) does not include heat conduction losses into the material near the kerf and, therefore, gives higher values for the speed than what usually are obtained in real conditions, especially for thickness more than 200 μm. In principle, the depth of penetration of the laser beam in silicon is about 300 μm. The dependence of the absorbance for the typical light spectrum as a function of Si layer thickness shows that almost 100% of the light is absorbed at thickness of 300 μm.[17] This means that whatever is the laser beam power and cutting parameters, wafers with thickness more than 300 μm cannot be cut with a single pass. Our experience shows that in order to obtain good cutting quality, the wafers should not be thicker than 250 μm. In principle, it is possible to cut wafers with standard thickness (about 780 μm) using the lasers available for the Synova machines, but for this purpose multiple pass should be used. Though, due to the worsen edge quality and broaden kerf width, dicing of thick wafers seems not very convincing application at the moment for the water-jet guided laser technology. Furthermore, the conventional saw is a constantly improving technique still providing satisfactory quality and dicing speed for wafers with standard thickness.

Table 3. Parameters of Haas Vectormark Q-switched Nd:YAG laser

Parameter	Nd:YAG laser
Pulse energy	2.6 mJ
Energy reproducibility	<2%
Average power	65 W
Pulse length	450 ns
Repetition rate	25 kHz

The symbols (diamonds) on Fig. 2 represent the dicing speed of blank Si wafers with different lasers at Synova's laboratory. The values do not follow the behavior of the theoretical curve, because they were obtained with different laser parameters and regimes (Q-switch and long pulse regime) and have only a representative feature of the best results obtained by Synova till now. These should be considered as maximum values that might be obtained in real conditions with the lasers available at the moment for the Synova laser dicing machines. In practice, only few applications require dicing of blank Si, GaAs or other compound semiconductor wafers, for which such speed is achievable in real production conditions. Most applications include structured wafers and in these cases the cutting speed depends on many additional factors, such as presence of oxide layers in the streets, type and thickness of the surface layers or treatment, backside metalization, surface relief, etc., which reduce the speed or require multiple pass with different laser energy or speed.

The Q-switched laser considered here is available at The Gem City Engineering Co., Dayton, Ohio, where, due to safety issues, all the demo-tests with GaAs wafers are to be done. The machines that Synova offers now might include lasers working in long pulse regime or Q-switch delivering output power up to 250 W (see table 1), and therefore, providing higher speed than the solid curve shown on Fig. 2.

The numerical estimation of the cutting speed for GaAs wafers gives lower speed values than Si, which is due mainly to the higher (more than twice) mass density of GaAs. Our experience confirms this tendency and, in practice, the difference between the cutting speeds is even higher than the theoretically predicted, due to the fact that GaAs is very fragile and brittle. Table 4 shows speed values for GaAs wafers obtained with the Vectormark Nd:YAG laser (Synova LDS-200 machine), at which the quality of the kerf is still high.

Table 4. Cutting speed of GaAs wafers (single pass)

Thickness (μm)	Speed (mm/s)
100	60
147	40
178	30
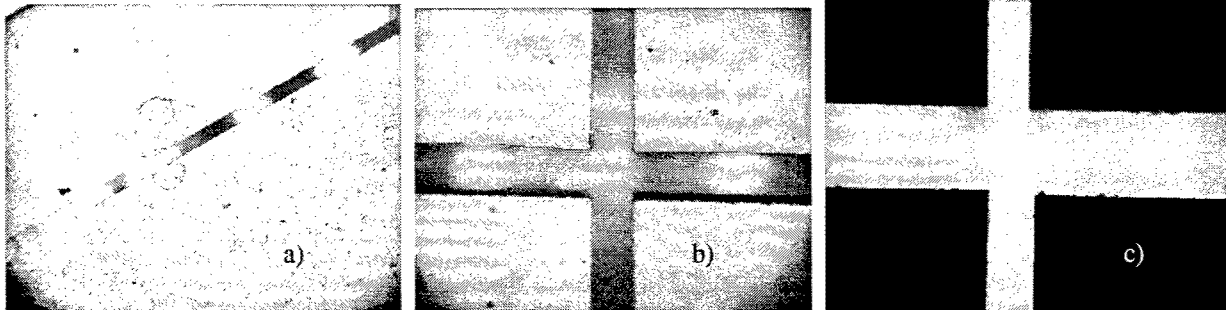
Fig. 3. GaAs wafer with complex layered structure with thickness 147 μmdiced with two passes with speed of 10mm/s and 60 mm/s, respectively: a) and b) 50 μm nozzle and water jet pressure of 300 bar; c) 50 μm nozzle (vertical line) and 75 μm nozzle (horizontal line).
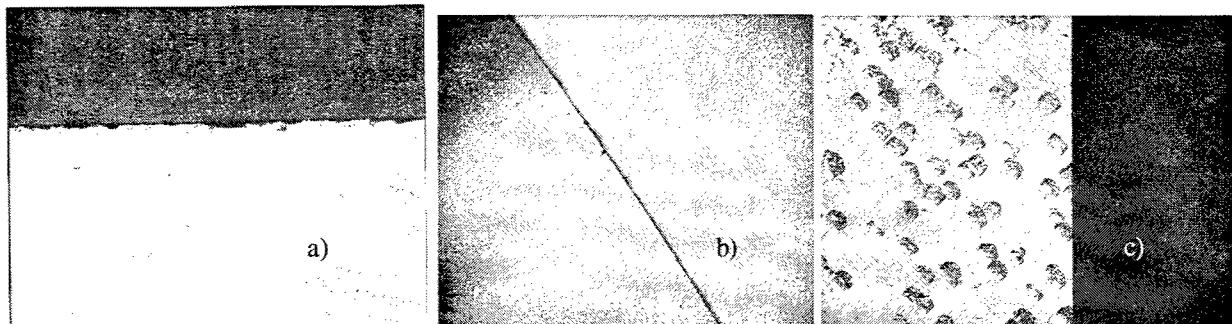
Fig. 4. Comparison of the front side quality with the saw. The wafers are GaAs/Ge with thickness of 178 μm and different top surfaces: a) saw cut with speed 1.8 mm/s, magnification 50 times; b) and c) laser MicroJet® kerf with speed of 15 mm/s, magnification 400 times. The wafers were not cleaned after cutting. No chipping or edge cracks are seen on b) and c). The speed factor vs. saw is 8.3. Customers require speed factor more than 4 to consider replacement of the existing saw equipment with the Laser MicroJet®.

Some examples of dicing of GaAs wafers are shown in Figures 3-6. Fig. 3 demonstrates dicing with the most used diamond nozzles with size of 50 and 75 μm. Fig. 4 compare the edge quality of dies cut with saw and laser MicroJet®, while Fig. 5 shows the backside edge quality in the case of backside metalization and blank GaAs/Ge wafer. The case of backside metalization usually requires lower speed and careful optimization of the dicing parameters in order to avoid chipping. Fig. 6 demonstrates the capabilities of the laser MicroJet® for cutting inner contours, which is important for singulating of multi-project wafers.

No backside metalization   With backside metalization
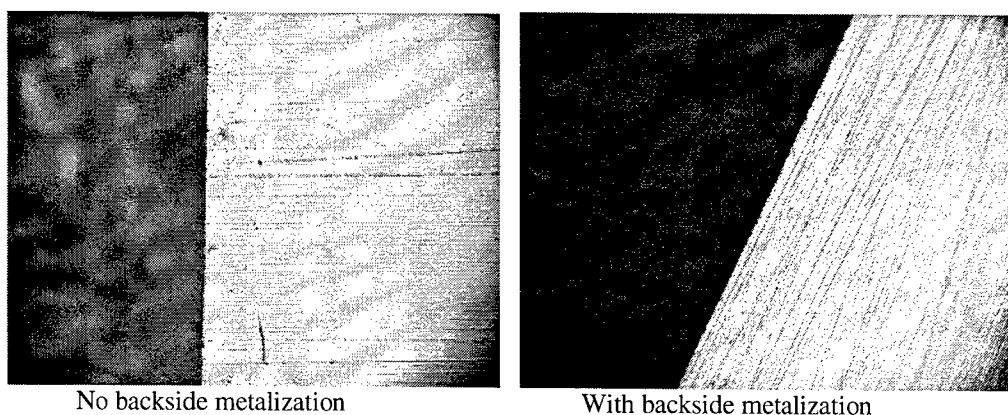
Fig. 5. Backside quality of GaAs/Ge wafer cut with the laser MicroJet®: wafer thickness 0.007" (178 µm), nozzle diameter 75 µm, water jet pressure 200 bar, speed 15 mm/s, magnification 400 times.
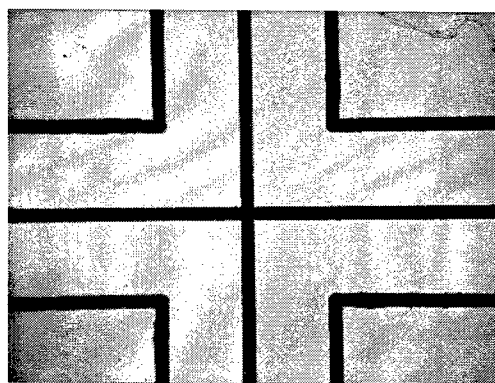
Fig. 6. Cutting of inner contours with the laser MicroJet®. Multi-layered structure on Silicon; laser pulse energy 2.5 mJ, speed 20 mm/s.

4. MECHANICAL DIE STRENGTH

We compare here the results on the fracture strength of silicon and GaAs/Ge dies cut with laser MicroJet® and saw. The data for Si were obtained by one of our European customers, a big chip manufacturer, while the data for GaAs/Ge were provided by one of our USA customers. The fracture strength of the silicon chips was investigated using two schemes shown in Fig. 7: (a) beam bending test and (b) ball bending test, while the GaAs/Ge dies were tested only with the ball bending test. At the point of loading, the top surface of the die is placed in a state of compression, whereas the bottom surface is in tension. The stress σ can be calculated from the die thickness d, the maximum bending moment M, and the moment of inertia of the cross section I, and for a rectangular die with width b and distance between the bearing points L (see Fig. 8) can be expressed as:

$$\sigma = \frac{Mc}{I} = \frac{3FL}{2bd^2} \quad , \tag{6}$$

where $c=d/2$ is the distance from the die center to outer edge, F is the applied load, $M=FL/4$ and $I=bd^3/12$. The fracture strength measurements consist in measuring the maximum load at which the die breaks and the elongation at the moment of break. Then the results are averaged for each group of dies consisting of 36 pieces. The average maximum load determines the mechanical stress, while the average elongation stands for strain. Thus, the results might be

presented as a stress – strain graph. The slope of the lines determines the Young's modulus or the Modulus of elasticity factor (see Fig. 9).

Force   Silicon Chip   Force

a) Beam Bending Test   b) Ball Bending Test
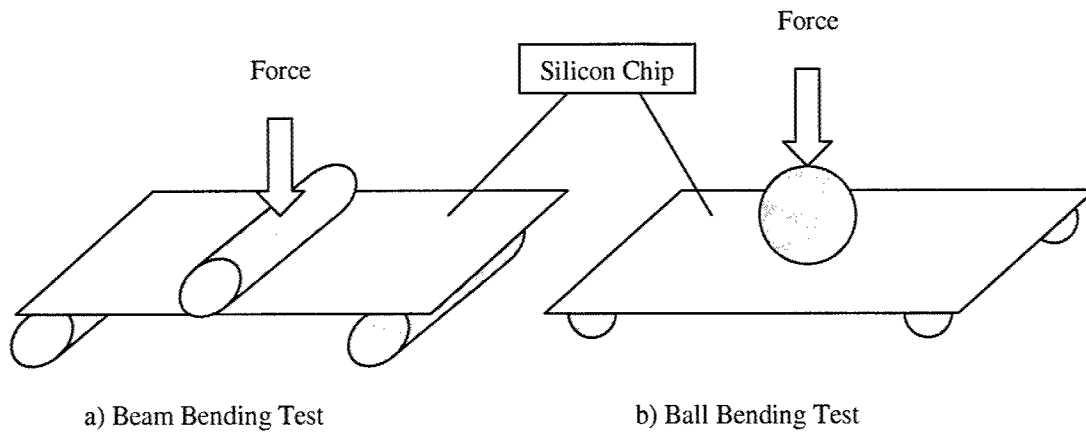
Fig. 7. Fracture strength test.

F   b

L/2   L/2   d
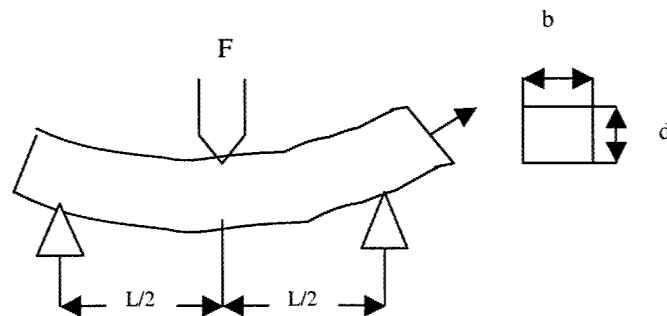
Fig. 8. Bending test of a rectangular die.

The results for the laser MicroJet dicing are compared with the results for saw dicing with resinoid blades on Figures 10 and 11 for silicon and GaAs/Ge dies, respectively. The absence of heat induced damages and micro-cracks is the reason for high fracture strength. It is seen that the laser MicroJet diced chips have significantly higher fracture strength than the diced with saw. Only in the case of backside metaliztion the dies cut with the lasser MicroJet[®] have shown lower strength, and the reason for this result is not completely clear yet. It is worth to explain here that the laser MicroJet[®] uses a UV laser tape, especially designed for Synova, not the conventional UV tape for saw dicing. The tape is curable with UV light and works very well with blank silicon or GaAs wafers. Though, we still have difficulties to remove from the tape dies with backside metalization. Our experience shows that after the UV exposure only the die edges are sticking to the tape, but not the die surface. We suppose that the high temperature at the boundary metal – tape during the cutting of the metal layer causes thermal damage of the adhesive layer and kills its UV sensitivity. The adhesive strength of the tape in the kerf area stays high and we have to apply force in order to remove the dies. We believe that during this forced removal of the dies, we introduce cracks, which are the cause of the easier break of the dies at lower load values. The manufacturer of the tape works hard on improving the tape properties, especially for the case of backside metalization. We also plan new experiments, which, we believe, will show higher fracture strength for the dies with backside metalization.
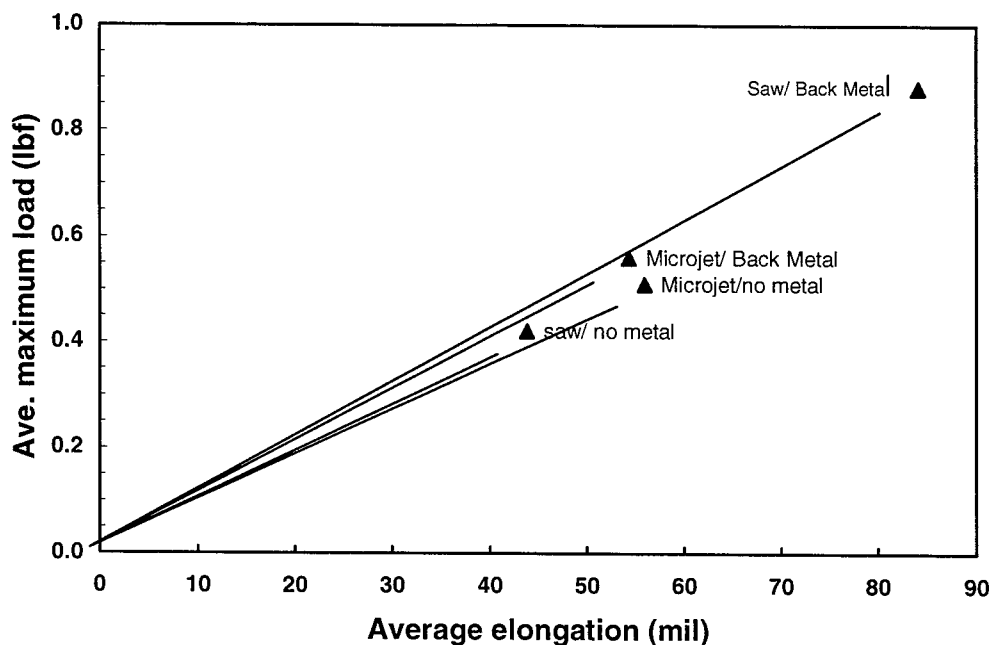
Fig. 9. Stress – strain measurements of GaAs/Ge dies cut with the laser MicroJet® and saw.

1. SUMMARY

The water-jet guided laser technology allows omni-directional and free-shape cutting, as well as processing of multi-project wafers. The laser MicroJet® provides lower tolerances, constant burr- and chipping-free cutting quality, more than 15 times faster dicing speed, as well as higher die fracture strength than the saw. At the moment the Synova technology is more suitable for dicing of thin semiconductor wafers, and, specifically, of GaAs wafers, which are fragile and brittle, and cause a lot of troubles to the saw dicing. The cutting parameters depend strongly on the wafer structure, the presence of oxide layers and backside metalization, and should be optimize for any type of wafers. More studies and improvements still need to be made, especially in the case of backside metalization, in order to meet the broad variety of requirements of our customers.

ACKNOWLEDGEMENTS
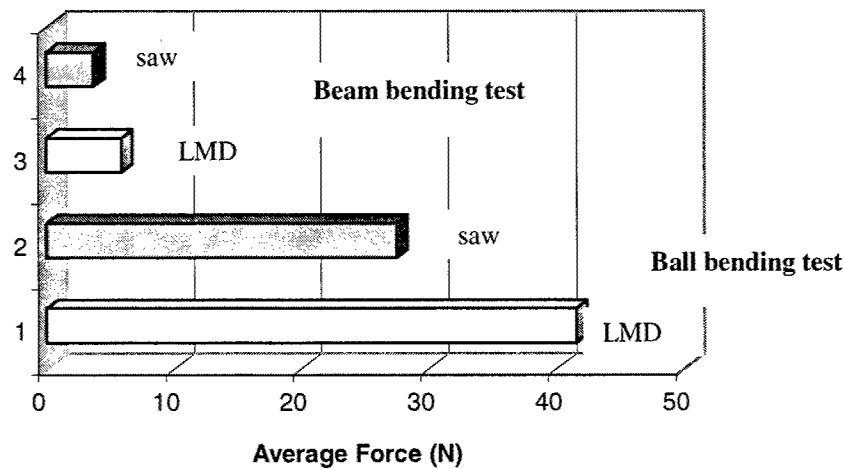
Fig. 10. Fracture strength of 100 micron thick Silicon dies obtained with laser MicroJet® dicing (LMD) and saw.
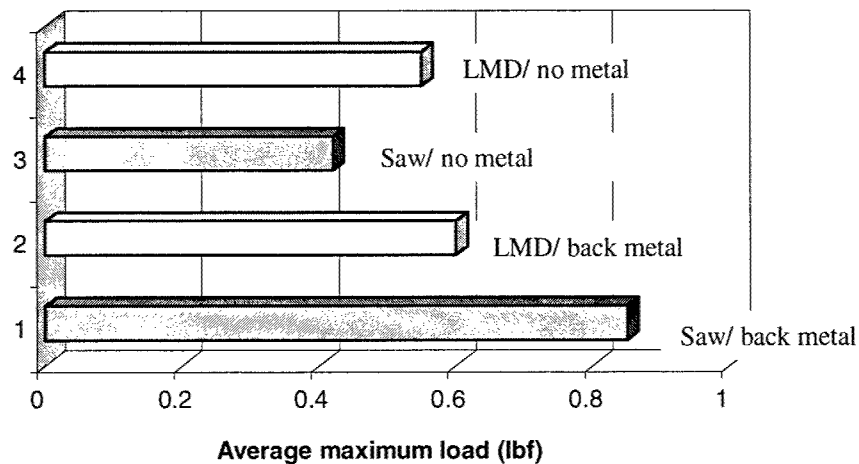
Fig. 11. Fracture strength of 178 micron thick GaAs/Ge dies obtained with laser MicroJet® dicing (LMD) and saw.

REFERENCES

1. R. Fox, "Dicing Improvements: Yield Enhancement, Throughput Increase and Die Size Reduction in M/A-COM's GaAs Fab", *Digest of Papers, GaAs Mantech Conference*, May 21-24, Las Vegas, pp. 48-51, 2001.
2. H. K. Tönshoff, A. Ostendorf, T. Wagner, "Structuring Silicon with Femtosecond Lasers", handout.
3. K. H. Leong, "F_2-laser applications at University of Toronto", Industrial Laser Solutions, October, pp. 21-24, 2001.
4. B. Richerzhagen, "Development of a System for Transmission of Laser Energy," *Ph. D. Thesis work*, EPFL, Switzerland, 1994.
5. B. Richerzhagen, G. Delacrétaz, R.P. Salathé, "Complete Model to Simulate the Thermal Defocusing of a Laser Beam Focused in Water," *Optical Engineering*, vol. **35**, No. 7, pp. 2058 – 2066, 1996
6. J. F. Ready (ed.), *LIA Handbook of Laser Materials Processing*, (1st ed.), p. 429, LIA Magnolia Publishing, Inc., 2001.
7. J. Singh, *Physics of Semiconductors and their Heterostructures.*, McGraw Hill, 1993.
8. K. Ng, *Complete Guide to Semiconductor Devices*, McGraw-Hill, 1995.
9. S. Sze, *Physics of Semiconductor Devices*, New York: Wiley, second ed., 1981.

10. M. Fischetti, "Monte Carlo Simulation of Transport in Technologically Significant Semiconductors of the Diamond and Zinc-Blende Structures-Part I: Homogeneous Transport," *IEEE Trans.Electron Devices*, vol. 38, no. 3, pp. 634-649, 1991.

11. T. González Sánchez, J. Velázques Pérez, P. Gutiérrez Conde, and D. Pardo Collantes, "Five-Valley Model for the Study of Electron Transport Properties at Very High Electric Fields in GaAs," *Semicond.Sci.Technol.*, **6**, pp. 862-871, 1991.

12. S. Adachi, "GaAs, AlAs, and $Al_xGa_{1-x}As$: Material Parameters for Use in Research and Device Applications," *J.Appl.Phys.*, **58**, pp. R1-R29, 1985.

13. S. Tiwari, *Compound Semiconductor Device Physics*, Academic Press, 1992.

14. A.S. Jordan, J. Cryst. Growth **71**, p. 551, 1985.

15. CRC Handbook of Chemistry and Physics, 69th Edition, CRC Press, Inc., 1989.

16. W. Miller, U. Rehse, K. Böttcher, Cryst. Res. Technol., **34**, pp. 481-489, 1999.

17. T. H. Wang, T.F. Ciszek, C. R. Schwrtfeger, H. Moutinho, and R. Matson, *Solar Energy Mat. And Solar Cells*, **41/42**, p. 19, 1996.

18. Cavalleri, K. Sokolovski-Tinten, J. Bialkowski, D. von der Linde, "Time of flight mass spectroscopy of femtosecond laser ablation of solid surfaces", SPIE Proceedings **3343**,

Laser bending of silicon

U. Löschner*, H. Exner*, E. Gärtner**, J. Frühauf**

*Hochschule Mittweida – University of Applied Sciences
Laserinstitut Mittelsachsen e.V.
Technikumplatz17, 09648 Mittweida, Germany

**Technical University of Chemnitz
Department of Electrical Engineering and Information Technology
09107 Chemnitz, Germany

Abstract

We are going to present a new technology for laser machining of silicon developed at the Laser Institute of Mittweida by a suggestion and in cooperation with the Technical University of Chemnitz, Department of Electrical Engineering and Information Technology. It allows the laser induced bending of microstructural silicon elements prepared by anisotropic wet etching. Bending of the element toward the incident laser beam occurs as a result of the laser induced thermal stresses in the material.

We investigated the influence of various process parameters on the bending angle. There is only a small range of laser power to generate bendings in silicon. We will show a variety of examples including multiple and also continuous bendings.

There are several essential advantages compared to conventional bending technologies: Laser bending is a contactless process without using additional tools or external forces. Because of the local laser treatment the heat flux to neighbouring material can be minimized so that the technology is suitable for machining of already finished microsystems.

This new technology opens up a new field of applications in microsystem technologies. It is possible to generate a clip-chip-mechanism to clip a chip in a holder. Other examples are the exact positioning of optical mirrors or other components, the production of electrostatic drives and sliding chips for micro optical benches.

Keywords: laser, bending, micromachining, silicon

1. Introduction

In the field of microsystem technology there is a growing demand for the micro processing of materials using lasers. Laser micromachining, for instance such as the drilling of microholes or the generation of microstructures in various materials is an established technology to produce microsystems [1,2].

In this paper we present a new technology to form silicon microstructure elements (mse) using laser induced thermal stresses caused by local laser treatment. This technique is well known for metallic parts. In the macroscopic field the laser is used to form large metal parts like plates and tubes needed in the prototype construction and the automobile industry. On a small scale there are some applications for mechanical adjustment of micro mechanical and micro optical components with lasers [3,4,5].

Up to now an application of this technology for silicon structures especially for microsystem technology is unknown.

2. Experimental procedure

The mse we used in the experiments were prepared by anisotropic wet etching at the Technical University of Chemnitz and Information Technology. They consist of one-side fastened bending elements made of single crystal silicon with a (100) orientation.

Under the condition to generate no melting we investigate characteristic process parameters like laser power, irradiation regime and thickness of the material. The results will give information about the reproducibility and the precision of the bendings in order to find application possibilities and limits of this technology in microsystem technology.

Fig. 1: Experimental set-up

The experimental set-up (see Fig. 1) consists of the laser source, a scanner system with objective lens, a sample holder with xyz-translation stage including a rotation axis and a device for measuring the bending angle. An Nd:YAG laser operating at 1064 nm wavelength was used for the experiments. It can work in the cw and the q-switched mode. The laser beam passes a xy-scanner and is focused onto the sample.

The current bending angle is measured in-situ by means of a ccd camera mounted laterally to the bending mse.

The irradiation regime used to generate the bending has a meander shaped geometry consisting of 10 lines with uniform distance as shown in Fig. 2. Begin and end of the lines are located outside of the bending area to avoid melting caused by acceleration effects of the laser beam scan. Depending on the desired size of the bending angle a specific number of consecutive scans of the regime is necessary.
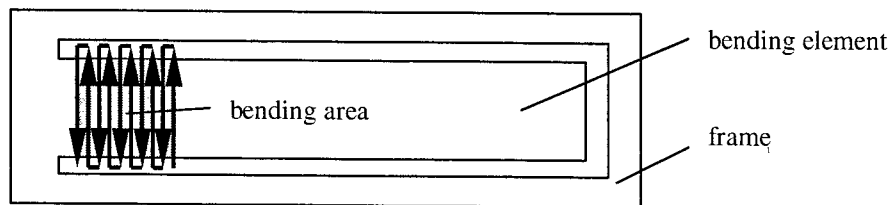
Fig. 2: Schematic microstructure element with meander shaped geometry (not full-scale)

3. Results and Discussion

3.1 Influence of the laser mode

Bending experiments in the q-switched laser mode were not successful up to now. Because of the short pulse duration of the laser (100 ns) melting and removal respectively occurs also with low average laser power in the range of 1 W at different pulse frequencies. No bending could be observed. Obviously the necessary thermal induced stresses cannot be produced with short pulses.

In the continuous laser mode (cw) bending occurs and the mse bends toward the incident laser beam. There is only a small range of laser power suited for bending. Too low laser power produces no bending. Melting of the surface occurs when the power is too high.

parameters	
mode:	cw
wavelength:	1064 nm
velocity:	10 mm/s
line distance:	5 μm
position:	6.8 mm
scans :	20
thickness:	100 μm

Fig. 3: Bending angle as a function of laser power

3.2 Laser power

These experiments were done on a 100 µm thick bending element using the irradiation regime described above applied at a distance of 6.8 mm from the clamping position.

There is a nearly linear correlation between laser power and bending angle as shown in Fig. 3. With increasing laser power the bending angle increases. The hindered heat flow at the edges of the bending element causes melting areas at the edges which become larger with rising laser power. Therefore, the parameter laser power is inappropriate to control the bending angle because expanded melting is undesired.

Fig. 4: Bending angle as a function of number of consecutive scans

3.3 Number of consecutive scans

We've found out that there is a dependence between bending angle and number of consecutive scans of the irradiation regime described above. In the experiments the number of scans were varied from 10 to 40.

The increasing of the number of consecutive scans results in larger bending angles (see Fig. 4). The bending angle gradually decreases with each additional scan so that the bending rate, defined as the rate at which the bending angle changed after consecutive scans, falls with rising number of scans. No linear dependence can be observed. There are two main reasons to explain the results. First there is a sinking temperature gradient between the irradiation area and the surrounding material with increasing machining time and therefore lower thermal stresses. Secondly associated with work hardening of the material the plasticity will be complicated

Fig. 5: Effect of line distance on the bending angle

with accretive bending because there is a reduction of possible displacement processes in the lattice planes.

3.4 Line distance

If we change the line distance of the meander shaped geometry so we obtain different values of the bending angle. In the experiments line distances range between 0 μm and 20 μm stepped in 5 μm. Fig. 5 depicts the bending angle as a function of the line distance of the meander shaped geometry. It is clearly seen that the largest bending angle is obtained at 5 μm line distance. Larger line distances cause nearly linear decreasing of the bending angle. Unexpected at 0 μm line distance the bending angle is approximately half of the value from that at 5 μm line distance. There are two basic reasons to explain this behaviour. First at 0 μm line distance the laser treatment is concentrated to one line on the bending element. Resulting in a pronounced work hardening the possible displacement processes in the lattice planes in a voxel are limited. Secondly with accretive machining time the temperature gradient between irradiation area and surrounding material is sinking. Thus there exists less thermal stresses and therefore smaller bending angles.

3.5 Machining velocity

The range of machining velocity is restricted by the energy input. Out of range either the energy input is too low and no bending occurs or too high and melting is generated.

The bending angle appeared runs nearly proportional to the machining velocity as shown in Fig. 6. Increasing machining velocity results in smaller bending angles. The faster the laser beam scans across the material the smaller is the temperature gradient between irradiation area and the surrounding material because sinking line energy. Finally there are less thermal induced stresses and lately smaller bending angles.
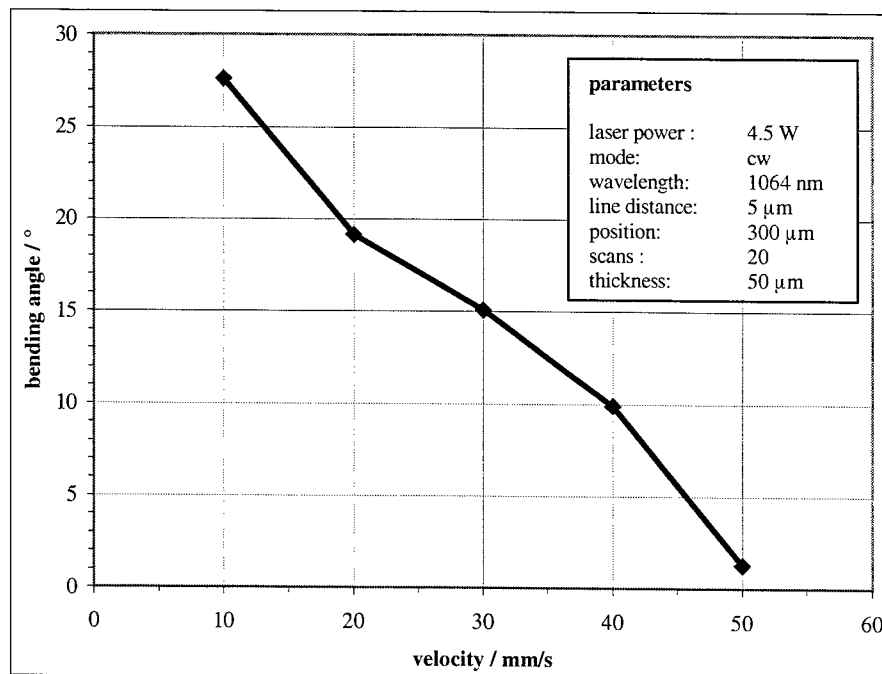
Fig. 6: Bending angle as function of machining velocity
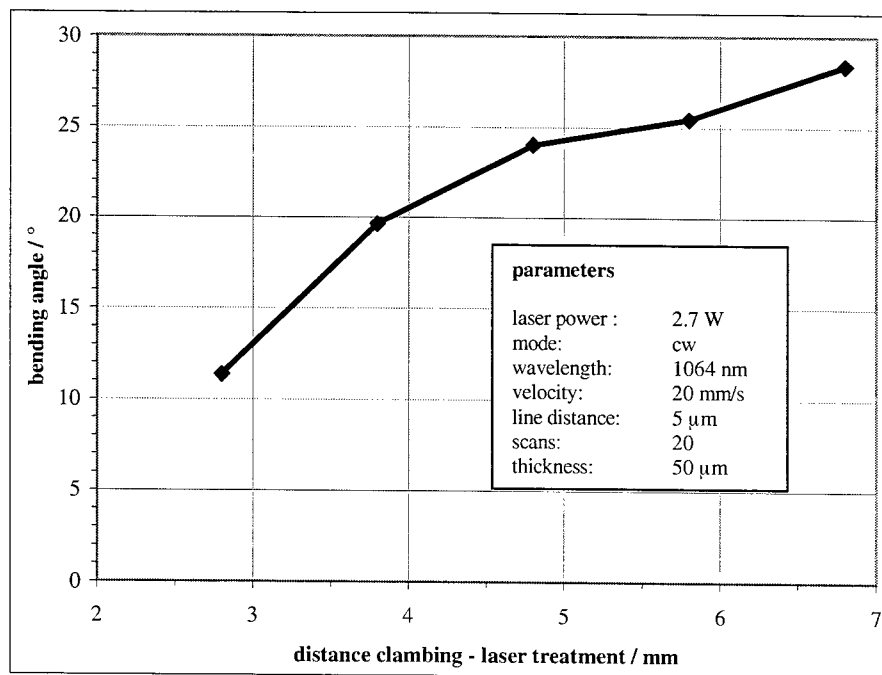
Fig. 7: Bending angle as a function of the position of laser treatment

3.6 Position of laser treatment

We define the distance to the clamping position of the bending element as the position of laser treatment. The bending angle directly depends on the position of laser treatment. Fig. 7 clearly demonstrates that the bending angle increases with growing distance of the position of laser treatment from the clamping. The effect is nonlinear. So the bending angle gradually increases with growing distance from the clamping position. Displacing the position of laser treatment nearer to the clamping more heat can flow from the bending element into the frame of the mse so less thermal induced stresses responsible for the bending are generated.

Fig. 8: Effect of the thickness of the bending element on bending angle

3.7 Thickness of the bending area

We found out that the bending angle strongly depends on the thickness of the bending element. With increasing thickness the bending angle becomes smaller as shown in Fig. 8. The geometrical moment of inertia immediately straight depends on the thickness of the bending element. Thicker bending elements causes larger moments of inertia. So the necessary forces and stresses must increase to generate equal bending angles.

3.8 Aging of the bending

To estimate aging of the bending we measured the bending angle immediately after machining and in certain time

time	0 s	20 s	30 s	1 min	10 min	1 h	1 d	4 d	28 d
bending angle	29.92°	29.92°	29.92°	29.92°	29.92°	29.92°	29.92°	29.92°	29.92°

Fig. 9: Bending angle as a function of the time

steps afterwards see Fig. 9. Up to now the bending angle remains constant so we can except near- and middle-term aging.

3.9 Reproducibility and accuracy

We bent 22 mse with identical parameters as shown in Fig. 10. The bending angles differ up to 4.6° and oscillate to an average value of 12.3°. The bending results show that the reproducibility and accuracy is insufficient for future applications in microsystems.

There are two reasons which can explain the results: First the laser power itself has a stability of about ± 2.5%. Second the thickness of the

Fig. 10: Frequency distribution of the bending angle from 22 mse

bending element differs in a range of ± 2%. Both facts influence the bending angle as reported above. To improve the reproducibility and precision a criterion of abruption is necessary which has to be generated when the desired bending angle is reached.

3.10 Bending radius

At all bended mse the bending radius was determined by optical profilometry by our co-authors. Fig. 11 depicts the
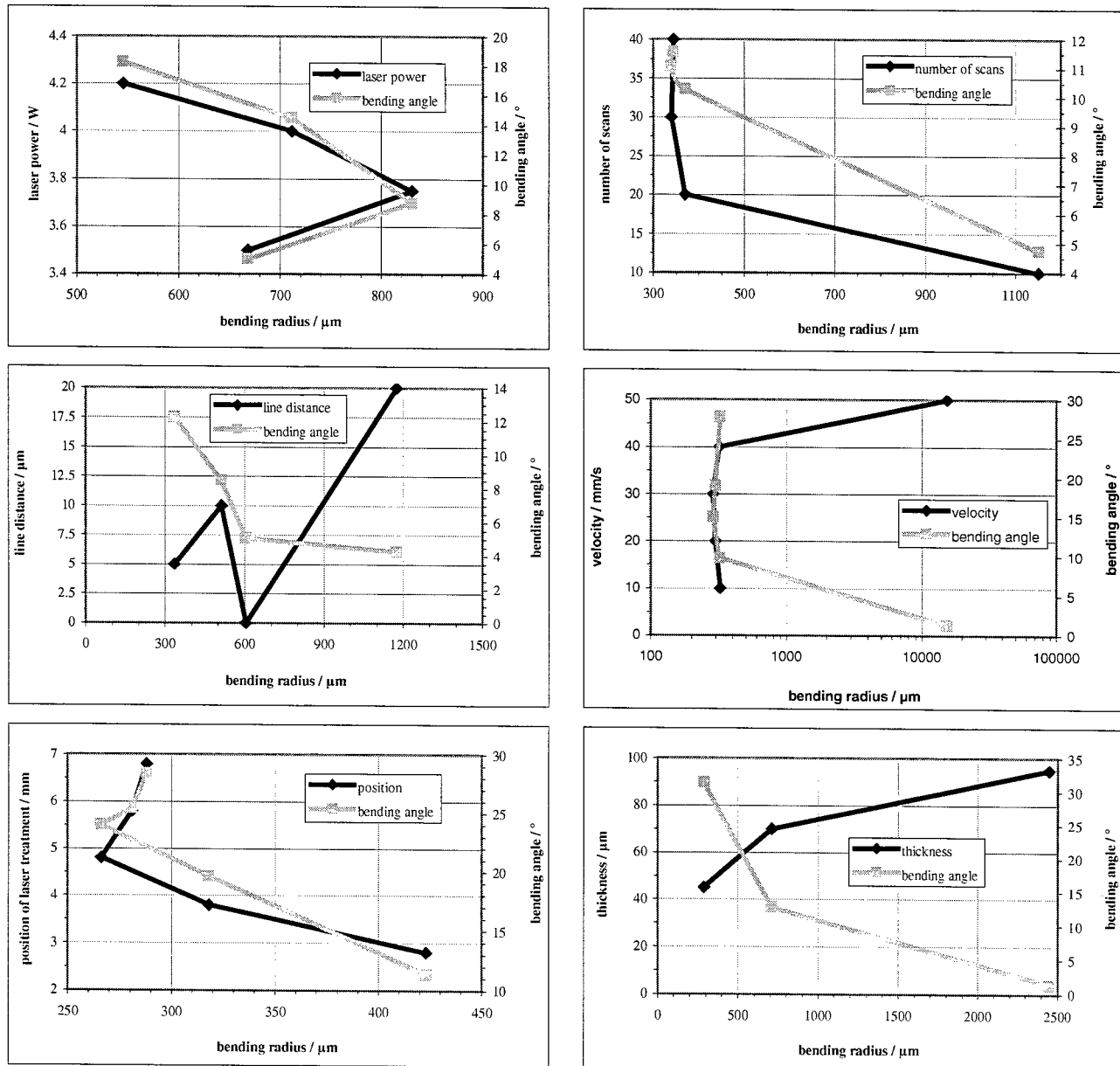
Fig. 11: Bending radii as a function of the process parameters and bending angle

bending radius as a function of the process parameters.

At first glance it seems that the bending radius depends on the process parameters as shown in Fig. 11. A detailed analysis revealed that the bending radius is always correlating with the bending angle, i.e. the larger the bending angle the smaller the bending radius shown in Fig. 12. Depicting the bending radii of all investigations as a function of the bending angles (see Fig. 12) the correlation is evident. The bending radius is independent on the process parameters.
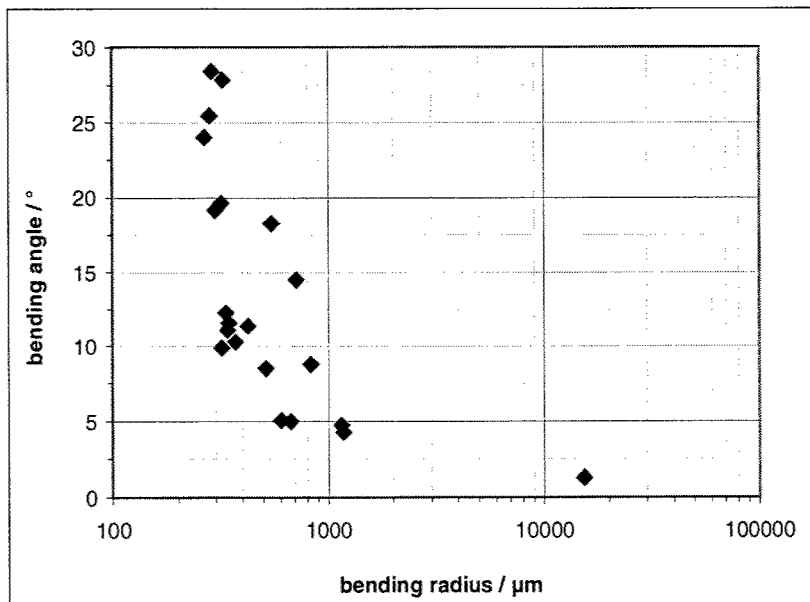
Fig. 12: Bending radii as a function of the bending angle

Bending angles larger then 10° have bending radii in the range 300 to 700 μm. Smaller bending angles result in increasing bending radii. We can notice that the bending radius simply depends on the bending angle.

4. Bending examples

First bending applications we implemented with this technology. The presented multiple bending in Fig. 13 shows single bendings both on the top side and on the bottom side. It is possible to generate steps and stairs respectively. For example the described multiple bending can pass through several wafer planes to execute mechanical or electrical tasks.

To produce an electrostatic drive made of silicon (see Fig. 14) a special shaped
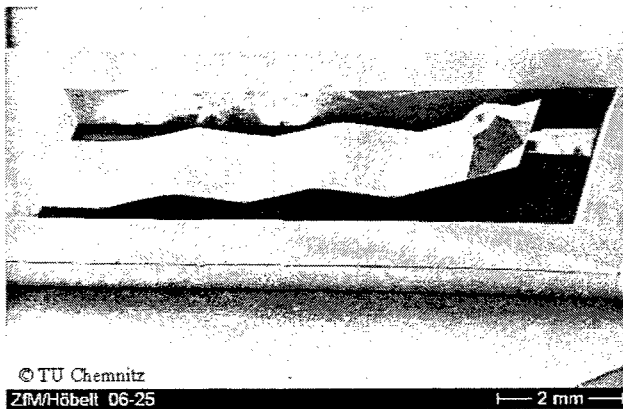
Fig. 13: Fivefold bending

Fig. 14: Continuous bending for use in an electrostatic drive
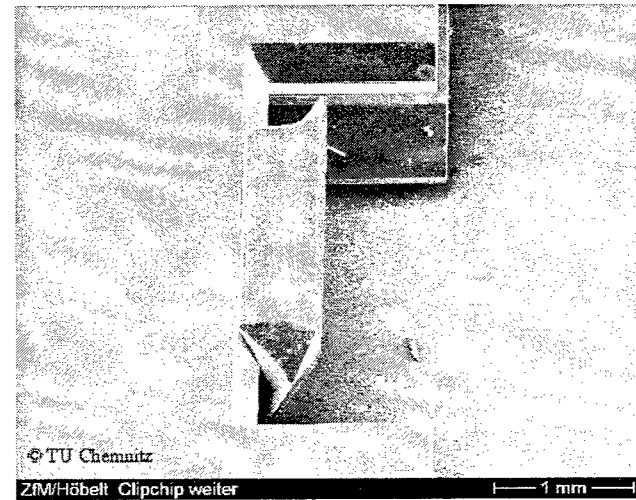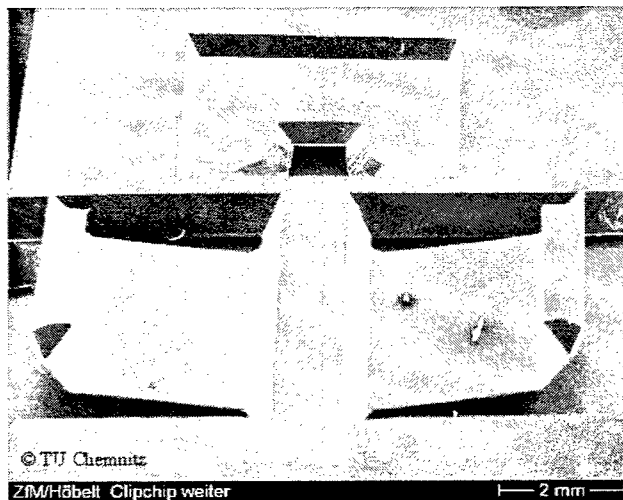
Fig. 15: SEM-micrograph of a clip-chip (left overview, right clipped chip)

electrode with a continuous curvature is necessary [6]. It was generated by means of a modified irradiation regime. A clip-chip mechanism (see Fig. 15) serves to mount components like chips. It is also possible to clamp a clip-chip on a guide block to operate as a slide in micro optical benches [7].

5. Conclusions

By means of local laser treatment we can form silicon caused by thermal induced stresses. In the continuous laser mode there is a small range of laser power suited to generate bendings. No bending can be observed when q-switched laser mode is used.

The bending angle strongly depends on the chosen parameters. Changing the number of consecutive scans, the machining velocity, the line distance, the position of laser treatment or the thickness of the bending element the bending angle can be controlled in a wide range. Up to this moment there is an insufficient reproducibility and precision of the bending angle. We couldn't find any near- and middle-term aging. The bending radius simply depends on the bending angle. First applications like multiple bendings, bendings with continuous curvature and clip-chips are realized.

Acknowledgement

References

[1]   B. Keiper, H. Exner, U. Löschner, Th. Kuntze; *Drilling of Glass by Excimer Laser Mask Projection Technique*, Journal of Laser Applications, Vol. 12, No. 5, October 2000, 189-193

[2]   R. Ebert, B. Keiper, U. Löschner, H. Exner; *Anwendungen der Lasermikrobearbeitung*, Lasermagazin 3/2001, p.38

[3]   Z. Mucha, J. Hoffman, W. Kalita, S. Mucha; *Laser forming of thick free plates*, LANE 97, Laser Assisted Net Shape Engineering 2, Proc. of the 30th Internat. CIRP Seminar on Manufacturing Systems,   Erlangen, D, Sep 23-24, 1997, vol. 30 (1997) p. 383-392

[4]   M. Otsu, T. Wada, K. Osakada; *Micro-bending of thin spring by laser forming and spark forming*, 51th General Assembly of CIRP, Nancy, F, Aug 19-25, 2001, CIRP Annals, Vol. 50 (2001) no. 1, p. 141-144

[5]   J. Widlaszewski; *Precise laser bending*, LANE 97, Laser Assisted Net Shape Engineering 2, Proc. of the 30th Internat. CIRP Seminar on Manufacturing Systems, Erlangen, D, Sep 23-24, 1997, vol. 30 (1997) p. 393-398

[6]   F. Bennini, J. Frühauf, W. Dötzel; *High force and large displacement electrostatic actuators with curved electrodes using silicon bulk micromachining,* Actuator 2000, Proceedings of the 7th International Conference on New Actuators, 19-21 June, Bremen, Germany, p. 87-90

[7]   E. Gärtner, J. Frühauf, E. Jänsch; *Mounting of si-chips with plastically bent cantilevers,* Proc. 11th Int. Conf. Solid State Sensors and Actuators, Munich, Germany, June 10-14, 2001, Digest of technical Papers Vol.1 1C3.08P, p. 206-209

Three-dimensional recording by femtosecond pulses in dielectrics

Saulius Juodkazis[a,b], Toshiaki Kondo[b], Vygantas Mizeikis[a,c],
Shigeki Matsuo[a,b], Hiroyuki Murata[b], and Hiroaki Misawa[a,b],

[a]Core Research for Evolution Science & Technology (CREST),
Japan Science & Technology Corporation (JST),
[b]Department of Ecosystem Engineering, University of Tokushima,
2-1 Minamijosanjima, Tokushima 770-8506, Japan
[c]Satellite Venture Business Laboratory, University of Tokushima,
2-1 Minamijosanjima, Tokushima 770-8506, Japan

ABSTRACT

Fabrication and characteristics of two-dimensional (2D) and three-dimensional (3D) periodic structures, recorded in the bulk of SU8 photoresist film by multiple-beam interference is described. Multiple beams (up to nine) were generated by a diffractive beam splitter. Recording was performed by ultrashort laser pulses with temporal width of 140 fs (FVWM) and central wavelength of 800 nm, derived from a Ti:sapphire laser. Intensity-dependent photomodification of the photoresist was due to single-photon as well as multi-photon (two and three) absorption. After the development, the exposed resist films contained free-standing 2D and 3D periodic dielectric structures with unexposed exposed regions removed by the development. Detailed examination of the samples has revealed close resemblance between their structure and the light intensity distributions in the multiple-beam interference fields, expected from the numerical calculations. Quality of the samples recorded by a single-photon absorption was lower than that of that of other samples, in particular due to poor development quality. The microfabrication method used in this work appears to be a suitable for obtaining photonic crystal templates.

Keywords: Photonic crystals, holographic recording

1. INTRODUCTION

Development of photonics is progressing at a steady pace, and currently is capable of delivering sophisticated optoelectronic devices, importance of which matches that of microelectronic devices.[1,2] Among the main tasks of photonics is spectral and spatial manipulation of electromagnetic radiation. Multi-dimensional diffraction gratings may be useful in realizing these tasks via dispersive and photonic band gap (PBG) effects.[3] Various techniques for the diffraction grating fabrication exist, but two-dimensional (2D) and three-dimensional (3D) gratings can be most conveniently recorded holographically in appropriate photosensitive media, such as crystalline material,[4,5] liquid crystals,[6,7] or photo-thermo-refractive (PTR) glass.[8]

Most of the earlier reports on holographic fabrication have concentrated on 1D structures, while the fabrication of 2D or 3D periodic structures has received somewhat less attention. In 1990, Burns et al.[9] demonstrated an interference technique, which allowed direct visualization of the 2D optical field intensity and a periodic arrangement of micrometer-sized polystyrene particles in the water assisted by optical forces. In this work, the periodically arranged particles were termed "optical crystals". Berger et al. have fabricated 2D hexagonal lattice in a thin layer of photoresist by interference of three beams at $\lambda = 325$ nm.[10] The resist layer was subsequently used as the mask for reactive ion etching, and fabrication of 2D PhC in GaAs with the depth of 3 μm. The lattice period was 2.66 μm, but in principle it could be downscaled to $\frac{2}{3}\lambda = 217$ nm. Similar techniques have been also used by others.[11]

Further author information: (Send correspondence to H. M.)
H. M.: E-mail: misawa@eco.tokushima-u.ac.jp, Telephone: (+81 88) 656 7389, Fax: (+81 88) 656 7598.
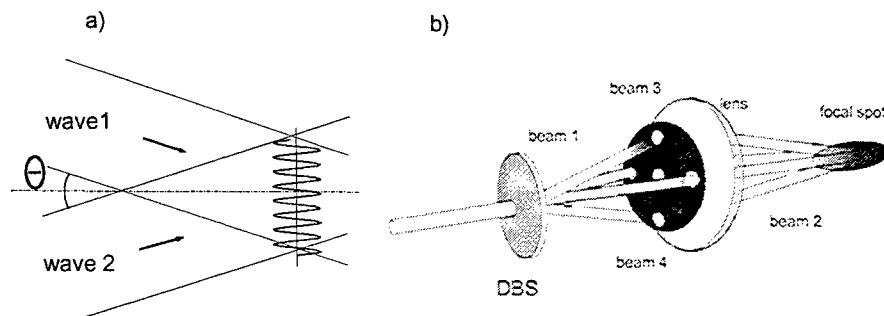
Figure 1. Interference of two coherent plane waves (a), use of diffractive beam splitter for obtaining multiple plane waves (b).

Fabrication of photonic crystal (PhC) structures by laser interference was first reported by Campbell *et al.*.[12] By using 355 nm nanosecond laser pulses, they obtained 3D fcc structures with a lattice constant of 922 nm in photoresist having a thickness of several tens of micrometers. Trigonal structures were also obtained for different angles between the beams. By using the fabricated structure as a template, they obtained an inverse periodic structure in TiO_2, which is known to a have higher refractive index than the photoresist. Holographic fabrication of PhCs was also performed in photopolymerizing resins,[13] where light irradiation leads to solidification of liquid polymers. Five overlapping waves were used to form 3D triangular lattice with hexagonal structure. The same authors also fabricated 2D and 3D PhC by laser interference using a simple setup based on a diffractive beam splitter (DBS). The initial laser beam was split by a DBS, and selected beams were gathered by two lenses. This setup is very simple and ensures equal optical path lengths of interfering beams, which is helpful when working with short laser pulses.

The present work focuses on the holographic recording of 2D and 3D gratings in photoresist films using interference of ultrashort laser pulses, obtained from a single pulse by a DBS, and employing non-linear absorption mechanisms. The experimental setup used is based on the DBS in the course of experiments in photoresist, performed with very similar optical setup. This paper is organized as follows. The principles on which laser microfabrication by holographic (or interference) recording are based, are described in Sect. 2. Numerical simulations of interference patterns created by five laser beams are given, and applicability of the holographic technique for the fabrication of 3D photonic crystal templates is examined using numerical modeling in Sect. 3. Sect. 4 describes the experimental setup and details of the fabrication process. The main results which describe generation of various light interference fields, and recording of four-beam and five-beam interference patterns in photoresist films are presented in (Sec. 5).

2. PRINCIPLES OF RECORDING BY INTERFERENCE

The basic principles of holographic laser fabrication technique are illustrated by the sketch in Fig. 1. Interference of two coherent plane waves 1 and 2 creates one-dimensionally (1D) periodic intensity pattern, $I(x)$, which depends on the coordinate x as

$$I(x) \propto I_1 + I_2 + 2\sqrt{I_1 \cdot I_2} \cos\left[\frac{2\pi x}{\Lambda} + \phi_{12}\right]. \tag{1}$$

$$\Lambda = \frac{\lambda}{2\sin(\theta/2)}, \tag{2}$$

where I_1 and I_2 are the intensities of the two waves, and Λ is the spatial period of the pattern, which depends on the laser wavelength, λ, and the angle between the wave propagation directions, θ. At intermediate angles $\theta \approx \pi/4$, Λ becomes comparable to the laser wavelength, reaching its upper limit $\Lambda = \lambda/2$ at $\theta = \pi$ (counter-propagating beams). The phase of the modulation pattern is controlled by the phase difference between the
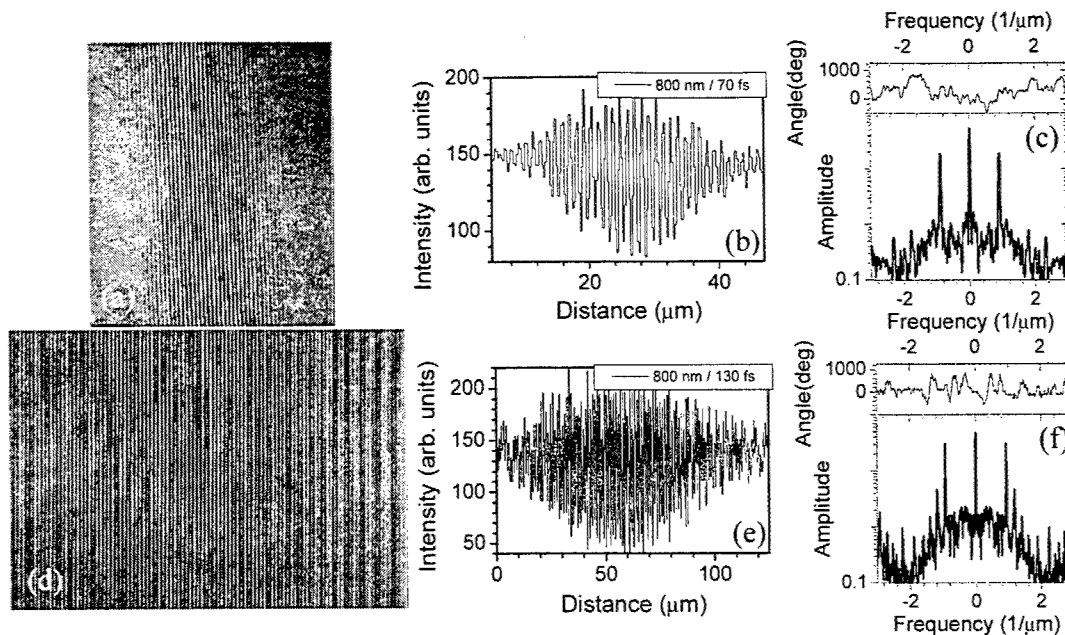
Figure 2. CCD images of the interference region at the tip of Fresnel biprism (a, d) with intensity cross sections across the fringes (b, e), and corresponding spatial frequency analysis by FFT given in (c, f). The duration of pulse incident on the biprism (with 110° angle at the tip) was about 130 fs (a-c) and 70 fs (d-f), respectively.

two waves, ϕ_{12}. By placing a photosensitive medium in the interference field, structure with periodically modulated optical density or refractive index can be recorded, and later used as a diffraction grating. It is helpful to note here, that if the recorded grating is subsequently illuminated by, for example, wave 2, one of its first-order diffracted waves will reproduce the wave 1, including the information about its phase. Recording of 1D diffraction gratings by two plane wave interference is therefore the simplest kind of holography. This simple method can be extended to produce much more complex periodic 2D and 3D patterns, if many waves propagating along carefully selected directions with different phases, are allowed to interfere. The setup which enables to achieve interference between multiple waves is sketched in Fig. 1, and will be described in more detail in Section 4. Such arrangement uses a diffractive beam splitter (DBS) which produces multiple, mutually coherent laser beams from a single input beam. The beams are subsequently focused by a lens into the bulk of photosensitive material. All of the beams deliver to the focal spot region of the focusing optics nearly plane waves, propagating at different directions. Thus DBS together with focusing optics automatically ensures vanishing difference between the optical paths of the beams, which is especially important if ultrashort laser pulses are used for the recording.[14] Indeed, an overlap of two ultra-short coherent pulses is determined by their longitudinal dimension, $l_p = c\tau_p$, which is about 30 μm for a 100 fs pulse. Hence, the width of the spatial overlap is $w = c\tau_p/\sin(\theta/2)$ for 2-beam interference. In contrary, for diffracted pulses the pulse front (an intensity front) is not perpendicular to direction of propagation (the wave front), i.e., the pulses are tilted, and the region of overlap is given $w = d/\cos(\theta/2)$, where d is the cross-section diameter of the beam. Thus, sub-mm-scale patterns can be routinely produced using even a tight focusing optics (with numerical aperture, $NA > 0.5$).

Figure 2(a) demonstrates interference patterns imaged on CCD camera for two interfering pulses, which were produced by passing a pulse via Fresnel bi-prism. Hence, this corresponds to interference of two pulses whose wave fronts (and pulse fronts) are perpendicular to the propagation direction, i.e. not tilted. The width of the light intensity distribution (b) was obviously dependent on the pulse duration. FFT analysis of intensity patterns (c) was used to determine the period, which was found $\Lambda = 1.06$ μm and 1.11 μm for 150 and 50 fs

pulses. This is very close to the expected value of 1.094 μm defined by refractive index 1.453 at 800 nm wavelength of 110° bi-prism.

Use of short pulse excitation together with beam focusing allows to achieve power densities, sufficient for inducing effective photomodification of initial material, optically transparent in the linear regime, via higher order non-linear absorption effects. As in the two-wave case explained above, periods of multiple-wave interference patterns depend crucially on their mutual convergence angles. θ . The latter can be controlled by changing the inter-beam distance prior to the focusing, or the focal length, which in turn requires to use lenses with various focal lengths and numerical apertures (NA). Axial depth of the interference region, and hence of the recorded structure, is proportional to the waist size of the interfering beams and inversely proportional to the angle θ. For short pulses, i.e., when l_p becomes smaller than the diameter of the beams, lateral size of the interference area may become somewhat reduced. In practice, structures with modulation periods below one micrometer, and containing tens of periods along all three directions are routinely achieved using fairly tight focusing optics with NA> 0.5. Complexity of the interference pattern depends on the number of participating waves, which can be changed by opening and closing various beams with a mask, as illustrated in Fig. 1 (b). Depth of the intensity modulation can be controlled by adjusting the intensities of the interfering beams. Different kinds of photosensitive materials can be used for the structure recording.

3. MULTIPLE-BEAM INTERFERENCE PATTERNS

3.1. Numerical simulations

In this section we will use simple numerical calculations to demonstrate the patterns that can be generated by multiple-beam interference, and to outline the main expectations for the experiments described later.

In general, spatial light intensity distribution in the multiple beam interference field can be expressed as follows:

$$I(\vec{r}) = \left\langle \left| \sum_{i=1}^{n} E_i \cos(\vec{k}_i \cdot \vec{r} - \omega t + \varphi_i) \right|^2 \right\rangle, \tag{3}$$

where E_i, k_i, φ_i are amplitude, wavevector and phase of the of the i-th field (beam), ω is the frequency, r the radius-vector, n the number of beams, and t is the time.

Figure 3 shows isosurfaces of the 3D light intensity distributions created by five interfering plane waves, calculated according to Eqn. 3. Since the structure recording will be done through a non-linear absorption, which usually occurs above well-pronounced threshold intensity, one can expect that at a certain irradiation intensity the isosurfaces depicted in the figure can be transformed into the boundaries between exposed and unexposed regions. The beam configuration used to obtain these results is illustrated in the sketch shown in Fig. 1 (b). At the entrance to the lens four of them are aligned on the corners of a square, while the fifth beam is located in its center. We have found that for achieving maximum modulation amplitude in this configuration the intensities of all four corner beams must be equal. At the same time, intensity of the central beam must be equal to the total intensity of the corner beams, i.e., four times higher. The numerical calculations have also revealed profound role of the phases of the waves on the structure of the interference fields, which is illustrated by cases (a,b,c) in Fig. 3. For the illustration purpose we show the case where phases of two beams located on the opposite corners of the square, begin to differ from the phases of the other beams. When phases of all beams are equal (Fig. 3 (a)), the periodic structure has body-centered tetragonal (bct) lattice with a single "atom" (a high-intensity parallipeped, extending along in the z-axis). To obtain a body-centered cubic (bcc) lattice, usually, a sharper focusing is needed. When phase difference up to $\pi/2$ is introduced for two beams (b,c), the periodic structure exhibits a smooth change, whereby the same bcc (or bct) lattice is retained, but an atomic basis, consisting of two high-intensity ellipsoids is formed. After a more detailed inspection such structure can be identified as a diamond structure (if bcc structure is formed by all equal phases beams). The transformation towards the diamond structure is interesting, since the latter is a highly promising candidate for the application in photonic crystals (PhC), and is difficult to obtain by most of the currently known PhC fabrication techniques. It is also obvious from the figure, that diamond structure will have a framework of cross-linked unexposed regions, and a framework of cross-linked exposed regions. This layout provides full access into
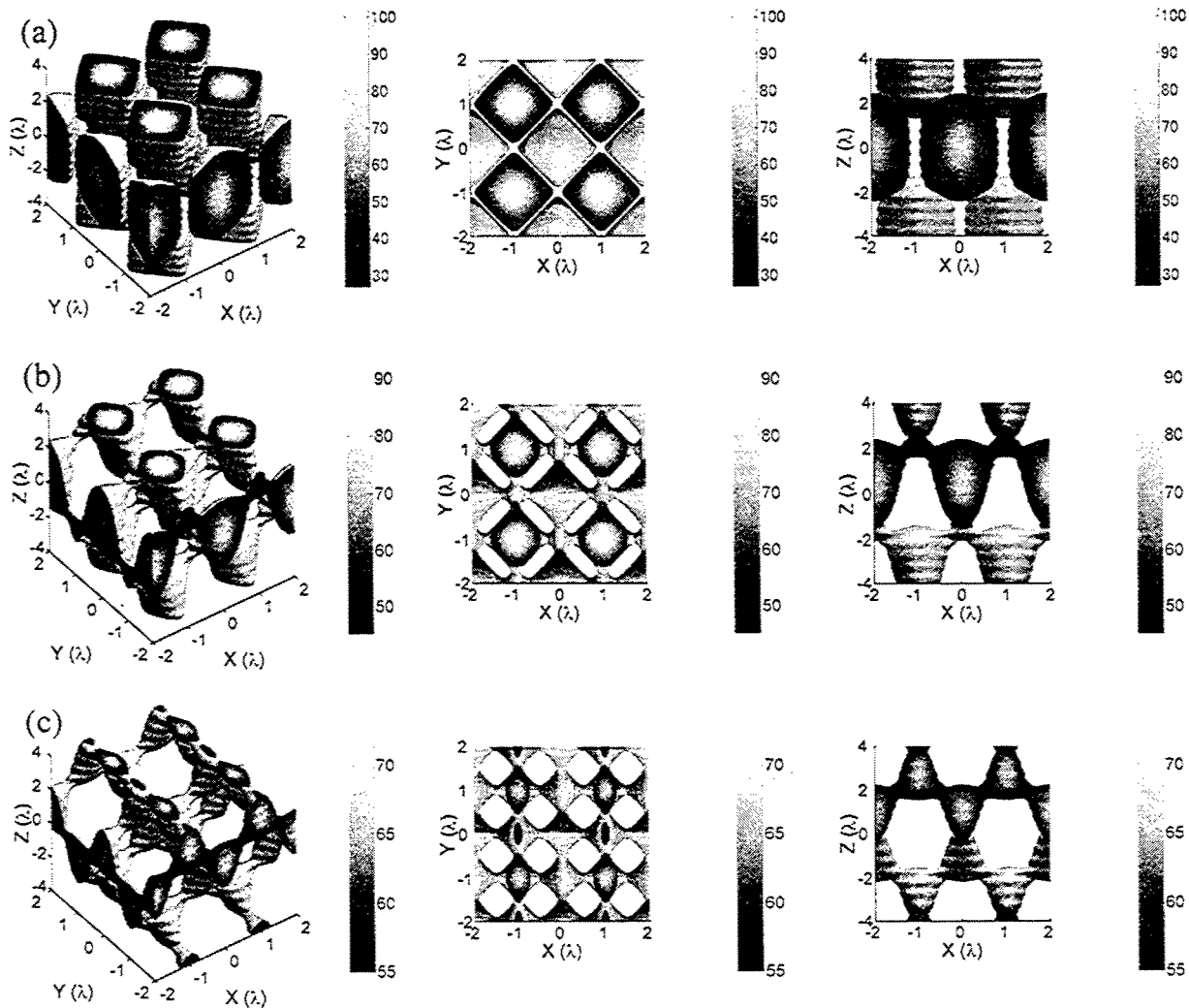
Figure 3. Spatial light intensity distributions generated by interference of five plane waves. The complex amplitudes of the central beam in all plots is $4I_0e^{-i0}$, while corner beams have different amplitudes: (a) all I_0e^{-i0}; (b) $I_0e^{-i\pi/4}$, $I_0e^{-i\pi/4}$; I_0e^{-i0}; I_0e^{-i0}); (c) $I_0e^{-i\pi/2}$, $I_0e^{-i\pi/2}$, I_0e^{-i0}, I_0e^{-i0}. The plots show iso-surfaces drawn at different intensities: 27 for (a), 45 for (b), and 52 for (c). The coordinates are given in units, normalized to the wavelength of the recording light, λ (note the difference between the scale of z-axis and x,y axes.). Maximum beam convergence angle $\theta_{air} = 60°$ was assumed for the calculations.

the structure for the developer solution. Moreover, after the development such structure is mechanically stable, and can be used as a template for the infiltration by high refractive index materials.

The above described example shows only a few simple possibilities existing among great variety of the lattice types that can be generated by multiple-beam interference. More examples will be given in the following sections devoted to the description and discussion of the experimental results.

3.2. Suitability for photonic crystals applications

In PhCs periodic modulation of the dielectric constant leads to the formation of photonic bandgaps PBG, or spectral ranges in which light waves cannot penetrate the PhC.[3] Since in general the PBG central wavelength
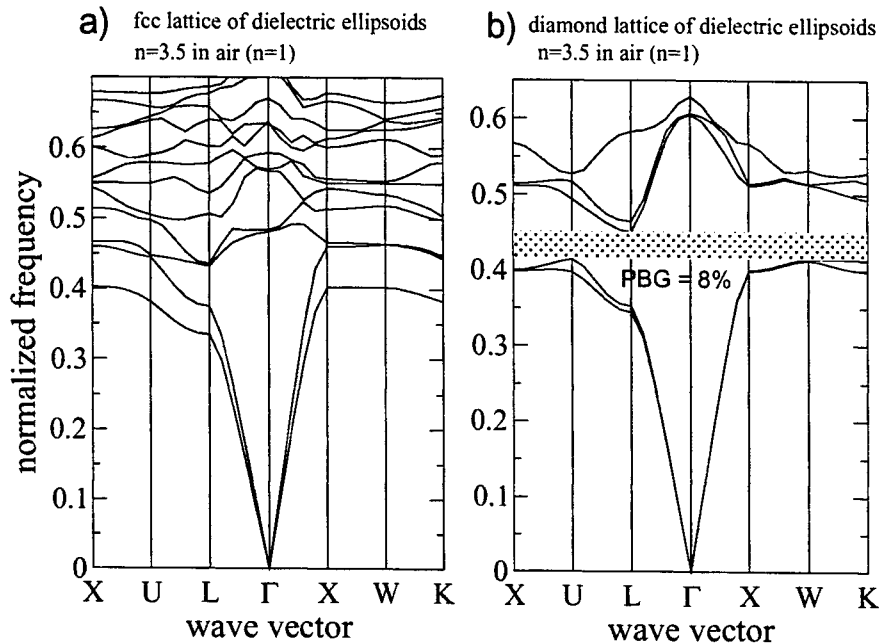
Figure 4. Calculated photonic band diagrams for silicon ellipsoids in air, forming (a) simple fcc, and (b) diamond lattices. The frequency axis is given in normalized frequency units $\omega a/(2\pi c)$, where ω is the frequency, a is the lattice period, and c is velocity of light. Elongation factor of the ellipsoids along the z-axis is 1.5.

is comparable to the modulation period. PhCs must have dielectric lattices with sub-micrometric periods and contain dielectric features of even smaller size. With these requirements, fabrication of 3D PhC structures may prove too difficult. Therefore much attention has been focused recently on search for novel PhC fabrication techniques which would enable easier fabrication of 3D periodic dielectric microstructures from bulk materials. As noted in the previous Section, in this regard holographic recording may provide interesting capabilities due to the possibility to obtain field distributions that have fcc and diamond type structures. The latter one is especially interesting, since it favors a large PBG, which opens at a refractive index contrast as low as 2 to 1.[15] In this section we shall briefly examine possibilities to use holographic microfabrication techniques in PhC fabrication. Intensity patterns shown in Fig. 3 (b,c), successfully transferred to SU8 photoresist, will create fcc and diamond lattices with a single ellipsoid (for fcc) or two ellipsoids (for diamond), filled by air, at each lattice site. The longer axis of ellipsoid will be oriented along the z-axis direction, the elongation factor will be about 1.5-2.0, depending on the beam convergence angle at the focal spot. In the $x - y$ plane ellipsoids will touch each other, such that empty regions (as well as unexposed regions) will be cross-linked. We used this description for numerical modeling of the photonic band diagrams of the fcc and diamond lattices.

It must be noted in advance, that bare framework of unexposed photoresist regions in air can not exhibit complete (direction-independent) PBG under any circumstances due to its relatively low refractive index contrast (1.5 to 1). Despite this circumstance, it is interesting to investigate whether or not such structure can be used as a template for infiltration by high refractive index materials. This option allows one to raise the refractive index contrast in the initial structure and has attracted much interest in relation with infiltration of self-organizing systems, like opals.[16] Semiconductor growth and processing technology provide the procedures required for effective infiltration of templates by high refractive index semiconductors, e.g.. chemical vapor deposition.[17] If the framework of infiltrated material is mechanically stable and self-supporting it is possible to remove the original template, thus further raising the refractive index contrast.

We assume that all these techniques are in principle applicable for holographically fabricated structures.
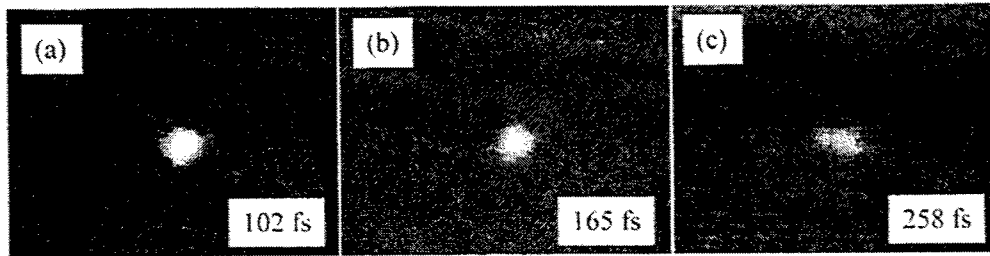
Figure 5. GRENOUILLE (*time × spectrum*) traces of fs-laser (*Tsunami* oscillator) pulses: at the output of oscillator (a), just before oil-immersion objective lens (b), and after the focus, which was placed inside cover glass (c). Pulse durations at FWHM retrieved by FROG algorithm are shown on each image. Horizontal size of the images corresponds to 1779 fs; the vertical - 33.7 nm.

and that air voids in the above described fcc and diamond templates can be filled by silicon ($n \approx 3.4$), and subsequently removed from the structure. Photonic band diagrams for these cases were calculated using a freely available software package (MIT Photonic Bands), that implements a targeted iterative eigensolver of Maxwell's equations on a plane-wave basis.[18] Two representative results of the calculations are shown in Fig. 4 for an fcc and a diamond cases. Perhaps the most important difference between these two plots is absence of the PBG in the first case and presence of the PBG in the second case. Both results are not very surprising, since it is known, that fcc (or opal) lattice composed of spherical dielectric elements can not open a PBG even at the refractive index contrast as high as 3.5 to 1. On the other hand, similar diamond lattice has a complete PBG (about 8% of its central frequency) when the refractive index contrast exceeds relatively low value of 2 to 1.[15] However, in the case regarded here dielectric elements are not spheres, but ellipsoids. Thus the result shown in Fig. 4 illustrates that while fcc lattice does not acquire additional robustness at these lattice parameters, the diamond lattice retains its capability of opening a complete PBG. This indicates that holographically recorded structures in principle can be used as templates for the PhC fabrication. However, much broader investigations are required for full assessment of their suitability. For example, we have found, that even for diamond structure, PBG tends to disappear when ellipsoid elongation factor approaches 2, hence the recording beams must converge at large angles, which may not always be possible to achieve. On the other hand, fcc lattice may still prove useful at different orientation of the ellipsoids, for example when their elongation is in the (111) direction, and the structure becomes similar to the diamond structure.

4. EXPERIMENTAL DETAILS

The layout of the optical setup used for the generation of multiple beam interference patterns and recording of periodic structures is described in detail in the literature.[19] Below we give brief descriptions of the main features of the optical system used, and of the samples and their processing.

4.1. Femtosecond light source

The light source for the experiments was a femtosecond Ti:Sapphire laser (Tsunami) with a regenerative amplifier (Spitfire), from Spectra Physics, which was tuned to the 800 nm wavelength, and produced pulses of $\tau_p = 130 \pm 10$ fs temporal length (FWHM) at the pulse repetition rate of 1 kHz. Prior to the experiments, temporal pulse spreading after passage through various dispersive elements (lenses, DBS) was evaluated. The temporal pulse length at different locations along the beam optical path and at the focus point was measured by the GRENOUILLE apparatus[20] from Swamp Optics, which recorded a convolution of temporal and spectral pulse shapes, and the pulse length was later retrieved using the frequency-resolved optical gating (FROG) algorithm from Femtosecond Technologies. For the measurements of the pulse duration at the focal spot, an additional solid immersion lens, not present during the structure recording, was employed in order to couple the strongly divergent beam into the GRENOUILLE. Figure 5 shows an example of the initial composite pulse image obtained by the GRENOULLE, and the subsequently extracted pulse durations at the output of the amplifier,
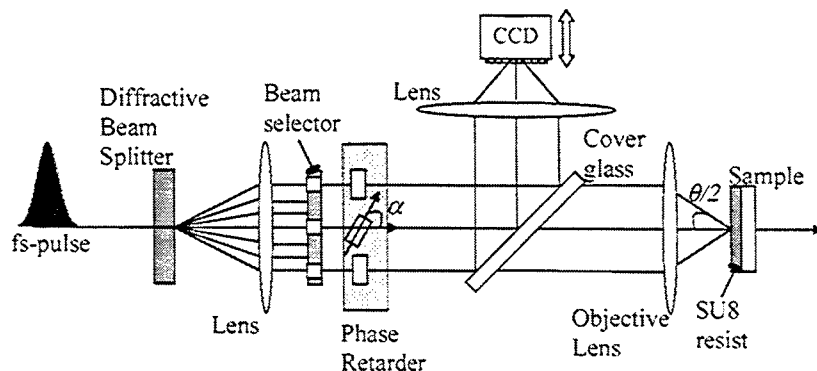
Figure 6. Optical setup for holographic recording of multidimensional periodic structures. Cover glass plates, tilted at variable angle α were used as phase retarders of the selected beams.

after passing through the optical alignment and other elements before the entrance to the microscope objective lens, and after the oil-immersion objective lens with $NA = 1.3$. In all cases FROG error was lower than 2%. Using this approach we have measured the pulse duration to be 160 ± 15 fs for $NA = 0.75$ objective lens used in the structure recording. The lenses and other parts of the optical setup introduce a pulse temporal stretching due to dispersion, since pulse duration at the output of the regenerative amplifier is 130 fs.

4.2. Generation and control of the interference fields

The key ideas about operation of the optical setup have been already outlined in Section 2. Its more detailed schematic picture is depicted in Fig. 6. The DBS divides a single input laser beam into several components, which are collected and focused into the material by a pair of lenses. The number of interfering waves and their relative phases are controlled by an aperture and phase retarder plates placed between the lenses. The aperture has a number of openings, which select the required beams and block the unwanted ones. The phase retarder plates are pieces of microscope cover glass, introduced into the beams at variable orientation angles α. A small part of the incident beams is split off by a larger cover glass plate, and is focused on a CCD for observation an a monitor. For inspection of 3D interference patterns the CCD camera was moved along the optical axis, and different cross sectional views of the structure were examined. The lens used for focusing the of the beams into the sample is a dry objective lens (Olympus UApo) with $20^\times$ magnification and numerical aperture $NA = 0.75$.

4.3. Samples and their exposure

Films of negative photoresist SU-8 (Microlithography Chemical Corp.), which is optically transparent for wavelengths $\lambda > 400$ nm, were used for the recording. The photoresist was spin-coated on cover-glass plates, and had thickness of about of $5 - 6$ μm. The samples were pre-baked prior to the optical exposure. After the exposure, the samples were post-baked in order to enhance photo-initiated crosslinking reaction. The development procedure resulted in removal of the exposed regions from the sample. Typical exposure parameters used in the experiments were: average laser power before the DBS 0.21 W, at the focal spot 1.67 mW (in the case of four beams). For the 150 μm diameter spot and $\tau_p = 150$ fs, this corresponds to the 2.4 mJ/cm^2 pulse energy density, and 1.6×10^{10} W/cm^2 power density. The exposure time was varied within the $5 - 90$ seconds interval. The fabricated samples were inspected by a scanning electron microscopy (SEM), for which a thin layer of Au (< 20 nm) was coated by sputtering on the sample.
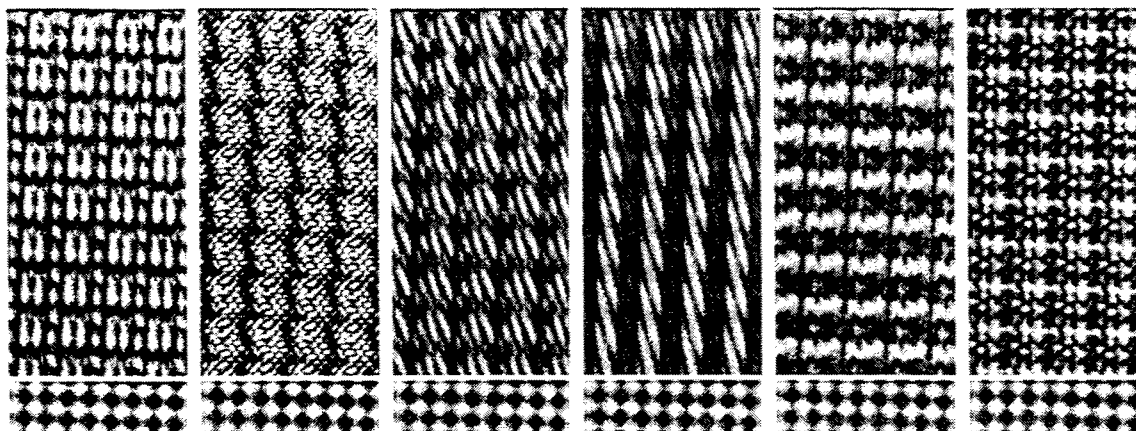
Figure 7. Two-dimensional CCD images of the interference patterns created by seventeen interfering beams, arranged into a cross at the entrance to the focusing lens. Phases of nine beams belonging to one bar of the cross were smoothly changed and corresponding intensity distributions are shown on the top row of the images. For a scale reference. interference patterns of four beams with no phase difference among them are also shown in the bottom row of the images.
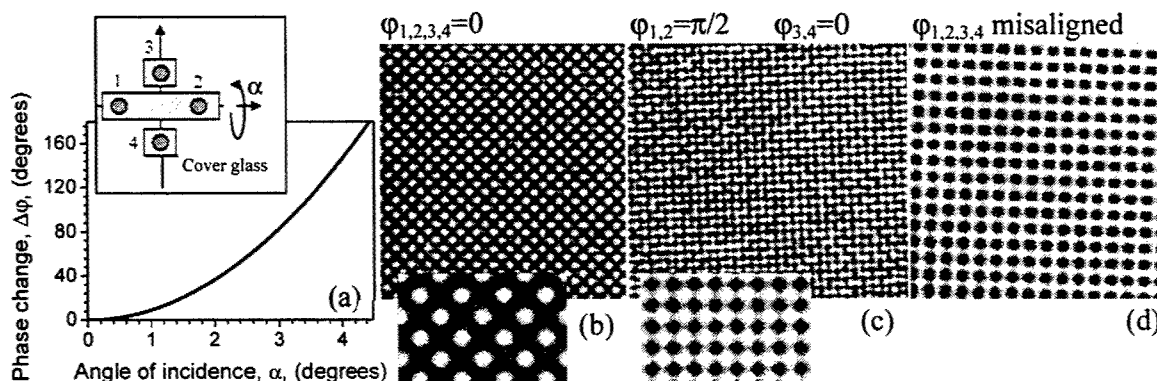
Figure 8. Illustration of phase control of the interfering beams by tilting cover glass plates (thickness 0.2 mm, refractive index 1.5). (a) shows the dependence of the beam phase on the glass tilt angle, the experimental configuration used is depicted in the inset, (b-d) CCD images of interference fields for various beam phases: (b) phases of all beams are equal, (c) phases of beams 1 and 2 shifted by $\pi/2$ with respect to those of beams 3 and 4, (d) when the optical path difference between the beam pairs (1,2) and (3,4) exceeds the coherence length. All CCD images were taken at the same magnification. Insets in (b) and (c) shows calculated intensity patterns for those cases.

5. RESULTS AND DISCUSSION

5.1. Manipulation and monitoring of interference fields

This section presents experimental examples of interference fields with 3D intensity distributions more complex than those inferred from the calculations in Section 3.1. Figure 7 shows interference patterns of 17 beams, aligned along the diagonals of the square shown in Fig. 1 (b). If along one bar of the cross the phases of the beams are smoothly and simultaneously varied, while along the other bar they remain fixed, the intensity distribution exhibits smooth transformations. The images shown in the figure were captured with a CCD camera, and phases of the beams were changed using the cover glass retarder element. The same figure also shows much simpler patterns generated by four-beam interference. All of the displayed patterns have distinct
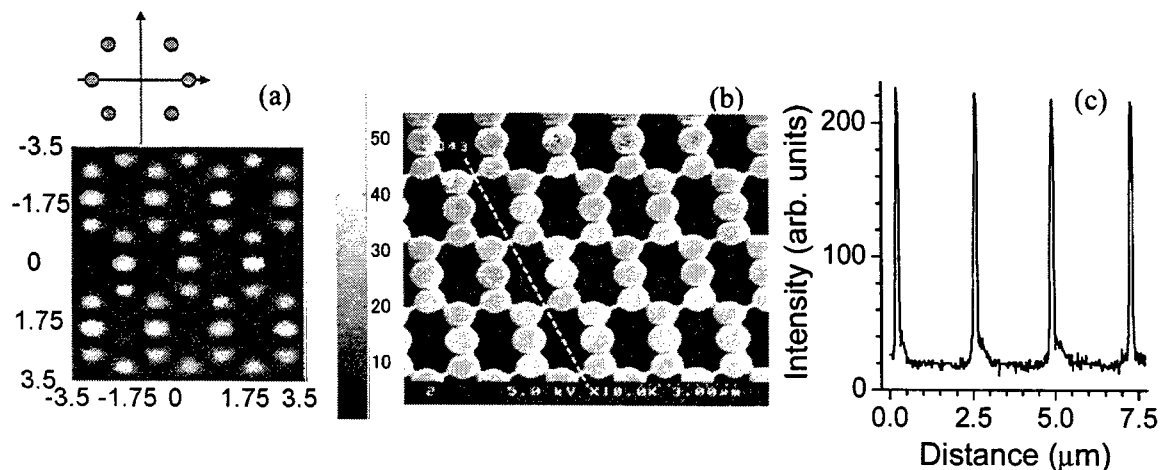
Figure 9. Calculated intensity profile (a) and fabricated (b) patterns of 6-beams interference. Scale in (a) is in wavelength for a $\theta/2 = 69°$. (c) Cross-section intensity profile along a dashed line in (b). The width of the intensity spikes is 220 nm (FWHM).
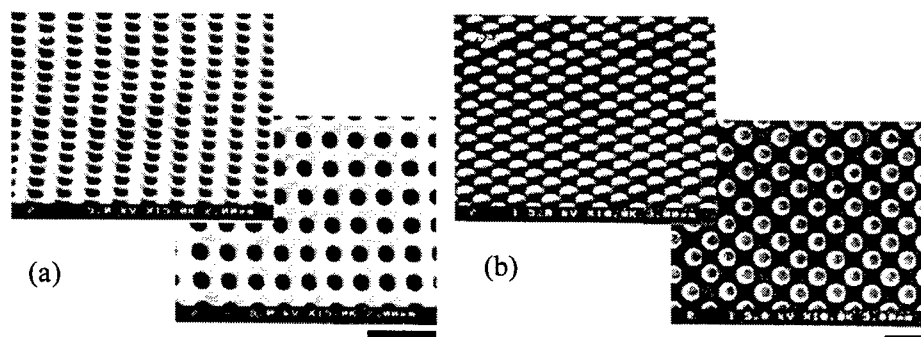
Figure 10. Perspective and top-view SEM images of periodic structures in SU-8 resist, (a) hole structure recorded by two consecutive exposures (beam pairs consisted of beams located on each diagonal of the square), (b) rod structure recorded by a single four-beam exposure. Focusing corresponded to a $\theta_{air}/2 = 32°$ angle. Scale bars are 2 μm.

periodic structure containing fine features, and can be recorded in a photoresist or other material. Four-beam configuration is actually more suitable for revealing the importance of phase control. This is illustrated by data and images shown in Fig. 8 (see explanations in the figure caption).

One may ask whether or not the images of interference fields taken by the CCD (Fig. 6) resemble the intensity distribution at the focus of the lens, where actual fabrication takes place. Of course, both distributions are not exactly the same; in the CCD image smallest features will be smeared by diffraction and therefore not visible. Nevertheless, larger features can be correctly imaged on the CCD, and for them one can expect close matching between the CCD image and the intensity distribution at the focus. Fig. 9 shows comparison between the calculated light intensity pattern created by six-beam interference and the pattern recorded in the photoresist after the development. As is evident from the figure, the size (about 220 nm) and shape of the features in both images match closely. The recording light wavelength was 800 nm, and the objective lens used had $NA = 0.25$.

5.1.1. Recording of periodic structures in photoresist

In holographic fabrication experiments we start from simpler 2D structures, that can be recorded by four beams, arranged on the corners of a square. By using four beams, two opposite pattern types can be recorded. One
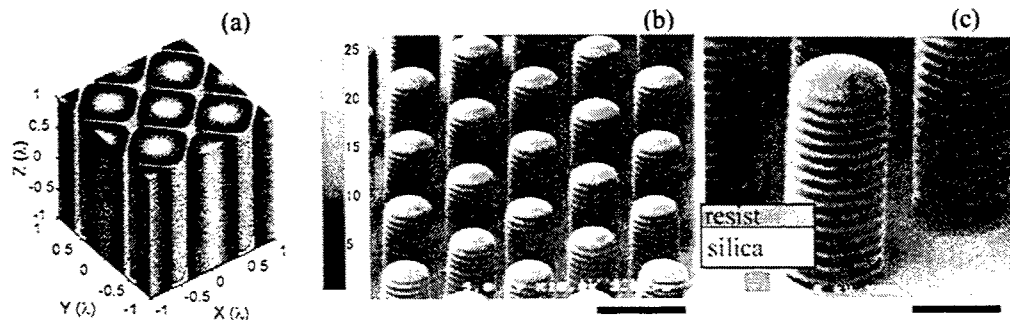
Figure 11. (a) Calculated light intensity distribution for four-beams interference at the mutual convergence angle $\theta = 69°$, (b-c) SEM images of the SU8 photoresist structures recorded by four beams (scale bars are 3 and 1.5 μm, respectively). The inset in (c) shows the geometry of the resist illumination.

of them contains periodically arranged holes in the resist film, while the second one consists of periodically arranged rods. Figure 10 shows the examples of two such patterns. The hole pattern was recorded by a combination of two consecutive two-beam exposures, and the rod pattern was recorded by a single four-beam exposure. The structures exhibit high degree of order and are reminiscent of some 2D PhC structures reported in various publications. Despite the fact that low refractive index of the photoresist will prevent occurrence of significant PBG effects, these structures may still be useful as templates for processing of high refractive index materials. It is helpful to remind here, that various lattices can generated by carefully controlling the phases of interfering beams. For 2D interference lattices these possibilities are considered in detail in the literature,[21] and for 3D structures some of them were outlined in Sect. 3. In the case of the 2D samples shown in Fig. 10, their structure, size and shapes were found to be very close to the ones expected from the calculations. For example, the lattice period (1 μm) was found to be exactly equal to the expected value of $\lambda/(\sqrt{2}\sin(\theta_{air}/2)) = 1.02$ μm. In fact, it should be possible to record the structure shown in Fig. 10 even if the phase difference is larger than the coherence length (see Fig. 8 (d)).

Figure 11 illustrates further the good agreement between the light intensity distribution and the experimentally obtained structures, and demonstrates excellent quality of the latter. The calculated intensity distribution shown in (a) clearly reveals rectangular arrays of nearly cylindrical high intensity regions. After the exposure and development only the array of rods, corresponding to exposed regions is left (b,c). Close-up SEM images shown in the figure also clearly reveal wavy side surfaces of the rods. These features are result of interference between the incident and reflected waves during the fabrication and their period is exactly given by the $\lambda/(2n) \simeq 270$ nm, where refractive index of resist is about $n = 1.5$.

Turning to the case of 3D holographic structures, we remind here that material in Sect. 3 demonstrated theoretically the possibilities to tune the structure type from simple fcc to diamond by controlling the phases of the recording waves. In practice it is not easy to demonstrate such transition because in fact phases of the recording beams are not constant over the entire lateral cross section of the irradiated area. Despite these difficulties we have succeeded in recording of diamond-like structures. This result is shown in Fig. 12. The images were taken using optical confocal microscopy. Unlike in the previous experiments, this time the recording was done with femtosecond pulses having 400 nm central wavelength. At 400 nm single-photon absorption is already significant, and due to this reason it was difficult to develop the exposed structures evenly. A 400 nm wavelength had been chosen for exposure in order to ensure a better cross-linking of the structure, however the experiment had proven that, in fact, a fundamental absorption caused too extensive cross-linking. Either one or two-photon exposures are used the dosage and intensity as well as the resist spin-coating and development procedures should be optimized for a better fabrication.

Unlike the diamond structure discussed above, most of the holographically fabricated microstructures are recorded via two-photon or multi-photon nonlinear absorption processes. The nonlinearity allows to expect successful recording of structures with smallest feature size below the "interference-limited" resolution of the
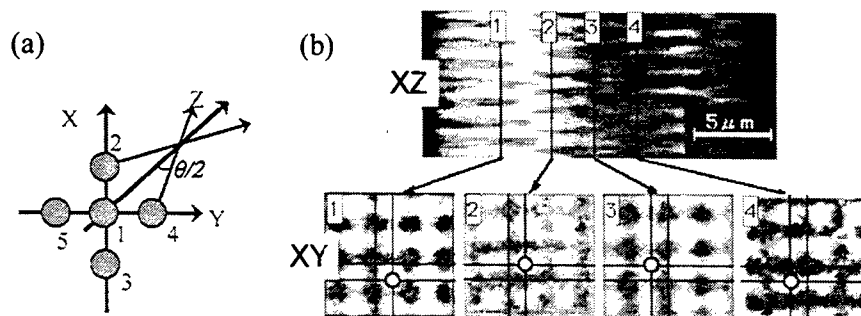
Figure 12. Recording of diamond-like structure by five-beam interference at the wavelength of 400 nm, where single-photon absorption is significant (a) geometry of the experiment, (b) cross-sectional views of the structure taken by optical confocal microscopy. The top image depicts cross-section along the z-axis direction, and the bottom images show $x - y$ plane cross-sectional images taken at z coordinates which correspond to different atomic planes.

multiple-beam optical field. Indeed, such resolution increase is a common consequence of absorption nonlinearity. and is often encountered in laser microfabrication of transparent dielectric materials.[22] Experiments, which explore this possibility are currently being performed in our laboratories, and the results will be reported in detail later. Preliminary confirmation of this possibility has been already obtained using four and six-beam recording of 2D patterns. Using the beam configuration, shown in Figure 8 we expect to be able produce interference patterns similar to those shown in Figure 7. For example, the bottom row of images in Figure 7 produced 2D interference patterns with period 1 μm. Six-beam pattern shown in Fig. 9(c) demonstrates a reproducible features with size of 0.22 μm way below the limit of diffraction for a given optics.

To conclude this section, we note that holographic recording can be useful not just for microstructuring of photoresist, but also for a broad range of other materials. Recently, we have found that thick phase gratings can be recorded by femtosecond pulses at 800 nm wavelength in photo-thermo-refractive (PTR) glass[23] by four-beam interference patterns.[24] The mechanism, responsible for the photosensitivity of the PTR glass (which has an Ce^{3+} absorption at the wavelength of 308 nm), is most probably related to the nonlinear absorption and ionization of the glass matrix, which provides electrons, necessary for a latent image formation.[25] Structures, recorded in PTR glass and SU-8 resist film, were practically identical. Readout of the holograms, recorded in glass indicated that they are phase holograms.[24] Their estimated parameters (refractive index modulation, period, and thickness) were consistent with the values calculated from the geometry of the experiment and from Kogelnik's coupled wave theory.[26]

6. CONCLUSIONS

We have demonstrated holographic recording of 2D and 3D periodic dielectric structures in the films of SU-8 photoresist using femtosecond laser pulses and both linear and non-linear absorption mechanisms. This technique enables simple recording of structures in a single procedure, which does not require sample or laser beam translation. We have also demonstrated that with multiple laser beams/pulses, it is possible to create very complex field patterns. Some of these patterns appear to be promising candidates for the microfabrication of photonic crystal templates, since their structure can be relatively easily tuned from 3D fcc to diamond type by adjusting the phases of constituent beams. We have demonstrated simple implementation of the facilities which allowed to achieve sufficient degree of control over the number of interfering waves, their amplitudes, phases. convergence angles and other parameters, and enabled successful recording of diamond structure.

We have also demonstrated holographic fabrication of 2D periodic structures, which consisted of circular holes or rods, and had very high structural quality. The holographic microfabrication technique appears to be versatile tool for bulk microstructuring of photoresist as well as other materials. In addition, it also promises to be suitable for surface microstructuring, highly demanded in the applications based on high-harmonics generation,

local field enhancement, electron field emission applications, etc. Furthermore, is spatial resolution can be enhanced by absorption nonlinearities and (in photopolymerizing materials) by proper choice of polymerization conditions. Recent reports indicate, that pattern auto-amplification effects occur under proper conditions.[27] In future the interference technique may gain further advantages if interactions between the recording waves and their components diffracted for the fabricated structure can be exploited. Such transient feedback effects may further decrease sizes of the peak intensity regions.

6.1. Acknowledgments

REFERENCES

1. E. Yablonovitch, "Inhibited spontaneous emission in solid-state physics and electronics," *Phys. Rev. Lett.* **58**(20), pp. 2059–2062, 1987.
2. N. Bloembergen, "From nanosecond to femtosecond science," *Rev. Mod. Phys.* **71**(2), pp. S283–S287, 1999.
3. E. Yablonovitch, "Inhibited spontaneous emission in solid-state physics and electronics," *Phys. Rev. Lett.* **58**, pp. 2059–2062, 1987.
4. N. Korneev, H. Veenhuis, K. Buse, and E. Krätzig, "Thermal fixing of holograms and their electrically assisted development in barium calcium titanate crystals," *J. Opt. Soc. Am. B* **18**(11), pp. 1570–1577, 2001.
5. M. A. Noginov, G. B. Loutts, K. Ross, T. Grandy, N. Noginova, B. D. Lucas, and T. Mapp, "Role of traps in photocoloration of Mn:YAlO₃," *J. Opt. Soc. Am. B* **18**(7), pp. 931–941, 2001.
6. C. M. Titus, J. R. Kelly, E. C. Gartland, S. V. Shiyanovski, and J. A. Anderson, "Asymmetric transmissive behavior of liquid-crystal diffraction gratings," *Opt. Lett.* **26**(15), pp. 1188–1190, 2001.
7. V. P. Tondiglia, L. V. Natarajan, R. L. Sutherland, D. Tomlin, and T. J. Bunning, "Holographic formation of electro-optical polymer-liquid crystal photonic ctrstals," *Adv. Mater.* **14**(3), pp. 187–191, 2002.
8. O. M. Efimov, L. B. Glebov, and V. I. Smirnov, "High-frequency bragg gratings in a photothermorefractive glass," *Opt. Lett.* **25**(23), pp. 1693–1695, 2000.
9. M. Burns, J.-M. Fournier, and J. Golovchenko, "Optical matter: Crystallization and binding in intense optical fields," *Science* **249**, pp. 749–754, 1990.
10. V. Berger, O.Gauthier-Lafaye, and E. Costard, "Photonic band gaps and holography," *J. Appl. Phys.* **82**, pp. 60–64, 1997.
11. P. Visconti, C. Turco, R. Rinaldi, and R. Cingolani, "Nanopatterning of organic and inorganic materials by holographic lithography and plasma etching," *Microelectron. Eng.* **53**, pp. 391–394, 2000.
12. M. Campbell, D. N. Sharp, M. T. Harrison, R. G. Denning, and A. J. Turberfield, "Fabrication of photonic crystals for the visible spectrum by holographic lithography," *Nature* **404**, pp. 53–56, 2000.
13. S. Shoji and S. Kawata, "Photofabrication of three-dimensional photonic crystals by multibeam laser interference into a photopolymerizable resin," *Appl.Phys. Lett.* **76**, pp. 2668–2670, 2000.
14. A. A. Maznev, T. F. Crimmins, and K. A. Nelson, "How to make femtosecondpulses overlap," *Opt. Lett.* **23**, pp. 1378–1380, 17 1998.
15. K. Ho, C. Chan, and C. Sokoulis, "Existence of photonic gaps in periodic dielectric structures," *Phys. Rev. Lett.* **65**, p. 3152, 1990.
16. K. Busch and S. John, "Photonic band-gap formation in certain self-organizing systems," *Phys. Rev. E* **58**, pp. 3896–3908, 1998.
17. M. Razeghi, *The MOCVD Challenge*, Adam Hilger, Bristol, 1989.
18. S. Johnson and J. D. Joannopoulos, "Block-iterative frequency-domain methods for maxwell's equations in a planewave basis," *Optics Express* **8**, pp. 173–190, 2001.
19. T. Kondo, S. Matsuo, S. Juodkazis, and H. Misawa, "Femtosecond laser interference technique with diffractive beam splitter for fabrication of three-dimensional photonic crystals," *Appl. Phys. Lett.* **79**, pp. 725–727, 2001.
20. P. O'Shea, M. Kimmel, X. Gu, and R. Trebino, "Highly simplified device for ultrashort-pulse measurement," *Opt. Lett.* **26**(12), pp. 932–934, 2001.
21. S. Matsuo, T. Kondo, S. Juodkazis, V. Mizeikis, and H. Misawa, "Fabrication of 3D photonic crystals by femtosecond laser interference," in *SPIE Proc. Photonic bandgap materials and devices (OPTO 2002) vol. 4655*, A. Adibi, A. Scherer, and S.-Y. Lin, eds., pp. 327–334, 2002.
22. T. Tanaka, H.-B. Sun, and S. Kawata, "Rapid sub-diffraction-limit laser micro/nanoprocessing in a threshold material system," *Appl. Phys. Lett.* **80**, pp. 312 – 314, 2 2002.
23. S. D. Stookey, "Photosensitive glass (a new photographic medium)," *Industrial and Engineering Chem.* **41**, pp. 856–861, 1949.

24. S. Juodkazis, V. Smirnov, T. Kondo, S. Matsuo, L. B. Glebov, L. N. Glebova, and H. Misawa, "Three-dimensional holographic recording in photo-thermo-refractive glass by femtosecond pulses," *Adv. Mat.* , 2002 (In press).
25. S. Juodkazis, "Optical properties of femtosecond laser irradiated photo-thermo-refractive glass," *Lithuanian Journal of Physics* **42**, pp. 119–126, 2 2002.
26. H. Kogelnik *The Bell System Technical Journal* **48**, p. 2909, 1969.
27. R. Sigel, G. Fytas, N. Vainos, S. Pispas, and N. Hadjichristidis, "Pattern formation in homogeneous polymer solutions induced by a continous-wave visible laser," *Science* **297**, pp. 67–69, 2002.

Ultrashort Pulse Laser Micromachining Testbed Development

J.G. Thomas[a], J. T. Schriempf[a], R. Gilmore[b]

[a] The Pennsylvania State University, Applied Research Laboratory, Electro Optics Center, 77
Glade Dr. Kittanning, PA 16201
[b] Extrude Hone Corporation, 1 Industry Blvd. Irwin, PA 15642

ABSTRACT

Ultrashort pulse or femtosecond laser materials processing is an emerging technology that potentially can produce substantial cost savings in the manufacture of a wide variety of Navy systems. A laser micromachining testbed facility utilizing two industrial laser systems, a Ti:Sapphire laser capable of producing pulses of less than 150 femtoseconds and a frequency tripled Nd:YLF laser (351 nm, ~50 nsec pulsewidth) has been established at the Electro Optics Center (EOC). The testbed provides the EOC with a facility for feasibility testing of laser micromachining applications and a resource for workforce training. In addition, the testbed provides a unique capability of evaluating ultrashort (150fs, long wavelength (775 nm)) pulses versus longer pulse, short wavelength (351nm), high photon energy pulses for micromachining applications. Comparison of processing by the femtosecond and uv solid state laser will reveal the optimal processing for an intended application where throughput, stability and quality of the process can be assessed.

Keywords: Ultrashort, femtosecond laser, Ti:Sapphire, laser micromachining, laser ablation

1. INTRODUCTION

Ultrashort pulse lasers provide an improved method of material ablation in which the shortness of the pulse (100-200 femtoseconds) and correspondingly high intensity (10^{12} W/cm^2) limit the amount of heat that is dissipated into the surrounding substrate. This allows very clean holes and features to be machined with little or no recast or heat affected zone (HAZ). A micromachining testbed was developed to provide a vehicle for the transfer of ultrashort pulse micromachining technology to industry. A previous project (Ultrashort Pulse Laser Beam Survey) had identified several areas where application of femtosecond laser processing could produce a high ROI for both DoD and commercial markets. These applications included improved micromachining of practically any solid material and modification of transparent materials for waveguides.

Femtosecond laser ablation for dielectric mask repair was the first commercial manufacturing application that had been implemented using ultrashort pulse laser technology[1]. It was a niche application where the lack of heat effects to the substrate was necessary to prevent a loss of transmission. ARL/EOC has identified another application, femtosecond laser drilling of fuel injector nozzles, as having a high ROI. The advantage of using an ultrashort pulse laser is the ease in backwall damage prevention for the nozzle as opposed to other conventional lasers. Implementation of the improved nozzles is expected to improve diesel engine performance, thereby decreasing fuel consumption and pollution emissions. Such characteristics are desired for Marine and Army transport vehicles.

Infrared focal plane arrays (IRFPA) are the basis for the DoD night vision sensors. Via holes are required on some of these IRFPAs and are done by ion milling but the yields are relatively low and the hole diameters and aspect ratios are not optimal. Laser drilling using femtosecond or short pulse ultraviolet lasers could potentially provide a high yield low cost solution.

The Electro-Optics Center, in collaboration with Extrude Hone (subrecipient) set up the micromachining testbed using both a femtosecond laser and a diode pumped frequency tripled uv laser to test and demonstrate feasibility of the two applications identified above. Extrude Hone developed the micromachining workstations for both lasers and applied their expertise in systems integration and manufacturing of fuel injector nozzles to the project.

2. FEMTOSECOND LASER WORKSTATION

The laser used for the femtosecond laser workstation is a Clark-MXR model CPA-2010, shown in Figure 1. The CPA-2010 is a chirped pulse amplified Ti:Sapphire laser system that incorporates a diode-pumped seed laser (mode-locked fiber laser), pulse stretcher, Ti:Sapphire regenerative amplifier, pulse compressor and Nd:YAG kHz pump laser head. It has an adjustable repetition rate that can be varied between 1 and 2 kHz. For all the testing done to date, a rep rate of 1 kHz was employed.
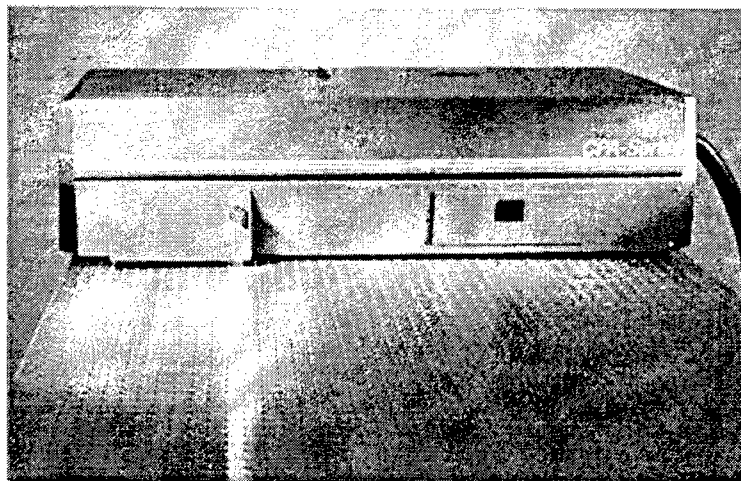
Figure 1. Clark MXR femtosecond laser

The laser emits at a wavelength of 775 nm with an average power of 1 watt at a repitition rate of 1 kilohertz. The pulse energy at this rep rate is approximately 1 millijoule (mJ). The minimum pulse width specified is 150 femtoseconds but was between 200 and 300 femtoseconds for most of our studies. The output beam diameter is approximately 6 mm and is slightly elliptical and the beam exiting the laser head is linearly polarized in the horizontal direction.

The layout of the femtosecond laser workstation with the input optics is shown is Figure 2.
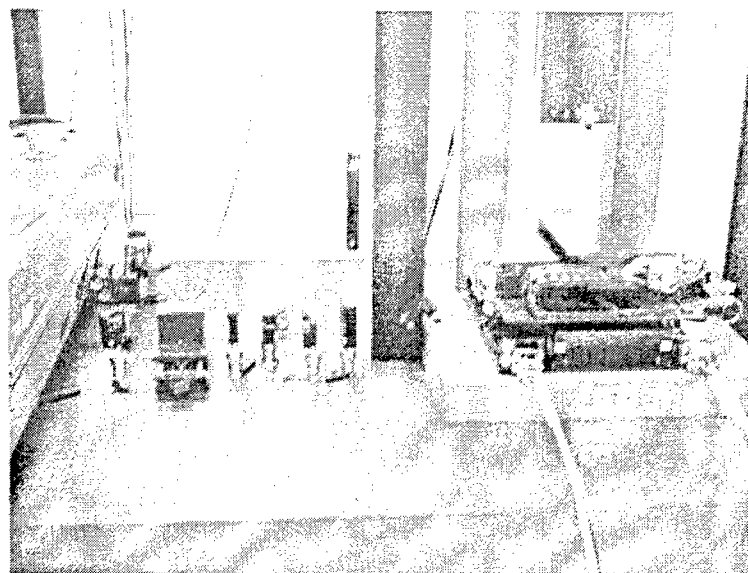
Figure 2. Femtosecond Laser Workstation

The workstation was designed to accommodate a wide variety of processing requirements. For instance, the z-axis stage has a total length of travel of 300 mm while the x and y axis stages are capable of 100 mm of travel. This provides a great deal of flexibility when mounting odd shaped parts or using longer focal length objectives.

A close up view of the input optics is shown in Figure 3. An uncoated window directs a small percentage of the beam to a beam diagnostic instrument from Swamp Optics, LLC. The Grenouille functions both as a standard laser beam analyzer where the beam intensity profile can be determined and as an ultrashort pulse analyzer that can measure the intensity and phase of the pulse at rates up to 20 Hz. This is accomplished through frequency resolved optical gating (FROG). The ultrashort laser pulse is characterized by interacting one or more pulses in a nonlinear medium. One pulse forms a "gate" that lets a time slice of the other pulse pass to a spectrometer. This signal pulse is spectrally resolved and recorded as a function of the delay between the input pulse and the gate. This record is called a spectrogram or FROG trace. An image of the FROG trace with the corresponding diagnostics is shown in Figure 4.
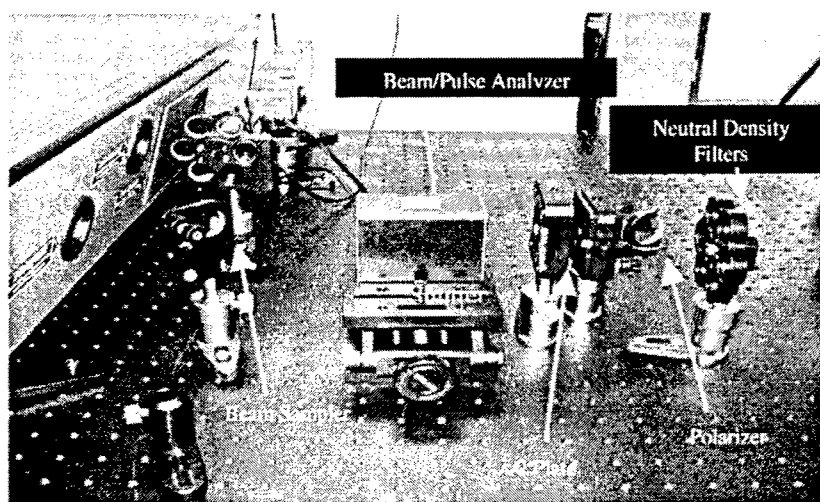
Figure 3. Femtosecond Laser Optics
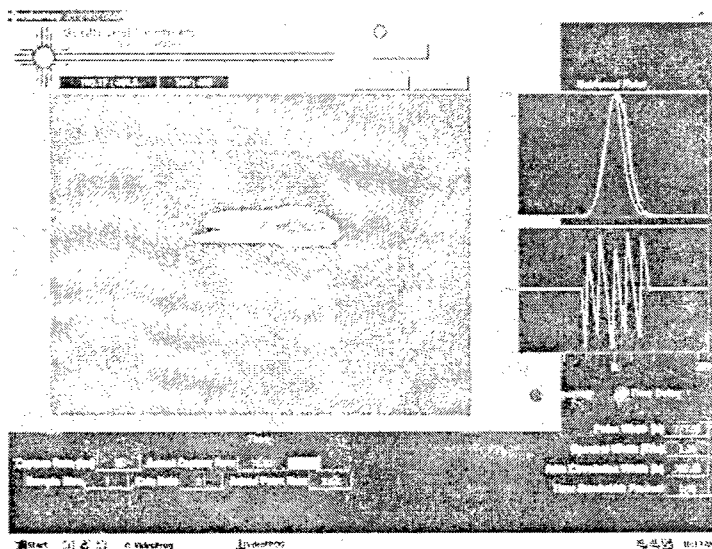
Figure 4. FROG Trace

After the beam sampler, the beam passed through a fast mechanical shutter capable of switching speeds of 1 millisecond. This was purchased from NM Laser Products Inc. and allowed a particular number of laser pulses to

reach the work surface. The beam then passed through a zero order half wave plate purchased from CVI Laser, model # QWPO-775-10-2 and through a CVI Laser polarizer, model # TFPK-775-PW-1025-C. This combination provided variable attenuation of the beam intensity that allowed us to accurately control the pulse energy. In addition, a series of neutral density filters was positioned after the polarizing components to allow more flexibility in controlling the pulse energy during machining.

After the neutral density filters, the beam was directed in the vertical direction by a dielectric coated fold mirror purchased from CVI Laser (model # TLM1-775-45-P-1025). Two other identical fold mirrors directed the beam along the z-axis stage. The beam then passes through a quarter wave plate converting the linearly polarized light to circular for symmetrical hole drilling. The focusing objective used was a Mitutoyo NIR 10X, long working distance microscope objective with an effective focal length of 20mm and a working distance of 30 mm.

The workstation itself consisted of a granite slab baseplate and granite bridge structure on which motor driven translation stages were mounted. The x and y stages were linear motor stages purchased from Aerotech and had a total travel length of 100 mm with a resolution of less than a micron and a positional accuracy of $\pm$ 1 micron. The z axis stage, a linear ball screw stage also purchased from Aerotech had a total travel of 300 mm with a resolution of 1 micron. Extrude Hone designed and manufactured the baseplate and bridge and integrated the motion control driver and electronics with the PC.

3. UV LASER WORKSTATION

The laser used for the uv laser workstation was a Q-switched, diode pumped, frequency tripled Nd-YLF laser purchased from Photonics Industries, Inc. Their model # DS10-351 emits at a wavelength of 351 nm with an average output power of around 4 watts at a repetition rate of 3 kHz and a pulse energy of 3 mJ. The rep rate was user adjustable from 1 to 10 kHz and the pulse width varied with rep rate with the minimum being approximately 50 ns at 1 kHz and broadening to about 200 ns at 10 kHz. The beam exiting the laser has a diameter of .9 mm.
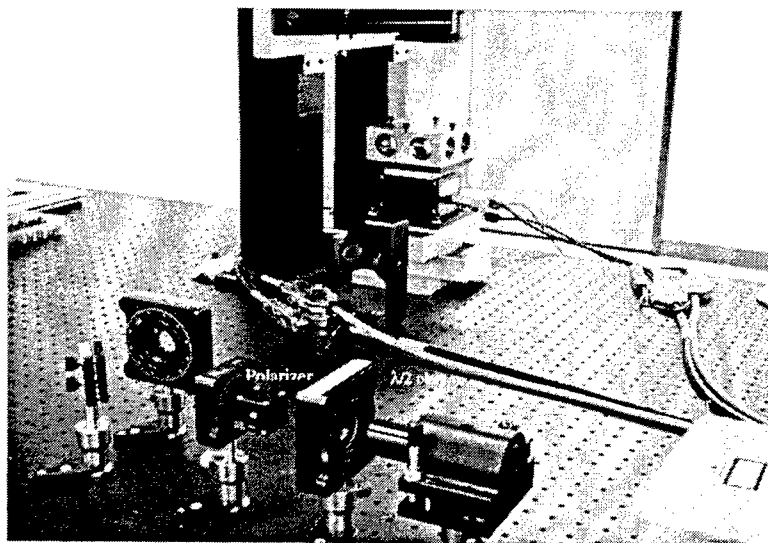
Figure 5. UV Laser, Optics, and Workstation

Upon exiting the laser, the beam passes through a 5X beam expander, and a half wave plate, polarizer combination. The laser, optics, and workstation are shown in Figure 5. The half wave plate/polarizer combination allows fine adjustment of the beam intensity. After a fold mirror, the beam passes through a quarter wave plate changing the linearly polarized light to circular polarization. Two fold mirrors then direct the beam into a galvonometric scan head consisting of two orthogonal mirrors that can be controlled via software to perform two dimensional patterning operations. The scan head , a HurryScan 10 from ScanLab AG.accommodates a maximum beam diameter of 10 mm and it's mirrors are optimized for 351 nm at a 45 degree incidence angle. The focusing lens attached to the scan

head is a 100 mm focal length f theta lens that focuses to a flat image surface over an area of 50 mm x 50 mm with a minimum spot size of 10 microns.

The x and y linear ball screw stages from Aerotech had a maximum travel of 50 mm with a resolution of .5 microns and a positional accuracy of $\pm$ 2 microns. A close up view of the uv workstation showing the scan head, lens and linear translation stages is shown in Figure 6.
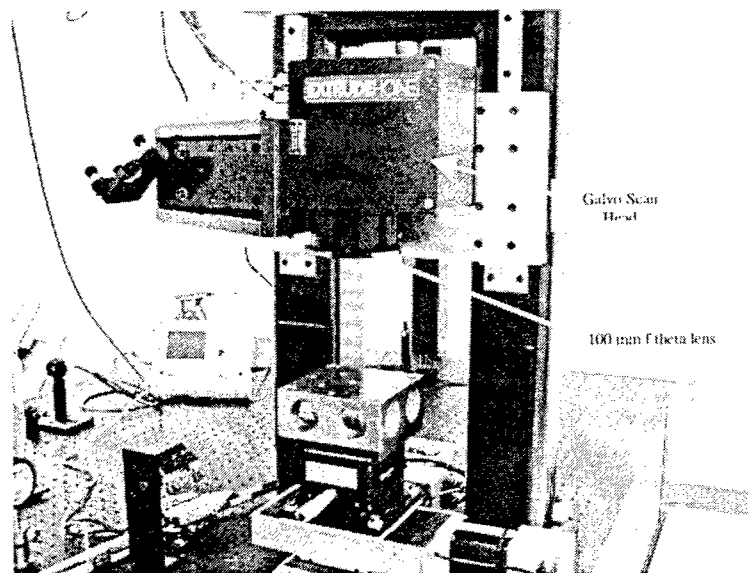
Figure 6. UV Laser Workstation Scan Head and Motion Control System

The z axis was controlled manually using coarse and fine adjustment control. The coarse adjustment provides 150 mm of travel through the use of a large lead screw that translates the entire scan head along slides mounted on the bridge. Fine adjustment control was obtained using a Coherent 61-0360 translation stage that provided 12.5 mm of vertical travel with 5 micron resolution. With this workstation, the focal distance was manually set and the beam was controlled using the HurryScan scan head.

3. RESULTS

3.1 Femtosecond laser workstation
In an earlier program exploring applications for ultrashort pulse lasers, hole drilling for diesel engine fuel injectors was identified as an application that could benefit from the unique advantages offered from femtosecond laser machining. A considerable improvement in diesel engine fuel economy can be realized with smaller and properly shaped fuel injector holes.

Via hole drilling in Mercury Cadmium Telluride (HgCdTe), currently being done using ion milling techniques, is another application identified that could benefit from ultrashort pulse laser machining. Using the current method of drilling, yields are relatively low and the minimum hole sizes to date are in the 25 micron diameter range. With array pixel sizes becoming smaller and smaller, the via hole diameters must shrink accordingly. A femtosecond laser should be capable of hole sizes on the order of 10 microns with relatively high aspect ratios.

As such, the initial testing using the femtosecond laser workstation centered around percussion drilling in stainless steel and HgCdTe. All of the tests to be discussed were done in air at atmospheric pressure.

The beam intensity profile exiting the laser is shown in Figure 7. The image was taken with the Grenouille device and examined with SensorPhysics laser beam analysis software.
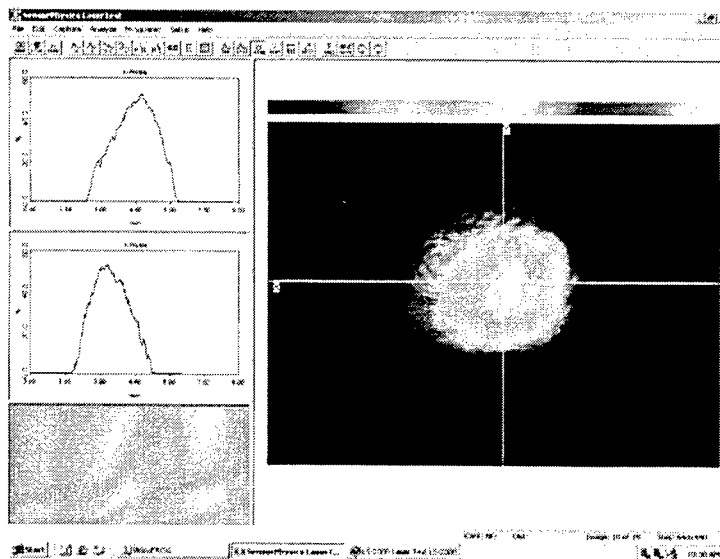
Figure 7. Femtosecond laser beam profile

As has been shown in the past, the advantage of femtosecond lasers is realized when it is used at or near the ablation threshold. At high fluences, there is a considerable amount of energy that is transferred to the substrate in the form of heat. There can be considerable melting and ejection of material during machining due to the high energy present in the wings of the pulse. Figure 8 shows the front and back side of a percussion drilled hole in 50 micron thick stainless steel using the femtosecond laser. The pulse energy for this test was set to 15 μJ, the pulse width was 200 femtoseconds and the rep. rate was set to 1 kHz. The objective lens was a 50 mm best form singlet lens from CVI Laser that was antireflection coated for minimum reflection at 775 nm.

Front   Back
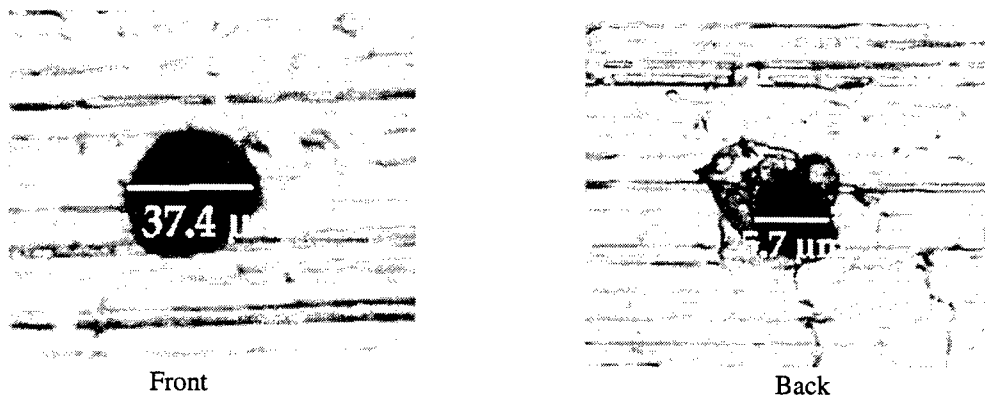
Figure 7. Percussion drilled hole in 50 μm thick stainless steel using femtosecond laser

Some debris can be seen at the output of the exit hole. In fact, debris was present in nearly all cases although most of the debris was loose and could be wiped away easily with alcohol or water.

To measure the drill rate, an experiment was performed where a known number of laser pulses were allowed to pass through to the work surface at a known laser energy and pulse width. Figure 8 shows that at a laser pulse energy of 100 μJ, a pulse width of approximately 200 fs, and a rep rate of 1 kHz, a 2 μm deep hole is drilled with 250 pulses corresponding to a drill rate of slightly less than .01 μm/pulse.

Figure 8. Drill rate of femtosecond laser at 100 µJ

To demonstrate the capability of the micromachining workstation, a two-dimensional pattern was input into a software program that generates code that controls the Aerotech stages. Figure 9 shows an example of this machining process. This pattern was drilled into 100 µm thick stainless steel using a pulse energy of 100 µJ. The overall length of this pattern was approximately 5 mm.

Figure 9. Example of femtosecond laser micromachining workstation

As mentioned previously, the other application we explored was the use of the femtosecond laser to drill via holes in HgCdTe. Figure 10 shows some examples of holes drilled in the material at two different pulse energies. The results show that smaller hole diameters are obtained at low pulse energies due to the fact that ablation only occurs near the peak of the intensity profile. At higher energies, melting can occur at the wings of the pulse. This also shows up as debris around the hole as the larger hole in Figure 10 shows. The lower three holes shown in Figure 10 are approximately 30 µm in diameter when the laser pulse energy was set to 1 µJ, the pulse width was about 200 fs and the rep rate was 1 kHz. The larger holes at the top of the Figure were generated at a pulse energy of 20 µJ. These holes were generated using the Mititoyo 10X objective lens. The chart on the right in Figure 10 shows a noncontact profile taken using a Zygo noncontact surface profiler of a hole drilled in HgCdTe at a pulse energy of 1 µJ.
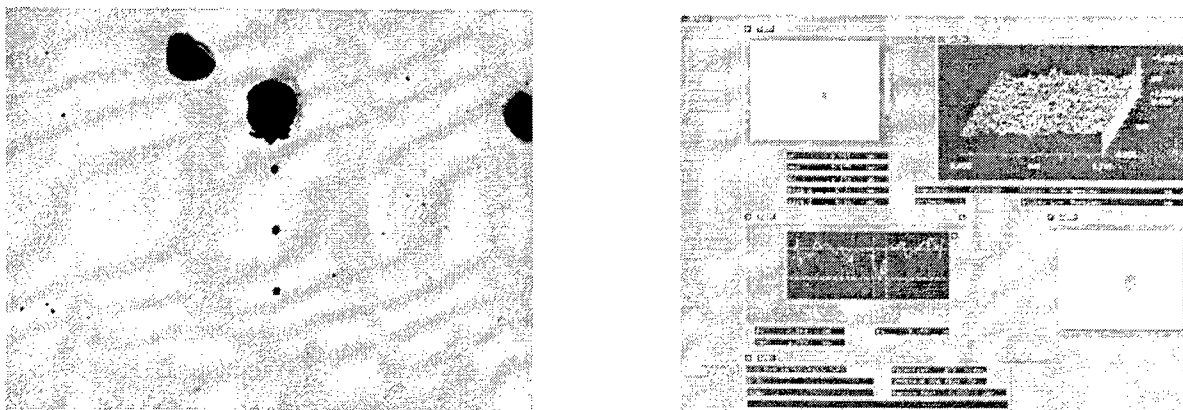
Figure 10. Holes drilled in HgCdTe using femtosecond laser

3.2 UV Laser Workstation

The second laser system utilized in the development of the micromachining testbed was a Q-switched, diode pumped, frequency tripled Nd:YLF laser purchased from Photonics Industries, Inc. Testing was limited with this laser because of problems with one of the harmonic crystals that caused the average power to degrade. We did perform percussion drilling tests at reduced pulse energies in HgCdTe and stainless steel, however.

Figure 11 shows the front and back side of a percussion drilled hole in 100 μm thick stainless steel using the uv laser at an average power of 1 Watt (pulse energy of approximately .75 mJ), a pulse width of 100 ns, and a rep rate of 3 kHz.
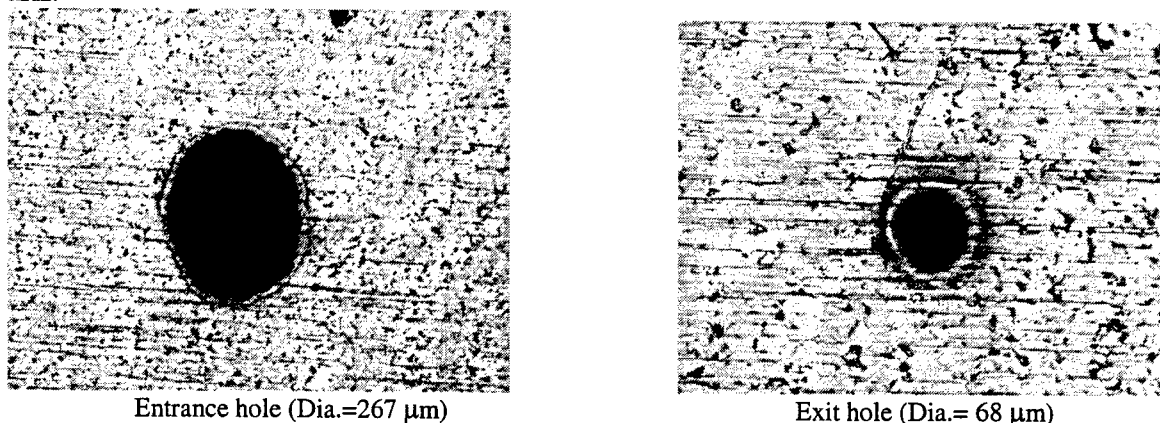
Entrance hole (Dia.=267 μm)

Exit hole (Dia.= 68 μm)

Figure 11. Percussion drilled hole in 100 μm thick stainless steel using uv laser

Figure 11 shows that there is a substantial amount of debris present on both the entrance and exit holes. This is due not only to the longer pulse length of the laser that produces substantial energy transfer in the form of heat to be transferred to the substrate but also the high intensity pulse that can cause melt at the wings of the pulse.

As described previously, the uv workstation uses a scanning galvonometric head to steer the beam over a flat 50 x 50 mm image plane. This system is typically used in laser marking and scribing applications. The mirrors in the scan head are controlled through software that reproduces two-dimensional patterns drawn in a computer aided design (CAD) program. The program also controls the laser shutter and rep rate so a prescribed number of pulses or traces can be passed. Figure 12 shows an example of the workstations capability. For this case, the laser was set to an average power of 4 W at a rep rate of 3 kHz and a pulse width of 100 ns. The machining was done in 100 μm thick stainless steel. The overall length of the pattern in the left figure was 5 mm. The figure on the right shows a closeup of the line generated on the far left of the pattern. The width of this line is approximately 36 μm
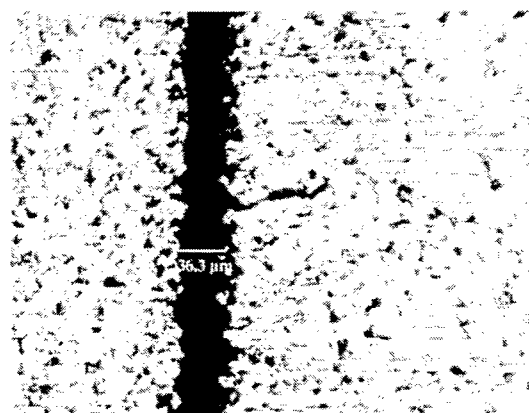
Figure 12. Example of uv laser workstation in 100 μm thick stainless steel

We also used the uv laser workstation to generate holes in HgCdTe to compare with those drilled using the femtosecond laser. Figure 13 shows holes drilled in a sample using the uv laser set to an average power of 50 mW (pulse energy ~ 17 μJ), a pulse width of 100 ns, and a rep rate of 3 kHz. From top to bottom, the number of pulses was varied from 60 to 30 to 15 to examine the effect additional pulses had on hole size. The diameter of the hole did not seem to be affected by the additional shots although the depth of the hole was.
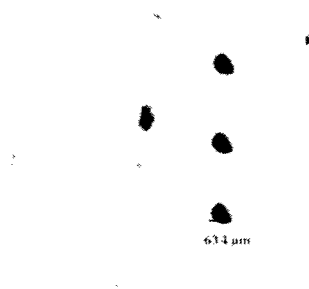
Figure 13. Percussion drilled holes in HgCdTe using the uv laser

The hole profile was examined using the Zygo noncontact profiler for the 60 pulse case above. Figure 14 shows the profile of the hole. Notice that the depth of the hole was approximately 2 μm which corresponds to a drill rate of about .03 μm/pulse. Increasing the number of pulses to 90 and 120 did not alter the drill rate. Also notice the amount of debris buildup around the edge of the hole indicating considerable melt eject. This is to be expected with the longer pulse lasers. Adjusting the pulse energy to be closer to the ablation threshold should reduce the amount of debris ejected from the hole.
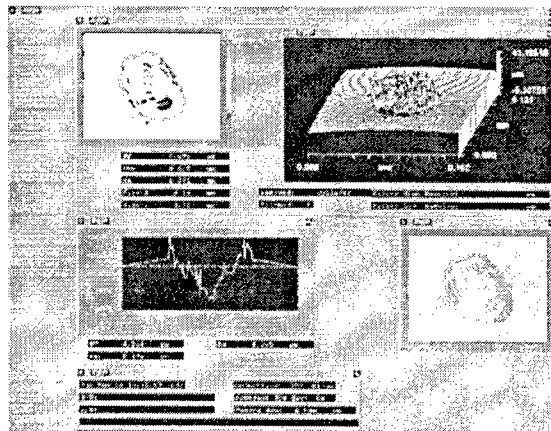
Figure 14. Surface profile of hole drilled in HgCdTe using uv laser (60 pulses)

4. CONCLUSIONS

An ultrashort pulse laser micromachining testbed has been developed at the Electro-Optics Center to examine the advantages of this technology for specific applications relevant to the military and commercial markets. Two of these applications are diesel engine fuel injector hole drilling and via hole drilling in infrared focal plane arrays. The material used to examine these applications were stainless steel and mercury cadmium telluride (HgCdTe). The two lasers selected for the testbed were a femtosecond laser from Clark-MXR and a frequency tripled Nd:YLF uv laser from Photonics Industries.

Initial results showed the capabilities of both workstations to generate two-dimensional patterns as well as percussion drilling of holes in both materials. A comparison of these results seems to show that the femtosecond laser can produce small feature sizes with very little debris and substrate damage when operated in the low pulse energy regime. Additional testing needs to be conducted with both laser systems to compare the results and to determine the most suitable candidate for that particular application.

5. ACKNOWLEDGEMENTS

REFERENCES

1. R. Haight, P. Longo, and A. Wagner, "Femtosecond lasers repair photomasks", Laser Focus World, p. 79 May, 2002.

Femtosecond laser machining of steel

Michelle L. Griffith[*], Mark T. Ensz, and Daryl E. Reckaway
Sandia National Laboratories, P.O. Box 5800, Albuquerque, NM 87185

ABSTRACT

Femtosecond laser processing is a promising new technology for the fabrication of micro-scale components from engineering materials, such as metals. In the femtosecond time regime, the ablation process is nearly a solid to vapor transition, thereby providing access to cut smaller features. Sandia National Laboratories has constructed a femtosecond laser microfabrication system to study the ability to produce microscale components in metals and glasses. In this paper, we will report on our initial studies to understand the metal ablation process with respect to manufacturing process parameters. With this understanding, we will show that femtosecond laser processing can fabricate complex components with fine feature detail and clean surfaces. A key finding in this work is the substantial effect of layer decrement on resulting recast material deposition when processing in air.

Keywords: femtosecond, laser, micro fabrication, micro machining, steel, rapid prototyping, layered manufacturing

1. INTRODUCTION

At Sandia National Laboratories, miniaturization dominates future hardware designs, and technologies that address the manufacture of micro-scale to nano-scale features are in demand. Currently, Sandia is developing technologies such as photolithography/etching (e.g. silicon MEMS)[1], LIGA[2], micro-electro-discharge machining (micro-EDM)[3], and focused ion beam (FIB) machining[4] to fulfill some of the component design requirements. As in the macro world, no one micro- or nano-scale process can do it all. Some processes are more encompassing than others, but each process has its niche, where all performance characteristics cannot be met by one technology. For example, micro-EDM creates highly accurate micro-scale features but the choice of materials is limited to conductive materials. With silicon-based MEMS technology, highly accurate nano-scale integrated devices are fabricated but the mechanical performance may not meet the requirements. Femtosecond laser processing has the potential to fulfill a broad range of design demands, both in terms of feature resolution and material choices, thereby improving fabrication of micro-components. One of the unique features of femtosecond lasers is the ability to ablate nearly all materials with little heat transfer[5], and therefore melting or damage, to the surrounding material, resulting in highly accurate micro-scale features.

For many years, Sandia has been involved in the development of laser-based rapid prototyping (RP)[6] and direct fabrication technologies[7-9] to build prototype parts, as well as small lot production components. The significant aspect of these technologies is the utilization of a computer model, sliced into two-dimensional cross-sections, to drive the fabrication process, where a part is fabricated layer by layer to create the three-dimensional shape. For example, we use these models to routinely fabricate polymeric three-dimensional representations for design verification and, in some instances, fabricate patterns for investment casting to obtain a metal component. Instead of using secondary processes, such as investment casting, to fabricate the final metal part, Sandia has developed a laser-based metal fabrication technology, known as Laser Engineered Net Shaping (LENS®)[7], to directly fabricate the metallic component. These technologies have greatly enhanced our ability to quickly fabricate parts but the size regime is typically on the macro-scale. The RP polymeric-based technologies are now scaled to the micro level but their properties do not typically meet the performance requirements of components that are of interest to Sandia. The LENS® process can produce parts down to the mm-scale but no smaller due to processing constraints.

At present, Sandia is developing a femtosecond laser micro-fabrication capability to expand into the micro-scale size regime for metals and glasses. We hope to produce accurate, reliable micro-components. To facilitate adoption of this technology in the manufacturing environment, further understanding is required to ensure routine fabrication of robust components with desired material properties. This requires understanding and control of the material behavior during

[*] mlgriff@sandia.gov; phone 1 505 284-2096; fax 1 505 844-5589

part fabrication. This paper describes our initial research to understand the ablation process of steels and to determine the correct path sequencing to drive the process in order to fabricate components with clean surfaces and accurate features.

2. EXPERIMENTAL

Figure 1 is a photo of our femtosecond laser micro-fabrication system. We are using a Hurricane femtosecond laser from Spectra-Physics. This laser provides a small footprint which is more amenable for the manufacturing environment with the following characteristics: 800 nm wavelength, 120 fs pulse width, 1 KHz frequency, up to 1 mJ energy, and approximately 4 mm output beam. This beam is transferred to the working envelope by a series of mirrors and is focused with a microscope objective. For this work, a 20X objective was used resulting in a minimum spot size of 40 microns at 975 mW. Smaller spot sizes are easily obtainable, but for this work a larger spot size was used to aid in understanding the ablation process.
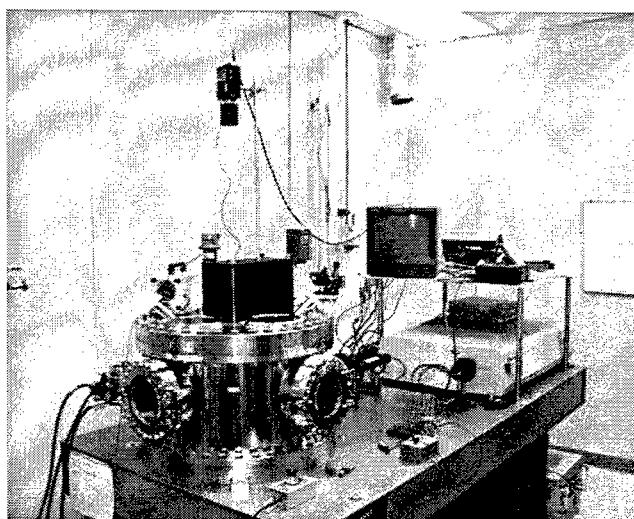
Figure 1. Sandia's femtosecond laser micro-fabrication system.

The beam is focused onto the working surface and X-Y stages manipulate the geometry in the plane, whereas the microscope objective is mounted to a Z stage to manipulate the beam position. These stages and objective are mounted inside a vacuum chamber for future environmental studies. It is well known that the environment utilized during processing has a dramatic effect on final feature definition through the enhanced removal of the ablated species[10]. For this work, all studies were done in air, where it is generally more difficult for the species to ablate away from the surface resulting in redeposition onto the sidewalls or top surfaces. It is beneficial to process in air for a variety of factors from simpler equipment (no vacuum/gas handling equipment) to easy sample exchange. Other researchers have found techniques[11] to provide good feature definition without species redeposition while processing in air. Appropriate techniques will be incorporated into our system in the future.

Stainless steel 304L foils were used for this work. Typically, 200 micron thick foils were used. The foils were mounted into a picture frame holder, where features ablated through thickness easily fall out of the foil for analysis. Full power (975 mW) was used for most studies. Since this work involves the utilization of traditional RP techniques, effects of travel velocity, layer decrement, and geometric features were studied. Sandia-developed software was used to define the path sequence for part fabrication. Simple machine language (M and G codes) was used for initial parameter studies. Ablated features were analyzed by optical and scanning electron microscopy. Width and depth of features were measured by interferometry techniques.

3. RESULTS

3.1 Velocity studies

For complex part fabrication, we will need to process parts in a layered manufacturing approach. A three-dimensional part is partitioned into two-dimensional cross sections and raster paths will further define each layer. In order to correctly choose the layer thickness and raster width (known as hatch) we need to understand the effect of velocity on feature width and depth. Single lines, 10 mm long, were drawn at various velocities and their width and depth measured using interferometry. Table 1 shows the velocity, width, and depth for the lines drawn. Figure 2 shows the morphology of the lines ablated.

Table 1. Effect of travel velocity on resulting width and depth of ablated line.

Velocity (mm/s)	Line Width (μm)	Line Depth (μm)
0.42	46	0
0.85	18/49	25
1.69	29/54	19
3.39	44/58	4.5

| (a) | (b) | (c) | (d) |
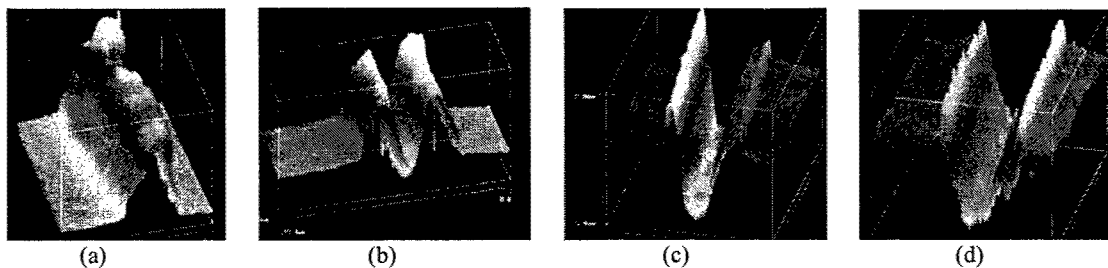
Figure 2. Interferometric data showing cross-sectional morphology of lines fabricated with varying velocities: (a) 0.24 mm/s. (b) 0.85 mm/s. (c) 1.69 mm/s, and (d) 3.39 mm/s. Data not on same scale for each velocity.

Depth was measured from the foil surface to an average depth within the channel. For the three fastest velocities, the first value in the line width column is the interior width, whereas the second is an indication of how much material was redeposited around the channel. As the velocity increases, this difference becomes negligible. As expected, increasing velocity results in decreasing depth with less redeposited species.

At the slowest velocity (0.42 mm/s), where one would expect the greatest depth, it appears that there is no ablation. Ablation depths are inconsistent at this velocity. Typically depth measurements are 40-50 microns for thick foils; however, plasma generation and particle collisions, can inhibit the species from escaping the channel. In the current example, the ablated species decelerated and redeposited across the channel opening. It is expected, if cross-sectional microscopy were performed, there would be a slot, approximately 45 microns deep, underneath this deposition. Even though more material is ablated at slower velocities, which could decrease fabrication time, the unreliability of clean channel formation is unfavorable for repeatable manufacturing.

3.2 A comparison of parameter sets on component fabrication

By utilizing a layered manufacturing approach, a three-dimensional shape is represented by two-dimensional cross-sections where each cross-section is represented by a raster pattern. There are two choices for volumetric material removal: 1) fast travel velocity and smaller layer decrement or 2) slow travel velocity and larger layer decrement. Processing speed is of great importance in the manufacturing environment, but so is final part resolution and cleanliness. Figure 3 shows a micrograph of a 200 micron thick comb geometry fabricated at 0.42 mm/s at 25 micron layer decrements. The comb geometry is reasonably accurate dimensionally, but as the figure shows, there is a large amount

of recast material along the sidewalls. Furthermore, it took twelve passes to ablate through the thickness or a discrepancy of 100 microns. This supports the concept that during fabrication some of the ablation energy is utilized to remove old material that has recast within the channel.

Figure 3. Comb geometry fabricated at 0.42 mm/s with 25 micron layer decrements. Comb arms are 200 microns wide with 250 micron spacings. For a 200 micron thick foil, it took 12 passes to ablate through thickness.

In contrast, as Figure 4 shows, a ratchet gear was fabricated at 1.69 mm/s and 5 micron layer decrements. The gear is both dimensionally accurate and has little recast material. The gear was cut through a 100 micron thick foil in 18 passes, or 90 microns, resulting in a more efficient process where energy is directly utilized to cut features. Even though the gear was cut from a 100 micron foil, it is apparent that the small layer increment is better for part fabrication. For this parameter set, the particles can volatize away from the channel without heavy plasma shielding or increased particle-particle collisions.
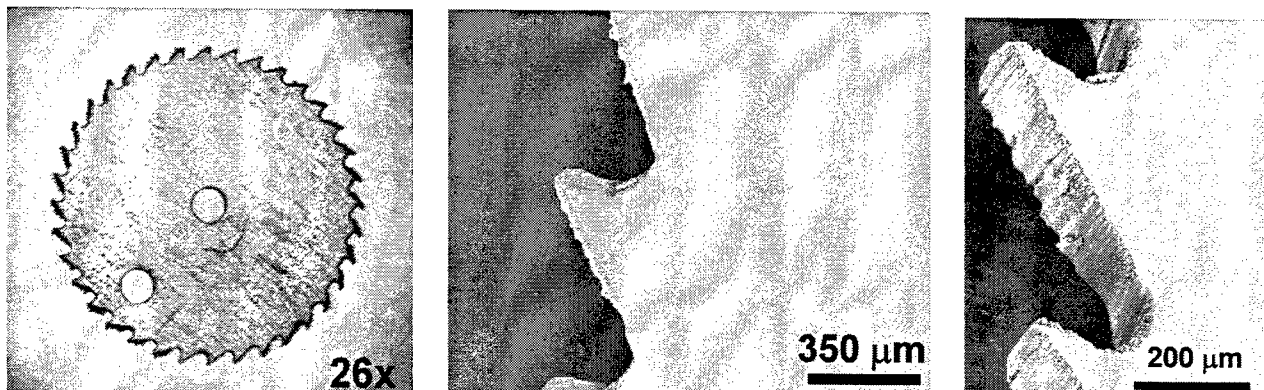
Figure 4. Ratchet gear fabricated in 100 micron thick foil using the following parameters: 1.69 mm/s, 5 micron layer decrement, 18 passes to ablate through thickness.

4. CONCLUSIONS

Initial studies show that femtosecond laser processing is a promising manufacturing technology to fabricate micro-components. We have demonstrated with a basic understanding of travel velocity and layer decrement on resulting channel morphology, complex shapes can be fabricated in stainless steel. A key factor in producing clean features is choosing the correct layer decrement that allows the ionized species to escape the channel.

ACKNOWLEDGEMENTS

REFERENCES

1. J. J. Sniegowski, "Moving the World with Surface Micromachining," *Solid State Technology*, February Issue, pp. 83-90. 1996.

2. J. Hruby, "LIGA Technology and Applications", *MRS Bulletin, Vol. 26, No. 4*, p. 337, 2001.

3. G. L. Benavides, L. F. Bieg, M. P. Saavedra, E. A. Bryce, "High Aspect Ration Meso-scale Parts Enabled by Wire Micro-EDM", *Journal of Microsystems Technologies, Vol. 8, No.6*, p. 395, 2002.

4. D.P. Adams, G.L. Benavides, "Micrometer-scale Machining of Metals and Polymers Enabled by Focused Ion Beam Sputtering", *Materials Research Society, V546, Symposium O Proceedings, April 1999*, pp. 201-205, 1999.

5. B. N. Chichkkov, C. Momma, S. Nolte, F. von Alvensleben, A. Tunnermann, "Femtosecond, Picosecond, and Nanosecond Laser Ablation of Solids", *Appl. Phys. A 63*, pp. 109-115, 1996.

6. C. L. Atwood, M. C. Maguire, M. D. Baldwin, "RP&M Applications at Sandia National Laboratories", *Stereolithography and Other RP&M Technologies*, Society of Manufacturing Engineers, Dearborn, Michigan, pp. 253-272. 1996.

7. M. L. Griffith, M. T. Ensz, J. D. Puskar, C. V. Robino, J. A. Brooks, J. A. Philliber, J. E. Smugeresky, W. H. Hofmeister, "Understanding the Microstructure and Properties of Components Fabricated by Laser Engineered Net Shaping (LENS)", *Materials Research Society, V625, Symposium Y Proceedings, April 2000*, pp. 9-20. 2000.

8. M. L. Griffith, M. T. Ensz, D. L. Greene, D. E. Reckaway, J. A. Romero, T. B. Crenshaw, L. D. Harwell, T. E. Buchheit, and V. Tikare, "Solid Freeform Fabrication using the WireFeed Process", *Proceedings of the Solid Freeform Fabrication Symposium, August, 1999*, University of Texas, Austin, TX, pp.529-536, 1999.

9. J. Cesarano, R. Seglaman III, P. D. Calvert, "Robocasting Provides Moldless Fabrication from Slurry Deposition", *Ceramic Industry 148*, pp. 94-102, 1998.

10. J. Sun, and J. P. Longtin, "Effects of Gas Medium on Femtosecond Laser Beam Delivery", *Proceedings of the 21st International Congress on Applications of Lasers and Electro-Optics, October 2002, LIA Publication #594*, Laser Institute of America, Orlando, Florida, paper 155734 on CD-ROM, 2002.

11. S. Nolte, C. Momma, G. Kamlage, A. Ostendorf, C. Fallnich, F. von Alvensleben, H. Welling, "Polarization Effects in Ultrashort-pulse Laser Drilling", *App. Phys. A 68*, pp.563-567, 1999.

Femtosecond laser processing tailored for biomedical materials and laser power delivery through optical fibers

M. Obara[1*], K. Ozono[1], M. Kanai[1], H. Sekita[1,2] ,P.A.Atanasov[1,3]

[1]*Keio University, Department of Electronics and Electrical Engineering, 3-14-1, Hiyoshi, Kohoku-ku,* Yokohama-shi, 223-8522 Japan

[2]Cyber Laser Inc., *2-45 Aomi, TIME24 Building, 4F N-5, Kotoku, Tokyo, 135-8073, Japan*

[3]*Institute of Electronics, Bulgarian Academy of Sciences, 72 Tsarigradsko Shose Blvd., Sofia 1784, Burgaria*

Abstract

We have been working on the tailored ablation processing of advanced materials using femtosecond lasers. Here we would like to focus on the femtosecond laser processing tailored for hydroxyapatite. Hydroxyapatite is a key material of human tooth and human bone. The human bone is made of hydroxyapatite oriented along the collagen. The micromachining of human bone is highly required for medicine. The medical issue is how to preserve the chemical property of the laser-ablated surface. By use of pulsewidth tunable femtosecond laser (50fs – 2ps, 1.5mJ, 1kpps), we compared the relative content of calcium and phosphorus. The relative content of calcium and phosphorus is kept unchanged before and after laser ablation. For these medical applications, the intense femtosecond laser delivery through optical fibers is required. It is theoretically shown that it is possible to deliver the 900 fs pulses of 0.1 mJ/pulse through a 1 m-long graded index fiber with a 200 μm core diameter if the fiber has the optimum refractive index profile. We therefore conclude that graded index multimode fibers give better spatial distributions of the output transverse mode than hollow fibers or step index multimode fibers, and can deliver larger pulse energy than single mode fibers.

Keywords: hard tissue ablation, tooth, bone, plastic surgery, fiber delivery, femtosecond laser

1. PROCESSING OF HYDROXYAPATITE

1.1. Introduction

The importance of ultrashort pulse lasers in the medical field has been enhanced over the years. One of the fields of interest is the removal of hard biological tissue, for example, bone or teeth. The human bone is mainly made of hydroxyapatite (HAp, $Ca_{10}(PO_4)_6(OH)_2$) oriented along the collagen. The human dental enamel

---

* E-mail: obara@obara.elec.keio.ac.jp; Phone: +81-45-563-1141; Fax: +81-45-566-1529; http://www.obara.elec.keio.ac.jp; Department of Electronics and Electrical Engineering, Keio University, 3-14-1 Hiyoshi, Kohokuku, Yokohama, 223-8522 JAPAN.

consists of 95 % HAp, 4 % water and 1 % collagen fibers, and human dentin contains 70 % HAp, 20 % collagen and 10 % water [1]. The micromachining of HAp is highly required for orthopedics and dentistry. The important medical issue is to preserve the chemical property of the machined (ablated) surface. If chemical properties of HAp change once, human bone or tooth cannot re-grow after laser processing [2]. Tanaka et al. have demonstrated the artificial synthesis of a material consisting of HAp and collagen with the same characteristic as the bone by self-organization process [2]. They experimentally revealed that the environmental conditions which promote the self-organization process are at 40°C and pH8-9 [2]. This result means that self-organization (re-growth) is hard to proceed in a human body when changing the phosphorus (P)/calcium (Ca) ratio in HAp, because change of the P/Ca ratio leads to the change in pH value in the vicinity of the artificial/real bone.

Conventional surgical instrument for cutting bone is mainly a mechanical saw and Er:YAG laser[3]. The use of saw has the following disadvantages [3]: It causes broader cut than the laser beam. Moreover, it deposits tissues, causing rather large defects. Especially in the skull region, the remaining deposit of metal shavings, resulting from the contact between saw-blade and skull bone, has a negative influence on the subsequent healing process. In the meantime, Er:YAG (2.94 µm, 100 µs) laser irradiation exhibits rough tooth surfaces with deep cracks (~300 µm)and with heat-affected zone, because the long-pulse, 2.94 µm laser is absorbed by the water in the enamel and dentin, resulting in the subsequent humidity explosion to get the enamel and dentin blown off [3-7].

Ultrashort laser processing of human dentin and enamel was experimentally investigated by Krueger et al. using a 300-fs, 615-nm pulse [8]. They observed scanning electron microscope (SEM) images of these hard tissues ablated with a 300-fs pulse compared to a 7-ns laser ablation. With 300-fs pulse ablation they demonstrated precise, smooth ablation without heat-affected zone. While only rough ablation surfaces with heat-affected zone were achieved with the long-pulse 7-ns pulse ablation. Perry et al. have also carried out a femtosecond laser (350 fs, 1053 nm, repetition rate: 10 Hz) ablation experiment of human dentin and enamel, and they demonstrated precise removal by 350-fs laser ablation compared to the nanosecond laser (1.4 ns, 1053 nm) removal [9,10]. Junbiao et al. have reported laser ablation of human dentin and enamel by use of a short pulse free electron laser (2 ps, 9.6 µm) and it is evident that there are changes in ratios of P to Ca in HAp before and after irradiation [11].

The previous papers have not reported the chemical content of P and Ca in bone or tooth [4-10]. Here, we would like to report on the demonstration of ablation processing of HAp using a high-intensity femtosecond laser with pulsewidth of 50 fs, 500fs and 2ps at a wavelength of 820 nm and at 1 kpps. We address the chemical properties of the ablated surface after ablation. It is found that there is no change of the chemical content of the ablated surface before and after ablation over the pulsewidth range used in this experiment. And we have also demonstrated ablation processing of human tooth using a high-intensity femtosecond laser with pulse width of 60 fs, and 2 ps at a wavelength of 820 nm and 1 kpps. Even with 2-ps pulses, non-thermal ablation has been demonstrated.

1.2. Experimental

In our experiments, we used a pulsewidth controllable (from 50 fs through 2 ps) Ti:sapphire laser operating at 820 nm, 1 kpps and about 1 mJ/pulse. The HAp on the xyz-stage was ablated in air to make a wide ablated area for X-ray Photoelectron Spectroscopy (JOEL, JPS-9000MC) observation. Each HAp sample was ablated with 20-shot laser pulses, and after laser ablation we measured chemical properties of the ablated surface using X-ray Photoelectron Spectroscopy (XPS). And we have demonstrated ablation processing of human tooth using a high-intensity femtoescond laser with pulsewidth of 60 fs and 2 ps. And ablated surface has been observed using Scanning Electron Microscope (SEM).

1.3. Results and discussion

By narrow-scan XPS we measured calcium 2p spectrum, phosphorus 2p spectrum, and oxygen 1s spectrum on the ablated HAp surface to observe quantitatively the chemical properties of the ablated surface. The narrow-scan XPS spectra of non-ablated and ablated surface of HAp are shown in Figs. 1 and 2. Figure 1(a) shows the comparison of calcium 2p1/2, 3/2 signals with each pulsewidth ablation. The calcium 2p3/2 signal shows 352.75 eV. The HAp was ablated at a laser
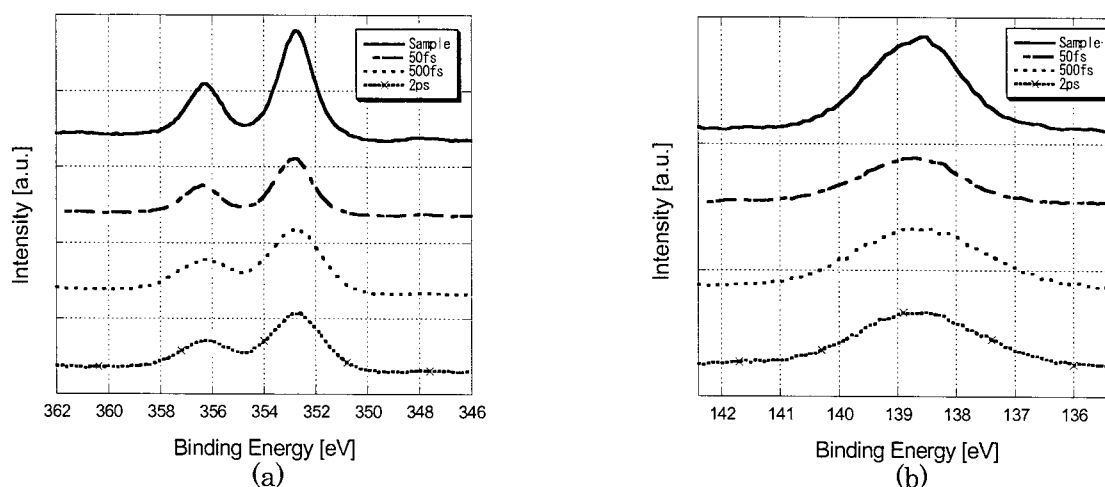
Fig.1 (a) Calcium 2p XPS narrow-scan spectra of non-ablated HAp sample, 50 fs laser ablated, 500 fs laser ablated, and 2 ps laser ablated HAp in air. (b) Phosphorus 2p XPS narrow-scan spectra of non-ablated HAp sample, 50 fs laser ablated, 500 fs laser ablated, and 2 ps laser ablated HAp in air. The HAp was ablated at a laser fluence of 3.2 J/cm^2 (6.4x10^{13}W/cm^2 at 50 fs), 3.3 J/cm^2 (6.6x10^{12}W/cm^2 at 500 fs) and 9.6 J/cm^2 (4.8x10^{12}W/cm^2 at 2 ps), respectively.

fluence of 3.2 J/cm^2 (6.4x10^{13}W/cm^2 at 50 fs), 3.3 J/cm^2 (6.6x10^{12}W/cm^2 at 500 fs) and 9.6 J/cm^2 (4.8x10^{12}W/cm^2 at 2 ps), respectively. These fluences are much above the ablation threshold fluence with respective pulsewidths. As can be seen in Fig. 1(a), we did not observe any difference in the calcium spectrum before and after the laser ablation. Figure 1(b) shows the comparison of phosphorus 2p spectrum. The phosphorus
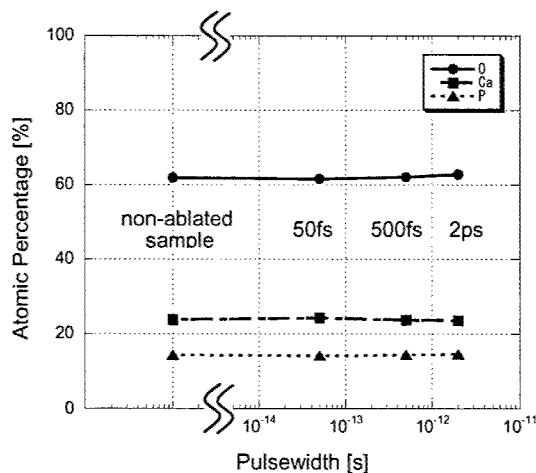
Fig.3 Plots of atomic percentage in the ablated HAp as a function of laser pulsewidth.
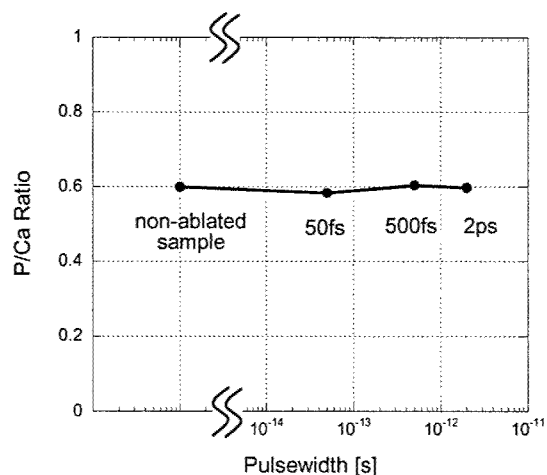
Fig.4 Plots of P/Ca ratio in the ablated HAp as a function of laser pulsewidth.

2p1/2 signal shows 138.65 eV in binding energy. In this experiment, we used the same laser fluence as in Fig. 1(a). We did not observe any difference in the phosphorus spectrum before and after the laser ablation.

Figure 2 shows the comparison of oxygen 1s spectrum. The oxygen 1s signal shows 536.87 eV in binding energy. In this experiment, we used the same laser fluence as in Fig. 1(a). We did not observe any difference in the phosphorus spectrum before and after the laser ablation.
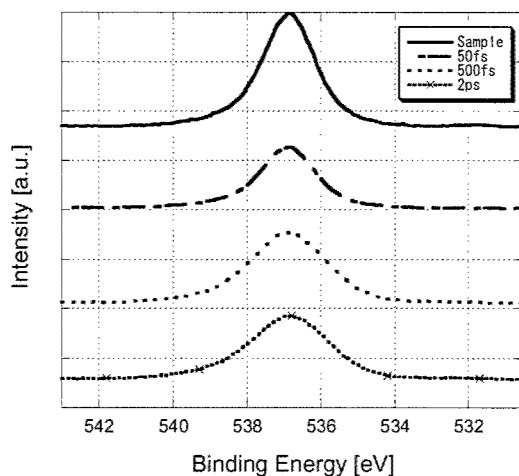
Fig.2 Oxygen 1s XPS narrow-scan spectra of non-ablated HAp sample, 50 fs laser ablated , 500 fs laser ablated, and 2 ps laser ablated HAp in air. The HAp was ablated at a laser fluence of 3.2 J/cm2 (6.4 x 10^{13}W/cm^2 at 50 fs), 3.3 J/cm^2 (6.6 x 10^{12} W/cm^2 at 500 fs) and 9.6 J/cm^2 (4.8 x 10^{12} W/cm^2 at 2 ps), respectively.

Figure 3 shows plots of atomic percentage as a function of irradiation laser pulsewidth. The data are normalized to the initial value of the non-ablated HAp sample. As can be seen in Fig. 3, each atomic percentage seems to be unchanged over the ablation pulsewidth range observed. Figure 4 shows plots of the P/Ca ratio as a function of irradiation laser pulsewidth. It is found that the P/Ca ratio is kept at 0.6 after ablation with pulsewidth ranging from 50 fs through 2 ps. According to the result shown in Fig.2, oxygen content is also kept unchanged after laser ablation. As a result, the structure of $Ca_{10}(PO_4)_6(OH)_2$ is preserved after laser ablation ranging from 50 fs to 2 ps pulse.

In our experiment, it is demonstrated that even with 2-ps, 1-kpps Ti:sapphire-laser ablation of the HAp the ablated surface has kept the chemical properties of the ablated surface unchanged. However, Junbiao et al. have reported that a 2 ps, 2856 MHz burst pulse free electron laser (FEL) at 9.66 μm decreased a fraction of phosphorus in the dental enamel ablated. The HAp has a resonant absorption wavelength at 9.66 μm. The laser energy of 2 ps pulse is about 1 mJ/pulse. The P/Ca ratio of the ablated human dentin surface by FEL is decreased. With the FEL ablation, the micro-pulse is 2 ps. Since its repetition rate is 2856 MHz, it is high enough to induce cumulative thermal effects due to the fact that the thermal diffusion time is in the order of microsecond.

In the case of femtosecond Ti:sapphire laser irradiation at 820 nm in our experiment, there is no resonant absorption by HAp itself, however, the peak laser intensity for 2-ps ablation reaches 4.8 TW/cm^2. Therefore, the main absorption is based on the multiphoton absorption process, which is nearly independent of its composition in HAp. Therefore, ultrashort pulse Ti:sapphire laser is attractive in clinical machining of bone and tooth.

Experimentally we have demonstrated ablation processing of HAp with pulsewidths of 50 fs, 500 fs, and 2 ps. Note that even in the case of 2-ps ablation, chemical properties of ablated surface have been kept unchanged. Our laser is operating at 1 kpps. Therefore, cumulative thermal effects are avoided, while with the 2 ps, 2856 MHz FEL ablation, it is high enough to induce cumulative thermal effects due to the fact that the thermal diffusion time is in the order of microsecond. Then, low energy density remaining between laser pulses (350 ps period) would induce selective ablation of phosphorus. Since laser pulsewidth is shorter than the heat diffusion time (10 - 100 ps), ablation occurs before heat conduction into the surrounding materials. Therefore, an extremely high energy density is stored and ablation takes places independently of the sort of element. Consequently, the chemical property of the ablated surface is preserved. Previously, Ozono et al. have demonstrated femtosecond laser ablation of GaN semiconductor without any change of chemical property of the ablated surface [12]. Hirayama et al. have also demonstrated femtosecond laser ablation of BN ceramics so that the ablated surface remains as the BN layer itself [13].

And we have also demonstrated ablation processing of human tooth using a high-intensity femtosecond laser with pulsewidth of 60 fs, 2 ps at a wavelength of 820 nm and 1 kpps. Figure 5 shows the SEM photograph of human tooth ablated with 60 fs and 2 ps pulses with the laser fluence of 3.5 J/cm^2, respectively. Even with 2-ps pulses, we can observe very sharp edge and we do not observe any cracks.

Our result would be very useful in clinical hard tissue processing application of femtosecond Ti:sapphire

lasers. Optical power delivery of ultrashort laser pulse through optical fibers, which has an energy enough to ablate hard/soft tissues, is a very hard task. It has not realized yet except metal-coated hollow fibers [14]. For medical endoscopic application, optical power fiber delivery techniques are required. Self-focusing in the silica glass is one of the reasons why ultrashort pulse transmission is not realized. Another reason is the self phase modulation, which causes pulsewidth broadening. A longer pulse (2 ps) ablation processing, which still can preserve the initial chemical properties of the ablated HAp surface and which can process the non-thermal ablation, would reach actual clinical applications using optical fiber power delivery [15].

(a)   (b)
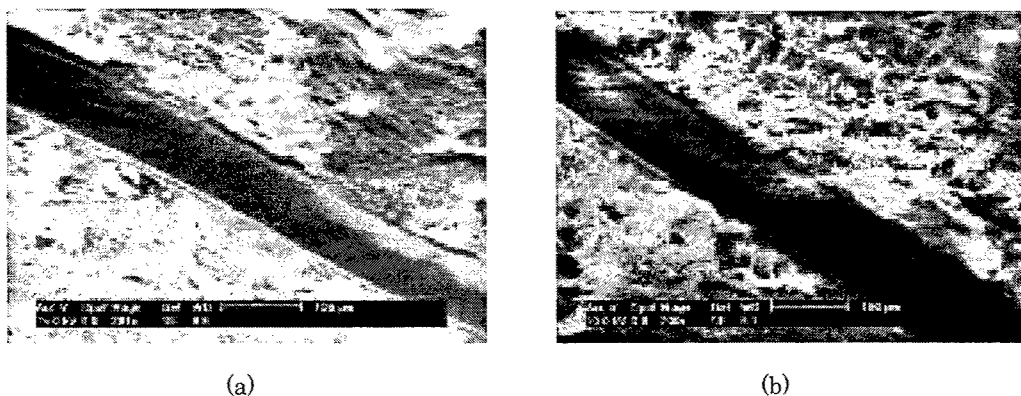
Fig.5 SEM photograph of human tooth ablated with Ti:sapphire laser. The laser fluence is 3.5 J/cm^2 (λ= 820 nm). (a) (τ = 60 fs (b)τ = 2 ps.

2. FEMTOSECOND LASER DELIVERY THROUGH OPTICAL FIBER

2.1. Introduction

Various results concerning femtosecond laser processing have been reported, attracting much attention from industrial and medical fields [16][17]. Especially, as the most popular femtosecond laser source (Ti:sapphire laser) has a central wavelength around 800 nm, which is a window wavelength of biological tissue, the photo dynamic therapy (PDT) using femtosecond laser pulses is expected as a efficient method in the field of cancer diagnosis and therapy in the future[18]. For these applications inclusive of hard tissue ablation, femtosecond laser delivery through optical fibers is required to freely transmit the intense pulses to the work. However, the free space guiding by use of mirrors / prisms is the only one available option so far. If we demonstrate an optical-fiber transmission, a considerable increase of the ease of use for these applications will be obtainable.

There are a few examples of transmission of femtosecond laser pulses through optical fibers. A 100 fs, 0.5 nJ pulse has been transmitted trough a 2 m long single mode optical silica fiber[19], and a 200 fs, 0.7 mJ pulse has been transmitted through a 1 m long *hollow* core multimode optical fiber[20]. However, the silica fiber has a transmission power limited by the small core diameter of the single mode optical fiber, while the hollow fiber

degrades the transmission beam profile. For the above-mentioned applications, it is important that the transmitted beam profile maintains a nearly Gaussian profile and is independent of fiber bending to increase the focused intensity.

In this chapter, we report on the study of high peak power femtosecond pulse delivery through a GI multimode fiber. We obtained a better spatial intensity profile of the output than hollow fibers and SI multimode fibers, and it is found that the GI-multimode fiber can deliver higher peak power than the single mode (SM) fiber transmission. We set the practical delivery parameter as 1 ps, 0.1 mJ/pulse and 1 m long fiber. It is confirmed that the frequency pre-down chirped pulse should realize this delivery by the numerical analysis.

2.2. Experimental
2.2.1. Laser system

To carry out the fiber delivery experiment, we used a Ti:sapphire laser with a chirped amplifier system pumped by the second harmonic wave of a Nd:YLF laser operating at a 1 kHz repetition rate, and at a 800 nm center wavelength. The maximum output pulse energy was 1.5 mJ for the single pulse and the pulsewidth could be varied between 50 fs and 3 ps by changing separation in the pulse compressor. The spatial intensity distribution of the amplified beam was close to the ideal TEM_{00} mode and the beam diameter was 8 mm. The output was linearly polarized.
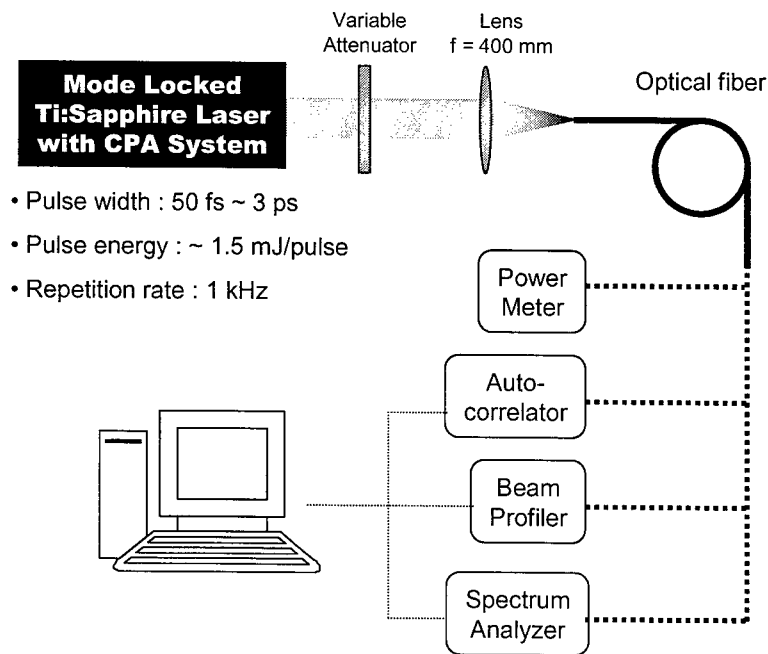
Fig.6. Experimental setup.

2.2.2. Experimental setup

The experimental setup is shown in Fig.6. The laser pulses were focused onto the entrance surface of the optical fibers with a BK7 glass lens (f = 400 mm). The input/output pulse duration, spectrum and spatial beam profile were measured by an autocorrelator (MINI, APE), optical spectrum analyzer (Q8381A, ADVANTEST) and a beam profiler (BeamStar, OPHIR), respectively. Measuring the pulsewidth with the autocorrelator, we used the intensity autocorrelation in order to avoid the effect of the frequency chirp of pulses. The step index (SI) multimode fiber with 1 mm core diameter (F-MMC, Newport) and the graded index (GI) multimode fiber with 62.5 μm core diameter (GIF625, THOR LABS) were used.

2.3. Experimental results

2.3.1. Spatial intensity profile

Figure 7(a) and 7(b) show output beam profiles from a 15 cm long silica SI multimode fiber with a 1
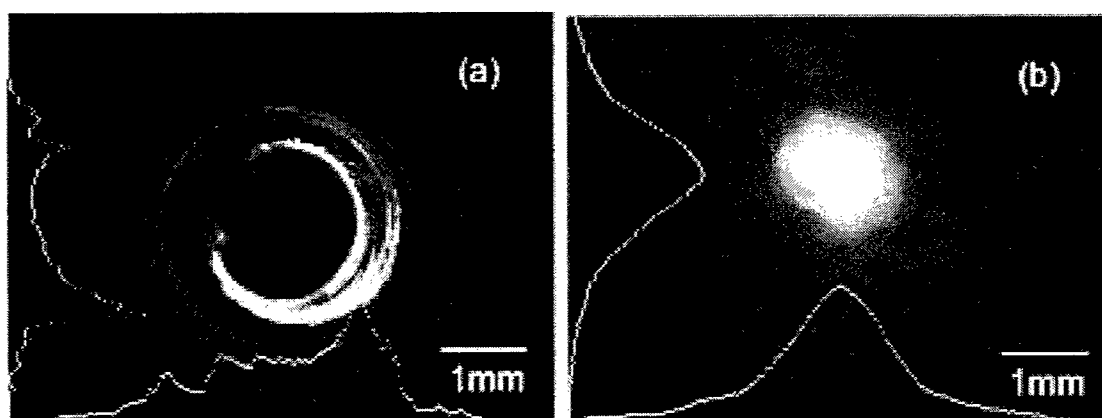
Fig.7. Output beam profile through (a) a straight silica SI multimode fiber with 1 mm core diameter and (b) a straight silica GI multimode fiber with 62.5 μm core diameter 20 mm distant from the end surface of these fibers. The input pulse is 1.7 MW (peak power) and 60 fs (FWHM).
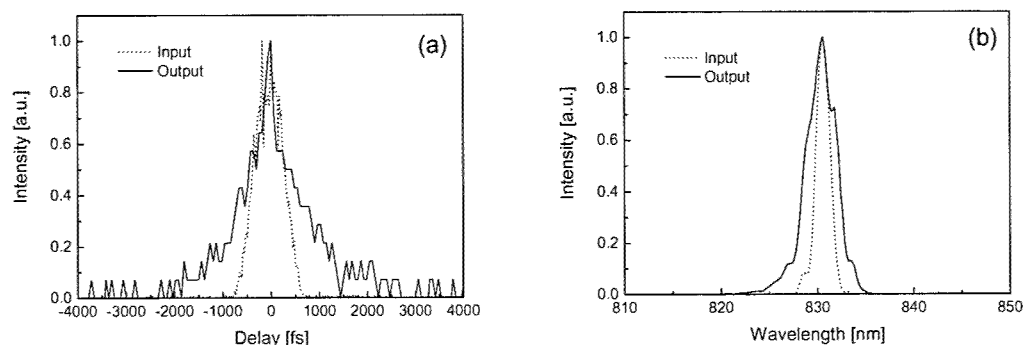
Fig.8. (a) The intensity autocorrelation traces and (b) the spectra of input / output pulse. The fiber length is 10 cm. The input / output peak power is 20 MW / 7.9 MW (10 μJ / 8.7 μJ).

mm core diameter (F-MMC) and GI multimode fiber with 62.5 μm core diameter (GIF625), respectively. The measurement was done 20 mm distant from the exit surface of these fibers. The incident peak power was 1.7 MW and the input pulsewidth was 60 fs. The annular beam profile from the SI multimode fiber is due to the interference of high-order modes. This is sensitive to the bending of the fiber. While the output beam profile through the GI multimode fiber is approximately Gaussian and is nearly independent of the bending. This characteristic cannot be shown in SI multimode fibers but in hollow fibers. Therefore, GI multimode fibers have the advantage of keeping better spatial intensity profile of the output than hollow fibers and step index (SI) multimode fibers.

2.3.2. Measurement of pulse broadening through GI multimode fiber

We have also performed measurements of the pulse duration and the spectrum. The dotted line in Fig. 8(a) represents the intensity autocorrelation trace of the input laser pulse with 500 fs Fourier limited pulse, while the solid line represents the output pulse after propagating through the 10 cm GI multimode fiber with a duration of 1.1 ps. Figure 8(b) shows the spectrum of the input and output pulse under the same conditions. The input peak power was 20 MW. The transmission loss is 0.65 dB.

2.4. Theoretical simulation by nonlinear Schrödinger equation

In our experiments, we could not get the autocorrelation trace when white-light generation occurred. The input peak power was over 20 MW (0.65×10^{12} W/cm^2) at that time. It has been reported that self-focusing in silica glasses occurs at input intensities in excess of 1×10^{12} W/cm^2 where the nonlinear refractive index is 3×10^{-20} m^2/W in silica[21]. Therefore, we assume that this intensity is a maximum input intensity that can be delivered through the GI multimode fiber.
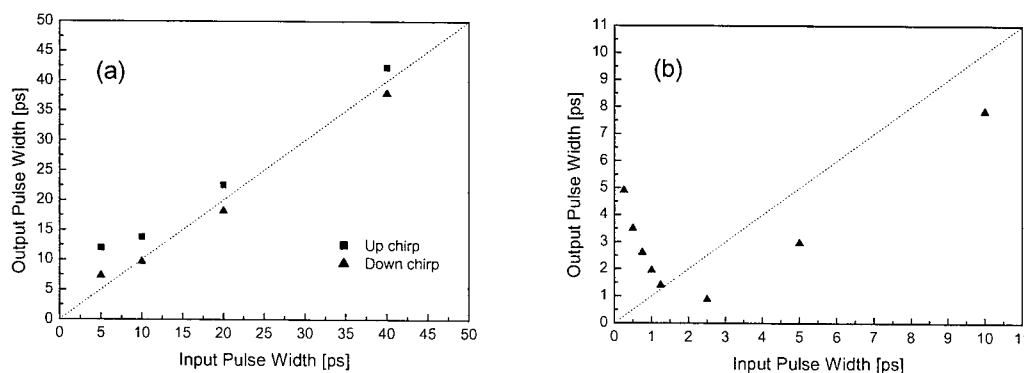
Fig.9. Calculated pulse broadening through a 1 m GI fiber for pre-chirped input pulse. The pulse energy is 0.1 mJ and the spectral width is 20 nm (the central wavelngth is 800 nm). (a) Core diameter : 62.5 μm, (b) Core diameter : 200 μm.

The nonlinear Schrödinger equation (NLSE) governs the behavior of pulses through optical fiber. In our numerical approach, we use the normalized NLSE

$$i \frac{\partial U}{\partial \xi} = \text{sgn}(\beta_2) \frac{1}{2} \frac{\partial^2 U}{\partial \tau^2} + \frac{i\beta_3}{6|\beta_2|T_0} \frac{\partial^3 U}{\partial \tau^3} - N^2 |U|^2 U \exp(-\alpha z) \tag{1}$$

where $\xi = z/L_d$ and $\tau = T/T_0$ represent the normalized distance and time variables, respectively. U is the normalized amplitude by using the definition $P_0^{1/2} \exp(-\alpha z/2) U(z, \tau)$. P_0 is the peak power of the input pulse and T_0 is the input pulsewidth. β_2 is the dispersion of the fiber. The dispersion length $L_d = T_0^2/|\beta_2|$ and the nonlinear length $L_{NL} = 1/\gamma P_0$ provide the length scales over which the dispersion and the nonlinear effect become important, respectively. γ is the nonlinear coefficient and is related to the nonlinear refractive index n_2 and the effective core area A_{eff}, as $\gamma = n_2 \omega_0 / c A_{\text{eff}}$. The parameter N is introduced by use of the definition $N^2 = L_d/L_{NL} = \gamma P_0 T_0^2 / |\beta_2|$. The index parameter N is normally used to compare the importance of the dispersion and SPM effects in the fiber.

We employed the split-step Fourier method [22] for NLSE and perform this calculation based on the assumption that the light remains in the lowest-order modes through the GI multimode fiber. This assumption is based on our experimental results shown in Fig. 6 and on the paper that the light remains in the lowest order modes even for a small bending diameters of GI multimode fibers when the fundamental mode is excited[23]. We performed this calculation and experiments under the identical conditions which are P_0=20 MW, T_0=500 fs for the input pulse and 10 cm of the fiber length. The calculated output pulsewidth was 0.97 ps where the measured pulsewidth was 1.1 ps. The experimentally measured pulsewidth is a little longer than the calculated one. This is mainly due to the fact that modal dispersion is neglected in the calculation. However, a reasonable estimation of pulse broadening is obtainable.

In practical use, the required fiber length to deliver pulses freely is considered to be no less than 1 m. Our experimental results show that Fourier limited 10 μJ, 500 fs input pulses are broadened to 1.1 ps. From this result, consequently, it is impossible to deliver the 0.1 mJ, 1 ps pulse through 1 m long fiber. Additionally, if the input pulses have larger energy or the fiber is longer, the pulse broadening increases because of both effects of self phase modulation and dispersion. In order to reduce these effects, we suppose the dispersion compensation by the frequency pre-down chirped pulse.

Then, we calculate the pulse broadening for 1 m GI multimode fiber. In Eq.(1), the frequency pre-chirped pulse is represented by

$$U(0, T) = \exp\left(-\frac{1 + iC}{2} \frac{T^2}{T_0^2} \right) \tag{2}$$

where C is the chirp parameter. The input pulse energy and the fiber length set at 0.1 mJ and 1 m, respectively. The pulse broadening is calculated by varying the chirp parameter C and the core diameter of GI multimode fiber. In addition, the central wavelength and spectral width are set to 800 nm and 20 nm, respectively, which are same
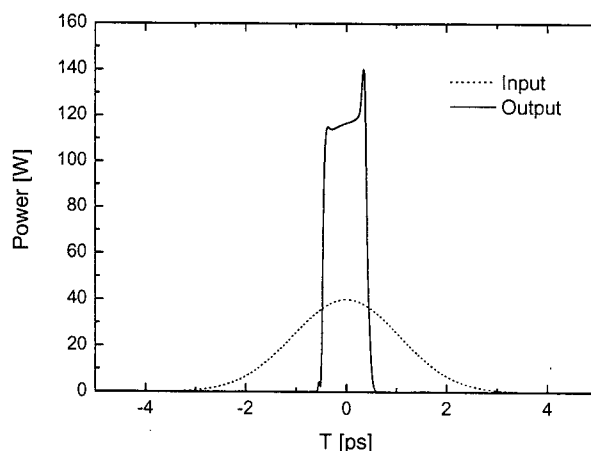
Fig.10. Calculated output pulse shape through a 1 m GI fiber (the core diameter : 200 mm) for pre-chirped input pulse. The pulse energy is 0.1 mJ and the spectral width is 20 nm (the center wavelength is 800 nm).

as our experimental condition.

Figures 9 and 10 show the plot of the pulse broadening with respect to the input pulsewidth for 1 m GI multimode fiber which has 62.5 μm and 200 μm core diameter, respectively.

In Fig. 9, the pulse compression was observed for pre-down chirped pulse, however, it is impossible to deliver the pulses which have shorter pulsewidth than 3 ps because the pulses go beyond the threshold intensity of the self-focusing due to the small core diameter. On the other hand, in Fig. 10, the output pulsewidth is compressed to 900 fs for the input pulse which has 2.5 ps pulsewidth (C=-50) by compensation of the dispersion. The shape of this output pulse is shown in Fig. 10. The asymmetric shape is due to the third dispersion. The output pulse peak power comes up to 140 MW, however, the intensity is 0.45×10^{12} W/cm^2 on the output surface of the fiber. This value is smaller than the typical threshold value of self-focusing (1×10^{12} W/cm^2) or our experimentally observed intensity of white light generation (0.65×10^{12} W/cm^2). Therefore, using the GI multimode fiber with a 200μm core diameter, it is theoretically demonstrated to deliver 0.1 mJ, 1 ps pulses through 1 m long fibers.

3. CONCLUSION

We have demonstrated ultrashort pulse Ti:sapphire laser ablation of HAp with pulsewidth of 50 fs, 500fs and 2ps at 820 nm and at 1 kpps. The HAp was ablated at a laser fluence of 3.2 J/cm^2 (6.4×10^{13}W/cm^2 at 50 fs), 3.3 J/cm^2 (6.6×10^{12}W/cm^2 at 500 fs) and 9.6 J/cm^2 (4.8×10^{12}W/cm^2 at 2 ps), respectively. Using XPS we have observed chemical properties of the ablated HAp surface. As a result it is found that the ablated surface is unchanged after laser ablation over the pulsewidth range used in this experiment. And we have also demonstrated

ablation processing of human tooth using a high-intensity femtosecond laser with pulsewidth of 60 fs, 2 ps at a laser fluence of 3.5 J/cm^2 at a wavelength of 820 nm and 1 kpps. Even with 2-ps pulses, non-thermal ablation has been demonstrated. Eventually, short-pulse (2 ps) Ti:sapphire lasers may be put in practical use as a more generic processing laser.

We have also described the results of the fiber delivery of intense ultrashort laser pulses. The 1.1 ps pulses of 8.7 µJ at 800 nm were delivered through a 10 cm GI multimode fiber with a 0.6 dB transmission loss. In the meantime, the output beam profile is nearly Gaussian and is independent of bending of the fiber. In addition, our calculated results indicate that it is possible to deliver the 900 fs pulses of 0.1 mJ through a 1 m GI fiber with a 200 µm core diameter if the fiber has the optimum refractive index profile. We therefore conclude that GI multimode fibers give better spatial distributions than hollow fibers or SI multimode fibers and can deliver larger energy than single mode fibers.

ACKNOWLEDGMENTS

REFERENCES

[1] H. Newesely: *Mechanisms and Action of Trace Elements in the Mineralisation of Dental Hard Tissues* (Zyma SA, Nyon, Switzerland 1972).

[2] J. Tanaka, M Kikuchi, *J. Surface Science Society of Japan*, Vol. 20, No. 9, 600 (1999).

[3] M. Stanislawki, J. Meister, T. Mitra, et al., *Appl. Phys. B*, Vol. 72, 115 (2001).

[4] S.Chaiyavej, H.Yamamoto, A.Takeda, et al., *Lasers in Surgery and Medicine*, Vol.27, 341 (2000).

[5] B. Majaron, D. Sustercic, Ml Lukac, et al., Appl. Phys. B, Vol. 66, 479 (1998).

[6] M. H. Niemz: *Laser-Tissue Interactions* (Springer, Berlin, Heidelberg 1996).

[7]K.M.Sasaki, A.Aoki, S.Ichinose, et al., *Lasers in Surgery and Medicine*, Vol. 31, 79 (2002).

[8] J. Krueger, W. Kautek, H. Newesely, *Appl. Phys. A*, Vol. 69, S403 (1999).

[9] M. D. Perry, B. C. Stuart, P. S. Banks, et al., *J. Appl. Phys.*, Vol. 85, No. 9, 6803 (1999).

[10] J.Neev, L.B.D.Silva, D.Feit, M.D.Perry, A.A.M.Rubenchik, B.C.Stuart, *IEEE J. Selected Topics in Quantum Electronics*, Vol.2, No.4, 790 (1996).

[11] Zhu Junbiao, Li Yonggui, Liu Nianquig, et al., *Nuclear Instruments and Methods in Physics Research A*, Vol. 475, 630 (2001).

[12] K.Ozono, M.Obara, A.Usui, et al., Optics Communications, Vol. 189, 103 (2001).

[13] Y.Hirayama, M.Obara, *J. Appl. Phys.*, Vol. 90, No. 12, 6447 (2001).

[14] Y. Matsuura, M. Miyagi, K. Shihoyama, et al., *J. Appl. Phys.,* Vol. 91, No. 2, 887 (2002).

[15] M.Kanai, L.Kamino, M.Obara, H.Sekita, "Intense ultrashort laser delivery through a multimode optical fiber for medical application," presented at APLS 2002, September 17-20, 2002, Osaka, Japan.

[16] K. König, I. Riemann, P. Fischer, and K. J. Halbhuber, *Cell. Mol. Biol.*, **45**, 195 (1999).

[17] N. I. Smith, K. Fujita, T. Kaneko, K. Katoh, O. Nakamura, S. Kawata, and T. Takematsu,, *Appl. Phys. Lett.*, **79**, 1208 (2001).

[18] Q. Xing, H. Wei, L. Chai, W. Zhang, N. Zhang, and C Wang, *Proc. SPIE*, **4276**, 42 (2001).

[19] S. W. Clark, F. Ö. Ilday, and W. Wise, *Opt. Lett.*, **26**, 1320 (2001).

[20] Y. Matsuura, M. Miyagi, K. Shihoyama, and M. Kawachi, *J. Appl. Phys.*, **92**, 887 (2002).

[21] O. M. Efimov, K. Gabel, S.V. Garnov, L. B. Glebov, S. Grantham, M. Richardson, and M. J. Soileau, *J. Opt. Soc. Am. B*, **15**, 193 (1998).

[22] G. P. Agrawal, "Nonlinear Fiber Optics" (Academic, San Diego, Calif., 1995).

[23] C. K. Asawa, and H. F. Taylor, *Appl. Opt.*, **39**, 2029 (2000).

Femtosecond pulsed laser induced phase transition in iron

Tomokazu Sano[*], Hiroaki Mori, Etsuji Ohmura, and Isamu Miyamoto

Graduate School of Engineering, Osaka University, Japan

ABSTRACT

Femtosecond pulsed laser induced phase transition in iron was investigated using electron backscatter diffraction pattern (EBSP) analyzing system in this study. Mirror polished surface of single crystalline iron (purity: 99.99%) was irradiated by femtosecond pulsed laser (wavelength: 800 nm, pulse width: 120 fs, fluence: 2.5 J/cm^2, intensity: 1.6×10^{13} W/cm^2, number of pulses: 2000 pulses) in argon atmosphere. Electron beam irradiated the mirror polished vertical section by using colloidal silica under the bottom of the laser irradiated part, and the electron backscatter diffraction pattern was analyzed to determine the crystalline structure. ε phase of hcp structure found to exist around 4 μm deeper from the bottom. γ phase of fcc structure was not detected. This result shows the shock induced by femtosecond pulsed laser irradiation causes the $\alpha \leftrightarrow \varepsilon$ phase transition. It is suggested that this experimental method has a potential to investigate the existence and its crystalline structure of high pressure and high temperature phase of iron (β phase).

Keywords: femtosecond pulsed laser, phase transition, shock compression, iron

1. INTRODUCTION

Iron under normal pressure and room temperature (α phase of bcc structure) changes to γ phase of fcc structure under high temperature and to ε phase of hcp structure under high pressure, respectively. Existence of new phase of iron under high pressure and high temperature (β phase) and its crystalline structure have been discussed in this decade [1-9].

Shock induced α to ε phase transition in iron was reported for the first time by Minshall [10], and the Hugoniots in these two phases were measured first by Bancroft *et al.* [11]. The $\alpha \leftrightarrow \varepsilon$ transition in iron under shock wave loading was widely reviewed by Duvall *et al.* [12]. Boettger and Wallace investigated the metastability and the dynamics of the shock induced $\alpha \leftrightarrow \varepsilon$ transition in iron, and they concluded that the metastable path for forward and reverse transitions in shocks is basically the same as that under quasistatic compression regarding metastability, and that phase transition relaxation time depends on shock strength regarding dynamics [13].

High pressure phase can be obtained as metastable state under shock compression and rapid quenching (SCARQ) in case of irreversible type of phase transition. Diamond was synthesized from graphite using this method [14]. Diffusionless and complete reversible type of phase transition under shock compression is correspondent with the phase transition under quasi-static high pressure at room temperature because heat activation is not needed to induce this type of transition. The *P-V* curve (the Hugoniot) of solids under shock compression with some correction of temperature is well consistent with the quasi-static one under 100 GPa. ε phase of iron, however, can not be obtained using SCARQ technique because the diffusionless and complete reversible type of phase transition can not be quenched and $\alpha \leftrightarrow \varepsilon$ transition of iron is this type of transition.

High power pulsed laser irradiation of metal induces shock wave in metal [15]. High power ns or sub-ns laser with the intensity of more than 10^{12} W/cm^2 driven shock induces pressure of sub-TPa [16,17]. Extremely dense distribution of twins in iron induced by two high power laser shocks was the observed, and occurrence of $\alpha - \varepsilon$ transition from the existence of short characteristic twins was inferred [18]. The $\alpha \leftrightarrow \varepsilon$ transition induced by high power laser shock was reported [19]. Crystallographic evidence, however, was not revealed.

Laser pulse acts as thermal pulse followed by rapid quenching in case of low power pulsed laser irradiation. Phase transition in iron thin film induced by ns pulsed KrF excimer laser was investigated using high resolution TEM, and the presence of the mixture phase of $\alpha + \gamma$ between α and γ phases was found [20]. It was found that the γ phase is

not quenched during normal $\alpha \rightarrow \gamma$ martensitic transformation, but during incomplete $\alpha \rightarrow \gamma$ transformation in the laser heating [21].

Femtosecond pulsed laser (fs laser) irradiation of metal induces transient recoil pressure loading on the surface, and after that shock wave as well as temperature wave propagates in the metal [22-24], i.e., high pressure and high temperature state can be achieved in metal irradiated by fs laser. Fs laser induced shock wave in metal thin films has been investigated using frequency-domain interferometry. Pressure of $0.1 - 0.3$ TPa induced by laser pulse (10^{14} W/cm^2, 120 fs) was inferred assuming the simultaneously measured particle velocity and shock velocity were along the Hugoniot, when Al thin film was irradiated by the laser pulse [25]. Rise times of shock wave in metal thin films induced by laser pulse (800 nm, $0.2 - 0.5$ mJ, 130 fs) was measured with sub-ps time resolution [26]. Dynamics of fs laser induced shock wave was investigated applying the ultrafast time resolved 2D interferometric microscopy to the measurement of shock wave breakout from metal thin film [27]. It is expected that a part of high pressure and high temperature phase is quenched due to its ultrafast process. Existence of β phase will be cleared and the crystalline structure can be determined if β phase exists achieving the ideal state which is believed to exist β phase.

The purposes of this paper are to investigate the fs laser induced phase transition in iron and to determine the transformed phase crystallographically. In this study electron backscatter diffraction pattern (EBSP) analyzing system was used to determine the crystalline structure. The principle of EBSP analysis is as follows; (0) Detector is equipped with SEM. (1) Sample, of which surface is polished using activator, is irradiated by focused electron beam with spot size of several nm in case of FE-SEM. (2) The diffracted channeling pattern, which depends on crystalline structure, generated from the irradiated point is detected through the screen. (3) Estimation of orientation is performed comparing to the crystal data set. (4) Finally crystalline structure is determined.

2. EXPERIMENTS

Polycrystalline iron (purity: 99.99%) was annealed at 900 °C under low pressure of 10^{-3} Pa for 72 hours to make crystalline grains larger. The obtained size of grains was the order of millimeter. This indicates that the laser pulse irradiates the single crystal because the spot diameter of the laser is small enough comparing to the grain size. Mirror polished surface of the iron target was irradiated by fs laser (wavelength: 800 nm, pulse width: 120 fs, fluence: 2.5 J/cm^2, intensity: 1.6×10^{13} W/cm^2, number of pulses: 2000 pulses) in argon atmosphere. The sample was embedded in resin after laser irradiation. Electron beam irradiated the mirror polished vertical section by using colloidal silica under the bottom of the laser irradiated part, and the electron backscatter diffraction pattern was analyzed to determine the crystalline structure.

3. RESULTS AND DISCUSSIONS

3.1 EBSP analysis

Results of EBSP analysis are shown in Fig. 1. Fig. 1(a) shows the SEM image of the laser irradiated part. Figure 1(b) shows the EBSP phase mapping data, where red, yellow and green colors indicate α, ε and γ phase, respectively. ε phase are scattered around 4 µm deeper from the bottom of the laser irradiated part. γ phase dose not exist. The diffracted channeling patterns at the point where ε phase exists are shown in Fig. 1(c). The orientation was determined for each pattern (Fig. 1(d)). This result also shows the existence of ε phase and the absence of γ phase. These experimental results indicate that only shock compression is effective for this phase transition.

The absorbed laser energy causes thermal diffusion, thermal melting, and ablation after the order of 1 ps, 10 ps, and 100 ps from the laser irradiation, respectively. This means shock wave driven by recoil pressure loading on the surface during ablation start to penetrate in the material after 100 ps from the irradiation. Temperature wave as thermal diffusion decreases steeply and disappears at sub µm deeper from the surface before ablation [23]. Shock wave penetrates in the non-disturbed material in the order of µm deeper from the surface. Thus, shock wave is under stable state and thermodynamically equilibrium in the area where ε phase exists. Shock compressed state under stable state and thermodynamically equilibrium is expressed by the Hugoniot function.

3.2 Calculation of shock temperature

In this section we derive the thermodynamic equation of state under shock compression. Characters used are as follows; P: pressure, V: specific volume, T: temperature, S: specific entropy, E: specific internal energy, C_V: constant-volume specific heat, γ: Grüneisen parameter, subscript 0: an ambient state, subscript H: a shock compressed state. Thermodynamic identical equation under shock compressed state is

$$TdS = dE + PdV. \tag{1}$$

An appropriate thermodynamic identity

$$TdS = C_V dT + \frac{\gamma}{V} C_V T dV, \tag{2}$$

is derived by Wallace derived [28]. Following Walsh and Christian [29], Eq. (1) is integrated from an ambient state 0 to a shock compressed state H along the Hugoniot. We have

$$\int_{S_0}^{S_H} T_H dS = (E_H - E_0) + \int_{V_0}^{V_H} P_H dV. \tag{3}$$

Conservation law of energy along the Hugoniot is expressed by

$$E_H - E_0 = \frac{1}{2}(P_H + P_0)(V_0 - V_H). \tag{4}$$

Substitution of Eq. (4) into Eq. (3) yields

$$\int_{S_0}^{S_H} T_H dS = \frac{1}{2}(P_H + P_0)(V_0 - V_H) + \int_{V_0}^{V_H} P_H dV. \tag{5}$$

Integrating Eq. (2) in the same way as in Eq. (1) gives

$$\int_{S_0}^{S_H} T_H dS = \int_{T_0}^{T_H} C_{VH} dT + \int_{V_0}^{V_H} \frac{\gamma_0}{V_0} C_{VH} T_H dV, \tag{6}$$

where it has been assumed that $\gamma/V = \gamma_0/V_0$. Derivations of Eqs. (5) and (6) with respect to V_H are equated to become

$$C_V \frac{dT}{dV} + \frac{\gamma_0}{V_0} C_V T = \frac{1}{2} \frac{dP}{dV}(V_0 - V) + \frac{1}{2}(P - P_0), \tag{7}$$

where subscript H is omitted. Shock temperature behind shock front T can be accurately calculated using this equation.

Calculated shock temperature T is shown in Fig. 2 with phase diagram of iron. Shock temperature is always below γ phase. This means that the shock driven by fs laser does not induce $\alpha \leftrightarrow \gamma$ transition. Shock temperature pass through ε phase, and β phase if it exists. This means that the shock driven by fs laser can induce $\alpha \leftrightarrow \varepsilon$ transition, and $\varepsilon \leftrightarrow \beta$ transition if it exists.

Fs laser induced shock compression can quench the ε phase which is theoretically impossible to obtain using SCARQ method. It may be due to quenching under metastable state during ultrafast process.

4. CONCLUSIONS

Femtosecond pulsed laser induced phase transition in iron was investigated using EBSP system in this study. Conclusions are as follows;
(1) ε phase of iron, which is theoretically impossible to quench under shock compression, was induced by fs laser irradiation.
(2) The ε phase was crystallographically confirmed using EBSP system.
(3) Shock compression driven by fs laser found to be effective for fs laser induced α ↔ ε phase transition in iron.
(4) The calculation results of shock temperature indicates that the shock driven by femtosecond pulsed laser can induce not only α ↔ ε transition but ε ↔ β transition if β phase exists.
(5) It is suggested that this experimental method has a potential to investigate the existence and crystalline structure of β phase.

REFERENCES

[1] S.K. Saxena, G. Shen, and P. Lazor, "Temperatures in Earth's core based on melting and phase transformation experiments on iron," Science 264, 405-407 (1994).
[2] S.K. Saxena, L.S. Dubrovinsky, P. Häggkvist, Y. Cerenius, G. Shen, and H.K. Mao, "Synchrotron x-ray study of iron at high pressure and temperature," Science 269, 1703-1704 (1995).
[3] C.S. Yoo, J. Akella, A.J. Campbell, H.K. Mao, and R.J. Hemley, "Phase diagram of iron by in situ x-ray diffraction: Implications for Earth's core," Science 270, 1473-1475 (1995).
[4] S.K. Saxena, L.S. Dubrovinsky, and P. Häggkvist, "X-ray evidence for the new phase beta-iron at high temperature and high pressure," Geophys. Res. Lett. 23, 2441-2444 (1996).
[5] S.K. Saxena and L.S. Dubrovinsky, "Detecting phases of iron," Science 275, 94-96 (1997).
[6] C.S. Yoo, J. Akella, A.J. Campbell, H.K. Mao, and R.J. Hemley, "Response to Detecting phases of iron," Science 275, 96 (1997).
[7] O.L. Anderson, "Iron: Beta phase frays," Science 278, 821-822 (1997).
[8] D. Andrault, G. Fiquet, M. Kunz, F. Visocekas, and D. Häusermann, "The orthorhombic structure of iron: An in situ study at high-temperature and high-pressure," Science 278, 831-834 (1997).
[9] S.S. Saxena and P.B. Littlewood, "Iron cast in exotic role," Nature 412, 290-291 (2001).
[10] S. Minshall, "Investigation of a polymorphic transition in iron at 130 k.b.," Phys. Rev. 98, 271 (1955).
[11] D. Bancroft, E.L. Peterson, and S. Minshall, "Polymorphism of iron at high pressure," J. Appl. Phys. 27, 291 (1956).
[12] G.E. Duvall and R.A. Graham, "Phase transitions under shock-wave loading," Rev. Mod. Phys. 49, 523 (1977).
[13] J.C. Boettger and D.C. Wallace, "Metastability and dynamics of the shock-induced phase transition in iron," Phys. Rev. B 55, 2840 (1997).
[14] H. Hirai and K. Kondo, "Modified phases of diamond formed under shock compression and rapid quenching," Science 253, 772-774 (1991).
[15] R.M. White, J. Appl. Phys. 34, 2123 (1963).
[16] F. Cottet and J.P. Romain, "Formation and decay of laser-generated shock wave," Phys. Rev. A 25, 576-579 (1982).
[17] F. Cottet, J.P. Romain, R. Fabbro, and B. Faral, "Measurements of laser shock pressure and estimate of energy lost at 1.05-μm wavelength," J. Appl. Phys. 55, 4125-4127 (1984).

[18] T. de Rességuier and M. Hallouin, "Interaction of two laser shocks inside iron samples," J. Appl. Phys. 90, 4377-4384 (2001).

[19] J.P. Romain, M. Hallouin, M. Gerland, F. Cottet, and L. Marty, "$\alpha \rightarrow \varepsilon$ phase transition in iron induced by laser generated shock waves," *Shock Waves in Condensed Matter – 1987* (Elsevier, New York, 1988), p. 787-790.

[20] V.S. Teodorescu, L.C. Nistor, J.Van Landuyt, and M. Dinescu, "TEM study of laser induced phase transition in iron thin films," Mater. Res. Bull. 29, 63-71 (1994).

[21] V.S. Teodorescu, I.N. Mihăilescu, M. Dinescu, N. Chitică, L.C. Nistor, J. Van Landuyt, and A. Barborică, "Laser induced phase transition in iron thin film," J. Phys. IV 4, 127-130 (1994).

[22] P. Celliers and A. Ng, "Optical probing of hot expanded states produced by shock release," Phys. Rev. E 47, 3547 (1993).

[23] A. Ng, A. Forsman, and P. Celliers, "Heat front propagation in femtosecond-laser-heated solids," Phys. Rev. E. 51, 5208 (1995).

[24] K. Widmann, G. Guethlein, M.E. Foord, R.C. Cauble, F.G. Patterson, D.F. Price, F.J. Rogers, P.T. Springer, R.E. Steward, A. Ng, T. Ao, and A. Forsman, "Interferometric investigation of femtosecond laser-heated expanded states," Phys. Plasmas 8, 3869 (2001).

[25] R. Evans, A.D. Badger, F. Falliès, M. Mahdieh, T.A. Hall, P. Audeberg, J.-P. Geindre, J.-C. Gauthier, A. Mysyrowicz, G. Grillon, and A.Antonetti, "Time- and space-resolved optical probing of femtosecond-laser-driven shock waves in aluminum," Phys. Rev. Lett. 77, 3359-3362 (1996).

[26] K.T. Gahagan, D.S. Moore, D.J. Funk, R.L. Rabie, S.J. Buelow, and J.W. Nicholson, "Measurement of shock wave rise times in metal thin films," Phys. Rev. Lett. 85, 3205-3208 (2000).

[27] K.T. Gahagan, D.S. Moore, D.J. Funk. J.H. Reho, and R.L. Rabie, "Ultrafast interferometric microscopy for laser-driven shock wave characterization," J. Appl. Phys. 92, 3679-3682 (2002).

[28] D.C. Wallace, "Irreversible thermodynamics of flow in solids," Phys. Rev. B 22, 1477-1486 (1980).

[29] J.M. Walsh and R.H. Christian, "Equation state of metals from shock wave measurements," Phys. Rev. 97, 1544-1556 (1955).
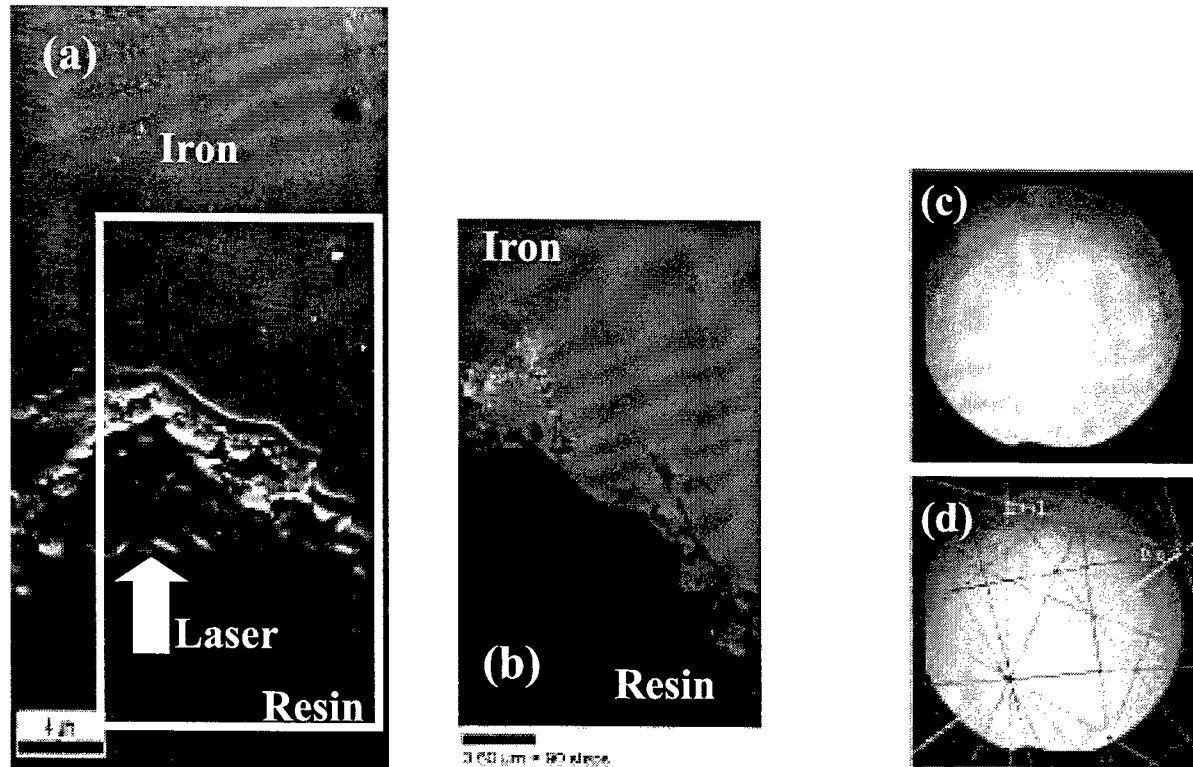
FIG. 1. (a) SEM image of laser irradiated part. Laser irradiated upwards in this image. The area surrounded by the lines were analyzed by EBSP system. (b) EBSP phase mapping data. Red: α phase, Yellow: ε phase, Green: γ phase, Black: resin. ε phase exists around 4 μm deeper from the bottom. γ phase dose not exist. (c) Diffracted channeling patterns at the point where ε phase exists. (d) Orientation was determined for each pattern. Red line: α phase, Purple line: ε phase.
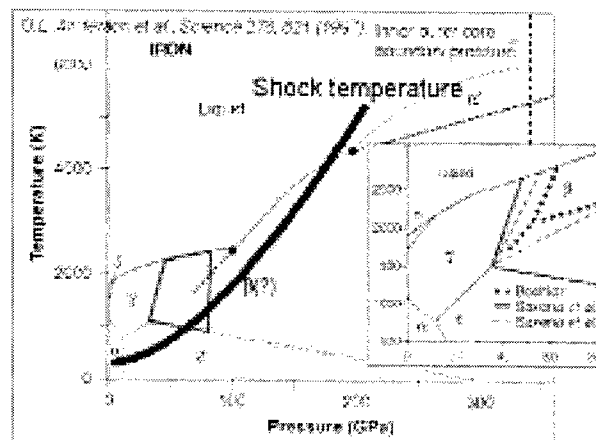
FIG. 2. Calculated shock temperature with phase diagram of iron.

Laser assisted nanofabrication

M. H. Hong, S. M. Huang*, B. S. Luk`yanchuk, Z. B. Wang, Y. F. Lu, T.C. Chong
Data Storage Institute, Agency for Science, Technology and Research, DSI Building, 5,
Engineering Dirvel, 10 Kent Ridge Crescent, Singapore 117608

ABSTRACT

Laser assisted nanofabrication for surface nanopatterning is investigated. To overcome the limitation of light wavelength, pulsed lasers were applied to combine with atomic force microscope (AFM) and nanoparticle self - assembled mask to achieve sub-30 nm patterning on the metallic surfaces. The mechanisms of the formation of nanostructure patterns are discussed. Progress on numerical simulation and physical modeling of laser assisted nanofabrication has been demonstrated. The method of AFM tip or particle enhanced laser irradiation allows the study of field enhancement effects as well as its potential applications for nanolithography.

Keywords: near field, Mie scattering, nanostructuring, laser irradiation

1.INTRODUCTION

In the last decade we have witnessed the revolutionary development of nanoscience. Many efforts have been spent for the problem of submicrometer or nanometer lithography. A lot of methods and techniques have been proposed and developed. Nanometer and atomic scale surface modification using optical resonance and near field effects is emerging as a new and promising method. For this method, one involves illuminating the tip of a scanning tunneling microscope (STM) or an atomic force microscope (AFM) with a pulsed laser. Structures with lateral dimensions below 30 nm and therefore well below half a wavelength, $\lambda/2$, could be produced underneath the tip [1-6]. The setup seemed to be promising for the study of field enhancement effects at sharp tips, a question of great interest in optics and surface structuring applications.

Another approach involves the illumination of micrometer or submicrometer sized spheres, which also allows the study of field enhancement effects as well as their application for nanolithography process. Theoretical examination of the dry laser cleaning showed that scattering of radiation by contaminant particles plays an important role in dry laser cleaning [7-10]. For example, a small transparent particle with size by the order of the wavelength may work as a lens in near field region. This permits to focus laser radiation into an area with size smaller than the radiation wavelength. This produces nonstationary 3D distribution of temperature and 3D thermal deformation of the surface. Recent experiments have shown that light enhancement can produce a hot spot, resulting in the formation of a small pit on sample surfaces using femtosecond or nanosecond pulsed lasers [11-14]. Near field optical enhancement needs a special consideration. It contains very rich physics, related to caustics, catastrophes and optical resonance effects.

In this study, we describe our results in laser assisted nanofabrication. Nanostructuring of metallic surfaces using optical resonance and near field effects is reported. The nanostructure fabrication on metallic surfaces using a pulsed laser in combination with an AFM is presented. Nanopatterns such as pits and multilines were created. Experimental results and mechanisms of nanostructure formation are discussed. On the other hand, nanostructures fabricated on metallic surfaces using nanoparticle self - assembled masks are exhibited. Pit arrays were created. Numerical simulation and physical modeling of optical near field effects under particles are also carried out. The experimental results show a good agreement with theoretical calculations.

2. EXPERIMENTS AND DISCUSSION

2.1 Laser nanoprocessing using AFM tips

*HUANG_Sumei@dsi.a-star.edu.sg; phone 65 68748204; fax 65 67771349

The experiments were carried out on a commercial scanning probe microscopy (SPM) system (Autoprobe CP, Park Scientific Instruments). The SPM probe head has an open architecture, which allows an external laser beam irradiation on the tip and sample directly. The sample is made of a gold film with a thickness of 20 nm on Si substrate. The metallic films were deposited by a hot evaporator. During imaging and nanoprocessing, the tip was fixed and the sample was moved via a tube scanner. A 532 nm Nd:YAG pulsed laser with a pulse duration of 7 ns was used. The maximum repetition rate of the laser is 10 Hz. The laser beam is vertically polarized. The laser beam was focused by a plano-convex lens (focus length f=20cm). The laser spot diameter, D_b, was estimated using the second harmonic divergence ($\alpha \cong 1.5 \times 10^{-3}$ rad) as $D_b \cong \alpha f \cong 300$ μm. The laser beam was focused on the tip apex. The laser alignment was performed under an optical charge coupled device microscope with high resolution. It was adjusted by observing the diffraction ring from the tip. The laser beam hits the sample surface at an incidence angle of $\theta_i \sim 80°$, measured from the surface normal. The SPM was operated in AFM mode. Boron doped silicon (0.001 Ω cm) tip (Park Scientific Instruments) was used in contact mode.

The laser beam is introduced to the gap between the tip and the gold sample. When the laser intensity is above a threshold value, one pulse can create one pit on the gold surface. We estimated a threshold level of ~ 7.5 MW/cm^2 for the Si tips (Park Scientific Instruments, Ultralevels^{TM}, cantilevel type A and B) in contact mode. Figure 1 shows two pits created by two laser shots. The nanoholes, from the left to the right, were created with the pulse intensity of 8 and 8.5 MW/cm^2, respectively. The height profiles of the nanohole are also shown in Fig. 1. The depths of both nanoholes are 3.5 and 4.9 nm, and their full widths are 16.0 and 20.8 nm, respectively. With further higher pulse intensity, the created nanohole becomes even deeper and wider. Figure 2 presents the two pits created by a single pulse with the laser intensity of 9 and 11 MW/cm^2, respectively. The height profile of both pits is also shown in Fig. 2. Their depths are 6.0 and 10.0 nm, and their widths are 28.0 nm and 43.0 nm, respectively.

In order to obtain continuous lines using a pulsed laser, the scanning speed must be slow enough. Figure 3(a) and (b) show AFM image and the height profile of a series of created lines on the gold surface, respectively. The laser beam with an intensity of 7.5 MW/cm^2 and a repetition rate of 10 Hz was used. The scanning speed was 0.02 μm/s. The line width is about 10 nm and the depth is about 3.5 nm as shown in Fig. 3. With the higher laser intensity, the continuous line created becomes wider and deeper. Figure 4 presents AFM image and the height profile of the lines created at a laser intensity of 8 MW/cm^2. The line width is about 17 nm and the depth is about 4.4 nm. We also studied nanopatterning of some polymer, magnetic and copper films on Si substrates using the above processing system. The results are similar to those on the gold films described above.

In our previous papers [4, 5], several possible factors and mechanisms of nanoprocessing with the pulsed laser irradiation of the AFM tip, such as tip heating and thermal expansion as well as sample surface heating and field enhancement, were analyzed and discussed in details. Based on our experiments, we think that the field enhancement mechanism is the main reason for this nanoprocessing. The enhanced field of the tip locally heats the sample to the melting and evaporation temperature in a nano-sized domain on the sample. And the thermal expansion of the tip also makes some contribution to the fabrication of the nanopatterns. The thermal expansion of the tip decreases the gap between the tip and the sample and increases the light intensity at the nanoprocessing point further, resulting in higher temperature in a nano-sized domain on the sample. On the other hand, the thermal expansion of the tip decreases the distance between the tip and grains, leading to an increasing repulsive force between them. If the laser intensity is very high and out of our process window, the mechanical contact force due to the thermal expansion of the tip might be a main reason for the patterning processing. This nanoprocessing depends strongly on the material properties of not only the tip but also the sample surface. The geometry parameters of the tip, the curvature radius of the tip, the solid angle of the probe cone also have a great influence on the final results.

2.2 Laser nanoprocessing using nanoparticle self - assembled masks

Monodisperse silica (SiO$_2$) and polystyrene (PS) spheres with diameters in the range of 140 nm to 1000 nm were used. These particles are transparent to the ultraviolet (UV) light. In the preparation of our samples, monodisperse SiO$_2$ or PS spheres were applied to the sample after the particle suspension had been diluted with deionized (DI) water. Isolated spheres at any desired concentration onto the substrate were deposited by controlled application of a colloidal suspension. Aluminum films (35 nm in thickness) on silicon substrates were used as samples and deposited by the sputtering method. The light source was a KrF excimer laser with a wavelength of 248 nm and pulse width of 23 ns. The laser fluence used was in the range from 100 to 800 mJ/cm^2. The 25 mm × 5 mm rectangular laser spot has a

uniform light intensity. The laser beam was incident normally on the sample with particles on the surface. Each sample was treated by a single laser pulse. During the laser irradiation, it was found that most of particles were removed from the sample surface. The sample was further ultrasonically cleaned before AFM and SEM measurements were done.

0.95 μm SiO_2 particles were applied onto an Al surface. The diameter of the SiO_2 particles is with a deviation of $\pm 5\%$. Figure 5 (a) shows a typical SEM morphology of a periodic pit array, formed after illumination of the colloidal monolayer on the Al surface with a single pulse. The laser fluence was 300 mJ/cm^2. The periodic pit array reflects the previous positions of the colloid spheres on the surface. With a higher magnification, SEM analysis shows that the diameter of the created hole is about 190 nm shown in Fig. 5 (b). The resultant holes are inhomogeneous in size to some extent. There is small change in the dimensions of the created holes. The AFM analysis reveals that depths of holes are about 3 nm. Monodisperse PS particles with a size of (140 ± 5) nm in diameter were applied to the second sample. After laser treatment by a single pulse at a laser fluence of 300 mJ/cm^2, holes were created on an Al surface and shown in Fig. 6. The depth and the diameter of the created holes are about 3 nm and 30 nm, respectively. When the laser fluenece is increased, for each kind of particle mentioned above, the hole becomes bigger and deeper.

The near-field light intensity is based on the solution of a boundary problem: a sphere particle on a flat semi-infinite substrate. Recently, an appropriate method was developed to solve this problem in our previous work [7 – 9, 11]. An accurate solution can be derived using this method. The electromagnetic field is the sum of both the scattered and the incident fields. The calculation shows that the multi-reflection of the Poynting vector between the particle and the substrate results in high intensity at the contacting point, and the full width at the half maximum for the intensity distribution is even smaller than that from the Mie solution. As it was shown in [7-9, 11], particle significantly changes the local intensity distribution. There are two easily understandable limiting cases. The first one refers to the geometrical optics limit, when the size of the particle (radius a) is significantly larger than the radiation wavelength, $a \gg \lambda$. For this case the intensity on the substrate can be estimated using ray tracing according to Snell's law and energy conservation [15, 16]. Assuming that a ray is incident on the spherical surface of a sphere (refractive index n, n $\neq$ 1, or 2) with an incidence angle θ_i, and it is refracted by the surface with a refraction angle inside θ_t the sphere, both angles are related by $\theta_t = \arcsin\left[\sin\theta_i / n\right]$. Upon the second refraction the ray leaves the sphere at a point with a polar angle of $\theta_o = 2\theta_t - \theta_i$ against the z-axis, and emerges from the sphere in the direction $\theta_{ou} = 2\theta_t - 2\theta_i < 0$. All the refracted rays form a caustic shown in Fig. 7. The caustic crosses the sphere at the angle θ_{om} given by the condition $\sin^2\theta_{om} = (4-n^2)^3 / 27n^4$. Corresponding angle of incidence θ_{im} is given by $\sin^2\theta_{im} = \left(4-n^2\right)/3$. We approximate the spot size on the substrate by caustic on the sphere: $w_g \approx a\sin\theta_{om}$. This yields the following formula.

$$w_g \approx a\sqrt{\frac{(4-n^2)^3}{27n^4}}. \tag{1}$$

By a similar way the further reflections can be taken into account. They produce new caustics. In Fig. 7, the caustics inside the particle are shown for two subsequent reflections. These effects are especially important for strongly oblique rays, as they have larger reflection coefficient.

Assuming that intensity within the caustic cone is homogenized by the imperfections of the sphere, reflections from the substrate, one can find an intensity enhancement factor [15,16]:

$$\frac{I_m}{I_0} \approx \frac{a^2}{w_g^2} \approx \frac{27n^4}{(4-n^2)^3}. \tag{2}$$

Further modifications of this approach can be developed, taking into account secondary scattering effects, caustics from multiple reflections. Another useful limit follows from the dipole approximation for small spheres, $a \ll \lambda$ [17]. Corresponding polarizability δ is given by

$$\delta = 4\pi a^3 \frac{n^2-1}{n^2+2}. \tag{3}$$

Using the formulas for scattered dipole radiation and considering interference with the incident plane wave one can find corresponding intensity distribution shown in Fig. 8. At the right side of the sphere at $z = a$, one obtains for intensity enhancement [15,16]

$$\frac{I_m}{I_0} \approx \left(1 + \frac{n^2 - 1}{n^2 + 2} q^2\right)^2 . \tag{4}$$

Here $q = 2\pi a / \lambda$ is the size parameter. Comparison of Eqs. (2) and (4) shows that for a refractive index $1.1 < n < 1.7$ transition to the geometrical optics limit occurs for the size parameter around $3.5 < q < 5.5$. In the paper [15] the smooth interpolation formula (transfer from the dipole approximation to geometrical optics) was suggested. Although it qualitatively explains the role of the particle size effect, the situation is more complex because of the structure of the field within the caustic cone.

For larger spheres, it is instructive to consider Mie scattering near the sphere as a diffraction pattern of a focal caustic. In [16] it was shown, that this interpretation remains fruitful even for rather small spheres. The diffraction focus, f_d, is shifted towards the sphere, and the intensity there has asymptotic dependence $I_{max} \propto ka$ for large Mie parameters ka. This is typical for (strong) spherical aberration [18] as the focus $f \propto a$. The focal caustic is axially symmetric and highly degenerate [19]. It contains a caustic surface of revolution with $I \propto (ka)^{1/3}$, and a caustic line along the z - axis. The former is due to meridional rays, while the latter is due to sagittal rays. As a result, (if $n > \sqrt{2}$) the intensity for all $a < z < f_d$ shows the same $I(z) \propto ka$ asymptotic behavior as the focal intensity I_{max} does.

For an equivalent aberrationless lens we find $I_{max} \propto (ka)^2$ in the focal point f, and a depth of focus of about λ. According to geometrical optics, the intensity decreases as $(z - f)^{-2}$. As $f \propto a$ at the surface of the sphere, $z = a$, this yields $I(a) \propto (\lambda/a)^2(ka)^2 \propto const(n)$. Thus, strong spherical aberration significantly decreases the focal intensity, but creates a high intensity line between the sphere and the focus. This result is also revealed by Mie calculations. This resolves the contradiction between the Mie results [11] and estimations based on geometrical optics [15] for the intensity on the z - axis behind the sphere. The prediction of geometrical optics is valid within the caustic cone, but not on the z-axis. From the experimental point of view, the intensity along the z-axis should be strongly decreased by imperfections or asymmetries of spheres, which destroy the degeneracy. If this is not the case, the hot spot under the sphere has a diameter $\sim \lambda$ and intensity $\propto ka$, surrounded by a plateau of (still enhanced) intensity with parameters described by the geometrical optics results Eqs. (1) and (2).

Additional corrections to this picture are due to optical resonance effect (see, e.g. [20, 21]). Optical resonances can be understood as resonances of the waves undergoing total internal reflection. The evanescent tails of these waves leaking outside the sphere may lead to a significant variation of the near-field intensity behind the particle. These variation depend on the size parameter shown in Fig. 9, while the limit of geometrical optics, i.e., Eq.(2), demonstrates only the dependence on the refractive index.

The near-field focusing is well described by the Mie theory [20]. Figure10 shows the intensity distribution around a "small" and a "big" particle, calculated from the corresponding Mie formulas. In both cases one can see the localization of energy in the region, which is smaller than the radiation wavelength (near-field focusing). The enhanced near-field intensity distribution in x-y plane under the particle is rather complex [7-10]. Nevertheless with the accuracy sufficient for further calculations it can be approximated by Gaussian function [11]:

$$S(x, y) = S_0 e^{-r^2/r_0^2} \tag{5}$$

Where r is radial coordinate and S_0 is the intensity enhancement factor.

If S_0 is known, the characteristic size of the high intensity area, i.e., radius r_0 in Eq. (5), can be estimated from the overall energy conservation condition. The geometrical cross-section of the particle is πa^2, area of the main lobe of scattered light can be expressed as πr_0^2. We denote the area of all the side lobes (with the same effective "brightness"

of scattering) as πr_1^2, here r_1 is effective radius. One can define r_1 in such a way that the ratio of corresponding areas gives the intensity enhancement factor $S_0 = a^2 / \left(r_0^2 + r_1^2 \right)$. Typically, variation of r_1 is within the limits: $0 < r_1 < r_0$ [11], i.e., majority of energy is concentrated near the center of caustic cone. This consideration yields the following estimation for radius r_0 :

$$a / S_0^{1/2} < r_0 < a / 2 S_0^{1/2} . \tag{6}$$

Factor S_0 calculated from the Mie theory is shown in Fig. 11. As it was found experimentally [11-14], the size of the region with field enhancement under the SiO_2 and polystyrene particles vary between 50 and 100 nm, in good agreement with Fig. 11 b.

3. CONCLUSIONS

Nanopatterning of metallic layers on silicon substrates has been demonstrated by laser irradiation under an AFM tip and self-assembled particle masks. Processing of structures with a lateral resolution down to 10 nm is realized on gold layers using AFM technique. The AFM tip nanoprocessing strongly depends on the geometry parameters of the Si tip, the optical and thermal properties of the sample, including the properties of the metallic layer and the substrate. Optical resonance and near-field effects in the interaction of particles with laser light have been studied and analyzed using geometrical optics, dipole approximation and Mie theory. Theoretical calculations of intensity distribution versus the particle size on the contacting area (substrate surface) are carried out. The limits of geometrical optics and dipole approximation are discussed. Experimental results of particle mask nanprocessing are explained and consistent well with those of theoretical calculation.

REFERENCES

1. A. A. Gorbunov and W. Pompe, Phys. Status Solidi A 145, 333 (1994).
2. J. Jersch and K. Dickmann, Appl. Phys. Lett. 68, 868 (1996).
3. Y. F. Lu, Z. H. Mai, G. Qiu, and W. K. Chim, Appl. Phys. Lett. 75, 2359 (1999).
4. S. M. Huang, M. H. Hong, Y. F. Lu, B. S. Luk'yanchuk, W. D. Song, and T. C. Chong, J. Appl. Phys. 91, 3268 (2002).
5. S. M. Huang, M. H. Hong, B. S. Luk'yanchuk, Y. F. Lu, W. D. Song, and T. C. Chong, J. Vac. Sci. Technol. B 20, 1118 (2002).
6. J. Jersch, F. Demming, and K. Dickmann, Appl. Phys. A 64, 29 (1997).
7. B. S. Luk'yanchuk, Y. W. Zheng, Y. F. Lu: *Proc. SPIE*, vol. 4065, 576 (2000).
8. B. S. Luk'yanchuk, Y. W. Zheng, Y. F. Lu: *Proc. SPIE,* vol. 4423, 115 (2001).
9. B. S. Luk'yanchuk, Y. W. Zheng, Y. F. Lu: RIKEN Review, No. 43, 28 (2002).
10. P. Leiderer, J. Boneberg, V. Dobler, M. Mosbacher, H. -J. Münzer, N. Chaoui, J. Siegel, J. Solis, C. N. Afonso, T. Fourrier, G. Schrems, D. Bäuerle: *Proc. SPIE*, vol. 4065, 249 (2000).
11. B. S. Luk'yanchuk, M. Mosbacher, Y. W. Zheng, H. - J. Münzer, S. M. Huang, M. Bertsch, W. D. Song, Z. B. Wang, Y. F. Lu, O. Dubbers, J. Boneberg, P. Leiderer, M. H. Hong, T. C. Chong, *Chapter 3* in: "Laser Cleaning", Ed. By B.S. Luk'yanchuk (World Scientific New Jersey, London, 2002), pp. 103-178.
12. M. Mosbacher, H. -J. Münzer, J. Zimmermman, J. Solis, J. Boneberg, P. Leiderer, Appl. Phys. A 72, 41 (2001).
13. Y. F. Lu, L. Zhang, W. D. Song, Y. W. Zheng, and B. S. Luk'yanchuk, JETP lett. 72, 457 (2000).
14. S. M. Huang, M. H. Hong, B. S. Luk'yanchuk, Y. W. Zheng, W. D. Song, Y. F. Lu and T. C. Chong, J. Appl. Phys. 92, 2495 (2002).
15. N. Arnold, *Theoretical description of dry laser cleaning*, EMRS Spring Meeting, Strasbourg, France, 2002 (to appear in Appl. Surf. Sci.).
16. B. S. Luk'yanchuk, N. Arnold, S. M. Huang, and M. H. Hong, 3- Dimensional effects in dry laser cleaning, to appear in Appl. Phys. A, 2002.
17. L. D. Landau, E. M. Lifshitz and L. P. Pitaevskii, *Electrodynamics of Continuous Media*, Pergamon Press, New York, 1984.

18. Yu. A. Kravtsov, Yu. I. Orlov, *Geometrical Optics of Inhomogeneous Media*, Springer, Berlin, 1990.
19. M. V. Berry, C. Upstill, in *Progress in optics*, Vol. 18, E. Wolf ed., Elsevier, North-Holland, 1980.
20. Born M., Wolf E., *Principles of Optics*, 7th Edition, (Cambridge University Press, 1999).
21. Kerker M., *Selected Papers on Light Scattering*, Proc. SPIE, vol. **951** (Part One), (1989), see Section 4 *"Optical Resonances"*.
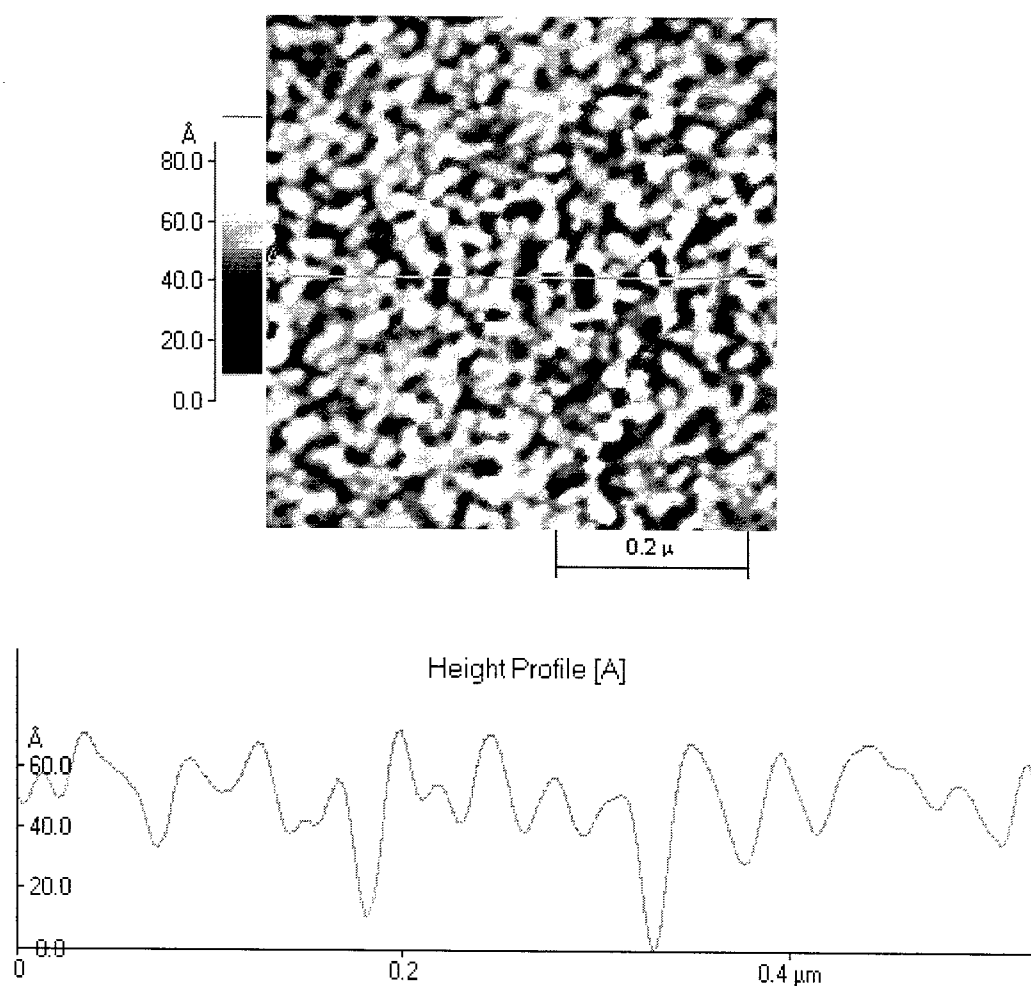
Fig. 1 AFM image and height profile of the nanoholes created by one pulse at laser intensities of 8 and 8.5 MW/cm^2, respectively.
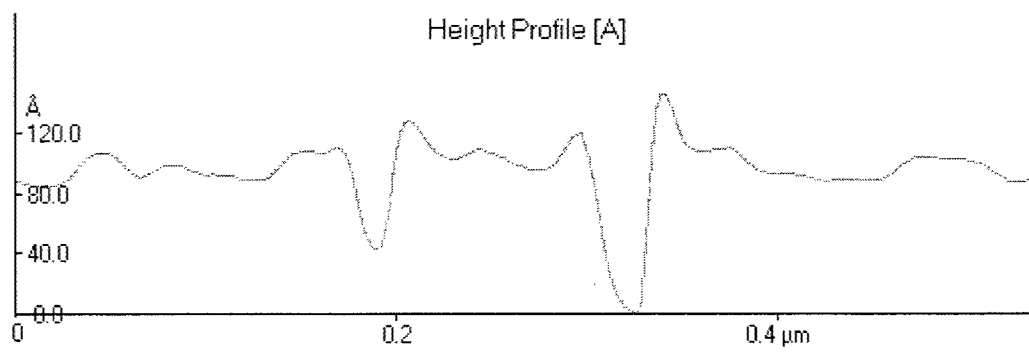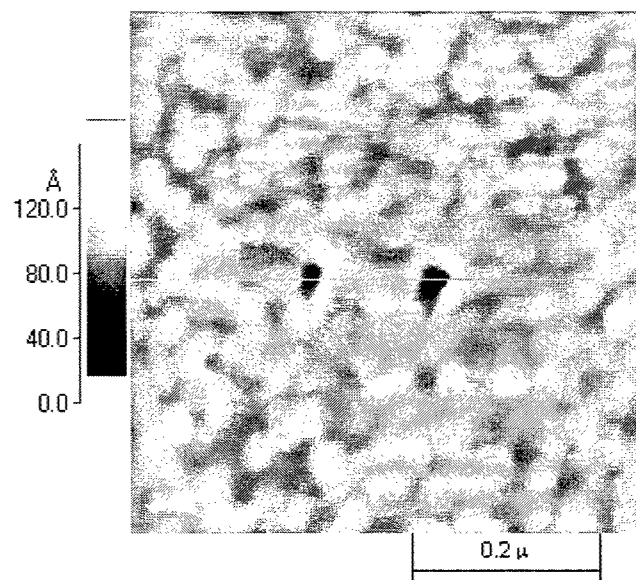
Fig. 2 AFM image and height profile of the nanoholes created by one pulse at laser intensities of 9 and 11 MW/cm^2, respectively.

(a)

(b)
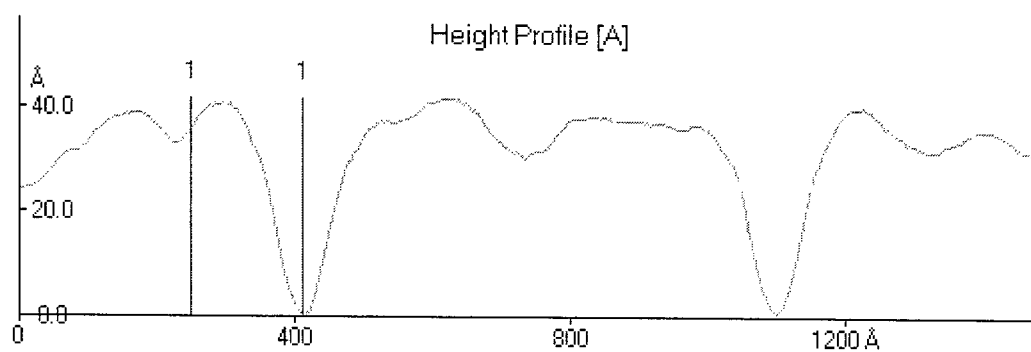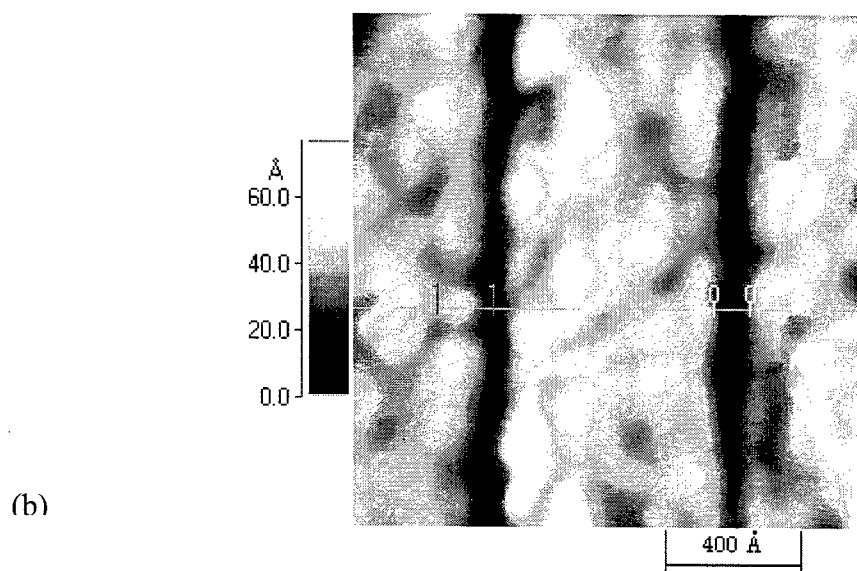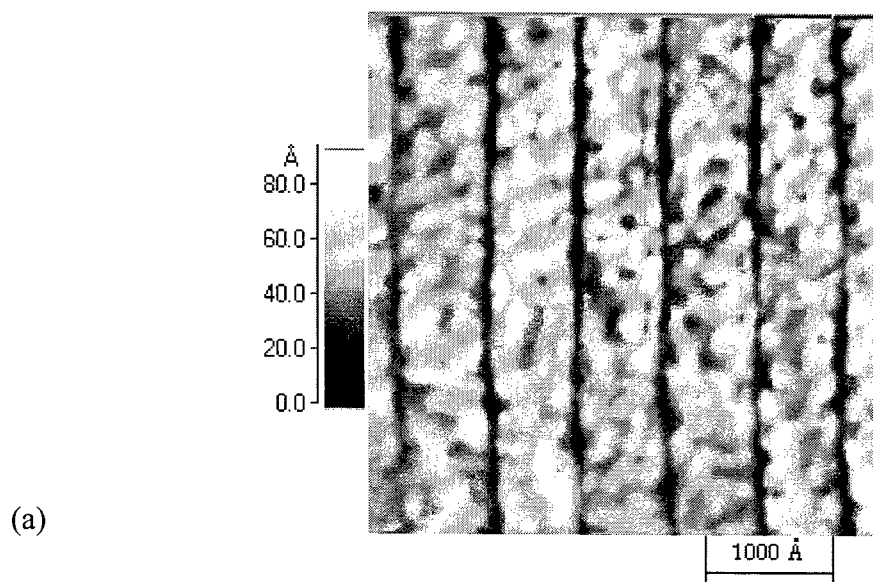
Fig. 3 AFM images (a) and height profile (b) of multi-nanolines created at a laser intensity of 7.0 MW/cm².
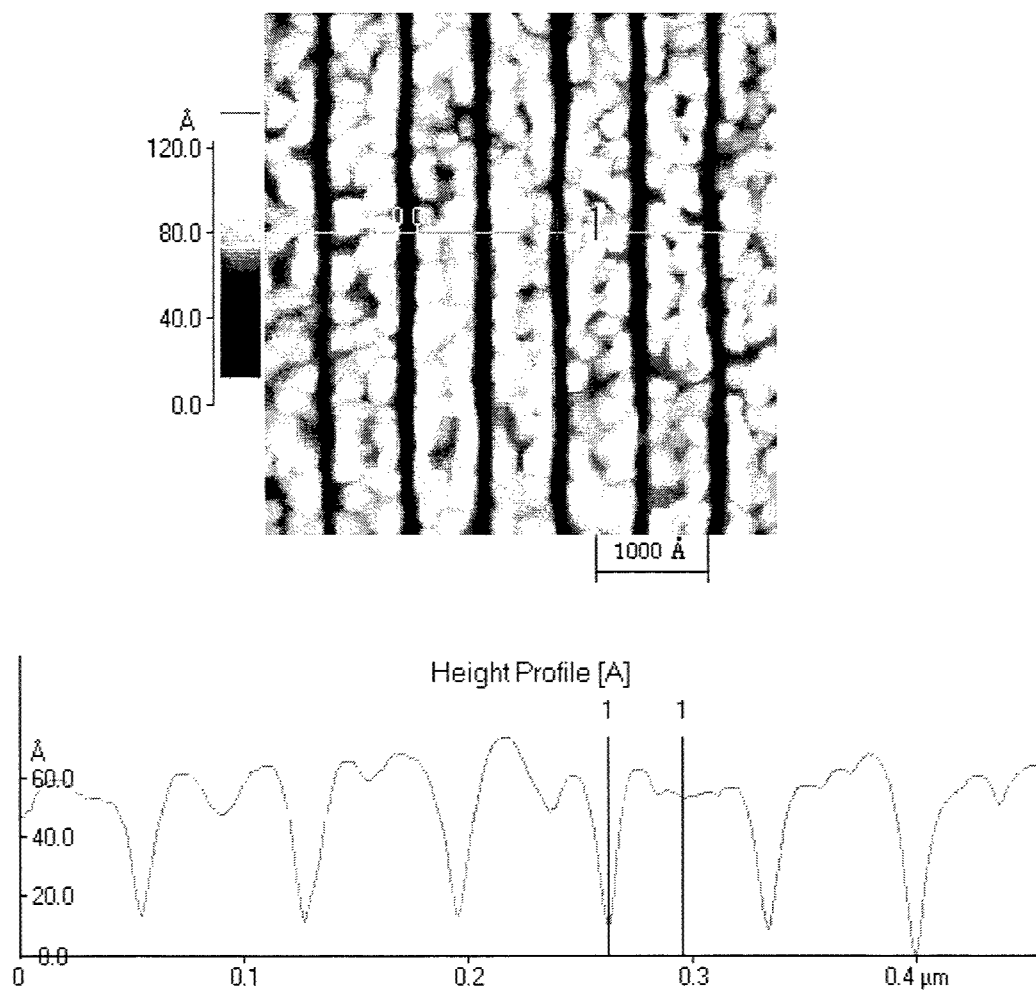
Fig. 4 AFM image and height profile of multi-nanolines created at a laser intensity of 8 MW/cm^2.
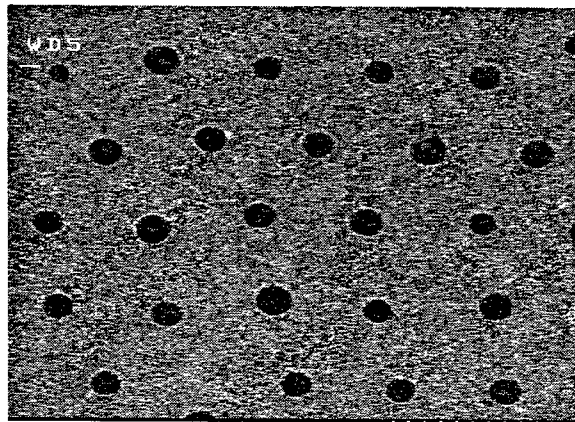
(a)   25.0 kV   X 20.0 k   1.50μm
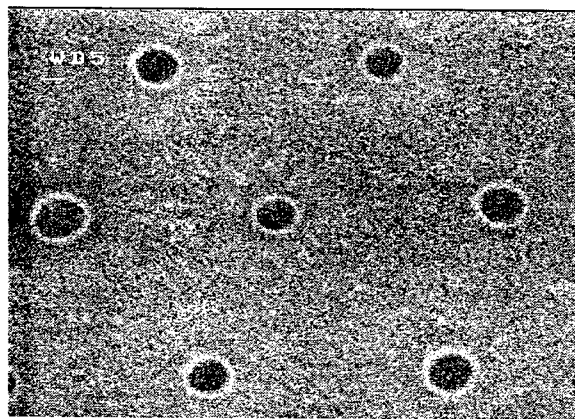
(b)   25.0 kV   X45.0 k   667 nm

Figs. 5 SEM images of periodic pit arrays formed after illumination of isolated 0.95 μm SiO_2 particles on an Al surface by a single pulse at a laser fluence of 300 mJ/cm^2.
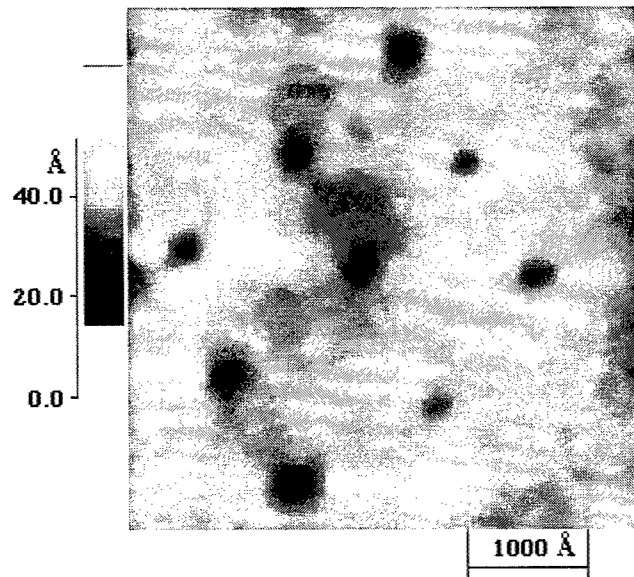
Fig. 6 AFM image of pits formed after illumination of isolated 140 nm PS particles on an Al surface by a single pulse at a laser fluence of 300 mJ/cm².
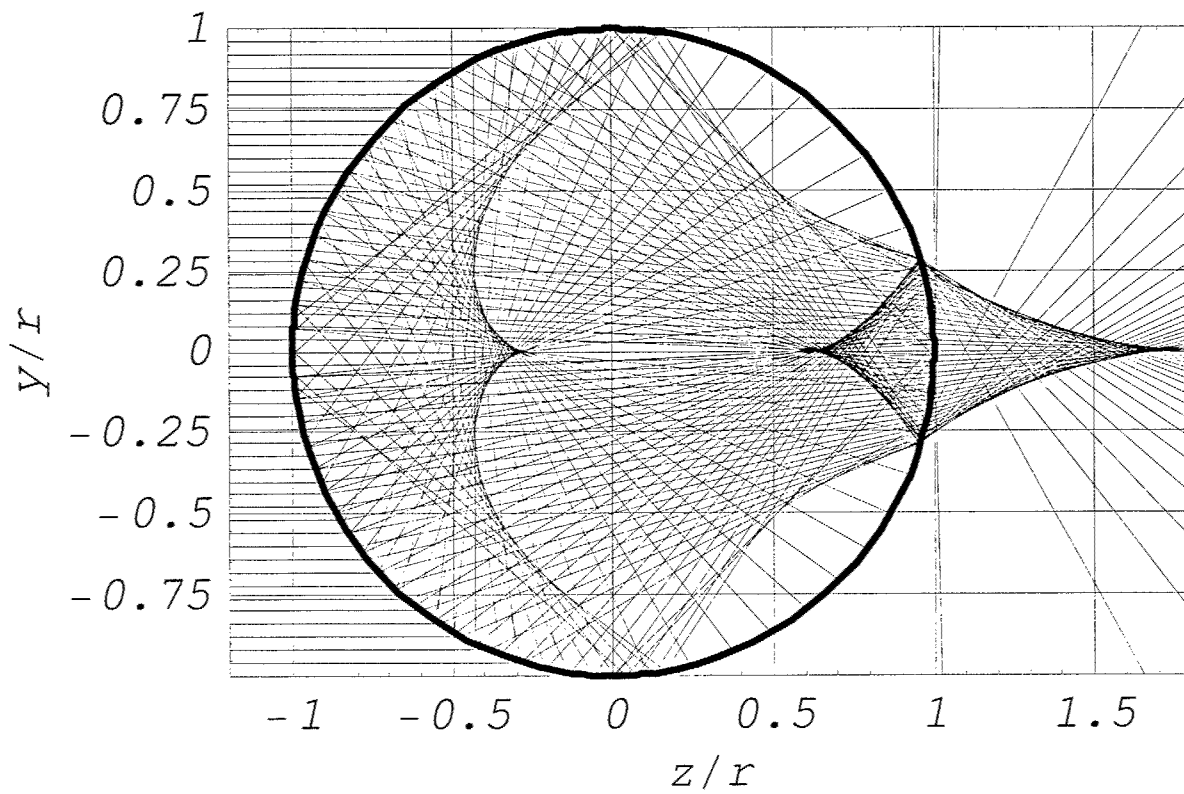
Fig. 7. Rays tracing for big particle $a \gg \lambda$ with a refractive index $n = 1.4$.
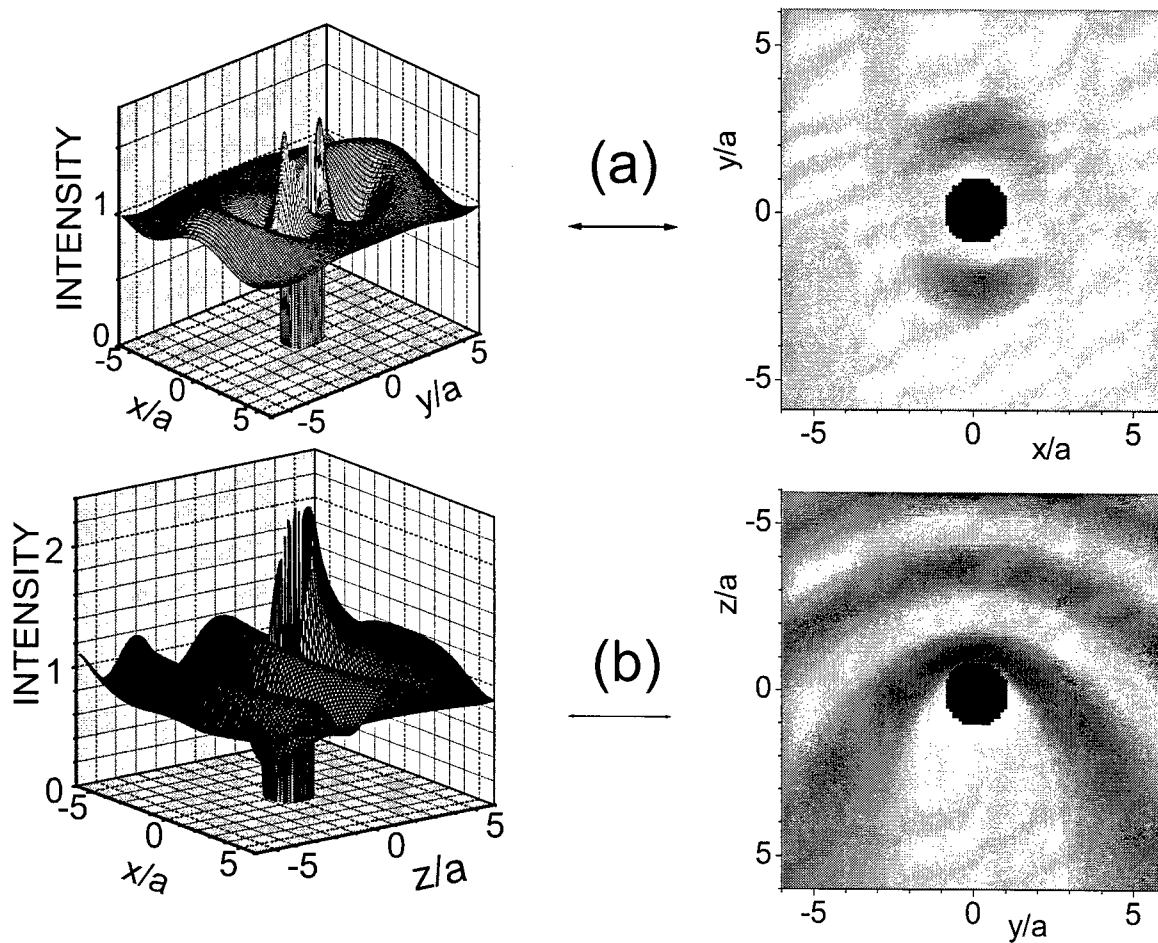
Fig. 8. 3D (left) and contour (right) plots for the intensity distribution under dipole approximation for small particle, $a/\lambda = 0.2$, with refractive index $n = 1.6$. Electrical vector in the incident plane is directed along the x-axis.(a) Distribution of intensity under the particle in x-y plane; (b) Distribution of intensity under the particle in z-y plane. Gradations of the intensity from small (dark) to high (light) values within the contour plots are given in logarithmic scale.
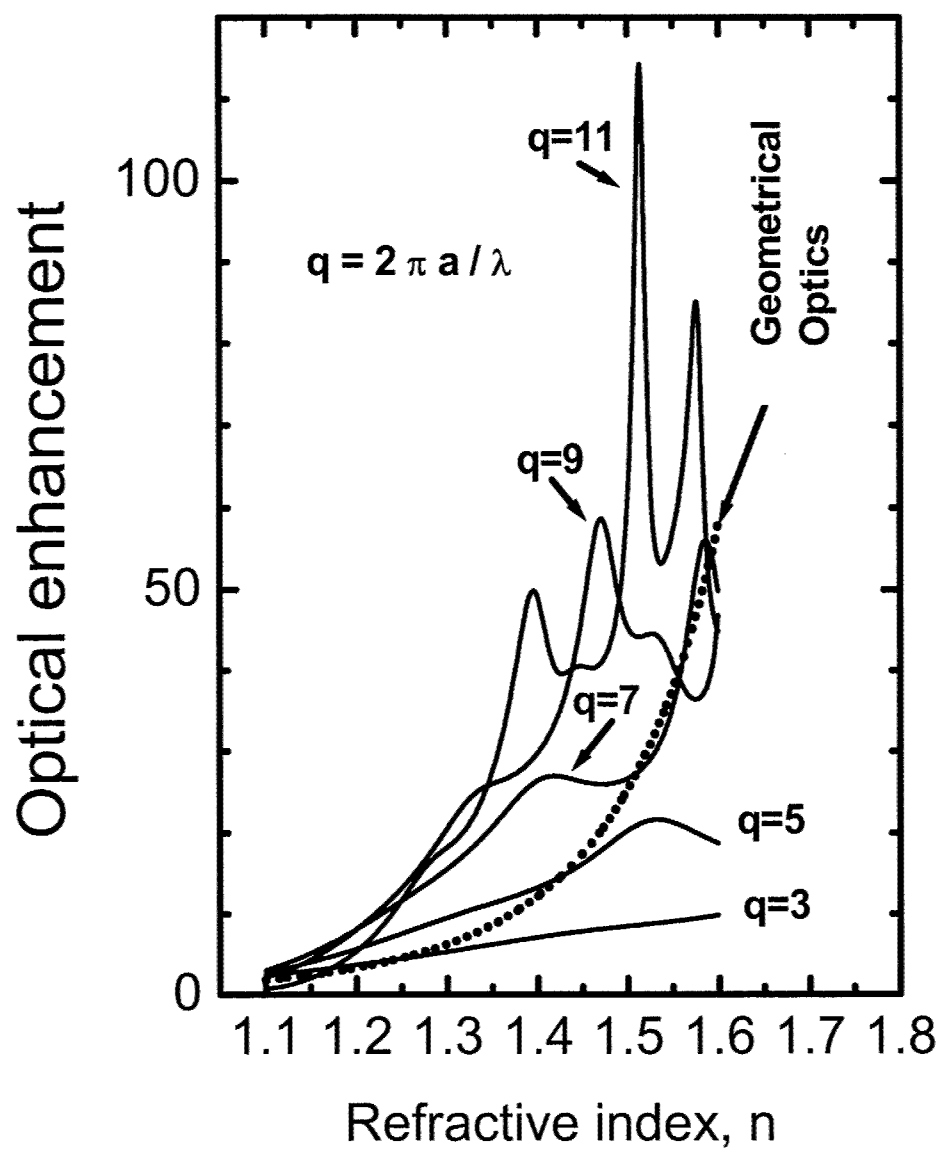
Fig. 9. Optical enhancement under the particle versus refractive index. Solid lines are calculated from the Mie theory for different values of the size parameter, q. Dotted curve – approximation of geometrical optics calculated from Eq. (2).
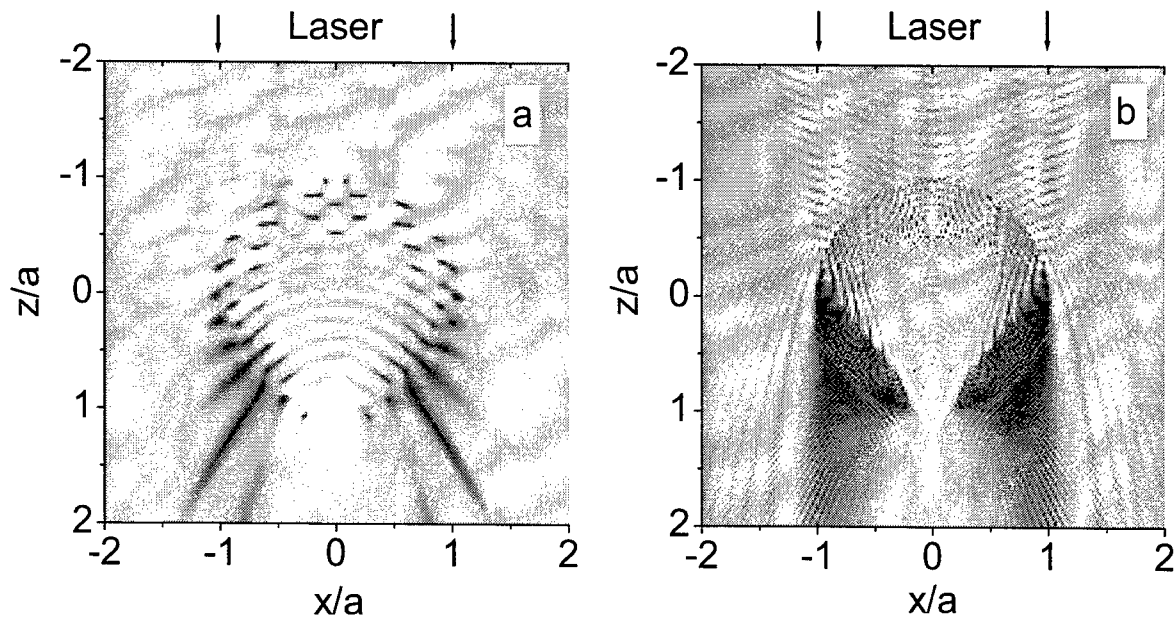
Fig. 10. The intensity distribution E^2, (z-axis along the radiation wave vector) around the particle with refractive index $n = 1.6$, radiation wavelength is $\lambda = 248$ nm. Gradations of the intensity from small (dark) to high (light) values are in logarithmic scale. (a) The particle radius is $a = 0.5$ μm, i.e. the size parameter $q = 2\pi a / \lambda = 12.67$; (b) The particle radius is $a = 5$ μm, i.e. the size parameter is $q = 2\pi a / \lambda = 126.7$.
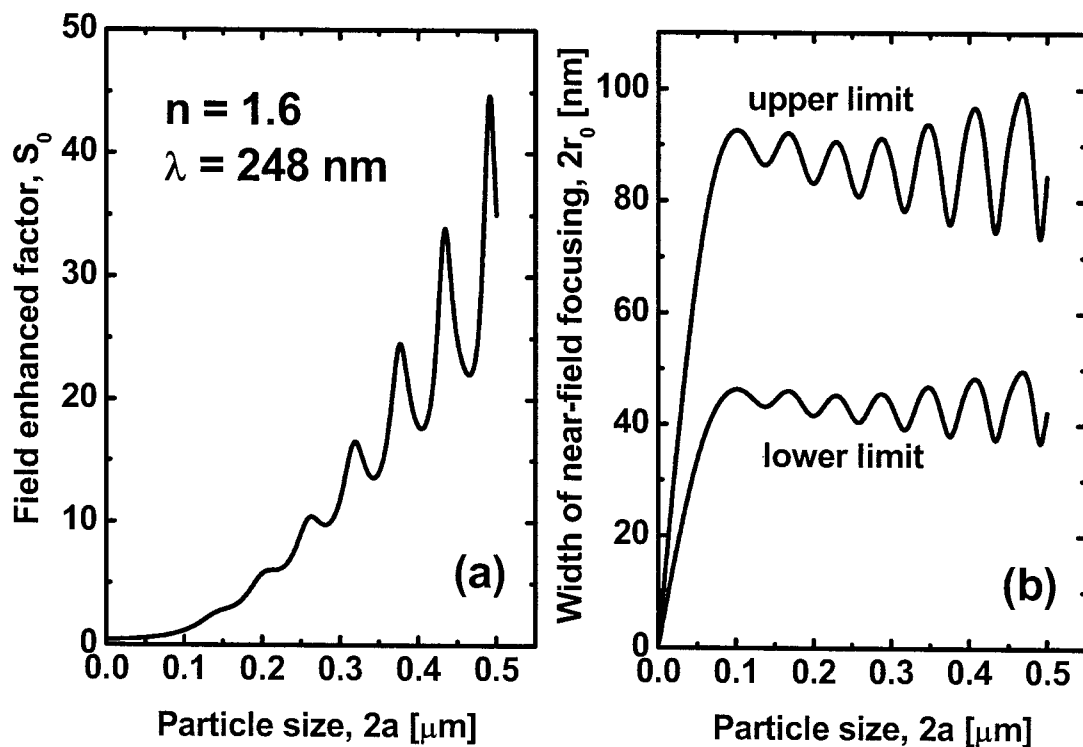
Fig. 11. Field enhancement factor, S_0 calculated from the Mie theory (a) and the width of near-field focusing (b) estimated from Eq. (6) for upper and lower limits. The refractive index $n = 1.6$ and the radiation wavelength $\lambda = 248$ nm.

Laser-Promoted Nanostructure Evolution and Nanoparticle Alignment

Anthony J. Pedraza, Jason D. Fowlkes, Stephen Jesse and Yingfeng Guan

Dept. of Materials Science and Engineering, The University of Tennessee, Knoxville, TN 37996-2200; Ph (865)974-7809; Fax (865)974-4115; e-mail apedraza@utk.edu

Abstract

A cone microstructure has been used as a template to generate nanotips and to promote nanoparticle alignment. A quasi-periodic array of nanotips is produced when the laser-induced cone microstructure is subject to chemical etching due to tapering of the cone tips. Nanoparticles can be produced on the surface of a silicon specimen by irradiating it in the presence of an inert gas atmosphere. The backscattered material that is re-deposited on the substrate, upon irradiation at fluences close to the melting threshold, is composed of a thin film intermixed with extremely small nanoparticles. Further irradiation promotes film clustering and nanoparticle formation. In the presence of cones, the nanoparticles become aligned into straight and long (~1 mm) lines whose spacing is close to the laser wavelength. This result suggested an ordering mechanism similar to that occurring for laser-induced periodic surface structures. The relation between nanoparticle line spacing and angle of incidence of the radiation supported this similarity. Nanoparticle ordering also was promoted by laser-enhanced chemical vapor deposition (LCVD) using polarized light, when a laser-induced periodic surface nanostructure was present in the substrate.

Introduction

A cone microstructure can form on the surface of silicon specimens upon pulsed-laser irradiated under a reactive SF_6 atmosphere, using either femto- or nanosecond pulses [1, 2]. This microstructure develops under certain irradiation conditions which include SF_6 pressure, laser fluence per pulse, and number of pulses [3]. For nanosecond laser irradiation, a surface modulation that exhibits crystallographic features initially evolves as the number of laser pulses is increased [4]. This initial morphology also develops when the irradiation is conducted under vacuum or inert gas atmosphere. As the number of pulses increases this wave structure further increases in amplitude but, at variance with non-reactive atmospheres, in SF_6 pits develop at the bottom of the valleys. Multiple reflections at the walls of the pits increase the local fluence causing a temperature increase at the bottom of the holes, thus enhancing the SF_6 etching and ensuing ablation. In addition, the multiple reflections and the confinement of gases in the holes, favors localized plasma formation. Plasma presence at the bottom of holes has been detected by an ICCD camera attached to a long focal distance microscope equipped with a UV transmitting lens [5]. Those two effects, very high heating at the hole-bottom and plasma evolution inside the hole, lead to holes that can reach hundreds of micrometers in depth after a few thousand pulses. Figure 1, which is a cross sectional image of a specimen irradiated under SF_6 at 0.5 bar pressure and a laser fluence of 2.7 J/cm^2 with 2000 pulses, reveals the presence of these very deep holes.
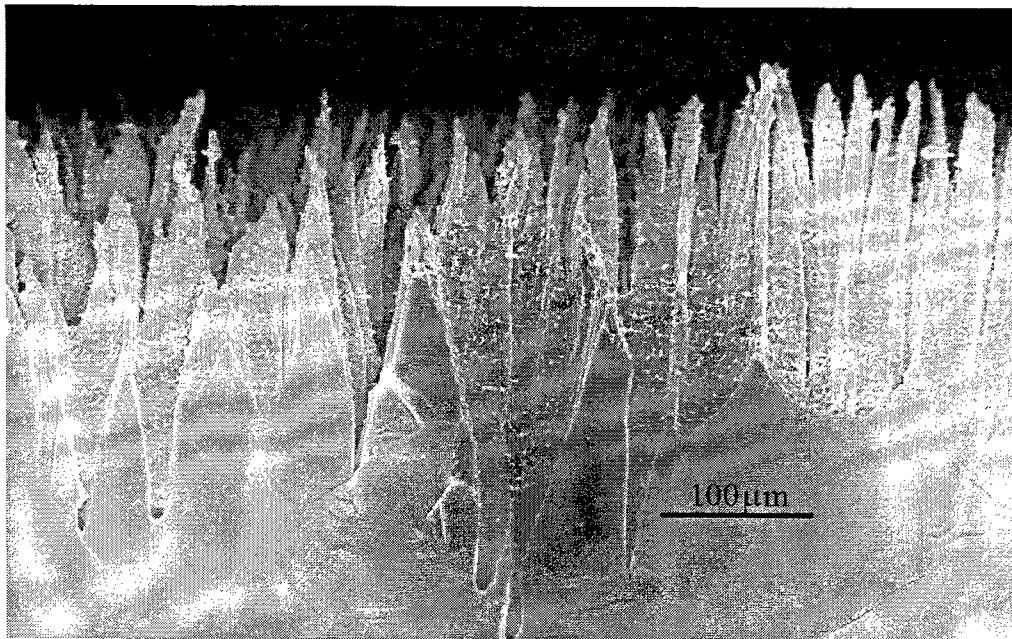
Figure 1. Cross sectional image of a cone microstructure. The Si specimen was irradiated at a fluence of 2.7 J/cm^2 with 2000 pulses under an SF$_6$ background pressure of 0.5 bar.

As a consequence of the etching-enhanced ablation that takes place preferentially at the hole-bottoms and the high pressure of the background gas that keeps the laser plume front at a distance of 50 to 80 μm away from the surface, a deposition process is initiated on the hillcrests as soon as the pits are formed [5]. Cone formation is favored there because the protruding portions receive a higher fluence than the slopes and are melted for the longest time [2]. Preferential re-deposition takes place at the tips of the growing cones because sticking is enhanced in melted areas. This preferential re-deposition leads to a cone structure that can reach several tens of micrometers above the initial surface, with a tip diameter of ~ 2 μm. The progress of microcone/microhole synergistic formation requires melting and re-solidification of the cone tip, which limits the smallest attainable tip size to the micrometer scale.

We have used these microstructures as templates to produce nanocolumns ~ 3 μm in height and ~ 150nm in diameter [6]. The nanocolumns where grown atop the microcone tips by drastically reducing the laser fluence to 0.5 J/cm^2 and the SF$_6$ background pressure to 10 Torr. Under these latter conditions, no microstructure evolves from a microscopically flat surface, and small overall changes occur in the cone/hole microstructure. Only the fine filaments develop, starting as a result of re-solidification of a very small melted pool at the cone tip and proceeding by a re-deposition process.

In this paper we will describe, first, two techniques to synthesize nanostructures using the microcone structure as: 1) a template for nanotips, and 2) an agent to induce the alignment of nanoparticles. This second procedure suggests a general technique to produce ordered nanoparticles. Thus, initial results show that Si nanoparticles are generated and forced into

alignment during chemical vapor deposition (CVD) of Si by irradiating the substrate while deposition is taking place.

Experimental Procedure

Boron-doped silicon substrates of {100} orientation were irradiated using a Lambda Physik LPX – 305i, KrF excimer laser (248 nm wavelength), with a pulse duration of 25ns. The beam emerging from the laser cavity was directed to an optic bench using a MgF_2-coated fused silica mirror. The optic bench contained an aperture, a fused-silica lens array, and the irradiation chamber. The rectangular aperture partly removed the low energy tails of the trapezoidal laser beam. The laser fluence was varied by adjusting the position of the fused-silica lens array relative to the sample holder in the irradiation chamber.

The experiments for generating nanoparticles were conducted using helium as background gas. For each laser irradiation cycle, the irradiation chamber was pumped to a base pressure of 1×10^{-7} Torr prior to introducing ultra-high purity (UHP) helium gas (99.999% pure) at a selected pressure. For most experiments, the substrates were first laser-microstructured in an SF_6 atmosphere, to produce a cone relief.

Ex-situ characterization studies were conducted using scanning electron microscopy (SEM), atomic force microscopy (AFM), and Auger emission spectroscopy (AES).

Etching of microstructured specimens was conducted in a 20% by weight KOH aqueous solution at 85 °C, for 20 minutes. Etching was profuse in the microstructured region of the specimen, and was followed by immersing the whole specimen in distilled water for 30 min. However, bubbling out of the microstructured region continued for the first 20 min of immersion.

Results and Discussion

1. Laser-induced cone microstructure as a template for nanotips

A cone/hole microstructure was grown on a 100-oriented silicon surface irradiating the specimen with 3000 pulses at 2.5 J/cm^2 under 0.5 bar of SF_6. When this hole/cone microstructure was etched with a KOH solution, as specified in the Experimental Procedures section, a structure exhibiting very remarkable crystallographic features was obtained. The etching cleared all of the cone surface irregularities produced by the redeposition and resolidification processes involved in their growth. The etched microcones appeared as stacks of 100 thin layers, quite similar in appearance to an Aztec pyramid (Figures 2a and b).

The directions of the squares that delineate the base of the cones and holes are, most probably, <100>. Due to the etching tapering action, the tips of the cones have become extremely thin. An HRSEM image shows that these tips are now ~25 nm in diameter, as seen in Figure 3.
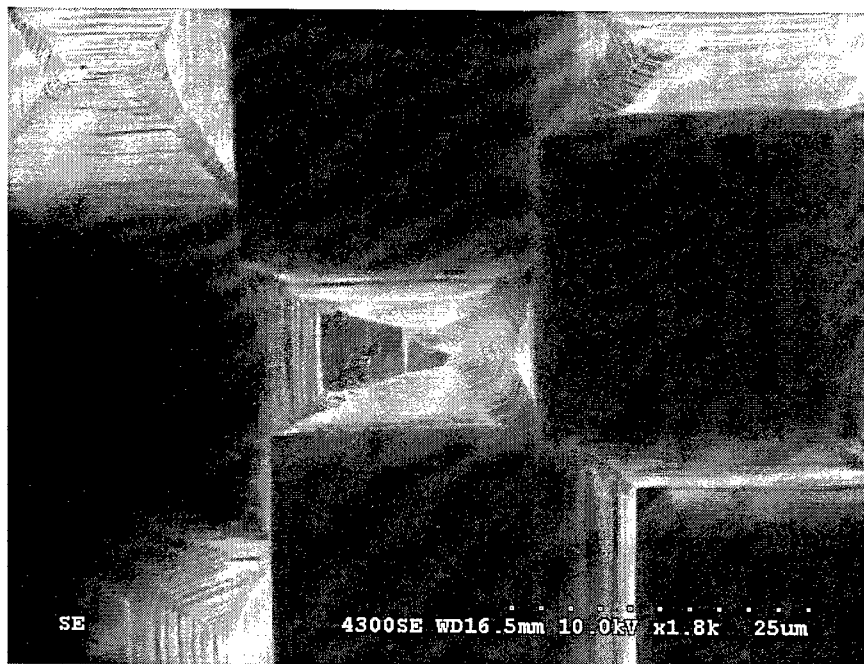
Figure 2a. Frontal view of a KOH-etched cone structure. The surface structure before etching was similar to that shown in figure 1. This specimen was irradiated with 3000 pulses, at 2.5 J/cm^2, under a 0.5 bar of SF$_6$.
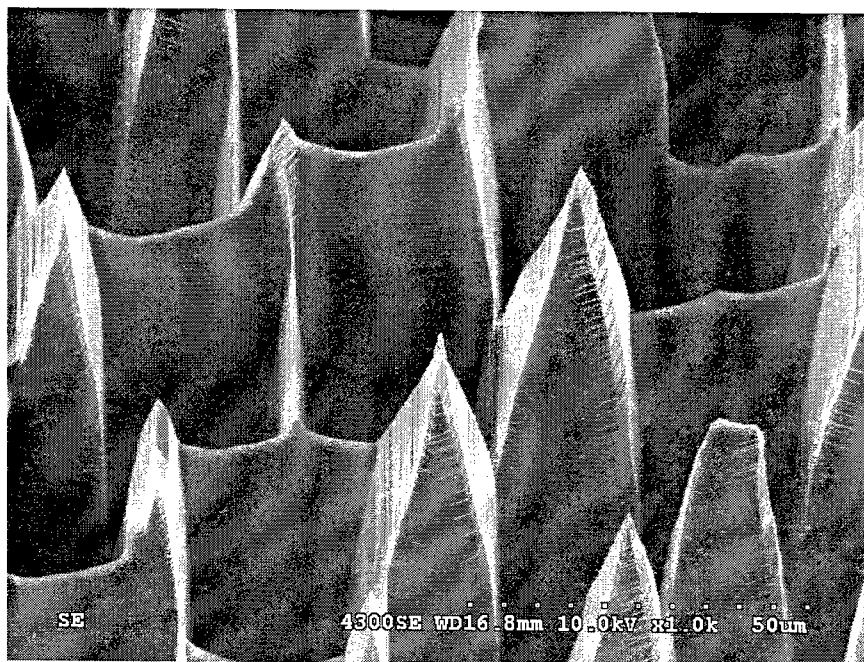
Figure 2b. Another view of the same specimen as that of fig. 2a, with the surface tilted by 30°.

Previous measurements using x-ray diffraction revealed that the cones were single-crystals that had the same orientation as the substrate [5]. This could be expected because the deposited material that causes the cones to grow is subjected to melting and re-solidification after each laser pulse [7, 2]. Consistent with those facts, after chemical etching, each cone appears as a stacking of 100 layers. The high aspect ratio of the etched cones with nanoscopic dimension tips make them very promising for their use in field emission applications.

Figure 3. High magnification of an etched cone-tip. Same specimen as that of Figure 2.

2. The cone microstructure as an agent to induce the alignment of nanoparticles

The cone microstructure can also be used to organize laser-produced nanoparticles into linear arrays. Two irradiation steps were followed: first, a microcone/microhole structure was generated under SF_6 as described in the introduction and, next, a region encompassing the microstructure was irradiated under UHP He at a much lower gas pressure and fluence. The cone microstructure remains essentially unaffected by the second irradiation step.

Figure 4 is a low magnification image of the cone microstructure and the surrounding region after irradiation at normal incidence using a fluence of 1 J/cm^2, in a background pressure of 10 Torr of He. As the irradiation proceeded, nanoparticles formed in the neighborhood of the microstructure and became aligned to form an ordered array. The insert of Fig 4, taken from the indicated area shows a high magnification SEM image of this array. The line spacing is approximately equal to the light wavelength, λ.

Figure 5 is a partial view of a sample irradiated also with 400 pulses and 1 J/cm^2 but at a pressure of 100 Torr of He. In this instance where a higher background pressure was used the entire region that surrounds the cone structure became covered with aligned nanoparticles. The angle of incidence in this instance was also close to 90° and the line spacing also is very close to λ.
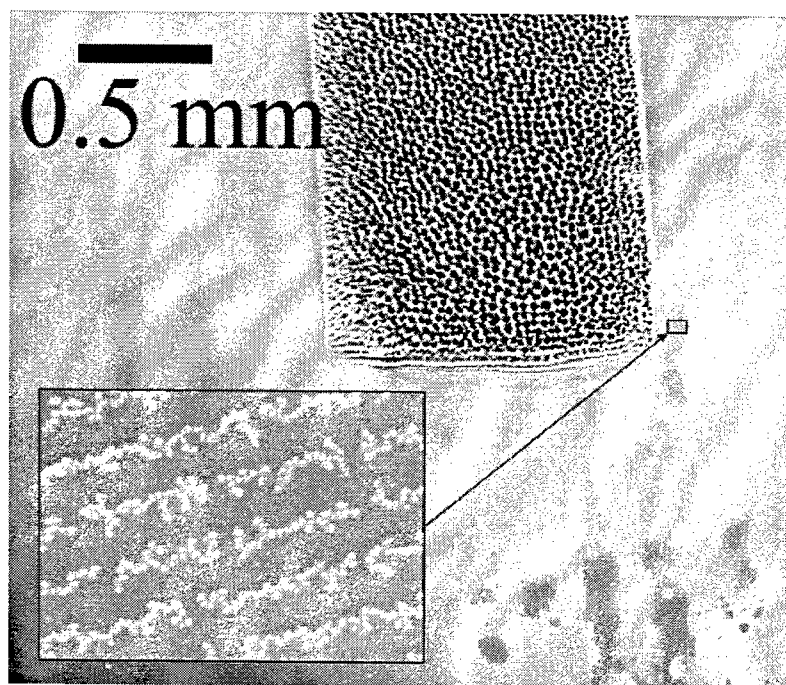
Figure 4. The two-step procedure to produce the nanoparticle alignment: The first irradiation generates the cone microstructure (upper right corner); the second irradiation that covers the entire area seen in the image promotes the formation of nanoparticles that surround the cone microstructure. The insert in the lower left corner, shows at high resolution the aligned nanoparticle structure. First irradiation: 2000 pulses, fluence 2.7 J/cm^2, 0.5 bar SF_6. Second irradiation: 200 pulses, fluence 1 J/cm^2, 10 Torr UHP He.

The fact that the line spacing is very close and in some instances equal to the laser wavelength points to a mechanism of formation similar to that of the laser induced periodic surface structures (LIPSS). The formation of LIPPS is the results of a non-homogeneous deposition of energy resulting from the interference between the refracted beam and two scattered waves parallel to the surface [7, 10-14]. A surface roughness is responsible for

scattering of waves parallel to the surface. A positive feedback between the production of the roughness and the energy distribution during irradiation must take place in order to develop LIPSS. In particular, if the incident light is p-polarized, and the angle of incidence of the light is θ, the line spacing Λ can be approximated by:

$$\Lambda = \frac{\lambda}{1 - \sin\theta} \qquad (1)$$

for a medium having a modulus of the dielectric coefficient much larger than 1 [7, 10], which is the case for silicon. Also, the polarization vector must run perpendicular to the direction of the nanoparticles lines.
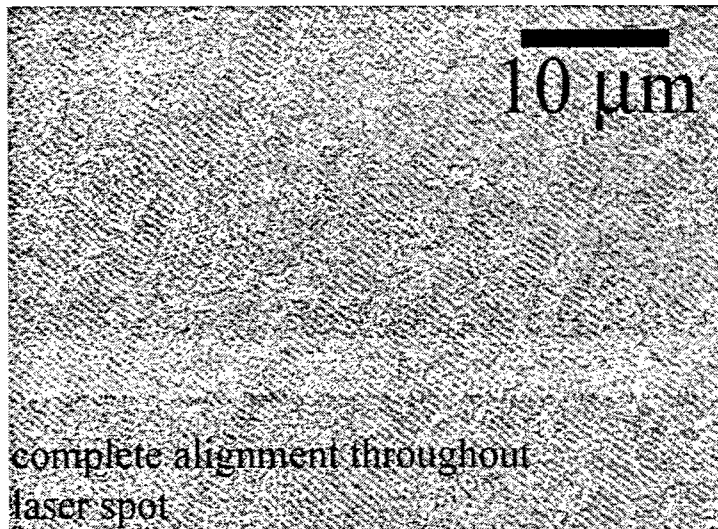
Figure 5. After 400 pulses at a laser fluence of 1 J/cm^2 under 100 Torr of UHP He, the region surrounding the cone microstructure is completely aligned.

The mechanism of formation of this nanoparticle arrays can be inferred from the nanostructure evolution in regions that are further away from the microstructure. Figure 6 is an image taken from one of these regions. A deposited film appears as a whitish area covering a portion of the image while, in another site, two intersecting strips are denuded of film but covered with nanoparticles. As one moves away from the strips' edges and toward the center of these film-free regions, the nanoparticles appear larger and become aligned. This result and other detailed experiments [8, 9] where the film has been detected during the initial irradiation stages indicate that film deposition precedes the formation of nanoparticles. As irradiation proceeds the film clusters forming nanoparticles which become aligned upon additional irradiation. The AFM images presented in Figs. 7a and b show a region where the transition to nanoparticle ordering is illustrated.
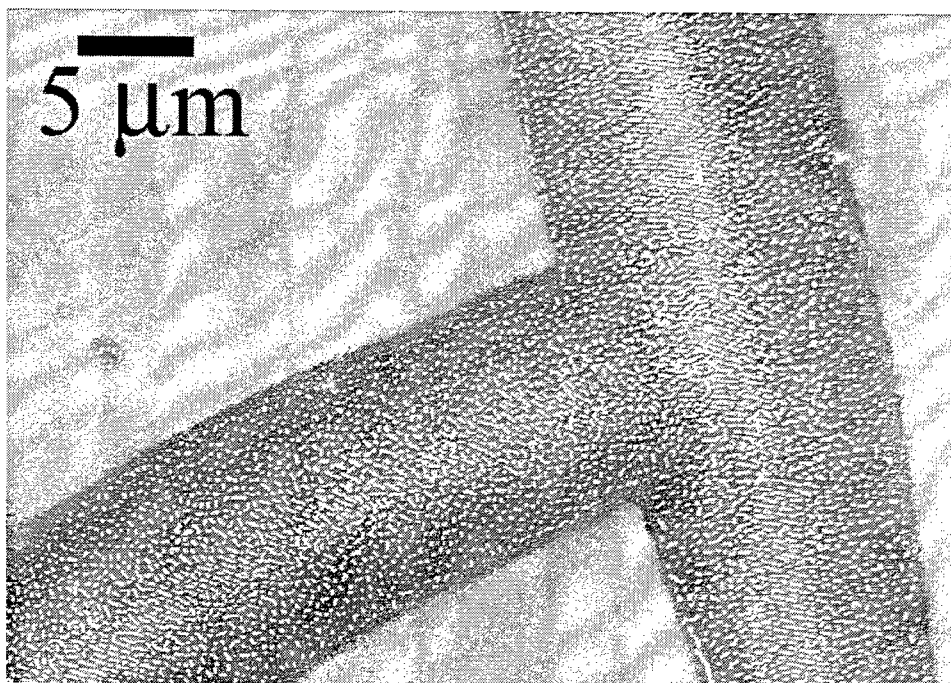
Figure 6. Specimen irradiated in UHP He at 100 Torr with 200 pulses, at a fluence of 1 J/cm^2. Prior to this irradiation a microcone structure was generated in the vicinity by irradiating the specimen with 200 pulses at 2 J/cm^2 in a 0.5 bar SF$_6$ atmosphere.
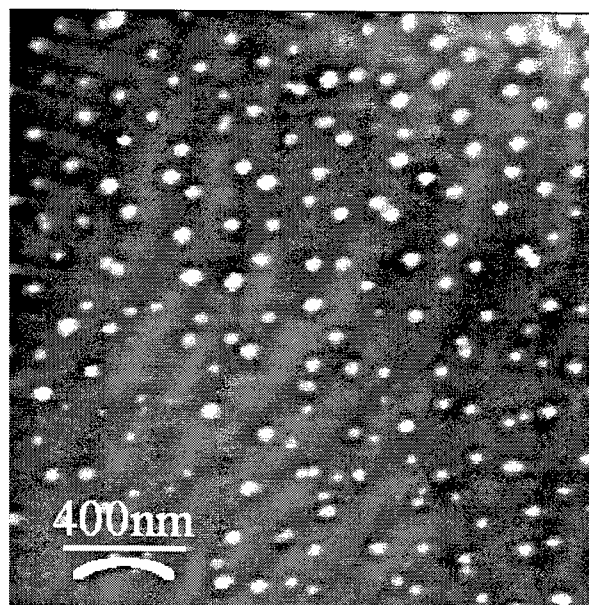
Figure 7a. AFM image of specimen irradiated with 200 pulses at a laser fluence of 1 J/cm^2 in UHP He at a pressure of 0.5 Torr.
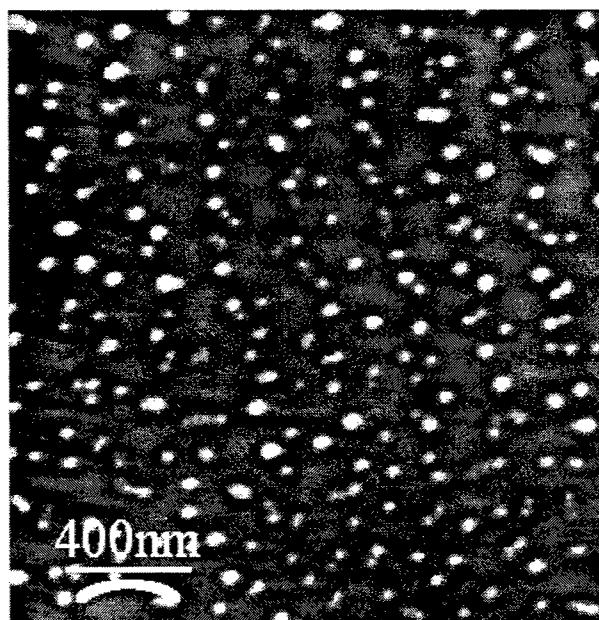
Figure 7b. AFM image in a region adjacent to that show in Figure 7a

In order to further investigate the similarities between nanoparticle ordering and LIPSS, nanoparticles lines were produced using p-polarized light. Figure 8 shows that there is close agreement between the measured line spacing and equation 1 as the angle of incidence was changed. These experiments suggest that laser light can be used to form and organize nanoparticles using films produced by other methods. In order to test these ideas a film was deposited using laser assisted chemical vapor deposition (LCVD). The process followed two steps. In both instances the silicon substrate was irradiated with p-polarized light. First, LIPSS were produced irradiating a silicon substrate with 400 pulses at a fluence of 0.8 J/cm^2. The structure obtained is shown in figure 9. Next, a gas consisting in Ar+10% silane was introduced in the chamber to a total pressure of 10 Torr and the specimen was irradiated with 1000 pulses at a fluence of 0.5 J/cm^2. During LCVD, silicon nanoparticles were deposited in the valleys and hills of the LIPSS structure (Fig. 10).

All our observations indicate that a very thin film gets deposited during laser irradiation of an area that includes the cone microstructure [8, 9]. As analyzed in the introduction the presence of cones promotes ablation at the bottom of the holes. A simple calculation using the microhole geometry shows that there is a four fold increase of the laser fluence at the hole-bottom relative to the nominal fluence, thus facilitating ablation there and film redeposition in the region around the microstructure.

. It is clear from the extensive work done on ripple formation that a non-uniform deposition of energy is produced during laser irradiation of a surface with micro- or nano-roughness. The light scattered from the very significant roughness of the deposited film will generate a random interference pattern with the refracted film. SEM and AFM images strongly suggest that the film clusters as it is being simultaneously deposited and irradiated and forms nanoparticles. The incipient order observed in the AFM image of figure 7b shows the tendency of the nanoparticles

to order and form lines. These lines are separated by a distance of ~ 230 nm very close to the wavelength suggesting a process controlled by non-homogeneous deposition of energy, similar to what happens during ripple formation. Figure 6 illustrates the evolution of the film, demonstrating that the nanoparticles grew in the substrate consuming the film and became aligned as they were irradiated. The nanoparticle array depicted in figure 5, that has line spacing very close to 248 nm and extends over microscopic regions, shows a very significant relation with the ripple formation.
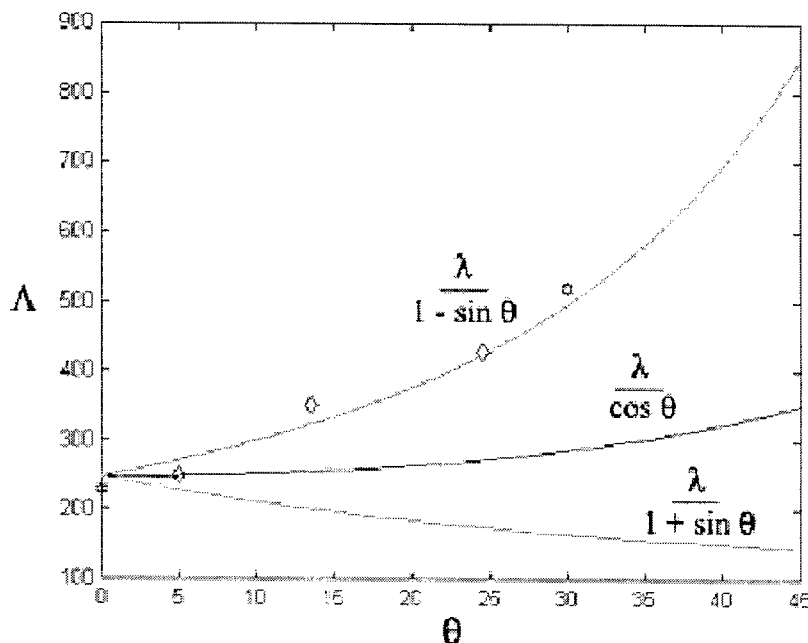
Figure 8. Nanoarray line spacing measurements as a function of the laser light angle of incidence. The line-spacing follows the relation $\dfrac{\lambda}{1-\sin\theta}$.

Summary and Conclusions

A cone microstructure has been used to produce nanotips when used as a template to build on. A quasi-periodic array of nanotips is produced by etching a laser-induced cone microstructure. An ordered array of cones can be produced by laser irradiating the substrate using a projection mask, thus giving way to generate an ordered array of field emission tips.

The cone microstructure also was used to promote nanoparticle formation and alignment when used as an external agent. The close agreement between the measured line spacing and equation (1) strongly suggested that nanoparticle alignment is caused by a non-homogeneous deposition of energy similar to what happens when LIPSS are formed. The nanoparticles seem to act as light scattering centers in a way similar to the LIPSS undulations. The preliminary

experiments on the ordering of nanoparticles produced during laser-induced chemical vapor deposition shows that nanosecond lasers can be used as tools to generate and induce ordering of nanoparticles.
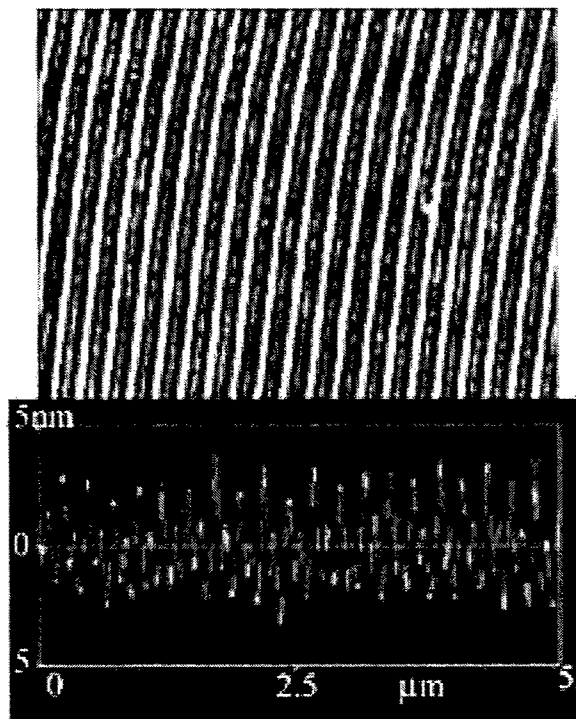
Fig. 9. AFM image of LIPSS formed in silicon under vacuum. Linearly polarized laser light at normal incidence. Laser wavelength: 248 nm, fluence: 0.8 J/cm^2, 400 pulses. Note: y-scale in nm; x-scale in μm
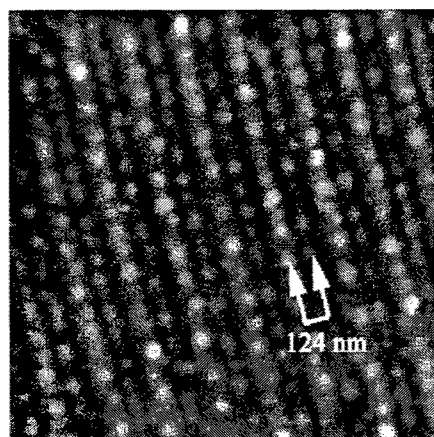
Figure 10. Laser-induced nanoparticle formation and alignment from a chemically-vapor deposited Si film. AFM image of the particle array shows spacing of λ/2.

Acknowledgments

References

1. T-H Her, R.J. Finlay, C. Wu, S. Deliwala, E. Mazur, Appl. Phys. Lett. **73**, 1673 (1998); T-H Her, R.J. Finlay, C. Wu, E. Mazur, Appl. Phys. A **70**, 383 (2000)
2. A.J. Pedraza, J. Fowlkes and D.H. Lowndes, Appl. Phys. Lett. **74,** 2322 (1999).
3. J. D. Fowlkes, A. J. Pedraza and D. H. Lowndes, Appl. Phys. Lett. **77**, 1629 (2000).
4. J. Pedraza, S. Jesse, Y. Guan, and J. D. Fowlkes, J. Mater. Res., **16**, 3599 (2001)
5. S. Jesse, A. J. Pedraza, J. D. Fowlkes and J. D. Budai, J. Mater. Res. **17**, 1002 (2002).
6. Anthony J. Pedraza, Jason D. Fowlkes and Yingfeng Guan, in SPIE International Proceedings on High Power Laser Ablation 2002, ed. C. R. Phipps, Vol 4760, 164 (2002).
7. S.A. Akhmanov, V.I. Emel'yanov, N.I. Koroteev, and V.N. Seminogov, Sov. Phys. Usp. **28**, 1084 (1986)
8. J. D. Fowlkes, A. J. Pedraza, D. A. Blom, and H. M. Meyer III, Applied Physics Letters 80, 3799 (2002), Virtual Journal of Nanoscale Science & Technology May 27, (2002).
9. A. J. Pedraza, J. D. Fowlkes D.A. Blom and H.M. Meyer III, J. Mater. Res. **17**, 11, 2815 (2002).
10. D. Bäuerle, Laser Processing and Chemistry, 3rd Ed., (Springer-Verlag) Ch. 28, p.571 (2000).
11. Z. Guosheng, P.M. Fauchet, and E. Siegman, Phys. Rev. **B 26**, 5366-5381 (1982).
12. J.E. Sipe, Jeff F. Young, J.S, Preston and H.M. van Driel,, Phys. Rev. **B 27**, 1141-1154 (1982).
13. J.F. Young, J.S. Preston, H.M. van Driel, and J.E. Sipe, Phys. Rev. **B 27**, 1155-2015 (1982).
14. S.R.J. Brueck and D.J. Ehrlich, Phys. Rev. Lett. **48**, 1678-1681 (1982).

Holographic fabrication of micron structures

using interfered femtosecond laser beams split by diffractive optics

Yoshiki Nakata[*a], Tatsuo Okada [a], Mitsuo Maeda [a]

[a]Graduate School of Information Science and Electrical Engineering,
Kyushu University,
6-10-1 Hakozaki, Fukuoka 812-8581, Japan
Tel:+81-92-642-3965, Fax:+81-92-642-3965
E-mail: nakata@photon.ees.kyushu-u.ac.jp

ABSTRACT

A line of periodic dot structure was fabricated on and inside materials by laser-induced modification with interfered femtosecond laser beams split by a diffractive optics. In addition, dot matrix and comb structures were fabricated with transportation of a sample at arbitrary speeds. These structures worked as transmission and reflection gratings. In addition, nanowires were fabricated by peeling the comb structure. Dot matrix was also formed by a single shot of laser ablation with four interfering beams.

Keywords: laser ablation, femtosecond laser, interference, holography, diffractive optics, micro-machining

1. INTRODUCTION

Laser ablation or solarization using femtosecond laser has been receiving great interests because it achieve nano-sized and damage-free material processing.[1,2] Recently, laser ablation and photo-polymerization using interfered femtosecond laser beams were utilized to form periodic structures.[3-7] In our experiments, long periodic structure with 6 mm in length was firstly processed with a single shot of laser ablation using femtosecond laser. In our experiments, a diffraction beam splitter was used to achieve a wide interfered region of femtosecond laser beams.[7]

In this paper, our recent results of the micro-processing using interfered femtosecond laser beams are presented. A line of periodic structure was processed on different materials in a single shot by interfered

* nakata@ees.kyushu-u.ac.jp; phone 81 92 642-3895; fax 81 92 642-3965; http://photon.ees.kyushu-u.ac.jp/index.html; Graduate school of ISEE, Kyushu university, 6-10-1 Hakozaki, Higashi-ku, Fukuoka, 812-8581 Japan

femtosecond laser beams split by a diffractive optics. Dot matrix and comb structures were formed by scanning on a gold film, and they the diffraction property was measured. By peeling the comb structure, nanowires were formed. In addition, dot matrix was formed by a single shot of laser ablation with four femtosecond laser beams.

2. EXPERIMENTAL SETUP

The experimental setup is shown in Fig. 1. We used a femtosecond laser with about 90 fs pulse width and center wavelength of about 800 nm from an amplified Ti:sapphire system. The frequency of the laser was 10 Hz. The original beam size was about 6 mm in diameter, and it was split by a diffractive optics which has 80 periods per mm. The first order beams were transferred and interfered on the surface of a sample placed on a XYZθ stage by two convex lens which have a focal length of 100 mm. To obtain a higher laser fluence to achieve laser ablation, a cylindrical lens was set between the lens and the stage. The focal length of the lens was 60 mm. The zero order beam was dumped between the convex lenses. All processes were done in air, and at room temperature. Gold thin film evaporated on a silica glass, polystyrene, sapphire, slide glass were used as sample, and processed structures was observed by an optical microscope or scanning electron microscope (SEM).
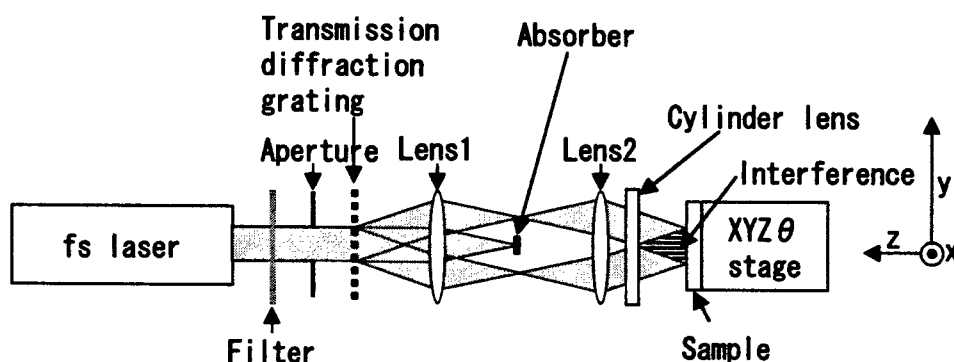
Figure 1: Experimental setup.

3. RESULTS

3.1 Processing of periodic dot structure on solids

Fig. 2 shows the periodic structures oricessed on polystyrene. Ablation laser energy was 0.9 mJ with two beams, and the process was done with single shot of laser. The laser were focused almost on the sample in (a), and defocused in (b). The beams were focused by cylindrical lens, so the shape at the focus point is

a line. When the surface of the sample was placed at the focus point, the resultant shape of the structure was a periodic dot structure, as shown in Fig. 2 (a). On the other hand, when the sample was moved from the focus point, the structure was elongated as shown in Fig. 2 (b). In this case, larger area was processed with a single shot of laser ablation. In each structure, the period was 6.25 μm.
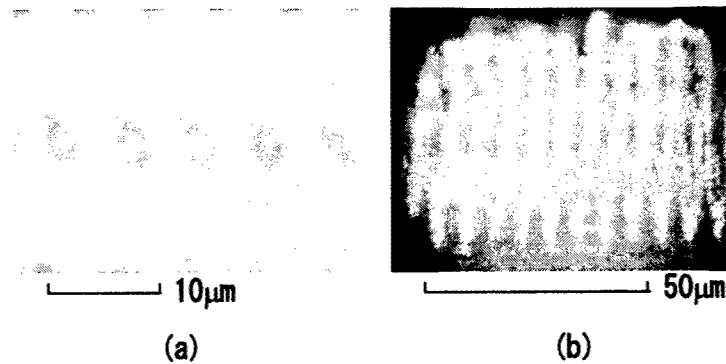
Figure 2: Periodic structures processed on polystyrene. They were focused on it in (a), and defocused in (b) during the process.
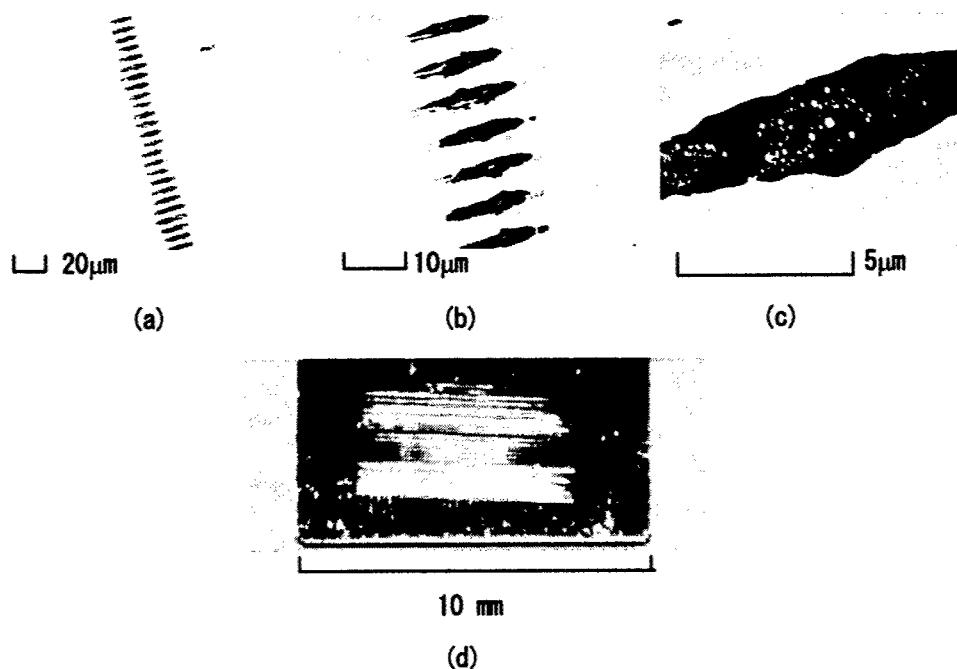
Figure 3: Periodic structures processed on gold film observed with different magnification. (a), (b) and (c) was observed with SEM, and (d) was observed with CCD camera.

Fig. 3 shows the periodic structure fabricated on a gold thin film evaporated on a silica glass substrate. The film thickness was 200 nm. The laser energy was 0.8 mJ with two beams, and the process was done with a single shot except Fig. 3 (c). These pictures were observed with different magnification. In Fig. 3 (a) and (b), a line of periodic holes with a shape of ellipsoidal is shown. The deviation of the figure of the holes is thought to be due to the non-uniformity of the original beam. In Fig. 3 (c), nano-sized gold particles can be seen inside the hole, which were produced by the melt or condensation of the gold vapor in the micro ablation plume. The length of this dotted line structure was 6 mm as shown in Fig. 3 (d), and which is longest structure fabricated by a single shot of interfered femtosecond lasers. This shows that the interference was achieved along the whole irradiated region, even the short spatial length of the laser.[7] This can be achieved in this configuration using diffractive optics. The ablated length corresponds to the original beam diameter.

Here, the period of interference pattern is $M\Lambda/2$, where M is imaging factor of two convex lenses, and Λ is the grating period of transmission grating.[7] So, with lessening these factors, smaller period of structure can be formed. In addition, enough high laser fluence to achieve laser ablation was obtained with small M without cylindrical lens. Fig. 4 shows the structure processed with smaller $M \fallingdotseq 0.16$ and $\Lambda = 15.5$ μm, and the period was about 1.2 μm. The total laser energy was 0.16 mJ with two beams, and the gold film thickness was 50 nm. It is quite interesting that the width of the formed line is only 0.3 μm, and which is smaller than the wavelength of the femtosecond laser. This is due to the multi-photon absorption process of the femtosecond laser.
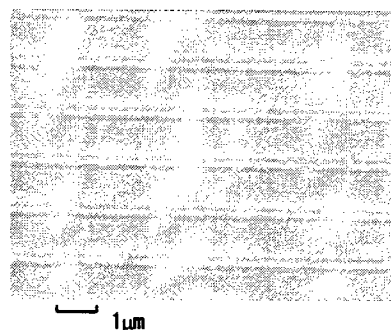
Figure 4: Periodic structure processed on a gold film.

Fig. 5 shows periodic structures processed on slide glass. Ablation laser energy was 0.8 mJ with two beams. Fig. 5 (a) was processed with a single shot, and Fig. 5 (b) was processed with dozen of shots. In both periodic dot structures were processed. With dozen of shots each hole was connected, but the cyclic structure can be seen at the side and bottom of the structure, as shown in Fig. 5 (b). Affection outside the

structure can be seen in Fig. 5 (b), which can be due to the thermal effect.
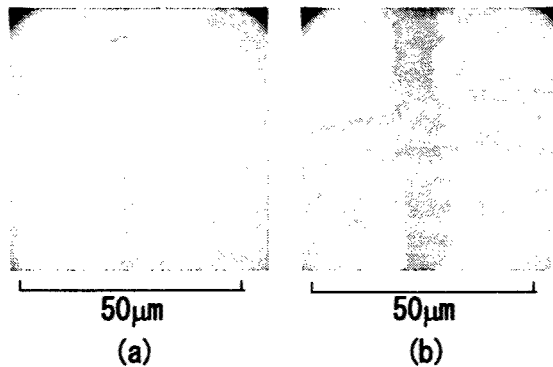
Figure 5: Periodic structures processed on a slide glass.

Fig. 6 shows the structures on a sapphire substrate processed with different number of shots. The laser energy was 1.8 mJ with two beams, and the number is shown at the underside. Here, when the energy was 0.8 mJ, no process was done. The surface was periodically holed, and the depth was deepened with the number of shots. The shape of the hole was ellipsoidal, and each hole was connected over 50 number of shots. Debris could be seen outside the holes, which were produced during the process.
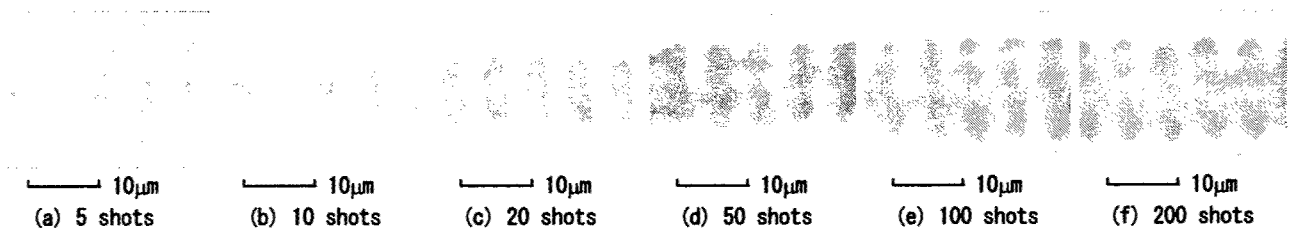
Figure 6: Periodic structures processed on a sapphire with different shot numbers.

3.2 Processing of periodic dot structure in solids

In the case of fabrication inside of silica glass, zero and two first order beams were used. The energy of zero order beam was 1.0 mJ, and that of first order beam was 0.7 mJ for each. The process was done with 10 shots, and strong white light of Raman scattering was observed during the process. The structure was processed at 8.5 mm deep from the surface of the sample.

The structure scattered a He-Ne laser light to every direction, so the structure is thought to be not only made of periodic change of refractive index, but also laser-induced small random damage. Fig. 7 shows the optical image of the structure formed inside silica glass observed from the same direction of incidence of the beams used in the process. The picture shows that the periodic structure was processed inside the

silica glass. The period of the structure was about 6.3 μm, and which is almost same with these processed on surfaces, which are shown in the former paragraphs. This is because that the changes of crossing angle and wavelength inside a material compensate exactly, which can be easily calculated using Snell's law.[6] In summary, the period is related only with an angle of the beams outside the sample, and not related with a kind of material or position. In addition, the structure worked as a diffractive optics with an incidence of a He-Ne laser, and this shows that the period of the structure is uniform. The diffraction efficiency of first order beams was 0.44 %, and that of second order beams was 0.04 %.
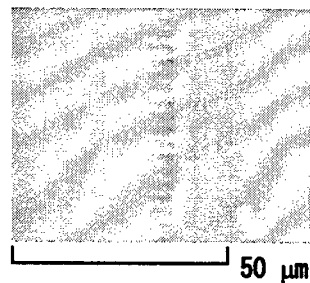
Figure 7: Periodic structure processed inside a silica glass.

Fig. 8 shows the periodic structures processed inside acryl with different shot numbers. Only the first order beams were used in the process, and the total energy was 1.3 mJ. The structures were processed at 2 mm deep from the surface. With 10 shots, periodic pit structure was formed as shown in Fig. 8 (a). The period was about 6.3 μm, which was the same with the case of silica glass. The defocusing of some pits is due to disperse in depth, and which was recognized in focusing during the observation. In addition, the sizes of the pit were dispersed. These are due to the inhomogeneity of the sample and femtosecond laser. With more shots, the pits were connected as shown in Fig. 8 (b) or (c), and this is the same in the case of the processing on a surface, which is shown in the former paragraphs.

(a) 10 shots (b) 20 shots (c) 50 shots
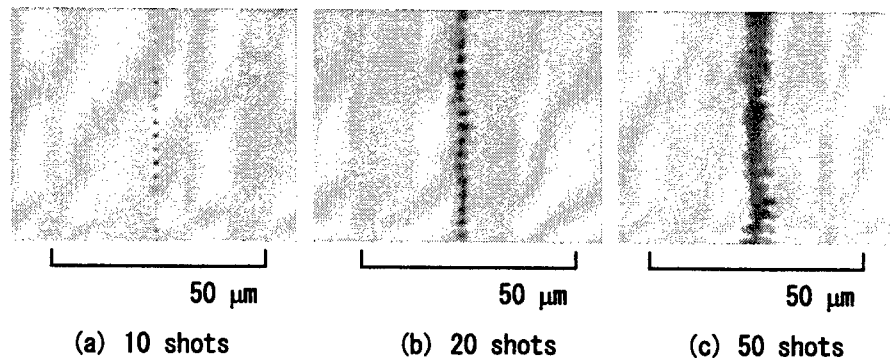
Figure 8: Periodic structures processed inside an acryl with different shot numbers.

3.3 Processing of dot matrix and comb structure and nano wire

By scanning a sample during the process, dot matrix structures were formed with successive ablations, as shown in Fig. 9 (a). The gold film thickness was 200 nm, and the scanning speeds during the processes were 107 μm/s. The ablation energy of the beams was about 0.6 mJ. A dot matrix was successfully formed in Fig. 9 (a). The large random dots are thought to be defects on the original film. Each horizontal line of dots was fabricated with a single shot of femtosecond laser. On the other hand, each vertical line of dots was formed by the transportation of the sample during the process, so the interval is related with the speed of the transportation. The deviation of the diameter in a horizontal line of dots is due to an inhomogeneity of the beams or the diffraction beam splitter, and the deviation in a vertical line of dots is due to the shot-to-shot fluctuation of the energy of the laser beams.

On the other hand, due to the inhomogeneity of the laser, the size of dots is larger at different point, then the dots are connected horizontally at that point. In addition, with slowing the scanning speed, the dots were connected vertically. As a result, small bits of gold film were left, as shown in Fig.9 (b). Here, the scanning speed was 39 μm/s.

(a) (b)
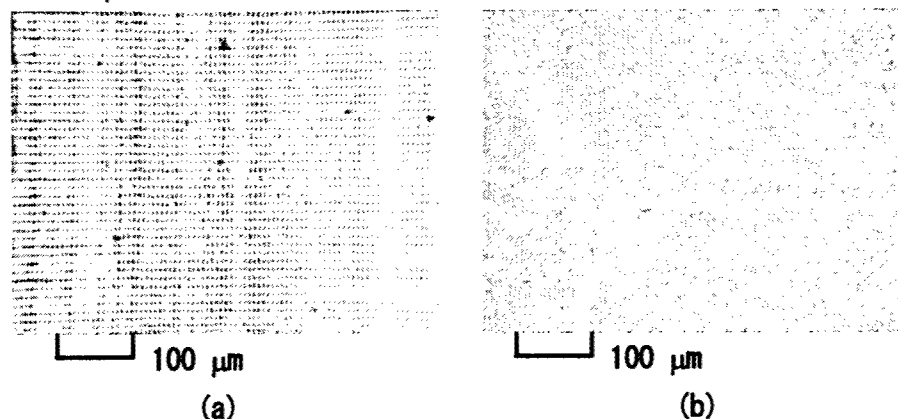
Figure 9: (a) dot matrix formed on a gold film with scanning the sample and successive laser ablation. The scanning speed was 107 μm/s. (b) small pits formed on a gold film with scanning with 39 μm/s and higher ablation fluence.

Fig. 10 shows the periodic structures processed with different scanning speeds of (a) 107, (b) 39, and (c) 8.3 μm/s. The ablation laser energy was 0.6 mJ with two beams. With slowing the transportation speed, the vertical interval is shortened, and then each hole is connected, and comb structure was formed as shown in Fig. 10 (c). Limitless long structure can be formed by scanning, and an arbitrary interval can be easily formed by changing the transportation speed.

(a) 107 μm/sec   (b) 39 μm/sec   (c) 8. 3 μm/sec
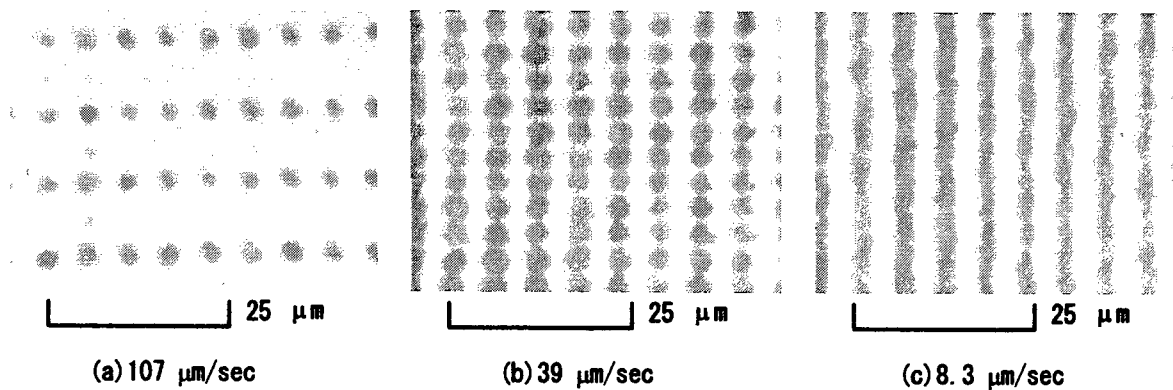
Figure 10: Periodic structures processed with different transportation speeds of (a) 107 μm/s, (b) 39 μm/s, and 8.3 μm/s.

These structures work as transmission and reflection grating, as shown in Fig. 11. The inset shows the top view of the experimental setup. The tested sample was the same with that in Fig. 10 (a). The sample was inclined at 30° against the He-Ne laser, and reflected and transmitted laser was projected on the screens. In the case of reflected laser, 9th vertically diffracted beams and 7th horizontally diffracted beams were visible on the screen. On the other hand, in the case of transmitted laser, 6th vertically diffracted beams and 4th horizontally diffracted beams were visible on the screen. The efficiency of reflected beams was 72.0 % of the incident beam, and that of transmitted beams was 6.1 %. So the total efficiency was about 78%, and the left was thought to be scattered and absorbed by the film or the silica glass substrate. The ratio of reflected and transmitted beams can be controlled by the diameters of the holes, which can be controlled by the energy of femtosecond laser used in the ablation process.
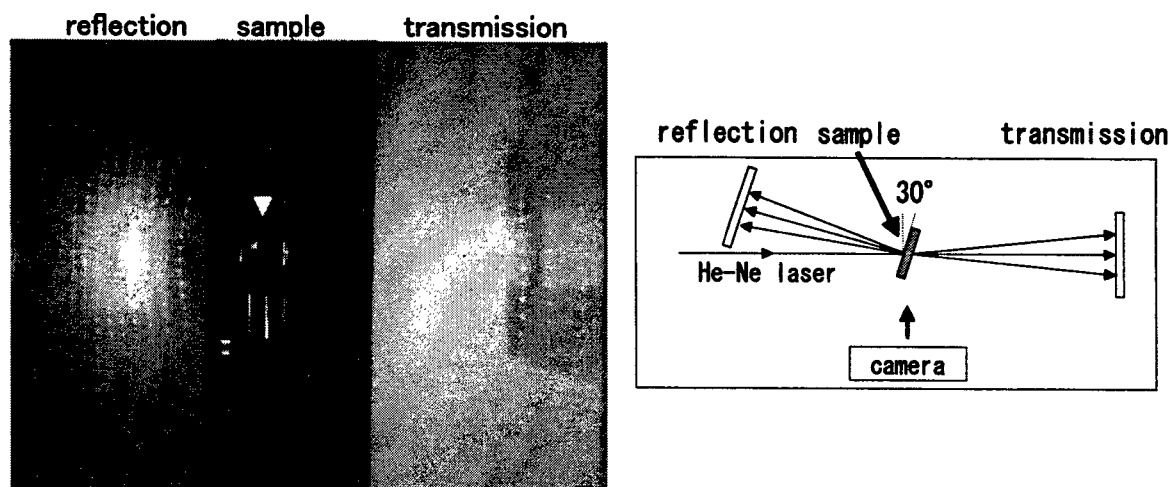
Figure 11: Diffraction patterns of reflected and transmitted He-Ne laser. Inset shows the top view.

In addition the diffraction pattern can be changed by the interval of dots, as shown in Fig. 12. The bracketed symbols correspond in Fig. 10. The inset shows the experimental scheme. The distance between a sample and the screen was 10 cm. The diffracted and transmitted laser irradiated the screen, and observed from the backside of the screen by CCD camera. Fig. 11 (a) shows the sample worked as diffractive optics for dot matrix, and which shows the dots are really holes, and the interval is uniform horizontally and vertically. Each diffraction angle followed the equation of $\theta_n=\sin^{-1}(n\lambda/d)$, where n is diffracted order, λ is wavelength of incident light, and d is the interval of the dots. So, when the interval was shortened, the diffraction angle was widened as shown in Fig. 11 (b). In the case of comb structure, the sample worked as a conventional transmission beam splitter as shown in Fig. 11 (c). The power distribution for each order of diffracted beam in Fig. 11 (c) is shown in the table under the inset.

In summary, the characteristics of formed diffractive optics can be changed by the energy of the process, the angle of the beams, focal length and focusing of the lens, transportation speed of a sample, spectrum of the laser, etc.. It is important that diffractive optics, which works as both transmission and reflection grating, can be formed within a single process.

(a) 107 μm/sec (b) 39 μm/sec (c) 8.3 μm/sec

order	-3	-2	-1	0	1	2	3
Power (μw)	0.5	3.7	46.3	102	48.4	4.4	1.0
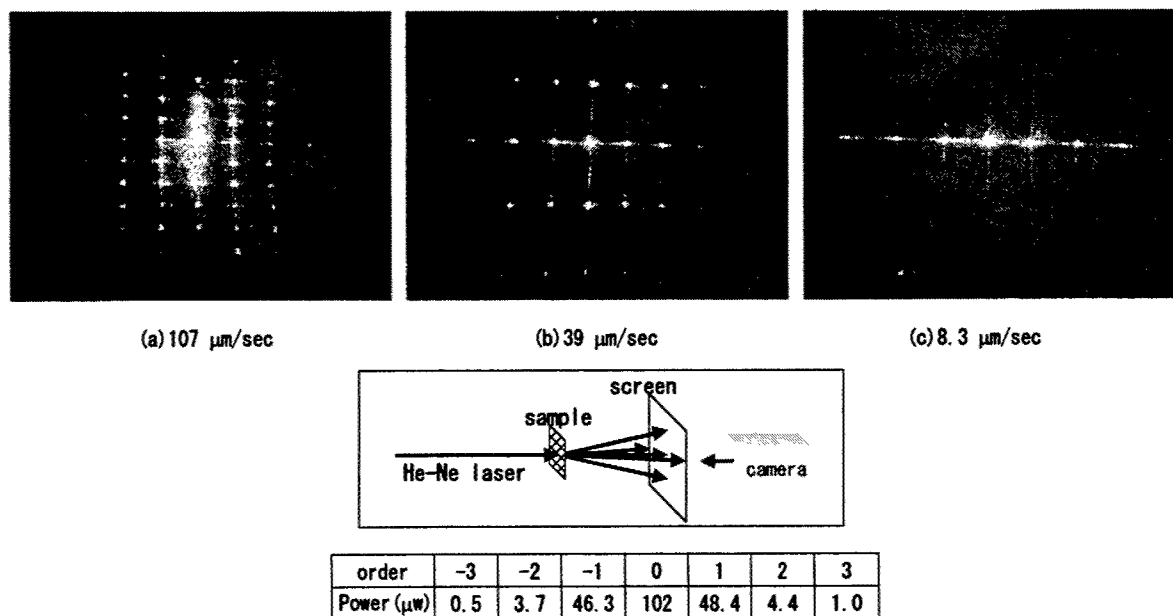
Figure 12: Diffraction patterns of transmitted He-Ne laser. The bracketed symbols correspond with those in Fig. 10. The inset shows the experimental scheme. The power distribution for each order of diffracted beams in Fig. 12 (c) is shown in the table under the inset.

By scratching the comb structure shown in Fig. 10 (c), nanowire can be formed as shown in Fig. 13. The optical image in Fig. 13 (a) shows that the wires were formed and bended. The SEM images in Fig. 13 (b) and (c) shows the width of the nanowires was about 2 or 3 μm. The thickness was 200 nm, which corresponds to that of the original film. The non-uniformity in width is due to the non-uniformity of the original comb structure, which is due to the fluctuation of laser energy and the vibration of the apparatuses during the process. The thickness will be thinned by using thinner film and the width will be more narrowed by modifying the experimental setup. It is important that this method, which can form nanowire, can be used for various materials which can form thin film with thickness in nano scale.
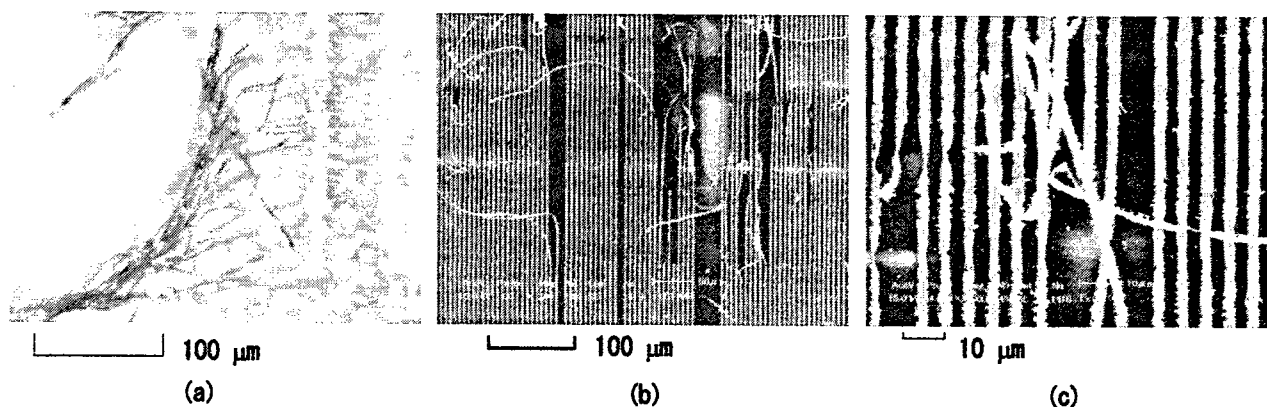
Figure 13: Images of gold nanowire observed by (a) optical microscope, (b) and (c) by SEM.

3.4 Processing of dot matrix structure with a single shot by four laser beams

By using two laser beams, a periodic dot structure can be processed with a single laser shot, as shown in the previous paragraphs. On the other hand, complex interference pattern can be formed at a surface by using more beams, then more complex structure can be processed. Here, we used 4 beams to produce dot matrix structure within a single shot.

Fig. 14 shows a dot matrix structure produced by a single shot of laser ablation. The ablation laser energy was about 0.3 mJ with four beams, and the diffraction angle between the beams opposite with each other was about 6 degree. The cylindrical lens was removed, and M ≒ 0.16. Periodic holes which have an interval of about 1.7 μm were formed. The shape of each hole was circle, and the size was almost 0.8 μm. In addition, this worked as transmission and reflection grating.
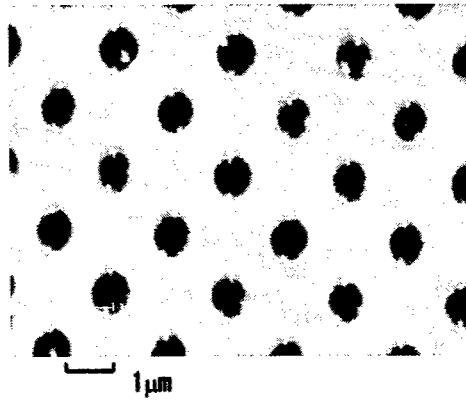
Figure 14: dot matrix structure processed by four laser beams.

4. SUMMARY

In summary, interfered femtosecond laser beams split by a transmission grating was used to process periodic structures. A line of periodic dot matrix and comb structures were successfully formed using two beams. In addition, a dot matrix was formed in a single shot by using four beams. These structures worked as diffractive optics, and this shows that the period is enough uniform to work as a diffractive optics. The smallest modified size was 0.3 μm, which was much smaller than the wavelength. In addition, nanowires were formed by peeling the comb structure.

Acknowledgment

REFERENCES

1. K. M. Davis, K. Miura, N Sugimoto, and K. Hirao, "Writing waveguides in glass with a femtosecond laser", Opt. Lett. **21**, pp. 1729-1731 (1996).

2. S. Küper and M. Stuke, "Femtosecond uv excimer laser ablation", Appl. Phys. B **44**, pp199-204 (1987).

3. K. Kawamura, T. Ogawa, N. Sarukawa, M. Hirano, and H. Hosono, "Fabrication of surface relief gratings on transparent dielectric materials by two-beam holographic method using infrared femtosecond laser pulsed", Appl. Phys. B: Lasers Opt. **71**, pp. 119-121 (2000).

4. T. Kondo, S. Matsuo, S. Juodkazis, and H. Misawa, "Femtosecond laser interference technique with diffractive beam splitter for fabrication of three-dimensional photonic crystals", Appl. Phys. Lett. **79**, pp. 725-727 (2001).

5. Y. Nakata, T. Okada, M. Maeda, ""Fabrication of dot matrix, comb and nanowire structures using laser ablation by interfered femtosecond laser beams", Appl. Phys. Lett., **81**, pp 4239-4241, (2002).

6. Y. Nakata, T. Okada, M. Maeda, "Formation of periodic structure inside silica glass and acryl by interfered femtosecond lasers", Jpn. J. Appl. Phys., to be published.

7. Y. Nakata, T. Okada, M. Maeda, "Line of periodic hole structure produced by laser ablation using interfered femtosecond lasers split by transmission grating", Appl. Phys. A, to be published.

Preparation of thin film GaAs on glass by pulsed-laser deposition

Bruno Ullrich[*a], Artur Erlacher[a], Satoshi Yano[a], Raoul Schroeder[a], Timofey G. Gerasimov[a],
Heather J. Haugan [b]

[a]Centers for Materials and Photochemical Sciences; Department of Physics and Astronomy,
Bowling Green State University, Bowling Green, OH 43403-0224,
[b]Air Force Research Laboratory; Materials & Manufacturing Directorate, AFRL/MLPS, Wright–
Patterson AFB, OH 45433-7707

ABSTRACT

One of the most straightforward methods possible is presented and investigated to form thin film GaAs. The film was deposited on unheated glass in vacuum (10^{-6} Torr) by the ablation from a GaAs wafer with the emission of a pulsed Nd:YAG laser (532 nm, 6 ns, 10 Hz). The photoluminescence, photocurrent, transmission and micro-Raman measurements of the films demonstrate that films with promising optoelectronic properties have been formed. Most importantly, from the viewpoint of light emitting and optoelectronic device production, the films show photoluminescence of comparable intensity with the bulk material without emissions owing to impurities, although the films show a rather flat absorption edge which indicates tail states. The observed photocurrent was in the µA/W range driven by rather moderate electric fields on the order of 100 V/cm. Concerning the material quality, the films have an extremely smooth surface as demonstrated with scanning electron microscopy. Grown GaAs films on glass substrates were amorphous evidenced by X-ray diffraction measurements, however, micro-Raman measurements showed crystalline phonon modes, suggesting that localized crystalline structure might co-exist in amorphous GaAs films.

Keywords: Thin film GaAs, pulsed-laser deposition, photoluminescence, photocurrent, transmission, X-ray diffraction Raman spectroscopy

1. INTRODUCTION

During the last two decades, the III-V semiconductor gallium arsenide (GaAs) has obtained almost the same importance as silicon (Si). GaAs and related compounds are of particular significance for high-speed digital and high-performance analog applications and specifically important for the production of laser diodes.[1-3] The state-of-the-art GaAs device production is mainly covered by rather expensive techniques such as molecular beam epitaxy (MBE), metal organic chemical vapor deposition (MOCVD) and related techniques since the layers grown by these two methods exhibit extreme uniformity and reproducibility.[4] Herein, pulsed-laser deposition (PLD) was studied as low-cost alternative to MBE and MOCVD to deposit GaAs on glass substrates. The employment of transparent substrates would considerably increase the flexibility of optoelectronic device structures because GaAs circuits on glass would allow free standing optically interfaced electronics and three dimensional optically clocked computer structures. Furthermore, the replacement of GaAs substrates with GaAs on glass, if deposited in the required quality, would considerably lower the production costs of GaAs devices by MBE and MOCVD. The employment of PLD for the formation of thin film GaAs is not intensively studied and only a few attempts have been reported.[5] In general, PLD has received much less attention than have other vaporization methods but is known for the formation of high quality stoichiometric material due to congruent explosive evaporation of component materials.[6] Examples for these are the high-T_c superconductor yttrium barium copper oxide (YBCO)[6] and the II-VI semiconductors cadmium sulfide (CdS),[7] zinc oxide (ZnO),[8] and zinc sulfide (ZnS).[9] In this paper, we present, as far as we are aware for the first time, the optoelectronic properties of thin film GaAs on glass formed by PLD.

---

[*] bruno@kottan-labs.bgsu.edu; phone: +1 419 372-7245; fax +1 419 372-9938; http://kottan-labs.bgsu.edu/

2. SAMPLE PREPARATION

Figure 1 shows the core arrangement of the PLD setup used. The distance between target and the fused silica glass substrates was 6 cm. The target was a p- type zinc doped (10^{19} cm^{-3}) GaAs wafer with a diameter of 50.8 mm (2 in.) and a thickness of 2 mm (0.08 in.). The material was ablated from the target with a laser fluence of 0.79-0.84 Jcm^{-2}, which was provided by the pulsed second harmonic emission (532 nm) of a Nd:YAG laser. The ablation spot size was 1.8×2.5 mm corresponding to an ellipse area of 3.5 mm^2. Pulse duration and repetition rate of the laser was 6 ns and 10 Hz, respectively. The ambient pressure during the ablation process was kept at 10^{-6} Torr and in order to avoid that holes are burned in the target it was rotating with 6 revolutions per minute. Figure 2 reveals the circular traces of the ablation beam on the target. The film was deposited to be 0.2 µm thick. The films were deposited at room temperature, however the glass substrates were probably heated to some degree form the interaction with the high-energetic plume.
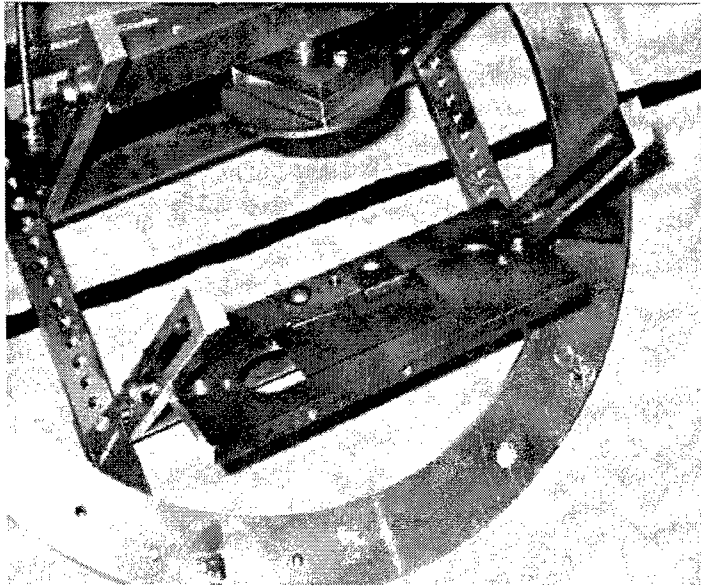
Figure 1: The core part of the PLD setup.
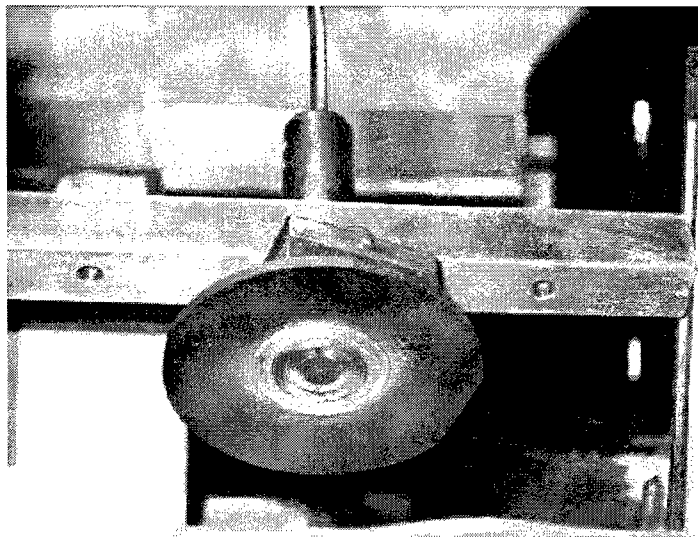
Figure 2: The circular traces of the laser beam on the target.

3. EMISSION PROPERTIES OF THE FILMS

Figure 3 shows the photoluminescence (PL) of the film in comparison to the target emission. It is seen that the film shows like the target a broad PL spectrum from the infrared spectral range to the visible region. The PL of the film and the target was excited with an intensity of 0.8 MW/cm^2 and 0.7 MW/cm^2, respectively employing the pulsed 532 nm emission of the laser used for PLD. The emission was detected with a fiber spectrometer with a resolution of 1 nm. The experiments have been performed in reflection geometry, i.e., the emission was collected from the surface of the sample.

It is seen that the target material shows a pronounced peak at 880 nm corresponding to the fundamental transition in GaAs. The second rather broad peak is eventually related to the heavy electron band, which is ≈0.3 eV above the light electron band.[10] Since the film does not show impurity related emission below the band-gap but not the pronounced gap emission at 880 nm, we believe that the PLD film is a rather intrinsic material with a shorter minority-carrier lifetime than the source material. The lack of the traditional band-gap emission can indicate disorder in the chemical bonding or an amorphous structure. That the film are of intrinsic nature is supported by the investigation of the stoichiometry using SEM. Examining various films, reasonably stoichiometric ratios Ga/As=1.1 have been found. However, due to the similar atomic weight of Ga and As, the stoichiometry determination with SEM is not extremely reliable and further investigations using other methods are required.
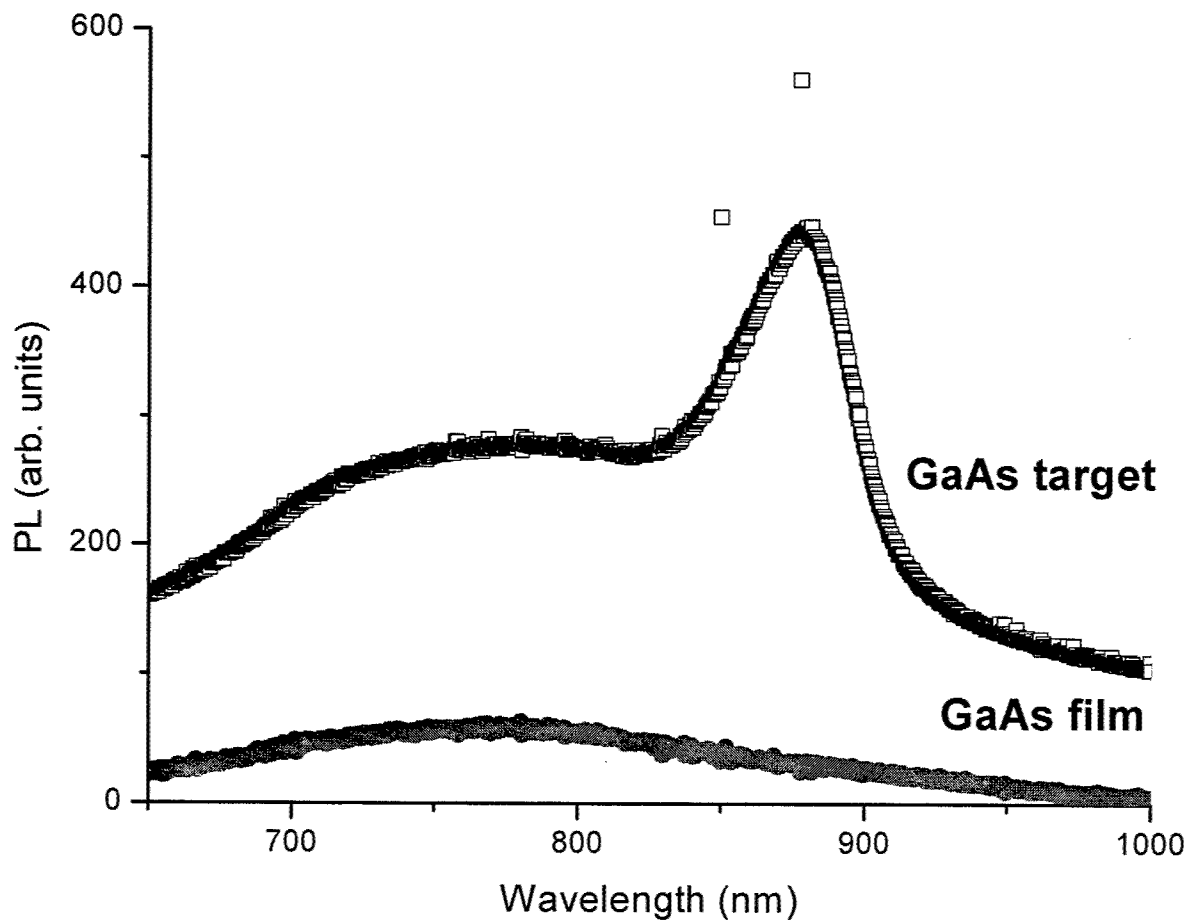
Figure 3: Film and target PL at room temperature achieved with an excitation at 532 nm. The spectra are shifted and shown in the same arbitrary units.

4. PHOTOCURRENT OF THE FILMS

The photocurrent of the film is shown in Fig. 4 for various applied electric fields. The experiments have been carried out with a Titanium:Sapphire laser pumped with a 30 W argon laser. The emission of the laser system can be tuned in the range of 790-930 nm and the impinging intensity was kept constant at 200 mW. The electric contact to the film was performed with evaporated aluminum electrodes with a gap of 1 mm between them. The bias was applied with a programmable voltage source and the photocurrent was measured with a pA-ammeter.

In many cases, the photocurrent decreases beyond the band-gap energy although the absorption increases. The contradictory behavior is caused by the increase of the recombination rate at the surface region of the material owing to dangling bonds and eventually present damages.[11] The rather flat spectra in the higher energy region in Fig. 4 indicate that in the film exhibits the same recombination rate throughout the film including the surface. Indeed, Fig. 5 shows the scanning electron microscope (SEM) picture of a typical film on glass. There is no particulate on the surface and the film is very smooth optically.
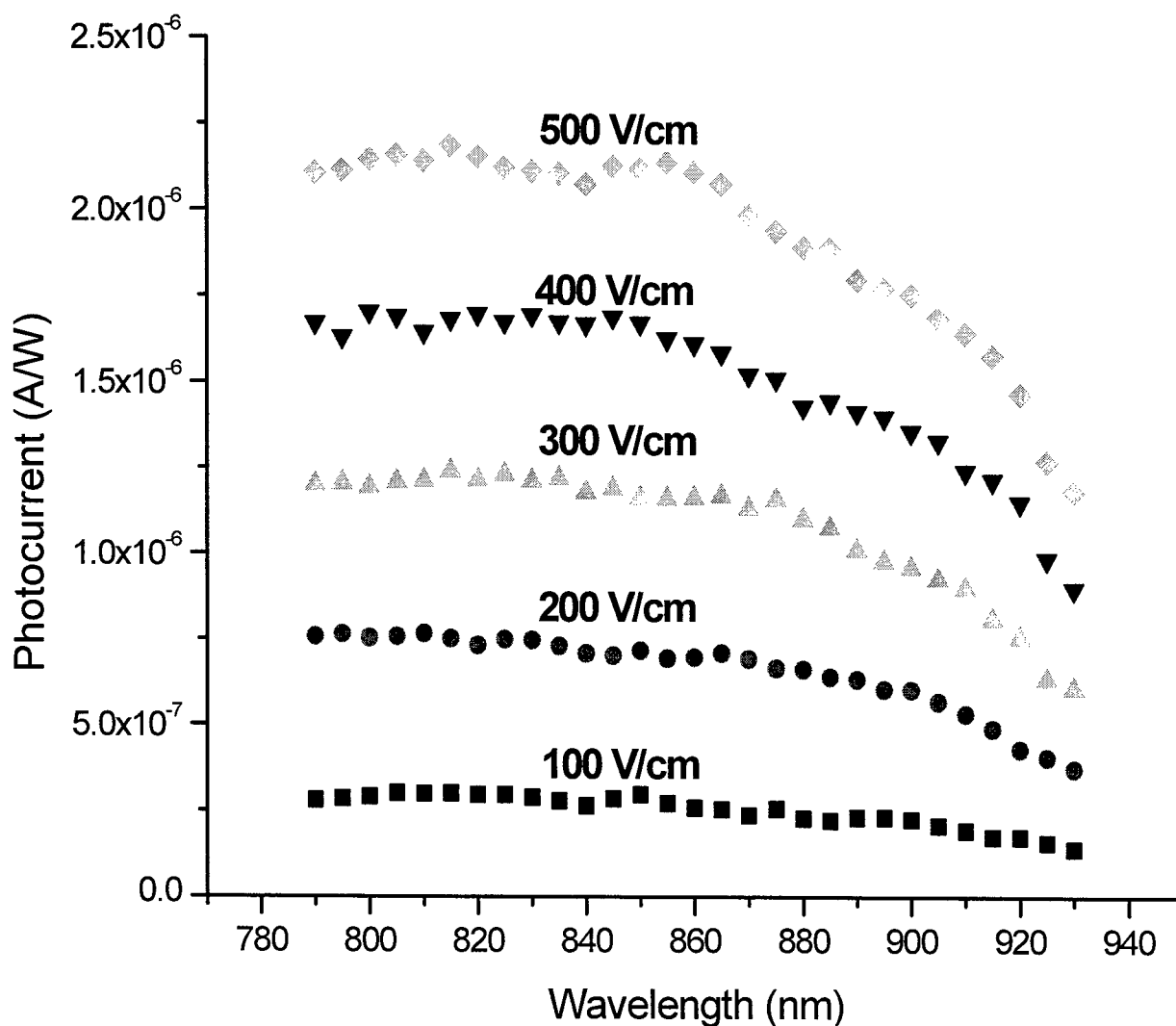
Figure 4: Photocurrent of thin film GaAs on glass at room temperature.
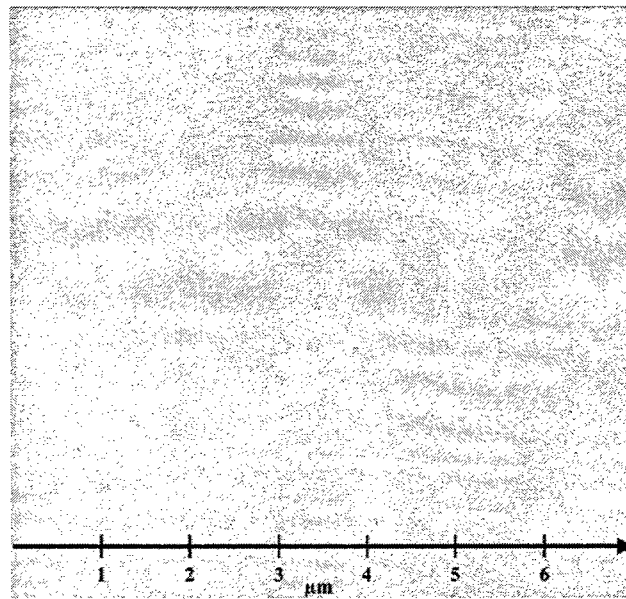
Figure 5: SEM picture of the GaAs film. Note the smoothness of the surface.

From Fig. 4 one might conclude that the slope of the absorption edge of the films is not very steep indicating tail states within the band-gap. This phenomenon of band edge flattening is known as Urbach's rule[12] and is more pronounced in thin film material than in single crystals. Figure 6 shows the transmission of the thin film and in agreement with the photocurrent spectra in Fig. 4 a rather flat rising absorption threshold is observed. The fundamental transition at 880 nm is weakly indicated by hump around 850 nm. The peak at 1000 nm does not correspond to an energy transition in the material but is caused by Fabry-Perot interference.
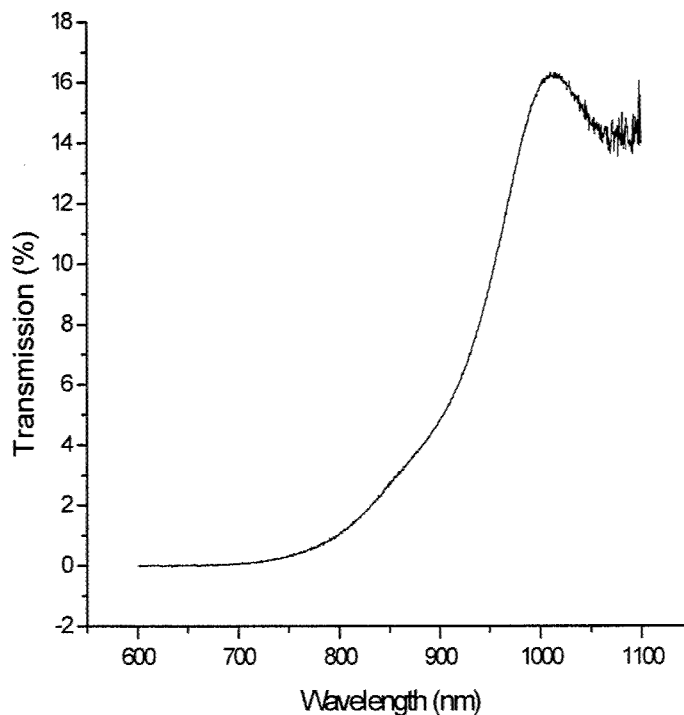
Figure 6: Transmission of thin film GaAs at room temperature. The measurement was carried out with an industrial photospectrometer.

5. STRUCTURAL PROPERTIES OF THE FILMS

The crystallographic qualities of the GaAs films were investigated by X-ray diffraction (XRD) measurements using a Rigaku diffractometer with CuKα radiation (λ=0.154054 nm). Theta-2theta scans were made in a range from 20 to 80 degree using 0.05° step size. Figure 7 shows XRD results of a θ-2θ scan. As can be seen in this figure, GaAs films grown on glass show a typical amorphous feature without evidence of crystalline structure.
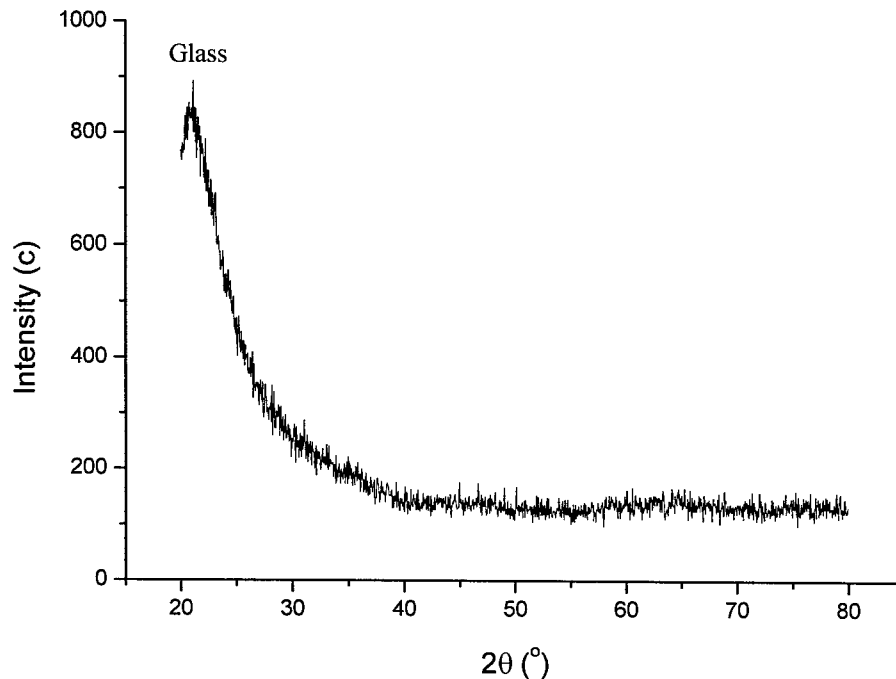
Figure 7: θ-2θ scan for a GaAs film deposited on a glass substrate.

The sample analyzed by XRD in Figure 7 was further investigated by Micro-Raman spectroscopy to obtain complementary information about crystalline distribution in the film. The system uses the 514.5 nm emission of an argon laser in a backscattering geometry. The output power of the laser was kept within 30 mW using a 50X objective with 1μm spot size and an integration time of 25 s. Measurements were taken at room temperature. Since the laser beam spot size is approximately 1 μm, micro-Raman measurements are area sensitive, especially for samples that may contain non-uniformities. By measuring several different areas on the sample, information about uniformity and crystalline distribution of the sample can be achieved.

In Raman scattering, disorder causes a breakdown of Raman selection rules and broadening of Raman peaks. Therefore, the shape and intensity ratio of phonon modes can be used to distinguish between amorphous and crystalline films. For instance, a single crystal GaAs [100]-oriented sample in the backscattering geometry only shows sharp longitudinal optical (LO) phonon mode expected around 295 cm^{-1}. The transverse optical phonon (TO) mode is forbidden on [100]-oriented films. However, the forbidden TO mode can be observed as a weak peak due to slight misorientation of a sample on occasion. Meanwhile, for the GaAs [110]-oriented single crystal, it is the other way around; the TO is allowed expected around 270 cm^{-1} and the LO is forbidden. Raman peaks from amorphous GaAs are very different from those of crystalline GaAs. For instance, Raman peaks from amorphous GaAs are very broad around 270 cm^{-1} because of disorder in a sample and the longitudinal optical phonon (LO) mode is not observable.

Figure 8 displays the Raman spectrum of a GaAs sample for the randomly selected area. The spectrum from the GaAs film shows the frequencies of approximately 270 and 295 cm^{-1}, which are the expected wave frequencies of the TO and LO Raman active phonons for crystalline GaAs, and suggesting the existence of crystal structure in the film. The presence of a strong TO peak in Figure 8 indicates that crystalline order in the film can be (110)-oriented or highly disordered (100)- orientation due to a low quality. It appears there is both a broad and sharp peak around 270 cm^{-1}. Therefore, the Raman spectrum indicates that both crystalline and amorphous volumes exist in the film, and it is hard to tell the orientation of the crystalline volume fraction with this technique.

It is not clear why XRD shows amorphous feature in the GaAs film but some crystalline features were observed in Raman measurements. However, we believe that GaAs film grown on glass substrate might be not uniform, and contains localized crystalline islands which give crystalline feature in micro-Raman measurements. The localized crystalline features however might not be strong enough to be easily detected with standard XRD measurements.
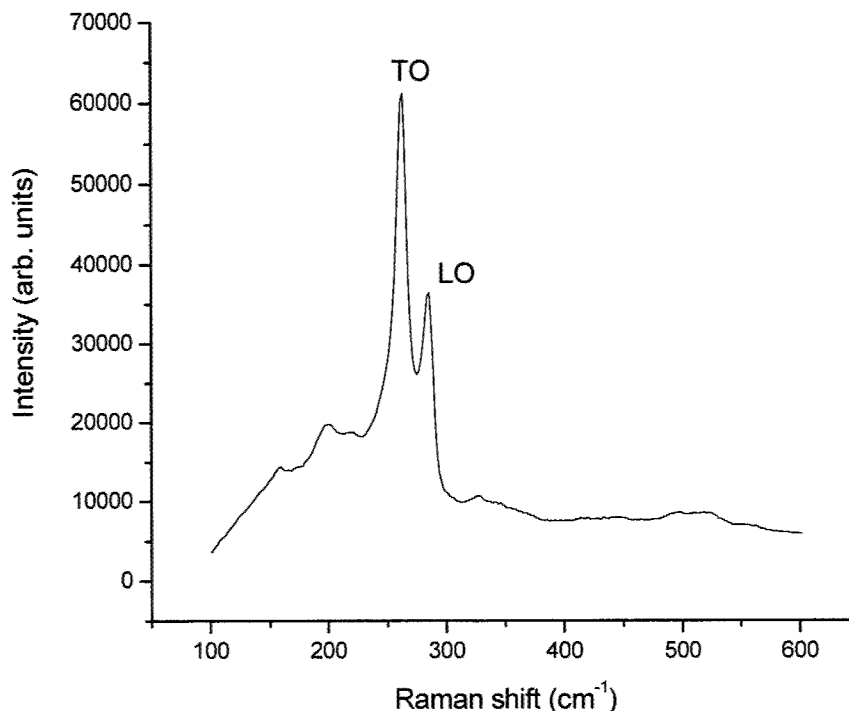
Figure 8: Raman spectrum obtained using 514.5 nm at 294 K for a GaAs film on glass substrate.

6. SUMMARY

We have presented an overview of the optoelectronic properties of thin film GaAs on glass formed by PLD. Emission, photocurrent, transmission and Raman properties have been reported at room temperature. The results address the advantage and versatility of PLD to form high quality light emitting GaAs films on amorphous and cheap substrates such as glass by fairly simple means. With respect to technological and industrial interests, it is worthwhile to stress that a large number of films can deposited out of one target. Hence, by replacing GaAs wafers by thin film GaAs on glass, the costs for electronic circuits would be drastically reduced. In order to use thin film GaAs on glass as host, films with satisfactory quality are required. On the basis of results shown in this paper, it appears that this goal is achievable with PLD.

ACKNOWLEGEMENT

REFERENCES

1. C. T. Wang (Ed.), *Semiconductor Technology*, p. 349, John Wiley & Sons, New York, 1990.
2. V. V. Mitin, V. A. Kochelap, and M. A. Stroscio, *Quantum Heterostructures*, p. 362, Cambridge, New York, 1999.
3. M. Quirk and J. Serda, *Semiconductor Manufacturing Technology*, p. 40, Prentice Hall, New Jersey, 2001.
4. J. Singh, *Semiconductor Optoelectronics*, p. 18, McGraw-Hill, New York, 1995.
5. D. B. Chrisey and G. K. Hubler (Eds.), *Pulsed Laser Deposition of Thin Films*, p. 260, John Wiley & Sons, New York, 1994
6. D. L. Smith, *Thin-film Deposition, Principles & Practice*, p. 394, MacGraw-Hill, Inc., New York, 1995.
7. B. Ullrich, R. Schroeder, H. Sakai, A. Zhang, and S. Z. D. Cheng, "Two-photon-excited green emission and its dichroic shift of oriented thin-film CdS on glass by laser deposition," *Appl. Phys. Lett.* **80**, pp. 356-358, 2002.
8. J. W. Tomm, B. Ullrich, X. G. Qiu, Y. Segawa, A. Ohtomo, M. Kawasaki, and H. Koinuma, "Optical and photoelectrical properties of oriented ZnO films," *J. Appl. Phys.* **87**, pp. 1844-1848, 2000.
9. S. Yano, R. Schroeder, B. Ullrich, and H. Sakai, "Absorption and photocurrent properties of thin film ZnS formed by pulsed-laser deposition on quartz," *Thin Solid Films* (in print).
10 S. M. Sze, Physics of Semiconductor Devices, p.13, John Wiley & Sons, New York, 1981.
11. C. Bouchenaki, B. Ullrich, J. P. Zielinger, H. N. Cong, and P. Chartier, "Preparation, characterization, and bistable photoconduction properties of thin CdS layers," *J. Opt. Soc. Am. B* **8**, pp. 691-700, 1991.
12. J. I. Pankove, *Optical Processes in Semiconductors*, p. 43, Dover Publications, Inc., New York, 1971.
13. M. Cardona (Ed.), *Light Scattering in Solids I*, p.227, Springer-Verlag, New York 1983

Laser Micromachining in the Microelectronics Industry: Emerging Applications

Pradeep K. Subrahmanyan

Electro Scientific Industries, Inc.

13900 NW Science Park Dr., Portland, OR 97007, USA

ABSTRACT

Emerging applications in the microelectronics industry impose special manufacturing requirements that are not well addressed by conventional manufacturing techniques. On the other hand, advances in laser technology, optics and beam steering combined with a better understanding of laser-material interaction make laser micromachining a viable, attractive, cost-effective and in some cases enabling technology to support these applications. This paper reviews some of the emerging applications in the microelectronics industry that are well served by laser micromachining and discusses the advancements in lasers, optics and beam steering that enable cost effective laser micromachining. It also discusses some open issues that are the subject of current and future research.

Keywords: Lasers, Micromachining, Microelectronics

1. INTRODUCTION

Various factors have been instrumental in the heightened interest in the application of laser micromachining to semiconductor manufacturing. These include developments on the laser and optics side as well as emerging applications in the semiconductor industry. We first review some of these applications, the special requirements these applications impose on the lasers, optics and beam steering, the economics of laser micromachining and finally some open issues that merit further study. The key applications in the semiconductor industry are :

- Scribing low-K dielectric materials
- Dicing thin silicon
- Drilling and slotting in thick silicon
- Dicing III-V materials
- Scribing ceramics
- Dicing released MEMS devices
- Direct write applications

For the purpose of this paper, our reference to laser micromachining will involve a beam vectoring approach. The beam vectoring approach is being accepted by the industry as the standard, and is our focus in this paper. A typical setup is illustrated in Figure 1. The vectoring setup usually comprises a high rep-rate(tens of KHz) solid-state laser steered to the work surface through a combination of stages and/or galvonometric scanners (galvos for short). The usual choice of the irradiance profile is that of a TEM_{00} Gaussian, however, certain applications demand alternate irradiance profiles. The other common technique usually comprises an excimer laser delivered to the work surface through a series of optics and masks. It involves high capital costs of the excimer, and the recurring costs of projection optics for various semiconductor designs.

Send correspondence to pks@esi.com
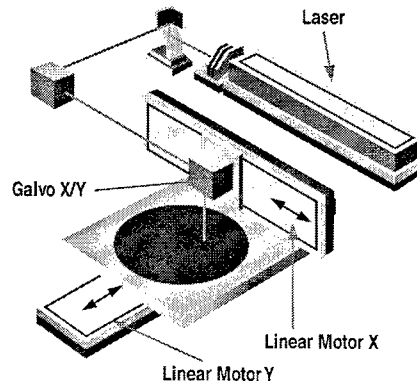
Figure 1. Schematic of a beam vectoring setup for laser micromachining

2. LASER MATERIAL INTERACTIONS

This section is meant to provide those new to the field with an understanding of the basic concepts. We further illustrate the interaction of 355 nm lasers with Silicon. Absorption of the photons emitted by the laser (3.49 ev @ 355 nm wavelengths) occurs by interaction with the valence electrons. These electrons in turn, undergo transitions between the ground and excited states. Detailed quantum mechanical models have been developed to describe the absorption process.[1]   The absorption and reflection of light propagating through a medium characterized by its complex refractive index $n - ik$, where both n and k are frequency-dependent is given by the Beer-Lambert law.[2]

$$I(z) = I_0 e^{-\alpha z} \tag{1}$$

where I_0 is the intensity at $z = 0$, and $I(z)$ is the intensity at a distance z from the origin. The attenuation coefficient

$$\alpha = \frac{4\pi k}{\lambda} \tag{2}$$

is directly proportional to the imaginary term in the refractive index and inversely proportional to the wavelength. The characteristic penetration depth is then given by $1/\alpha$. For silicon,

$$
\begin{aligned}
k \ (\lambda = 355) &= 2.92 \\
\alpha &= 0.103 \ \text{nm}^{-1} \\
\alpha^{-1} &= 9.67 \ \text{nm}
\end{aligned}
$$

the small penetration depths due to its strong absorption indicate that surface effects will dominate. In such cases, surface roughness and composition are also very important in determining the coupling of laser radiation to the substrate. Equation 1 is however valid only when I_0 is much less than the intensity at which non-linear effects may become significant. At UV wavelengths in condensed media, this limit implies $I_0 \leq 10^4$ W/cm^2. At intensities higher than this value, it is possible to involve the sequential or simultaneous absorption of two or more photons. When two-photon effects dominate, equation 1 can be used to compute $I(z)$ with α replaced by $\alpha^{(2)}$[3] where

$$\alpha^{(2)} = \text{constant} \times I_0 \tag{3}$$

so that the absorption coefficient is intensity dependent. The value of the constant is determined by factors such as the intrinsic strength of nearby one-photon transitions, the population difference between initial and final two-photon states and the frequency of the transition. Two-photon absorption coefficients have been measured for selected materials.[4] With most modern commercial lasers, multi-photon effects are important.

As an example, let us consider a 355 nm laser TEM$_{00}$ beam with an average power at 10 W at a pulse repetition frequency (PRF) of 10 KHz, with a pulse width of approximately 25 ns, and a spot size of 15 μm.

The irradiance profile for a TEM$_{00}$ Gaussian beam is given by

$$I(r) = I_0 e^{-2r^2/\omega_0^2} = \frac{2P}{\pi\omega_0^2} e^{-2r^2/\omega_0^2} \tag{4}$$

where I_0 is the irradiance at the center of the spot and ω_0 is the so-called $1/e^2$ radius of the beam where the beam irradiance has fallen to $1/e^2$ (13.5%) of its peak value (I_0). For the case of this computation, we assume further that the temporal profile of the pulse is rectangular, although in reality it is not. The resulting irradiance profile is plotted in Figure 2 and the resulting irradiance magnitudes clearly demonstrate that multi-photon effects are important. Whereas the absorption of a material is related only to the imaginary part of the complex refractive
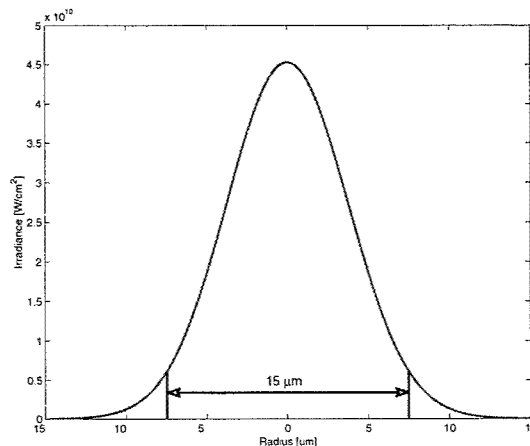
Figure 2. Example of a TEM$_{00}$ beam with a spot size of 15 μm, a pulse energy of 1000 μJ and a pulse width of 25 ns

index, the reflectivity depends on both the real and imaginary parts. For normal incident light, the reflectivity, R is computed from

$$R = \frac{(n-1)^2 + k^2}{(n+1)^2 + k^2} \tag{5}$$

To make things even more complicated, the reflectivity and absorption coefficients in Silicon are found to increase dramatically with temperature for energies between the indirect bandgap (1.12 eV) and the direct gap (3.4 eV). This is attribute to increasing phonon population at elevated temperatures with an attendant increase in the rate of indirect transitions.

The absorbed UV radiation can now interact with the substrate causing both photochemical and photothermal effects. At the high intensities obtained in today's commercial lasers as illustrated in figure 2, both effects contribute to ablation. Brannon[5] provides a qualitative understanding of UV laser-material interaction. Duley[67] provides a more rigorous reference for those interested in getting a basic understanding of the ablation mechanisms and underlying fundamental limitations. We reproduce a few excerpts of relevance for completeness here, especially relating to photothermal effects.

First, we define a few thermal properties of materials. Of specific importance is the thermal diffusivity κ,

$$\kappa = l_{\mathrm{mfp}} v = \frac{K}{\rho C_p} \tag{6}$$

where K is the thermal conductivity in W/mK, ρ is the density in Kg/m^3 and C_p is the specific heat in J/KgK. We can now compute the thermal diffusion length given by

$$L = \sqrt{4\kappa\tau} \tag{7}$$

where τ is the time of interest (i.e., pulse width for example). For silicon, $\kappa = 0.866 \ cm^2/s$ and L = 2.94 μm at a pulse width of 25 ns. For most purposes, the interaction of a laser pulse with the substrate can be treated

as an axisymmetric problem. The temperature T as a function of spatial coordinates distance r and z into the substrate can be obtained by solving the heat equation[8]

$$\rho C_p \frac{\partial T(r,z,t)}{\partial t} = K(t)\nabla^2 T + A(r,z,t) \tag{8}$$

subject to appropriate boundary conditions, where A is the heat source term due to the laser pulse. Excited electron states decay into phonons rapidly causing heating of the substrate. This raises the surface temperature very rapidly at heating rates on the order of 10^{10} K/s. In most cases, especially in the case of silicon, all the laser radiation is converted to heat in a time far shorter than the time for the heat to diffuse one absorption depth. In such a case

$$A(z,t) = (1-R)I(r,t)\alpha e^{-\alpha z} \tag{9}$$

We usually obtain the solution to the the 2-D form of the heat equation (axisymmetric) numerically. A typical temperature distribution in the case of machining thin silicon is illustrated in figure 3.
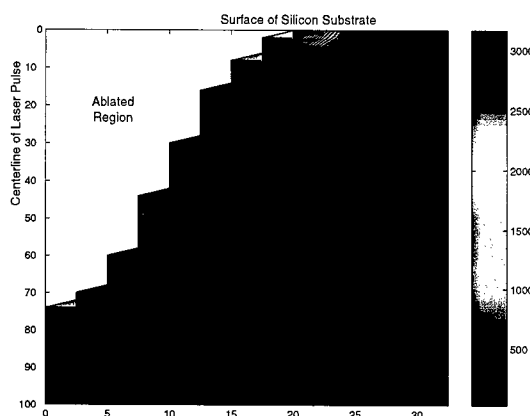
Figure 3. Numerical solution to the 2-D heat equation illustrated on a semi-infinite piece of silicon. A Gaussian laser pulse with pulse parameters using commercially available lasers is used in the simulation.[9] Notice the Heat affected zone (HAZ) is restricted to tens of μm.

3. APPLICATIONS

In this section, we discuss four key applications, each of which has different demands on laser micromachining.

3.1. Low-K Dielectric Scribing

The semiconductor industry is quickly approaching a point at which conventional silicon dioxide dielectrics are inadequate for the job for which they are intended: insulating metal interconnects in an ever-increasing scale of integration and increased speed as well. A cross-section SEM image of a processed wafer is reproduced in Figure 4 from the Intel Technology Journal.[10] Figure 4 is a 6-high stack. Intel has already made public its move to a 7-high stack at the 90 nm node. Figure 4 also serves to illustrate the interconnect problems faced by the industry. It lies in the resistance-capacitance (RC) delay that slows down processing due to the increased capacitance as wires crowd closer together. An insulator with a lower dielectric constant (κ) than the value of 4.2-4.5 for silicon dioxide is required primarily for the realization of the full benefits of copper dual-Damascene technology. Low-K materials, Fluorinated Silicate Glass (FSG), with κ=3.7 have been in production since the 250 nm node and were introduced into the 180 nm node with copper dual Damascene. The measurable performance benefit derived from FSG spurred the aggressive introduction of lower-κ materials (κ ¡ 3.0) at the 130 nm node with organic spin-on polymers (SOP) and both spin-on and PECVD inorganic/organic hybrid materials. A roadmap of low-κ dielectric technology is reproduced from the "International Technology Roadmap for Semiconductors, ITRS 2001"[11] in Figure 5.
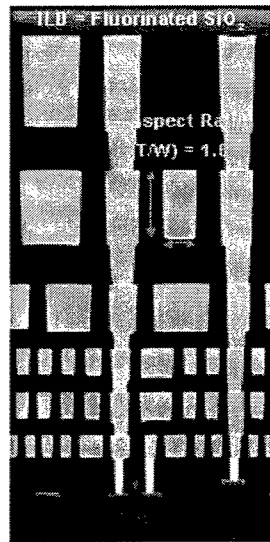
Figure 4. Cross-section SEM Image of a Low-κ dielectric/metal stack reproduced from Thompson *etal.*[11]

However, the integration of new low-κ dielectrics needed for performance enhancement bring numerous reliability concerns that include thermally or mechanically-induced cracking or adhesion loss, poor mechanical strength, moisture absorption, time-dependent behavior leading to reliability concerns, texture effects and poor thermal conductivity. Of these, the thermally or mechanically induced cracking/adhesion loss and moisture absorption are key limitations to the use of existing singulation technology. With dicing saws, large tensile and shear stresses are imparted at the cut zone which lead to significant cracking and adhesion loss leading to delamination of the metal and low-κ layers. Besides, the use of coolant during the sawing process leads to moisture absorption and a time-dependent behavior. One approach to reduce the mechanically induced delamination is by reducing the saw speed, thus hindering the throughput and productivity significantly. However, problems with moisture absorption and yield still remain. The industry has been looking for a technology alternative that could eliminate the issues with mechanical dicing saws. Besides the move to lower κ materials, which is driving the industry to look for alternate technology, the increase in the number of layers is another contributing factor as well. Alternate technologies under evaluation include laser ablation, and dry etching. Dry etching has other problems with preferential etches in the lateral direction due to the multiple layers of metal and low-κ dielectric. Issues with the laser include thermally induced delamination and cracking, however, these are being resolved and laser scribing appears to be the best positioned to succeed.

There are two flavors of low-κ scribing. These are illustrated in Figure 6. In the first scheme, two laser scribes are laid out on either side of the street. Streets are usually wide since low-κ dielectrics are at least initially finding application in logic elements such as microprocessors which have significant test structures in the streets. The laser scribing scribes through the low-κ metal stack and stops at the silicon. The sawing process cuts through the center of the street and cuts through the low-κ metal stack and the silicon and singulates the wafer. In this approach, cracks could exist in the street between the saw kerf and the laser kerf, but the laser kerf serves as a crack stop and ensures that these cracks do not propagate into the dice and affect the electrical performance of the integrated circuit.

In the second scheme, the laser kerf is laid down the center of the street to be wider than the saw kerf by about 10 μm. Again, the laser scribes through the low-κ and the metal layers and stops at the silicon. Following the laser scribe, the saw cuts through the silicon and singulates the wafer. This scheme has the added advantage of ensuring that the saw blade does not get loaded by soft dielectrics that might be used, thus ensuring lower cost of operation and better reliability of the sawing process itself. The disadvantage however is the requirement of a fairly wide trench to be cut in the low-κ metal stack ($¿$ 85 μm). Figure 7 illustrates the second approach with a scanning electron micrograph (SEM). The low-κ dielectric scribing application is a classic one that involves

Low-K Technology Roadmap

| | 2001 | 2003 | 2005 | 2007 | 2009 | 2011 | 2013 |

Porous Organic Polymer
Porous Inorganic
Porous Organic Polymer
Organosilicate Glass
Porous Inorganic
Organic Polymer
Porous Organic Polymer
Organosilicate Glass
Organic Polymer
Organic Polymer
Methyl Silsesquioxane
Hydrogen Silsesquioxane
Fluorinated Silicate Glass
Silicon Carbide
Silicon Dioxide
Silicon Carbide
Silicon Nitride

▦ Research   ■ Development   ☐ Qualification

Figure 5. Low κ technology roadmap reproduced from ITRS 2001[11]
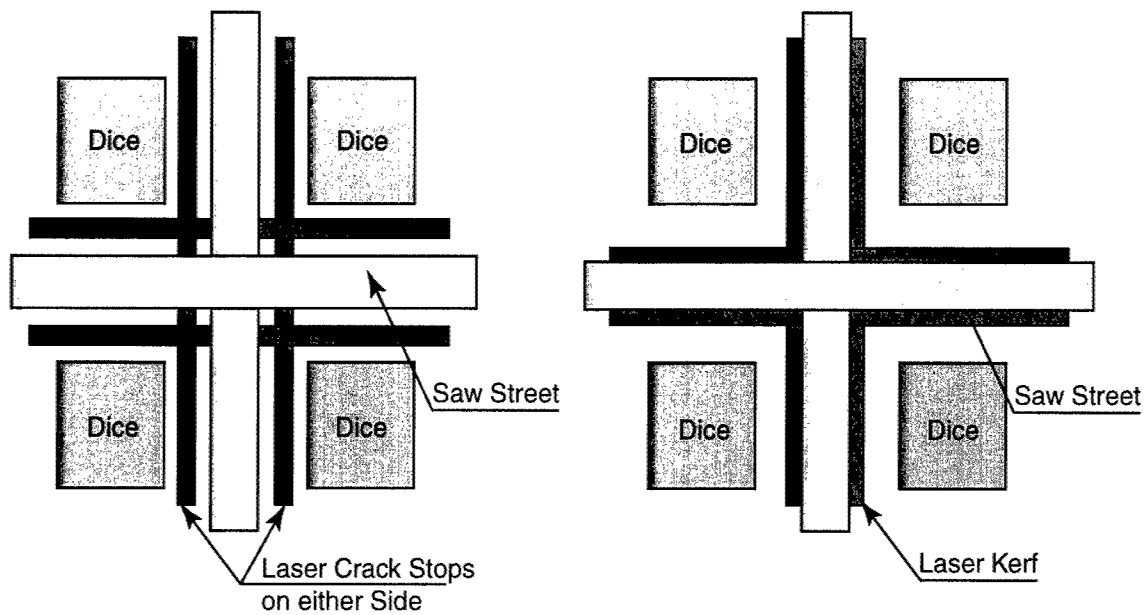
Figure 6. Two low-κ dielectric scribing schemes. On the left is shown a scheme where the laser scribes on either side of the saw street, and any cracks that emanate from the subsequent sawing down the center stop at the laser scribe. On the right is shown a scribe whose width is larger than the saw blade width. This scheme also helps avoid loading the saw while dicing soft dielectric materials.
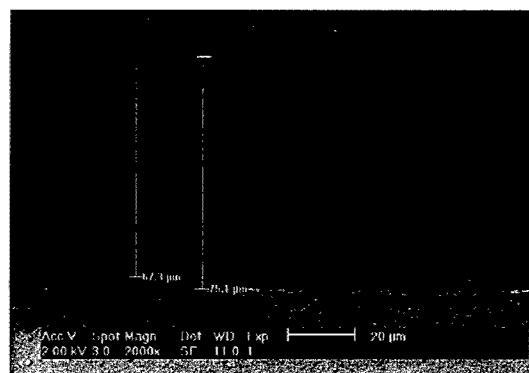
Figure 7. SEM of a trench cut in a low-K dielectric stack. Note the clean edges and the lack of delamination.

lasers, optics, laser-material interaction, heat-transfer and elasticity theories. To get an appreciation for the problem, consider the use of a Gaussian profile as shown in Figure 2 to machine the trench shown in Figure 7. The width of the trench needs to accomodate the subsequent dicing process and is usually not achieved by a single run of the Gaussian beam over the substrate. Figure 8 illustrates three runs of a Gaussian beam side by side to achieve the desired width of the trench. The width is set by the ablation threshold of the stack (denoted by I_{th}. However, the Gaussian has the side-effect of providing a heat source outside the region to be ablated due to its tails. The source term for the heat equation due to these tails can be removed by use of a different irradiance profile, such as a top-hat profile whose width is tailored to be the desired width of the trench. This
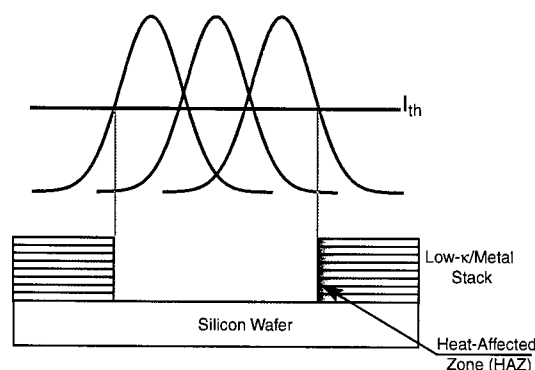
Figure 8. Illustration of the heat affected zone due to heating by the tails of the Gaussian beam while machining a trench in a low-κ dielectric stack.

brings with it additional considerations due to the increased thermal gradients which lead to delamination due to residual thermal stresses in the stack. Proprietary techniques have been developed which allow machining of low-κ dielectric materials without cracking and delamination to produce the clean trenches illustrated in Figure 7. Laser ablation for low-κ dielectric scribing is actually both an enabling and cost-effective solution.

3.2. Thin Silicon Dicing

The semiconductor industry is working towards thin silicon in various areas. Most of the semiconductor circuits are formed on silicon on a very thin epitaxial layer. The bulk of the silicon in the wafer really plays no role in the performance of the circuit and in some cases actually hinders good performance of the circuit. In most cases, the thickness of the silicon is decided by the diameter of the wafer. Typically 200 mm wafers are 625 μm thick while 300 mm wafers are 750 μm thick. The thickness is decided by the need to preserve mechanical integrity of the wafer during the sawing of the wafer from the silicon crystal and subsequent processing to develop the integrated circuits. There are three main drivers behind the move to thin silicon :

- First, there is a slowdown in the ability to decrease the size of the transistors, since a lot of the technologies are reaching the end of the road. Given the fact that the areal density of an integrated circuit can only go so far, efforts are being made to stack the circuits, so there is vertical growth of packages.

- Second, in power-hungry devices such as RF circuits and power devices, there is a need to get the circuits closer to the heat sinks. Silicon's thermal conductivity is about 50 % that of Aluminum and 35 % that of copper. The ability of such circuits to withstand large currents and high frequencies is going to be dictated by their ability to conduct heat away from the active area. This is made possible by moving the device closer to the metal heat sink by reducing the thickness of the silicon.

- Third, in the proliferating market of smart cards, there exists a need to get thin circuits so they can be laminated onto a plastic card - the thickness requirement here is completely due to form factor and reliability due to the reduced flexural stresses.

Thinning is typically done on the backside of the wafer and can be done either prior to or after IC fabrication. For our purpose, we classify anything less than 200 μm thick to be thin silicon. At larger wafer diameters that are required for economy of production, it becomes very hard to handle thin silicon wafers reliably. So, the thinning is done subsequent to the IC fabrication. However, the industry is struggling with problems in the singulation of such wafers. Normally, silicon wafers are sawed using a diamond saw. As the thickness of the silicon decreases, there is an increase in the vibration of the wafer during the sawing. This leads to problems with chipping and breaking of the dice. The industry has been seeking either extensions of sawing technology or technology alternatives to improve throughput and yield during the singulation process. One of the early technologies that was proposed as a solution is the "Dicing Before Grind (DBG)", patented by Mitsubishi and licensed by Disco. Here, the wafer is partially diced subsequent to IC fabrication and prior to grinding the backside. The depth of dicing is more than the desired final thickness of the wafer. During the grinding process on the backside, the wafer is mounted on a film frame and the dice become fully singulated when ground to final desired thickness. This approach does not work very well for thickness of the silicon below 150 μm due to a significant amount of backside chipping during the grinding process.
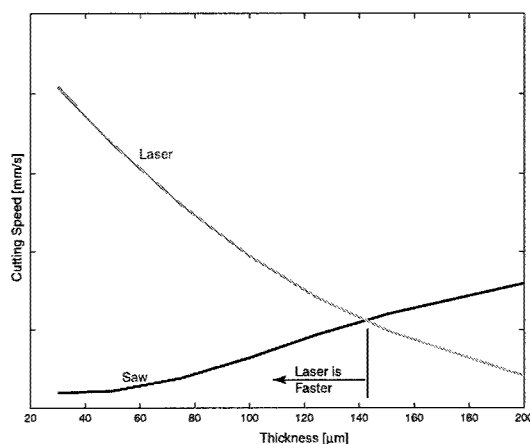
Figure 9. Thin Silicon Cutting Speeds - Comparison of laser and saw cutting speeds. The actual numbers have not been reported to preserve confidentiality. The graph shows the laser delivering higher throughput for thickness below 150 μm.

As wafers become thinner, the smaller aspect ratio actually works to the advantage of the laser, and the laser delivers a higher throughput as illustrated in Figure 9. The other important requirement in dicing thin silicon is to ensure minimal interaction with the tape, since these wafers are usually mounted on tape frames prior to dicing. Manufacturers such as Lintec already offer polyolefin tape for use with UV lasers. However, care needs to be taken while setting up the process recipe to ensure minimal interaction of the laser with the tape while ensuring complete singulation of the dice. Again, with productivity gains by going to thinner silicon, laser ablation is turning out to be the process of choice for dicing thin wafers.

3.3. Compound Semiconductor Scribing and Dicing

Compound semiconductors are starting to find increased application in RF and optical devices. The biggest application is in the light emitting diode (LED) market where the substrates used are Gallium Arsenide (GaAs), Sapphire, Gallium Phosphide (GaP), and Silicon Carbide (SiC). In these applications, the cost of the substrate is high and the value of the wafers following epitaxy is even higher. However, due to the hexagonal symmetry, mechanical scribe and break leads to poor yield. Sawing on the other hand uses up too much valuable real estate that could otherwise be used to make real devices. The key here is the ability to maintain optical quality of the surfaces. This is best done by applying sacrificial layers of material such as photoresist or poly-vinyl alcohol (PVA) to the surface prior to laser ablation followed by stripping of the layer. Again, minimal tape interaction is a requirement, especially given the transparent characteristics of some of the substrates at UV wavelengths.

3.4. Thick Silicon Slotting & Via Drilling

In thick silicon, the biggest applications are in creating slots for ink ject cartridges and for via drilling. The inkjet printing industry is undergoing rapid technology changes to keep pace with the consumer demand. One of the biggest demands has resulted from the proliferation of digital cameras and images in digital form. The average customer now wants to process images digitally while still retaining the ability to generate prints. Key to the success of digital photography and digital image editing has been the inkjet printing industry, which has managed to increase the resolution of affordable color printers to produce photographic quality prints at reasonable speeds. Current day photographic quality printing cartridges boast of an impressive 4800x1200 dots per inch (DPI). To keep pace with an aggressive DPI roadmap, the inkjet cartridge industry has had to place more than a thousand nozzles per head and have firing speeds up to 40,000 drops/second. The requirement of higher DPI in the cartridges lends to a rethinking of the manufacturing paradigm.

During operation of the cartridge, the ink from the ink well flows into a slot from where it is sucked or forced into various channels and directed to the print surface through a nozzle. The slot is machined into the silicon itself and various circuit elements responsible for the firing of the nozzle are fabricated right next to the slot. In fact the manufacturing operation is sequenced in such a manner that the slotting operation is done after all the circuit are formed. Current technology uses grit blasting to fabricate these slots. In this procedure, highly pressurized grit is forced through a ceramic nozzle that is held right over the wafer surface. This is a dirty, mechanical process that reduces the yield and causes defects such as chipping in the slot as well. It is also limited in placement accuracy, and offers poor process control over the shape and size of the slot due to wear and tear of the nozzle itself by the abrasive action of the grit. As the DPI increases, the length of the channels from the slot to the nozzles needs to be controlled, and the aforesaid problems with grit blasting form a technology/productivity barrier. The industry has been evaluating alternative approaches to the problem of slotting. They expect good slot quality, no chipping or cracking, good control over slot placement and good process control. The key here is in the ability to deliver throughput exceeding that of grit blasting machines and offering all the advantages of better process control and better placement.

The market for drilling interconnect vias (in Si ICs and Si interposers) is beginning to emerge. A small number of customers have expressed interest in this area. Applications for interconnect vias are varied and include laying ground planes on the back side, provision for an optical interconnect, chip scale packaging etc. Customers are in the early stages of development for these products.

REFERENCES

1. G. Herzberg, *Electronic Spectra and Electronic Structure of Polyatomic Molecules*, Van Nostrand Reinhold, 1966.
2. J. Birks, *Photophysics of Aromatic Molecules*, Wiley-Interscience, London, 1970.
3. A. Yariv, *Quantum Electronics*, John Wiley & Sons, New York, third edition ed., 1989.
4. D. Friedrich, "Two-photon molecular spectroscopy," *Journal of Chemical Education* **59**, p. 472, 1982.
5. J. Brannon, *Excimer Laser Ablation and Etching*, no. M-10, American Vacuum Society, 1993.
6. W. Duley, *UV Lasers : Effects & Applications in Materials Science*, Cambridge University Press, 1996.
7. W. Duley, *CO_2 Lasers : Effects & Applications*, Academic Press, New York, 1976.
8. J. Ready, *Effects of High Power Laser Radiation*, Academic Press, New York, 1971.
9. Y. Sun, "Simulation of laser ablation - private conversations." 2002.
10. S. Thompson, M. Alavi, M. Hussein, P. Jacob, C. Kenyon, P. Moon, M. Prince, S. Sivakumar, S. Tyagi, and M. Bohr, "130,nm logic technology featuring 60,nm transistors, low-k dielectrics, and cu interconnects," *Intel Technology Journal* **6**, pp. 5–13, May 2002.
11. Sematech, "International technology roadmap for semiconductors - interconnect," tech. rep., 2001.

CAD/CAM software for an industrial laser manufacturing tool

Ines Stassen Böhlen[a], Jim Fieret[a], Andrew Holmes[b], Kin Wei Lee[b]
[a]Exitech Ltd., Oxford Industrial Park, Yarnton, Oxford OX5 1QU, UK;
[b]Imperial College of Science, Technology and Medicine, Dept. of Electrical
and Electronic Engineering, Exhibition Road, London SW7 2BT, UK

ABSTRACT

A facility for rapid prototyping of MEMS devices is crucial for the development of novel miniaturised components in all sectors of high-tech industry, e.g. telecommunications, information technology, micro-optics and aerospace. To overcome the disadvantages of existing techniques in terms of cost and flexibility, a new approach has been taken to provide a tool for rapid prototyping and small-scale production: Complex CAD/CAM software has been developed that automatically generates the tool paths according to a CAD drawing of the MEMS device. As laser ablation is a much more complicated process than mechanical machining, for which such software has already been in use for many years, the generation of these tool paths relies not only on geometric considerations, but also on a sophisticated simulation module taking into account various material and laser parameters and micro-effects. The following laser machining options have been implemented: cutting, hole drilling, slot cutting, 2D area clearing, pocketing and 2½D surface machining. Once the tool paths are available, a post processor translates this information into CNC commands that control a scanner head. This scanner head then guides the beam of a UV solid-state laser to machine the desired structure by direct laser ablation.

Keywords: Laser micromachining, rapid prototyping, UV solid-state laser, CAD/CAM laser processing software

1. INTRODUCTION

The vision is old: You design your 2½D-device in a CAD-program, you select the material and the laser parameters, and some clever software generates the code for the laser machine to produce your device. This would open up many possibilities for rapid prototyping and small-scale production and give you finally the full flexibility you expect from a laser tool.

The vision is old – and has years ago been realized for other tools such as mills and routers. Even for certain operations of a laser, e.g. welding and cutting, such software has been developed. But if you want to use the laser like a milling tool and machine pockets and 2½D structures, things become more complex; a simulation module is needed to be able to predict the result of a certain machining operation.

We have tackled this problem, using existing CAD/CAM software (alphaCAM by Licom Systems Ltd.) as a basis for our graphical user interface (GUI). Using the application programming interface (API) to communicate with the alphaCAM software, we generate our own tool paths. For the simpler machining operations as hole drilling and slot cutting, we have incorporated our experience with different machining strategies and provide a high degree of flexibility to make it easy to experiment with different parameter sets; our area clearing function is able to process extensive and complex structures; for the most complex machining operations – pocketing and 2½D surface machining – we rely furthermore on our simulation module for feedback on the effect of machining along the envisaged tool paths. Once the tool paths are generated, they are translated into CNC commands.

Our CAD/CAM software LaseCAM has been developed for a purpose-built laser micromachining tool, the Exitech M1000. The main features of this tool are: A small footprint, a UV solid-state laser and a scanner head with a short focal length f-theta lens to achieve spot sizes of a few μm. But the LaseCAM software is not restricted to the use with this particular tool: it has already been widely used on other systems with or without scanner head and with lasers of various wavelengths.

2. LASER ABLATION VERSUS MILLING

Laser ablation as a process has many advantages over mechanical machining, certainly in the area of micromachining. Apart from being a non-contact technique, it allows a wide range of materials to be machined and very small dimensions and high resolution and accuracy to be achieved. Open tool paths are easily achieved by simply switching the laser off while moving to the starting point of the next tool path rather than lifting the tool out of the workpiece. And it is not necessary to drill pilot holes in order to move the tool into position in the first place.

On the other hand, laser ablation is a much more complex process than for example milling. Figure 1 illustrates in a schematic and simplified way the differences between milling and laser ablation. Whereas with milling, the result of a
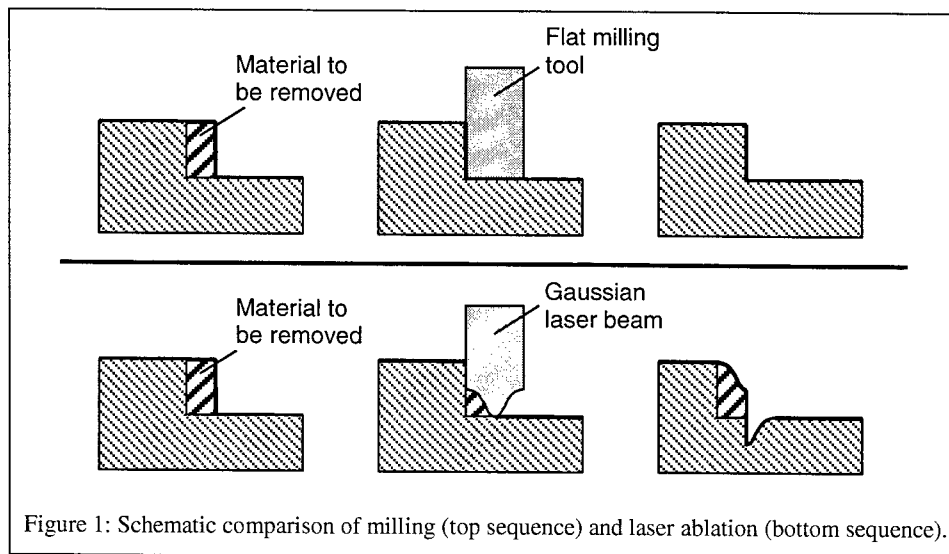
Figure 1: Schematic comparison of milling (top sequence) and laser ablation (bottom sequence).

machining operation is completely determined by the geometry and the position of the tool, this is not so with laser ablation. One fundamental issue is the depth control: Given the length of a milling tool you can easily position it so that it will remove material exactly down to a predefined absolute z-level. A laser beam, however, machines down to a certain depth relative to the surface – wherever the surface is. In particular, overlap of tool paths results in extra depth. Similarly, with milling the profile of the cut is entirely determined by the shape of the milling tool. With laser ablation, on the other hand, there are many factors that influence the profile of the cut: The beam profile and shape, laser parameters such as the pulse repetition rate and the shot overlap, physical properties of the material (e.g. optical penetration depth, thermal diffusivity), the curvature of the tool path (the cut will be deeper at the inside of a curve due to higher shot overlap) and the shape of the surface of the substrate.

To sum up: There is no way of determining the result of laser ablation along a given tool path other than simulating shot by shot what happens to the work piece. And if you cannot predict what happens if you machine along a given tool path, there is no way to find the tool paths for producing a predefined shape.

3. SIMULATION MODULE

The role of the simulation module is to predict the shape of the surface remaining after a specified machining operation, given information about the initial surface shape, the material ablation characteristics, the tool path, the laser parameters and the beam delivery optics. As noted above, the only general approach to this problem is to consider the effect of each successive pulse on the evolving surface. An important consideration here is that the volume of material removed by each pulse is very small, so that for structures of any practical use the number of shots required is typically very large (often in excess of 10^6). Consequently, simulations based on run-time implementation of semi-rigorous physical models of the ablation process can be ruled out on grounds of computation time. Such models have been used extensively in the

past by researchers to explain observations of ablation by plane illuminating beams [1,2]; however, for an industrial prototyping tool where the operator is looking for immediate feedback, much faster calculations are required. Our current approach is to propagate the surface in response to each pulse using an etch function that relates the material removal rate to the local fluence and surface orientation. This etch function may be derived from experimental measurements or from physical modelling. The key steps in the simulation process are outlined below.

The first task is to determine the fluence distribution over the illuminated region of the surface. The normal approach for direct-write machining of a complex structure is to remove material layer by layer. In this case the focus is normally adjusted for each successive layer so that the average surface level of the region to be machined corresponds to the focal plane of the optical system. The fluence in the vicinity of this plane may be determined by classical imaging theory; furthermore, for the important case of a focussed solid-state laser beam, a Gaussian profile may be assumed with good results. Calculation of the fluence over a 3D region around the focal spot allows for local height variations in the surface. This is necessary in regions where there are large height variations (e.g. at steps in the machined surface), because the fluence is reduced and the spot size is increased outside the focal plane. The fluence calculation ignores the presence of the workpiece, and consequently it only needs to be done once for a given optical set-up (i.e. combination laser beam profile, aperture if applicable, and lens).

Once the fluence distribution is known, the local material removal rate is estimated based on the etch function of the material in question. In the simplest case, a classical *Beer's law* ablation curve is assumed, i.e.

$$d = \begin{cases} \dfrac{1}{\alpha} \ln\left(\dfrac{F}{F_T} \right) & F > F_T \\ 0 & \text{otherwise} \end{cases}$$

where d is the depth to which material is removed, and F is the fluence at normal incidence. This kind of etch function is specified by just two parameters: an effective absorption length α and a threshold fluence F_T. Alternatively, more realistic ablation curves - either measured or generated by physical modelling - can be stored as data pairs. Some account has to be taken of the angle of incidence, and in the absence of measured data we simply take the component of fluence in the direction of the local normal to the surface. This assumption has been used previously when modelling excimer laser ablation of microstructures, and has been shown to give reasonable agreement with experiment, at least for some common polymer materials [3,4]. A third option for estimating material removal, which we have not yet implemented, would be to store measured single pulse ablation crater profiles, covering a range of spot sizes and pulse energies. This would clearly require more data storage, but would be expected to yield the most accurate simulation results.

For the purposes of simulation, the surface is described by a rectangular matrix containing the surface height at each point on a rectangular grid. For each incident pulse, the sub-set of points on the surface that is affected by material removal is determined (i.e. points for which the normal component of fluence is above threshold), and only these points are processed. Each point is propagated in the direction of the local normal by a distance corresponding to the local etch depth. For example, in the case of a simulation based on Beer's law ablation curves, the point with position vector **S** on the surface moves to **S'** where:

$$\mathbf{S'} = \mathbf{S} + \frac{1}{\alpha} \ln\left(\frac{F \cdot \hat{\mathbf{n}}}{F_T} \right) \hat{\mathbf{n}}$$

$\hat{\mathbf{n}}$ being the local unit normal into the surface. Interpolation is used to move the propagated points **S'** back onto the original regular grid before arrival of the next pulse.

The simulation approach just described, while fast, clearly contains many simplifying assumptions. Most importantly,
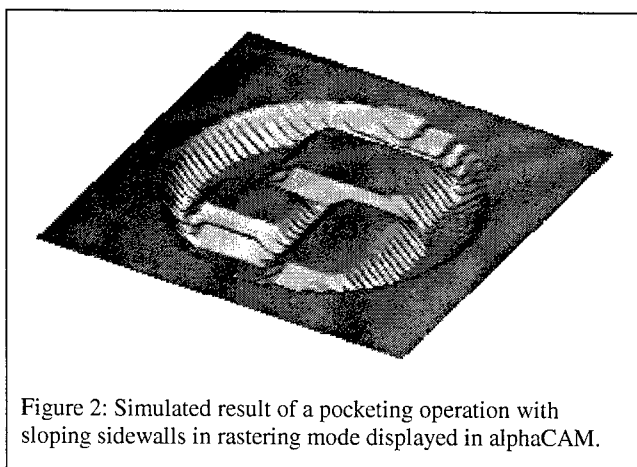
Figure 2: Simulated result of a pocketing operation with sloping sidewalls in rastering mode displayed in alphaCAM.

we neglect the possibility that reflections from the directly illuminated region may cause material removal elsewhere on the surface. This is reasonable on parts of the surface that are almost normal to the incident beam, but is likely to break down in steeply sloping regions. Consequently, the simulator predictions are expected to be less accurate in the vicinity of steps in the surface, and in cavities with high aspect ratios (i.e. ratios of depth to width). On the other hand, the simulator should perform well on the bottom surface of an open cavity, making it useful for optimising the tool path to remove unwanted surface height fluctuations arising from the beam profile and pulse overlap.

4. TOOL PATH GENERATION

When going from a CAD drawing of the desired device to the CNC commands that will produce this device, tool paths – curves along which the tool will move – are generated as an intermediate step. As we generate these curves, we have to take into account the width of the cut in order to compensate for it.

4.1 Cutting
In terms of tool path generation, cutting is certainly the easiest machining option. According to the width of the cut and the machining side defined by the user, the cut is offset from the contours defined by the CAD drawing. Applications are widespread; one example is the manufacture of the apertures used on the Exitech M1000.

4.2 Hole drilling
Drilling micro-holes has many applications, such as fuel injector systems, probe cards and vias in silicon and ceramics.

Unlike a mechanical drill, the laser beam has often a smaller diameter than the hole to be drilled and more sophisticated techniques than percussion drilling are used. When using helical trepanning, an incoming and an outgoing arc are added
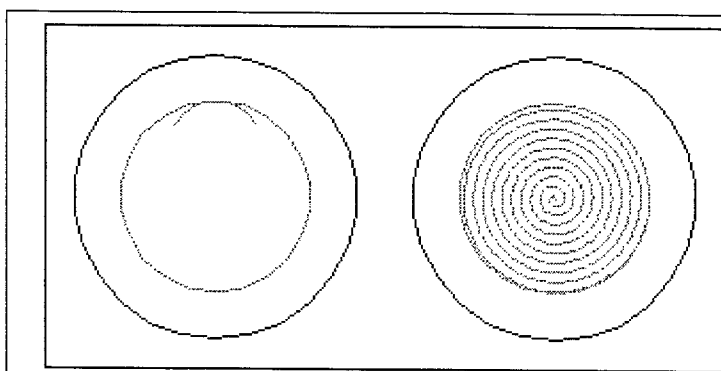
Figure 3: Tool paths for trepanning (left) and spiraling (right).

40 μm
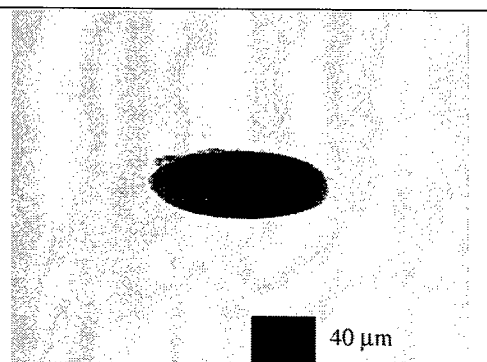
Figure 4: ∅ 107 μm hole drilled in silicon.

to achieve good edge quality. A spiraling technique is used to remove the material starting at the centre of the hole; this avoids a deep narrow cut along the edge, out of which it is hard to expel further material. These techniques are well known, but our software makes it easy to adjust various parameters (e.g. the number of revolutions of the spiral) and to try the new configuration by translating it directly into scanner commands.

4.3 Slot cutting

Figure 5: Tool path (grey) for rastering a slot (black).

Figure 6: Slot cut in Silicon using the rastering technique.
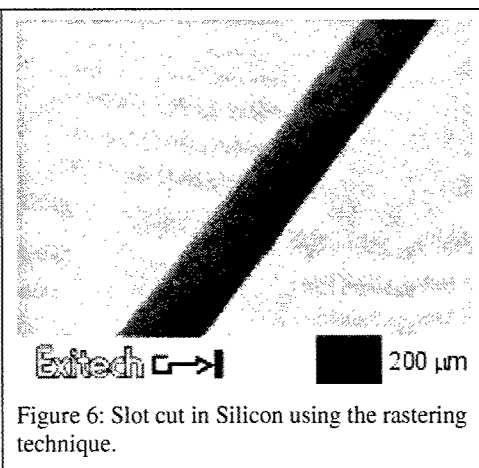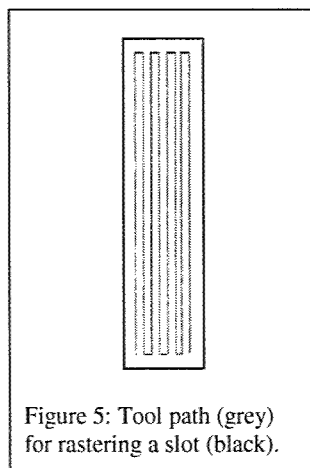
In many cases, the most efficient way to machine a slot is not cutting along its edges, but raster scanning the whole slot. This technique is the analogue to the spiraling technique for hole drilling and has the same effect: Material is removed from the whole area of the slot in order to avoid a narrow cut. Again, it is not the technique itself that is innovative, but the ease of use and convenience provided by our software.

As an example of an application for slot cutting we can mention the machining of ink feeding slots for ink jet printer heads.

4.4 2D area clearing

2D area clearing is mainly used for single shot processes where no depth control is required, e.g. for patterning of transparent conductive oxide (TCO) layers on glass or flexible substrates as required for flat panel displays.

Tool paths are generated that allow all the material in the areas defined by the borderlines in the CAD drawing to be removed. In the case of nested borderlines, we build up a tree structure reflecting which borderline is inside which. This allows us to identify the different regions, each of which is delimited by an outer border and possibly contains islands. The user can choose the distance between the cuts according to the size of the beam and select between a rastering (Figure 8) and a contouring option (Figure 11).
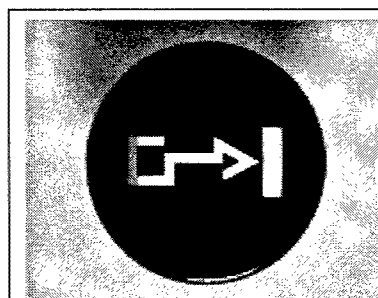
Figure 7: Back-lit panel display button (black paint on clear plastic).
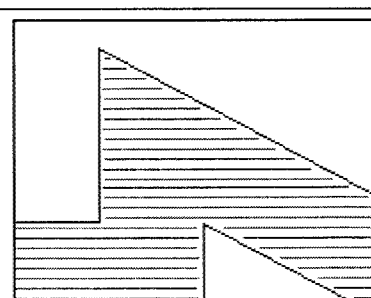
Figure 8: Tool paths (grey) for machining the logo in Figure 7 (detail). Rastering mode.
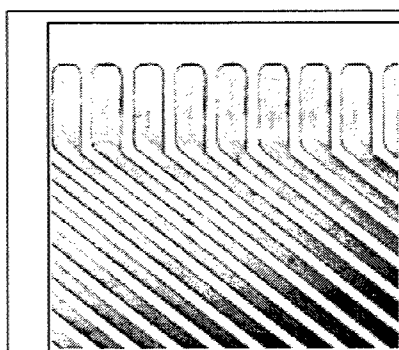
Figure 9: Fan-outs machined into TCO on display panel.
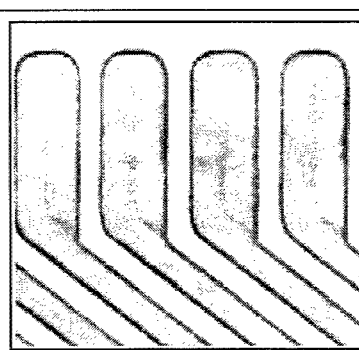
Figure 10: Detail of Figure 9.
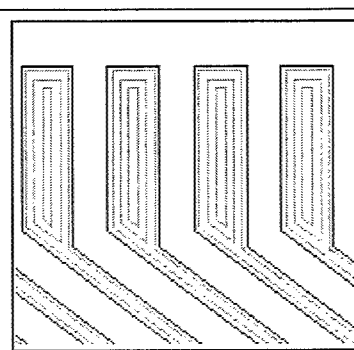
Figure 11: Borderlines (black) and tool paths (grey) for the fan-outs shown in Figure 10. Contouring mode.

The main difference to similar functions that are commercially available is that the LaseCAM area clearing function can deal with much more extensive and complex structures (e.g. a ∅ 80 mm clock display containing 217 borderlines and requiring about 42 m of tool paths in total).

4.5 Pocketing and 2½D surface machining
As with the area clearing operation, the user can choose between a contouring and a rastering mode; in the case of pocketing, there are the options of vertical or sloping sidewalls. The work on these operations is ongoing.

The tool paths are generated layer by layer: The first layer of tool paths is derived from the contours given in the CAD-drawing in the same way as the tool paths for area clearing. Then the machining along these tool paths is simulated and the result compared to the desired device. This comparison is quantified by calculating the differences between the machining depth achieved so far and the machining depth specified by the drawing at each pixel of the simulation grid. The next step is to derive from this "matrix of remaining machining depth" the contours for the second layer of tool paths. These contours are the borders of the areas where the remaining machining depth is above a certain threshold. In order to translate the discrete information from the matrix of remaining machining depth into the continuous curves needed to generate further tool paths, we use edge detection and edge linking algorithms similar to those known from image processing applications. Once the contours have been derived, the second layer tool paths are generated as before. Again, machining along these tool paths is simulated and the result compared to the device in the drawing, etc.

With a circular beam, the machining depth at the centre of the cut is greater than close to the edges due to higher shot overlap; in the case of a Gaussian beam profile, this effect is even more pronounced as the intensity decreases with the distance from the centre of the beam. In order to average out these differences in machining depth, the tool paths of subsequent layers are offset with respect to each other.

To avoid extra machining depth caused by increased shot overlap, the tool paths can be enhanced by trimming them at acute angles and speeding up the scanner movement (to reduce shot overlap) where the tool paths are too close together.

Figure 12: Fragments of tool paths that cause extra machining depth: Acute angle (left) and two fragments close together (right). The grey scale in the schematic drawing of the corresponding shots reflects the amount of shot overlap.
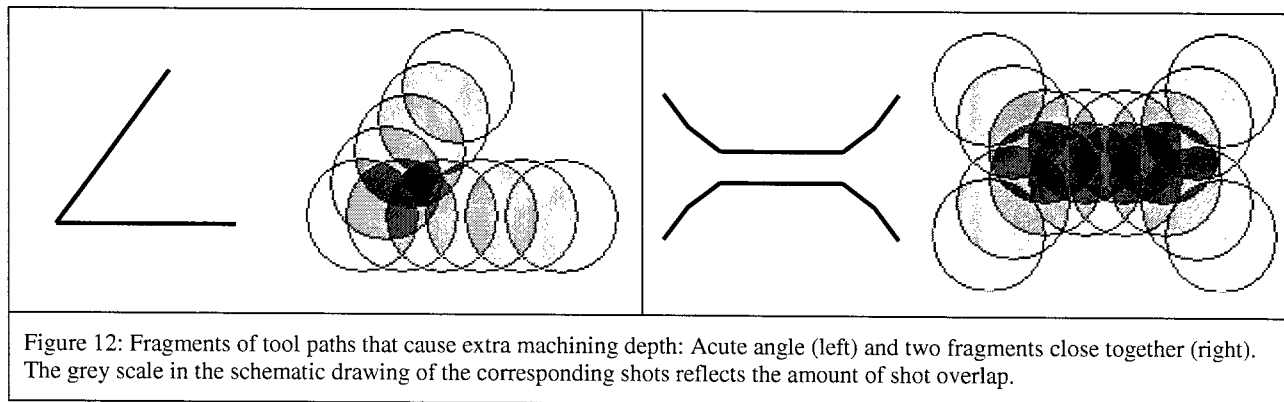
Applications for the pocketing and 2½D surface machining operations include embossing tools, micro injection molding tools and devices for passive alignment.

5. SCANNER POST PROCESSOR

Once the tool paths are available as geometric information, they have to be translated into CNC commands to control the tool. In our case, these are commands for the scanner head. As the scanner is not able to machine along curved lines, all the arcs in the tool paths have to be approximated by straight lines. The user can specify the maximum chord error that can be accepted.

In case the device to be machined is larger than the scan area, the machining area has to be subdivided into "tiles" of the size of the scan area and the tool paths have to be broken up into pieces that are entirely within one of the "tiles". This makes it possible to machine the desired device in a step and scan process, stitching the "tiles" together.

If the system on which the LaseCAM software is used does not have a scanner, other post processors are available that translate the tool paths as geometries into other languages, e.g. into commands for the Aerotech UNIDEX 500 motion controller.

6. GRAPHICAL USER INTERFACE

The graphical user interface (GUI) provided by the alphaCAM software has been customised in order to allow the user to access the functionality of LaseCAM by means of menu items and buttons. Many user forms have been created to make it convenient for the user to edit and enter parameters and to choose between different options.
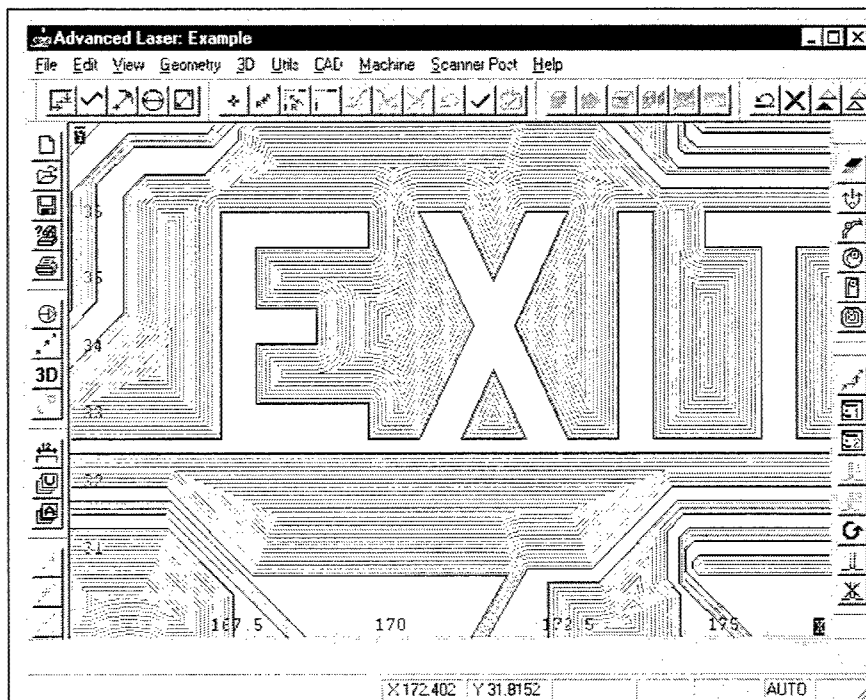
Figure 13: Screen shot of the GUI of the LaseCAM software showing another example for the area clearing operation (borderlines in black, tool paths in grey).
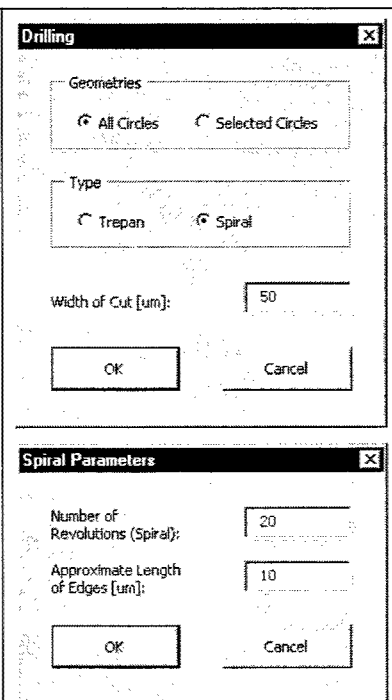
Figure 14: Examples of user forms.

7. EXITECH M1000 LASER MICROMACHINING TOOL

The Exitech M1000 laser micromachining tool was specifically designed as a small footprint workstation integrating the LaseCAM software described in this paper.

The Exitech M1000 tool (Figure 15) is a compact, floor mounted unit. It incorporates a Q-switched UV solid-state laser source. The laser beam is delivered to the workpiece via a scanner head for rapid beam displacement. A very short focal length telecentric f-theta lens (f = 30 mm) makes it possible to achieve a spot size of 2 - 3 μm at 266 nm wavelength. The size of the scan field is about 10 x 10 mm. There is a maximum of flexibility for the lay-out of the optical path: One option is to image an aperture with x 100 demagnification using an aperture changer, which allows a variety of different spot sizes and shapes to be generated at the workpiece. To achieve the smallest spots, direct focusing of the Gaussian

beam is used. Figure 16 shows the optical layout for these two versions. Precision X and Y stages are used for step and scan operations. Various system diagnostics such as an alignment camera, height sensor with autofocus and a power meter are integrated.

The machine is built on a rigid platform with a granite gantry. The laser, all critical optical components, the stages and the scanner head are attached to the granite structure for stability and freedom from vibration. An enclosure makes this tool class 1 laser-safe.
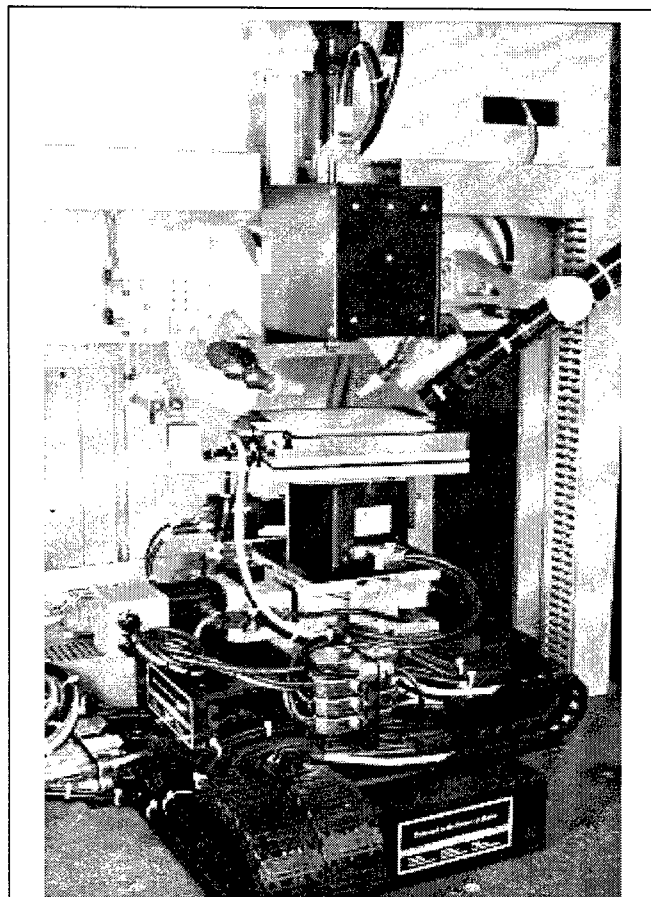
Figure 15: View into the Exitech M1000 micromachining tool.
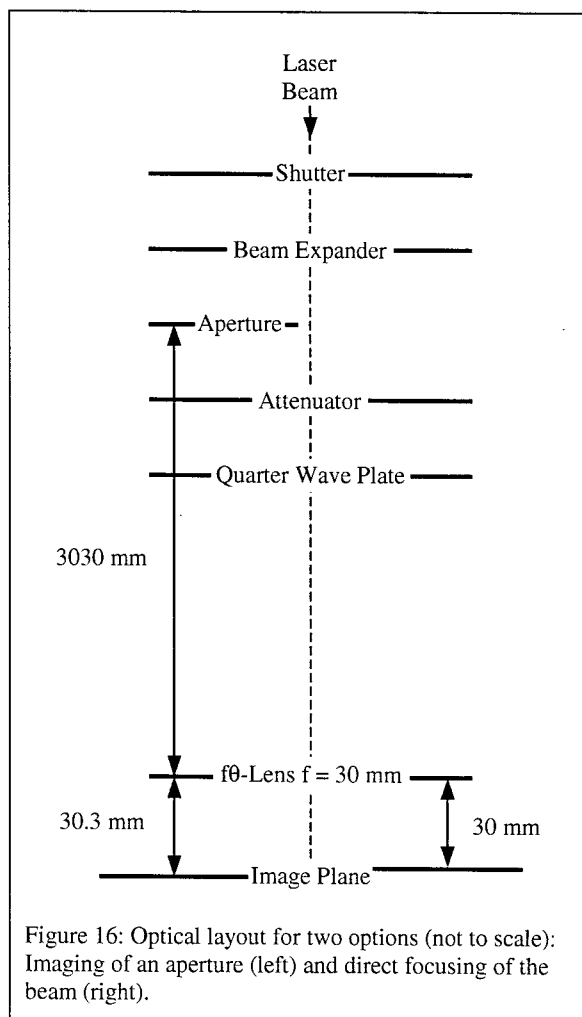
Figure 16: Optical layout for two options (not to scale): Imaging of an aperture (left) and direct focusing of the beam (right).

It should be noted, though, that the LaseCAM software developed for this workstation can also be used on other systems with or without scan head and with lasers of different wave lengths suited to the respective application.

8. CONCLUSIONS

User-friendly CAD/CAM software for a novel laser micromachining tool concept has been developed on a commercial CAD/CAM platform. The LaseCAM software automatically generates laser beam tool paths for 2D and 2½D structures, relying on a simulator module for the more complex machining operations. These tool paths are then translated into motion control commands for conventional motor-driven stages or for x-y laser scanners, or a combination of both. The use of state-of-the-art scanners with short focal length f-theta (telecentric) lenses and deep-UV diode-pumped solid-state lasers (266 nm) allows high resolution, accurate micromachining of most metals, ceramics, polymers and electronic

compounds. Applications include micro-hole drilling, thin-film patterning, micro rapid prototyping and micro injection molding tool manufacture.

REFERENCES

1. S. R. Cain, F. C. Burns, C. E. Otis, *On single-photon ultraviolet ablation of polymeric materials*, J. Appl. Phys. 71(9), pp. 4107-4117, 1992

2. G. H. Pettit and R. Sauerbrey, *Pulsed ultraviolet laser ablation*, Appl. Phys. A 56, pp. 51-63, 1993

3. P.E. Dyer, D. M. Karnakis, P. H. Key and P. Monk, *Excimer laser ablation for micro-machining: geometrical effects*, Appl. Surf. Sci. 96-98, pp. 415-419, 1996

4. C. Paterson, A. S. Holmes, R. W. Smith, *Excimer laser ablation of microstructures: a numerical model*, J. Appl. Phys. 86(11), pp. 6538-6546, 1999

ACKNOWLEDGEMENTS

Micromachining of liquid crystal polymer film with frequency converted diode-pumped Nd:YVO₄ laser

Mingwei Li[a], Ken Hix[b], Larry Dosser[b], Kevin Hartke[b], Jim Blackshire[c]

[a]Spectra-Physics, Inc., 1305 Terra Bella Ave., Mountain View, CA 94043;
[b]Mound Laser & Photonics Center, Inc., P.O. Box 223, Miamisburg, OH 45343;
[c] Materials & Manufacturing Directorate, Wright Patterson Air Force Base, OH 45433

ABSTRACT

Liquid crystal polymer (LCP) is a new and innovative material being used as an alternative to polyimide in the flexible circuit industry. LCP has many intrinsic benefits over polyimide including lower moisture absorption and improved dimensional stability. However, LCP is very resistant to chemical milling or etching. As a result, other methods for processing the material are being investigated including laser micromachining. In this paper, three frequency converted diode-pumped solid-state (DPSS) Nd:YVO₄ lasers at 355 nm were used to micromachine a LCP film and a copper/LCP laminate. Of them, two are Q-switched lasers operating in the nanosecond regime and the other a mode-locked laser in the picosecond regime. The Q-switched lasers can be operated at pulse repetition rates of 1 to 300 kHz while the mode-locked system is operated at 80 MHz. The micromachining experiments consisted of cutting the 50 µm thick LCP film, cutting the 18 µm thick copper on the film, and drilling micro-vias through both the copper coating and the film substrate. The laser/material interactions and processing speeds were studied and compared. The results show that, compared to polyimide film of the same thickness, LCP film can be more efficiently processed by laser micromachining. In addition, each laser has a unique advantage in processing LCP based flexible circuit materials. The Q-switched lasers are more capable of processing the copper coating while the mode-locked laser can cut LCP film faster with the smallest kerf width.

Keywords: Liquid crystal polymer, laser micromachining, diode-pumped, Q-switched, mode-locked

1. INTRODUCTION

New flexible circuit materials are currently being developed and implemented as a result of the need for smaller, faster, and more flexible electronic devices[1-3]. The current material being used in most flexible circuit applications is polyimide. Polyimide has been widely used because of its inherent strength, electrical resistance, and flexibility. However, the material has met some short falls as new high frequency, environmental sensitive applications develop. Liquid crystal polymer (LCP) has come to the market with many advantages over polyimide including improved flexibility and dimensional stability, low moisture absorption, low dielectric constant and loss factor, equivalent coefficient of thermal expansion with copper, and resistance to corrosive environments[1-3]. Of all the benefits, the resistance to corrosive environments has also been considered a hindrance because chemical milling is widely used to process the material into a flexible circuit[1-3]. This problem has brought forth further research in the area of laser materials processing of LCP.

Previous reported researches on laser processing of LCP laminate and composite have only briefly discussed laser drilling using Excimer laser or Nd:YAG laser at 1064 nm fundamental wavelength[2-4]. In the current study, laser micromachining of LCP based materials was approached using three frequency converted Nd:YVO₄ UV lasers having a wavelength of 355 nm. This approach was taken because of the expected strong absorption of UV light by LCP[2-4]. In addition, diode-pumped solid-state (DPSS) lasers are currently commercially available and can be used for multiple tasks in the LCP flexible circuit manufacturing process. With the high speed processing requirements of flexible circuit manufacturing, a comparison was made between Q-switch and mode-locked DPSS lasers. These lasers operate in two very different pulse width and pulse repetition rate ranges, which are deemed important for high speed processing of LCP. Micromachining experiments were conducted to cut the LCP film only, to cut a copper coating off the film

surface, and to percussion drill micro-vias. Cutting the film only was investigated for use in cutting out a flexible circuit from a web production line. The metallic coating removal was examined for applications in direct-write circuit prototyping. Finally, micro-via drilling was looked into for connecting multiple layers in a circuit.

2. EXPERIMENTAL

A Q-switched HIPPO H10-355Q laser and a mode-locked Vanguard laser were used to conduct the comparison micromachining studies at the Spectra-Physics Applications Lab. Another Q-switched Navigator YHP40-355Q laser was used at Mound Laser & Photonics Center to conduct the similar micromachining experiments. All three are diode-pumped Nd:YVO$_4$ lasers at 355 nm UV wavelength, manufactured by Spectra-Physics, Inc. The HIPPO UV laser can be operated from 15 to 300 kHz with a typical pulse width of approximately 12 ns and an average power of greater than 5 W at 50 kHz. The Navigator UV laser can be operated from 1 to 100 kHz with a typical pulse width of approximately 35 ns and an average power of greater than 3.5 W at 20 kHz. The "quasi-cw" mode-locked Vanguard UV laser produces an average power of 4 W at output, with a repetition rate of 80 MHz and a pulse width of 10 ps. For the purpose of this study, the HIPPO is designated as Q-switched laser A, the Navigator as Q-switched laser B, and the Vanguard as mode-locked laser.

During all experiments, a beam expander was used to expand the output beam to approximately 10 mm in diameter and a ¼ waveplate was placed right after the beam expander to make the beam circularly polarized. A galvanometer based scan head (SCANLAB hurrySCAN 10) was then used to move the beam. A telecentric objective of 100 mm focal length was used to focus the beam, producing a focal spot of approximately 15 μm in diameter. Average power on samples at various pulse repetition frequencies (PRF) was measured after all the beam train optics. The laser parameters used in the experiments were summarized in Table 1. Note that the maximum power at each repetition rate for each laser was used for the experiments.

Table 1. Laser parameters used in micromachining experiments

Laser	Product name	PRF (kHz)	Average power on sample (W)	Pulse energy (μJ)	Pulse width (ns)	Peak power (kW)	Fluence on sample (J/cm^2)
Q-switched laser A	HIPPO	40	4.95	123.75	11.00	11.25	70.03
		50	5.04	100.80	12.00	8.40	57.04
Q-switched laser B	Navigator	5	1.00	200.00	30.00	6.67	113.18
		20	3.50	175.00	35.00	5.00	99.03
		40	2.23	55.75	40.00	1.39	31.55
		50	1.74	34.80	50.00	0.70	19.69
Mode-locked laser	Vanguard	80000	3.50	0.04	0.01	4.38	0.02

The 50 μm thick LCP film and 18 μm thick copper/50 μm thick LCP laminate were provided by Mound Flextek, Inc. The copper was plated with 0.5 μm thick tin. For straight line cutting experiments on LCP and copper, a series of 10 mm long cuts were made and the scan speeds were decreased gradually until the laser cut through the materials. Same sets of experiments were always repeated along both the extruded direction of LCP and the transverse direction (to the extruded direction) to observe possible directional effects on cutting speeds. For percussion drilling experiments, a series of 3 x 3 hole matrices were made and the drilling dwell times were increased gradually until the laser drilled through the materials.

All the cuts and micro-vias were examined using optical microscopes. Selected cuts and micro-vias were also analyzed with a white-light interferometer. The interferometer uses an optical interferometry technique termed 'white-light interferometry', which involves the interference of reference and object beams of light. Instead of using a highly coherent, monochromatic light source, a partially coherent, polychromatic light source is used (Figure 1). Because polychromatic light has a short coherence length, interference fringes appear only when the optical pathlength difference between the sample and reference surface is close to zero. As shown in Figure 1, the 'white-light' interference pattern

involves an additional envelope function due to the polychromatic light that has a maximum fringe contrast at exactly zero pathlength difference between the sample and the reference surface. By monitoring the fringe contrast as the sample is vertically scanned through focus, a precise measure of the local focal position can be measured, and the topographic features can be mapped out.
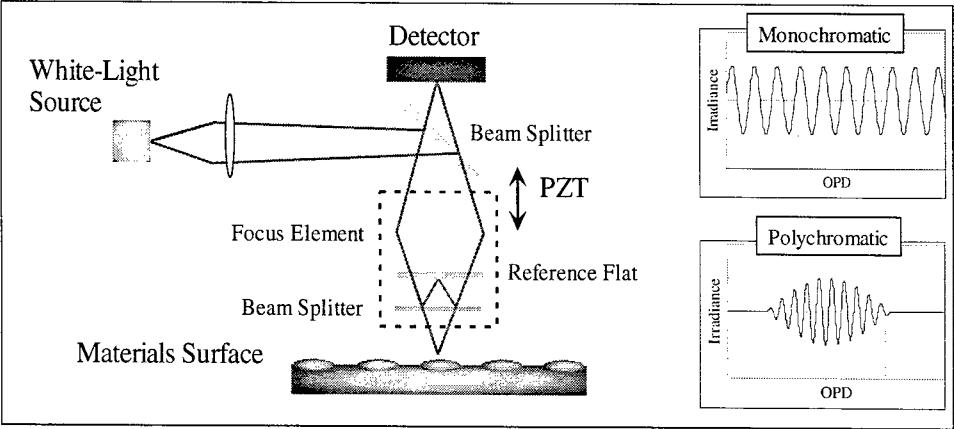
Figure 1. Schematic diagram of white-light interferometry system

3. RESULTS AND DISCUSSION

3.1 Cutting 50 μm thick LCP film

3.1.1 Q-switched laser A

The short pulse Q-switched laser A was used to cut the LCP film at 50 and 40 kHz. The scan speeds and pulse overlaps were shown in Table 2.

Table 2. Cutting speeds and pulse overlap used in LCP film cutting experiments

Q-switched laser A			Q-switched laser B					Mode-locked laser	
Scan speed (mm/s)	Pulse overlap		Scan speed (mm/s)	Pulse overlap				Scan speed (mm/s)	Pulse overlap
	40 kHz	50 kHz		5 kHz	20 kHz	40 kHz	50 kHz		80 MHz
1000	-0.67	-0.33	200	-1.67	0.33	0.67	0.73	2000	0.9983
500	0.17	0.33	150	-1.00	0.50	0.75*	0.80	1000	0.9992
400	0.33	0.47	125	-0.67	0.58*	0.79	0.83	900	0.9993
300	0.50	0.60	100	-0.33	0.67	0.83	0.87*	800	0.9993
200	0.67*	0.73*	75	0.00	0.75	0.88	0.90	700	0.9994*
150	0.75	0.80	50	0.33	0.83	0.92	0.93	600	0.9995
100	0.83	0.87	25	0.67*	0.92	0.96	0.97	500	0.9996
								400	0.9997

* Where the LCP film was cut through, i.e., the maximum cutting speed was obtained

At 50 kHz and 5.04 W, the cutting depths increased almost linearly with decreasing scan speeds, after the pulses began to overlap at 500 mm/s (Figure 2). When the scan speed dropped to 200 mm/s with a pulse overlap of 0.73, the laser cut through the LCP film with relatively clean edge (Figure 3). No black carbonization was evident at this speed. When the speed was further decreased to 100 mm/s, the laser left a much wider cut with carbonization along the edge. No apparent difference was observed between the extruded direction and the transverse direction of the film.

At 40 kHz and 4.95 W, the cutting efficiency seemed to be a bit lower. At 200 mm/s and a pulse overlap of 0.67, the laser cut through the LCP film along the extruded direction but did not along the transverse direction. At the same speed such as 100 mm/s, the cuts made at 40 kHz appeared to have a bit less carbonization along the edge than those made at 50 kHz, although the difference was quite small. Compared to 50 kHz, although the increase in pulse energy at 40 kHz (Table 1) should allow a greater amount of material to be removed per pulse, the decrease in pulse overlap (Table 2) more than offset this effect, resulting in slightly lower maximum cutting speed (to cut through the LCP film).

Figure 2. LCP cutting depth as a function of scan speed for Q-switched laser A at 50 kHz (5.04 W), as measured by white-light interferometer

(a)

(b)
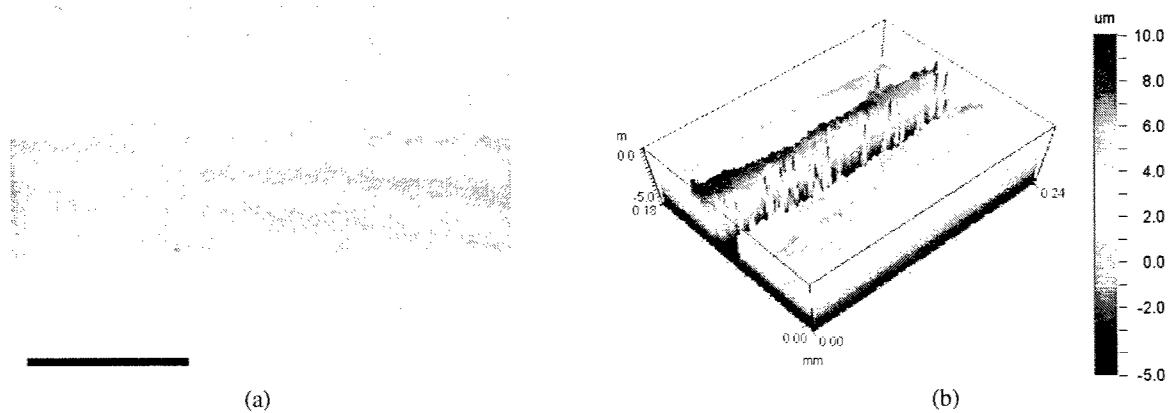
Figure 3. LCP film cut by Q-switched laser A at 50 kHz (5.04 W) and 200 mm/s: (a) 200x micrograph with a 100 μm scale and (b) 3D plot generated by white-light interferometer

3.1.2 Q-switched laser B

The longer pulse, lower power Q-switched laser B was used to cut the LCP film at 50, 40, 20, and 5 kHz (Tables 1 and 2). The scan speeds were varied from 200 mm/s to 25 mm/s (Table 2), since the maximum cutting speed obtained for this laser was expected to be lower than that for the Q-switched laser A.

At 50 kHz and 1.74 W, minimal splattering was observed compared to the cuts made at the same repetition rate by the Q-switched laser A, presumably due to lower average power (and lower pulse energy) of the Q-switched laser B. The laser cut through the LCP film at a maximum speed of 100 mm/s with a pulse overlap of 0.87.

At 40 kHz and 2.23 W, again, very little splattering and carbonization were produced. The laser cut through the LCP film when the scan speed was decreased to 150 mm/s with a pulse overlap of 0.75 (Figure 4). This speed was the fastest cutting speed obtained for the Q-switched laser B, although the average power was not the highest at this repetition rate.

At 20 kHz and 3.50 W, it seemed that higher pulse energy and less pulse overlap at this repetition rate produced a lot more splattering at faster scan speeds. As the scan speed was decreased, the splattering became less pronounced. Carbonization and some internal discoloration were present and, as with the Q-switched laser A, both effects became more pronounced as the scan speed was reduced. The maximum cutting speed at which the laser cut through the LCP film was 125 mm/s with a pulse overlap of 0.58 (Figure 5). No difference was observed between the extruded direction and the transverse direction of the film. Although the laser had much higher average power and pulse energy at 20 kHz, the maximum cutting speed – 150 mm/s was obtained at 40 kHz. Therefore, more pulse overlap at 40 kHz should have played a more important role in determining the cutting speed. Also note that, compared to the Q-switched laser A, the Q-switched laser B only had less than half of the average power at 40 kHz (Table 1) but its maximum cutting speed was ¾ of that obtained for the Q-switched laser A. This may indicate that the longer pulse width of the Q-switched laser B is more efficient in cutting this kind of "soft" polymer materials.

At 5 kHz and 1.00 W, the laser began to cut through the LCP film at 50 mm/s, with significant splattering (Figure 6). However, it appeared that the laser could only cut completely through at 25 mm/s with a pulse overlap of 0.67. Compared to the cuts obtained at 20 kHz, the cut kerf seemed to be wider (Figures 5 and 6).

Since the maximum cutting speed for the Q-switched laser B to cut through a standard 50 μm thick polyimide Kapton film was 80 mm/s[5,6], the laser, operating at 20 to 40 kHz, could cut a LCP film of the same thickness faster. This result shows that thin LCP film can be more efficiently processed by Q-switched DPSS lasers than its polyimide counterpart. This may be due to the fact that LCP has a stronger UV absorption as a result of its unique structure. Also, LCP has a higher thermal conductivity than standard polyimide film[3], which may cause faster heat dissipation in regions surrounding the cuts and thus more melting or vaporization of the material. Clearly, more detailed studies are needed to explain the different laser/material interactions between LCP and polyimide.
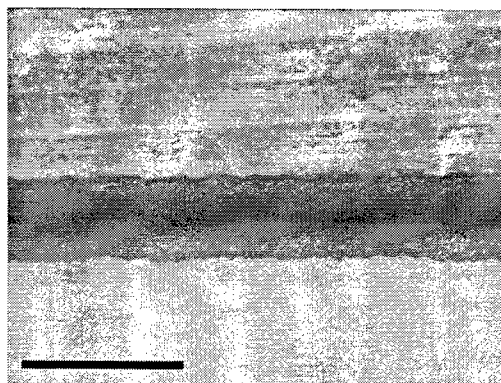
Figure 4. LCP film cut by Q-switched laser B at 40 kHz (2.23 W) and 150 mm/s: 200x micrograph with a 100 μm scale
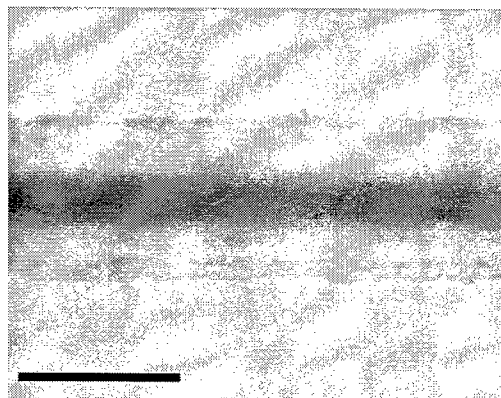
Figure 5. LCP film cut by Q-switched laser B at 20 kHz (3.50 W) and 125 mm/s: 200x micrograph with a 100 μm scale

(a)

(b)
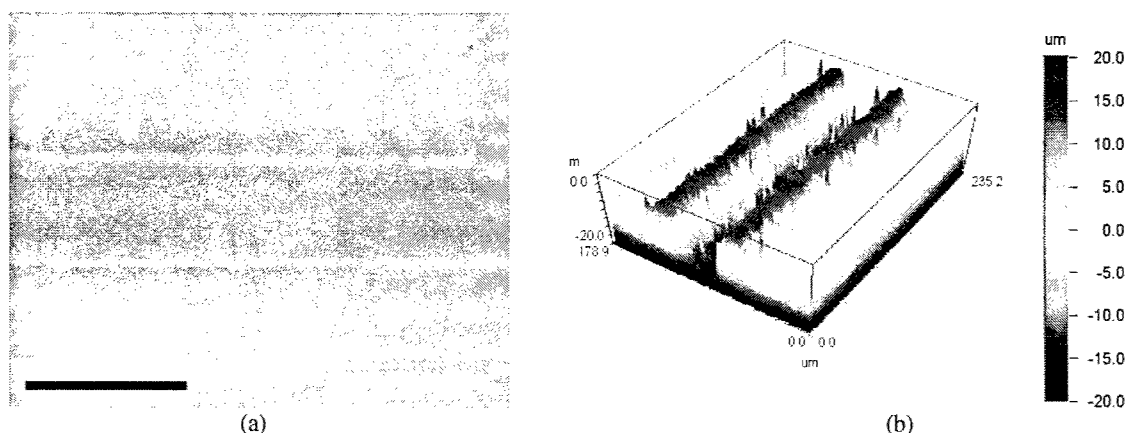
Figure 6. LCP film cut by Q-switched laser B at 5 kHz (1.00 W) and 50 mm/s: (a) 200x micrograph with a 100 μm scale and (b) 3D plot generated by white-light interferometer

3.1.3 Mode-locked laser

The mode-locked laser operates at an ultra-high repetition rate of 80 MHz while its pulse energy is almost four orders of magnitude lower than that of the Q-switched lasers A and B (~40 nJ compared to ~100 μJ), resulting in a high degree of pulse overlap that does not vary much over the range of the experimental scan speeds (Table 2). Due to the expected high cutting speed of the laser[5,6], the scan speeds were varied from 2000 mm/s to 400 mm/s (Table 2). As expected, the cutting depth increased gradually with decreasing scan speeds (Figure 7). When the speed dropped to 800 mm/s, the laser began to cut through the LCP film. At 700 mm/s, the film was completely cut through with a very clean edge and a narrow kerf – approximately 15 μm wide (Figure 8).

Compared to the maximum cutting speeds obtained using the Q-switched laser A (200 mm/s) and B (150 mm/s), the mode-locked laser was much faster in cutting the film and provided much better cut quality (Figure 8). Note that the Q-switched laser A had higher average power and the Q-switched laser B had almost the same average power, compared to the mode-locked laser. This confirms that the mode-locked laser is a lot more efficient in processing thin polymer films than Q-switched UV lasers of similar power level, as first discovered in a previous study[5,6].

In addition, when the same mode-locked laser was used, the maximum speed in cutting a 50 μm thick polyimide film was 600 mm/s[5,6], lower than the maximum cutting speed obtained on the 50 μm thick LCP film. This proves again that LCP film can be processed faster by UV lasers than polyimide film of the same thickness (see Section 3.1.2).
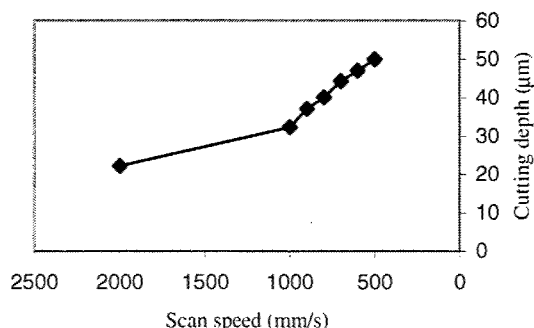
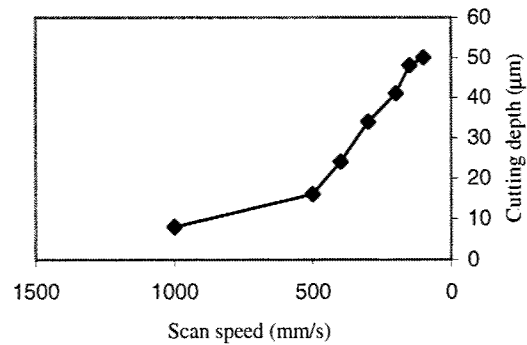
Figure 7. LCP cutting depth as a function of scan speed for mode-locked laser at 80 MHz (3.50 W), as measured by white-light interferometer

(a)   (b)
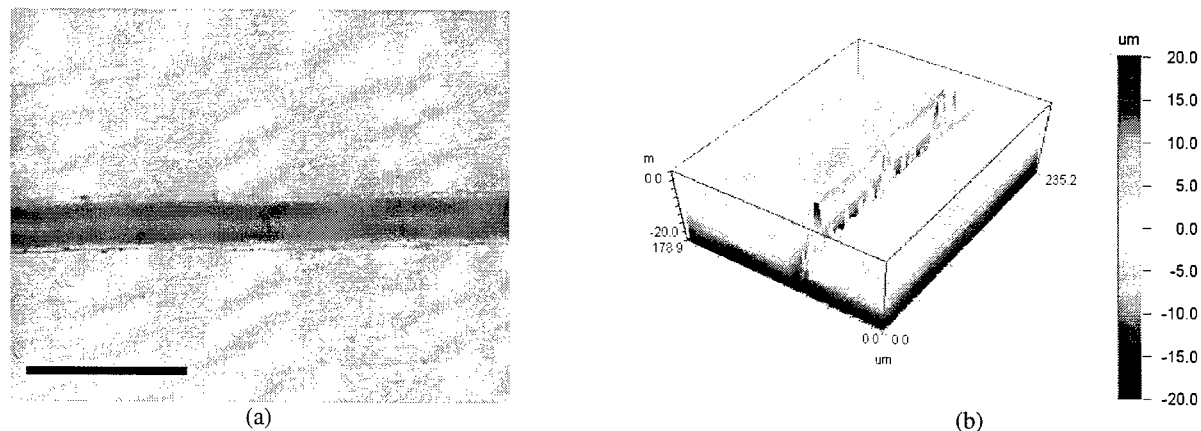
Figure 8. LCP film cut by mode-locked laser at 80 MHz (3.50 W) and 700 mm/s: (a) 200x micrograph with a 100 μm scale and (b) 3D plot generated by white-light interferometer

3.2 Cutting 18 μm thick copper/50 μm thick LCP laminate

3.2.1 Q-switched laser A

In addition to cutting LCP film, the short pulse Q-switched laser A was used to cut the copper/LCP laminate at 50 and 40 kHz. The scan speeds and pulse overlaps were shown in Table 3.

Table 3. Cutting speeds and pulse overlap used in copper/LCP laminate cutting experiments

Q-switched laser A			Q-switched laser B		Mode-locked laser	
Cutting speed (mm/s)	Pulse overlap		Cutting speed (mm/s)	Pulse overlap	Cutting speed (mm/s)	Pulse overlap
	40 kHz	50 kHz		20 kHz		80 MHz
500	0.17	0.33	200	0.33	500	0.9996
400	0.33	0.47	150	0.50	400	0.9997
300	0.50	0.60	125	0.58	300	0.9998
200	0.67	0.73	100	0.67	200	0.9998
150	0.75	0.80	75	0.75*	150	0.9999
100	0.83	0.87*	50	0.83	100	0.9999
75	0.88*	0.90**	25	0.92**	75	0.9999
50	0.92**	0.93			50	1.0000

    * Where the copper coating was cut through
    ** Where the whole copper/LCP laminate was cut through

At 50 kHz and 5.04 W, when the cutting speed dropped to 100 mm/s with a pulse overlap of 0.87, the laser appeared to completely cut through the copper coating (Figure 9). The width of the cut was about 20 μm. At 75 mm/s, the laser began to cut through both the copper and the LCP.

At 40 kHz and 4.95 W, as in the case of cutting LCP film (see Section 3.1.1), the cutting efficiency seemed to be a bit lower. At 100 mm/s, there appeared to be still copper residue left in the grooves. At 75 mm/s, the laser did not cut through both the copper and the LCP. Finally at 50 mm/s, the whole laminate including the copper and the LCP was cut through.
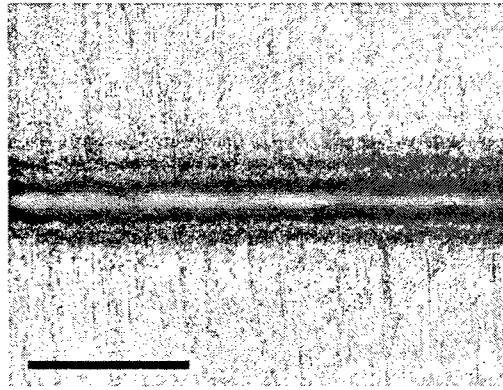
Figure 9. Copper coating (on LCP substrate) cut by Q-switched laser A at 50 kHz (5.04 W) and 100 mm/s: 200x micrograph with a 100 μm scale

3.2.2 Q-switched laser B

The longer pulse, lower power Q-switched laser B was also used to cut the copper/LCP laminate at 20 kHz (Table 3). The scan speeds were varied from 200 mm/s to 25 mm/s.

At 20 kHz and 3.50 W, when the speed was reduced to 75 mm/s, the cut was through the copper and just exposed the LCP at the bottom of the cut (Figure 10). The cut kerf and heat-affected zone were relatively wide compared to the through cut made by the Q-switched laser A (Figure 9). At 25 mm/s, the cut was completely through both the copper and the LCP.

(a)

(b)
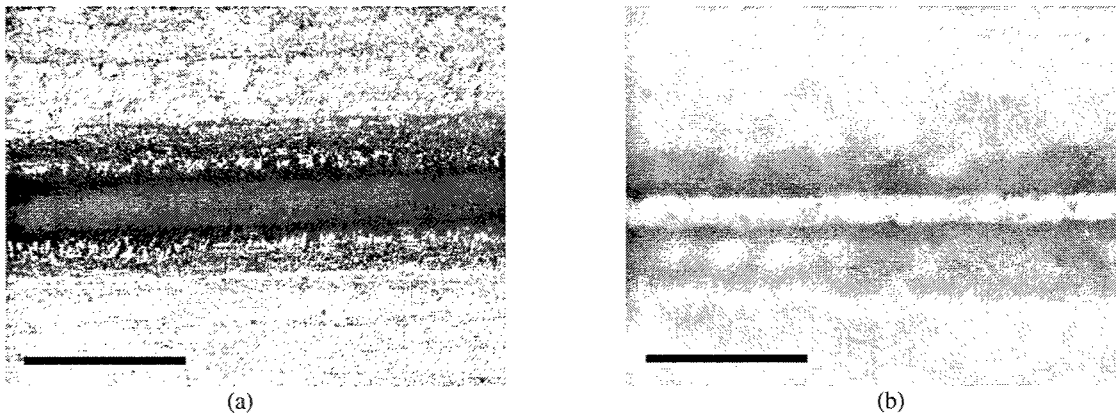
Figure 10. Copper coating (on LCP substrate) cut by Q-switched laser B at 20 kHz (3.50 W) and 75 mm/s: (a) 200x micrograph with a 100 μm scale – top and (b) 200x micrograph with a 100 μm scale – bottom

3.2.3 Mode-locked laser

The mode-locked laser was also used to scribe the copper of the laminate (Table 3). The laser did not cut through the copper coating at any scan speeds, leaving only shallow grooves on the copper surface. This result is consistent with previous obtained results that the mode-locked laser is very inefficient in processing copper compared to Q-switched DPSS lasers[5,6].

3.3 Micro-via percussion drilling using Q-switched laser A

3.3.1 Micro-via drilling in 18 µm thick copper/50 µm thick LCP laminate

The Q-switched laser A was used to drill micro-vias in the copper/LCP laminate. The repetition rate was 50 kHz and the power on materials was 5.04 W. At 0.10 ms drilling dwell time, the laser appeared to drill through the 18 µm thick copper coating completely and exposed the LCP substrate (Figure 11). The via hole opening was approximately 20 µm in diameter. Since there were only 6 pulses within 0.10 ms, the copper removal rate was 3 µm/pulse. This usually high removal rate was likely a result of the high peak power of the Q-switched laser A due to its short pulse width at high repetition rates (Table 1).

At 0.15 ms dwell time, the laser began to drill through both the copper and LCP (Figure 12). The entrance diameter of the vias was about 20 µm and the exit about 5 µm (Figure 12). At 0.25 ms dwell time, the entrance became 25 µm in diameter and the exit about 15 µm (Figure 13).
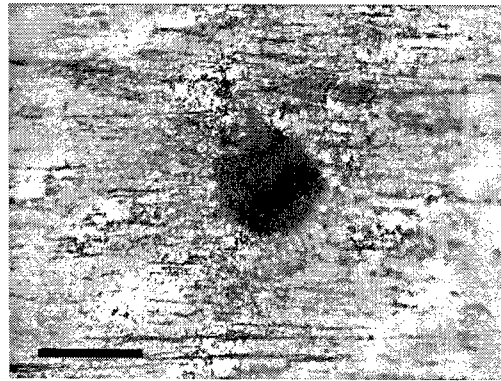
Figure 11. Micro-vias drilled in copper/LCP laminate by Q-switched laser A at 50 kHz (5.04 W) and 0.10 ms dwell time: 500x micrograph with a 25 µm scale

(a)   (b)
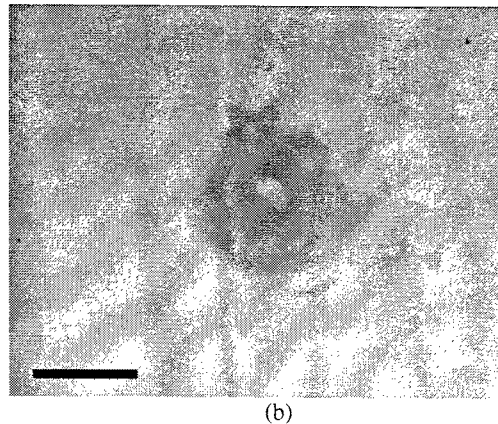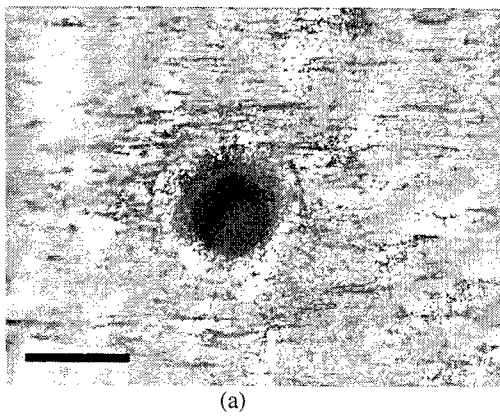
Figure 12. Micro-vias drilled in copper/LCP laminate by Q-switched laser A at 50 kHz (5.04 W) and 0.15 ms dwell time: (a) 500x micrograph with a 25 µm scale – entrance (copper side) and (b) 500x micrograph with a 25 µm scale – exit (LCP side)

(a)   (b)
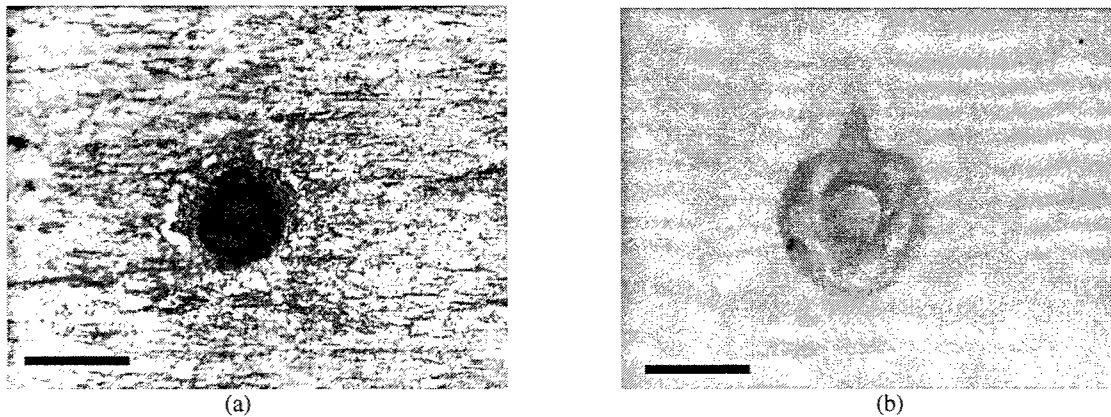
Figure 13. Micro-vias drilled in copper/LCP laminate by Q-switched laser A at 50 kHz (5.04 W) and 0.25 ms dwell time: (a) 500x micrograph with a 25 μm scale – entrance (copper side) and (b) 500x micrograph with a 25 μm scale – exit (LCP side)

3.3.2 Micro-via drilling in 50 μm thick LCP film

At 50 kHz and 5.04 W, the same Q-switched laser A was also used to drill micro-vias in the LCP film. At 0.04 ms (3 pulses), the laser began to drill through the 50 μm thick film (Figure 14). The entrance diameter at this time was about 5 μm and the exit about 3 μm (Figure 14). Since the hole diameter was smaller than the focal spot size of 15 μm, only the center of the beam was effective in ablating the material within such a short dwell time. The micro-vias became bigger with increasing drilling dwell time. At 0.30 ms (16 pulses), both the entrance and exit diameter were approximately 20 μm (Figure 15).

(a)   (b)
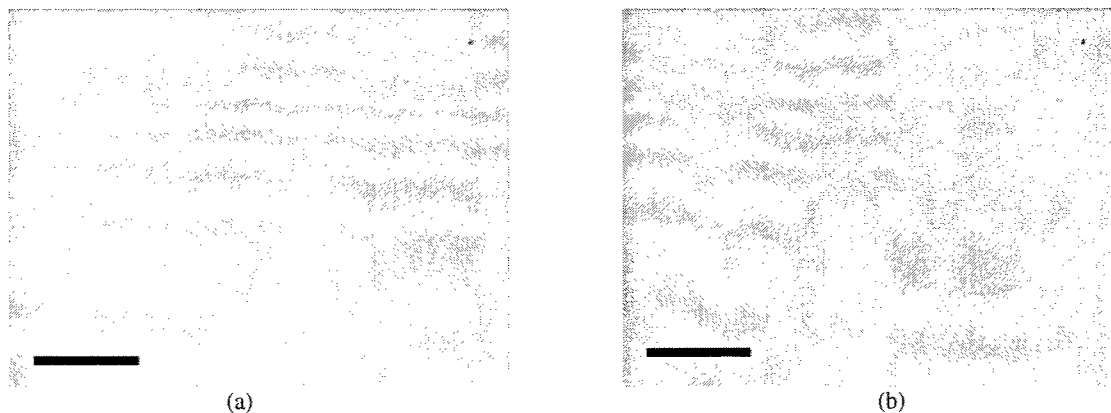
Figure 14. Micro-vias drilled in LCP film by Q-switched laser A at 50 kHz (5.04 W) and 0.04 ms dwell time: (a) 500x micrograph with a 25 μm scale – entrance and (b) 500x micrograph with a 25 μm scale – exit

(a)   (b)
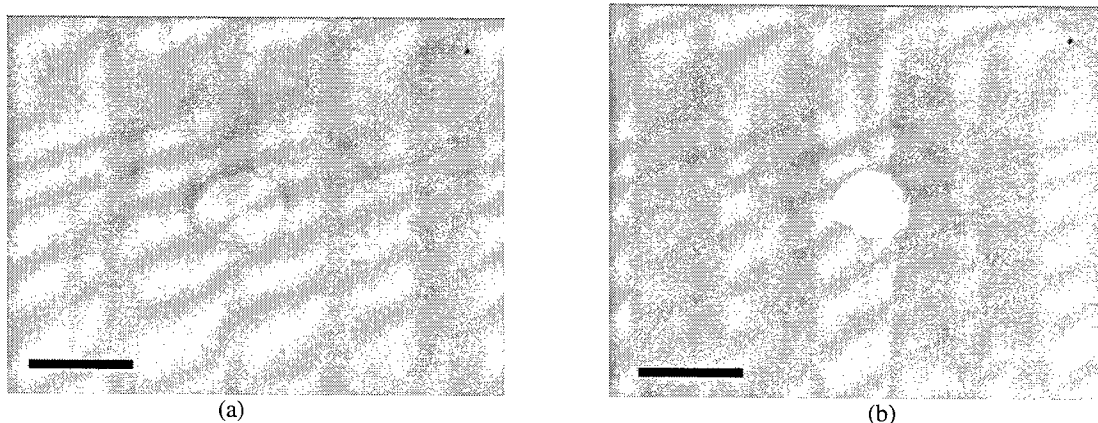
Figure 15. Micro-vias drilled in LCP film by Q-switched laser A at 50 kHz (5.04 W) and 0.30 ms dwell time: (a) 500x micrograph with a 25 μm scale – entrance and (b) 500x micrograph with a 25 μm scale – exit

3.3.3 Micro-via drilling in 50 μm thick polyimide film

For comparison, the Q-switched laser A was also used to drill micro-vias in a 50 μm thick polyimide (Kapton) film. At 50 kHz (5.04 W) and 0.04 ms dwell time, the laser began to drill through the film. The entrance diameter of the holes was about 6 μm and exit about 2 μm. At 0.30 ms dwell time, the entrance diameter was about 20 μm and exit about 8 μm. Although the minimum drilling time needed to drill through the polyimide film was the same as that needed to drill through the LCP of the same thickness, the hole exits in general were smaller and the holes were more tapered in the polyimide, given the same dwell time. This shows once again that LCP is easier to process with DPSS UV lasers than polyimide (see Sections 3.1.2 and 3.1.3).

4. SUMMARY

Two Q-switched and one mode-locked frequency converted 355 nm lasers were used to investigate the laser cutting and drilling applications in LCP film based materials.

Compared to the polyimide film of the same thickness (50 μm), the LCP film can be more efficiently processed by DPSS UV lasers, as demonstrated by cutting experiments using both the Q-switched and the mode-locked Nd:YVO$_4$ lasers and percussion drilling experiments using the Q-switched laser.

The maximum cutting speed to cut through the LCP film was 200 mm/s for the Q-switched lasers and 700 mm/s for the mode-locked laser. In addition, the cuts obtained by the mode-locked laser were cleaner and narrower than those by the Q-switched lasers, with nearly no heat affected zone. This result is consistent with previous reported findings that the mode-locked laser is more efficient in processing polymer materials than its Q-switched counterparts[5,6]. Both Q-switched and mode-locked lasers can be effectively used to cut out LCP film based flexible circuits.

The maximum cutting speed to cut through the copper coating of the copper/LCP laminate was 100 mm/s for the Q-switched lasers. However, the mode-locked laser could not ablate the copper effectively. This is also consistent with the previous reported results[5,6]. For direct circuit structuring in copper, Q-switched lasers should be used.

During percussion drilling of micro-vias, the short pulse high peak power high repetition rate Q-switched laser demonstrated a very high material removal rate in both copper and LCP. This will enable potential high throughput in micro-via drilling processes. The same laser can be used to drill either copper or LCP or both, offering a great deal of versatility in circuit manufacturing.

REFERENCES

1. E.C. Culbertson, "A new laminate material for high performance PCBs: liquid crystal polymer copper clad films", *Proc. 45th Electronic Components and Technology Conference*, pp. 520-523, Las Vegas, 1995.
2. K. Brownlee, P.M. Raj, S.K. Bhattacharya, K. Shinotani, C.P. Wong, and R.R. Tummala, "Evaluation of liquid crystal polymers for high performance SOP application", *Proc. 52nd Electronic Components and Technology Conference*, pp. 676-680, San Diego, 2002.
3. P. Nevrekar, "Liquid crystalline polymer: the next generation of high-performance flex circuit materials", *CircuiTree*, **15**, pp. 46-54, April 2002.
4. T.M. Yue and K.C. Chan, "Laser drilling of liquid crystal polymer composites", *Polymer Composites*, **19**, pp. 11-17, 1998.
5. M. Li, A. Held, and M. Keirstead, "A comparison study of micromachining using mode-locked and Q-switched diode pumped solid state ultraviolet laser", *Proc. 21st International Congress on Applications of Lasers & Electro-Optics – ICALEO 2002*, in press, Scottsdale, 2002.
6. M. Li, A. Held, and K. Hartnett, "UV laser micromachining: Q-switched or mode-locked?", *Industrial Laser Solutions for Manufacturing*, **17**, pp. 23-27, December 2002.

Femtosecond laser micromachining of silicon for MEMS.

M. El-Bandrawy[1] and Mool C. Gupta[2] Applied Research Center, College of Engineering and
Technology, Old Dominion University
12050 Jefferson Ave., Newport News, VA, 23606

ABSTRACT

Laser micromachining of n-type silicon wafer was studied using femtosecond laser operating at 400 and 800 nm wavelengths. The fundamental wavelength was used to fabricate a diaphragm of 4 mm diameter using a computer controlled galvo head. The laser pulsewidth was 110 fs, repetition rate of 1 kHz, and maximum average power of 2 W. The experiments were done in air and in vacuum environment. The samples were examined with optical microscope and surface profilometer. Experiments were also done with doubling the laser beam frequency using LBO crystal to get 400nm wavelength. Using a 10 nm resolution stage, high numerical aperture microscope objective, we were able to fabricate 235 nm wide lines with 600 nm depth.

Keywords: Laser, Micromachining, Silicon, MEMS, Femtosecond, Ultrashort pulses, Ablation, Grating.

1. INTRODUCTION

Lasers are extensively used for micromachining of various materials. However there have been very few studies reported in achieving submicron features using laser micromachining. This difficulty is due to the minimum spot size that can be achieved due to the diffraction effects. In the case of femtosecond laser the machining feature is not only controlled by the focus spot size but also by the laser pulse width. Getting smaller features requires that the thermal diffusion length be much smaller than the optical absorption depth[1]. This condition is satisfied with the femtosecond laser pulse width, as the optical absorption length is ultimately much higher than the thermal diffusion length. Another feature of using the femtosecond laser is that, the laser energy can be precisely controlled so, the ablation can take place by a part of the energy in the focus spot[2]. This allows us to go beyond the diffraction limit of the laser beam. Theoretical and experimental studies[1-8] have been performed to understand the interaction of the femtosecond laser with materials in order to fabricate linewidth below the diffraction limit. Laser micromachining of submicron features will provide a new precise machining tool to be used in the microelectronic mechanical systems (MEMS) field. This direct writing method can be used to obtain optical grating of different shapes and different periods. Ngoi et al[1] reported a linewidth of about 500 nm with depth of about 100 nm but the lines suffered discontinuity. The experiment was done in vacuum at 400 nm wavelength using femtosecond laser of pulsewidth 150 fs and repetition rate of 1 kHz.

2. EXPERIMENTAL SETUP

2.1 Galvo machining of the diaphragm

The experimental setup as shown in figure 1 consists of a Ti-sapphire femtosecond laser operating at 1 kHz repetition rate, with a fundamental wave length at 800 nm and pulse width of 110 femtosecond. The pulse energy was 2 mJ. The laser power was precisely varied using a half waveplate and a polarizer. The laser beam was passed through a quarter waveplate to insure the circular polarization state. Constant monitoring of the power and the beam profile was done using beam splitters and attenuators. Finally computer controlled scanning mirrors were used to scan the beam. A desired CAD file was created in the computer that controls the mirrors motions. The beam was focused to 100 μm spot diameter using a 100 mm plano convex lens. The sample was placed in a vacuum chamber and the focus position could be varied using a z-stage.

---

[1] Electronic mail: Elbandrawy@hotmail.com ; phone 1 757 269-5632; Fax 1 757 269-5644
[2] Electronic mail: mgupta@odu.edu ; Phone 1 757 269-5645; Fax 1 757 269-5644
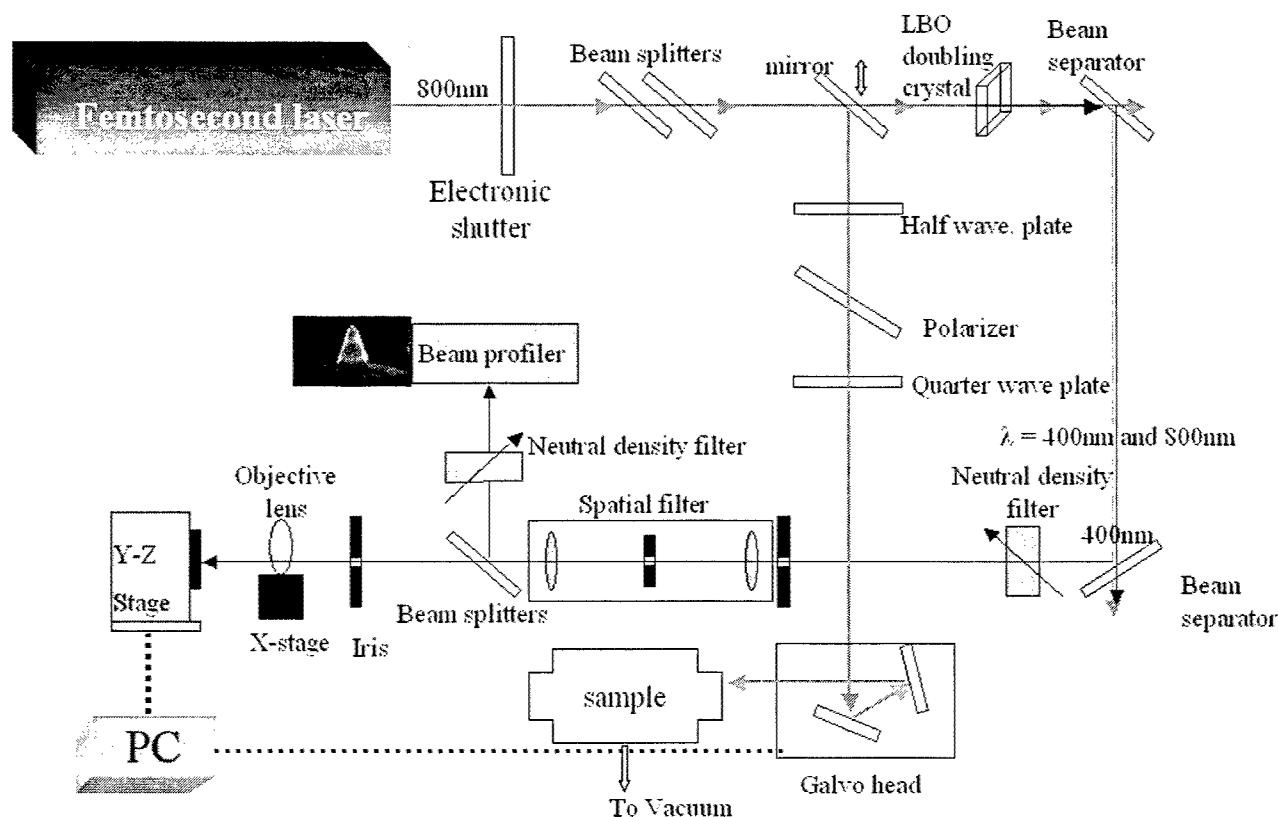
Figure (1) micromachining setup

2.2 Submicron grating fabrication

Figure 1 shows the micromachining set up used for obtaining the submicron grating lines. The laser beam was frequency doubled using LBO crystal of thickness 250 micron. The 400 nm beam was separated using a pair of surface coated mirrors then subjected to a spatial filter consisting of two plano convex lenses with focal length of 200 and 150 mm respectively. The beam was focused by the first lens to pass through a 75 μm pinhole then re-collimated with a 150 mm plano convex lens. The filtered beam was refocused again using a microscope objective lens with a numerical aperture of 0.85. The sample was fixed on a Y-Z stage with a resolution of 10 nm and the scan speed was 50 μm/sec. The focus position was varied using an X stage with a 1 micron resolution. The laser power of the machining pulses was controlled using a neutral density filter. Here we did not use the half waveplate mentioned earlier for controlling power, as we wanted to keep the ratio of fundamental wavelength to the second harmonic constant. If the half waveplate is used then the doubling efficiency of the crystal will be decreased. The beam power was measured using a calibrated photodiode of high sensitivity just before beam was focused by the objective lens.

3. RESULTS AND DISCUSSIONS

3.1 The Diaphragm

The diaphragm micromachining experiment was done in air and in vacuum at different laser powers. The surface roughness was measured using a stylus surface profiler. The scan speed was 100 μm/sec and laser focus spot size was ~ 100 μm in diameter. The results in figure 2 and 3 show that; lower surface roughness is obtained for machining in vacuum as compared to in air. Also the lower the laser machining power the lower the roughness. The surface roughness increases rapidly for machining in air due to the plasma formation, which affects the machined surface. The ablated depth was found to be linear with the applied laser power.
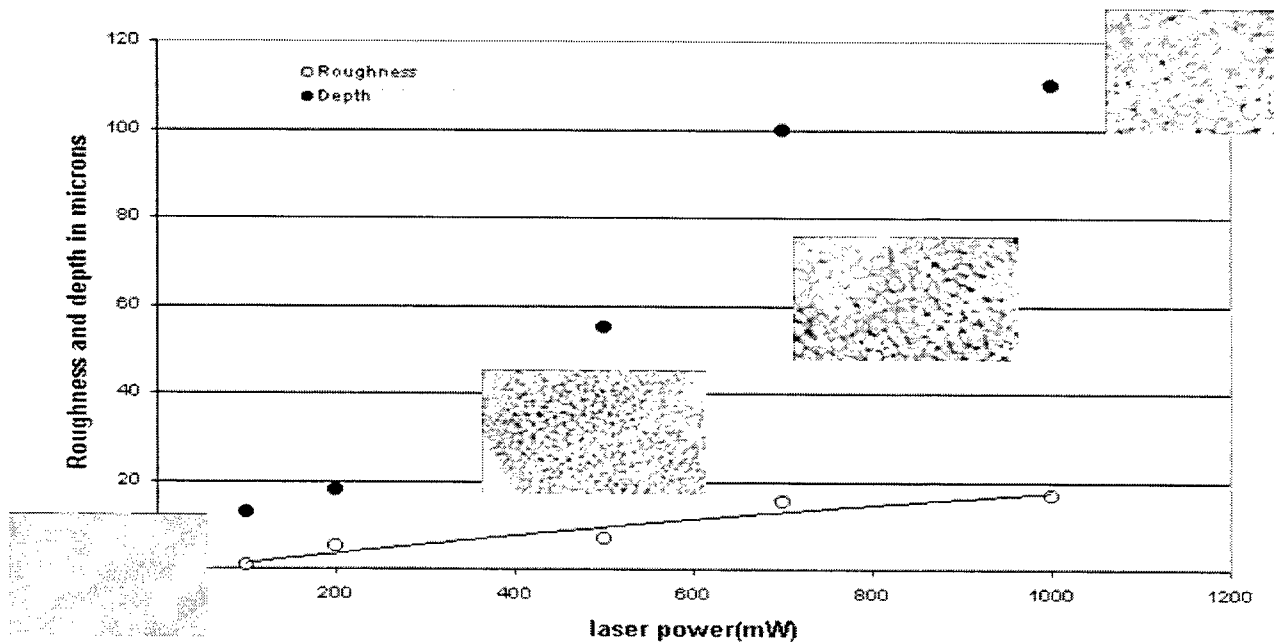
Figure (2) variation of roughness and depth with femtosecond laser power (micromachining was done in air).
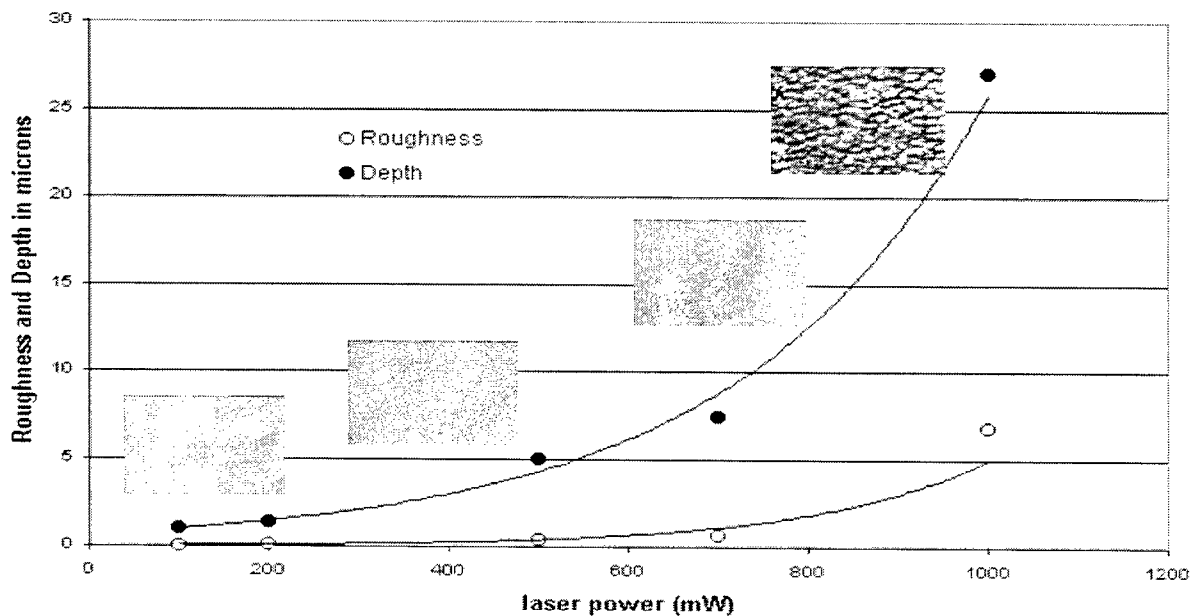
Figure (3) variation of roughness and depth with femtosecond laser power (micromachining was done in vacuum).

3.2 The submicron grating fabrication

A focus study was done by micromachining lines on the silicon wafer at different positions of the lens with respect to the sample. The focus run was performed at laser power of 5 mW. The laser power used to fabricate the submicron grating was 2 mW. The sample was translated at a speed of 50 μm/sec. Figure 4 shows that the depth of focus is about 10 microns. The linewidth is smaller at the focus point and then becomes wider as the sample moves away from the focus.

Moving away from the focus will increase the spot size, lowering the power density at the sample. Due to the Gaussian profile of the beam not all of the focus spot play a role in ablating the material. Only the central part of the beam has the energy above the ablation threshold.
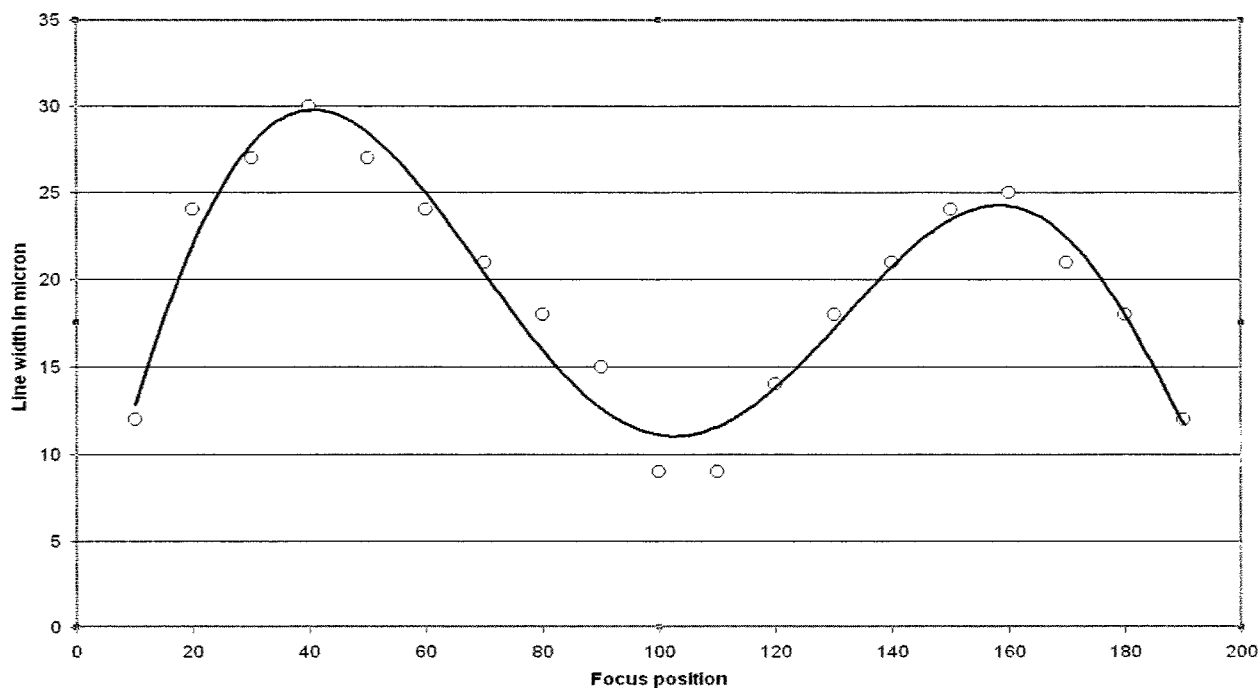
Figure (4) variation of linewidth with focus position using microscope objective of 0.85 numerical aperture.
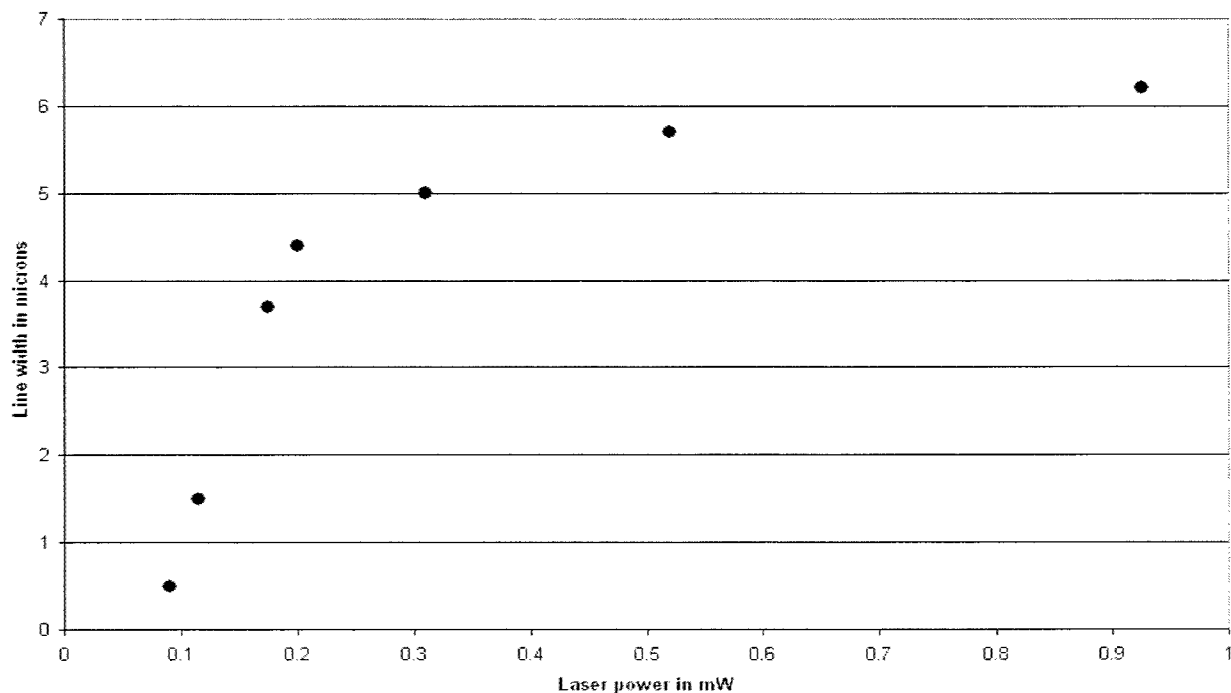
Figure (5) variation of linewidth with laser power

To study the effect of the laser power on linewidth, a sample was translated at 50 μm/sec under the beam and the laser power was carefully varied. It was noticed that the linewidth increased rapidly with the laser power and then saturated as shown in figure 5.

Laser micromachined lines under the optimum conditions were examined using an atomic force microscope (AFM). Figure 6 shows profile of a single line fabricated by femtosecond laser. The waviness in the line is due to the effect of the stepper motor. The depth of the line was about 200 nm and width as 390-450 nm. The rim around the line was ~ 40 nm in height.
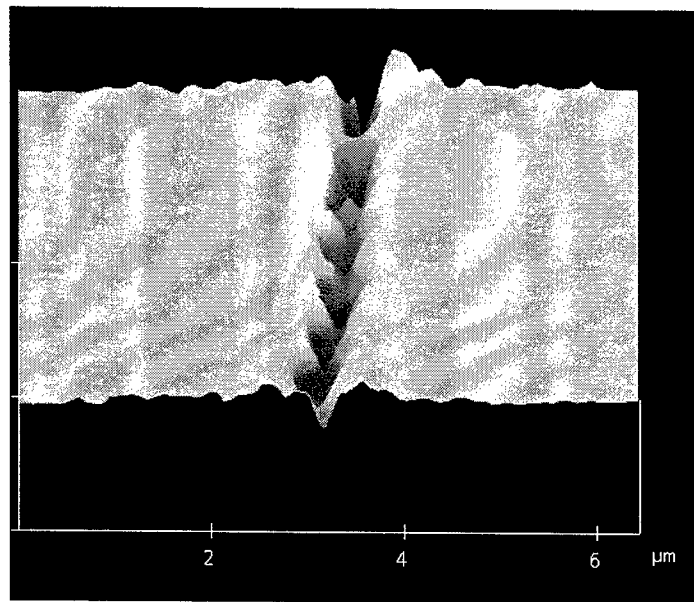
Figure (6) AFM photograph of femtosecond laser micromachined line.

Different grating periods were obtained by changing the laser parameters. Figure 7 shows a 2 micron linewidth grating obtained at ~ 3 mW laser power using a 0.65 NA objective lens. Figure 8 shows the depth profile of a 235 nm grating linewidth fabricated by femtosecond laser. The laser power was 88 μW.
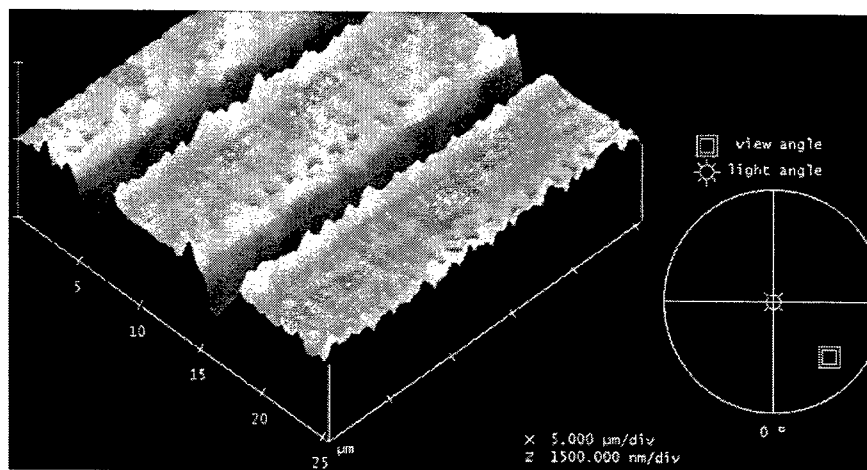
Figure (7) AFM photograph of 2 μm grating.
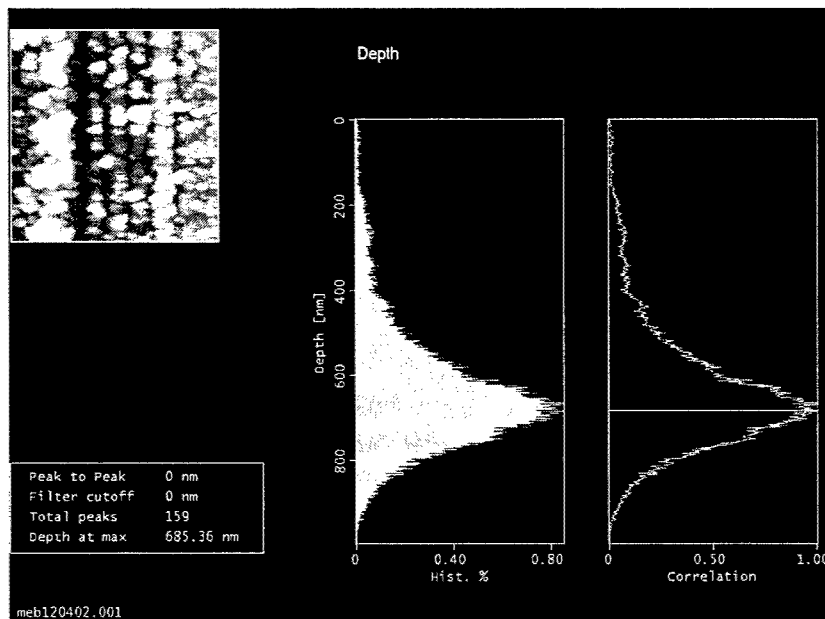
Figure (8) Depth profile of lines (linewidth = 235 nm).

4. CONCLUSIONS

The effect of air and vacuum on the silicon micromachining process using a femtosecond laser was studied. Micromachining in vacuum gave lower surface roughness than in air. Also a decreased in the rim on the edges was observed. A diaphragm was fabricated under vacuum at different laser powers with a low surface roughness. Using 400 nm wavelength spatially filtered femtosecond laser beam, a 235nm x 800nm grating was fabricated with a depth of 600 nm. Grating lines below the diffraction limit were achieved. Spatially filtering femtosecond laser beam was found to be an important step for submicron feature fabrication.

ACKNOWLEDGMENTS

REFERENCES

1.Bryan K.A. Ngoi, K. Venkatakrishnan, L.E.N. Lim and B. Tan, "Submicron Micromachining on Silicon Wafer Using Femtosecond Pulse Laser" *Journal of Laser application*, **13** No. 1, 41-43, 2001.

2. J. Bonse, S. Baudah, J. Kruger, W. Kautek and M. Lenzer, "Femtosecond laser ablation of silicon-modification threshold and morphology", *Appl. Phys. A*, **74,** 19-25, 2002.

3. Xinbing Liu "Ultrafast Lasers as a Versatile Processing Tool" *Proceeding of SPIE*, **3888**, 198-209, 2000.

4. K. Shihoyama, A. Furukawa, Ph. Bardo and A.A. Said, " Micromachining with Ultrafast Lasers", *Proceeding of SPIE*, **4088**, 140-143, 2000.

5. D.Von der Linda and K. Sokolowshi-tinten, "The physical mechanisms of short-pulse laser ablation", *Applied Surface Science*, **154-155,** 1-10, 2000.

6. J. Kruger and W. Kautek, "The Femtosecond Pulse Laser: a New Tool for Micromachining" *Laser physics*, **9** No. 1, 30-40, 1999.

7. Zhao Jianxin, Huettner Bernd and Menschig Arnd, "Micromachining with ultrashort laser pulses" *Proceeding of SPIE*, **3618**, 114-121, 1999.

8. S.Ameer-Beg, W. Perrie. Srathbone, J. Wright, W. Weaver and H.Champoux " Femtosecond laser micromachining of materials", *Applied Surface Science,* **127-129,** 875-880, 1998.

Sub-surface 3d structures by laser-induced modification of the optical properties of transparent materials

David Ashkenasi[*a], Hans-Jürgen Hoffmann[b], Dieter Krause[c], and Gerhard Müller[a]

[a]Division Applied Laser Technology,
Laser- und Medical-Technology GmbH, Berlin, Germany;
[b]Institut für Werkstoffwissenschaften und –technologien,
Technical University, Berlin, Germany
[c]Schott, Mainz, Germany

ABSTRACT

A new field in laser processing is opened by this method of modifying the optical properties, i.e. the refractive index, absorption- and scattering-coefficient, inside the material. Focusing ultra short laser pulses inside the transparent media allows to control and modify their optical properties. This is referred to as nik-engineering[TM], relating the experimental technique to changes of the complex refractive index $(n + ik)$. Three dimensional patterns of the $(n + ik)$ modifications can be achieved in the subsurface region even on a microscopic scale. New results in nik-engineering obtained in our application laboratory are presented using different optical materials. The results in laser nik-engineering of photo-chromic glass using ultra short laser pulses at a wavelength of 800 nm are presented to the best of our knowledge for the first time. We discuss the results and the possibilities of nik-engineering and consider the technological relevance with respect to decorative work, micro-tagging, and other functional structures.

Keywords: laser processing, nik-engineering[TM], sub-surface modification, damage threshold, ultra short laser pulses, photo-chromic glass.

1. INTRODUCTION

The availability of ultra short laser pulses (e.g. < 1 ps pulse width) has stimulated a growing interest in exploiting the femtosecond technology for micro-machining. Ultra short laser pulses (USLP) offer several advantages for precision micro-fabrication. Due to lower energetic thresholds for sub-picosecond ablation and the controllability of laser pulse width the amount of energy deposited into the processed sample can be localized and optimized. This reduces some disadvantageous thermal effects and minimizes energy diffusion,[1] so that very clean microstructures can be achieved. In addition, non-linear optical effects can be exploited, such as self focusing, which is relevant for transparent dielectric materials. Our study is guided by the generally accepted picture for the excitation of dielectrics with ultra short laser pulses with wavelengths in the near infrared spectral region: the initiating excitation mechanism is due to multi-photon absorption, either via morphological or structural defect states in the band gap or by interband transitions, which causes electron heating and additional ionization due to electron impact.[2,3] This is followed by an energy transfer from the "hot" electronic system into the lattice by electron-phonon coupling and subsequent heating of the sample.[4]

Corresponding author: * d.ashkenasi@lmtb.de; phone: +49 30 67053-6; fax: +49 30 67053-500; http://www.lmtb.de; Schwarzschildstr. 8, D-12489 Berlin, Germany;

The interaction between USLP and dielectrics is usually based on experimental studies on "pure" materials, such as sapphire, fused silica, fluorides and certain glasses. The thresholds for laser-induced surface and bulk damage has been investigated until now predominately in respect to cracks, voids, density changes, defect accumulation etc.[2-5] In the present paper, however, a new field of laser-induced (sub-surface) modification is presented: a persistent local change in the optical properties while the glass matrix remains "unharmed". In the following, results on this new type of laser-induced modification concerning the complex refractive index (nik-engineering[TM]) is described to our knowledge in the case of photo-chromic glass for the first time.

2. EXPERIMENT AND RESULTS

The experimental set-up is shown schematically in Fig. 1. A femtosecond laser system (Spectra Physics / Quantronix) generates ultra short laser pulses (0.17 ps) at a repetition rate up to 1 kHz with a single pulse energy of 1 mJ at 800 nm. A shutter (Uniblitz) and an attenuator are used to control the number of laser shots (N) and the single pulse energy (E), measured with an energy monitor device (LTB, Berlin) located near the sample surface. A Galilean telescope reduces the laser beam diameter approximately by a factor of 7. The sample is irradiated with USLP with a measured circular $1/e^2$ diameter of 500 µm (Gaussian intensity distribution). In addition, the beam of a 1mW cw He-Ne laser is aligned in the propagation path of the ultra short laser pulses to monitor the interaction between the laser beam and the material using a combination of an optical far-field microscope, a CCD-camera, and a video monitor. The material discussed in this paper is the photo-chromic glass "D6526 super brown" from Schott, Germany, which is utilized to fabricate self-adjusting sun-glasses. The transmittance of photo-chromic glasses is reduced by UV illumination (sun-light). A few minutes after the UV illumination is blocked, the photo-chromic glass recovers to its original optical transparency; thus, the photo-chromic effect is reversible. More details on the photo-chromic effect related to the laser-induced modifications are presented in the discussion. The glass sample is placed on a XY translation stage for vertical and horizontal translation. Except surface cleaning using methanol, no additional preparation of the 10 mm thick and curved photo-chromic glass blanks is required prior to the experiment.
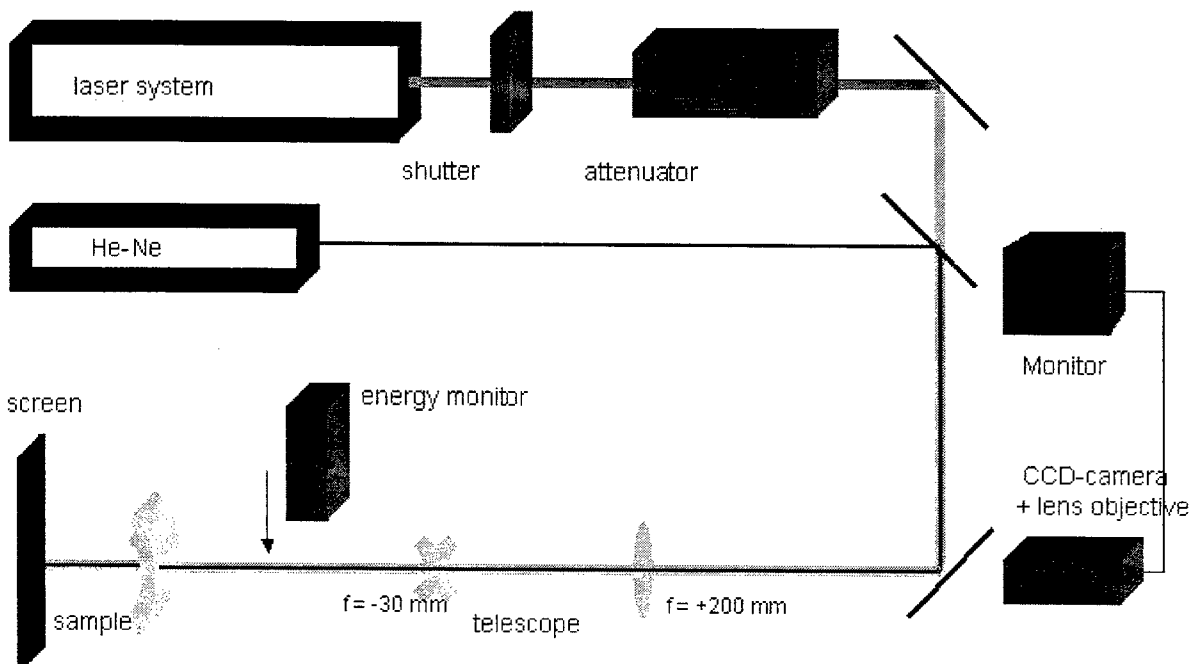
Fig. 1: Schematic illustration of the experimental set-up

At single laser pulse energy $E = 200$ µJ and a pulse width $\tau_p = 0.2$ ps, corresponding to a laser fluence of 100 mJ/cm^2 and a peak intensity of 0.5 10^{12}W/cm^2, the sample was irradiated with different pulse numbers N ranging from $N = 60$ to 10^5 shots per individual site, each 2 mm apart. The first $N = 60$ laser pulses induce a first irreversible modification in the sample only, which is called "bleaching" in this paper. The areas bleached by the ultra short laser pulses are difficult to detect unless the photo-chromic glass is held in sun-light. Using UV excitation the glass still darkens, except in the bleached volume (!). Fig. 2 depicts examples of sub-surface structuring using the effect of laser-induced bleaching to mark the photo-chromic sample (Zeiss logo). The laser-induced bleaching eliminates the photo-chromic effect permanently throughout the sample depth.

Fig. 2: CCD camera image of laser modified photo-chromic glass sample (10 mm thick) several minutes after is was held under sun-light. The region surrounding the modifications (two Zeiss logos of size 3mm x 3mm) are darker due to the (reversible) photo-chromic effect.
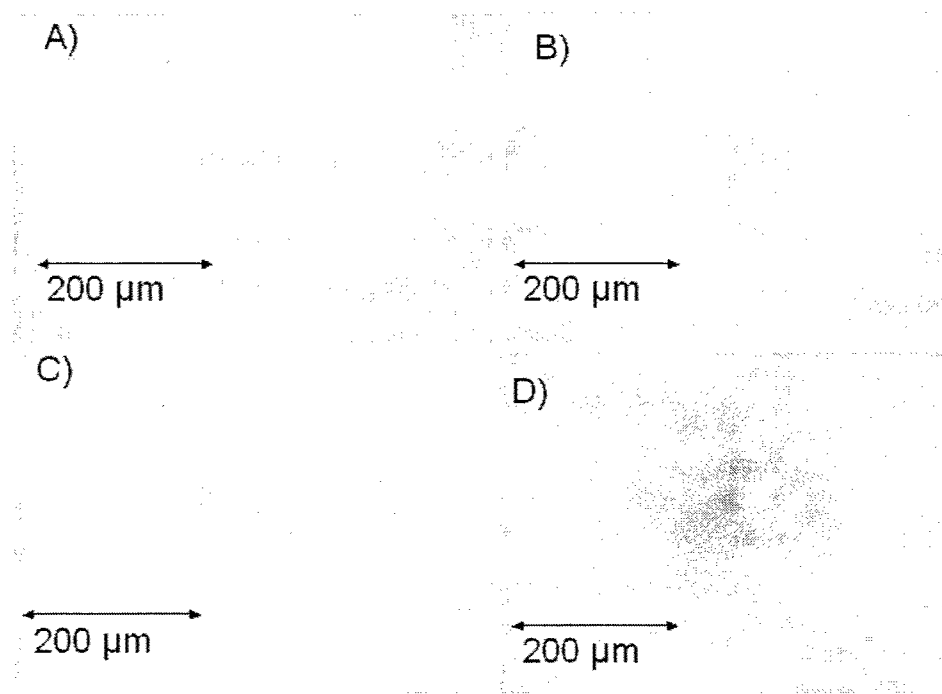
Fig. 3: Micrograph of laser modified photo-chromic glass, which has been irradiated using ultra-short laser pulses of 0.2 ps pulse duration and single pulse energy of 200 µJ at different pulse numbers N: A) $N = 2000$, B) $N = 5000$, C) $N = 10^4$, and D) $N = 10^5$.

With increasing shot numbers, a second type of permanent modification in the photo-chromic sample is obtained. Inside the bleached volume darkening of the glass is observed, quite different from the photo-chromic effect. Fig. 3 depicts the different stages of this second type of modification. After $N = 2000$ laser pulses on a single site, Fig. 3 A, an ensemble of dark micro dots or spots can be observed inside the bleached volume with an optical microscope. This persistent darkening effect is intensified with increasing shot number, see Fig. 3 B to D, where the micro dots increase in size and density. The individual dot size and the density seem to correspond with the fluence profile of the ultra short laser pulses.

Several additional observations have been made in this study, during and after propagation of the sub-ps laser pulses into the photo-chromic glass:

- generation of white light (super continuum) throughout the cylinder volume of ultra short laser pulses propagating inside the photo-chromic glass,
- photo-chromism during and after excitation even several mm outside the cylinder volume of ultra short laser pulses propagating inside the photo-chromic glass,
- photo-chromism recovers and remains active outside the laser illuminated cylinder volume,
- in situ observation of stray light of the He-Ne laser source from the cylinder volume during ultra-short pulse excitation,
- no modifications or ablation on the surface,
- no signs of micro cracking or internal stress such as birefringence observed,
- bleaching (in-active photo-chromic volume) observed at low fluence, multi-shot ($N = 6000$) threshold 3 to 6 µJ (1.5 to 3 mJ/cm^2) at 0.2 ps and 800 nm,
- persistent darkening in bleached volume observed at higher fluence, multi-shot ($N = 6000$) threshold 150 to 200 µJ (75 to 100 mJ/cm^2) at 0.2 ps and 800 nm,
- the darkening effect is seen as brown micro dots.
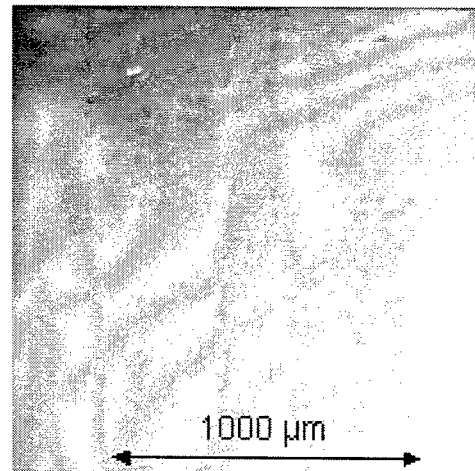
Fig. 4: Micrograph of laser modified photo-chromic glass, bleached and darkened using ultra short laser pulses at 0.2 ps and 200 µJ per pulse. Processing speed: 0.25 mm/s; repetition rate: 1 kHz.

To investigate the influence of accumulated energy, several areas of 3mm x 3mm were scanned at different single pulse energies E, processing speeds, and cycle numbers. The combination of the last two parameters sets the average shot number per site N_{ave}. The accumulated fluence $F_{acc} = F \times N_{ave}$ results from the product of single pulse fluence F (= single pulse energy $E/(\pi (250)^2 10^{-8})$ J/cm^2) times the average number of laser pulses per site N_{ave}. Fig. 4 depicts a laser darkened area inside the photo-chromic glass at $E = 200$ µJ ($F = 100$ mJ/cm^2) and $N_{ave} = 20000$. Processing the glass sample at single pulse energies of $E = 14$ and 75 µJ resulted in a bleaching effect only. This is observed even for relatively high average number of pulses $N_{ave} = 20000$, hence, an accumulated fluence of $F_{acc} > 650$ J/cm^2. This level of accumulated fluence is above the threshold obtained for the additional darkening effect using larger single pulse energies $E = 150$ and 200 µJ. The threshold for the darkening effect is in this case 600 J/cm^2. Hence, a minimal single pulse fluence is required to initiate the darkening effect in the laser bleached area. At a single laser pulse fluence of 100 mJ/cm^2, e. g., the darkening increases with the cycle number and decreases with the processing speed. The processing speed, however, has a stronger influence than the cycle number.

The laser-induced modifications inside the photo-chromic glass depend strongly on the pulse width used to irradiate the glass sample. Fig. 5 depicts micrographs of the laser modified volume using sub-ps and ps laser pulses at a single pulse energy of 200 µJ and the number of laser pulses on a single site of $N = 6000$. At a pulse width of 0.43 ps (0.23×10^{12} W/cm^2) the darkening effect disappeared, only the bleaching effect is observed. With increasing laser pulse width the bleaching effect is still noticeable, however, it is less pronounced in the case of 3.2 ps (0.03×10^{12} W/cm^2) compared to 0.43 ps.
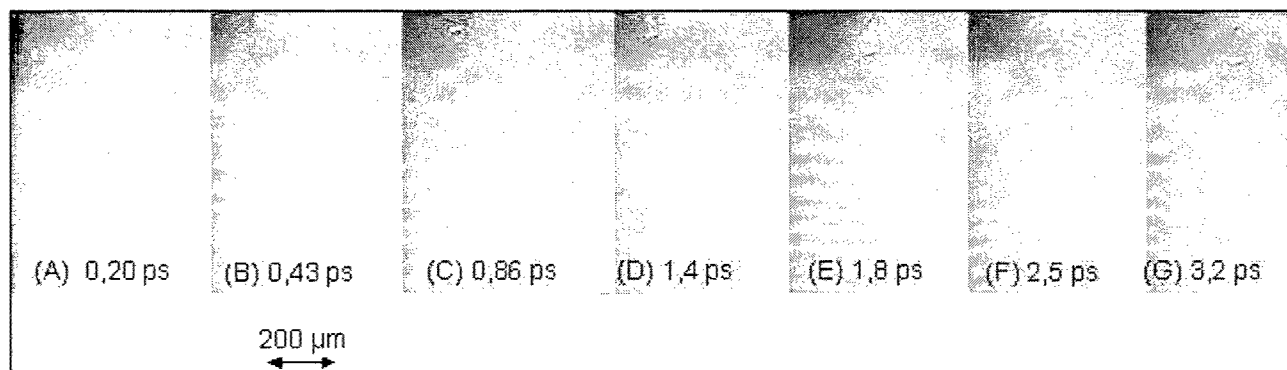
Fig. 5: Micrographs of laser modified photo-chromic glass using ultra short laser pulses at a pulse width between 0.2 ps and 3.2 ps. Single pulse energy = 200 µJ, laser fluence = 100 mJ/cm^2, number of shots $N = 6000$.

3. DISCUSSION

The results in laser-induced sub-surface persistent modification of optical properties, presented in the last section seem to be surprising. Similar experiments were conducted using nanosecond laser pulses in the IR (1064 nm) and UV (355 nm) spectral regions. The laser light generated by a *q-switch* Nd:YAG laser system was focused into the photo-chromic sample. As expected for photo-chromism, UV laser light causes darkening of the glass. However, the transmittance is not reduced persistently and the optical properties retain their original state after the UV irradiation of 10 ns laser pulses has been turned off. Increasing the laser fluence to about 10 J/cm^2 the glass matrix is damaged. One can see internal cracking and the development of voids. Even if any bleaching effect has occurred in this case, it might be masked by the damage in the glass matrix. To reach a peak intensity range of 10^{12} W/cm^2 with laser pulses of 10 ns, the laser fluence must be almost 10000 times higher compared to a laser pulse of 0.2 ps. This comparison makes clear that USLP provides conditions for high peak intensity and strong excitation of the material at a relatively low laser fluence, modifying the photo-chromic centers without necessarily causing internal damage of the glass matrix. The influence of the peak intensity is significant, as can be seen in Fig. 5. Therefore it is most appropriate to consider the (multi shot) threshold for bleaching and darkening also in terms of the peak intensity, 0.02×10^{12} W/cm^2 and 0.5×10^{12} W/cm^2, respectively, at a pulse width of 0.2 ps.

For better understanding of the relevant laser-material interaction mechanisms, one has to take a closer look at the material conditions, in this case the photo-chromic oxide glass (alkali-alumo-boro-silicate) doped with silver halides.[6] The presence of silver and halogen ions (Cl- and Br-) in the order of 0.1 to 1 % and copper ions in the order of several 1/100 % by the mass in the matrix is necessary to provide for photo-chromism. Depending on the composition of the matrix, the melting temperature of the photo-chromic glasses may range from 1200 to 1450°C. The formation of photo-chromic centers is driven by phase separation; the mechanism is discussed in detail by R. Pascova and I. Gutzow.[7] With the presence of photo-chromic centers the UV absorption edge is shifted. For an optimum performance of a self-adjusting sun-glass the diameter of the photo-chromic centers is between 10 and 25 nm. Assuming a diameter of 20 nm and an amount of 0.4 mass % distributed to photo-chromic centers, one can estimate that 5×10^{15} photo-chromic centers are present per cm^3 of the glass with an average distance of 125 nm. Each of these photo-chromic centers contains

approximately 10^5 silver ions. The performance of present photo-chromic glasses is characterized by Fig. 6a and 6b showing radiation-induced changes of the spectral transmittance and its dependence on time at a wavelength of 555 nm.[8] Photo-electrons and –holes are created during UV excitation. The lifetime of the photo-electrons is increased, since the copper ions are known as efficient traps for photo-holes. Since the recombination traffic is blocked, the photo-electrons are trapped at the interface between the silver halide particle and the glass matrix. Silver ions are attracted by the photo-electrons and form silver atoms after recombination. Eventually, a silver layer is formed, which is responsible for the broad band absorption (Fig. 6a).

After switching off the irradiation (excitation) regeneration mechanisms cause a reverse reaction. An electron is re-emitted from the silver speck and combines with the Cu^{2+} ion or a hole is emitted from the Cu^{2+} ion and diffuses to the silver speck. In both cases, a neutral silver atom of the silver speck is transformed into Ag^+, which diffuses back into the interior of the photo-chromic center.
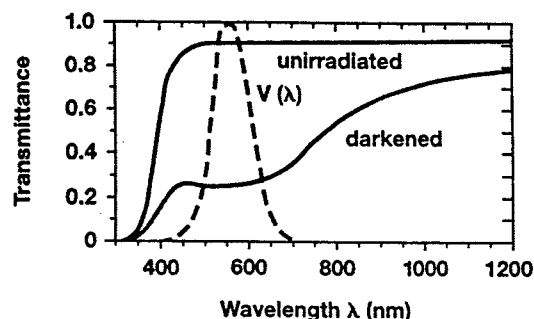
Fig. 6a: Transmittance of a commercially available photo-chromic glass as a function of the wavelength during and after solar irradiation for about 15 minutes at normal incidence (sample thickness = 2mm, room temperature). The dashed curve indicates the spectral sensitivity for photopic vision of the human eye.[8]
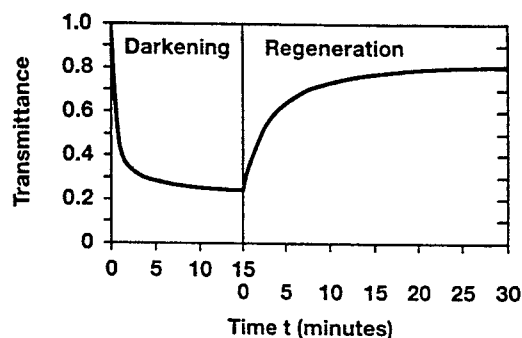
Fig. 6b: Kinetics of the transmittance of a commercially available photo-chromic glass (Fig. 6a) for the wavelength 555 nm after switching on and off the solar irradiation at room temperature.[8]

Fig. 7 illustrates schematically a preliminary model explaining the experimental observations on the photo-chromic glass after USLP excitation. Ultra short laser pulses with a wavelength of 800 nm propagate through the glass sample containing photo-chromic centers with a diameter of 20 nm, as illustrated in Fig. 7A. Efficient non-linear 2-photon excitation of the silver halide is expected at the peak intensity $> 10^{10}$ W/cm^2. In addition, a super continuum originating from the interaction of USLP with the glass matrix is also generated. Therefore, the blue and UV spectral part of the super continuum have to be considered as additional sources of excitation. For example, the off-axis radiation of the super continuum could explain the observed reversible photo-chromism **outside** the irradiated diameter 500 µm. Fig. 7B depicts the situation expected for the usual photo-chromic reaction. The photo-electron density increases at the interface silver halide and glass matrix. The picture in Fig. 7B illustrates a silver-ion drifting toward the negatively charged interface (photo-electron) to form neutral silver atom. Under low intensity conditions, i.e. sun-light irradiation, photo-chromic darkening takes place and lasts for minutes, see Fig. 6b. However, in the present case, photons of the USLP interact with the photo-chromic center in a time interval of only 0.2 ps. The photo-electron density at the interface between silver halide and the glass matrix increases drastically. Due to the slower mobility, silver ions are unable to follow the pace of the photo-electrons. Band filling of the conduction band of the photo-chromic centers is expected: the negative potential at the interface increases and will reach a level to force the photo-electrons to move into the glass matrix. This leads to the situation illustrated in Fig. 7C: electrons are distributed and trapped in the glass matrix around the silver halide. Positive silver ions are now able to escape the interface barrier and diffuse into the glass matrix. There.

they will recombine with the photo-electrons to form neutral silver atoms. The radial silver ion diffusion is enhanced by increasing Cu^{2+} ion density inside the silver halide. This loss mechanisms of silver ions from the silver halide is responsible for a size reduction of the photo-chromic center, as indicated in Fig. 7C. After switching off the irradiation (excitation), a regeneration mechanism as in the "classic" situation for a photo-chromic center is not possible for the "escaped" silver atoms. The loss process for the photo-chromic center is irreversible (at room temperature), yielding a further reduction of the silver halide during multi-shot excitation. A photo-chromic center with a diameter sufficiently below 10 nm does not show efficient photo-chromism; thus, at this stage the bleaching effect is obtained. In consequence, the intense excitation and ionization of the silver halide causes the partial or perhaps even a complete non-thermal destruction of the nano-particle similar to a Coulomb explosion.[4]
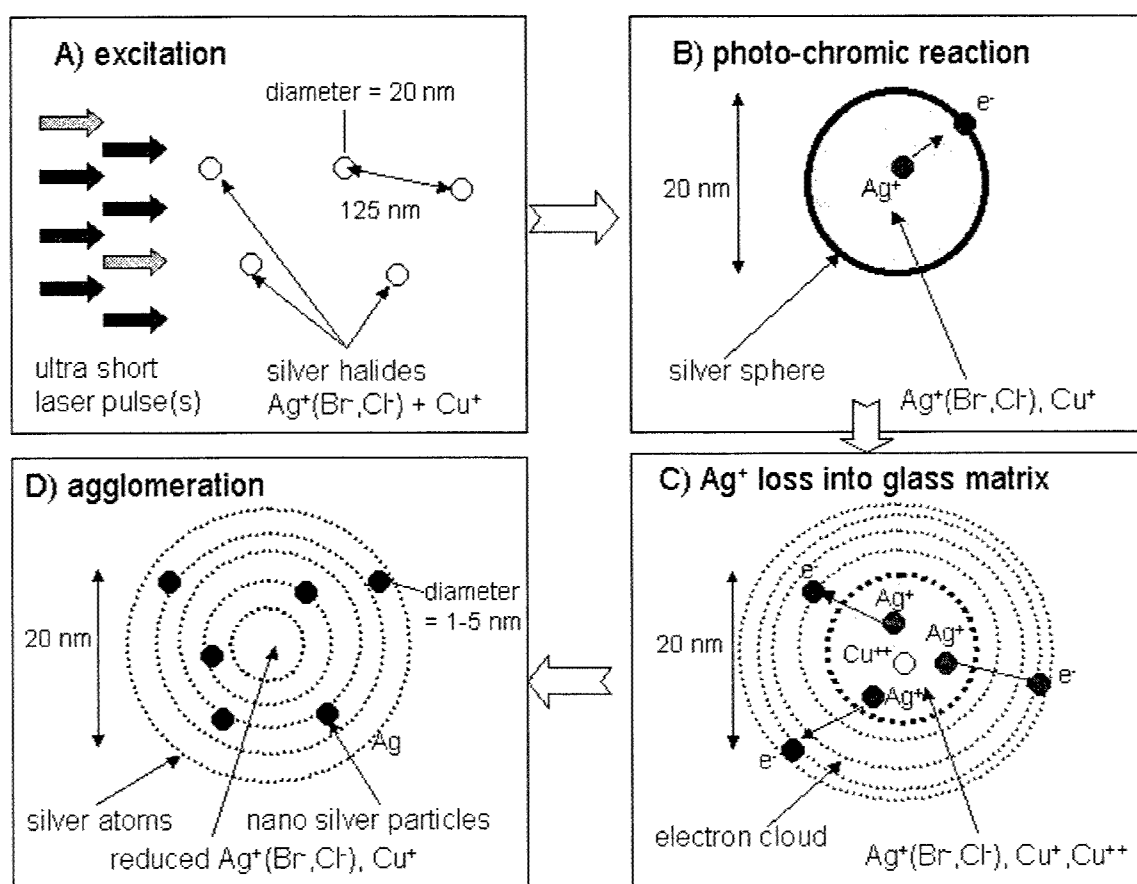
Fig. 7: Schematic illustration of the events responsible for A) laser excitation. B) photo-chromic reaction. C) Ag+ loss into the glass matrix (bleaching) and D) agglomeration of silver atoms (persistent darkening).

The micrographs in Figs. 3 and 4 demonstrate an additional effect in the bleached volume at a laser fluence of 100 mJ/cm^2 and an intensity of 0.5x10^{12} W/cm^2 after several 1000 laser pulses: a persistent darkening in form of dots. A thermal response related to the laser fluence could induce the following: An increase in the mobility of the silver atoms and silver clusters in the glass matrix around the remnant silver halide. An agglomeration mechanism of the silver atoms (and small clusters) will then yield silver nano-particles, as illustrated in Fig. 7D. It is expected that the silver nano-particles stabilize in sizes from 1 to 5 nm.[9,10] In addition, the thermal response enhances its destruction of the original silver halides which are stable only below 800°C. A temperature gradient inside the silver halide would additionally

contribute to its destruction. This process can act as an additional source for silver atoms and clusters, which agglomerate into larger silver nano-particles inside the glass matrix. In conclusion, the strong excitation, scaling with laser *peak power density*, initiates the conversion of the silver halide nano-particle into many silver atoms (or very small clusters) inside the glass matrix. The subsequent thermal response, scaling with the laser *fluence*, accounts for improved conditions for silver agglomeration, hence, the development of nano silver particles, estimated to be smaller than 5 nm. Based on the above model, laser modification remains confined to the glass constituents, in this case the silver halides.
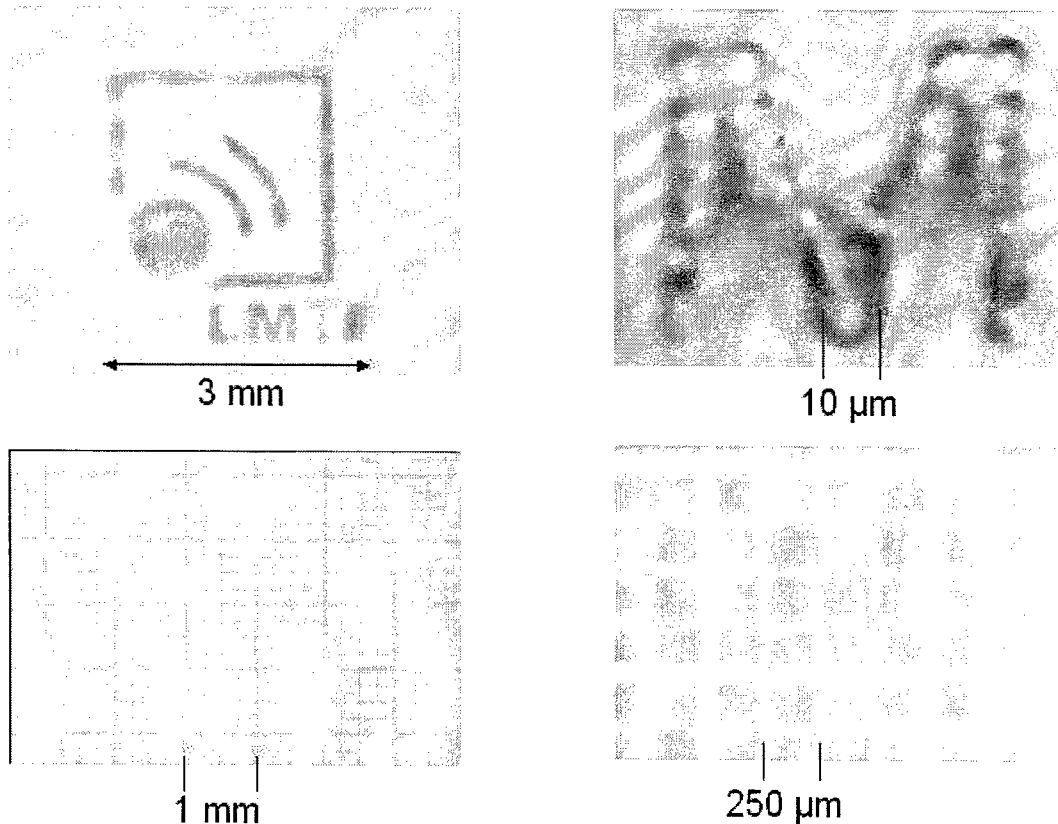
Fig. 8: Micrographs of laser-induced sub-surface modifications inside a special glass made by Schott, Germany: examples of nik-engineering (patent pending). Top left picture: LMTB company logo throughout the 3 mm thick sample; top right: enlargement of the "M" in the logo; bottom pictures: micro scale in the same glass, processed at a spacing of 250 μm.

Besides of (invisible) sub-surface tagging, other applications are possible for commercial usage. Fig. 8 depicts examples of nik-engineering in a different material, a special glass from Schott, Germany. The top microscope picture of Fig. 8 shows the logo of the LMTB fabricated using a cut mask and placed in front of the sample during scanned laser illumination. The bottom picture depicts an example of a sub-surface micro-scale generated in direct writing method. The line thickness scales with the single pulse energy. The mechanisms responsible for the laser sub-surface processing are quite similar to the photo-chromic material discussed above. There is also the believe that the visible changes in the optical properties inside this special glass originate from laser-induced modifications in the glass constituents. The observed alterations are due to a laser-induced reduction and/or conversion of the original (prior to USLP excitation) nano-particles into single atoms, clusters, or other nano-particles inside the glass matrix.

4. SUMMARY

The method of laser-induced sub-surface modification of the optical properties, i.e. the change in the complex refractive index, is referred as nik-engineering[TM]. Irradiation of photo-chromic glass with ultra short laser pulses (USLP) with a wavelength of 800 nm and a pulse width of 0.2 ps leads to two different observations: 1) a bleaching effect, i.e. the photo-chromism is unattainable throughout the volume of USLP excitation; 2) a persistent darkening, i.e. the occurrence of dark dots inside the bleached volume at larger laser fluence and number of USLP on identical site. The laser fluence (and peak intensity) threshold for both types of modification are identified as 1.5 to 3 mJ/cm^2 (about 0.01×10^{12} W/cm^2) for the bleaching and 75 to 100 mJ/cm^2 (about 0.5×10^{12} W/cm^2) for the persistent darkening, which was not observed at 100 mJ/cm^2 for pulse widths of 0.43 ps. The model presented in this paper for the first time explains the experimental observations. It follows the concept of a strong electronic excitation of a nano-particle, in this case a silver halide photo-chromic center with a diameter of about 20 nm. The large peak intensity forces the photo-electrons to move into the glass matrix. Silver ions will follow and neutral silver atoms are formed outside the photo-chromic center. Repetitive excitation will result in size reduction of the silver halide (i.e. bleaching) and the increasing temperature inside the glass matrix will provide for agglomeration of silver atoms to develop nm large silver particles (i.e. persistent darkening). Further examples of nik-engineering -using a different type of special glass- demonstrate the commercial potential of this new method. Additional experimental and theoretical investigations in our facilities will be continued to check and improve the current state of our interpretation and demonstrate the technological relevance with respect to optically functional nano-structures.

ACKNOWLEDGEMENT

REFERENCES

1) E.E.B. Campbell, D. Ashkenasi, A. Rosenfeld, *Lasers in Materials Science* (Trans Tech Publications, Switzerland, 1999), pp. 123-144, 1997.

2) B.C. Stuart, M.D. Feit, A.M. Rubenchik, B.W. Shore, M.D. Perry, *Phys. Rev. Lett.* **74**, pp. 2248, 1995.

3) A.-C. Tien, S. Backus, H. Kapteyn, M. Murnane, G. Mourou, *Phys. Rev. Lett.* **82**, pp. 3883, 1999.

4) R. Stoian, D. Ashkenasi, A. Rosenfeld, E.E.B. Campbell, *Phys. Rev. B* **62**, pp. 13167, 2000.

5) B.C. Stuart, M.D. Feit, S. Herman, A.M. Rubenchik, B.W. Shore, M.D. Perry, *Phys. Rev. B.* **53**, pp. 1749, 1996.

6) H.J. Hoffmann: Photochromic Glass, p. 273-288, *The Properties of Optical Glass* (ed. H. Bach – N. Neuroth), Schott Series on Glass and Glass Ceramics, Springer Berlin, 1995.

7) R. Pascova and I. Gutzow, "Modelluntersuchungen zum Bildungsmechanismus fototroper Silberhalogenidphasen in Gläsern", *Glastechn. Ber.* **56**, pp. 324-330, 1983.

8) H.J. Hoffmann. "The use of silver salts in photochromic glasses", in Studies in Organic Chemistry (ed. H. Dürr – H. Bouas-Laurent), Vol. **40**, pp. 822-854, 1990

9) U. Kreibig. "Small silver particles in photosensitive glass: their nucleation and growth", *Appl. Phys.* **10**, pp. 255-264, 1976

10) T.P. Seward III. "Coloration and optical anisotropy in silver-containing glasses", *J. Non-Crystalline Solids* **40**, pp. 499-513, 1980

Fabrication of diffractive optical elements by ArF-laser ablation of fused silica

József BÉKÉSI, Dirk SCHÄFER, Jürgen IHLEMANN*, Peter SIMON

Laser-Laboratorium Göttingen, Hans-Adolf-Krebs-Weg 1, 37077 Göttingen, Germany

ABSTRACT

Excimer laser ablation at 193 nm is used for the generation of a surface relief structure on fused silica with the aim to fabricate diffractive optical phase elements to be applied for efficient laser materials processing. Though there are several problems to achieve high aspect ratio material removal at this laser wavelength (193 nm) in a scarcely absorbing material (fused silica), ablation of sub-μm depth, as it is needed to generate the appropriate phase delays of diffractive phase elements (DPE) for UV-applications, is possible without cracking. Applying a machining process corresponding to a bitmapped DPE design generated by an Iterative Fourier Transform Algorithm (IFTA), the fused silica surface is patterned on a 128 x 128 pixel^2 area with a pixel size of 12.5 x 12.5 μm^2. The step height of this two level DPE has to be adapted to the combination of the wavelength, at which the element will be applied, and the refractive indices of the DPE-material and the environment. The example DPE is designed as a 10 x 10 focus raster generator for a UV-femtosecond laser operating at 248 nm. Using this DPE in combination with a 25x Schwarzschild objective, the parallel drilling of micron sized holes in stainless steel and other metals is demonstrated.

Keywords: diffractive optical elements, laser ablation, fused silica, femtosecond laser

1.   INTRODUCTION

Diffractive optical elements (DOE) gain increasing importance in various fields of beam shaping or illumination control, like microscopy, laser lithography, or laser material processing [1]. They are mainly used either for efficient utilization of light, for beam homogenization, or for correction purposes in combination with refractive systems. In laser micromachining applications based on mask projection systems (like excimer laser drilling of ink jet nozzles) DOEs may be used for the efficient illumination of the mask. Especially, if the mask has a non-uniform distribution of areas of transmission, the minimization of losses can be accomplished by DOEs distributing the light only into these areas of interest. In addition, DOEs enable laser micro machining with ultrashort pulses without vacuum, whereas geometrical imaging leads to air breakdown in the focus at high intensities [2].

Diffractive optical elements make use of the diffraction of light at small structures. They can be characterized as amplitude or phase elements. Diffractive phase elements (DPE, often named kinoforms), may consist of a pattern of refractive index variation or of a surface relief structure. This surface relief may be continuous or, mainly due to the ease of fabrication, can have a binary or a multilevel structure. The simplest kinoform to be used at a wavelength λ is a binary surface relief structure on a material of refractive index n with a depth modulation of d = λ / 2(n-1). Lateral structure dimensions are of the order of 5 to some 10 λ, depending on the optical configuration and the coherence parameters of the light for which the DPE is designed.

*jihle@llg.gwdg.de; phone +49 551 503544; fax +49 551 503599; www.llg.gwdg.de

For a DPE to be used in the visible spectral range, surface structures with a depth of about 0.5 μm and lateral dimensions of 5 μm are required. In the case of polymeric materials, these dimensions are easily accessible by (single pulse) excimer laser ablation. Some attempts have already been made to fabricate DPEs by laser ablation, either on the basis of pixel by pixel irradiation [3-4] or image based using chrome masks [5] or dielectric masks [6-7]. Recently the laser shaping of diamond for IR diffractive optical elements has been demonstrated [8].

Mass fabrication of plastic DPEs is easily performed by replication techniques. But the fabrication of a high quality master DPE for replication, or of an original in glass (quartz) material is rather complicated and expensive. Time consuming lithographic methods (exposure, etching etc.) are required, and for the etching of fused silica special equipment is needed. Therefore less complex fabrication techniques are desired.

Also for fabricating DPEs which can be used for UV laser applications, it is necessary to structure fused silica or other materials with high UV transmission. In this paper we describe the fabrication of DPE by laser ablation of fused silica, and the application of these elements for the drilling of micron sized holes in metals with a UV ultrashort pulse laser system.

2. DESIGN OF DIFFRACTIVE OPTICAL ELEMENTS

Various concepts are applied for the design of diffractive optical elements. The most frequent applications are the generation of homogeneous intensity in specified areas or the generation of a multi beam array (beam splitter or fan-out element). A beam splitter consisting of an array of six sub-apertures has been presented to generate four spots for a micro machining application [9]. In this example alternating binary gratings with horizontal and vertical grooves have been used to shape a KrF excimer laser beam, i.e. different parts of the signal originate from light coming from different sub-apertures. This concept is similar to the composition of simple geometrical objects to more complex intensity signals with a DPE based on geometrical optics [10]. In contrast to this method we use the Iterative Fourier Transform Algorithm (IFTA), which is capable of forming nearly any arbitrary intensity distribution [11]. If this concept is used in combination with the segmentation of the beam in sub-apertures, every sub-aperture contributes to the whole signal distribution.
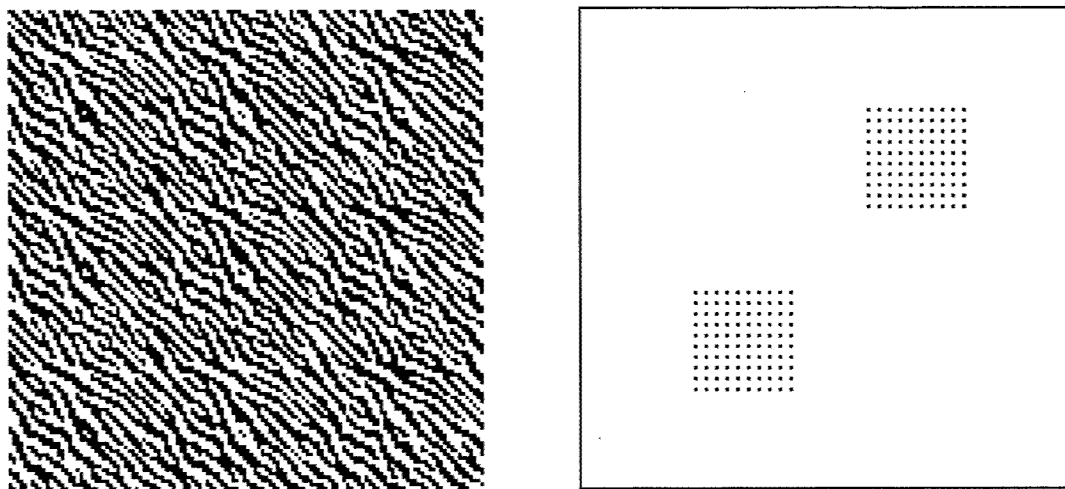
Fig. 1   IFTA-designed binary bitmap and computer simulated reconstruction showing the intensity distribution in the signal plane

For the demonstration of the producibility of a DPE in fused silica by laser ablation, a comparatively simple intensity pattern was selected. It consists of a 10 x 10 fan-out element (focus raster generator). The calculated phase distribution

is represented by a 128 x 128 binary bitmap. A two level DPE always causes a point symmetric intensity distribution (fig 1). The DPE can be designed as a Fraunhofer-element, i.e. the intensity distribution is reconstructed in infinity, or as a Fresnel-element, i.e. the plane of reconstruction has a finite distance from the element. A Fraunhofer-element can be used in combination with a lens to transfer the reconstruction from infinity to the focal plane of this lens. To be used with optimal diffraction efficiency at a wavelength λ, the relief step height of a binary DPE has to be $d = \lambda/2(n_r - n_0)$, if n_r is the refractive index of the DPE-material and n_0 the refractive index of the environment. For example, for a reconstruction wavelength of $\lambda = 248$ nm and fused silica ($n_r = 1.51$) in air ($n_0 = 1$) the required step height is $d = 244$ nm.

3.   FABRICATION OF DIFFRACTIVE OPTICAL ELEMENTS

For the application of DPEs in transmission in the ultraviolet spectral range, the use of UV-transparent substrates is necessary. The most common UV-substrate material is fused silica. However, the UV-transparency of fused silica complicates its machinability by laser ablation, because precise ablation requires absorption of the laser radiation. Though laser machining with comparatively long wavelengths was applied to fused silica for the purpose of hole drilling [12], the precise removal with sub-μm depth control requires at least deep UV lasers. The F_2-laser emitting at 157 nm is well suited for this task, because the photon energy of 7.9 eV matches the band gap of the material [13]. In this case beam delivery requires CaF_2-optics and an O_2-free beam path, which complicates the process. Alternatively, femtosecond titanium-sapphire lasers were applied for the ablation of quartz material [14]. This leads to good results for hole drilling, but the beam properties are not optimal for the ablation of flat spots with smooth surface, as they are needed for a DPE.
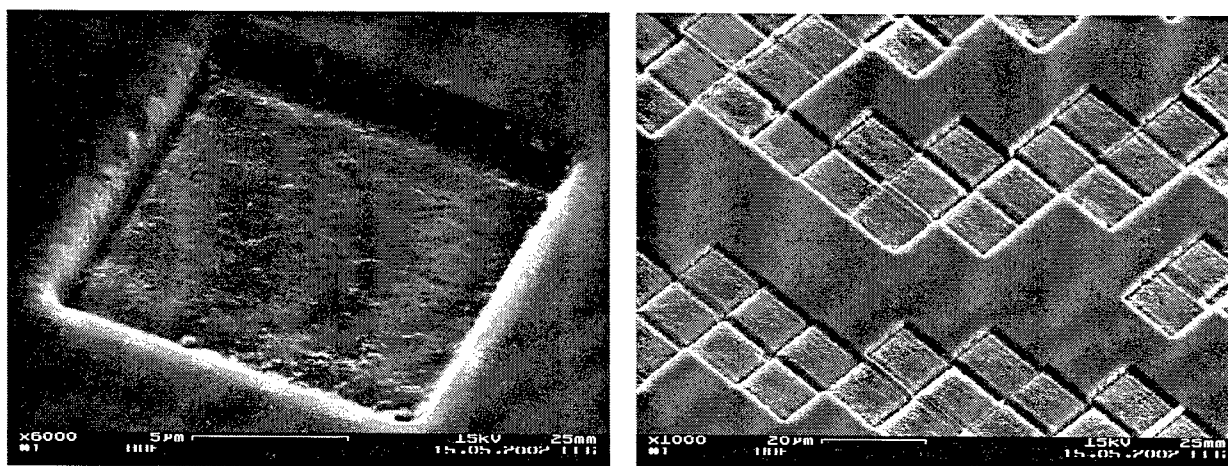
Fig. 2   Ablation of fused silica by 193 nm ablation (19 J/cm², 2 pulses per pixel)

    (a) Single ablation spot ("pixel"), 12.5 x 12.5 μm²   (b) Part of the binary DPE pattern

The ArF-excimer laser (nanosecond pulse duration) was also successfully applied for fused silica ablation [15]. The advantage of the excimer laser is its practically flat top beam profile, which enables the desired homogeneous ablation on a square spot by mask projection technique. Due to weaker absorption compared with the F_2-laser, the ablation threshold of fused silica at 193 nm (ArF-laser) is three times higher, about 3 J/cm². This is already a fluence leading to dielectric breakdown with ns-pulses, so that the removal process is likely dominated by plasma mediated ablation [16]. The minimum ablation rate is about 200 nm/pulse, which complicates the precise adjustment of the ablation depth to a desired phase delay value. Furthermore the probability of the formation of cracks after a certain number of pulses is rather high. Apparently these cracks appear only after the accumulation of defects after application of several pulses per

position, so that the ablation spot after one ore two pulses looks very clean and smooth, especially if a high laser fluence is used. Due to these restrictions concerning the adjustment of a proper phase delay by tuning the ablation depth, another parameter has to be adjusted. This is the refractive index of the surrounding medium. If instead of air, water or a water-solvent mixture is used, the appropriate phase delay can be adjusted for a given step height by tuning this refractive index.

The calculated phase level distribution in bitmap form (fig. 1) was transferred into a surface relief on fused silica (Suprasil 1) by ablating pixel by pixel with the 193 nm-laser. With a pixel size of 12.5 μm x 12.5 μm the total size of the DPE is 1.6 mm x 1.6 mm. For each pixel to be ablated, two pulses of about 19 J/cm^2 were applied reaching an ablation depth of 900 nm (fig. 2). Then, if the surface profile is immersed in water ($n_0 = 1.37$ at 248 nm), the step height condition for application at 248 nm is matched quite well. Before application the surface was cleaned from ablation debris by slightly polishing it with window cleaning powder.

4.   UV-FEMTOSECOND LASER ABLATION WITH DIFFRACTIVE OPTICAL ELEMENTS

In many cases of high resolution laser processing the pulse duration is the limiting factor for precision and resolution. If lateral spreading of the absorbed energy out of the irradiated zone occurs during the laser pulse, the fabrication of accurate structures is prohibited. The extension of the heat affected zone scales with the square root of the pulse duration. For materials with high heat conductivity, e.g. metals or semiconductors, even a pulse duration of some nanoseconds is still too long to generate sub-micron features [17-19]. Therefore short pulse laser systems like Ti:Sa lasers are more and more applied for micro machining of metals. On the other hand, the optically achievable resolution scales inversely with the wavelength. Roughly speaking, no lateral features significantly smaller than the laser wavelength can be created. Obviously, a laser system combining short wavelength and short pulse duration, represents the best prerequisite for sub-micron processing of metallic solids. Such a system is given by a UV-femtosecond excimer laser system operating according to the following scheme [20]: The output of a commercial Ti:Sa system (500 μJ pulse energy and 150 fs pulse duration at 745 nm) is frequency tripled to 248 nm and then amplified in a KrF-excimer module. In a three-pass amplification scheme the pulse energy is increased to about 30 mJ. Though the system can be operated at 300 Hz, resulting in an average power of about 10 W at 248 nm, the processing speed is limited, if the laser beam is focused to a small spot, and structures are "written" sequentially, e.g. drilling holes one after the other. A parallel process like mask imaging is much faster and more efficient. However, in applications with a small filling factor of the mask (large opaque areas with only a few transparent regions) a large amount of laser radiation is lost at the mask and the process becomes rather inefficient. In these cases, a diffractive phase element, which except for Fresnel reflections at the surfaces and diffraction losses, transfers the whole laser energy to the workpiece, may provide a much more efficient and therefore faster process.

| Ti:Sa-Laser with frequency tripling | → | KrF amplifier | → | Diffractive phase element | → | Schwarzschild objective | → | Work piece |
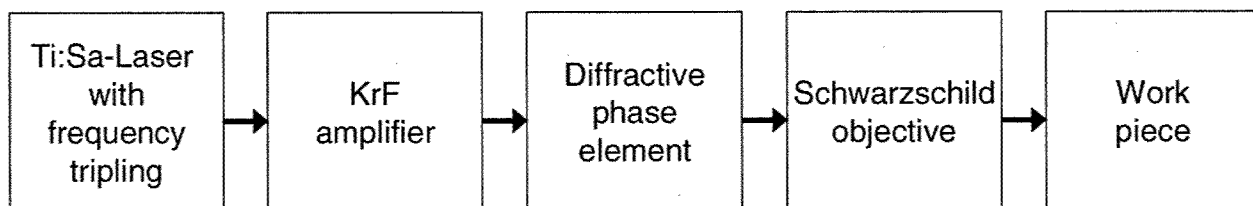
Fig. 3   Scheme of the maskless parallel hole drilling with UV-femtosecond-laser

To demonstrate this method, the UV-femtosecond laser was used for maskless simultaneous drilling of a 10 x 10 hole array with the DPE shown in figures 1 and 2. The process scheme is shown in fig. 3. The DPE was used here in combination with a 25x Schwarzschild objective (NA = 0.4). This achromatic focusing system serves for high resolution and is essential with the use of ultrashort pulses to avoid pulse front distortions, which would deteriorate the

signal pattern. The results of patterning stainless steel and nickel are shown in figure 4. The micron-sized holes have a spacing of about 4 μm.

(a)

(b)
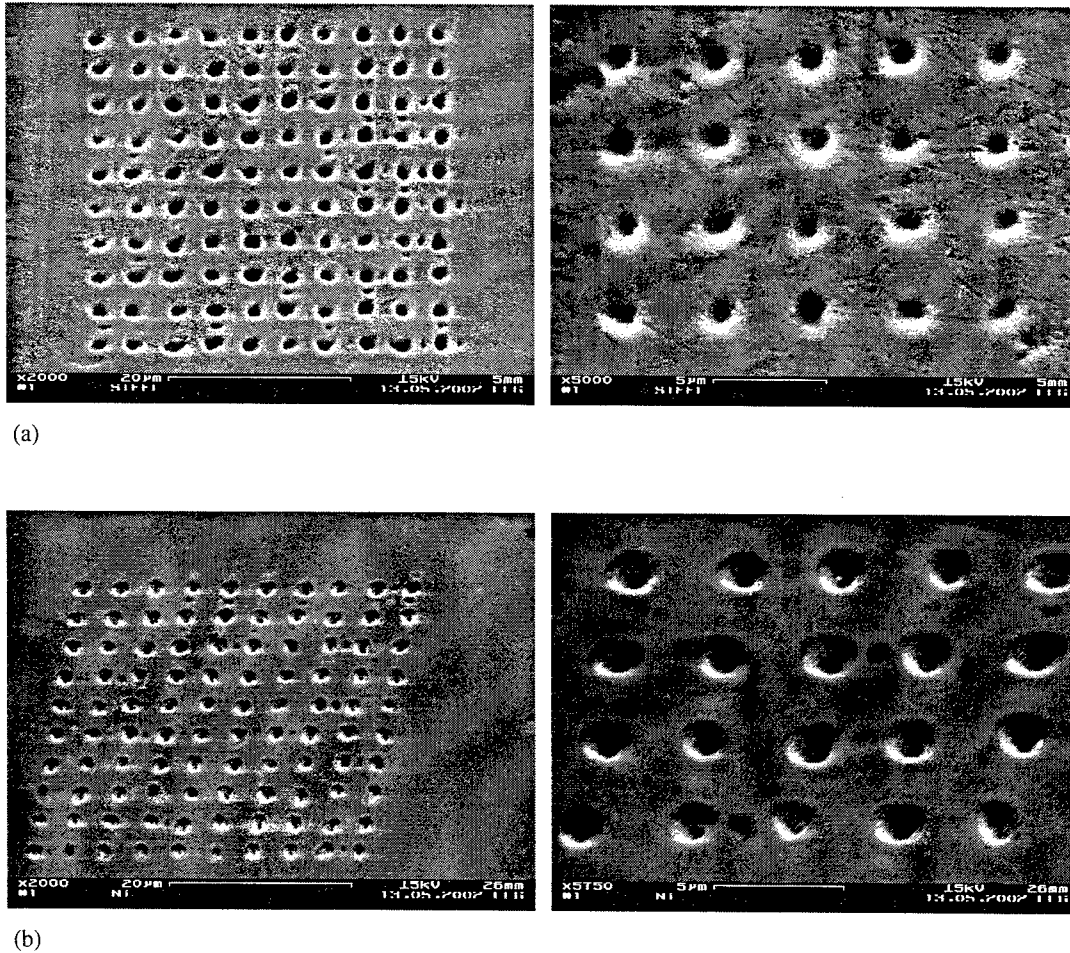
Fig. 4   10 x 10 hole arrays (pitch 4 μm) in metals, generated by UV-ultrashort pulse laser with diffractive phase element

(a)   Stainless steel, 248 nm, 300 fs, 780 mJ/cm², 100 pulses

(b)   Nickel, 248 nm, 300 fs, 520 mJ/cm², 50 pulses

5.   SUMMARY

Diffractive phase elements (designed on the basis of IFTA) for UV-laser applications can be made by laser machining of fused silica. ArF-excimer laser ablation leads to smooth and clean pixel patterns, though the possibilities of precise adjustment of the ablation depth are limited. The adjustment of the phase delay is therefore assisted by tuning the refractive index of the environment of the DPE. The performance of the elements in maskless laser processing is demonstrated by parallel drilling of micron-sized holes in metals using a UV-femtosecond laser.

REFERENCES

[1] J. Turunen, F. Wyrowski eds., *Diffractive Optics for Industrial and Commercial Applications*, Akademie Verlag Berlin 1997.

[2] C. Momma, S. Nolte, G. Kamlage, F. von Alvensleben, A. Tünnermann, "Beam delivery of femtosecond laser radiation by diffractive optical elements", *Appl. Phys. A* **67**, 517-520 (1998).

[3] G.P. Behrmann, M.T. Duignan, "Excimer laser micromachining for rapid fabrication of diffractive optical elements", *Appl. Opt.* **36**, 4666-4674 (1997).

[4] N.A. Vainos, S. Mailis, S. Pissadakis, L. Boutsikaris, P.J.M. Parmiter, P. Dainty, T.J. Hall, "Excimer laser use for microetching computer-generated holographic structures", *Appl. Opt.* **35**, 6304-6319 (1996).

[5] X. Wang, J.R. Leger, R.H. Rediker, "Rapid fabrication of diffractive optical elements by use of image-based excimer laser ablation", *Appl. Opt.* **36**, 4660-4665 (1997).

[6] D. Schäfer, J. Ihlemann, K. Mann, G. Marowsky, "Excimer laser patterned dielectric masks for the fabrication of diffractive optical elements by laser ablation", *Appl. Phys. A* **69**, S319-S322 (1999).

[7] J. Ihlemann, D. Schäfer, "Fabrication of diffractive phase elements for the UV-range by laser ablation patterning of dielectric layers", *Appl. Surf. Sci.* **197-198**, 856-861 (2002).

[8] V.V. Kononenko, V.I. Konov, S.M. Pimenov, A.M. Prokhorov, V.S. Pavelyev, V.A. Soifer, B. Lüdge, M. Duparré, "Laser shaping of diamond for IR diffractive optical elements", *Proc. SPIE* **4426**, 128-138 (2002).

[9] A.-K. Holmér, S. Hård, "Laser-machining experiment with an excimer laser and a kinoform", *Appl. Opt.* **34**, 7718-7723 (1995).

[10] T. Dresel, M. Beyerlein, J. Schwider, "Design and fabrication of computer-generated beam-shaping holograms", *Appl. Opt.* **35**, 4615-4620 (1996).

[11] F. Wyrowski, "Diffractive optical elements: iterative calculation of quantized, blazed phase structures", *J. Opt. Soc. Am. A* **7**, 961-969 (1990).

[12] C. Buerhop, B. Blumenthal, R. Weismann, N. Lutz, S. Biermann, "Glass surface treatment with excimer and CO_2 lasers", *Appl. Surf. Sci.* **46**, 430-434 (1990).

[13] J. Ihlemann, S. Müller, S. Puschmann, D. Schäfer, M. Wei, J. Li, P.R. Herman, "Fabrication of submicron gratings in fused silica by F_2-laser ablation", *Appl. Phys. A* 2003, in press.

[14] H. Varel, D. Ashkenasi, A. Rosenfeld, M. Wähmer, E.E.B. Campbell, "Micromachining of quartz with ultrashort laser pulses", *Appl. Phys. A* **65**, 367-373 (1997).

[15] J. Ihlemann, B. Wolff-Rottke, P. Simon, "Nanosecond and femtosecond excimer laser ablation of fused silica", *Appl. Phys. A* **54**, 363-368 (1992).

[16] L. Dirnberger, P.E. Dyer, S. Farrar, P.H. Key, P. Monk, "Laser ablation studies of magnesium oxide", *Appl. Surf. Sci.* **69**, 216-220 (1993).

[17] S. Preuss, A. Demchuk, M. Stuke, "Sub-picosecond UV laser ablation of metals", *Appl. Phys. A* **61**, 33-37 (1995).

[18] J. Krüger, W. Kautek, "Femtosecond-pulse laser processing of metallic and semiconducting thin films", *Proc. SPIE* **2403**, 436-447 (1995).

[19] P. Simon, J. Ihlemann, "Machining of submicron structures on metals and semiconductors by ultrashort UV-laser pulses", *Appl. Phys. A* **63**, 505-508 (1996).

[20] J. Békési, S. Szatmari, P. Simon, G. Marowsky, "Table-top KrF amplifier delivering 270 fs output pulses with over 9 W average power at 300 Hz", *Appl. Phys. B* **75**, 521-524 (2002).

Laser processing of photonic & micro-electronic components using multiple visible and UV wavelength source

E.K. Illy[*], G Rutterford, & M.R.H. Knowles
Oxford Lasers Ltd., Abingdon Science Park, Abingdon, OX14 3YR, U.K.

ABSTRACT

Laser processing using a multiple visible and UV wavelength copper laser source is presented with particular emphasis on photonic and microelectronic applications. Visible micromachining of ceramics and diamond are discussed in addition to UV micromachining/microfabrication of germanium doped silica, sapphire and kapton.

Keywords: laser micromachining, copper vapor laser, microelectonics, fibre Bragg gratings, dicing

INTRODUCTION

Laser micromachining is today an industrially accepted and widely available resource. Nevertheless lasers still offer a unique advantage for processing next generation photonics and microelectronics components. Micron feature sizes are readily achieved with most laser sources and coupled with excellent resolution and accuracy, high power, low heat deposition, precision beyond mechanical methods, and high efficiency, the use of lasers for machining is an obvious choice. In addition, coupling the laser energy into the material by understanding the materials absorption and interaction characteristics, can mean the optimum laser wavelength can be identified. Due to the high band gap of materials frequently used in the manufacture of photonics and microelectronics components, laser wavelengths in the visible to UV part of the spectrum are most efficient for processing. In particular, visible radiation is highly suited to machining the ceramics used in laser diode mounts and fibre array connectors while, UV wavelengths are ideal for fabricating fibre bragg gratings (FBG) in silica fibre. Thus a laser source offering both visible and UV wavelengths has extensive capabilities.

The industrially proven copper vapor laser (CVL) enables multiple discrete wavelengths in both the visible and UV (578, 511, 255, 271, 289nm) to be accessed, making it a highly favourable source for use in processing the many different materials used in the manufacture of photonic and microelecrtonic components. This paper describes a wide range of applications in opto-electronic component manufacture which have been laser processed using a CVL.

MICROMACHINING METHODS

The fundamental visible wavelengths of the CVL at 511nm and 578nm have been used widely for laser

---

micromachining and extensively reported over the past 20 years[1,2,3,4]. More recently, micromachining and fabrication of FBGs using the second harmonic of 511nm and 578nm, at 255nm and 289nm respectively, has also been presented[5,6,7].

From the fundamental wavelengths second harmonics can be generated using the nonlinear crystal super beta barium borate (s-BBO). In addition to the second harmonics, the sum frequency generation of the fundamentals can produce 271nm. The high repetition rate (6-20kHz) and moderate average power (1-20W) of the copper laser, means the low pulse energy (~10-50µJ) is advantageous for precise removal of material in a controllable manner. Typical operating parameters of the LM100 (511 & 578nm) and FBG*Ultra* (255nm, optional 271 & 289nm) are shown in Table 1.

	Visible		UV		
Wavelength (nm)	511	578	255	271	289
Average power (W)	10-20	3-7	0.3	0.3	0.15
Pulse duration	40ns		30ns		
Repetition rate (standard)	6-20kHz		6kHz		
Peak power	>10kW		1kW		
Temporal coherence length	40mm		40mm		
Spatial coherence	-		1mm		
Beam diameter	25mm		2mm		
Divergence	0.05mrad		0.5mrad		
Polarization ratio	random		>100:1		
Power consumption	4kW		4kW		

Table 1: Parameters of the LM 100 (visible) & FBG*Ultra* (UV) high beam quality configuration.

The high resolution and precision required for laser micromachining and fabrication of FBGs, means excellent average power stability as well as excellent beam pointing stability are imperative. The pointing stability of the FBG*Ultra* has been shown to be better than 10µrad, while the passive power stability is 0.3% rms over 1 hour and 1.0% rms over 8 hours. These values enable efficient inscription of complicated Bragg gratings by phase mask or interferometric methods, as well as the production of micro resolution structures for micromachining applications.

In general, laser micromachining is performed by focussing the beam to a small spot of high intensity, using this to melt/ablate the material. Methods for achieving this can be loosely categorised as either percussion or trepanning techniques. By the percussion method, the sample is exposed for a fixed period while stationary. More often than not, an object is imaged to produce the required pattern or hole. By the trepanning method, the beam or sample is translated during the beam exposure period to produce round holes, a method often referred to as micro-drilling. Further translating the sample, while trepanning or not, is often referred to a micro-cutting. A schematic of these methods is shown in Figure 1.
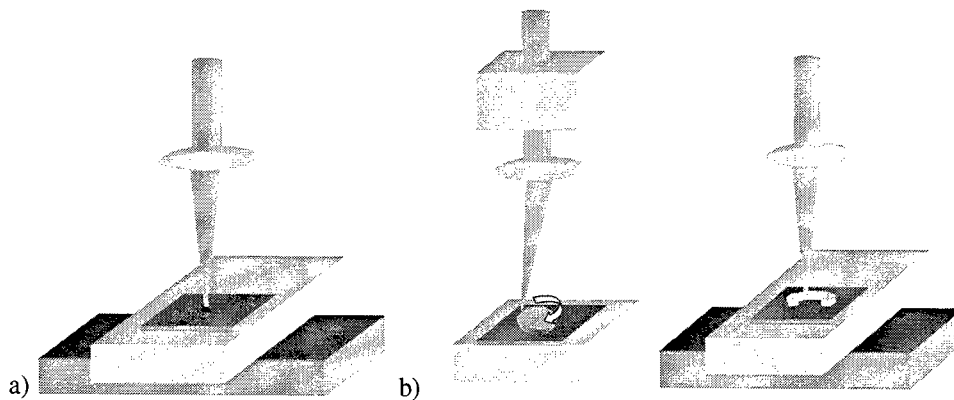
Figure 1: Schematic of methods for laser machining by a) percussion & b) trepanning of sample.

For visible laser micromachining averages powers from 10-20W are used in conjunction with a 150mm focal length BK7 achromat lens and computer controlled Aerotech translation stages. For UV micromachining, average powers ranging from 100mW – 1W are used depending on the material. High quality microscope objectives are used to deliver the beam to the computer controlled stages. Analysis is typically performed using optical microscopy and scanning electron microscopy.

For the fabrication of fibre bragg gratings (FBG) average powers of ~250mW in a high beam quality configuration are used in conjunction with a 300mm focal length cylindrical lens focussed parallel to the fibre axis. Analysis of FBGs is performed in real-time using an optical spectrum analyser (OSA) in conjunction with a broadband light source that is launched through the fibre. The reflectivity of the grating is measured as a function of time from which a value of the refractive index modulation (Δn) can be calculated.

PROCESSING USING 511 & 578NM WAVELENGTHS

During the laser processing of metals, ceramics, diamond and composites both 511nm and 578nm beams are typically combined to utilise maximum power. The combined visible lines are highly suited to machining ceramics that are used in laser diode mounts and fibre array connectors for photonics applications.

Ceramics

Although ceramics can be laser processed using both infrared and visible wavelengths, glassification often results using the longer infrared wavelengths. Glassification results in a 'recast' layer that can reduce accuracy and induce cracking, however, can be avoided by using shorter visible wavelengths thereby enabling efficient laser processing of such materials. High precision and accuracy are demonstrated using the visible wavelengths from the CVL in the manufacture of ceramic laser diode mounts and fibre terminators. The processes of micro-milling, micro-cutting and micro-drilling are all combined for the manufacture of the mount shown in Figure 2a. The hole diameter is 50±1μm, while the milling angle is 45°. The total size of the part is 5mmx 2mm with a neck width of 1mm. An example of ceramic fibre-optic ribbon terminators are shown in Figure 2b. Ceramic 640μm thick was machined to produce 127μm diameter holes with high taper angle in the upper half of the hole and parallel sides on the lower half of the hole, on a 120μm pitch. The precision and reproducibility required for such an application means that

alternative mechanical methods can not be used. These components are typically used to align fibres where loss of alignment translates to signal loss.
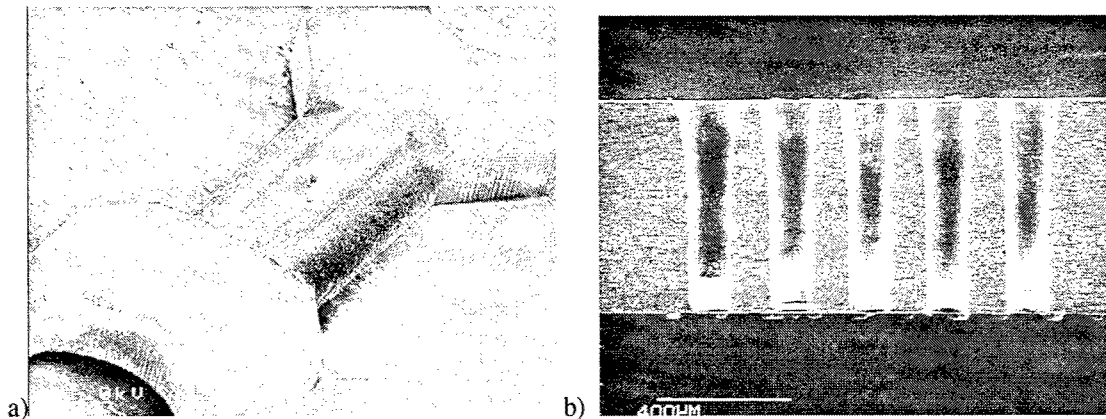
Figure 2: a) Ceramic laser diode mount & b) ceramic fibre terminator (cross-section) machined using visible CVL beam.

CVD Diamond and composites

Diamond is an inherently stable pure insulator with resistively values similar to aluminium nitride and is often used in advanced packaging of photonic components. Diamond's extreme hardness can only be machined using laser light with high power and adequate photon energy. This makes laser processing of diamond possible using the visible wavelengths of the CVL. An example of CVL processed diamond in shown in Figure 3a for use as a heat spreader for alignment of the fibre to the diode. The sample is 0.3mm thick and 0.5mm x 0.75mm squares were machined with low taper and minimal graphitization for electrical isolation. Another example of processing 200μm diameter holes in diamond is shown in Figure 3b.
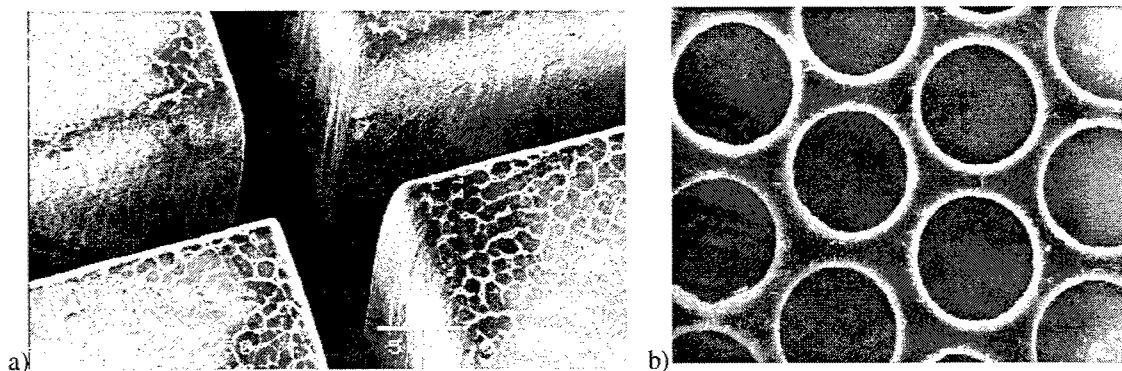
Figure 3: a) Diamond heat spreaders & b) 200um diameter holes machined using visible CVL beam.

Ceramic and metal composites, eg aluminium/silicon carbide, have been machined for use in high-spec circuit boards. Holes of diameter 50μm have been processed in a couple of seconds. Other ceramics such as aluminium nitride, silicon nitride and silicon carbide have been readily machined for applications such as component substrates and wafer probe cards. Materials such as copper, stainless steel and aluminium are also readily machined using the visible wavelengths of the CVL[2,10]. The higher absorption of metals and alloys in the visible enables efficient coupling of photon energy with lower heat deposition into the

sample. As metals and alloys are used in a foray of applications within photonics and microelectronics, laser processing using the visible wavelengths is regularly applied.

PROCESSING USING 255NM & 271NM WAVELENGTHS

Materials processing and component fabrication using deep UV wavelengths has abundant applications in both photonic and microelectronics industries. In particular, the high UV absorption of polymers and glasses materials results in a principally photochemical ablation process thereby producing high quality features with micron resolution. By comparison, non-linear processes have been attributed to efficient processing of semiconductor materials.

Bragg gratings

Fibre Bragg gratings (FBG) are phase perturbations within the core of the optical fibre resulting from a UV induced refractive index modulation. This refractive index modulation means a single wavelength (or channel) satisfying the Bragg condition can be selected and therefore FBGs find applications as filters in multiplexing/demultiplexing components of optical networks.

Of the three UV wavelengths available from the UV-CVL, 255nm is most suited to the manufacture of FBGs due to the high absorption of germanium doped silica at this wavelength. The high pulse rate of the CVL means that peak powers are moderate and, in addition to the high absorption of silica fibre at 255nm, that write times are fast. Furthermore, the low pulse energy means fibre strength and component lifetime is maintained.

The methods for producing FBGs using the UV-CVL has been extensively discussed elsewhere[8,10] and will not be described in detail here. By using either the phase mask method or interferometric methods complex grating profiles can be produced for use as specialised filters in optical network devices. In general, the phase mask method is used for simplicity, however, the principal limitation is the fixed wavelength of the grating. In some instances when flexibility is routinely required, the interferometric technique is used to write gratings over a wide range of Bragg wavelengths. This flexibility in grating wavelength surpasses the rather complicated optical arrangement, however, requires good coherence from the writing source. In addition, the zeroth order, which reduces the fringe visibility and thus refractive index modulation, can be removed using the interferometric technique.
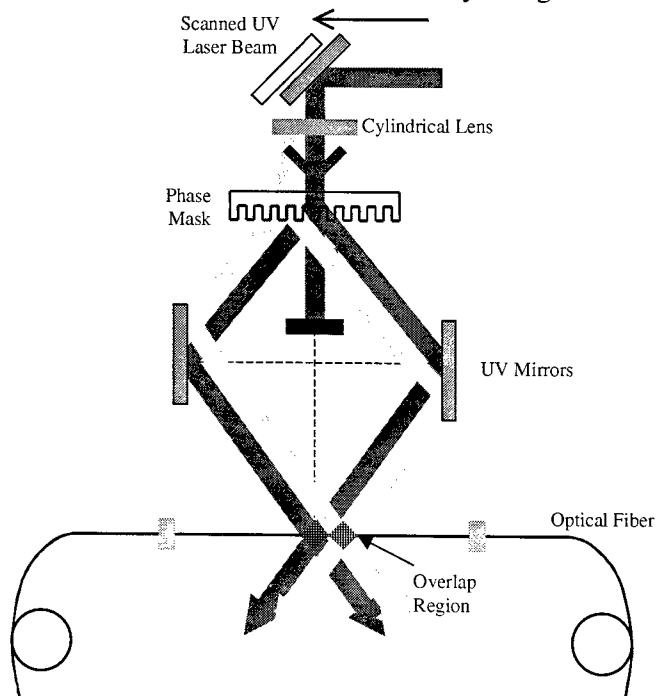
Figure 4: Schematic for writing FBGs using the UV-CVL in a scanning interferometric arrangement.

The interferometric technique can be further expanded to produce custom optical filters, again with flexibility in grating wavelength as well as grating bandwidth. By scanning the beam along the phase mask a semi-apodised narrowband filter can be produced[11]. A schematic of this arrangement is shown in Figure 4.

The filter bandwidth requirements mean that gratings need to be of the order of 15-35mm for use at 50GHz and 25GHz channel spacing respectively. In the above experiment the grating length was limited by the small diameter (1") turning mirrors and therefore the beam was only scanned ~3mm, however, this method could still be scaled to longer gratings. A slow velocity (0.01-0.02mm/s) was used due to low reflectivity of the mirrors. The total average power delivered to the fibre was only 60mW. By scanning the beam, it is also possible to 'soften', or apodise, the boundaries of the grating to produce an ideal rectangular bandpass filter in a similar method to that used to apodise scanned gratings using the phase mask technique. An example of a non-apodised filter is shown in Figure 5.
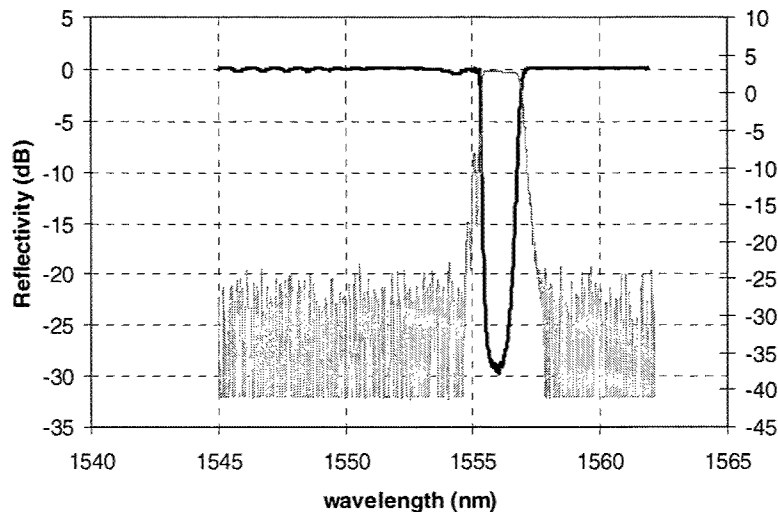
Figure 5: Reflection and transmission profiles for a non-apodised scanned grating of length 3mm, velocity 0.02mm/s written in H$_2$ loaded B/Ge co-doped fibre.

The reflectivity of the grating shown in Figure 5 is ~30dB with a bandwidth of ~1.6nm. The reflection profile shows evidence of some apodisation possibly due to the gaussian beam profile present when focussed onto the fibre. Filters produced by the scanning method for commercial components, such as 25GHz filters, have been previously presented[12].

The longer UV wavelengths of 271nm and 289nm available from the UV-CVL enable grating writing in materials other than silica and lends to the possibility of inscription through the protective coating layers of optical fibre and wafer based devices.

Substrate Dicing
The high average UV powers delivered by the UV-CVL allow fast translation velocities and high quality wall finish to be achieved when scribing sapphire and GaN substrates that are often used in photonics applications such as blue light emitting diodes (LEDs) and microarray LEDs. The high intensities achievable in the UV enable non-linear processes, and therefore efficient micromachining of these hard materials is possible.

Laser dicing of substrates is rapidly emerging as the choice for manufacturing LEDs. The narrow kerf, typically 10μm, is an order of magnitude smaller than the resulting kerf using conventional diamond sawing techniques. This means high component density is feasible thus significantly reducing the cost of manufacturing.

An example of cross-sections from scribing sapphire and GaN using 255nm from the UV copper laser is shown in Figure 6. The kerf width was <30μm, the thickness of the sapphire wafer was 0.3mm and GaN wafer was 0.25mm. The scribe velocity was 0.05mm/s in the sapphire and 1mm/s in the GaN.
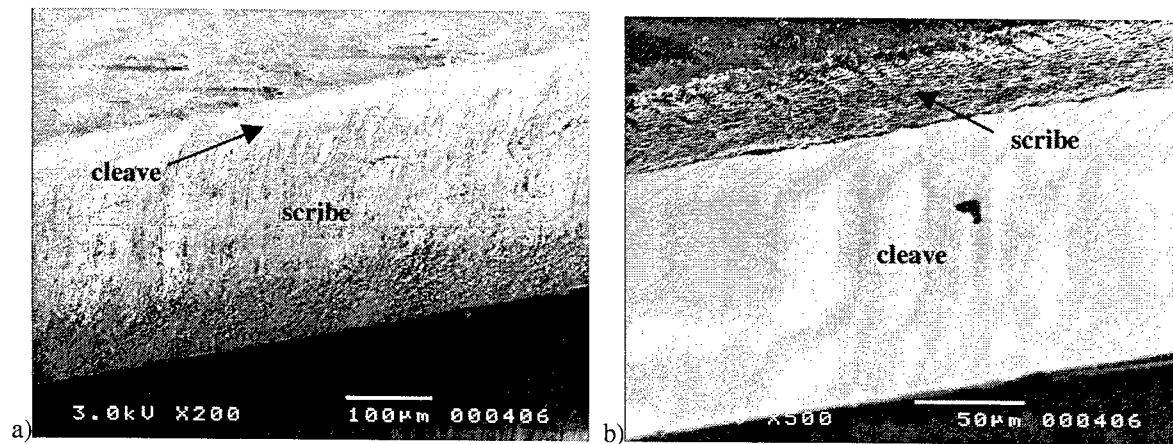
Figure 6: Sapphire scribing of a) 0.3mm thick sapphire & b) 0.25mm thick GaN using the UV-CVL (images courtesy of Institute of Photonics, University of Strathclyde, Glasgow, UK).

No thermal damage to the component was reported after laser scribing[13]. Kerf widths of <15μm have been achieved for ~30μm deep scribes in 0.1mm thick sapphire at velocities in excess of 5mm/s.

From the scribing data (ie scribe depth, velocity and width), the etch rate (μm/pulse) of sapphire can be calculated for use with a laser source at 6kHz. This data is shown in Figure 7.
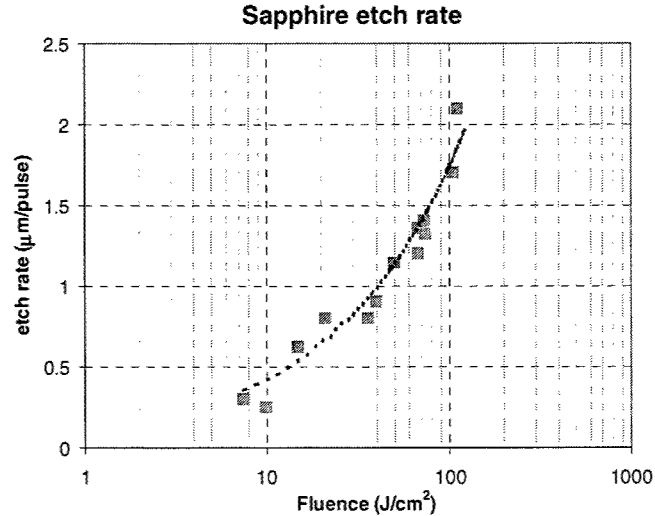
Figure 7: Etch rate data for scribing sapphire using the UV-CVL at 6kHz.

Polymers

The excellent insulating properties of polymers mean they are routinely used in the manufacture of multi-layer microelectronic components. The high UV absorption of these polymers such as kapton (PI) and mylar (PET) mean they can be easily machined away from the conducting copper layers, without damaging these connecting tracks. Holes with typical diameters of 50μm as well as shapes are readily produced using the percussion method in conjunction with imaging an object. The imaging method guarantees roundness and reproducibilty, while the low pulse energy of the UV-CVL is used to control the depth with micron resolution and the high pulse rate allows fast exposure times. Exposure times are typically of the order <50ms for drilling >100μm thick kapton. Examples of holes and squares are shown below in Figure 8.
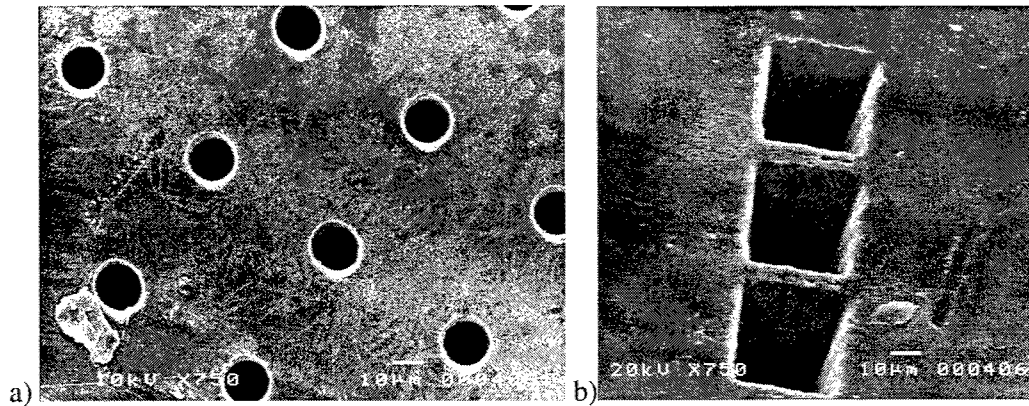
Figure 8: SEM of a) 20um diameter holes & b) 50um squares (note irregularity in quality of object is evident) in kapton.

CONCLUSIONS

Laser materials processing using visible wavelengths of 511nm and 578nm of the copper vapor laser has been demonstrated as an effective, precise and efficient process for the micro-processing of materials often used in the manufacture of photonics and microelectronics components. The UV wavelengths also available from the CVL at 255nm, 271nm and 289nm have applications in the fabrication of Bragg gratings and dicing photonic components as well as micromachining polymers for microelectronic manufacture. These applications demonstrate the versatility of the frequency doubled copper laser in the manufacture of photonic and microelectronic devices.

References

1. M.R.H. Knowles, A.J. Kearsley., R. Foster-Turner., J.E. Abbott, J.M. Boaler., K.H. Errey, "Visualization of small hole drilling using a copper laser," *Proceedings of ICALEO 94* **79,** 352-361, (1994).

2. M.R.H. Knowles, R. Foster-Turner, A.I. Bell, A.J. Kearsley, A.P. Hoult, S.W. Lim, and H. Bisset, "Drilling of shallow angled holes in aerospace alloys using a copper laser," *Proceedings of ICALEO 95* **80,** 321-330, (1995)..

3. D. Kapitan, D. W. Coutts and C. E. Webb, "On pulsed laser ablation of metals: comparing the relative importance of thermal diffusion in the nanosecond-femtosecond regime," *Conference on Lasers and Electro-Optics – Europe* paper CThH76 (1998).

4. J.J. Chang, B.E. Warner, E.P. Dragon and M.W. Martinez, "Precision micromachining with pulsed green lasers," J. Laser Applications **10,** 285-291 (1998).

5. A.C. Glover., D.W. Coutts, D.J. Ramsay and J.A. Piper, "Progress in high-speed UV micro-machining with high repetition rate frequency doubled copper vapour lasers," *Proceedings of ICALEO 94* **79,** 343-351, (1994).

6. A.C. Glover,.M.J. Withford, E.K. Illy and J.A. Piper "Ablation threshold and etch rate measurements in high-speed ultra-violent micro-machining of polymers with uv-copper vapour lasers," *Proceedings of ICALEO 95* **80,** 361-370, (1995).

7. Paddison C.J., Dawes J.M., Brown D.J.W., Withford M.J., Trickett R.I. and Krug P.A., Electronics Letters 34 (1999), pp. 2407-2412.

8. Booth H.J., Illy E.K., Knowles M.R.H., Purves, G.T., Kearsley, A.J., Proc. ICALEO, Laser Inst. America, M203 (2001).

9. M.R.H. Knowles, A.I. Bell,.G. Rutterford, G. Foster-Turner and A.J. Kearsley, "Advances in copper lasers for micromachining," *Proceedings of ICALEO 97* **82,** (1997)

10. E. K. Illy, H. J. Booth, M. R. H. Knowles. 'Laser processing of photonics components using a multiple UV wavelength source' proceedings ICALEO LIA M602 Oct 2002.

11. F Floreani et.al. 'Effects of intrinsic apodisation in chirped fibre Bragg gratings fabricated using scanning holograpgic set-up' Proceedings Photon 02 OP2.1.4 Cardiff 2 Sept 2002.

12. E. K. Illy, H. J. Booth, G. Rutterford , & M. R. H. Knowles. 'Laser processing of photonics components with copper lasers' proceedings Photonics Fabrication Europe SPIE Brugge 28-31Oct 2002.

13. E.Gu et.al. 'UV copper laser micromachining and dicing of sapphire, GaN and micro LED devices'. To be published.

Subsurface photorefractive effect in LiNbO$_3$ under high- power 248 nm laser irradiation

Alexander M. Razhev*[a], Sergey N. Bagayev[a], Iosif B. Barkan[b],
Dmitry V. Petrov[b], Andrey A. Zhupikov[a]

[a] Institute of Laser Physics SD RAS, Lavrentyev aven. 13/3, Novosibirsk, 630090, Russia
[b] Institute of Semiconductor Physics SD RAS, Lavrentyev aven. 13, Novosibirsk, 630090, Russia

ABSTRACT

A phenomenon of a strong irreversible variation of the refractive index ($\triangle n \approx - 0,2$) in a subsurface layer of the lithium niobate crystal has been observed. The effect arises under the strong absorption of high-power radiation with wavelength 248 nm of KrF excimer laser. The characteristics of the subsurface photorefractive effect (SPRE) were identified by using the data on measurements of the reflection coefficient of a crystal and of the diffraction efficiency of a recorded phase grating. About 40% of niobium and oxygen atoms has been found to be displaced from the lattice points in the 350±50 Å subsurface layer. This phenomenon was used for creation of some integrated optics elements.

Keywords: 248 nm excimer laser, crystal LiNbO$_3$, subsurface irreversible variation of the refractive index

1. INTRODUCTION

Lithium niobate is among the most interesting and important materials of nonlinear and integrated optics, electro- and acoustooptics and holography. Over the recent years this material has been attracting attention of many researchers because of the possibility of producing high-efficiency broadband waveguides and optical elements of integrated optics. The following methods of microelectronics are successfully used here: diffusion of titanium atoms into the subsurface layer of a crystal [1], ion implantation [2] and ion implantation in combination with chemical etching [3].

A volume photorefractive effect (VPRE) [4,5] was first discovered in LiNbO$_3$, which is the reversible of the refractive index $\triangle n$ arising in a crystal under the action of laser radiation in the visible range [6]. Depending on the radiation intensity $I = 10^{-1} \div 10^3$ *W/cm^2* and its dose $D = (1 \div 10^3)$ *J/cm^3* the magnitude $\triangle n$ varies in a wide range from 10^{-6} to 10^{-3}. Its sensitivity to the VPRE ($S = \triangle n/D$) has been increased by 2 or 3 orders by doping LiNbO$_3$ with iron and impurities [7]. The time of relaxation of $\triangle n$ depends on the crystal temperature [8,9], the impurity concentration [10,11] and ranges from 10^{-4} s to several months. In addition, $\triangle n$ relaxes when the crystal is illuminated with photorefractive radiation due to photoconductivity [7,12]. In all cases the time of relaxation is changed by varying the specific resistance of the crystal. The VPRE is now widely used in new developments in holography (stationary [7,8] and dynamic [11] volume phase recording media), in optical data processing [13], and quantum electronics [14]. With the laser pulse in the visible range with $I = 1 - 30$ MW/cm^2 the time of formation of $\triangle n$ decreases down to $t \sim 10^{-8}$ s [15], while the sensitivity to the VPRE does not change practically, i.e., the law of reciprocity is fulfilled: $\triangle n \sim It = D$. The same law is fulfilled with higher intensities (40-60 MW/cm^2), but here, the probability of crystal destruction with formation of micro cracks and cavities increases.

A significant difference in the mechanisms and characteristics of the subsurface and volume effects is a strong (by several orders) change of the volume density of the absorbed energy. Complex measurements, including optical interference methods and methods of radioactive physics have been made for the main characteristics of the phenomenon to be determined.

The present paper described the results of investigations of the phenomenon of irreversible variation of the refractive index in the subsurface of a crystal LiNbO$_3$ under the action high-power radiation with wavelength 248 nm KrF excimer laser and the application of the phenomenon for creation of some integrated optical elements.

*razhev@laser.nsc.ru; phone 7 3832 341214; fax 7 3832 332067

2. METHODOLOGY

2.1 Light reflection

An expression for the coefficient of light reflection from the crystal surface containing the subsurface layer of thickness δ in the approximation of a homogeneous dielectric film is of the form [16]

$$R = (r^2_{12} + r^2_{23} + 2r_{12}r_{23}\cos2\beta)/ \text{ x } (1 + r^2_{12}r^2_{23} + 2r_{12}r_{23}\cos2\beta) \tag{1}$$

For normal incidence

$$r_{12} = (n_1 - n_2)/(n_1 - n_2), \; r_{23} = (n_2 - n_3)(n_2 + n_3), \; \beta = 2\pi n_2\delta/\lambda, \tag{2}$$

where: n_1, n_2, n_3 are the refractive indices of air, layer, and crystal, respectively. In this notation, the refractive index variation of interest is expressed as

$$\triangle n = n_2 - n_3 \tag{3}$$

It is impossible to find unambiguously $\triangle n$ and δ from (1), because R is the periodic function of $(n_3 + \triangle n)$. Additional optical measurements, e.g., light diffraction, are therefore required here. The analysis of (1) shows that $\triangle R < 0$ only in cases where $\triangle n < 0$.

2.2 Light diffraction

Let us consider the diffraction of coherent light (wave vector **k**) by two-dimensional phase periodic grating of thickness δ (Fig. 1) (d is the grating period along the both coordinates, a and b are the lengths of the sections with different refractive indices n_2 and n_3, respectively).
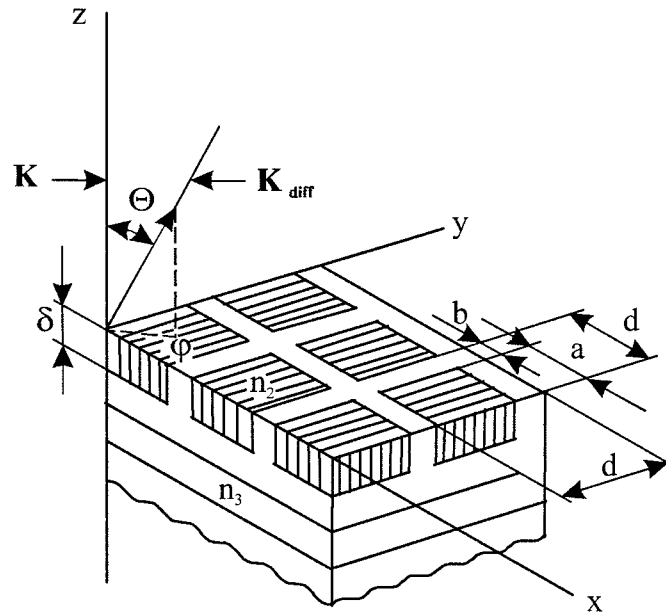
Figure 1: Two-dimensional phase diffraction grating with thickness δ $n_1 = 1$, n_2 is the refractive index of the a·a·δ square cell, n_3 is the refractive index of the crystal substrate

It can be shown that the intensity of the diffracted radiation with the wave vector $\mathbf{k}_{dif}$ is of the form:

$$I_{dif} = (I_0/N^2X^2_dY^2_d)\sin^2(NX_d/2)/\sin^2(X_d/2)\sin^2(NY_d/2)/\sin^2(Y_d/2) \text{ x}$$
$$x[\sin^2X_a + \sin^2X_b + 2\sin X_a\sin X_b\cos(2\gamma - X_d)] \; x \; [\sin^2Y_a + \sin^2Y_b + 2\sin Y_a\sin Y_b\cos(2\gamma - Y_d)], \tag{4}$$

where:

$$X_a = \pi a \sin\Theta \cos\varphi/\lambda$$
$$X_b = \pi b \sin\Theta \cos\varphi/\lambda$$
$$X_d = \pi d \sin\Theta \cos\varphi/\lambda$$
$$Y_a = \pi a \sin\Theta \sin\varphi/\lambda$$
$$Y_b = \pi b \sin\Theta \sin\varphi/\lambda$$
$$Y_d = \pi d \sin\Theta \sin\varphi/\lambda$$

N is the number of cells in the grating, γ is the difference in phase:

$$\gamma = \pi \triangle n \, \delta/\lambda \tag{5}$$

The positions of the diffraction maxima satisfy the condition:

$$X_d = m\pi$$

$$Y_d = l\pi \qquad m, l = 0; \pm1; \pm2; \tag{6}$$

The diffraction pattern has the form of a symmetric grating the points of which are described by (6). In this case the greatest diffraction intensity is observed in four symmetric directions (when one of the indices m or l is zero, the second ±1) and described by the expression:

$$I_{dif} = (4I_0/\pi^2) \sin^2\gamma \sin^2(\pi a/d) \tag{7}$$

From (7) with $\gamma \ll 1$ the diffraction efficiency η is:

$$\eta = I_{dif}/I_0 = 4(\triangle n \, \delta/\lambda)^2 \sin^2(\pi a/d) \tag{8}$$

The product ($\triangle n \, \delta$) can thus be found from the measurements of the diffraction efficiency, which, in combination with the measurements of the reflection coefficient under certain restrictions imposed on the quantity δ, allows a determination of $\triangle n$ and δ.

3. EXPERIMENT

3.1 Preparation of samples
We studied optically polished, single-domain $LiNbO_3$ crystals both undoped and doped with iron, chromium and others. The 1 mm plates of the y- and z-cuts were examined. The plates were carefully degreased and irradiated in air.

3.2 Experimental technique
The SPRE was realized by the radiation from a high-power UV laser (KrF, 248 nm, 5 ns, 1-20 MW/cm^2). In order to measure the reflection coefficient, the crystal sample was irradiated by the homogeneous radiation through a mask with a 3 x 6 mm^2 aperture. A two-dimensional phase periodic grating was produced by irradiating the crystal surface through the wire mask grating with a period $d = 22$ μm (the ratio of the window width to that of the baffle is $a/b = 2$). The reflection coefficient and the diffraction efficiency were measured by using the collimated radiation from a He-Ne laser at 0.63 μm under normal incidence.

4. RESULTS AND DISCUSSION

4.1 Influence intensity and dose of laser radiation to the refractive index
In all irradiated crystals we observed a decrease of the reflection coefficient of both ordinary and extraordinary waves (R_0 and R_e, respectively). With allowance for (1) the decrease of $R_{0,e}$ indicates that $\triangle n_0$, $\triangle n_e < 0$. In this case $\triangle n_0$ and $\triangle n_e$ exceed by 2 or 3 orders those measured in the known VPRE [4.5]. It should be noted that $\triangle n$ contains two

components, reversible and irreversible ones. The reversible component, which is about 5% of the irreversible one, is of the same nature as that in the VPRE [4] and relaxes with heating the crystal up to 170°C. In this work we examine the irreversible component the magnitude of this component has not significantly changed for one and a half years. In addition, the visible 20 MW/cm^2 radiation causing relaxation of the VPRE does not affect Δn in this case. The typical temperature of annealing of this component is about 500°C, the annealing time 30 min.

The reflection coefficient is nonlinearly dependent on an irradiation dose D (Fig. 2) and reaches saturation at a dose of about 1 J/cm^2 and intensity of 20 MW/cm^2.
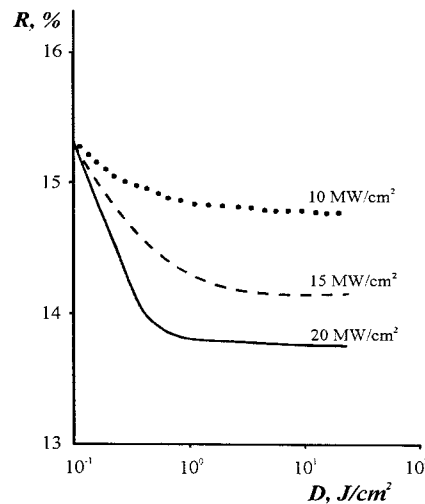
Figure 2: Dependence of the reflection coefficient of LiNbO3 with 0,05 wt.% of chromium on the dose of irradiation by an UV laser (249 nm) for different intensities

The reflection coefficient is nonlinearly dependent on the radiation intensity at the same dose of 1 J/cm^2 (Fig. 3). The effect has an evident threshold for character: the threshold for the crystal with the 0,05 wt.% Cr impurity is 8-10 MW/cm^2. The threshold for crystal destruction is above 30 MW/cm^2. It should be noted that the magnitude of the threshold for the formation of the SPRE is largely dependent on the stoichiometric and impurity composition of the crystal and conditions of its thermo chemical treatment. The effect is reproducibly induced by the radiation at a quantum energy larger than the forbidden band with (> 4 eV). At quantum energy smaller than 4 eV the threshold of formation of the SPRE is close to that of crystal destruction.
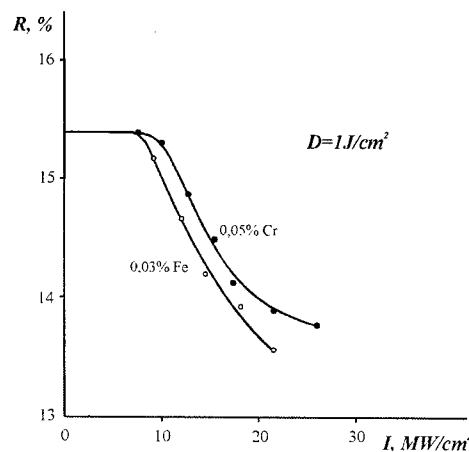
Figure 3: Dependence of the reflection coefficient on intensity at the same irradiation for the crystals with different impurities

The diffraction efficiency and, hence, the magnitude of the induced difference in phase on the grating also increase nonlinearly with the irradiation dose and reach 0,02%.

As has been noted above, for the determination of the main characteristics of the layer $\triangle n$ and δ from measurements of the reflection coefficient and the diffraction efficiency it suffices to solve the system consisting of (1,8). To solve unambiguously this system, the determination of the range of variation of δ is required. The following typical parameters may be used to restrict this range.

4.2 Light Absorption length in the crystal
Because of the high absorption coefficient of the crystal ($\alpha > 10^5$ cm^{-1}) at a wavelength 248 nm, we failed to measure its value. The value of α obtained by extrapolating the results from [17] ranges from 10^5 to 10^6 cm^{-1}, which corresponds to an absorption length of $10^2 - 10^3$ Å.

4.3 The depth of the perturbed layer in the crystal arising under the laser radiation
In order to determine this depth we examined here the spectra of backward Rutherford scattering of helium atoms. It has been found that about 40% of niobium and oxygen atoms are displaced from the lattice points in the 350 ± 50 Å subsurface layer.

Based on these considerations one can restrict the range of δ variation by the value of 1000 Å and solve the system of equation for $\triangle n$ and δ by using the experimentally measured value $\Delta R_0 = -1,5\%$ and $\eta = 0,026\%$ in saturation, with:

$$D = 1 \text{ J/cm}^2 \text{ and } I = 20 \text{ MW/cm}^2$$

$$\triangle n_0 = -0,18, \quad \delta = 300\pm30 \text{ Å} \tag{9}$$

Taking into account that δ in (9) is close to the perturbed layer depth, one can assume that the mechanism of SPRE is bound up with a sufficiently high concentration of the crystal structure point defects. Besides, a good correlation between the layer thickness and the absorption depth is indicative of a high volume density of the absorbed energy. Estimations show that about ten absorbed photons with a quantum energy exceeding interatomic bond energy are consumed per atom.

This is more than enough for the formation of the high concentration of the point defects. The possibility of this mechanism has been shown in [3] under ion implantation of the LiNbO$_3$ crystal. With nitrogen ions (150 keV, 4 x 10^{16} N$^+$/cm^2 the following parameters of the layer have been obtained: $\triangle n = -0,16, \delta = 0,25$ μm.

4.3 Diffractive gratings performance
Results of study of some diffractive structures parameters made by two ways are described below. In the first way an irradiations of z- cut LiNbO$_3$ crystal samples were made through a periodic phase mask (the period 6 microns) made on a quartz plate by an ion etching of photo resist mask. The phase mask densely nestled on a surface of a crystal LiNbO3, as spatial coherence of excimer laser radiation was low. In experiments the relative diffraction efficiency of a grating induced in subsurface layer of a crystal depending on number of irradiation pulses at power density on a surface of a sample ~ 9 MW/cm^2 in 1 and 2 orders was measured (Fig. 4).

The formation of the gratings with two periods in subsurface layer of a LiNbO$_3$ crystal was experimentally revealed. One period was equal and another was twice shorter than that at a mask. The grating with the period equal to the period of a mask forms as result of interference between a past beam (the 0 order) and one of the diffractive beams of the first order. The grating with the twice shorter period is caused as a result of interference between beams of + 1 and -1 orders. The primary formation of the grating on a LiNbO$_3$ crystal surface with the twice shorter period seem to cause by high efficiency of a phase mask.

Depending on number of irradiation pulses the diffractive efficiency of this grating formed on a surface of the LiNbO$_3$ crystal has the saturation at 12-16 pulses. The presence at an irradiation of a constant background. i.e. wave of the 0-th order. lead to a decrease of the induced grating efficiency with the growth of number of an UV radiation pulses.
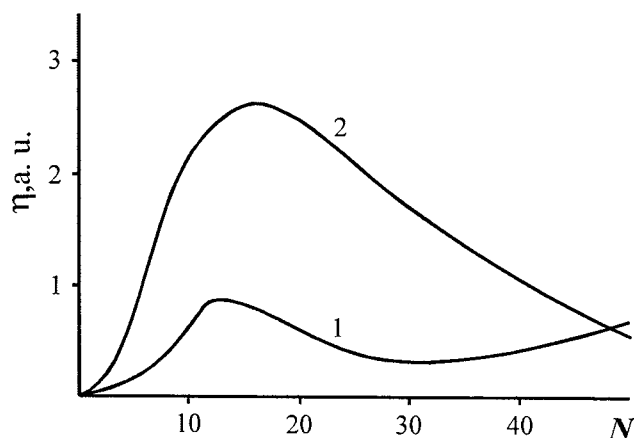
Figure 4: The dependence of the grating diffractive efficiency on the number of pulses in the 1 order (curve1) and in the 2 order of the diffraction (curve2).

For the same reason and also because of occurrence the corrugation on the irradiated sample surface the estimation of the variation of a refractive index value due to variation of absolute value of efficiency in these experiments was complicated.

The experiments on influence of the UV radiation to losses in waveguides made by diffusion of titan in $LiNbO_3$ have been performed. The value of losses in single mode waveguides was shown to be without changing so long as the doze of an irradiation does not reach saturated value of Δn. The excess of this level of an irradiation results in appreciable increase of losses basically at the expense of light dispersion.

We shall note also following experimental fact. In the irradiated zone the speed of etching of lithium niobate is higher than this one in not irradiated zone. In our experiments a relief with depth ~ 0,1 microns has been formed after irradiation of the sample by 10 pulses with power density of 8 MW/cm^2, when there is no deformation of a surface, and after the etching during 20 minutes in an acid at temperature of 20 C.

In the second way the irradiation of the X-cut of $LiNbO_3$ samples was carried out through an aluminum mask put on a surface of a crystal. Previously the single mode optical waveguide was made by the diffusion of the titan on this surface. The configuration of the diffraction grating strokes was designed by method of geometrical optics, which should couple out from waveguide the falling on it directed wave and to focus on some distance from a substrate (Fig.5). The dimensions of a grating were 1x1 mm. Optical length of a way from the center of a grating till a focus was 10 mm. The grating was made by the photolithography etching in an aluminum mask. The thickness of a mask was 200 nm that provided reliable protection of a waveguide surface from the UV of radiation at 10 ns pulse duration, power density of 20 MW/cm^2 and total doze of 6 J/cm^2.

The collimated beam of light (polarization TE) was entered into waveguide through a prism. The distribution of light intensity near to focus was measured by scanning glass waveguide by a diameter about 8 microns (Fig. 6). The size of a focal spot on an axis X was 30 microns that is approximately three times higher of a diffraction limit. The efficiency of a grating determined as the intensity of light in focus to intensity of a directed mode falling on a grating has been measured. The efficiency of a grating was 1%. Assuming the depth of the disturbed layer arising at a laser irradiation is 350 angstrem, it is possible to estimate the values of bond coefficient for typical single mode waveguides in $LiNbO_3$ and to find the efficiency of transformation in the radiated wave. This efficiency is close to one obtained experimentally. The ways of an efficiency increasing are clear: reduction of waveguide depth (in particular, by using the waveguides made by a proton exchange), increase of grating length, optimization of its geometry, the use of UV radiation with the higher penetration depth into $LiNbO_3$ crystals.

In summary we shall note, that the opportunity of local influence by UV radiation on various parts of the integral-optical circuits on a basis $LiNbO_3$ represents a simple and accessible method of tuning of some elements of these circuits.
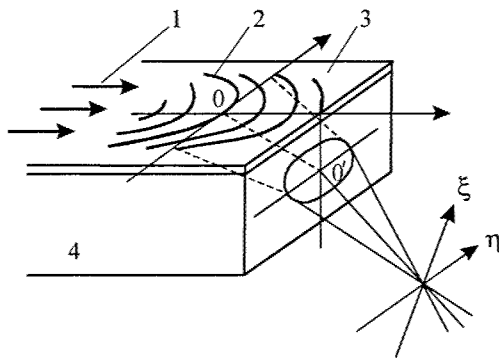
Figure 5: Diffractive element; 1- optical mode; 2 – focusing diffractive grating; 3 – waveguide Ti-LiNbO$_3$; 4 – lithium niobate crystal.
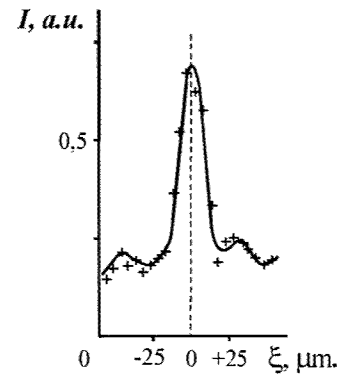
Figure 6: The distribution of light intensity near to focus.

6. CONCLUSION

A phenomenon of a strong irreversible variation of the refractive index ($\triangle n \approx - 0,2$) in a subsurface layer (thickness ~300 Å)of the lithium niobate crystal has been observed. The effect arises under the strong absorption of high-power (20 MW/cm^2) radiation with wavelength 248 nm of KrF excimer laser. The characteristics of the subsurface photorefractive effect (SPRE) were identified by using the data on measurements of the reflection coefficient of a crystal and of the diffraction efficiency of a recorded phase grating. About 40% of niobium and oxygen atoms has been found to be displaced from the lattice points in the 350±50 Å subsurface layer. The phenomenon discovered may be applicable in integrated optics, e.g., in manufacturing phase elements, gratings and etc. (in practical waveguides), if the effective layer thickness is about 1 μm. For this purpose, apparently, longer-wavelength radiation should be used, e.g., with λ = 282 nm (XeBr laser) the absorption length in crystal is 1 μm.

REFERENCES

1. R.V. Schmidt. I.P. Kaminov, *Appl. Phys. Lett.*, **25**, pp. 458-460,1974.

2. D.T.Y. Wei, W.W. Lee, L.S. Bloom, *Appl. Phys. Lett*, **25**, pp. 329-331, 1974.

3. G. Gots, H Karge, *Nucl.Instrum. Measurements*, **209/210**, pp. 1079, 1983

4. I.A. Ashkin, G.D. Boyd, J.M. Dziedzic, et.al, *Appl. Phys. Lett.*, **9**, pp. 72-74, 1966.

5. F.S. Chen, *J. Appl Phys.*, **38**, pp. 3418-3420, 1967.

6. H.B. Sereze, R.B. Goldner, *J. Appl Phys. Lett.*, **22**, pp.626-629, 1973.

7. W.Phillips, J.J. Amodey, D.L. Staebler, *RCA Rev.*, **33**, pp. 94-98, 1972.

8. J.J. Amodey, D.L. Staebler, *Ferroelectrics*, **3**, pp. 107-110, 1972.

9. I.B. Barkan, S.I. Marennikov, M.V. Entin, *Phys. Stat. Solidi.*, **38**, pp. 139-144, 1976.

10. A.M. Glass, D. von der Linde , T.J. Negran, *Appl. Phys. Lett.*, **25**, pp. 233-235, 1974.

11. I.B. Barkan, S.I. Marennikov, M.V. Entin, *Phys. Stat. Solidi.*, **45**, K17, 1976.

12. H Kurz, *Ferroelectrics*, **8**, pp. 437-440, 1974.

13. N.V. Kukhtarev. S.Zh. Odulov, *Pisma ZhETF*, **30**, pp. 6-9, 1979.

14. S.Zh. Odulov, M. S. Soskin, *Pisma ZhETF*, **37**, pp. 243-246, 1983.

15. P. Shah. T.A. Rabson, F.K. Tittel, T.K. Gaylord, *J. Appl Phys. Lett.*, **24**, pp.130-132. 1974.

16. M Born, *Optik*, Springer, Berlin, 1933.

17. D. Redfield. W.J. Burke, *J. Appl Phys.*, **45**, pp. 4566-4571, 1974.

Single Step Direct-Write Photomask Made From Bimetallic Bi/In Thermal Resist

Glenn Chapman[1], Yuqiang Tu

School of Engineering Science, Simon Fraser University, Burnaby, BC V5A 1S6, Canada

ABSTRACT

A new single step direct-write photomask process has been proposed by using Bi/In bimetallic thermal resist which turns almost transparent with high energy laser exposure. The Bi over In metallic films, each layer ~40 nm thick, were DC-sputtered onto quartz mask plate substrates in a single pump-down chamber. Before laser exposure the Bi/In had 2.91 Optical Density. Bi/In is a bimetallic thermal resist and hence shows near wavelength invariance exposure sensitivity from Near IR to UV light. For Bi/In exposure, up to 0.9 W Argon laser (514 nm) beam was focused by an f=50 mm lens to a 10 micron spot. When writing a mask the Bi/In coated sample was placed on a computer-controlled high accuracy X-Y table and the pattern was raster-scanned by the laser at 10mm/sec. After exposure the Bi/In film became nearly transparent (0.26 OD) at I-line (365 nm) wavelength, and remained conductive. Bi/In photomasks have been used together with a standard mask aligner to pattern the oxide and Al layer during the manufacturing of test solar cell devices in the lab. Experiments also showed that annealing the as-deposited films at 90°C before laser exposure increase the Bi/In transparency.

Keywords: Direct-write photomask, Thermal Resist, Bimetallic Thin Film.

1. INTRODUCTION

Previous research has found that bimetallic layers of Bismuth on Indium creates an inorganic thermal resist with many interesting properties[1,2,3]. When exposed to laser pulses at energies equal to that of organic resists the Bi/In film is converted into a new material with quite different characteristics from the unexposed areas. It is chemically different enough that development in a diluted RCA2 solution ($HCl:H_2O_2:H_2O=1:1:48$) removes the unexposed areas with an excellent etch selectivity[4]. The remaining resist is also highly resistant to alkaline-based anisotropic silicon etching[3]. Yet potentially even more useful is the extremely large change in the optical absorption with the exposed areas becoming nearly transparent[1]. This suggested the possibility of using Bi/In resist as a direct write photomask.

Photomasks with smaller features, better controlled linewidth, fewer defects and lower cost are required by the microfabrication and micromachining industries. A conventional photomask consists of an insulating/transparent substrate, and a surface covering/patterning film, most commonly Cr. While quartz and glass have been widely used for decades as the mask substrates, many different kinds of materials have been used as the surface imaging layer. Drexler [5] heated up the exposed silver-halide emulsion to 250°C and the emulsion became visually transmissive to yellow-orange light in both silver and non-silver clear areas, but opaque in the silver areas to ultraviolet wavelengths. CrO, CrON, MoSi and MoSiON have been reported to be used to make single-layer attenuated phase-shift masks[6,7].

However Cr has been the most widely used covering materials in the wafer fab industry[8,9,10]. The typical Cr photomask manufacturing process involves the blank mask preparation: Cr and Cr oxide deposition, photoresist coating, resist baking, laser or e-beam direct-writing, resist development, metal layer dry or wet etching, resist stripping and cleaning[8,9]. There are many issues with current photomask and its preparation processes. Firstly, it is difficult to minimize the defect counts, as there are 5 – 9 operation steps involved in making a photomask and each step can introduce process defects and particles. Secondly, mask damage from ESD (electrostatic discharge) has long been a concern. Although a lot of effort has been spent in making the photomask and the pellicle set conductive by adding conductive films, conductive frames, conductive dust pellicles, etc.[10,11], ESD damage can be more problematic due to the shrink of the feature size. To make things even worse is that masks for 157 nm lithography will be kept in ambient atmospheres nearly free of water, which will increase the risk of ESD damage to masks[12]. Thirdly, although Cr dry

etching has become a standard mask making process step, the loading effect is still a serious problem. The chrome etch rate changes with the ratio of clear area to opaque area on the mask, which can seriously affect the precise Critical Dimensions (CD) control[13]. Fourthly, the cost of masking is escalating. A 0.18 μm binary photomask for critical layers costs $8000 – 22,000, and those for non-critical layers cost $18,000 - $20,000. OPC (Optical proximity correction) and PSM (phase shift mask) add substantially to these prices[14]. In order to solve all these issues people in the semiconductor industry have to explore new processes and new materials. Takaoka, et al[15], proposed a sol-gel combined with DTR (diffusion transfer) process. A liquid containing metal oxide was applied to the substrate, and this dried and heated coating would act as a physical development nucleus layer into which the silver complex compound was diffused to form a silver film at the unexposed area. Plasma etching is not necessary. However it still involves more than 5 steps.

In this paper, a novel single step direct write photomask made from bimetallic Bi/In thermal resist is reported. Unlike conventional mask lithographic steps for patterning, Bi/In itself is a thermal activated optical material, hence patterns can be directly written onto the film, and the exposed Bi/In area becomes more transparent. Mask defects can be drastically reduced due to much fewer steps are needed in the preparation process. Moreover because both the exposed and unexposed Bi/In are conductive, there is inherently not ESD problem with this type of photomask. Obviously the manufacturing cost of Bi/In photomask is much lower than conventional masks. Bi/In is a potential photomask material for semiconductor industry. This paper investigates the resist itself to create a V-groove solar cell, and briefly looks at the mechanism behind the large optical changes.

2. Bi/In BIMETALLIC THERMAL RESIST

The Bi/In bimetallic resist concept (see Figure 1(a)) starts with the deposit of two thin (15-150 nm) film layers of materials whose combined phase diagram contains a eutectic, an alloy with a melting point local minimum below that of either metal[16]. The Bi/In phase diagram has a eutectic of 72°C at 22% bismuth and a local temperature minimum of 112°C at 53% bismuth[17]. In the resist the two film ratios are chosen to match these eutectic compositions. When exposed to a short laser pulses of ~7 mJ/cm^2 under a photomask or direct laser writing (Figure 1(b)) the exposed area will absorb the light energy and with sufficient power heat up to above the Bi/In eutectic temperature. At the end of the laser pulse, the resist layers will cool and solidify as the altered alloy. The material in the unexposed area, where the light is blocked by the photomask, will remain the same as two-layer structure. Tests show that the alloy have different chemical and optical properties than Bi or In. In resist applications two development etch solutions have been found[4] which will attack the areas of unexposed resist more aggressively than the exposed areas. As Bi/In film gets very transparent after high power laser exposure, which makes it material for making direct-write photomasks[2] and development is not needed.

The BiIn bimetallic films were prepared on glass slides and quartz using a Corona DC sputter machine that has 5 targets installed and can deposit multilayer films without an air break, creating the structures of Figure 1(a). The target materials used are two inches in diameter 99.99% Bi and 99.99% In. The substrates were RCA1 and RCA2 cleaned before deposition, and then baked for 20 minutes at 120°C to remove moisture. The vacuum chamber was pumped down to a base pressure of 6×10^{-7}Torr before sputtering. During deposition, the chamber pressure was kept at 4mTorr with an Ar gas flow rate of 10 sccm. The deposition rate for the bismuth, and indium was determined, as shown in Table 1, by
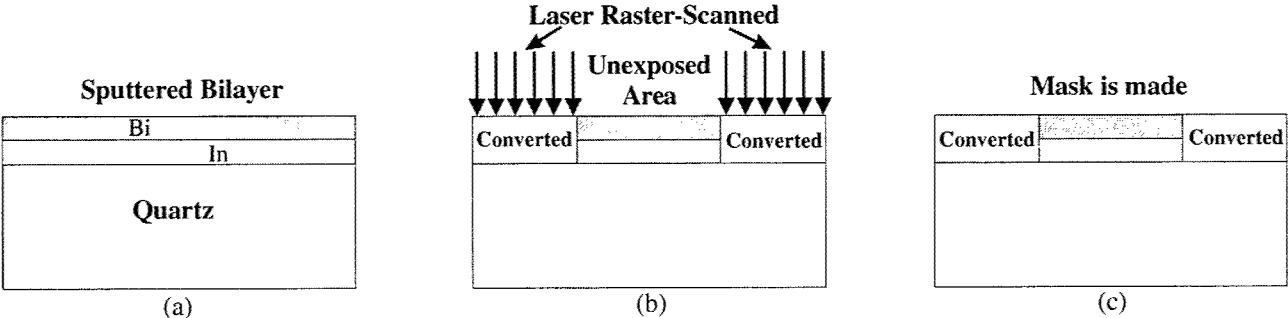

Figure 1. The mask making process steps. (a) Bi and In are DC-sputtered on quartz or glass with a bilayer structure. (b) Bi and In form an alloy when exposed to laser, and the unexposed area remains to be bilayer structure. (c) The exposed area becomes transparent after laser exposure, the unexposed Bi/In is opaque. The mask is then made.

Table 1. Bi and In Sputter Rate

Metal	Argon Pressure	DC bias	Current	Watt·Min	Deposit rate Å/W·min
Bi	4mTorr	470V	0.23A	2500	12
In	3mTorr	450V	0.23A	2500	4

sputter depositing thick films on glass slide substrates for 2,500W·min and measuring the film thickness with a KLA-Tencor AS5 profilometer.

Since the In sputter rate (4Å/W·min) was lower than that of Bi (12Å/W·min), a different sputter power was used for Bi and In sputtering in order to give a better control of film thickness. To prepare a 40nm/40nm BiIn film, the DC voltage was 500V and the current was 0.2A to sputter In, and to sputter Bi, the DC voltage was 350 V and current was 0.07A. The actual DC sputter powers for the Bi and In depositions were 24.5W and 100W, respectively.

The properties of the deposited films are very stable. Reflection and transmission measurements were made on a daily basis for three bilayer samples held at room temperature, under a 60W light bulb (about 10cm away) and immersed in a bath of liquid nitrogen (77°K). The reflection and transmission were measured on both the front (exposed to air) and back (on the glass substrate) surfaces, no significant changes were observed in transmission or reflection in any of the samples. A rigid shelf lifetime test has been carried out at 50°C and >90% humidity condition for over 200 hours, and no changes of the sample properties were observed[1]. Such stability is very important for photomasks.

3. LASER EXPOSURE

While Bi/In is a sensitive thermal resist much lower power is needed to create an etch resistant material with some transparency for a resist, while higher powers are required to maximize the change in optical characteristics. Also as a thermal resist Bi/In is wavelength invariant in laser exposure energy required for the reaction[3] Hence in this application an Argon CW laser running at 514 nm was used to expose the Bi/In films. The 2.5 mm diameter laser beam was focused by different lens (5×, 50× objective lens and 50 mm lens, dependent on the feature size) onto the sample to create higher power densities.
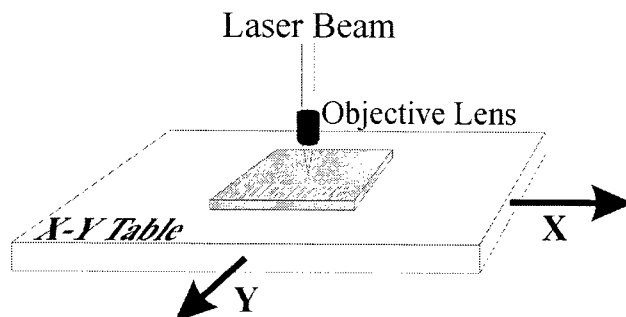
Figure 2. Exposure setup. The laser beam was focused by a 50 objective lens. The sample was placed on an X-Y table, while the laser beam was fixed.

The waist of the focused beam is from 2 μm to 10 μm. The laser beam was fixed during the scanning. The sample was placed on a computer-controlled high precision (±0.1μm) X-Y Z table, and the table moved back and forth along X direction at a constant speed, with a small incremental step along Y direction after each scan (Figure 2). Thus the laser beam raster-scans the sample to make a pattern. Different patterns can be made by writing computer control scripts or by using our proprietary table control software which takes bitmap image as the input file and the X-Y table will move accordingly so that the same image can be written on the sample. Three parameters contribute to a successful mask making: table moving speed, laser power and Bi/In film thickness. The table moving speed is similar to the exposure time in steppers or aligners. In the experiment it was kept at 1 cm/sec. The power of the Argon laser used for the scanning is from 0.3W to 0.9W when using 50 mm lens. The film thickness chosen is 40 nm / 40 nm.

When the laser beam hits the bilayer film part of the light will be reflected at each interface, and some light will be absorbed and converted into heat and the rest will transmit through the film. It is the absorbed portion of the light that exposes the film by heating up the metal. At laser powers above the threshold for reaction the physical and chemical properties of converted Bi/In films change and most importantly for masks it becomes almost. transparent compared to

the unexposed Bi/In[1]. As covered in section 8 the heat converts the Bi/In into an transparent alloy or alloy oxide[18], while the unexposed area remained bilayer structure. Figure 1 shows the two steps to make a Bi/In direct-write photomask. Step 1 is the blank mask preparation: Bi and In are deposited onto quartz or glass substrate. Step 2 is the laser raster-scan: exposed area gets converted and turns to be more transparent, and the unexposed remains the same. In order to protect the pattern a protection layer such as SiO2 can be sputtered onto the mask surface after the pattern writing.

4. OPTICAL CHARACTERISTICS OF Bi/In FILMS

The large optical property difference between the exposed and unexposed bimetallic thermal resist Bi/In films is attractive since this can be utilized in many fields such as optical storage and direct-write photomask materials. It is observed that the light transmission increases rapidly with the laser exposure power. To characterize the optical properties of Bi/In films before and after laser exposure a Varian CARY 3E spectrometer was used to measure the absorption through the Ar CW raster scanned area and the unexposed area on the film. Figure 3 shows the Optical Density (OD) versus the transmission light wavelength for a 40 / 40 nm Bi/In film on a glass slide after exposure to Ar laser of different power. The top curve is the as-sputtered 40 / 40 nm Bi/In film, which is around 2.6 – 2.8 OD from 400 nm to 800 nm wavelength. The second, third and fourth curves are the OD's of films exposed to Ar laser of 300, 450, and 600 mW, respectively. As the power of the laser exposure increases, the OD of the exposed area reduces, and saturates at a minimum level where all of the material in the layers is converted. The absorption spectrum for the converted layers in the range from 400 nm to 800 nm reaches a minimum value of less than 0.1 OD at an exposure intensity of 600 mW. This shows a change in the OD of larger than 2.5 orders in terms of transmitted light power. An ideal direct-write photomask for i-line applications should have ~ 3 OD for unexposed area and < 0.25 OD for exposed area. The OD of unexposed 40/40 nm Bi/In at 365 nm (i-line) is 2.94 and that of area exposed with 600 mW Ar laser is 0.43. In order to improve the transparency of the exposed area while keeping the OD of the unexposed area, many methods are under investigation, such as adding different gases and elements during film sputtering, various substrate temperatures during exposure, finding the optimized film structure (thickness and order of deposition), etc.

It is found that annealing the Bi/In samples at 50 to 90°C for a period of time in the air before laser exposure helps reduce the optical density of the exposed area. An experiment comparing the OD of the oven-annealed and non-annealed samples was carried out. Two different Bi/In samples were used: one was 40/40 nm and the other was 15/15 nm film, all deposited on glass slides. Each sample was cut into 2 halves for comparison. One half was Ar laser scanned as-deposited and the other half was heat-treated at 90°C for 72 hours before laser scanning. In this way the influence of the fluctuation of film thickness from sample to sample was eliminated. Table 2 lists the OD comparison experiment results measured at i-line wavelength. The "Laser Power" column shows the Ar laser power that was used to expose the films. The "OD (Non-annealed)" column shows the OD of the films that were exposed as-deposited with different laser power. The "OD

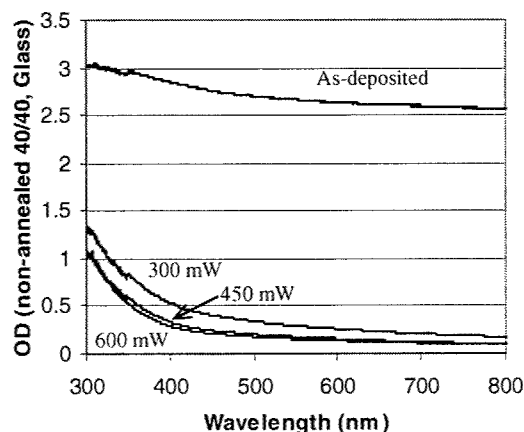Figure 3. Optical absorption (300 nm to 800 nm) through 40/40 nm (non-annealed) Bi/In deposited on glass slide exposed by Ar laser with different power. From top to bottom: 0, 300, 450, and 600 mW. The sample was not heat-treated.
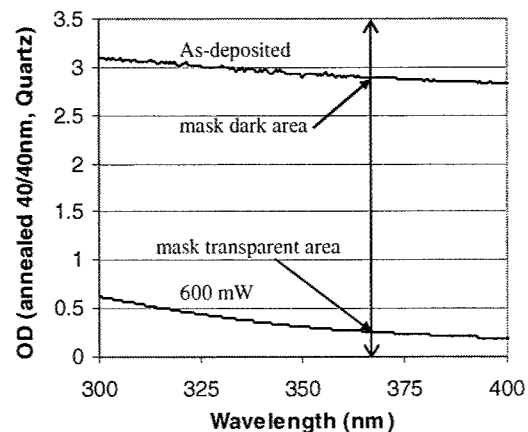
Figure 4. Optical absorption through annealed 40/40 nm Bi/In on quartz substrate, in the range of 300 nm to 400 nm. The top curve is the OD for unexposed, and the bottom is exposed with 600 mW Ar laser.

(Annealed)" is the OD of the films that were first heat-treated and then exposed with different laser power. The last column shows the percentage of OD reduction from non-annealed films. One can see that the OD of 40/40 nm film after 600 mW laser exposure dropped 8.42% from 0.435 to 0.398, while the unexposed area only dropped 0.81% and was still above 2.9. Similar results were also found for 15/15 nm films, although the OD drop for unexposed area (23.21%) was much larger than that of 40/40 nm film. The annealing mechanism that brings down the OD of films both before and after exposure is not fully understood at this moment. As the optical absorption of glass slides start to increase rapidly

Table 2. Comparison of Optical Density (OD @ i-line) between oven-annealed and non-annealed Bi/In films deposited on glass slides.

Film Type	Laser Power (mW)	OD (Non-annealed)	OD (Annealed)	OD Reduction %
40 / 40 nm Bi/In	0	2.936	2.913	0.81%
	300	0.726	0.515	29.13%
	450	0.492	0.431	12.34%
	600	0.435	0.398	8.42%
15 / 15 nm Bi/In	0	1.142	0.877	23.21%
	75	0.504	0.499	0.98%
	150	0.299	0.266	11.18%
	300	0.227	0.155	31.84%
	450	0.170	0.158	7.14%
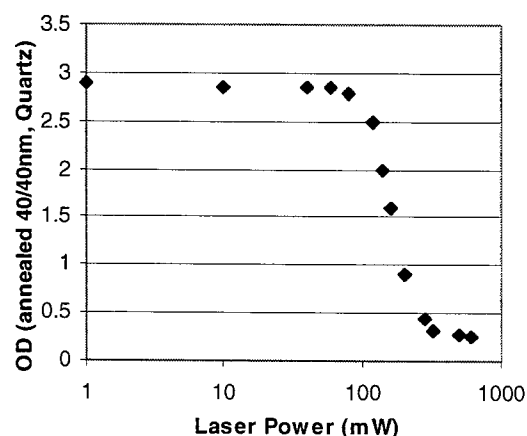
Figure 5. 40/40 nm Bi/In film optical absorption vs laser power at wavelength 365 nm. Absorption drops drastically at around 100 mW laser power and gradually saturates after 300 mW. The film was deposited on quartz and was annealed at 90°C for 72 hours.
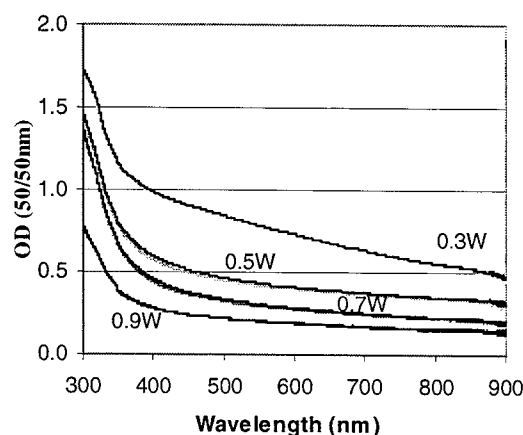
Figure 6. Optical spectrum before and after the shelf test. The spectrum lines before and after the shelf test overlap with each other, showing that the film optical property is stable.

after 450 nm wavelength, Bi/In was deposited on quartz substrates in order to make photomask for i-line applications. Tests showed that with quartz as the substrate the OD of exposed area was 0.260 and unexposed area 2.911 at 365 nm wavelength. Figure 4 shows the OD of unexposed and 600 mW laser exposed area of annealed Bi/In on quartz sample in the wavelength range of 300 nm to 400 nm. It is also seen that the optical absorption of annealed quartz sample at 300 nm is much lower than that of non-annealed glass sample.

Figure 5 shows a curve of optical absorption versus laser writing power at the wavelength of 365 nm which is very important for determining the direct write laser power requirements. It is noticed that when the laser is below 50 mW the Optical Density (OD) of the film does not change. The X-Y table moves with the speed of 10 mm/sec and the laser beam is focused to a small spot with 20 µm in diameter with 50 mm lens, hence 50 mW of Ar laser power yields around 5J/cm^2 power density (for exposure times of milliseconds). Converted masks are stable to exposure during mask use as the mask making powers are much higher than typical industrial exposure power density (10 – 100 mJ/cm^2) and While the exposure times is much shorter. Thus in mask applications the Bi/In temperature is raised far less than during the mask making exposures, thus the photomask stability and reliability will be maintained. The absorption drops sharply

around 100 mW writing power, and it quickly saturates from 300 mW onwards and the optical density stabilizes around 0.26 OD on quartz substrates. With such low absorption levels the Bi/In resist has met the needs for a direct write photomask for 365 nm applications where the converted areas can directly be used as the mask "openings" without development. Both the unexposed and exposed films were reported to be very stable[2]. A shelf test was carried out in order to test the stability of the exposed area. The Bi/In films raster-scanned with different Ar laser power were kept in an environment of 70°C and ~100% humidity for 7 days. The optical spectrum was measured before and after the shelf test. As shown in Figure 6, the spectrum curves before and after the shelf test overlap each other. The transmission rate barely changed and the optical property is stable as is required for photomasks.

5. ELECTRICAL PROPERTIES OF Bi/In

Electrostatic discharge damage in conventional chrome masks is caused by the charge accumulation in the transparent non-conductive quartz area. Although a lot innovative technique has been applied to alleviate the problem, it is extremely difficult to eliminate ESD. However, Bi/In direct-write photomasks are free from ESD problem as both exposed and unexposed Bi/In films are conductive, which cover the whole mask surface. The sheet resistance of the exposed and unexposed samples was measured using a MP0705A four-point probe from Wentworth Labs, which is connected to an HP 3478A multimeter. The bilayer film was sputter-deposited on glass slides with 30 nm equally thick Bi on top of the In layer. The sheet resistance was first measured on the unexposed Bi/In film (named as Bi/In 30/30 U in Table 3), and then on the Ar laser raster-exposed areas (as Bi/In 30/30 E in Table 3). The laser power was 0.20W. The resistances of single layer Bi and In films of thickness 15 nm, 30 nm, and 45 nm were also measured. It is noticed that the resistivity of the thinner Bi and In films is higher than that of bulk materials, dropping significantly as the films get thicker. This can be attributed to the fact that the oxidized part of the film is more significant in thinner films than in thicker films. It is noticed that the exposed films are slightly more conductive that unexposed films.

Table 3. Sheet resistance and resistivity

	Bi (15nm)	Bi (30nm)	Bi (45nm)	In (15nm)	In (30nm)	In (45nm)	Bi/In 30/30 U	Bi/In 30/30 E
Sheet resistance (Ω/sq)	484.7±39	171.0±13	79.6±5	32±3	9.3±0.9	3.5±0.2	82.8±6	80.8±5
Film resistivity (Ωcm)	7.27×10^{-4}	5.13×10^{-4}	3.58×10^{-4}	4.91×10^{-5}	2.79×10^{-5}	1.56×10^{-5}	4.97×10^{-4}	4.85×10^{-4}
Bulk resistivity (Ω cm)	1.3×10^{-4}			8.0×10^{-6}			-	-

6. PREPARATION OF Bi/In DIRECT-WRITE MASK

To demonstrate that the Bi/In bilayer film can be used as a direct write material for practical fabrication applications, several photomasks have been made on glass slides and quartz substrates. Figures 7 – 11 show a mask made with the following conditions:

- 40 / 40 nm Bi/In deposited on quartz;
- Heat treated for 72 hours at 90°C (open air);
- Argon laser raster-scan power = 600 mW;
- 50 mm lens used to focus Argon laser before hitting the film, beam size = 10 μm;
- X-Y table moving speed (along X direction) = 1 cm/sec;
- Raster-scan increment (along Y direction) after each scan = 8 μm.

Figure 7 is a front-lit picture of the whole 1×1.6 cm direct-write Bi/In photomask. The laser-scanned areas are darker that the unexposed area from the front-lit picture. Figure 8 is a back-lit image of the mask, showing clearly the patterns. Figure 9 is an enlarged front-lit picture showing one of the patterns of 51μm line and space exposure structure. Figure 10 was taken with both front and back lights on, showing vertical lines in the exposed area that were generated by the laser raster-scan for a 25 μm line and space test structure. However, the raster-scan lines disappeared when only the back-light was on, as shown in Figure 11, and are not visible in exposed regular organic resist patterns from this masks (refer to Figure 12). One can also clearly see the smallest feature in the back-lit picture which is a 2 μm wide space. This width is really only the limits of the mask creation program not that of the resists.. Although we have not carried out experiments to find out the smallest feature size possible with the Bi/In film, TEM (Transmission Electron Microscopy) analysis showed that the grain size of the Bi/In film is 150 nm, indicating that the smallest feature can be ~ 150 nm[18]. In order

Figure 7. Front-lit picture of the 1×1.6 cm direct-write photomask made on a quartz plate coated with 40/40 nm Bi/In. The bilayer film was heat-treated for 72 hours at 90°C before laser exposure.
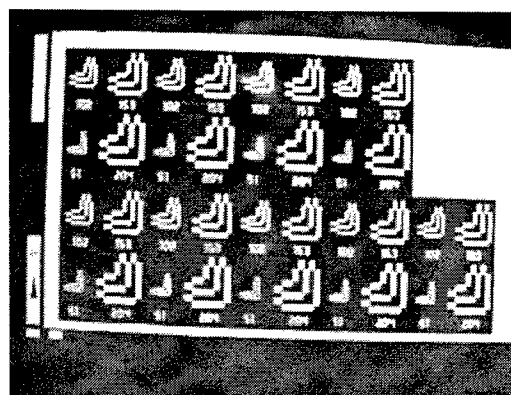
Figure 8. Back-lit image of the same mask in Figure 7.
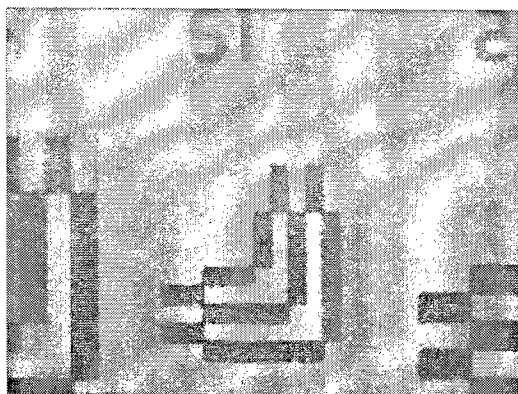
Figure 9. Enlarged front-lit picture of the direct-write photomask The width of the line at the middle is 51 μm.
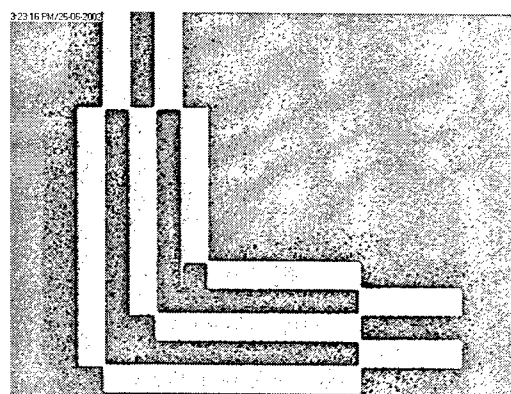
Figure 10. Front-lit & back-lit image of a pattern on the mask with 25 μm wide lines. Vertical raster-scanned lines can be seen in the exposed areas.

Dark area
2.91 OD

Transparent
area 0.26 OD
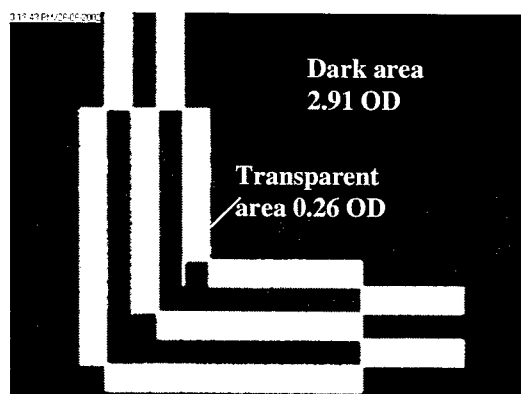
Figure 11. Back-lit image of the same pattern in Figure 10. No raster-scan lines can be seen in the exposed areas. The thinnest line near the center is only 2 μm wide.
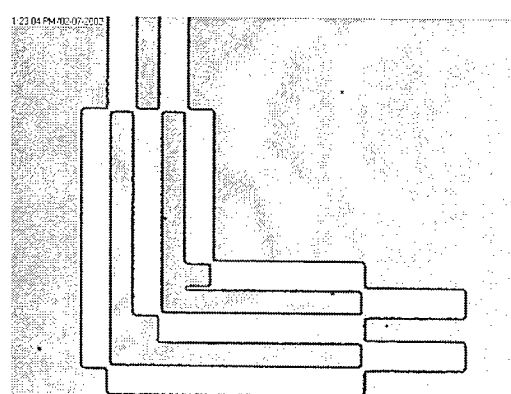
Figure 12. Shipley SPR2FX-1.3 photoresist has been successfully patterned with the same mask. This is the pattern after developed in Shipley MF-319.

to test the direct write photomask, a Quintel 4" mask aligner with a 365 nm Hg source was used to expose a Shipley SPR2FX-1.3 photoresist coated on a chrome film. With a 15 seconds exposure time and a 10 mW/cm^2 light intensity, a good pattern was made in the photoresist. These are comparable exposure parameters to those required for processing a chrome mask with the same features. Figure 12 shows the pattern on the Shipley photoresist after developed in developer Shipley MF-319 for 30 seconds.

7. MAKING TEST SOLAR CELLS WITH Bi/In DIRECT-WRITE MASK

To better demonstrate the applications of Bi/In film as a thermal resist, a Si anisotropic etching mask material, a direct-write photomask material, and its compatibility with conventional CMOS processes, we have made surface textured solar cells as test devices, as shown in Figure 13.

The first step was to make parallel V-grooves on a silicon wafer. Bi/In resist was deposited on the wafer and laser patterned, followed by a diluted RCA2 solution (HCl:H_2O_2:H_2O=1:1:48) development removing the unexposed Bi/In. This developed Bi/In acted as an etch masking process layer on a (100) n-type silicon wafer for anisotropic etching in TMAH at 85°C for 30 minutes, followed by standard cleaning and HF dip to strip the Bi/In mask layer. The second step was to create diodes in the V-grooved area. Boron diffusion was carried out after the wet oxidation and oxide definition lithography. Last step was the metallization process. Bi/In was used as the direct-write photomasks for the lithography of the oxidation and metallization layers. The oxide definition mask was created under the same condition as the one reported above. In order to pattern the Al layer a direct write dark field Bi/In mask was used together with a negative photoresist AZ-5214. The process is as following:

- Spin coat 1.4 μm thick AZ-5214 onto the wafer;
- Soft bake at 120°C for 60 seconds;
- Exposure Bi/In mask for 30 second at $P_{365nm} = 10$ mW/cm^2;
- Hard bake at 120°C for 45 seconds;
- Flood exposure (without mask) for 10 seconds at $P_{365nm} = 10$ mW/cm^2;
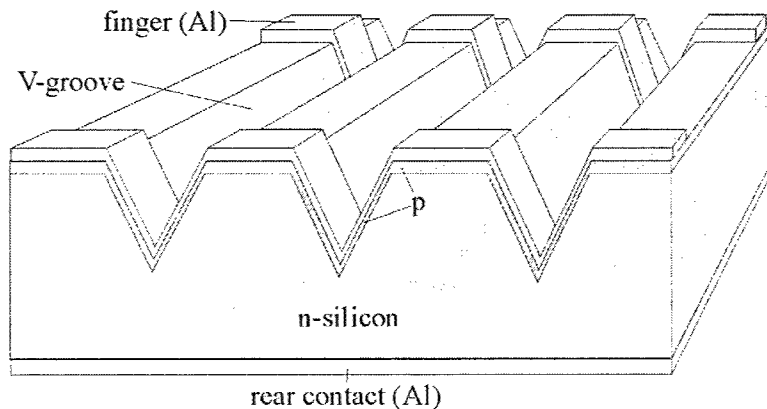- Developed in MIF for 30 seconds.

Figure 13. V-groove surface textured solar cells are made on a (100) n-type silicon wafer by using Bi/In as the patterning and masking material.
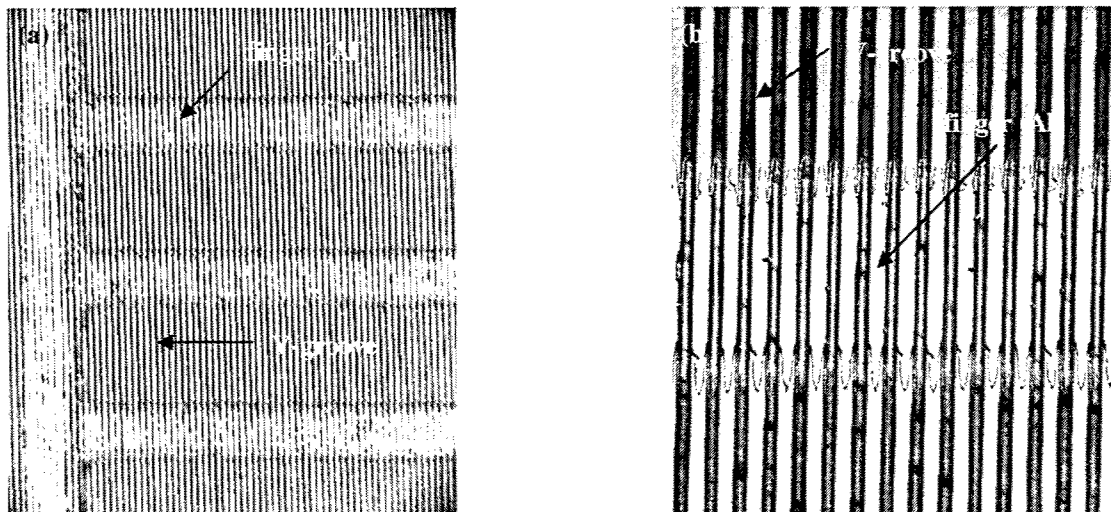

Figure 14. Optical pictures of part of the solar cell. (a) 50× image. The thin vertical lines are the V-grooves. The thick horizontal white lines are Al contacts; (b) 200× image. The V-grooves can be seen.

Illumination power (W/m² at 600nm)	Open Circuit Voltage (mV)	Short Circuit Current (mA)
0	0	0
9.75	135	3.8
19.37	280	8.1
40.82	320	10.4
87.87	352	11.2

Table 4. V-groove solar cell electrical performance.

Figure 14 are two optical pictures of part of a solar cell. The vertical fine lines are the V-grooves and the while thick horizontal lines are Al contacts. In order to provide a reference to compare with, normal solar cells were also produced on the other half of the same silicon wafer without being patterned with Bi/In films. Measurement results show that the 1.5 cm² v-grooved solar cell gives 280 mV open circuit output voltage and 8.1 mA short circuit current under normal florescent tube light at 25°C, which is a fully functioning solar cell. These test results are identical to the reference cells. Table 4 shows the detail of the electrical performance of the cells.

8. STRUCTURAL ANALYSIS OF Bi/In FILM

For photomask applications it is important to maximize the Optical Density change, and have the converted minimum OD values extend to the shortest wavelength. Hence it is important to understand the conversion mechanism of Bi/In when exposed to laser. Recent work has shown that the eutectic alloy may be only part of the mechanism.

Profilometry test was carried out on 40 nm thick single Bi, single In layer and 40/40 nm Bi/In bilayer that were DC-sputtered onto silicon substrates. Results show that single Bi film is smooth with Ra = 20 Å, while single In layer is very rough with Ra = 218 Å, as shown in Figure 15. Bi/In, due to the roughness of In is much rougher than Bi, but smoother than In layer, with Ra = 100 Å. The laser scanned Bi/In film gets rougher than the unexposed film, with Ra = 200 Å. Figure 16 shows a profile across the exposed and unexposed area of 40/40 nm Bi/In film (raster-scan laser power = 1.5W with 5× objective lens, scan speed = 1cm/sec, and Y direction increment = 5 μm). Area on the left side of the high peak is laser exposed and that on the right is as-deposited. One can see that the roughness increases after laser exposure and that the exposed area is slightly thicker than the as-deposited area.
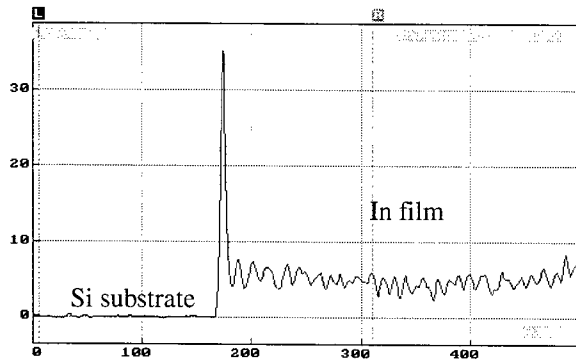
Figure 15. Profilometry result of 40 nm thick, as-deposited, single layer In on silicon substrate. On the left side of the high peak is the Si substrate and the right side is the In film, Ra = 218 Å.
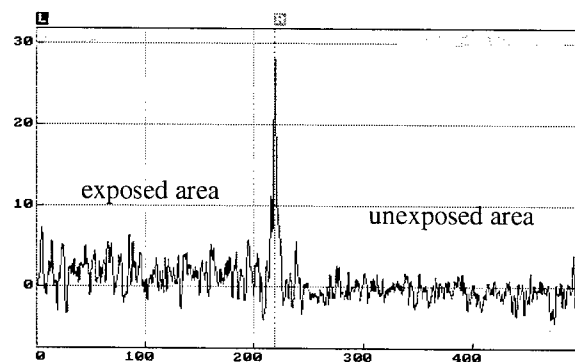
Figure 16. A profile across the exposed and unexposed area of 40/40 nm Bi/In film. Area on the left side of the high peak is exposed, while the right is unexposed.

Recent work by the authors, done in collaboration with Prof. K. Kavanagh at Simon Fraser University and Dr. W. Lennard at University of Western Ontario has explored the structural behavior of the Bi/In films before and after laser exposure[18]. Bi/In films were prepared on different substrates, such as glass slides and silicon wafers. As the laser exposure of Bi/In is a thermal process, furnace annealing of Bi/In films in the air at 150, 200 and 246°C for 3 hours was also carried out in order to compare them with the laser exposed samples. The composition and microstructural characteristics were investigated using profilometry test, atomic force microscopy (AFM), x-ray diffraction θ-2θ scans (XRD, Cu Kα_1), Rutherford backscattering spectrometry (RBS) (2 and 3 MeV He^{++}), and nuclear reaction analysis (NRA, $^{16}O(d,p)^{17}O$).
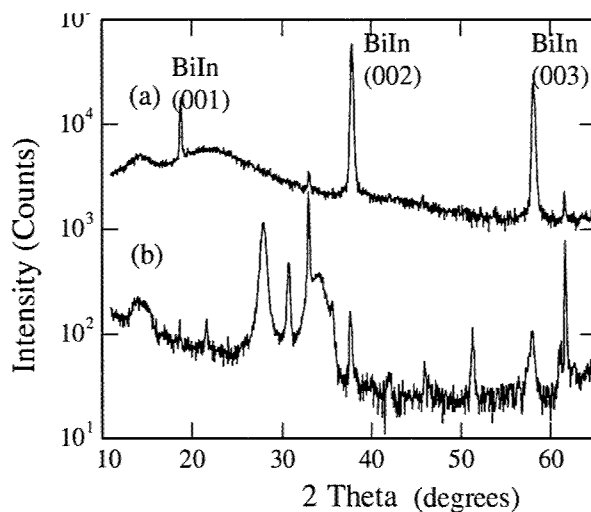
Figure 17. X-ray diffraction θ-2θ scans of BiIn bilayers (45/45 nm) deposited on silicon (a) as-deposited displaced by a factor of 10, and (b) laser exposed in air.

AFM measurements showed that both as-deposited and Argon laser-scanned 12/12 nm Bi/In films are rough (12 nm RMS) with feature sizes of 150 nm. It was noticed that the Bi/In film turned slightly transparent after annealing at 246°C for 3 hours. However it was much less transparent than the laser exposed Bi/In film, indicating a different process than the laser conversion. XRD scans shown in Figure 17 showed the as-deposited films display strong diffraction peaks consistent with BiIn alloy formation. After laser exposure new reflections develop that begin to match some of the known BiIn oxide structures in powder diffraction databases.

RBS spectra and simulation of the data from the as-deposited, furnace annealed at 150°C, 246°C and laser exposed 120/120 nm bilayer films are shown in Figure 18, 19, 20 and 21, respectively. The results for the as-deposited films in Figure 18 clearly show that In is detected on the surface even though it is deposited first, next to the substrate. This is consistent with the severe roughness observed with the profilometry and AFM results of In film. The simulation results showed that the as-deposited film had a 2.5 nm In_2O_3 surface layer and a 200 nm thick $Bi_1In_{1.4}O_{0.06}$ film beneath it. It is interesting to notice that after furnace-annealing at 150°C and 246°C for 3 hours, the film structure does not change (as shown in Figure 19 & 20), except that the top In_2O_3 layer gets a little thicker, which is 18 and 28 nm, respectively. After laser exposure oxidation of the films was detected as seen in Figure 21. The simulated spectrum was generated by a target film with a 2.5 nm thick surface layer of In_2O_3 and a $BiIn_{0.6}O_6$ /$Bi_{0.3}InO_6$ bilayer of average thickness 200 - 245 nm

Figure 18. The experiment and simulated RBS spectra of as-deposited 120/120 nm thick Bi/In bilayers on Si.
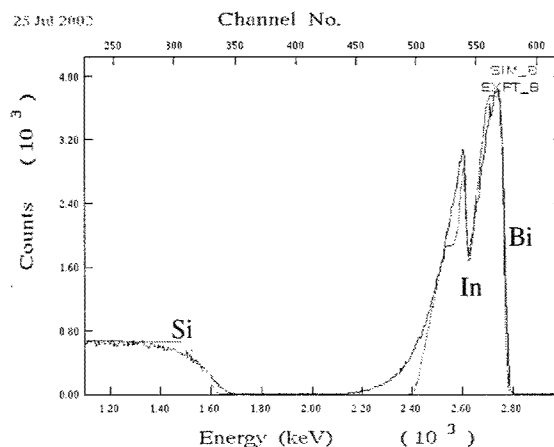
Figure 19. The experiment and simulated RBS spectra of 120/120 nm Bi/In bilayers on Si, furnace–annealed at 150°C.
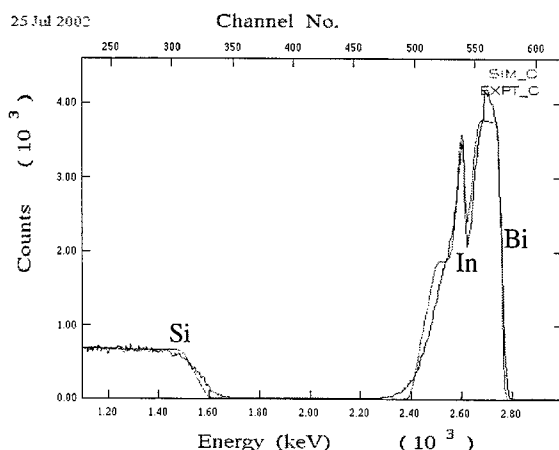
Figure 20. The experiment and simulated RBS spectra of 120/120 nm Bi/In bilayers on Si, furnace–annealed at 246°C.
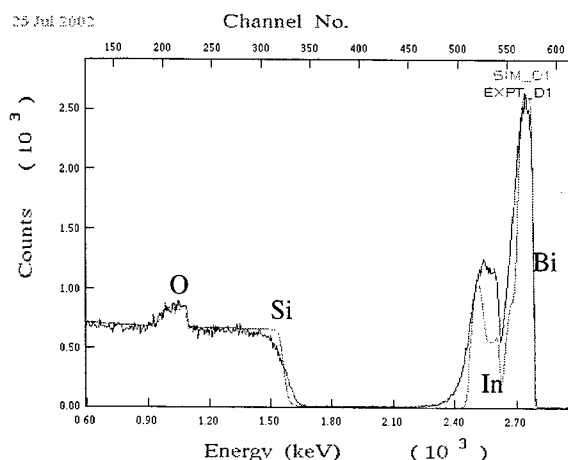
Figure 21. The experiment and simulated RBS spectra of 120/120 nm thick Bi/In bilayers on Si, laser annealed with 0.95 W power and laser beam focused with a 50× objective lens.
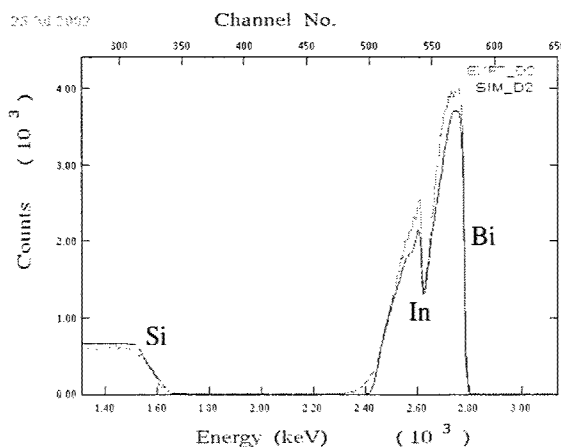
below it. Table 5 summarizes the oxygen content obtained from both the NRA and RBS data. There was considerably less oxygen in the furnace-annealed films. Furnace annealing at higher temperature will be conducted in future, as the actual laser exposure temperature could be much higher. It is unknown at this moment whether oxygen is a necessary part of the conversion of Bi/In to a transparent film, as laser exposure tests in a vacuum (50 mTorr) and reducing atmosphere (Nitrogen+10% Hydrogen) showed that the Bi/In films still turned equally transparent after exposure. More stringent vacuum tests will be conducted in future.

Table 5. RBS/NRA results of O concentration.

Sample	[O] NRA $(10^{17}$ at./cm$^2)$	[O] RBS $(10^{17}$ at./cm$^2)$
as-deposited	0.22	0.27
150° furnace anneal	0.87	0.84
200° furnace anneal	0.80	0.70
250° furnace anneal	1.5	1.3
Laser annealed	9.5	13.5

9. CONCLUSION

It has been demonstrated that Bi/In bimetallic thermal resist, which turns transparent with high energy laser exposure, can be utilized as a direct-write photomask material for microfabrication applications. With heat treatment at 50 to 90°C before laser exposure, the Optical Density of Bi/In can reach 0.26 at i-line after laser writing, while keeping the unexposed area around 2.91 OD. Working solar cells were successfully made by using Bi/In photomasks together with a standard mask aligner to pattern the oxide and Al layer. XRD and TEM analysis results show that BiIn alloy forms in the as-deposited Bi/In film. RBS and NRA results indicate that the laser conversion of Bi/In could be an oxidation process as large amount of oxygen was found in the laser-exposed Bi/In film. However, it is not known yet whether oxygen is necessary to make Bi/In film transparent. Stringent vacuum test and high temperature furnace annealing test need to be done in future to confirm it.

10. ACKNOWLEDGMENT

Reference:

[1] M. V. Sarunic, G. H. Chapman, Y. Tu, "A Prototype Laser Activated Bimetallic Thermal Resist For Microfabrication", Proc. SPIE Vol. 4274, pp 183-193, January, 2001.

[2] G. H. Chapman, Y. Tu, M. V. Sarunic, "BiIn: a Sensitive Bimetallic Thermal Resist", Proc. SPIE Vol. 4345, pp 557-568, 2001.

[3] G.H. Chapman, Y. Tu, and M.V. Sarunic " Bi/In Bimetallic Thermal Resists for Microfabrication, Photomasks and Micromachining Applications", Proc. SPIE Vol. 4690, pp 465-476, San Josa, CA, Mar., 2002.

[4] Y. Tu, G.H. Chapman, and M.V. Sarunic. "Bimetallic Thermally Activated Films for Microfabrication, Photomasks and Data Storage", Proc. SPIE Vol. 4637, pp 330-340, 2002.

[5] Jerome Drexler, "Method for making thermochromic photomasks", United States Patent No. 4,225,659, September 30, 1980.

[6] Masayuki Nakajima, et al, "Attenuated phase-shifting mask with a single-layer absorptive shifter of CrO, CrON, MoSiO and MoSiON film," Proc. SPIE Vol. 2197, pp 111-121, 1994.

[7] F. D. Kalk, R. H. French, H. U. Alpay, G. Hughes, "Attenuated Phase-Shifting Photomasks Fabricated from Cr-Based Embedded Shifter Blanks", Proc. SPIE Vol. 2254, pp 64-70, 1994.

[8] Yamazaki Teruhiko, et al, "Manufacture of photomask", Japan Patent No. 55-143560, Aug.11,1980.

[9] Kato Tadao, et al, "Manufacture of photomask", Japan Patent No. 55-144245, Nov. 11, 1980.

[10] Erwin Deng, Sylvia Hwang, "Photomask Structure", United States Patent No. 6,440,617, August, 2002

[11] Hiroyuki Miyashita, et al., "Halftone phase shift photomask comprising a single layer of halftone light blocking and phase shifting", United States Patent No. 5,604,060, February 18, 1997.

[12] "International Technology Roadmap of Semiconductor 2001, Lithography", International SEMATECH, 2001.

[13] Jung-Min Sohn, et al, "Process Technology for Next Generation Photomask", Jpn. J. Appl. Phys. Vol. 37 Pt. 1, No. 12B pp 6669-6674, 1998.

[14] Robert N. Castellano, "The photomask industry: minimizing a crisis in escalating costs", Solid State Technology, pp 44 – 48, Aug 2002

[15] Kazuchiyo Takaoka, et al, "Photomask material, photomask and methods for the production thereof", Unite State Patent No. 6,303,262, October 16, 2001

[16] G. H. Chapman, M. V. Sarunic, Y Tu, "Dry Multilayer Inorganic Alloy Thermal Resist for Lithographic Processing and Image Creation", PCT patent application WO 02/06897 A2, applied for Jan 24, 2002.

[17] Max Hansen, Constitution of binary alloys, McGraw-Hill, 1958.

[18] Y. Tu, M. Karimi, N. Morawej, W. N. Lennard1, T. W. Simpson1, J. Peng, K. L. Kavanagh, and G. H. Chapman, "Wavelength-Invariant Resist Composed of Bimetallic Layers", accepted by MRS Fall Meeting, Boston, 2002.

Surface micro-fabrication of silica glass by excimer laser irradiation of toluene solution

Hiroyuki Niino[*], Yoshimi Yasui, Ximing Ding, Aiko Narazaki, Tadatake Sato, Yoshizo Kawaguchi and Akira Yabe

Photoreaction Control Research Center (PCRC)
National Institute of Advanced Industrial Science and Technology (AIST)

ABSTRACT

Laser-induced backside wet etching of silica glass plates was performed by the excitation of a pure toluene solution with a ns-pulsed KrF excimer laser at 248 nm. Well-defined grid micropattern was fabricated without debris and microcrack around the etched area. To understand the etching mechanism, the formation and propagation of shockwave and bubble were monitored by time-resolved optical microscopy at the interface between the silica glass and the toluene solution after laser irradiation. Transient high-pressure as well as high-temperature generated by UV laser irradiation plays a key role in the etching process.

Keywords: laser ablation, ns-pulsed UV laser, micro-machining, fused silica, shockwave, bubble, time-resolved optical microscopy

1. INTRODUCTION

Laser ablation continues to grow as an important technique for film deposition, micromachining and surface modification for various materials.[1] However, laser ablation is limited to photon-absorbing materials and has difficulties in the processing of the materials which are transparent at the wavelength of the laser.[2] In the search for a simpler and effective method on laser-induced material processing, there are several approaches to the use of pulsed lasers from the viewpoint of conventional laser ablation,[3] vacuum UV laser processing,[4-5] plasma-assisted UV ablation,[6-9] and femtosecond laser micromachining.[3,10]

Recently, we have developed a one-step method to microfabricate a silica glass plate which we called *laser-induced backside wet etching* (LIBWE) upon irradiation with a ns-pulsed UV excimer laser.[11-19] Our idea of LIBWE is based on the deposition of laser energy on the surface of silica glass during the ablation of a dye solution. Figure 1 shows the experimental setup for LIBWE method. As the UV absorption of silica glass was negligible, an incident laser beam penetrated through the glass plate, resulting that dye molecules in the solution were excited upon the laser irradiation. When the dye solution was ablated upon the laser irradiation with a sufficient fluence, the etching on a surface layer of the silica glass was achieved. The etch depth increased linearly with the number of laser shots. The etch rate of the material was typically 0.1–25 nm/pulse, which was dependent on irradiation conditions such as laser wavelength, laser fluence, and dye concentration. We have succeeded in the micro-fabrication of such transparent materials as silica glass,[11,14-18] quartz,[12] calcium fluoride,[14] fluorocarbon resin,[13] and saphire.[19] The advantages of our LIBWE method are as follows, (i) micro-fabrication without debris and cracks formation at an atmospheric pressure, (ii) simplification of pre-/post-treatment for a target substrate, (iii) large area irradiation with a conventional ns-excimer laser through a mask projection. In addition, we are able to select a dye solution from various liquids of pyrene/acetone,[11,12,14,15,19] pyrene/THF,[13] pyranine/water,[16] naphthalenesulfonic acid/water,[17] toluene[18] upon the irradiation with KrF and XeCl excimer lasers.

In this paper, we have investigated an extension of liquid media to include an organic solution without dye molecules. Commercialized high-purity toluene, which was simple and inexpensive, was used for this purpose. As toluene is a popular compound in both scientific research and practical use, a large number of optical and thermal parameters have been reported. In addition, we intended to analyze laser-induced transient phenomena at the interface between silica glass and toluene solution by time-resolved optical microscopy.

2. EXPERIMENTAL

A fused-silica glass plate (Tosoh SGM Co., ES grade) with a thickness of about 2 mm and a diameter of 20 mm was used as a sample. A KrF laser (Lambda Physik, EMG201MSC, λ= 248 nm, FWHM 30 ns) was used as a light source. The repetition rate of laser irradiation was set at 5 Hz. A square mask of 2.9 × 2.3 mm^2 was used to investigate the etch rate. Depth profiles were measured with a Stylus instrument (Taylor-Hobson, Talystep). A copper grid with an array of 46 × 46 μm^2 holes was used to etch a grid pattern. An organic solvent, toluene (Wako Pure Chemical Industries Ltd., S grade), was used without further purification.

The transient optical images of toluene ablation were monitored by time-resolved back illumination technique.[20] The solution in a quartz cubic cell was irradiated with a KrF laser through a pinhole and the irradiated diameter was 170 μm. A dye solution (Rhodamine B in ethanol) pumped with a XeCl laser (Lambda Physik, Compex102, λ= 308 nm) provided a peak emission at 560 nm with the duration of 25 ns, which was used for back illumination. The delay time between the KrF laser and the XeCl laser was regulated with a digital delay and pulse generator (Stanford Research Systems, DG535). By changing the delay time, the time-resolved images of the ablation process were taken with a conventional CCD camera (Nikon, Coolpix 990) and a microscope (Olympus, SZ6045TR or Mitsutoyo, VMU-V+M Plan Apo 5X). Emission spectrum of toluene excited by KrF laser irradiation was detected using a CCD spectrophotometer without a time-gated function (Hamamatsu, PMA-11).
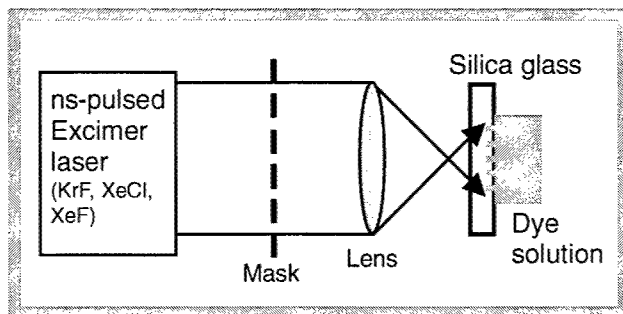
Figure 1: Schematic drawing of experimental apparatus.

3. RESULTS AND DISCUSSION
3.1. MICRO-FABRICATION OF SILICA GLASS

Figure 2 shows that well-defined etching free of debris and microcracks were fabricated by KrF laser irradiation using a pure toluene solution. When a grid mask was used for patterning, an array microstructure was fabricated on a silica glass, as shown in Fig. 3. The relationship between the etch depth and the number of laser pulses indicates a linear function within the investigated range.[18] The slopes of the straight lines in Fig. 3 correspond to etch rates at each of the given laser fluences.[18] As the etch rate increased linearly with laser fluence, the threshold fluence for toluene was extrapolated to be 0.19 J cm^{-2}. This excellent linearity affords the potential to be used for fine etch depth control in applications, such as the fabrication of 3-dimensional structures, currently done using a contour or gray scale mask.[21,22]

The etch rate in the case of toluene solution was about 30 % higher than that obtained in acetone solution of pyrene dye at concentration of 0.4 M, while the absorption coefficient of pure toluene (α= d^{-1}= 0.11 μm^{-1}) is about one seventh of that of the pyrene solution (0.78 μm^{-1})[11]. It is noted that, during LIBWE process with hundreds of laser shots, black-colored fine particles were gradually formed and suspended in the toluene solution, while the particles were not observed in such dye solutions as pyrene derivatives. Raman spectrum of the particles showed two broad peaks at 1354 cm^{-1} and 1603 cm^{-1}, suggesting that carbon soot was produced from toluene photolyzed by UV laser irradiation.
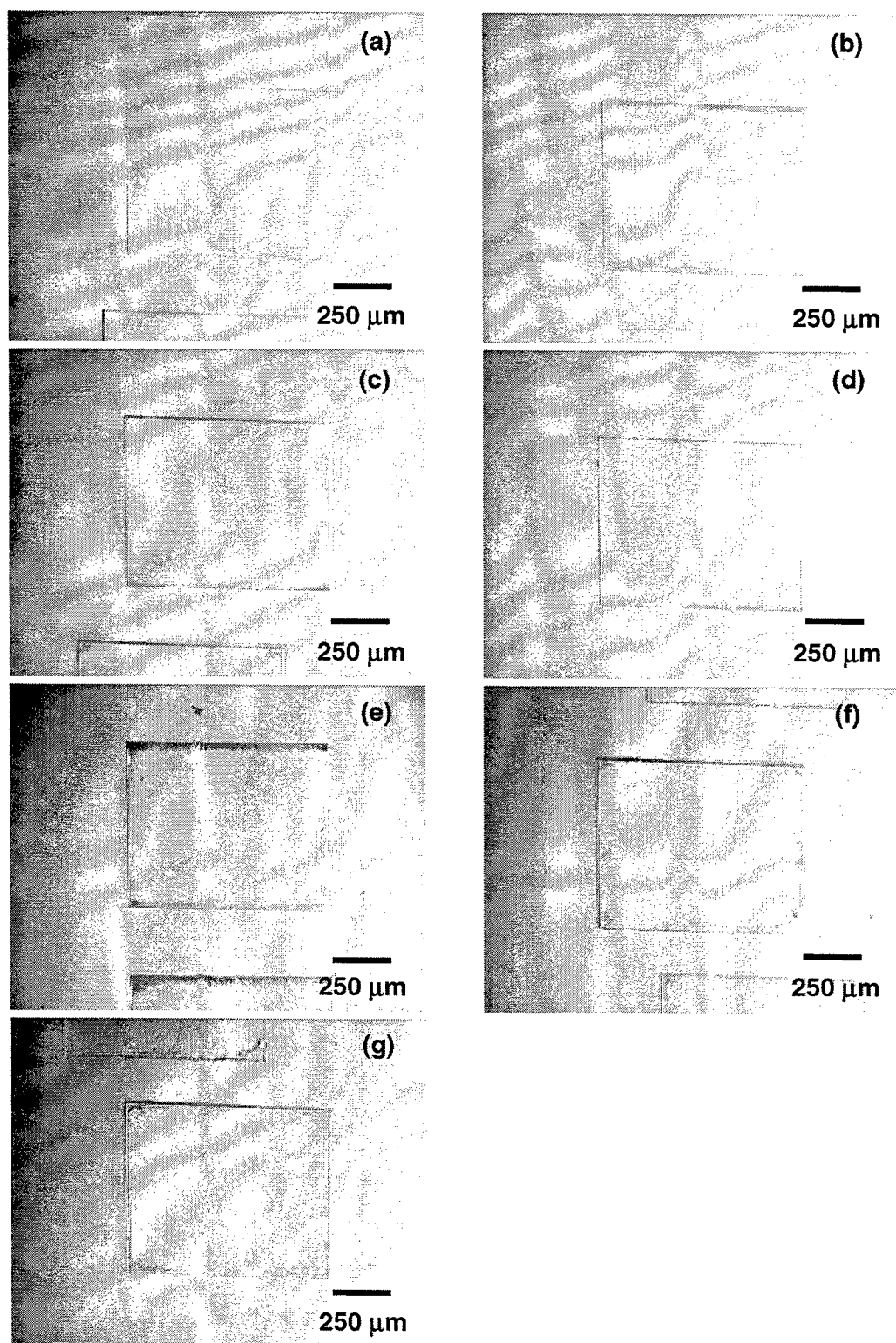
Figure 2: Optical micrographs of silica glass etched by LIBWE method with a pure toluene solution upon the irradiation of KrF excimer laser; (a) 0.4 J cm^{-2}, 500 shots (etch depth: 4.1 μm), (b) 0.6 J cm^{-2}, 200 shots (2.2 μm), (c) 0.8 J cm^{-2}, 200 shots (3.7 μm), (d) 1.0 J cm^{-2}, 100 shots (4.1 μm), (e) 1.14 J cm^{-2}, 50 shots (1.4 μm), (f) 1.2 J cm^{-2}, 100 shots (2.9 μm), (g) 1.46 J cm^{-2}, 50 shots (2.0 μm).
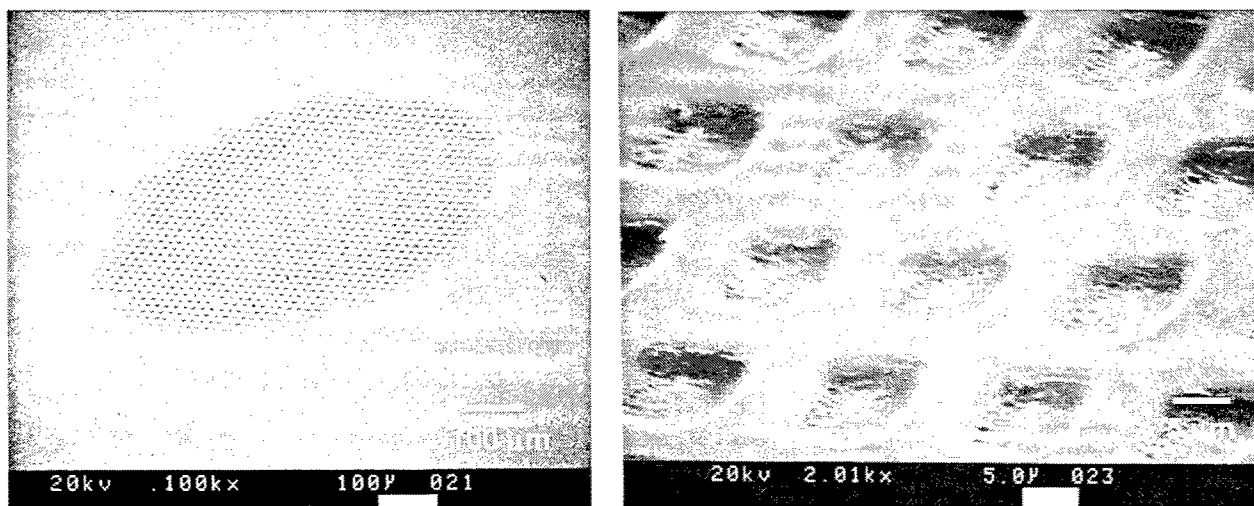
Figure 3: SEM pictures of silica glass surface-structured by LIBWE method with a pure toluene solution upon the irradiation of KrF excimer laser at 720 mJ cm^{-2} with 300 pulses (etch depth: 4.5 μm).

3.2 IN-SITU OBSERVATION OF LIQUID ABLATION

The laser ablation of a toluene solution was monitored by a back-illumination technique with a optical microscope. Figures 4 and 5 show temporal side-view images of toluene ablation at the delay time between 100 ns and 110 μs after KrF laser irradiation at fluence of 1.6 J cm^{-2}. The formation of shock wave and vapor bubble was observed around the interface between silica glass and toluene liquid. Initial velocities of expansion for shock wave and vapor bubble were ca. 1.4 km s^{-1} and 200 m s^{-1}, respectively. At the delay time of 50 μs, vapor expansion reached the maximum size of 600 μm on the glass (Fig. 5), and the vapor dome shrunk gradually up to 110 μs. Top-view observation of Figs. 6 and 7 supported these finding.[23] From both the top-view and side-view detection, it was indicated that shock wave and vapor bubble were hemi-spherically expanded on the glass surface. As shown in Fig. 9, the formation and propagation of shock wave and vapor bubble were also observed upon the laser irradiation at the fluence of 600 mJ cm^{-2}.

Interestingly, upon the laser irradiation at 100 mJ cm^{-2}, we have found several specific phenomena (Fig. 8). First, a tiny small size of bubble was formed. The maximum size of the bubble at 100 mJ cm^{-2} was ca. 30 μm at the delay time of 5 μs (V_{jet} = ca. 40 m s^{-1}). Second, the shock wave was hardly discernible by the microscopy. Third, the soot in the solution was observed negligibly. Toluene solution was still color-less and transparent upon 10,000 shots irradiation. These three findings are clearly distinct from those upon the laser irradiation above 190 mJ cm^{-2}. Masuhara and co-workers reported that threshold fluence for nanosecond-pulsed KrF excimer laser ablation of a pure toluene solution was 35 mJ cm^{-2} in ambient air.[24]

Figure 4: Side-view images of toluene ablation taken by time-resolved optical micrographic technique at a delay time (Δt) between 0 and 1200 ns after the irradiation of KrF excimer laser at the fluence of 1.6 J cm^{-2} (Laser beam size: 170 μmϕ).

Figure 5: Side-view images of toluene ablation taken by time-resolved optical micrographic technique at a delay time (Δt) between 2 and 110 μs after the irradiation of KrF excimer laser at the fluence of 1.6 J cm^{-2} (Laser beam size: 170 μmφ).

Figure 6:   Top-view images of toluene ablation taken by time-resolved optical micrographic technique at a delay time (Δt) between 50 and 1000 ns after the irradiation of KrF excimer laser at the fluence of 1.6 J cm^{-2} (Laser beam size: 250 µm square).[23]

Figure 7: Top-view images of toluene ablation taken by time-resolved optical micrographic technique at a delay time (Δt) between 2 and 130 μs after the irradiation of KrF excimer laser at 1.6 J cm^{-2} (Laser beam size: 250 μm square).[23]
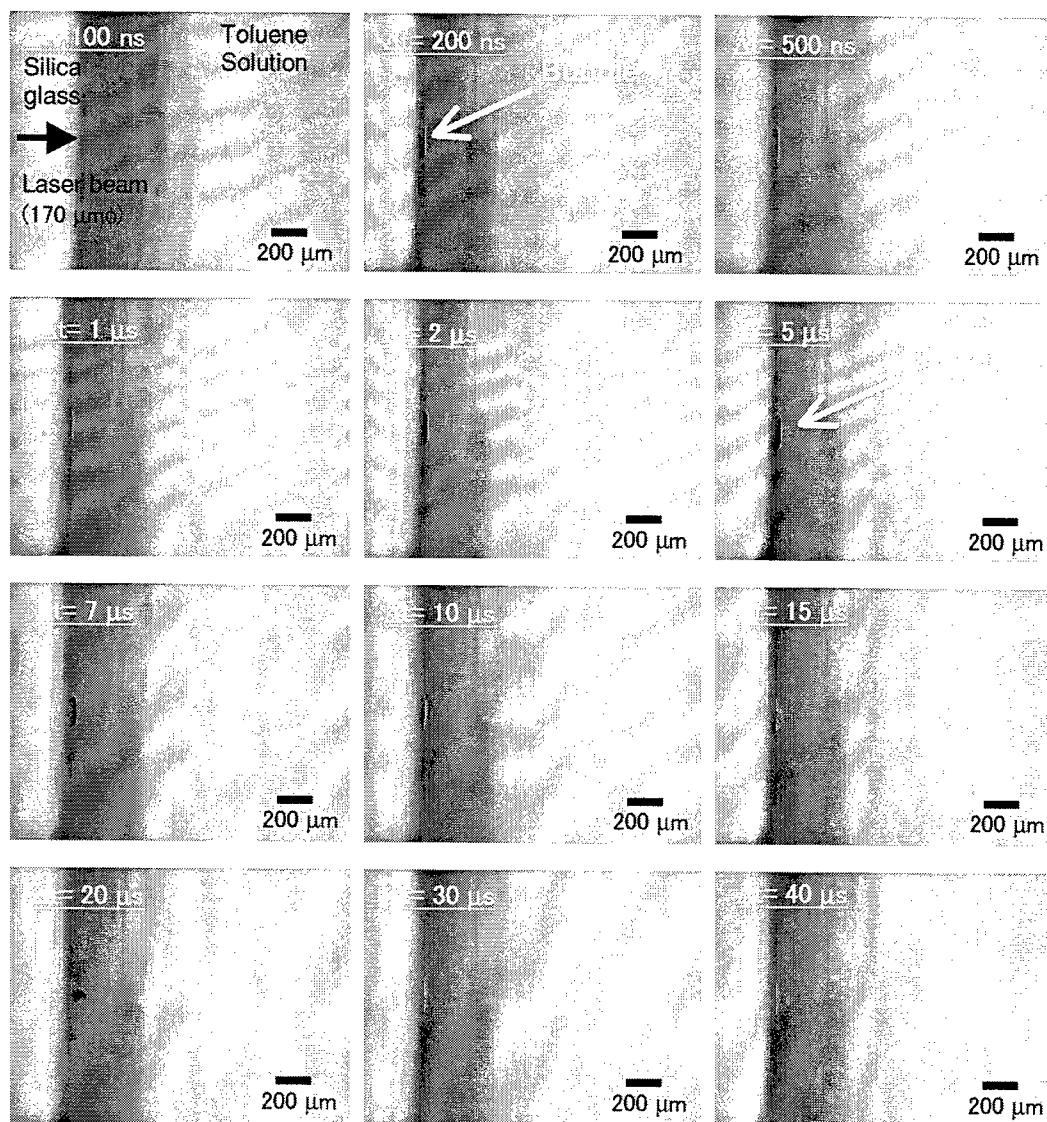
Figure 8: Side-view images of toluene ablation taken by time-resolved optical micrographic technique at a delay time (Δt) between 100 ns and 40 µs after the irradiation of KrF excimer laser at the fluence of 100 mJ cm^{-2} (Laser beam size: 170 µmϕ).
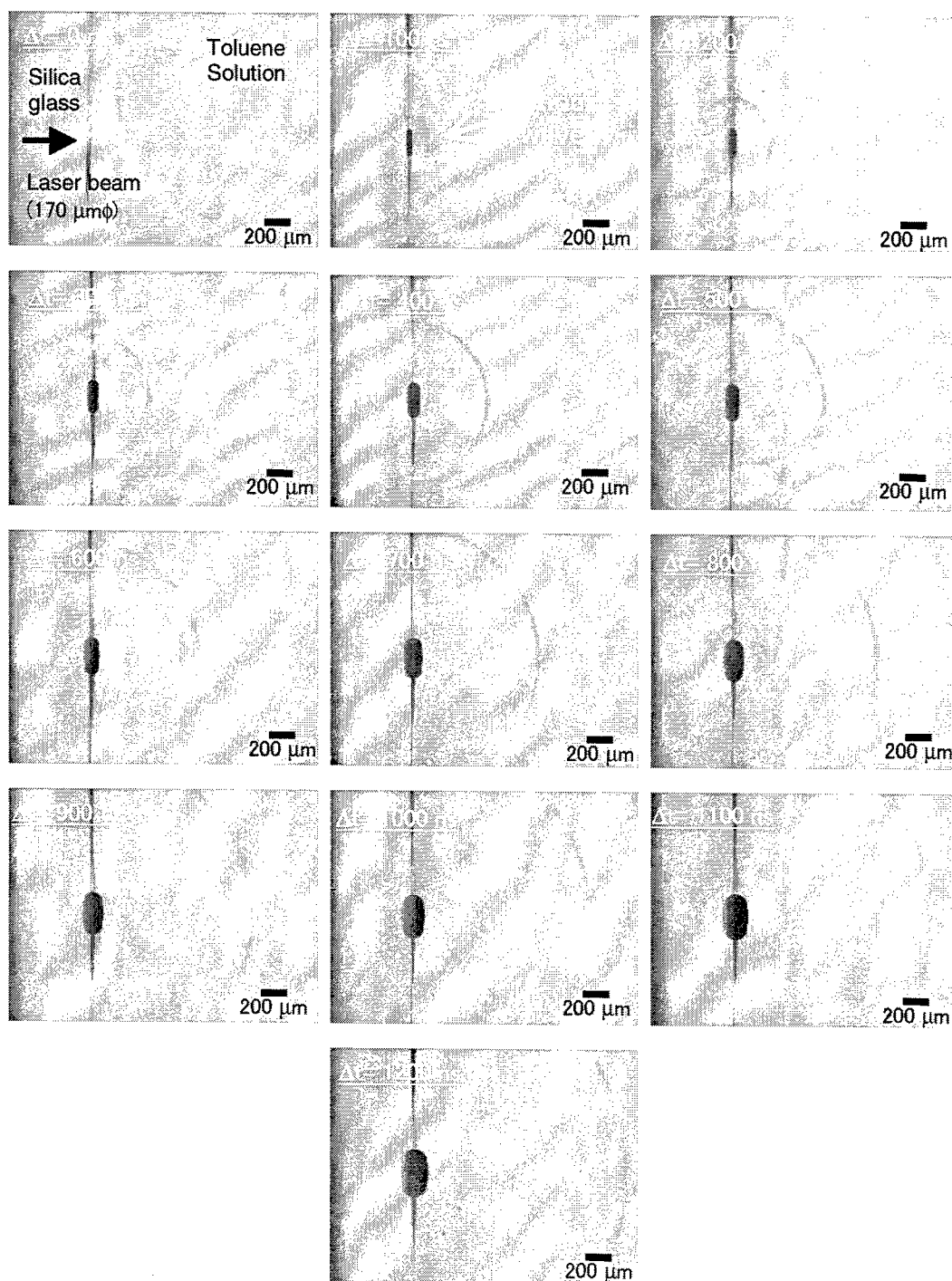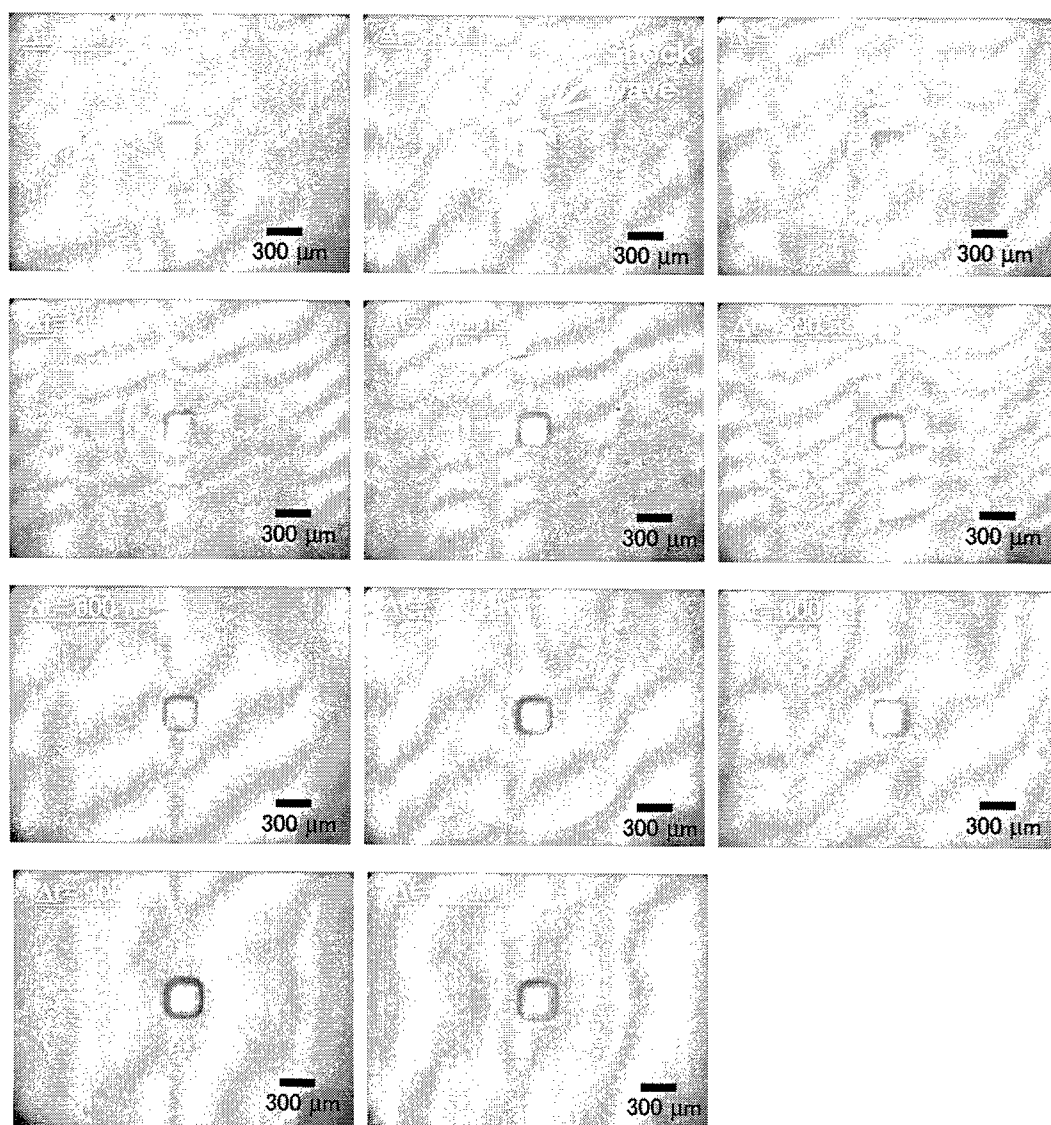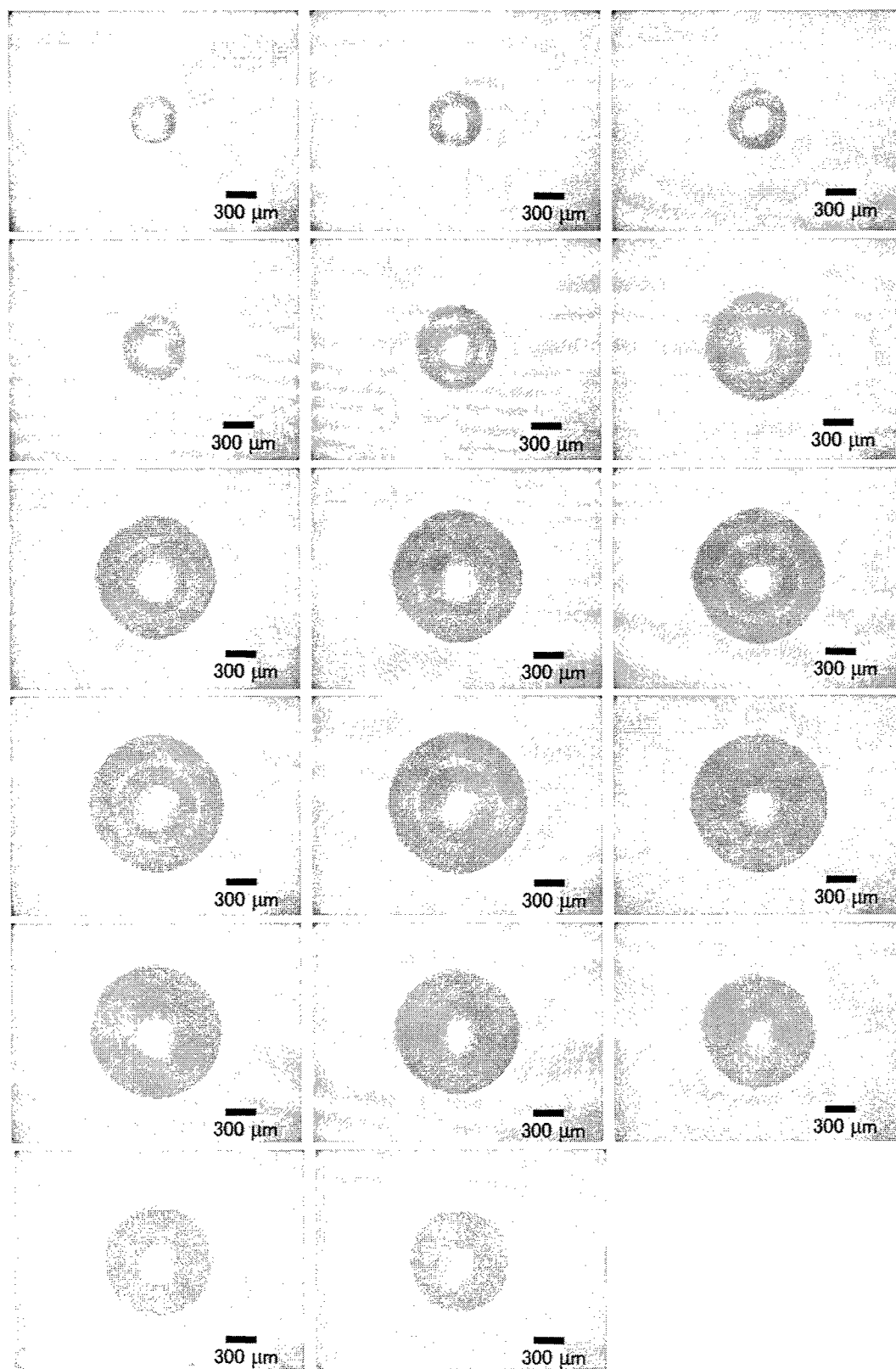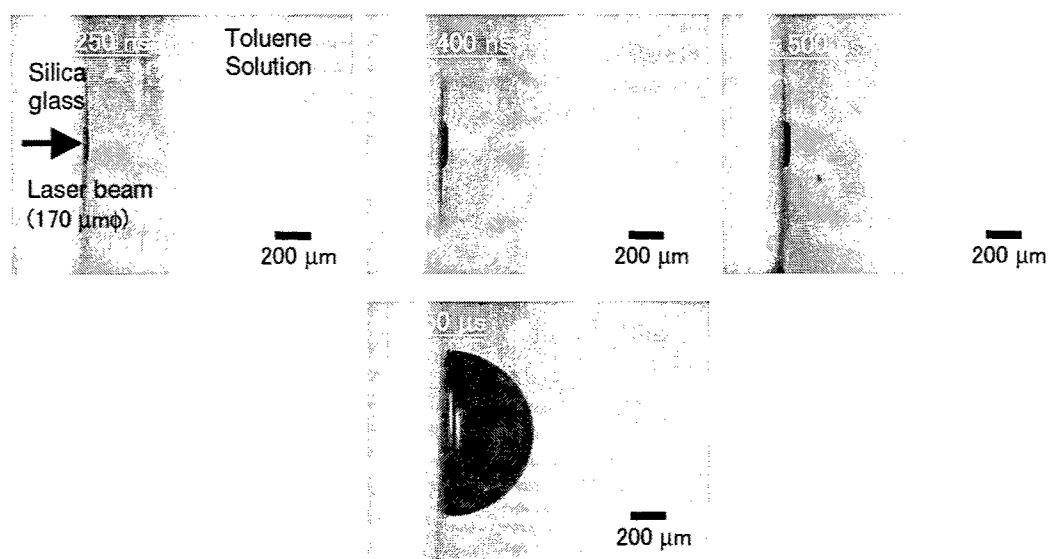
Figure 9: Side-view images of toluene ablation taken by time-resolved optical micrographic technique at a delay time (Δt) between 250ns and 50 μs after the irradiation of KrF excimer laser at the fluence of 600 mJ cm^{-2} (Laser beam size: 170 μmϕ).

The impact pressure of the liquid jet can be estimated roughly from the following formula:[25]

$$P = \rho \cdot C \cdot V_{jet},$$

where ρ and C are the density of toluene and the acoustic velocity in toluene (ρ= 0.86 g cm^{-3} and C= 1300 m s^{-1} at 300 K), respectively. A velocity V_{jet} of 200 m s^{-1} corresponds to a pressure of 220 MPa. When we assume another simple model where incident photon energy was totally converted to thermal energy for vaporizing toluene without decomposition of the molecular structure, the initial pressure and temperature of toluene bubble upon the laser irradiation at fluence of 1.6 J cm^{-2} was estimated to be $\sim$100 MPa and $\sim$1000 K from the calculation based on the state equation using thermal properties of toluene molecule such as heat capacity and heat of evaporation. These two types of estimates suggest that the laser irradiation of toluene solution provided a unique environment under a transient high pressure and temperature. Figure 10 shows that initial pressure of toluene ablation has an excellent linear relation against the laser fluence, suggesting that such a transient high pressure propagation plays a key role for silica glass etching.

In addition, when the laser beam was incident into the solution at 0.19 J cm^{-2} and 1.6 J cm^{-2}, the ratio between the number of incident photons (I) and the number of toluene molecules (N) in the unit volume for the penetration depth was calculated to be I/N= 0.05 and 0.4, respectively (The penetration depth (d) of pure toluene at the wavelength of 248 nm was estimated to be d= 8.9 μm on the basis of single photon absorption (d=$M_w/\varepsilon\rho$; M_w= 92 g mol^{-1}, ρ= 0.86 kg dm^{-3}, ε= 120 mol^{-1} dm^3 cm^{-1} (hexane solution)).[26] This means that LIBWE process was mainly based on a single-photon event. Figure 11 shows the luminescent spectrum of a pure toluene liquid. This was ascribed to the emission of benzyl radical,[24] which was mainly produced by the photochemical decomposition of toluene molecule by a single UV photon at 248 nm.
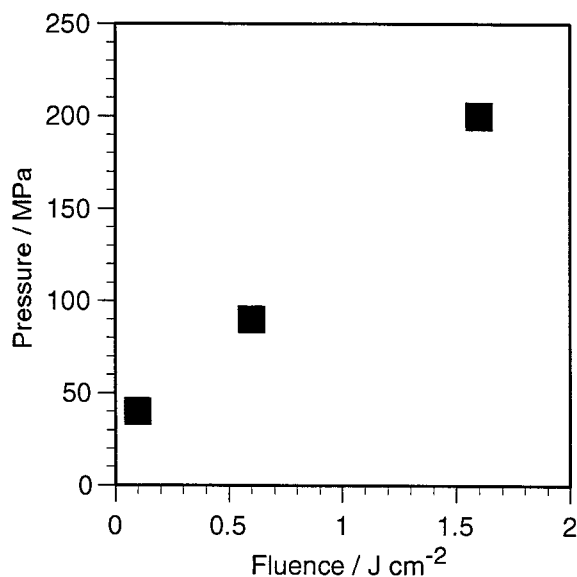
Figure 10: Estimated initial pressure of toluene ablation as function of KrF excimer laser fluence.
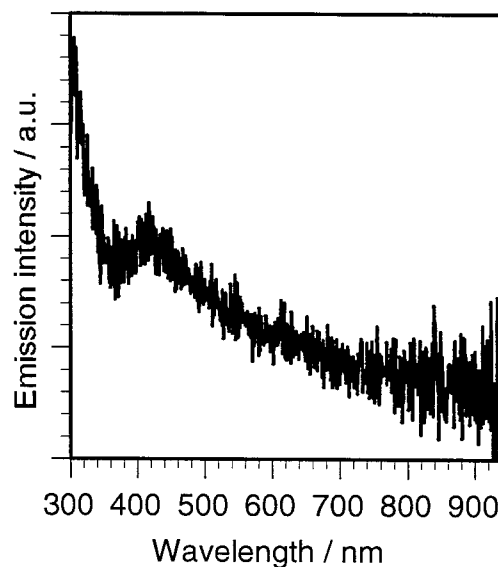
Figure 11: Emission spectrum of a pure toluene solution excited by KrF excimer laser irradiation at 1.6 J cm^{-2}.

5. CONCLUSION

We demonstrated a new technique for silica glass etching by use of ns-pulsed laser ablation of toluene solution. Our LIBWE method has several advantages compared to previous methods for micromachining of transparent materials; a lower laser fluence and higher etch rate, a constant etch rate, sharp edges for micro-pattern, free from cracks and debris, and so on. This is a one-step simpler process at ambient pressure, which seems to be profitable for mass production.

REFERENCES

1. D. Baeuerle, "Laser Processing and Chemistry", Springer, Berlin, 1996.
2. J. Ihlemann, B. Wolff-Rottke, "Excimer laser micromachining of inorganic dielectrics", Appl. Surf. Sci. 106, pp.282-286, (1996).
3. J. Ihlemann, B. Wolff, P. Simon, "Nanosecond and femtosecond excimer laser ablation of fused-silica", Appl. Phys., A54, pp.363-368 (1992).
4. P. R. Herman, R. S. Marjoribanks, A. Oettl, K. Chen, I. Konovalov, S. Ness," Laser shaping of photonic materials: deep-ultraviolet and ultrafast lasers", Appl. Surf. Sci., 154–155, pp.577-586 (2000).
5. K. Sugioka, S. Wada, H. Tashiro, K. Toyoda, A. Nakamura, "NOVEL ABLATION OF FUSED QUARTZ BY PREIRRADIATION OF VACUUM-ULTRAVIOLET LASER-BEAMS FOLLOWED BY 4TH HARMONICS IRRADIATION OF ND-YAG LASER", Appl. Phys. Lett., 65, pp.1510-1512 (1994).
6. J. Zhang, K. Sugioka, and K. Midorikawa," Direct fabrication of microgratings in fused quartz by laser-induced plasma-assisted ablation with a KrF excimer laser", Opt. Lett., 23, pp.1486-1488 (1998).
7. J. Zhang, K. Sugioka, and K. Midorikawa, "High-speed machining of glass materials by laser-induced plasma-assisted ablation using a 532-nm laser", Appl. Phys., A67, pp.499-501 (1998).
8. J. Zhang, K. Sugioka, and K. Midorikawa, "Laser-induced plasma-assisted ablation of fused quartz using the fourth harmonic of a Nd+: YAG laser", Appl. Phys., A67, pp. 545-549 (1998).

9. J. Zhang, K. Sugioka, and K. Midorikawa. "High-quality and high-efficiency machining of glass materials by laser-induced plasma-assisted ablation using conventional nanosecond UV, visible, and infrared lasers", *Appl. Phys.*, **A69**, pp.S879-S882 (1999).

10. H. Varel, D. Ashkenasi, A. Rosenfeld, M. Waehmer, E. E. B Campbell, "Micromachining of quartz with ultrashort laser pulses", *Appl. Phys. A*, **65**, pp.367-373 (1997).

11. J. Wang, H. Niino, A. Yabe, "One-step microfabrication of fused silica by laser ablation of an organic solution", *Appl. Phys.*, **A68**, pp.111-113 (1999).

12. J. Wang, H. Niino, and A. Yabe, "Micromachining of quartz crystal with excimer lasers by laser-induced backside wet etching", *Appl. Phys.*, **A69,** pp.S271-S273 (1999).

13. J. Wang, H. Niino, A. Yabe, "Microfabrication of a fluoropolymer film using conventional XeCl excimer laser by laser-induced backside wet etching", *Jpn. J. Appl. Phys.*, **38**, pp.L761-L763 (1999).

14. J. Wang, H. Niino, A. Yabe, "Micromachining of transparent materials with super-heated liquid generated by multiphotonic absorption of organic molecule" *Appl. Surf. Sci.*, **154-155**, pp.571-576 (2000).

15. Y. Yasui, H. Niino, Y. Kawaguchi, and A. Yabe, "Microetching of fused silica by laser ablation of organic solution with XeCl excimer laser", Appl. Surf. Sci., 186, pp.552-555 (2002).

16. X. Ding, Y. Yasui, H. Niino, Y. Kawaguchi, and A. Yabe, "Laser-induced back-side wet etching of fused silica with an aqueous solution containing organic molecules", *Appl. Phys.*, **A75,** pp. 437-440 (2002).

17. X. Ding, Y. Kawaguchi, H. Niino, and A. Yabe, "Laser-induced high-quality etching of fused silica using a novel aqueous medium", *Appl. Phys.*, **A75**, pp.641-645 (2002).

18. H. Niino, Y. Yasui, X. Ding, A. Narazaki, T. Sato, Y. Kawaguchi, and A. Yabe, "Surface micro-fabrication of silica glass by excimer laser irradiation of organic solvent", *J. Photochem. Photobiol. A: Chem.*, in press.

19. X. Ding, T. Sato, Y. Kawaguchi, and H.Niino, "Laser-induced Backside Wet Etching of Sapphire", *Jpn. J. Appl. Phys. Pt.2*, **42(2B)**, (2003) in press.

20. Y. Tsuboi, H. Fukumura, H. Masuhara, "Nanosecond imaging study on laser-ablation of liquid benzene", *Appl. Phys. Lett.*, **64,** pp.2745-2747 (1994).

21. R. Böhme, A. Braun, K. Zimmer, "Backside etching of UV-transparent materials at the interface to liquids", *Appl. Surf. Sci.*, **186**, pp.276-281 (2002).

22. K. Zimmer., R. Böhme, A. Braun, B. Rauschenbach, F. Bigl, "Excimer laser-induced etching of sub-micron surface relief gratings in fused silica using phase grating projection", *Appl. Phys.*, **A74**, pp.453-456 (2002).

23. In Figs. 6 and 7, the area of the laser irradiation on silica glass corresponds to a bright spot (square) at the center of pictures. This visible emission was ascribed to the luminescence of toluene liquid excited by KrF laser irradiation. The shadow image of shock wave and bubble expansion was superimposed onto the luminescence because our CCD-camera equipment has no time-gated function. The luminescent spectrum in the visible region is shown in Fig. 11.

24. Y. Tsuboi, K. Hatanaka, H. Fukumura, H. Masuhara, "The 248-nm excimer-laser ablation of liquid benzene-derivatives: A relation between ablation threshold and molecular photochemical reactivity", *J. Phys. Chem.*, **98**, pp.11237-11241 (1994).

25. J. C. Isselin, A. P. Alloncle, A. Autric, "On laser induced single bubble near a solid boundary: Contribution to the understanding of erosion phenomena", *J. Appl. Phys.*, **84**, pp.5766-5771 (1998).

26. H.-H. Perkampus, "UV-vis Atlas of Organic Compounds", 2nd Edn., VCH, Weinheim, p.338 (1992).

Diode-pumped TEM$_{00}$ mode solid state lasers and their micromachining applications

Norman Hodgson, Mingwei Li, Andrew Held, Arnd Krueger
Spectra-Physics, Inc., Solid State Laser Business Unit
1305 Terra Bella Avenue, Mountain View, CA 94043

ABSTRACT

During the last decade, diode-pumped TEM$_{00}$ mode solid state lasers have gained widespread application in micromachining of dielectrics and metals. Commercial systems with output powers of up to 40W at 1064nm, 20W at 532nm, 15W at 355nm and 2W at 266nm, repetition rates of up to 400kHz and pulse durations between 10ns and 100ns are now being used in numerous micromachning applications. In addition, industrial applications of modelocked lasers are starting to emerge. This paper will give an overview of the state-of the art of diode-pumped TEM$_{00}$ mode solid state lasers and their applications in micromachining.

Keywords: diode-pumped solid state lasers, micromachining, ultrafast lasers, Q-switching, modelocking

1. INTRODUCTION

Since their introduction more than a decade ago, there have been continuous improvements in the performance and reliability of diode-pumped TEM$_{00}$ mode solid state lasers. The advent of reliable higher power diode bars, the optimization of diode-pumped laser designs as well as improvements in the quality of laser crystals and nonlinear crystals has led to a tenfold increase in TEM$_{00}$ mode power at 1064nm and its harmonic wavelengths (Fig.1). Diode-pumped TEM$_{00}$ mode solid state lasers are now being used in numerous industrial applications such as via hole drilling, PCB structuring, stereolithography, disk texturing, resistor trimming, memory repair, scribing, cutting and marking (Table 1). Industrial requirements for higher output power is mainly driven by a demand for increased processing speeds. Consequently, the higher output power needs to be realized with a corresponding increase in repetition rate. In addition shorter pulse durations down to 100fs are gaining more importance in a variety of applications as the heat affected zones is reduced leading to a better processing quality.
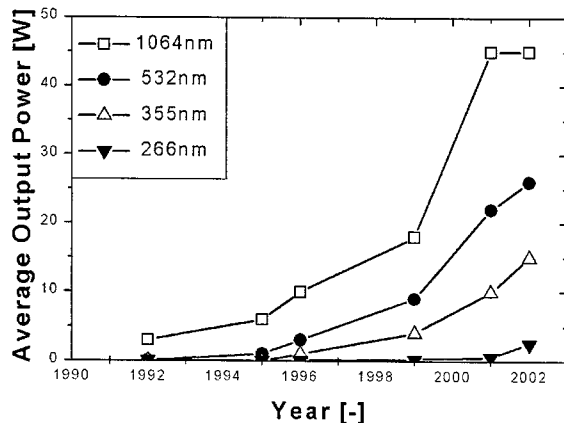
Fig. 1 Maximum output power in TEM$_{00}$ mode operation of commercially available, diode-pumped solid state lasers.

2. INDUSTRIAL MARKET FOR TEM$_{00}$ MODE DPSSLs

The Optoelectronics Report [1] estimates that the 2002 worldwide market size for diode-pumped solid state lasers (DPSSLs) was about 192 million US$, with a forecast for 2003 at around 215 million US$. At present, the majority of DPSSLs are TEM$_{00}$ mode lasers. Within this market segment, the main industrial applications can be divided into three categories: computer and micro-electronics (PCB fabrication, resistor trimming, memory repair, disk texturing, solar cell scribing, semiconductor wafer processing), industrial manufacturing (stereolithography, marking, drilling, cutting) and printing. Table 1 gives an overview of the current industrial applications for diode-pumped solid state lasers.

Wavelength	Power	Pulse Duration	Repetition Rate	Applications
Q-switched lasers				
1320 nm	0.4-1.0 W	5 – 20 ns	10-20 kHz	memory repair
1064 nm	1 – 35 W	5 – 100 ns	1 – 100 kHz	resistor trimming, memory repair, marking, solar cell scribing, disk texturing, diamond cutting
532 nm	0.5 - 20 W	5 – 70 ns	1 – 50 kHz	marking, PCB structuring, drilling, cutting
355 nm	0.2 – 10 W	5 – 50 ns	15– 100 kHz	via hole drilling, stereolithography, silicon marking, silicon dicing
266 nm	0.5 – 2.0 W	5 – 30 ns	15– 100 kHz	drilling, marking, inspection, wafer processing
Modelocked lasers				
800 nm	0.5 – 2 W	100 fs	80 MHz	multiphoton imaging, thin film metrology, optical coherence tomography
800 nm	0.5 – 1.5 W	100 fs	1-5 kHz	machining of nozzles, photo mask repair
355 nm	0.2 – 4 W	10 ps	80 MHz	PCB production, printing, FBG production, cutting of foils
cw Lasers				
1064 nm	5 – 15 W	0.1µs-100µs	5 – 40 MHz	printing
532 nm	2 – 10 W	N/A	N/A	wafer inspection, disk texturing, image recording, medical
266 nm	0.2 – 0.5 W	N/A	N/A	wafer inspection, FBG production, DVD disk mastering

Table 1: Commercially available diode-pumped TEM$_{00}$ mode solid state lasers and their industrial applications.

3. TEM$_{00}$ MODE DPSSL TECHNOLOGY

The majority of diode-pumped TEM$_{00}$ mode lasers are end-pumped designs, where Neodymium doped YAG or Vanadate crystals are pumped at 808nm through one or both of the endfaces. Pump powers of up to 30W per end face and pump spot diameters of 0.5mm-1.5mm provide high small-signal gains of greater than 4.0 and stored energies of up to 10mJ. Thermal lensing of the active medium limits the maximum output power in TEM$_{00}$ mode per laser crystal to about 25W. Higher output powers per crystal of up to 60W are possible, but only by limiting the pump power range within which the laser remains in a stable zone, a design strategy that is generally avoided in industrial lasers. A layout of a high power TEM$_{00}$ mode laser is depicted in Fig.2 [2-4]. Two Vanadate crystals are end-pumped with a maximum pump power of 26W per side. In cw operation this system provides a maximum IR power of about 48W in TEM$_{00}$ mode operation, corresponding to an optical efficiency (emitted 1064nm power to incident 808 nm pump power) of 46%. Q-switching of the cavity is accomplished with an acousto-optical modulator (AOM), resulting in repetition rates between 10 kHz and 130 kHz and pulse durations of 50-150 ns.

Neodymium doped Vanadate is the crystal of choice for high repetition rate operation (>20kHz), due to its high gain and relatively short lifetime of the upper laser level (100μs). In high gain lasers, the maximum repetition rate can be increased to 500 kHz by undercoupling the resonator. Higher repetition rates are difficult to achieve due to the limited gain recovery time between pulses. In applications that require lower repetition rates and higher pulse energies, Nd:YAG or Nd:YLF are utilized due to their longer lifetime of 230μs and 480μs, respectively.

Due to the high peak power of Q-switched IR lasers (10s of kW), external harmonic generation in LBO can be used to generate TEM$_{00}$ mode emission at 532nm and 355nm. Conversion efficiencies (IR to harmonic wavelength) of greater 60% at 532nm and greater 25% at 355nm, result in maximum output powers in excess of 20W and 10W, respectively (Fig.3). Higher efficiencies can be attained with intra-cavity harmonic generation, a technology that is inherently more complicated. In addition, the improvement in the quality of CLBO and the advent of methods to handle its hygroscopy have recently resulted in commercially available 266nm Q-switched lasers with output powers in excess of 2 Watts [5] (Fig.4).
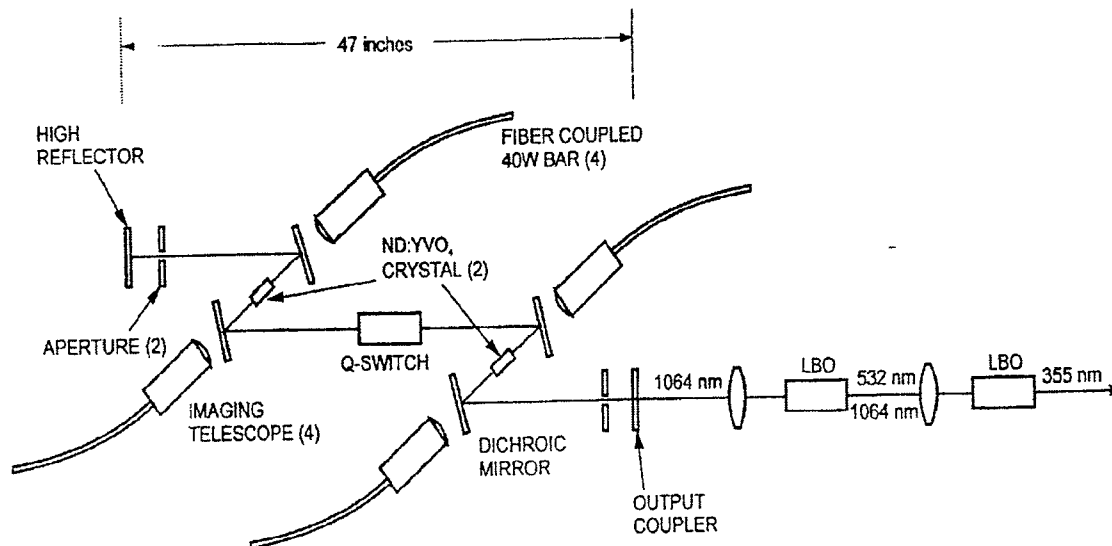
Fig.2 Layout of a high power, Q-switched DPSSL in TEM$_{00}$ mode operation with external third harmonic generation.
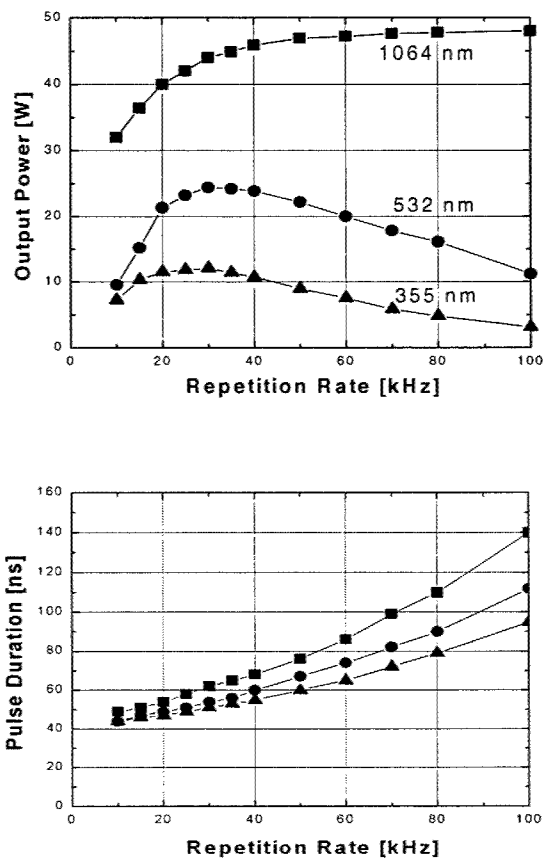
Fig.3 Average output power and pulse duration of the end-pumped Q-switched Vanadate laser of Fig.2. Green and UV output is generated using extra-cavity harmonic generation in LBO.
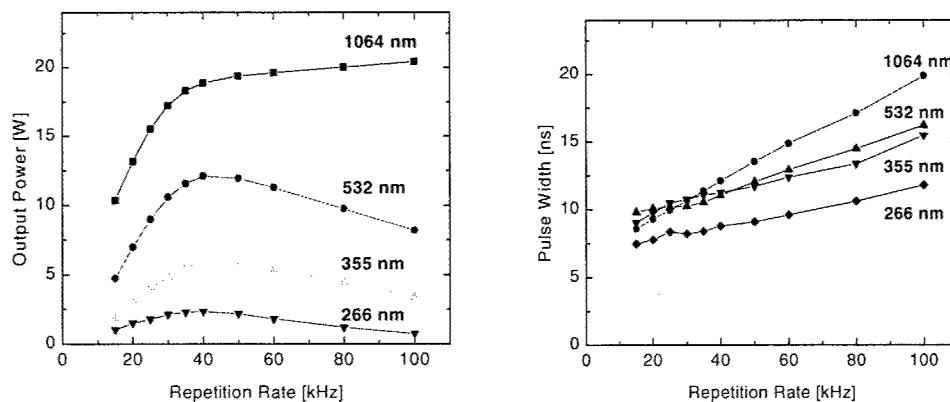
Fig.4 Output power an pulse durations of a short-pulse, Q-switched Vanadate laser in TEM00 mode operation at the fundamental and its harmonic wavelengths (Spectra-Physics' HIPPO).
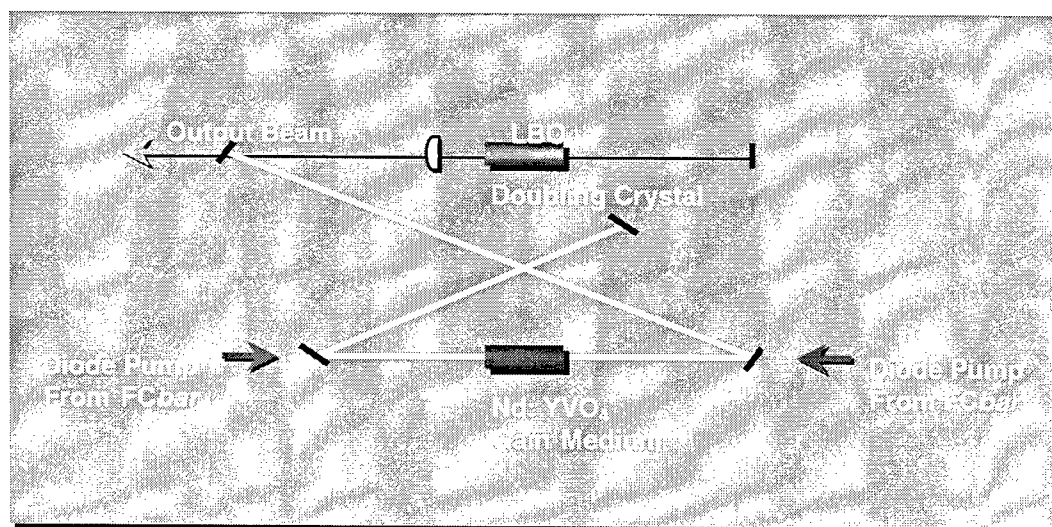
Fig.5 Intracavity doubled cw Vanadate laser with 10W TEM_{00} mode output power at 532nm.
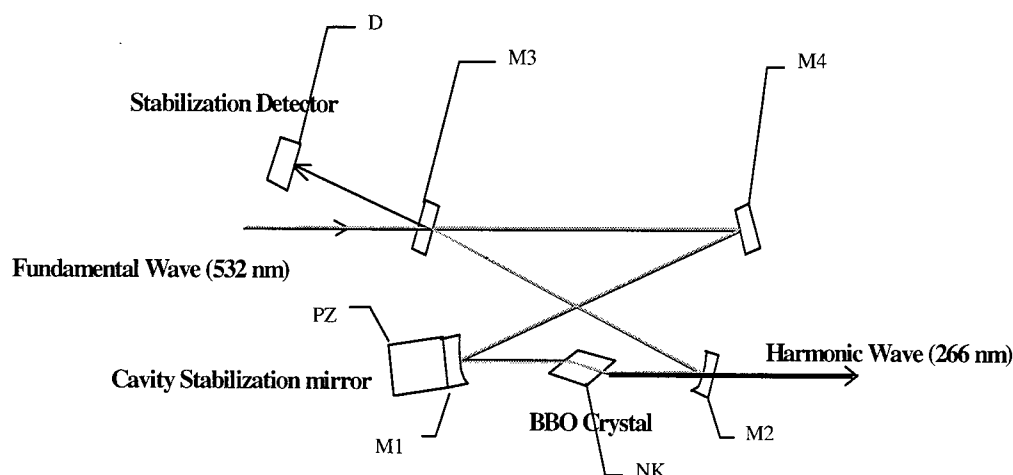
Fig.6 Resonant doubling of 532nm in a ring-cavity with BBO. The length of the build-up cavity has to match the resonator length of the green pump laser to get constructive interference.

Industrial applications of TEM_{00} mode cw lasers at 1064nm are limited to the printing industry, where external modulation and scanning of the laser beam is used to write 10 micron pixels on specially coated, IR sensitive printing plates. However, this technology is now being replaced by direct diode systems, leaving the vast majority of cw applications of TEM_{00} mode lasers in the green and the UV wavelength ranges. With the current IR power levels, the nonlinear crystal must be placed inside the laser cavity to obtain useful second harmonic power levels. Beginning with the Millennia introduction by Spectra-Physics in 1996, cw 532nm lasers are now well established with output powers of up to 10W and very low optical noise of less than 0.04% (Fig.5). The use of an external build-up cavity with BBO as the nonlinear crystal allowed the introduction of industrial 266nm cw lasers with output powers of up to 500mW (Fig.6).

Another route to higher green and UV power is provided by modelocking a cw Vanadate laser (Fig.7). The latest SBR (saturable Bragg reflector) mirror technology enables simple mode-locking that is robust enough for demanding industrial applications. Since the peak power of these lasers are similar to those of Q-switched systems, mode-locked Nd:Vanadate lasers allow for efficient frequency doubling and tripling. TEM_{00} mode output powers of 20W in the IR, 10W in the green and up to 4W at 355nm are now commercially available. The high repetition rate of 80MHz and pulse durations of 10ps allow these lasers to replace bulky ion lasers in many cw ultraviolet applications.
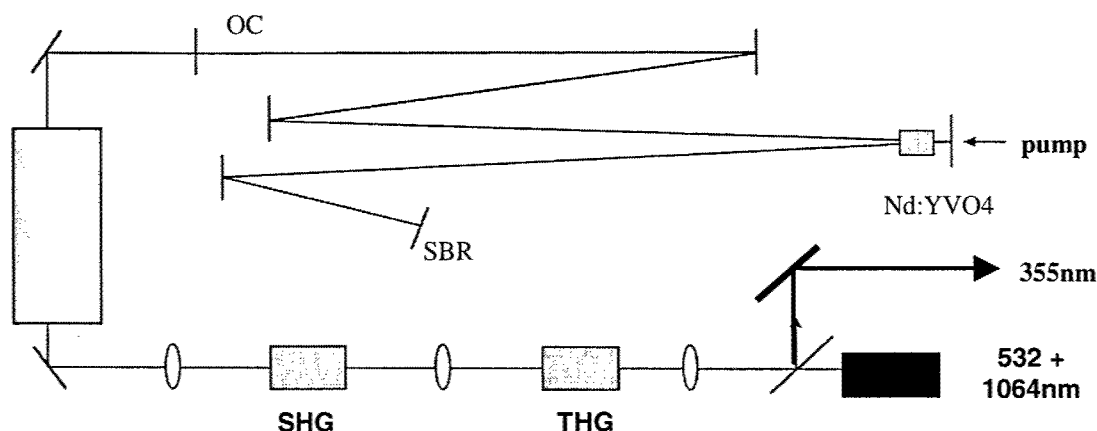
Fig.7 Layout of a modelocked Vanadate laser with external third harmonic generation (Spectra-Physics Vanguard). The resonator length of 1.8m results in a repetition rate of 80MHz at pulse durations of 10ps. An amplifier (left) is used to increase the IR output power to 20W. At 355nm, this system delivers an average output power in excess of 4W.

The relatively long pulse duration of 10ps of these modelocked systems is a result of the limited bandwidth of Nd:Vanadate. By using Ti:sapphire, with its 1000 times larger bandwidth, pulse durations of less than 10fs can be attained at emission wavelengths ranging from 720 to 960nm.. One of the disadvantages of this technology is the need for a green pump source. Since green pump diodes are not commercially available, the sapphire has to be pumped with a cw green DPSSL, adding considerably to the overall system cost. Industrial mode-locked oscillators are offered as one-box systems with the green pump laser incorporated that provide output powers of up to 1.5W at repetition rates of 80MHz and pulse durations between 50 and 100fs. Due to the low pulse energies of tens of nJ, applications of these oscillator systems are limited to thin film thickness measurement and two-photon microscopy, both applications that prohibit any irreversible interaction with the work sample. Normally, micromachining requires much higher pulse energies of 10s of microJoules, energy levels that can only be attained by amplification of the oscillator pulses and reduction of the pulse repetition rate to below 10 kHz.

An industrial, one-box modelocked amplifier system that provides an average output power of 1.25W at 5 kHz with pulse durations of 100fs is depicted in Fig.8. An electro-optic modulator is used to pick pulses from a 1W, 80MHz, 80fs, oscillator at a repetition rate of 5kHz. After stretching the pulses in a pair of gratings from 80fs to 100ps, the pulses are fed into a regenerative Ti:sapphire amplifier to increase the pulse energy from 18nJ to 260µJ. Subsequent compression in the grating pair results in pulse durations of about 100fs.

Despite the complexity and the cost of such a system, there is an emerging industrial market, mainly due to the requirement of heat affected zones that are much smaller than those generated by standard Q-switched lasers [6]. Current applications include nozzle drilling and photomask repair. Penetration into applications in which Q-switched lasers are currently being used would require a cost reduction by at least of a factor of three as well as an increase of the repetition rate to 10s of kHz. Both requirements cannot be met with the current technology. However, recent advances in modelocked Yb doped disk lasers may result in more cost-effective solutions in the near future, due to the fact that these materials can be directly pumped with infrared diodes.
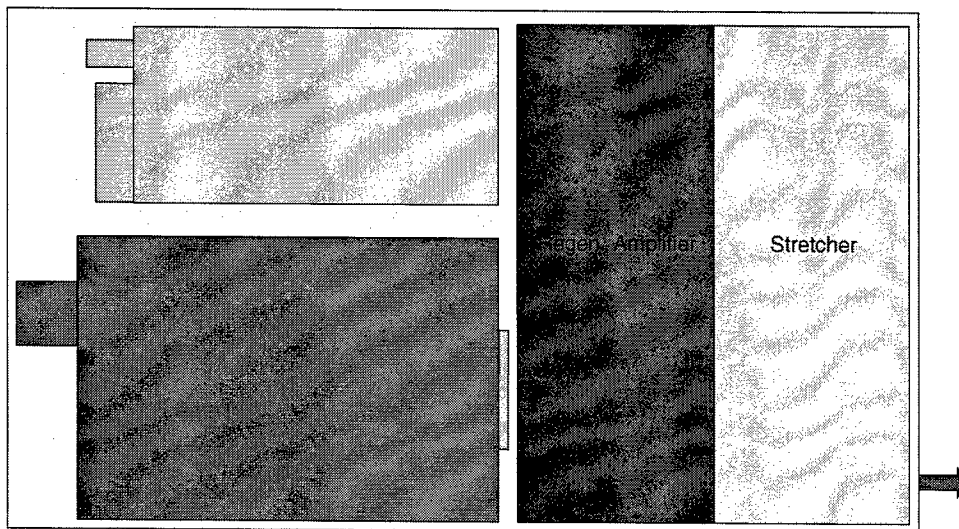
Fig.8 System architecture of an ultrafast laser system (Spectra-Physics Hurricane) with >1 W output power at 1kHz or 5kHz and 50-130fs pulse duration. A: Diode-pumped, Q-switched 532nm pump laser with 10W output power, B: 1W, 80MHz, 80fs Ti:sapphire oscillator. Oscillator pulses are picked with an E-O modulator and amplified in a regenerative amplifier after stretching the pulses to >200ps. Subsequent pulse compression generates pulse durations of about 100 fs. Length and width of the whole system is 132 cm and 71 cm, respectively.

4. APPLICATIONS
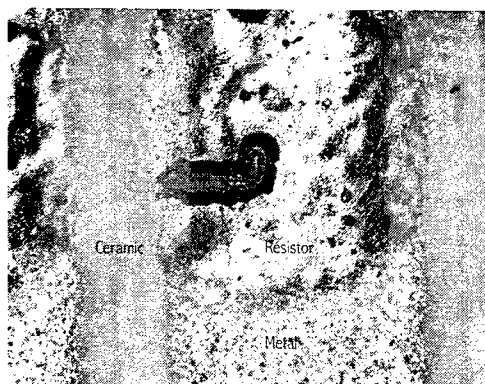
Fig.9 Trimming of a surface mounted resistor using a Q-switched 1064nm laser with 6W average output power at 10kHz and 60ns pulse duration. The horizontal cut provides coarse trimming, the vertical cut in direction of the current flow provides fine adjustment of the resistance. Length of the resistor in direction of the current flow is 1mm. A panel with on the order of thousand resistors is trimmed in 10s of seconds including online measurement of the resistance.
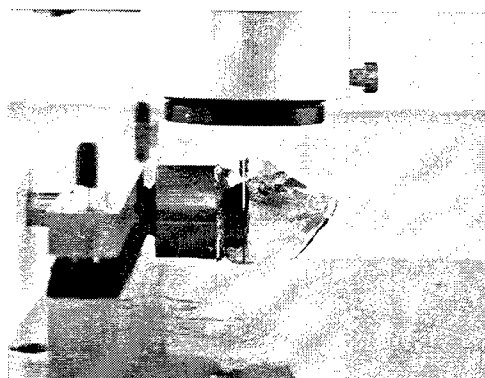
Fig.10 Cutting of a diamond using a Q-switched 1064nm Nd:YAG laser. Repetition rate: 10 kHz, output power: 12W, pulse duration: 70ns (Courtesy of CNC Laser, Belgium).
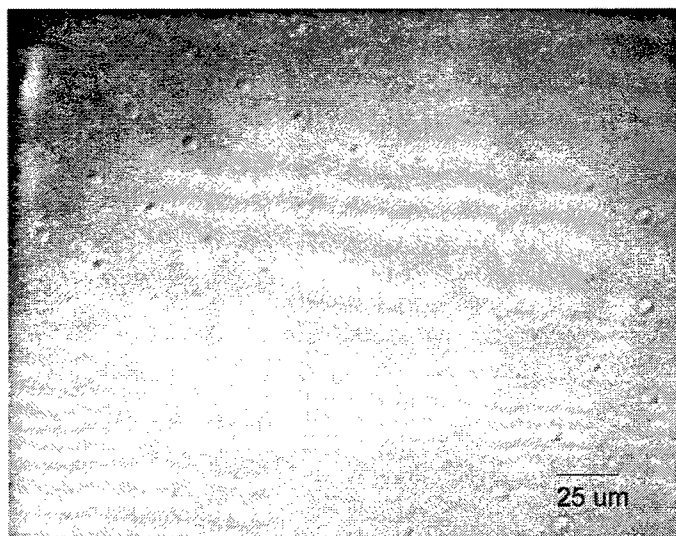
Fig.11 Computer disk texturing using a Q-switched 1064nm Nd:Vanadate laser with 4W average power at 135kHz and 80ns pulse duration. Each pulse generates a crater-shaped bump that is 5nm high and 4 micron wide. Several 10,000 bumps are generated on both sides of the disk in a 5-10mm wide annulus near the disk center (landing zone of the read/write head).
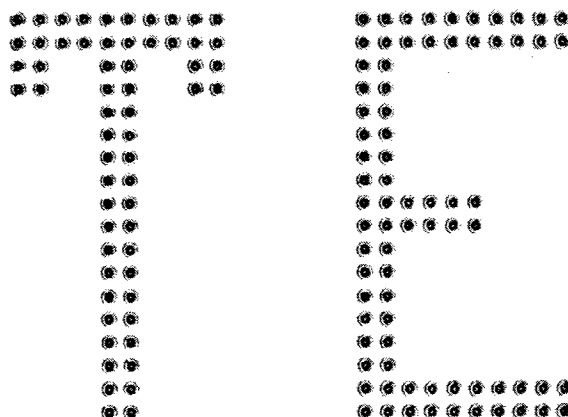
Fig.12 Precision marking of silicon using a 6W Nd:YAG laser at 10kHz repetition rate and 70ns pulse duration Spot diameters are 70 microns (courtesy of Intergen).
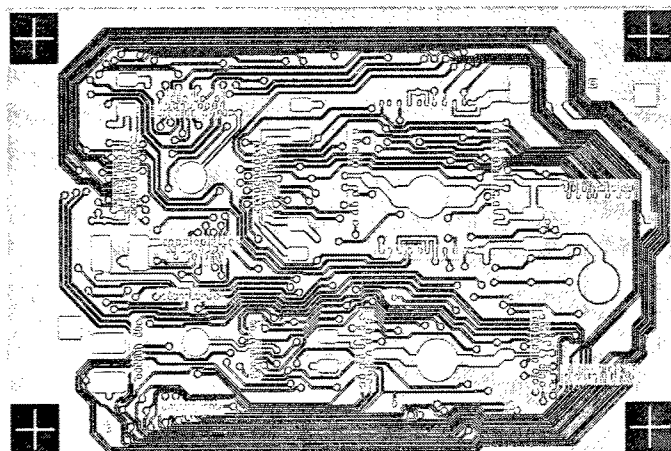
Fig.13 Structuring of a PCB using a 9W Q-switched, 532nm Nd:Vanadate laser at 60kHz repetition rate and 35ns pulse duration. The dark lines mark the areas in which the laser has ablated the copper layer (courtesy of Siemens Dematic, Germany).
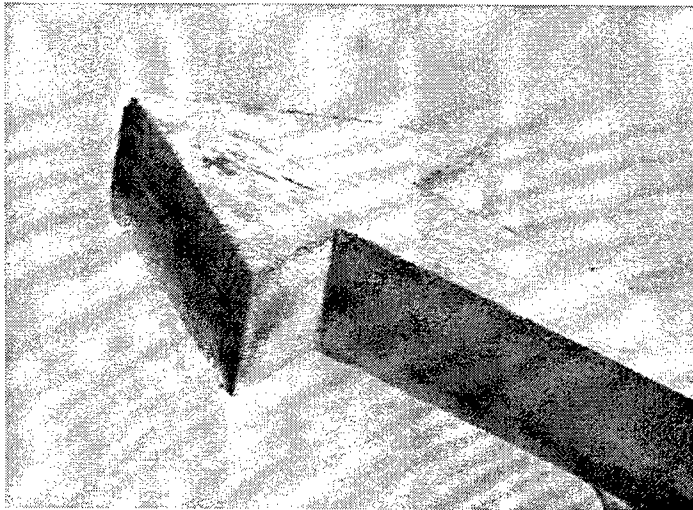
Fig.14 Machining of a silicon waver using a 20W Q-switched 532nm Nd:Vanadate laser at 30kHz repetition rate and 50ns pulse duration. The wafer thickness is 525 microns, cutting speed: 0.064mm/s (courtesy of Exitech, UK)
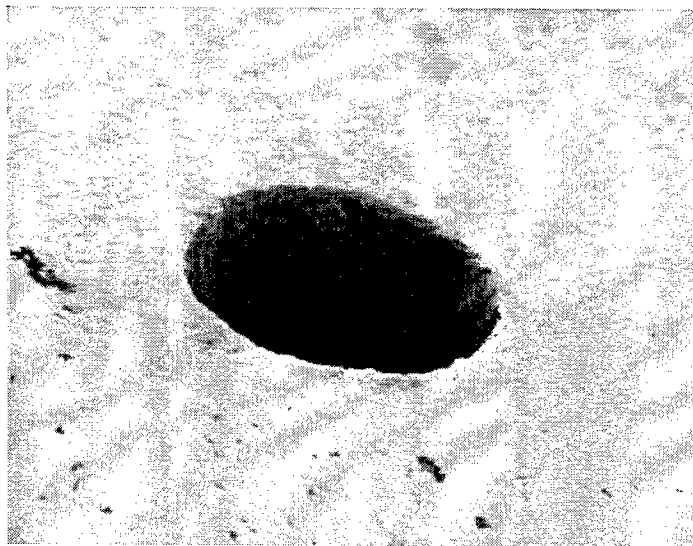
Fig.15 Trepanning drilling of a through hole in a 1mm think silicon nitride substrate using a 20W Q-switched 532nm Nd:Vanadate laser at 30kHz and 55ns pulse duration. The hole diameter is 100 microns (courtesy of Exitech, UK).
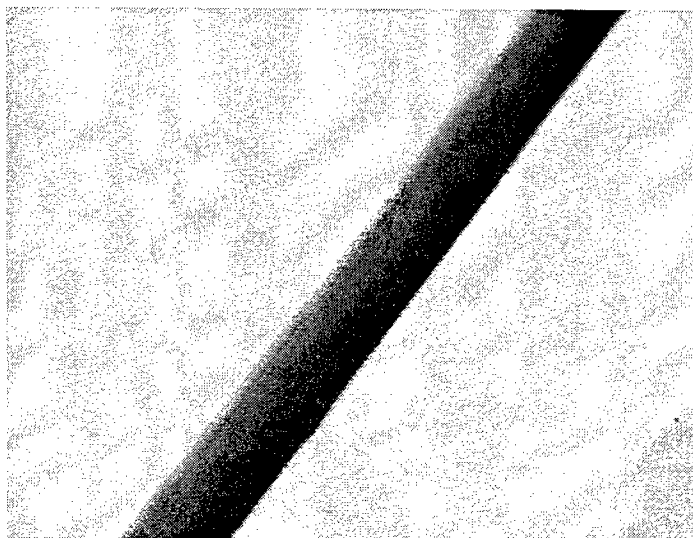
Fig.16 Machining of 200 micron wide trenches in 525 um thick silicon wafers with a 11W 532nm Q-switched Nd:Vanadate laser at 50 kHz repetition rate and 13ns pulse duration (courtesy of Exitech,UK).
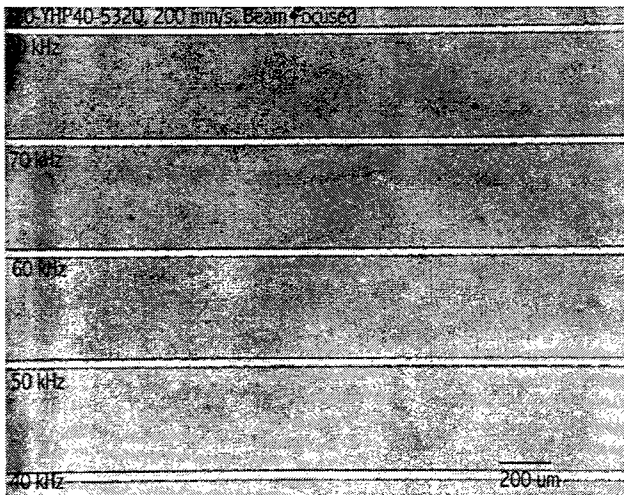
Fig.17 Scribing of indium tin oxide coating (ITO) on a flat panel display substrate using a 9W Q-switched 532nm Nd:Vanadate laser at different repetition rates, cutting speed: 200mm/s.
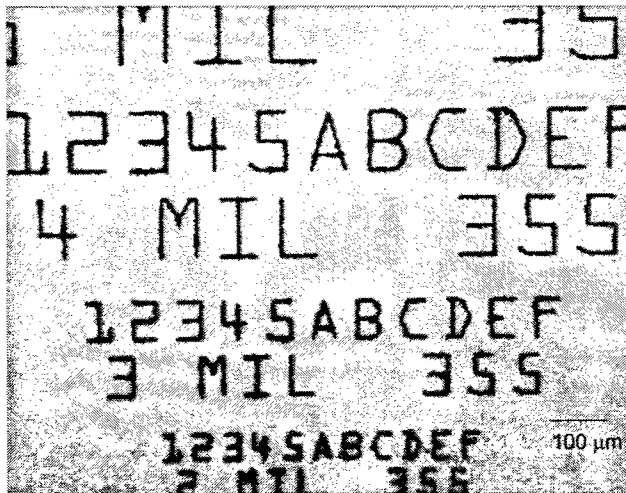
Fig.18 Precision marking of a hard disk slider using a 1W Q-switched 355nm Nd:Vanadate laser at 35kHz repetition rate and 6ns pulse duration (courtesy of Control Micro Systems).
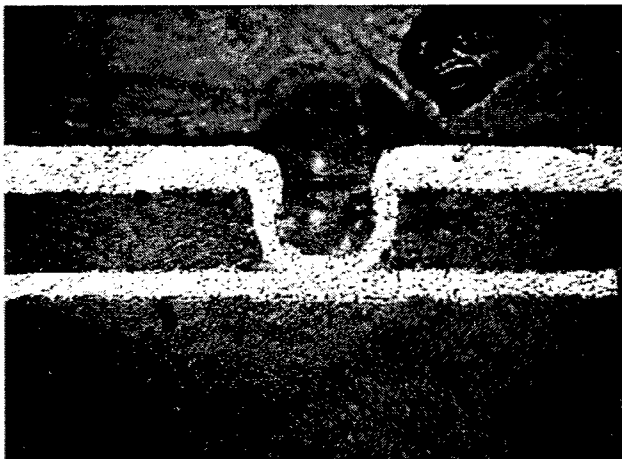
Fig.19 Trepanning drilling of blind via in multi-layer PSB using a 4W Q-switched 335nm Nd:Vanadate laser at 20kHz repetition rate and 35ns pulse duration. The via hole was drilled through a 18μm thick copper layer and 60μm thick dielectric. The hole was copper plated after drilling (courtesy of Exitech, UK).
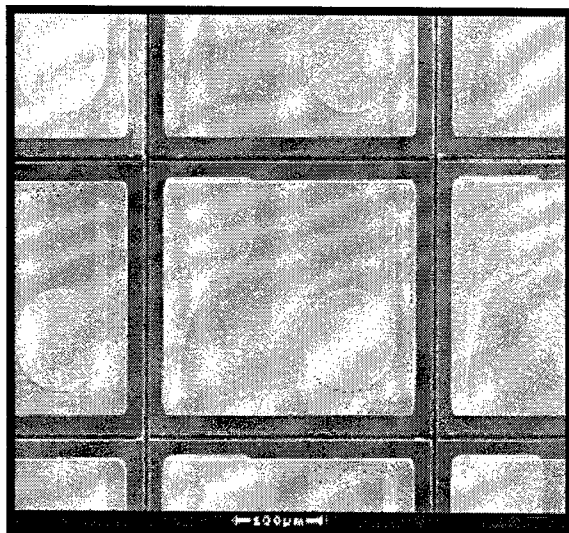
Fig.20 Dicing of sapphire wafer using a 2W Q-switched 266nm Nd:Vanadate laser at 50kHz repetition rate and 10ns pulse duration [7]. Cut width is 5μm, cutting speed: 30mm/s (courtesy of JPSA).

400 um
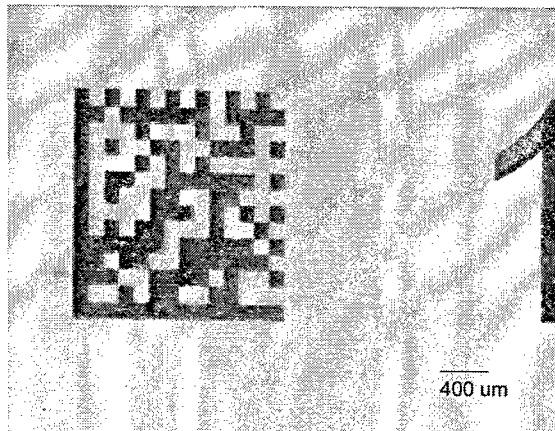
Fig.21 Marking inside flat panel display glass using a 4W 355nm Q-switched Nd: Vanadate laser at 20 kHz and 35 ns pulse duration.

Fig.22 Stereolithography using a 1W Q-switched 355nm Nd:Vanadate laser at 35kHz and 6 ns pulse duration. The prototypes are grown by curing layers of resin, 100 microns at a time.
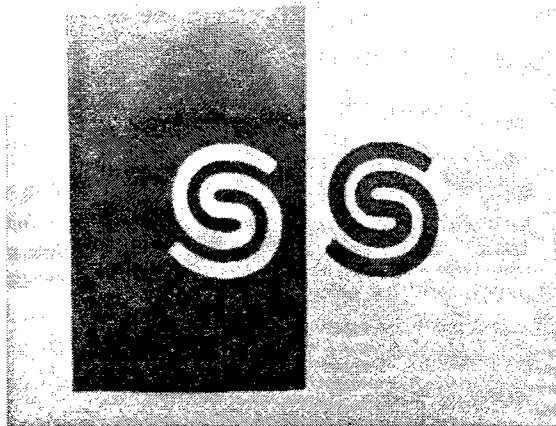
Fig.23 Cutting of a 50 micron thick polyimide film using a 4W mode-locked 355nm Nd:Vanadate laser with 80MHz repetition rate and 10ps pulse duration. The cutting speed is 600mm/s.

200 um

200 um
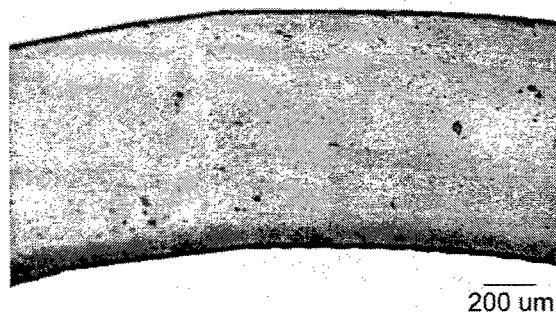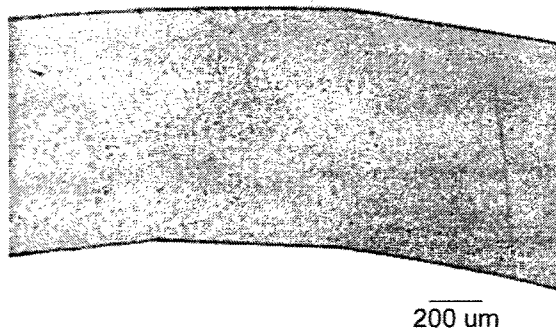
Fig. 24 Detail of the cut shown in Fig.18 (left). The right photograph shows the cutting results for the same material using a 4W Q-switched 355nm Nd:Vanadate laser at 20kHz, 35ns pulse duration and a cutting speed of 80mm/s.
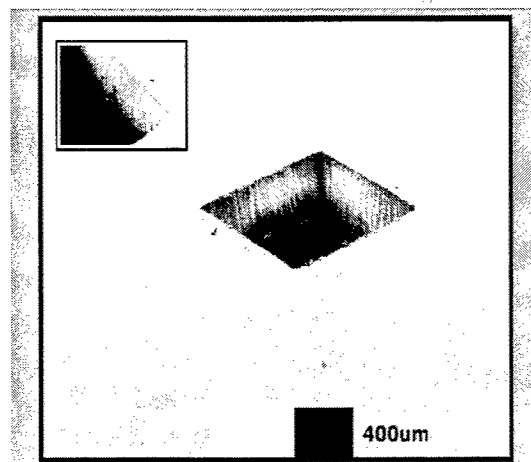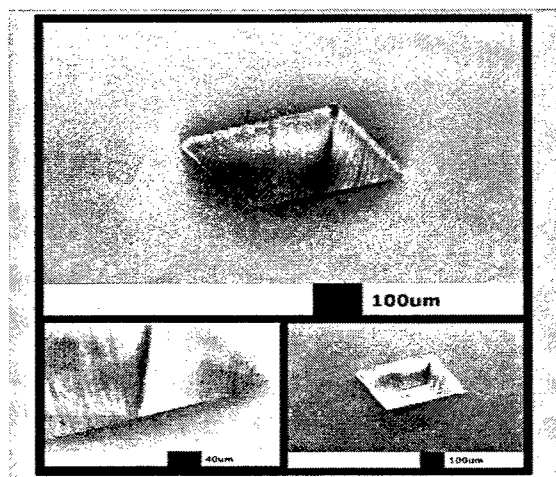
Fig. 25 Machining of fused silica (left) and stainless steel (right) using a 1W, 1kHz ultrafast laser at 800nm with 100fs pulse duration (Spectra-Physics' Hurricane, courtesy of Exitech, UK).
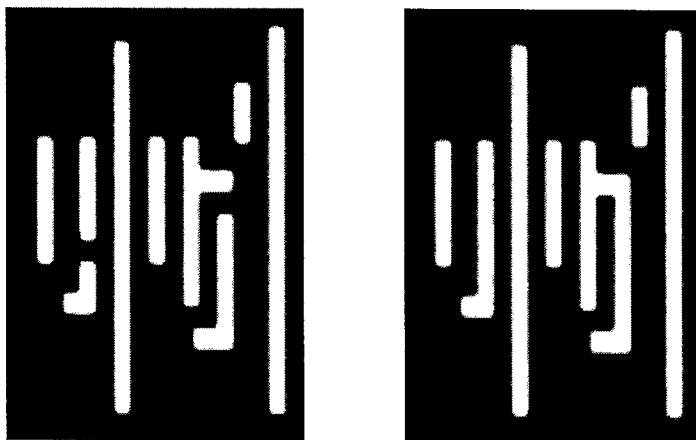
Fig.26 Repair of chromium-on-fused-silica photomasks for deep-ultra-violet photolithography. The absorber material is removed with a doubled ultrafast laser at 400nm. The line width is 0.75 μm [8].
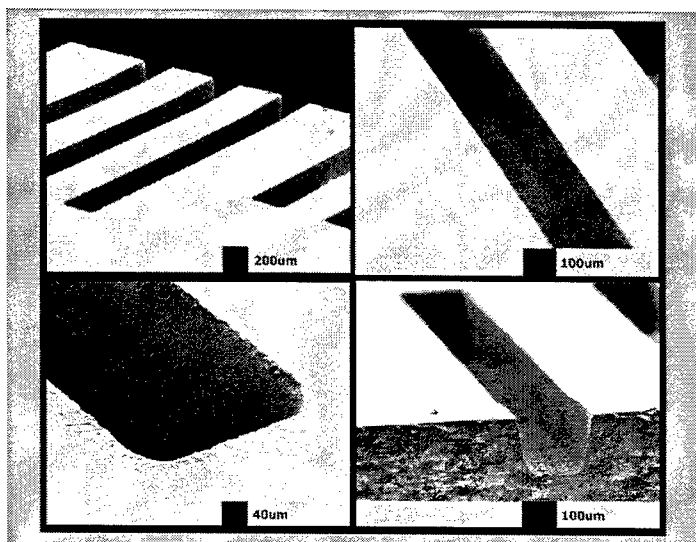
Fig.27 Processing of PMMA using a 1W, 1kHz ultrafast laser at 800nm with 100fs pulse duration (Spectra-Physics' Hurricane, courtesy of Exitech,UK).

5. CONCLUSION

The maturation of diode-pumped solid state lasers has led to a widespread use in material processing while creating new applications due to their low noise, high power performance at high repetition rates. At present, the state of the art in diode-pumped TEM_{00} mode infrared lasers is 40W average output power at 20-100kHz with peak power rms noise of 1% in Q-switched operation. Higher repetition rates of up to 400 kHz are available commercially with an output power of greater 8W. Harmonic generation using LBO or CLBO in extra- or intra-cavity arrangements has increased the output power to 20W at 532nm, 15W at 355nm and 2W at 266nm. Whereas in the last years, the trend of Q-switched lasers has been towards higher output power and higher repetition rates, the current focus lies more on the realization of more cost-effective systems with improved performance, especially shorter pulse durations. The current trend towards shorter Q-switch pulses (<10ns) at high repetition rates (>50kHz) and high output power (>20W) will certainly continue, and can only to a certain extent be satisfied with Vanadate oscillators, This may lead to the industrial use of oscillator/amplifier arrangements, where pulse duration and output power can be optimized separately.

Industrial applications for modelocked Vanadate lasers emitting at 355nm are now emerging in areas dominated by ion lasers. Pulse durations of 10ps and a high repetition rate of 80MHz, similar scanning speeds as compared to cw lasers can be used. Output powers of 20W at 1064nm, 10W at 532nm and 4W at 355nm can be attained using passive modelocking with saturable Bragg reflectors. Penetration of ultrafast lasers into the micromachining market is still limited by the high cost and the complexity of the Ti:sapphire amplifier systems. However, these systems have found industrial applications in processes where sub-micron machining accuracies are required and the heat affected zone (HAZ) generated by Q-switched lasers is too large. In addition to the small HAZ, the high peak power of ultrashort pulses lead to a strongly nonlinear interaction, resulting in strong absorption of materials that are generally transparent for Q-switched pulses.

REFERENCES

1. Optoelectronics Report, vol.10, no.1, January 2003
2. N. Hodgson et al., *High power TEM$_{00}$ mode operation of diode pumped solid state lasers*, Proc. SPIE 3611, 119-131, 1999
3. W.L. Nighan, N. Hodgson, E. Cheng, D. Dudley, *Quantum –limited 35W, TEM$_{00}$ Nd:YVO$_4$ laser*, CLEO 1999, Technical Digest, p.1, OSA 1999
4. N. Hodgson, D. Dudley, L.Gruber, W. Jordan, H. Hoffman, *Diode end-pumped, TEM$_{00}$ Nd:YVO$_4$ laser with output greater than 12W at 355nm*, CLEO 2001, Technical Digest, 389-399, OSA 2001.
5. A. Petersen, S. Utter, C. Ihli, N. Hodgson, *High reliability, high repetition rate 266nm output from a diode-pumped solid-state laser*, CLEO 2002, Technical Digest, 87-88, OSA 2002
6. P. Feru, A. Fry, *Ultrafast technology delivers OEM lasers*, Laser Focus World 5/02, 77-83, 2002
7. J. Park, P. Sercel, *High-speed UV laser scribing boosts blue LED industry*, Compound Semiconductor, Dec. 2002
8. R. Haight, P. Longo, A. Wagner, Laser Focus World 5/2002, p. 79, 2002

High quality laser micro drilling of metals and ceramics with maximum aspect ratio

Alexander Binder*[a], Thomas Metzger[#a], Holger Kern[a], David Ashkenasi[a], Gerhard Müller[a],
Thomas Riesbeck[b], Hans-J. Eichler[b],

[a]Laser- und Medizin-Technologie GmbH, Berlin, Schwarzschildstraße 8, 12489 Berlin, Germany;
[b]Optisches Institut, Technische Universität Berlin, Strasse des 17. Juni 135, 10625 Berlin, Germany;

ABSTRACT

To meet the industry's demand for reducing machine cycle lengths concerning laser-drilling a Nd:YAG Master-Oscillator Power-Amplifier (MOPA)-system was developed at the LMTB-laboratories that emits high-power peak-pulses at excellent beam-quality. Presently, the output power of the oscillator (10W@1064nm) with a beam-quality of $M^2=1.3$ is amplified to 95W@1064nm with $M^2=2.3$ and a single pulse energy up to 500mJ. The pulse duration can be varied between 26 and 230ns. On account of the excellent beam quality, frequency conversion resulted in 49W@532nm and 4.8@266nm. The MOPA-System is used for laser micro drilling experiments into metals and ceramics where the influence of the beam quality on the geometrical shape of the hole is investigated and compared with applications conducted with similar laser systems. Additionally means in optimizing the drilling process such as burr-minimizing and melt-reduction were introduced. Furthermore, experiments using tapered drilling technique are undertaken. A maximum aspect ratio of 1:200 in stainless steel was obtained.

Keywords: laser-material-micro-machining, high-aspect ratio, master-oscillator-power-amplifier, ceramics.

1. INTRODUCTION

During the last decades, systems generating laser pulses proved to be an excellent tool for drilling into various kinds of metals and ceramics with outstanding quality. Compared to conventional drilling methods laser drilling is excelling in respect to difficult to mechanically machine materials and to the limitations in conventional micro machining of many material classes. The laser represents an outstanding working tool when tapered holes are desired, which for traditional drilling would require extra-designed perpendicular faces. At present conventional boring of metals is limited to a minimum diameter of 10 μm, whereas laser drilling reaches beyond the 1 μm margin. Other novel drilling techniques need complicated boundary conditions (electron beam drilling: vacuum) or restrict the variety of material (electro-chemical drilling and electric discharge machining (EDM): electrical conductivity).

Micro processing with solid state lasers is typically conducted in a direct writing alignment. The laser beam is focused down to the μm range to provide optimal spatial energy localization. Diffraction limited processing suggests a very good beam quality, i.e. TEM_{00} mode output. This can be easily provided with Nd:YAG laser systems at moderate average powers of 10 W and above. Basically, the choice of the laser parameters, e.g. wavelength, pulse width, average power and repetition rate, depends not only on the excitation state of the material, which is actually (peak) intensity related. Very importantly, an optimization of the relevant parameters depends also significantly on the desired material reaction. Therefore, the demand for laser systems combining high average laser power with very good beam quality and providing high flexibility in the repetition rate and single pulse energy for specific application as high aspect drilling is gaining constantly.

* corresponding author: a.binder@LMTB.de; phone ++49-30-67053-461; fax ++49-30-67053-500; www.LMTB.de
# present address: Institute for Optics, Gusshausstraße 27/387, 1040 Wien, Austria

As an example using a ms-500 W flashlamp pumped Nd:YAG laser at a repetition rate of 100 Hz 5 mm-deep drillings into steel with an average diameter of 400μm are obtained resulting in an aspect ratio of just 1:12. Due to the beam quality of M² = 75 the quality of the bore hole is poor. Investigations on ms-flashlamp pumped systems with enhanced beam quality resulted in aspect ratios up to 1:65 and 1:120 with slab-lasers [1]. It was found that with these systems the beam quality decreased with a repetition rate higher than 10 Hz. The following chapter introduces our ms-pumped MOPA-system which provides a constant and excellent beam quality at a pump frequency of 100 Hz. Applying additional q-switch with bursts varying between single and 40 burst pulses (resulting in average repetition rates from 100 Hz to 4 kHz) ns-pulses make drillings with aspect ratios up to 1:200 possible.

2. MASTER-OSCILLATOR POWER-AMPLIFIER-SYSTEM

To meet the industry's demand for reducing machine cycle times, a high power laser system with excellent beam quality was originally developed at the LMTB GmbH, Berlin [2] and [3]. In co-operation with the Institute for Optics at the Technical University of Berlin (TU Berlin), the Nd:YAG master oscillator power amplifier (MOPA) design is being permanently improved aiming at shorter pulse duration, higher average power and improved long-term stability [4] and [5]. The MOPA-layout is sketched in Fig. 1.
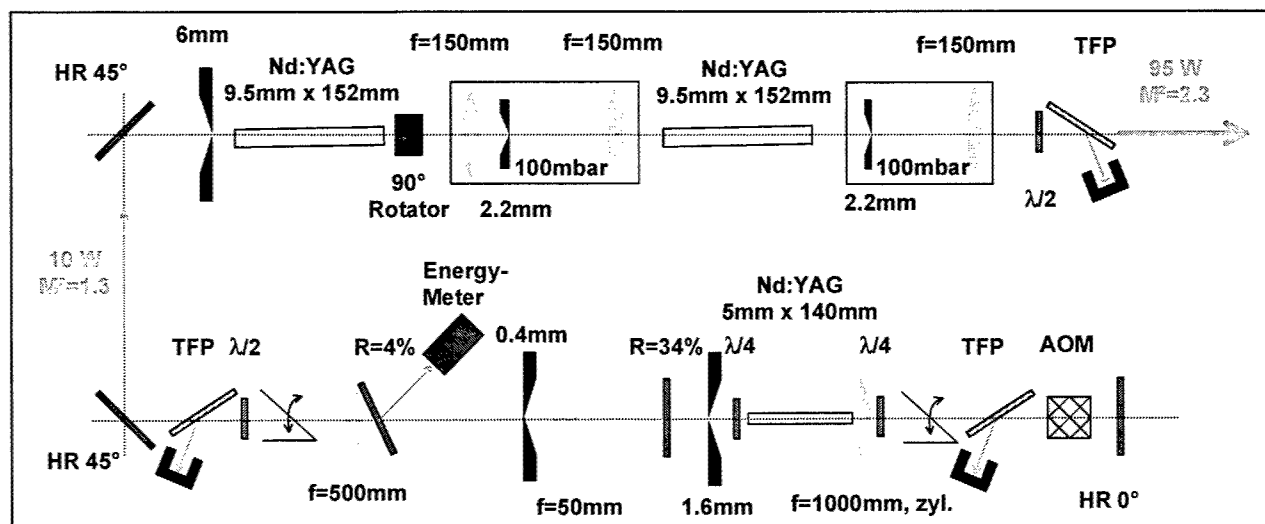
Fig. 1: Schematic diagram of the optical assembly of the MOPA laser system.

2.1 Oscillator

The oscillator set-up consists of a flash-lamp pumped Nd:YAG resonator which is q-switched by an AOM. The pulse duration can be varied between 31 and 230 ns. The repetition rate is variable between 100 Hz and 5 kHz. In multimode configuration the oscillator emits an average power of 60 W. With an internal aperture of 1.6 mm the beam quality results in M² = 1.35 at averagely 10 W. The Nd:YAG crystal is located between two λ/4-plates (passed by circularly polarized laser beam) also to avoid spatial hole-burning. An additional cylindrical lens is positioned next to the crystal for mode volume enhancement, aiming at higher output power while saving the sound beam quality. An internal thin-film polarizer defines the linear output polarization. In order to minimize the divergence of the output beam it passes a 1:10 telescope (type Kepler) with an 0.4 mm aperture in the focus. External power scaling is accomplished using a combination of revolving λ/2-plate and external thin-film polarizer.

2.2 Amplifier

The amplifier consists of two flash-lamp pumped cavities which are slightly tilted off the optical axis to prevent autonomous laser activity. In the single-pass set-up, birefringence compensation in the amplifier is necessary, which is obtained by mounting a quartz-rotator between the cavities. The repetition rate can be set between 100 Hz and 5 kHz with pulse duration between 31 and 230 ns. The original oscillator TEM_{00} laser beam is amplified to 95 W @ 1064 nm with $M^2 = 2.3$ and a pulse energy up to 500mJ @ 100 Hz. On account of the excellent beam quality frequency conversion results in 49 W @ 532 nm and 4.8 W @ 266 nm, respectively.

2.3 Signal-sequence

The sequence cascade of the signals is built up by two frequency generators. The first sets the pulse-frequency for the triggering of the power supply for the flash-lamps of the amplifier (start signal). After a certain time (delay I) the power supply for the oscillator flash-lamps is triggered. After another time lag (delay II), the second frequency generator opens within a period of 1 ms the AOM, which is modulated at a variable burst-frequency. The number of burst pulses results of the burst frequency and the duration of the pump pulse. For example the 100 Hz frequency of the flash-lamps and a number of 40 burst pulses result in an average repetition-rate of 4 kHz. The signal sequence is illustrated in Fig. 2.
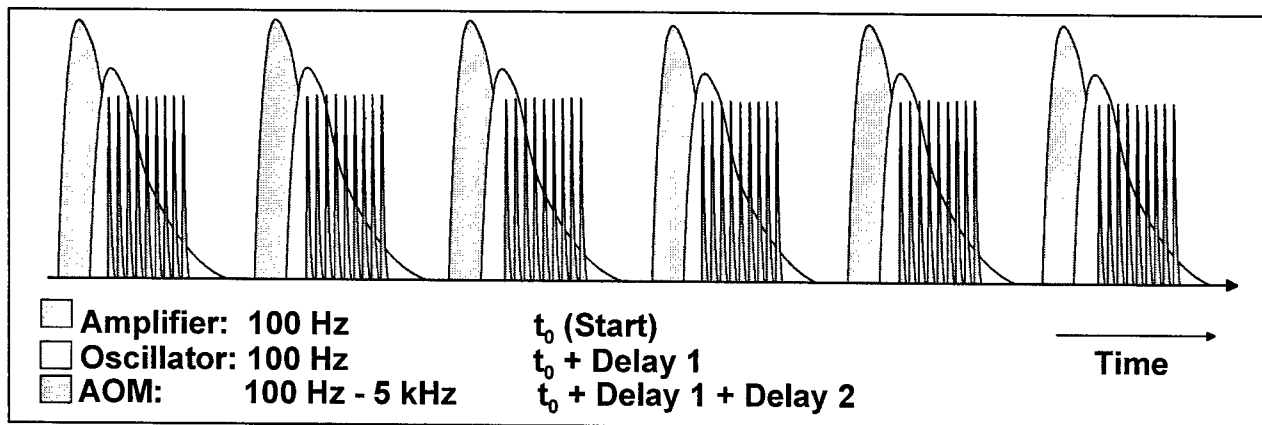
Fig. 2: Signal sequence of the oscillator-amplifier arrangement.

3. EXPERIMENT

3.1 Master Oscillator Arrangement

In oscillator arrangement without amplification the average power of ca. 10 W is sufficient for micro structuring in a depth of several 100 μm. For example, more than 1000 drillings within 1 mm^2 in stainless steel of 100 μm thickness, see Fig. 3 A), were obtained. Another application is shown in Fig. 3 B): For further mask projection with an excimer-laser the LMTB-logo was cut into tungsten with a letter high of just 130μm. These few examples illustrate the very good beam quality of the master oscillator system which is a big premise for an efficient power amplification, necessary to laser machine in greater depths and/or higher processing speeds.
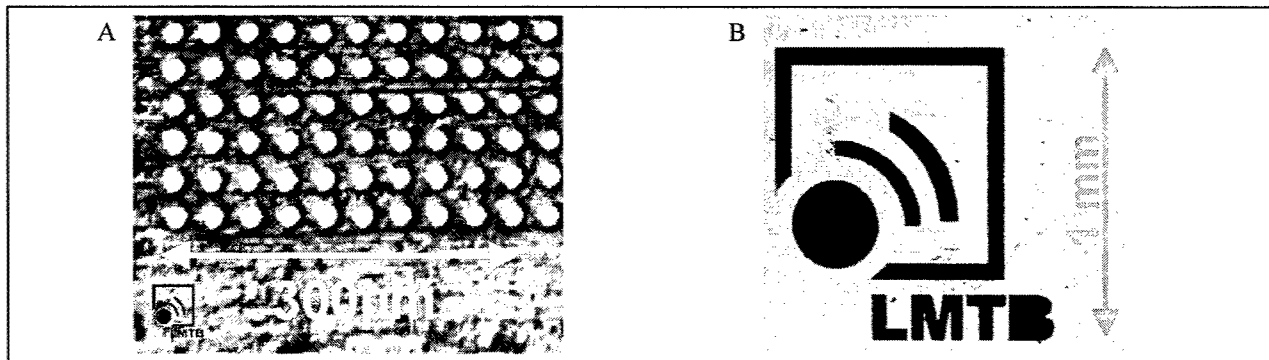
Fig. 3: Examples of micro structuring in oscillator-mode (TEM_{00}) without amplification. A): stainless-steel micro-sieve with a number of 1032 20 µm-drillings on a square millimeter. B): LMTB-logo cut in tungsten.

3.2 Power Amplifier Arrangement

The MOPA system was used for high aspect laser micro drilling studies into metals and ceramics. Ablation rates in dependence of energy density and ambient pressure were determined. In comparison with similar q-switch Nd:YAG-systems the influence of beam quality on the geometrical shape of the hole was investigated. Additionally, means for optimizing the drilling process such as burr-minimizing and melt-reduction were investigated. Furthermore, taper drilling experiments were made.

Drilling into metals

A maximum aspect ratio of 1:200 was obtained in stainless steel gaining 20 mm depth at an average bore-hole diameter of 100 µm, see a cross-section in Fig. **4** A. With a repetition rate of 100 Hz and a pulse energy of 0.5 J an average ablation rate of 300 nm per pulse was observed. Laser micro drilling of metals in that range could replace EDM for generating wire-forging nozzles. Fig. **4** B illustrates an example of a bore-hole in copper resulting from processing in ambient pressure. Bore-holes in copper are needed e.g. for cooling sockets of high-power laser diodes. A 2-mm-sheet of Ni-based alloy was drilled into at an angle of attack of 45°, cross-section is shown in Fig. **4** C. Drilling time in ambient pressure is 20 s. Potential applications here are located in the domain of energy engineering concerning cooling nozzles in turbine blades.

Reduced ambient pressure

Investigations on drilling into metals were undertaken both at 1000 mbar and in low-pressure (< 100 mbar). Fig. 5 shows the achieved drilling-speeds under different air pressure. Laser drilling after approx. 10 s significant higher ablation rates under low-pressure conditions are observed. In the case of copper the drilling speed at 1000 mbar is about 60-75 % of the drilling-speed at 100 mbar regarding the drilling time 75-240 s. Even more drastic is the difference during the first 15 s and 35 s drilling time, where at low pressure the ablation rate expanded by a factor of 2. A maximum drilling depth of 6.6 mm at 1000 mbar and 8.6 mm at 100 mbar respectively was reached after 4 minutes. Consistent laser micro drilling of steel at low-pressure until the ablation rate falls to zero leads to micro holes at a depth of 20 mm compared to 9.5 mm @ 1000 mbar.
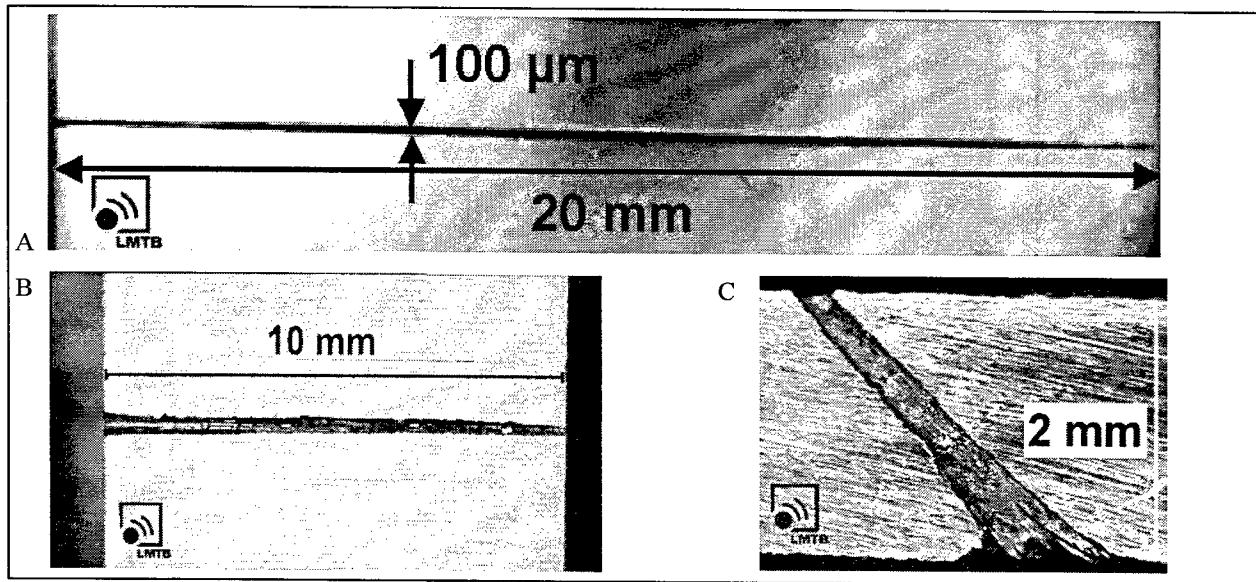
Fig. 4: A): Drilling into stainless steel at 1000 mbar with an aspect ratio of 1:200. Laser parameters: repetition-rate: f_{REP} = 100 Hz; average power: P_{LAVG} = 80 W; focus-radius: ω_F = 90 μm; fluence: E/A = 8 kJ/cm²; drilling time t = 600 s. B): Drilling into copper with an aspect ratio of 1:50. Laser parameters: repetition rate f_{REP} = 3,5 kHz; average power: P_{LAVG} = 70 W; focus radius: ω_F = 72 μm; fluence: E/A = 125 J/cm²; drilling time t = 1200 s. C): Tapered drilling into Ni-based alloy. Laser parameters: repetition rate: f_{REP} = 3,5 kHz; average power: P_{LAVG} = 70 W; focus radius: ω_F = 72 μm; fluence: E/A = 85 J/cm²; drilling time t = 20 s.
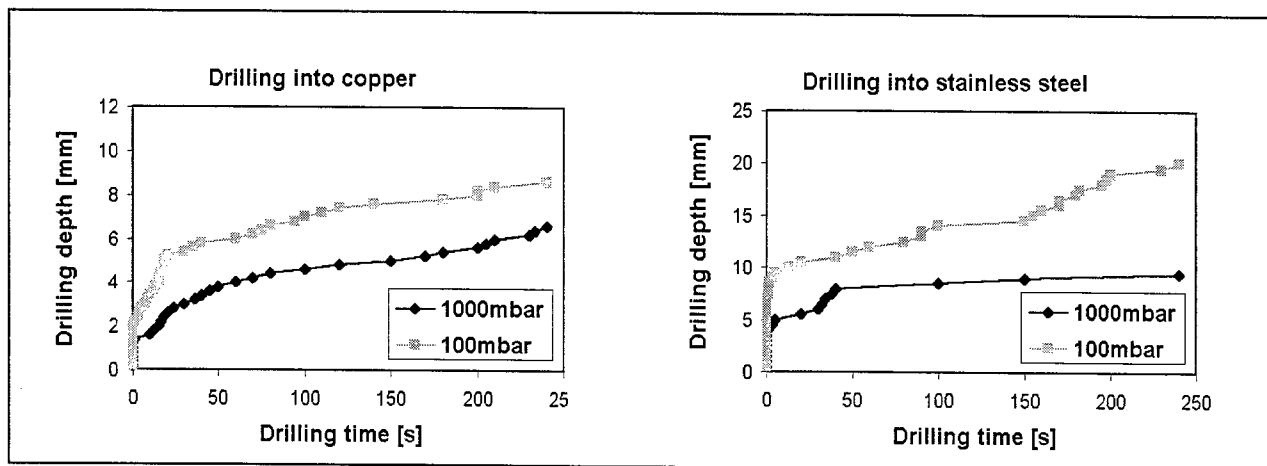
Fig. 5: Depth of ca. micro hole (diameter ca 100 μm) over the laser drilling time at different ambient pressures in copper and stainless steel. Laser parameters: repetition rate: f_{REP} = 3,5 kHz; average power: P_{LAVG} = 70 W; focused laser beam radius: ω_F = 72 μm; fluence: E/A = 125 J/cm².

Drilling into ceramics

The MOPA-system proved to be highly efficient for drilling micro holes into ceramic materials, which are difficult to machine using conventional methods. Fig. 6 illustrates the bore-holes into aluminum-oxide and aluminum-nitride in at different energy densities using the MOPA laser system. Note that to improve the visualization of the extremely lean geometry the horizontal axis in Fig. 6 was expanded so that the diameter of the hole scales in μm whereas the depths are indicated in mm. For Al_2O_3 a maximum drilling depth of 18.5 mm at an aspect ratio of 1:140 was obtained. The average diameter of the bore-hole is about 130 μm with a considerable shell crater of more than 250 μm at the entrance. For AlN the acquired bore-hole is more constant in diameter, the maximum drilling depth reaches 15.8 mm at an aspect ratio of 1:175.
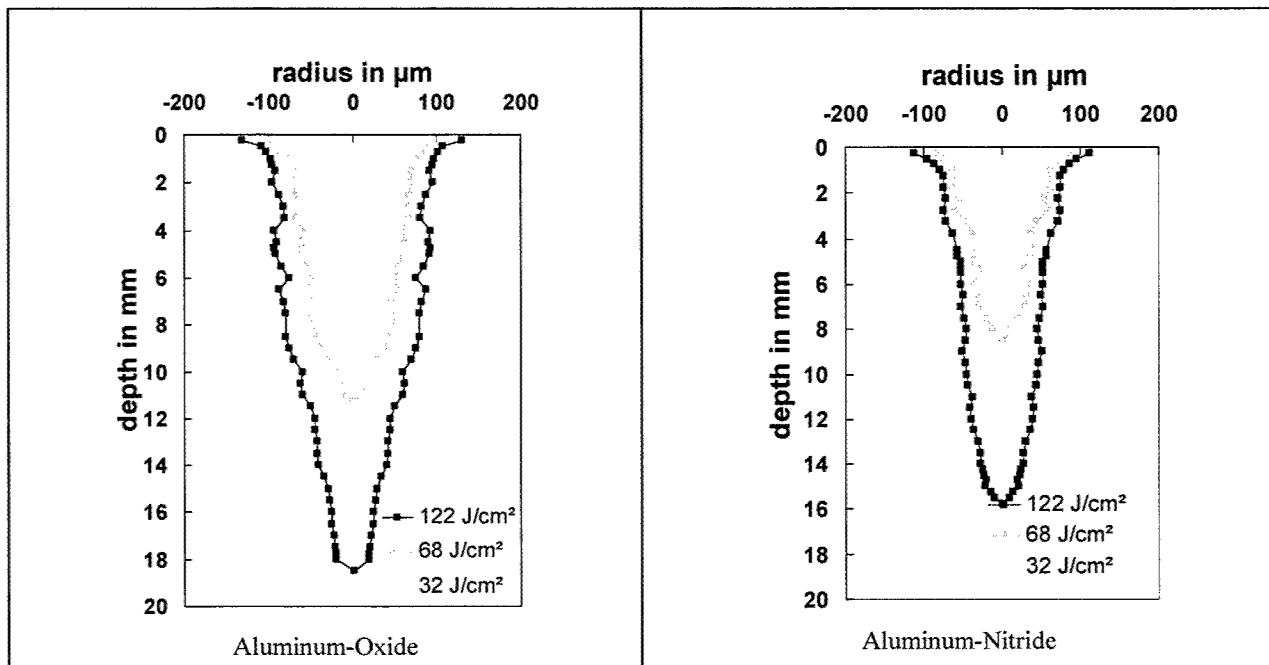
Fig. 6: Distorted progression ([μm] versus [mm]) of the bore-holes resulting from laser micro drilling into Al_2O_3 and AlN at different fluence using the MOPA system. Laser parameters: repetition rate: f_{REP} = 4 kHz; pulse duration: τ = 127 ns; average power: P_{LAVG} = 80 W; focus-radius: ω_F = 72 μm; focal length lens: f = 250 mm; drilling time t = 210 s.

Fig. 7 shows several top views of 250μm thick AlN-disks taken out of a stack the drilling process. On the right hand side of **Fig. 7** the corresponding bore hole geometry is illustrated (note: distorted scale with μm versus mm!). After a crate-like geometry during the first millimeter the geometry becomes nearly parallel with an inclination of about 0.2° from 2 mm to 14 mm. From 14 mm depth on till the bottom of the drilling the diameter decreases faster. The pictures of the upper region of the drilling show a fairly circular shape. Dark spots surround the hole, the darkened area increases with depth. In deeper regions of the drilling considerable fraying can be observed. In some investigated specimen even a fillamentation of the bore channel into smaller holes was found. This phenomenon was noticed in all drilling studies where the process saturated at maximum depth. With increasing pulse energy the maximum depth due to saturation (i.e. ablation rate $\rightarrow$ 0) increases.
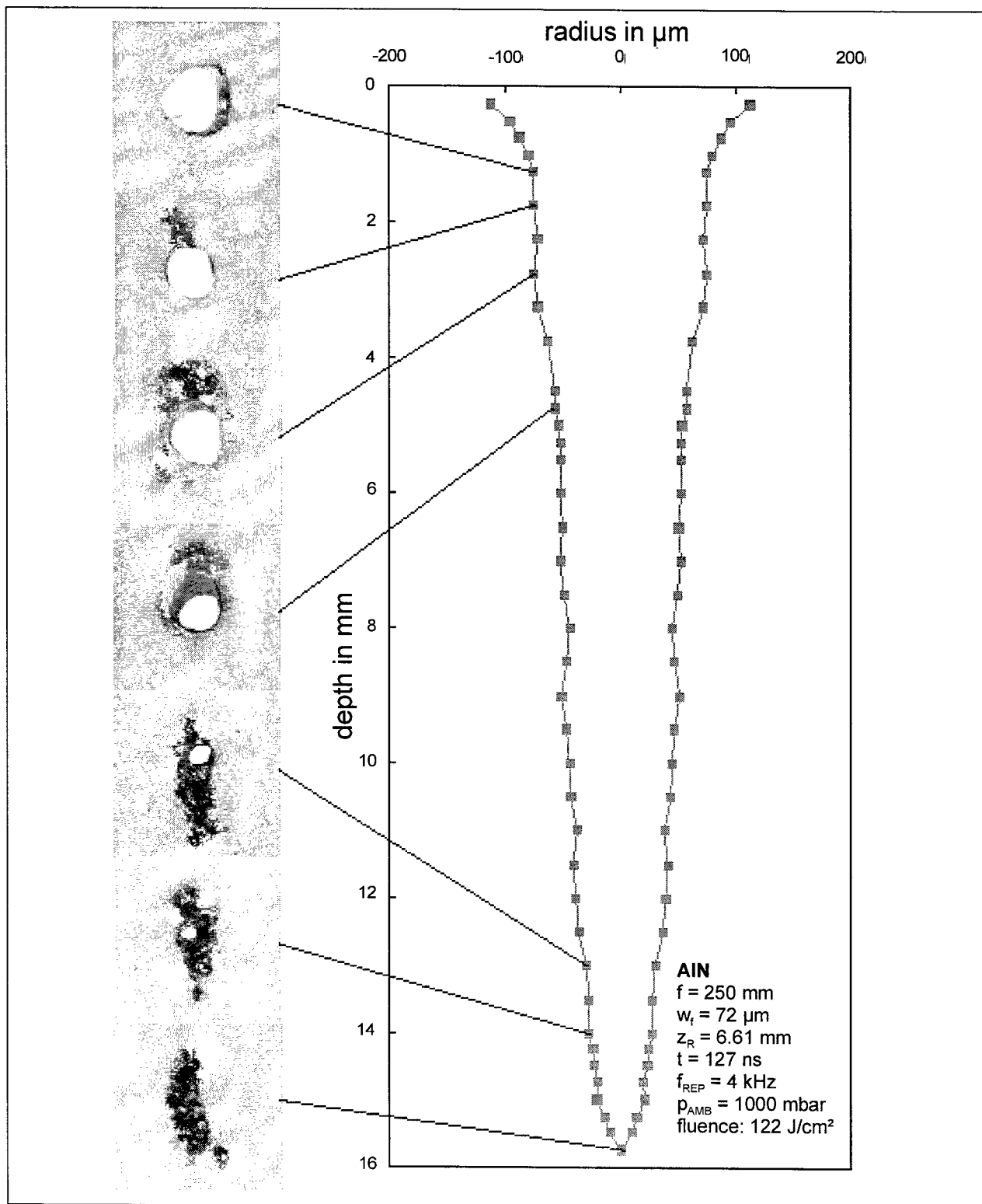
Fig. 7: Top views of some example specimen taken from stacked AlN-disks and the corresponding bore hole geometry.

Influence of beam quality

To determine the influence of laser beam quality in high aspect laser micro drilling, comparative drilling studies into AlN and Al_2O_3 using a non-commercial 100 W double-rod Nd:YAG laser system (LMTB) [6] and [7]in multimode configuration were conducted. The MOPA-system achieves significant deeper and leaner holes at identical laser parameters, except for the difference in beam quality, which lies one order of magnitude apart (MOPA: $M^2 = 2.3$; double-rod: $M^2 = 20.5$). The focal diameter ($2 \, \omega_F = 145 \, \mu m$) and the repetition rate ($f_{REP} = 1.5$ kHz) was identical in both cases. The pulse duration, $\tau_{MOPA} = 127$ ns compared to $\tau_{2\text{-}ROD} = 119$ ns, is considered to be too similar to have a strong effect in the different micro drilling results. Fig. 8 - Fig. 10 show the dependence of the bore-hole geometry on the beam quality of the laser. Drilling diameters twice the size using the MOPA laser system are obtained at lower beam quality when energy densities approach 50 J/cm² (Fig. 9). The MOPA-system reaches drilling-depths which exceed those obtained with the 2-rod laser (Fig. 8). With the 2-rod the achievable aspect-ratio lies about 1:20, whereas the MOPA-system obtains at least 1:70 till 1:150 (Fig. 10).
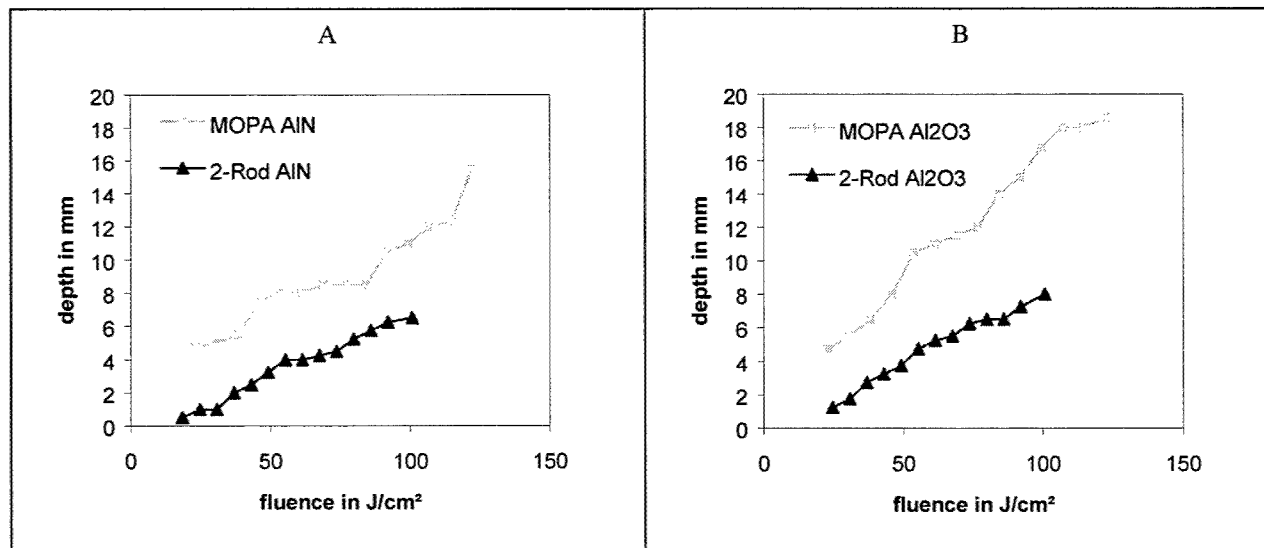
Fig. 8: Comparison of the MOPA laser system ($M^2 = 2.3$) with a Nd:YAG 2-rod laser system ($M^2 = 20.5$): Drilling depth with respect to different fluence for drilling into A) AlN and B) Al_2O_3.
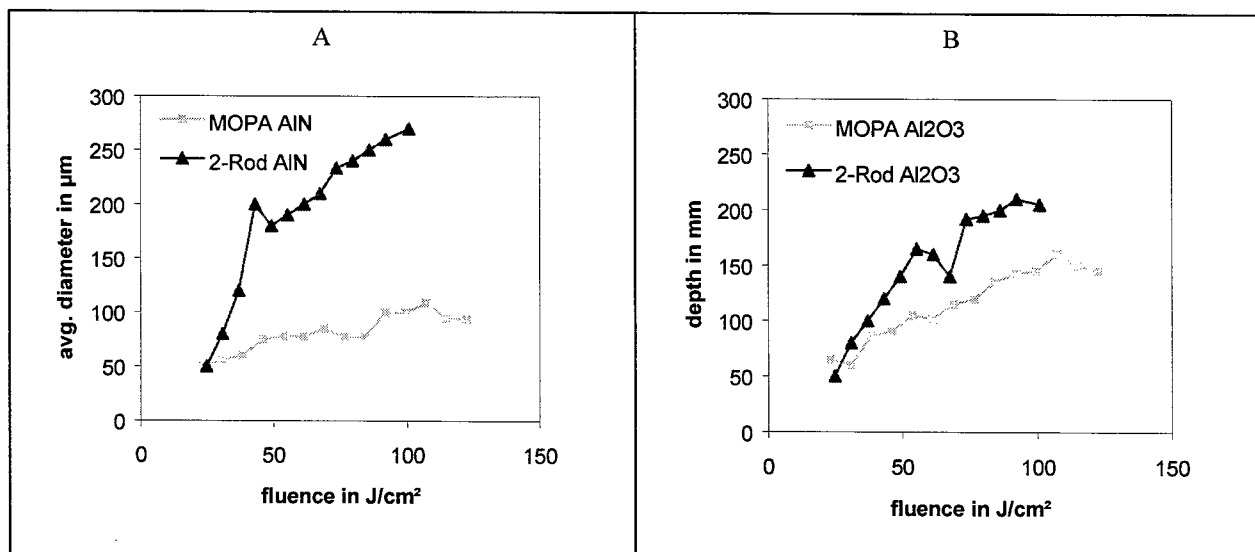
Fig. 9: Comparison of the MOPA-system ($M^2 = 2.3$) with a Nd:YAG 2-rod-system ($M^2 = 20.5$): Average diameter with respect to different fluence for drilling into A) AlN and B) Al_2O_3.
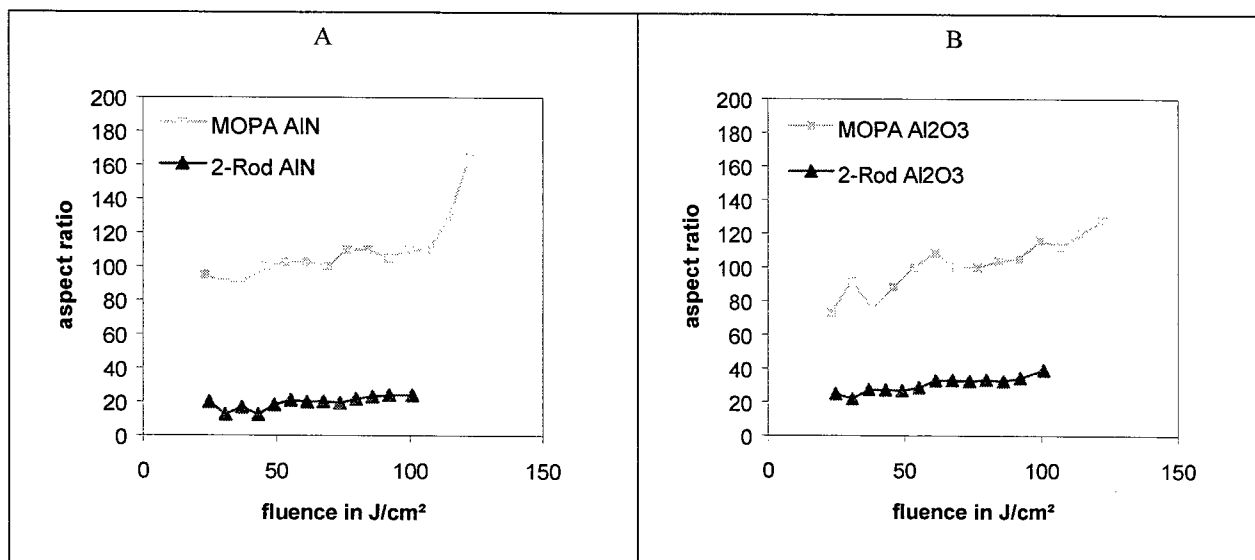
Fig. 10: Comparison of the MOPA-system ($M^2 = 2.3$) with a Nd:YAG 2-rod-system ($M^2 = 20.5$): Aspect ratio with respect to different fluence for drilling into A) AlN and B) Al_2O_3.

4. OUTLOOK: FIBER PHASE CONJUGATE MIRRORS

Further improvement on extraction efficiency and beam quality is achieved using silica fibers as phase conjugate mirrors (PCM) [8]. Fig. 11 illustrates schematically the MOPA laser system set-up with a fiber-PCM replacing a high reflecting mirror in the amplifier chain. After double pass amplification in the power amplifier the average power is increased to 125 W with a beam quality of $M^2 = 2.2$, compared to 85 W at $M^2 = 2.3$ in a the single pass configuration. Due to the stimulated Brilluoin scattering (SBS) mechanism, phase distortions -originating in the pumped laser rods and

forthcoming optics- are in theory completely compensated after double passing the amplifier. In practice, the oscillator beam quality is slightly deteriorated during double pass amplification, however the improvement compared to the case single pass amplification is notable.
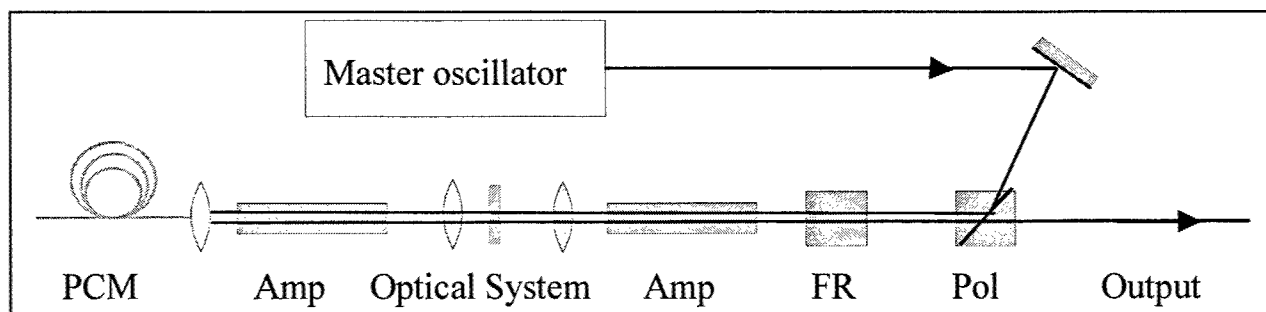
Fig. 11: Schematic set-up of double pass amplifier chain with phase conjugate mirror (PCM), two amplifier rods (Amp), faraday rotator (FR) and polarizor cube (Pol).

Presently, studies on laser material micro machining (LM^3) using the improved MOPA configuration are conducted in the LMTB application laboratory at the Technical University Berlin. First preliminary results on laser micro drilling using laser systems with PCM technique in the power amplifier set-up are very promising. As further perspective, additional effort is being placed on a "turn-key table" laser design of a 100 W MOPA system with outstanding beam quality for innovative LM^3.

5. SUMMARY

Due to excellent beam quality in "just"-oscillator arrangement a precise tool for micro-structuring is available. In amplifier arrangement the high-power MOPA-system proved the potential of drilling at an aspect ratio up to 1:200. Ablation rates and the quality of the drillings can be enhanced when "soft"-vacuum about 100 mbar is applied. The influence of beam quality on the obtainable aspect ratio was demonstrated for AlN and Al$_2$O$_3$ in comparison of the MOPA-system ($M^2 = 2.3$) with a Nd:YAG double rod laser system ($M^2 = 20.5$). Applying fiber phase conjugate mirrors results in enhanced extraction efficiency and beam quality avoiding the use of mostly toxic SBS-cells.

6. ACKNOWLEDGEMENTS

REFERENCES

1. HOLTZ, R.; JOKIEL, M.: "Optimized laser applications with lamp-pumped pulsed Nd:YAG lasers". *ICALEO 2002*, Laser Institute of America, 2002 (in print).

2. SEIDEL, S.; KUGLER, N.: "Nd:YAG 200 W average-power oscillator-amplifier system with stimulated Brillouin-scattering phase-conjugation and depolarization compensation". *J. Opt. Soc: Am.* **14**, no.7, 1997

3. SEIDEL, S. SCHIRMACHER, A.; MANN, G.; NURSIANI; RIESBECK, T.: "Optimized resonators for high-average power high-brightness Nd:YAG lasers with birefringe compensation". *SPIE 3267*, 1998.

4. BINDER, A.; METZGER, T.; ASHKENASI, D.; MÜLLER, G.; RIESBECK, T.; RISSE, E.; EICHLER, H.-J.: "Nd:YAG nd Nd:YAP Solid-State Laser Systems with High Beam Quality and High Average Output Power by Fiber Phase Conjugate Mirrors". *ICALEO 2002*, Laser Institute of America, 2002 (in print).

5. BINDER, A.; METZGER, T.; ASHKENASI, D.; MÜLLER, G.; RIESBECK, T.; EICHLER, H.-J.: "High Aspect-Ratio Laser-Drilling of Micro-Holes with a Nd:YAG Master-Oscillator Power-Amplifier (MOPA) System". *ICALEO 2002*, Laser Institute of America, 2002 (in print).

6. KUGLER, N.; DONG, S.; LÜ, Q.; WEBER, H.: "Investigation of misalignment sensitivity of a birefringence-compensated two-rod Nd:YAG laser system", *Appl. Opt. 36*, pp. 9359-9366, 1997.

7. ASHKENASI, D.; BINDER, A.; JABER, H.; KERN, H.; METZGER, T. MÜLLER, G.; MÜLLER, N.; ZIEGERT, A.: "Laser processing of ceramic and crystalline wafer substrates for microelectronic applications", *SPIE 4977* (in print) 2003.

8. RIESBECK, T.; RISSE, E.; EICHLER, H.J.: "Pulsed solid-state lasersystem with fiber phase conjugation and 315W average output power", *Applied Physics B* (Laser and Optics) **73**, pp. 847-849, 2001

Laser based manufacturing of high-accuracy electrodes in brittle materials

C. Kulik, A. Ostendorf, F. Meyer

Laser Zentrum Hannover e.V. (LZH), Hollerithallee 8, 30419 Hannover, Germany

ABSTRACT

Dielectric sensors with smallest electrode structures are used to monitor several technical applications. Thus, durable substrate materials are essential for the exploitation of the sensors in hostile process environment. Here, ceramics and different glasses show ideal material properties, but are difficult-to-machine in the micrometer range. UV-laser beam sources are well suited for an economic manufacturing of micro-structures in these brittle materials. Especially, advanced laser tools like excimer- and frequency converted solid-state lasers show excellent machining results.

This paper presents the development of new laser based production techniques and innovative process chains for the fabrication of distinctive electrode structures in high stable materials. Two different machining concepts are shown. A conductive Indium Tin-Oxide (ITO) layer with a thickness of about 600nm has been structured with a KrF excimer laser ($\lambda = 248$ nm, H = 5 J/cm²), without damaging the underlying borosilicate glass substrate. The dimension of the electrodes and insulation channels of the sensor are as small as 50µm. For the second approach of manufacturing a dielectric sensor, aluminum oxide as a bulk substrate materials has been machined with the same laser type. No thermal damage was observed by an operating fluence H = 20 J/cm². The obtained extreme durable embedded-electrode-type sensor can be completed by filling the cavity with conductive material by standard electroplating techniques. For the manufacturing process, a high flexible NC-controlled machining concept is presented, which allows a time and pulse minimized fabrication as well as an optimization of the surface quality of the micro-sensor, including a process optimization via simulation.

Keywords: laser based micro-machining, brittle materials, sensor manufacturing, UV-laser, electrodes

1. INTRODUCTION

In modern production lines, a standardized and reproducible fabrication quality is more and more sufficient to meet the aim of minimum failure production. Therefore, different types of sensors are employed to monitor the manufacturing process and provide a constant product quality. Dielectric sensors, like interdigital capacitors, are widely used for monitoring the change of dielectric fields depending on varying material properties. **Fig. 1** shows the principle geometry of an interdigital capacitor. The sensor consists of two electrically insulated parts, which electrodes form a grid. Supplying an alternating voltage at the contact pads, an electromagnetic field interacts between the electrodes as seen in **Fig. 2**. The amplitude of the electromagnetic signal corresponds with a variation of the dielectric constant ε_1 of the surrounding material, in which ε may change it's value due to geometrical or chemical variations. This type of sensor is commonly used for monitoring the properties of fluids or gases [1], but also for monitoring e.g. the state of cure of thermosetting composites. The multiple number of applications for this sensor consist, among others, of detecting gas composition, oil level control or analyzing the viscosity of fluids. Some applications present a hostile environment. Therefore, the sensor has to be resistant against aggressive impacts as e.g. high temperature and pressure or corroding fluids. To provide a durable and reliable monitoring system for this range of applications, extremely resistant substrate materials have to be used.

For such dielectric sensors made from brittle materials like glass or ceramics, special manufacturing techniques are required. Laser micro-machining with wavelength in the UV range has been proved to be an accurate and efficient tool for structuring this difficult-to-machine materials [2, 3, 4, 5].The combination of UV-wavelength, which is strongly absorbed by brittle material, and ns-pulse duration allows a high machining resolution and pulse peak power of several megawatts along with an extremely small heat effective zone. These outstanding characteristics enable a highly precise structuring of bulk brittle materials in the micrometer range without thermal induced damage like cracks.
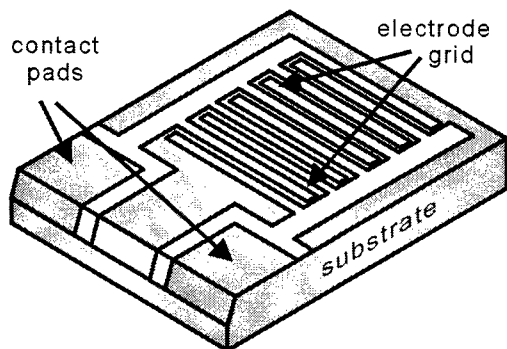
Fig. 1: Principle sketch of a dielectric sensor (interdigital capacitor).
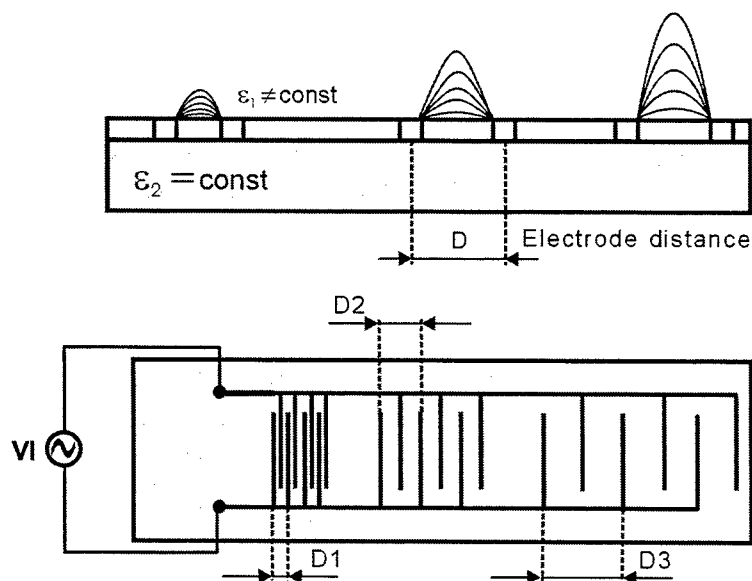
Fig. 2: Example for the influence of the electrode distance on the penetration depth of the electric field.

2. ELECTRODE BASED SENSORS

Sensors based on the detection of variations in electrical fields are capable monitoring material properties of certain substances, since the field strength E corresponds directly to the dielectric constant ε of the substances itself (ε_1 in **Fig. 2**). The variation of ε is directly linked to the material state of the substance surrounding the sensor. Due to this fact, the measurement of ε allows a detection of the variation in the surrounding material (oil level detection, content of gases) or the modification of material properties (viscosity of fluids, cure of liquid polymers), since the value of ε is directly effected by this matters.

The penetration depth of the sensor relates, in addition to the dependency on the dielectric constant ε, on the leakage field which depends of the distance D of the sensing electrodes as demonstrated in **Fig. 2**. It can be observed that by increasing distance D between the electrodes, the penetration depth of the field rises as well. Using multiple electrode width for the monitoring process, the material state in different distance from the sensor surface can be analyzed. This is essential for guarding inhomogeneous processes like the cure of viscous fluids, where the state of cure is in general dependent on the distance to the outer boundary layer of the fluid. This type of interdigital capacitor has a high potential for monitoring complex cure cycles of composite materials, as used in injection molding or pultrusion. For achieving an appropriate capacitance, the electrode width and distance has to be in the range of some 10μm. For reproducibility reasons, the electrode edge has to be smooth and straight, which becomes exponentially more difficult with smaller dimensions. An advanced micro-manufacturing process is therefore essential.

During the monitoring process, the sensor is provided with an alternating voltage of a defined amplitude. The characteristic spectrum outlined in **Fig. 3** can be received by measuring the imaginary impedance at different frequency ranges with an impedance analyzer. Each slope represents an impedance spectrum at a certain time and therefore specified state of cure. The upward shift of the different spectra with increasing cure time ends at a static value, when the conversion has finished (complete cure of polymer).

When monitoring conversion cycles of composite materials, high peak temperatures up to several hundred degrees may appear. This temperature causes major damage to most of the available dielectric sensors, which consist of metal electrodes (e.g. gold, copper) based on a polymer substrate (e.g. PI). These sensors have to be disposed after use in the cure cycle and are not appropriate for monitoring the process at all.
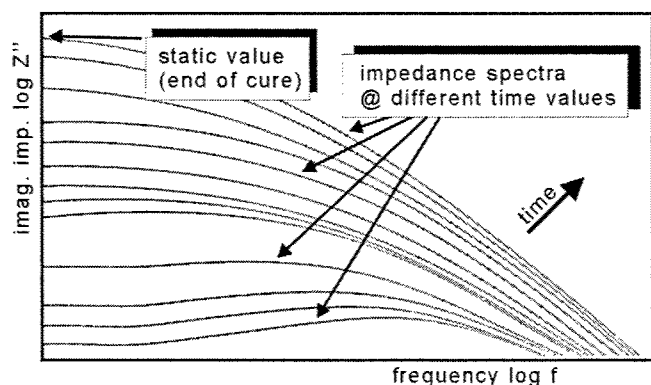
Fig. 3: Sketch of the evolution of the imaginary impedance spectrum measurement during isothermal cure of a composite material.
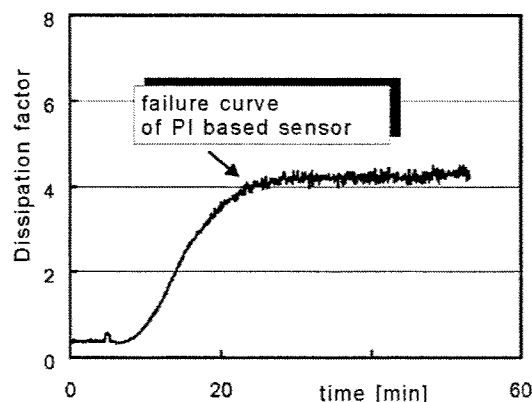
Fig. 4: Variation of the dissipation factor of an interdigital capacitor on polymer substrate at holding temperature 220°C [6]. (Courtesy Gyeongsang National University, South Korea)

The service temperature of sensors with a polymer substrate is limited to the glass transition temperature of the substrate, since the material properties may vary at this temperature [6]. The variation of the dissipation factor for a polymer based interdigital capacitor at high temperature is shown in **Fig. 4**. At about 8 minutes after starting the monitoring process, the variation of the dissipation factor begins. After 25 minutes, the substrate of the sensor has been carbonized. Therefore, this type of sensor is inappropriate for monitoring the cure of composites at high temperatures. To prevent a damage of the sensor due to thermal stress, an improvement of the substrate material has to be made. Several technical ceramics and glasses are ideal materials for hostile environment. With high heat resistant of some hundred degrees, an extremely low expansion coefficient in the range of 10^{-6} °K^{-1} and high specific volume resistivity ($10^{10}..10^{16}$ $\Omega *$ cm), these materials fulfill the high requirements on a durable and reliable sensor design. This durability qualifies the sensor as well for monitoring cycles with high standardized quality management as frequently found e.g. in aircraft industries.

3. LASER BASED MANUFACTURING OF ELECTRODES IN BRITTLE MATERIALS

In combination with a controlled micro-positioning system, UV-lasers become a highly precise, flexible and versatile tool for manufacturing micro-structures in brittle materials, required e.g. for interdigital condensers [7]. For the examinations, a 4 axis precision handling system has been employed. A positioning resolution of 0.1µm and repeating accuracy of 0.5µm allows exact and reliable micro-machining. As a ceramic substrate, aluminum oxide (Al_2O_3, Rubalit®) was chosen and structured with an krypton-fluoride (KrF) excimer laser (Type LPX325i, Lambda Physik, wavelength $\lambda = 248$nm, max. pulse repetition rate $f_P = 250$Hz, pulse duration $\tau = 20$ns). For the machining of glasses and other materials that transmit radiation at 248nm, argon-fluoride (ArF) excimer lasers with $\lambda = 193$nm are available [4]. Furthermore quartz, which is even more difficult to ablate due to its extremely high UV-transparency, can be structured with wavelength as short as 157nm (F_2 excimer laser) [8, 9].

Another outstanding laser tool for micro-structuring of for example technical ceramics, are frequency converted diode-pumped solid-state lasers (DPSSL). Here, the UV- sources, third harmonic (3ω, 355nm) and especially the frequency quadrupled (4ω, 266nm) lasers allow excellent machining results. Though lower pulse energy compared with standard excimer lasers (factor $10^2..10^3$), a repetition rate up to 100.000Hz enables, combined with a fast laser-scanner imaging tool, high machining speed. The gaussian type beam profile of DPSSL can be focused to spots as small as some micrometers, which allows the production of complex micro-structures. For wider ablation geometries, the gaussian nature of the beam is less suitable than the top head profile of excimer lasers, since the non-homogenous intensity may cause irregularities for machining plane areas. Therefore, the intensity profile can be adjusted to an optimal ablation result by using diffractive optical systems. These specialized optics provide a process adapted optimization of the gaussian beam of the DPSSL. The achieved homogenized beam profile shows a similar ablation characteristic as provided by excimer lasers.
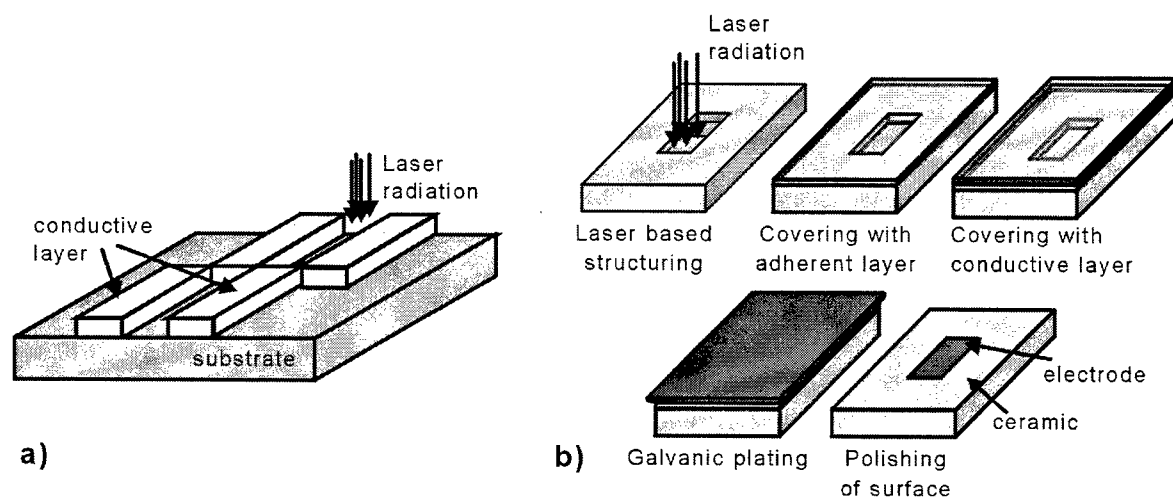
Fig. 5: Sketch of sensor design with electrode formation by a) surface structuring, b) embedded electrodes.

There are two major laser based manufacturing techniques for implementing the sensor structure. One method is to completely cover a suitable substrate with a conductive layer like gold, copper or conductive oxides like ITO or SnO_2 and remove the layer partially to form the desired sensor structure (**Fig. 5a**). This procedure is less time and cost intensive, since the conductive coating can be removed with laser radiation, and post processing usually is not necessary. An alternative technique for the sensor design is to machine the bulk substrate material to create a cavity of the desired sensor structure. In a following process step, the formed cavity can be filled with a conductive material (gold, copper, nickel) by standard electroplating processes (embedded electrodes). This technique is more complex, because the electroplating process consists of multiple steps, as explained in **Fig. 5b** (sputtering of adhesive layer → polishing of surface → sputtering of start layer for electroplating process → filling cavity with conductive material (electroplating) → polishing of entire structure). This sensor type is more durable, since the electrodes are embedded into the bulk substrate material. The improved wear resistance may be fundamental for application with a strong abrasive force, as in pultrusion machines, where the curing material is in direct contact with the surface of the dielectric sensor.

excimer laser	: KrF , λ = 248 nm	strategy	: NC-controlled production
pulse duration	: τ_H = 20 ns	Sensor dimension	: 19 mm x 19 mm
demagnification	: β = 1:40	contact pads	: copper (500 nm)
electrode width	: 50 µm	insulation channel	: 50 µm
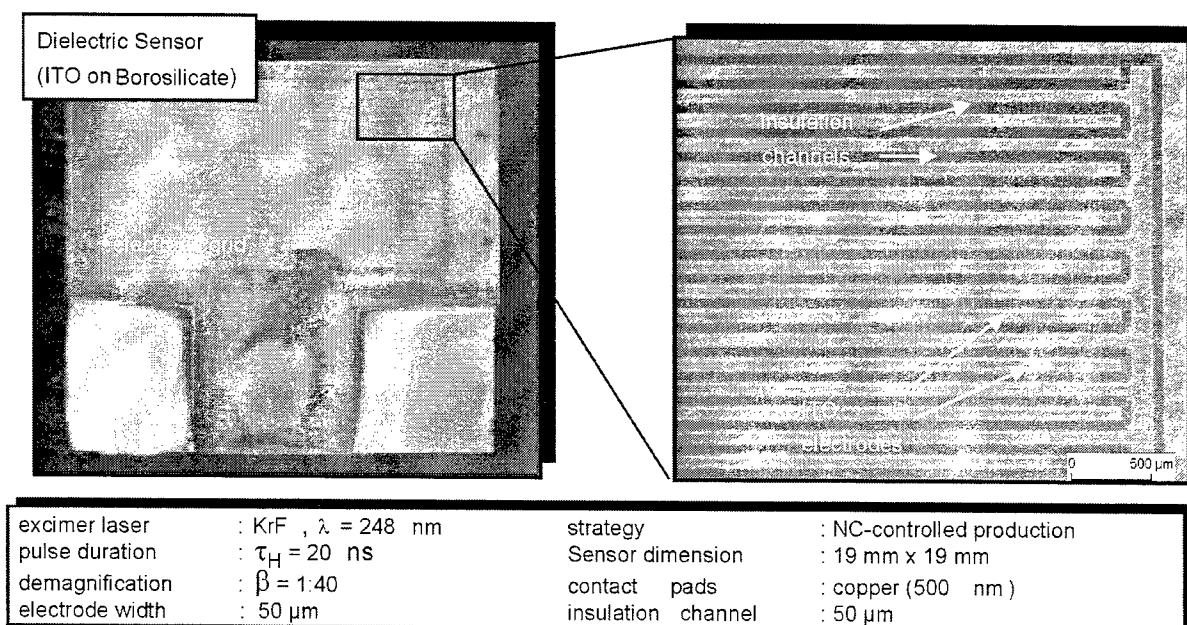
Fig. 6: Surface structured dielectric sensor.

The result of a surface structured dielectrical sensor can be seen in **Fig. 6**. The sensor structure has been achieved by ablating a conductive surface layer (Indium Tin-Oxide, ITO, square resistance $R_{sq} = 10\Omega$/sq., layer thickness ~ 600nm) partially with a KrF excimer laser (fluence H = 5 J/cm²). The sensor substrate was borosilicate glass (BoroFloat33, Schott). A sketch of the sensor geometry is outlined in **Fig. 1**. The microscope picture on the right side of **Fig. 6** shows the insulation channels achieved at a square ablation area of 50μm x 50μm with an overlap of 50%. A 500nm thick copper layer was sputtered onto the rectangular contact pad to ensure a reproducible transition resistance for the connection of the sensor with an impedance analyzer. For this sensor geometry with 100 electrodes on a 15mm x 10mm grid area (capacitance C = 40..42pF), a machining time of 25min has been obtained. For a proper machining result, two repetitions were necessary for writing the sensor geometry into the material. Whereas a fluctuation of the fluence in the range of ±0.3 J/cm² was tolerable.

As shown in **Fig. 2**, different electrode dimensions and distances are required to serve various sensor properties like sensitivity and sensing depth. For an optimal machining process, the raw beam of the laser has to be shaped in the lateral range of a few 100μm up to some millimeters. With an image ratio of 1:40, this corresponds with a spot size of about 5μm to 250μm. This was realized by using a flexible rectangular mask. The mask can be operated by NC-code and therefore enables a time-minimized, economic manufacturing.

The rectangular ablation is the basis for manufacturing an embedded-electrode-type of sensor from a bulk material. **Fig. 7** shows exemplarily an ablation area with three different ablation dimensions in aluminum oxide as a substrate material, minimum latitude as small as 10μm. The process was driven defocused, since an electrode geometry with shallow flank angles was required in the specific application.
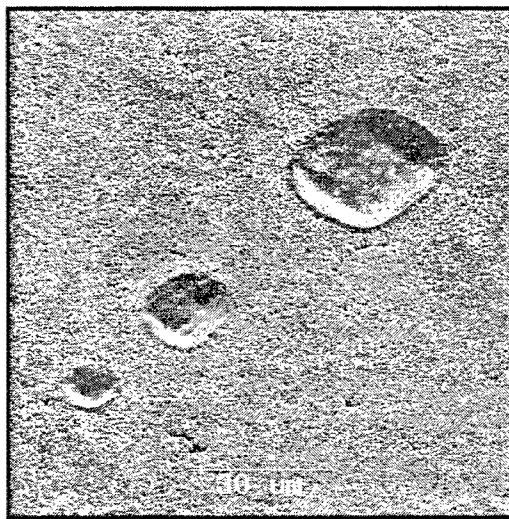
Fig. 7: Different defocused ablation sizes with flexible mask system. (Source LZH)
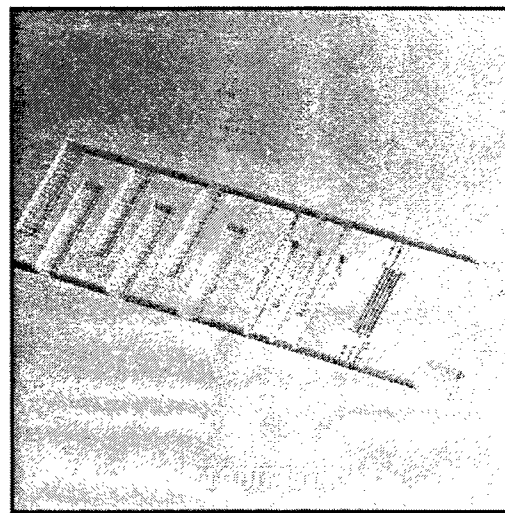
Fig. 8: Laser machined electrode grid in aluminum oxide. (Source LZH)

For the manufacturing of a complete sensor geometry, the work piece is moved relatively to the stationary laser beam. NC controlled xy-stages are used to determine the defined positioning with an accuracy in micrometer range. A SEM picture of the electrode grid of an embedded-electrode-type sensor structure in the bulk material aluminum oxide is displayed in **Fig. 8**. The fabrication was carried out with an KrF-excimer laser at a fluence of 20 J/cm². The machining result indicates smooth ablation edges and a plane ground of the cavity. Since the effort of implementing a suitable NC-code rises exponentially with increasing complexity of sensor geometry, software interfaces have been developed, which transform a CAD model of the desired micro-structure into NC-data. **Fig. 9** shows a general schematic of the transformation process.
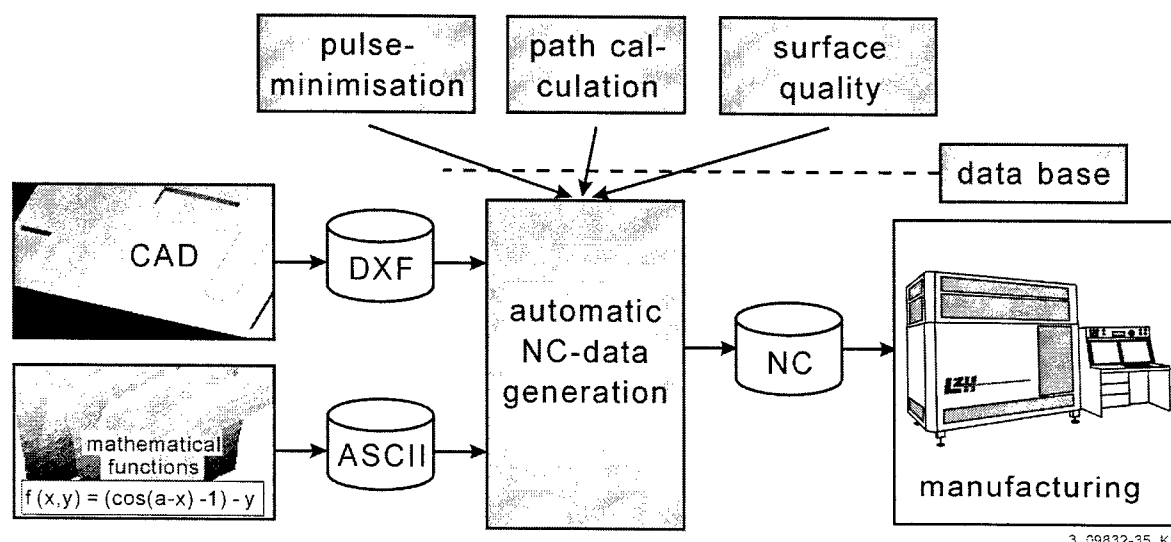
Fig. 9: Block diagram of the automatic NC-data generation [7].

Models of the desired micro-structure, provided as standardized files containing geometry descriptions can be transferred to the interface. The software tool automatically generates the NC-code considering several optimization algorithms. These algorithms are provided from databases which are linked to the software. The optimization of the NC-data allows a pulse minimization and path optimization of the manufacturing process. Using this method, the number of single pulses was reduced significantly compared with the number of pulses without minimization algorithm [7]. Due to their low repetition rates, the duration for machining of complex micro-structures often exceeds several hours. Hence, the aspect of reducing the number of laser pulses is essential for the micro-structuring with excimer lasers to allow an economical manufacturing process. In addition to this advanced, process adapted CAD-CAM system, a 3D-simulation of the generated NC-code for the production of electrodes can be performed. The simulation is essential, since for each different electrode geometry and machined material, specified manufacturing parameters are required to receive an optimized machining result. Slightly varied parameters result in distinct modification of surface quality for the slope and ground area of the structure, as well as process time or damage of the bulk material. By optimizing the process parameters before starting the cost and time intensive machining process, rejects can be avoided.

Fig. 10 shows a screenshot of the simulation tool with a generated 2D image of a sensor demonstrator geometry. Laser specific parameters like wavelength, fluence or demagnification ratio can be modified by the software. The given simulation was calculated for $\lambda = 248$ nm, $H = 20$ J/cm² and a ratio of 1:40. The machining depth for a desired area of the structure can be displayed on the screen. The right side of the figure shows a 3D simulation of the electrode geometry, on which the surface quality can be studied. The simulation is generated from the information provided of the CAD model of the structure and the process parameters. Due to the availability of this optimization tool, a reduced development time can be achieved, which is even more important for products with short life-cycles.
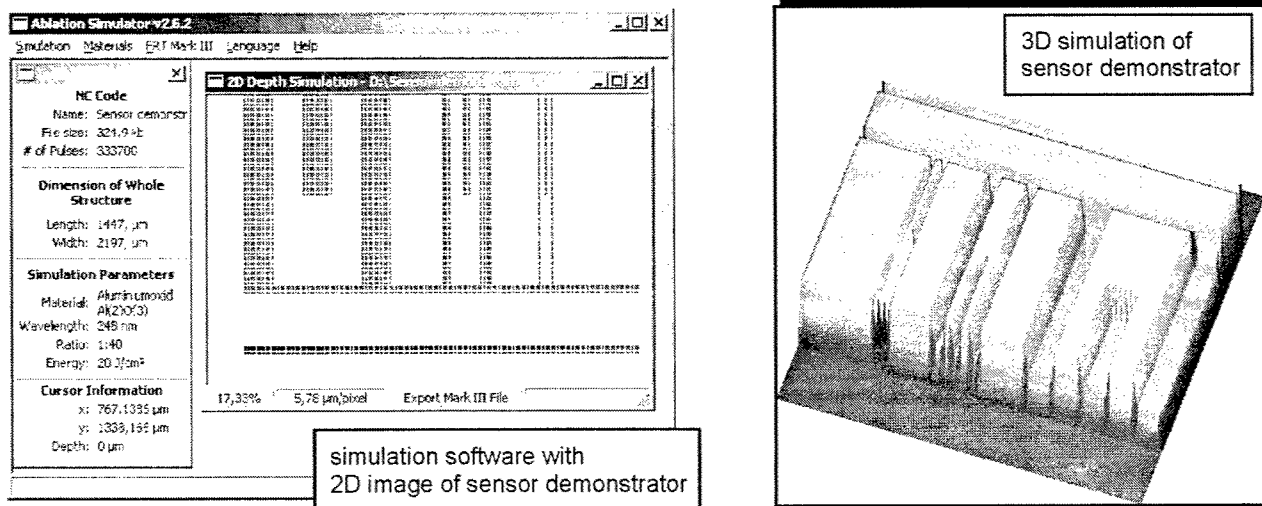
Fig. 10: Screenshot of simulation software with 2D view and 3D simulation of sensor demonstrator geometry.

4. CONCLUSION & OUTLOOK

In this paper, laser based fabrication techniques for dielectric sensors (interdigital capacitors) have been presented. Due to the usage of brittle materials as substrate material, sensors for rough environment applications, such as high pressures or temperatures, can be fabricated. It has been shown that UV-laser sources are an excellent tool for machining these materials with a structure resolution in micrometer range. Two laser-assisted manufacturing concepts for electrode based sensors have been introduced. The first one is to structure a conductive layer on top of a durable substrate material. By ablating the negative image of the desired electrode structure, an appropriate sensor geometry can be achieved. As a top layer, material conductive oxides like ITO or SnO_2 as well as metals (copper, gold) can be machined in the micrometer range. For the second technique, the brittle bulk substrate material has to be machined to create a cavity of the desired sensor structure. The received positive image of the electrode geometry can be metallized in a following step with standard electroplating processes. This multi process technique is more time- and cost intensive that the direct structuring of the surface layer, which usually has no need on post processing. However, the embedded electrode structure of electroplated sensor type is more durable versus abrasion force or thermal stress.

For an optimal machining result, an automated laser based manufacturing cycle has been introduced. Complex micro-structures have been designed by commercial CAD-systems and provided to a software interface. This interface converts the sensor model into appropriate NC-code for the control of the employed micro-machining center. Since different electrode geometries and machined materials need special NC-code adaption, a 3D-simulation of the machining result can be created to verify the optimum parameters for the NC-code generation.

Especially excimer and frequency converted diode-pumped solid-state lasers provide an outstanding ablation characteristic for a precise machining of technical ceramics (wavelength range 355, 266, 248nm) and even several glasses (193, 157nm). Due to high repetition rates up to 100,000 Hz, the possibility of using fast beam guiding systems and furthermore a comparable low acquisition cost, DPSSLs have a great potential of improving the economic viability of the fabrication. For an optimized machining result, the gaussian intensity profile of DPSSL can be homogenized by diffractive optics, which provides a flat hat ablation charakteristic, comparable with excimer lasers. The examinations should lead to a successful transference of the process from high quality excimer laser machining with its lower machining speed due to repetition rate and xy-stage restrictions to a DPSSL process with comparable fabrication results. This transference of laser based manufacturing of complex electrode geometries to a solid-state laser driven process realizes a high accurate, reproducible and economically improved sensor fabrication.

5. ACKNOWLEDGEMENTS

6. REFERENCES

1. Endres, H.-E. ; Hammerl, E.; Drost, S. M. M. et al.: Reinigungssensor für die CIP-Reinigung. In: dmz 13 (2002), pp. 34-38.

2. Tönshoff, H.K.; von Alvensleben, F.; Graumann, C.; Willmann, G.: *High precision laser machining of ceramics.* In: *Proc. of SPIE*, No. 3414, Opto-Contact Workshop, (1998) Québec, pp. 51-59, ISBN 0-8194-2868-X

3. Tönshoff, H.K.; Graumann, C.; Rinke, M.: *NC-controlled production of smooth 3-D surfaces in brittle materials with 193 nm-Excimer Laser.* In: *SPIE's International Symposium on Micromachining and Microfabrication*, (1998) Santa Clara

4. Rinke, M.: *Glasbearbeitung mit ArF-Laserstrahlung.* 1. Aufl. Düsseldorf: VDI, 2000. - ISBN 3-18-355002-4

5. Kulik, C.: *Bearbeitungsstrategien für die lasergestützte 3D-Mikrostrukturierung technischer Keramik.* 1. Aufl. Düsseldorf: VDI, 2002. - ISBN 3-18-362102-9

6. Choi, J.; Kim, I.; Lee, D.: Devolopment of the simple dielectric sensor for the cure monitoring of the high temperature composites. In: *Journal of Materials Processing Technology* 132 (2003), pp. 168-176.

7. H.K. Tönshoff, F. von Alvensleben, M. Rinke, K. Körber, C.Kulik: *Machining Concepts for Three-Dimensional Micro-Structuring with Pulsed UV Lasers.* Proc. of MicroEngineering 99, (1999) Stuttgart, pp. 176-182. ISBN: 3-00-004950-9

8. Ostendorf, A.; Stamm, U.; Temme, T.: *Precision Machining of Innovative Materials Using 157 nm Excimer Laser Radiation.* In: 2nd *International Symposium on Laser Precision Microfabrication*, LMP 2001 Singapore, SPIE 4426 (2002), pp.449-452.

3D microstructuring inside photosensitive glass by use of a femtosecond laser for lab.-on-chip applications

Ya Cheng[*a], Koji Sugioka[a, b], Masashi Masuda[a, b], Katsumi Midorikawa[a], Masako Kawachi[c], Kazuhiko Shihoyama[c], and Koichi Toyoda[b]

[a]RIKEN, The Institute of Physical and Chemical Research, Hirosawa 2-1, Wako, Saitama 351-0198, Japan
[b]Tokyo University of Science, Yamazaki 2641, Noda, Chiba 278-8510, Japan
[c]HOYA PHOTONICS CORPORATION, Hikawacho 3-5-24, Toda, Saitama 335-0027, Japan

ABSTRACT

In this paper we show that a femtosecond laser enables us to form true three-dimensional microstructures embedded in a photosensitive glass Foturan for lab.-on-chip applications. The Foturan glass has superior properties on transparency, hardness, chemical and thermal resistances, and biological compatibility. After exposure to the tightly focused laser beam, latent images are written inside the glass. Modified regions are developed by a post baking process and then preferentially etched away in an ultrasonic solution of 10% hydrofluoric acid in water. By use of this technique, we fabricated various true 3D microstructures including microfluidic components and microoptics inside the Foturan glass. However, the microchannel fabricated inside glass by scanning focal spot of a femtosecond laser perpendicularly to the direction of laser propagation gets an elliptical shape with a cross section of large aspect ratio, owing essentially to a longitudinal distribution of the focal spot produced by an objective lens with numerical aperture of 0.46. We demonstrate that the aspect ratio can be effectively improved by use of a slit-assisted irradiation method. Lastly, we show that 3D microoptics are fabricated inside the Foturan glass, which enhances the function of lab.-on-chip.

Keywords: 3D microstructuring, photosensitive glass, lab.-on-chip, femtosecond laser, aspect ratio, microchannel

1. INTRODUCTION

It has been a trend to use highly miniaturized and integrated systems in biomedical and biotechnical applications. These systems are called lab.-on-chip or micro total analysis systems (μ-TAS). A lab.-on-chip uses integrated microfluidic components, such as microchannels, microcells, micropumps and micromixers, to conduct biological or chemical analysis of nanoliter-size even picoliter-size samples with high performance[1]. Currently, fabrication of lab.-on-chip relies on planar microfabrication techniques like micromaching, micro-moulding, and photolithography *etc*. Although these techniques have been well established and are suitable for surface microfabrication, the fabrication of true three-dimensional (3D) microstructures requires multilayer and multistep processes including stacking and fusing substrates. Since it is known that femtosecond (fs) laser can internally modify transparent materials using the multiphoton absorption process, laser direct writing becomes a promising and simple approach for embedded 3D microstructuring. It has been reported that microchannels inside fused silica were fabricated by fs laser irradiation followed by post chemical etching in a hydrofluoric (HF) acid solution[2], or by water-assisted laser backside drilling[3]. To induce microexplosion inside the fused silica, these techniques require high laser intensity and low scanning speed. In comparison with the silica glass, a photosensitive glass may be a more attractive candidate material because it can be modified by much lower laser fluence as well as much higher scanning speed. Consequently, cost can be reduced while throughput can be increased.

In fact, the history of the photosensitive glass and its fabrication can be ascended to half century ago. Stooky at Corning did the earliest work in development of this material in 1950s[4]. Now there are over 5,000 varieties of these glasses and one of the most successful commercializations of today is manufactured by Schott Corporation and sold under trade name Foturan[5, 6]. It is composed of lithium aluminosilicate glass and doped with trace amount of silver and cerium. The cerium (Ce^{3+}) ion plays an important role of photosensitizer, which releases an electron to become Ce^{4+} by exposure to

---

[*] ycheng@postman.riken.go.jp; phone +81-48-467-9495; fax +81-48-462-4682; www.riken.go.jp

UV light irradiation. Some silver ions obtain the free electrons to form silver atoms. In a subsequent heat treatment, first the silver atoms diffuse and agglomerate to form clusters at about 500 $^\circ$C; then the crystalline phase of lithium metasilicate grows into the amorphous glass matrix using the silver clusters as nucleus at about 600 $^\circ$C. As this crystalline phase of lithium metasilicate is much more soluble in a dilute solution of hydrofluoric acid than the glass matrix, it can be easily etched away. Usually, the exposure process in a two-dimensional (2D) microfabrication of Foturan is a UV lamp photography step. And for the 3D microfabrication, a pulsed UV laser direct write technique has been established by Helvajian and his co-workers[6].

Since the UV light is resonant with the absorption wavelength of the Foturan glass, it induces linear absorption from the surface, and decreases the fabrication precision. On the contrary, an exposure process employing a fs laser confines the absorption region inside transparent materials by a multi-photon process, resulting in a more precise fabrication of true 3D microstructures[7-8]. In this paper, we show that sophisticated and complicated 3D microstructures for the lab.-on-chip applications are fabricated within Foturan glass by a fs laser operated at near-infrared wavelength. We also demonstrate how to control the uniformity and the aspect ratio of the microchannels by use of advanced irradiation methods.

2. THE PROCESSING PARAMETERS

The experiments were carried out on a commercial fs laser workstation at Hoya Photonics Corporation, as shown in Fig.1. The laser wavelength, pulse width and repetition rate were 775nm, 140±5fs and 1kHz, respectively. To guarantee a high beam quality, the 6mm diameter of the output laser beam was reduced to 3mm by an aperture in front of the focusing system. The focusing system was a 20X microscope objective with a numerical aperture (N.A.) 0.46. Sample under fabrication was translated by a PC controlled XYZ stage at a resolution of 0.5μm. The fabrication process was displayed on the PC monitor by a charge coupled device (CCD).
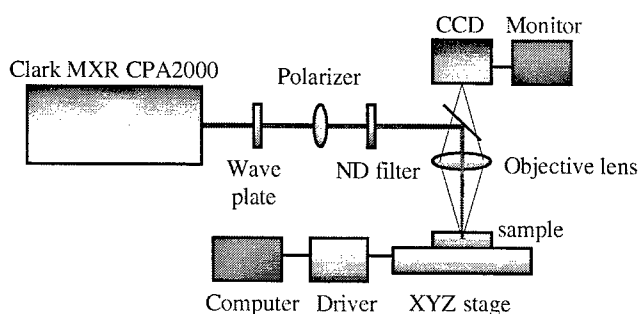
Fig. 1. Experimental setup.
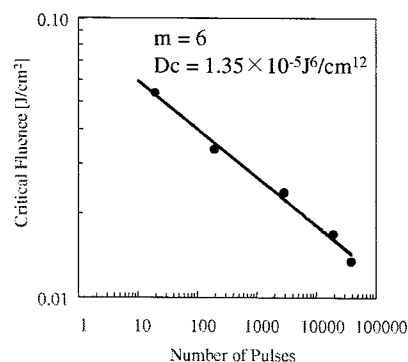
Fig. 2. Dependence of critical fluence on number of pulses in logarithmic scale.

The first step of this work was to check the critical dose of the photoreaction, because the high precision was only achievable using laser pulse energy just over this critical dose. A critical dose is defined as the lowest dose necessary for the modification of the Foturan glass at the exposed region. In the model developed by Fuqua *et al.*, this critical dose is a constant which merely depends on material composition and process parameters, and can be written as below [6]:

$$D_c = F_c^m N ,$$
(1)

where F_c is the critical fluence and N is the number of pulses. To determine the critical dose, we irradiate the Foturan sample with the fs laser at different pulse energies and shot numbers, then baked the sample and treated the sample by chemical etching. Under the microscope, it was clearly shown that for a given number of shots there existed a threshold of the pulse energy over which a visible etched mark could be formed on the glass sample. From this threshold and the spot size of the laser beam, the critical fluence can be determined. Figure 2 is a log-log plot of the critical fluence versus the number of pulses. When we fitted the data by Eq. 1, the slope disclosed a six-photon process $D_c = F_c^6 N$, where the constant $D_c \approx 1.35 \times 10^{-5}$ J^6/cm^{12} was the critical dose according to the laser parameters in our

experiments. An earlier investigation of a pulsed UV laser (355nm) irradiation[6] disclosed a two-photon process $D_c' = F_c'^2 N$ with $D_c' = 9 \times 10^{-6} \, J^2/mm^4$. This discrepancy implies that the mechanism of the photoreaction activated by the near-infrared fs laser is distinct from that by the UV light irradiation. Nevertheless, the enhanced nonlinearity is beneficial to the internal fabrication and the resolution, because the absorption region could be confined to a very small region inside the glass by use of the tightly focused beam, and the modified area could be much smaller than the laser focal spot if the pulse energy is controlled close to the critical dose.

Another necessary condition for a high precision is a large etching selectivity between the exposed and unexposed regions. We directly measured this parameter by comparing the etching rates of exposed and unexposed regions on a same sample. For several laser parameters in our experiments, the exposed regions showed a similar etching rate about 35 times as high as that of the unexposed region, as shown in Fig. 3. Based on the critical dose and the etching rate, we determined the processing parameters.
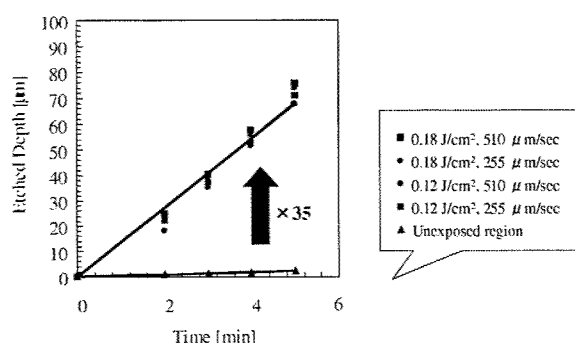
Fig. 3. Etching selectivity between exposed and unexposed regions.
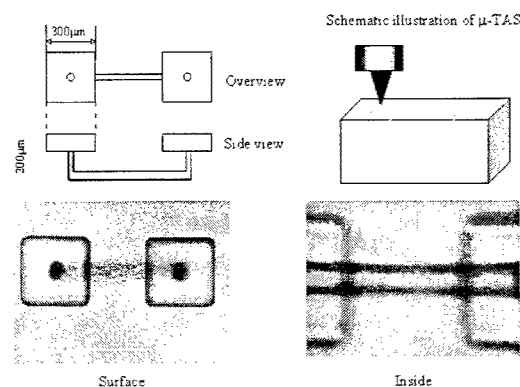
Fig. 4. Micrograph of a bridge-like microstructure. Through microchannel and two microcells with sharp edges were structured. Neither debris nor cracks were found.

3. MICROFLUIDIC COMPONENTS APPLICATIONS

In the first instance, we applied this technique to fabricate a bridge-like microchannel embedded 200μm below the surface, with which two microcells were connected on the sample surface, as shown in Fig. 4. To form the microchannel inside the glass, first the sample was translated along parallel direction of laser propagation from the surface to the depth of 200μm, next it was moved perpendicularly to the direction of laser propagation to form the horizontal channel in the schematic diagram, finally it was translated along the laser propagation direction again until the laser focal spot left the sample surface. Then, the square microcells on the sample surface were formed by translating the sample to the laser focal spot line by line at a pitch of 10μm. The scanning speed for the processing was 510μm/s at which 50 pulses overlapped at the same position, and the laser fluence was set at 78mJ/cm² which was derived from the critical dose. After the exposure step, the sample was subjected to a programmed heat treatment. First, the temperature was ramped from room temperature to 500°C at 5°C/min and held at 500°C for one hour; then it was raised to 605°C at 3°C/min and again held for one hour. After the sample cooled to the room temperature, it was soaked in a 10% HF solution to take an ultrasonic bath for 90 minutes. Crystalline phase of lithium metasilicate was totally etched away in this step. Lastly the sample was cleaned in distilled water and dried by nitrogen gas flow. Over exposure to the HF solution for somewhat long time caused broadening of the fabricated channel.

By the same procedures and same parameters, large scale, more complicated microstructure with microchannels as long as ~2800μm was successfully fabricated, as shown in Fig. 5. To avoid the over etching effect, the total time for chemical processing was shortened to 45 minutes. Thus the diameter of the microchannels was reduced to 45μm. Notably, from the overview picture of the structure in Fig. 5, one can see that this diameter was almost unchanged in the full length of the fabricated channel, namely, the long channels were formed almost without taper. It indicates that it is

possible to get a high uniformity even for such a large-scale microstructures by optimization of the processing parameters in both exposure and chemical etching, which was thought as one of the main issues in this approach[8].

Figure 6 shows a microstructure with a vertical-configuration which has not only embedded microchannles but also embedded microcells. The microstructure has a total height of 2000μm, as same as the thickness of the Foturan sample. The vertical channels were tapered, because it took 90 minutes to remove the large volume of the internal material. Thus the opening part of the microstructure had an etching time much longer than the central part. The inhomogeneous etching time resulted in the tapered structure.
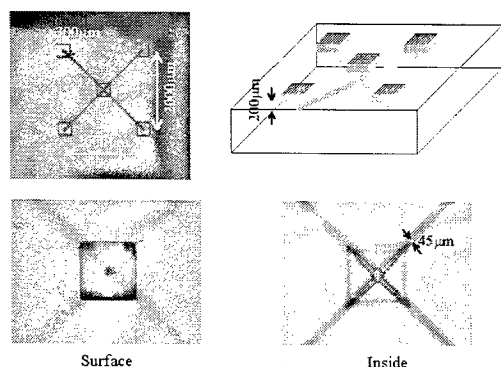
Fig. 5. A large-scale crossed-channel microstructure.
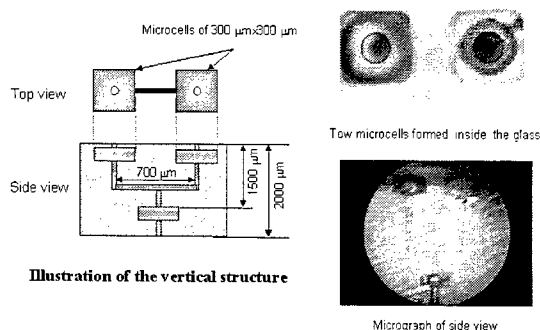
Fig. 6. A microstructure with a vertical configuration.

Fortunately, recently Masuda *et al.* have reported that increasing the irradiation area at the tapered region can reduc e the taper significantly[9]. Figure 7 shows a structure the same as that in Fig. 6 but fabricated with a multi-scanning process. At the central part of each vertical channel, we used additional four scans to increase the modified area as well as the etching speed. The scanned four traces were distributed symmetrically around the central channel with a lateral shift of 10μm, with its side view illustrated in the inset of Fig. 7. It is obvious that the improved microstructure is almost free of taper. Generally speaking, if a structure has a complicated configuration and a large internal volume, thus requires a long chemical etching time over one hour, use of the dose-compensated irradiation method becomes important to achieve the high uniformity.

The true 3D microfabrication technique even makes it possible to structure a movable component within an embedded chamber by a one-step fabrication, which has also been demonstrated by Masuda *et al.* recenly[9]. Figure 8 shows a prototype of a microfluidic device with switchable microchannels. A movable glass plate indicated by the arrow plays the role of a valve, which is controlled by use of gas flow. When the plate is moved to the right side, it blocks the right channel then only the left channel is available, and vice versa. To fabricate the movable plate, we first used the fs laser to scan the hatched area illustrated in the inset, then baked and etched the sample. The device was intendedly designed large for a clear demonstration of the function. Besides microfluidic components, movable micro mechanical components like microturbin and microgear can be also structured in this way.
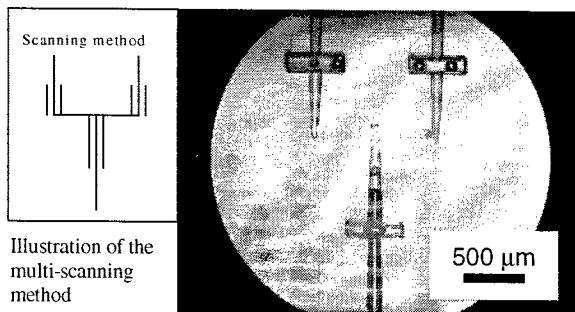
Fig. 7. A vertical microstructure fabricated by use of the multi-scanning method
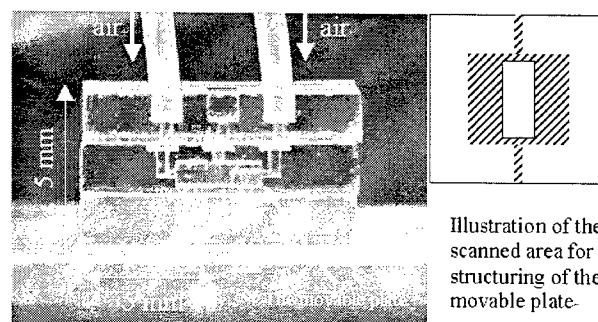
Fig. 8. A prototype of a microfluidic device with a movable plate as a valve.

4. CONTROL OF THE ASPECT RATIO OF MICROCHANNEL

In general, the cross-sectional profile of the fabricated microchannel shows an elliptical shape with a large ellipticity[7-8]. For instance, a horizontal "Y" branched microstructure and its cross-section are shown in Fig. 9a and b, respectively. It reflects a channel width of 17μm and a depth of 71μm (aspect ratio of 4.2). For flexible manufacture of μ-TAS, the aspect ratio should be controllable. In essence, the high aspect ratio is attributed to a longitudinal distribution of the spatial intensity of a beam focused by an objective lens with numerical aperture of 0.46. The use of a higher N.A. lens should reduce the aspect ratio, but the working distance would become very short (several hundred μm), which would make the formation of integrated 3D structures difficult. In this section, we demonstrate that control of the aspect ratio can be realized by use of a slit-assisted irradiation method[10].

3-D Y-branched structure
fabricated in the photosensitive
glass (focusing on surface)

(a)

Cross Sectional Shape of
embedded Microchannel

(b)
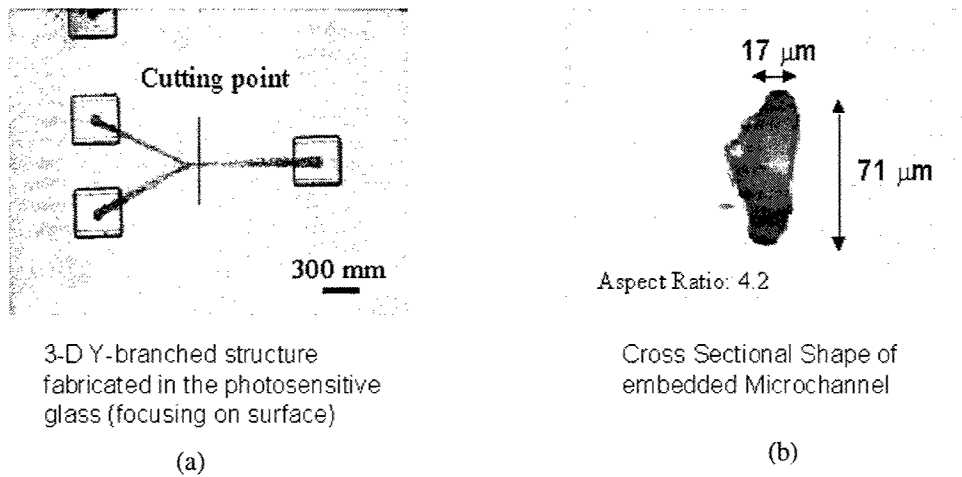
Fig. 9. (a) A horizontal "Y" branched microchannel structure embedded 300μm below the sample surface.
(b) Cross-section of the microchannel. The cutting point is indicated in Fig. 7a.

As the aspect ratio of the fabricated microchannel reflects the energy distribution near the laser focus, the key point in controlling the aspect ratio is to modify the energy distribution near the laser focal spot, namely, laterally expand the focal spot in the direction perpendicular to the channel. From the principle of diffraction[11], this can be accomplished by use of an elliptical aperture instead of the circular aperture in front of the focusing system. However, a two-dimensional diffraction theory therein cannot describe the longitudinal distribution of the laser field near focus. Fortunately, this problem can be easily solved by Gaussian optics. First, for a circular Gaussian beam with its beam waist in the input plane of the lens, the energy distribution near the focal point can be expressed as[12]

$$I_c = \frac{1}{(1+\frac{z^2}{z_0^2})} \exp[\frac{-2(x^2+y^2)}{w_0^2(1+\frac{z^2}{z_0^2})}] \quad , \tag{2}$$

where the coordinate origin is at the geometrical center of the focal point, $w_0 = \lambda/(f^* \cdot \pi)$ is the new beam waist at the focal point, $z_0 = kw_0^2/2$ is the corresponding Rayleigh length, f^* is the numerical aperture of the focal lens, and λ and k are the wavelength and wave vector, respectively. In addition, we assume that the full width of the incident laser beam is the same as the aperture of the focusing lens, based on the practical observation in our experiments.

Similarly, for an elliptical Gaussian beam with its major axis in the X direction and minor axis in the Y direction, the new energy distribution near the focal point can be expressed as

$$I_e = \frac{1}{\sqrt{(1+\frac{z^2}{z_0^2})}} \cdot \frac{1}{\sqrt{(1+\frac{z^2}{z_0'^2})}} \exp[\frac{-2x^2}{w_0^2(1+\frac{z^2}{z_0^2})}] \exp[\frac{-2y^2}{w_0'^2(1+\frac{z^2}{z_0'^2})}] , \qquad (3)$$

where again we assume that the effective full width along the major axis of this elliptical beam is the same as the lens aperture, and the beam waist is in the input plane of the lens. In Eq. 3, w_0 and z_0 are the same as those in Eq. 2, but there are two new arguments, $w_0' = (R_x / R_y) \cdot w_0$ and $z_0' = k w_0'^2 / 2$. Here, R_x is the radius along the major axis of the elliptical beam and R_y that along the minor axis. For simplicity, peak intensities are assumed to have a value of one in arbitrary units for both Eqs. 2 and 3.

Computer simulations were carried out by use of Eqs. (2) and (3). Figures 10a-b compare the longitudinal distributions at the focal points of a circular incident beam and an elliptical incident beam, where the numerical aperture of the lens was set at $f^# = 0.46$ and the aspect ratio of the elliptical Gaussian beam was set at $R_x / R_y = 6$. It is shown that the energy distribution near the laser focal point becomes more symmetrical in Fig. 10b. Therefore, the aspect ratio of the microchannel could be improved by adopting this novel irradiation mode.
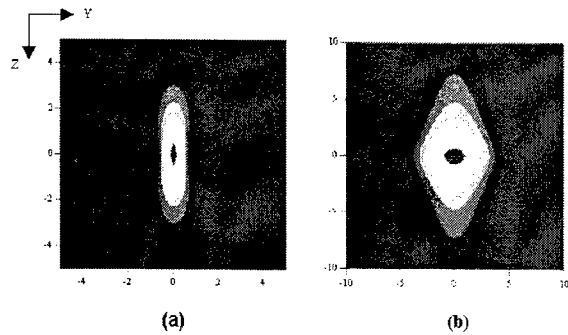
Fig. 10. Computer simulations of energy distributions near the laser foci produced by (a) a circular Gaussian beam and (b) an elliptical Gaussian beam. Units on both Y and Z axes indicate wavelength. Please note that the ranges of axes are different in (a) and (b).
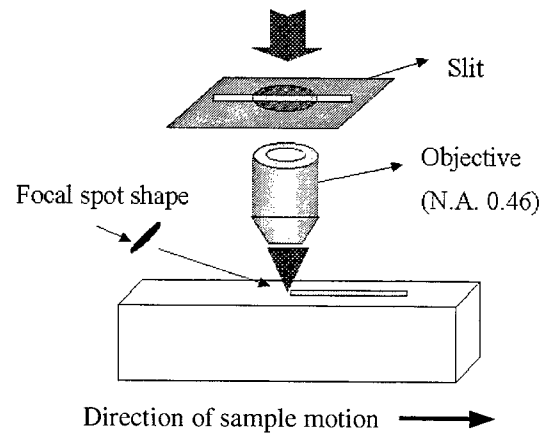
Fig. 11. Schematic diagram of the silt-assisted irradiation system.

To confirm the effectiveness of the above simulations, the experiments were carried out by using a focusing system as shown in Fig 11. In this experiment, we merely used a slit to simulate the elliptical beam shape, which was placed through the beam center and parallel to the direction of sample motion. The Foturan samples were translated three-dimensionally by the PC-controlled XYZ-stage at a scanning speed of 250μm/s. The postprocessing procedures were all the same as those aforementioned.

For comparison, we first adjusted the laser pulse energy to 490nJ and fabricated one structure without the slit. The side view and cross section are shown in Figs. 12a-b, respectively, revealing an aspect ratio of ~3. Then, we inserted a long slit (>3mm) of 0.5mm width above the objective lens and raised the laser energy to 2200nJ/pulse to fabricate a same structure. Since only 22% of the light could pass through the slit, the laser fluence injected into the sample was virtually unchanged. The side view in Fig. 12c shows that the height of the horizontal channel of the second structure is only

about half of that of the first one. The cross section in Fig. 12d shows a reduced aspect ratio of ~1.6. The height of the horizontal channel in Fig. 7 was reduced by this technique, too.

(a)　　　　(b)

(c)　　　　(d)
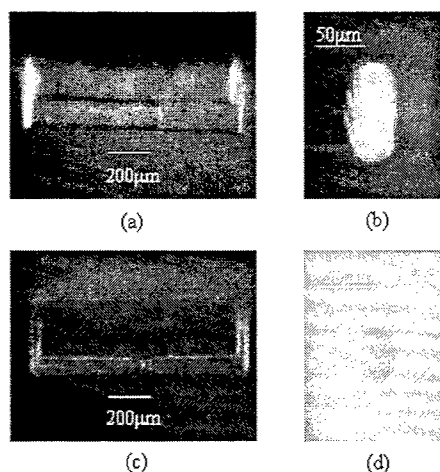
Fig.12. Micrographs of two microchannel structures. (a) Side view and (b) cross section of the microstructure fabricated without a slit. (c) Side view and (d) cross section of the same structure fabricated with a slit of 0.5mm width. Irregular shadow inside the channel was caused by water remaining after etching and cleaning.

(a)　　　　(c)

(b)
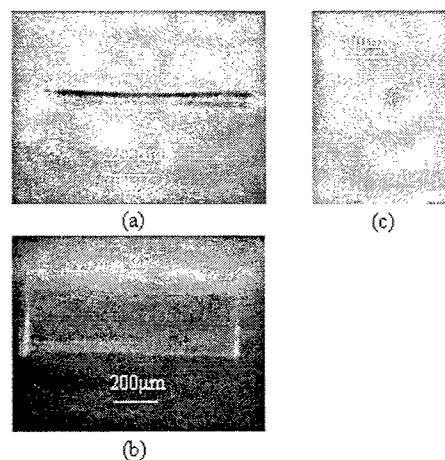
Fig.13. Micrograph of a microchannel structure fabricated with a slit of 0.2mm width: (a) top view, (b) side view, and (c) cross section.

Moreover, by adjusting the width of the slit, the aspect ratio of the focal spot could be varied, enabling us to form microchannels with different ellipticities. For the fabrication of the third microstructure, we changed the slit width to 0.2mm and raised the laser pulse energy to 10,500nJ. In consideration of the transmission efficiency of the slit, the actual pulse energy injected into the sample was about 890nJ. Figure 13 shows that the channel aspect ratio was further reduced to ~1.3. In addition, the size of the cross section decreased in spite of the higher actual pulse energy, because the narrower the slit, the wider the diffraction pattern. This effect expanded the focal spot, consequently, lowered the average intensity in the vicinity of the focal point and reduced the area in which laser irradiation exceeded the critical dose for modification. This result implies that not only aspect ratio but also fabrication precision can be improved with the use of a suitable slit.

5. MICROOPTICS APPLICATIONS

The feature of the internal modification by use of a fs laser facilitates the structuring of not only 3D microfluidic components, but also 3D microoptics inside the glass material. First, we fabricated a 45° micromicrror embedded in the Foturan glass as shown in Fig. 14a. To form this structure, we scanned parallel lines from the upper surface of the sample to the bottom of the sample. The interval between two adjacent lines in the Foturan glass was 15μm. Thus in consideration of the sample thickness of 2000μm, we scanned 140 parallel lines as total to form a through structure. The laser pulse energy and the scanning speed was set at 700nJ and 500μm/s, respectively. After the laser irradiation, the sample was subjected to the heat treatment and the subsequent chemical processing. The time for the chemical etching was 1 hour. Finally, we rinsed the sample in the distilled water and dried it with nitrogen gas flow.

To examine the optical property, we polished the sidewalls of the sample. Then we used a Helium-Neon (He-Ne) laser to check the beam spot reflected from the internal etched surface. The 45° incident angle led to a total reflection. The optical path is indicated by the lines with arrows in Fig. 14a. In Fig. 14b, a test screen is placed at a distance of 10mm from the end of the Foturan glass, on which the reflected beam spot is pointed by the arrow. The size of the beam spot is larger than that of the incident laser beam, implying that the reflected beam is strongly divergent during the propagation. Since the crystallites of the lithium metasilicate developed by the heat treatment must be grown to a certain

size (a few microns) to form a connected etchable network[6], etching of the crystallites leaves behind a rough surface (see Fig. 15a). This high roughness causes strong scattering and the concequent divergence and loss of the light, therefore, it must be improved for the microoptics application.

(a)   (b)   (c)
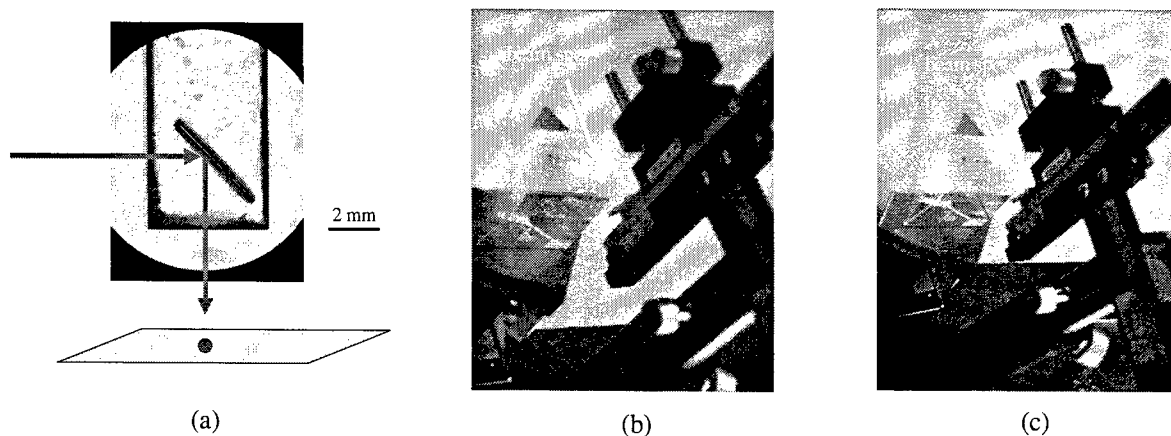
Fig.14. 3D micromirror fabricated inside the Foturan glass. (a) Overview of the structure. The optical path is indicated. (b) Reflected beam spot from the sample without annealing. (c) Reflected beam spot from the sample with annealing.

We solved this problem by a special annealing processing. After the chemical processing, we baked the Foturan sample again. The temperature for the annealing was lower than that for the crystallization. First, the temperature was ramped to 570°C at 5°C/min and held at this temperture for 5 hours, then it was reduced to 370°C at 1°C/min. After the sample cooled to room temperature, we examined the optical property again. The result is shown in Fig. 14c. It is obvious that the size of the reflected beam spot is much smaller than that from the sample without the annealing, indicating an improvement of the divergence. A more direct evidence of the reduction of the roughness is shown in Fig. 15a-b, in which the morphologies of the etched surfaces with and without the annealing are compared. One can see that after the annealing, the etched sample surface is comparable to a polished glass surface, though there is still a few ripples in the central region. Consequently, the optical property can be improved by the annealing process. Recently, it has also been reported that an annealing process can remove SiO_x nanostructures on a silicon surface[13].

(a)   (b)
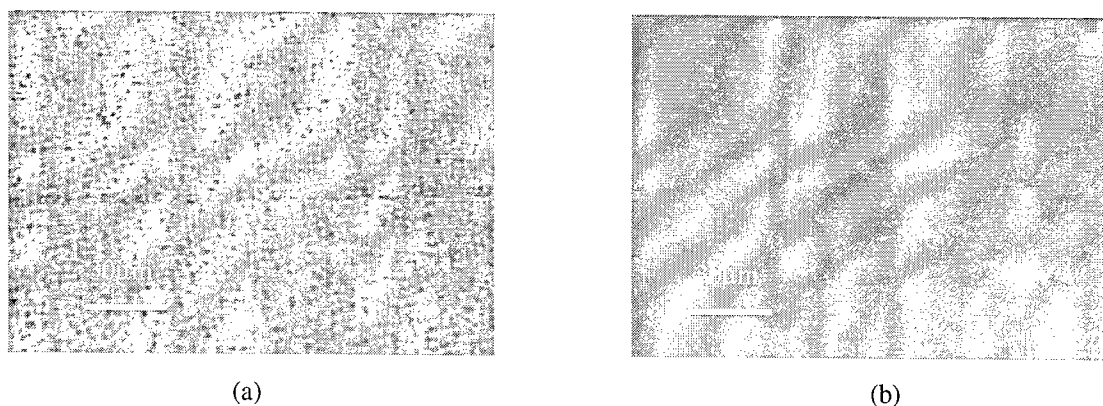
Fig.15. Morphologies of the etched surfaces of the Foturan glass after exposure to fs laser and the programmed heat treatment. (a) Without the annealing processing. (b) With the annealing pro cessing.

By the same procedures, we fabricated an optical circuit as shown in Fig. 16a. Three 45° micromirrors were structured within an area of only 4mm×5mm, and this size can be further reduced without any difficulty. We choose this size because the beam diameter of the He-Ne laser is over 1mm. The input laser beam is turned 270° by the three total

reflections, then transmitted to the test screen which is placed 5mm away from the end of the sample, as shown in Fig.16b. The beam spot is also indicated by the arrow.

(a)

(b)
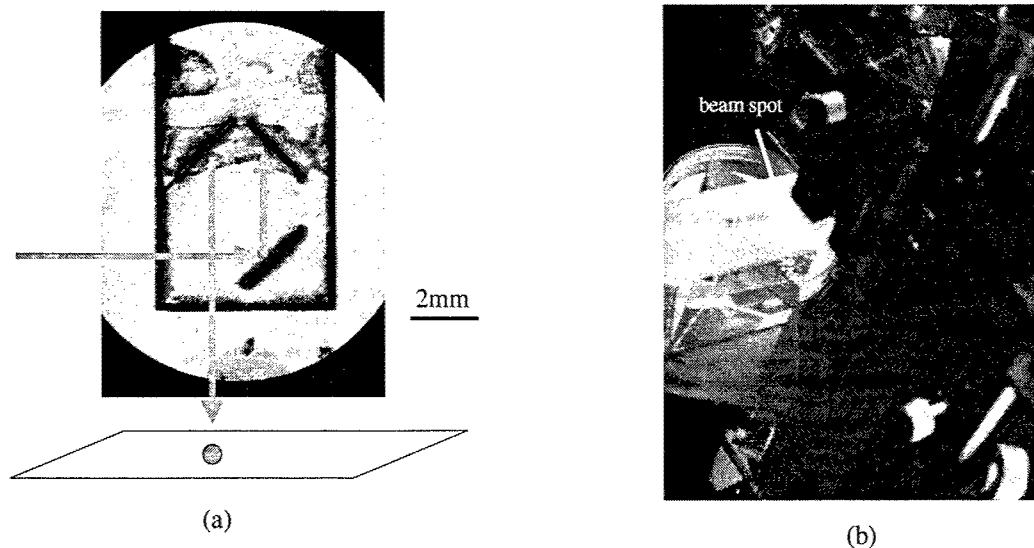
Fig.16. Microoptical circuit fabricated inside the Foturan glass. (a) Overview of the structure. (b) Reflected beam spot on the test screen.

The capability of structuring internal microoptics extends the function of lab.-on-chip, because many biological analyses like fluorescence detection and photoabsorption spectroscopy rely on optical means[14]. Moreover, the internal microoptics could see more applications in the field of optoelectronics. Recently, a variety of microoptical components for intergrated optics application have been fabricated inside the glass materials by use of fs laser, such as waveguide[15], grating[16], Fresnel zone[17] and so on. One could insert these components into the above optical circuit. Since the micromirrors bend the light in a small area without significant optical loss, the size of the integrated optical device can be effectively reduced.

6. CONCLUSIONS

In conclusion, we demonstrate the feasibility of true 3D microstructuring in Foturan glass by use of a fs laser operated at near-infrared wavelength for lab.-on-chip applications. Advanced irradiation methods, such as multi-scanning method and slit-assisted focusing method, are developed for control of the uniformity of the large-scale microfluidic structure and the aspect ratio of the cross-section of the microchannel. A prototype of a microfluidic device with movable component within the embedded chamber is fabricated and its function is demonstrated. Moreover, 3D micromirror is structured inside the Foturan glass. An optical circuit with a size of 4mm×5mm is presented in which the direction of light propagation is turned 270°. In future, the microfluidic circuit and the microoptical circuit can be integrated onto one chip, making it possible to enhance the functions of both lab.-on-chip and optoelectronic device.

REFERENCES

1. M. A. Burns, B. N. Johnson, S. N. Brahmasandra, K. Handique, J. R. Webster, M. Krishnan, T. S. Sammarco, P. M. Man, D. Jones, D. Heldsinger, C. H. Mastrangelo, and D. T. Burke, "An integrated nanoliter DNA analysis device," *Science*, **282**, pp. 484-487,1998, and the references therein.
2. A. Marcinkevicius, S. Juodkazis, M. Watanabe, M. Miwa, S. Matsuo, H. Misawa, and J. Nishii, "Femtosecond laser-assisted three-dimensional microfabrication in silica," *Opt. Lett.* **26**, pp. 277-279, 2001

3. Y. Li, K. Itoh, W. Watanabe, K. Yamada, D. Kuroda, J. Nishii, and Y. Jiang, "Three-dimensional hole drilling of silica glass from the rear surface with femtosecond laser pulses," *Opt. Lett.* **26**, pp. 1912-1994, 2001

4. Stooky, "Photosensitively opacifiable glass," *U.S. Patent* 2684911, 1954

5. See *http://www.mikroglas.com/foturane.htm*

6. H. Helvajian, P. D. Fuqua, W. W. Hansen, and S. Janson, "Laser microprocessing for nanosatellite microthruster applications," *RIKEN Review*, **32**, pp. 57-63, 2001

7. M. Masuda, K. Sugioka, Y. Cheng, N. Aoki, M. Kawachi, K. Shihoyama, K. Toyoda, H. Helvajian, and K. Midorikawa, "3D microfabrication in photosensitive glass by femtosecond laser," *Appl. Phys. A.* (to be published)

8. Y. Kondo, J. Qiu, T. Mistsuyu, K. Hirao, and T. Yoko, "Three-dimensional microdrilling of glass by multiphoton process and chemical etching," *Jpn. J. Appl. Phys.* **38**, pp. L1146-1148, 1999

9. M. Masuda, K. Sugioka, Y. Cheng, T. Hongo , M. Kawachi, K. Shihoyama, A. Takahashi, K. Toyoda, and K. Midorikawa, "3D microfabrication of photosensitive glass by femtosecond laser (2)," *The 63rd Autumn Meeting of The Japan Society of Applied Physics, Niigata Univ., Japan, Sep. 24- 27,* 2002

10. Y. Cheng, K. Sugioka, K. Midorikawa, M. Masuda, K. Toyoda, M. Kawachi, and K. Shihoyama, "Control of the cross-sectional shape of a hollow microchannel embedded in photostructurable glass by use of a femtosecond laser," *Opt. Lett.* **28**, pp. 55-57, 2003

11. M. Born and E. Wolf, *Principles of Optics, 7th edition*, pp443-446 (Cambridge University Press, Cambridge, 1999)

12. G. Laufer, *Introduction to Optics and Lasers in Engineering* (Cambridge University Press, New York, 1996)

13. C. Wu, C. H. Crouch, L. Zhao, and E. Mazur, "Visible luminescence from silicon surfaces microstructured in air," *Appl. Phys. Lett.* **81**, pp. 1999-2001, 2002

14. J. M. Ruano, V. Benoit, J. S. Aitchison, and J. M. Cooper, "Flame hydrolysis deposition of glass on silicon for the integration of optical and microfluidic devices," *Anal. Chem.* **2000, 72**, pp. 1093-1097, 2000

15. K. M. Davis, K. Miura, N. Sugimoto, and K. Hirao, "Writing waveguides in glass with a femtosecond laser", *Opt. Lett.* **21**, pp. 1729-1931, 1996

16. D. Homoelle, W. Wielandy, A. L. Gaeta, E. F. Borrelli, and C. Smith, "Infrared sensitivity in silica glasses exposed to femtosecond laser pulses", *Opt. Lett.* **24**, pp. 1311-1313, 1999

17. W. Watanabe, D. Kuroda, K. Itoh, and J. Nishii, "Fabrication of Fresnel zone plate embedded in silica glass by femtosecond laser pulses", *Opt. Express* **10**, 978-983, 2002

Fabrication of Microstructures in FOTURAN using Excimer and Femtosecond Lasers

Joohan Kim, Halil Berberoglu and Xianfan Xu[*]

Department of Mechanical Engineering, Purdue University

ABSTRACT

We discuss laser fabrication of microstructures in photoetchable glass-ceramics, FOTURAN. A KrF excimer laser ($\lambda = 248$ nm, $\tau = 25$ ns) is used for surface micromachining, and a femtosecond laser ($\lambda = 800$ nm, $\tau = 80$ fs) is used for fabricating three-dimensional structures. Other aspects of the machining, such as the fluence and crystallization depth resulting from these two methods are presented. A detailed analysis of the absorption process of both lasers in FOTURAN is discussed.

Keywords: Photoetchable glass-ceramics, excimer laser, femtosecond laser, FOTURAN

1. INTRODUCTION

Photoetchable glass-ceramics are very promising materials for fabrication of a variety of microsystems. They have high Young's Modulus, transparency in the visible wavelengths, and good thermal and electrical insulation properties. In addition, their good chemical stability, biocompatibility, and high melting temperatures enable the fabricated micro-devices to be used in corrosive and high temperature environments for many biological, chemical and military applications. As an example, photoetchabe glass-ceramics have been used in the display technology for making high aspect ratio spacers in field emission displays (FED) [1].

It is desirable to find alternative ways, other than the conventional lithographic methods, that will prove to have distinctive advantages for effective micro-structuring of these materials. In this work, laser beams are used for changing material properties locally and the main material removal is done by chemical etching in the machining process of the photoetchable glass-ceramics. Therefore, this method combines advantages of two processes: fast local patterning on the material using laser beams and efficient material removal using wet etching. Moreover, 3D machining inside of the photoetchable glass-ceramics by focusing laser beam inside the material is another main advantage. This 3D machining eliminates many difficult assembly steps in fabricating MEMS devices. Laser based micro-fabrication in FOTURAN has been studied for fabricating miniature satellites and other micro-devices [2, 3]. Embedded 3D structures such as Y or H shaped inter channels have been produced with femtosecond lasers [4, 5]. Femtosecond lasers are very useful for making micro-structure inside of the photoetchable glass-ceramics due to its low absorptivity at the laser length ($\lambda = 800$ nm) except at the focal point where the laser intensity is high enough to cause multiphoton absorption. On the other hand, the UV excimer laser can be used for fabricating structures on a large material surface due to the high absorptivity at that wavelength ($\lambda = 248$ nm). In our research, these two different processes for photoetchable glass-ceramics are studied and are presented. A detailed analysis of the absorption process of both lasers in FOTURAN is discussed.

2. PRINCIPLES

The photoetchable glass-ceramics used for our study, FOTURAN, is manufactured by Schott Co. The basic idea behind processing of FOTURAN is to create a way to induce unisotropic etching. Glass is an amorphous material, meaning there are no specific directions within its structure to create directionally specific etching. However, by locally

---

[*] Correspondence: xxu@ecn.purdue.edu. Phone: (765) 494-5639, Email: xxu@ecn.purdue.edu

modifying this amorphous structure, it becomes possible to change its etching characteristics and therefore to create designed structures. In FOTURAN this is achieved by creating a local crystalline phase that etches about 20 times faster than the amorphous one. The process of FOTURAN traditionally requires three main steps, namely photosensibilization, heat treatment, and etching.

2.1 Photosensibilization

Photosensibilization is the first step in structuring FOTURAN, where the structure to be created is written and/or projected into the material with a suitable light source. During illumination, local temperature rise induces the formation of Ce^{3+} ions. These ions are stabilized by Sb_2O_3 and other reducing agents:

$$2Ce^{4+} + Sb^{3+} \leftrightarrow 2Ce^{3+} + Sb^{5+}$$ (1)

The unstable Ce^{3+} ion in return act as a sensitizer. Once it absorbs enough photon energy from a laser beam, it gives away one electron going into the stable Ce^{4+} form.

$$Ce^{3+} + h\nu \rightarrow Ce^{4+} + e^-$$ (2)
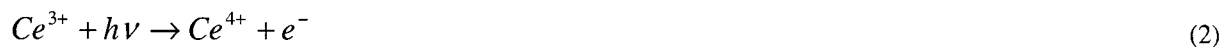
The created electrons are then absorbed by the silver ions which are reduced to silver atoms.

$$Ag^+ + e^- \rightarrow Ag$$ (3)

The resulting silver atoms act as nucleation sites around which lithium-metasilicate can be crystallized during the heat treatment step.

2.2 Heat treatment

Following the photosensibilization step, FOTURAN is heat treated for the lithium-metasilicate to crystallize around the silver nucleation cites. During this step, it is desired to obtain as small crystal size as possible to reduce surface roughness after the etching step. This is quite important for creating micro structures since uncontrolled crystal sizes ranging from 1-10µm are possible. Also it is believed that the crystal sizes can affect the etch ratio between the crystalline phase and the amorphous phase. Although there is no exact recipe for the heat treatment process, several procedures have been proposed in the literature [6]. Accordingly, FOTURAN is first heated up to 500°C at a rate of 5°C per minute. During this portion of the heat treatment, silver atoms diffuse to form silver clusters in the exposed regions. After staying at this temperature for about an hour, the temperature is ramped up to 605°C at a rate of 3°C. At this temperature, crystallization is most efficient and the FOTURAN is held at this temperature for about an hour. Finally the sample is brought back to the room temperature in an uncontrolled manner. Fuqua et al. [6] also mentioned that the formed crystals would have a lower density so internal stresses and surface roughness would show up to a degree depending on the size of the structures.

2.3 Etching

The final step in the structuring of FOTURAN is the etching step. In this step, the crystalline regions are etched away with hydrofluoric acid (HF).

$$Li_2SiO_3 + 8HF \rightarrow 2LiF + H_2SiF_6 + 3H_2O$$ (4)

In literature, there are several different concentrations and schemes suggested for etching. Dietrich et al. suggested using a solution of 10% HF with ultrasonic support or spray etcher at room temperature [7]. Fuqua et al. suggested using 5% HF at 40°C [6]. Both sources quote an etch ratio of 20 to 1. Dietrich et al also quoted a 10 µm/min etch rate for structures having a diameter greater than about 500 µm. The quoted etch rate decreases as the dimensions of the

structure gets smaller since HF can not reach in as effectively. This is the biggest problem for creating arbitrary 3D structures as it can become quite difficult to get the etchant to every part of the structure without broadening the easily accessible sections.

3. EXPERIMENTS AND RESULTS

The lasers used are an excimer laser and a femtosecond laser. For creating 2D structures using the excimer laser, an image can be irradiated directly on the FOTURAN surface with a pre-machined mask. In this case, the actual size of a feature is limited by the crystallized grain size after the heat treatment which is around a few microns. A well defined structure can be obtained directly when the size is above 10 μm. On the other hand, a primitive beam pattern such as a circular shape can be used for direct writing. This method was used for both excimer and femtosecond laser processing. Various features can be printed on or inside the material with a proper focusing lens and high precision moving stages which are controlled by a pre-defined computer program
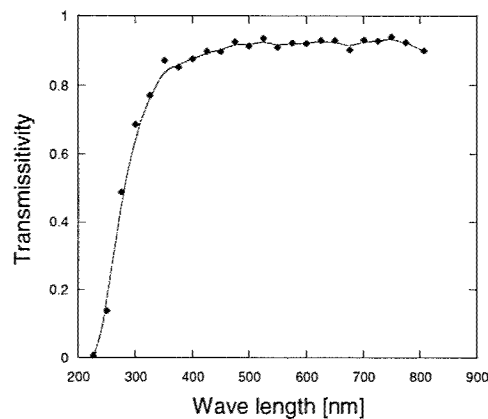
Fig. 1. Transmission characteristic.

Figure 1 shows the transmissivity of a FOTURAN sample of 0.2 mm thick with respect to wavelength measured using a spectral photo meter. At the wavelength of 248 nm for the KrF excimer laser, the transmissivity is 2.6 %, indicating that most of energy at this wavelength is absorbed in the material and the crystallized region is formed on the surface. The crystallization of 3D structures by focusing the beam at this wavelength is rather difficult due to the very low transmissivity at this wave length. A high magnification objective lens can be used, however the depth of the crystallized region is shallow, around 10 - 100 μm. A femtosecond laser at the wavelength of 800 nm has a high transmissivity (> 90 %), and the loss is due to surface reflection. When the femtosecond pulses are focused to a tight spot, multiphoton absorption allows effective absorption of the illuminated light causing the reaction shown in Eq. (2). The effective volume where this reaction can take place depends on the depth of focus and the intensity of the focused laser beam. In general, only a small volume of material can be photosensitized by a single pulse, therefore, scanning this volume in three dimensions is needed to create a true 3D structure.

3.1 Excimer laser process for 2D machining

The excimer laser used has a wavelength of 248 nm, a pulse length of 25 ns, and fluences ranging from 0.1 J/cm^2 to 1.5 J/cm^2. A mask with a pattern of a cross in a circle was used for demonstrating projecting 2D patterns on the FOTURAN specimen. The laser beam passed through the mask was condensed with a lens and irradiated on the specimen. Different numbers of laser pulses and fluences were applied to evaluate their effects. The irradiated specimens were heat treated was and then developed in a 5 % HF solution for 10 min to 20 min, depending on the crystallized depth of the structure.

The specimen after heat treatment and etching process is shown in Fig 2. The dark area in Fig. 2 (a) is the crystallized region after the heat treatment. More pulses or higher fluence produces a darker region and the depth of crystallization region grows. However, the increase of the depth is not linear.

Figure 3 shows SEM pictures of the etched specimen. The wall surface has many craters where crystallites were formed. Their diameters are on the order of a few microns, which dictate the roughness of the structure. The surface of crystallized region is smoother than that of non-crystallized region as shown in Fig. 3 (b). It is expected that a smoother surface can be obtained when a higher fluence is used for crystallization or other heat treatment parameters are applied.

(a)   (b)
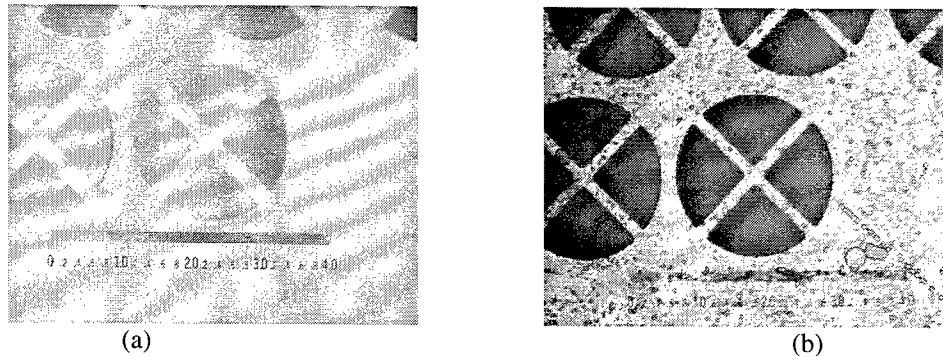
Fig. 2. Patterns on the specimen: after heat treatment (left) and after etching process (right). Full size of scale is 400 μm and excimer laser fluence is 0.1 J/cm^2

(a)   (b)
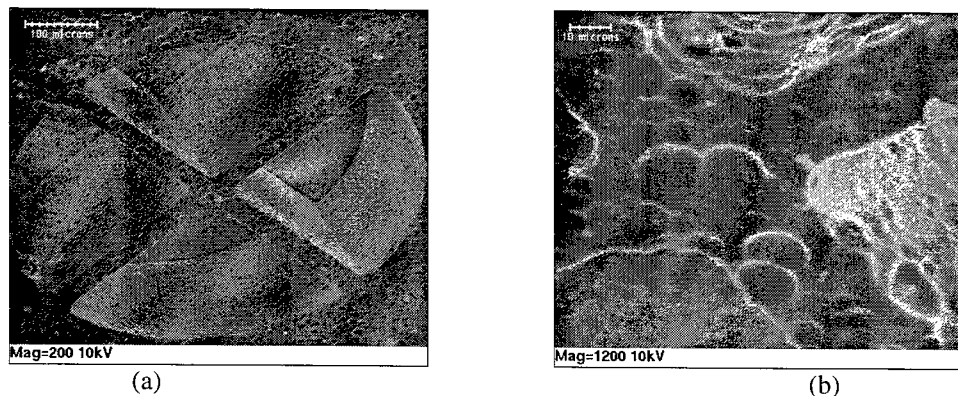
Fig. 3. SEM pictures of the etched specimen with the excimer laser process.

The depth of the final structure such as a micro channel is related to the level of crystallization and the etching time. In order to obtain an expected surface structure, it is desired to control the depth of the crystallization region and etch away only the crystallized region. The crystallization depth with respect to fluence is shown in Fig. 4. As expected, the trend represents that the higher the fluence, the deeper crystallization region. The relationship between fluence and crystallization depth follows the simple Beer's Law of radiation absorption as:
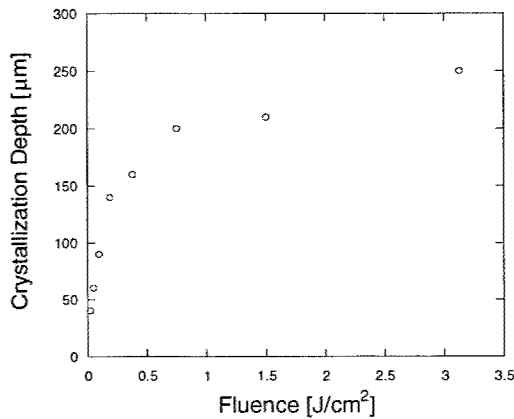
Fig. 4. Crystallization depth as a function of laser fluence
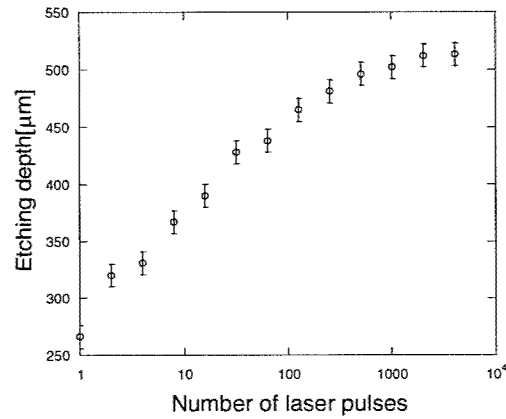
Fig. 5. Etch depth as a function of the number of laser pulses

$$\frac{I}{I_0} = e^{-\alpha \cdot x} \tag{5}$$

where I is the fluence inside the material at a distance x from the surface, I_0 is the incident fluence, and α is the absorption coefficient. Using a curve fit of the data, the threshold fluence (I_{th}) and absorption depth (α) can be found to be 0.011 J/cm^2 and 0.0225 µm^{-1} respectively. The etching depth with respect to the number of laser pulses is shown in Fig. 5. An increase of the etch depth with respect to the number of pulses is observed. This could be due to the fact that the crystallized region by previous pulses changes the absorption coefficient of the material. However, as the number of pulses becomes higher, the etching depth levels off.

3.2 Femtosecond laser process for 3D machining

Multi-photon absorption is one of the forms of nonlinear absorption where two, three or more photons are absorbed in a stepwise manner or simultaneously by atoms or molecules. In this way, instead of absorbing a single photon of high energy, similar chemical reactions can occur by absorbing a number of photons of lower energy. This is exactly the case in FOTURAN irradiated by femtosecond laser pulses. Instead of absorbing high energy UV photons, same chemical reactions can be brought about by absorbing multiple near-IR photons.

In order to investigate the multi-photon absorption process, a simple experiment was designed to determine how many photons are actually involved in the process. In this experiment, it is assumed that absorption is related to the incident intensity I as:

$$\frac{dI}{dx} = -\alpha I^n \tag{6}$$

where I the incident intensity in Wcm^{-2}, α is the nonlinear absorption coefficient, n is the number of photons absorbed and x is the distance from the surface to which the laser is incident on measured in cm. Integrating this expression over the sample length L gives Eq. 7 which can be utilized together with the data to determine the n and α.

$$I^{(1-n)} - I_0^{(1-n)} = (n-1)\alpha L \tag{7}$$

In parallel with Eq. (6) and Eq. (7), an experiment is conducted to investigate the multiphoton absorption process. The schematic of the experimental setup is given in Fig. 6.
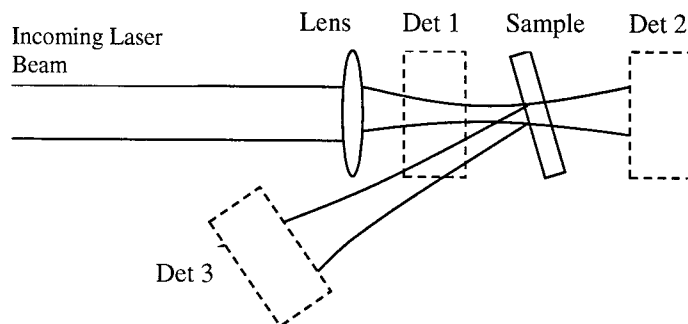
Fig. 6. The schematic of the multi-photon absorption experiment setup.

In this setup, the sample is slightly tilted so that the reflected portion of the intensity could be detected easily. The detector used in the experiment is a power meter. The same detector is used at three different locations namely De.1, Det 2 and Det 3 to measure the input power, the transmitted power, and the reflected power, respectively. The lens used is a 200 mm focal length biconvex lens which gives a spot size of 39 μm. For this lens, the Rayleigh length is about 6.3 mm which provides a weak focusing condition for the 3 mm FOTURAN sample. In this experiment transmission measurements up to surface ablation, which took place for input fluences greater than 4 J/cm^2, were conducted. The obtained transmitted power versus input power is shown in Fig. 7. From this figure, it can clearly be seen that above about 1 Jcm^{-2} there is a regime change. This regime change is due to the optical damage, distinct from the ablative damage is occurring. The data point at 1.1 J/cm^2 is thought to be caused by an experimental error. A similar trend change can also be observed in Fig. 8 which shows the plot of transmittance versus input fluence.
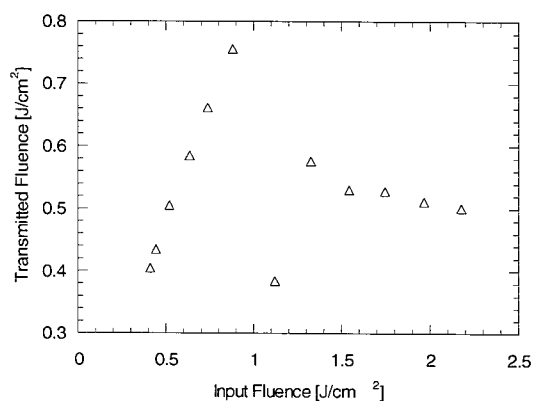
Fig. 7. Plot of transmitted power versus input power
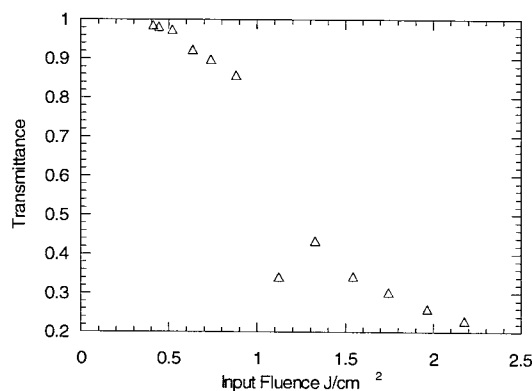
Fig. 8. Plot of transmittance versus input fluence

From Fig. 8 it can also be seen that the first three data points correspond to a transmittance of about 1 which indicates that there is no absorption. Therefore, the data for input fluence between 0.6 J/cm^2 and 1 J/cm^2 was utilized in investigating the multiphoton absorption process. Due to the difficulty in analytically solving Eq. 7, a code was written to perform a nonlinear fit to the data and estimate the value of n and α. This method estimated the value of n to be 3.22 and the value of α to be 1.66x10^{-7} cm^{3}W^{-2}. This result clearly signifies that the multi photon absorption process in FOTURAN is a three photon process. With this model, the predicted and the measured transmitted power versus the input power are presented in Fig. 9.
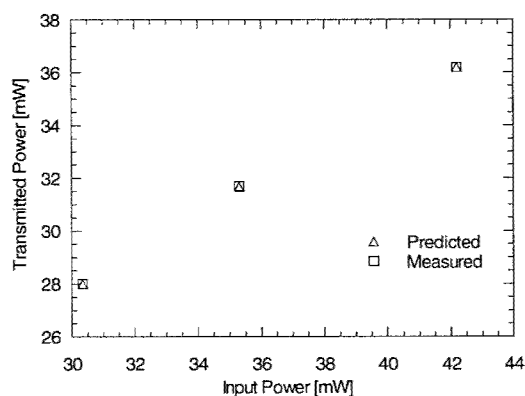
Fig. 9. Comparison of the predicted and measured values for the transmitted power using a three photon model

Characterization experiments are needed to get an idea on how the crystallization depth and width change with laser intensity, write speeds and how different heat treatment conditions affect the overall crystal structure. Also the etch rates of regions with different photosensibilization and heat treatment conditions need to be identified. The study presented here is a preliminary study to get an idea on the effect of these factors. For standardization of the parameters, an exhaustive series of experiments need to be designed and performed to confirm the reliability and repeatability of the parameters.

The first experiment conducted is designed to get the cross sectional width and the depth of the crystallized region with respect to laser power and write speed. During this experiment, a Mitutoyo M Plan Apo -20x microscope objective is utilized which gives a spot size of 2 μm. After the photosensibilization, the sample is heat treated with the same procedure above. After the heat treatment step, the sample can be visually inspected to determine the crystallized region and the respective dimensions. Lines with five different power levels and four different speeds are used.

The results of the experiment are presented in Fig. 10 and Fig. 11. From these figures, it seems that the line thickness is dependent on fluence. However for different speeds at a fixed fluence, this relation changes in a power form. These results suggest that for a given laser fluence, the line thickness increases to an ultimate value with increasing number of pulses. This is pictured in Fig. 12. Some error could have been introduced in the line measurements for lower fluence levels and high write-speeds, for which the resolution of the measuring technique was not sufficient to distinguish the occurring changes.
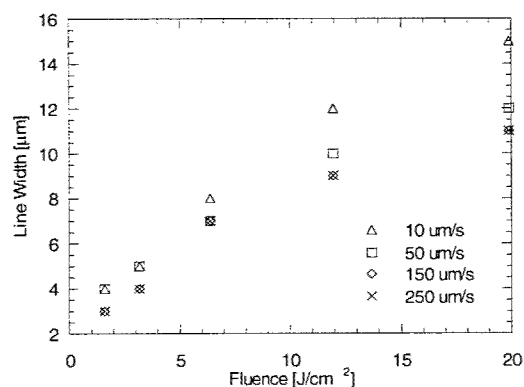
Fig.10. Line width as a function of laser fluence and write speed
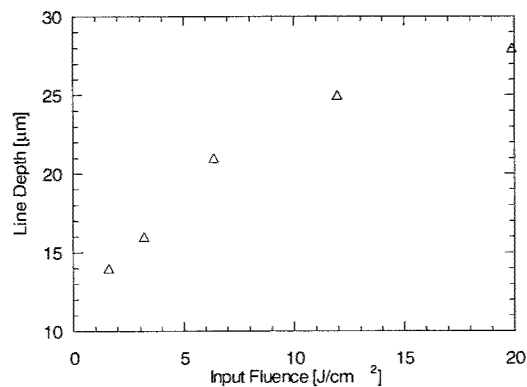
Fig. 11. Line width as a function of fluence when the speed is fixed at 50 μm/s
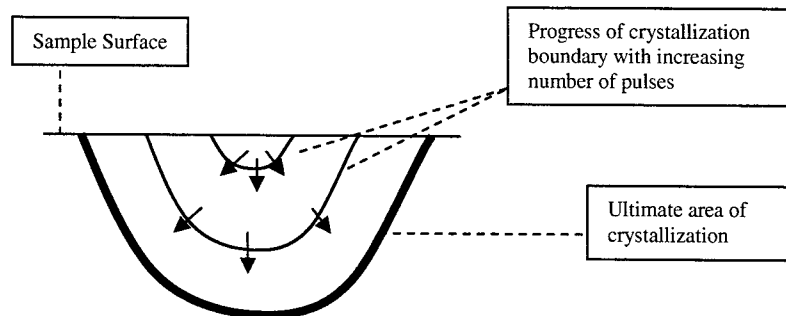
Fig. 12. The Progression of line thickness and depth.

The second experiment conducted investigated the etch depth as a function of laser photosensibilization fluence and write-speed. Results of the experiment are presented in Fig. 13. During the experiment, the samples are etched for 20 minutes and the profiles are measured using a profilometer. From these results, it can be seen that the etch depth decreases with decreasing fluence and increasing write-speed. The trend for the write-speed suggests that the longer a particular area is irradiated, i.e. more pulses per area, the deeper it etches. This is the same as observed in the excimer laser experiment, where the etch depth also increases with the number of laser pulses. Also similar to the excimer laser experiment, with higher intensity nucleation occurs in a deeper region. Therefore, using high fluence would allow higher aspect ratio features to be created.
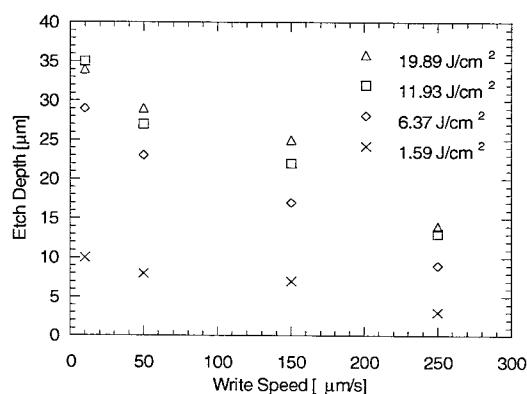
Fig. 13. Etch depth comparison for different photosensibilization fluences and write-speeds.

The etched surface quality with femtosecond laser process can be seen in Fig. 14, where a coral type of texture is observed right after etching. This type of surface is an indication of localization and not uniform distribution of nucleation cites. In order to obtain smoother etch surfaces, a second heat treatment was done on the samples. The idea was to melt the surface slightly without warping the structure. The samples were heated in an oven to 650°C for half an hour and cooled to room temperature. The surface quality of the samples before and after the second baking process can be seen in Fig. 14. Also, the Nomarski pictures of the etched unexposed sample surface before and after the second heat treatment process are shown in Fig.15. It is thought that a second laser scanning of the etch walls, without ablating, will give smoother surfaces required for micro fluidic or micro optical applications. However, for some applications, a rough surface might be beneficial, especially for coating the surfaces, where surface roughness will increase the mechanical bond strength of the coating.
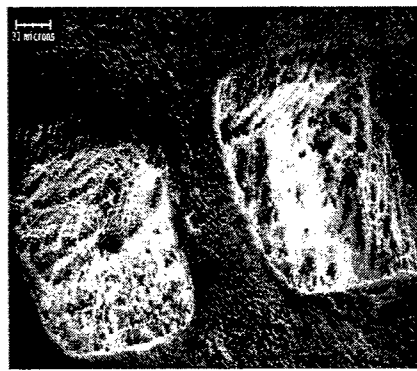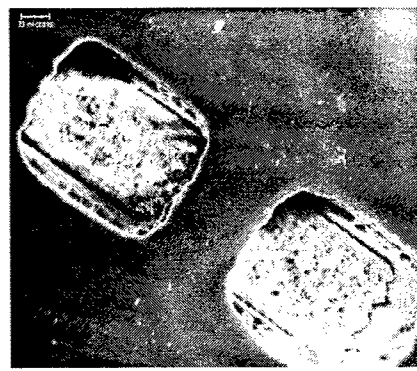
(a)   (b)

Fig. 14. SEM photos of the etched specimen with the femtosecond laser process: (a) before and (b) after the second heat treatment.
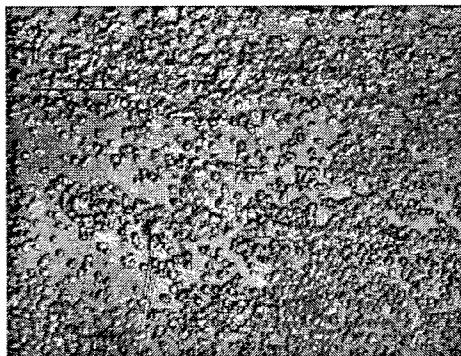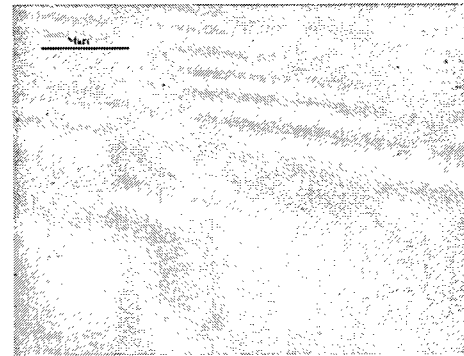
(a)   (b)

Fig. 15. Nomarski pictures of surface quality (a) before and (b) after second baking taken with 40x objective.
The length of the scale bar is 24 μm.

3D micro-structuring using femtosecond pulses is demonstrated by creating a U-shape channel in FOTURAN. After getting an understanding about the parameters involved in utilizing femtosecond pulses to structure FOTURAN, a U-shape channel was designed to demonstrating 3D machining. The dimensions of the design are given in Fig. 16. The channel was written in FOTURAN with 3.18 J/cm^2 at a speed of 50 μm/sec. These correspond to line width of 5 μm and line depth of 16.5 μm. Therefore, the digital machining program parameters were adjusted accordingly to write the U-shape channel structure. The etching is performed in 5% hydrofluoric acid (HF) solution for about 45 min. On different samples fabricated, the progress of etching is observed as presented in Fig. 17. In Fig. 17a the arms of the U-shaped channel are etched and the etching of the connecting bottom layer has not started yet. In Fig. 17b, the etching of the connecting layer is progressing. In Fig. 17c the etching of the bottom connecting layer has been completed creating the 3D U-shaped channel in FOTURAN.
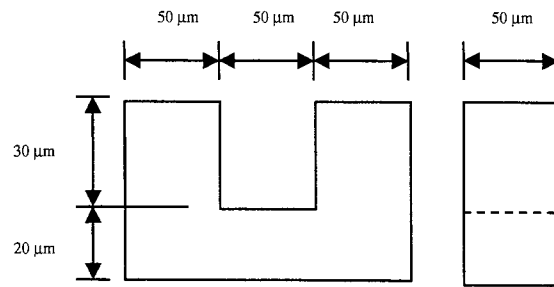
Fig. 16. The design of the U-shape-channel

(a)

(b)

(c)
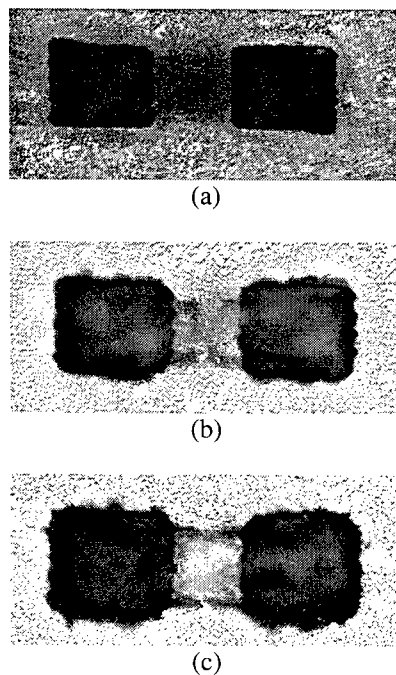
Fig. 17. Nomarski pictures of the etch progress of the U-shape channel.

4. CONCLUSIONS

We have demonstrated the laser processing characteristics of photoetchable glass-ceramic, FOTURAN, utilizing an excimer laser and a femtosecond laser. The different wavelengths of the laser demonstrated different process characteristics. The excimer laser irradiation at the wavelength of 248 nm has a very low transmissivity in FOTURAN so it is useful to fabricate micro structures on the surface. On the other hand, a very high transmissivity and multiphoton absorption of femtosecond laser irradiation in the wavelength of 800 nm make it possible to produce a 3D structure by focusing the irradiation inside the specimen. Along the way, parameters required for processing FOTURAN with excimer and femtosecond pulses are obtained. The threshold fluence and relations between fluence and crystallization dimensions were obtained.

5. ACKNOWLEDGEMENTS

6. REFERENCES

1. Y-R. Cho, J-Y. Oh, H-S. Kim and H-S, "Micro-etching technology of high aspect ratio frameworks for electronic devices," *Mat. Sci. Eng. B*, **64**, pp. 79 - 83, 1999.
2. P. Fuqua, S. W. Janson, W. W. Hansen and H. Helvajian, "Fabrication of True 3D Microstructures in Glass/Ceramic Materials by pulsed UV Laser Volumetric Exposure Techniques," *SPIE*, **3618**, pp. 213 - 220, 1999.
3. W. Hansen, P. Fuqua, F. Livingston, A. Huang, M. Abraham, D. Taylor, S. Janson and H. Helvajian, "Laser Fabrication of Glass Microstructures," *The Industrial Physicist*, June/July, pp. 18 - 21, 2002.
4. Y. Kondo, J. Qiu, T. Mitsuyu, K. Hirao and T. Yoko, "Three-Dimensional Microdrilling of Glass by Multiphoton Process and Chemical Etching," *Jpn. J. Appl. Phys.*, **38**, Pt. 2 (10A), pp. L1146 - L1148, 1999.
5. A. Marcinkevicius and S. Juodkazis, "Femtosecond laser-assisted three-dimensional microfabrication in silica," *Opt. Lett.*, **26** (5), pp. 227 - 279, 2001.
6. P. D. Fuqua, D. P. Taylor, H. Helvajian, W. W. Hansen and M. H. Abraham, "A UV Direct-write Approach For Formation of Embedded Structures in Photostructurable Glass-ceramics," *Mat. Res. Soc. Symp. Proc.*, **624**, pp. 79- 86, 2000.
7. T. R. Dietrich, W. Ehrfeld, M. Lacher, M. Kramer and B. Speit, "Fabrication technologies for microsystems utilizing photoetchable glass," *Microelectron. Eng.*, **30**, pp. 497 - 504, 1996.

Thermal and Fluid Processes of a Thin Melt Zone during Femtosecond Laser Ablation of Glass

Adela Ben-Yakar[*a], Anthony Harkin[c], Jacqueline Ashmore[c], Mengyan Shen[b], Eric Mazur[b], Robert L. Byer[a], and Howard A. Stone[c]

a Applied Physics Department, Ginzton Laboratory, Stanford University, CA, USA 94305
b Department of Physics and Division of Engineering and Applied Sciences, Harvard University, Cambridge, MA, USA 02138
c Division of Engineering and Applied Sciences, Harvard University, Cambridge, MA, USA 02138

ABSTRACT

Microfluidic channels on borosilicate glass are machined using femtosecond lasers. The morphology of the ablated surface is studied using scanning microscopy. The results show micron scale features inside the channels. The formation mechanism of these features is investigated by additional experiments accompanied by a theoretical analysis of the thermal and fluid processes involved in the ultrafast laser ablation process. These studies indicate the existence of a very thin melting zone on glass and suggest that the surface morphology is formed by the plasma pressure-driven fluid motion of the melting zone during the ablation process.

Keywords: Femtosecond, laser, ablation, microfabrication, rim, glass, borosilicate, thin film, microchannels, microfluidics

1. INTRODUCTION

Microchannels fabricated on glass have a growing importance in the miniaturization of microfluidic devices for chemical and biological micro-total-analysis systems[1-3]. In most cases, the chips are fabricated using traditional multilayer and multistep photolithographic techniques. On the other hand, laser micromachining using ultrafast pulses offers a single-step method for direct writing of microchannels on glass. Using this laser ablation technique the fabrication speed can considerably be increased and geometries with variable depth and high-aspect ratio not possible through traditional microlithographic techniques can easily be achieved.

However, detailed morphology studies[4] of the laser-machined microchannels have demonstrated that micron-size features were formed inside the channels and the walls of the ablated surfaces were not smooth. It is necessary to investigate the formation mechanism of these small surface features to control and understand the micro-machining process using ultrafast lasers. We have performed a theoretical analysis of the thermal and fluid processes involved in the ultrafast laser ablation to explain and understand the experimental observations.

2. EXPERIMENTAL RESULTS

We carried out the experiments on borosilicate glass (Borofloat™ 1.1 mm thick, Precision Glass and Optics, Ltd.). The substrates were cleaned ultrasonically with alcohol before the experiments. After the ablation, the debris was removed with a 0.5 Molar sodium hydroxide (NaOH) solution (a very weak etching for about 20 minutes) followed by an alcohol rinse in the ultrasonic bath.

---

[*] adela@stanford.edu; phone: +1 (650) 723-0161; fax: +1 (650) 723-2666

The glass samples were irradiated with 800-nm 100-200-fs pulses from a regeneratively amplified Ti:sapphire laser with the surface of the sample positioned to be normal to the direction of the incident beam. Following irradiation, the samples were analyzed with a scanning electron microscope (SEM). The laser beam was delivered to the surface by a long working distance objective lens (Mitutoya, 5x, NA=0.14) attached to a microscope. On the surface of the target, the focused beam had a Gaussian spatial beam profile with a $1/e^2$ radius of $w_0 = 5.9$ μm[4]. The experiments were performed in a vacuum chamber at pressures below 10^{-4} mbar. A continuous channel was formed by moving the sample with a scanning speed of $v_{ss} = 1.5$ mm/s at 1 kHz laser repetition rate. The average number of pulses overlapping at the same spot was $N_{eff} = 6$. The resulting channel has a width of 9.6-μm and a depth of 2.5-μm. Figure 1 shows a typical surface morphology of a microchannel produced with 200-fs pulses at an average laser fluence (energy per unit area) of 12 J/cm^{2}. The most pronounced feature of the microchannel surface morphology (Fig. 1) is related to its non-smooth walls that have a surface roughness of the order of 1-μm.

An important clue explaining the mechanism of the microfeature formation could be determined from how the glass surface responds to a single laser pulse irradiation. Figure 2 presents SEM images of a crater generated with a single 100-fs laser pulse. The center of the crater demonstrates a smooth surface profile, whereas around the crater a 50-nm tall rim is raised above the surface. A detailed visualization of the elevated rim is shown in Figs. 2b and 2c. The observations suggest that the rim is a resolidified splash of a molten layer generated during the ablation process. In ultrafast laser ablation, the rapid energy deposition to the material allows material removal before significant heating of the bulk material occurs. Still, enough energy is deposited in the undamaged part of the material to create a shallow molten zone below the ablated area. We discuss the level of the material heating and estimate the melt depth. We present characteristic time scales of various mechanisms causing the melt to flow outwards to create the rim and show representative numerical simulations of fluid flow in a thin molten layer.

3. THEORETICAL MODELING AND DISCUSSION

A theoretical model is described to characterize the detailed thermal and flow processes associated with the first laser pulse. The goal is to identify the nature of the rim formation around the laser ablated craters and suggest ways (such as modification of the laser profile) to eliminate it. To estimate the melt thickness, optical light penetration and heat conduction into the material were taken into account. A thin film model is then proposed to predict the temporal evolution of the melt surface. The amount of the melt flow to the crater edge depends on the viscosity, the thickness of the molten layer, and the pressure distribution above the surface.

3.1. Heat transfer calculations

Absorbed laser energy and its partition
To calculate the thickness of the molten layer, the partition sequence of the absorbed laser energy must be determined. Specifically, we need to know what fraction of the laser energy remains in the bulk of the material and how this energy dissipates from the illuminated regime.

Vidal et al.[5] modeled the fluid and thermal dynamics of a laser-induced plasma for an aluminum target ablated with a 100-ps laser pulse. Their numerical simulation results provide the partition of the absorbed laser energy as a function of time. Typically after a few microseconds they found that most absorbed laser energy is used to move the ambient gas (~ 70%). A significant fraction of the absorbed energy (~ 20%) is lost in radiation and a small fraction (~ 10%) of the absorbed energy remains in the target as thermal energy.

However, to estimate the partition of the absorbed laser energy in the case of femtosecond laser ablation of glass, a further complicated numerical solution is required. We propose to use an effective optical light penetration depth to estimate the fraction of the incoming laser energy which remains in the glass as the thermal energy.

Optical light penetration depth

The volume/depth, where the laser energy is deposited initially, can be calculated using the effective absorption coefficient of the material. According to the Beer-Lambert law, which provides a convenient means to quantify the penetration depth of the absorbed laser energy, light attenuates with depth z according to

$$F_a(z) = A F_0^{avg} \exp(-\alpha_{eff} \cdot z) \tag{1}$$

where A is the surface absorptivity, α_{eff} is the effective material absorption coefficient (α_{eff}^{-1} is the effective optical penetration depth), F_0^{avg} is the average laser fluence (energy per unit area), and F_a is the laser fluence absorbed by the material.

Absorptivity of fused silica when exposed to high intensity ultrashort pulses, has been numerically calculated and experimentally measured by Perry et al.[6] They have demonstrated that when the incident intensity is high above threshold, a large portion of the energy can be reflected back into the ambient gas (due to the formation of a critical plasma density early in the pulse or in other words due to the induced skin effect). The reflectance of a fused silica surface using 10^{14} W/cm^2 of laser irradiance is estimated to be around 70%. Since a similar laser irradiance level is used in the current experiments, we can assume that only 30% of the incident beam gets absorbed by glass $(A = 0.3)$.

The value of the effective optical penetration depth, α_{eff}^{-1}, for borosilicate glass can be taken from our previous studies[4]. The ablation threshold measurements yield a linear relationship between the ablation depth, h_a, and the laser fluence according to

$$h_a = \alpha_{eff}^{-1} \ln\left(\frac{F_0^{avg}}{F_{th}^{avg}}\right) \tag{2}$$

where F_0^{avg} is the average fluence of the incident beam and F_{th}^{avg} is the average ablation threshold fluence ($F_{th}^{avg} = 1.7$ J/cm^2 for borosilicate glass)[4]. The slope of the linear fit to the experimental data points provides an optical penetration depth of $\alpha_{eff}^{-1} = 224$ nm for borosilicate glass (780-nm and 200-fs laser pulses in the fluence range of $F_0^{avg} = 10 - 30$ J/cm^2).

We may assume that the absorbed laser energy that penetrates beyond the measured ablation depth remains in the material as heat. Since the laser fluence at the ablation depth is equal to $F_a(z = h_a) = A F_{th}^{avg}$, the value of the thermalized energy remaining in the material as heat is

$$E_{heat} = A F_{th}^{avg} \cdot \pi w_0^2, \tag{3}$$

where w_0 is the $1/e^2$ laser beam radius at the surface. Thus a fixed amount of laser fluence about $A F_{th}^{avg} = 0.5$ J/cm^2 will be heating the undamaged part of the material independent of the incident laser fluence in the range of $F_0^{avg} = 10 - 30$ J/cm^2. At near threshold fluences, a larger amount of energy is expected to heat the material beyond the ablation depth as the surface absorptivity increases at lower fluences[6].

Melt depth

The ultrafast laser ablation process can be separated in two independent processes: absorption of the incoming light and dissipation of the heat. Initially electrons in the conduction band are excited with the absorbed laser energy. Only after the laser pulse is gone, energy is transferred from the high energy electrons to the lattice. Within a few picoseconds the excited electrons equilibrate with the ions (lattice) before any significant energy is dissipated by the heat diffusion into the material. The resulting initial equilibrium temperature (T_{eq}) can then be calculated according to the optical penetration depth of the laser light;

$$T_{eq}(z) = \frac{F_a(z)}{\rho C} = \frac{A F_0^{avg}}{\rho C \cdot \alpha_{eff}^{-1}} \exp\left(-\frac{z}{\alpha_{eff}^{-1}}\right) \qquad (4)$$

assuming a constant heat capacity C. Melting occurs in a volume of heated material when the temperature exceeds the melting temperature (T_m). The glass transition temperature is used here as the melting temperature. Also note that the glass materials do not have a latent heat of melting. So, all the absorbed energy goes into melting.

Figure 3 shows a schematic illustration of the incident laser beam attenuation with depth and the resulting initial temperature distribution inside the glass material. When the material is illuminated with an ultrashort laser pulse, a high-temperature and high-pressure plasma is formed above the surface, presumably down to the ablation depth. The ablated material is removed by the expansion of the plasma. Below the plasma there is a thin zone of a molten glass with an initial thickness of $h_m(t=0) = 0.5$ μm, calculated using Eq. 4 (as the depth with temperature $T_{eq} > T_m$).

Following the cessation of ultrafast energy input, the melting process continues as the heat flows out of the initial light penetrated region. The speed at which the heat diffuses determines the melting front. Since the melting front moves with the heat source the heat penetration into the material will determine the variation of the melt thickness.

By taking $A F_{th}^{avg}$ as the laser fluence that remains in the part of the material that is not ablated, the heat flow out of the regime can then be calculated by solving the one-dimensional (1-D) heat diffusion equation. The cooling at the top of the melt zone is assumed to be negligible because of the presence of the high temperature plasma. During the expansion, the plasma cools from some very high initial temperature to the ambient temperature which takes place in tens of microseconds.

Assuming the heat capacity, C, the thermal conductivity, k, and therefore the thermal diffusivity, $D = k/\rho C$ to be constant we can calculate the temperature distribution in the part of the material that is not ablated. Using the one-dimensional conduction model described by Nolte et al.[7] the equilibrium temperature as a function of $\tilde{z} = z - h_a$ is

$$T_{eq}(\tilde{z}) \cong \frac{A F_{th}^{avg}}{\rho C} \frac{1}{l^2 - \delta^2}\left[l \exp\left(-\frac{\tilde{z}}{l}\right) - \delta \exp\left(-\frac{\tilde{z}}{\delta}\right)\right] \qquad (5)$$

where $l = \sqrt{D \cdot t}$ is the heat penetration depth and $\delta = \alpha_{eff}^{-1}$ is the optical penetration depth. Note that the temperature distribution at $t=0$ is exactly the initial temperature distribution calculated previously according to the Beer-Lambert law. The variation of the melt depth can then be calculated as a function of time using Eq. 5.

Figure 4 presents a plot of melt depth variation with time for two different laser fluences thermalized in the material as heat; $F_{heat} = A F_{th}^{avg} = 0.5$ and $F_{heat} = A F_{th}^{avg} = 1.0$ J/cm^2. The melting process continues briefly for 1-3 μs and then solidification begins. These calculations provide us an estimate for the order of magnitude of two important characteristic scales of the melt zone:

1. Characteristic melt depth h_m (or h_0) of the order of 1 μm.
2. Characteristic melt life time τ_m of the order of 5-10 μs.

3.2. Fluid dynamics calculations

Thin film model
Here we treat a one-dimensional model of the fluid motion, which should be a good approximation since the molten layer has a depth much smaller than its radius. The free surface of the molten fluid is described by $z = h(x,t)$ and the lubrication approximation can be used to describe the fluid motion. The evolution equation is

$$h_t + \frac{\partial}{\partial x}\left(\frac{\gamma_x h^2}{2\mu} - \frac{dp}{dx}\frac{h^3}{3\mu}\right) = 0 \tag{6}$$

where μ is the viscosity, γ is the surface tension, and $p(x)$ is the time independent pressure of the plasma above the free surface. We have neglected the capillary contribution in the last term since this would only be important at late times when larger curvatures form. Also, because of the complicated dynamics of the plasma, for this initial modeling we assume that the plasma pressure field at the liquid surface is independent of time. When a temperature distribution, $T(x)$, is imposed along the surface, then

$$\gamma_x = \frac{d\gamma}{dx} = \frac{d\gamma}{dT}\frac{dT}{dx}. \tag{7}$$

If $\gamma_T = d\gamma/dT$ is constant and we neglect temperature effects on the viscosity, then we have

$$h_t + \underbrace{\frac{\gamma_T}{2\mu}\frac{\partial}{\partial x}\left(T_x h^2\right)}_{\text{Marangoni flow}} - \underbrace{\frac{1}{3\mu}\frac{\partial}{\partial x}\left(\frac{dp}{dx}h^3\right)}_{\text{pressure-driven flow}} = 0. \tag{8}$$

The first term accounts for the surface tension gradients (Marangoni flow) due to the uneven heating of the surface and the second term accounts for the motion due to the pressure gradients exerted by the plasma onto the molten material. Characteristic time scales associated with the Marangoni flow and the pressure-driven flow are

Marangoni flow:
$$\tau_M \sim \frac{\mu L^2}{|\gamma_T|T_m h_0} \tag{9}$$

Pressure-driven flow:
$$\tau_p \sim \frac{\mu L^2}{p_0 h_0^2} \tag{10}$$

where $|\gamma_T|$ is the absolute value of the temperature coefficient of surface tension, h_0 is an average melt depth, L is a typical radial dimension, and p_0 is an average plasma pressure. The values of material properties of borosilicate glass are summarized in Table 1. For an average melt depth of $h_0 \approx 1\,\mu\text{m}$ as estimated in the previous section and an average plasma pressure of $p_0 \sim 100$ atm (typical plasma pressure drops from millions of atmospheres to about ~20 atm during the first 200-ns of its expansion[8]) we obtain

$$\frac{\tau_M}{\tau_p} = \frac{|\gamma_T|T_m}{p_0 h_0} \approx 0.5 \times 10^3. \tag{11}$$

The characteristic time scale for Marangoni flow is two to three orders of magnitude longer than the one for the pressure-driven flow. It is clear from this estimate that the plasma pressure above the free surface acts to move the fluid much more quickly than surface tension. This suggests that once an expanding plasma is formed above the glass surface during a laser ablation process of glass, the spatially varying plasma pressure will control the evolution of the free surface at the interface. In the context of laser texturing of silicon surfaces in the absence of ablation, however, the pump formation was attributed to the Marangoni flow in thin films created by nanosecond laser pulse heating[9].

Furthermore, the surface tension coefficient of borosilicate glass is positive in contrast to the normally observed negative values of most pure liquids. This means that the thermocapillary flow (Marangoni flow) in laser irradiated glass surfaces would actually drive fluid from the cold periphery to the hot center of the melt. Therefore, if the thermocapillary forces would act faster, a competition would have existed between the pressure gradients pushing on the surface and the thermocapillary forces.

After identifying that the effect of the thermocapillary flow is negligible during a laser ablation process, the surface evolution equation can be simplified to:

$$h_t - \frac{1}{3\mu}\frac{\partial}{\partial x}\left(\frac{dp}{dx}h^3\right) = 0 .\tag{12}$$

If the bottom substrate of the molten fluid is not flat and given by $z = b(x,t)$ the evolution equation for the surface of the fluid becomes

$$h_t - \frac{1}{\mu}\frac{\partial}{\partial x}\left[\frac{dp}{dx}\frac{(h-b)^3}{3}\right] = 0 .\tag{13}$$

Nondimensionalizing the time, length, height, and pressure by characteristic values

$$t \to \tau_p t', \qquad x \to Lx', \qquad h \to h_0 h', \qquad b \to h_0 b', \qquad p \to p_0 p' \tag{14}$$

leads to the following nondimensional equation

$$h_t' - \frac{\partial}{\partial x'}\left(\frac{dp'}{dx'}\frac{(h'-b')^3}{3}\right) = 0 .\tag{15}$$

Numerical simulation results

Numerical calculations of Eq. 15 are performed on an unbounded domain for a pressure distribution given by $p = \exp(-x^{10})$ which approximates closely a top hat profile that should be a reasonable approximation to the plasma pressure. The initial interface between the plasma and the melt is shaped and the molten layer has the same thickness as the ablation depth. The initial shape of the free surface initially is assumed to be $h(x) = 1 - 0.5\exp(-15x^{10})$ and the shape of the bottom substrate is described by $b(x) = 0.9 - 0.8\exp(-x^{10})$. The results, presented in Fig. 6, indicate that a rather tall rim (at the height of $0.25h_0 \approx 250\,\text{nm}$) develops for a pressure-driven flow within a short time $t = 8\,\mu\text{s}$ (we have assumed $L = 10\,\mu\text{m}$). There is a clear consistency between the rim formation time scale and the melt life time. This provides an indication that the rim is formed by the pressure gradient of the plasma within the life-time of the melt.

From the characteristic time scale, τ_p, (Eq. 10) one can identify the parameters that might effect the rim formation. One of the parameters is the melt thickness. A thinner melt zone will slow down the rim formation, and may even eliminate it.

4. CONCLUSIONS

The morphology of the single-shot ablated areas revealed a smooth and shallow crater surrounded by an elevated rim. From these experimental observations, conclusions could be drawn on the ablation mechanism of borosilicate glass. We argued that a very thin melt zone existed during the ablation process and calculated the thermal and flow properties of this thin melt zone. In these calculations, several characteristic time constants associated with ablation, melting, and flow processes were determined. The comparative values revealed that fluid would have enough time to move from the center of the melted region (the center of the crater) to the edge by way of a pressure-driven flow depositing a thin rim around the ablated area, where the origin of the pressure gradient is the high pressure above the surface.

ACKNOWLEDGEMENT

REFERENCES

1. D. J. Beebe, G. A. Mensing, and G. M. Walker, "Physics and applications of microfluidics in biology." *Annu. Rev. Biomed. Eng.* **4**, p. 261-286, 2002.
2. J. Voldman, M. L. Gray, and M. A. Schmidt, "Microfabrication in biology and medicine." *Annu. Rev. Biomed. Eng.* **1**, p. 401-425, 1999.
3. N. Giordano and J.-T. Cheng, "Microfluidic mechanics: progress and opportunities." *J. Phy.: Condens. Matter* **13** R271-R295
4. A. Ben-Yakar and R. L. Byer, "Femtosecond laser micromachining of microchannels on borosilicate glass." *Submitted for publication to J. of Appl. Phys.*, 2002.
5. F. Vidal, S. Laville, B. Le Drogoff, T. W. Johnston, M. Chaker,O. Barthélemy, J. Margot, M. Sabsabi, " Modeling of ablation plasmas for various laser pulse lengths." *From presentation in the Annual meeting of OSA*, Long Beach, CA, 2001.
6. M. D. Perry, B. C. Stuart, P. S. Banks, M. D. Feit, V. Yanovsky, and A. M. Rubenchik, "Ultrashort-pulse laser machining of dielectric materials." *J. of Appl. Phys.* **85** (9), p. 6803-6810, 1999.
7. S. Nolte, C. Momma, H. Jacobs, A. Tunnermann, B. N. Chichkov, B. Wellegehausen, and H. Welling, "Ablation of metals by ultrashort laser pulses." *J. Opt. Soc. Am. B* **14** (10), p. 2716-2722, 1997.
8. F. Vidal, S. Laville, T. W. Johnston, O. Barthelemy, M. Chaker, B. Le Drogoff, J. Margot, M. Sabsabi, "Numerical simulations of ultrashort laser pulse ablation and plasma expansion in an ambient air." *Spectrochimica Acta Part B*, **56**, p. 973-986, 2001.
9. T. Schwarz-Selinger, D. G. Cahill, S. C. Chen, S. J. Moon, and C. P. Grigoropoulos, "Micron-scale modifications of Si surface morphology by pulsed-laser texturing", *Physical Review B*, **64**, pp.155323, 1999.
10. W. D. Kingery, "Surface tension of some liquid oxides and their temperature coefficients", *J. Am. Cerm. Soc.*, **42**, pp. 6-10, 1959.

Table 1: Properties of borosilicate glass (Borofloat©) with chemical composition of 81% SiO_2, 13% B_2O_3, 2% Al_2O_3, and 4% Na_2O.

Properties	Symbol	Units	Values
Density	ρ	kg/m^3	2.23×10^3
Melting temperature	T_m	K	1500
Viscosity	μ	Pa $\cdot$ s	$\approx 10^3$ at $T_m = 1500$ K $\approx 10^2$ at $T = 2000$ K
Surface tension	γ	J/m^2	0.28 [10]
Temperature coefficient of surface tension	$\partial \gamma / \partial T = \gamma_T$	N m^{-1} K^{-1}	$+3.4 \times 10^{-5}$ [10]
Thermal conductivity	k	W m^{-1} K^{-1}	1.25 (at 300 K) 1.6 (at 600 K)
Specific heat	C	J kg^{-1} K^{-1}	1000 (at 600 K)
Thermal diffusivity	$D = k/\rho C$	m s^{-2}	7.2×10^{-7} (at 600 K)
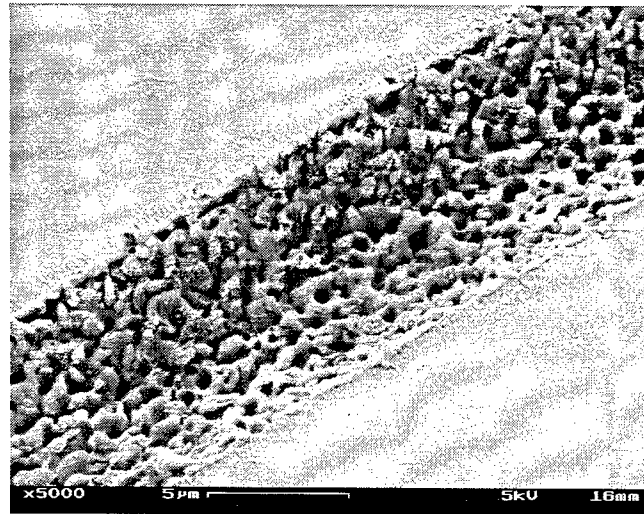
Figure 1: Surface morphology of a microchannel fabricated on borosilicate glass using 800-nm and 200-fs laser pulses. The channel is about 9.6-μm wide and about 2.5-μm deep. The effective number of overlapping pulses was about $N_{eff} = 6$ and the average laser fluence was 12 J/cm^2.
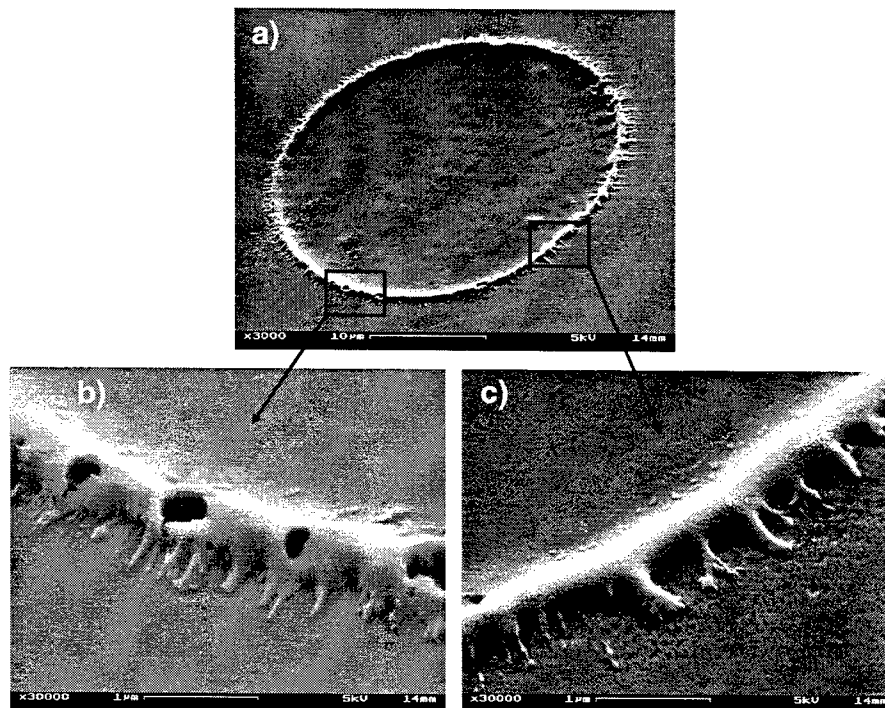
Figure 2: SEM images of a crater generated with a single laser pulse. (a) The whole crater at 3000× magnification and (b,c) two higher resolution SEM images (30,000× magnification) focused on the rim formed around the crater. The laser fluence was $F_0^{avg} = 34$ J/cm^2.
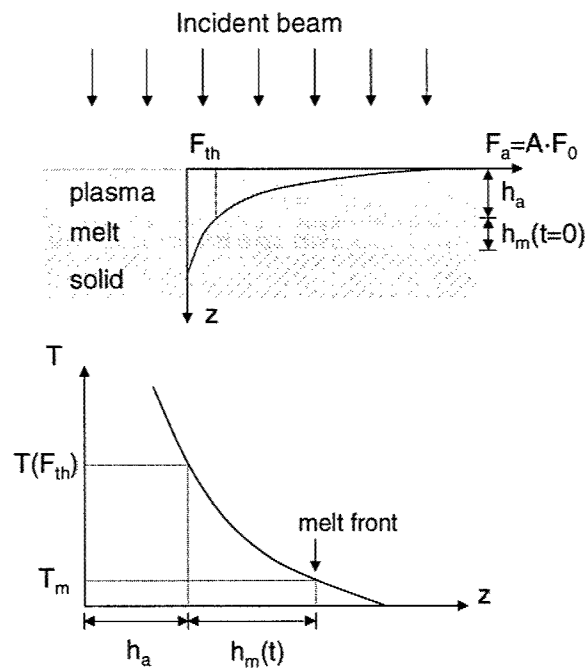
Figure 3: Laser absorption according to Beer-Lambert law and the resulting initial temperature distribution inside the material.
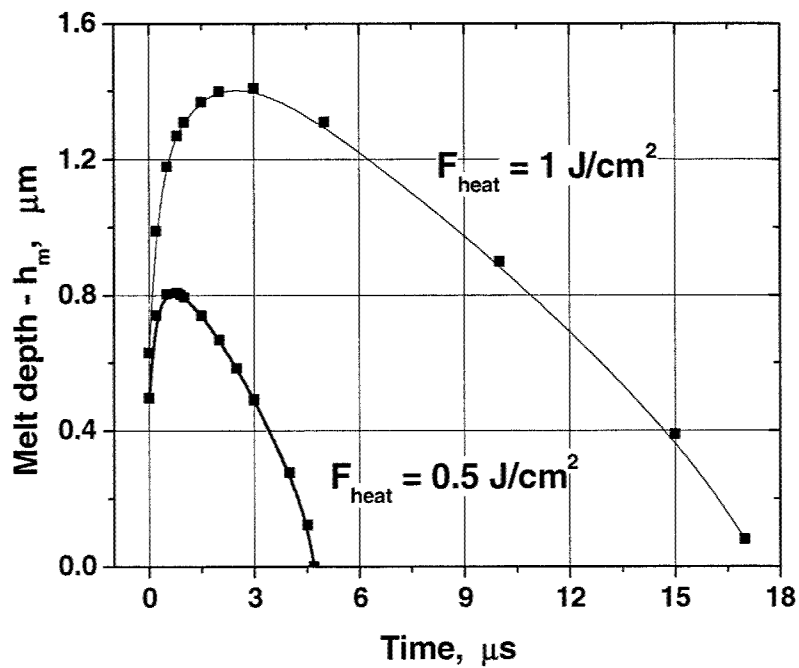
Figure 4: Calculated values of the melt depth variation with time for two different laser fluences that remain in the target (borosilicate glass) as thermal energy.
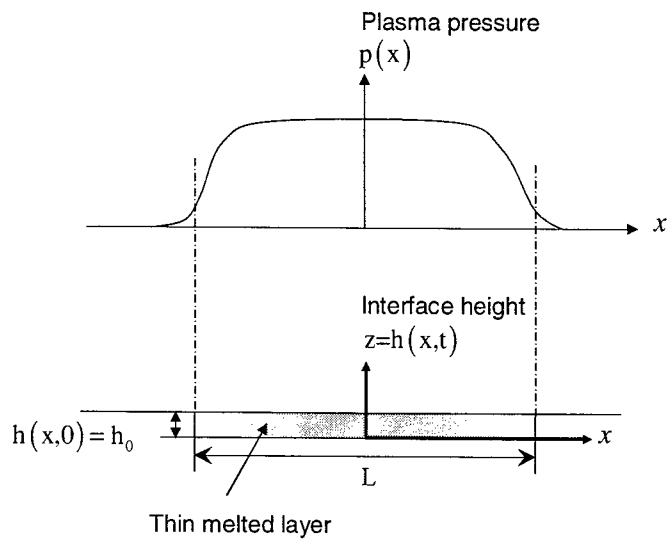
Figure 5. Description of parameters used in the thin film model to calculate the free melt surface evolution.
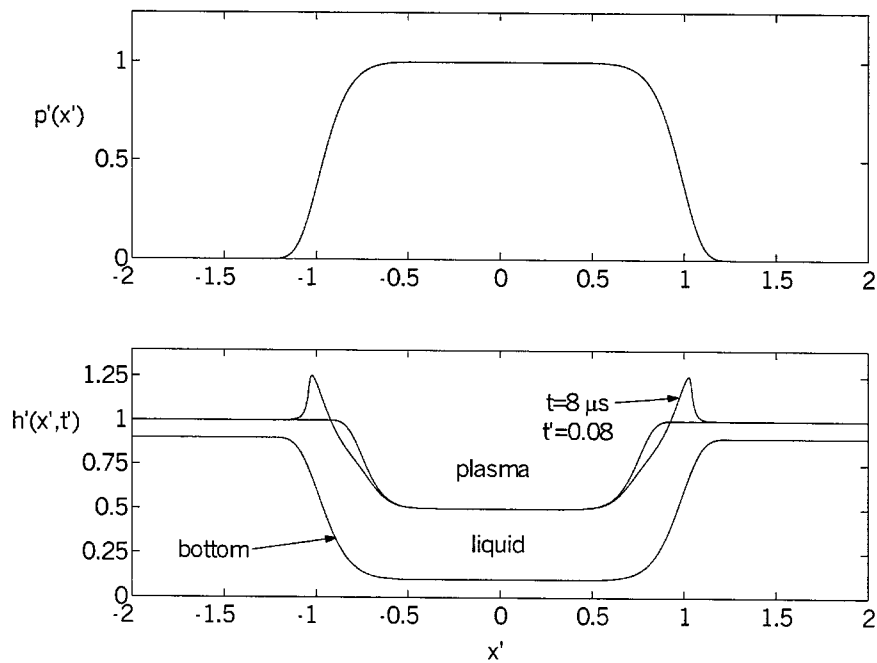
Figure 6. Numerical solution of pressure driven melt flow (Eq. 15) for a crater with a shaped bottom. The plasma pressure is shown in the top plot and is given by $p'(x') = \exp(-x'^{10})$. The bottom plot shows the evolution of the free surface at $t = 0$ and 8 μs. The crater is only half full of liquid (the rest got ablated).

Direct laser-assisted processing of polymers for micro-fluidic and micro-optical applications

W. Pfleging, J. Böhm, S. Finke, E. Gaganidze, Th. Hanemann, R. Heidinger, K. Litfin

Forschungszentrum Karlsruhe, Institute for Materials Research

P.O. Box 3640, D-76021 Karlsruhe, Germany

ABSTRACT

In the microscopic world the need of functional prototypes increases, e.g. as a precondition for a mould insert fabrication for micro-injection moulding. In this work the direct fabrication of prototypes made from polymers with an accuracy down to the micrometer range will be presented. For this purpose the direct patterning or modification of polymers with UV-laser radiation is performed for applications in fluidic and micro-optics. Different UV laser sources such as excimer and frequency-multiplied Nd:YAG were used.

In the case of complex designs for fluidic applications it is powerful to use Nd:YAG laser radiation as patterning tool because of their high laser repetition rates: CAD data from complex fluidic designs were transmitted directly via CAM module into the polymeric surface. Because of the very small laser pulse duration of about 400-500 ps the thermal-induced damage during ablation decreases significantly. Process parameters, ablation rates and attainable surface qualities for capillary-electrophoreses chips will be presented.

With the aid of a motorised aperture or a rotating mask system, excimer laser radiation is used to enable a well defined patterning of grooves with sharp edges and smooth sidewalls. The direct ablation of polymethylmethacrylate (PMMA), as well as the laser induced modification of the polymeric chemistry is used for the preparation of passive integrated-optical waveguides. Two types of concepts of waveguides are discussed: 1. Laser patterned grooves are filled with index matched materials which leads either to an increase or a decrease of the refractive index relative to pure PMMA. 2. Localised laser-induced polymer modification leads immediately to an integrated waveguide with higher refractive index. Both types of waveguides-concepts are characterised by their optical properties, which will be discussed in detail.

Keywords: excimer, Nd:YAG, rapid manufacturing, polymer ablation, polymer modification, polymer waveguides, refractive index variation, micro fluidic, micro optics

1. INTRODUCTION

The microsystem technology (MST) market is characterised by rapidly changing requirements regarding lower production costs, decreasing lead times and increasing accuracy of products. For the immediate future up to 2015 main fields of MST-applications will be in the powerful expanding sectors of IT peripherals, life science, telecommunications, automation, automotive and environmental monitoring [1]. Currently most of the established products like sensors or actuators are silicon based, but the non-silicon microcomponents or microsystems, especially the polymer ones, enter market. Conventional methods for the production of microoptical and microfluidical components include microstructuring mainly by etching. Depending on the materials used, e.g. silicon, glass or polymers, etching is often a time consuming and labour intensive procedure. The techniques of rapid prototyping (RP), rapid tooling (RT) and rapid manufacturing (RM) are increasingly used in MST in order to adapt the processes to the aforementioned requirements. In particular the LIGA technique, developed in the mid-eighties at the Forschungszentrum Karlsruhe GmbH, allows for the economic mass production of microstructured components with large aspect ratios (height to width), structural details in the submicron range and a precision better than 2 microns in the final plastic product [2-5]. LIGA is a German acronym and stands for lithography with x-ray synchrotron radiation, electroplating (German: *Galvanoformung*) and moulding (German: *Abformung*) using different replication processes like reaction moulding, hot embossing or injection moulding [6]. On the other side, the layer manufacturing techniques such as stereolithography are being developed [7], and exhibit the capability of producing MST devices. However, there are still limitations regarding the materials (curing) and constrains regarding the feature sizes and accuracy. It is though that the combination of layer manufacturing and laser ablation could be a suitable alternative for micropatterning of polymers and other materials. In addition the laser can be used to locally modify optical, electrical or

---

*Correspondence: Email: wilhelm.pfleging@imf.fzk.de Fax: ++49-7247-82-7288

mechanical properties.

Besides the above mentioned fields of application, microoptics and microfluidic in bio-analytics, are of particular interest [8,9]. In this paper new approaches to laser-assisted processes for applications in microfluidics, i.e. Capillary Electrophoresis (CE-) Chips, and microoptics, i.e. integrated monomode waveguides, will be presented. The use of new mask techniques for direct laser patterning as well as the use of new laser radiation sources for laser induced material modifications are being discussed.

2. THEORETICAL BACKGROUND

2.1 Laser ablation – polymer selection

UV laser radiation is often used for direct micropatterning of polymers. The interaction between the UV laser radiation and the material can generally be described as a combination of a pyrolytical and a photolytical process [10]. The pyrolytical process is characterised by an increased amount of debris formation and a significant thermal damage of the polymer. Therefore the dominating mechanism should be the photolytical. The non-thermal contribution can be enhanced by two technical measures: increasing the laser photon energy and/or decreasing the laser pulse duration. Typical UV laser radiation sources are excimer and frequency tripled (3ω) and quadrupled (4ω) Nd:YAG.

Photolytical ablation is based on direct bond breaking of e.g. C-C, C-O or C=C groups or the laser excitation of so called "chromophores". The bond breaking is determined by the wavelength used [11]. The strength of the C-C bond is of about 3.6 eV, which is in the range of the wavelength of the 3ω Nd:YAG laser. The 3ω Nd:YAG operates at 355 nm and 4ω Nd:YAG laser at 266 nm. Ablation is carried out by focusing the laser beam onto the surface, whereby the intensity distribution is Gaussian. In addition to the solid state lasers, excimer lasers also operate in the UV wavelength range. In contrast to Nd:YAG laser radiation, the excimer laser beam shows a flat top intensity distribution. This requires the use of masks and enables the formation of μm-sized structures. The work described in this paper was performed with KrF (248 nm) and ArF (193 nm).

For the UV-laser assisted direct fabrication of CE-Chips different types of polymers as possible materials were investigated, e.g. polyetheretherketone (PEEK), polysulfone (PSU), polyimide (PI) and polymethylmethacrylate (PMMA). These materials are of industrial interest. PEEK, PSU and PI are good absorbers for KrF excimer laser radiation as well as for 4ω Nd:YAG laser radiation. For microoptics as well as for microfluidics the use of PMMA is one of the most wanted materials. In general good surface qualities are necessary for both application field. Therefore the direct laser-assisted patterning of PMMA is only reasonable with rather low wavelengths and thus requires the use of ArF-excimer or F_2-excimer (157 nm) laser radiation. With respect to an economic process, the use of ArF-excimer is preferred. Besides the direct patterning via ablation, the localised modification of the outer surface of PMMA, i.e. the increase of refractive index n, is of fundamental interest and is performed for the fabrication of integrated monomode waveguides. Direct patterning of PI with 3ω Nd:YAG laser radiation is investigated for the for the direct fabrication of CE-Chips as well as for the fabrication of polymeric mould inserts which is described elsewhere in more detail [12].

2.2 Microfluidical Components

Conventional microfluidic devices (e.g. Lab on Chip devices) are usually made of glass, silicon or quartz [13]. They are used for biological and chemical analysis. CE-Chips for example enable the handling of small volumes of liquids (10^{-9}-10^{-12} l) which is necessary for separation and detection operations. Micropatterning of Si based components requires wet chemical etching which is limited by restriction regarding the crystallographical orientation. Another drawback is the amount of processing steps (polymer coating, baking, lithography, etching, stripping,...) which have to be performed. In order to ensure the performance, microfluidic devices require a high level of cleanness. Therefore disposable components can be seen as an economical alternative. Processing times and cost can be significantly decreased by using polymers [13].

Polymers can easily be patterned in a one step process (laser ablation) and also be economically replicated by micro injection moulding techniques. Since there are no restriction with respect to the crystallographical orientation, the flexibility of new structural design increases dramatically and due to the low costs disposable components can be produced.

2.3 Microoptical Components

Currently there is a strong demand for refractive index adjustable polymers with improved transmission properties in the visible and NIR range. In the first one only PMMA (n=1.491), polycarbonate (PC, n=1.584), cycloolefinic copolymers (COC, n=1.53) and certain polyesters (n=1.55-1.56) show optical transmission in the visible around 90% or better. A large refractive index mismatch between plastic optical fibres or polymer waveguides and fused silica (n=1.46) or semiconductor

based optoelectronic devices (n > 2) results in an enhanced fresnel coupling loss. Therefore an adjustment of the polymer's refractive index should reduce the total optical loss in a microoptical system.

The basic principle of the wave propagation in waveguides is the total internal reflection. The lightwave is propagated if the angle of incidence i with respect to the normal to the core-cladding interface exceeds the critical angle i_c given by $\sin i_c = n_{cladding}/n_{core}$, where $n_{cladding}$ and n_{core} are refractive indices of cladding and core materials, respectively and $n_{cladding} < n_{core}$. The coupling to the waveguide from the external source (optical fibre) through the medium with a refractive index n_0 is realized if the light beam is confined within the numerical aperture of the waveguide defined by $NA = n_0 \sin\theta_m = (n_{core}^2 - n_{cladding}^2)^{1/2}$ determining a maximal acceptance angle θ_m with respect to the waveguide axis. At a given wavelength λ a condition for the monomode operation of the waveguide is expressed by a parameter $V=(2d/\lambda)NA<1$ with d being the waveguide dimension. Consequently waveguide dimensions d and refractive index differences $\Delta n = n_{core}-n_{cladding}$ need to be small for monomode waveguide operation (for $n_{core} = 1.5$, and $\Delta n = 0.005$ the needed waveguide dimension is as small as $d \approx 6 \mu m$ at the telecommunication wavelength @1550 nm).

In this work we studied two different strategies for the production of monomode waveguides: direct writing of grooves in polymers with diameters and depth up to 10 μm and subsequent filling with index matched materials; localised laser-induced modification of polymer surface leading to an increase of refractive index.

3. EXPERIMENTAL PROCEDURE

3.1 Laser parameters - ablation

The excimer laser ablation is performed with a laser micromachining system (Exitech PS2000) which operates with a Lambda LPX 210i as radiation source. Different mask techniques are used in order to obtain the desired pattern. Direct optical imaging by using complex mask structures or motorised masks are established. Furthermore, a motorised rotating mask is used which enables the creation of complex structures with high precision. The desired geometry is unwound to the circumference of the mask and it rotates with a determined velocity. Depending on the desired overlap the work piece velocity is synchronised to that of the mask. This procedure enables the production of rather complex structures in a continuous process, which eliminates start-stop problems. This mask technique is used for the patterning of large complex structures. Another technical option is the use of a motorised aperture mask. The CAD data can be directly transmitted into the polymeric surface. The aperture consists of four independent shields which can be positioned with μm accuracy. This mask technique is a precise processing technique for the fabrication of well defined groove structures such as curved grooves and grooves with a variation of cross section. This flexible technology is a scanning technology ("direct laser writing") and needs no additional masks, but the processing time may be long compared to the direct optical imaging of a large mask geometry. The best attainable surface roughness during excimer laser patterning may be in the in the range of R_a=50-60 nm [14]. This is an excellent condition for the laser-assisted fabrication of integrated monomode waveguides and CE-Chips. Figure 1 shows an example of a CE-Chip design.
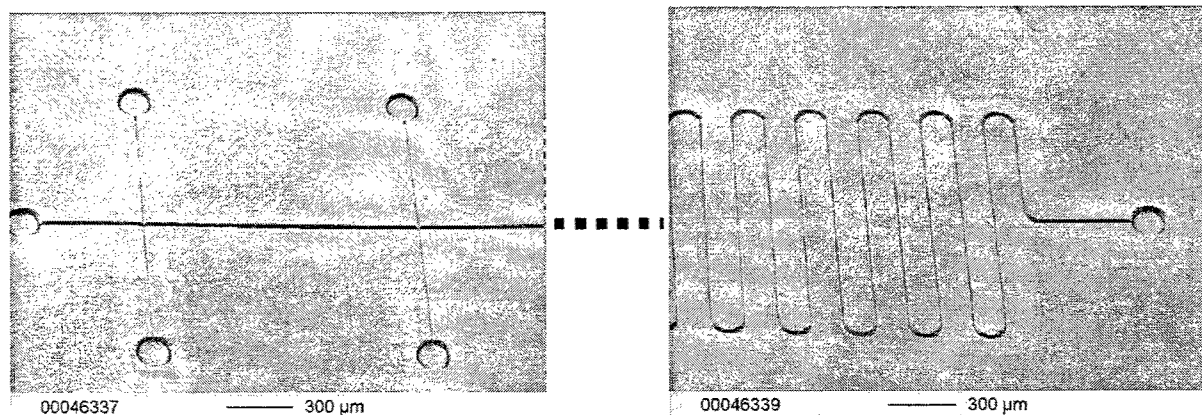

Figure 1: Examples of CE-Chip designs (Design from Greiner Bio One GmbH, FRG) produced in PI by laser ablation via direct writing (3ω Nd:YAG).

Because of small laser repetition rates (<100 Hz) the scanning process may be too slow. In this case it might be a better option to use a 4ω or 3ω Nd:YAG laser where repetition rates up to 2000 Hz are possible. This could cause a reduction of

processing time of more than one order of magnitude. First investigations on polymer ablation and modification of PMMA were carried out with a PowerChip Nano UV (JDS Uniphase) with a pulse width of about 400-500 ps and a pulse energy of about 10-20 µJ. The high laser fluence of >40 J/cm² enables polymer ablation as well as ablation and drilling of glass, steel and ceramics. Because of the small pulse width a significant reduction of thermal contribution in the ablation processes was expected.

3.2 Methods of refractive index matching
3.2.1 Laser assisted modification
As recently shown by other work groups [15], UV laser radiation can be used for the modification of the optical properties of PMMA. In our studies the refractive index was increased locally by either using a contact mask technique or scanning a pre-determent area with a focused laser beam. The PMMA specimens used were characterised by an initial refractive index of 1.491. Modification was then carried out using excimer and Nd:YAG lasers operating at wavelengths of 193 nm, 248 nm and 266 nm. The total number of laser pulses, which is directly related to the photon dose, varied between 1000 and 12000 pulses. The experiments were carried out at laser fluence of 6-17 mJ/cm². and laser repetition rates of about 5 Hz, 10 Hz (excimer) and 1500 Hz (4ω).

3.2.2 Filling with nano-sized ceramics
Different strategies can be pursued a refractive index modification. A polymer synthesis should allow for a tailoring of the optical properties depending on the used monomeric synthons (homopolymer, copolymer, blockpolymer, etc.). A further cross-linking between the polymer chains should increase the density and as a consequence the refractive index. Furthermore, the method described here uses nano-scaled ceramics with large intrinsic refractive indices and average particle sizes smaller 40 nm, i.e. $\lambda/10$ of the visible range. Mie and Rayleigh scattering of the particles should be hindered due to the small particle sizes.

The discussed nano-sized particles are listed in Table 1. The primary particle diameters range between 7 and 30 nm. Due to the large surface area an enhanced agglomeration is expected. In case of soft agglomeration improved stirring methods can desagglomerate the larger particles.

Filler	Ø d50 [nm]	n	Type & manufacturer	Filler	Ø d50 [nm]	n	Type & Manufacturer
ZrO_2	30	2.20	VP-Degussa	Aerosil 90	20	1.45	Degussa
Al_2O_3	13	1.76	C-Degussa	Aerosil 200	12	1.45	Degussa
				AerosilR8200	7-14	1.45	Degussa

Table 1: Used nano-sized fillers.

Generally the reactive resin Plexit55 (35wt% PMMA solved in MMA) is further thinned with MMA monomers (ratio Plexit55:MMA = 8:2) to reduce viscosity and simplify the stirring process. A reasonable way to characterize these nano-powders is to evaluate high resolution pictures from the Transmission Electron Microscope. Furthermore, the structure (high or low), the allocation of agglomerates and there the rate of dispersion can be determined. Another way to examine the structure and the free surface of the filler particles is the application of an Atomic Force Microscope, which will be used in the course of filler characterisation.

3.3 Methods of optical characterisation
Light transmission characteristics are typically determined by measurements of signal amplitudes [16]. An instructive indicator for the guiding properties are near-field patterns registered at the end of the waveguide component with an infrared camera. Quantitative information is generally obtained with narrow line lasers and broadband detectors or by broadband sources with filtering at the detection branch.

As signal transmission measurements yield an effective attenuation which includes coupling losses at the fibre to waveguide interfaces (reflection, limited acceptance angles) as well as scattering and absorption in the waveguides, it is convenient to characterise the performance of the components by the insertion loss defined as the logarithmic ratio of the power at the output fibre relative to the input fibre, i.e. insertion loss [db]: $10 \cdot \log(P_{out}/P_{in})$.

The advent of tuneable laser sources with low source spontaneous emission (SSE) allow fast amplitude measurements with a high dynamic range and wide sweep intervals. Combining these sources with interferometric systems bear the additional potential of simultaneous amplitude and phase measurements and give access to polarisation dependent loss and wavelength dependent signal delay [17]. As 'Photonic All-Parameter Analysers' are not yet standard characterisation equipment, the determination of the effective optical properties of (modified) waveguide materials are commonly determined by inspections of slap-size specimens which provide larger areas with homogeneous optical properties. Common methods are m-line spectroscopy and local transmission measurements.

Optical characterisation of the planar polymer waveguides with respect to insertion and coupling losses is carried out by means of the commercially available Wavelength Domain Component Analyser (WDCA) Agilent 86082A (figure 2). The system is a combination of a tuneable laser source (TLS) operating in a wide wavelength range 1495 nm $<\lambda<$ 1639 nm and a multi-channel Optical Spectrum Analyser (OSA). High wavelength resolution of 1 pm and high dynamic range of 65 dB allow precise quantification of the losses. The planar polymer waveguide is fixed to a sample holder, whereas the both FC/PC connectors terminating the input and output single-mode fibres (standard 9/125 µm) are manually positioned by a five axes $XYZ\Theta\Psi$-alignment system in order to obtain maximum transmitted signal. The losses of the optical line (launching optics: fibres, connectors, adapters) are calibrated before each measurement, so the insertion loss is directly measured by the WDCA.

Extinction loss of polymer plates is measured in a wide wavelength range by means of commercially available VIS (380 nm $<\lambda<$ 1000 nm) and NIR (1100 nm $<\lambda<$ 1750 nm) spectrometers. For large area illumination of the polymer plates the input and output fibres are terminated by gradient index (GRIN) lenses yielding beam spot diameters of ~400 µm.
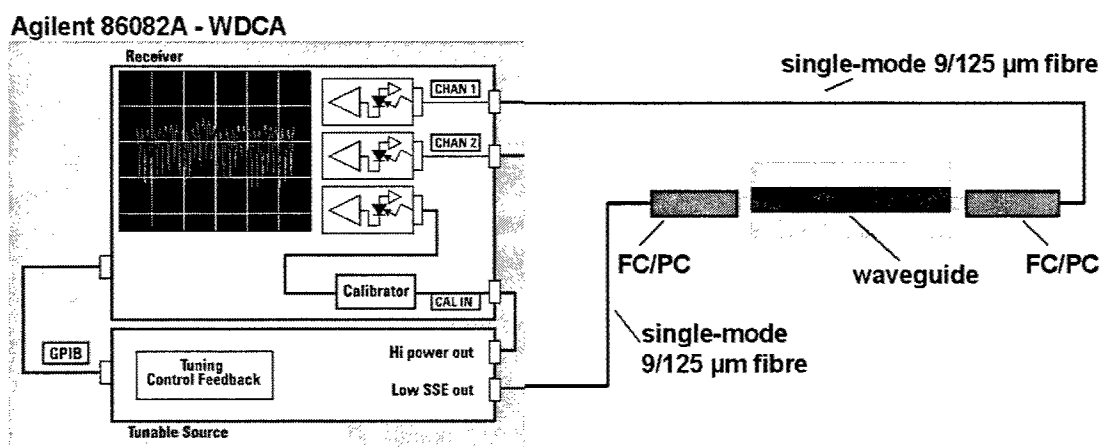
Figure 2: Experimental set-up for optical characterisation of planar polymer waveguides. The waveguide is fixed on the sample holder, whereas the both FC/PC connectors are positioned by a five axes $XYZ\Theta\Psi$-alignment system.

4. RESULTS AND APPLICATIONS

4.1 Laser ablation - fabrication of polymeric CE-Chips

For the fabrication of small grooves with well defined depth and surface quality the appropriate laser fluence, pulse overlap during scanning and laser wavelength had to be determined. First the laser ablation rates for PMMA were determined using the excimer laser operating at 193 nm and 248 nm as well as for the 3ω and 4ω Nd:YAG laser operating at 355 nm and 266 nm respectively. The results are summarised in figure 3. The surface roughness was determined by profilometry and is also shown in the graphs.
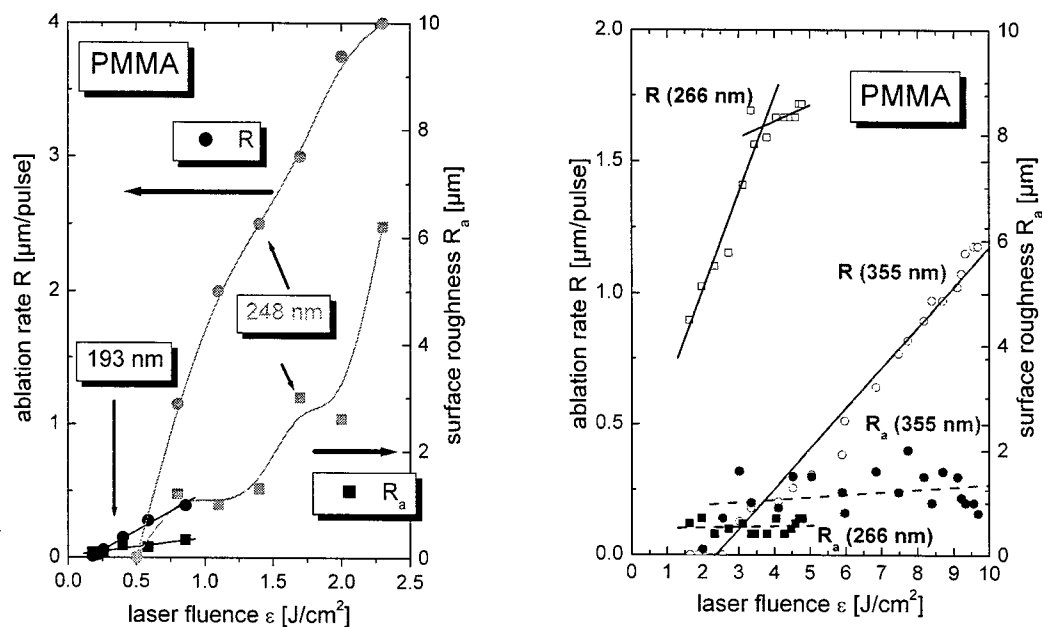
Figure 3: Ablation rate and surface roughness of PMMA as function of laser fluence for different wavelengths (193 m, 248 nm, 266 nm, 355 nm) and different pulse length (excimer: 20-25 ns; Nd:YAG: 400-500 ps).

The best surface quality is obtained for 193 nm which is caused by a pure photolytically driven ablation process. A surface roughness of about $R_a=200$ nm is desirable for optical applications and is related to small ablation rates of about 150 nm/pulse (laser fluence up to 0.4 J/cm^2). With increasing laser fluence an ablation rate as well as the surface roughness increase. For laser fluence up to 1 J/cm^2 a surface roughness of $R_a=300$ nm was obtained which is sufficient for fluidical applications. By using 248 nm the fluence threshold of ablation was found to be significantly higher. Furthermore the surface roughness increase by an order of magnitude compared to 193 nm indicating that the dominating mechanism is pyrolytical. 248 nm laser radiation is thus not suitable for ablation of PMMA for these applications. A smaller pulse length is thought to increase the photolytical contribution. Therefore the 3ω and 4ω Nd:YAG laser with pulse length of about 400-500 ps was used. While the graph for 266 nm shows a linear stage for low laser fluence and a saturation of ablation rate at a fluence above 3 J/cm^2, the curve for 355 nm is linear. This indicates that the ablation mechanism for 266 nm is combination of photolytic and pyrolytic whereas that for 355 nm is mainly pyrotlytic. The surface roughness also reflect the different process mechanisms: high surface roughness for 355 nm and lower roughness for 266 nm. However, the quality of the grooves produced so far does not meet the requirements. The ablation mechanism is not yet fully understood, it is thought that the pyrolytical contribution is still too high. The Gaussian profile also accounts for a higher surface roughness.

Laser ablation was used to produce components for microfluidical applications, such as CE-Chips. Several structures were produces either with the Excimer laser or a 3ω, 4ω -Nd:YAG laser. Figure 4 shows an example of two crossing sections of CE-Chips made by different mask techniques. It can be seen in the left photo, that there is a not avoidable position problem which leads to an overlap as indicated by the arrows. The rotary mask approach, which is a modified mask dragging technique, enabled a reproduction of the desired geometry without any distortion.
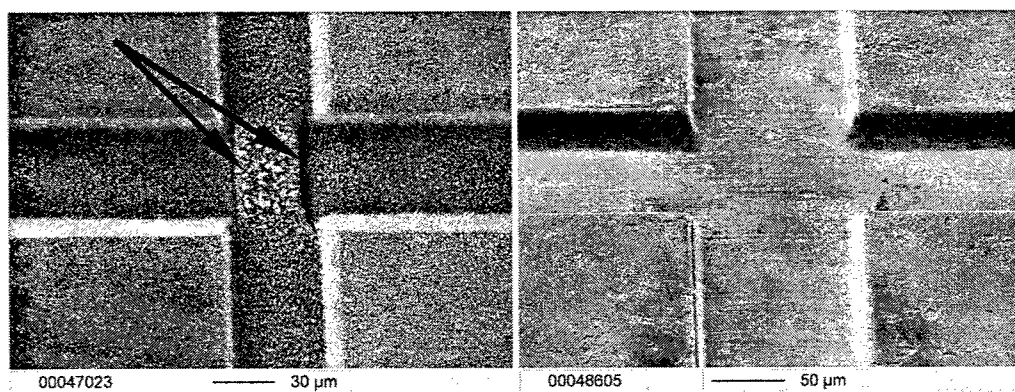
Figure 4: Examples of crossing sections of polymeric CE-Chips fabricated by excimer laser ablation using different mask techniques. Left: flexible motorised mask; right: rotary mask.

4.2 Integrated waveguides

4.2.1 Filling of grooves with index matched materials

For microoptical applications the width of the generated grooves is significantly smaller that for microfluidics. In order to get monomode waveguides the lateral structure size should be in the range of 10 µm. Figure 5 shows grooves obtained by excimer laser ablation (193 nm) with varying fluence. The inserts reveal the influence of processing gas on debris formation. It can be seen from the micrographs that the surface quality meets the requirements for the optical application.
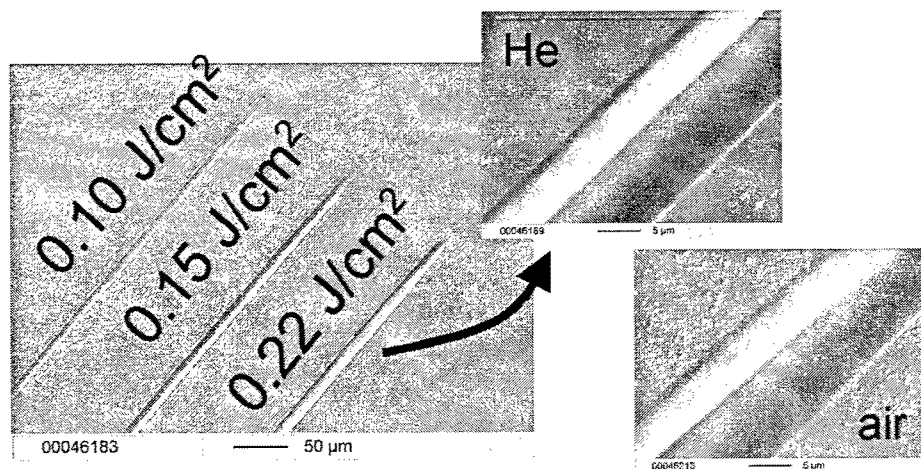
Figure 5: Grooves in PMMA produced by excimer laser ablation using different fluence and a wavelength of 193 nm.

Resins filling

The machined grooves were filled with liquids and covered with a PMMA plate. Several index matching liquids and curing PMMA/MMA were used to form waveguide structures. First working waveguide structures have been realised with an oil having a refractive index of n=1.509 @1550nm (figure 6). After filling and covering first measurements showed insertion loss down to 8dB for a 25mm groove. Due to chemical reaction of the oil with the substrate the transmission loss increased within a few days. Fillings with modified PMMA/MMA and curing by the use of UV have failed so far due to cracks and voids in the waveguiding structure. These problems were caused by volume contraction during the curing process and high strain in the cured sample.
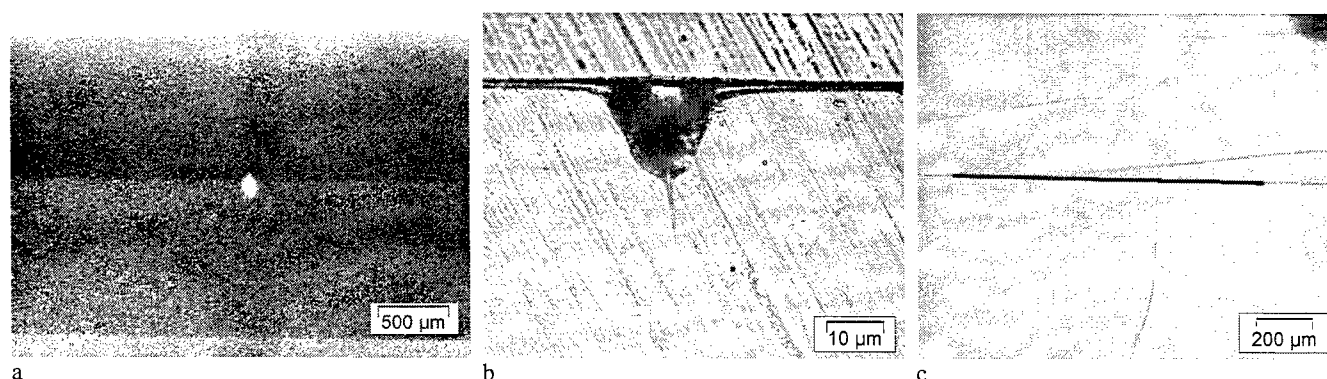
Figure 6a: Side view of a polymer waveguide filled with oil and covered with PMMA. Picture was taken by an IR camera @1550nm.
Figure 6b,c: Side view and top view of a polymer waveguide containing cracks and voids caused by cured modified PMMA.

Nano particle filled polymers

In order to fill the laser patterned grooves, the viscosity of the filler has to be sufficiently low. The viscosity of the oil (described in the previous section) is smaller by a factor of ten in comparison to the used pure Plexit55. In order to achieve good filling results with ideally no air inclusions the Plexit55 was diluted with MMA. A further reduction of viscosity leads to disadvantages in tensile strength of the cured composite. Mixing PMMA-based reactive resins and nano-powder leads in general to a tremendous increase in viscosity. Viscosity raises with increasing filling degrees. The nano-sized particles interact as mixing points for the polymer chains, the average free chain length is significantly reduced.

Until now two different filling tools are available. Either a turbine stirrer can be used to admix the nano-powders and Plexit55 or diluted systems respectively, or a dissolver stirrer comes into operation. Though the dissolver stirrer has the disadvantage of slowly mixing the powders into the matrix, the quality of dispersion is excellent. This is illustrated in Table 2, where the attenuation data of the old method (turbine stirrer) is compared to the data of the dissolver stirrer.

	PMMA	5 wt% R8200	10 wt% R8200
Old method	0.2 dB/mm	4.0 dB/mm	2.9 dB/mm
Optimised method	0.2 dB/mm	1.1 dB/mm	1.7 dB/mm

Table 2: Comparison of attenuation data of AerosilR8200 in PMMA.

In order to get these attenuation data, the filled Plexit55 has to be cured which is carried out with UV-induced reaction moulding yielding a solid PMMA nano-particle filled composite. After that process the generated dies with high surface quality are ready for optical measurements like determination of attenuation, refractive index or transmission.

Variation of the refractive index

Filling PMMA with silica reduces the refractive index, all the other fillers increase the refractive index. Figure 7 shows that a total variation of the refractive index $\Delta n=0.005$ can be achieved. For this reason the criterion of total reflection in a monomode waveguide is fulfilled.
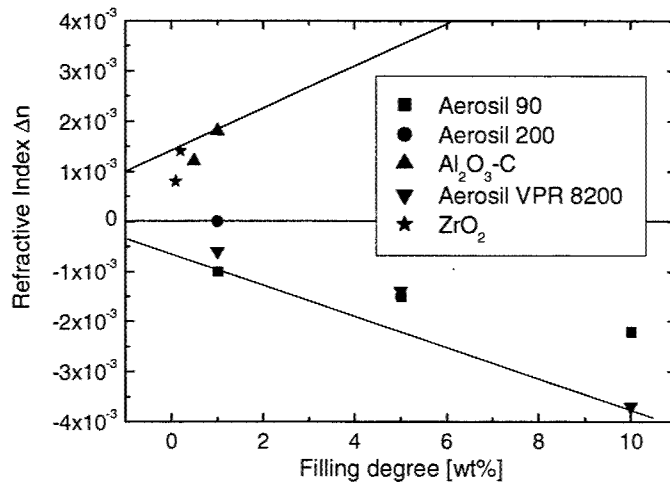
Figure 7: Variation of the refractive index as a function of the filling degree.

4.2.2 Change of refractive index by laser induced polymer modification

Preliminary results of the laser induced polymer modification are presented in figure 8. The graph shows that the refractive index could be raised by approximately $\Delta n=0.009$. As described in section 2.3 the minimum Δn for monomode waveguides should be about 0.005. The graph reveals that the use of both wavelengths resulted in a sufficient increase of the refractive index. However, it should be noted that modification with 248 nm is significantly faster and the possible change of Δn is larger. As of yet the depth distribution of the refractive index has not been examined. In ongoing studies this aspect will be investigated in more detail.
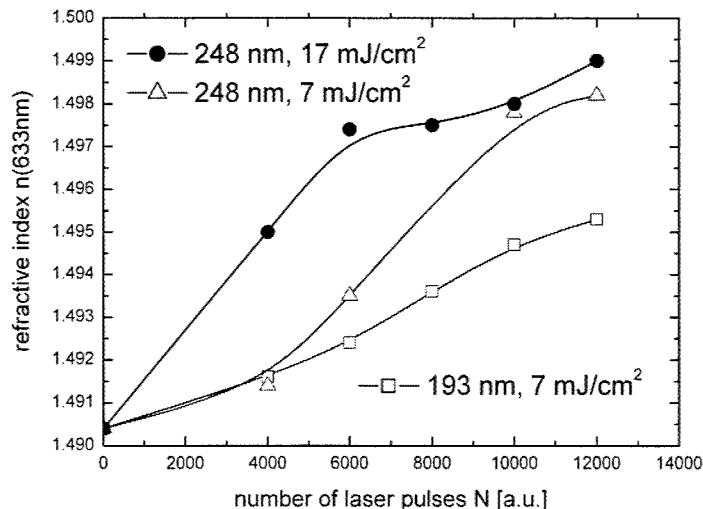
Figure 8: Change of refractive index of PMMA as function of laser radiation dose for 248 nm and 193 nm.

By means of laser lithography and direct writing operating waveguide structures were achieved. Polymeric waveguides with a length of 10 mm were fabricated by excimer laser beam illumination through the Cr/SiO_2 mask at 248 nm. Figure 9a shows the near-field pattern of the waveguide. The image is captured by an infrared camera at 1550 nm and shows waveguiding at the desired wavelength. The transmission characteristics of the waveguide as determined by WDCA yielded 13 dB insertion losses at 1550 nm. This is to be compared to the insertion loss of 33 dB of the polymer plate without guiding structure. As the coupling losses of each waveguide interface are to be expected below 1 dB the major performance limitations are thought to be in the structural imperfections of the Cr/SiO_2 mask or in the surface finish of end-faces of the

polymer plate. Alternatively polymer waveguide of the same length has been fabricated by 4ω Nd:YAG laser beam direct writing, which increases the flexibility with respect to geometry. Another advantage of this approach is a significantly lower processing time due to the high laser repetition rate of about 2000 Hz. The output near-field pattern in figure 9b shows a divergent beam profile. This indicated that the observed insertion loss of 24 dB is mainly due to not optimised waveguide geometry.

a   b
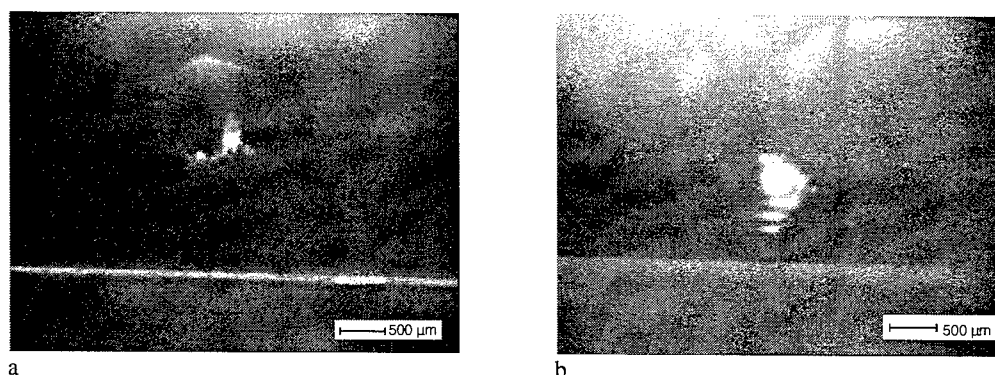
Figure 9a. End-face of the polymer waveguide fabricated by laser beam illumination through the Cr/SiO_2 mask at 248 nm. The output near-field pattern is pictured by an infrared camera at 1550 nm. Figure 9b. End-face of the polymer waveguide fabricated by laser beam direct writing at 266 nm.

5. CONCLUSIONS & OUTLOOK

Laser material processing by means of ablation and modification was found to be a very suitable tool to reach lower production costs, to decrease lead times and to increase the accuracy of products. In this work this was shown for applications in microfluidics and microoptics. One of the main problems of conventional techniques is the limited flexibility regarding complex designs. The presented work reveals that with new mask techniques this problem can be overcome. In addition the use of 3ω and 4ω Nd:YAG with high laser repetition rates and short laser pulses enables the "direct writing" of complicated structures. These new concepts were successfully applied in microoptics and microfluidics. In the case of microfluidics the results of this work form the base of a new approach for the production of disposable devices.

It has been shown that integrated monomode waveguides can be manufactured in one process step as well as in a two step process. The two alternative routes investigated were: laser-induced local change of refractive index and the combination of laser micropatterning of grooves and subsequent filling. First light transmission integrated waveguide structures were fabricated by laser micromachining. Best results with respect to insertion loss were obtained with grooves filled with index matched liquids. Waveguides formed by local index modification in PMMA by laser lithography and direct writing are found to be promising but require further process optimisation.

REFERENCES

1.   R. Wechsung, H. Wicht, Market Analysis for microsystems 1996-2002, http://www.emsto.com/market-analysis/index.html, 2000.

2. R. Bruek, N. Rizvi, A. Schmidt, *Applied Microtechnology, LIGA – Laser – Micro Precision Engineering*, Carl Hanser Verlag, München, FRG, 2001.

3. W. Menz, J. Mohr, O. Paul, *Microsystem Technology*, Wiley-VCH Verlag GmbH, Weinheim, FRG, 2001.

4. G. Tschulena, *Mikrosystemtechnik: Grundlagen, Praxis, Trends*, Hüthig Verlag, Heidelberg, FRG, 1999.

5. U. Wallrabe, H. Dittrich, G. Friedsam, T. Hanemann, J. Mohr, K. Mueller, V. Piotter, P. Ruther, T. Schaller, W. Zißler, "RiBCon®: Micromolded easy-assembly multi fiber connector for single- and multimode applications", *Proc. of SPIE Integration and Packaging of MEMS/MOEMS* **4408**, pp. 478-485, 2001.

6. T. Hanemann, M. Heckele, V. Piotter, "Current Status of Micromolding Technology", *Polymer News* **25**, pp. 224-229, 2000.

7. M. Farsari, F. Claret-Tournier, S: Huang et.al., "A novel high-accuracy microstereolithography method employing an adaptive electro-optic mask, *J. of Mat. Proc. Technol.* **107**, pp. 167-172, 2000.

8. S. Sinzinger, J. Jahns, *Microoptics*, Wiley-VCH, Weinheim, FRG, 1999.

9. W. Ehrfeld, V. Hessel, H. Löwe, *Microreactors*, Wiley-VCH, Weinheim, FRG, 2000.

10. D. Bäuerle, *Laser processing and chemistry*, pp. 221-257, Springer-Verlag, Berlin Heidelberg New York, 2000.

11. M. Wehner, *Excimer Laser Technology: laser sources, optics, systems and applications*, pp.107-112, D. Basting (Ed.), Lambda Physik AG, Göttingen, FRG, 2001

12. W. Pfleging, T. Hanemann, W. Bernauer, M. Torge, „Laser Micromaching of Polymeric Mold Inserts for Rapid Prototyping of PMMA-Devices via Photomolding", *Proc. of SPIE* **4637**, pp318-329, 2002.

13. H. Becker, and W. Dietz, "Microfluidic devices for µ-TAS applications fabricated by polymer hot embossing", *SPIE Proc. Microfluidic Devices and Systems* **3515**, pp. 177-182, 1998.

14. W. Pfleging, T. Hanemann, M. Torge, W. Bernauer, „Rapid Fabrication and Replication of Metal, Ceramic and Plastic Mold Inserts for Application in Microsystem Technologies", accepted (19.08.02) for publication in *Journal of Mechanical Engineering Science* **217** Part C.

15. C. Wochnowski, S. Metev, S. Sepold, "UV-laser-assisted modification of the optical properties of polymethylmethacrylate", *Applied Surface Science* **154-155**, pp. 706-711, 2000.

16. L. Friedrich, P. Dannberg, C. Wächter, Th. Hennig, A. Bräuer, W. Karthe, "Directional coupler device using a three-dimensional waveguide structure", *Optics Communication* **137**, pp. 239-243, 1997.

17. Agilent Technologies; Product description: Agilent 81910A, Photonic All-parameter Analyser, http://www.tmintl.agilent.com/npl/Npl29Mar02.shtml.

Modeling electrical characteristics of laser tuned silicon microdevices

Michel Meunier [a,b], Mathieu Ducharme [a] and Jean-Sébastien Bernier[a]

[a] École Polytechnique de Montréal, Laser Processing Laboratory, PO Box 6079, Succursale. Centre-ville, Montréal (Québec), Canada, H3C 3A7
[b] LTRIM-Technologies, 440 Blvd Armand Frappier, suite 140, Laval, Québec, Canada, H7V 4B4

ABSTRACT

Highly accurate resistances can be made by iteratively laser inducing local diffusion of dopants from the drain and source of a gateless field effect transistor into its channel, thereby forming an electrical link between two adjacent p-n junction diodes. These laser tuned microdevices have been electrically characterized and their current-voltage (I-V) behaviors are linear at low voltages and sublinear at higher voltages where carrier mobility is affected by the presence of high fields. Considering that the microdevice is a one dimensional trap less n+ υ n+ structure, we have developed a theoretical current-voltage equation that satisfies these experimental results.

Keywords: Laser trimming, laser tuned microdevices, laser induced diffusible resistance, microelectronics, highly accurate resistance.

INTRODUCTION

Due to the inevitable fabrication process variabilities, analogue microelectronics circuits' functionalities are frequently altered and trimming techniques have to be used to accurately adjust some microdevices' characteristics. We have recently proposed a new technique to finely tune analogue microelectronics' circuits that presents the advantages of being very accurate, using very small die area, and being easily integrated into any actual CMOS processes without additional fabrication steps [1-5]. A patent disclosing the detailed device structure and creation method has been recently accepted [3]. In this paper, after reviewing the principle of the technique, we present the electronic characterization and modeling of these new microdevices. We show that they present an excellent linear current-voltage behavior at usual microelectronics' voltages and that at higher voltages, the sublinear behavior is due to a saturation of the majority carriers' velocity.

PRINCIPLE OF THE LASER TRIMMING METHOD

The laser trimming technique shown schematically in Figure 1 is performed on a device structure consisting of a gateless MOSFET fabricated by a conventional CMOS process [1,2]. For a n-type resistor, the device structure consists of two highly doped regions formed by implantation inside a p-well, resulting in two p-n junctions facing each other. Before the laser trimming operation, the only current that can flow through the device is the p-n junctions leakage current, resulting essentially in an open circuit. Focusing a laser beam on the gap region between the two junctions causes melting of the silicon, resulting in dopant diffusion from the highly doped regions to the lightly-doped gap region. Upon removal of the laser light, the silicon solidifies, leaving the diffused dopants in a new spatial distribution forming an electrical link between the highly doped regions. This laser-diffused link constitutes the tuned microdevice. Tight control of process parameters is necessary to create efficiently these laser tuned microdevices while avoiding damage to adjacent devices and structures. These parameters are the laser spot size, the pulse duration, the laser power, the number of laser expositions and the position of the laser spot relatively to the device. By varying the parameters between each laser intervention, one can accurately control the tuning of the device. Scanning electron microscopy and transmission electron microscopy show that the laser process has no effect on the dielectric multilayers nor on the dielectric/silicon interface[2,6].
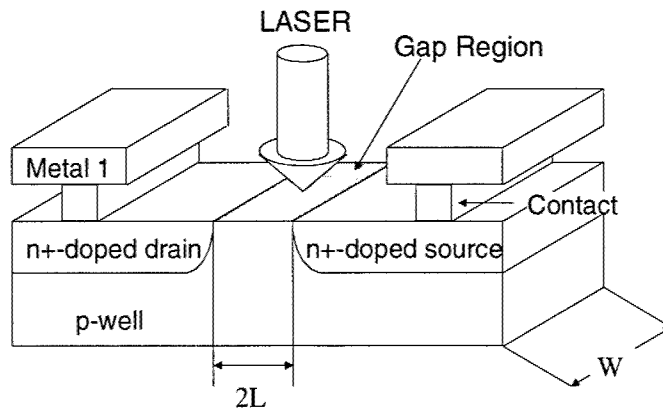
Figure 1 Schematics of the laser tuned microdevices technique

ELECTRICAL CHARACTERIZATION

Current-voltage (I-V) characteristics have been measured using a Hewlett Packard 4155A semiconductor parameter analyzer with a four-wire test procedure on samples placed in a Faraday cage at room temperature. The I-V curves of typical laser tuned resistances are presented in Figure 2. Devices with few kΩs in resistance present an excellent linearity over the range of voltages normally used in microelectronics (±1.5V). In Figure 3, I-V characteristics of tuned resistances with nominal gap between 0.6 μm and 1.4 μm are plotted up to 7.5 volts, the maximum applicable voltage on our test chip before breakdown. They showed a non-linear behavior primarily related to the carrier velocity saturation at moderate fields. The lines on this figure correspond to the model presented in the next section.
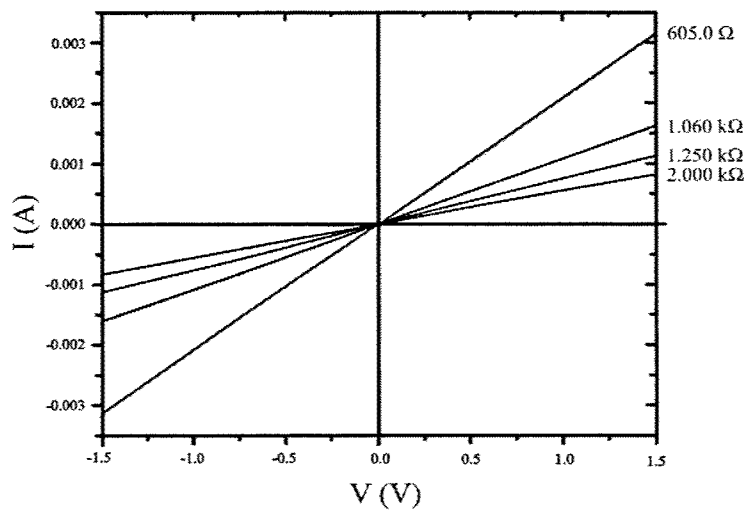
Figure 2: Current-voltage characteristics of four laser diffusible resistances at low voltages (< 1.5V) usually used in microelectronics.
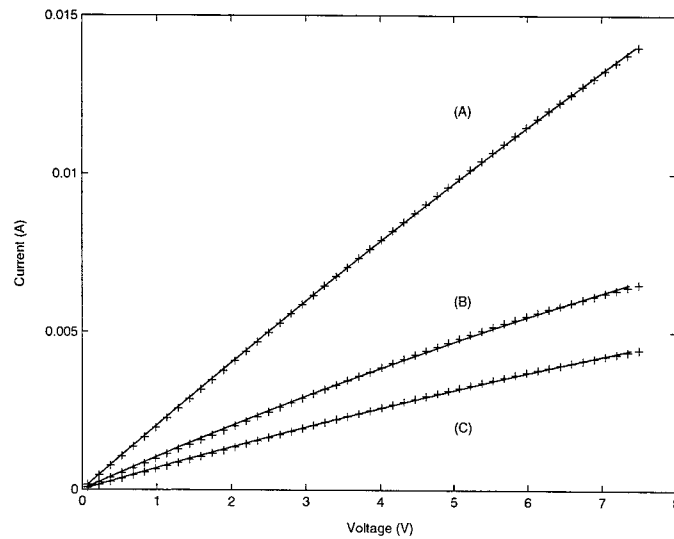
Fig. 3 Current-voltage (I-V) plot of the experimental data (crosses) and fitted model (line) for three typical laser-tuned resistors of parameters, 500, 1000, 1500 Ω. The lines are calculated from the model introduced below with the following characteristics:
(A) $R = 500\Omega$, $N_D = 1.45 \times 10^{18} \text{cm}^{-3}$, $L = 0.6\mu\text{m}$; (B) $R = 1\text{k}\Omega$, $N_D = 5.02 \times 10^{18} \text{cm}^{-3}$, $L = 1.0\mu\text{m}$;
(C) $R = 1.5\text{k}\Omega$, $N_D = 2.66 \times 10^{18} \text{cm}^{-3}$, $L = 0.6\mu\text{m}$.

MODELING THE LASER TUNED MICRODEVICES

The laser has the effect of diffusing dopants from the source and drain into the channel as shown schematically on the top part of figure 4. After diffusion, the microdevice presents a n+ υ n+ (or p+ π p+ depending on the highly doped region type) structure with non-abrupt junctions. As it is quite often done in a first analysis of a microdevice, one can approximate this device by a one dimensional structure with two abrupt junctions, as shown in Figure 4.
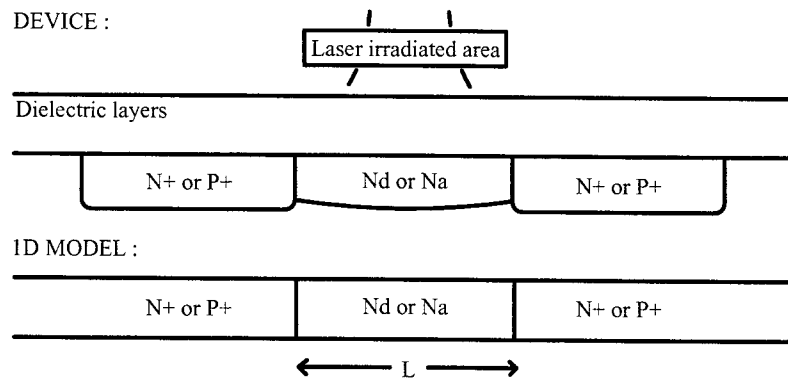
Fig. 4 Schematics of the one dimensional model applied to the geometry of a laser-diffused resistor.

The J-V relation of a n+ υ n+ structure has been extensively studied in the past [7-12]. Single carrier transport can be described by the drift-diffusion equation where the diffusion current is ignored and by a field dependent mobility expression based on the Canali et al. model [13]. An impurities' concentration dependent low field mobility model was also used [14]. Mobility degradation is implicitly assumed since important electric fields as high as 10^5V/cm are applied on the laser-tuned resistors. Therefore, the current density is given by:

$$J = nq\frac{\mu_0 E}{1 + |E/E_C|} \tag{1}$$

where q is the elementary electrical charge, E_C is the electric field necessary to observe mobility degradation and μ_0 the low field mobility. At low applied electric field E, we observe an ideal ohmic relation. The charge-trap density is considered small enough to be ignored and current continuity yields to $dJ/dx = 0$. By combining equation (1) with Poisson's equation, where all the impurities N_D are ionized (leading to $n = N_D$ at room temperature), we obtain the differential equation:

$$J = q\left(N_D - \frac{\varepsilon}{q}\frac{d}{dx}E\right)\frac{\mu_0 E}{1+|E/E_C|}.$$

(2)

where ε is permittivity of the semiconductor. We then make the "virtual cathode approximation" which stipulates that the electric field is equal to 0 at $x = 0$ and a transcendent solution is obtained by integration of the differential equation (2):

$$-\hat{j}\hat{x}\left(\frac{1}{\hat{j}}-1\right)^2 = \left(\frac{1}{\hat{j}}-1\right)\hat{e} + \ln\left(1-\left(\frac{1}{\hat{j}}-1\right)\hat{e}\right)$$

(3)

with the dimensionless variables :

$$\hat{j} \equiv \frac{J}{qN_D\mu_0 E_C},$$

(4a)

$$\hat{e} \equiv E/E_C,$$

(4b)

$$\hat{x} \equiv \frac{-xN_D q}{\varepsilon \cdot E_C}.$$

(4c)

A solution J(V) is very hard to obtain because we do not have a direct relation between J and E. In previous studies, this solution was investigated only in certain asymptotic conditions because of its nature and complexity of its numerical resolution. Unfortunately, most of the current-voltage (J-V) plot of a typical laser-diffused resistor is within the transition between pure ohmic conduction and the effect of mobility degradation and space-charge-limited current. This transition cannot be only evaluated in asymptotic conditions.

It is reasonable to consider that for a positive applied voltage V we will get negative values of J, E and E_C. Since

$$-\hat{j}\hat{x}\left(\frac{1}{\hat{j}}-1\right)^2 \leq 0, \quad \forall \hat{x} \quad and \quad \forall \hat{j},$$

(5)

the logarithmic term will always dominate on the right hand side of equation (4) in our case. We can then approximate our transcendent solution by

$$-\hat{j}\hat{x}\left(\frac{1}{\hat{j}}-1\right)^2 \approx \ln\left(1-\left(\frac{1}{\hat{j}}-1\right)\hat{e}\right).$$

(6)

It is now possible to express the electric field $E = dV/dx$ as a function of the current density, yielding after integration over the device's length L to the V-J relation:

$$V = \frac{E_C^2\varepsilon}{N_D q}\frac{-\hat{j}^2}{(\hat{j}-1)^3}\left\{\exp\left(\frac{-\hat{x}_L}{\hat{j}}(\hat{j}-1)^2-1\right)+\frac{\hat{x}_L}{\hat{j}}(\hat{j}-1)^2-1\right\}$$

(7)

where

$$\hat{x}_L \equiv \frac{-LN_D q}{\varepsilon E_C}.$$

(8)

This equation was applied to fit the experimental curves of Figure 3 with only N_D and E_C as free parameters. The three fitted curves give values of N_D between 10^{18}cm^{-3} and $5\times 10^{18}\text{cm}^{-3}$ which correspond to the expected doping level

in the melted region after the laser induced dopant diffusion from the highly doped regions of 5×10^{19} cm^{-3}. The excellent fit suggests that equation (7) described very well the electrical behavior of the laser tuned microdevices.

CONCLUSIONS

Highly accurate resistors compatible with CMOS technology can be easily made by laser inducing dopant diffusion. These new microdevices have very linear I-V curves at the usual microelectronics operating voltages and present non-linear behavior due to carrier velocity saturation. Experimental results are well described by a simplified analytical solution of the one dimensional trap-less n+ υ n+ or p+ π p+ diodes' model.

REFERENCES

[1] M. Meunier, Y. Gagnon, A. Lacourse, Y. Savaria et M. Cadotte, " A new laser trimming process for microelectronics", Proceedings of the SPIE, Volume 4274, 385-392 (2001)

[2] M.Meunier, M. Cadotte, M. Ducharme, Y. Gagnon, A. Lacourse, " Laser induced diffusible resistance: device characterization and process modeling" Proceeding of the SPIE, Volume 4637, 75-81(2002).

[3] M. Meunier, Y. Gagnon, Y. Savaria, A. Lacourse and M. Cadotte, A New Laser Trimming Process for Microelectronics" Applied Surface Science, 186, 52-56 (2002)

[4] Y. Gagnon, M. Meunier, Y. Savaria, "Method and Apparatus for Iteratively and Selectively Tuning the Impedance Integrated Semiconductor Devices Using a Focused Heating Source" US Patents 09/332,059 and PCT # 06042-002-WO-1 by LTRIM Technologies Inc. (2001)

[5] M. Meunier, M. Cadotte and M. Ducharme "Laser tuned silicon microdevices for analogue microelectronics", Riken Review, Volume 50, 53-56 (2003)

[6] M. Meunier, M. Ducharme , J-Y. Degorce, Y. Liao and A. Lacourse "Laser induced local modification of silicon microdevices: a new technique for tuning analogue microelectronics" Proceeding of the SPIE, (2003)

[7]M. A. Lampert, P. Mark, Current Injection in Solids, New York, Academic, (1970)

[8] A. Van der Ziel, "Space-Charge-Limited Solid-State Diode", Semiconductors and Semimetals, vol.14, pp.195-247. (1979)

[9] G.T. Wright, Solid State Electron, 2, p.165. (1962)

[10] S.M. Skinner, J. Applied Physics, 26, p.498. (1955)

[11] M. Lampert and A. Rose, Phys. Rev., 121, p.26 (1960)

[12] G. Krieger, P. Niles, "Diffused Resistors Characteristics at High Current Density Levels – Analysis and Applications", IEEE Trans. Electron Devices, vol.36, pp.416-423. (1989)

[13] C. Canali, G. Majni, R. Minder, and G. Ottaviani, "Electron and hole drift velocity measurements in Silicon and their empirical relation to electric field and temperature", IEEE Trans. Electron Devices, vol.ED-22, pp.1045-47. (1975)

[14] G. Masetti, M. Severi, and S. Solmi, "Modeling of Carrier Mobility Against Carrier Concentration in Arsenic-, Phosphorus- and Boron-Doped Silicon", IEEE Trans. Electron Devices, Vl.ED-30, pp.764-769. (1983)

Synthesis of Metal Oxides Nanoparticles by Laser Ablation
— Nanoparticle-Assisted Deposition of Nanostructured ZnO —

Tatsuo Okada, Mitsuhisa Kawakami, Agung Budi Hartanto, Yoshiki Nakata
Kyushu University, Faculty of Information Science and Electrical Engineering,
Fukuoka 812-8581, Japan

ABSTRACT

This paper describes a new growth method of ZnO nanorods. Firstly ZnO nanoparticles were synthesized in an oxygen and He background gas by laser ablation. These nanoparticles were used to deposite nanostructured-ZnO thin films. Under an optimized deposition conditions, ZnO nanroods with a diameter of about 300 nm and 6 μm in length have been synthesized without any catalyst by nanoparticle assisted laser ablation deposition. The laser action was observed in the nanorods under an optical excitation at 355 nm, indicating a high quality of the crystal.

Keywords: ZnO, Nano-particles, Nano-rods, laser ablation, imaging, stimulated emission, Rayleigh scattering

1. INTRODUCTION

Metal oxides semiconductors such as ZnO, GaN, SnO_2 and so on have been paid a great interest for opto-electronic applications like photo-diodes, lasers, sensors and so on. Recently nanostructures of these metal oxides such as nanoparticles, nanoballs, naowires and nanorods has been fabricated by various techniques [1-6]. Among them, laser vaporization in a background gas is one of the powerful technique for the fabrication of such nanostructures. Although the laser vaporization in a background gas, nanoparticles are ineviatvely formed in the gas phase by condensation of the vapor, less attention has been paid for the role of nanoparticles in synthesizing nanostructures.

In this paper, we describe a synthesis of ZnO nanorods by nanoparticle-assisted laser ablation deposition in a background gas. In the growth of nanodods, the formation and the transport of ZnO nanoparticles played an important role. The characteristics of ZnO thin films and nanorods synthesized under various deposition conditions were analyzed by XRD, SEM and photo-luminescense. The laser action of ZnO narods under photo-excitation is also described. Finally the formation of ZnO nanoparticle was investigated by Rayleigh scattering imaging, in order to understand the growth mechanism of ZnO nanorods.

2. FORMATION OF ZNO NANOPARTICLES

A sintered ZnO target (99.99%) was ablated in an oxygen or He background gas in the range from 1 Torr to 10 Torr by a KrF excimer laser with a fluence of about 3 J/cm^2. The repetition rate of the laser was 20 Hz. The distance between the target and the substrate was set to be 20 mm. In the present experiment, the films were deposited at higher background pressure than that used by other groups. There are many reports on the fabrication of ZnO thin films by many research groups, but most of them fabricated the ZnO thin films at a low background pressure of less than 1 Torr [7-14]. Nanostructured ZnO films were deposited on a (0006) sapphire substrate or SiO_2 substrate heated up to 800 ℃. The crystallinity of the films were analyzed by XRD and the surface morphology was observed by SEM. The optical properties were investigated by the photoluminescence under the excitation at 355 nm from a frequency tripled Q-switched Nd:YAG laser.

The formation of nanoparticles was confirmed by visualizing the nanoparticles using Rayleigh scattering imaging diagnostics, as described below. Nanoparticles formed in the background gas were irradiated by a sheeted probe-laser beam from a XeCl excimer laser at 308 nm, as shown in Fig. 1. The Rayleigh scattered light from the nanoparticles was imaged on a time-gated and image-intensified CCD camera through a spectral filter. Thus the spatial distribution of the nanoparticles at a given time after ablation was obtained in single shot. The temporal behavior can be obtained by changing the delay time between the KrF laser and the XeCl laser shot by shot [15-18].

Figure 2 shows examples of Rayleigh scattered images at 1 ms after ablation at different background gas pressures. As the background pressure increased, stronger Rayleigh scattered signals were observed, indicating that larger nanoparticles were formed in a higher background gas. At 1 Torr, the distribution of nanoparticles was diffuse, but
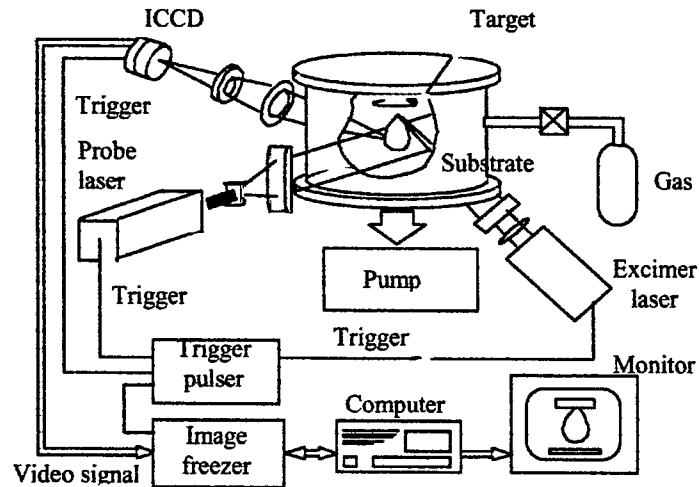
Fig. 1   Experimental setup for imaging diagnostics of ZnO nanoparticles.

Oxygen pressure [Torr]
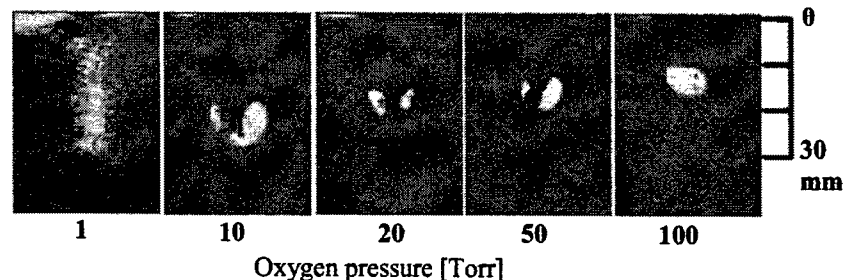
Fig.2   Rayleigh scattered images of ZnO nanoparticles formed in O_2 background gas 1 ms after ablation.

characteristic mushroom-shaped distributions were observed as the pressure increased.   When He was used as a background gas, no Rayleigh scattered signal was observed until the pressure increased more than 30 Torr, indicating that less and smaller nanoparticles were formed in He background gas than in oxygen background gas.

3. SYNTHESIS OF ZNO NANORODS BY NANOPARTICLE-ASSISTED DEPOSITION

3.1 Characteristics of ZnO thin films and nanorods

All the films appeared white, indicating that the films have a structure of the order of the visible wavelength.   The XRD spectra of the ZnO films are shown in Fig. 3 (a) for films deposited at 400, (b) 500, (c) 600 and (d) 700 ℃ in a oxygen background gas.   All the films were deposited for 30 minutes.   Films deposited at a temperature higher than 500 ℃ show only the refraction peaks from [0002] and [0004], indicating that films are highly c-axis oriented.   The c-axis oriented films were also obtained on SiO_2 substrate.   Films deposited at 400 ℃ was also preferentially c-axis oriented, but the lines from [1000],   [1001] and other planes were also observable.

The SEM images of ZnO films deposited at different substrate temperature are shown in Fig. 4 (a) for 400 ℃, (b) 500 ℃, (c) 600 ℃ and (d) 700 ℃.   These films are the same as shown in Fig. 1.   The film deposited at 400 ℃ has the rough surface that consists of a ball-like structure with a size of less than 1 μm.   It looks that the balls themselves consist of small particles with a size of less than 100 nm.   This aggregation agrees with the results of the XRD, as shown in Fig. 2 (a) that consisted of diffractions from different crystal planes.   Thus the film deposited at 400 ℃ was made up from a random aggregation of crystallized nanoparticles.   We believe that the particles with a size of 100 nm in Fig. 3 (a) are the aggregation of the nanoparticles form in a background gas, shown in Fig. 2.   When the substrate
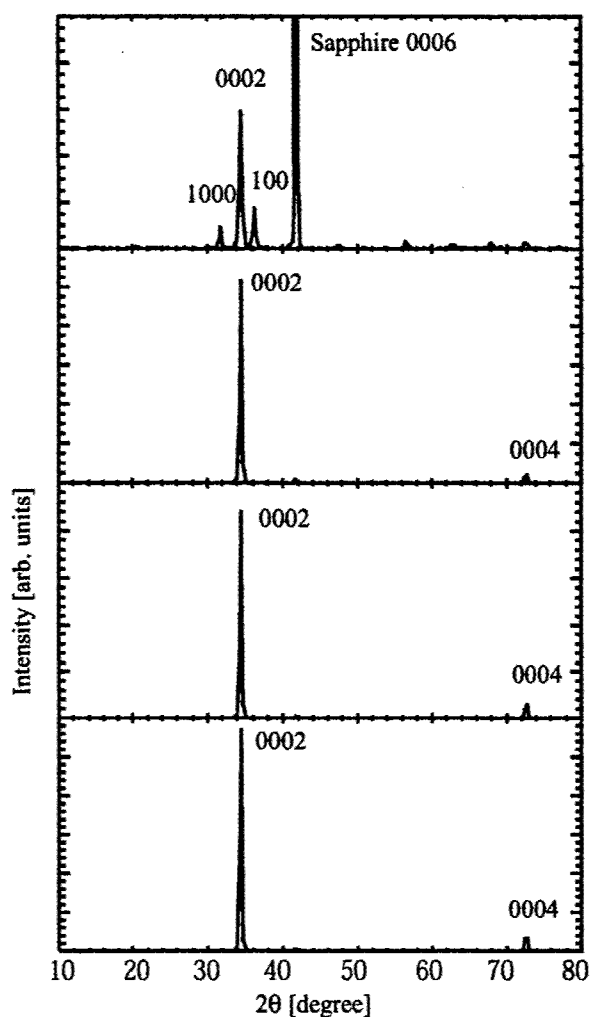
Fig. 3 XRD spectra of ZnO films deposited at different substrate temperature of 400 ℃, 500 ℃, 600 ℃ and 700 ℃ in oxygen background gas.

temperature increased at 500 ℃, the grains with a size of around 500 nm dominates the film surface and the hexagonal structure of the ZnO crystal was clearly observed. However, there were still small particles stacked on the grains. When the substrate temperature increased further up to 600 ℃, films were fully covered by the hexagonal crystals with a size of 100-700 nm. At 700 ℃, hexagonal crystals have more uniform size with an average size of around 300 nm. It is also observed that hexagonal crystals were isolated each other. At a substrate temperature of higher than 600 ℃, there was no trace of nanoparticles on the films and it is thought that nanoparticles were fused into the hexagonal crystals. The cross sectional SEM image of the film deposited at 700 ℃ is shown in Fig. 5, and Fig. 6 shows the SEM image of single ZnO nanorod. Although each hexagonal crystal grew from the substrate, it is thought that some different layer exists between the substrate and the rod. This is suspected from the fact that a thin plate that have no hexagonal shape remains at the substrate end of the rod in Fig. 6. Thus ZnO nanorods were easily synthesized by the laser ablation technique without any catalyst. It is obvious from the XRD spectrum in Fig. 3 (d) that nanorods were c-axis oriented. The length of the nano-rods was very uniform and it was about 6 μm in the present film. We believe that the present length of the nanorods is limited only by the deposition time of 30 minutes and no difficulty is expected in obtaining the longer nano-rods simply by elongating the deposition time.

Figure 7 shows SEM images of ZnO rods deposited on sapphire substrate and SiO₂ substrate. Both were c-axis
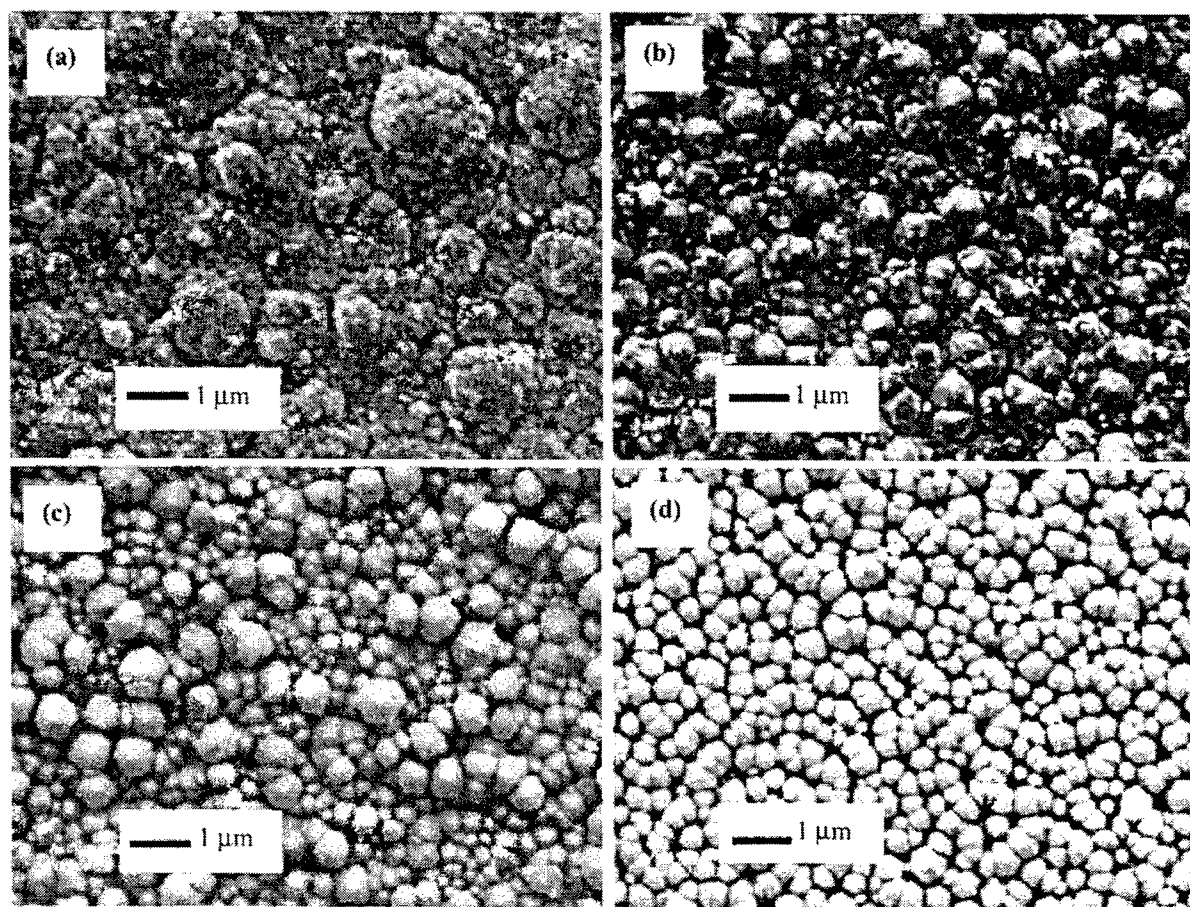
Fig. 4 SEM images of ZnO films.

Fig. 5 Cross sectinal SEM image of ZnO.
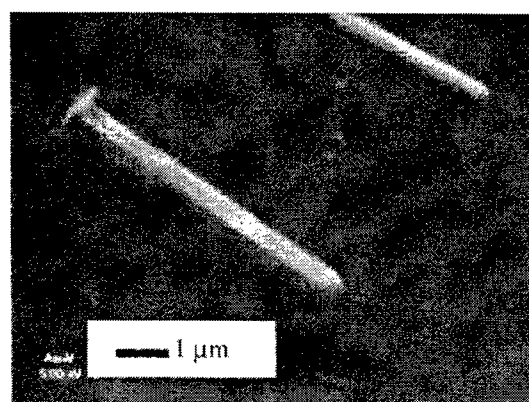
Fig. 6 Single ZnO nanorod.
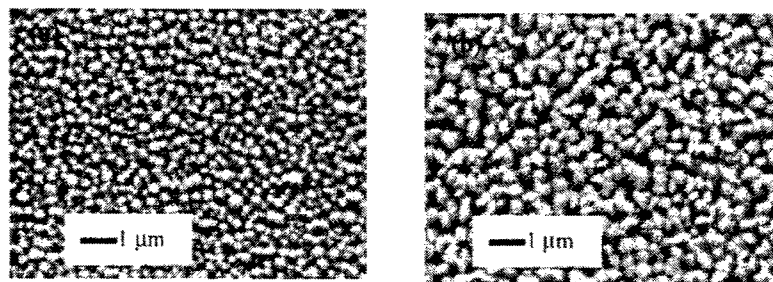
Fig. 7   SEM images of ZnO rods on sapphire (a) and SiO₂ (b).

oriented.   On SiO₂ substrate, it looks that two or three rods are stuck each other.   On the sapphire substrate, on the

other hand, each rod was isolated well.

3.3 Discussion on growth mechanism

Based on the above results, we propose the following growth mechanism.   Figure 2 clearly shows that nano-particles are formed in the gas phase and transported on to the films.   In the SEM image shown in Fig. 4 (a) for the films deposited at 400 ℃, the films are made up of randomly aggregated particles.   It is though that these particles are the trace of the aggregated nano-particle in the background gas, as schematically shown in Fig. 8 (a).   In spite of the formation of particles in the gas phase and of their transportation on to the substrate, on the other hand, the films deposited at the substrate temperature of higher than 500 ℃ were crystallized and well c-axis oriented. This indicates that the surface reaction of the nanoparticles transported on a heated substrate plays an important role in the growth of nano-rods.   For instance, the melting temperature of the bulk ZnO crystal is around 1800 K, but nano-particle ZnO crystal may have lower melting temperature.   This may enable to grow nanorods by melting and fusing the nano-particles stuck on the substrate at a relative lower temperature of 700 ℃ compared with other technique, as shown in Fig. 8 (b).
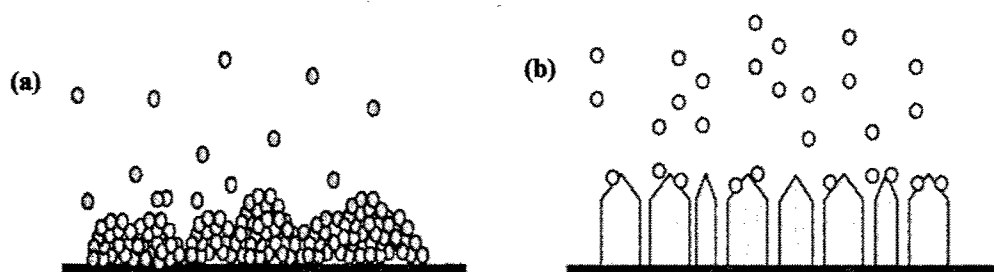
Fig. 8 Growth from nanoparticles at low substrate temperature (a) and at high sbstrate temperature (b) where nanoparticles fused into crystal due to low melting temperature.

4.   OPTICAL PROPERTIES AND LASER ACTION

The photoluminescence spectra under the excitation at 308 nm by a XeCl laser are shown in Fig. 9. All films showed the characteristic fluorescence spectra near the band-gap of 380 nm.   The fluorescence intensity was stronger from the nano-rod films than from the ball-like or the grained film.   It was also observed that the peak wavelength shifted from 380 nm to 388 nm when the structure was changes to the nano-rods.   When nanorods were pumped by a frequency-tripled Q-switched Nd:YAG laser at 355 nm, apparent spectral narrowing was observed with an increase of pump energy, as shown in Fig. 10.   The emission intensity showed a typical threshold characteristics as hsown in Fig.
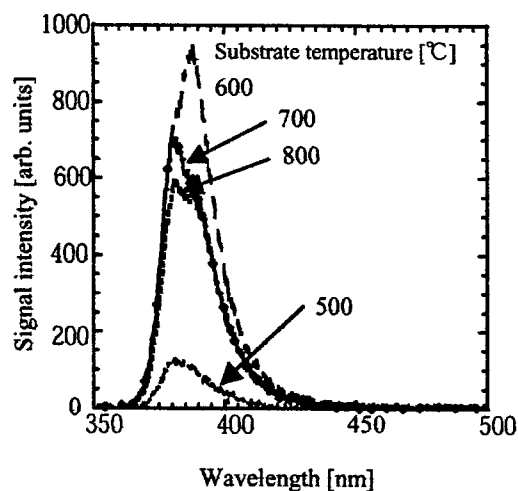
Fig. 9 Photoluminescence spectra.
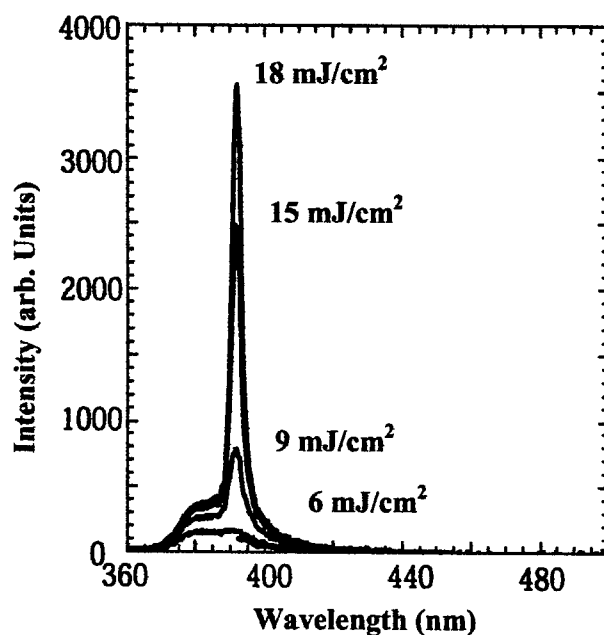
Fig. 10 Stimulated emission from ZnO nanorods.

11. These results indicates the onset of the stimulated emission in ZnO nanorods.

5. CONCLUSION

In conclusion, ZnO nanorods were successfully synthesized by nanoparticle-assisted pulsed-laser deposition. Crystallized and c-axis oriented ZnO nanorods with a size of about 300 nm in an average diameter and of 6 μm in length were grown on sapphire substrates heated at around 700 $°C$ without any catalyst. The characteristic photoluminescence spectra were observed from the nano-rods near the ZnO band-gap around 390 nm. These nanorods will be a promising material for nano-electro-optic devices. We have also confirmed by the Rayleigh scattering imaging
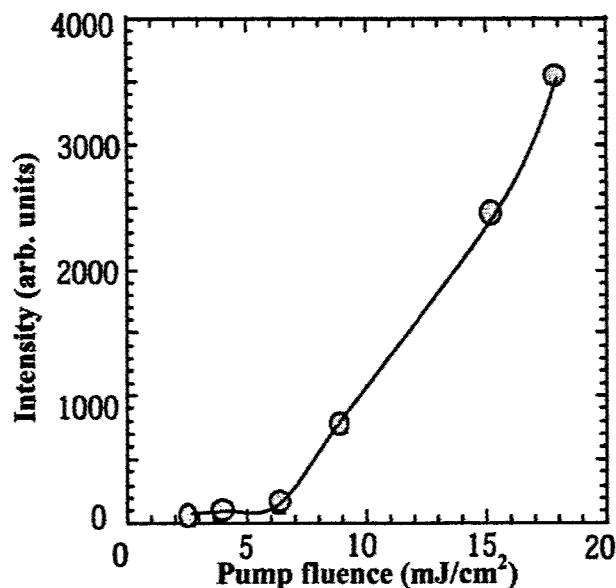
Fig. 11 Emission intensity as a function of pump fluence.

that the ZnO nanoparticles were formed in a background gas during the nano-rod deposition.

ACKNOWLEGEMENT

REFERENCES

1. H. Cao, J. Y. Xu, D. Z. Zhang, S.-H. Chang, S. T. Ho, E. W. Seeli, X. Liu and R. P. H. Chang, Phys. Rev. Lett. **84**, 5584 (2000).
2. Y. C. Kong, D. P. Yu, B. Zhang, W. Feng and S. Q. Feng, Appl. Phys. Lett. **78**, 407(2001).
3. Y. W. Wang, L. D. Zhang, G. Z. Wang, X. S. Peng, Z. Q. Chu and C. H. Liang, J. Crystal Growth **234**, 171(2002).
4. M. H. Huang, S. Mao, H. Feick, H. Yan, Y. Wu, H. Kind, E. Weber, R. Russo and P. Yang , Science **292**, 1897(2001).
5. J. J. Wu and S. C. Liu, Adv. Mater. **14**, 215(2002).
6. P. Yang, H. Yan, S. Mao, R. Russo, J. Johnson, R. Saykally, N. Morris, J. N. Morris, J. Pham, R. He and H. J. Choi, Adv. Funct. Mater. **12**, 323(2002).
7. S. Hayamizu, H. Tabata, H. Tanaka and T. Kawai, J. Appl. Phys. **80**, 787(1996).
8. M. Kawasaki, A. Ohtomo, I. Okubo, H. Koinuma, Z. K. Tang, P. Yu, G. K. L. Wang, B. P. Zhang and Y. Segawa, Mater. Sci. Eng. **B56**, 239(1998).
9. J. F. Muth, R. M. Kolbas, A. K. Sharma, S. Oktyabrsky and J. Narayan, J. Appl. Phys. **85**, 7884(1999).
10. X. W. Sun and H. S. Kwok, J. Appl. Phys. **86**, 408(1999).
11. S. Choopun, R. D. Vispute, W. Noch, A. Balsamo, R. P. Sharma, T. Venkatesan, A. Iliadis and D. C. Look, Appl. Phys. Lett. **75**, 3947(1999).
12. Y. R. Ryu, S. Zhu, D. C. Look, J. M. Wrobel, H. M. Jeong and H. W. White, J. Crystal Growth **216**, 330(2000).
13. S. Im, B. J. Jin and S. Yi, J. Appl. Phys. **87**, 4558(2000).
14. Y. R. Ryu, S. Zhu, J. D. Budai, H. R. Chandrasekhar, P. F. Miceli and H. W. White, J. Appl. Phys. **88**, 201(2000).
15. J. Muramoto, T. Inmaru, Y. Nakata, T. Okada and M. Maeda, Appl. Phys. Lett. **75**, 751 (1999).
16. Y. Nakata, J. Muramoto, T. Okada and M. Maeda, J. Appl. Phys. **91**, 1640(2002).
17. M. Kawakami, Agung Budi Hartanto, Y. Nakata and T. Okada, Jpn. J. Appl. Phys. Part 2, (2003) to be published.

Effect of VUV F$_2$ laser irradiation on fluoride crystal

Yoshizo Kawaguchi, Aiko Narazaki, Tadatake Sato, and Hiroyuki Niino

Photoreaction Control Research Center (PCRC)
National Institute of Advanced Industrial Science and Technology (AIST)
Tsukuba Central 5, Tsukuba, Ibaraki 305-8565, Japan

ABSTRACT

The early stage of optical damage caused by F$_2$ laser irradiation on the wide bandgap fluoride crystal, CaF$_2$, is investigated and compared with the case of ArF laser irradiation. Besides a blue emission band due to self-trapped exciton, sharp emission lines appear and grow at a fluence of about 2 J cm^{-2}, showing the initiation of the optical damage and growth of plume from the F$_2$-laser-irradiated surface of CaF$_2$. There exist cracks and melted structures on the laser-damaged surface, which are caused by thermal stress and vaporization due to laser absorption and following local heating.

Keywords: CaF$_2$, F$_2$ laser, optical breakdown, laser ablation, optical damage

1. INTRODUCTION

Micro- and nano-fabrication using short wavelength lasers are much in progress. In the ULSI manufacturing process, photo-lithography is the key technology for the fine patterning of the electronic circuits on Si, where the resolution of the patterns are proportional to the wavelength of the light source and a light source with shorter wavelength is strongly required. Now a KrF excimer laser (λ = 248 nm) is widely utilized on a stepper, a photolithography system with a mask projection technique, a system with an ArF excimer laser (λ = 193 nm) is almost ready, and a F$_2$ laser (λ = 157 nm) is scheduled on the road map of the ULSI manufacturing process. Besides photolithography, application of the F$_2$ laser for micro- and nano-fabrication is vigorously investigated. Herman's group constructed a ×25 demagnification projection system for the F$_2$ laser beam including a Schwarzschild optics and a beam homogenizer, and fabricated a micro-cylindrical lens and buried waveguide in fused silica.[1,2] Recently, Ihlemann et al. reported fabrication of submicron gratings in fused silica by direct irradiation of the F$_2$ laser with the above projection system.[3] Sugioka's group reported microfabrication of fused silica at high efficiency by simultaneous irradiation of F$_2$ and KrF lasers.[4,5] Dyer et al. reported machining of PMMA, soda lime glass, and NaCl by F$_2$ laser ablation.[6,7]

With shorter wavelength, the interaction of light with materials becomes stronger in general. The optical materials transparent in the deep ultraviolet (DUV) to vacuum ultraviolet (VUV) region are limited, and the resistance of these materials against the laser irradiation is a very severe problem. Cumulative irradiation of the laser beam with the laser fluence just below the damage threshold often causes optical breakdown, so-called incubation effect.[8] For the F$_2$ laser, the available optical materials are F-doped fused silica and fluoride crystals, typically CaF$_2$, MgF$_2$, and BaF$_2$. An F-doped fused silica, named as modified silica, has several times larger transmittance at 157 nm compared with conventional fused silica containing OH groups, and is expected to be applied to the substrate of a photomask for the F$_2$ laser lithography.[9,10] BaF$_2$ is still under development on the crystal growth with high quality. MgF$_2$ is commercially available and shows large transmittance at 157 nm, though it shows large birefringence and is not suitable for lenses. CaF$_2$ is now the most promising material for optical components including lenses for the F$_2$ laser lithography. Furthermore, CaF$_2$ is also used as a second material for the ArF laser lithography, applied to compensate for the chromatic aberration with the optics made of fused silica.

There exist a certain amount of reports on CaF_2 regarding the band structure, the nature of defects and self-trapped excitons,[11-18] ArF-laser induced absorption and photoluminescence,[19-21] optical breakdown and laser ablation under KrF or ArF laser irradiation.[22-25] However, there are few works on the interaction between the F_2 laser beam and CaF_2 crystal,[26] which is well worth to be executed.

In the previous works, we investigated the optical breakdown of NaCl crystal and fused silica under KrF laser irradiation,[27-30] and that of CaF_2 crystal under ArF laser irradiation.[31] Here, we report the early stage of optical breakdown in CaF_2 crystals under F_2 laser irradiation and compare the result with the case of ArF laser irradiation.

2. EXPERIMENTAL

A schematic diagram of the experimental setup for the F_2 laser irradiation is shown in Fig. 1. A substrate of VUV grade CaF_2 single crystal (random cut, thickness = 1.6 mm) which was polished to the optical quality, was used as a sample, and mounted into a vacuum chamber made of acrylic resin. The F_2 laser (Lambda-Physik, LPF-200) was operated with the pulse duration of about 20 ns FWHM and the pulse energy of about 50 mJ at maximum. Maximum deviation of the pulse energy from pulse to pulse was about 10 %, which limited the accuracy of the laser fluence. The laser beam passed through a window into the vacuum chamber, transmitted the attenuator plate, and was focused with a plano-convex lens (f = 83 mm) onto the sample. These optical components were made of VUV grade CaF_2 to keep high transmittance against the F_2 laser beam, typically 80 – 85 % at 157 nm. The laser fluence was controlled by changing the tilted angle of the attenuator plate against the laser beam. Because the F_2 laser beam is strongly absorbed by the oxygen gas, the beamline should be evacuated or purged with nitrogen gas. After evacuation with a turbo-molecular pump, the vacuum chamber was purged with a flowing nitrogen gas (nominal purity 99.999 %).
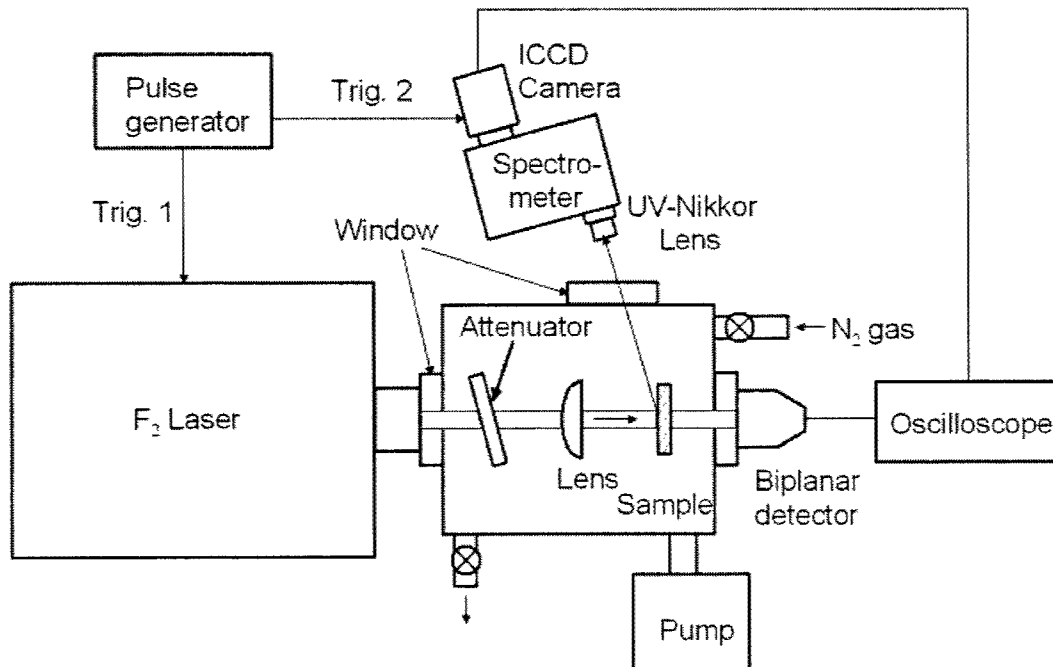
Fig. 1: Experimental setup.

The onset of the optical breakdown on the surface of CaF_2 was observed by monitoring the appearance of the line spectra due to micro-plume from the sample. Light emitted from the sample was focused with a UV-Nikkor lens, and a space-resolved emission spectrum from the laser-irradiated region was acquired with a gated, ICCD camera (Roper, PIMAX-512) attached to a spectrometer (Acton, SpectroPro-150). For a measurement of wide-range spectrum with a sacrifice of the resolution, a grating of 150 grooves mm^{-1} was used. For high-resolution measurement, a grating was switched to that of 1200 grooves mm^{-1}. The adjustment of the delay between the firing of the laser pulse and the gating of the ICCD camera was executed with a pulse generator (Stanford Research, DG-535) while monitoring the waveform of the laser pulse with a biplanar detector (Hamamatsu Photonics, R1193U-54). The laser-damaged surface of the sample was gold-coated and observed with the secondary electron microscope (SEM: Akashi, Alpha 30A).

3. RESULTS AND DISCUSSION

Figure 2 shows optical emission spectra in CaF_2 single crystal under F_2 laser irradiation at various fluences. The ICCD camera was triggered 100 ns after the firing of the laser pulse, and the gate time was set to 10 μs. At low fluence, the emission consisted of a broad, blue band centered at 290 nm and a red band which is a 2nd order line of the blue band. The blue band decayed within 10 μs at room temperature. This blue band is ascribed to relaxation luminescence of the self-trapped exciton (STE) in CaF_2.[17] STE luminescence in CaF_2 was also observed under ArF
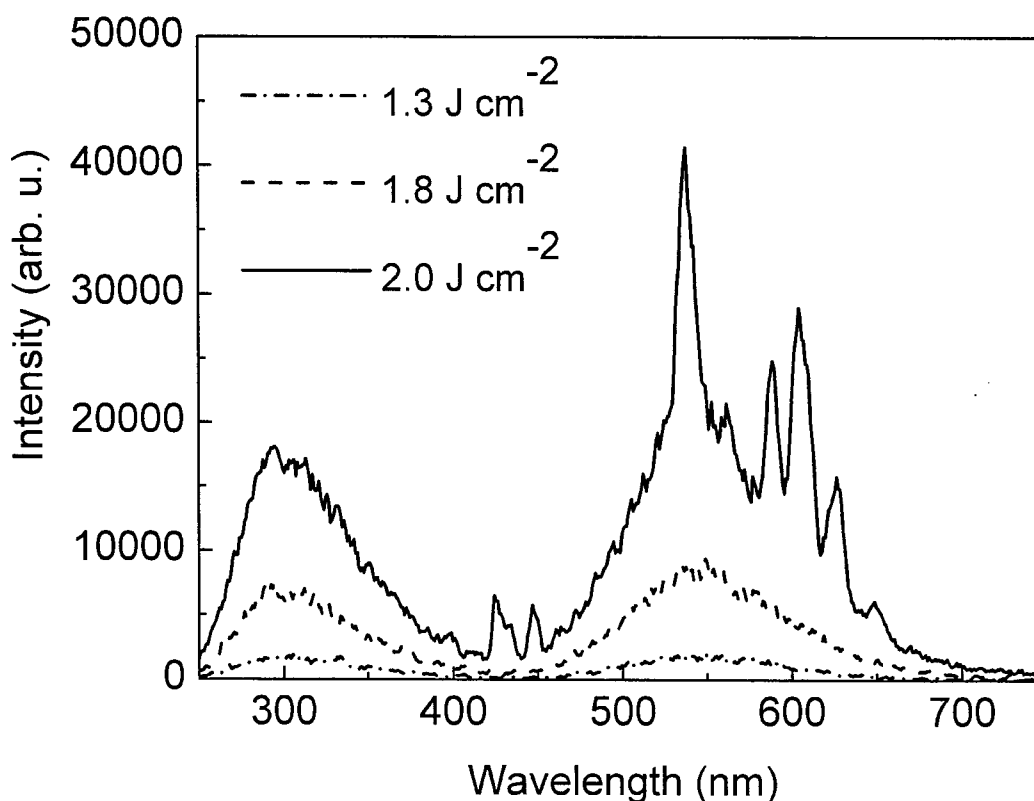
Fig. 2: Optical emission spectra in CaF_2 under F_2 laser irradiation at various fluences.
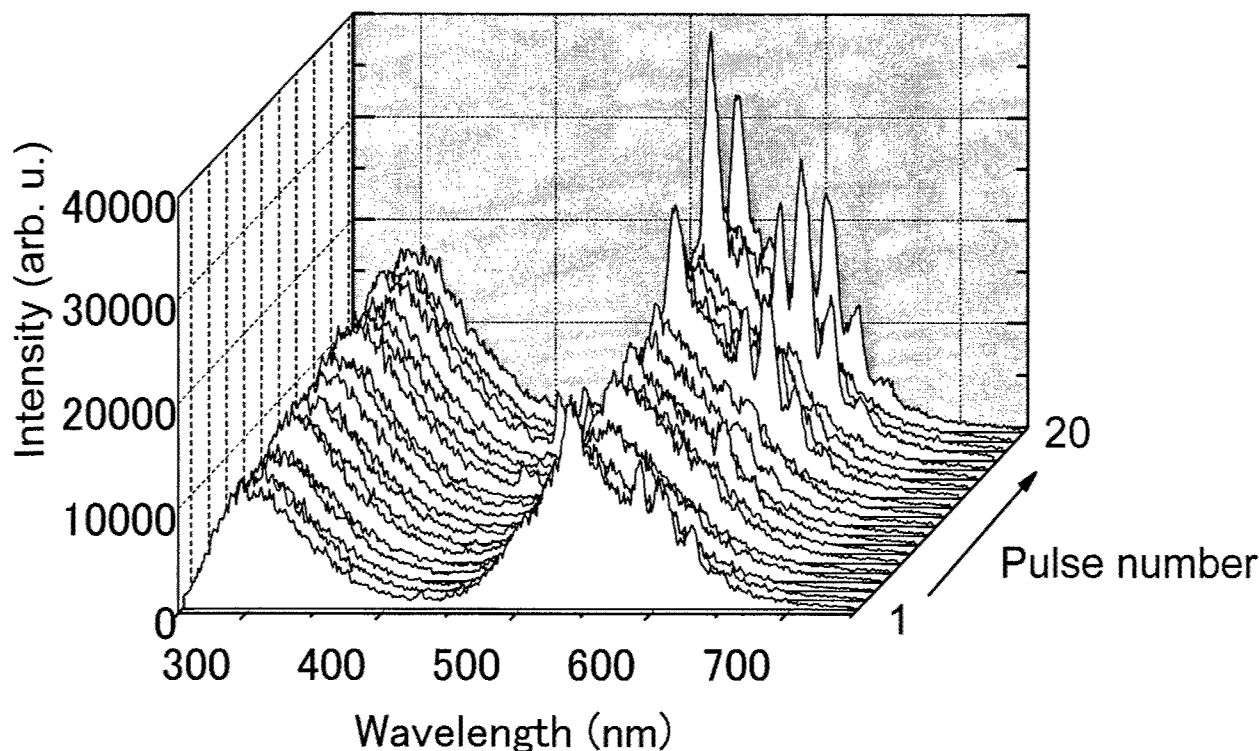
Fig. 3: Optical emission spectra in CaF_2 vs. pulse number under F_2 laser irradiation at 2.0 J cm^{-2}.

laser irradiation, but it did not appear under KrF laser irradiation.[31] The bandgap of CaF_2 is about 12 eV.[11, 12] Thus, band-to-band excitation is achieved by two-photon excitation or defect-mediated two-step excitation under ArF (hv = 6.4 eV) or F_2 (hv = 7.9 eV) laser excitation, while even the energy of the two photons, 10 eV, is not enough to overcome the bandgap in case of KrF laser (hv = 5.0 eV). Similar result is reported and discussed based on the calculated electronic band structure of CaF_2 by Görling et al.[26] At 2.0 J cm^{-2}, sharp emission lines appeared at 424, 449, 536, 589, 603, and 628 nm and overlapped the blue band. They are mainly assigned to relaxation luminescence of the excited Ca atoms and Ca$^+$ ions within the experimental accuracy,[32] showing the occurrence of the optical breakdown and the emission of ablated species from the surface. The line spectra disappeared within several μs, reflecting the diffusion of the plume in the air.[33]

After irradiation of 10 pulses at 1.3 J cm^{-2} and 1.8 J cm^{-2}, optical emission spectrum in CaF_2 at 2.0 J cm^{-2} was observed. The result for each pulse of the F_2 laser is shown in Fig. 3. Line spectra appeared on the first pulse, weakened on the second pulse, and disappeared on the third pulse. After the appearance and disappearance from pulse to pulse several times, the emission lines grew to very strong ones. This phenomenon was also observed under ArF laser irradiation.[31] It should be that F_2 laser irradiation creates electron-hole pairs, and part of them will convert to metastable defects, enhance laser-absorption and cause optical damage accompanying micro-plume with the emission of the line spectra from the near-surface region. Two-photon excitation by the F_2 laser also causes electron desorption on the surface region,[12] which also encourages defect formation, enhances laser-absorption and initiation of the optical damage. While, laser absorption will sometimes work to reconstruct defects to more stable structures and depress the line emission. Moreover, the enhancement and depression of the line spectra may be partly due to the fluctuation of the pulse energy of the F_2 laser. With the cumulative irradiation of the F_2 laser pulses, the concentration of defects will finally increase with the progress of the damage, and result in the strong line emission due to large plume from the surface region.

Fig. 4: SEM image of the laser-damage region by F_2 laser irradiation in Fig. 3.

Fig. 5: SEM image of the laser-damaged region after the occurrence of the laser ablation by the irradiation of the first pulse of the F_2 laser at 2.0 J cm^{-2}.

Figure 4 depicts the SEM image of the laser-damaged surface by F_2 laser irradiation in Fig. 3. The electron beam was irradiated at the incident angle of 60° to the surface. The surface contained severely melted undulations, and 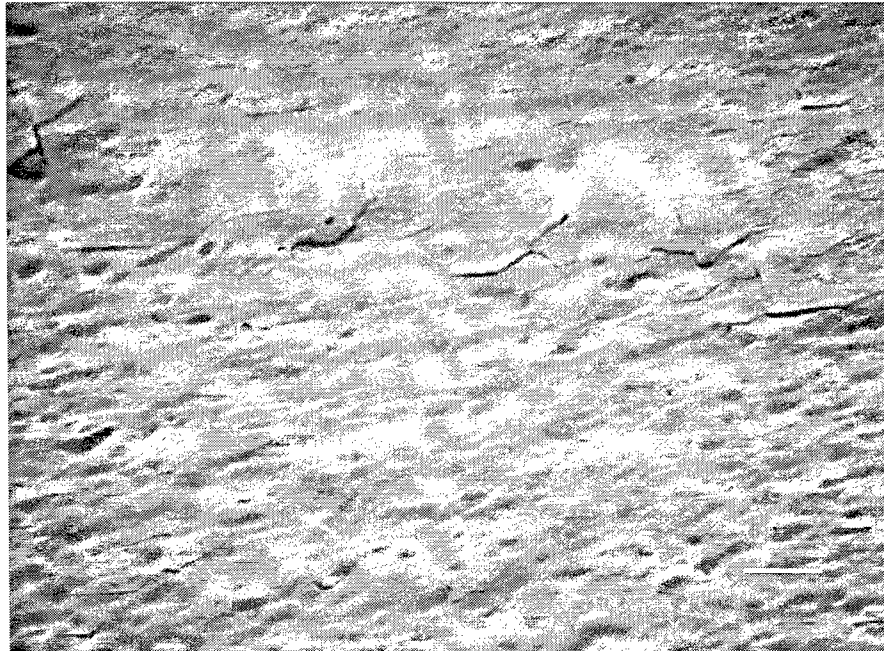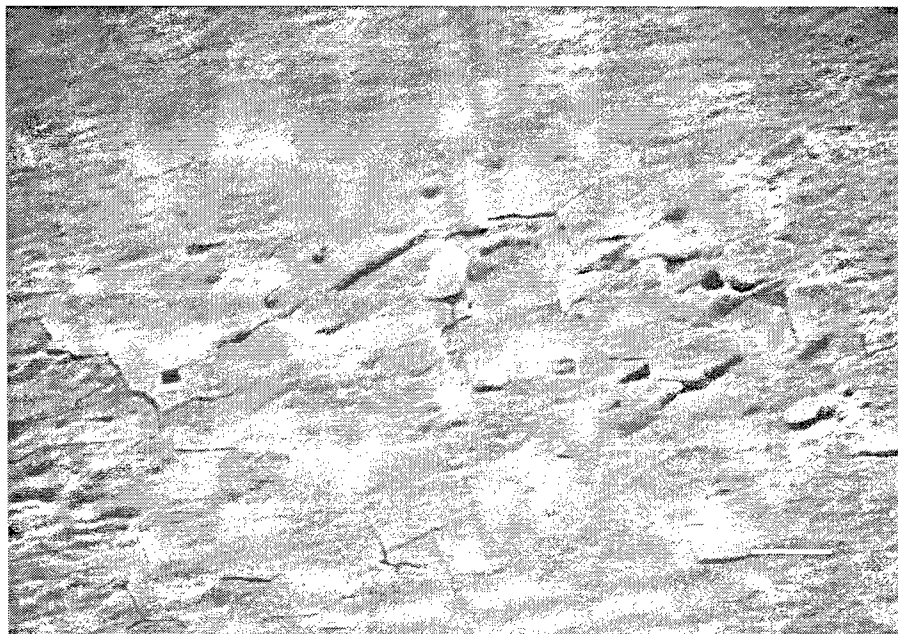there were small pits caused by vaporization of the particles from the surface region. Several cracks due to thermal stress were also observed. This result shows very large thermal effect by the cumulative irradiation of up to 20 pulses at 2.0 J cm^{-2}.

When the F_2 laser beam was irradiated to the other region of the sample, a weak emission of the line spectra appeared from the first pulse of the F_2 laser irradiation when the fluence was increased to 2.0 J cm^{-2}. Figure 5 shows the SEM image in this damaged region where the laser irradiation was stopped after the appearance of the line spectra. The undulation of the surface was not so severe compared to that in Fig. 4, following the gentle damage by irradiation of single pulse at 2.0 J cm^{-2}. The surface showed many cracks due to thermal stress. There also existed several triangular craters due to spallation of the surface layer, similar to the rectangular craters in NaCl and MgO.[28, 34] Large thermal stress generates cracks along the crystallographic axes where the mechanical endurance is lower, and creates triangular flakes which are removed from the damaged surface. In Fig. 4, melting of the surface by the irradiation of additional laser pulses possibly made triangular craters obscure. In case of optical damage by irradiation of a KrF laser or an ArF laser,[23, 24, 31] there are many triangular flakes and cracks on the damaged surface compared to the case of F_2 laser irradiation where the melted structure is more prominent. It may be that larger absorbance for the F_2 laser results in shorter penetration depth at 157 nm and that the absorbed energy is concentrated on the shallower region of the surface and promotes local heating more efficiently, resulting in severer melted structure in addition to the spallation of the surface layer. Unfortunately, the two-photon absorption coefficient at 157 nm for a VUV grade CaF$_2$ crystal is unknown, and detailed discussion is a problem to be solved.

4. CONCLUSION

Under cumulative irradiation of the F_2 laser, the optical damage in CaF$_2$ single crystal initiated at a fluence of about 2 J cm^{-2}. The appearance and disappearance of micro-plume from pulse to pulse was observed, similar to the case of ArF laser irradiation. The laser-damaged surface showed melted structure with cracks, showing the effect of local heating and thermal stress by the F_2 laser irradiation. The knowledge on the interaction of the CaF$_2$ crystal with the F_2 laser will help to clarify the applicability of the crystal for optical components in the VUV laser lithography and VUV laser machining.

5. ACKNOWLEDGEMENTS

6. REFERENCES

1. J. Li, P. R. Herman, X. M. Wei, and K. P. Chen, "High-resolution F_2-laser machining of micro-optic components", *Proc. of SPIE* 4637, pp. 229-234, 2002.
2. X. M. Wei, K. P. Chen, D. Coric, P. R. Herman, and J. Li, "F_2-laser microfabrication of buried waveguide structures in transparent glasses", *Proc. of SPIE* 4637, pp. 251-257, 2002.
3. J. Ihlemann, S. Müller, S. Puschmann, D. Schäfer, M. Wei, J. Li, and P. R. Herman, "Fabrication of submicron gratings in fused silica by F_2-laser ablation", Appl. Phys. A DOI: 10.1007/s00339-002-1467-8, 2002.
4. J. Zhang, K. Sugioka, T. Takahashi, K. Toyoda, and K. Midorikawa, "Dual-beam ablation of fused silica by multiwavelength excitation process using KrF excimer and F_2 lasers", *Appl. Phys. A* 71, pp. 23-26, 2000.

5. K. Sugioka, T. Akane, K. Obata, K. Toyoda, and K. Midorikawa, "Multiwavelength excitation processing using F_2 and KrF excimer lasers for precision microfabrication of hard materials", *Appl. Surf. Sci.* **197**, pp. 814-821, 2002.

6. P. E. Dyer, S. M. Maswadi, H. V. Snelling, and C. D. Walton, "Glass micromachining using the VUV F_2 laser", *Proc. of SPIE* 4637, pp. 218-227, 2002.

7. P. E. Dyer, S. M. Maswadi, and C. D. Walton, "VUV F_2 laser ablation of sodium chloride", *Appl. Phys. A* DOI: 10.1007/s00339-002-1889-3, 2002.

8. R. W. Webb, L. C. Jensen, S. C. Langford, and J. T. Dickinson, "Interactions of wide band-gap single crystals with 248 nm excimer laser radiation. I. MgO", *J. Appl. Phys.* **74**, pp. 2323-2337, 1987.

9. M. Mizoguchi, L. Skuja, and H. Hosono, "F-doped and H_2-impregnated synthetic SiO_2 glasses for 157 nm optics", *J. Vac. Sci. Technol. B* **17**, pp. 3280-3284, 1999.

10. H. Hosono and Y. Ikuta, "Interaction of F_2 excimer laser with SiO_2 glasses: Towards the third generation of synthetic SiO_2 glasses", *Nucl. Instrum. Meth. Phys. Res. B* **166-167**, pp. 691-697, 2000.

11. G. W. Rubloff, "Far-ultraviolet reflectance spectra and the electronic structure of ionic crystals", *Phys. Rev. B* **5**, pp. 662-684, 1972.

12. R. T. Poole, "Electronic structure of the alkaline-earth fluorides studied by photoelectron spectroscopy", *Phys. Rev. B* **12**, pp. 5872-5877, 1975.

13. R. A. Heaton and C. C. Lin, "Electronic energy-band structure of the calcium fluoride crystal", *Phys. Rev. B* **22**, pp. 3629-3638, 1980.

14. D. L. Staebler and S. E. Schnatterly, "Optical studies of a photochromic color centers in rare-earth-doped CaF_2", *Phys. Rev. B* **3**, pp. 516-526, 1971.

15. J. M. G. Tijero and F. Jaque, "Thermal and optical properties of the F_A and $(F_2^+)_A$ centers in Na-doped CaF_2 crystals", *Phys. Rev. B* **41**, pp. 3832-3836, 1990.

16. V. Denks, A. Maaroos, V. Nagirnyi, T. Savikhina, and V. Vassiltsenko, "Excitonic processes in pure and doped CaF_2", *J. Phys. Condens. Matter* **11**, pp. 3115-3125, 1999.

17. K. S. Song and R. T. Williams, *Self-trapped excitons*, 2nd ed. (Springer, Berlin, 1996), p. 96

18. R. Lindner, R. T. Williams, and M. Reichling, "Time-dependent luminescence of self-trapped excitons in alkaline-earth fluorides excited by femtosecond laser pulses", *Phys. Rev. B* **63**, pp. 075110-1-075110-7. 2001.

19. M. Mizoguchi, H. Hosono, H. Kawazoe, and T. Ogawa, "Generation of optical absorption bands in CaF_2 single crystals by ArF excimer laser irradiation: Effect of yttrium impurity", *J. Vac. Sci. Technol. A* **16**, pp. 3052-3057, 1998.

20. M. Mizoguchi, H. Hosono, H. Kawazoe, and T. Ogawa, "Time-resolved photoluminescence for diagnosis of resistance to ArF excimer laser damage to CaF_2 single crystals", *J. Opt. Soc. Am. B* **16**, pp. 1153-1159, 1999.

21. N. Komine, S. Sakuma, M. Shiozawa, T. Mizugaki, and E. Sato, "Influence of sodium impurities on ArF excimer-laser-induced absorption in CaF_2 crystals", *Appl. Opt.* **39**, pp. 3925-3930, 2000.

22. J. Reif, S. Petzoldt, A. P. Elg, and E. Matthias, "The role of defects in laser surface damage thresholds of fluoride crystals", *Appl. Phys. A* **49**, pp. 199-204, 1989.

23. H. Johansen, S. Gogoll, E. Stenzel, M. Reichling, and E. Matthias, "SEM-analysis of fracture features formed in excimer-laser induced surface damage in CaF_2", *Radiat. Effects and Defects Solids* **139**, pp. 151-156, 1995.

24. S. Gogoll, E. Stenzel, M. Reichling, H. Johansen, and E. Matthias, "Laser damage of CaF_2 (111) surfaces at 248 nm", *Appl. Surf. Sci.* **96-98**, pp. 332-340, 1996.

25. M. Reichling, J. Sils, H. Johansen, and E. Matthias, "Nanosecond UV laser damage and ablation from fluoride crystals polished by different techniques", *Appl. Phys. A* **69**, pp. S743-S747, 1999.

26. C. Görling, U. Leinhos, and K. Mann, "Comparative studies of absorptance behaviour of alkaline-earth fluoride at 193 and 157 nm", *Appl. Phys. B* **74**, pp. 259-265, 2002.

27. J. T. Dickinson, Y. Kawaguchi, M. L. Dawes, and S. C. Langford, "Onset of laser plume formation at 248 nm on cleaved single crystal NaCl: Evidence for highly localized emissions", Proc. of SPIE **3935**, pp. 38-46, 2000.

28. Y. Kawaguchi, M. L. Dawes, S. C. Langford, and J. T. Dickinson, "Interaction of wide bandgap single crystals with 248 nm excimer laser irradiation. VII. Localized plasma formation on NaCl single crystal surfaces", *J. Appl. Phys* **89**, pp. 2370-2378, 2001.

29. Y. Kawaguchi, S. C. Langford and J. T. Dickinson: Plume formation and optical breakdown on KrF excimer laser irradiated silica glass, *Proc. of SPIE* **4274**, pp. 258-265, 2001.

30. Y. Kawaguchi, A. Narazaki, T. Sato, H. Niino, A. Yabe, S. C. Langford, and J. T. Dickinson, "The onset of optical breakdown in KrF-laser-irradiated silica glass", *Appl. Surf. Sci.* **197-198**, pp. 50-55, 2002.

31. Y. Kawaguchi, A. Narazaki, T. Sato, H. Niino, and A. Yabe, "Onset of laser ablation in CaF_2 crystal under excimer laser irradiation", *Proc of SPIE 4637*, pp. 13-20, 2002.
32. D. R. Lide, *CRC Handbook of Chemistry and Physics*, 81st ed. (CRC Press, Washington, D. C., 2000).
33. D. R. Elmer, S. C. Langford, and J. T. Dickinson, "Interaction of wide band gap single crystals with 248 nm excimer laser radiation. V. The role of photoelectronic processes in the formation of a fluorescent plume from MgO", *J. Appl. Phys.* **81**, pp. 1495-1504, 1997.
34. J. T. Dickinson, L. C. Jensen, R. L. Webb, M. L. Dawes, and S. C. Langford, "Interactions of wide band gap single crystals with 248 nm excimer laser radiation. III. The role of cleavage-induced defects in MgO", *J. Appl. Phys.* **74**, pp. 3758-3767, 1993.

Semiconductor laser crystallization of a-Si:H

B. K. Nayak, J. McLeskey, A. Selvan, B. Eaton and M. C. Gupta[a]
Applied Research Center, Old Dominion University, Newport News, Virginia 23606
R. Romero and G. Ganguly, BP Solar, Toano, Virginia 23168

ABSTRACT

Results of semiconductor laser crystallization of a-Si:H on transparent conducting fluoride doped tin oxide coated glass are discussed. A-Si:H films were prepared by plasma enhanced chemical vapor deposition. Laser crystallized films of a-Si:H were characterized by X-ray diffraction and optical microscopy. Semiconductor laser crystallization process as compared to well-established excimer laser offers low cost large area technology for solar cell, display and other applications. Longer wavelength of diode lasers (805 nm) allows light to penetrate deeper in the films for crystallization of thicker films required for enhanced light absorption.

Keywords: a-Si, a-Si:H, Laser crystallization, Diode laser, Solar cells, Semiconductor laser.

1. INTRODUCTION

Amorphous silicon is deposited on inexpensive substrates like glass or plastic for mass production of large area solar cells and display applications. For photovoltaic applications it is often desirable to produce cells with higher film thickness for better light trapping[1]. The requirement of low temperature deposition on these substrates results in amorphous films. However, due to the amorphous nature of the deposited films the device performance deteriorates due to carrier recombination. To avoid such recombination and at the same time keeping higher film thickness for significant light absorption necessitates a post processing. Large grain sizes are required, in case of thin film transistors (TFT's)[2] as well as for photovoltaic applications for improved performance[3]. Laser Crystallization is an attractive technique to produce device quality poly-silicon for photovoltaic and display applications[4]. Excimer laser crystallization is a well-established technology for producing poly-Si on glass. However, due to the very high absorption of excimer laser wavelength (248-316 nm) in a-Si:H, only a very thin layer (sub micron) could be crystallized. Although, some improvements in excimer laser technology have been reported to achieve crystallization of thicker films and/or large grain sizes, but they are not practical[5] due to their high processing cost.

Semiconductor lasers operating at near infrared wavelength (805 nm), on the other hand provide an opportunity to crystallize thicker films due to higher penetration of light in to the film at this wavelength. In addition to this, these lasers are very compact for large area robotic controlled applications and relatively lower cost.

2. EXPERIMENTAL

The amorphous silicon layers were deposited on plane glass and TCO (Fluoride doped tin oxide: SnO_2:F) coated glass, using low temperature Plasma Enhanced Chemical Vapor Deposition (PECVD) technique. The hydrogenated amorphous silicon (a-Si:H) films were deposited at a rate of 1 A°/s in hydrogen diluted silane environment at about 200° C. The samples were crystallized using a highly efficient laser diode bar from Nuvonyx (model PB-40) with maximum CW power of 50 Watts, conversion efficiency 50%, pulse width in the range of 100 μs – CW, pulse repetition rate of 0-2 KHz, operating at central wavelength of 805 nm. The laser was operated in pulse mode with repetition frequency of 1500 Hz and pulse width of 300 μs at the average power of 45 W. The samples were placed on a high precision computer controlled X-Y stage with a stepper resolution of 100 nm. The laser beam was focused on the sample through a plano-convex lens of 15 mm focal length. The spot size on the sample surface was approximately 1 mm x 80 μm. The photograph of experimental setup is shown in fig. 1. The sample was scanned at

[a] Electronic mail: mgupta@odu.edu ; phone: 757-269-5645; fax: 757-269-5644

a speed of 2.5 mm/s. The linear translation between two consecutive laser shots was approximately 1.67 μm. Crystallization was performed at room temperature and in air. The laser fluence was ~17 J/cm^2. Note here that there was a necessity to have very high input laser fluence because of relatively lower absorption at 805 nm. A 2.54 × 2.54 cm^2 area of a-Si:H film was crystallized by scanning the sample under the laser beam.

3. RESULTS

The optical microscope picture of laser-crystallized surface is shown in Fig. 2. A clear distinction between laser treated to untreated region is apparent from the figure. X-Ray diffraction (XRD) was carried out on the laser treated/untreated samples to study the structural modification induced by laser treatment. The Rigaku Miniflex 2005 X-ray diffractometer with Cr target was used for our experiment. Fig. 3. Shows the X-ray diffraction results, before and after laser treatment of the sample. Fig. 3 (a) shows the X-ray diffraction result for a-Si:H film (2 μm thick) deposited on glass substrate. An expected broad amorphous peak was observed. However, after laser treatment, three peaks corresponding to (111), (311) and a (331) could be observed in Fig. 3 (b), confirming the crystallization of a-Si:H on glass. The (111) orientation was observed to be predominant peak over both (311) and (331) crystal orientations. Some samples of a-Si:H of 0.5 μm thickness were deposited on SnO2:F coated glass for laser crystallization. After crystallization (220) peak was observed in addition to (111) and (311) peaks. However, (331) peak was absent. The light absorption of the sample at 805 nm wavelength was estimated from spectrophotometeric measurements and was compared with already published literature values for both SnO2:F glass[6] and a-Si[7]. It was found that there was not a very significant amount of absorption at this wavelength. The measurements for 500 nm a-Si:H film on 950 nm SnO_2:F coated glass substrate showed reflection value of 43.5% and, transmission as 36 %. So absorption and scattering, amounts to only 20.5%. With average power of 45 watt laser output no crystallization was observed when tried to crystallize 500 nm thick a-Si:H film deposited on glass. So SnO_2:F layer play a critical role in crystallization process. In order to estimate the grain size of the sample after laser treatment, Secco etching (solution: 3 parts of H_2O, 2 parts of HF 50%, 1 part 0.15 mol solution of $K_2Cr_2O_7$ in H_2O) was applied to the samples. Grains of the order of 5 μm in size were observed from AFM images taken on Secco etched samples[8]. Raman back scattering experiments were carried out on laser treated samples and a sharp peak at 522 cm-1 further confirmed the crystallization.. From the Raman spectrum the crystalline fraction of the laser treated sample were calculated to be 87 %[8].
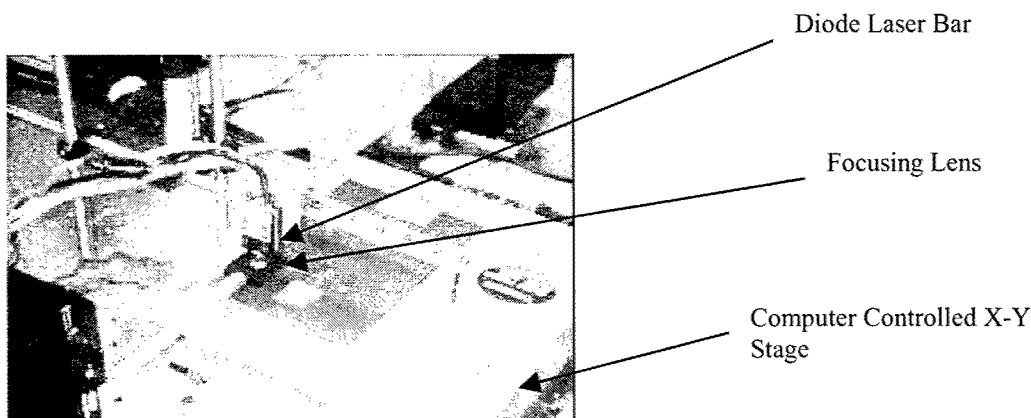
Fig. 1. Photograph showing diode laser crystallization set up

50 um
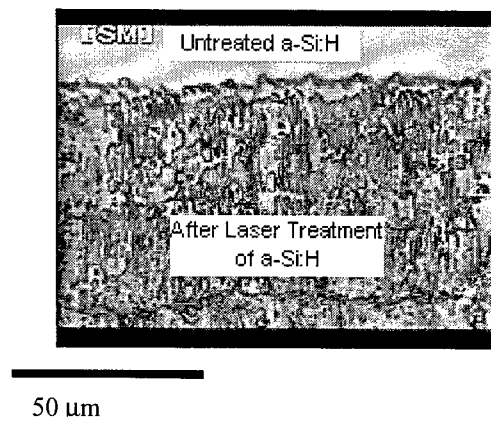
Fig. 2. The optical micrograph of diode laser crystallized a-Si:H on SnO$_2$:F coated glass
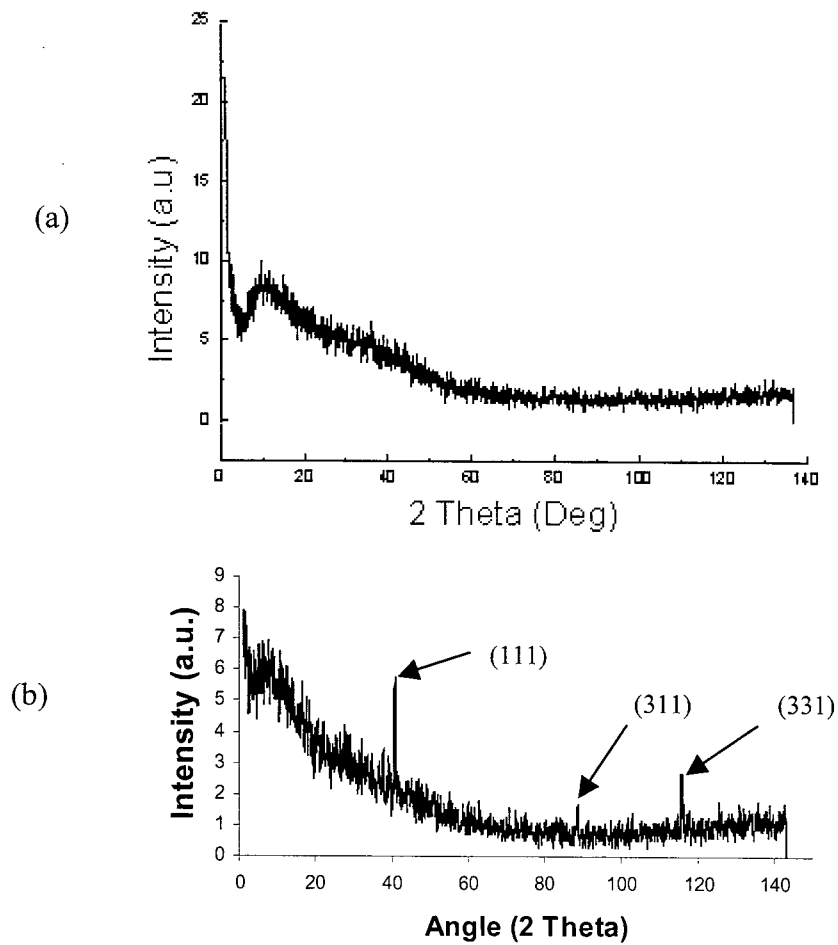
Fig. 3. The X-Ray diffraction results for (a) a-Si:H film (2 µm thick) deposited on glass substrate (b) after laser treatment. (111), (311) and (331) peaks emerged because of laser treatment.

4. CONCLUSIONS

a-Si:H film on conducting tin oxide coated glass and uncoated glass substrate was crystallized using 805 nm wavelength from a compact, low cost semiconductor laser. X-ray diffraction and Raman measurements confirm the crystallization of films. Films as thick as 2 μm have been successfully crystallized. The electrical properties of the film and effect of dopants on crystallization process are being investigated.

ACKNOWLEDGEMENTS

REFERENCES

1. G. Andra, J. Bergmann, F. Falk, E. Ose, Thin Solid Films **318**, 42-45 (1998).
2. S. D. Brotherton, J. R. Ayres, M. J. Edwards, C. A. Fisher, C. Glaister, J. P. Gowers, D. J. McCulloch, and M. Trainor, Thin Solid Films **337**, 188 (1999).
3. R. B. Bergmann, Appl. Phys. A **69**, 187 (1999)
4. S. D. Brotherton, D. J. McCulloch, J. B. Clegg, and J. P. Gowers, IEEE Trans. Electron Devices **40**, 407 (1993).
5. M. Matsumura, Chang-Ho Oh, Thin Solid Films **337**, 123, (1999).
6. K. Von Rottkay, M. Rubin, Mater. Res. Soc. Symp. Proc., **426**, 449 (1996).
7. St. Kanev, Z. Nenova, K. Ivanova, S. Koynov, Solar Energy Materials and Solar Cells, **36**, 277-187, (1995).
8. B. K. Nayak, B. Eaton, J. A. Anna Selvan, J. McLeskey, R. Romero, G. Ganguly and M. C. Gupta[a], Submitted to Appl. Phys. Lett.

---

[a] Electronic mail: mgupta@odu.edu

Femtosecond Laser Interferometric Processing of Nd:GGG Planar Optical Waveguide

K. Oi, M. Obara[*]

Department of Electronics and Electrical Engineering,

Faculty of Science and Technology, Keio University

3-14-1 Hiyoshi, Kohoku-ku, Yokohama, 213-8522, Japan

[*]e-mail: obara@obara.elec.keio.ac.jp

Tetsumi Sumiyoshi

Cyber Laser, Inc., 2-45 Aomi, Times24 4F-N-5, Kotoku, 135-8073 Japan

ABSTRACT

Surface relief type gratings for input laser coupling were fabricated on the PLD deposited 2 at. % Nd:GGG thin film optical waveguide by femtosecond laser interferometric processing. The morphology and coupling efficiency were experimentally evaluated. A clear periodic structure with a fringe period of ~ 800 nm and height of ~ 100 nm was obtained for a surface relief type grating induced on the target surface with a fluence of 0.92 Jcm^{-2}. The coupling efficiency of an 808 nm-centered laser diode pumping light into the 1.35 μm thick film was measured as a function of the incident angle. Three coupling peaks were observed at 57°, 65° and 77°, each being the coupling to the TE_0, TE_1 and TE_2 modes respectively. Each peak had a large FWHM and a maximum coupling efficiency was 3 %.

Keywords: Interferometric ablation, Femtosecond laser processing, Grating coupler, Waveguide laser, Neodymium doped gallium gadolinium garnet.

1. INTRODUCTION

These last few years, various studies have reported that near-infrared femtosecond pulses have a large potential for micro-processing of advanced materials [1]~[15]. Femtosecond laser processing has shown to have the following characteristics: 1) In the case of femtosecond laser pulses, the primary energy transfer to the electrons occurs before the heat relaxation, resulting in the ablation with a minimized heat affected zone (HAZ) [1], [10]; 2) The fact that focused femtosecond laser pulses have an extremely high peak intensity easily leads to nonlinear phenomena and therefore photon energy can be absorbed by any materials having no linear absorption but via non linear absorption such as multiphoton absorption and moreover, processed area below diffraction limit can be obtained [1]; 3) In addition, recent studies have also reported the possibility of submicron accuracy ablation [1]. These characteristics prove this laser to be an innovative tool for high precision processing. Recently, Kawamura et al. have shown the possibility to induce sub-micron period surface relief type grating (SRG) on transparent bulk materials by shingle shot IR femtosecond laser holographic ablation [12] ~ [15]. This holographic technique has revealed to have the following advantages: high productivity because it is a single shot process, and the adjustability of the grating period by the simple tuning of the colliding angle of the two beams [15].

The input/output coupling of a free space propagating laser beam to the waveguide modes is one of the essential technologies for the integration of photonic devices. Optical coupling methods using high index prisms or micro-lenses have both advantages such as ease of use for the former and a high coupling efficiency for the latter. However they require additional optical components and, therefore, restrict the integration capability. Although it requires complicated calculation and design, one of the devices that answer to the requirements of the principle of integrated optics is the grating coupler. Consisting of a simple sub-micron periodic structure, there are two major categories of grating coupler: index modulation type gratings and surface relief type gratings.

The aim of this study is to use femtosecond laser processing in order to improve the integration capability of a thin
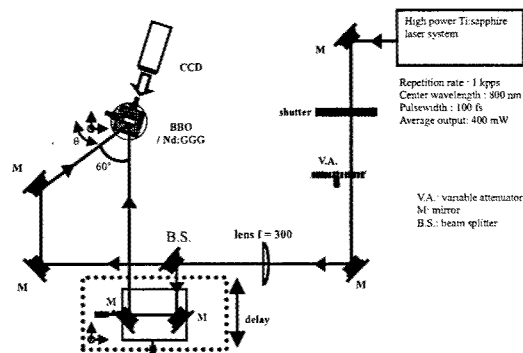
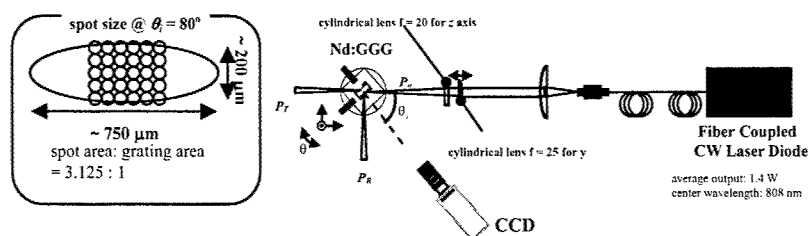Fig. 1   Schematic of the optical setup for the grating fabrication.

Fig. 2   Schematic of the optical setup for the measurement of the coupling efficiency.

film laser waveguide. Etched relief type grating coupler for input coupling is fabricated by femtosecond laser interferometric processing.

2. MATERIALS AND METHODS

2.1 Fabrication method
In this study, the target material is a neodymium doped gallium gadolinium garnet (Nd:GGG) thin film laser waveguide fabricated by a pulsed laser deposition (PLD) on YAG substrate, with a thickness of 1.35 ~ 5 μm. It is a target having possibility as lasing source (pumping at 808nm, lasing at 1.06 μm) for opto electronic integrated circuit (OEIC) applications. Details concerning the PLD fabrication method of the laser waveguide are published by Ishida et al. [16]. A schematic of the optical setup for fabrication is shown in Fig. 1. The laser source is composed of a green laser (SPECTRA PHYSICS; Millennia) pumped Kerr lens mode locked Ti:sapphire laser (FEMTO; Femtosource Pro) with a frequency of 76 MHz, producing 10 fs pulses, then amplified by a home-made chirped pulse amplification system pumped by the second harmonic of a Q-switched Nd:YLF laser (B.M.Industry) operating at a center wavelength of 800 nm, pulsewidth of 100 fs full width at half maximum (FWHM), repetition rate of 1 kHz and an average output of 400 mW. The ablation threshold and absorption process of 1.35 μm thick 2 at. % Nd doped Nd:GGG thin film deposited on a 500 μm thick YAG substrate by PLD is first evaluated for normal incidence case. For the fabrication of gratings, the laser pulse is split into the two identical intensity beams using a beam splitter and then crossed at the target surface. The beam is focused before splitting using a plano-convex lens with a focal length of 300 mm in order to make a spot size of ~ 50 μm. The overlap of the split two pulses is confirmed by the generation of the second harmonic from a 30 μm thick BBO crystal. Each grating is induced by single shot process in air, and the fluence is varied using a variable optical attenuator. The crossing angle θ is calculated from equation $\Lambda = \lambda/2\sin(\theta/2)$, where λ is the writing beam wavelength. Since the grating period is set to 800 nm, the crossing angle resulted to 60°. The induced grating is designed for the coupling of an incident laser centered at 808 nm and the phase matching condition; $\beta = \beta_m + 2q\pi/\Lambda$ (β: propagation constant of the incident light [17], β_m: propagation constant of the mth propagating mode, q: grating order and Λ: grating period) is satisfied when the incident angle of the coupled light ranges between 55° to 75°. This wide range of coupling angle is due to the large refractive index difference between the waveguide (1.97 @ 808 nm) and the substrate (1.82 @ 808 nm) and the thickness of the waveguide (1.35 ~ 5 μm). The written grating is evaluated using an optical microscope and atomic force microscope for morphology observation, and the coupling efficiency of an 808 nm laser diode light is experimentally evaluated.
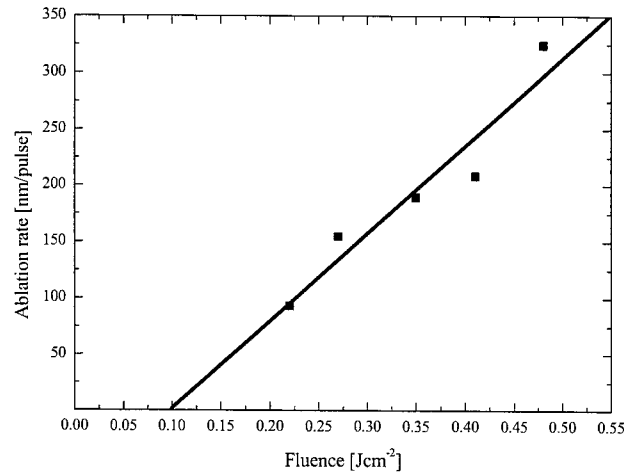
Fig. 3   Variation of the ablation rate as a function of the ablation fluence.
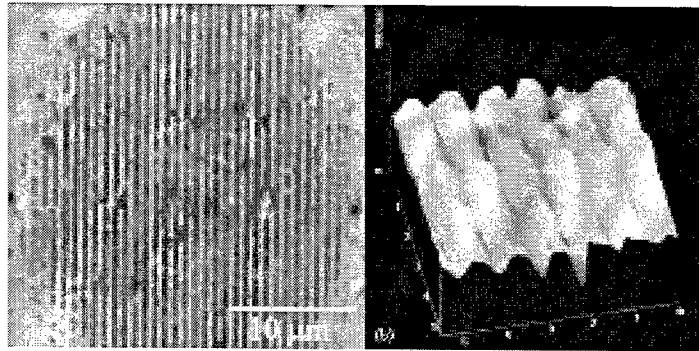
Fig. 4   (a) Optical microscope image of an SRG induced with a fluence of 1.55 Jcm-2,
and (b) AFM image of an SRG induced with a fluence of 0.64 Jcm-2.

2.2 Coupling evaluation method

The optical setup for the evaluation coupling efficiency of an s-polarized 808 nm centered LD light is shown in Fig. 2. The LD light is once collimated using a plano-convex lens with a focal length of 3.8 mm and then refocused at the SRG area using two cylindrical lenses (f = 20 mm, f = 25 mm for the vertical axis and horizontal axis, respectively). The coupling efficiency η_{total} is assumed to be a fraction of the incident light neither reflected nor transmitted (P_R and P_T as shown in Fig. 2) and corrected by taking into account of the loss P_{L0} caused even without any SRG, defined as

$$\eta_{total} \approx \frac{P_o - (P_T + P_R) - P_{L0}}{P_o} \tag{1}$$

where P_0 is the total power of the incident light.

3. RESULTS AND DISCUSSION

The variation of the ablation rate as a function of the fluence is plotted in Fig. 3. The plot represents the experimental results where the solid line is a fitting. The fitting shows that the ablation threshold of the Nd:GGG thin film is around 0.1 Jcm^{-2}. The linear fitting also shows that the absorption process is likely to be linear absorption caused by the Nd doping.   Shown in Fig. 4 (a) is an optical microscope image of an SRG induced on the target surface with a fluence of 1.55 Jcm^{-2}. An AFM image of an SRG induced on the target surface with a fluence of 0.64 Jcm^{-2} is shown in Fig. 4 (b).
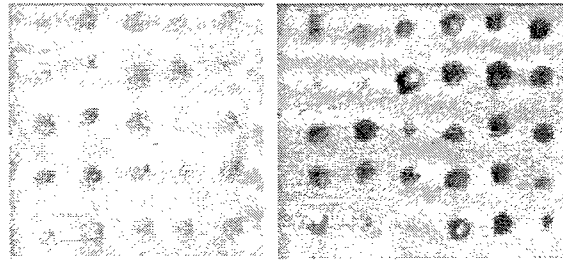
Fig. 4   Optical microscope image of, a) 5×5 matrix pattern with each grating induced with a fluence of 0.82 Jcm-2 (left) and b) 5×6 matrix pattern with each grating induced with a fluence of 0.92 Jcm-2 (right) on a 1.35 μm thick film.

Fig. 5   Mode dispersion curves for a 1.35 μm thick Nd:GGG.

Fig. 6   Variation of the coupling efficiency.

A clear periodic structure with a fringe period of ~ 800 nm can be observed in both cases. The AFM image shows that the depth of the grooves 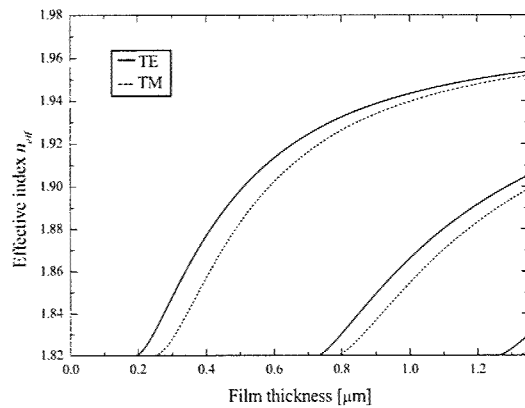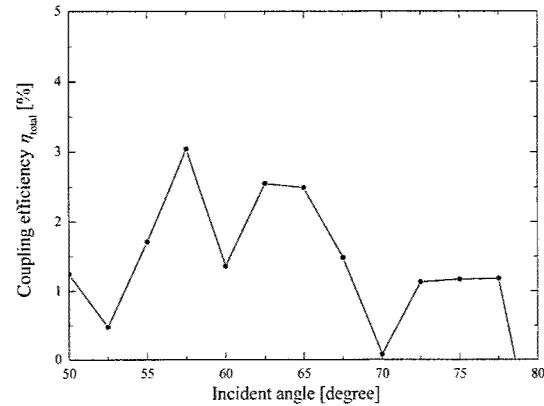h is ≥ 100 nm. SRGs have been induced with fluences from 0.41 Jcm^{-2} to 2.99 Jcm^{-2}, and gratings with depth as deep as 140 nm has been obtained. Since the calculated maximum distance of the evanescent wave outside the waveguide h_c became 130 nm, the obtained grating depth seems to be appropriate. However, at high ablation fluences above 2 Jcm^{-2}, cracks were generated on the waveguide surface, restricting the fluence to be set at a moderate value. In Fig. 4 is shown a schematic of optical microscope images of SRGs arranged as a) 5 ×5 matrix pattern with each grating induced with a fluence of 0.82 Jcm^{-2} and b) 5×6 matrix pattern with each grating induced with a fluence of 0.92 Jcm^{-2} on a 1.35 μm thick Nd:GGG film. When the beam is launched into an area without any SRG, no light was possible to be observed at the waveguide end surface. This suggests that the laser is coupled to the waveguide. However, a scattered light was also observed at the substrate area, being evident that some of the input light has been coupled into the substrate's guiding modes. This miss-coupling might be caused by the fact that the input light was focused at the SRG surface so as to have an incoming beam with a range of incident angle. Since the coupling only occurs at a specific incident angle, a part of the residual light might be coupled to the substrate's guiding modes. In Fig. 5 is shown the calculated dispersion curves for a 1.35 μm thick Nd:GGG film where the solid lines represent the TE modes and dashed lines represent the TM modes. The calculated phase matching incident angle are ~ 55°, ~ 63° and ~ 70.5° for TE modes. In Fig. 6 the variation of the coupling efficiency η_{total} as a function of the incident angle when the incident light is launched through the 5× 6 matrix pattern SRGs is shown. Here, the coupling efficiency is an average of 4 coupling measurements and 3 loss measurements. Three clear peaks can be recognized with a maximum η_{total} of ~ 3 %. The coupling of the incident light to each propagation mode can be identified. From the spot area: unit grating area ratio, the coupling efficiency of each grating can be estimated as 9.375 %. The more than 5° FWHM is mainly caused by the large focusing. The actually low η_{total} of 3 % is due to the fact that neither the incident beam profile nor the grating length are optimized for efficient coupling.

4. CONCLUSION

Although the coupling efficiency is low, the fabrication of surface relief type grating for input coupling of the pump light to a Nd:GGG optical waveguide by femtosecond laser interferometric processing has been achieved. By optimizing the grating parameters and incident pump light parameter, a more efficient coupling efficiency might be obtained.

5. AKNOWLEDGEMENTS

6. REFERENCES

[1] A. Ostendorf, "Precise structuring using femtosecond lasers", *Review of Laser Engineering* **30**, no 5, 221 (2002).

[2] B. N. Chichkov, C. Momma, S. Nolte, F. Von Alvensleben and A. Tuennermann, "Femtosecond, picosecond and nanosecond laser ablation of solids", *Appl. Phys. A* **63**, no 2, 109 (1996).

[3] J. Krüger, W. Kautek, M. Lenzner, S. Sartania, C. Spielmann and F. Krausz, "Laser micromachining a barium aluminium borosilicate glass with pulse durations between 20 fs and 3 ps", *Appl. Surf. Sci.*, no 127-129, 892 (1998).

[4] K. Ozono, M. Obara, A. Usui and H. Sunakawa, "High-speed ablation etching of GaN semiconductor using femtosecond laser", *Opt. Comm.* **189**, no 1-3, 103 (2001)

[5] K. Miura, J. Qyu, H. Inouye, T. Mitsuyu and K. Hirao, "Photowritten optical waveguides in various glasses with ultrashort pulse laser", *Appl. Phys. Lett.* **71**, no 23, 3329 (1997).

[6] S. Guizard, A. Semerok, J. Gaudin, M.Hashida, P. Martin and F. Quere, "Femtosecond laser ablation of transparent dielectrics: measurement and modelisation of crater profiles", Appl. Surf. Sci., no 1- 4, 364(2002).

[7] H. Misawa, "Functionalization of transparent dielectric materials by femtosecond fabrication with super-resolution", *Review of Laser Engineering* **30**, no 5, 239 (2002).

[8] K. Sugioka, "Comparison between DUV/VUV and femtosecond laser processing of dielectrics and semiconductors", *Review of Laser Engineering* **30**, no 5, 226 (2002).

[9] C. B. Schaffer and E. Mazur, "Micromachining using ultrashort pulses from a laser oscillator", *Optics and Photonics News* **12**, no 4, 20 (2001).

[10] Y. Hirayama and M. Obara, "Heat effects of metals ablated with femtosecond laser pulses", *Appl. Surf. Sci.* **197-198**, 741 (2002).

[11] V. Schmidt, W. Husinsky and G. Betz, "Dynamics of laser desorption and ablation of metals at the threshold on the femtosecond time scale", *Phys. Rev. Lett.* **85**, no 16, 3516 (2000).

[12] K. Kawamura, T. Ogawa, N. Sarukura, M. Hirano and H. Hosono, "Fabrication of surface relief gratings on transparent dielectric materials by two-beam holographic method using infrared femtosecond laser pulses", *Appl. Phys.* **B 71**, no 1, 119 (2000).

[13] K. Kawamura, N. Ito, N. Sarukura, M. Hirano and H. Hosono, "New adjustment technique for time coincidence of femtosecond laser pulses using third harmonic generation in air and its application to holograph encoding system", Rev. of Scien. Inst. **73**, no 4, 1711 (2002).

[14] K. Kawamura, N. Sarukura, M. Hirano, N. Ito and H. Hosono, "Periodic nanostructure array in crossed holographic gratings on silica glass by two interfered infrared-femtosecond laser pulses", Appl. Phys. Lett. **79**, no 9, 1228 (2001).

[15] Y. Li, W. Watanabe, K. Yamada, T. Shinagawa, K. Itoh, J. Nishii and Jiang Yongyuan, "Holographic fabrication of multiple layers of grating inside soda-lime glass with femtosecond laser pulses", *Appl. Phys. Lett.* **80**, no 9, 1508 (2002).

[16] Y. Ishida, S. Fukaya, T. Shimoda and M. Obara, "Fabrication of Nd:Gd$_3$Ga$_5$O$_{12}$ and self Q-switched Nd,Cr:Gd$_3$Ga$_5$O$_{12}$ laser waveguides by pulsed laser deposition method", *Proceedings of the SPIE - The International Society for Optical Engineering* **4184**, 530 (2001).

[17] T. Tamir, *Integrated Optics*, pp 90 - 118, Springer-Verlag (1979).

Femtosecond laser ablation processing of x-cut LiNbO₃ substrates for optical communication devices

Riichi Kitano, Kazue Ozono, Minoru Obara, and Hiroyuki Tsuda
Electronics and Electrical Engineering, Keio University
3-14-1 Hiyoshi, Kohoku, Yokohama 223-8522, Japan

ABSTRACT

We have studied femtosecond laser ablation characteristics of LiNbO₃ for the first time. LiNbO₃ is ferroelectric material with large optical nonlinearity and Pockels effect. The femtosecond laser ablation is very useful to fabricate various optical devices including the optical modulator and the tunable optical filter for optical communication systems because the thermal damage around the irradiated area is small due to the short pulse width, and the sub-wavelength structures may be formed by the multi-photon excitation. In our experiments, the femtosecond Ti:Sapphire laser system (Energy 0.14 mJ/pulse, Wavelength 800 nm, Pulse duration 60 fs, Repetition rate 1 kHz) based on the chirped-pulse amplification (CPA) technique was used. The aperture with a diameter of 5 mm was imaged onto the LiNbO₃ surface by the objective lens in the air. We observed ablation holes by the scanning electron microscope and the profilometer. We have found no damage around the holes and the clear boundary between ablated area and non-ablated area was observed. Those features are very useful for precise material processing. The bottom face of the holes was relatively flat. The etching rate was 0.93 micrometer/pulse and proportional to the number of the laser pulse. The results showed that the femtosecond laser ablation is an innovative tool for manufacturing LiNbO₃-based optical devices.

Keywords: LiNbO₃, femtosecond laser, ablation, processing, optical waveguide, optical communication

1. INTRODUCTION

1.1 LITHIUM NIOBATE FOR OPTICAL DEVICES

To realize the next generation photonic network, it is necessary to develop optical devices such as wavelength division multiplexers (WDM), optical filters, which are used for optical signal processing and routing at each node connected by optical fibers[1]. The planar lightwave circuit (PLC) is usually made of SiO₂ layers[2]. SiO₂ is a general material for optical waveguides, and inexpensive and easy for processing. But it is difficult to fabricate SiO₂ to active devices such as modulators. LiNbO₃ is ferroelectric material with large optical nonlinearity and Pockels effect. Therefore, it is useful for the optical modulator and the wavelength converter[3] for optical communication systems. For example, the wavelength division multiplexer can be integrated with the optical modulator array (Fig. 1). The optical filter can be integrated with the wavelength converter with the quasiphase matched (QPM) waveguides (Fig. 2).
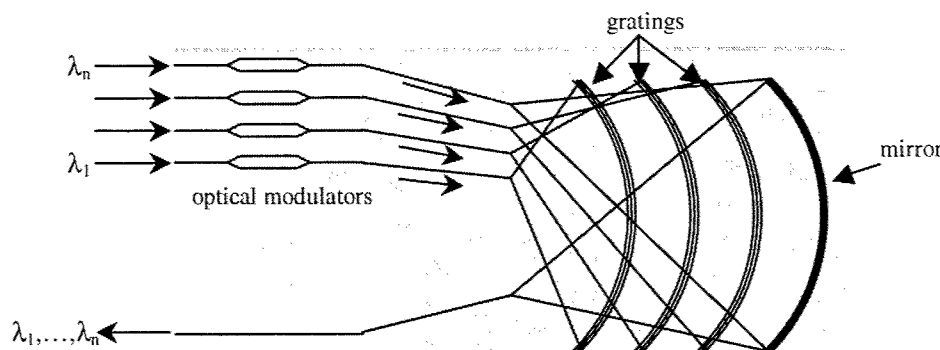

Figure 1: Schematic view of the wavelength division multiplexer integrated with the optical modulator array.
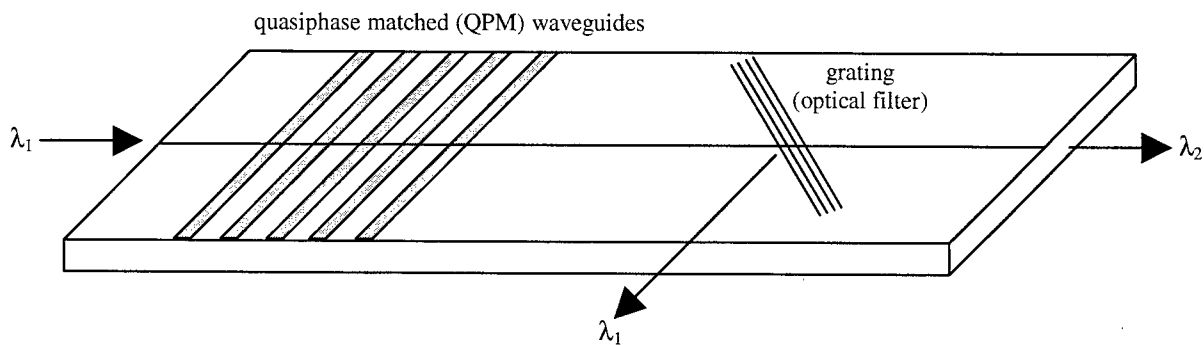
quasiphase matched (QPM) waveguides

Figure 2: Schematic view of the optical filter integrated with the wavelength converter.

1.2 FEMTOSECOND LASER ABLATION

The femtosecond laser ablation is very useful to process various materials. There are many advantages of using femtosecond laser pulses. The thermal damage around the irradiated area is small due to the short pulse width. The sub-wavelength structures may be formed by the multi-photon excitation. Much less input energy is required to produce the material removal because of high peak power[5, 6]. We propose the use of the femtosecond laser ablation for manufacturing optical devices. Recently, the fabrication of gratings on the $LiNbO_3$ substrate was achieved by using the two-beam interference[7]. It proved that the femtosecond pulse is a useful tool for processing $LiNbO_3$. Therefore, we need to investigate detailed characteristics of the femtosecond laser ablation of $LiNbO_3$. In this paper, we have studied femtosecond laser ablation characteristics of $LiNbO_3$. We observed ablation holes by the scanning electron microscope (SEM), atomic force microscope (AFM), and the profilometer.

2. EXPERIMENTAL

A schematic diagram of the experimental set-up is shown in Fig. 3. The laser used in our experiments was a Ti:Sapphire oscillator-amplifier system based on the chirped-pulse-amplification technique (CPA)[8]. This system consists of the femtosecond oscillator, the Nd-YLF pump laser, and the amplifier system (CPA). The output power varies up to 1W. The center wavelength was 800 nm. The repetition rate was 1kHz. Mirrors guided the amplifier output light. Through the aperture, the neutral density filter (ND filter), and the electrical shutter, the beam (linearly polarized light) was focused onto the $LiNbO_3$ -x face on the stage by the objective lens in the air. The pulse duration, which was measured by the autocorrelator, was 60 fs just before the laser-focusing lens. From the backside of the target, the illuminated surface was observed by the objective lens and the CCD camera. The stage and the shutter were controlled synchronously by the personal computer. The laser-focusing lenses were the x20 objective (the aperture diameter 5 mm), the x100 objective (the aperture diameter 2 mm), and the plano-convex lens (focal length f = 50.4 mm).

To observe the damage around the ablated holes, the morphology of the bottom face, and the boundary between ablated area and non-ablated area, the laser beam illuminated the target by the x20 objective. At the focal point, the Gaussian beam diameter was estimated 17μm by relation between the diameter of the holes and the pulse energy[9].

We experimented varying the fluence and the number of pulses with the plano-convex lens (focal length f = 50.4 mm). The depths of holes etched by femtosecond pulses with various fluence were measured by the atomic force microscope (AFM), and the profilometer.

To make holes as small as possible, x100 objective was used. At the beam waist, the beam diameter was 6μm.
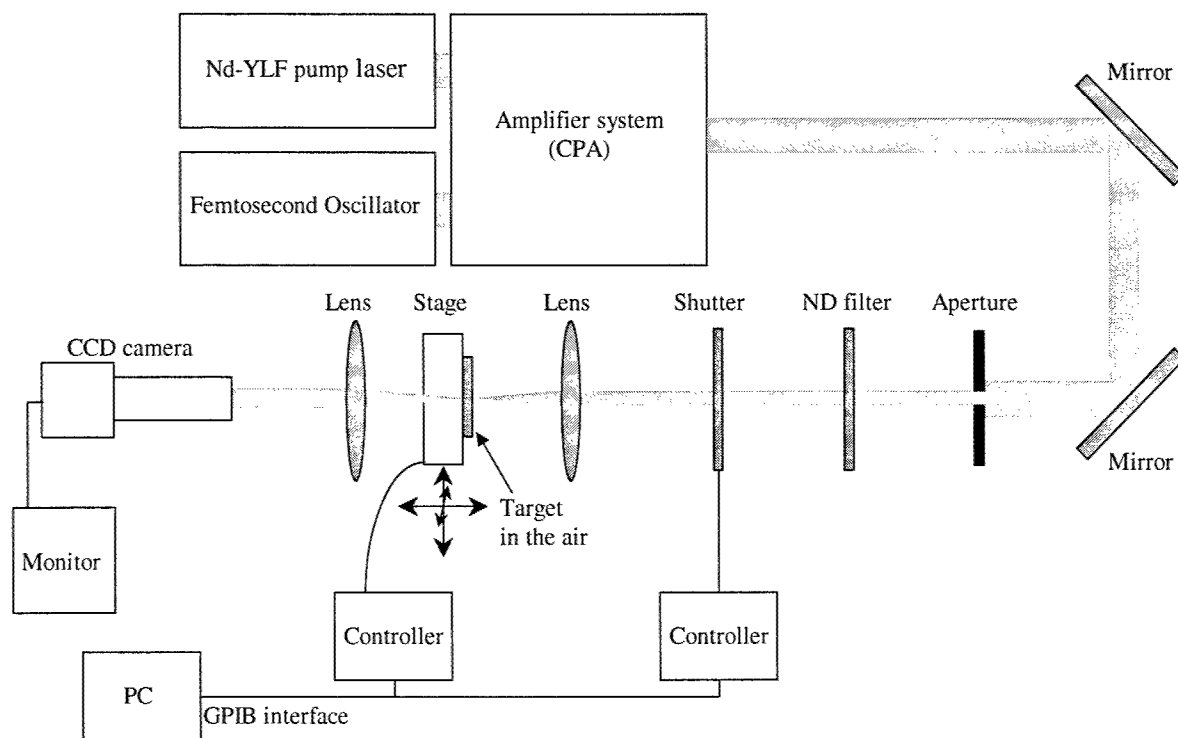
Figure 3: Schematic illustration of the experimental set-up.

3. RESULTS AND DISCUSSION

3.1 SURFACE MORPHOLOGY

Figures 4 (a)-(i) show the SEM photographs of the structures on the LiNbO$_3$ substrate obtained by the laser processing using the x20 objective as the laser-focusing lens. We have found no damage around the holes, where the clear boundary between ablated area and non-ablated area was observed (Fig. 4 (a)~(e),(g)). The multi-photon excitation contributed to the formation of the clear boundary.

At the fluence of 9.7 J/cm^2, radial stripes were observed, which may be the deposits of the ablation plume. At the high fluence of 9.7 J/cm^2, with 128 shots (Fig. 4(i)), there was damage (small craters) around the hole. Because the aperture focused at the focal point to Gaussian beam profile by the Fourier transform, and the high frequency component around Gaussian profile exceeded the threshold fluence.

In all photographs, there were periodic ripples on the bottom surfaces of the holes. The spacing of the ripples was 770 nm. The ripples were with a spacing corresponding to the wavelength of the laser light. The ripples originated from the interference between the incident laser light and the scattered wave along the interface[4, 5].

a) F=3.1 J/cm^2, N=32 b) F=3.1 J/cm^2, N=64 c) F=3.1 J/cm^2, N=128

d) F=6.1 J/cm^2, N=32 e) F=6.1 J/cm^2, N=64 f) F=6.1 J/cm^2, N=128

g) F=9.7 J/cm^2, N=32 h) F=9.7 J/cm^2, N=64 i) F=9.7 J/cm^2, N=128

Figure 4: SEM pictures after the laser processing of LiNbO$_3$ at 800 nm, 60 fs using the x20 objective as the laser-focusing lens in the air for three different fluence: 3.1 J/cm^2 (top), 6.1 J/cm^2 (middle), and 9.7 J/cm^2 (bottom); SEM photographs of holes produced with 32 shots (left column), 64 shots (middle column), and 128 shots (right column).

3.2 ETCHING RATE

Figure 5 shows the ablation depths as a function of the number of laser shots (N = 2-16) for LiNbO$_3$ in the air. The laser-focusing lens was the plano-convex lens (f = 50.4 mm). The depths were measured by the profilometer. For the low fluence (1.1 J/cm^2 and 1.4 J/cm^2) the substrate etching processes were in the gentle ablation phase. For the high fluence (2.0 J/cm^2 and 4.1 J/cm^2) the ablation depth increased dramatically. The crossover from the gentle ablation phase to the strong ablation phase takes place[4, 5].

The etching rate is shown in Fig. 6. The etching rate increased dramatically when the laser fluence was over 2.0 J/cm^2. The ablation threshold of 0.63 J/cm^2 was obtained. The energy band gap of LiNbO$_3$ is 3.635 eV. Because the laser photon energy of hν = 1.55 eV at 800 nm, the 3 photon excitation makes the ablation possible. In this case, the relationship between the amount of the ablated material and the laser fluence is nonlinear.
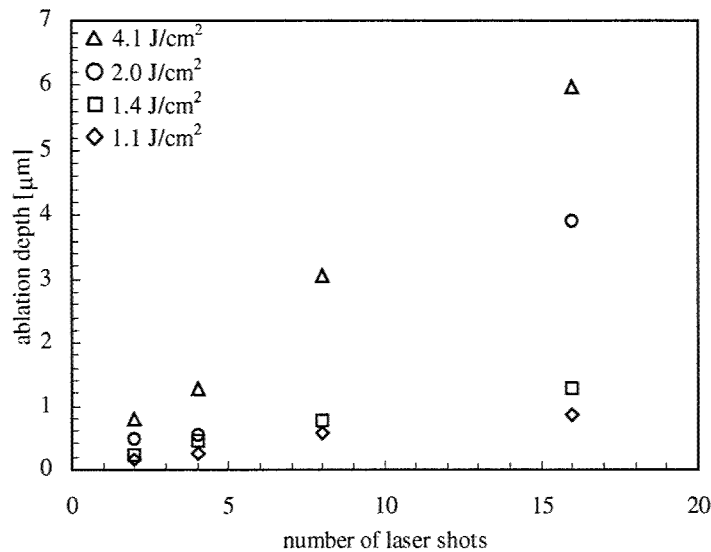
Figure 5: The ablation depths as a function of the number of laser shots (N = 2-16) for LiNbO$_3$ at 800 nm. 60 fs in the air and at four fluences (1.1, 1.4, 2.0, and 4.1 J/cm^2). The laser-focusing lens was the plano-convex lens (f = 50.4 mm). The depths were measured by the profilometer.
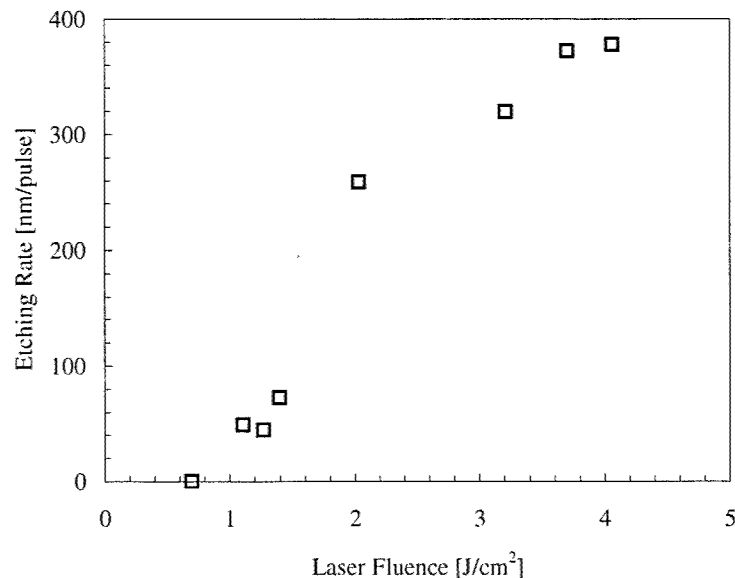
Figure 6: The etching rate as a function of the laser fluence for LiNbO$_3$ at 800 nm. 60 fs in the air. The plano-convex lens (f = 50.4 mm) was used.

3.3 MICROSCOPIC PROCESSING

Figures 7(a)~(f) show SEM pictures after the laser processing of $LiNbO_3$ with 8 and 16 shots of pulses with a wavelength of 800 nm and a pulse duration of 60 fs using the x100 objective. At the highest fluence (Fig. 7(a)), the deposit was observed around the hole. The amount of the deposit was reduced for the lower fluence (Fig. 7(b)). There was no deposit for the lowest fluence (Fig. 7(c)), and the hole with the diameter of 1 µm was obtained. This can be applied to optical devices such as optical filters, which have gratings with 1 µm period. The aspect ratio of the holes was so high that neither the atomic force microscope (AFM) nor the profilometer could measure the depth.

Figure 8 shows the diameters of holes as a function of the laser fluence using the x100 objective as the laser-focusing lens in the air. The relation between the diameter of the modified area D and the laser fluence F is $D^2 = 2\omega_0^2 \ln(F/F_{th})$, where ω_0 is $1/e^2$ beam radius, F_{th} is modification threshold fluence. Fig. 8 indicates this relation. We found that the laser-processed area could be controlled by the laser fluence.

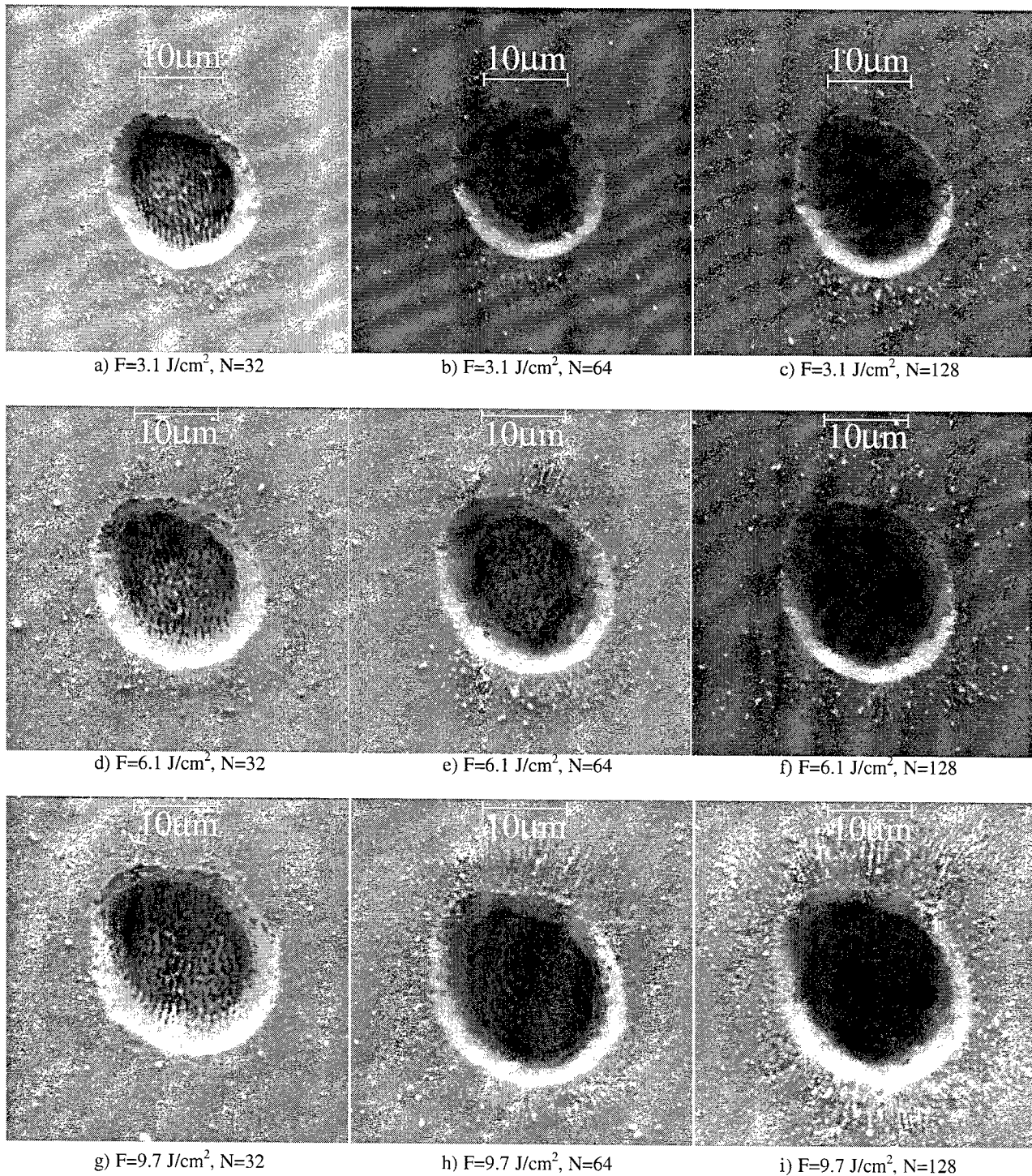|		
(a) F=2.7x10^2 J/cm^2, N=8	(b) F=87 J/cm^2, N=8	(c) F=4.2 J/cm^2, N=8
(d) F=2.7x10^2 J/cm^2, N=16	(e) F=87 J/cm^2, N=16	(f) F=4.2 J/cm^2, N=16
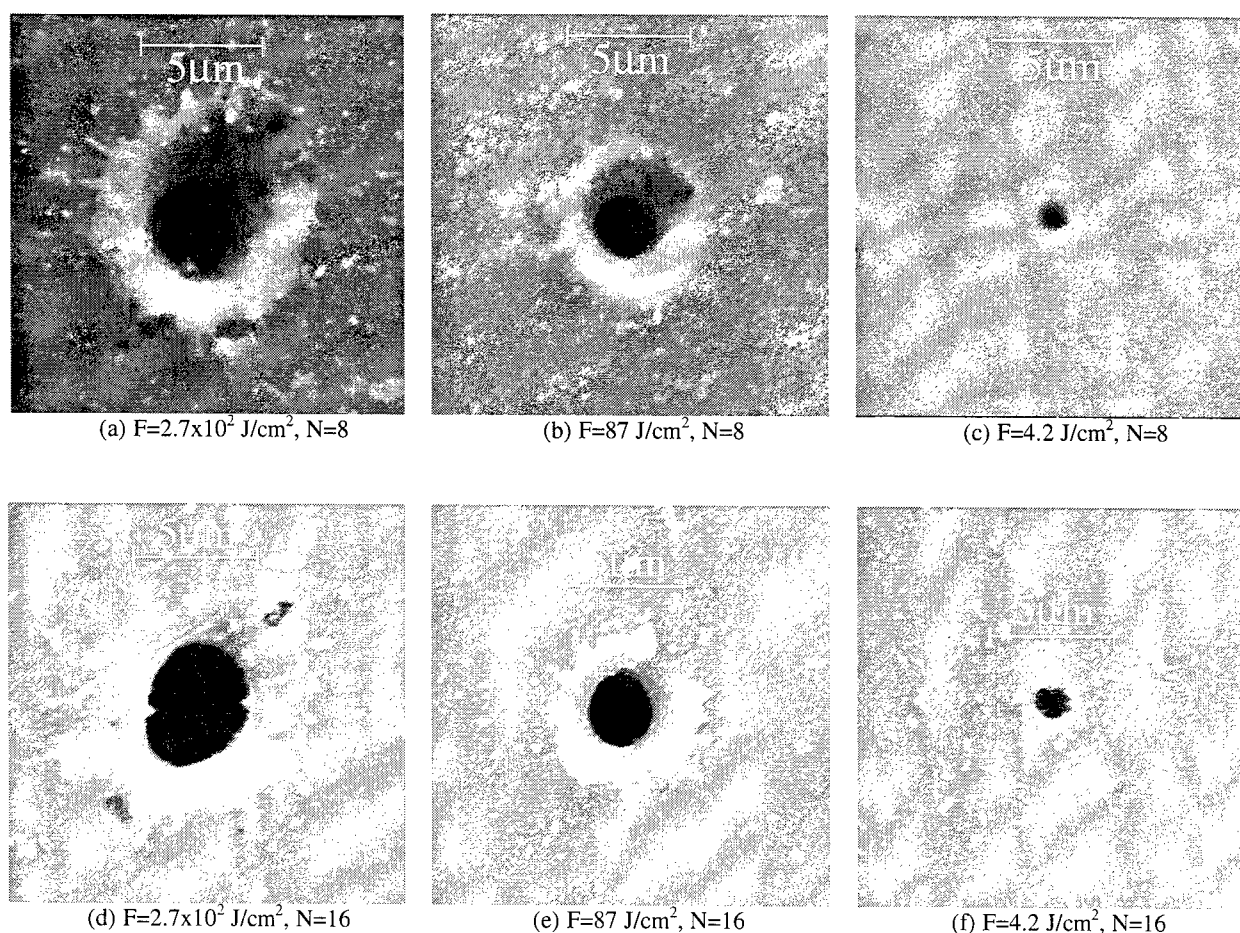
Figure 7: SEM pictures after the laser processing of $LiNbO_3$ at 800 nm, 60 fs using the x100 objective as the laser-focusing lens in the air for three different fluence: 2.7x10^2 J/cm^2 (left column), 87 J/cm^2 (middle column), and 4.2 J/cm^2 (right column); SEM photographs of holes produced with 8 shots (top), and 16 shots (bottom).
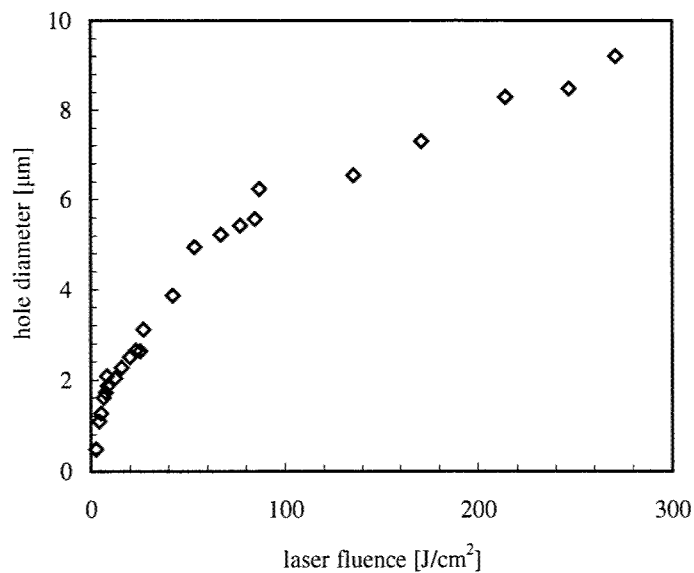
Figure 8: The hole diameters as a function of the laser fluence after the laser processing of $LiNbO_3$ with 8 shots of pulses with a wavelength of 800 nm and a pulse duration of 60 fs using the x100 objective as the laser-focusing lens in the air. The diameters were taken from SEM analysis.

4. CONCLUSION

We have studied laser ablation characteristics of $LiNbO_3$ for the femtosecond pulses with a wavelength of 800 nm and a pulse width of 60 fs, using the x20 objective lens, the x100 objective, and the plano-convex lens (focal length f = 50.4 mm) as the laser-focusing lens. We have found no damage around the holes and the clear boundary between ablated area and non-ablated area was observed. The bottom face of the holes was relatively flat, and there are ripples with the period corresponding to the laser wavelength. Two ablation phases are observed. At low laser fluence and small number of laser shots a gentle ablation can be seen. At high fluence with multiple laser shots there is an abrupt change to a much stronger ablation. Between both phases there is clear difference in the etching rate per pulse. The ablation threshold of 0.63 J/cm^2 was obtained. The relation between the modified area and the laser fluence was in good agreement with the theory. The size of the processing area can be controlled by the laser fluence. Fine processing of 1μm was achieved by using x100 objective lens. These results showed that the femtosecond laser ablation is an innovative tool for manufacturing $LiNbO_3$-based optical devices such as wavelength division multiplexers (WDM) and optical filters.

ACKNOWLEDGEMENTS

REFERENCES

1. Tsuda, Obara, PCT/JP01/10824.

2. Yoshinori Hibino, "Planar Lightwave Circuits for Photonic Networks," *CERAMICS JAPAN*, **37**, 355-360, 2002.

3. Bo Chen, Chang-Qing Xu, Bing Zhou, Yasukazu Nihei, Akinori Harada, "All-Optical Variable-In Variable-Out Wavelength Conversions by Using MgO:LiNbO$_3$ Quasiphase Matched Wavelength Converters," *Jpn. J. Appl. Phys.*, **40**, L1370-L1372, 2001.

4. D. Ashkenasi, A. Rosenfeld, H. Varel, M. Wahmer, E.E.B. Campbell, "Laser processing of sapphire with picosecond and sub-picosecond pulses," *Applied Surface Science*, **120**, 65-80, 1997.

5. E.E.B.Campbell, D.Ashkenasi, A.Rosenfeld, "Ultra-Short-Pulse Laser Irradiation and Ablation of Dielectrics," *Mater. Sci. Forum*, **301**, 123-144, 1999.

6. H. Kumagai, K. Midorikawa, K. Toyoda, S. Nakamura, T. Okamoto, M. Obara, "Ablation of polymer films by a femtosecond high-peak-power Ti:sapphire laser at 798 nm," *Appl. Phys. Lett.*, **65**, 1850-1852, 1994.

7. K. Kawamura, T. Ogawa, N. Sarukura, M. Hirano, H. Hosono, "Fabrication of surface relief gratings on transparent dielectric materials by two-beam holographicmethod using infrared femtosecond laser pulses," *Appl. Phys. B*, **71**, 119–121, 2000.

8. T. Imahoko, K. Furusawa, M. Kamata, M. Obara, "Development of automatic pulsewidth-controllable ultrashort laser system," *IEICE Technical Report*, **100**, LQE2000 14-25, 49-54, 2000.

9. S. Baudach, J. Bonse, W. Kautek, "Ablation experiments on polyimide with femtosecond laser pulses," *Appl. Phys. A*, **69[Suppl.]**, S395-S398, 1999.

Optical Waveguide Fabrication Inside Transparent Materials by Use of Plasma Channeling Induced by Tailored Femtosecond Laser

Masanao KAMATA, Kosuke OHTA, Minoru OBARA
Department of Electronics and Electrical Engineering, Faculty of Science and Technology,
Keio Univerisity, 3-14-1 Hiyoshi, Kohoku-ku, Yokohama 223-8522, Japan
*Email: obara@obara.elec.keio.ac.jp

Hiroshi SEKITA
Cyber Laser, Inc. 2-45 Aomi, TIME 24 4F-N-5, Kotoku, 135-8073 Japan

Abstract

With a loosely focused femtosecond laser, refractive index change is induced in silica glass without any scanning process. By decrease numerical aperture of the incident laser, the induction of irregular structure can be avoided such as clacks and spatial splitting of the induced refractive index change region. We demonstrate controlling of the refractive index change by optimizing the numerical aperture and input energy and input pulsewidth and laser shot number. A new method of fabrication of photonic devices in silica glass is proposed.

1. Introduction

Internal modification of transparent materials by femtosecond laser (fs) were recently reported [1,2]. Fs laser has a very high peak power and the increase of refractive index change is caused by the nonlinear absorption in wide band gap materials such as silica glass that have no linear absorption in the visible region of the spectrum. Although the physical mechanism of the refractive index change is still under investigation, the refractive index change induced by fs laser pays much attention because it enables to fabricate optical waveguides arbitrarily inside transparent materials [3,4]. This technique applied to photonic devices such as couplers[5,6], photonic crystals [7].

There are two methods of the induction of refractive index change by fs laser. One method is using a large numerical aperture (NA) lens and another method is to use a small NA lens [8,9]. The former has high controllability because the absorbed energy is confined in a very small volume, but the modified region is limited to near the surface due to the very short focal length of the large NA lens. The latter allows focusing fs laser pulses deep inside the transparent material because of a long focal length, but the control of the induction of refractive index change is a very difficult task because plasma channeling occurs and it is likely to induce spatial splitting of refractive index change. Plasma channeling is an intensity dependent nonlinear phenomenon in which an intense pulsed laser beam is self-guided for a length longer than the Rayleigh range along the laser propagation axis inside the material. Refractive index change induced by plasma channeling has elongated profile along the optical axis. In order to control refractive index change using fs laser induced plasma channeling, it is indispensable to grip the nonlinear propagation inside the transparent material.

In this paper we demonstrate waveguides fabrication without any scanning process by controlling the nonlinear propagation of fs laser pulses. This method allows photonic device fabrications such as optical waveguides, internal gratings, and couplers deep inside transparent materials.

2. Experiment
A. Automatic pulsewidth variable fs laser

The experiments were performed with the automatic pulsewidth variable fs laser we developed. It is based on chirped pulse amplification (CPA) technique which produces 50fs~1ps, 0.5mJ, at a wavelength of 800nm. The laser consisted of a Kerr-lens mode-locked Ti:sappire laser followed by a Q-switched Nd:YLF laser pumped regenerative amplifier in CPA
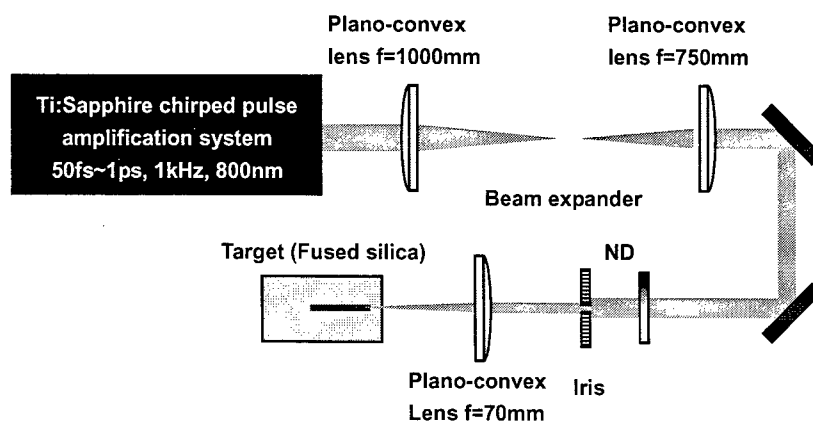
Fig.1 Schematic of the experimental setup for waveguides fabrication in fused silica samples. ND: neutral density filter.

architecture. The pulsewidth can be varied by adjusting a distance of gratings in a pulse compressor using computer controlled stepping motors. The pulsewidth was characterized by second harmonic generation cross-type autocorrelator. The spectral width of the output laser pulses was 30nm and the beam diameter was 4.3mm. The laser pulse energy stability was better than 5%.

B. Experimental setup for the induction of refractive index change

We investigated induction of refractive index change in terms of experimental parameters such as the effective numerical aperture, incident laser pulsewidth, energy, and irradiation time to control the behavior of plasma channeling. The apparatus for the experiments is illustrated in Figure1. The beam diameter was decreased to 3.2mm by a 4:3 beam expander. The laser pulses were focused by a plano-convex lens with a focal length of 70mm and geometric focal point was located 5mm inside the sample surface. The pulse energy was adjusted by neutral density filter. The beam diameter just before the focusing lens was adjusted by iris. The polished fused silica (40×20×10mm) samples were mounted on a metal target holder on a triaxial micromanipulator. The side edges of the samples were polished to observe the modified region by an optical microscope.

The induced refractive index change was measured by the method of Homoelle et al. [3]. On the assumption that the fabricated waveguides are step-index waveguides, the induced refractive index change Δn is described as follows for small Δn,

$$NA = \sqrt{2n\Delta n} , \tag{1}$$

NA was measured by the cone of the output light from the fabricated waveguide coupled by a He-Ne laser.

3. Results and discussion
A. Effective numerical aperture dependence

Figure 2 shows the microscopic photographs of the refractive index change region at different effective numerical apertures. Effective numerical aperture was varied by adjusting the beam diameter before the focusing lens under the condition of fixed incident pulsewidth (100fs), energy(20μJ), and irradiation time(10min). When the beam diameter is 3mm, multiple splitting of refractive index change was induced and it is seen that beads are sitting along the modified region as shown in Figure 2(a). When the beam diameter is 2mm, beadslike structure was generated but multiple splitting of refractive index change was not induced as shown in Figure. 2 (b). When the beam diameter is 1mm, irregular structure was not induced and refractive index change straight as a line was induced.

These results can be understood as described below; Beam focus of fs laser pulses before focal point in
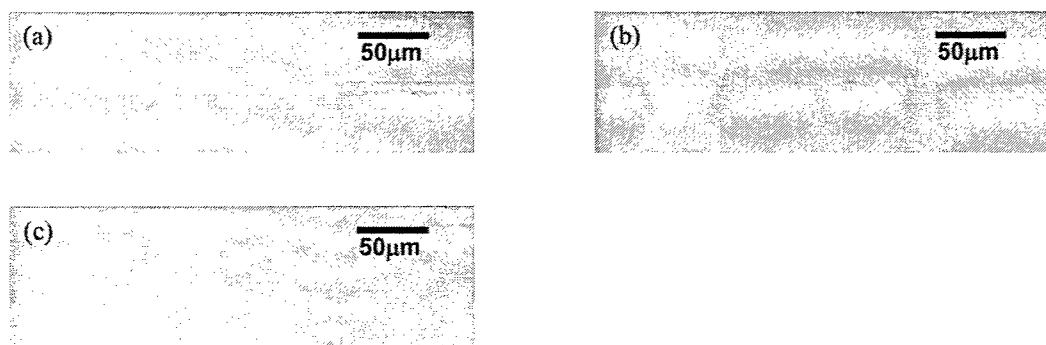
Fig.2 Microscopic photographs of refractive index change region. (a) beam diameter 3mm, (b) beam diameter 2mm, (c) beam diameter 1mm.

transparent materials is governed by self-focusing by Kerr-nonlinearlity and linear-focusing by a lens. Strength of self-focusing is in proportional to the beam diameter [10]. Geometrical focal diameter of lens for collimated beam is given by

$$D = \frac{4\lambda f}{\pi \omega}, \tag{2}$$

where D is the beam diameter just before the lens, ω is the beam diameter at focal point, and f is focal length of a lens. Figure 3 shows the relationship between the beam diameter before lens and the focal diameter using equation (1). Focal diameter becomes smaller as the beam diameter before lens increases. Moreover, self-focus should be considered and it results in more tight focus. Then plasma defocusing becomes stronger than self-focusing result in unstable propagation over the focal point as the spatial and temporal splitting of laser pulses [11]. The beam diameter was fixed to 1mm in the following experiments.

B. Incident pulsewidth dependence

Figure 4 and Figure 5 show the dependence of modification depth and modification length on the incident laser pulsewidth at a fixed incident energy (20μJ), irradiation time (10min). The incident laser pulsewidth varied from 150fs to 300fs. The modification depth means the distance from the entrance surface at which the modification starts. Modification depth became shorter as the pulsewidth was decreased as shown in Figure 4(a). This effect can be explained by considering self-focusing because strength of self-focusing depends on the peak power of the incident laser pulses. Therefore, modification starts earlier when the incident laser pulsewidth is decreased. The diameter of modified region was
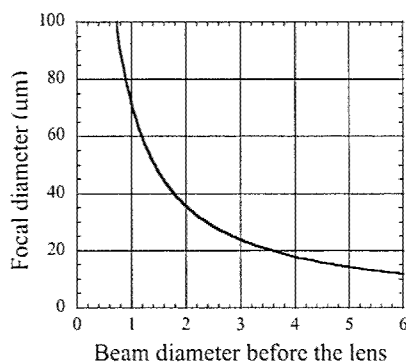
Fig.3 Relationship between the beam diameter before the lens and the focal diameter. Focal length of lens is 70mm.
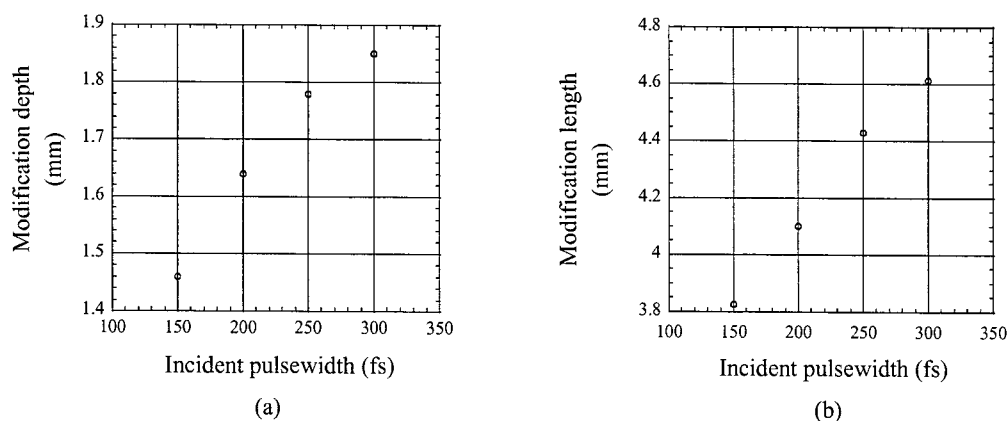
Fig.4 Relationship between the incident pulsewidth and (a): the modification depth, (b): the modification length.

1mm

Fig.5 Microscopic photograph of the modified region at different incident laser pulsewidths.

5μm approximately in each incident laser pulsewidth. The modification length became longer as the incident laser pulsewidth was increased as shown in Figure 4(b). The reason for increasing the modification length with increasing laser pulsewidth is unclear at this moment and further work is in progress.

C. Incident energy dependence

Figure 6 shows the dependence of the modification depth and the modification length on the incident pulse energy at a fixed incident laser pulse width (100fs), irradiation time (10min). The incident energy varied from 5μJ to 20μJ. Modification depth became shorter as the incident energy was decreased as shown in Figure 6(a) as the same reason as described above. The modification length became longer as the incident energy was increased as shown in Figure 4(b).
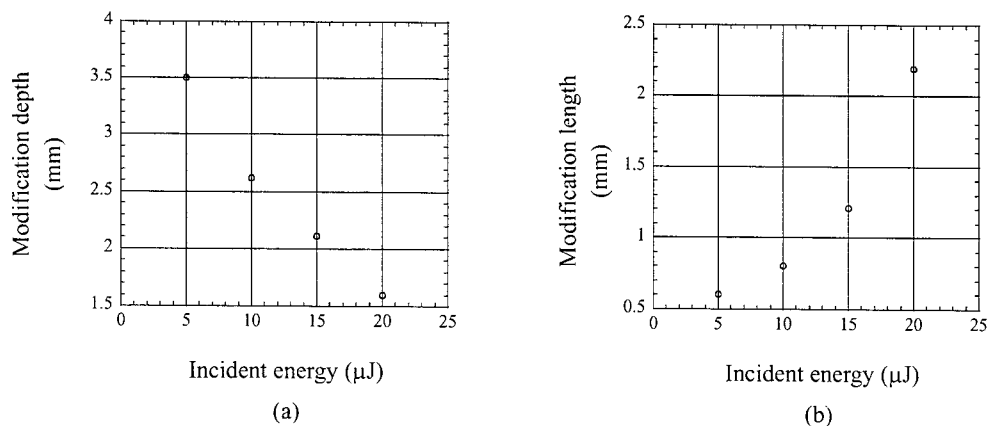
Fig.6 Relationship between the incident energy and (a): modification depth, (b): modification length.
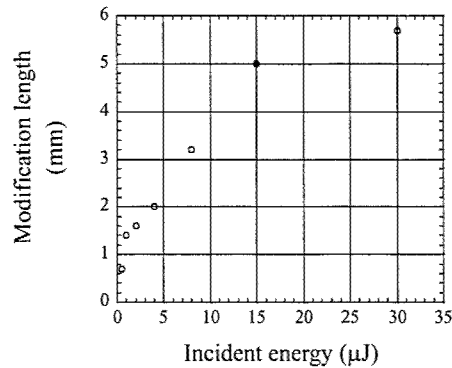
Fig.7 Relationship between the irradiation time and modification length

The diameter of the modified region varied slightly from 5μm to 8μm as the incident energy was increased. The reason for increasing the diameter of the modified region with increasing incident energy is dependent on the diameter of the laser induced plasma on the energy of the incident pulse when catastrophic collapse occurs [12].

D. Laser irradiation time dependence

Figure 7 shows the dependence of the modification length on the laser irradiation time at a fixed incident energy (20μJ), incident pulsewidth (100fs). The laser irradiation time varied from 0.5min to 30min. The modification depth was 1.35±0.1mm at the each laser irradiation time. The modification length became longer as the laser irradiation time was increased. The elongation was saturated after 30min as reported by Yamada et al. [9]. The diameter of the modified region was under 5μm at each laser irradiation time.

E. Induced refractive index change

Figure 8 shows a far field pattern of the output light from the fabricated waveguide at 633nm. The refractive index change Δn measured by the method described previously is 5.0×10^{-3}. The normalized frequency [13] is under 2.405 over 800nm under the condition that Δn is 5.0×10^{-3} and the core diameter of the fabricated waveguide is 5μm. Thus the fabricated waveguides can work as a single-mode waveguide for 850nm that is the wavelength of VCSEL (Vertical Cavity Surface Emitting Laser).
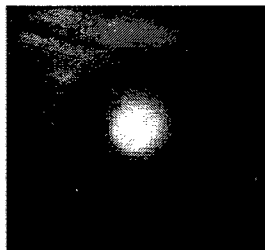
Fig.8 Far field pattern of the output from the fabricated waveguide at 633nm.

5. Conclusion

In conclusion, optical waveguides with the length of up to 6mm and the diameter of up to 8µm were fabricated inside fused silica using fs laser induced plasma channeling without any scanning process. The induction of irregular refractive index change can be controlled by reducing the effective numerical aperture. The length, position and core diameter of the fabricated waveguide are controllable by the incident laser pulsewidht, energy, and irradiation time. This method allows photonic device fabrication such as optical waveguides, internal gratings, and couplers deep inside transparent materials for access network.

Acknowledgement

References

[1]. K. M. Davis, K. Miura, N. Sugimoto, and K. Hirao, "Writing waveguides in glass with a femtosecond laser", Opt. Lett. **21**, 1729 (1996).

[2]. E. N. Glezer, M. Milosavjevic, L. Huang, R. J. Finlay, T. H. Her, J. P. Callen, and E. Mazur, "Three-dimensional optical storage inside transparent materials", Opt. Lett. **21**, 2023 (1996).

[3]. D. Homoelle, S. Wielandy, and Alexander L. Gaeta, N. F. borrelli and Charlene Smith, "Infrared photosensitivity in silica glasses exposed to femtoseconed laser pulses", Opt. Lett. **24**, 1311 (1999).

[4]. Chris B. Schaffer, Andrew Brodeur, Jose F. Garcia, and Eric Mazur, "Micromachining bulk glass by use of femtosecond laser pulses with nanojoule energy", Opt. Lett. **26**, 93 (2001).

[5]. Alexander M. Streltsov and Nichoral F. Borrelli, "Fabrication and analysis of a directional coupler written in glass by nanojoule femtosecond laser pulses", Opt. Lett. **26**, 42 (2001).

[6]. K. Minoshima, Andrew M. Kowalevicz, Ingmar Hartl, Erich P. Ippen, and James G. Fujimoto, "Photonic device fabrication in glass by use of nonlinear materials processing with a femtosecond laser oscillator", Opt. Lett.**26**, 1516 (2001).

[7]. H. B. Sun, Y. Xu, S.Juodlazis, K. Sun, M. Watanabe, S.Matuso, H. Misawa, "Arbitrary-lattice photonic crystals created by multiphoton microfabrication" Opt. Lett, **26**, 325 (2001).

[8]. S. H. Cho, H. Kumagai, I. Yokota, K. Midorikawa, M. Obara, "Observation of self-channeled plasma formation and bulk modification in optical fibers using a high-intensity femtosecond laser", Jpn. J. Appl. Phys. Lett. **37**, L737 (1998).

[9]. K. Yamada, W. Watanabe, T. Toma, and K. Itoh, J. Nihii, "In situ observation of photoinduced refractive-index changes in filaments formed in glasses by femtosecond laser puses", Opt. Lett. **26**, 19 (2001).

[10]. J. H. Marburger, "Self-Focusing: Theory", Prog. Quatum. Electron. **4**, 35 (1975).

[11]. K. Ishikawa, H Kumagai and K. Midorikawa, "High-Power regime of femtosecond –laser pulse propagation in silica: Multiple-cone formation" Phys. Rev E. 66, 56608 (2002).

[12]. N. Bloembergen, "Laser induced electric breakdown in solids", IEEE. J. Quantum . Electron. **QE-10**,375 (1974).

[13]. G. P. Agrawal, "Nonlinear Fiber Optics" (Academic Press, San Diego, 1995).

F$_2$-Laser Micropatterning of Chrome-Coated CaF$_2$ for Vacuum-Ultraviolet Masks

Andrew Yick[*], Jianzhao Li, Peter R. Herman

Department of Electrical and Computer Engineering, University of Toronto,
10 King's College Road, Toronto, ON, M5S 3G4, Canada.

ABSTRACT

Chrome-on-quartz optics serve multi-functions including high-resolution masks for UV lithography. At the next node down, F$_2$-laser lithography demands alternate high-transparency substrates such as wide-bandgap CaF$_2$. We present here a direct-write method of F$_2$-laser ablation for selective removal of 110-nm thick chrome films on CaF$_2$ and SiO$_2$ (fused silica) substrates. Laser-processing parameters are presented for micropatterning of the chrome film with minimal damage to the underlying substrates. Damage thresholds, ablations rates, incubation processes, and surface morphology of the chrome and CaF$_2$ are described together with methods that reduce ablation debris and collateral damage. Laser-patterned masks are tested in a 157-nm optical projection system at 30-mJ/cm^2 fluence for sub-micron laser structuring of glass and other materials.

Keywords: F$_2$ laser, 157 nm, ablation, micropatterning, chrome masks, calcium fluoride, fused silica

1. INTRODUCTION

Chrome mask patterning currently requires several multi-step processes that include direct e-beam or CW laser scanning of resist layers, followed by resist development and sample etching to form the desired pattern. Laser ablation is an alternate approach that can potentially shape high-resolution structures in a single processing step. Direct writing of thin chrome layers for photomasks has been studied by Venkatakrishnan et al.[1] using a Ti:sapphire chirped-pulse amplified ultrafast laser. Ultrafast lasers are currently used at IBM for photomask repair,[2, 3] taking advantage of the short-pulse interactions to avoid damage to the underlying quartz substrate. Laser ablation further affords means for shaping phase-shift masks (PSM's) through precise removal of the bulk substrate surface but has not been applied to the author's knowledge.

New photomask nanofabrication tools are now required for microelectronic lithography and micromachining applications emerging for the vacuum-ultraviolet (VUV) F$_2$ laser. The present paper was motivated by our own group's requirement for rapid fabrication of high-resolution photomasks to support a laser nanofabrication program based on the short-wavelength F$_2$ laser. VUV photomasks require wider bandgap optical materials such as CaF$_2$ to provide high transparency at the short 157-nm wavelength. The F$_2$ laser was applied here to exploit the strong interactions of 7.9-eV photons and the promise of high-resolution features of 157-nm light to micro-pattern structures onto Cr-on-CaF$_2$ and Cr-on-SiO$_2$ (fused silica) photomasks. Direct ablation of CaF$_2$ was also investigated for the first time with 157-nm radiation for defining phasemask features. Laser micromachining of CaF$_2$ surfaces has been studied by Böhme et al.[4] by laser-induced backside wet etching (LIBWE) in a pyrene-acetone solution while Ashkenasi et al.[5] applied a 780-nm Ti:sapphire laser of varying pulse width (200 fs – 8 ns) for direct ablation. Laser ablation characteristics are reported for a wide range of laser exposure conditions for both Chrome and CaF$_2$ materials. Laser-fabricated Cr-on-CaF$_2$ and Cr-on-SiO$_2$ photomasks were tested in the F$_2$-laser optical projection system, producing 800-nm surface-relief features on soda-lime glass.

*Andrew Yick: Phone: (416) 978-7039, Fax: (416) 971-3020, Email: andrew.yick@utoronto.ca

2. THE F₂-LASER PROCESSING SYSTEM

The optical processing system [6, 7] consists of an F_2 excimer laser (Lambda Physik LPF220i), a beam delivery system by MicroLas Lasersystems GMBH, and precision target positioning tools. Homogenizing elements in the beam delivery system uniformly illuminate a 6 mm × 6 mm area in the mask plane, which was projected by a 25× demagnifying Schwarzschild lens to the target surface. An on-target laser fluence of up to 7 J/cm^2 was available, which was presented together with a red light energy component of 10-20% generated by helium-buffered laser gas. Laser energy was monitored with pyrometer detectors (Molectron Detector Inc., MaxBlack J25LP-MB-1187 and EPM1000 Laser Energy Meter). Since oxygen strongly attenuates 157-nm radiation, the chamber was flushed with transparent nitrogen gas. Target samples were placed outside the chamber in front of a nozzle that also flushed the lens-to-target beam path with transparent nitrogen gas. Samples were positioned with 50-nm precision three-axis stages (Newport TSPI100 with MM4006 controller). Target positioning and laser exposures were controlled with a computer and a DAQ card (National Instruments PCI-6035E) using either Labview or Visual Basic software. Further details are provided in Ref. [6, 7].

3. CaF₂ ABLATION WITH 157-nm RADIATION

Laser interactions with the photomask substrates without the Chrome coatings were first investigated for two purposes:

1) to identify maximum exposure conditions that might avoid damage to the optical surface, setting an upper limit to exposures when patterning the chrome coating, and

2) to examine the surface morphology and ablation depth control at higher fluence exposures, and thereby ascertain the potential for generating smooth excisions only 10's of nanometer deep for potential PSM applications.

Since comprehensive studies of F_2-laser micromachining of fused silica have been reported by our group in the past,[7] only ablation characteristics for CaF_2 are presented here.

Due to the large ~12eV bandgap of the calcium fluoride, the 7.9-eV photon interactions will largely be dictated by the impurity and defect states in the crystal. CaF_2 windows of 2" diameter, 4-mm thickness, and 60-40 scratch-and-dig (COHERENT Inc., 36-1790-000) were ablated with square-shaped holes of three sizes of 120 µm, 80 µm and 40 µm. With the laser red light component factored out, on-target fluences of 1 to 7 J/cm^2 were applied with various pulse numbers of 1 to 350. The crystal orientation was not known.
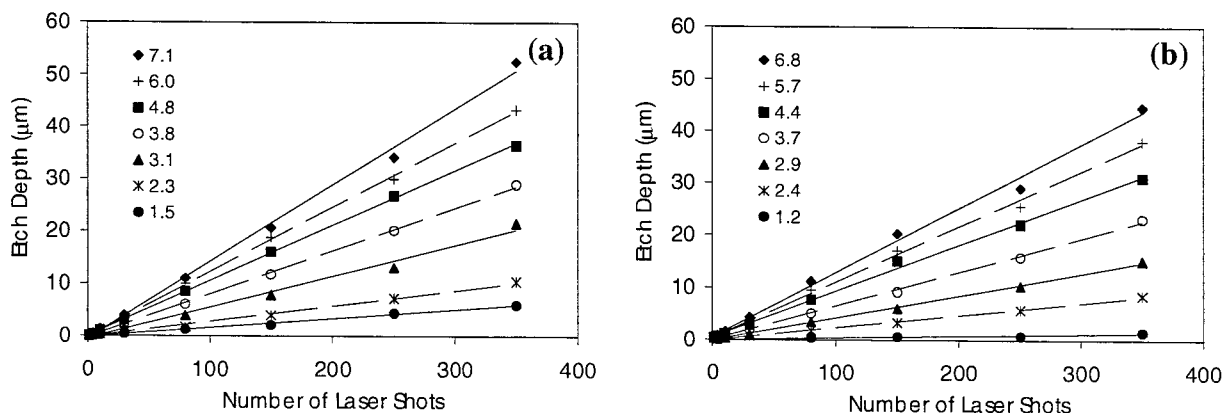
Figure 1: The F_2-laser etching depth of calcium fluoride for (a) 120-µm squares at fluences from 1.5 to 7.1 J/cm^2 and (b) 40-µm squares at fluences from 1.2 to 6.8 J/cm^2. The legend shows fluence values in J/cm^2. Note the linearity of the hole depth with pulse number.
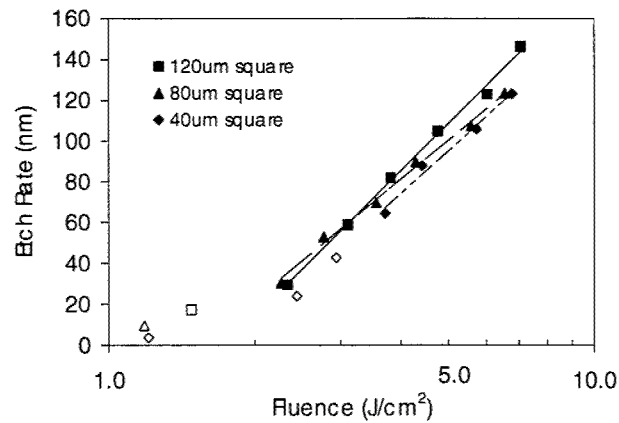
Figure 2: Ablation rate of calcium fluoride under 157-nm radiation for three different spot sizes. The solid points are those that show prompt ablation after one laser pulse, whereas the hollow points are those that required several 'incubation' pulses to initiate material removal.
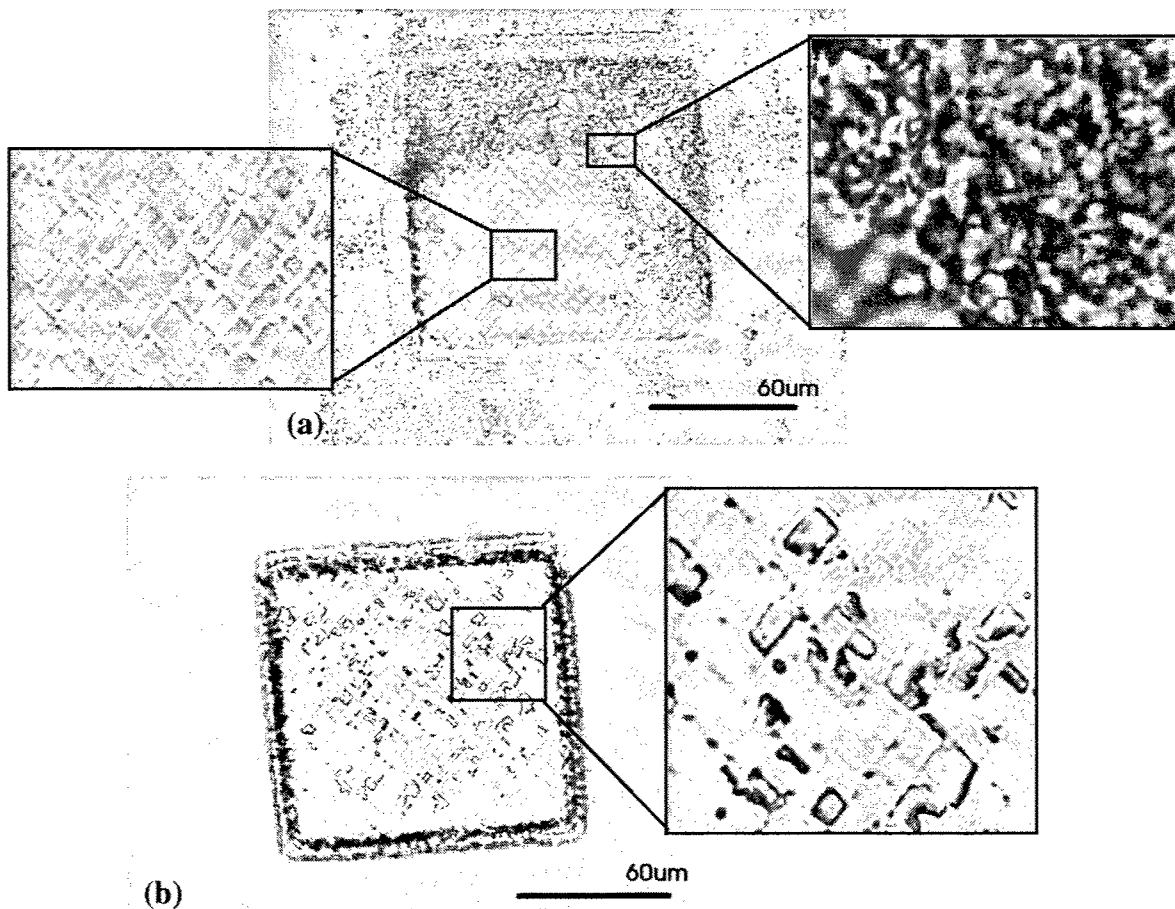
Figure 3: Microscope images of a typical 120-μm × 120-μm ablated hole in calcium fluoride (a) before, and (b) after 10 minutes of ultrasonic cleaning in DI. Note the surface microfracturing along the preferred crystal directions. See text for further details.

Laser ablation depths were determined by a Veeco Dektak 3 stylus profilometer and an optical microscope and are reported in Figures 1a and b for the 120-μm and 40-μm sized squares, respectively. Prompt ablation was generally noted at fluence values exceeding ~3 J/cm^2, while numerous 'incubation' pulses were required at lower fluence values before the onset of material removal. Once ablation was initiated, all etch depths increased linearly with the number of pulses, an attractive response for controlling surface relief size and shape in a laser micromachining application. The slope in these linear regions provided the etching rates, D, which are plotted in Figure 2 for the three hole sizes. The open data points represent fluence values where several incubation pulses were required to initiate ablation. The overall data indicate a slight decrease in ablation rate and a requirement for more incubations pulses as the spot size decreases.

Under prompt ablation conditions (solid data points in Figure 2), the etch rates closely followed a logarithmic fluence dependence of

$$D = R \log\left(\frac{F}{F_{th}}\right),$$
(1)

where D is the etch rate (nm/ pulse), R is a rate constant, F is the on-target 157-nm laser fluence in J/cm^2, and F_{th} is the threshold fluence for ablation. An average over all three hole sizes yielded $R = 216$ nm and $F_{th} = 1.7$ J/cm^2 for Eq. 1. (The incubation data were ignored and the 10-20% red energy component was factored out due to the high transparency of this radiation in CaF$_2$.) Etching rates as low as 10-nm/pulse were noted under incubation conditions, opening a window of opportunity for the controlled fabrication of phase masks in CaF$_2$.

Examination of the CaF$_2$ morphology under F$_2$-laser ablation reveals a highly mechanical process for material removal with only little evidence of thermal interactions. An absence of molten splatter or bonded debris within and outside the ablated hole suggests little generation of molten CaF$_2$ during the laser interaction. Material removal appeared dominated by ejection of solid CaF$_2$ pieces, evidenced by the loose shards surrounding the excised area as shown in Figure 3a. These shards can be easily moved by tilting the sample and are seen collected to one side of the hole near the top of Figure 3a, with an expanded view shown in the right inset. Figure 3b shows complete removal of this material for the same hole after 10 minutes in an ultrasonic DI bath. More striking is the ~3-μm period tiling structure of the laser-treated surface as seen in the left inset of Figure 3a before cleaning. Note that the ultrasonic cleaning further loosens small shards of this tiling structure as seen in the inset of Figure 3b, suggesting a weak bounding to the underlying surface. The SEM micrographs in Figures 4b and 4c show higher resolution features such as a wavy surface relief and small vertical steps at the tile interfaces. Such terraced tiling and cracking effect was also observed and analyzed in detail by Gogoll et al.[8] in 248-nm laser ablation of CaF$_2$, where microfracturing along the (111) cleavage planes was explained by a thermoelastic model.

Evidence of an explosive mechanical removal process is also noted by large voids and cracks occasionally seen at the bottom of holes processed above 6 J/cm^2, as shown in Figure 4a. A large void covering ~30% of the hole bottom is seen at the top right corner extending deeper than the relatively flat bottom surface. The rough top edges of the hole and the absence of debris in the SEM micrograph of Figure 4b offers further evidence of the non-thermal nature of the ablation.

A cursory investigation revealed that surface roughness at the hole bottom was sensitive to the single-pulse laser fluence and less dependent on the depth of the hole. Samples radiated at 6 J/cm^2 had a >100-nm rms roughness over a 200μm^2 area for a hole depth of ~1 μm. This roughness diminished to ~10-nm rms for single-pulse fluences below 2J/cm^2 over a 200μm^2 area of a similar depth hole. These values compare with a native flatness of ~5-nm rms over a 200μm^2 area and suggest that only low-fluence exposures of < 2 J/cm^2 offer an adequate degree of depth control for surface profiling to optical quality. No discernable damage to the CaF$_2$ surface was in evidence for fluences below < 1 J/cm^2, suggesting a potentially wide fluence window for removing Chrome coatings without substrate damage for photomask fabrication as examined in the next section.

4.Cr-on-CaF₂/SiO₂ MASK PATTERNING

CaF$_2$ (Coherent, 2" dia x 4mm thick) and fused silica (ESCO Products, 1" dia. x 160-μm thick) windows were coated with a ~110-nm thick chrome film by Accucoat Inc. and patterned by F$_2$ laser ablation to test the fabrication of VUV photomasks. The 157-nm transmittance of the blank substrates were ~82% for the CaF$_2$ window and ~63% for the fused silica cover slip.

An atomic force microscope (AFM) image of Cr-coated CaF$_2$ is shown in Figure 5a after a single VUV pulse at 6 J/cm^2. While the chrome was effectively removed in the exposed area, surface roughness and tiling structure were generated in the CaF$_2$ substrate at this high fluence. Fluence exposure of the CaF$_2$ masks was then reduced to below the prompt ablation threshold of CaF$_2$ of F_{th} = 1.7 J/cm^2, as described in the previous section, with the hope to avoid such damage. For such low VUV fluence, the presence of a helium buffer gas in the laser generated a notable background red-coloured beam, presenting a ~0.6-J/cm^2 fluence on the target. This fluence was also sufficient to remove the opaque Cr layer in a single pulse even with the 157-nm radiation completely blocked. Further work is underway with a neon gas mix that eliminates the red-light component.
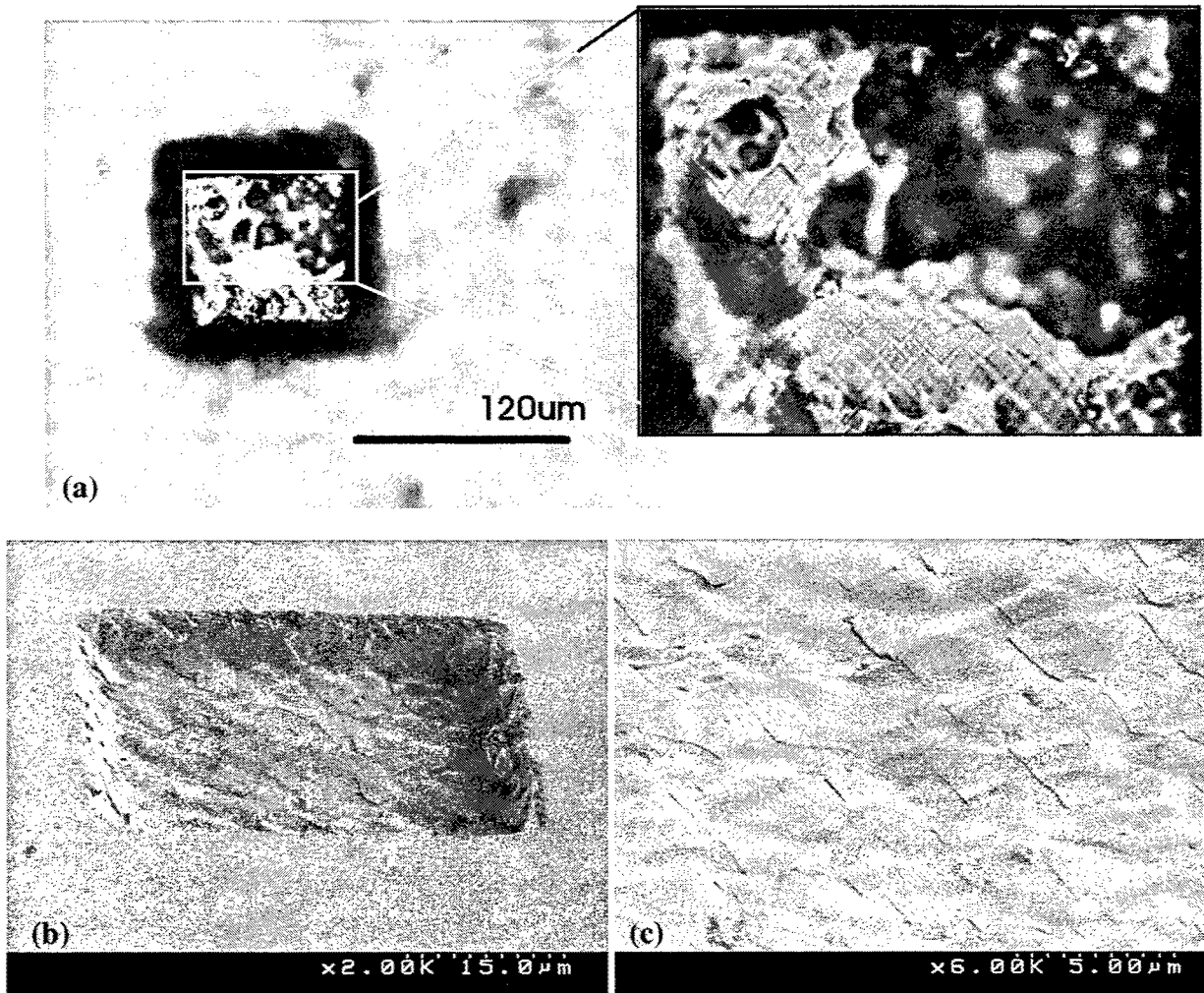
Figure 4: Microscope image (a) of a void extending beyond the flat portion of the fabricated CaF$_2$ hole, seen occasionally at high fluence. SEM micrographs (b,c) showing the tiling structure typical in an ablated CaF$_2$ hole (40 μm) at different magnifications.

The patterned square holes in the Chrome had a metallic hue in the hole, constituting incompletely removed Chrome that could be readily cleaned by a second laser pulse. Visible colour changes were noted with each laser pulse suggesting the generation and removal of metallic debris. Surface damage to the underlying CaF_2 substrate, such as the tiling in Figures 3 and 4, was not noted with red-only exposure. However, the addition of small amounts of VUV radiation (0.6 J/cm^2) such that the combined red plus 157-nm fluence remained below the ablation threshold for CaF_2 (F_{th} = 1.7 J/cm^2) was sufficient to tile the substrate and damage the surface in a single laser pulse as shown in Figure 5b. The high opacity of the chrome layer therefore serves to lower the prompt damage threshold for the CaF_2 substrate, narrowing the processing window for defining high quality photomask features.
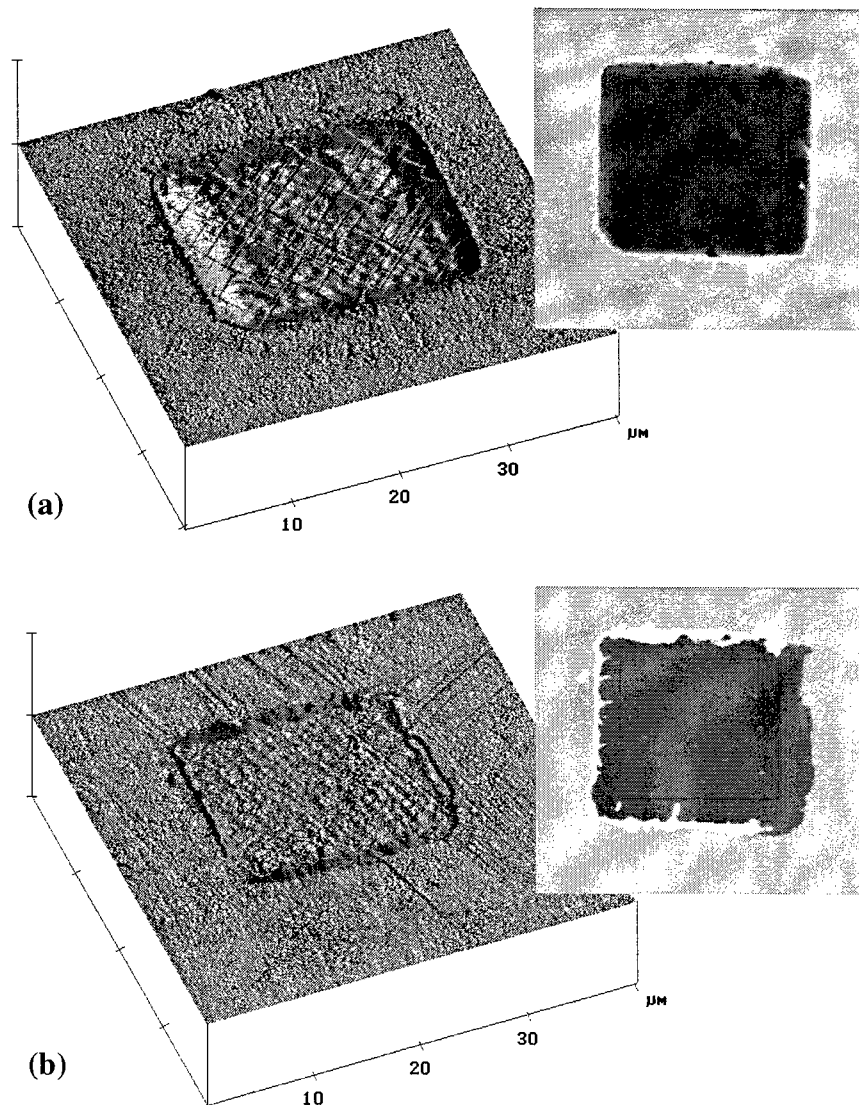
Figure 5: AFM image of thin Cr-on-CaF_2 ablated with (a) a single 157-nm pulse at 6 J/cm^2, and (b) a combined red and VUV pulse of F = 1.2 J/cm^2, after ultrasonic cleaning. The tiling effect is also present in (b), but the surface flaking has much smaller amplitude than at 6 J/cm^2 (a), and not readily visible here.

Recall that low fluence ablation of CaF_2 provided the lowest surface damage with minimal substrate surface roughness of ~10-nm rms (over a 200-μm^2) for ablation depths of up to 1 μm. This roughness value represents an optical quality of <λ/10 for 157nm, which is sufficient for several optical applications. The addition of the Chrome layer decreased the quality of the laser-ablated surfaces. Further, a comparison of Figure 5a and 5b shows a noticeable difference in the edge definition of the thin chrome layer. The ablation edges are much cleaner and well defined and there exists little residual Chrome in the ablation areas for the high fluence (6 J/cm^2) exposure. For low fluences (0.6J/cm^2), small cracks in the Cr layer were observed radiating out from the ablation perimeter. During ultrasonic cleaning, these edges become torn and reduced the masking resolution to ~ 2 μm. Additionally, small micron-sized droplets of chrome were observed in the processed area, adding to the effective surface roughness. Because of these effects, the flatness of the laser treated surfaces was ~70-nm rms and ~12-nm rms for singe-pulse exposures of 6 J/cm^2 and 1.2 J/cm^2 (red plus 157 nm), respectively, over an ~200 μm^2 observation area. This compares with a native ~5-nm roughness (rms) of the CaF_2 blank over a similar area. Fluence optimization for photomask fabrication therefore favours higher fluence for high contrast and high resolution at the expense of higher substrate surface damage and scattering loss.

The laser mask fabrication process is a very simple and quick procedure that allows direct writing from computer design in just minutes. To test F_2-laser mask writing, a mask design was laid out with a computer graphics program in a two level bitmap of size 173 x 130 pixels, creating the logo "University of Toronto F_2 microfabrication laboratory" shown in Figure 6. The logo included a diamond structure of the dense alternating checkerboard design shown in Figure 6b. A MATLAB script generated the sequence of moves to map each pixel and generate 20-μm ablation squares on both Cr-on-CaF_2 or Cr-on-SiO_2 mask samples. The total laser exposure was ~17 minutes. A microscope image of Cr-on-CaF_2 and a Cr-on-SiO_2 mask patterns under microscope backlighting are shown in Figure 7. For low fluences of ~1 J/cm^2, not all the chrome material was removed and neighbouring pixels were outlined by splattered or redeposited micron-sized chrome droplets. This undesired effect added to the effective surface roughness of neighbouring ablated pixels as shown in the close-up view of the patterned Cr-on-SiO_2 mask in Figure 7 (right). This debris effect was worse for the SiO_2 substrate than for the CaF_2 substrate. It may be possible to eliminate the chrome debris by ablating samples in vacuum as demonstrated by Venkatakrishnan et al.[1]
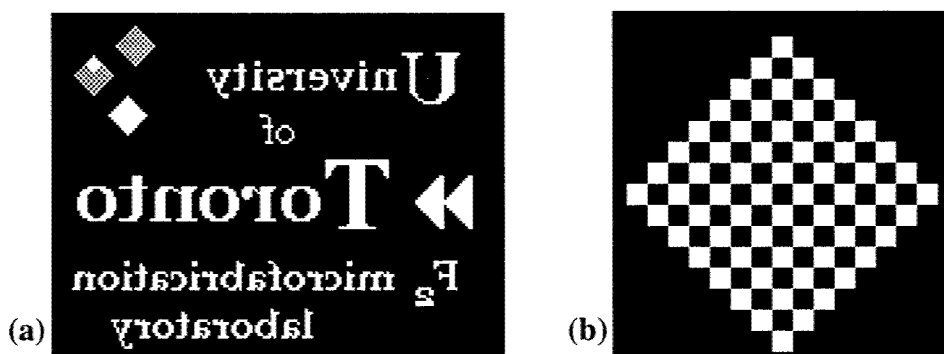
Figure 6: MATLAB processed computer bitmap image of a logo (a) and enlargement (b) of the uppermost diamond pattern in the top left corner.

5. Cr-on-CaF₂/SiO₂ MASKS FOR GLASS MICROFABRICATION

Both the Cr-on-CaF_2 and Cr-on-SiO_2 masks were tested in the F_2 laser processing system at fluences of up to 30 mJ/cm^2. Without optimization, the best quality mask provided a low transmittance of only ~20 - 25% which compares to loss estimates of 70-75% for the Cr-on-CaF_2 mask and 60-68% for the Cr-on-SiO_2 mask when accounting for bulk and Fresnel losses. The discrepancy suggests large scattering and absorption losses by the micron-sized chrome droplets, surface roughness at the edges of overlapping pixels, and the surface roughness of the laser-damaged CaF_2 crystal, especially after tile uprooting during ultrasonic cleaning. Further investigation of methods to control surface

roughness through in-vacuum ablation, lower fluence exposures, and gentler cleaning methods is underway. Masks processed at fluences >6 J/cm^2 yielded surface scattering losses of >80% at 157 nm and did not yield sufficient fluence for testing the ablation of glasses.

Figure 7: Microscope image in backlighting of a laser patterned Cr-on-CaF$_2$ mask (a) and an enlargement (b) of the diamond structure in the uppermost left corner of the same logo on a Cr-on-SiO$_2$ mask.

Laser photomasks offering the highest transmission were tested as projection masks for F$_2$-laser ablation of standard soda-lime microscope glasses using single laser pulses at a fluence of 1.0 J/cm^2 (or 1.4 J/cm^2 including red energy). Figure 8 shows a faithful reproduction of the mask features onto the laser-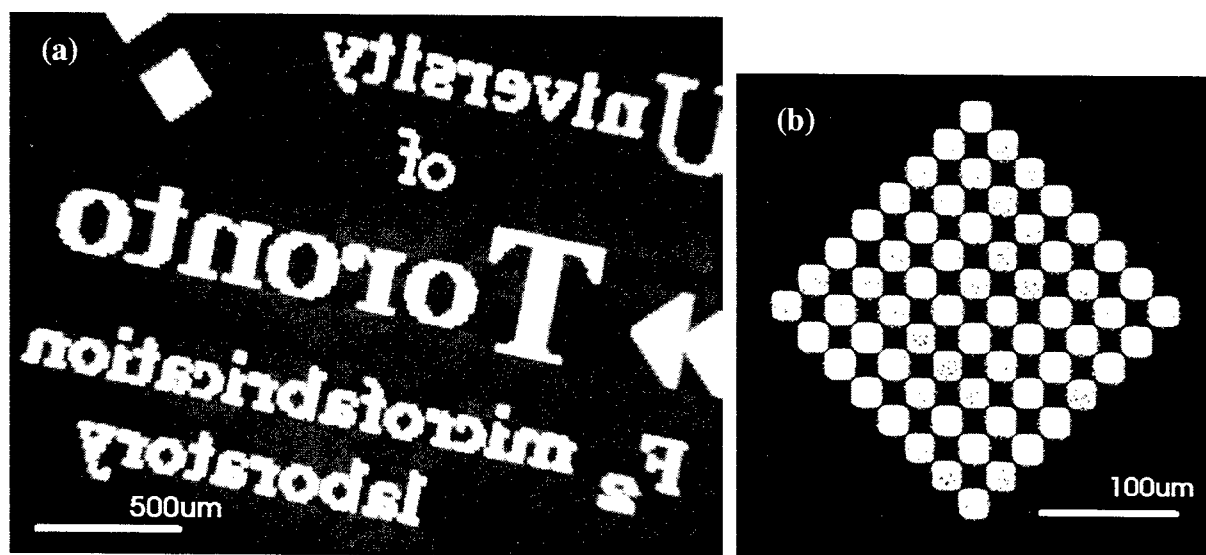patterned glass under microscope front lighting. An enlarged AFM view of the uppermost diamond figure, showing the full detail of the checkerboard pattern is shown in Figure 9 (top) together with Cr-on-SiO$_2$ mask pattern (bottom) that created it. The micron-sized chrome droplets in the photomask were too small after 25x demagnification to affect the glass patterning. A surface profile of the ablated glass regions in Figure 9 (top-right) reveal an ~130nm depth modulation with a peak-to-peak separation of 1.6 μm horizontally and 1.1 μm diagonally, corresponding to sub-micron pixel features of smaller than ~800 nm. Smaller features are currently being investigated.

6. DISCUSSION AND CONCLUSION

F$_2$-laser radiation provides predictable ablation rates in CaF$_2$ that follows Eq. 1 with an ablation threshold fluence of F_{th} = 1.7 J/cm^2 and a rate of R = 216 nm. Material removal is largely mechanical that leaves loose crystal debris around the ablated surfaces that are easily removed. Undesirable surface roughness arose from tiling of small parallelogram flakes on the bottom of the processed surface, an effect observed also in CaF$_2$ by Gogoll et al.[8] with 248-nm irradiation and Ashkenasi et al.[5] with ultrafast irradiation.

Patterning of Cr-on-CaF$_2$ and Cr-on-SiO$_2$ masks have been demonstrated here by F$_2$ laser ablation yielding about 25% transmittance at 157 nm. Even with such losses, these masks were able to define <800 nm features on laser-ablated standard soda-lime glass. For practical use in laser systems, further study is required to reduce surface damage, improve transmittance, sharpen the chrome edges, and minimize the ablation debris on the photomask surface. Lower fluence 157-nm exposures in the absence of the red contamination light may improve some of these features while more benign cleaning methods that effectively remove chrome droplets without dislodging the CaF$_2$ surface tiles as in the present ultrasonic case are desirable. Ablation under vacuum conditions is know to reduce debris[1] and may also yield a lower processing threshold for the chrome film removal. Chemical methods of debris removal were not tested

here. The observation of CaF_2 ablation rates as small as ~10 nm/pulse bodes well for future applications of structuring CaF_2 phase masks where precise $\lambda/2$ depth excisions are required.

In summary, preliminary investigation of F_2-laser ablation of Cr-coated CaF_2 and fused silica substrates showed good promise for generating several micron features in photomasks for F_2 laser processing applications. Further work is required to reduce laser damage and the concomitant surface scattering losses that reduce the VUV transmittance of the laser-generated masks to ~25% in the present case. With further optimization, F_2-laser ablation may also serve to define phase-mask features in the CaF_2 substrate, that together with the laser-patterned Chrome, enhances the optical resolution of the photomask.

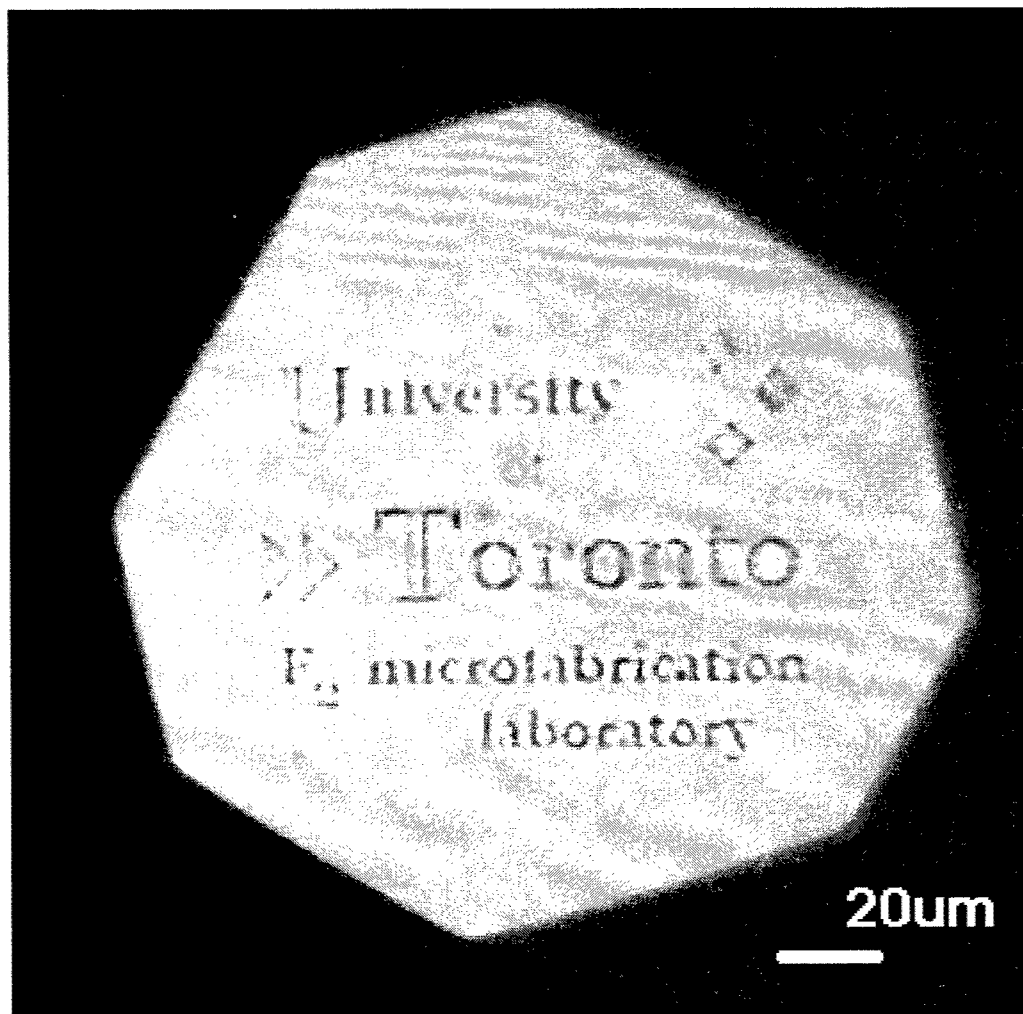**Figure 8:** Microscope image in top lighting of a logo ablated in soda-lime glass with one laser pulse through the fused silica mask.

7. ACKNOWLEDGEMENTS
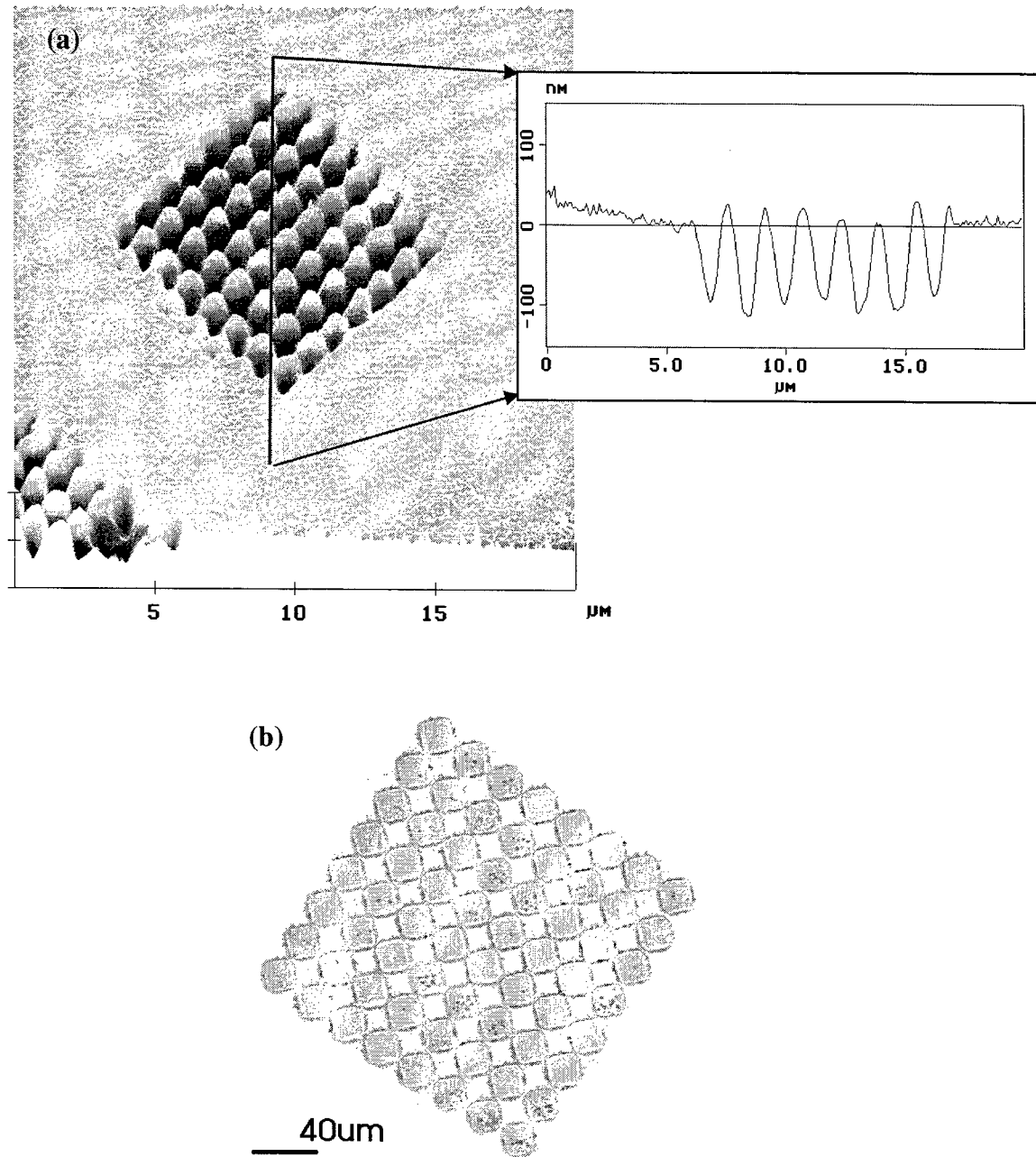
Figure 9: AFM profile of the diamond–shaped logo ablated into soda-lime glass (a) by F_2 laser ablation using the laser-patterned Cr-on-SiO_2 mask shown in (b). Note the micron-sized chrome droplets inside some of the open squares in the photomask.

8. REFERENCES

1. Venkatakrishnan, K., et al., *Laser writing techniques for photomask fabrication using a femtosecond laser.* Appl. Phys. A, **74**, 2002, p. 493-496.
2. Haight, R., et al., *MARS: Femtosecond laser mask advanced repair system in manufacturing,* J. Vac. Sci. Technol. B, **17**, 1999, p. 3137-3143.
3. Wagner, A., R. Haight, and P. Longo, *MARS2: An advanced femtosecond laser mask repair tool,* IBM Res. Report, **RC 22562,** 2002, p. 1-12.
4. Bohme, R., A. Braun, and K. Zimmer, *Backside etching of UV-transparent materials at the interface to liquids.* Appl. Surf. Sci., **186**, 2002, p. 276-281.
5. Ashkenasi, D., et al., *Pulse-width influence on the laser-induced structuring of CaF_2 (111),* Appl. Phys. A, **63**, 1996, p. 103-107.
6. Herman, P.R., et al.,*F_2-lasers: high-resolution optical processing system for shaping photonic components.* in *Laser Appl. in Microelectronic and Optoelectronic Manuf. V*, SPIE **4274** (2001) p. 149-157.
7. Herman, P.R., et al. *Processing applications with the 157-nm fluorine excimer laser.* in *Excimer Lasers, Optics, and Applications*, SPIE **2992**, 1997, p. 86-95.
8. Gogoll, S., et al., *Laser-damage of cleaved and polished CaF_2 at 248 nm*, Methods Phys. Res. B, **116**, 1996, p. 279-283.

Direct laser marking on ROM media for identification

Sumio Nakahara*[a,c], Yoshihiro Okino[a], Masaaki Takita[b], Shigeyoshi Hisada[c] and Takeyoshi Fujita[c]

[a]HRC, Kansai University, Suita, Osaka 564-8680, Japan
[b]Takita R&D Ltd., Ibaraki Osaka 567-0878, Japan
[c]Dept. of Mechanical Engineering, Kansai University
*E-mail: nakahara@ipcku.kansai-u.ac.jp

ABSTRACT

In order to attempt the direct laser marking for ROM media like a compact disk for identification, various laser heating was carried out against a thin metallic film in the transparent medium. As heat sources for the processing, a semiconductor laser excitation YAG laser (532 nm wavelength of second harmonic, max 150 mW), semiconductor lasers (780 nm, up to 2 W), and an Ar ion laser (514.5 nm, max 2000 mW), etc. were used. The media under consideration on laser marking is an aluminum thin film reflector layer, which was sandwiched between a polycarbonate (PC) of 1.2 mm and a protection film of 5 μm thickness. The aluminum thin film (Al) is 100 nm in thickness. The obtained laser marking sizes were less than 1 μm and were evaluated using SEM and AFM. The observation samples inside a transparency resin were obtained by tearing off a protection film, and the surfaces of the bared PC and protection film were examined. The surface conditions and cross sections of laser-marking area were observed. It seems that the heated aluminum thin film were melted and a hole arose. Then a cavity was not observed from SEM cross-section observation in the marking area. It became clear that the holes were filled with PC by SEM and AFM observation. These results indicate the possibility of heat localization at the Al-PC interface and also significant heat penetration into the PC substrate itself.

Keywords: Laser marking, Aluminum thin film, ROM medium, Transparent resin, AFM, SEM, Polycarbonate

1. INTRODUCTION

When the laser began to put it to practical use as an industrial application, the possibility of laser marking to a variety of industrial materials has been examined. For about ten years, like IC package, the label method and the ink-marking method have been replaced by the laser marking rapidly in the electronics industry. At first, the laser-processing device for marking was large-scale. The object mark size was big. In recent years the laser and the optics system of focus make it to high performance. It came to be able to make it to low-cost with the speed-up of the processing. Moreover, it has come to be applied to a micro processing area including small parts of various materials. The merit of the laser marker is as follows. The laser marking differs from the marking method, which uses ink, and does not need the solvent at all. Therefore, it is environment-friendly. Because ink does not soak, the recycling of the material is easy. The kind and the time of the process can be greatly reduced. It differs from the method to use ink. Marking does not disappear because it changes the material in quality by the laser light. A micro marking outside the area of the ink jet can be easily done. Therefore, it is the best for marking to small electronic parts. Because operating it with the computer can easily do the input change, the content of marking is suitable to mass production for the many kinds of products. It is possible to contribute to the improvement of productivity by high-speed marking. Moreover, because the maintenance work is comparatively easy, the labor saving and the useful automation are easy. It can mark a wide material such as the metal, the resin, ceramics, the semiconductor, paper, and the glass.

Recently, the mark size is made minute by an advanced processing technology's having progressed. It is applied to a variegated field such as marking of the silicon wafer and jewels. In the field of the optical disk, it is tried to mark the CD-ROM medium by the request of the society for making to identification in various organizations [1-3]. This kind of marking should fulfill not only the mark, but also the role of the signal. Therefore, the marking size and pit formation accuracy that should be equal to a pit-size (<1 μm) of a CD signal are demanded. Moreover, to maintain durability, which is the feature of CD-ROM, the result of laser marking should avoid damaging the composition of the disk, especially the protection film. The heat model analysis of organic compact disk writable media of B. J. Bartholomeusz [4], pit formation model of T. S. Chung [5], and heat stress mechanism of K. E. Evans [6] were presented by the content concerning the laser marking about the organic dye thin film used for CD-R and CD-RW in the early research. Though those were presented by the content concerning the laser marking, the one of the CD-ROM medium is not found.

In this study, to write the signal for identification in the CD-ROM medium by the laser marking, it aimed to examine details of the formed pit part when marking it. To achieve this, using scanning electron microscope (SEM) and atomic force microscope (AFM), the laser processing part of the metallic thin film in the transparent medium resin was observed in micron area, and the thermal deformation behavior by the laser processing was examined. We place this laser processing to the laser marking from the point of identification of CD-ROM.
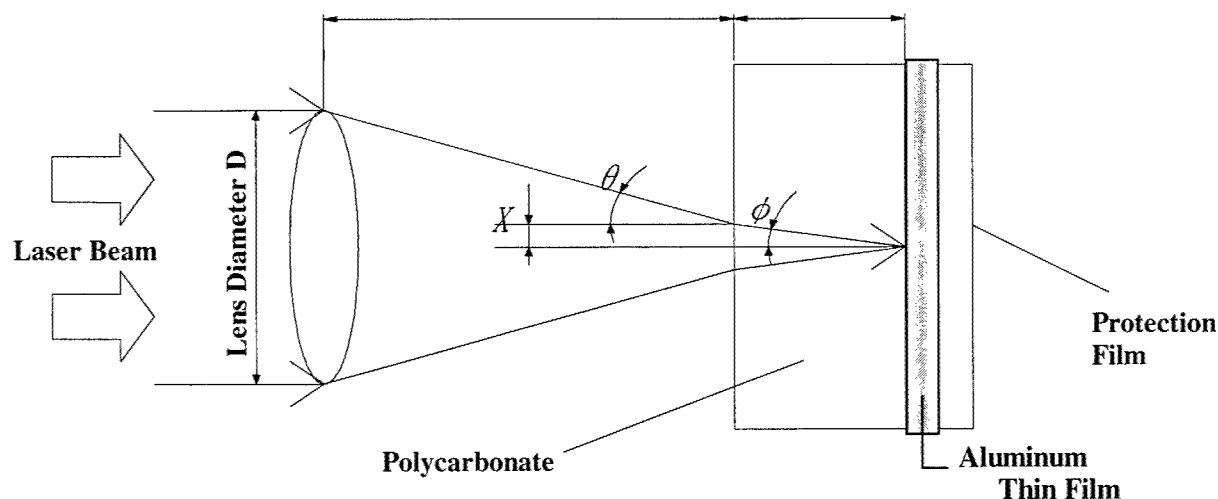
Fig. 1 Schematic diagram of the focusing beam and CD-ROM Specimen.

2. EXPERIMENTAL

2.1 Laser device for processing

Figure1 shows the outline of the sample and optical system for the experiment. The heat sources for the processing were a diode pumped YAG laser (MAX 150 mW) with wavelength 532 nm of second harmonic (SHG), a diode laser (780 nm, 80-100 mW: single mode and 2 W: multi-mode), Ar ion laser (514.5 nm, MAX 2000 mW), and the N_2 laser pumped dye laser (pulse laser, 5 nsec, and Max 300 mJ). Generally the laser marking is the processing to the surface of the material. However in this experiment the laser marking is the processing to the material in the transparent resin through the polycarbonate.

2.2 ROM media as sample

As a ROM media sample, a commercial available compact disc (CD) was used as the processing sample. An aluminum (Al) metallic thin film placed between a polycarbonate in thickness of 1.2 mm and a protection film (ultraviolet curing resin) in thickness of 5 μm was laser-processed through the polycarbonate. The size of the sample is 120 mm in the diameter and 1.2 mm in the thickness. The aluminum metallic thin film is about 100 nm.

3. RESULTS

In the case of the laser processing of the semiconductor laser ($\lambda = 780$ nm, the multimode, and 1000 - 2000 mW), the marking size was 60 - 70 μm because there was 1 μm x 200 μm in the source size of light. For YAG laser (SHG) with the maximum power is 150 mW, it cannot mark the sample because of the loss of the optics system. By using both an optical microscope focusing system and the N_2 pumped dye laser ($\lambda = 610$ nm, pulse width = 5 nsec and pulse energy = 300 mJ), the laser marking into a sample was conducted with an adequate irradiation power using ND filter. However, it is difficult in the degree of the pit pattern formation because the oscillation repetition rate is very low. Optical photographs of signal pits of commercial available CD and laser-marked pits of CD by an Ar ion laser are shown in Fig. 2. Dot lines indicate signal pits in Fig.2(a) and laser-processed pits in Fig. 2(b). It seems that the mark of the same size as the signal pit of CD is obtained with the Ar ion laser (λ =514.5 nm, TEM00) with good beam quality of the source of light. The width of the pit of CD is about 0.6 μm and track pitch is 1.6 μm. An aluminum metallic thin film is adhered to the protection film side in Figure 3(a). Aluminum in the laser irradiation part melts, and the pit is formed. In the part of the rim around the pit, the swelling was observed. The peeped protection film through the pit is smooth and not damaged. In the part of the polycarbonate side corresponding to it, the laser irradiation part swelled with convex, and the hollow was observed in a surrounding part. It is confirmed to cause this phenomenon in the large range as the input power grows.
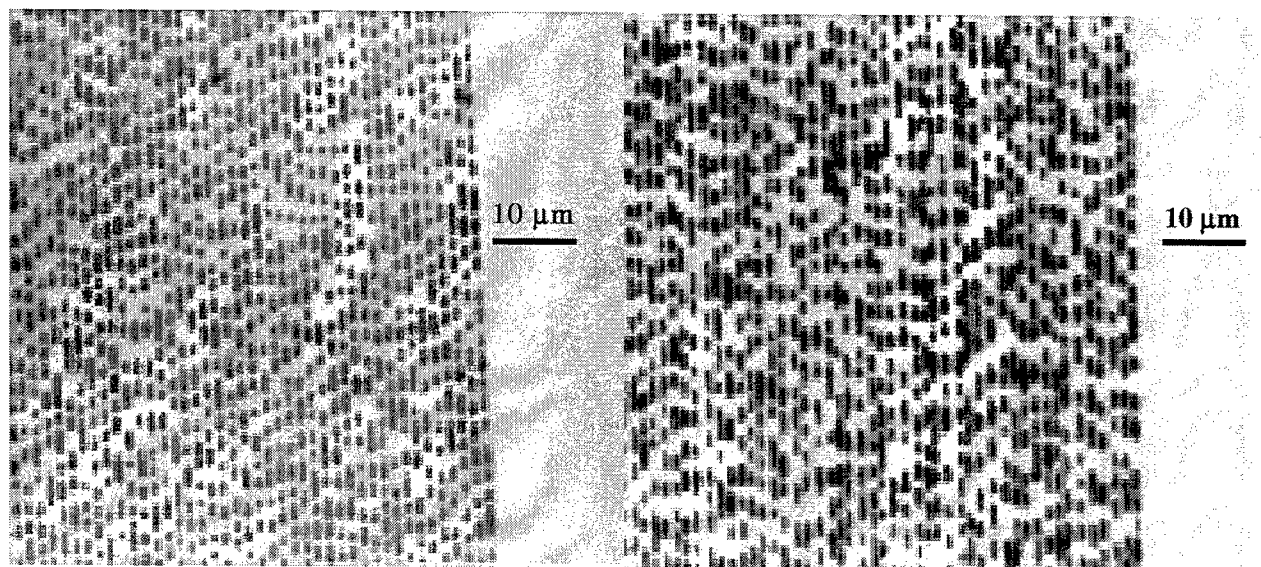
(a) CD-ROM signal pits.   (b) Laser Marking pits.

Fig. 2   Optical microscope images.   Pit width = 0.6 μm, Track pitch = 1.6 μm
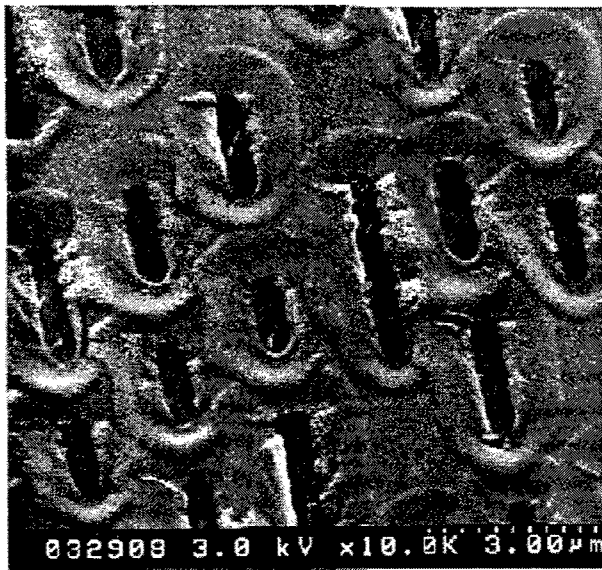
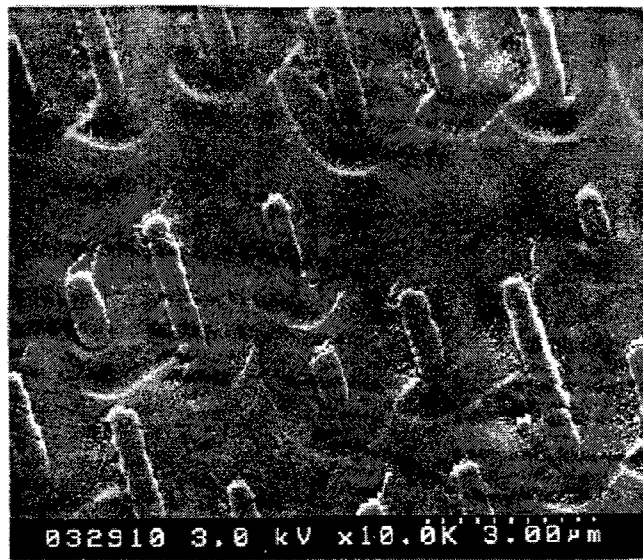Fig. 3(a) protection film side.   Fig. 3(b) Polycarbonate side.

Fig. 3   SEM images of peeled area of PC and protection film. Aluminum thin film is adhered to side of protection film.

In order to examine quantitatively this ruggedness, an information of the height was examined in detail by using AFM. Figure 4 shows typical images of AFM. In this Fig.4(a), as well as the result of SEM, the polycarbonate side was swelled with convex., it is understood to cause the hollow in a surrounding part. Examining this ruggedness, as shown in Fig.4(b), a ruggedness amount is <100 nm, the swelling will be caused like having thrust the aluminum thin film aside. The result is thought to be one of factors that the pit is formed to the aluminum thin film. Next, the cross-section observation in the pit formation part of the marking part was conducted using SEM. Figure 5 shows the cross-section image of pit. The upper part is PC side in the cross-section photograph, and the lower side is a protection film side. A horizontal white line in the photograph is aluminum thin film (~100 nm). In the cross-section observation, there is no Al film in the laser irradiation area. The boundary of PC and the protection film was not observed. However, it was confirmed that there was no cave in the inside. The Al film of neighborhood where the laser was irradiated was compared with the center part. It found that the Al film of neighborhood, where the laser was irradiated, swells thick compared with the center part with the polycarbonate side. This corresponds to the convex part on the PC side that can be confirmed even by the SEM observation and the AFM observation of the sample peeled off. Figure 6 is a model chart of the thermal deformation behavior of the observation result. The heat absorbed to aluminum is transmitted to the PC side and the protection film side by the thermal conduction. Though PC on the laser irradiation side is good for the transparency of the laser wavelength, it is thought that slight absorption and scattering are accompanied, and the temperature rises to the vicinity of the softening point. It is about 420 K in temperature of the glass metastasis point and 500 - 520 K in melting point of PC.

It is thought that the material flow is generated when the temperature exceeded melting point. It is thought that the surface tension is generated as aluminum dissolves, PC expands to the pit formation part with the material flow of PC, and it infiltrates to the Al film area. To confirm it further, the heat flow analysis with a material flow is needed.
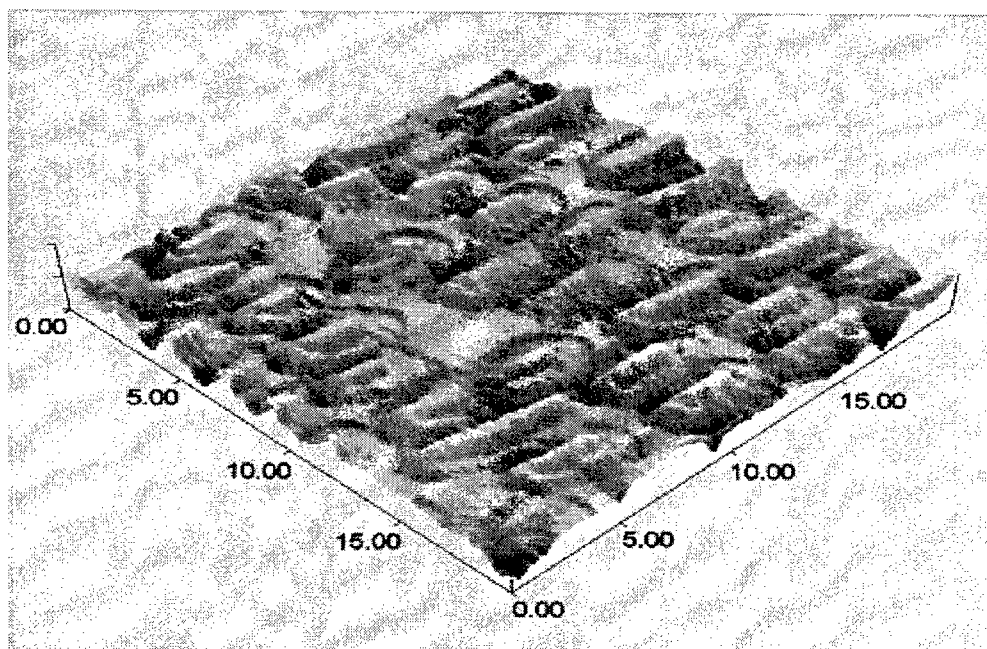
Fig. 4(a). 3D Image of PC side on laser marked CD -ROM.
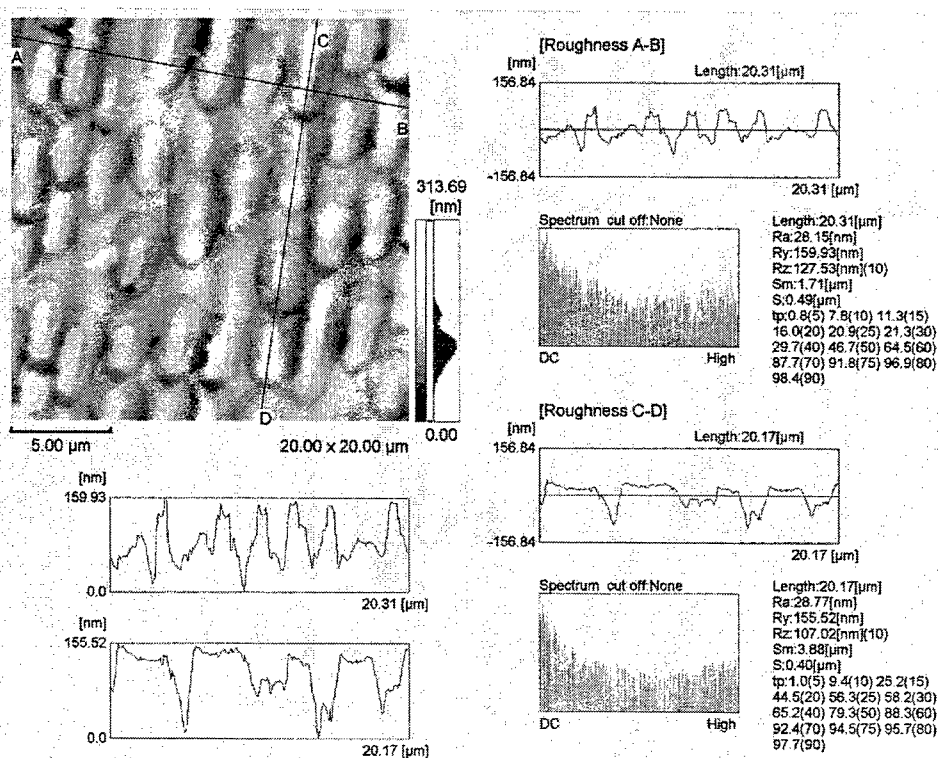
Fig. 4(b). Top view of PC side

Fig. 4 AFM images of laser marking recorded on a CD material. Surface of PC was peeled off protection film.
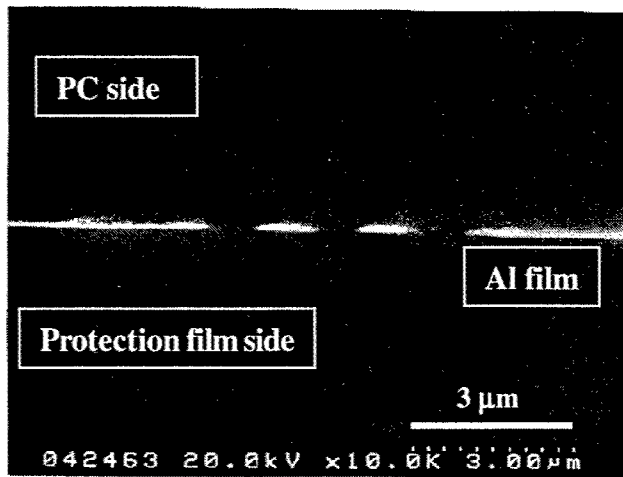
Fig. 5 Cross-section SEM images : White lines in the center of photos are Al thin film (100 nm), the upper part of the line is PC, and the lower part is protection film.
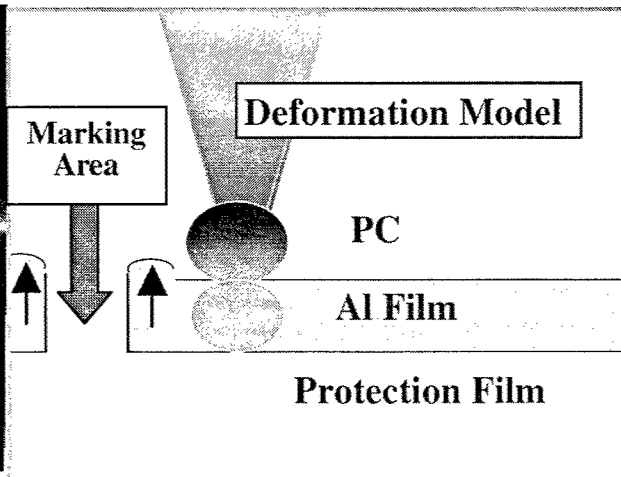
Fig. 6 Pit formation model during laser marking process

4. SUMMARY

The laser marking in the CD-ROM medium for identification was conducted. The results of observing the processing situation through SEM and AFM are as follows:

It was confirmed to be able to form the pit to the aluminum thin film in a transparent medium without damaging the protection film from SEM and the AFM observation.

The deformation of the polycarbonate according to the pit formation of the aluminum thin film was confirmed from SEM and the AFM observation.

An excellent result was comparatively obtained with Ar ion laser (λ =514.5 nm, 450 mW).

Though the diode laser of a single mode is desirable on the device composition, the power is small now with 100 mW or less. It seems that 150 mW or more is necessary on the surface of the sample.

ACKNOWLEDGEMENT

REFERENCES

(1) Sumio Nakahara, *et al.*, 6th Kansai University HRC symposium, pp.74-79(2002.3).

(2) S. Nakahara, *et al.*, LAMP 2002 Technical Digest, p.45, (2002.5).

(3) Press release: (2002.5) . Http://www.sony.co.jp/SonyInfo/News/Press/200205/02-021/

(4) Brian J. Bartholomeusz, Appl. Optics., 31(7), pp.909-918, (1992.3).

(5) Tai-Shung Chung, J. Appl. Phys., 60(1), pp.55-60, (1986.7).

(6) K.E. Evans, J. Appl. Phys., 63(10), pp.4946-4950 (1988.5).

Heat-affected zone of metals ablated with femtosecond laser pulses

Yoichi Hirayama, and Minoru Obara*

Dept. of Electronics and Electrical Engineering, Keio Univ./

3-14-1 Hiyoshi, Kohoku-ku, Yokohama, 223-8522, Japan

ABSTRACT

The melted area is found on the surface ablated by nanosecond and picosecond laser pulses. However, the heat effect is little on the ablated surface in the case of femtosecond laser due to non-thermal ablation process. Heat-affected zone of metallic bulk crystal ablated with femtosecond Ti:sapphire laser pulses is experimentally studied. As a result of XRD (X-ray diffraction) measurements, the XRD peak signal of the area ablated with Ti:sapphire laser becomes smaller than that of the crystalline metal sample. While the crystallinity of the metal sample is crystalline before the laser ablation, the crystallinity in the ablated area is *partially* changed into the amorphous form. Because the residual pulse energy that is not used for the ablation process remains, leading to the formation of thin layer of melt phase. The melt layer is abruptly cooled down not to be re-crystallized, but to transform into the amorphous form. It is evident that the area ablated with femtosecond laser is changed into the amorphous metal. Additionally XRD measurements and Ar^+ etching are performed alternately to measure the thickness of the amorphous layer. In the case of iron, the thickness is measured to be 1 µm approximately, therefore heat-affected zone is quite small.

Keywords: heat-affected zone, femtosecond laser, ablation, metal, amorphous, XRD, Ar^+ etching

1. INTRODUCTION

Significant advancement of tunable solid state lasers and the chirped pulse amplification (CPA) technique by using Ti:sapphire, Cr:LiSAF and Cr:LiCAF laser media has led to the challenging phase of application research. The application fields opened up high-intensity physics[1], ultrashort pulsed laser ablation[2,3], and so on. Ultrashort pulsed laser ablation is one of the most promising technologies among femtosecond laser applications because the ablation physics is drastically different from those governing conventional nanosecond pulsed laser ablation. Generally, the electron-lattice relaxation time in metals is 1-10 ps[4,5]. Therefore, the mechanism of femtosecond laser ablation differs from that of longer pulsed laser ablation. Thermal ablation occurs when the laser pulsewidth is longer than the electron-lattice relaxation time. The importance of the pulsewidth compared to the electron-lattice scattering time and the thermal diffusion time corresponding to the skin depth was pointed out by Stuart et al.[6] In a wide band-gap insulator under strong laser irradiation, direct observation of multiphoton absorption by free electrons was reported[7].

Moreover, femtosecond laser ablation of materials with high thermal conductivity is of paramount importance[8,9],

*obara@obara.elec.keio.ac.jp; phone +81-45-563-1141 ext. 42226; fax +81-45-566-1529

because the chemical composition and properties of the area ablated with femtosecond laser is kept unchanged[9, 10]. The material processing by femtosecond laser can well control the heat-affected zone of the dielectric materials. Regarding metal ablation, the residual energy left in the metal, which is not used for ablation, will induce liquid phase, resulting in the amorphous/polycrystalline phase of the metal during re-solidification. The heat transfer in metals irradiated by subpicosecond laser pulses is theoretically simulated based on the two-temperature diffusion model[11] and in the case of gold it is *experimentally* demonstrated that the heat effects exist after femtosecond laser irradiation[12]. However, the heat-affected zone at the area ablated with femtosecond laser is not evident.

In this study, we would like to report on the heat-affected zone of metallic bulk crystals ablated with femtosecond Ti:sapphire laser. Due to the heat effects induced by laser pulses, the ablated bottom area is partially converted into the amorphous metals from the sample crystalline metals.

2. EXPERIMENTAL

The laser used in our experiments is a commercially available titanium-sapphire (Ti:sapphire) laser, with a chirped pulse amplification (CPA) system pumped by the second harmonic of a Nd:YLF laser at a 1 kpps repetition rate. The pulsewidth, the center wavelength and pulse energy is 100 fs, 800 nm and 1.0 mJ, respectively. The intensity autocorrelator and the powermeter at the exit of the amplifier periodically monitor the drifts of the pulsewidth and output energy in order to ensure stable pulse energy on a target. To control the pulse energy, we used optical neutral density filters. Thus, the laser parameter is confirmed prior to the ablation experiments. An 80-mm-focal-length fused silica convex lens is used to focus the attenuated laser pulses onto the targets. The irradiation number of laser pulses is controlled by a mechanical shutter. Metallic bulk crystals used here is gold, silver, copper and iron. The crystallinity of Au, Ag and Cu is poly-crystalline, and the crystallinity of Fe is single crystalline. The thermal properties of these metals are listed in Table 1[13]. All ablation experiments are performed in air at room temperature. In measurements, we use X-ray diffraction (XRD, Rigaku RAD-C) and argon ion etching apparatus (JEOL Ltd. Model 9000-MC) to observe the crystallinity and the heat-affected zone of the ablated area. After the ablation experiments, the crystallinity of the

Table 1 Thermal and electrical properties of metals[13]

	Thermal conductivity at 300K [W/cmK]	Electrical resistvity at 300K [10^{-8} Ωm]	Heat capacity at 298K [J/cm³K]	Lattice constant [Å]	Melting point at 760Torr [°C]	Boiling point at 760Torr [°C]
Au	3.17	2.271	2.49	4.0786	1064	2856
Ag	4.29	1.629	2.47	4.0862	962	2162
Cu	4.01	1.725	3.45	3.615	1085	2562
Fe	0.802	9.98	3.53	2.8664	1538	2861

ablated area is measured using XRD. Additionally, in order to estimate the heat-affected zone, we perform the XRD measurements after the ablated area was etched using Ar^+ etching apparatus.

3. RESULTS AND DISCUSSION

3.1 Ablation rate of metals

The dependence of the ablation rate on the laser fluence is investigated in order to characterize the ablation process. Fig. 1 shows the ablation rates of Au, Ag, Cu, and Fe[12]. Ablation depth is measured using a mechanical stylus (Dektak-3030). The estimated ablation rate is an average value of 300 laser shots. In the case of Au, Ag, and Cu ablated with Ti:sapphire laser, it is observed that the ablation rate has two different ablation regimes, as reported by Nolte, *et al.*[14] and Furusawa *et al.*[8] The characteristic depth of the two different ablation regimes is explained by the optical skin depth (penetration depth) and the thermal diffusion length, which is determined by the peak electron temperature in the framework of the two-temperature model. However, it is not found for Fe that there are two ablation rate regimes like other metals, because of its small thermal conductivity. Therefore we perform ablation experiments for three laser fluences (below the threshold fluence, low fluence regime, and high fluence regime) determined by each metal. After that, the crystallinity at the ablated area is measured using XRD.

3.2 Results of XRD measurements

As a result of XRD measurements, the XRD peak signals of the bottom area ablated with femtosecond Ti:sapphire laser is found to be much weaker than that of the crystalline metal sample, as shown in Figs. 2-5. XRD measurement of Ag sample is shown in Fig. 2. Figs. 3-5 indicate XRD measurements of Ag at the area ablated in the
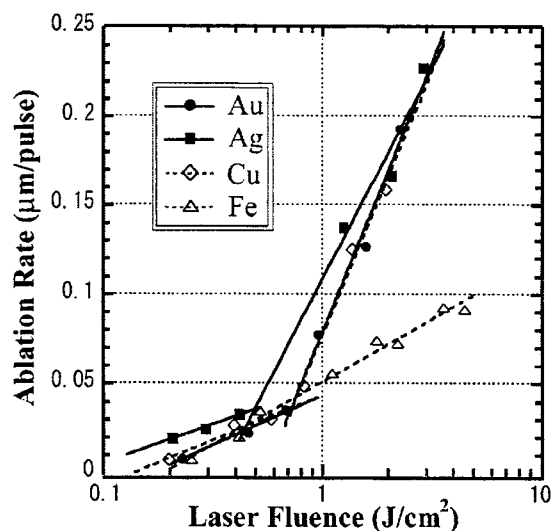

Fig. 1 Plots of ablation rate per pulse as a function of Ti:sapphire laser fluence for Au, Ag, Cu, and Fe.

Fig. 2 XRD signals of Ag sample before laser ablaion.
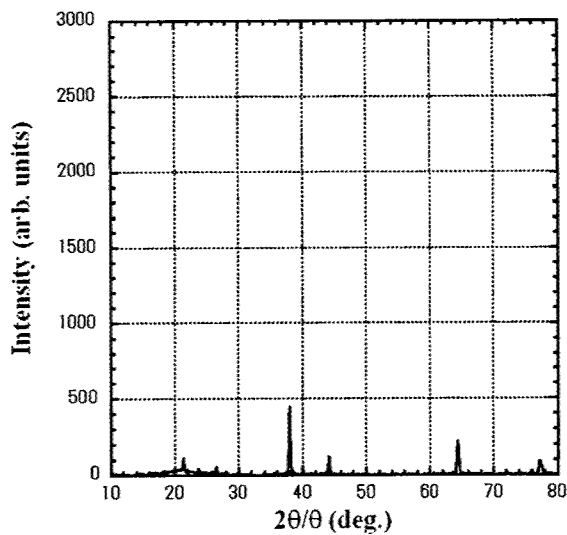
Fig. 3 XRD signals of Ag after laser ablation. The laser fluence is 1.48 J/cm² (high fluence regime).

Fig. 4 XRD signals of Ag after laser ablation. The laser fluence is 0.32 J/cm² (low fluence regime).

laser fluence of high fluence regime (1.48 J/cm^2), low fluence regime (0.32 J/cm^2) and below threshold fluence (0.058 J/cm^2), respectively. Although these figures show the XRD signals of Ag, the same results are obtained in the case of Au[12] and Cu as well. There are some large peak signals in Fig. 2, because Ag sample is poly-crystal. Although the crystallinity of the metal sample used is poly-crystalline before the laser ablation, the crystallinity at the ablated area is *partially* changed into the amorphous. The residual laser energy absorbed that did not contribute to the ablation process remains, leads to the formation of thin layer of melt phase. The melt layer is abruptly cooled down not to be re-crystallized, but to be amorphous. It is evident that the area ablated with femtosecond laser is converted into amorphous metals. This mechanism would be similar to the melt-quenching generally used as the fabrication method of

Table 2 Absorption coefficients and skin depth of metals at the wavelengths of X-ray used in XRD and Ti:sapphire laser

	At 0.15406 nm (the wavelength of X-ray used in XRD)		At 800 nm (the wavelength of Ti:sapphire laser)	
	Absorption coefficient [cm^{-1}]	Skin depth [μm]	Absorption coefficient [cm^{-1}]	Skin depth [μm]
Au	4006	2.50	7.25×10^5	0.0138
Ag	2290	4.37	9.21×10^5	0.0109
Cu	460	21.7	8.36×10^5	0.0120
Fe	2396	4.17	5.72×10^5	0.0175

amorphous metals. This experimental result is consistent with the theoretical results reported by Furukawa *et al.*[15] who performed the simulation of metal ablation by femtosecond laser and found to form the melted layer at the ablated area.

In the case of Fe, the results of XRD measurements has only one large peak signal, as shown in Figs. 6 and 7. Fig. 6 shows XRD measurement of Fe sample, and Fig. 7 indicates XRD measurement of Fe at the area ablated in the laser

Fig. 5 XRD signals of Ag after laser ablation. The laser fluence is 0.058 J/cm^2 (below threshold fluence).
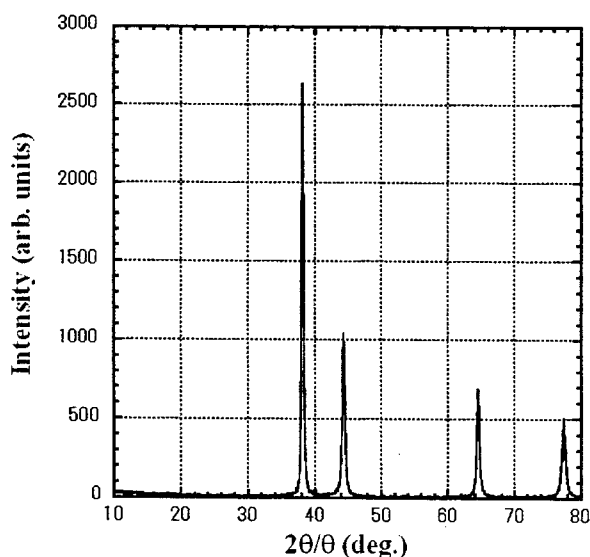

Fig. 6 XRD signals of Fe sample before laser ablation.

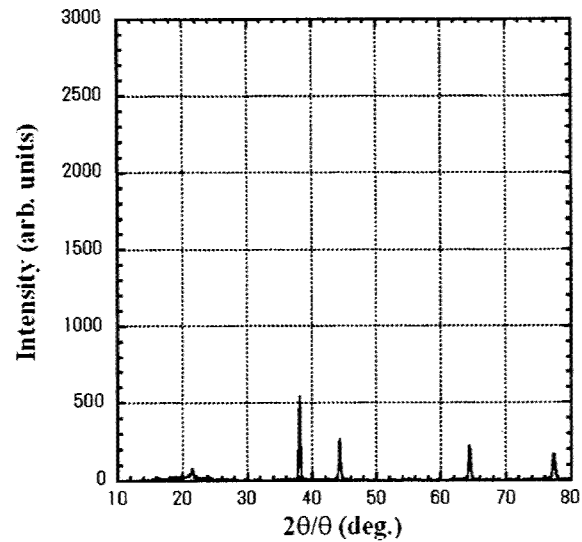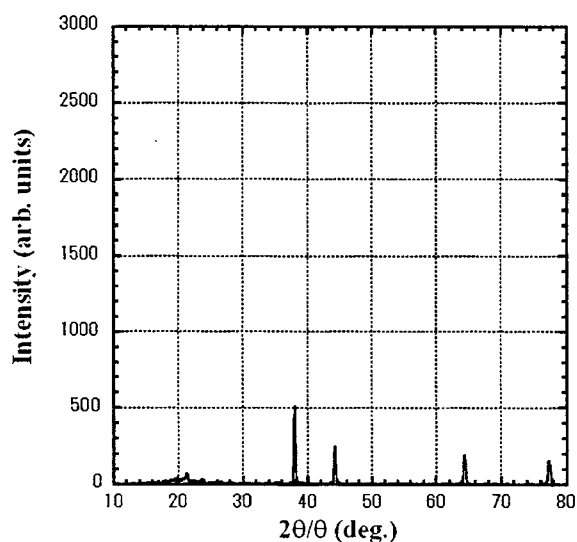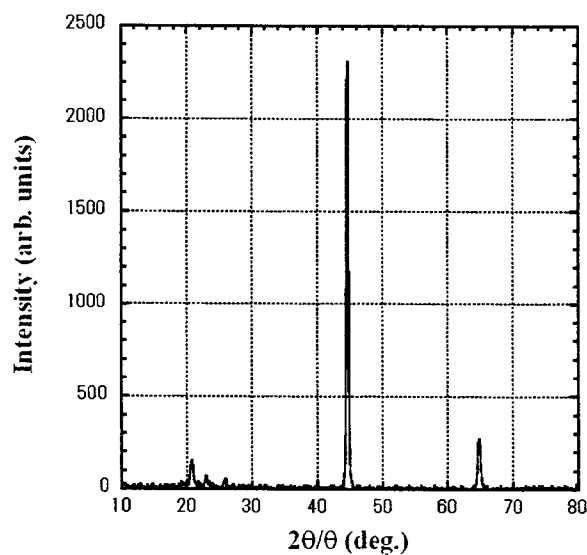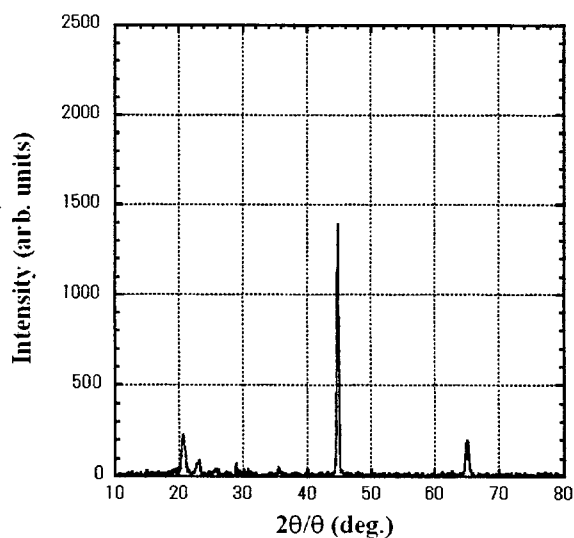Fig. 7 XRD signals of Fe after laser ablation. The laser fluence is 2.39 J/cm^2 (high fluence).
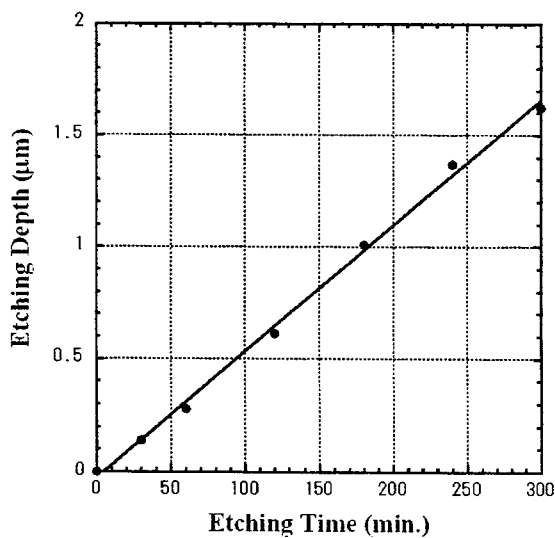
Fig. 8 The dependence of etching depth on the etching time for Fe. The etching rate is 0.337 μm/hour.

fluence of 2.39 J/cm^2. Because the crystallinity of Fe sample we used is single crystal. While the XRD signal of the complete amorphous material has no peak, the results we obtained show weak peak signals. The optical absorption coefficient of metals at 800 nm of Ti:sapphire laser is much larger than that at the wavelength of X-ray we used to measure, as listed in Table 2[13]. Because the energy of Ti:sapphire laser is absorbed only by very thin depth near the surface, that area changes into amorphous form after the laser ablation. Therefore, the results of small peak signals are obtained by XRD measurement, because the crystalline part under the amorphous layer changed by laser ablation is also measured.

3.3 The thickness of amorphous layer

At first, we investigate the etching rate of argon ion etching apparatus used in this experiments. The dependence of the etching depth on the etching time is shown in Fig. 8. It is calculated from this figure that the etching rate is 0.337 μm/hour.

Next, in order to estimate the thickness of the amorphous layer, the laser-ablated area etched using Ar$^+$ etching apparatus is measured by XRD. The surface of Fe sample etched by Ar$^+$ etching is measured using XRD whether the XRD peak signal is changed by etching or not. It is found that the XRD peak intensities have hardly any changes, as shown in Fig. 9. The XRD peak signals at the area ablated in the laser fluence of 2.39 J/cm^2 after Ar$^+$ etching are shown in Fig. 10. The XRD peak intensity after Ar$^+$ etching is gradually increasing and is saturated. Fig. 11 indicates the standardized signals of the XRD peak intensities in Fig. 10, and full width of half maximum (FWHM) of each signal is listed in Table 3. When the etching time is long, FWHM is gradually narrowing, and is saturated. Because the saturated values of the XRD peak intensity and FWHM in Figs. 10 and 11 are close to the XRD peak intensity and FWHM of the
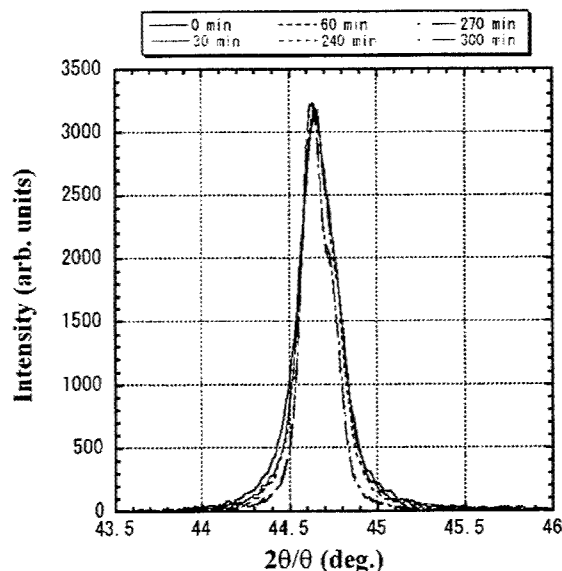
Fig. 9 The relationship between XRD peak signals of Fe sample and etching time.
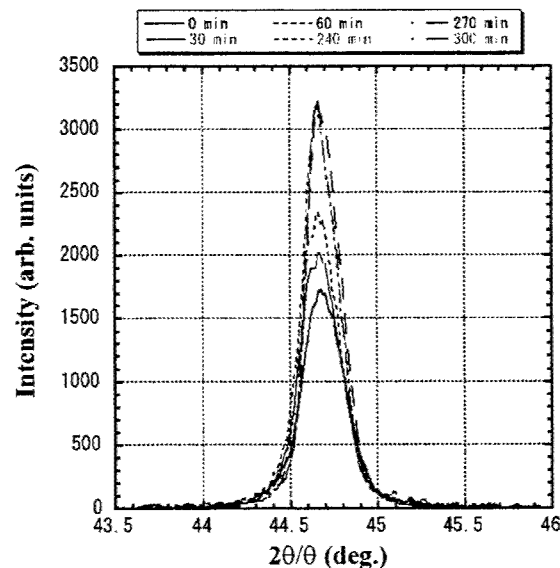
Fig. 10 The relationship between XRD peak signals at the ablated area and etching time. Laser fluence is 2.39 J/cm^2.
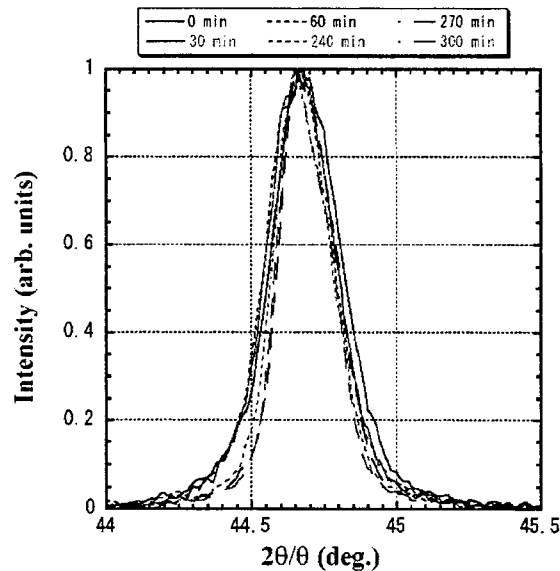
Fig. 11 The relationship between the normalized signals and etching time.
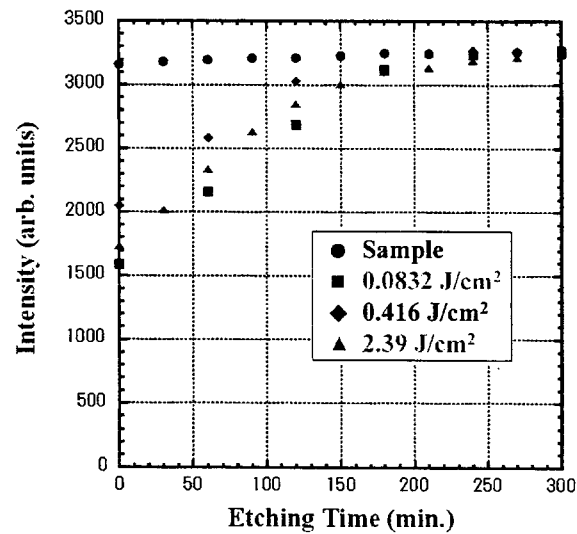
Fig. 12 Plots of the XRD peak intensities as a function of etching time.

Fe sample, the amorphous layer fabricated by laser ablation is removed by etching and the crystalline part appears on the surface.

The dependence of XRD peak intensity on etching time for Fe sample and three laser fluences are shown in Fig. 12. The thickness of amorphous layer is evaluated from Figs. 8 and 12, as listed in Table 4. In the fluence below the threshold fluence, the whole energy irradiated on the target is absorbed because the laser ablation does not occur. However, in the case of the energy over the threshold fluence, the residual laser energy which did not contribute to the ablation is left. Therefore the thickness of amorphous layer for the laser fluence below threshold fluence is larger than that for low and high fluence. It depends on the laser fluence, and is measured to be 1 μm, approximately. Therefore it is found that heat-affected zone by the femtosecond laser is quite small.

Table 3 FWHM of XRD signals in Fig. 11.

Etching time [min.]	Depth [μm]	FWHM
0	Surface	0.277
30	0.169	0.273
60	0.337	0.261
240	1.348	0.223
270	1.517	0.228
300	1.685	0.217

Table 4 The thickness of amorphous layer estimated.

Laser fluence [J/cm²]	0.0832	0.416	2.39
The thickness of amorphous layer [μm]	1.033	0.798	0.937

4. CONCLUSION

Heat effects and heat-affected zone of metallic bulk crystals of ablated with 100-fs Ti:sapphire laser pulses is experimentally studied. As a result of XRD (X-ray diffraction) measurements, the XRD peak signal of the area ablated with Ti:sapphire laser is smaller than that of the crystalline metal sample. While the crystallinity of the metal sample is crystalline before laser ablation, the crystallinity in the ablated area is *partially* changed into the amorphous form. It is evident that the area ablated with femtosecond laser is changed into amorphous metals. This formation mechanism would be the same as the melt-quenching generally used as the fabrication method of amorphous metals. The thickness of the amorphous layer is measured to be only 1 μm, approximately.

ACKNOWLEDGE

REFERENCES

1. B. E. Lemoff, G. Y. Yin, C. L. Gordon III, C. P. J. Barty, and S. E. Harris, "Femtosecond-pulse-driven 10-Hz 41.8-nm laser in Xe IX," *J. Opt. Soc. Am. B* **13**, 180-184, 1996.

2. W. Kautek, and J. Krueger, "Femtosecond pulse laser ablation of metallic, semiconducting, ceramic, and biological materials," *Proc. SPIE* **2207**, 600-611, 1994.

3. B. C. Stuart, M. D. Feit, A. M. Rubenchik, B. W. Shore, and M. D. Perry, "Laser-induced damage in dielectrics with nanosecond to subpicosecond pulses," *Phys. Rev. Lett.* **74**, 2248-2251, 1995.

4. S. D. Brorson, A. Kazeroonian, J. S. Moodera, D. W. Face, T. K. Cheng, E. P. Ippen, M. S. Dresselhaus, and G. Dresselhaus, "Femtosecond room-temperature measurement of the electron-phonon coupling constant lambda in metallic superconductors," *Phys. Rev. Lett.* **64**, 2172-2175, 1990.

5. G. L. Eesley, "Generation of nonequilibrium electron and lattice temperatures in copper by picosecond laser pulses," *Phys. Rev. B* **33**, 2144-2151, 1986.

6. B. C. Stuart, M. D. Feit, S. Herman, A. M. Rubenchik, B. W. Shore, and M. D. Perry, "Optical ablation by high-power short-pulse lasers," *J. Opt. Soc. Amer. B* **13**, 459-468, 1996.

7. P. Daguzan, S. Guizard, K. Krastev, P. Martin, G. Petite, A. Dos Santos, and A. Antonetti, "Direct observation of multiple photon absorption by free electrons in a wide band-gap insulator under strong laser irradiation," *Phys. Rev. Lett.* **73**, 2352-2355, 1994.

8. K. Furusawa, K. Takahashi, H. Kumagai, K. Midorikawa, and M. Obara, "Ablation characteristics of Au, Ag, and Cu metals using a femtosecond Ti:sapphire laser," *Appl. Phys. A* **69**, 359-366, 1999.

9. Y. Hirayama, H. Yabe, and M. Obara, "Selective ablation of AlN ceramic using femtosecond, nanosecond, and microsecond pulsed laser," *J. Appl. Phys.* **89**, 2943-2949, 2001.

10. K. Ozono, M. Obara, A. Usui, and H. Sunakawa, "High-speed ablation etching of GaN semiconductor using femtosecond laser," *Opt. Commun.* **189**, 103-106, 2001.

11. A. P. Kanavin, I. V. Smetanin, V. A. Isakov, Yu. V. Afanasiev, B. N. Chichkov, B. Wellegehausen, S. Nolte, C. Momma, and A. Tünnermann, "Heat transport in metals irradiated by ultrashort laser pulses," *Phys. Rev. B* **57**, 14698-14703, 1998.

12. Y. Hirayama, and M. Obara, "Heat effects of metals ablated with femtosecond laser pulses," *Appl. Surf. Sci.* **197-198**, 741-745, 2002.

13. D. R. Lide, *CRC Handbook of Chemistry and Physics 82nd ed.*, Chapter 12, CRC Press, Boca Raton, 2001-2002.

14. S. Nolte, C. Momma, H. Jacobs, A. Tünnermann, B. N. Chichkov, B. Wellegehausen, and H. Welling, "Ablation of metals by ultrashort laser pulses," *J. Opt. Soc. Am. B* **14**, 2716-2722, 1997.

15. H. Furukawa, and S. Uchida, "Simulation of metals by femtosecond laser ablation," *Reports on The 280th Topical Meeting of LSJ*, **RTM-0046**, 46-49, 2000.

Excimer and femtosecond pulsed laser induced forward transfer process of metal thin film

Hirokazu Yamada, Tomokazu Sano*, Etsuji Ohmura, Isamu Miyamoto

Graduate school of engineering, Osaka university,
2-1 Yamada-oka, Suita, Osaka 565-0871, Japan

ABSTRACT

The investigation of laser induced forward transfer (LIFT) process using femtosecond pulsed laser comparing with that using excimer laser is reported. Ni thin film of several hundreds of nanometer thickness, which is deposited on fused silica substrate, was irradiated by single pulse of KrF excimer laser (wavelength: 248nm, pulse width: 30ns) or femtosecond pulsed laser (wavelength: 800nm, pulse width: 120fs), and transferred to a Si acceptor substrate. It is shown that laser beam profile affected the removal of thin film. It is revealed that adhesion of particles was inhibited using femtosecond pulsed laser in comparison with the case of excimer LIFT process.

Keywords: Laser-induced forward transfer (LIFT), Thin film patterning, Direct writing

1. INTRODUCTION

Many direct-write technologies have been studied for their ability to transfer and/or process any types of material over any surface with precision resolution in a functional structure or working device.[1] Laser induced forward transfer (LIFT) is one of these technologies and was first performed by Bohandy et al. in 1986.[2] LIFT techniques using picosecond - microsecond pulsed laser have been investigated by many researchers due to its unique process and the ability to fabricate microstructures. LIFT process consists of the sequence of the three events. First, laser beam is irradiated on metal thin film through a transparent support substrate and thin film is removed (Removal process). Second, thin film is transferred to an acceptor substrate placed parallel to a support substrate (Transfer process). Finally, thin film is hit on an acceptor substrate, and deposits there (Deposit process). LIFT process can be performed in air and under room temperature without generating poisonous gases. Using mask projection method, optional patterns can be transferred on an acceptor substrate in optional size. Various thin films, such as metals (Al.[3,4] Au.[5] Cu[2]!$Cr.[6,7] Sn.[6] V.[6] Ti.[6,7] Pd.[8] W.[9-12] Ni[13,14]), semiconductor (Ge[15]), and superconductors (YBaCuO, BiSrCaCuO[16]), diamond particles,[17] laser dye (Rhodamine 610[18]), were deposited using picosecond - microsecond pulsed laser.

In addition to fabrication of deposited materials, the mechanisms of LIFT process have been investigated. Bullock et al. photographed images of the Al vapor plume using shadowgraph and interferometer system[19,20] and revealed that the damage of a support substrate was occurred by laser irradiation. This damage limited the transmitting fluence and affected the edge velocity of the plume. Nakata et al. photographed the images of Au particles using two-dimensional laser-induced fluorescence (2D-LIF) method.[21] It was revealed that the velocity of atoms exceeds 2km/s and the velocity of emissive particles was about 100m/s. Adrian et al.[22] and Baseman et al.[23] calculated the temperature distribution in thin film during laser heating using finite difference and finite element method, respectively. They suggested that thin film was heated and vaporized by laser beam at the interface between thin film and a support substrate, and the pressure reached a value enough for thin film to be removed and propelled thin film from a support substrate.

On the other hand, LIFT techniques using femtosecond pulsed laser have been investigated by few researchers. Metal (Cr[24,25]), metal oxide (In$_2$O$_3$[24,26]), and organic material (PMMA[27]) thin films were deposited using femtosecond pulsed laser. Zergioti et al. fabricated microstructure, such as computer-generated holographic pattern.[24,25] computer-generated multilevel structure,[24] micrograting,[26] and so on. They investigated plume

---

Further author information: (Send correspondence to Tomokazu Sano)
E-mail: sano@mapse.eng.osaka-u.ac.jp, Telephone: +81 6-6879-7535

dynamics through imaging plume[28] and shadowgraph of plume[29] using Intensified CCD camera. Ejected material was highly directional with narrow angular divergence. It was revealed that the material velocity was 370±12m/s and the blast wave velocity was 396±10m/s in transfer process. In addition to these studies, it is needed to investigate femtosecond LIFT process itself to get more comprehension.

In this paper, the investigation of femtosecond LIFT process is reported comparing with excimer LIFT process.

2. EXPERIMENTAL PROCEDURE

Excimer laser induced forward transfer (excimer LIFT) setup is shown in Figure1. Metal thin film was irradiated by a single pulse of KrF excimer laser beam (wavelength: 248 nm, pulse width: 30ns) with flat-top profile using mask projection method.
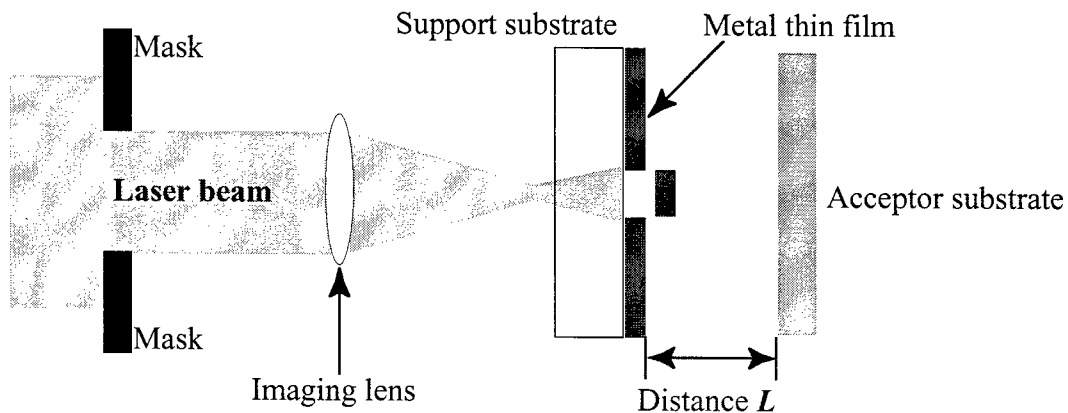
Figure 1. Schematic illustration of excimer laser induced forward transfer process.

Femtosecond laser induced forward transfer (femtosecond LIFT) setup is shown in Figure2. Ti:Sapphire laser beam (wavelength: 800nm, pulse width: 120fs) was oscillated at 1 hertz. Metal thin film is irradiated by a single pulse of laser beam.
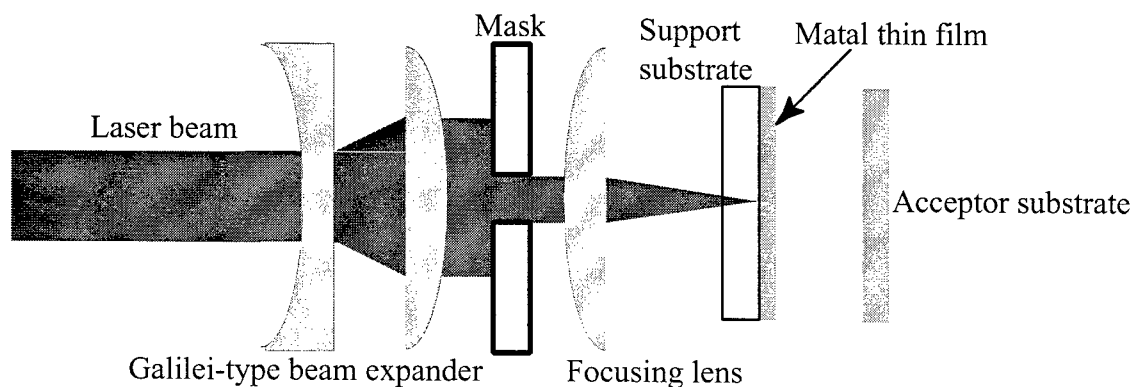

Figure 2. Schematic illustration of femtosecond pulsed laser induced forward transfer process.

Ni thin film was deposited on fused silica substrates of 2.3 mm thickness using ion sputtering method. The removed thin film was deposited on Si wafers as acceptor substrates. Laser fluence, F and distance L, which is

the distance between thin film and an acceptor substrate were varied from 0.8 to 2.7 J/cm^2 and 0 to 500μm, respectively. The experiments were performed in air at room temperature.

3. RESULTS AND DISCUSSIONS

3.1. Excimer laser induced forward transfer process

Figure3(a) shows the optical microscope image of the deposited material. The white square in this figure shows the size of laser-irradiated zone. The size of deposited material was equal to that of laser-irradiated zone, and droplets spread outward. In order to evaluate the resolution of deposited material, we defined distance d_1 as the distance between the edge of the laser irradiated zone and the outer edge of droplets. In our previous work,[13] it was revealed that making distance L shorter, distance d_1 became shorter and the resolution of a deposited material was improved. 3(b) shows the SEM image of deposited material. Particles were transferred circularly around the deposited material. We found that the diameter of particles-transferred zone was 4 - 8 times as long as the width of deposited material under the condition that distance L was larger than 10μm. Therefore, adhesion of particles made worse the resolution of deposited materials dramatically.
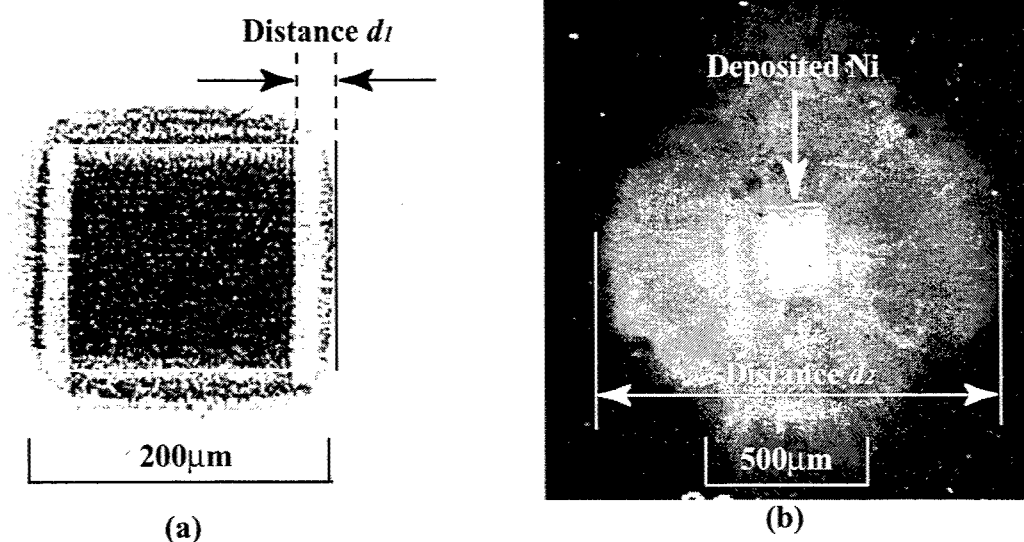
Figure 3. Optical microscope(a) and SEM(b) image of deposited material. Ni. Thickness of thin film: d=180nm, Distance L=20μm. Fluence: F=1.5J/cm^2(a), 0.8J/cm^2(b), respectively.

To investigate the reason why particles are transferred around a deposited material, we photographed the images of the plume, which is generated by laser irradiation, using image intensified CCD camera. Under the condition of no acceptor substrate, the plume was moving forward. On the other hand, the plume was prevented from moving forward by an acceptor substrate and expanded outward under the condition that an acceptor substrate was placed. Details of this experiment were described in our previous work.[13,14] Taking the behavior of the plume and the distribution of particles into account, it is considered that particles were contained within the plume and transferred around a deposited material when the plume expanded outward.

Consequently, we can inhibit the transfer of particles if we are able to prevent the plume from expanding outward. And so, we operated LIFT technique under the condition that distance L was 0μm, that was, thin film was in contact with an acceptor substrate. Figure4(a) shows the image of the deposited material, which was obtained under the condition that distance L was 0μm. The square in this figure shows the size of laser spot. Under this condition, particles were not seen around the deposited material. It was obvious that the deposited material has clear contour in comparison with the deposited material fabricated under the condition that distance L=10μm. When the LIFT technique was performed under the condition that distance L was

0μm, it is considered that the plume was trapped between thin film and the support substrate and solidified there. Therefore, particles were not expelled outside and not transferred around the deposited material. This optimum fluence was equal to that of the conventional LIFT technique, which was evaluated in our previous work.[13] Detailed investigation was done at our recent work.[14] However, this process restricts the applications by the contact of an acceptor substrate with thin film.

Figure 4. SEM images of deposited materials. Ni, d=230nm, F=1.7J/cm^2, (a)L=0μm, (b)L=0μm.

3.2. Femtosecond pulsed laser induced forward transfer process

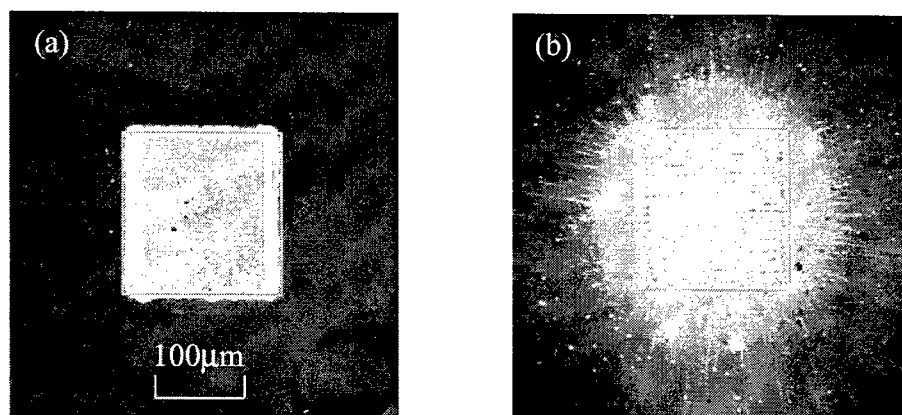Figure5 shows the optical microscope image of the deposited Ni. The black circles in these figures show the size of laser-irradiated zone. In the condition that thin film was in contact with an acceptor substrate, droplets were not seen. The size of deposited Ni became larger as laser fluence became larger. As laser beam has Gaussian beam profile, it is considered that removed zone of thin film become larger making laser fluence larger.

On the other hand, droplets spread widely around the deposited material in the condition that distance L was larger than 10μm. The size of deposited Ni was smaller than that of laser irradiated zone. The relationship between the size of deposited material and laser fluence was different from each other in two cases. In other words, the size of deposited Ni did not depend on laser fluence in this case. It is considered that thin film which was irradiated by the center of laser spot become deposited material and the other part of thin film become droplets.

Then, we changed mask whose diameter 5mm into that whose diameter 1mm. Using smaller mask, the center part of laser beam was only irradiated on thin film. Figure6 shows the optical microscope image of the deposited Ni. Spread of droplets was inhibited in the case that distance L was 10μm. From these results, it was revealed that removal of thin film was affected by Gaussian beam profile of femtosecond pulsed laser. It is considered that droplets-transferred zone become smaller as laser intensity approaches a constant value in laser irradiated zone.

Figure7 shows the SEM images of the deposited Ni. Particles are seen around deposited Ni in both condition (distance L=0, 10μm). We found that the diameter of particles-transferred zone was about 3 times as long as that of deposited material. It was revealed that spread of particles was smaller than that in the case of excimer laser.

In order to investigate the difference of spread of particles between excimer LIFT process and femtosecond LIFT process, we measured the intensity of reflected HeNe laser in excimer LIFT process. At first, we irradiated HeNe laser beam on thin film through support substrate. Then, HeNe laser beam reflected on the surface of thin film. The intensity of reflected laser beam was detected by Si photodiode. Secondly, we irradiated excimer laser beam on the thin film where HeNe laser was irradiated. We measured the change of the intensity of HeNe laser in the removal process of thin film. The detail of experimental setup was described in our previous work.[13]
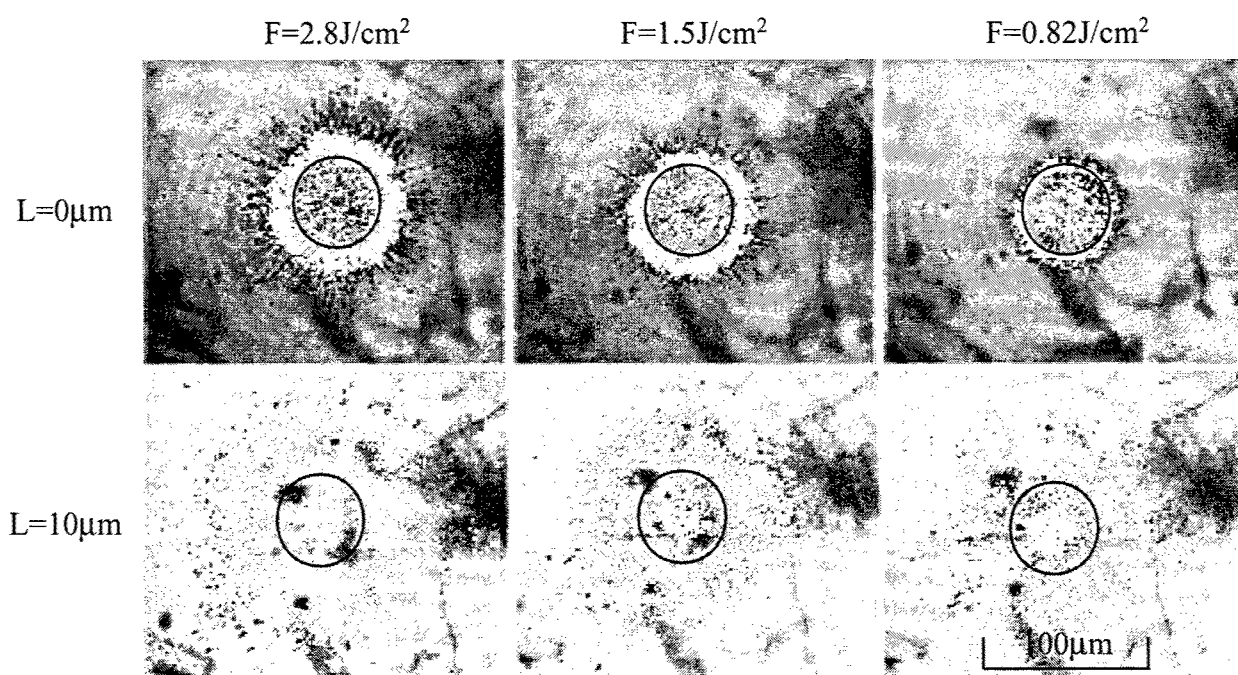
Figure 5. Optical microscopic images of deposited materials. Ni, d=120nm, L=0, 10μm, F=2.8, 1.5, 0.82J/cm^2, mask diameter=5mm.
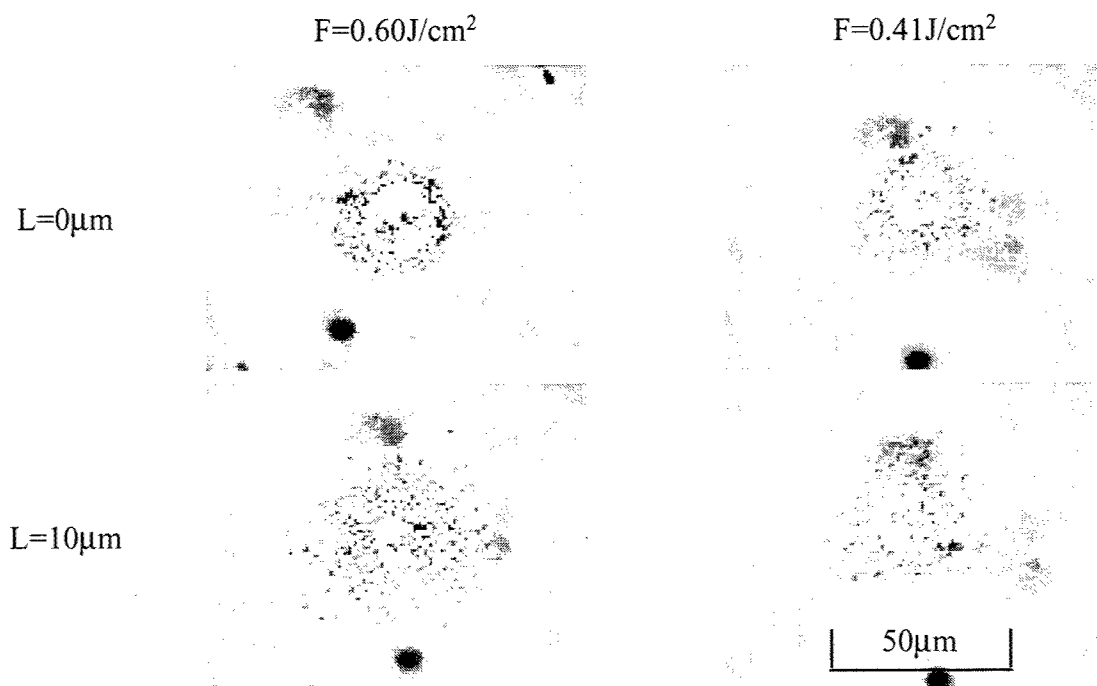
Figure 6. Optical microscopic images of deposited materials. Ni, d=120nm, L=0, 10μm, F=0.6, 0.41J/cm^2, mask diameter=1mm.

Figure8 shows the result of the measurement of intensity of HeNe laser. After excimer laser irradiation, the intensity of HeNe laser decrease steeply, then remains constant. The time when the intensity of HeNe laser finishes to decrease meant the end of removal of thin film. In this time, the intensity of excimer laser reached the peak value. So, only half of the energy of excimer laser pulse was used to remove thin film. Therefore, during the latter of laser irradiation, it is considered that energy is used for ablation of material and plume generation is encouraged in excimer LIFT process. On the other hand, it is considered that absorbed energy are used for thin film removal effectively in femtosecond LIFT process as pulse width is 100 fs. Thus, heating of generated plume was inhibited. Consequently, adhesion of particles was inhibited by irradiating femtosecond pulsed laser beam.

There is another advantage for using femtosecond pulsed laser. Heat damage of deposited material can be minimized irradiating femtosecond pulsed laser beam. This allows femtosecond LIFT process to be used for various application.

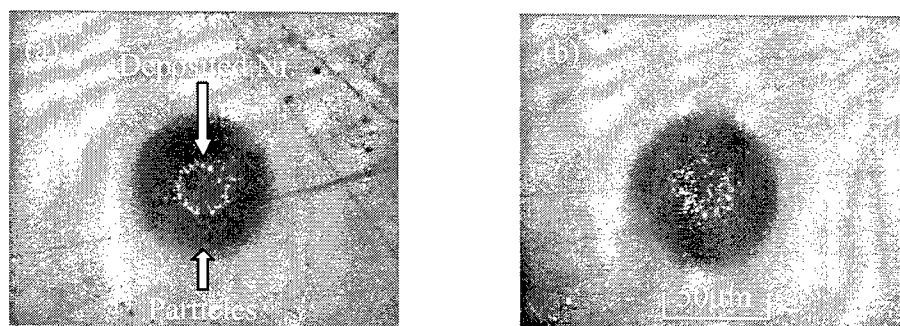Figure 7. SEM images of deposited materials. Ni, d=120nm. L=0, 10μm, F=0.41J/cm^2, mask diameter=1mm.
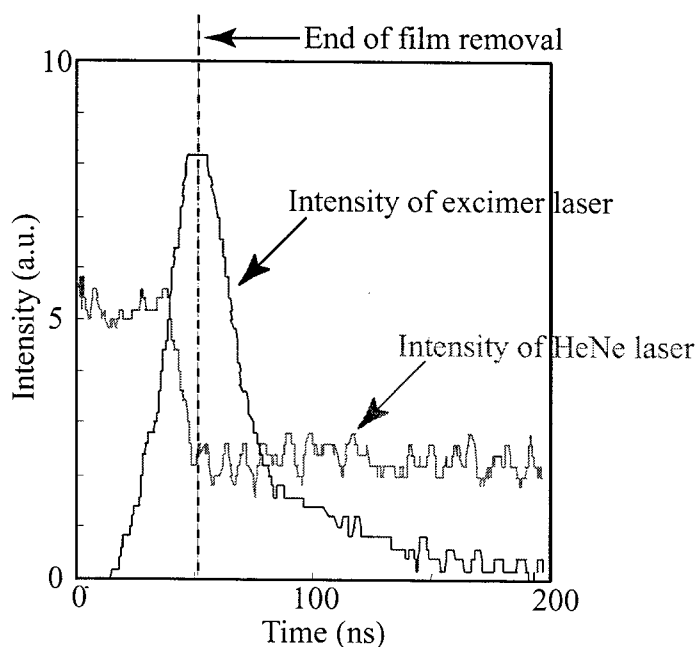

Figure 8. The result of the mesurement of intensity of HeNe laser after excimer laser irradiation. Au. d=140nm. F=0.80J/cm^2.

4. CONCLUSIONS

Effect of laser beam profile on the removal of thin film is indicated by the change of distribution of droplets. Irradiating the center of laser beam, that is, the part where change of intensity is low, adhesion of droplets is inhibited in the case of using laser beam which has Gaussian beam profile. The shape of the deposited material changed depending on the gap between thin film and an acceptor substrate. In the condition that there was the gap, adhesion of particles was inhibited using femtosecond pulsed laser. From the measurement of the intensity of reflected HeNe laser, it is revealed that half of the energy of excimer laser pulse was used to remove thin film and the other energy encouraged plume generation. Moreover, heat damage can be minimized using femtosecond pulsed laser, and these are the advantages for various applications.

ACKNOWLEDGMENTS

REFERENCES

1. A. Pique and D. Chrisey, *Direct-write technologies for rapid prototyping applications*, Academic press, 2002.
2. J. Bohandy, B. Kim, and F. Adrian, "Metal deposition from a supported metal film using an excimer laser," *J. Appl. Phys.* **60**, pp. 1538–1539, 1986.
3. V. Schultze and M. Wagner, "Blow-off of aluminium films," *Appl. Phys. A* **53**, pp. 241–248, 1991.
4. V. Schultze and M. Wagner, "Laser-induced forward transfer of aluminium," *Appl. Surf. Sci.* **52**, pp. 303–309, 1991.
5. T. Sano, I. Miyamoto, H. Hayashi, and H. Ochi, "Analysis of excimer laser patterning process of Cu thin film," *Proceedings of SPIE* **3933**, pp. 356–364, 2000.
6. P. Mogyorósi, T. Szörényi, K. Bali, Z. Tóth, and I. Hevese, "Pulsed laser ablative deposition of thin metal films," *Appl. Surf. Sci.* **36**, pp. 157–163, 1989.
7. Z. Kántor, Z. Tóth, and T. Szörényi, "Laser induced forward transfer: the effect of support-film interface and film-to-substrate distance on transfer," *Appl. Phys. A* **54**, pp. 170–175, 1992.
8. H. Esrom, J. Zhang, U. Kogelschatz, and A. Pedraza, "New approach of a laser-induced forward transfer for deposition of patterned thin metal films," *Appl. Surf. Sci.* **86**, pp. 202–207, 1995.
9. Z. Kántor, Z. Tóth, and T. Szörényi, "Deposition of micrometer-sized tungsten patterns by laser transfer technique," *Appl. Phys. Lett.* **64**, pp. 3506–3508, 1994.
10. Z. Kántor and T. Szörényi, "Dynamics of long-pulsed laser transfer of micrometer-sized metal patterns as followed by time-resolved measurements of reflectivity and transmittance," *J. Appl. Phys.* **78**, pp. 2775–2781, 1995.
11. Z. Kántor, Z. Tóth, and T. Szörényi, "Metal pattern deposition by laser-induced forward transfer," *Applied Surf. Sci.* **86**, pp. 196–201, 1995.
12. Z. Tóth, T. Szörényi, and A. Tóth, "Ar$^+$ laser-induced forward transfer (LIFT): a novel method for micrometer-size surface patterning," *Applied Surf. Sci.* **69**, pp. 317–320, 1993.
13. T. Sano, H. Yamada, T. Nakayama, and I. Miyamoto, "Experimental investigation of laser induced forward transfer process of metal thin films," *Appl. Surf. Sci.* **186**, pp. 221–226, 2002.
14. H. Yamada, T. Sano, T. Nakayama, and I. Miyamoto, "Optimization of laser-induced forward transfer process of metal thin films," *Appl. Surf. Sci.* **197-198**, pp. 411–415, 2002.
15. Z. Tóth and T. Szörényi, "Pulsed laser processing of Ge/Se thin film structures," *Appl. Phys. A* **52**, pp. 273–279, 1991.
16. E. Fogarassy and C. Fuchs, "Laser-induced forward transfer of high-T$_c$ YBaCuO and BiSrCaCuO superconducting thin films," *J. Appl. Phys.* **66**, pp. 457–459, 1989.
17. S. Pimenov, G. Shafeev, A. Smolin, V. Konov, and B. Vodalaga, "Laser-induced forward transfer of ultra-fine diamond particles for selective deposition of diamond films," *Applied surface science* **86**, pp. 208–212, 1995.

18. Y. Nakata, T. Okada, and M. Maeda, "Transfer of laser dye by laser-induced forward transfer," *Jpn. J. Appl. Phys.* **41**, pp. L839–L841, 2002.

19. A. Bullock, P. Bolton, and F. Mayer, "Time-integrated reflectivity of laser-induced back-ablated aluminum thin film targets," *J. Appl. Phys.* **82**, pp. 1828–1831, 1997.

20. A. Bullock and P. Bolton, "Laser-induced back ablation of aluminum thin films using picosecond laser pulses," *J. Appl. Phys.* **85**, pp. 460–465, 1999.

21. Y. Nakata and T. Okada, "Time-resolved microscopic imaging of the laser-induced forward transfer process," *Appl. Phys. A* **69**, pp. S275–S278, 1999.

22. F. Adrian, J. Bohandy, B. Kim, A. Jette, and P. Thompson, "A study of the mechanism of metal deposition by the laser-induced forward transfer process," *J. Vac. Sci. Technol.* **B5**, pp. 1490–1494, 1987.

23. R. J. Baseman and N. M. Froberg, "Time-resolved transmission of thin gold films during laser blow-off," *Appl. Phys. Lett.* **55**, pp. 1841–1843, 1989.

24. I. Zergioti, S. Mailis, N. Vainos, P. Papakonstantinou, C. Kalpouzos, C. Grigoropoulos, and C. Fotakis, "Microdeposition of metal and oxide structures using ultrashort laser pulses," *Appl. Phys. A* **66**, pp. 579–582, 1998.

25. I. Zergioti, S. Mailis, N. Vainos, C. Fotakis, S. Chen, and C. Grigoropoulos, "Microdeposition of metals by femtosecond excimer laser," *Appl. Surf. Sci.* **127-129**, pp. 601–605, 1998.

26. G. Koundourakis, C. Rockstuhl, D. Papazoglou, A. Klini, I. Zeigioti, and N. Vainos, "Laser printing of active optical microstructures," *Appl. Phys. Lett.* **78**, pp. 868–870, 2001.

27. T. Mito, T. Tsujita, H. Masuhara, N. Hayashi, and K. Suzuki, "Hollowing and transfer of polyimide methacrylate film propelled by laser ablation of triazeno polymer film," *Japanese journal of applied physics* **40**, pp. L805–L806, 2001.

28. I. Zergioti, D. Papazoglou, A. Karaiskou, N. Vainos, and C. Fotakis, "Laser microprinting of InOx active optical structures and time resolved imaging of the transfer process," *Applied surface science* **197-198**, pp. 868–872, 2002.

29. D. Papazoglou, A. Karaiskou, I. Zergioti, and C. Fotakis, "Shadowgraphic imaging of the sub-ps laser-induced forward transfer process," *Applied physics letters* **81**, pp. 1594–1596, 2002.

Spontaneous UV radiation source based on pulsed discharge in xenon

M.I. Lomaev, D.V. Rybka, V.F. Tarasenko, A.A. Lisenko

High Current Electronics Institute, 4, Akademichesky Ave., 634055 Tomsk, Russia;

e-mail: VFT@loi.hcei.tsc.ru; lomaev@loi.hcei.tsc.ru

ABSTRACT

Experimental results obtained in study of spontaneous UV radiation source based on high-current pulsed discharge in xenon developed for irradiation of diamond crystal to convert it into conductive state are presented. It is shown that at the pressure of about 450 Torr radiation of Xe lines predominate in UV range of discharge radiation spectrum. The part of radiation energy in the range of 200-250 nm with respect to the radiation energy of the whole range recorded (200-650 nm) may reach 50%. The maximum density of radiation power was 185 kW/cm^2. At pressure increasing up to 1200 Torr, the part of thermal radiation increases too. In this case the part of radiation energy in the range of 200-250 nm does not exceed 20%.

Keywords: UV emission radiation, pulsed xenon lamp, efficiency

1. INTRODUCTION

Recently, the sources of spontaneous radiation based on pulsed or continuous discharges in gases or vapor-gas mixtures are widely spread and applied. First of all, among such sources are mercury (of high or low pressure, with admixtures or without), sodium, and metal-halogen lamps. Second, widely used are hydrogen and deuterium, sulfuric lamps, and lamps based on high-current discharge in inert gases, and some other lamps as well [1-4]. The peculiarities of pulsed lamps based on a discharge in heavy inert gases is the high radiation power and small size of gas-discharge volume that allows use of focusing optical elements to concentrate radiation at the objects irradiated; and radiation spectrum including either thermal or non-thermal radiation. Discharge in xenon has the highest potential gradient and the lowest voltage drop in near-electrode areas, being most profitable with respect to lamp efficiency [1]. It is appropriate to employ the peculiarities of Xe pulsed lamps in development of a cheap efficient radiation source meant for controlling diamond-crystal based high-voltage switch [5-8]. Used as a switch, the diamond crystal possesses a high electrical strength, thermal conductivity, mechanical and irradiation strength as well. This promises creation in future of compact high-voltage switches based on diamond crystals. Nowadays, it has been shown a possibility of such switch controlling by an electron beam and UV-range lasers [9,10]. At serial production of such switches, electron beams and lasers are not suitable due to high cost . In connection with all said above, it is necessitated to develop a cheap pulsed UV-range source meant for diamond-based switching. And it is desirable to have the major part of radiation in the wavelengths range of $\lambda < 225$ nm that corresponds to the fundamental absorption band of the diamond [11, 12].

Spectral radiation composition of pulsed lamps in heavy inert gases is determined by a number of parameters such as composition and pressure of operating medium, energy characteristics and excitation pulse time dependencies, transmission spectrum of materials from which the lamp bulb is made. This paper is devoted to investigation of excitation pulse parameters and pressure effect on spectral and energy characteristics of pulsed xenon lamp. Energy and time characteristics of excitation pulse varied by changing of charging voltage, storage capacity and electrical circuit inductance. The effect of operating medium pressure was studied using sealed-off lamps with xenon pressure of 450 and 1200 Torr.

2. EXPERIMENTAL SET-UP

The block-scheme of experimental set-up is shown in Fig. 1. It includes a LC generator (1) allowing formation of voltage pulses with adjustable parameters on voltage value, duration, p.r.r, and stored energy. The sealed-off spherical Xe lamp (Xe pressure is 450 or 1200 Torr, interelectrode gap is 4 mm, bulb's diameter is 1 cm) was a load for generator. The bulb was made of quartz with transparency in the range of 200-250 nm not less than 85 %. Electric and optical characteristics of discharge were recorded on lamp operation. The system of registration of optical characteristics had a multichannel spectrum registration device – a spectrometer based on MUM monochromator and photodiode line FUK (2) connected to a personal computer, a coaxial photoelement FEK-22 SPU (3), a monochromator MDR-23, and a photomultiplier FEU-100
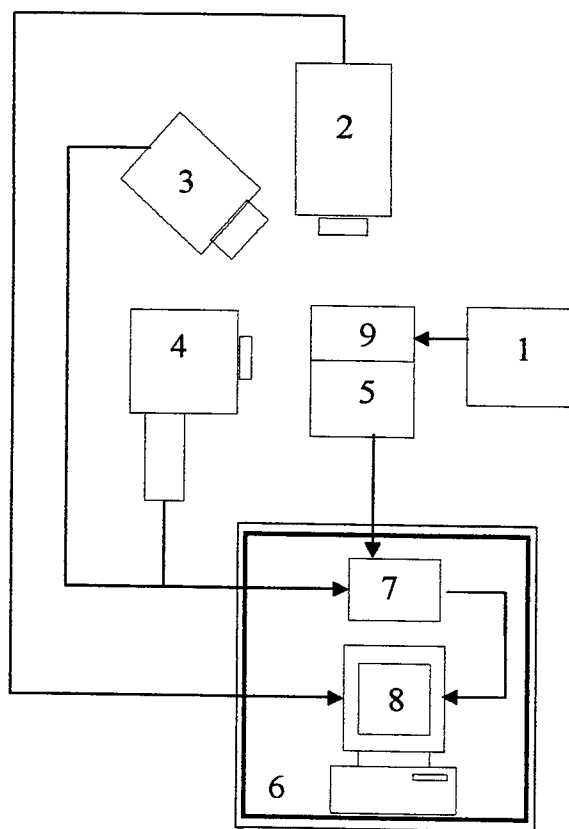
Figure 1: Block scheme of experimental set-up:
1 – Power supply; 2 – multichannel spectrum registration device; 3 – FEK – 22SPU; 4 – monochromator MDR-23 and FEU – 100; 5 – current and voltage measurements system; 6 - electromagnetic noise defense box; 7 – oscilloscope TDS 3032; 8 – personal computer PC; 9 – Xe lamp
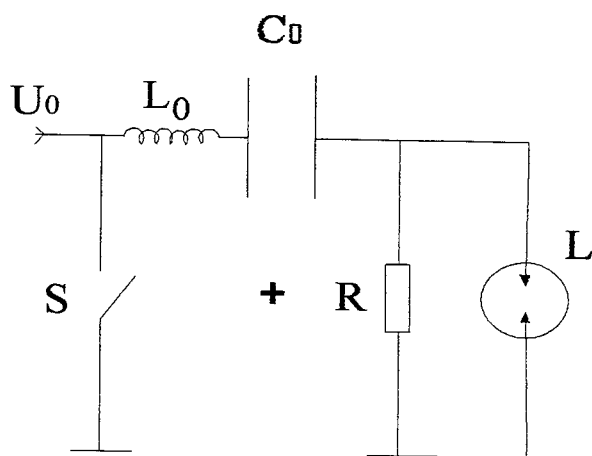

Figure 2: Eclectic scheme of LC generator: U_0 – charging voltage; R – charging resistor; S – switch; L_0 – circuit inductance; C_0 - storage capacity; L – Xe lamp.

(4). The spectrometer is meant for recording the integral-in time radiation spectrum in the range from 190 to 800 nm in relative units. The spectrometer function spectral halfwidth did not exceed 0,15 nm, the spectral width of simultaneous registration range in an impulse was ~ 70 nm. The FEK-22 SPU was used for recording power time dependencies of spectrum-integral radiation pulse of gas discharge plasma. The spectral-sensitivity curve for this device is known to be from 200 to 650 nm in absolute units. Data collection obtained from FEK -22 SPU and spectrometer provides to define radiation energy spectral distribution in absolute units in the wavelength range from 200 to 650 nm. The monochromator MDR -23 and FEU-100 were used for recording of emission radiation pulse time dependencies at different wavelengths. The spectral half width of the MDR -23 and FEU-100 function did not exceed 0,02 nm. Besides that, in the pulse-repetitive mode of lamp operation and diffraction grating rotation with constant velocity, the great collection of data on radiation time dependencies in different spectral areas with discreteness of 0,07 nm was obtained. That provided at further data processing to get power spectral distribution for arbitrary moment of time with respect to the pulse radiation start as well as radiation energy. The data on spectral distribution of energy were obtained at integration of radiation power oscillograms in time being analogous to the results taken with multichannel recorder.

The recording system of discharge current pulses and electrode voltage of the lamp (5) consisted of a current shunt, Rogovsky coil, and resistance voltage divider, correspondingly. Electric pulses were given to digital oscilloscope TDS-3032 (7), connected to PC (8). In order to diminish electrical pickup effect, the oscilloscope and PC were placed in electromagnetic noise defense box (6), and power supply of the recording equipment was realized from the network one-to-one transformer.

The electric circuit of the set-up including LC generator is presented in Fig. 2. The charging voltage U_0 varied in the range from 5 to 20 kV, storage capacitance C_0 changed within 17 - 233 nF. Excitation pulse duration τ at stored energy from 2 to 5 J was determined by the values of C_0 and discharge circuit inductance L_0 comprising ~1,1 µs (circuit №1), ~ 600 ns (circuit №2) and ~350 ns (circuit №3).

3. EXPERIMENTAL RESULTS AND DISCUSSION

The major part of experiments was carried out using a sealed-off lamp at xenon pressure of 450 Torr. Fig. 3 shows oscilloscope traces of discharge current pulses, electrodes voltage of the lamp, calculation excitation power curve, as well as oscilloscope traces of radiation
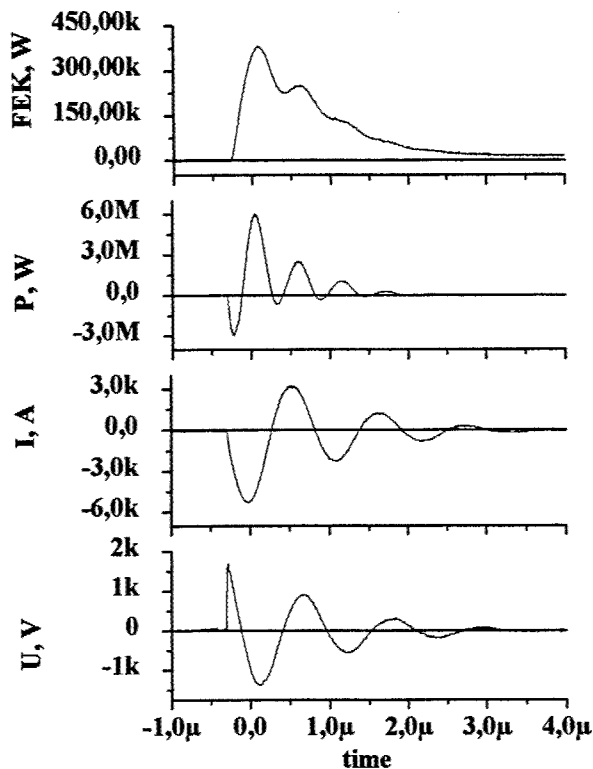
Figure 3: Oscilloscope traces of voltage (U), current (I), spectra integrated radiation power (FEK), and calculated curve of excitation power (P). Electric circuit N1, $U_0 = 5$ кV, $C_0 = 233$ nF

Figure 4: Spectral energy density of Xe lamp emission radiation. Electric circuit N1, $C_0 = 233$ nF, $U_0 = 5$ kV

pulse recorded by FEK-22 SPU in case of circuit №1 ($\tau \sim$ 1,1 μs). Spectral energy distribution of radiation taken by spectrometer for this case is shown in Fig. 4. It is seen from the figure that both thermal radiation and non-thermal one are presented in the spectrum. The pulse radiation energy in the area recorded of 200 – 680 nm was 1 J. In the range of 200 – 250 nm, there is about $\sim$ 35 % of radiation energy belonging in the main to xenon line. The peaking value of power radiation density in these conditions was $\sim$ 185 kW/cm^2. With reduction of excitation pulse duration τ up to 0,6 – 0,35 μs. (circuits № 2, 3), some transformation of radiation spectrum is observed. Fig. 5 represents spectral distribution of radiation energy obtained at excitation pulse duration of $\sim$ 0,6 μs. Oscilloscope traces of voltage pulse, current discharge, radiation pulse and calculated curves of excitation power are demonstrated in Fig. 6. As in the previous case, in the range of wavelengths of 200 – 250 nm, there is a similar number of intensive Xe lines possessing $\sim$ 50 % of radiation energy in the range 200 – 680 nm comprising $\sim$ 215 mJ. Perceptible decrease in radiation energy is related to efficiency decreasing of energy input into the gas discharge plasma. The efficiency values η of the input energy transformation into radiation in the range 200 – 250 nm shows that in the both cases, in the first ($\tau \sim$ 1,1 μs) and the second ones ($\tau \sim$ 0,6 μs) it makes up $\sim$ 8 %. At further decreasing of excitation pulse duration ($\tau \sim$ 0,3 μs), spectral distribution of radiation energy does not essentially change. However, the value η did not exceed $\sim$ 5 %, and the total energy of radiation in the range of recording was $\sim$ 180 mJ. It may be supposed that in this case plasma is being heated up to high temperature values so that the maximum of spectral distribution of thermal radiation falls to VUV spectrum range and is not recorded. The non-thermal radiation share (luminescence) becomes less. An increase in thermal radiation share takes also place with Xe pressure growth. Thus, at Xe pressure of 1200 Torr and $\tau \sim$ 1,1 μs the radiation energy in the range of 200 – 250 nm is not higher than 20 % of the total energy of recording band. At the same time, an intensive continuum is observed in visible and near UV spectrum ranges.

To use the lamp as a switch controlling light source it is intended to know pulse radiation time dependencies in the wavelength range of $\lambda <$ 250 nm. As it is seen from the Fig. 4, 5 in this spectral range non-thermal radiation predominates in this spectral range. Fig. 7 presents oscilloscope traces of radiation pulses taken from different spectral parts for $\tau \sim$ 1,1 μs. The corresponding spectral areas are indicated on calculated spectrum of radiation energy in Fig. 8. The calculated integral radiation pulses for the ranges 190 - 320 nm and 320 - 610 nm are presented in Fig. 10. Radiation pulse property in long-wave region is the greater pulse duration at FWHM and high relative intensity in afterglow. This may explain the fact that switching pulse duration occurs to be shorter than that of radiation pulse recorded by FEK-22 in the range of 200-600 nm [13].
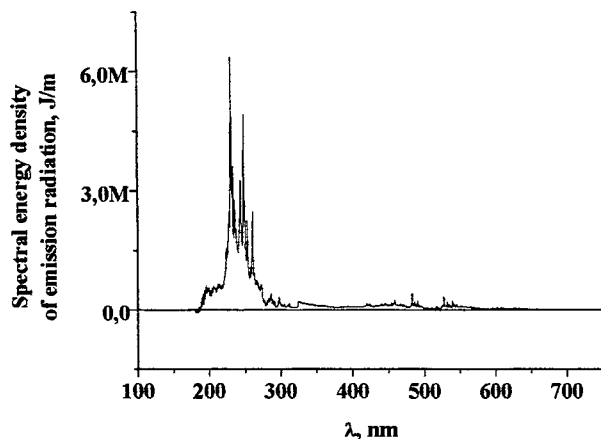
Figure 5: Spectral energy density of emission radiation.
Electric circuit N2, $U_0 = 18$ κV, $C_0 = 17$ nF
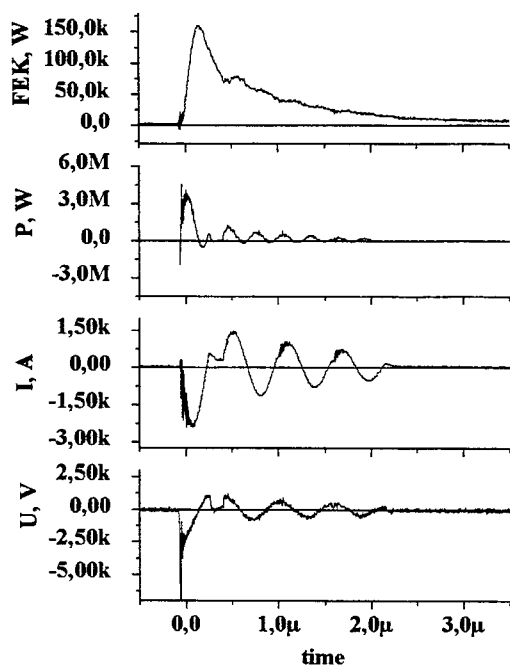
Figure 6: Oscilloscope traces of voltage (U), current (I), spectra integrated radiation power (FEK), and calculated curve of excitation power (P). Electric circuit N2, $U_0 = 18$ κV, $C_0 = 17$ nF
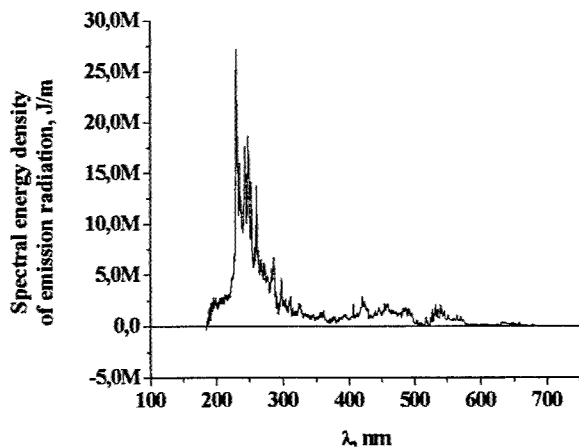
4. CONCLUSION

In this work, studies on spectral, energy, and time dependencies of pulsed discharge in Xe were performed. The maximum specific power was 185 kW/cm^2 at total radiation energy of ~ 1 J in the range of 200 – 680 nm. Intrinsic efficiency of the UV-source at 200-250 nm was ~ 8 %, pumping pulse duration was ~ 1,1 μs. Developing UV pulsed sources for diamond based switching it is expedient to use radiation of Xe lines dominating in the mentioned above spectral range.
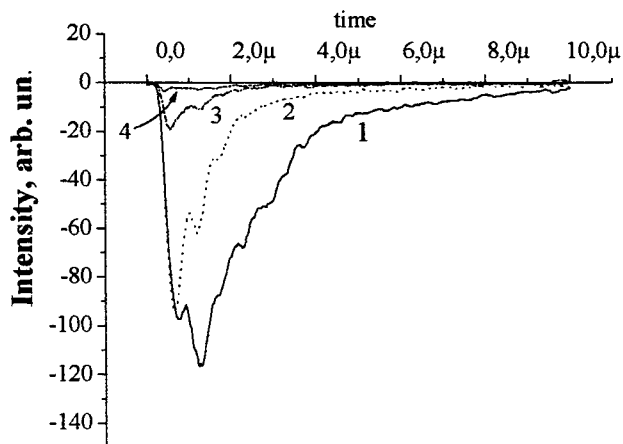
Figure 7: Oscillograms of emission radiation at λ = 230 nm (1), 272 nm (2), 212 nm (3), 462 nm (4); $C_0 = 233$ nF, $U_0 = 5$ kV.

ACKNOWLEDGEMENTS
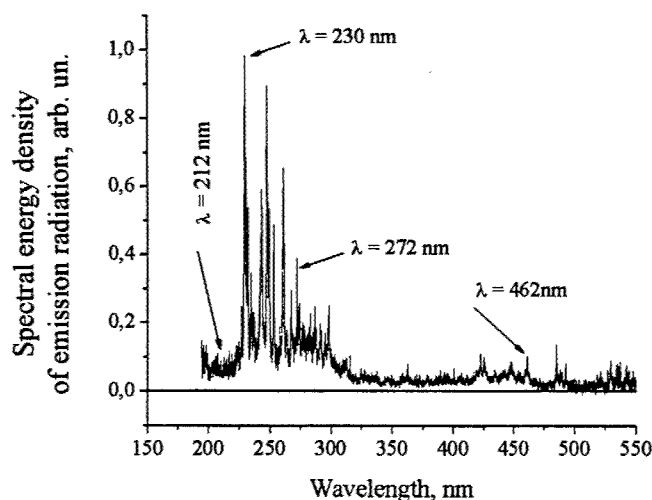
Figure 8: Spectral energy density of Xe lamp emission radiation. The results obtained by integration of radiation intensity oscillograms taken from different spectrum parts (spectral shift $\Delta \lambda \sim 0{,}07$ nm).
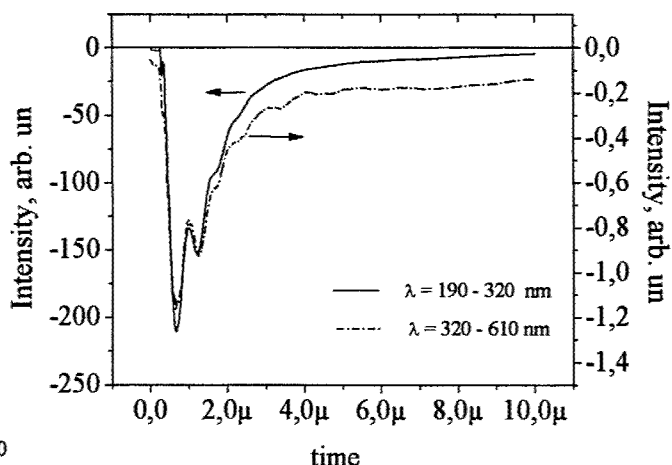
Figure 9: The calculated radiation pulses obtained in the ranges 190 - 320 nm and 320 - 610 nm.

REFERENCES

1 G.N. Rochlin, *Discharge Light Sources*, Moscow, 1991.

2 *Reference book on lighting technology*. Ed. by Yu.B. Izenberg, M.: Energoatomizdat, 1983.

3 *Pulsed light sources*. Ed. By I.S. Marshak. M.: Energy, 1978.

4 *Encyclopaedia of low-temperature plasma. Introductory volume IV*. Ed. By B.E. Fortov. Moscow, publ. "Nauka", MAIK "Science/Interperiodicals", 2000, p. 233.

5 P.K. Bharadwaj, R.F. Code, H.M. van Driel, E. Walentynowicz "High voltage optoelectronics switching in diamond", Applied physics letters, **43**, p. 207, 1983.

6 P.-T. Ho, C.H. Lee, J.C. Stephenson, R.R. Cavanagh "A diamond optoelectronic switch", Optics Communications, **46**, p. 202, 1983

7 P.K. Bharadwaj, R.F. Code, H.M. van Driel, E. Walentynowicz "High voltage optoelectronics switching in diamond", Applied physics letters, **43**, p. 207, 1983.

8 J. Glinski, X.-J. Gu., R.F. Code, H.M. van Driel "Space-charge-induced optoelectronics switching in IIa diamond" // Applied physics letters, **45**, №3, p. 260, 1984.

9 R. R. Prasad, J. Schein, S. W. Gensler and M. Krishnan. "Optically triggered diamond switches", Proc. of the 12th IEEE Pulsed Power Conf., Monterey, CA, USA, p. 142, 1999

10 E. I. Lipatov, A. N. Panchenko, V. F. Tarasenko, J. Schein, M. Krishnan "Diamond detector photosensitivity to laser radiation in the 220-355 nm region", Quantum Electronics, **31**, p. 1115, 2001.

11 J.E. Field, *The properties of diamond*. Lnd.: Academ. Press, 1979.

12 G.B. Baksht, G.N. Bezrukhov, Yu.A. Klyuev, A.M. Nalyotov, V.I. Nepsha. *Natural and synthetic diamonds*, M.: Nauka, 1986.

13 E.I. Lipatov, D.V. Rybka, A.N. Panchenko, M.I. Lomaev, V.F. Tarasenko, J. Shein, M. Krishnan. "Diamond detector switching by UV radiation", Theses of lectures and papers of the 8-th International Workshop on Luminescence and Laser Physics, Irkutsk, Russia, p. 57, 2002.

Formation of Periodic Structures on Glass with Laser Irradiation

Y.Z. Peng[a,b], C.W. An*[a], D.J. Wu[a], M.H. Hong[a], Y.F. Lu[a,b], T.C. Chong[a,b]

[a] Data Storage Institute, DSI Building, 5 Engineering Drive 1, Singapore 117608

[b] Electrical and Computer Engineering Department, National University of Singapore, Singapore 117576

ABSTRACT

Regular and tidy periodic structures have been directly induced on glasses using a CW CO_2 laser beam with linear polarization. It is experimentally shown that precise periodic structures with the period of several microns can be formed by means of well-set laser parameters. The orientation of the periodic structures formed is the same as that of the laser polarization no matter what the scanning direction is. The occurrence of periodic structures is very sensitive to laser power level and scanning velocity. To obtain appropriate periodic patterns, a combined condition of laser energy and scanning velocity must be satisfied. The period, width and height of the structures are dependent on processing parameters. An interesting phenomenon is that the period decreases with increasing scanning velocity. Permanent relieves with periods, widths and heights varied with the laser parameters are also studied.

Keywords: periodic structures, glass, laser fabrication.

1. INTRODUCTION

Laser fabrication of surface periodic structures is an attractive subject in the field of laser materials interaction, especially for forming regular and tidy periodic structures because they are expected to be more valuable. The appearance of spontaneous periodic surface structures has been produced in metals, semiconductors and dielectrics by laser processing methods, from the spectrum wavelength of ultraviolet to middle infrared, with pulse length ranging from pico-second to CW operation. These concerns of surface ripples are reviewed to be an area of both theoretical and experimental interests since 1970s [1]. From theories and experiments, it is known that the ripples or periodic structures are related to the interference effect (coherent structures), and several models have been used to explain these phenomena, which mainly concentrated on the role of laser coherence, polarization and the surface morphology. For example, Sipe and his co-workers concentrated their studies on the surface-scattered wave mode [2]. Some people took account of materials properties. They suggested that surface plasmons or surface polaritons could produce the ripples. For instance, Maracas argued that there is a standing acoustic wave pattern corresponding to the axial mode beat frequencies of their ruby laser, resulting in a periodic melting of their GaAs samples [3]. Paul suggested that the charge resulted in a sinusoidally varying perturbation to the applied laser field in the vicinity of the defect, and this perturbation is the greatest along the laser polarization. The maxima in the perturbation field will exceed the damage threshold, and a permanent ripple pattern in the surface will form [4]. Though periodic

*an_chengwu@dsi.a-star.edu.sg; phone 0065 6878204;fax 0065 67771349

structures or ripples have been studied for a long time, none has been done on the large dimensional regular grating like periodic structures. The previous interest mainly concentrated on the periodic surface damage patterns, on surface ripples of thin films, which are in small area.

Glass, the most important optical material, is a kind of metastable liquid material and is an absorber for CO_2 laser beam. The study of periodic structures on glasses is one of the possible applications for the optical material [5]. Different from previous studies, our study is focused on the formation of periodic structures on glasses, which are regular and tidy, and can be fabricated in a large area. It is a precise, fast and flexible way to create grating structures on glasses compared to the conventional methods. This paper analyses laser processing parameters dependent periodic structures on glasses. Experimental results and investigations show that their orientation, periods, widths and heights are mainly dependent on laser polarization, power and scanning velocity. The particular interest is that the laser parameters dependent periodic structures seem to show a different behavior from the previous general work.

2. EXPERIMENTAL SETUP

The specimens used in the experiment was plain glasses. The schematic diagram of the experimental set-up is shown in Fig. 1. A linearly polarized CW CO_2 laser beam with the wavelength of 10.6 μm was used as an irradiation source. The laser beam was delivered by an optical system and a lens of 50 mm focus length was used to focus beam onto the surface of glass substrate. A beam expander was used to make experimental condition more suitable to induce the periodic structures. An attenuator was used to adjust the laser dose to the glass substrate. By tuning the laser output and setting the beam attenuator, the laser beam energy onto the substrate can be adjusted. A x-y stage with resolution of 1 μm/s was used to change the scanning velocity. A power meter was used to measure the laser energy in front of the lens. A series of steps was carried out to ensure that the system is well set since the occurrence of periodic structures is very sensitive to the processing parameters. The experiment was carried out in open air. The resulting patterns were observed by an optical microscope (Olympics BH2-HLSH), and their profiles were measured by an Alpha-Step 500 profilometer (Tencor Instruments).
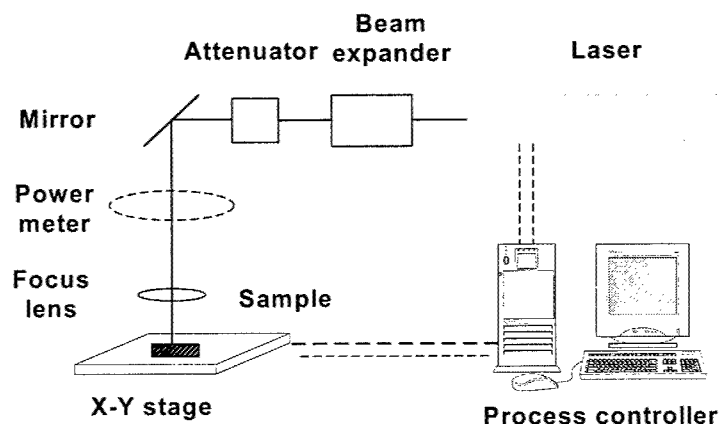

Fig.1   Schematic diagram of the experimental system

3. EXPERIMENTAL RESULTS

Precise structures in the form of relief modulation with the periods of the order of wavelength can be formed at normal incidence of laser irradiation on the glass substrate. Fig. 2(a) shows a typical micrograph of periodic structures by the laser beam scanning the glass surface in the vertical direction of its polarization. We can see that the periodic structure lines are regular and tidy, which are different with the previous results. It is shown that the periodic structure lines are vertical to the laser scanning direction, i.e. parallel to the laser polarization. We got another kind of result by the laser beam scanning the glass surface in the parallel direction of its polarization, as shown in Fig. 2(b). Both the results show that the orientation of the formed periodic structure is the same as that of laser polarization no matter what the laser scanning direction is. However, different scanning way results in different structure.

(a) ———▶ **Laser scanning direction**   (b) ———▶ **Laser scanning direction**
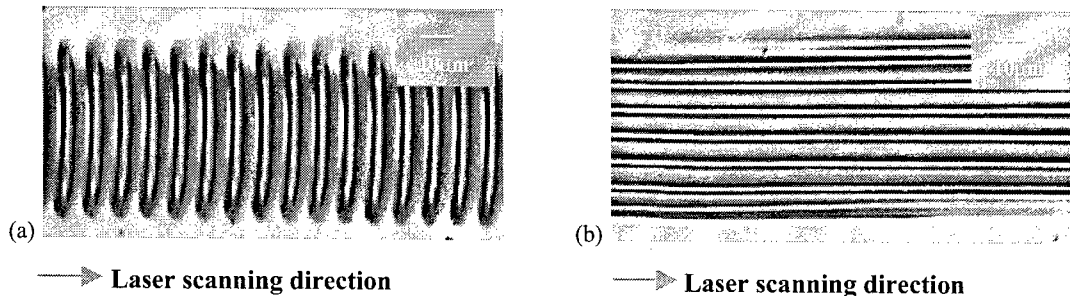
Fig. 2 micrographs of periodic structures formed on glass surface with laser irradiation.

(a) Transverse structure formed with laser scanning direction vertical to its polarization.

(b) Longitudinal structure formed with laser scanning direction parallel to its polarization.

To obtain regular and tidy periodic structures, the laser processing system must be well set. Furthermore, the periodic structures could be formed only within a certain range of scanning velocity and laser power, schematically shown as the shaded area in Fig. 3(a), which is obtained in the case when the laser scanning direction is vertical to its polarization. It is noticed that to obtain appropriate periodic patterns, a combined condition of laser energy and scanning velocity must be satisfied. When laser power, P is very small, no strip lines can be observed. The periodic structures could be observed only when laser power is larger than a critical value, P_{thl}. Conversely, when laser power is larger than P_{thh}, periodic structures could not be observed either. In this case, only a damaged strip line can be resulted. Furthermore, for each power level, there exists a range of velocity within which the periodic structures could be observed. That is to say that a lower velocity limit (V_{thl}) and an upper velocity limit (V_{thh}) exist. Fig. 3(b) shows the corresponding micrographs with different velocities when laser power is set as 0.28 w. The number near the picture represents the condition marked in Fig. 3(a), respectively. We can see that periodic structures began to tangle together when v is just less than V_{thl}. However, with increasing velocity ($v > V_{thl}$), the periodic structures tend to become regular and tidy, and the structure lines becomes straight. But more higher velocity ($v > V_{thh}$) will lead to shallow and not in their integrity structures, as shown in Fig. 3(b)-3. However there exists a power level by which we can get the largest velocity range. We call it optimum condition. It is 0.28 w in our experiment. Under this optimum condition, the periodic structures can be fabricated in the largest velocity range. The optimum power level line divides the occurrence area into two parts, area A (lower power level) and area B (higher power level), as

shown in Fig. 3(a). It is noticed that area B is larger than A. In the area B, in order to obtain the available periodic structures, both the lower and the upper velocity limits decrease as the laser power increases. This behavior is just opposite to that in area A. In addition, it constructs an interesting map in the figure. If a line L is set at the critical velocity value (almost 40 µm/s in our experiment), when the velocity locates below the critical one (left side in Fig. 3(a)), the periodic structures can be formed either at a higher laser power or at a lower laser power. There is a break in the middle of the laser power range. On the other hand, at the right hand, the power is of a continuous range in the middle part.

It is observed that the orientation, period, strip width and height could be controlled precisely by controlling the laser parameters. Fig.3 (c-e) show the relationship of the period, strip width and height with laser power and scanning velocity. From Fig. 3(c), the period decreases with increasing scanning velocity. It increases first with laser power and reaches the maximum at the optimum power level (0.28 w), and then decreases with further increasing power. This product does not accord with previous general report. As shown in Fig .3 (d), the strip width tends to decrease with increasing scanning velocity, and increase with laser power. The width increases faster at lower power range than at higher power range. The most clear periodic structures can be obtained at the inflection point. Fig. 3(e) shows the dependence of trip height on scanning velocity. The strip height decreases with scanning velocity. On the other hand, the height tends to increase with power until a certain threshold power value (0.28 w in our experiment), after which it decreases with increasing power. D is used as quasi "real" laser dose, which is defined as $D = \dfrac{P}{w \times v}$, where P is laser power, w strip width and v scanning velocity. Its relationship with power is shown in Fig. 3(f). It is indicated that D tends to decrease with P (<0.28w) and v. D decreases sharply when P is less than 0.28 w.
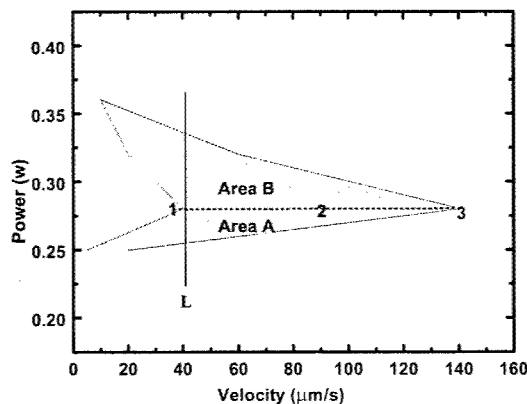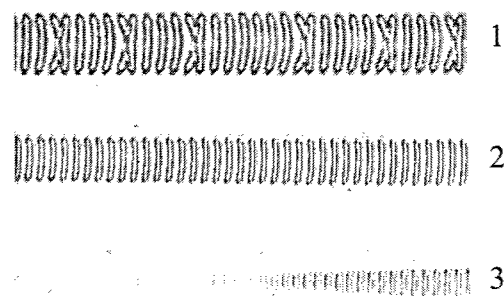
(a)   (b)
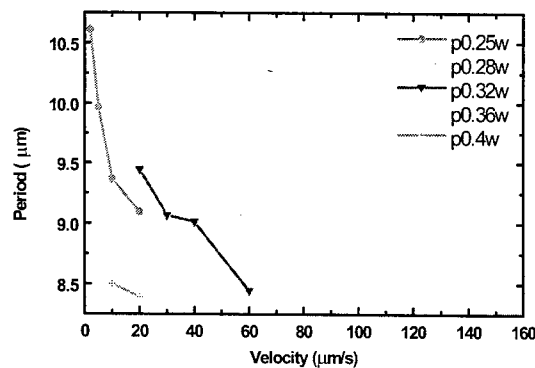
(c)
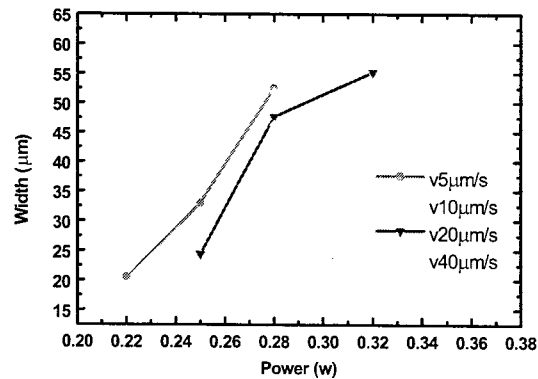
(d)
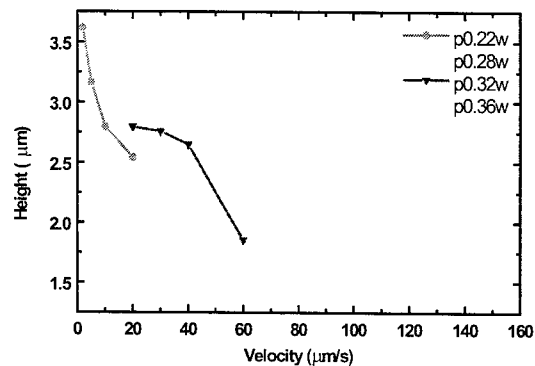
(e)
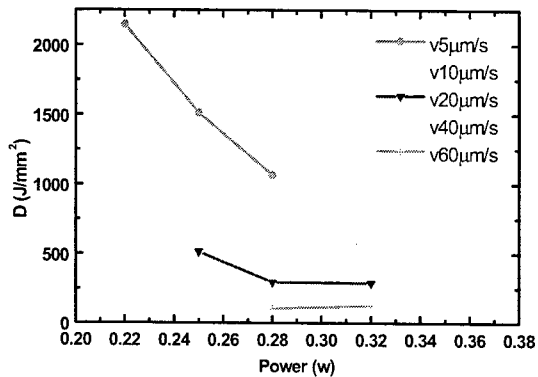
(f)

Fig. 3 Dependence of the periodic structures on laser powers and scanning velocities. (a) Map of experimental conditions for forming tidy and clear periodic structures. (b) Micrographs of periodic structures with different velocities when P is 0.28 w. Points 1, 2 and 3 represent corresponding experimental conditions marked in Fig. 3(a), respectively. (c) Dependence of period on laser scanning velocity and laser power. (d) Dependence of strip width on laser power and laser scanning velocities. (e) Dependence of strip height on laser scanning velocity and laser power. (f) Relationship of laser dose D with laser power and scanning velocity.

4. DISCUSSION

4.1 Mechanism

It is popularly thought that the periodic structures (coherent structures) arise from the interference between the incident light and the scattering light. Under the condition that there exists inevitable roughness surface, the interference will result in non-uniform energy distribution on the surface of grating like pattern, which can be given by standard diffraction theory. The most commonly used formula is $\Lambda = \lambda/(n \pm \sin\theta)$ [1, 6, 7], where Λ is the period, λ is the wavelength of laser, n the refractive index of the material, and θ the incident angle of the light. Furthermore,

under the normal incident condition, the laser excited a surface electromagnetic wave (SEW) on the surface and the period structures can be determined simply by $\Lambda=\lambda/n_{sew}$. Here n_{sew} is the SEW refractive index. In our experiments, when CO_2 laser beam incident on the surface of glass, the laser excites a SEW, and the interference of this wave with the laser wave leads to a spatially heating of the surface (temperature wave). This surface temperature wave will result in thermal expansion and corresponding pressure wave which argments the fluctuational start of the surface acoustic wave (SAW). This SAW will give rise to feed back to the SEW, which will result in frequency shift. The fluctuational excitation of a SAW gives rise to surface- relief modulation with a significant growth when positive feedback conditions are satisfied [7]. A static standing wave is related to the regular periodic structures. That is to say, the induced periodic structures arise from the coupling between the optical and thermal effect, which involves nonlinear optical effect of glass. It is not only the result of interference of the lights but also the feedback from the material that is important to induce the periodic structures; not only the normal scattering but also the nonlinear scattering that involves in the formation of the periodic structures. On the other hand, glass is a kind of material with strong cohesive bonds and ions in glasses are mutually polarized and the electrons surrounding the ions are asymmetrically distributed [8, 9]. The vibration of molecules could be considered as dipoles' vibration, called vibrators. The nonlinear E field distribution would drive these vibrators. When CO_2 laser beam is incident on glass, it is in absorptive state, and can induce strong polarization process that causes a dispersion in the dielectric constant or refractive index, with an associated increase in propagation loss or absorption, which is associated with a change in mass density. That is responsible for the behavior of the periodic structures in our experiments.

4.2 The dependence of period

It is of a lot of interest here to note that the period decreases with the scanning velocity. A possible qualitative explanation of this effect is given here. The scattered light is considered as a Doppler wave with frequency shifted through reflection from an acoustic wave front. Furthermore the acoustic wave is considered as a vibration wave, which is considered as the dipole movement of molecules. These ideas are illustrated schematically in Fig. 4. The effect may be observable if it is in the state with deep absorption which will result in high temperature sensitive absorption or heat loss [10]. On the other hand, as velocity increases, temperature tends to decrease due to the decrease of laser dwell time τ_l by the formula $\tau_l=2a/v$, where a is the beam spot size, v the scanning velocity [6]. Because the viscosity of silicate glass increases with decreasing temperature very much (viscosity$|_{800}=10^6$ poise, viscosity$|_{1000}=10^4$ poise) [9], the damping constant of the material increases with velocity. Since susceptibility or diffraction index of glass is related to this damping constant in the nonlinear scattering, they may follow this change, which leads to a decrease in period.

4.3 The occurrence of periodic structures

We found that the occurrence of periodic structures requires a combined condition of laser power and scanning velocity, and these critical values surround a closed area in which the periodic structures can be fabricated properly. There exists the highest velocity range in the optimum state. When the laser power is away from this state, the velocity range will be compressed and decreased a lot. We suppose that the formation of the regular and tidy
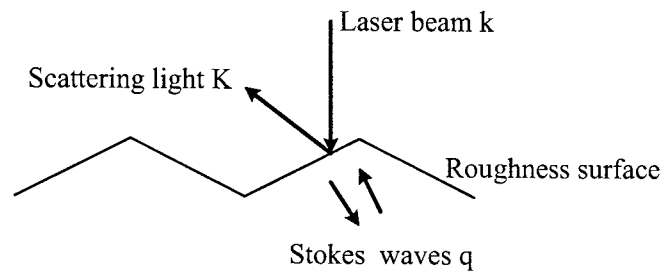
Fig.4 Schematic mechanism of scattering from an acoustic wave

periodic structures is an issue of coherent structure and it is temperature dependent sensitively. There must exist temperature thresholds, T_{th}. Under the low temperature threshold, T_{thl}, the periodic structures can not be induced because the material is stiffen and hard to deform due to high viscosity. Conversely, high temperature ($T > T_{thh}$) will run the risk of glass overflowing and make the periodic structures lines tangled together, where T_{thh} is the high temperature threshold. That is to say, the velocity limits relate to the temperature dependent surface gradient which will balance the resistance from gravity and density matter. Hence the velocity limits seems the product of the thermal effect.

The question is why the power limits exist? Probably, P_{th} is related to the feedback which is important to the formation of a standing wave, thus to the formation of a static surface structure. Because only when a critical value of pumping is exceeded, a positive feedback can lead to an exponential growth in the surface acoustic wave amplitude [11]. In our experiment, the critical threshold is $\sim 10^4$ J/cm^2.

The optimum condition is possibly the resonance condition and sensitive to heat loss. As have been discussed above, the induced SAW have a frequency related to the intensity of the laser power intensity. Thus, the power limits may be related to whether the resonance condition is satisfied. With increasing the difference in frequency, the interference conditions may not be satisfied and the standing wave may not be static formed. Hence the static surface structure will not be observed. In area B, as power increases, more heat is lost due to high conductivity at high temperature. The increased energy input may not keep pace with the increase of heat loss. This may be the possible reasons for explaining why with increasing laser power, to get the periodic structures, both the lower and upper velocity limits must decrease. On the other hand, in area A, lower power domains. Thus, with decreasing power, energy input decreases, which will lead to lengthen the required irradiation time to get the enough energy to pump for a enough positive feedback. Thus, the P_{th} seems the product of the interaction of the lights and the thermal properties of materials.

4.4 Periodic structures orientation

In our experiments, the periodic structure lines are parallel to the laser polarization. This result is consistent with other author' results and consists with the polarization theory. In our case, the SEW is taken by the fields diffracted by surface roughness. The formation of the nonlinear polarization from the coupling of the stokes and laser beam is automatically phase matched, and the polarized vibrators just keep up with the oscillation process associated with

the E component in electromagnetic field. Because material's polarization responds to the E component of electromagnetic wave, the time dependent polarization must follow that of the electric field. Hence the periodic structure orientation will be the same as the polarization all the time.

4.5 The dependence of line width and height

It shows that the strip width and height decrease with the scanning velocity and increase with the laser power, especially when the laser power is very small. The maximum clear periodic structures can be obtained in the optimum power condition. The behaviors of strip width and height dependence on velocity is the product of thermal effect. As the substrate is a kind of insulator material, the temperature near the position of the laser beam increases with decreasing velocity due to the increase in the dwell time. And this will lead to a high surface temperature on the surface of glass. As temperature increases, thermal conduction and thermal diffusion lead to increaser effective area. Their behavior dependence on power seems related to the heat propagation, which has been discussed in section 4.3.

5. CONCLUSIONS

The experiment was conducted to scan directly on a glass substrate by a CW CO_2 laser with linear polarization. It is experimentally shown that precise periodic structures with the periods of several microns can be formed by means of well-set laser parameters. The orientation of the periodic structure formed is the same as the laser polarization no matter what the scanning direction is. The occurrence of periodic structures requires a combined condition of laser power and scanning velocity, and these critical values surround a closed area within which the periodic structures could be fabricated properly. And this area is divided into two areas, higher power area and lower power area by the optimum power condition line. In the lower power area, the velocity limits increase with laser power. In contrast, the velocity limits decrease with laser power in the higher power area. In this optimum state, there exists the highest velocity range. When the laser power are away from this state, the velocity range will be compressed and decreased a lot. It is of a lot of interest here to note that the period decreases with scanning velocity.

REFERENCES

[1] Zhou Guosheng, P.M. Fauchet, A.E.Siegman, "Growth of spontaneous periodic structures on solids during laser illumination", *Phys. Rev. B*, **26**, pp. 5366-5381, 1982.

[2] J.E.Sipe, J.F.Young, J.S.Preston, H.M.van Driel, "Laser-induced periodic surface structure. I Theory", *Phys. Rev. B*, **27**, pp. 1141-1154, 1983.

[3] G.N.Maracas, G. L. Harris, C. A. Lee, R.A, McFarlane, "On the origin of periodic surface structure of laser annealed semiconductors", *Appl. Phys. Lett.*, **33**, pp. 453-455, 1978.

[4] Paul A. Temple, M. J. Soileau, "Polarization charge model for laser-induced ripple patterns in dielectric materials", *IEEE J. Quan. Elec.* **QE-17**, pp. 2067-2071, 1981.

[5] D.J.Wu, C. W. An, M. H. Hong, W. J. Wang, Y. Z. Peng, Y. F. Lu, "Grating fabrication with CW CO_2 laser irradiation" *Proceedings of SPIE*, **4915**, pp. 266-271, 2002.

[6] D. Bauerle, *Laser Processing and Chemistry*, Springer-Verlag, New York, 2000.

[7] P.E. Dyer, R.J. Farley, "Periodic structures in the excimer laser ablative etching of polymers", *Appl. Phys. Lett.* **57**, pp. 765-767, 1990.

[8] Joseph H. Simons, Kelly S. Dotter, *Optical Materials*, Academic Press, 2000.

[9] C.L. Babcock, etc. *Silicate Glass Techology Methods*, John Willey & Sons, Inc. 1977.

[10] R.L.Sutherland, *Handbook of Nonlinear Optics*, Marcel Dekker, Inc., 1996.

[11] V.I Emel'yanov, V. N. Seminogov, "Laser excitation of coupled surface electromagnetic and acoustic waves and of static surface structures in solids", *Soviet Physics JETP*, **59**, pp. 598-604, 1984.

Opportunities and challenges for laser technology in microelectronics and photonics

Willem Hoving[*],
Philips Centre for Industrial Technology - CFT,
Glaslaan 2, P.O.Box 218, Building SAQ-p,
5600 MD Eindhoven, The Netherlands.

ABSTRACT

Industrial manufacturing with the aid of laser technology has found many applications in the microelectronics industry during the last three decades. At Philips the main application fields are laser spot welding and marking. Several novel fields are strongly coming up due to the high demands in the microelectronics and (flat) display industry that cannot be met with conventional technologies. In this paper we give an overview of the present status of laser technology in electronics manufacturing and of innovative developments for new applications in microelectronics and photonics.

Keywords: laser materials processing, micro-spot welding, spike-welding, adjustment, separation, cleavage, laser mass transfer, process control.

1. INTRODUCTION

Laser materials processing is a broad and rapidly evolving technology area where many innovative applications are developed (Figure 1). This offers new possibilities in manufacturing. In most cases laser processing is contactless, force free and very localised. The method is software controlled and therefore flexible to changes, e.g. of parts geometry or
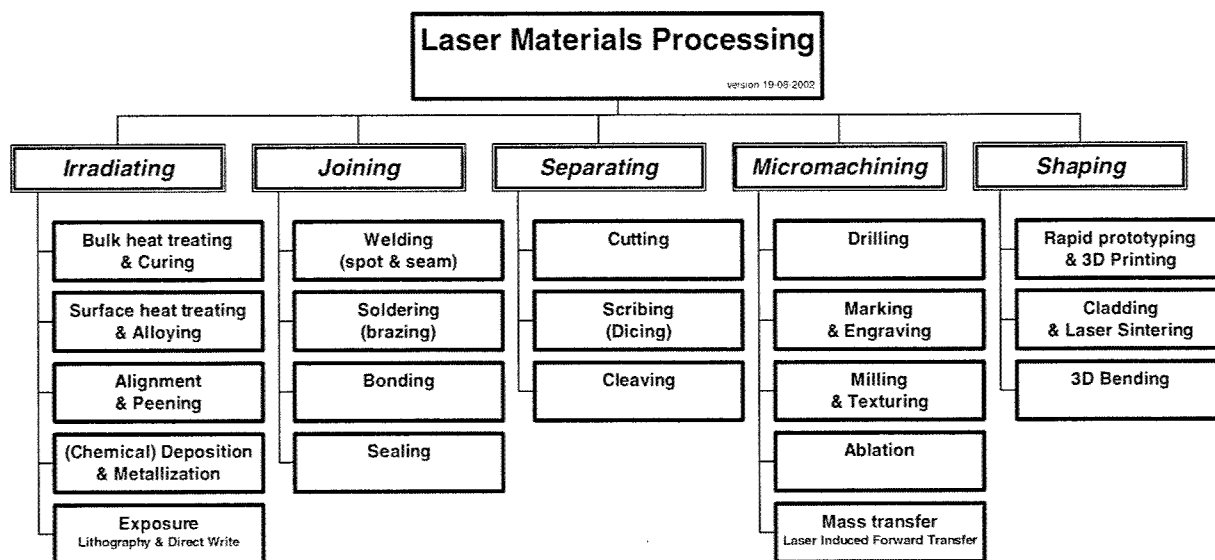

Figure 1: Laser materials processing is a broad and rapidly evolving technology area. Lasers are used for irradiating, joining, separating, micromachining and shaping of very diverse materials. Many innovative applications are developed.

---

material. The initial investment costs are often higher compared to conventional technologies. Cost price advantages with laser technology come from high yield, the high up-time of the equipment, the flexibility and short process times, and the replacement of several conventional process steps by one single laser process step. New developments in microelectronics and photonics manufacturing focus on cost reduction, enhanced quality, product miniaturization and reduction of the time-to-market. In the following paragraphs we address the opportunities and challenges for laser technology in these areas.

2. LASER MICRO-WELDING.

Laser micro-welding is extensively used in mass production of metal assemblies and sub-assemblies. Some examples are shown in Figure 2. Driven by a continuing trend towards miniaturisation, new products are designed that require micron and sub-micron accuracy's in a mass production environment. If such a high dimensional accuracy is desired, the thermo-mechanical distortions during melting, subsequent cooling and shrinkage of the parts have to be taken into account by designing the correct weld geometry.
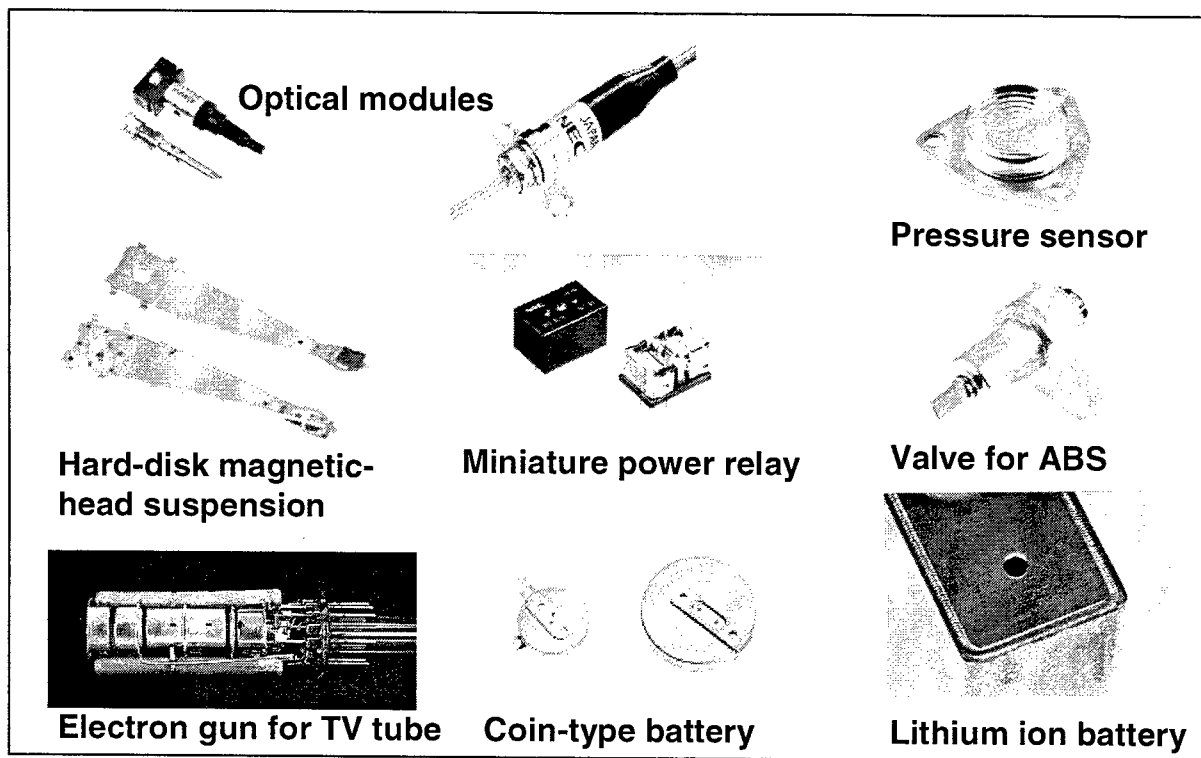
Figure 2: Several applications of laser micro-welding [Courtesy of NEC Corp].

2.1. Reduction of product contamination.

An issue for laser micro-welding is product and tool contamination due to debris from the welding process. A good approach to minimize this contamination is by finding an optimal process setting such that a 'calm weld' is obtained: it is important to avoid excessive evaporation or spattering of the molten material. This is accomplished by utilising the proper laser intensity during all subsequent phases of the welding process (pulse shaping), and by assuring an appropriate, annular intensity distribution in the focal spot of the laser beam (beam shaping). Using this strategy, local overheating of the metal is avoided, so that the material will remain at its melting temperature and below its evaporation temperature. This leads to a small plume and low product contamination, Figure 3.
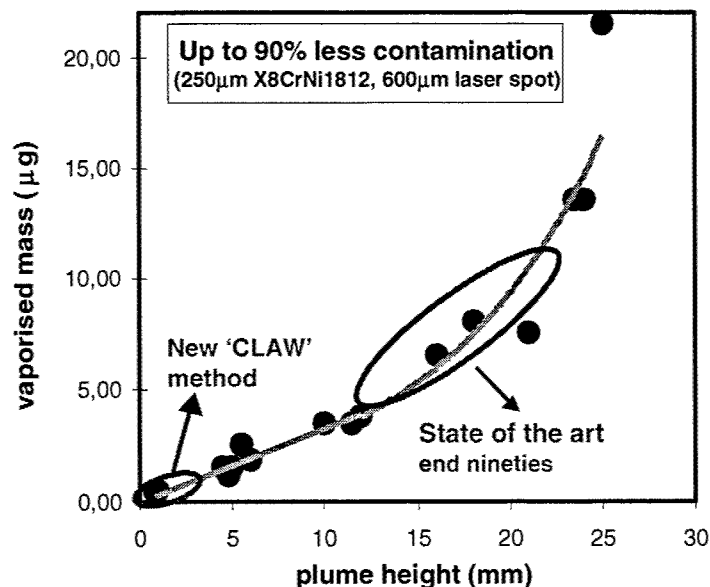
Figure 3: In the EU-funded project 'CLAW' a new micro-spot welding method was developed which gives 90% cleaner welds[1].

2.2. *Laser spike-welding, a novel welding method to bridge large gaps.*

A critical process parameter for laser micro-welding is the allowable gap between the product parts. This used to be 20 – 40 % of the top layer thickness at most. A novel welding recipe was found that overcomes this limitation for the overlap penetration geometry /1/. Firstly, a quiet pool of molten metal in the top material (directly irradiated by the laser beam) is made using the approach of the previous paragraph. This molten volume is pushed then within a few tenths of milliseconds towards the lower material by applying a high peak ('spike') in the incident laser beam intensity (Figure 4). With this so-called 'spike-welding' method, large gap tolerances can be bridged in production.
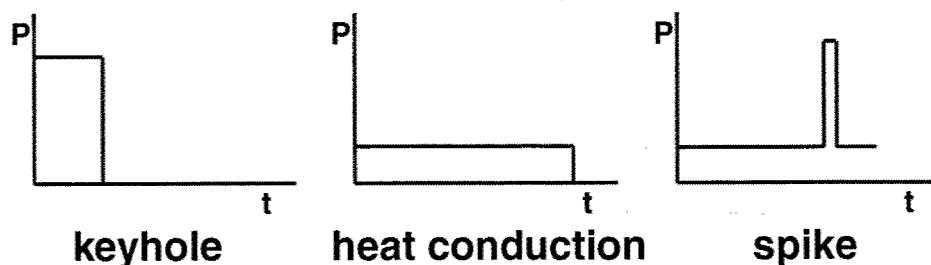
Figure 4: Different modes of micro-welding. In laser spike-welding a 'calm melt' is generated first in the top material. A short high peak ('spike') is superimposed on the incident laser beam intensity, which pushes the molten material across the gap between the product parts utilizing the recoil pressure of the generated metal vapour /1,2/.

Variable gaps are the result of dimensional tolerances of the product parts and the clamping tools. Figure 5 shows cross sections of spike-welds in 250μm thick X8CrNi1812 stainless steel. All welds have been made with the same energy, E=6.7J. The spot diameter is 600μm. The pulse-shape is a 20ms basic pulse of 325 W onto which a 1650W, 0.3ms wide spike is super-imposed at 14ms. The spike creates a narrow, approximately 10mm high plasma plume. Depending on

---

[1] CLAW = "Clean and Low Distortion Accurate Welding of micro-parts", see the Acknowledgements.

the ratio of laser spot diameter to the top plate thickness, gaps of 100% of the top layer thickness and more can be bridged. With conventional keyhole penetration welding this is only 20-40% at most. So, with spike-welding the gap between the metal plates can be increased by a factor of 2.5 to 5. In this way a powerful and attractive welding technique for joining of thin metal plates is available. The laser spike-welding method can handle larger production tolerances. It enables novel and cheap product designs, and also welding of dissimilar materials /1,2/.

Gap:	0 μm (0 %)	125 μm (50 %)	250 μm (100 %)
Strength:	100N	89N	59N
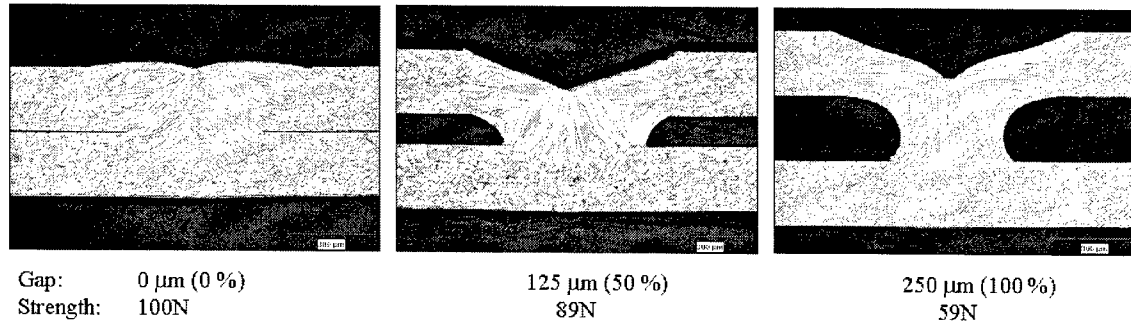
Figure 5: Cross-sections of laser penetration spike-welds in 250 μm thick sheets of X8CrNi1812 stainless steel. All welds have been made with the same laser pulse-shape, see text.

2.3. Real-time control of micro-welding processes.

It is difficult to obtain a robust micro-welding process for thin copper parts due to their low absorption coefficient for the laser light and their high thermal conductivity at room temperature. Moreover, these properties change in an unfavourable way when the material reaches its melting temperature, see Figure 6. This makes micro-welding of delicate copper parts a very critical process.
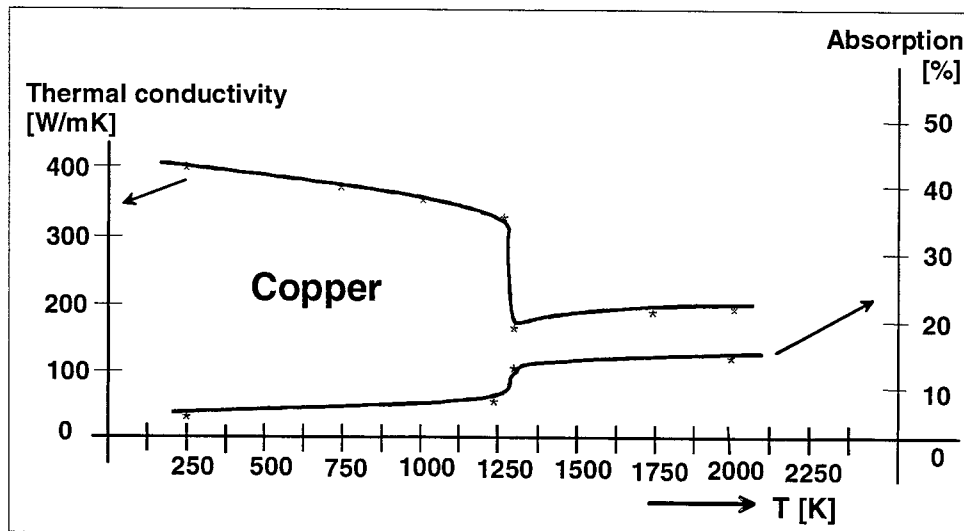
Figure 6: Thermal conductivity and absorption properties of copper for laser irradiation at a wavelength of 1.06 μm. Both properties change abruptly and in an unfavourable way with regards to the stability of the process when the material reaches its melting temperature /3/.

Real-time process control using multiple sensors that probe and control the progress of the weld, help to improve the yield in production. Signals recorded during spot-welding of a copper lead-frame show features that exhibit a strict relation with the evolving welding process, and which are used as input data for adaptive and real-time control functions. An industrial laser welding head for real-time process control is shown in Figure 7. It incorporates several
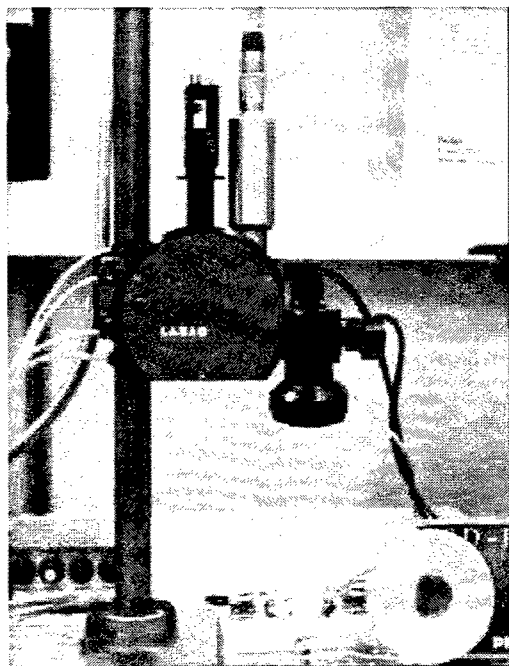
process sensors. The sensors are used to determine and control the different phases of the micro-spot welding process: 1) the pre-melting or heating phase, 2) the melting or fusion phase, and 3) the post-melting or cooling phase. Hardware and software for real-time process control for micro spot-welding of delicate copper parts was developed in the EU-funded project 'SLAPS'[2] /3/. The technology platform can also be used for other demanding processes, and is not limited to laser applications.

Figure 7: Picture of an industrial welding head for real-time controlled micro-spot welding. It incorporates a CCD camera, a small scanner for 'aim and shoot', and several integrated sensors /3/.

3. LASER ADJUSTMENT.

It is a well-known phenomenon that the application of small amounts of heat to metal products can introduce permanent thermo-mechanical deformations of the product parts. These effects can be utilized for mechanical alignment or trimming in the micron and sub-micron range /4/. The technology is has already widespread applications in several industries for adjusting digital video heads, relay switches, hard disk drive components, and optical components where mechanical methods are not accurate enough or too cumbersome. The example in Figure 8 of the miniature reed switch

illustrates that laser adjustment can also be applied to adjust component which are enclosed in a glass housing. The conventional production process of reed switches shows a large spread for the v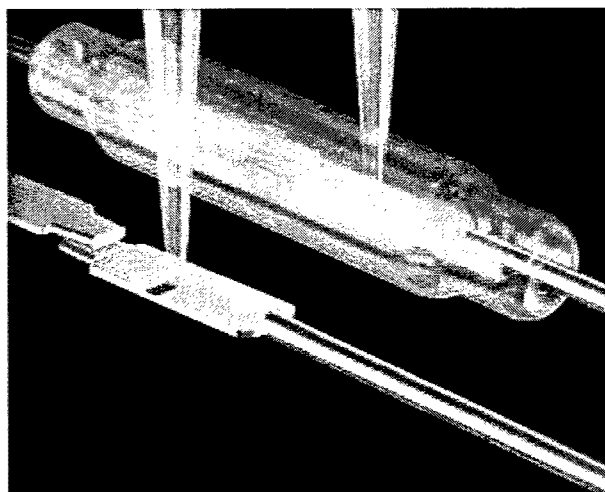alue for the magnetic field, expressed in Ampere-Windings (AW), where these switches open and close. This spread causes less efficient and complex production logistics. Laser adjustment offers the means to manipulate the AW-values by adapting the gap of assembled switches inside the glass enclosure and within a fraction of a second. By proper choice of the laser wavelength, pulse properties and irradiation strategy it is possible to adjust the gap between the two peddles with roughly one-micron accuracy. It is shown that this can be done without damaging the glass enclosure or affecting the lifetime of the switch. Application of this new technology results in a much more efficient production process and just-in-time delivery to the customer.

Figure 8: Schematic picture of the laser adjustment process for reed switches /5/, where the distance between the metal contacts is set by applying a laser beam through the glass housing.

Figure 9 illustrates a more elaborated laser-adjustment application for a photonics component where the laser

adjustment technology is used for trimming the angular orientation of a small lens mounted on a metal lens-holder with typical dimensions of several millimetres. The angle of the lens of Figure 9 can be fine-adjusted by applying a sequence of short laser pulses at the lower positions of the lens holder indicated in the picture /4/. As a first step, the lens holder is micro-welded into the optical product within an angular accuracy range of about 10 milliradians. Then the clamping tools are removed. A fully-automatic laser adjustment process is used to obtain the desired position with sub-millirad accuracy, whereby also the residual stresses are removed. Laser irradiation takes place from one side, where there is access to the product, and at a distance from the lens such that lens contamination will be avoided.

Laser irradiation areas
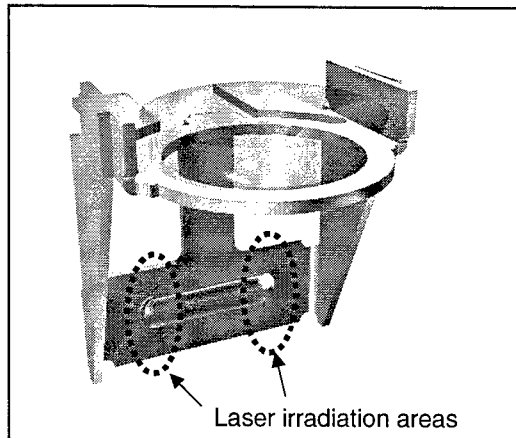
Figure 9: Micro-lens holder designed in the EU-funded project 'AMULET'[3] for accurate laser adjustment of the angular position of the lens, see text. The outer dimensions of the real product are a few millimetres.

4. LASER SEPARATION.

4.1.   Laser cutting.

Laser technology offers an accurate and flexible tool for separation of materials by cutting, scribing or cleaving. Laser cutting of metals is a standard technology in many mechanical job-shops, and for the manufacture of medical instruments (e.g. vascular stents). Several separation methods can be used for brittle materials. One method is full laser cutting using a pulsed solid-state laser with a very good beam quality and high pressure gas through a small nozzle. Figure 10 shows results for a 0.4 mm thick sapphire substrate where a cut width of only 10μm is reached without making micro-cracks in the weak sapphire wafer.
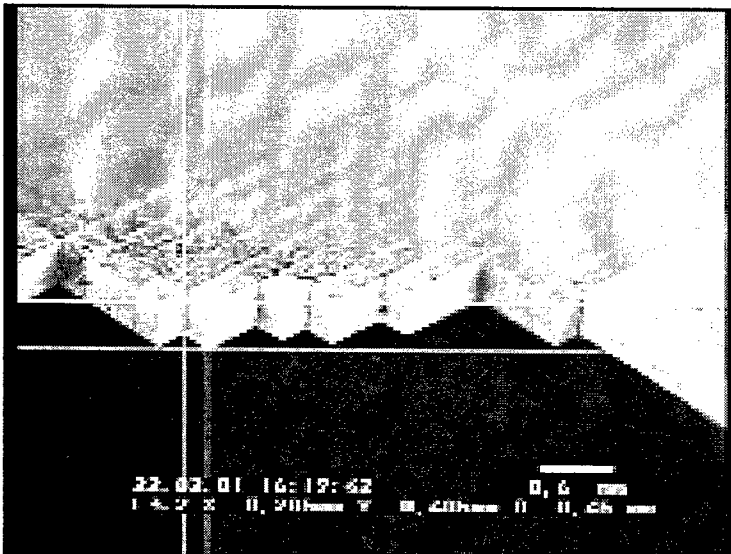
Figure 10: Laser cut parts of 300 μm x 400 μm from a 400 μm thick sapphire substrate. The cutting process was done using a pulsed Nd:YAG laser with a wavelength of 1.06 μm [Courtesy of Lasag].

---

[3] AMULET = 'Accurate Manipulation Using Laser Technology', see the Acknowledgements.

4.2. Laser scribe and break.

Conventional technology (Scribe & break) — Laser cleaving

Glass
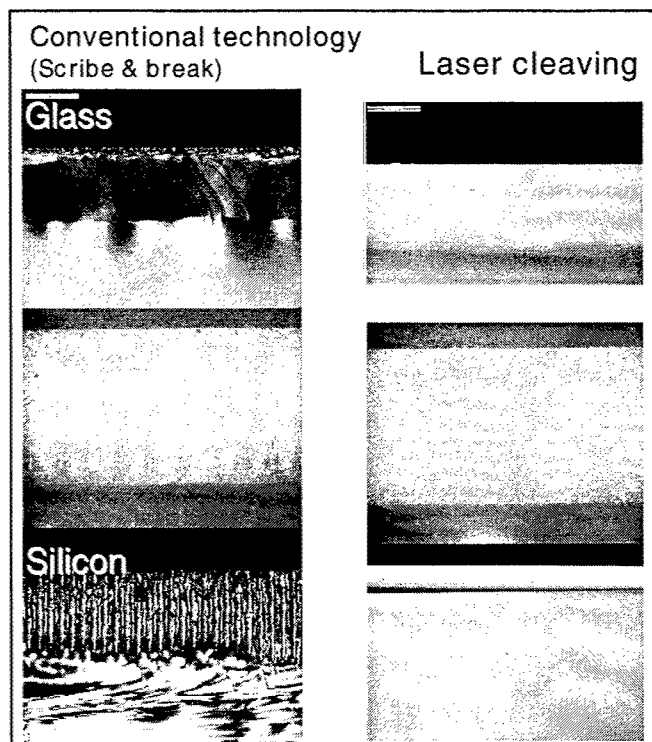
Silicon

The middle and bottom pictures of Figure 11 show typical cross-sections of singulation experiments with alumina and silicon samples that have been scribed first at the surface by a pulsed laser, and that are subsequently broken. With decreasing substrate thickness very high laser-scribe speeds of 150 mm/sec and higher can be used. This makes the laser scribe and break (LS&B) method interesting for industrial dicing of next-generation electronic substrates. No process fluids are needed. It is expected that laser technology will replace the mechanical sawing methods for substrate thicknesses below about 250 μm. The flexible silicon substrates have a thickness down to 50 μm or less.

Figure 11: Cross sections of glass (top), alumina (middle) and silicon (bottom) substrates that have been singulated by scribing and subsequent breaking (left) or by laser cleaving (right). The glass sample in the top left corner had been scribed by mechanical means.

4.3. Laser cleaving of brittle materials.

Laser cleaving has established itself as a technology for glass singulation in the automotive and display industries. Large-area laser heating using a CO_2 laser and subsequent strong local cooling by means of a gas or liquid is used to guide and propagate a cut though a brittle material (Figure 12). In this laser cleaving-method there is no material loss, so the effective cut width is zero. Furthermore the edge quality is very good with no chipping or cracks, and it has a high mechanical strength. The cleaving-method can be used for any brittle material. The right pane of Figure 9 shows the comparison with the scribe and break method for glass, alumina and silicon.
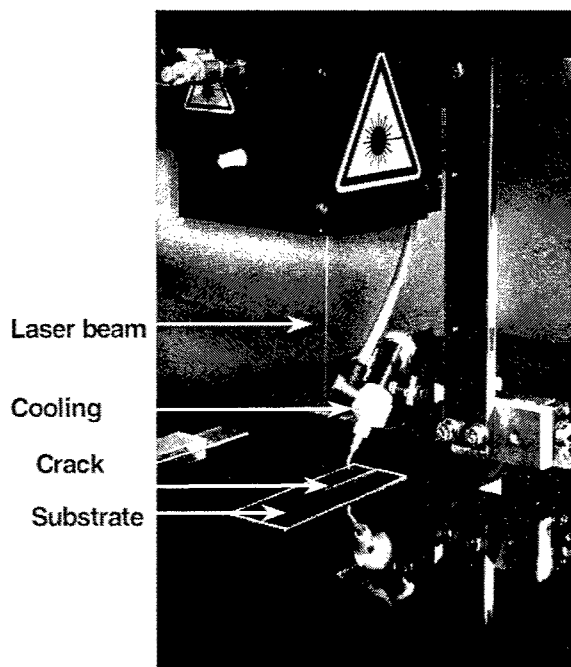
Laser beam

Cooling

Crack

Substrate

Figure 12: Picture of a set-up for laser cleaving of glass substrates showing the beam from a CO_2 laser and the nozzle for the cooling medium [Courtesy of Schott AP].

5. LASER MARKING AND LASER MASS TRANSFER.

Laser-induced colour-generation in plastic materials from the bulk volume can be achieved by foaming or bleaching, see Figure 13. In many cases however the quality of the colour (brightness) is not satisfactory, so that new methods need to be explored. An interesting candidate is laser-induced transfer of colours from a colour-containing donor-

medium to the product. This 'laser mass-transfer' method is well established in the paper printing industry for colour proofing. Laser induced transfer of colours is entering the flat-panel display industry now for making the black-matrix and the red, green and blue colour-filters of liquid crystal displays, Figure 14.
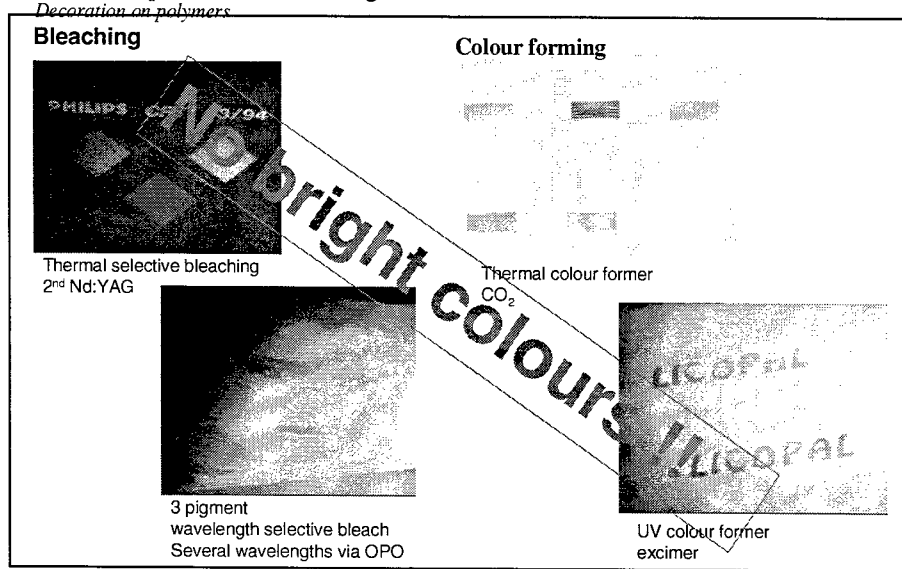
Figure 13: Methods where colours are generated from the bulk plastic material lead to dull colours, or need a white background. Laser induced transfer of colours might be a solution.
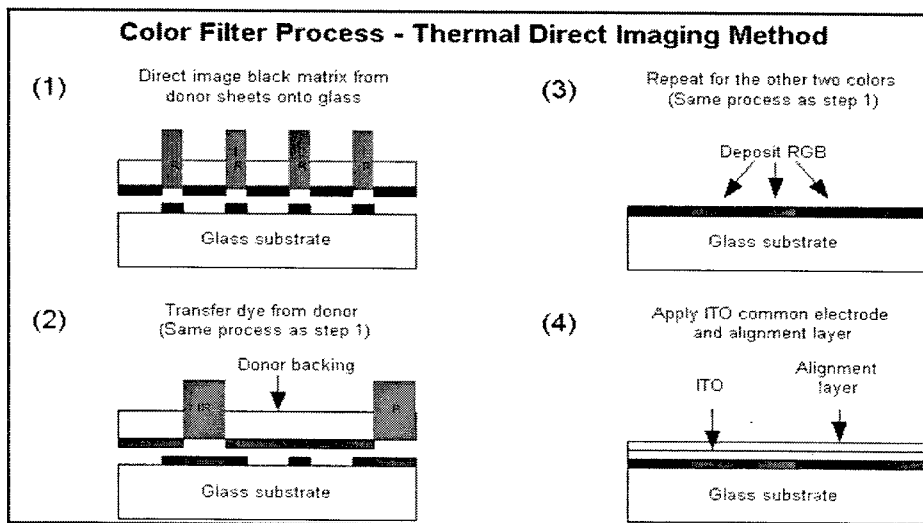
Figure 14: Laser induced transfer of the black matrix (1), and the red, green and blue dyes (2-3) onto glass substrates. This is a new method for making colour filters for LCD panels [Courtesy of CREO /6/].

6. OUTLOOK

The proceeding decades showed a strong effort in firstly developing new types of laser sources, and then finding application fields for these (technology push). Nowadays, the main focus lies at the industrial applications, where laser technology replaces conventional processes, or enable new products.

Emerging areas for laser materials processing in microelectronics and photonics are:

- **Irradiating:** building microstructures and micro-components by inkjet printing of nano-crystalline particles followed by laser sintering; silicon laser re-crystallization for display applications; structuring/local annealing of thin layers; maskless lithography using laser direct write.

- **Joining:** sealing of glass (lamps/displays), polymers (displays), ceramics (lamps), and plastic housings (consumer products, medical and domestic appliances); micro-assembly of semiconductor modules and micro-electromechanical devices using laser micro-joining, laser forward-transfer of components, and laser micro-adjustment.

- **Separating:** via hole drilling of electronic substrates (one of the fastest growing application fields); scribing, dicing and cleaving of glass (flat displays / lamps) and modern electronic substrate materials (silicon, sapphire, alumina, ceramics, AlN).

- **Micromachining:** finishing of plastic housings with unique textures; customisation of products by full-colour flexible decoration at packaging centres; additive and subtractive structuring of thin layers by direct-writing and by ablation and milling; trimming of embedded passives (resistors, capacitors, inductors) in multi-layer substrates; laser direct-write of electronic structures (metals, polymers, glass (frit), functional materials, phosphors) and lithography masks; laser cleaning of semi-conductor and optical components; laser processing, waveguide writing and sub-surface marking of polymers and glass substrates for future photonics devices; milling and texturing of surfaces (feature/structure sizes of 1 µm or below) for tribologic and decorative purposes.

- **Shaping:** micro-cladding and sintering to locally improve the properties of cheap products.

- and many other things.

In addition to this non-exhaustive list, where laser technology is used for processing materials and as a manufacturing tool, one can observe that an interesting new application field of high-power lasers is opening up, namely the laser as part of new consumer and professional products. Due to the compactness, reliability and price/performance of modern lasers, these become serious candidates as components of products for health care, (bio)medical analysis and projection display applications. The laser materials processing community will play an important role here. It knows how to judge and develop the new technical possibilities of, for example, the high-power diode-lasers as light and energy sources in these products, as well as the laser safety aspects.

ACKNOWLEDGEMENTS

REFERENCES

/1/. D.K.Dijken, W.Hoving and J.Th.M. de Hosson, "Laser penetration spike welding – A welding tool enabling novel process and design opportunities", Photon Processing in Microelectronics and Photons Conference, San Jose, January 2002 in Proceedings of SPIE Vol. 4637 (2002), pp. 555 – 560. Laser spike-welding is a patent pending technology.

/2/. D.K.Dijken, W.Hoving and J.Th.M. de Hosson, Journal of Laser Applications, Vol. 15, No 1 (2003).

/3/. A.H.M. Blom, P. Dunias, P.G. van Engen, W.Hoving, J. de Kramer, "Process spread reduction of laser micro spot welding of thin copper parts using real-time control", this conference.

/4/. W.Hoving, "Accurate Manipulation using Laser Technology" in Laser Assisted Net Shape Engineering 3, Proceedings of the LANE 2001, edited by M.Geiger & A.Otto, Miesenbach-Verlag Bamberg 2001, pp. 113 – 124 (2001).

/5/. E.C.M.Verhoeven, H.F.P. de Bie and W.Hoving, "Laser adjustment of reed switches: micron accuracy in mass production", Proceedings of the LEF'99 Conference ("Laser in der Elektronikproduktion & Feinwerktechnik", Erlangen, March 1999, Miesenbach Bamberg, pp. 169-179 (1999).

/6/. E.Elizur, D.Gelbart, "Thermal lithography for flat panel display manufacturing", Proceedings of the SID'02 meeting, SID 02 Digest, pp. 1055 – 1057.

Laser beam welding of thermoplastics

U.A. Russek[*a], A. Palmen[a], H. Staub[a], J. Pöhler[a], C. Wenzlau[a], G. Otto[a], M. Poggel[a], A. Koeppe[a], H. Kind[a]

[a] Fraunhofer-Institut für Lasertechnik ILT, Steinbachstr. 15, D-52074 Aachen, Germany

ABSTRACT

Current product development showing an ever shrinking physical volume is asking for new, reliable joining technologies. Laser beam technologies conceal innovative solutions to overcome limitations of conventional joining technologies. Laser beam welding of thermoplastics offers several process technical advantages. The joining energy is fed contact-less into the joining area, avoiding mechanical stress and thermal load to the joining partners. The energy is supplied spatially (seam width on the order of 100 μm) and timely (interaction time on the order of ms) very well defined. Different process strategies are possible leading to flexibility, product adapted irradiation, short process times and high quality weld seams as well as to high integration abilities and automation potentials. During the joining process no vibration, no thermal stress, no particle release takes place. Therefore, destruction of mechanically and electronically highly sensitive components, such as microelectronics, is avoided. The work place pollution is neglectable compared to other joining technologies, such as gluing (fume) or ultrasonic welding (noise, pieces of fluff). Not only micro-components can be welded in a reproducible way but also macro-components while obtaining a hermetic sealing with good optical appearance.
In this publication firstly, an overview concerning process technical basis, aspects and challenges is given. Next, results concerning laser penetration welding of polymers using high power diode lasers are presented, while comparing contour and simultaneous welding by experimental results and the on-line process monitoring.

Keywords: laser, thermoplastics, contour welding, simultaneous welding, on-line process monitoring

1   INTRODUCTION

Laser beam welding of thermoplastics as an alternative and innovative joining technology has been already considered in the early years of laser technology. However, conventional polymer welding technologies solved the joining challenges of those days and cost considerations did avoid the breakthrough of laser beam welding as well. Today, several joining demands can not be met by conventional technologies, but with laser radiation in operation. Additionally, availability, efficiency and expenditures of laser beam systems did improve drastically. Therefore, laser welding of thermoplastics has experienced an increasing industrial interest and acceptance for about ten years. [1][2][3][4] Numerous fields of applications such as in electronics and automotive industry have been established for years, like the well known electronic key or keyless-go card. [5][6] However, not all technological challenges got over at present. Still, several hurdles have to be cleared to exploit laser beam welding of thermoplastics even more. In the following, the basics of laser beam welding of thermoplastics will be illustrated, while giving an idea concerning the opportunities and limits of this innovative welding technology. Later on, two different welding strategies, contour and simultaneous welding, will be compared briefly regarding the used laser system, the experimental welding results as well as the on-line process monitoring.

2   BASICS OF LASER BEAM WELDING OF THERMOPLASTICS

2.1   Process technical basics and equipment
2.1.1 Laser beam based joining process
Laser beam welding of thermoplastics may be structured from different points of view:
- joint geometry: butt joint or overlap joint (see below)
- nature of irradiation: contour, quasi-simultaneous, simultaneous and mask welding (see below)
- applied laser source: high power diode laser, CO_2-laser, Nd:YAG-laser, Holmium-YAG laser (see Ch.2.1.2)

---

[*] russek@ilt.fhg.de; phone: ++49-241-8906-158; fax: ++49-241-8906-121, http://www.ilt.fhg.de

- joining partner stability: form stable[1] or flexible (like thin layers applied in packaging industries and life science)
- size of the joining partners: micro or macro parts
- dimensions of the weld seam: micro (seam width < 200 μm) or macro welding
- nature of thermoplastic joining partners combination. It may be distinguished between welding similar (such as PA / PA, PC / PC, PP / PP) or dissimilar thermoplastics[2] (such as ABS / PC, ABS / PMMA). In the following only welding of similar thermoplastics is considered.

Generally, all thermoplastics are laser weldable, if the optical, thermal and geometrical properties are suited to the process needs. Therefore, amorphous, partially crystalline, glass-fiber reinforced thermoplastics are weldable. Color substances and additives may be able to arrange product specific aspects and process technical requirements.

Laser beam welding of thermoplastics uses the transformation of electro-magnetic energy (laser radiation) into heat energy to plastify (melt) the thermoplastic joining partners spatially and timely defined within the joining area. There are in principle two different joint geometries to distinguish: the overlap joint and butt joint (Fig. 1), but the overlap joint has prevailed against butt joint geometry. First the overlap welding process is illustrated, followed by reasons for rarely using butt joints. Fig. 1 shows the basic overlap and butt joint geometry.
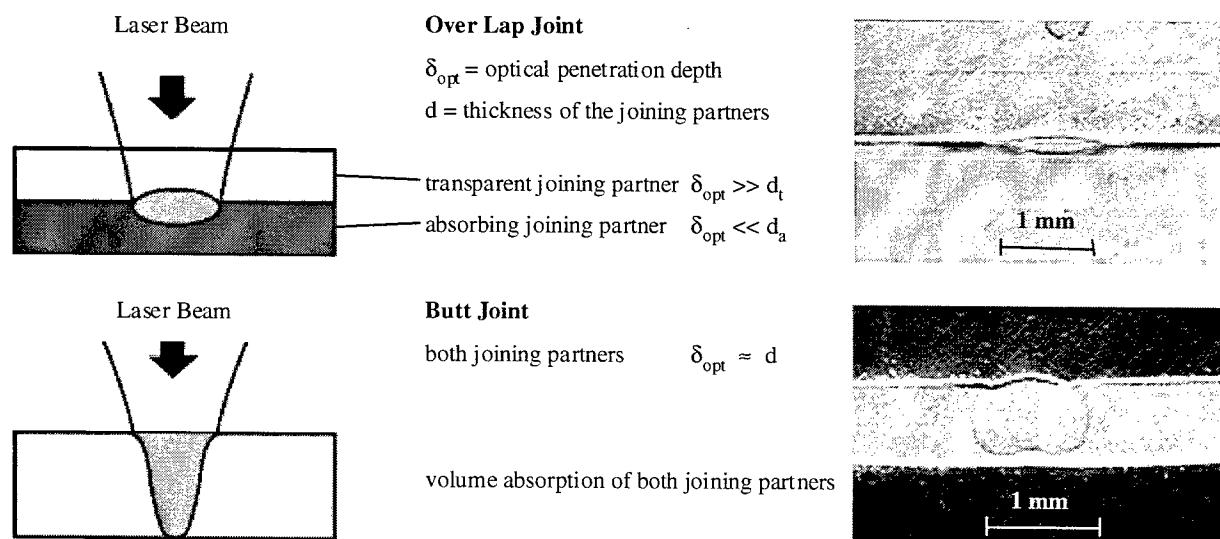
Fig. 1 Differences of the two joint geometries (overlap and butt joint) concerning joining partner position, optical penetration depth δ_{OPT} (see 2.2.2) as well as optical appearance of the weld seam (depicted by means of microtom cuts) [source: ILT]

By applying overlap welding two joining partners with different optical properties for the used laser wavelength are joined, as depicted in Fig. 1. The first irradiated – the (laser) transparent – joining partner, has to have the following optical properties: low degree of reflection, absorption and scattering centers and as a result high degree of transmission leading to guiding the laser beam to the second – the (laser) absorbing – joining partner with minimal energy loss and scattering influence. The absorbing joining partner has to show low degree of reflection and transmission and as a result high degree of absorption. Scattering is here of secondary importance because of the small optical penetration depth δ_{OPT}.

---

[1]   "Form stable" means a thermoplastic joining partner has a thickness causing a reasonable mechanical stability. Actually, it gives the opportunity to distinguish between thin, flexible as well as thick, stable joining partners. The thicker the transparent joining partner, the larger its necessary optical penetration depth for the applied laser radiation to transport enough electro-magnetic energy on to the absorbing joining partner.

[2]   If joining dissimilar thermoplastics is intended the polymer compatibility has to be considered. Whether polymer compatibility is given may be answered from several investigations documented in [8], [9]. The compatibility of different polymers depends mainly on the molecular interactions of atoms and molecules, the so called secondary valence forces. [8] Laser beam welding offers the opportunity of welding thermoplastics and thermoplastic elastomers, since laser welding does not require mechanical generation of heat, while most conventional polymer welding techniques do. [10]

First, both joining partners are put in a clamping device in close contact. The laser beam accessibility of the entire weld seam has to be guaranteed. The joining energy (laser radiation) is brought into the joining area through the transparent joining partner, which experiences, if at all, neglectable warm up. The joining area corresponds to the interface or the contact area, respectively, between the joining partners. There, the electro-magnetic energy of the laser radiation is transformed into heat energy by the absorbing joining partner[3]. The energy transformation occurs due to absorption within the polymer matrix but, while considering laser wavelengths on the order of 800-1100 nm, mainly due to additives such as carbon black, color pigments and infrared absorbers. The locally and timely defined energy input causes a plastification of the absorbing partner without putting mechanical, chemical or thermal stress into the seam environment. Due to the absorption within the absorbing partner local temperature and volume increase take place, which causes an expansion of the plastified material and a close contact between absorbing and transparent joining partner. Now, by means of heat conduction the transparent partner warms up and plastifies, too. To guarantee the heat conduction between the joining partners a close contact is imperative. Only small gaps may be bridged (2.2.4). The weld seam adapted clamping device presses the joining partners via a static pressure evenly against each other while minimizing the gap between the joining partners. It is the only mechanical load on the partners. The clamping device fulfills two further tasks. On the one hand, it keeps both joining partners fixed in their final position during the joining process, while guaranteeing reproducible positioning and small production tolerances. [4] On the other hand, the clamping supplies a pressure against the thermal expansion within the joining area. Volume expansion and clamping pressure result in an inherent joining pressure, which is besides an appropriate temperature necessary for obtaining a material conclusive joining. High-quality weld seams are obtained by means of sufficient generation of plastified material as well as enough interaction time to establish diffusion processes. The fulfillment of these conditions is reached by means of appropriate selection and adjustment of the variable influencing quantities, such as optical and thermal properties, laser power, intensity distribution, feed rate or interaction time and part tolerances (avoiding gaps). Process adapted design minimizes process times and increases weld quality.

The state of common plastification of joining partners in close contact allows thermal change of place as well as diffusion processes [12] leading to molecule chain penetration of the joining partners within the interaction area, which forms after the solidification a high-quality, material conclusive joining.

The plastified volume and therefore the needed joining energy for butt joint geometry is larger than for the overlap geometry[5]. For overlap joints only a layer of about $30 - 300$ µm thickness is plastified within the border area of the joining partners, while the layer thickness depends on the type of thermoplastic, optical penetration depth and applied process parameters. Applying butt joint welding both joining partners have to be plastified along their entire butt joint area. Furthermore, even small changes of the optical penetration depth δ_{OPT} may cause large deviations of the process parameters or the process results, respectively (see Ch. 2.2.4). δ_{OPT} may be changed easily by small deviations of the amount of additives applied to the basic polymer. Due to this the irradiation geometry and the absorption behavior the energy density and temperature distribution but especially the plastified volume over the material thickness may change. An uneven plastification layer may cause generation of inherent tensions. Additionally, exact positioning of the joining partners may be more critical for butt joints. Therefore, overlap joint has prevailed against butt joint.

Following reflections consider overlap joint geometry.

There are four main irradiation methods to distinguish. Tab. 1 and Tab. 2 are giving a summarizing overview.

The contact-less and locally restricted energy input distinguishing all laser beam processes avoids thermal load or damaging of the joining partners as well as the joining surrounding. Therefore, joining of sensitive components which for example contain electrical sensors, microelectronic or photonic parts, are weldable without impairing their functionality. Applying contour welding feed rates up to 25 m/min [6], while for simultaneous welding process times on the order of 0,5 s are realized already. [7]

---

[3] Absorption occurs with the speed of light. However, the energy transformation efficiency depends on the number of interaction centers per volume corresponding (1. approx.) to the optical penetration depth. But. temperature rise and plastified volume depend on the interplay of optical penetration depth. thermal conduction of the thermoplastics as well as the heat transition between them. interaction time, laser power and intensity distribution.

[4] Really. there are two opportunities. First. both joining partners are fixed in their final position during the entire process. Secondly. applying a melting or adding way. after plastifying the entire weld seam (quasi-simultaneous and simultaneous welding). Applying melting or adding way offers some advantages. such as compensating existing gaps due to parts tolerances as well as on-line process control while detecting path and pressure. However. the weld seam needs constructional preparation especially if the welding bulge has to be hidden. Additionally. applying melting or adding way may increase entire welding time.

[5] Actually. there are two strategies generating a butt joint to distinguish. One without any macroscopic motion of the joining partners as depicted in Fig. 1. The other one is similar to hot plate welding.

Contour Welding is the most widespread irradiation method. The weld seam geometry is covered sequentially with a single laser beam which generally is focused into the joining area, which is locally heated generating a small plastified volume (Fig. 2). The sequential motion may be performed by the laser beam, the clamped joining partners or a combination of both, while applying handling systems or robots. Appropriate handling systems allow welding of 3-d seam geometries. Gaps between the joining partners have to be avoided. Therefore, the design of the weld seam area and the manufacturing of the joining partners (shrinkage, tolerances) are of crucial relevance.
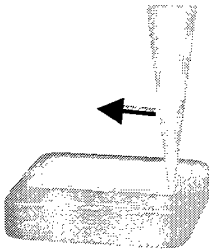

Fig. 2
Schematic depiction of contour welding
[source: ILT]

Characteristic features
- design freedom (flexibility in weld contour design)
- on-line process monitoring via pyrometry
- on-line process control via pyrometry and power feedback loop
- low optical expenditure
- lower laser power required
- dynamic motion system required
- cycle times corresponding to feed rate / weld seam length
- low gap bridging capability

Applied laser beam sources
- high power diode laser either with or without fiber coupling and with different shapes of the applied intensity distribution
- Nd:YAG-lasers either with or without fiber coupling offering higher beam quality than diode lasers

Variable parameter (after defining materials and their properties)
- laser power, feed rate, wavelength, intensity distribution, working distance, clamping pressure

Typical process data applying high power diode lasers
- spot size > 500 µm
- laser power < 200 W
- feed rates < 25 m/min
- interaction time > 1 ms

Mask Welding - Especially, generating narrow seams (≈ 100 µm) and complex seam designs in micro technology, biology and life science employment of masks is preferred. A mask between laser beam source and joining partners guarantees an irradiation only of areas to be welded (Fig. 3). High power diode lasers with a collimated, homogeneous, line-shaped intensity distribution are preferred for this irradiation method. The resolution or the smallness, respectively, depends on the thickness of the transparent joining partner, the optical and thermal properties of both joining partners, the intensity distribution as well as the arrangement laser source, clamping device and mask.

weld seam
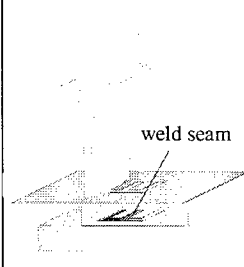
Fig. 3
Schematic depiction of mask welding
[source: ILT]

Characteristic features
- extra expenditure for mask design and manufacture as well as positioning system
- design freedom (flexibility in weld contour design)
- on-line process monitoring and control via pyrometry is limited
- low optical expenditure (but generating a homogeneous, line shaped intensity distribution)
- high laser power required
- dynamic motion system required (often only one axis required)
- cycle times corresponding to feed rate / weld seam length
- low gap bridging capability

Applied laser beam sources
- high power diode laser with or without fiber coupling and different shapes of the intensity distribution

Variable parameters (after defining materials and their properties)
- laser power, feed rate, wavelength, intensity distribution, working distance, clamping pressure

Typical process data applying high power diode lasers
- spot size   line shaped intensity distribution, in fast axis: Gaussian, in slow axis: top hat width > 500 µm, length < 40 mm
- laser power < 200 W
- feed rates < 10 m/min
- interaction time $> 2,5$ ms

Tab. 1 Illustrating the irradiation method mask and contour welding and their performance as well as characteristics

Quasi-Simultaneous (Scanning Method) – Guiding the laser beam by means of fast galvano-scanning mirrors system over an arbitrary 2-dimensional weld seam contour within a limited scanning field is called quasi-simultaneous welding (Fig. 4). A F-Theta-Optic ensures the focal spot of the laser beam lying at each point of the scanning field plane within this plane. By choosing the correct interplay of scanning speed and laser power, the entire weld seam may be brought in a plastified state. Since the laser beam runs several times over the entire seam contour per time unit, losses of heat removal by thermal conduction may be made up for by the supplied electro-magnetic energy which is transformed into heat via absorption. Because of plastifying the entire weld seam part tolerances may be compensated for depending on the weld seam and environmental design.	

Fig. 4 Schematic depiction of quasi-simultaneous welding	Characteristic features • extra expenditure for scanning system • design freedom while assuming the entire weld seam contour is within the scanning field • no on-line process monitoring or control via pyrometry and power feedback loop • low optical expenditure (if Nd:YAG-laser applied) • high laser power required • no dynamic motion system required, if entire seam contour within scanning field ($< 300 \times 300$ mm^2) • cycle times corresponding to feed rate / weld seam length • marked gap bridging capability Applied laser beam sources • Nd:YAG-lasers offer higher beam quality than diode lasers • high power diode laser are cheaper than Nd:YAG-lasers Variable parameter (after defining materials and their properties) • laser power, feed rate, wavelength, intensity distribution, working distance (scanning field), clamping pressure, working with or without melting or adding way, preservation time Typical process data • spot size depending on laser source: diode lasers > 500 µm, Nd:YAG-lasers > 20 µm • laser power > 200 W • feed rates < 10 m/s • interaction time depending on spot size and scanning speed: diode > 50 µs, Nd:YAG > 2 µs

Simultaneous Welding - The compact and modular set up of high power diode lasers permits simultaneous laser welding. The entire weld seam is irradiated as a whole and welded with one single laser pulse. Apart from short process times, which are of interest for big lot production, simultaneous welding allows a more moderate irradiation (interaction). Additionally, it promises wider process windows, marked bridging capability as well as enhanced weld strength compared to contour welding. By means of appropriate beam forming and guiding a homogeneous intensity distribution fitting to the entire weld seam geometry has to be generated, which represents the challenge of the simultaneous process.[6] Assessing efficiency of simultaneous welding aspects, such as size of the weld seam, required laser power and cycle time, have to be considered. Because of plastifying the entire weld seam part tolerances may be compensated depending on the weld seam and environmental design.	

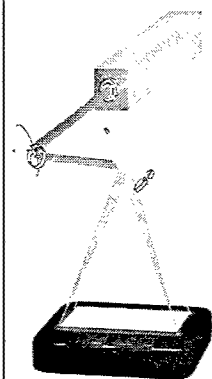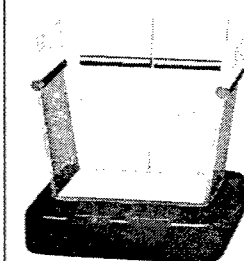|	
Fig. 5 Schematic depiction of simultaneous welding [source: ILT]	Characteristic features • extra expenditure for beam forming or guiding system • limited design freedom • on-line process monitoring and control via IR-camera • high entire laser power required • no dynamic motion system required, renunciation of trouble-prone components (fiber, handling, ...) • short cycle times independent on weld seam length • marked gap bridging capability Applied laser beam sources high power diode laser modules either with or without optical beam shaping and guiding system while generating a homogeneous intensity distribution over the entire weld seam Variable parameter (after defining materials and their properties) • laser power, irradiation time (interaction time), timely shape of the irradiation pulse (pulse sequence), wavelength, intensity distribution, working distance, clamping pressure, working with or without melting or adding way, preservation time Typical process data applying high power diode lasers • weld seam width > 500 µm • laser intensity > 100 W/cm^2 • irradiation time > 50 ms – 1s (the more laser power available, the shorter process times possible)

Tab. 2 Illustrating the irradiation methods quasi-simultaneous and simultaneous welding, their performance and characteristics

2.1.2 Laser beam sources

Different laser beam sources mainly operated in continuous wave mode are available for laser beam welding of thermoplastics. Laser beam welding of thermoplastics is known since the early years of laser technology. However, first systematic investigation are dating from the early nineties. [1],[2],[3],[4] In the beginning CO_2- and Nd:YAG-lasers have been in operation. Since CO_2-laser radiation ($\lambda = 10,6$ μm) experiences a very small optical penetration depth in all thermoplastics it has mainly been used for welding thin thermoplastic films and foils of packaging industry, either in overlap or butt joining geometry. Using CO_2-laser radiation for welding form stable polymers would cause inefficient heating times as well as extended heat influenced areas. Nd:YAG-laser radiation ($\lambda = 1,064$ μm) penetrates uncolored thermoplastics of several millimeters thickness, while experiencing only small absorption, which allows the overlap joining process. Therefore, Nd:YAG-lasers have been used for welding form stable thermoplastics. In these early years, laser welding of thermoplastics has not been efficient compared to conventional technologies and has only been employed in special cases. However, laser beam welding of thermoplastics experienced a renaissance with the appearance and availability of high power diode lasers, which are compact (small), reliable, efficient, easy to handle as well as simple to integrate into industrial applications. [6] High power diode lasers offer wavelengths in the range from 750 - 1800 nm [11], while 800, 940 and 980 nm are the typical employed wavelengths. [6] In this wavelength range uncolored thermoplastics show a marked transparency which is only limited by the thickness of the transparent joining partner, the additives added during the manufacturing process of the thermoplastic and the scattering due to the crystallinity of the thermoplastic. [12] Absorption may be adjusted via color pigments such as carbon black (see 2.2 and 2.3). Another laser source occasionally employed is the so called Holmium-YAG laser, which emits laser radiation of 2 μm wavelength. Normally, at this wavelength the optical penetration depth for uncolored thermoplastics is larger than for CO_2-laser radiation but smaller than for radiation in the range of 800 – 1100 nm. Therefore, it allows laser beam welding of two transparent joining partners to a certain extend. [13] One reason preventing industrial use are the costs of this laser beam source. [13]

In all, because of the increased demands on novel products and processing courses as well as the increased availability and efficiency of laser sources both CO_2-lasers and high power diode lasers are the mainly employed laser sources for laser beam welding of thermoplastics today. But still, at the time most applications use high power diode lasers. Not at least it is a question of their favorable cost development [6] as well as the small laser power[6] and beam quality required for joining thermoplastics. Due to this, these laser sources are more and more industrially accepted and employed. Additionally, like Nd:YAG-laser radiation, high power diode laser radiation can be guided via glass fiber cables, facilitating the implementation into existing process courses, such as employment of robots. Therefore, the following remarks are mainly concentrating on the employment of diode lasers[7] for laser beam welding of form stable thermoplastics.

2.1.3 Process applications in industry and additional process equipment

Several companies recognize the advantages as well as the industrial demand and interest of laser beam welding and offer laser systems or entire welding plants. Within Germany about 75 production plants have been put into operation in the last 5 years, approximately. Potential applications welded with laser radiation belong to industries, such as [5],[6]:
- automotive industry (rear light, liquid container, connectors, electronic keys, dashboard, bumper),
- electronics industry (electronic housings, sensors, switches),
- medical industry (dialysis components, injection needles),
- building trade (polymeric windows, large dowels, pump housings),
- household goods (funny glasses, polymeric dishes, shavers).

Besides joining partners, laser beam source, electrical and cooling devices additional equipment is necessary, such as:
- handling or robot system guiding the laser beam (contour or mask welding), scanner system (quasi-simultaneous welding), laser module positioning units as well as beam forming and guiding system (simultaneous welding),
- clamping device, guaranteeing correct fixing and positioning of the joining partners. There are different concepts available, which may be adapted to the actual geometry and needs of the joining partners [5],
- supply and removal system, ensuring an easy handling, while raising automation and throughput,
- on-line process monitoring (see also Ch. 3.3 and 4.3). There are different on-line process monitoring concepts available using signals from the process, such as melting or adding way, clamping pressure or heat radiation.
- laser safety conditions have to be fulfilled.

---

[6] Generally, less than 200 W laser power at the work piece are sufficient for laser beam welding of thermoplastics. However, high power diode laser with powers up to 5 kW are available at the time. [6]

[7] A terse overview of high power diode lasers for laser beam welding of thermoplastics can be found in. [6]

2.2 Process technical considerations
2.2.1 Laser beam adapted design
In obtaining high-quality welds applying laser beam welding of thermoplastics different design technical aspects have to be considered compared to conventional welding technologies, while certain requirements have to be fulfilled, such as:
- constructional or laser adapted design of the joining partners
  - demands on the product reconcile with laser adapted design of the joining partners and the weld seam geometry,
  - guaranteeing clamping and positioning of the joining partners during the irradiation process,
  - considering that joining partners are welded in their final position (if not working with melting way)
  - avoiding or minimizing gaps between the joining partners (if not working with melting way),
  - ensuring accessibility, avoiding beam obstructing parts between laser source and joining area,
- polymer specific design of the joining partners
  - guaranteeing welding suitability of the joining partners (polymer compatibility),
  - considering the influence of processing conditions on crucial demands for laser beam welding of thermoplastics,
  - matching the physical properties (optical, thermal, mechanical) to the laser beam process (overlap joining),
  - considering type, concentration, distribution and size of additives,
  - avoiding impurities[8] and moisture[8] (especially for Polyamide) within the thermoplastics,
- method depending factors of process influence:
  - irradiation method and joint geometry,
  - laser beam source (i.e. wavelength, power) and laser welding plant,
  - joining parameters as well as their clamping strategy, parts supply and removal.

If intending to apply laser beam welding for an existing or new product the laser beam adapted design has to be considered early, in order to use the process technical opportunities and advantages.

2.2.2 Optical and thermal properties
Laser beam welding has to rely on other physical properties of the joining partners than conventional welding technologies. The optical and thermal properties are the most important properties to consider for laser beam welding. The optical properties of the employed materials have to allow the overlap process regarding the used laser beam wavelength. Dyes, crystallinity, additives and other ingredients added to the basic thermoplastic influence the optical properties. On the other hand, they allow adapting the optical properties to the process technical needs. Considering welding of different thermoplastics their polymer compatibility has to be given.

An important measure is the optical penetration depth δ_{opt}. It is defined as the length within a material in direction z of the beam propagation where the original radiation flux Θ_0 is reduced to 1/e. Corresponding to Lambert´s Law [5]:

$$\text{(Eq. 1)} \quad \Theta(z) = \Theta_0 \cdot \exp(-\delta_{opt} \cdot z)$$

The extinction of the original radiation flux Θ_0 is caused by scattering and absorption. Since both physical phenomena appear at the same time it is difficult to separate them. From the physical point of view, absorption is the damping of electro-magnetic waves while propagating through a spatially extended media. Here, absorption takes place because of the interaction of electro-magnetic laser radiation and matter (thermoplastic). Due to dielectric and magnetic losses of the media absorbed energy is transformed into heat energy. In contrast to absorption scattering causes a change of the original intensity distribution due to an interaction of laser radiation and matter. The latter means a change of the original beam propagation behavior of the laser radiation. While scattering is negligible within amorphous thermoplastics, it is of relevance within partial crystalline thermoplastics. Crystalline super structures (spherulites) causing the scattering (a sort of multiple reflection)[9]. The original optical path becomes changed, while the optical path within the scattering medium becomes lengthened. This again causes an increased absorption. Therefore, the absorption increases either with growing degree of crystallinity or at the same degree of crystallinity but smaller (and therefore more) spherulites. Together both

---

[8] Impurities may influence physical properties in a negative and non-reproducible way. Thermoplastics absorb water from the atmospheric humidity. Absorbed water within the thermoplastics may evaporate within the joining area during the process. This may cause formation of bubbles in the weld seam leading to strength minimization and may worsen optical appearance.

[9] GF-reinforced thermoplastics show also marked scattering of the laser radiation. Glass fibers or spheres are transparent for laser radiation in the range of 800–1100 nm. But because of their shape (geometry) they act as an refractive or diffractive structure. The higher the concentration or the smaller the size at the same concentration, resp., the more evident the scattering. In general, the scattering effect is mainly dependent on size, shape, concentration as well as distribution of the scattering centers.

effects (absorption and scattering) cause a broadening of the original intensity distribution and a decrease of the original intensity. Due to scattering broadened intensity distribution may cause broader weld seams. Loss of laser power due to scattering and absorption within the transparent joining partner causes an increased original laser power to guarantee sufficient laser energy for plastification within the joining area[10]. Furthermore, the more laser energy is absorbed per length (volume) within the transparent joining partner, the larger the risk of burning the transparent thermoplastic. Due to this coherences the process window becomes smaller. This example already shows the importance of the optical properties of the thermoplastics to be laser beam welded. Therefore, knowledge concerning influencing the optical properties, while adapting them to the laser beam process is a crucial point of laser beam welding of thermoplastics. The optical penetration depth depends on the actual utilized thermoplastic (chemical compound, chemical ingredients), the morphology of the thermoplastic (e.g. degree of crystallinity) and the processing of the thermoplastic, the used laser wavelength and furthermore, it depends on the nature, quantity (concentration), size and distribution of the added substances, such as color additives as well as flame retardant, filling and reinforcement materials.[11]

While considering thermal properties of thermoplastics, such as melting and decomposition behavior, mechanical strength vs. temperature, phase transition, heat conductivity, thermal expansion coefficient as well as the viscosity, welding of thermoplastics is quite different from welding metals. [8] The temperature within the joining area has to be kept over melting and below decomposition temperature. Therefore, this temperature range may be pretty small. [8] The mechanical strength vs. temperature for thermoplastics is different for amorphous and partial crystalline thermoplastics. Especially, there are no distinct phase transition for amorphous thermoplastics like for metals. Considering the short interaction times of laser radiation with the thermoplastic as well as the low heat conductivity of polymers[12] on the order of $0,1 - 1$ W/(m·K), the intensity distribution is imaged into an energy density profile corresponding to a temperature profile within a layer of the dimension of the optical penetration depth.[13] The large thermal expansion coefficients of thermoplastics do not only support the mixing and diffusion of the thermoplastics to be welded, but also may cause inherent tensions because of shrinkage, even after long periods of time after solidification. Viscosity of plastified (molten) thermoplastics is much larger than for molten metals, therefore, molten thermoplastics do not flow and mix sufficiently within the available interaction time without any external force, such as inherent pressure (see Ch. 2.1.1).

In summary, fulfilling optical and thermal process requirements is mandatory for obtaining high-quality welds.

2.2.3 Process parameter line energy

Describing process behavior as well as determining process window location and extension the "characteristic curve" is commonly used, at present, while displaying strength versus line energy (Fig. 6). Line energy is defined as laser power per feed rate[14]. However, line energy is not a comprehensive process parameter, since it does not take all influencing aspects in consideration, such as beam shape, intensity distribution and process time scales. Therefore, process comparison is limited. There is a necessity for an improved process describing parameter, which considers the interplay of:

- material: physical and chemical properties
- process performance: interaction time(s), feed rate
- laser: power, intensity or intensity distribution
- product: joining partner, seam design

At present, investigations finding a more profound parameter are performed[15]. Fig. 6 also shows microtom cuts of PP samples, while the cuts have been performed for different line energies (numbers 1 – 4). Even if line energy is not an optimal process parameter, pictures in Fig. 6 show a clear dependence of the welding result on line energy.

---

[10] Scattering causes an increased reflection of the laser radiation at the transparent joining partner in all. The degree of surface reflection calculated by means of Fresnel Equations is given to about 8 %, independent on the scattering behavior of the thermoplastic itself. Due to the scattering within the thermoplastic also back scattering occurs ("volume reflection"), which can be "measured as reflected radiation". Therefore, it has been taken into consideration that this radiation also gets lost for the welding process.

[11] Changing the optical properties of the thermoplastic joining partners, while adapting them to both the laser beam process and the intended product design, means in general also changing other physical properties.

[12] The heat conductivity of metals is 3 – 4 orders of magnitude larger than for thermoplastics.

[13] Actually, two time scales have to be considered. On the one hand the time scale of interaction between laser radiation and thermoplastic at a certain point, corresponding to the energy input. On the other hand the time scale of heat conduction, corresponding to energy transportation away from the interaction area.

[14] For contour welding line energy is defined as laser power per feed rate, while it is defined as laser power per irradiated length times interaction time for simultaneous welding.

[15] Process modeling may be able to give more insight into relevant physical phenomena and quantities to consider. [14]
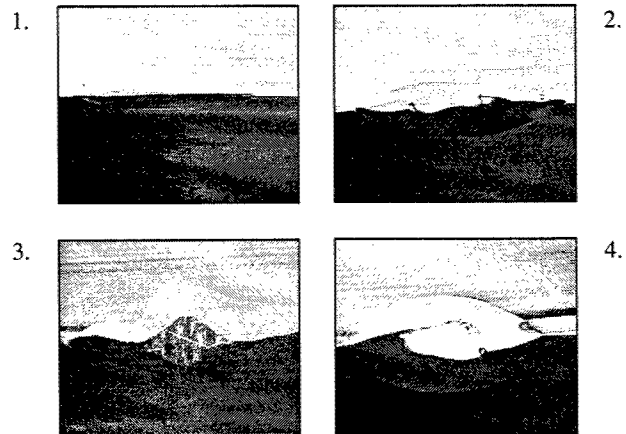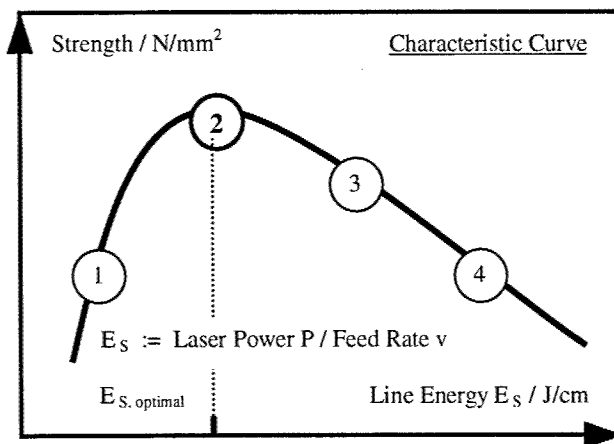
Fig. 6 left: Characteristic Curve – strength vs. line energy E_S – depicting position and extension of the process window
1. adhesion - no weld, 2. optimal weld adjustment, 3. optimal adjustment left - bad weld, 4. decomposition - bad weld
right: corresponding microtom cuts of welded PP samples [source: ILT]

2.2.4 Gap bridging capability

Gaps between the joining partners influence the joining process and its result by avoiding a close contact and therefore thermal conduction between the joining partners, while causing overheating of the absorbing joining partner. Gaps are especially problematic while applying contour welding. It is necessary to avoid gaps. For example, gaps are due to:

- manufacturing process (injection pins, shrinkage),
- parts tolerances,
- clumsy clamping.

There are strategies improving gap bridging capability to a certain extend. Firstly, clever weld seam design may minimize worsening weld quality because of gaps. Secondly, appropriate injection molding conditions and tools may optimize joining partner tolerances. Thirdly, proper adjustment of the optical properties improves process performance and gap bridging capability. For example, while performing systematic examinations on gap bridging capability, PP of different carbon black concentrations have been investigated. In summary, the lower the carbon black concentration (cbc),

- the larger the optical penetration depth, $\delta_{OPT} \propto 1 / cbc$
- the larger the (possible) molten volume, $\delta_{OPT} \propto$ molten volume
- the more moderate the temperature rise, $\delta_{OPT} \propto 1 / \nabla T(x,y,z)$
- the larger the gap bridging capability.   molten volume $\propto$ bridging capability

But this is only valid to a certain extend and at the expense of line energy necessary for melting

$$\delta_{OPT} \propto E_{S. optimal} \quad \text{(see Fig. 7)}$$

Depending on the carbon black concentration and the applied welding strategy, different gap sizes have been bridgeable: 150 µm for a circular spot (contour welding) and 250 µm for a line shaped spot (contour welding).

The less colors of joining partners are weldable the less design freedom obtainable. At the moment several colors are weldable by coincidence or by e.g. adding infrared absorbers[16] (IRA) to the absorbing partner. However, not all color combinations are weldable. Several investigations are focussing on this topic to widen design freedom. Besides applying IRA, another method is based on the approach that a certain color may be achieved by different pigments as well as different pigment arrangements. Generally, there is a gap between acceptable color and weldability of the joining partners for increasing IRA concentration or color pigment arrangement. Several research projects are focused on this topic.

In summary, the optical penetration depth δ_{opt} depends on the carbon black concentration. Besides, infrared absorbers offer the possibility of adapting δ_{opt} to the applied wavelength without influencing the color of the parts. The goal is making gap bridging capability as well as color arrangement predictable for a certain application as well as optimum carbon black and IRA concentration or color pigment arrangement determinable.

---

[16] Infrared absorbers are pigments added to the basic polymer before injection molding. There are different types of IRA available, which show a marked absorption at a certain wavelength or wavelength range. The mean value of the size of the IRA pigments is about 0.5 µm, while showing a pretty sharp Gaussian distribution between 0.3 and 0.7 µm.
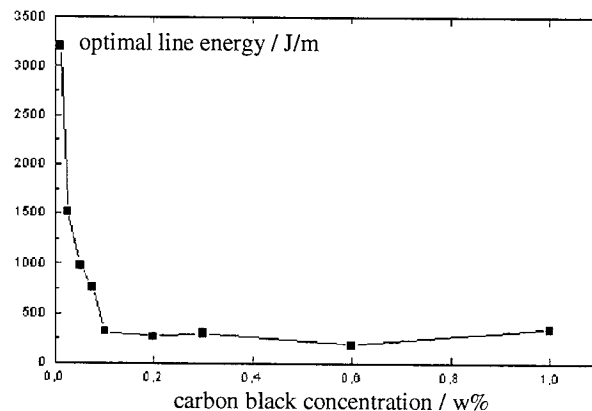
Fig. 7 Optimal line energy vs. carbon black concentration (cbc) for contour welding. The higher cbc, the smaller optical penetration depth. The lower cbc, the more line energy necessary for welding. [source: ILT]

2.3 Process technical challenges

As mentioned above certain requirements have to be met for an efficient application of laser welding of thermoplastics. From this, current challenges to increase the employment potential are :

- improving adaptation of the joining partners design to the welding process,
- beam guiding and beam forming of high power diode laser radiation to achieve simultaneous welding process,
- producing finer (thinner) weld seams for micro applications, such as in life science and medical industry, while using either mask technology or laser sources of higher beam quality, such as fiber lasers,
- strategies improving gap bridging capability of large thermoplastic parts,
- improvement of the pre-, on-line and post process monitoring as well as control,
- extension of the automation potential,
- adapting laser system and equipment to users' needs,
- extending colors of the joining partners which are still laser beam weldable. This maybe is the most important issue.

Several national and international research and development projects are focused on these topics. Therefore, there are good chances to overcome current limitations in the near future.

3 CONTOUR WELDING

3.1 Laser system, materials and samples

Welding flat samples (2x30x60 mm³) a fiber coupled high power diode laser (Rofin DF x06) supplying up to 60 W is applied generating an intensity distribution of Gaussian[17] shape (spot diameter 800 μm, wavelength 940 nm). Welding the rectangular sample boxes (20x20x40 mm³) a fiber coupled high power diode laser supplying 50 W is applied (Gaussian shape, spot diameter 800 μm, wavelength 803 nm). Investigation of flat test samples is focused on obtaining information concerning gap bridging behavior (capability), while the weld is a 17 mm straight line. Investigation of the sample boxes is used for density and burst pressure tests, while the weld seam is rectangular 20 x 40 mm². [7] Three materials are investigated: PA, PC and PP, without any additives. The joint geometry is always overlap. The absorbing joining partners are colored black by adding carbon black. The handling system provides a maximum feed rate of 4 m/min.

3.2 Experimental results

Contour welding experiments are performed in overlap joint geometry at a constant clamping pressure, while varying laser power, feed rate and the gap size. The quality examination of welded samples may be performed by means of destroying or non-destroying investigations. Non-destroying examinations are, i.e.: visual, ultrasonic, x-ray, tightness,

---

[17] The intensity distribution at the fiber end is of top hat shape. Depending on the imaging optic the intensity distribution in the focal spot distinguishes from the top hat shape. Image distortions causing a more or less Gaussian shape of the intensity distribution.

thermographic methods, laser scanning microscopy and computer tomography. Destroying examinations are, i.e.: tensile strength tests, burst pressure tests, microtom cuts, grinding and polishing of cross sectional cuts for microscopy.
The flat samples of PA, PC and PP are colored with different carbon black concentrations resulting in different optical penetration depths. In a first approach, different optical and thermal properties resulting in distinguished gap bridging capabilities, illustrated in Tab. 3. A gap be regarded as bridgeable if the strength of the obtained weld is at least 80 % of the strength for no gap.

Material	carbon black concentration in weight percent	optical penetration depth in μm (@ 808 nm)	optical penetration depth in μm (@ 940 nm)	bridged gap in μm
PA	0.2	52	61	50
PC	0.2	60	71	100
PP	0.7	43	46	50

Tab. 3 Summarizing overview of carbon black concentration, optical penetration depth and bridged gap for the investigated flat samples, while applying contour welding.

The carbon black concentration of the contour welded sample boxes is kept constant at 0.3 w.%. The welded boxes are tested concerning tightness and burst pressure. Tab. 4 gives a summary. Fig. 8 shows the obtained burst pressure vs. the line energy for PA, while three laser powers are investigated. Fig. 9 illustrates microtom cuts of the weld seam for PA sample boxes welded with 3.6 W (see corresponding curve in Fig. 8).

Material	carbon black concentration in weight percent	optical penetration depth in μm (@ 808 nm)	maximum burst pressure in bar of tight boxes
PA	0.3	47	10
PC	0.3	55	7
PP	0.3	71	8

Tab. 4 Summarizing overview of carbon black concentration, optical penetration depth and maximum burst pressure for the investigated sample boxes, while applying contour welding.
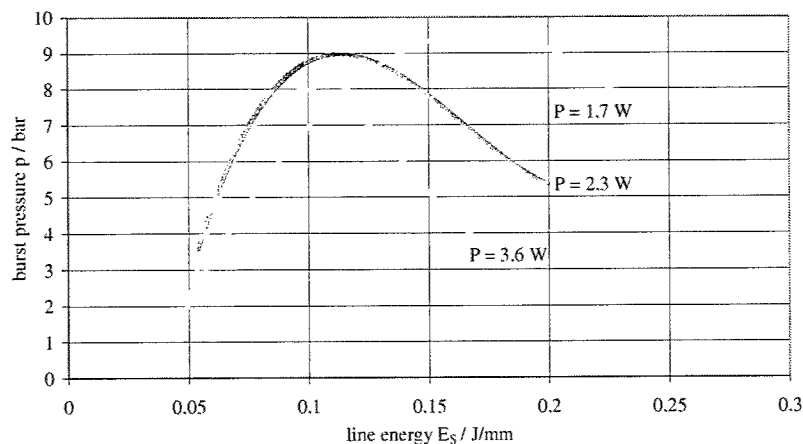

Fig. 8 Burst pressure p vs. line energy E_S for contour welded sample boxes of PA for three different laser powers [source: ILT]
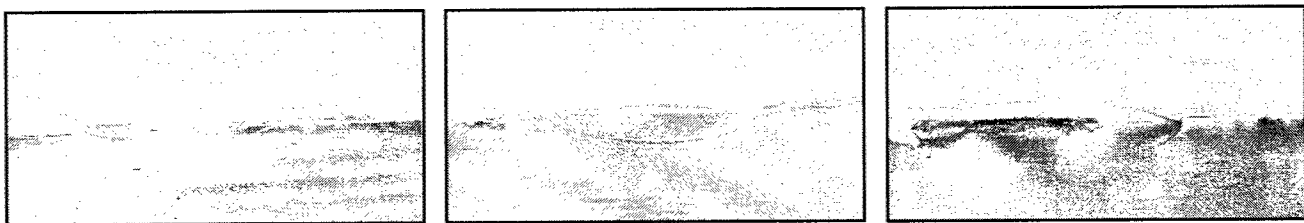

Fig. 9 Microtom cuts of contour welded PA samples (P = 3.6 W). From the left to the right increasing line energy E_S corresponding to constant laser power P but decreasing feed rate v. left: sticking, middle: good weld, right: decomposition (in the center of the heat affected zone). The entire length of depicted microtom cut areas is equivalent to about 1 mm. [source: ILT]

3.3 Process monitoring and control

The temperature range allowing welding of thermoplastics lies between melting and decomposition temperature. This range may be small (only few 10 °C). A process related signal presenting itself for process monitoring and control is the heat radiation emitted out of the irradiated area. The heat radiation can be detected by means of pyrometry.[18] [5][6] If the joining partners are well adapted to the process, which means bridgeable gaps, constant optical properties as well as no acceleration phases during welding, the detected heat radiation signal stays almost constant.[19] However, changes of the optical properties, the gap size or the feed rate along the weld seam contour lead to a decreasing or increasing heat radiation signal. This in turn corresponds to deviations of the weld seam quality. Therefore, the idea consists in using the heat radiation signal as input for a closed feedback loop, while adapting (controlling) the laser power to keep the temperature in the joining area within the appropriate temperature range guaranteeing a high-quality weld. However, certain requirements have to be met for successful on-line process monitoring and control via pyrometry, such as:

- only heat radiation reaching the detector can be measured,
- the detector integrates the measured heat radiation over the imaged area,
- the detector does not perform any spectral resolution,
- the obtained signal is only a measure of the temperature in the irradiated area,
- after process parameters adapted to achieve a good weld a corresponding reference signal has to be defined.

In summary, on-line process monitoring and control via pyrometry for contour welding is a helpful tool to guarantee high-quality weld seams if employment requirements are fulfilled as well as adapted to process technical demands.

4 SIMULTANEOUS WELDING

4.1 Laser system, materials and samples

There are different strategies possible to accomplish simultaneous welding, such as direct irradiation (without any beam shaping after the high power diode laser module), applying classical optics, employing mask technology and application of fiber bundles. At the moment, direct irradiation is the most common method, since sophisticated laser beam guiding and laser beam forming systems are not well matured so far. Applying direct radiation, the challenge consists in positioning the single high power diode laser modules to the weld contour, which consists of straight lines. Additionally, the untreated intensity distribution of the single diode laser modules has to allow lining up the single intensity distributions, while avoiding inhomogeneities in the entire intensity distribution. Employing simultaneous welding also offers the possibility of not generating a closed weld seam contour but several single joints at a time (simultaneous tacking).

Here, while performing simultaneous welding experiments with flat test samples one and with sample boxes six high power diode laser modules are used. All six modules are identical, supplying at a wavelength of 808 nm a maximum output power of 15 W, while generating a intensity distribution in about 100 mm working distance which has the shape of a straight line (20×1 mm^2). The six modules are arranged in a way they irradiate the entire rectangular weld seam contour of the sample box (20×40 mm^2). The applied laser system allows individual steering and interlock control of the laser modules. [7] Investigated materials and test samples are the same like for contour welding.

4.2 Experimental results

Simultaneous welding experiments are performed in overlap geometry at a constant clamping pressure, while varying entire laser power, irradiation time and gap between flat specimen. Corresponding to experimental results of contour welding, the largest gap investigated is 150 μm. Since it is bridged for all three thermoplastics maybe even larger gaps are bridgeable with simultaneous welding. Therefore, first systematic investigations already show simultaneous welding offers larger process windows, an increased gap bridging capability as well as slightly higher weld strength than contour welding (illustrated in Fig. 10, right). Simultaneous welding of the sample boxes assists this statement. Tab. 5 gives a summary (like Tab. 4). Fig. 10 shows the obtained burst pressure vs. the line energy for PA, while three laser powers are investigated. Fig. 11 illustrates microtom cuts of the weld seam for PA sample boxes welded with 62 W (see corresponding curve in Fig. 10).

---

[18] In principle, the heat radiation signal may used to determine the temperature in the joining area. However, this requires a great deal of measurement technique, while specifying the spectral behavior of all heat radiation spectrum influencing components of the beam path of the radiation. Additionally, this expenditure is not necessary. The obtained signal supplies sufficient information.

[19] In general, changes in the emitted (detected) heat radiation due to fluctuations of the laser power are neglectable.

Material	carbon black concentration in weight percent	optical penetration depth in μm (@ 808 nm)	maximum burst pressure in bar of tight boxes
PA	0.3	47	16
PC	0.3	55	10
PP	0.3	71	10

Tab. 5 Summarizing overview of carbon black concentration, optical penetration depth and burst pressure for the investigated sample boxes, while applying simultaneous welding.
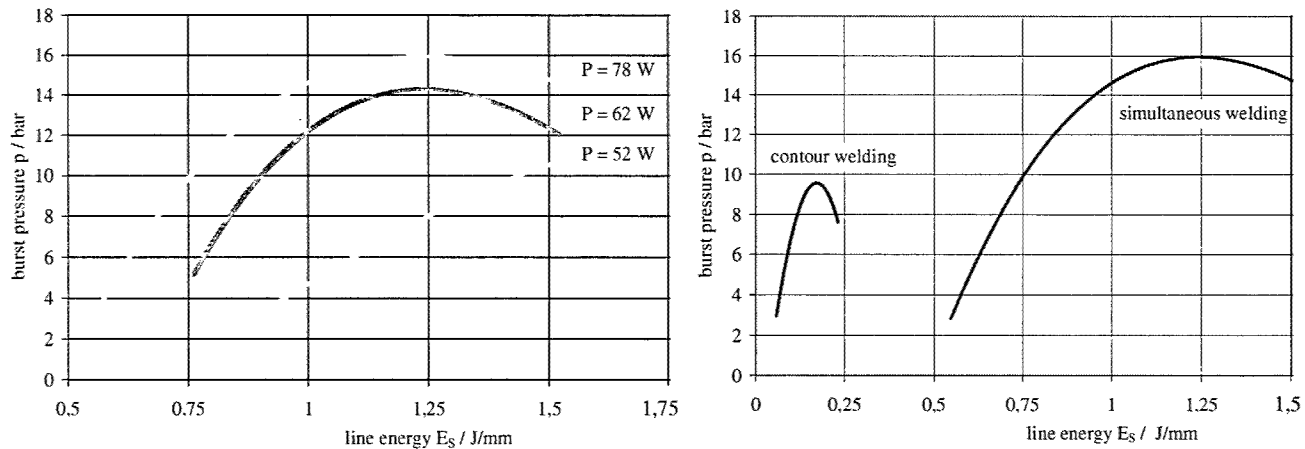
Fig. 10 left: Burst pressure p vs. line energy E_S for simultaneously welded sample boxes of PA [source: ILT]
right: Burst pressure p vs. line energy E_S for contour and simultaneously welded PA sample boxes [source: ILT]
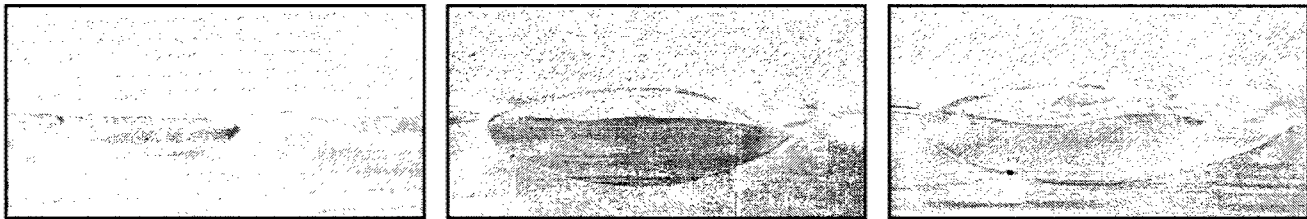
Fig. 11   Microtom cuts of simultaneous welded PA samples. From the left to the right increasing line energy E_S corresponding to constant laser power P and irradiated length l but increasing irradiation period t. left: sticking, middle: good weld, right: hole forming. The length of the depicted microtom cut areas is equivalent to about 1 mm. [source: ILT]

Applying an analytical thermodynamic process modeling program (developed at the ILT) for contour and simultaneous welding, experimentally found statements are verified. Energy and temperature density distribution as well as the volume extension of flat specimen resulting from the absorption of the laser radiation are calculated. [14] The input of heat increases the volume of the absorbing polymer. While looking on the overlap joint geometry this extension is related to the ability to bridge a gap between the joining partners. The extension of the heated polymer as well as the heat flow into the transparent joining partner, if gap bridging occurs, are calculated and so a measure for gap bridging capability is obtained. Calculations offer the determination of the process window. For example: choosing PP with 0,3 w.% carbon black, a laser power of 22 W (800 μm spot), a feed rate of 7 m/min corresponding to a line energy of 193 J/m a gap of 30 μm will be bridged. Simultaneous welding offers extended process windows as well as an increased gap bridging capability compared to contour welding. For example, calculations show for PP with 0,3 w.% carbon black, a laser pulse of 15 W (spot dimension 1,5 x 15 mm^2) and 0,3 s irradiation period (E_S = 300 J/m) a gap bridging capability of 60 μm. [14]

4.3 Process monitoring and control

The entire weld seam has to be monitored if applying simultaneous welding, while monitoring an interaction area of less than 1 mm diameter applying contour welding[20]. Different approaches delivering a spatially dissolved, process related signal allowing on-line process monitoring (or control) for simultaneous welding have been discussed, while detecting the clamping pressure changes or the heat radiation emission during the process, such as piezo techniques, while detecting and monitoring the change of the clamping pressure during the welding process, detector rows along the weld seam (heat radiation), modified pyrometry systems (heat radiation), IR-camera system (heat radiation).

Even if a spatially dissolved, process related signal would be available, two further aspects have to be taken into account. How does the entire monitored weld seam contour correspond to an area which could be controlled and adjusted ? - The challenge of simultaneous welding lies in skilful beam guiding and forming, while obtaining homogeneity over the entire intensity distribution by irradiating the entire weld seam contour at once. Another goal is to obtain a high grade of radiation mixing of all diode laser emitters, so emitter failures do not affect the intensity distribution locally but globally. Each diode laser bars consist of several individual emitters, which show differences in their emitting behavior. If homogeneity and mixing of the irradiating intensity distribution are given a locally adjustment of the intensity distribution becomes difficult. This challenges have to be solved due to appropriate beam guiding and forming (see 2.3).

How could an on-line process control be put into practice ? - Corresponding the obtained signals either an adjustment of the process parameters or the intensity distribution has to be performed or it has to be distinguished between good and bad parts, i.e. a quality control. This could be achieved by adjusting either the irradiation time, the entire laser power or the laser power of an extract from the entire weld seam contour.

Applying an IR-camera (Thermosensorik GmbH) a spatially dissolved, process related signal is obtained. A sample box of PC is irradiated simultaneously with six diode laser modules. The irradiation period is about 0,6 s, while the entire laser power is 80 W. Fig. 12 shows the IR-camera image taken in the moment the lasers turned off. It indicates the heat radiation emitted from the irradiated rectangular seam geometry. Although, at the corners a higher heat radiation emission is detected, the entire weld seam is tight and withstands a burst pressure of about 10 bars. However, high temperature at the corners as well as the not perfect homogeneity of the intensity distribution corresponding to the emitted heat radiation along the straight segments may cause reduced weld quality. Areas of sticking, good weld and decomposition may alternate. Therefore, the adaptation of the intensity distribution to the weld seam geometry needs improvement. However, applying IR-camera supports individual adjustment of the laser modules to the seam contour, gives a measure of the temperature in the welding area during the process as well as indicates process failures, such as melt burr because of a gap or overheating. Especially, the process adapted software of the IR-camera system permits quick data calculations and therefore sophisticated on-line process control and post process inspection. [15]
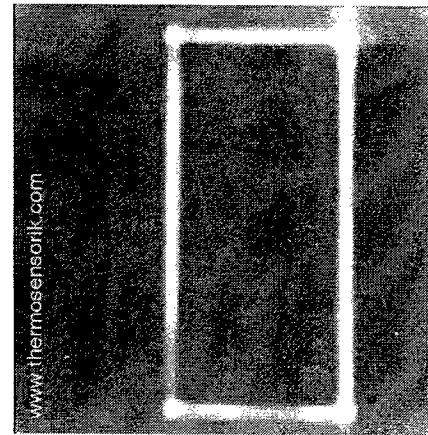

Fig. 12 IR-camera picture of the simultaneously irradiated, rectangular weld seam (20 x 40 mm^2) of a PC sample box. The picture is taken just when all six high power diode laser modules are turned off.

5   CONCLUSIONS

Laser beam welding offers specific process technical advantages compared to conventional joining technologies. However, laser beam welding will and can not replace existing technologies. It has to be seen as a complementary technology with process inherent advantages and disadvantages. Exploiting the numerous advantages certain requirements have to be met, such as laser adapted design, matching the optical properties, guaranteeing clamping and positioning during the irradiation process and ensuring accessibility of the joining area by the laser beam. The imperative challenges for research and development are, at present: producing thinner weld seams for micro applications, while using mask technology or different laser beam sources, extension of colors of the joining partners which are still laser beam weldable, strategies improving gap bridging capability of large plastics parts and improvement of the pre-, on-line and post process monitoring. Contour welding is the most widespread irradiation method. It presents high-quality weld seams while offering flexibility (freedom of design) as well as on-line process monitoring and control via pyrometry. Simultaneous welding asks for an additional challenge to complete the process: clever beam forming and guiding, to achieve a homogeneous and mixed

---

[20]   The signal delivered by pyrometry corresponds to an integration of detected heat radiation over the area imaged onto the detector.

intensity distribution over the entire weld seam contour. However, simultaneous welding offers shorter process times, extended process windows and a marked gap bridging capability. On-line and post process monitoring as well as on-line process control may be achieved by IR-thermography.[21] Current product development, as in microelectronics and photonics industry, is challenged by tasks which often can not be accomplished with traditional tools and therefore asking for new, reliable joining technologies. Keywords are increasing packaging density and decreasing physical volume both corresponding to a sensitive joining environment, efficiency and big lot productions. Laser beam technology offers innovative solutions to overcome limitations of conventional technologies. The process technical progress of the last years as well as current industrial applications and demands are giving reason to the justified assumption of increasing employment of laser beam welding of thermoplastics in the near future.

ACKNOWLEDGEMENTS

REFERENCES

[1]   R.M. Klein, *Bearbeitung von Polymerwerkstoffen mit infraroter Laserstrahlung*, PhD Thesis RWTH Aachen, Fraunhofer-Institut für Lasertechnik ILT, Germany, (1990)

[2]   W.W. Duley, R.E. Mueller, „CO$_2$ laser welding of polymers", Polymer Engineering and Science, Mid-May 1992, Vol. 32, No.9, p. 582 – 585 (1992)

[3]   P.A. Atanasov, „Laser welding of plastics – theory and experiment", Optical Eng. 34/10, p. 2976-2980, (1995)

[4]   C.J. Nonhof, „Laser welding of polymers", Polymer Eng. SCI 34/20, p. 1547-1549, (1994)

[5]   U.A. Russek, G. Otto, M. Poggel, "Verbindliche Nähte – Automatisiertes Fügen von Kunststoffen mit Hochleistungs-Diodenlasern", Laser Praxis, 1/2001, p. 14 - 16, (2001)

[6]   F. G Bachmann, U.A. Russek, "Laser welding of polymers using high power diode lasers", Proceedings Photonics West, (2002)

[7]   U.A. Russek, H. Staub, A. Palmen, „Simultanschweißen von Kunststoffen mit Hochleistungs-Diodenlasern - Qualitativ hochwertige Schweißverbindungen bei kurzen Prozesszeiten", to be published elsewhere, (2003)

[8]   G. Menges, E. Haberstroh, W. Michaeli, E. Schmachtenberg, „ *Werkstoffkunde Kunststoffe* ", 5. völlig neu überarbeitete Auflage. Chap. 12, Carl Hanser Verlag, München Wien, (2002)

[9]   H. Saechtling, *Kunststoff Taschenbuch*, 27. Ausgabe, Tab. 5.6, Carl Hanser Verlag, München Wien, (1998)

[10] D. Hänsch, H. Pütz, H.G. Treusch, Harte und weiche Kunststoffe mit Diodenlaser verbinden, Kunststoffe 88, Carl Hanser Verlag, (1998)

[11] www.Laser 2000.de, contact@laser2000.de, Dr. C. Keusch, Tel. ++49-8153-405-24, christopher.keusch@laser2000.de

[12] D. Hänsch, *Die optischen Eigenschaften von Polymeren und ihre Bedeutung für das Durchstrahlschweißen mit Diodenlaser*, PhD Thesis RWTH Aachen, Fraunhofer-Institut für Lasertechnik ILT, Germany, (2001)

[13] J. Brune, "Thermoplastische Kunststoffe schweissen", Laser Praxis 51, Juni, (2000)

[14] U.A. Russek, M. Aden, "Thermodynamic process modeling of laser beam welding of thermoplastics", to be published elsewhere, (2003)

[15] U.A. Russek, A. Palmen, B. Spellenberg, M. Lopez Saenz, "Process monitoring of simultaneous laser beam welding of polymers using an IR-Camera-System", to be published elsewhere, (2003)

[16] H. Haferkamp, A. von Busse, M. Hudstedt, E. Haberstroh, R. Lützeler, "Bestimmung der Laserschweißeignung von Kunststoffen mit einem thermographischen Verfahren", Der Praktiker, 10, (2002)

---

[21]   Thermography may also used to determine laser welding suitability of thermoplastics, see [16].

[**]   spellenberg@thermosensorik.de; phone: ++49-9131-691-407; fax: ++49-9131-691-419, http://www.thermosensorik.de
Thermosensorik GmbH, Am Weichselgarten 7, D-91058 Erlangen, Germany, info@thermosensorik.de

Laser Beam Soldering – An Attractive Alternative to Conventional Soldering Technologies

Lüdger Bosse[*a], Andreas Koglin[a], Alexander Olowinsky[a], Volker Kolauch[b], Michael Nover[b],

[a] Fraunhofer Institute for Laser Technology ILT, Steinbachstrasse 15, 52074 Aachen, Germany
[b] TechnoFusion GmbH, Kreuzweg 60, 47809 Krefeld, Germany

ABSTRACT

Laser beam soldering (LBS) is a non-standard manufacturing process for electronic packaging and interconnection technology today. Due to the actual trend towards complex and cost intensive products, LBS gains more attention for certain applications in this field. For mass production in automotive applications a fully automated and temperature controlled LBS process was developed. The achieved results are discussed with respect to quality, reliability and process efficiency and compared to established micro flame (hydrogen) soldering technology.

The development of the LBS process is presented. The process window is optimized using High Speed Video Imaging. Temperature signals are logged by means of pyrometry. The processed parts are evaluated with metallographical assessment of solder joint quality. Especially cross sections reveal the fine grained structure and the shape of the meniscus of the solder joints. The reliability is proven using shear strength tests and thermally induced strain cycles. Conclusively, LBS is a stable, reproducible process for applications requiring controlled and locally restricted heat input. The thermal and mechanical stress is reduced in comparison to conventional techniques.

1. INTRODUCTION

Electronic modules for the automotive environment are subjected to very special requirements in terms of performance, functionality and miniaturization on the one hand, and reliability and durability on the other hand. Especially the area under the hood calls for solutions with high-end properties in consideration of thermal conditions. As a consequence thereof the demands on the material choice, the packaging and interconnection technology are very sophisticated.

Thick-film or hybrid circuits have a high level of integration and an excellent performance in harsh environments (Ref. 5). This special kind of circuits consist of screen printed layers of conductive, dielectric or resistive materials on alumina (Al_2O_3) or infrequent on beryllia (BeO) substrate. These layers are applied in form of an ink or paste, are subsequently dried and sintered at high temperatures, where they form a strong bond with the substrate. Thus a double-sided substrate with multilayers and integrated resistors is obtained to which housed components can be soldered and naked dice can be bonded. For conductor tracks gold, silver, silver-palladium and silver-platinum pastes are used depending on the interconnection technology and resistance. The thickness of conductive layers are in the region of 10 μm for a fired track. For extremely high conductance tracks a thick print is used. These can be realized with a thickness up to 80 μm.

The interconnection from the substrate to the next package level, which is usually a plastic housing, is achieved by either a thick wire or ribbon bonding or soldered leads. Up to now the established types of soldering technologies are micro flame soldering and reflow soldering. The former allows the leads to be integrated into the housing but is a sequential process (Ref. 4). The latter is a parallel process, but the leads cannot be part of the housing. Since high temperature solder is used for automotive applications with maximum ambient temperature of 140 °C, the plastic typically will not withstand the required reflow temperatures (Ref. 5).

Already a few years ago LBS has been reported to be a feasible process in assembly of electronic components, thick-film hybrid circuits in particular (Refs. 1-2). However, no detailed report on implementation of LBS in a fabrication line for this kind of products is available. The purpose of this investigation is to assess the manufacturing feasibility of LBS in comparison to established joining technologies.

---

* bosse@ilt.fhg.de; phone +49 (0)241 8906-305; fax +49 (0)241 8906-121; www.ilt.fhg.de

2. EXPERIMENTAL SETUP

1. Specimen

The specimen used in the experiments is an automotive microelectronic module (alternator regulator realized in thick-film technology) with solder pads printed on an alumina substrate (Fig. 1). The housing has seven terminal leads to be soldered to the substrate. The dimensions and the compositions of the terminal lead and the solder pad are shown in Table 1. The entire alumina substrate is glued by a heat conducting adhesive to an aluminum base plate.
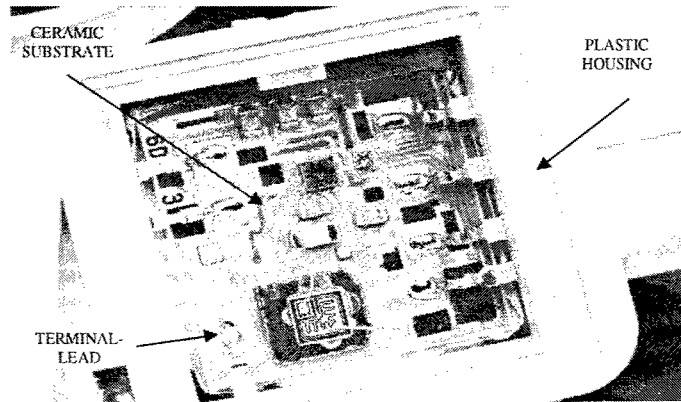

Fig. 1 Automotive microelectronic module in a plastic housing - alternator regulator –

Table 1 Specimen Data

Part name	Thick Film Alternator Regulator
Materials	
Terminal Lead	SAE CA 260 brass, ½ hard, Nominal composition is 70%Cu-30%Zn, 1.0 mm wide x 0.3 mm thick, tin-plated. The end is semicircular in shape with a 0.5 mm radius
Solder Pad	Sn10Pb88Ag2, 2.0 mm x 2.0 mm x 0.2 mm thick, melting point: 268 °C (solidus) / 290 °C (liquidus)
Alumina Substrate	94 % nominal Al_2O_3, 0.5 mm thick
Aluminum Base Plate	AA 3003-H14
Plastic Housing	Polybutylene terephthalate with 30% glass fiber (PBT-GF30)

2. Procedures

The major components of the experimental set-up are a fiber coupled, continuous wave (cw) diode laser system and a processing head with an integrated pyrometric and power sensor (Fig. 2).
The diode laser system has a maximum optical output power of 500 W, which can be modulated by controlling the pump current. The diode laser radiation emitted from the optical fiber is collimated by a lens (lens 1) and reflected by a deflecting mirror (mirror 1). A part of the laser radiation is transmitted by the deflecting mirror (mirror 1) and collected by a power detector integrated for online monitoring. The power detection is realized by a silicon photodiode. electronically intensified by a transimpedance amplifier circuit. The collimated laser beam passes through a galvanometer scanner and is focused by a f-Theta lens on the lead/solder pad area to generate the joint. The circular focus geometry of the laser beam is aligned to the center of the semicircle at the end of the terminal lead (Fig. 3). The working distance between the optics and the laser beam interaction area is about 80 mm. Using an image projection ratio of 1:2 the minimum focal diameter is 1.2 mm, which is the double fiber core diameter of 0.6 mm.
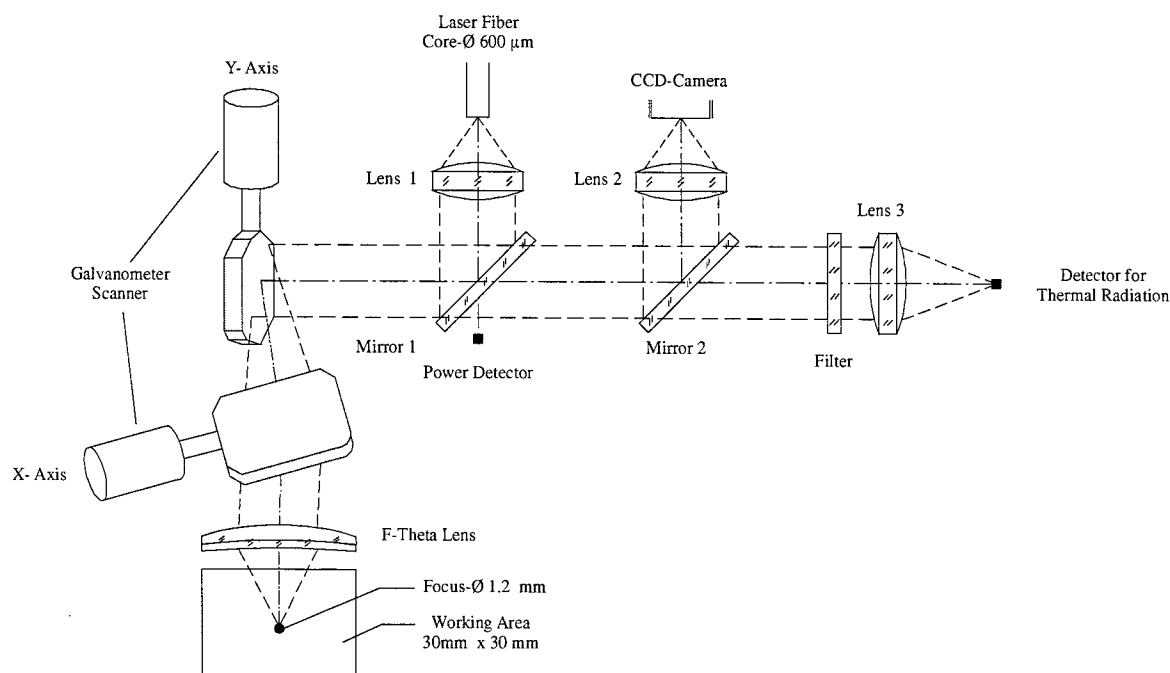
Fig. 2 Structure of the processing head

The thermal radiation emitted from the surface follows the beam delivery system of the galvanometer scanner and passes through the deflecting mirrors (mirror 1, mirror 2), which are transparent for this wavelength range. After passing the deflecting mirrors the thermal radiation is focused by a lens (lens 3) on a photo detector (Ex. InGaAs, peak wavelength 2.3 µm). The output signal of the detector is conditioned by a logarithmic amplifier circuit. Laser radiation reflected from the irradiated surface is blocked by optical filters. The integrated pyrometric sensor is conditioned for laser beam applications with process temperatures in the range of 150 °C, e.g. welding of plastics or soft-soldering. The pyrometric sensor is calibrated by means of a standardized black body and the response time of the sensor is about 1 ms at 150 °C.

The surface of the lead/solder pad area is imaged onto a CCD camera via a deflecting mirror (mirror 2).

The terminal leads are formed and prepared for soldering by precise bending and tin-plating. As shown in Fig. 3 the terminal leads are positioned applying a low pressure on the corresponding solder pads. A small amount of flux (low concentrated adipic acid) is applied to the lead/solder pads before soldering. In contrast to the state-of-the-art micro flame soldering process and the quoted LBS process of hybrid circuits no extra preheating of the specimen is necessary (Refs. 1, 2, 4).

The sequences of the LBS process are visually recorded by high-speed imaging. During the experiments the recording rate was 4500 frames/s. Important test conditions are summarized in Table 2.

Table 2 Test Conditions

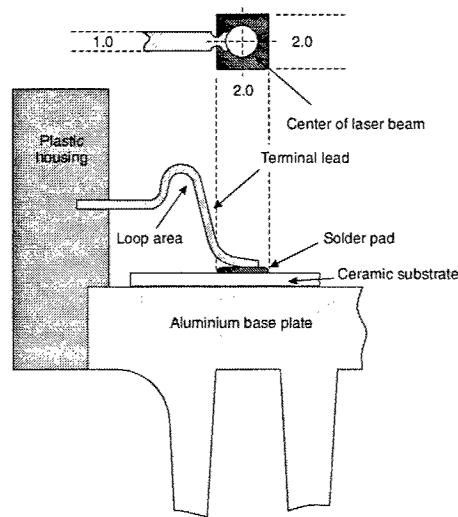| Beam Spot Diameter	1.2 mm @ $1/e^2$ (focal position)
Basic Conditions	no extra preheating no shielding gas against oxidation
Flux	Adipic acid (1.5%)
Terminal Lead/Solder Pad Contact	0.75 mm vertical deflection of the lead (corresponding contacting force ranged from approximately 50 to 150 g, depending on the length of terminal lead)

Fig. 3 Solder joint configuration (dimensions in mm)

3. DATA AND RESULTS

The thermal behavior of the examined specimens is significant for the LBS process. Due to the harsh environments under the hood the materials and the geometry are adapted and optimized. On the one hand the thermal characteristics of the specimens guarantee the field-tested functionality and on the other hand determine conditions of the soldering process.

To get a prediction of the thermal behavior during the soldering process the temperature distribution caused by laser irradiation is simulated (commercial software[1]). Using the specified data as input for the simulation, the following snapshot of thermal behavior of an irradiated contact is computed (Fig. 4, left hand side). The right hand side of Fig. 4 shows a cross sectional view of a soldered joint.
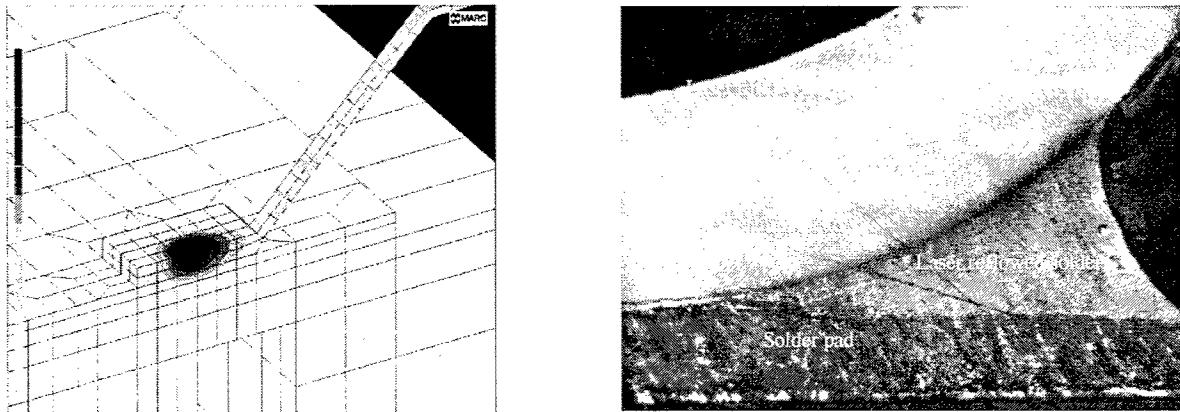

Fig. 4 (left) Snapshot of the thermal behavior of an irradiated contact (computed)
(right) Cross sectional view of a soldered joint;
Optical power: 80 W, irradiation time: 1000 ms, focal diameter: 800 μm.

Apart from the thermal properties of the substrate the results of the simulation imply that the terminal leads consisting of 0.3 mm thick tin-plated copper behave like heat sinks. Even through a temperature of slightly more than 600 °C was applied, the solder pad on the ceramic substrate exceeds the melting point of the solder alloy only very localized (Fig. 4,

---

[1] Marc Mentat   MSC Software Corporation
               Marc   Nonlinear Finite Element Solver with Parallel Processing
               Mentat   Graphical User Interface to the Marc Nonlinear Finite Element Solver

left hand side). Due to this special fusibility of the solder pad quantitatively appointed by the selected process parameters and the given system properties it is very complex to generate a sufficient solder joint. The maximum duration of the irradiation is predetermined by the work cycle of the production line, whereas the lower limit of laser beam power is given by the needs of melting an adequate area of the solder depot. The upper limitation of the supplied power is exceeded if signs of overheating or cracks in the ceramic substrate occur. According to these demands a suitable process window has been found in context of a feasibility study. The reliability and quality of the determined combination of process parameters could be proven by means of high-speed imaging and metallographical analyses of solder joints. In Fig. 5 selected frames of the joining area during irradiation are represented.
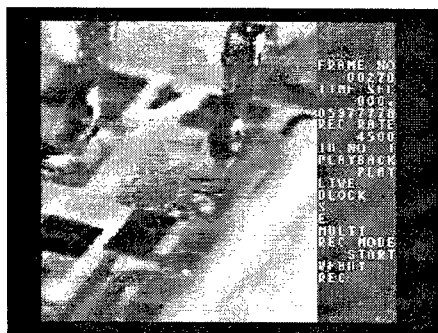
Frame 270: Lead/solder pad (initial situation)

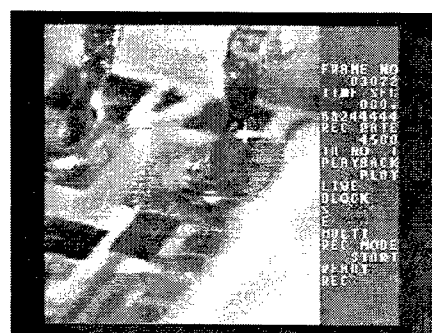Frame 290: Tin-Plating reaches the melting temperature

Frame 353: Thermal activation of the applied adipic acid and outgassing of the volatile components of the solder depot

Frame 637: Wetting of the terminal lead

Frame 1469: Appearance of a bubble

Frame 3072: Soldered joint (final state)

Fig. 5 Selected frames of the joining area during irradiation; irradiation time: 600 ms.

Apart from the interconnection requirements a high production rate has to be ensured by the LBS process to remain attractive for mass production. For this reason the total process period, especially the irradiation time, has to be as short as possible. But to achieve a sufficient solder joint with reduced irradiation time the laser power has to be increased. To avoid the hazard of superheating the laser power has to be limited and controlled. Therefore the thermal radiation from the interaction zone is detected and analyzed in more detail. In a series of experiments the following features could

reproducibly be observed in the recorded pyrometric signal. A typical profile is presented in Fig. 6, where the laser is switched on at time t = 0.2 s. At point [A] the reduction of the ascending slope indicates the beginning activation of the applied adipic acid. The second changing in the pyrometric signal at point [B] is related to the onset of localized melting of the solder pad and outgassing of volatile components. Due to the continued energy input by the laser beam the terminal lead reaches the wetting temperature (point [C]). In the next phase there is a sudden improvement in heat dissipation due to the wetting of the terminal lead, which often results in a temperature decrease (point [C] to [E]). At point [D] a gas bubble consisting of volatile components steps out of the molten solder. The variation of the signal curve following point [E] is induced by self-optimizing the surface tension and by superheating of the molten solder pool. After the laser beam is switched off at t = 1.2 s, very high cooling rates are observed. This high rate is caused by the optimized heat transfer into the aluminum base plate. At point [F] the solder solidifies. The change of the descending slope in the signal curve at the crystallization point [F] is known from the thermal analysis of solidification reactions in literature (Refs. 6-7).
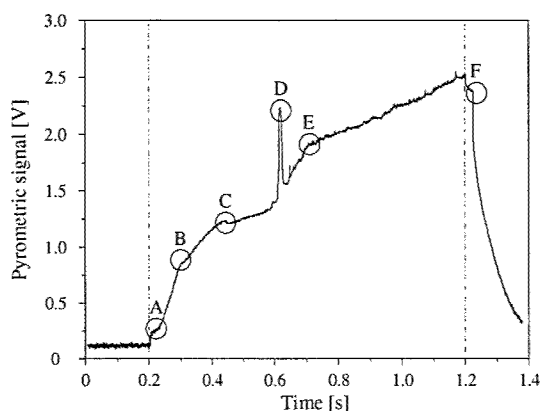

Fig. 6 Pyrometric signal detected during soldering; irradiation time: 1000 ms.

In order to quantify the achieved quality of the solder joints, simple tensile/shear tests are accomplished. In Fig. 7 the arrangement for the tensile/shear tests (left) and exemplarily a force/elongation diagram of a laser soldered specimen (right hand side) is represented. A defined traction is applied by a curved wire. Furthermore the arisen places of failure are drawn in. The breaking strain is exceeded either at the terminal lead, at the area of reduced diameter, or within the reflowed solder pad. Since the strains can not clearly be dedicated to be tensile or shearing stresses, the measured data are only meaningful in direct comparison. Therefore the obtained results are only to be understood as necessary and not as sufficient evaluation criteria.
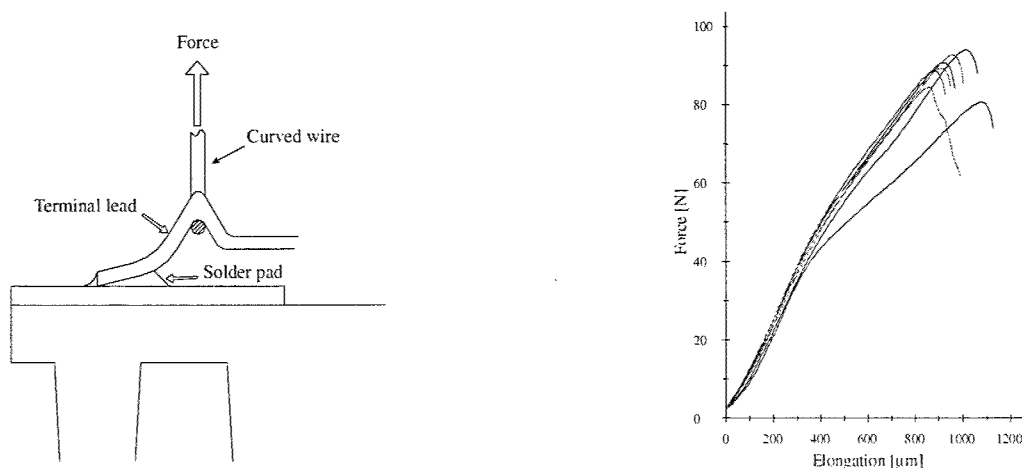

Fig. 7 (left) Arrangement for the tensile/shear tests in principle;
(right) Example of a force/elongation diagram of a laser beam soldered specimen; irradiation time: 300 ms.

Table 3 summarizes the obtained results of maximum tensile shear stress (Rm) related to specific terminal leads. The table represents in detail the average values (Xm), the standard deviation (S) and the coefficient of variance (v). Due to the fact, that usually the given reference values are reached or even exceeded with at least one process parameter set, the potential of LBS can be shown.

Table 3 Average value of maximum tensile shear stress (R_m) of micro flame or laser beam soldered specimen*

R_m [N]	Micro flame soldered specimen (references)	Laser beam soldered specimen			
		Irradiation time 1000 ms manual fluxing	Irradiation time 400 ms manual fluxing	Irradiation time 300 ms manual fluxing	Irradiation time 300..1000 ms automatic fluxing
Terminal 1					
X_m	87.5 (6)	88.7 (8)	78.5 (8)	84.4 (8)	88.1 (6)
S	5.1	3.6	7.9	8.3	4.0
v	5.9	4.1	10.0	9.8	4.5
Terminal 2					
X_m	87.4 (6)	84.0 (8)	78.4 (8)	81.8 (8)	86.8 (6)
S	1.8	4.9	6.1	8.9	3.4
v	2.0	5.8	7.8	10.9	3.9
Terminal 3					
Xm	85.5 (6)	77.2 (8)	76.8 (8)	80.4 (8)	85.0 (6)
S	3.6	10.0	7.7	9.1	4.6
v	4.3	12.9	10.1	11.4	5.4
Terminal 4					
Xm	81.9 (5)	79.1 (8)	81.6 (8)	80.5 (8)	79.2 (6)
S	3.7	1.35	0.7	1.8	2.6
v	4.5	1.71	0.9	2.2	3.3
Terminal 5					
Xm	91.2 (6)	89.3 (8)	88.3 (8)	84.7 (8)	92.8 (6)
S	1.7	4.8	7.7	6.8	0.8
v	1.8	5.4	8.7	8.1	0.9
Terminal 6					
Xm	92.4 (5)	93.5 (8)	93.3 (7)	93.3 (7)	91.8 (2)
S	1.4	1.4	1.1	0.9	0.1
v	1.5	1.5	1.1	1.0	0.1
Terminal 7					
Xm	79.5 (5)	89.0 (8)	93.9 (8)	92.4 (8)	80.0 (6)
S	1.7	4.4	1.1	1.4	4.1
v	2.1	4.9	1.1	1.5	5.1

* (n) Number of considered terminals – the remaining ones are used for the metallographical assessment.

4. CONCLUSION

The presented work shows that LBS is an attractive alternative in comparison to conventional soldering technologies for the presented kind of challenging soldering tasks. Apart from the well-known advantages of LBS, controlled and localized heat input as well as reduced thermal and mechanical stress, the achieved data and results prove quantitatively the potential of this technology. The statistically implemented tensile/shear tests on the one hand and the randomly carried out metallographical assessments on the other hand point out the high quality of laser beam soldered joints. Moreover, all tested specimens have successfully passed a standardized, thermally induced strain cycles trial (1000 cycles, –40 °C to +140 °C).

Due to the consequently performed parallel recordings of pyrometric signals and high speed imaging advanced process knowledge concerning LBS of hybrid circuits was acquired. In order to achieve a reliable and stable process it is inevitable to be able to monitor process relevant signals online. In addition it is necessary to relate the detected signal characteristics to physical and chemical phenomena in the beam interaction area. Previously reported methods for closed-loop controlled LBS are now applicable for this kind of specimens (Ref. 6). Based on the powerful combination

of the fast adjustment of laser power and closed-loop temperature control it will be possible to improve the stability of LBS and to produce hybrid circuits with constant high quality solder joints. The pyrometric signal, the laser power and the correlation of both can be used to compensate deviations of the process relevant values of the specimens and to differentiate between good and bad solder joints. In opposition to the established micro flame soldering one hundred percent online-control is feasible. As quality assurance considerations become more and more important this in particularly essential for industrial processes.

For future work this knowledge will be used to optimize the rate of LBS joints and consequently the level of process control. The long-term objective is to provide a highly flexible production cell for mass production that simplifies automation and production employing closed-loop controlled LBS.

ACKNOWLEDGEMENTS

REFERENCES

1. D. U. Chang, "Method of Laser Soldering", *United States Patent*, **4,531,044**, 1985.
2. D. U. Chang, "Experimental Investigation of Laser Beam Soldering", *Welding Journal*, **October**, pp. 33-41, 1986.
3. D. A. Davis, "Interconnection Construction to Thick Film Substrate", *United States Patent*, **4,470,648**, 1984.
4. J. Engbring and D. Jedritza , "Gehäusemontage von Keramikhybriden mit Hilfe eines Flammlötprozesses, *VTE* **3**, pp. 130-135, 1998.
5. P. Sommerfeld, D. Jendritza, S. Hell, "Advanced Packaging and Interconnection Technologies for Automotive Microelectronic Modules", *Advanced Microsystems for Automotive Applications*. **99**, pp. 111-119, 1999.
6. L. Bosse, A. Schildecker, A. Gillner, R. Poprawe "High quality laser beam soldering", *Microsystem Technologies*, **7**, pp. 215-219, 2002.
7. L. Bosse, A. Gillner, R. Poprawe, "Adapted time-power profile for laser beam soldering with solder paste", *Proceedings of SPIE*, **4406**, pp. 76-81, 2001.

Out of the SHADOW: Watch Parts in the Spotlight
Laser Beam Micro Welding of Delicate Watch Components

Thorsten Kramer[*], Alexander M. Olowinsky[**]

Fraunhofer Institute for Laser Technology ILT, Aachen, Germany

ABSTRACT

Conventional joining techniques like press fitting or crimping require the application of mechanical forces to the parts which, in combination with the tolerances of both parts to be joined, lead to imprecision and poor tensile strength. In contrast, laser beam micro welding provides consistent joining and high flexibility and it acts as an alternative as long as press fitting, crimping, screwing or gluing are not capable of batch production. Different parts and even different metals can be joined in a non-contact process at feed rates of up to 60 m/min and with weld seam lengths from 0.6 mm to 15.7 mm. Due to the low energy input, typically 1 J to 6 J, a weld width as small as 50 μm and a weld depth as small as 20 μm have been attained. This results in low distortion of the joined watch components.

Since the first applications of laser beam micro welding of watch components showed promising results, the process has further been enhanced using the SHADOW technique. Aspects of the technique such as tensile strength, geometry and precision of the weld seam as well as the acceptance amongst the -mostly conservative- watch manufacturers have been improved.

Keywords: Micro Technology, Laser, Micro-Parts, Mounting and Connecting Technique, Joining, Welding, Metals

1. INTRODUCTION

1.1. SHADOW

Watch manufacturers are challenged to offer a short time to market and a flexible and cost effective fabrication. The ability to switch fast from one design to the next is the prerequisite for modern and competitive manufacturing. In particular, rapid, flexible, reliable and precise joining techniques are vital to fulfill this goal. Common joining techniques reach their limits in flexibility, reproducibility, preparation and cycle time. At present the following joining techniques are deployed in watch manufacturing:

- Gluing
- Screwing
- Press fitting
- Crimping
- Flanging
- Riveting

Gluing demands a pre-treatment to prepare the joint areas of both partners. The small amount of adhesive is difficult to handle: both getting always the same amount of adhesive and keeping the environment (air temperature and humidity) stable set high requirements to the machine set-up. After joining the parts have to be cleaned as well.

All further techniques mentioned above apply mechanical forces to the parts which may lead to a distortion of the parts. An active position control is not possible and the tolerances of both parts may accumulate. The joining tools wear out and need to be re-machined if a single part is modified. Therefore reducing the distortion of the part as well as its contamination is one more challenge a new joining technique has to face.

Laser beam micro welding offers outstanding advantages such as a non-contact process and no wear-out and is a flexible joining technique in terms of energy deposition, part geometry and material. There are two welding techniques currently known: pulsed mode (pm) and continuous wave (cw) welding. Pulsed mode welding generates a joint seam by a series of overlapping single pulses. It is relatively slow and limited by the repetition rate of the laser beam source

---

[*] thorsten.kramer@ilt.fraunhofer.de; phone +49 241 8906 -407; fax +49 241 8906 -121;
Fraunhofer Institute for Laser Technology ILT, Steinbachstr. 15, 52074 Aachen, Germany
[**] alexander.olowinsky@ilt.fraunhofer.de; phone +49 241 8906 -491; fax +49 241 8906 -121;
Fraunhofer Institute for Laser Technology, Steinbachstr. 15, 52074 Aachen, Germany

typically $f_P < 200$ Hz and $f_P = 1\,000$ Hz at maximum using Nd:YAG laser beam sources. The beam diameter in the focus ranges approximately from $2w_f = 50$ μm to $2w_f = 400$ μm and weld widths between $b = 100$ μm and $b = 800$ μm can be obtained. Short laser pulses of a few milliseconds in duration lead to a small heat affected zone (HEZ). The fast heating and cooling phases may lead to high tensile and compressive stresses resulting in a distortion of the parts. Since the material cools down beneath its solidus temperature between two successive laser pulses, each pulse has to melt the material again and thus a high amount of energy is deposited in the parts. This high energy input may lead to a distortion of the part. At the transition from solid to liquid and if the temperature of the melt exceeds evaporation temperature droplets may be ejected from the melt and lead to debris on and contamination of the parts. State-of-the-art Nd:YAG laser beam sources are capable of pulse forming, i.e. the varying of the power over the pulse duration. With a process adapted pulse form the energy input as well as the maximum melt temperature can be adjusted.

In continuous wave welding a constant laser power is applied and the parts are moved relatively to the laser beam to generate a weld seam. Depending on the laser power and the feed rate the energy input in the parts varies. The so-called line energy q is the ratio of laser power P_{av} and feed rate v_f:

$$q = \frac{P_{av}}{v_f} \tag{1}$$

If the line energy is low, either the laser power P_{av} is low or the feed rate is v_f high, the energy deposited in the parts is low and at a constant line energy the heat affected zone can be minimized by increasing laser power P_{av} as well as feed rate v_f. The maximum feed rate is only limited by physical effects such as humping and goes up to 50 m/min.

The continuous process can be described as steady state, the energy input is lower, the probability of droplet ejection is smaller and the surface of the weld is smoother and more uniform. The lengths of the weld seams in micro applications are in the range of only a few millimeters, therefore the process time is smaller than 50 ms.

The beam quality of pulsed laser sources is better by a factor of two compared to the beam quality of a continuous wave laser source at the same laser power, e.g. a pulsed laser source with an average output power $P_{av} = 60$ W and a maximum pulse power $P_H = 3\,000$ W has a beam quality $M^2 = 30$ (10 mm·mrad) whereas a continuous wave laser source with an average output power $P_{av} = 3\,000$ W has a beam quality $M^2 = 75$ (25 mm·mrad). The better the beam quality (the smaller the value) the smaller the beam diameter in the focus at a constant focal length. The minimum beam diameter in the focus is $2w_f = 200$ μm, thus weld widths are down to $b = 300$ μm.

Regarding the investment costs a pulsed laser sources is half the price of a continuous wave laser source and in general the use of a continuous wave laser beam source for micro applications is not efficient.

As a consequence the optimum laser beam welding technique should combine the machine related advantages such as good beam quality and pulse forming with the continuous process management. This means to create a continuous weld seam using pulsed laser radiation source at high feed rates and is called SHADOW technique. The time dependent power of a single pulse generates weld seams of up to 15.7 mm in length.

1.2. Fundamentals

In general, two welding processes are differentiated: heat conduction welding and deep penetration welding. They are distinguished by the so-called aspect ratio r, the ratio of weld depth s to weld with b:

$$r = \frac{s}{b} \tag{2}$$

Figure 1 shows the weld depth s depending on the Intensity I for continuous wave CO_2-laser radiation at a feed rate $v_f = 10$ mm/s. The laser power was kept and the beam diameter was varied from $2w = 800$ μm down to $2w = 80$ μm. At a certain intensity I_{thres} the weld depth s increases rapidly, a keyhole is generated and the process switches from heat conduction to deep penetration welding. The threshold intensity I_{thres} is depending on the material, the laser source and the feed rate. For micro welding applications the increase in weld depth is much smaller. For a certain weld with a keyhole may no longer be generated or the absorption of the laser radiation within the keyhole may not be dominating the process because the diameter and the depth of the keyhole are too small. The absorbed laser power $A_\lambda \cdot P_{av}$ is apportioned to three parts: power required to keep up the keyhole P_k, power for welding P_w and heat conduction loss P_{HL}:

$$A_\lambda \cdot P_{av} = P_k + P_w + P_{HL} \tag{3}$$

The power P_k required for the upkeep of the key is constant and small compared to the power P_w for welding and the heat conduction loss P_{HL}. For large beam diameters $2w_f$ the heat conduction loss is low and the factor f_{HL} of heat conduction loss can be calculated by

$$f_{HL} = \frac{\arctan\left(\frac{\sqrt{8\kappa t}}{w}\right)}{\frac{\sqrt{8\kappa t}}{w}} \qquad (4)$$

for a Gaussian intensity distribution.

Figure 1:
Weld Depth
Depending on
Intensity
CO_2 laser radiation
$\lambda = 10.6\ \mu m$
$P_{av} = 2\ 000\ W$
$v_f = 10\ mm/s$
protection gas:
helium
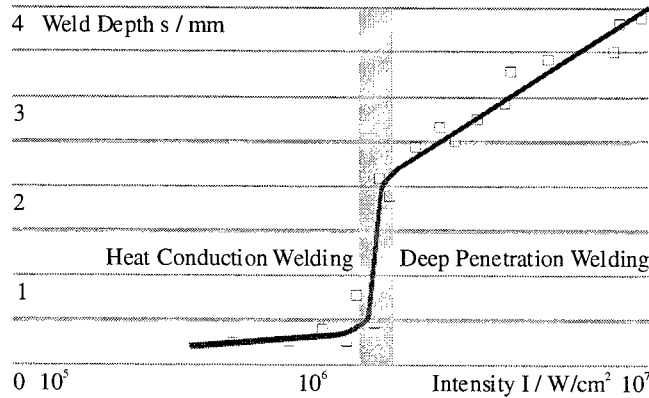
Figure 2:
Heat Conduction
Loss Depending on
Beam Diameter

$\tau_h = 20\ ms$
temperature conductivity
■ stainless steel   copper
$\kappa = 3.79 \times 10^{-6}\ m^2/s$ $\kappa = 114.8 \times 10^{-6}\ m^2/s$
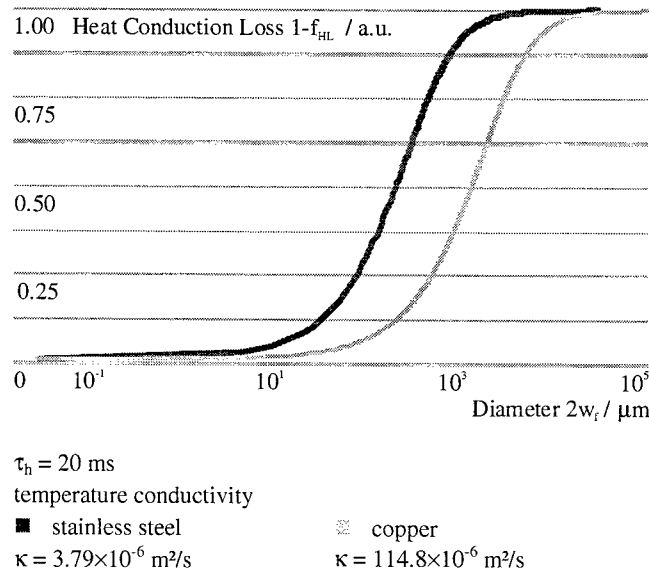
Figure 2 shows the factor $1\text{-}f_{HL}$ of heat conduction loss depending on the beam diameter $2w_f$ at a pulse duration $\tau_H = 20\ ms$ for stainless steel and copper. At a value $1\text{-}f_{HL} = 1$ there is no heat conduction loss. For beam diameters in the range of $2w_f = 100\ \mu m$ the factor of heat conduction loss can not be neglected.

2. EXPERIMENTAL SET-UP

Two experimental set-ups have been used to weld the delicate watch components. Set-up A comprises a pulsed laser source, a prototype Lasag KLS 246 RTPS, and the high speed axis, as shown in Figure 3. The laser beam is focused by

an optics with a focal length of f = 100 mm onto the surface of the workpiece. The beam diameter in the focus is down to $2w_f = 60$ μm. The focusing optics can be revolved. The high speed axis is capable of turning up to 13 500 rpm with a concentric running of 2 μm. The watch parts to be welded can be inserted into a workpiece holder and are kept in position by means of vacuum.

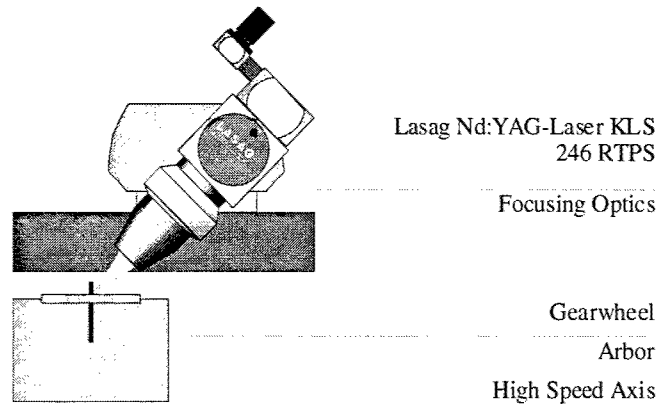**Figure 3:**
Schematic Drawing
of Set-up A

Lasag Nd:YAG-Laser KLS
246 RTPS

Focusing Optics

Gearwheel
Arbor
High Speed Axis

Figure 4:
Schematic Drawing
of Set-up B

Scanner

Balancier
Workpiece Holder
Lasag Nd:YAG-Laser
SLS 200 C32
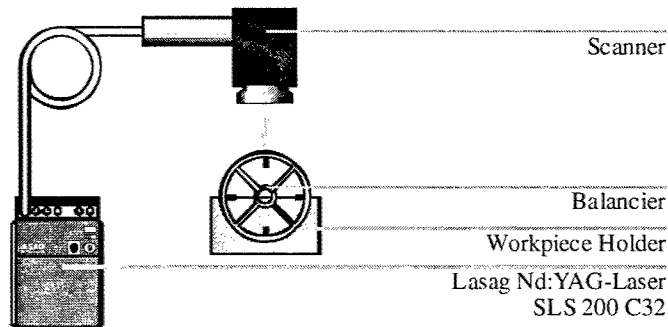
Figure 4 shows set-up B. The Nd:YAG laser radiation is transferred from the laser beam source, a Lasag SLS 200 C32, to a two axis galvanometer scanner by a fiber with a core diameter of 100 μm. The f-Theta focusing lens of the scanner has a focal length of f = 80 mm. Therefore the beam diameter in the focus is approximately $2w_f = 80$ μm.

Figure 5:
Experimental
Set-up A

Monitoring CCD-Camera

Lasag Nd:YAG-Laser KLS
246 RTPS

High Speed Video System
Focusing Optics

Diode Laser Illumination
Workpiece Holder
Vacuum System
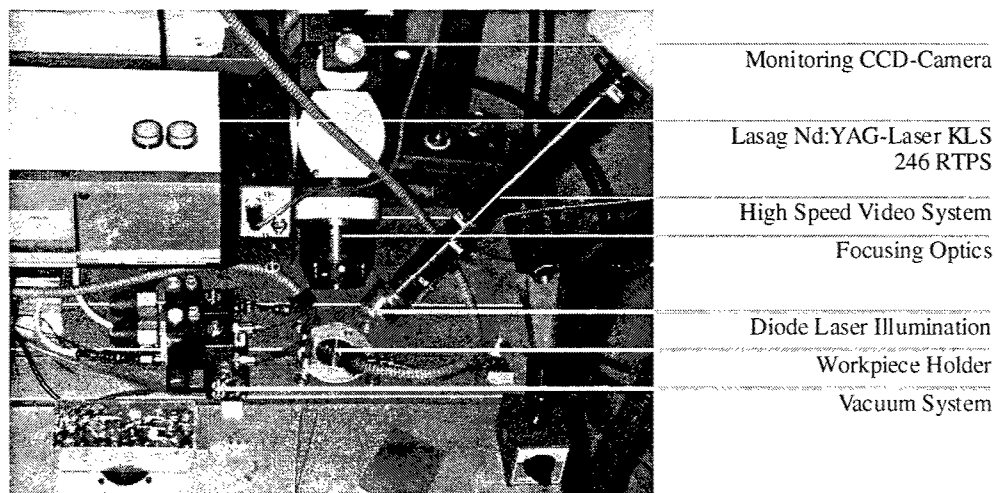
Figure 5 shows the experimental set-up A. For process monitoring a high speed video systems was used and the watch parts had to be illuminated by means of diode laser radiation. The reference curve of the pulse form can be defined on the laser control PC and the true pulse form was monitored on an oscilloscope.

3. WATCH COMPONENTS

3.1. "Balancier": Balancer

In the watch movement the "balancier" is connected to a spiral spring and oscillates bi-directional. It defines the speed of the watch and consists of a ring and four small pins, so-called "tiges", as shown in Figure 6. These pins have to be joined the ring. At present the pins are welded from the top side of the ring by a single Nd:YAG laser pulse. The diameter of the ring is $d_r = 9.60$ mm and the height of the ring is h = 700 μm. The diameter of the pins is d = 350 μm. The weld needs to be at least (700 - 350)/2 μm = 175 μm deep and the pin is only connected on one side. Subsequently the top side of the ring is turned as reference and the contact surface of the ring is turned to nominal diameter. The mounting of the pin into the ring is visible on the contact surface.

The reject due to welding defects is in the range of two percent at a production of one million parts per annum and therefore sums up to approximately 20 000 parts per annum. Each balancier costs EUR 10. That leads to a deficit of EUR 200 000 per annum.

Figure 6:
Balancier
SHADOW Weld
Turned
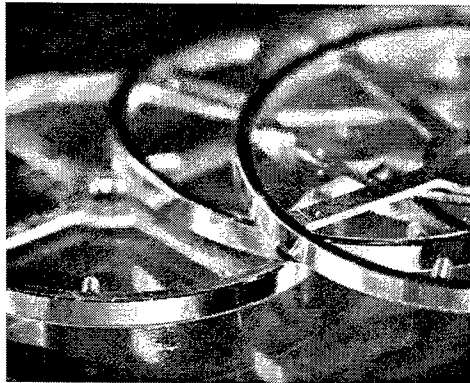
Material
Ring   CuBe2
            h = 700 μm
Pin   CuBe2
            d = 350 μm

Figure 7:
Balancier
SHADOW Weld
Q = 2.0 J
τ_H = 6.5 ms
N = 3
v_f = 35 m/min
α = 0°
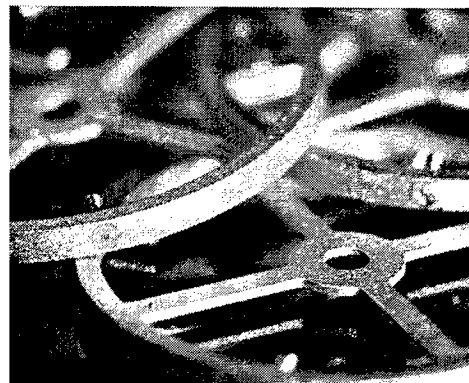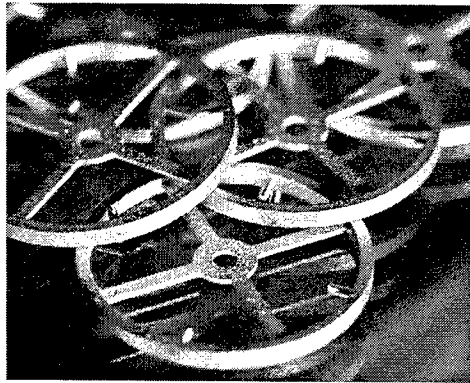
Figure 8:
Balancier
SHADOW Weld
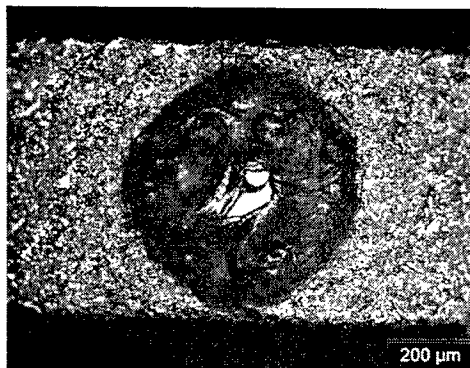
Alternatively the pins can be joined to the ring by a SHADOW weld around the pin on the outer diameter of the ring, the contact surface. On a laboratory set-up, set-up B, a first test series of 1 000 pieces has successfully been performed

using the SHADOW technique. Figure 7 and Figure 8 show SHADOW welded balanciers. The reject due to welding defects has been reduced to one percent with the potential to further reduction and thus EUR 100 000 can be save per annum. In addition to this financial aspect, there is an esthetical aspect as well. Since the weld is performed on the contact surface and this surface is turned after welding, the joint is not visible.
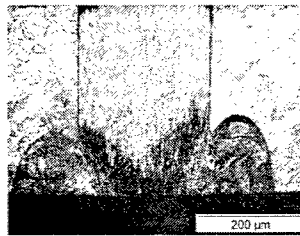
The laser beam describes a circle on the contact surface of the balancier defined by a diameter of the weld d_{weld}. The laser pulse hits the surface with an energy $Q = 2.0$ J and a pulse duration $t_H = 6.5$ ms. At a given feed rate v_f and diameter of the weld d_{weld} the pulse duration suffices for a number N of turns.

The quality of the weld is defined by two parameters: the torque and the look after turning. The minimum torque required is $T_{min} = 0.24$ N·cm. The SHADOW welds have an average torque of $T_{ave} = 0.50$ N·cm which exceeds the required minimum torque by a factor of two and the weld depth is s =300 μm. Figure 9 shows cross-sections of two SHADOW welded balanciers after the final turning. The number of turns was kept fixed at N = 3, but the diameter of the weld d_{weld} was varied. The sample on the right hand side differs from that on the left hand side in the shape of the weld depending on the diameter of the weld d_{weld} and the feed rate v_f, respectively.

Figure 9:
Balancier
SHADOW Weld
Cross-section
Torque
T = 0.50 N·cm
Weld Depth
s = 300 μm
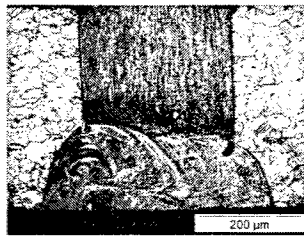
d_{weld} = 0.3 mm	d_{weld} = 0.4 mm
Q = 2.0 J	Q = 2.0 J
N = 3	N = 3
τ_H = 6.5 ms	τ_H = 6.5 ms
v_f = 26 m/min	v_f = 35 m/min
$\alpha = 0°$	$\alpha = 0°$

Besides the appearance of a keyhole the aspect ratio defines the kind of welding process, heat conduction welding or deep penetration welding. The depth of the welds is about the same but the width of the weld on the right hand side is only half of that on the left hand side. The smaller diameter d_{weld} of this weld leads to the accumulation of the deposited energy in the middle of the pin and the heat conduction is restricted. The aspect ratio is 0.5 and the dominating effect must have been heat conduction. The aspect ration of the weld on the right hand side is 0.85 which is an indicator for deep penetration welding. The structure in the molten region does not give any evidence for the appearance of a keyhole. Depending on the weld speed and the material the heat conduction into the workpiece perpendicular to the surface may be higher than the heat conduction to the sides. This means that for micro welds the traditional differentiation of heat conduction and deep penetration welding is no longer true. Further investigation will be carried out to proof this fact.

3.2. "Indicateur de Jour": Day Indicator

The day indicator is the part of the watch movement to which the clock face is glued. It consists of a disc and a gearwheel both made of brass. The disc is t = 80 μm thick and has an outer diameter of d_d = 17.20 mm and an inner diameter of d = 4.3 mm. The gearwheel is d_g = 9.50 mm in diameter.

For the welding of the indicator set-up A came into operation. The gearwheel is placed into the workpiece holder and the disc is position on top. The high speed axis revolves the parts at 3 000 rpm so that one revolution is done in τ_H = 20 ms and the corresponding feed rate is v_f = 40 m/min. The laser radiation hits the parts at an angle of $\alpha = 45°$, the pulse energy sums up to Q = 11.8 J. Figure 10 shows SHADOW welded indicators. The surface of the weld is not as smooth as it could be due to the pulse duration limit of τ_H = 20 ms. The high feed rate is at the transition to humping. If the feed rate can be reduced the surface of the weld gets smoother and more uniform. Moreover, the four additional holes normally required for riveting disturb the continuous process of SHADOW welding.

Figure 11 shows indicators after the testing of the tensile strength. A minimum force to tear disc and gearwheel apart of $F_{min} = 2.5$ N is prescribed. The average strength of the SHADOW welded indicators is F = 36 N which is higher by a factor of almost 15 and can be enhanced by reducing the feed rate as discussed above.

Figure 10:
Indicateur de Jour
SHADOW Weld
Q = 11.8 J
$\tau_H = 20$ ms
N = 1
$v_f = 40$ m/min
$\alpha = 45°$

Material
Disc   Ms61Pb
        t = 80 µm
Wheel Ms61Pb
        d= 4.3 mm
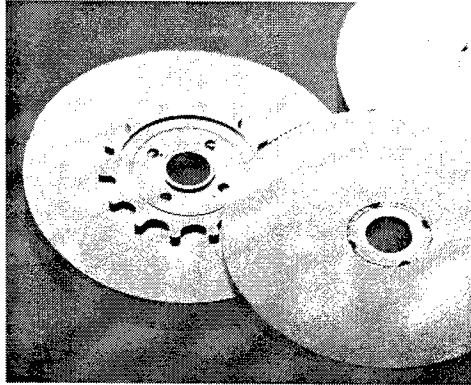
Figure 11:
Indicateur de Jour
SHADOW Weld
Strength
F = 36 N
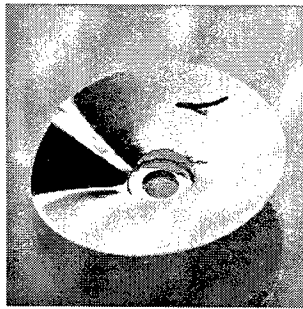
Figure 12:
Indicateur de Jour
SHADOW Weld
Cross-section
Weld Depth
s = 100 µm
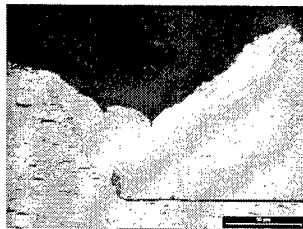
Q = 11.8 J
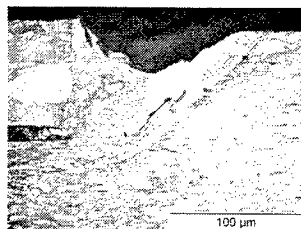$\tau_H = 20$ ms
N = 1
$v_f = 40$ m/min
$\alpha = 45°$

Q = 11.8 J
$\tau_H = 20$ ms
N = 0.75
$v_f = 30$ m/min
$\alpha = 45°$

Figure 12 shows to cross-sections; the thin part on top is the disc. The indicator on the left hand side was welded at the maximum feed rate of $v_f = 40$ m/min whereas the indicator on the right hand side was welded at a reduced feed rate of $v_f = 30$ m/min. The shape of the weld on the left hand side looks heat conduction dominated and has a depth of approximately s = 80 µm. Only the sides of disc and gearwheel have been joined, such that the joint can be described as a butt joint. A lower feed rate leads to a deeper weld as shown in the picture on the right hand side. The shape and the aspect ratio of 1.0 indicates that it is already in the deep penetration welding region. The weld reaches down to the bottom of the disc and into the gearwheel and the weld depth thus is s = 100 µm at minimum. The weld is no longer a butt joint but more an overlap joint. Even though the weld seam covers only 75% of the circle the strength of F = 30 N is about the same as the entirely welded indicators. The strength of the weld in a complete circle must be accordingly higher.

3.3. "Roue Seconde": Seconds' Hand Gearwheel

The seconds' hand gearwheel comprises a gearwheel and an arbor. The gearwheel is made of brass and has a diameter of $d_g = 3.0$ mm and a thickness of $t = 120$ μm. The arbor is made of stainless steel and has a diameter of $d = 300$ μm. Figure 13 shows SHADOW welded examples.

Figure 13:
Gearwheel – Arbor
SHADOW Weld

Material
Arbor   S 20 AP
 $d = 300$ μm
Wheel   Ms61Pb
          $t = 120$ μm
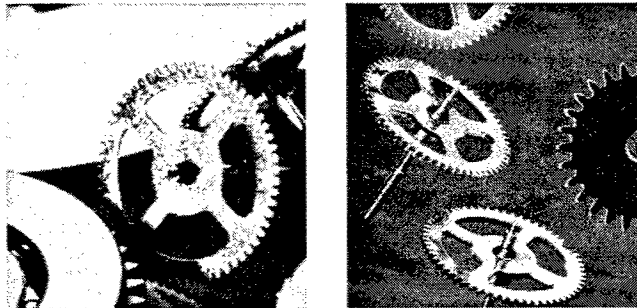
To demonstrate the advantages of the SHADOW technique the seconds' hand gearwheel was alternatively welded in the conventional pulsed mode technique. The tensile strength of the weld was the criterion to define both welds as comparable. The strength is up to $F = 130$ N. In SHADOW technique the energy is $Q = 1.3$ J at a pulse duration $\tau_H = 20$ ms. The part only turns once and the feed rate is $v_f = 3.3$ m/min. The pulsed mode technique requires a total energy $Q_{tot} = 7.3$ J to achieve this strength. At a repetition rate $f_P = 100$ Hz 130 single pulses of $P_H = 112$ W and $\tau_H = 0.5$ ms need to be applied to the parts. Therefore the processing time is $t = 1.3$ s.

Figure 14:
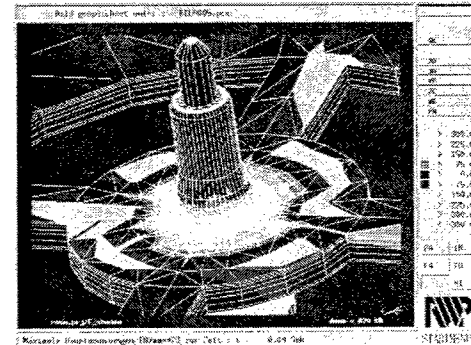Gearwheel – Arbor
Comparison of
Temperature and
Stress

Pulsed Mode   **SHADOW**

Temperature at the end of processing
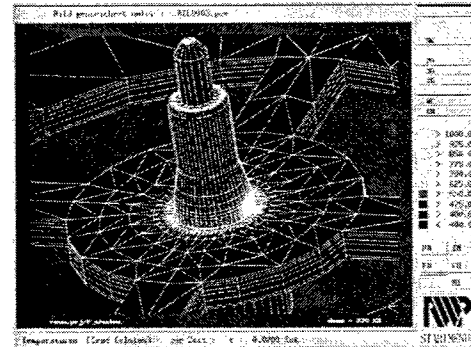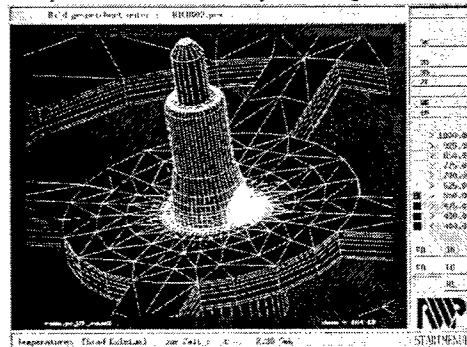
Stress after complete temperature equalization

Theses sets of parameters were used to simulate both welding processes. The simulations have been accomplished by RWP. Figure 14, Figure 15 and Figure 16 show the results. On the left hand side of the figures the final state of the

pulsed mode welding and on the right hand side that of the SHADOW welding is displayed. Th temperature of the parts at the end of the processing is significantly different. In pulsed mode welding a large area of the parts is heated up, whereas in SHADOW welding only a small area around the laser spot is heated. In combination with the alternating heating and cooling the pulsed mode welding induces a lot more stresses into the parts. The area where the laser induced stresses occur is larger and the kind of stress is different. In pulsed mode welding there are mainly strong tensile stresses in the gearwheel indicated in red, in SHADOW welding the gearwheel is only little affected and the stresses are limited to a small area around the weld. In both cases the final state looks almost rotationally symmetric, but the time development is responsible for the degree of distortion. Figure 15 displays the distorted seconds' hand gearwheel after complete temperature equalization with a magnification of 20. The origin position is plotted in light green. The pulsed mode welded parts show a noticeable distortion. The angle of distortion of the arbor is $\theta = 0.50°$. Using SHADOW welding the distortion can be minimized, there is only little difference between the origin and the final state. The angle of distortion of the arbor is $\theta = 0.03°$ and thus smaller by more than a factor of 15.
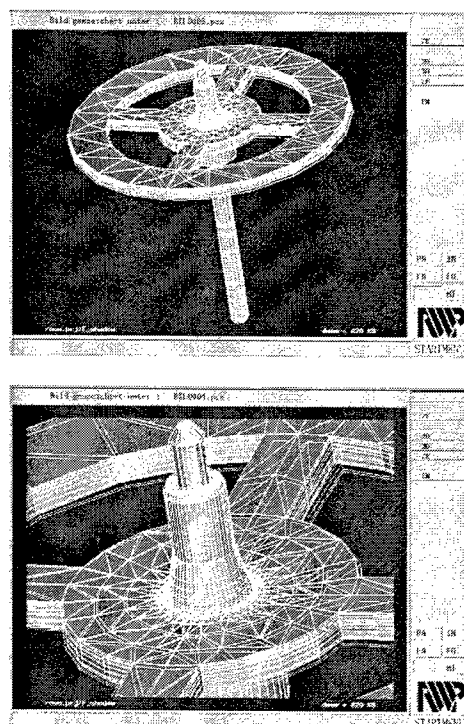
Figure 15:
Gearwheel – Arbor
Comparison of
Distortion

Pulsed Mode
Distortion after complete temperature equalization
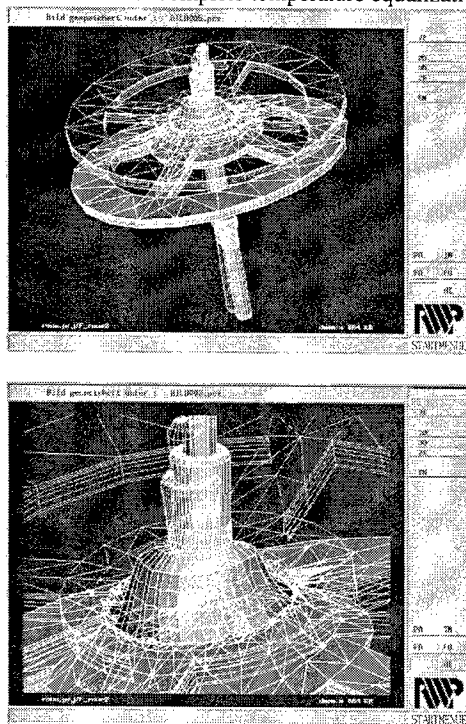
SHADOW

$P_H = 112$ W
$\tau_H = 0.5$ ms, $f_P = 100$ Hz
$N_P = 130$, $t = 1.3$ s
$Q_{tot} = 7.3$ J
$\alpha = 45°$

$v_f = 3.3$ m/min
$\tau_H = 20$ ms
$N_P = 1$
$Q = 1.3$ J
$\alpha = 45°$

The alternation in temperature at a certain point in the middle of the weld in pulsed mode welding is shown in Figure 16. There is an increase in the average temperature up to $T_{ave} = 1\ 000$ °C superposed by the spikes of each single pulse. The maximum temperature is evaporation temperature $T_{max. pulsed} = T_{eva} = 2\ 750$ °C.
During SHADOW welding the average temperature reaches only $T_{ave} = 500$ °C and the maximum temperature of $T_{max. SHADOW} = 1739$ °C is far below evaporation temperature. The diameter of the laser beam on the surface of the gearwheel is $2w_f = 100$ µm. At the given feed rate $v_f = 3.3$ m/min the interaction time can be calculated to approximately $t = 2$ ms. The peak power of the pulse is $P_H = 120$ W, which is in the same range as the pulse power during pulsed mode welding and the intensity $I = P_H/A = 1.5×10^4$ W/cm² seems to be the lower limit for brass welding. With a decrease in the spot diameter down to $2w_f = 60$ µm the peak power may be reduced to $P_H = 45$ W. In addition,

an increase in the feed rate up to $v_f = 30\,000$ rpm means a time of circulation $t = 2$ ms which is a tenth of the pulse duration τ_H the examples shown were welded with. The interaction time thus could be reduced to $t = 0.13$ ms.

The welding of the balanciers lead to the conclusion that welding the small watch with three turns per pulse. This leads to a consistent heating of the parts and may be described as quasi-simultaneous welding. The consistent heating is necessary to ensure minimum distortion.

Figure 16:
Gearwheel – Arbor
Temperature
Depending on
Time
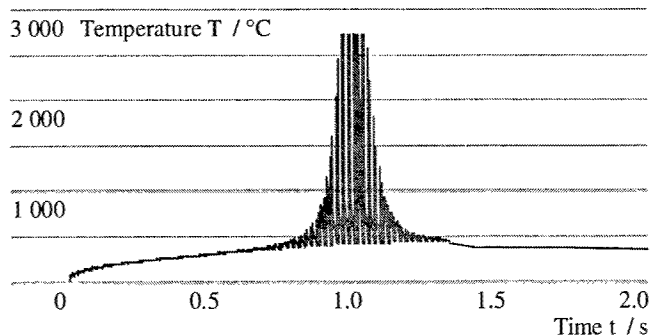
Pulsed Mode
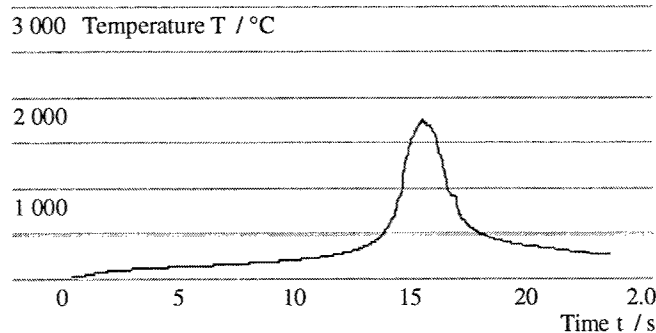
SHADOW

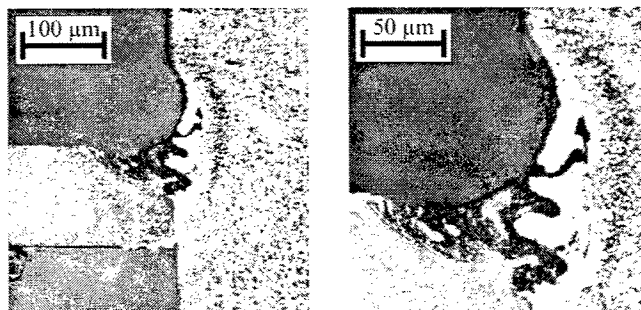**Figure 17:**
Gearwheel – Arbor
SHADOW Weld
Cross-section

Figure 18:
Overlap Joint
EDX-Analysis
[Atom-Percentage]

Material
Top   CrNi 18 10
         d = 250 μm
Bottom Ms61Pb
         d = 250μm

Pos.	Cr	Fe	Ni	Cu	Zn
A	20	68	10		
1	1	3	1	62	33
2	1	1		63	35
3	15	52	7	20	4
4	19	66	10	3	
B				63	37

Cross sections of the parts were made to determine the source of the high weld strength. Figure 17 shows an example. The depth of the weld is only $s = 65$ μm at a weld with of $b = 135$ μm. There is no mixture of brass and steel

identifiable. Both fused materials can clearly be separated. The interface is determined by the dynamics of the fused materials.

Since same kind of interlocking cannot be the only source of the joint mechanism, overlap welds of brass and stainless steel sheets were carried out. The cross sections of these welds were studied with respect to the elements (chromium, iron, nickel, copper and zinc) by means of energy dispersive X-Ray analysis (EDX). Figure 18 shows a cross section of an overlap brass steel joint with the typical look of variantly brass and steel regions. The measuring points are indicated. A is bulk brass, B is bulk steel and 1 to 4 are in the joint area. At measuring points 1 and 2 there is only a negligible fraction of chromium, iron or nickel, i.e. these are bulk brass regions. At measuring point 4 it's vice versa, the fraction of copper and zinc can be neglected and here is a bulk steel region. Measuring point 3 shows the presence of all elements analyzed, it's a mixture of brass and steel. The short-time interaction allows an alloying despite the incompatibility of those two metals and this indicates that macro-features may not be transferred to micro applications.

3.4. Ball Bearing

Watch movements comprise several kinds of bearings. The ball bearing shown in Figure 19 is one of the smallest and consists of an inner and an outer cage both made of CuBe2. Within these two cages five balls are positioned with a defined clearance. The clearance is adjusted by moving the outer cage relatively to the inner cage up and down while flanging the ball bearing.

Figure 19:
Ball Bearing
SHADOW Weld

Material
Inner Cage
 CuBe2
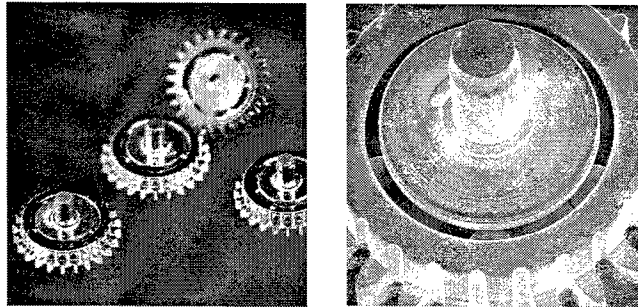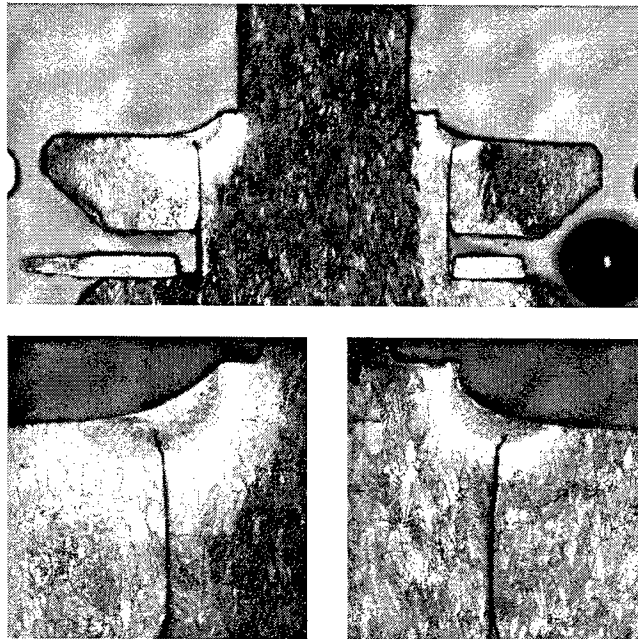 d = 0.6 mm
Outer Cage
 CuBe2
 d = 3.0 mm

Figure 20:
Ball Bearing
SHADOW Weld
Cross-section
Q = 2.0 J
τ_H = 5.0 ms
N = 1
v_f = 25.4 m/min
α = 45°

Alternatively the ball bearing can be welded in the flanging area. Inner and outer cage are positioned at the defined clearance and both parts are SHADOW welded as shown in the SEM-picture an the right hand side of Figure 19. Cross sections of a welded ball bearing are shown in Figure 20. The semicircular shape indicates heat conduction welding.

The gap between the inner and the outer cage reaches into the weld. The strength of the SHADOW welded ball bearings is $F_S = 90$ N, the flanged ball bearings stand $F_F = 75$ N.

Especially for these small ball bearings the adjusting of the clearance by moving the parts leads to a high reject rate. The outer cage is moved up and down by a crank of a lever and the balls hit the surface of the outer cage which may lead to a violation of the surface and in the long run to a malfunction of the ball bearing. If the cages can be positioned at the defined clearance and can be welded with the application of mechanical forces the reject rate may be reduced drastically.

4. CONCLUSION

SHADOW welding is a stable and robust process and reduces distortion as well as contamination due to low and accurate energy deposition into the components. This has been proofed by FEM simulations. The high feed rate leads to a low processing time. Deploying a well-priced pulsed laser for quasi continuous wave welding results in low operation costs. SHADOW welding is a cost effective process for the mass production of micro-parts. Several watch components have successfully been welded using the SHADOW technique. For the welding of the balancier the reject rate has been reduced to less than half of that of the welding process used in production. Even very small and delicate parts and materials combinations have been welded. The non-contact SHADOW welding offers a series of new possibilities for mounting and connecting watch components with respect to flexibility and without the application of mechanical forces.

ACKNOWLEDGEMENTS

REFERENCES

1. Thorsten Kramer, Alexander M. Olowinsky, Friedrich Durand, "SHADOW – A New Welding Technique" in *Photon Processing and Photonics*, Koji Sugioka, Malcom C. Gower, Richard F. Haglund, Jr., Alberto Piqué, Frank Träger, Jan J. Dubowski, Willem Hoving, Editors, Proceedings of SPIE Vol. 4637, p. 545-554 (2002)
2. Alexander M. Olowinsky, Thorsten Kramer, Friedrich Durand, " Laser Beam Micro Welding in Watch Industry" in Photon Processing and Photonics, Koji Sugioka, Malcom C. Gower, Richard F. Haglund, Jr., Alberto Piqué, Frank Träger, Jan J. Dubowski, Willem Hoving, Editors, Proceedings of SPIE Vol. 4637, p. 571-580 (2002)
3. Alexander M. Olowinsky. Thorsten Kramer. Nicolas Dumont. Henning Hanebuth. "New applications of laser beam micro welding", Proceedings of ICALEO 2001, Jacksonville, Florida USA
4. Arnold Gillner, Lüdger Bosse, Thorsten Kramer, Alexander M. Olowinsky, Michael Wild, "Laser micro joining of advanced micro systems", Proceedings of ICALEO 2000, Dearborn, USA
5. Willem Hoving, "Laser Applications in Micro-Technology" in CIRP – Journal of Manufacturing Systems, 1999, Vol. 28, No. 1
6. J. Rapp, "Fügetechniken an Automobilkomponenten", LEF '99 Tagungsband, 1999
7. "Laser beam micro welding as a new interconnection technique", Microelectronics International, No.39, pp. 44 ff January 1996
8. I. Miyamoto, H. Maruo, Y. Arata, "Beam absorption mechanisms in laser welding", Proc. SPIE, Laser Processing: Fundamentals, Applications and Systems Engineering, 3-6 June 1986
9. Mathias Glasmacher, "Prozeß- und Systemtechnik zum Laserstrahl-Mikroschweißen", Meisenbach Verlag, Bamberg, 1998
10. F. Dausinger, "Strahlwerkzeug Laser: Energieeinkopplung und Prozeßeffektivität", Teubner Verlag, Stuttgart, 1995
11. W. Kalita, "Structural and Mechanical Properties of CO_2-Laser Welded Joints in Difficult-To-Weld Metals", Welding International 1996, Vol. 10
12. E. Schubert, "Lasergestütztes Fügen von Werkstoffkombinationen", Bleche, Rohre, Profile 1999, Vol. 46
13. J. F. Lancaster, "Metallurgy of Welding", Chapman & Hall, 1993

Process spread reduction of laser micro-spot welding of thin copper parts using real-time control

Antoon Blom[a], Paraskevas Dunias[a], Piet van Engen[a], Willem Hoving[a], Janneke de Kramer[b].
aPhilips Centre for Industrial Technology, Glaslaan 2, Eindhoven, The Netherlands
bEindhoven University of Technology, Den Dolech 2, The Netherlands

ABSTRACT

In present-day industry, particularly in the area of microelectronics packaging and assembly, there is a strong demand for highly reliable, miniature joints of thin copper parts. Laser welding could be the perfect solution for making such joints if this process were not highly sensitive to various parameters, such as the reflectivity of the copper workpiece, the gap between the product parts to be welded and the laser-power density. The robustness of the process is further limited because two important product properties (reflectivity and heat conductivity) change strongly during welding.

An investigation has been performed to increase the robustness by means of real-time feedback control, based on several parameters that are monitored simultaneously during the process. It is shown how this drastically decreases the influence of the above-mentioned variations with "heat conduction" welds. The control algorithm was based on an approximate model of the (non-linear) welding process. In addition, it is shown how adaptive feedforward control is required to cope with the limited response time of the system. Finally, some remarks are made on experiences iterative learning control.

This investigation was part of the European co-operation project SLAPS[1], performed within the framework of the IMS/Brite-Euram III programme. The support from the European Commission and the IMS regional offices is gratefully acknowledged.

Keywords: laser welding, micro-spot welding, copper welding, process control

1. INTRODUCTION

Laser micro-spot welding is a joining technology that uses a laser beam to heat the workpiece parts to be joined.. Here, very high power densities are reached in the laser spot, capable of realising a melt in and a fusion of the workpiece materials in a few or even fractions of a millisecond. The combination of small welding spots and the short process times lead to a small heat-affected zone, which makes this technique an ideal candidate for small delicate parts that require well-controlled physical dimensions or geometrical stability.

The development of a robust process for novel applications needs experts on this technology to prepare the processes and to obtain stable operation with a high up-time for the production equipment. The state of the art technology uses feedforward controlled laser output power. A certain power profile as a function of time and/or position on the workpiece is used in specific cases to improve performance.

To make laser technology more easily accepted in industry, there is a drive to introduce self-tuning characteristics to the laser processing equipment, making the system more robust to changing parameters in the process. The introduction of feedback techniques based on information from the process is necessary to achieve this goal. Some form of process monitoring has to be introduced and the process signals have to be analysed and related to the actual conditions of the process at that moment. Having feedback control in place opens up new options as this will allow the processing of materials that show a very narrow processing window or do not even have a stable process at all. The laser micro-spot welding of bare copper using Nd:YAG laser sources is such a process. Because copper is an important material in the electronics industry, Philips CFT has invested considerable effort in the development of laser spot welding technology using Nd:YAG sources with feedback control, resulting in stable operating processes.

---

[1] SLAPS: Self tuning and user independent LAser material Processing unitS

2. PROBLEM DEFINITION

At the moment, only a limited number of applications are running using laser micro-spot welding on copper with the commonly used Nd:YAG laser sources. Two main reasons can be identified for this situation:

1. The process has a few parameters, which show significant variations from workpiece to workpiece.

The power of the laser beam is only partly absorbed by the surface of the workpiece. The absorption coefficient for the 1064 nm radiation from the Nd:YAG source by pure copper is about 5%. Measurements have shown that relative variations up to 10% can be expected on this figure, depending on the storage and treatment of the material.

The parts to be joined have to be brought together. The remaining distance between the parts is always subjected to some variation, affecting the heat diffusion through the structure and, in the end, the (start of the) fusion process.

2. The process behaviour changes dramatically during phase changes.

Copper has a high heat conductivity, which necessitates short process times (i.e. high laser power) to keep the energy input and the heat-affected zone small. The absorption coefficient of copper depends on the temperature, which changes abruptly when going through the solid–liquid phase change. A similar behaviour is present in the thermal conductivity, however with an opposite sign. This means that, at changing state, the absorption of laser radiation increases, while the thermal conductivity decreases, leading to a very fast increase of the local material temperature when the input laser power remains constant. Without taking precautions, the process very quickly runs into evaporation of the copper at the centre of the spot weld and, soon afterwards, into an uncontrollable keyhole welding regime.

A sudden increase of laser power absorption also occurs when the process runs into the keyhole welding regime. The evaporated material pushes the liquid material aside, thus creating a dent and, finally, a hole. This 'black' hole leads to almost full absorption of the laser beam energy.

The problems related to the first group (absorption of laser energy) could be tackled by introducing a kind of pre-processing to the workpiece surface, leading to a better-defined absorption for Nd:YAG (laser structuring, blackening with ink), or by selecting a laser source with a shorter wavelength, leading to a higher and more reproducible absorption coefficient (frequency doubled or tripled Nd:YAG). The effects of group two are purely defined by the material and process behaviour as such and have to be accepted. Although solving the laser in-coupling problem will be a very important step in getting the process under control, it will not cure all problems with the laser spot welding of copper parts.

3. METHODOLOGY

The approach followed in the SLAPS project to tackle the problem is to introduce a feedback controlled laser power source, on the basis of measured process parameters. The major drive for this choice is the consideration that this is a way to control process variations originating from workpiece variations, material properties and process conditions.

As stated in chapter 2, the problems related to laser spot welding of copper are caused by a number of different parameters and process conditions. Based on the problem definition presented, we can extract the following list of important parameters and process conditions, which are of crucial importance to the process behaviour:
- Absorption coefficient of the workpiece surface for the laser light,
- Heat diffusion through the workpiece structure,
- Distance between the parts to be welded,
- Solid-liquid phase change (changing physical properties),
- Liquid-vapour phase change (condition for keyhole operation).

It is obvious that a number of sensors are needed to detect the behaviour/presence of this set of process parameters and process conditions. This set of sensor signals is used to keep the process under control, by measuring the behaviour of process parameters on the one hand (energy absorption and surface temperature) and process conditions on the other hand (solid-liquid phase change, liquid-vapour phase change).

4. PROCESS & MONITORING

4.1. Process behaviour

Laser (micro) spot welding is a frequently-used joining technology for miniature welds on small products. The typical characteristic of this joining technology is that the laser beam remains focused on the same spot during processing. The processing times are short, in the order of 0.5 – 20 ms. Several different welding types are used in industry, among which the standing edge weld, overlap fillet weld and overlap penetration weld are the most important, see Figure 1.

Standing edge

Overlap fillet
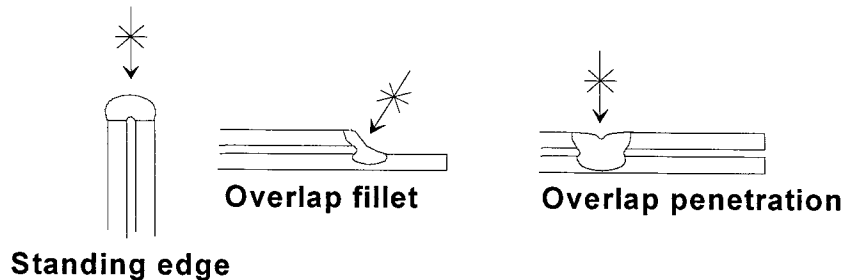
Overlap penetration

Figure 1 Laser spot welding geometries

The overlap penetration weld is the most critical geometry because the distribution of the laser energy over the workpiece is heavily influenced by the interface between the two metal parts. This type of spot weld geometry has been used throughout the research programme of SLAPS on micro-spot welding. Figure 2 shows a kind of time-resolved process condition overview of the micro-spot welding process for the overlap penetration geometry.

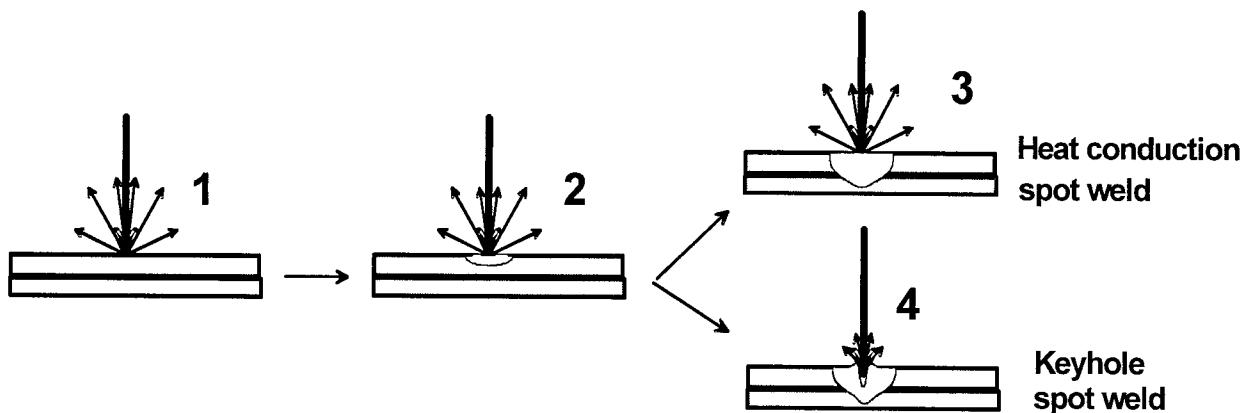**1** **2** **3 Heat conduction spot weld** **4 Keyhole spot weld**

Figure 2 Time resolved process phases for micro-spot welding

Phase 1, is the pre-melting phase. For most materials, the absorption increases with temperature, so the process more or less accelerates during heating. For copper, the transition from solid to liquid introduces a steep change in process behaviour. The energy absorption increases while the heat distribution decreases, leading to a rapid temperature rise when going into liquid phase (with constant input power). Figure 3 and Figure 4 show the behaviour of laser power absorption and heat diffusion as a function of temperature for stainless steel and for copper, to indicate the major difference [1], [2]. The process runs rather stably on stainless steel products due to the physical behaviour of this material. The absorption coefficient for the 1064 nm light of the Nd:YAG lasers is quite high and the thermal conductivity is low compared to other metals: The energy is accepted easily, while it remains more or less locally concentrated. In contrast to stainless steel, copper shows a step-wise change of both the thermal conductivity and the energy absorption at the solid-liquid phase change. Both effects have an accelerating influence on each other, leading to a kind of avalanche behaviour on the local temperature of the material. Unless precautions are taken by lowering the

laser power significantly, the centre part of the sot will soon go into the keyhole operation, often leading to liquid material exploding from the weld spot.
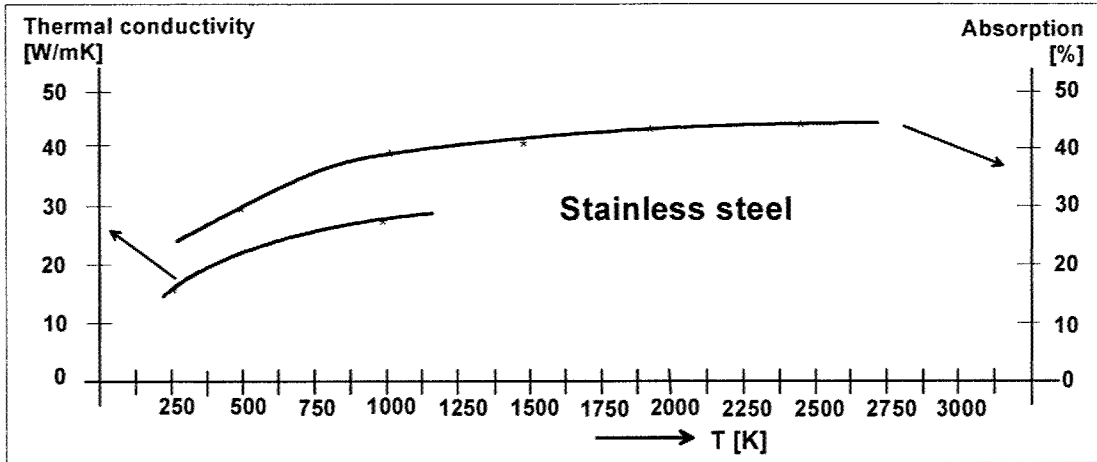

Figure 3 Thermal conductivity and absorption properties for stainless steel
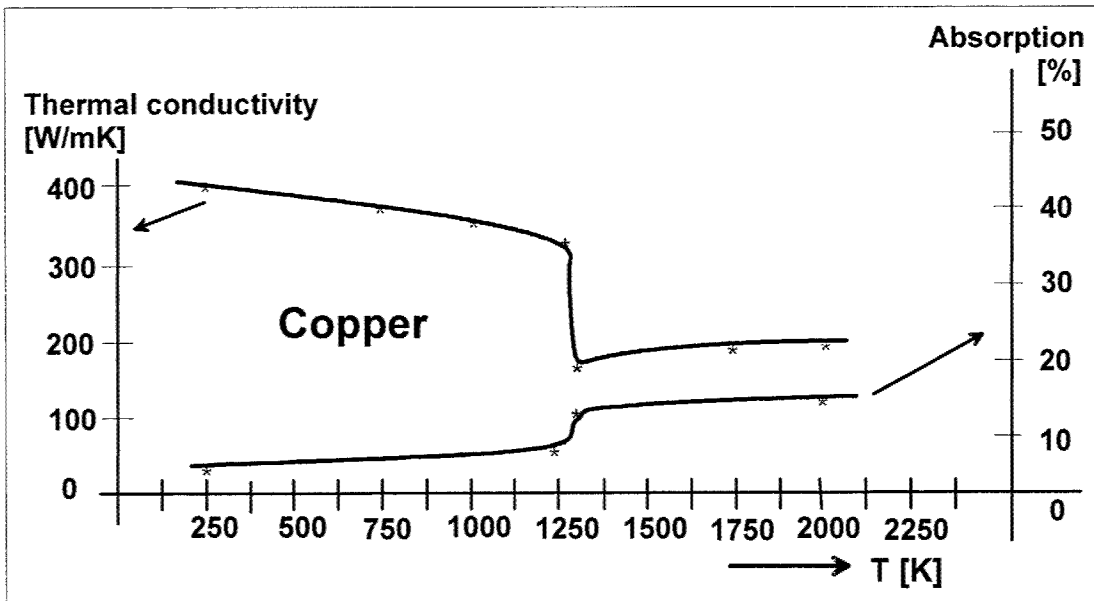

Figure 4 Thermal conductivity and absorption properties for copper

Phase 2, is the melting phase, where the top material within the spot area is initially partly solid and partly liquid, while expanding to completely liquid at the end.

Phase 3, indicates the accomplished heat conduction weld. There is hardly any vaporisation, leaving the surface more or less undistorted and flat.

Phase 4, indicates the situation in the case of keyhole spot welding. The recoil pressure of the vaporised material pushes the liquid aside, catching the laser beam.

As indicated in the aforementioned overview of process phases, the absorption coefficient changes from phase to phase. The initial absorption coefficient can vary, depending on the history of the copper material. Reducing the laser power immediately at the moment of melting is important to keep the process in stable operation. However, this moment depends on the amount of power absorption during the initial phase and even a 10% variation (which can be expected from normal oxidation) can be sufficient to cause stability problems. Problems can be reduced by improving and securing the absorption of the 'initial' material by means of a pre-treatment, such as oxidising, etching, sandblasting or coating. As soon as melting occurs, the effects of the pre-treatment will disappear.

When the process goes into keyhole operation, a second change in absorption starts, taking the laser absorption up to almost 100 % in the case of deep keyhole processing.

Introducing a pre-treatment on the material will give a better-defined absorption during the in-coupling phase. Once molten, the disturbing effects of other process parameters, such as the gap between the parts, are still acting on the process. The SLAPS technology relies on the introduction of real-time feedback control techniques to handle the initial absorption variations as well as on other process parameter variations such as gap variation, affecting the heat diffusion through the structure. Figure 5 shows a representation of the absorption variation when the spot welding process runs through the sequential phases. The figure indicates the effect of the initial absorption on the following process.
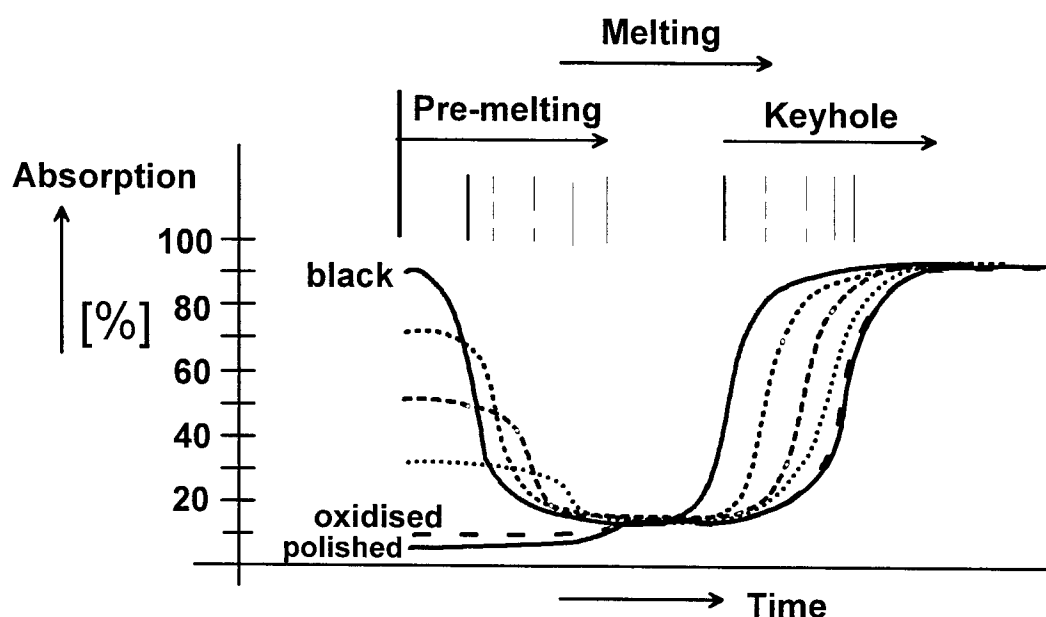

Figure 5 Absorption of laser energy over time, depending on the actual process phase

It is evident that the exact time instants of the critical phase changes vary and this is where the feedback control technique will help to align the laser source output to the evolving process.

Heat conductive welding of copper has been realised at Philips CFT by using feedforward operation and by limiting the range of process disturbance by initial absorption variation. This process uses a relatively large spot size compared to the workpiece thickness. Using the same weld type for the SLAPS work gives the option to compare the performance of the feedback controlled process directly with the feedforward operated process and thus establish an opinion about the performance improvement with feedback operated spot welding. The geometries used for the experiments and performance verification involved combinations of copper sheets of 100 and 50 microns thick.

4.2. Process monitoring

For effective process monitoring aiming for process control, it is vital to implement sensors that detect information that is linked to the critical process phenomenon mentioned in the previous paragraph. The table below presents the identified important process parameters and process conditions to detect and the related sensing system used on the set-up.

Process parameter or process condition to be measured or detected	Related physical property or properties	Implemented sensor
Absorption coefficient of the workpiece	Laser power to the workpiece Reflected laser power from the workpiece	Germanium photodiode Germanium photodiode
Heat diffusion through the workpiece, Surface temperature. Distance between the parts to be welded	Infra-red emission from the surface	InGaAs photodiode
Solid-liquid phase change (changing physical properties)	Reflected laser power form the workpiece Infra-red emission from the surface	Germanium photodiode InGaAs photodiode
Liquid-vapour phase change (condition for keyhole operation)	Optical emission from vapour	Silicon photodiode

Absorption coefficient of workpiece
On-line measurement of the absorption coefficient of the workpiece surface cannot be done with high accuracy. The practical set-up does not permit the measurement of all reflected laser power. As shown in Figure 6, only the reflected power that returns into the aperture of the optical system is measured. The input laser power is measured reliably with a sensor behind the first mirror, detecting a fixed fraction of the incoming laser power passing this mirror. Only an indicative value for the absorption coefficient can be extracted when monitoring the reflected laser signal over a certain period.

Heat diffusion through the structure, Surface temperature
The applied laser energy will diffuse through the workpiece structure, resulting in a certain temperature gradient profile in the workpiece structure. This profile is hardly accessible by on-line measurements, but some information about the heat distribution can be extracted by looking at the dynamic response of the surface temperature. Small variations in heat diffusion cannot be resolved. however the actual existence of metallic contact between the two copper sheets can be detected. Verification tests have shown that the InGaAs sensor used in our set-up can detect emissions from the surface down to temperature levels of about 600 °C.

Solid-liquid phase change
Two sensors in the set-up are used to detect the crucial solid-liquid phase change. As soon as the surface within the weld spot changes state, the reflection properties of the material changes instantly. The specular reflection from the surface decreases at the expense of the diffuse reflection. This can be recognised from the implemented laser power reflection sensor, showing a rapid decrease of the signal at the moment of melting (beam perpendicular to the surface).

There is a fixed relation between the surface temperature and the moment of melting for each specific material. This also means that the infra-red emission can be used to trace the melting event. This option is used for the implemented control module.

Liquid-vapour phase change
The most straightforward method of detecting vapour formation is to detect the optical emission from the evaporated cloud above the weld spot. This has been done with a coaxial sensor and with an off-axis sensor. The advantage of the off-axis method is that this measurement can be decoupled from the surface emission much more effectively. compared to the coaxially implemented sensor. The off-axis sensor was used in our control loop.

Besides the optical sensors mentioned above, other sensors have also been tested and evaluated. However. these sensors seemed to be less favourable for reasons of complex signal processing (microphone) or signal consistency (eddy current detection of weld pool penetration).
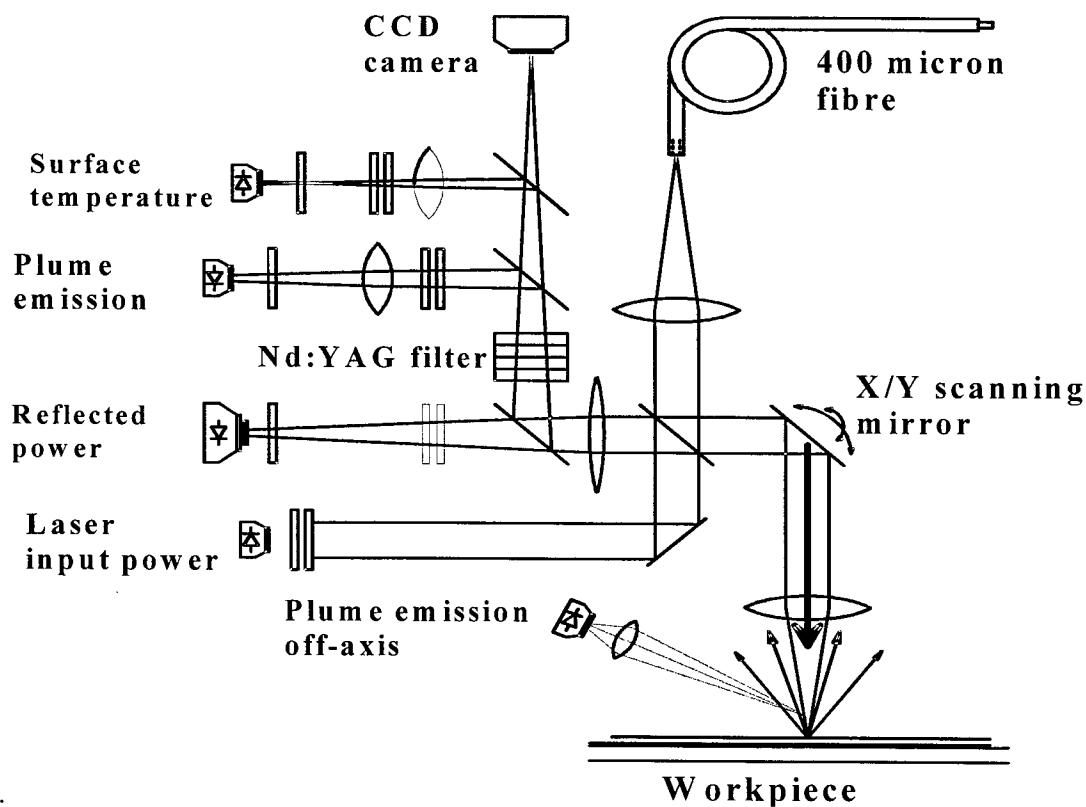
Figure 6 Implementation of sensors on spot welding set-up

The development of the processing head with the implementation of the sensors has been an activity of the Lasag AG company, in co-operation with the Institute of Applied Optics of the École Polytechnique Fédérale Lausanne (EPFL-IOA), both in Switzerland and partners in the SLAPS project for the spot welding application. A CCD camera gives a view of the welding spot and can be used in combination with machine vision techniques to align the position of the welding beam accurately on the workpiece by moving the two scanner mirrors in the processing head.

5. SIGNAL PROCESSING

All sensors have local preamplifiers and the amplified signals are fed to a filter unit, which performs straightforward anti-aliasing filtering for all sensor signals. Moreover, a comb filter processes the signals from the optical sensors. This filter suppresses the fundamental frequency and all higher harmonics of the switched mode power supply current to the flash lamps of the laser unit. The laser power modulation caused by the chopper frequency is thus completely suppressed in the sensor signals and does not disturb the control loop. Hardware filtering is selected for this application as it is expected that the full processing performance of the controller is needed for the control action as such.

In this case, the controller hardware is the DAP5200a signal acquisition processor board from Microstar Laboratories. This board provides 8 analogue input channels with two AD converters with 14-bit resolution and a sampling frequency up to 400 kHz (50 kHz per channel when all are used). Two analogue output channels are provided to drive actuators. In our case, only one is used for the power set point to the laser unit. The processing of the input data and generation of the output signal runs on the onboard processor.

6. CONTROL STRATEGY

It is not without reason that so much attention has been paid to the fact that the absorption coefficient of the material changes considerably throughout the spot welding action. When realising a closed loop operation, this means that a similar variation in the loop gain is in fact present. Loop gain variations as indicated in the previous chapter cannot be handled satisfactorily by one single controller. For best performance, the controller has to be adapted to the loop gain of the process in each phase. Based on this thought, the control strategy of Figure 7 has been proposed.
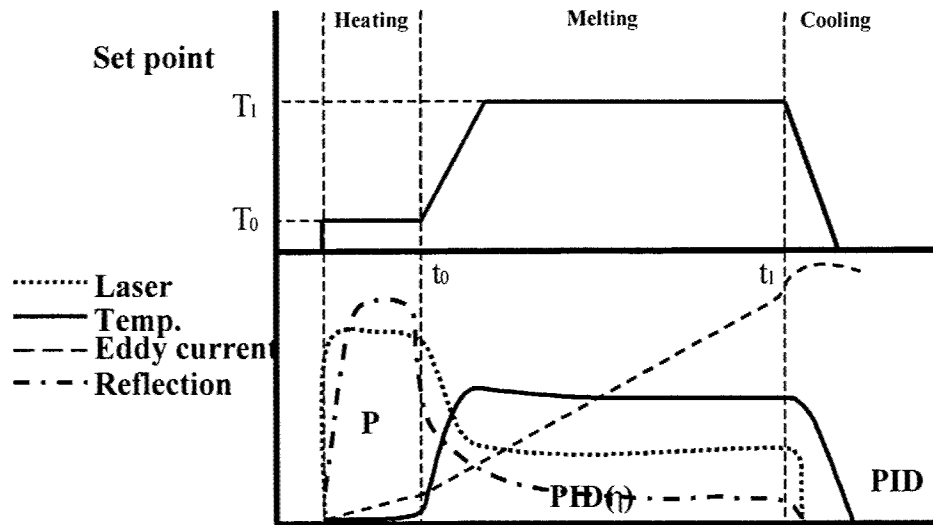
Figure 7 Control strategy for micro-spot welding

Each of the three process phases 'heating' or 'Pre-melting', 'Melting' and 'Cooling' has its own controller settings. The first problem to solve is to safely pass through the pre-melting phase. The material has to be heated from room temperature to a temperature just above melting temperature, without the process becoming unstable due to the solid-liquid phase change difficulties described in chapter 4. This is achieved over the proportional controlled heating phase. As soon as the measured temperature exceeds a pre-set threshold value, the heating phase is accomplished and the melting phase is started. This phase controls the laser power such that the measured surface temperature follows the set point contour. The PI controller takes the temperature from just above melting up to the desired fusion temperature and keeps it there for a certain period. The third phase takes the temperature down, according to a linear slope.

6.1. Controlling the welding process

A general diagram of the control scheme for the welding process is depicted in Figure 8.

Three different control modes are applied for different purposes. Traditional feedback control (including common feed-forward support) has been used to enforce the welding process to track a given temperature trajectory during the welding phase of the process.

Besides this, an adaptive control scheme was employed to change from one controller to another when the process changes from one state (solid) to another (molten) and back again to the solid state. Finally, the feedforward signal is adapted after each weld, based on the control error that occurred in each trial, in other words an Iterative Learning Controller.

6.1.1. Feedback control

Model:
The process consists of three subsystems: the laser equipment, the welding process and the temperature sensor.

The laser accepts an analogue input voltage of 0-6 V as a set point for an internal laser controller that controls the laser power, corresponding to 0-6 kW laser power. Identification measurements indicated that the laser behaves according to a first order system with an additional delay.
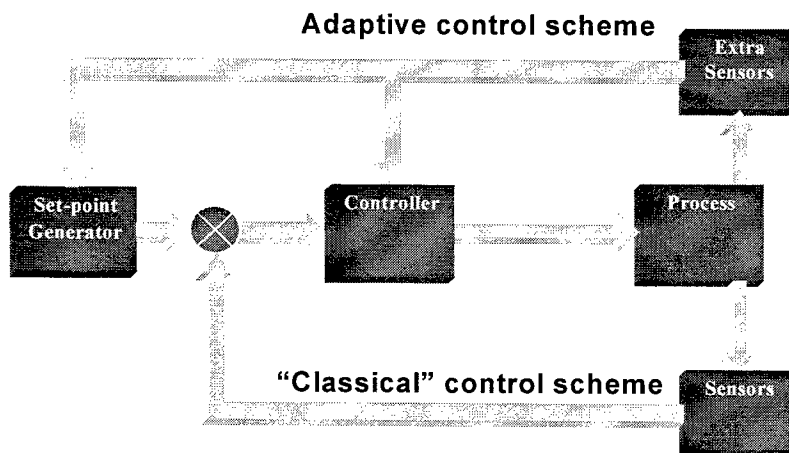
Adaptive control scheme

Figure 8 Block diagram of the control loop

The welding process model was derived on the basis of step and sinus excitation data, gathered during the molten phase of the welding process. The model found is a second order system with two zeros.

The pyrometer used for the surface temperature measurement was modelled (actually, calibrated) using a molten copper bath. A reference temperature signal was obtained using a thermocouple temperature sensor. The results of this investigation confirmed the theoretical model, which states that the temperature is proportional to the fourth square root of the surface radiation from the weld spot. The combination of all identification results leads to the following total model:

$$H = \frac{\sqrt[4]{S}}{L} = e^{-td\,s} \frac{K}{\tau_L s + 1} \frac{(\tau_{w1}s+1)(\tau_{w2}s+1)}{(\tau_{w3}s+1)(\tau_{w4}s+1)}.$$

Where:
K = 1.46, td = 196 μs, τ_L = 0.137 ms (f_{w1} = 1162 Hz), τ_{w1} = 1.061 ms (f_{w1} = 150 Hz), τ_{w2} = 0.108 ms (f_{w2} = 1469 Hz), τ_{w3} = 1.730 ms (f_{w3} = 92 Hz), τ_{w4} = 0.335 ms (f_{w4} = 475 Hz)
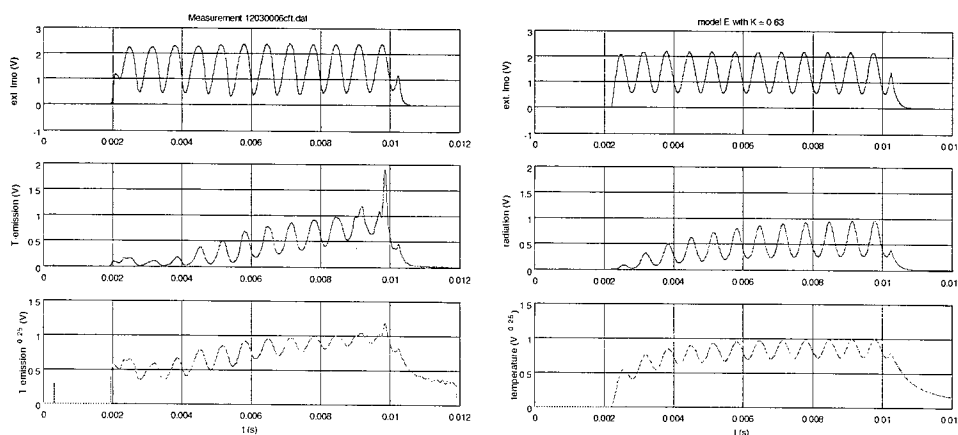

Figure 9 Examples of input and output signals of the process and the corresponding simulation signals

Feedback Controller Design:
The feedback controller had to be designed because of the large model uncertainty. The resulting controller is a PI controller with a proportional part Kp of 3.3, and a cut-off frequency at 200Hz, leading to a controlled process with 260 Hz bandwidth. The Nyquist plot shows that the controlled process appears to have a gain margin of more than 6 dB and a phase margin of more than 45 degrees, see also Figure 10.
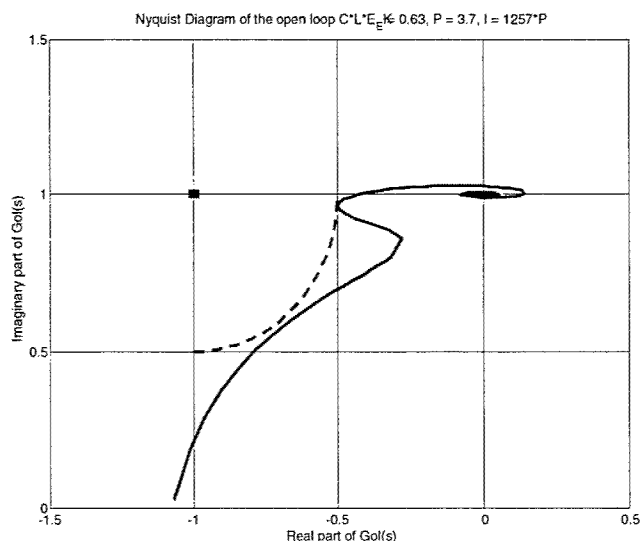

Figure 10 Nyquist diagram of the controlled process

Testing of the basic controller:
The implemented controller was tested on two kinds of overlap penetration welds. The first one was a weld of two sheets of 100 μm thick copper; the second was a weld of a 100 μm thick sheet on a 50 μm thick copper foil. Figure 11 shows an example of the temperature signal for a controlled weld of a 100 μm thick sheet on a 50μm thick foil.
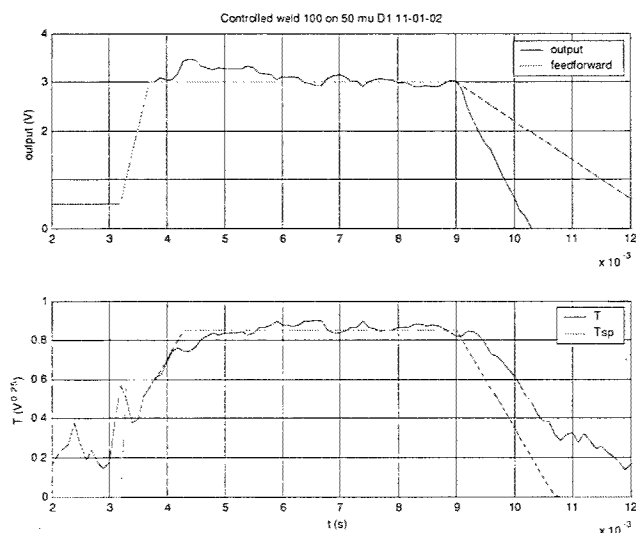

Figure 11 Example of controlled weld temperature and controller output

Although most of the welds done with a controlled system appeared to have a good and reproducible quality, several welds were much too small. Especially the performance on dirty (i.e. contaminated and oxidised) sheets had to be improved. The basic controller has been extended to improve its performance. It was noticed that the length of the melting phase affected the weld quality. The weld quality could be improved if a sensor signal could be found from which the optimum melting phase length could be determined on-line. In the next session, the extension of the feedback controller using such sensor information will be discussed.

6.1.2. Adaptive Control

Process Phases

As explained in chapter 4, the process changes drastically when the material passes from the solid state to the liquid phase, where the real fusion of the materials takes places. In line with this, different process phases have been defined, each having its own model and, consequently, its own controller configuration.

Pre-melting or heating phase

In the pre-melting phase, the laser power is kept constant until the material starts to melt. A *P-regulator* is employed here. The finishing moment of the pre-melting phase is extracted from the reflected laser light signal or from the surface temperature signal, see chapter 4.

Melting Phase

The melting phase may be the most important phase because this is where the actual welding takes place. The real control action starts here, defining the laser power set point in such a way that the measured surface temperature follows a defined profile. The aim during this phase is to bring the temperature to the desired level and then keep it constant until the moment the melt has reached a sufficient penetration depth. As mentioned before, the length of the melting phase determines the quality and reproducibility of the weld. The implemented controller adapts the melting phase length for optimum reproducibility of the weld quality, based on the monitored absorbed laser energy. The absorbed energy is calculated by integrating the difference between the laser input power and the reflected laser power. Figure 12 depicts an example of signals from two welds, showing a clear absorption behaviour during the welding phase. When the reflection increases during the melting phase, the length of that phase also increases in such a way that the total absorbed energy remains constant between the different welds.
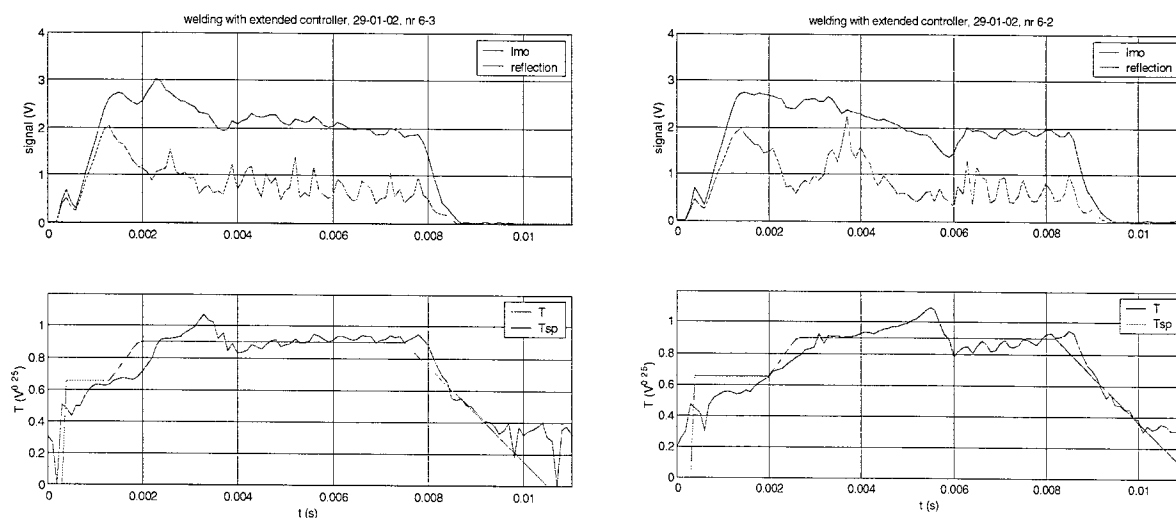

Figure 12 Phase regulation based on absorbed energy

Post-melting or cooling phase
In this phase, the melting phase is terminated with a certain cooling trajectory. For the copper welding application, the cooling trajectory is not important for the quality of the joint. This is why a simple PI controller is used to support the cooling phase. Nevertheless, the cooling temperature trajectory can be very crucial for other applications.

6.1.3. Iterative Learning Control

With the extended controller implemented, the reproducibility of the weld diameters has improved substantially, but the temperature still shows a large deviation from the reference at the beginning of the melting phase. Iterative learning control (ILC) was employed to suppress the systematic disturbances that cause reproducible deviations of the temperature trajectory with respect to the set point profile. In ILC, the error of the previous trail (in this case, the previous weld) is used to update the feedforward action off-line [4]. If the systematic errors are larger than the random errors, the error will reduce. The applicability of ILC is studied by looking at the systematic and the random errors. This investigation showed that ILC can indeed be applied.
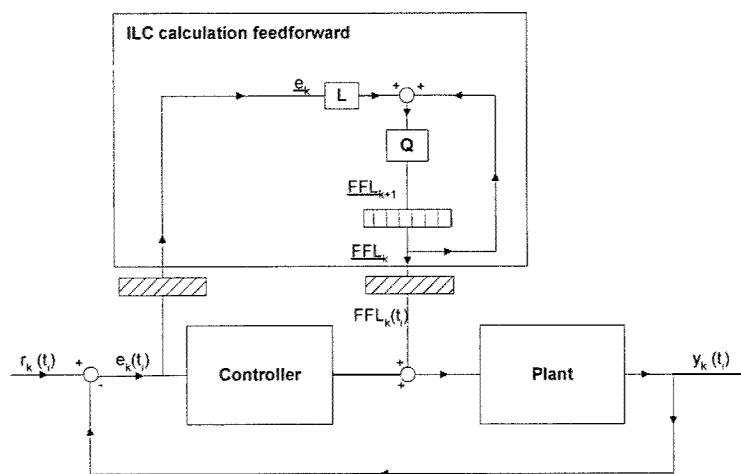
Figure 13 ILC general diagram

Iterative Learning Control applicability
ILC can be a powerful tool if the level of the systematic errors is large compared to the level of the random errors. Therefore, the repeatability of the error was investigated. Two series of 20 or 19 welds were made for four gap sizes (0, 20, 40 and 60 μm) on clean and polluted copper, respectively. Figure 14 depicts an example of such a set of error signals. For the clean sheets, the error is very reproducible, especially in the first 2 ms of the melting phase. The reproducibility of the errors reduces when gaps are introduced, but is still visible.

ILC has been implemented and tested in different configurations. An example of the obtained results is depicted in Figure 15, where the tracking behaviour of the system is visualised before and after the introduction of ILC.

The general observations regarding the ILC performance were as follows: From the control point of view, ILC performs well by means of better tracking performance. However, when a gap is present between the copper sheets, the weld quality decreases, although the tracking performance is improved. Although further experiments have to be done on this issue, the most likely explanation is that the surface temperature is maintained so well that there is hardly any mechanical excitation from vaporisation caused by an overshoot on the temperature. The top sheet simply melts and that's it: no wetting is initiated in the case of a gap between the parts.
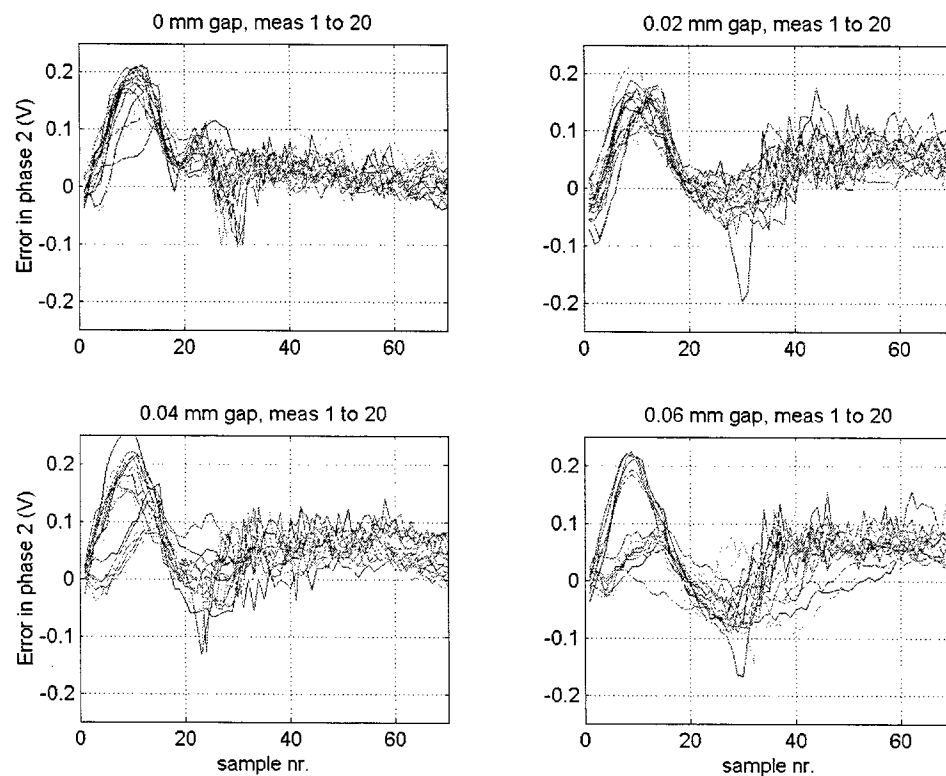
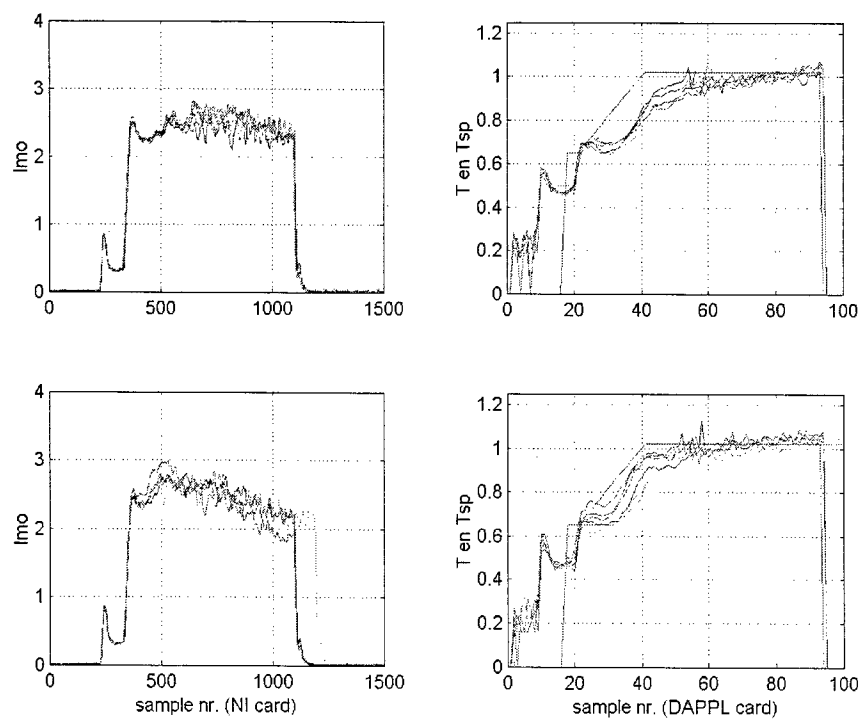Figure 14 Error signals in melting phase, for welds on clean copper

Figure 15 Learning experiment no gap, trials 1-5 and 6-10, learning starts at trial 6

7. TESTS AND RESULTS

The basis for our verification tests was the comparison of state of the art feed forward operated heat conduction spot welding using a certain fixed pulse shape, with the new feedback controlled spot welding technique. The tests were made on both clean copper sheets and on copper sheets that were polluted. Spacers of 20, 40 and 60 microns thick were used between the sheets to force a specific gap. The experiments showed that the actual size of the gap did not introduce much differentiation in the welding results. The fact that there is a gap is dominant. Table 1 shows the 'clean' version of the experiments of welding 100 onto 50 microns. Table 2 shows the results of similar experiments for polluted sheets. The third column presents the spread in weld diameter measured at the lower side of the joined sheets, when welding from the top. This figure is a good measure of the reproducibility of the welding process. The fourth column simply gives the percentage of bad or failing welds.

Table 1 Performance verification on clean copper sheets 100 onto 50 microns

Gap	Strategy	Good Welds	Bad welds
[μm]		Spread Dl(σ) [%]	Number [%]
0	Pulse shape	8	0
0-60	Pulse shape	24	28
0	Controlled	3	0
0-60	Controlled	4	0

Table 2 Performance verification on polluted copper sheets, 100 onto 50 microns

Gap	Strategy	Good Welds	Bad welds
(μm)		Spread Dl(σ) %	Number %
0	Pulse shape	41	7
0-60	Pulse shape	38	47
0	Controlled	7	0
0-60	Controlled	8	5

Table 1 shows that the open loop operating process performs well when there is no gap between the parts. The disturbing effect of the gap (heat distribution through the structure) is effectively handled by the feedback-controlled process.

A similar effect can be seen when polluted copper is used, introducing an extra disturbance during the pre-melting phase (see table2). A significant improvement of the joining technique is achieved using the controlled process, although the reproducibility with extra gap variations is no longer adequate on polluted copper.

8. CONCLUSIONS

The achieved results show that real-time feedback control on laser spot welding can improve the performance of the process significantly. The suppression of disturbances from the gap between the parts is remarkable. The introduced Iterative Learning Control concept shows a high potential. Optimisation with respect to the temperature profile required must still be done to obtain the full performance of this technique.

9. ACKNOWLEDGEMENTS

10. REFERENCES

[1] Y.S. Touloukian, R.W. Powell, *Thermophysical properties of matter, Vol. 1 Thermal conductivity, Metallic Elements and alloys*, IFI/Plenum, USA, 1970

[2] Data from publications in magazines:
     Kikuo Ujihara , Journal of applied physics, Volume 43 no 5, May 1972
     Journal of Laser applications, No. 9 1977.

[3] A concept for Hydrodynamic Model of Keyhole Formation, Icaleo 1994 (641-650)
     V.V. Semak, J.A. Hopkins, M.H. McKay, T.D. McKay
     Center for laser Applications, The University of Tennessee Space Institute, Tullahoma.

[4] M. Steinbuch, *Iterative learning control*, course notes TU/e, 2001.

3D-MID and Process Monitoring for Micro Joining Applications

A. Ostendorf, W. Specker, M. Stallmach, J. Zeadan

Laser Zentrum Hannover e.V., Hollerithallee 8, D-30419 Hannover, Germany

Introduction

Nd:YAG solid-state lasers have been integrated in many seam welding applications. They provide a good ability of integration into existing manufacturing sequences and allow its easy automation. Appropriate process monitoring systems are needed to decrease necessary user intervention, to ensure a high machine availability and to realize a zero defect production. In the electronics industry, laser spot welding techniques using pulsed Nd:YAG-lasers have been established in mass production applications, for example in manufacturing of electron gun components for TV monitor tubes over the last 25 years. They require different strategies and methods for process monitoring systems [1]. Apart from these integrated laser spot welding applications, there is a current demand for new technologies to join micro components onto 3-dimensional (3-D) circuit substrates and to connect electrical plugs. In recent years, laser spot joining techniques have emerged as a viable option for packaging electrical and mechanical microparts, such as surface mounted devices (SMDs) and casings. Under most conditions, laser spot welding provides more durability as well as thermal and mechanical stability compared to traditional packaging techniques, such as simultaneous soldering [2, 3]. Additionally, under less ideal conditions, the packaging quality can be inconsistent, resulting in the need for optimization and monitoring of the weld parameters under different conditions [4, 5]. In order to achieve a stable process during packaging of electrical components despite their weak absorption of laser radiation and different surface qualities, a process monitoring system should be needed.

1. Motivation

Monitoring systems for laser welding processes have been successfully implemented in single joining applications such as seam welding of car body parts in the automotive industry [6]. An easy transfer of the established process monitoring methods to laser spot welding applications as used in the electronics industry is not possible because of the limited system reliability with regard to the required defect detection. Usually, the evaluation of the process signals is based on empirically defined thresholds, because the dependence of the process signals on the beam-material interaction is only insufficiently known.
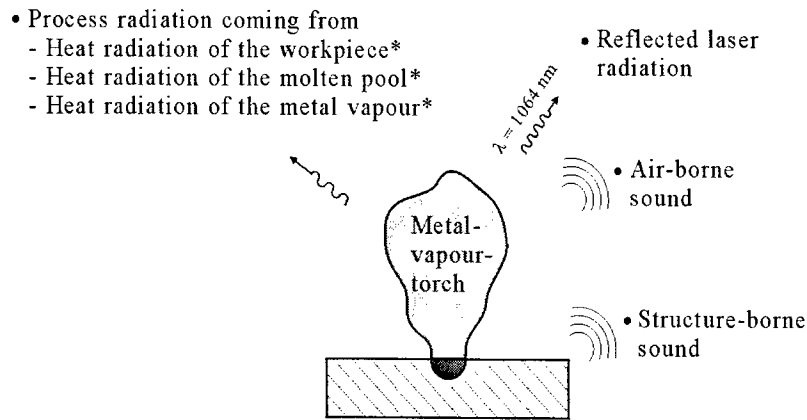
Therefore experimental work is carried out to investigate the process during laser spot welding of electron gun subcomponents and SMD components onto printed circuit boards. A process model is developed describing the laser induced evaporation and the related emission of process radiation. In this matter, the optical process signals are evaluated.

2. Laser spot welding processes

During Nd:YAG-laser spot welding processes, the laser beam is transmitted via a flexible glass fibre trough an appropriate focussing optics onto the workpiece. With appropriate parameters the joint is generated by a single laser pulse. In general, two types of laser spot welding processes are distinguished: Heat conduction welding and deep penetration welding. During heat conduction welding, the laser radiation is absorbed at the surface of the workpiece. The sheets are welded by heat conduction only. Laser induced evaporation can be seen on the surface of the workpiece. For small workpieces the mechanical strength of the penetration generated by a laser spot can be adequate for the connection of the two parts joined. Apart from mechanical joining of two parts, an electrical connection can be carried out using this technique.

3. Process signals during laser beam welding

The interaction between laser beam and the material causes emissions from the process area. Among other emissions, optical and acoustical process signals are emitted which can be measured with appropriate sensors. They are evaluated and recorded by computer programs. The signals contain information about the beam-material interaction so that appearing welding defects can be detected during the process and recorded for each single workpiece. Figure 1 shows a selection of detectable emissions which can be used as process signals.

- Process radiation coming from
  - Heat radiation of the workpiece*
  - Heat radiation of the molten pool*
  - Heat radiation of the metal vapour*

- Reflected laser radiation

$\lambda = 1064\ nm$

- Air-borne sound

Metal-vapour-torch

- Structure-borne sound

*The heat radiation of all sources superpose in the visual and infrared spectral range and lead to the emission of process radiation

Figure 1: Selection of different emissions arising during Nd:YAG-laser beam welding

The back-reflected laser radiation is the amount of the radiation of the laser source which is not absorbed by the material. Acoustic sound can be divided into air-borne and structure-borne emissions. They are caused by the surface of the laser induced metal vapour. The metal vapour and the molten pool emit continuous radiation in the visible and infrared range of the spectrum [8]. During Nd:YAG-laser welding, the process radiation is mainly determined by the heat radiation of the metal vapour [7, 8]. Only a small amount of ionised metal atoms is observed whose emission can be neglected. The advantage of measuring optical signals can be seen in the non-contact measurement without interfering the process itself. For Nd:YAG-laser welding applications, the flux density of the process radiation is used as process signal in this paper. It is defined as flux of the heat radiation emitted from the metal vapour detected by the optical sensor.

4. Process monitoring systems for laser spot welding applications

In general, commercially used as well as on laboratory scale, available process monitoring systems have a similar structure. An optical sensor is used to record the flux density of the secondary radiation emitted by the process. The flux density is converted by the photo diode into an electrical signal. Most common used photo diodes for this application are made of silicon providing a spectral response between $\lambda = 400$ nm and $\lambda = 1100$ nm [1, 7, 8, 9]. With optical filters, the sensitivity of the photodiode can be limited to certain spectral ranges of interest. The high time resolution and dynamic offered by photo diodes with short rise times of about 10 ns is sufficient for spot welding processes in which a pulse duration of typically 1 ms to 20 ms are applied. The amplified signals are transferred to the PC equipped with a data acquisition board. The evaluation and documentation of the signals are carried out cost effectively by dedicated evaluation programs [6, 9].

Applying this method, irregularities during the welding process leading to weld defects can be detected and documented for each spot weld. Systematic variations of the process parameters as well as randomly caused changes of process

influences can be detected. Different signal characteristics, such as mean, standard deviation or the coefficient of variation are suitable indicators in this context.

The position of the sensor determines whether the observation of the process area is carried out co-axially or off-axially to the laser beam (figure 2). During off-axial measurements of the process radiation, positions and orientations of the optical sensor and its distance to the weld pool can be varied so that the observation of the process under several angles between workpiece and welding head are possible. Dependent on the observation position either just the metal vapour above the keyhole or even the metal vapour in the keyhole itself during deep penetration welding is detected. During signal evaluations even small changes in the sensor alignment has to be taken into account at off-axial measurements of the process radiation which in practice is hardly possible [7].
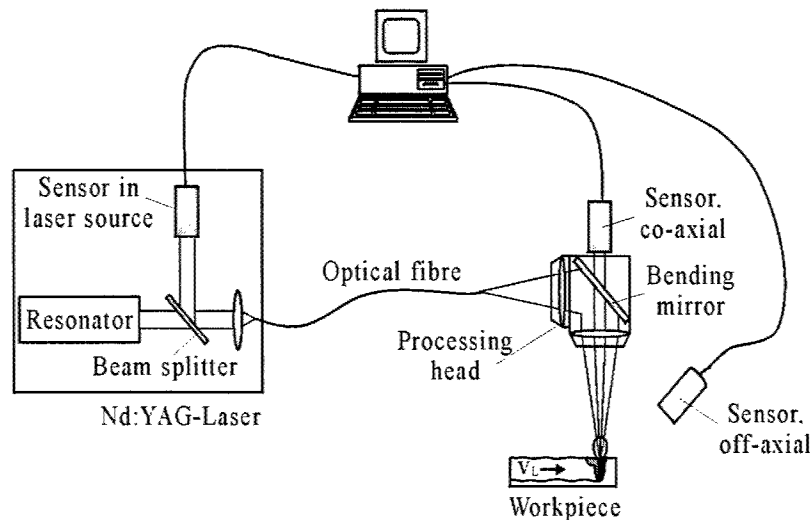

Figure 2: Sensor integration for process monitoring systems

At coaxial configurations of the sensor, the optical path of the weld pool observation corresponds to the direction of the incident laser beam. The process radiation is coupled out by an appropriate optical component, such as a beam splitter or a bending mirror. If the optical sensor is integrated into the laser source, the process radiation is guided back through the same optical fibre as the laser beam itself [8]. The advantage of the coaxial process observation lies in minor requirement of adjustments. After a confocal pre-alignment, the sensor is insensitive to external influences, such as misalignment or contaminations.

5. Process monitoring applied in mass production of electron guns for TV tubes

A typical industrial application for spot welding with Nd:YAG-laser radiation can be seen in the manufacturing of electron gun components for television picture tubes [1, 7]. The subassembly of an electron gun is joined by up to 150 laser spot welds. The process consists of heat transfer welding, therefore a capillary as seen in deep penetration welding is not present. The grating of an electron gun is made of a 0.2 mm thick FeNi42-metal sheet (figure 3). The nominal pulse energy of the laser beam source applied during the welding process amounts $Q = 7.6$ J.

The optical sensor is placed behind the bending mirror of the optical welding head (figure 2 and 5). The signal path of the radiation flux density during the process dependent on the pulse energies $Q = 7.1$ J, $Q = 7.6$ J and $Q = 8.0$ J is given in figure 4.

Laser : pm Nd:YAG, HL124 P	Beam guidance : Fibre, d = 0.6 mm
Pulse energy : Q = 7.6 J	Operation mode: Single pulse
Pulse duration: t_H = 5 ms	Material : FeNi42, s = 0.2 mm
Beam forming : Prism, f_k = f_f = 100 mm	Weld geometry : Overlap weld
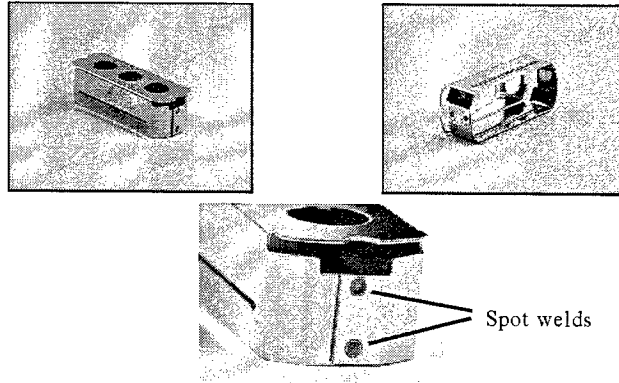
Spot welds

Figure 3: Electron gun grating for TV tubes with welding points

Each signal displayed is the calculated average of 20 measured signals from 20 spot welds. Figure 4a shows the flux density of secondary radiation without gap between the workpieces to be joined, whereas a gap of 70 μm was present during the measurements of figure 4b. All averaged signals show the identical characteristic course. After an approximate linear rise of the flux density the signal passes its maximum before decreasing again. Signals measured at samples with a gap of 70 μm, the maximum reaches a higher value than those with no gap. The rise of the signal is dependent on the applied pulse energy. This can be used for monitoring of the welding process. Independent of an existing gap a larger positive rise of the flux density can be seen at higher pulse energies applied. A small rise of the flux intensity indicates a not sufficient pulse energy at the workpiece to perform the welding process. Possibilities to classify the gratings with gap can be derived from the evaluation of the signal maximum.

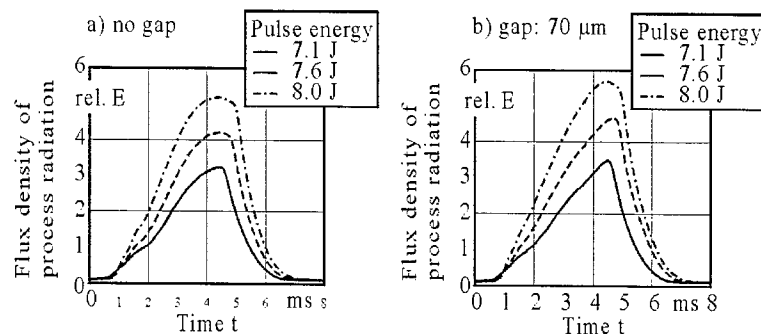| Laser : pm Nd:YAG, HL124 P	Beam guidance : Fibre, d = 0.6 mm
Pulse energy : Q = varied	Operation mode: Single pulse
Pulse duration: t_H = 5 ms	Material : FeNi42, s = 0.2 mm
Beam forming : Prism, f_k = f_f = 100 mm	Samples : n = 20

Figure 4: Flux density of secondary radiation dependent on the pulse energy

The integration of the optical sensor into a production line for manufacturing electron guns was carried out as shown in figure 5.
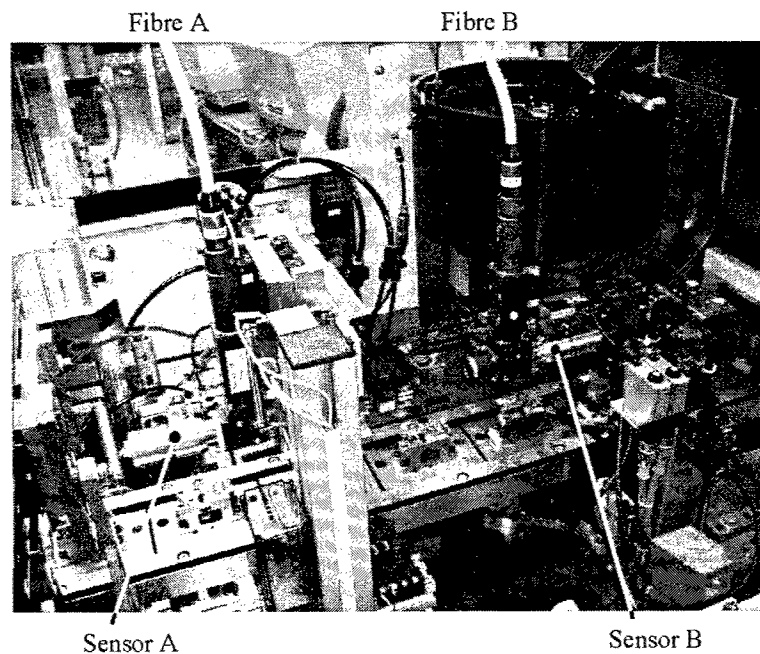
Figure 5: Sensor integration in a production line for manufacturing electron gun components for TV monitor tubes

5.1 Process model

At heat conduction welding, the metal vapour escaping and expanding from the interaction area can be seen as source of the heat radiation emitted. After the end of the laser pulse, the torch of the metal vapour condenses within a duration of 1.5 ms and the emitted heat radiation extinguishes. Therefore the rate of evaporation is of particularly importance for the heat radiation. To determine the heat radiation, influenced by the pulse energy and the existing gap, the model of the laser induced evaporation rate according to Aden is used [11]. The absorbed laser beam radiation leads to an evaporation of material in the so-called evaporation front, which is a 1 µm thick layer of material. The evaporation front moves, comparable to a burning wave, with the speed v_D into the material. Under stationary circumstances, the speed v_D is proportional to the evaporation rate and therefore majorly determines the heat radiation. The pulse energy or an existing gap affects the speed of the evaporation front influencing the evaporation rate and the emission of heat radiation. The flux density of heat radiation is measured as process signal by the optical sensor. The rise at the start of the process signal can be explained by the radial expansion of the evaporation front until a quasi-stationary state of equilibrium is achieved. The rise at high pulse energies is bigger, because the pulse power (here proportional to the pulse energy) influences the velocity of the evaporation front as well. Therefore the volume of metal vapour and process signal increase faster. Existing gaps between the metal sheets cause a change in the equilibrium conditions at the evaporation front with increasing velocity of the evaporation front due to a different thermal conduction behaviour in the workpiece. This leads to an increase of the process signal with time delay after the start of the laser pulse as well.

6. Connecting SMD-leads on 3-dimensional circuit substrates

Another typical industrial application is the welding of microcomponents, such as SMD with Nd:YAG-laser radiation. The process consists of heat transfer welding as well, because a deep penetration weld would generate too much heat causing damage to the microcomponents.

6.1 Pattern and substrates specification

In the experiments, laser welds were created to join the leads of standard SO16-SMDs to the contact lands of the circuit substrate. The laser beam direction is perpendicular to the SMD-lead (figure 6). To obtain reproducible results, the optical behaviour and physical characteristic of the welding areas must be similar [12]. The SMD's specifications are listed in table 1. The lands fixed onto the circuit substrate are made off copper with varying thickness between different substrates.
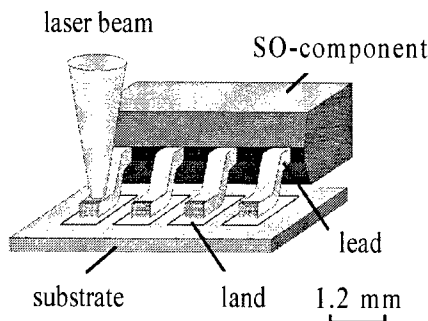

Figure 6: Experimental set-up (schematic)

Lead thickness	0.25 mm
Lead width	0.49 mm
Contact surface	0.1 mm^2 (approx.)
Pitch distance	1.27 mm
Material	Fe: ~ 59% Ni: ~ 40%
Coating	Sn/Pb

Table 1: SMD-specification

The substrate is made off metallized and structured Poly-imid (PI) foils. Copper contact lands are created on the surface of the substrate using different plating processes which are also used for 3-dimensional moulded interconnection devices (3-D MID). In order to protect the lands from oxidation, they are coated with a few microns thick tin layer, a common technique in industrial batch production. The thickness of the metallized layer is an important parameter for the laser welding process because of the thermal balance between the metallized layer and the SMD's lead.

6.2 Applied equipment and system technology

To conduct the welding experiments, a lamp-pumped Nd:YAG-laser, model 200 SLSC60 from Lasag AG Switzerland, is used. The beam is guided through an optical fibre to a 50 mm focusing optics creating a 200 μm spot diameter. Table 2 shows further specifications of the laser whereas table 3 gives the parameters that are varied during the experiments.
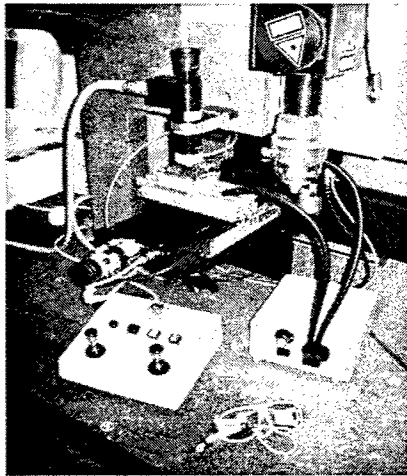
Laser type	Nd:YAG, pulsed
Wavelength λ	1064 nm
Pulse duration (τ_H)	0.1 .. 20 ms
Repetition rate (f_p)	0.1 .. 1000 Hz
Max. pulse energy (Q)	10 .. 50 J
Pulse power @ 3 ms	2 .. 5.5 kW
Average output power (P)	50 .. 220 W
Fibre optics diameter	400 μm

Table 2: Laser specifications [10]

Figure 7: Laser welding system (set-up) [10]

Pulse energy (Q)	1 .. 20 J
Pulse duration (τ_H)	1 .. 10 ms
Number of pulses (n)	1 .. 6
Repetition rate (f_p)	1 .. 30 Hz

Table 3: Process parameters for the welding tests

6.3 Experimental work on 3D-MID components

The difficulty in laser beam welding of micro components in mass production can be seen in an unstable process. Figure 8 shows the process window for successful welds on two different substrates. The process window is given by the black area marked in the graphs. Using a PI-foil, as shown in the left diagram, the process window is narrow. By using a PA-T PCB foil the parameter window of good welds increases. But for transferring the results into 3-D MID applications the PI foil is the better alternative. The reasons for the increased process window are related to a better heat resistance of the substrates.
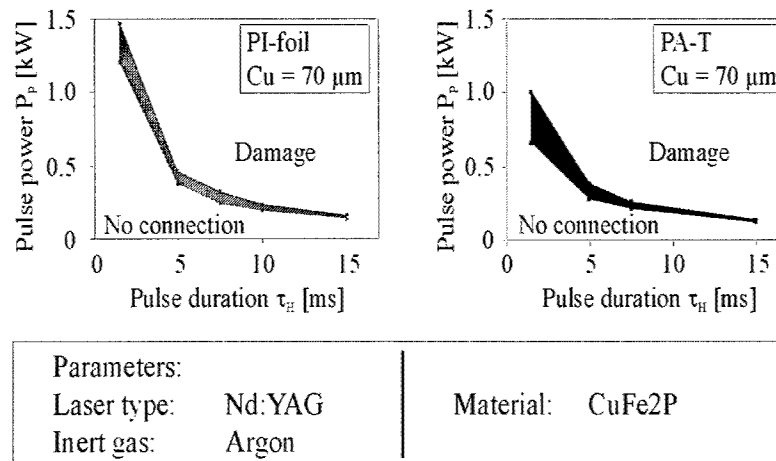

Figure 8: Area of good laser spot welds of flip-flop SMD on different substrates

6.4 Process control

For process control and quality assurance purposes, an optical sensor on the base of a silicon photo diode is used to measure the radiation emitted from the work piece. The sensor measures at frequency of 50 kHz which is equivalent to 250 measurements over a 5 ms pulse duration. Figure 9 shows the generated signals of several welds with different quality achieved which are separated into good welds in the left diagram and bad welds in the right diagram. All welds were made using the identical parameter set. When the weld quality is similar, both the shape and the magnitude of the signal detected by the sensor are similar as well. However, when the signal from a bad weld is compared to a good weld, the signals are different. In the laboratory, this technique has shown promising results for about 100 welds.

For automation of the process and quality control, reference data is required which is usually obtained by running a wide range of experiments. A comparison of the results have to be made to create a correlation between the process signal and the weld quality. When welding in batch production, the detected process radiation will be evaluated to determine good and bad welds achieved.

The detected signals in figure 9 show 3 relevant areas. Area I shows a high peak, which reaches 14 volts in about 0.25 ms. This effect appears due to the melting of the tin film on the leads. Area II lasts for nearly 3 ms. In this time the NiFe leads are heated. The heating first does not primarily affect the emission of process radiation. Therefore the sensor signal stays approximately constant. In area III the sensor signal increases again to about 4 volts in 1 ms. This behaviour represents the melting of the NiFe leads. At the same time, metal vapour is generated leading to a strong increase of heat radiation and thus to a rise of the signal. Details of the data evaluation of the process signals and the algorithms for quality classification are shown in [7].
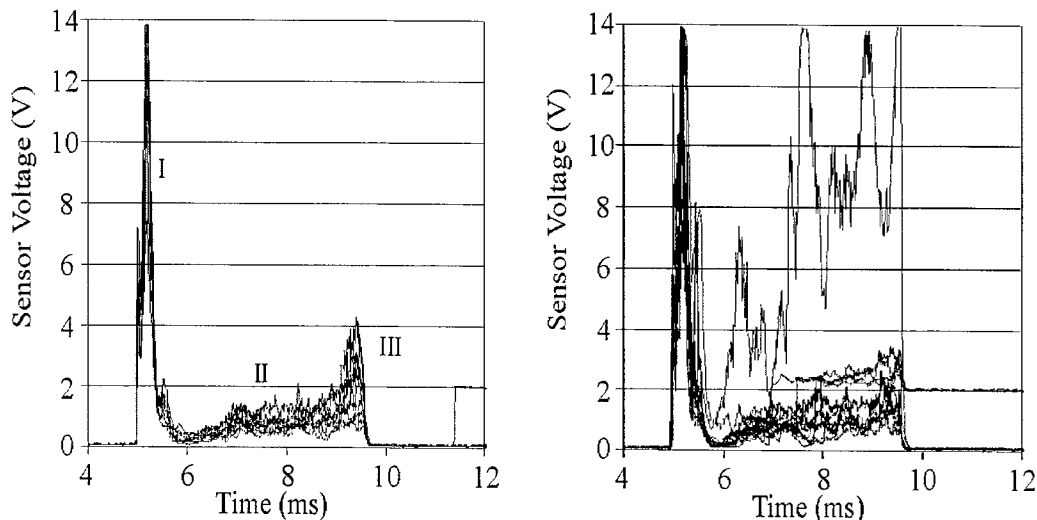

Figure 9: Reproducibility of detected process signals during laser spot welding of 3D-MID components

Figure 10 shows pictures of the welding process recorded by a high speed camera. The first shot shows a high metal cloud. This section refers to the highest peak, produced by the controller of the laser system. The second picture displays the process radiation already decreased so that the vapour also decreases. The third and fourth picture show a rising amount of metal vapour generated. This section can be related to section II of figure 9. Looking at the fifth picture, a higher process beam can be seen which correlates to the course of figure 9.
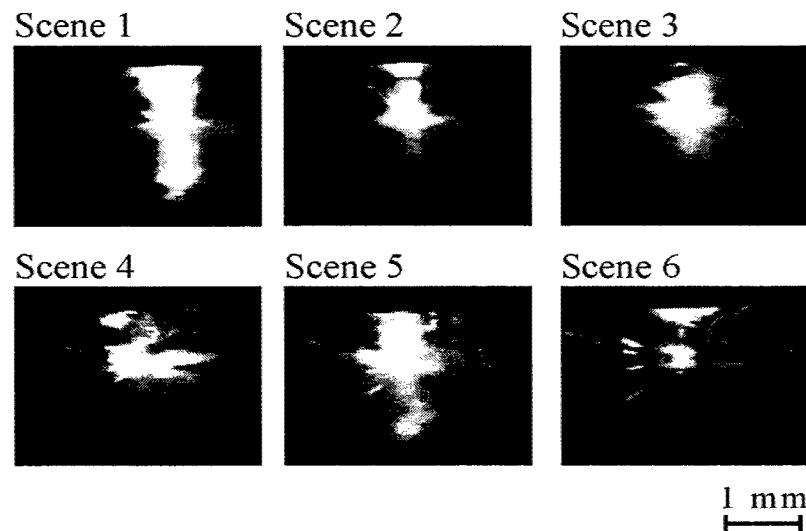
Figure 10: The 3D-MID welding process recorded with a high speed camera

Conclusion

Laser spot welding processes are a part of automated production lines. This leads to a strong demand for automated process monitoring which can be performed by measuring the process signals. In this paper the process flux density of the heat radiation from the metal vapour was used as a characteristic process quantity. An optical sensor was integrated into a welding head in the production line for laser spot welding of electron guns. The influence of different pulse energies and gaps to the process signals was investigated. A process model was developed to understand the origin of process radiation leading to the process signals caused by the laser induced evaporation.

Furthermore, in this paper laser spot welding with respect to its use for three-dimensional circuit substrates is examined. The goal is to create joints for handling-temperatures exceeding 150 °C which cannot be created using conventional soldering techniques with tin-lead solder.

Laser welding allows process parameter optimization without using a filler metal. However, because of errors due to varying gap sizes and surface conditions, there are still difficulties in the reproducibility of consistent high quality joints. An integration of a process control system into the process set-up provides a method for quality inspection during welding.

References

[1]   J. Griebsch, L. Schlichtermann, M. Jurca, et al.: *Quality Assurance of Industrial Spot Welding with Pulsed Nd:YAG-Laser.* Proc. of ICALEO 1996, Detroit, LIA, Laser Institute of America, p. 164-173.

[2]   B. S. Yilbas, et al.: *Laser spot welding of electrical wires.* MATADOR, Proc. of the 33rd International MATADOR Conf., Manchester, GB, 2000, p. 455-460.

[3]   K. H. Leong, et al.: *Predicting threshold laser beam irradiances for melting and welding.* Laser materials processing conf. ICALEO '97, Vol. 83: 1997; p. 1-8.

[4]   C. Lampa, et al.: *Nd:YAG Laser welding of aluminium to copper.* Joining Technologies of Dissimilar Materials and Structural Integrity Problems of So Jointed Materials, 2001 International Conf., Ljubljana, SLO, July 12, 2001, Welding in the World, Vol. 45: 2001; p. 109-116.

[5]   S. Spruk, et al.: *Laser induced reaction between Fe layer and CuNi30Mn1Fe alloy.* Kovine Zlitine Tehnologije, Vol. 29: 1995, No. 3 / 4; p. 427–430.

[6]   F. Behr: *Qualitätskontrollsysteme für das Laserstrahlschweißen..* ILT, AKL Aachener Kolloquium für Lasertechnik, EuroLaser, Gruetter, 2000, p. 115-128.

[7]   W. Specker: *Prozeßüberwachung beim Schweißen mit Nd:YAG-Lasern.* Düsseldorf, VDI-Fortschrittsberichte, Reihe 2., ISBN 3-18-361402-2. Diss, University of Hannover, Germany, 2002.

[8]   J. Schumacher: *Untersuchungen zum Schweißen mit gepulsten Hochleistungs-Nd:YAG-Lasern.* Düsseldorf, VDI-Fortschrittsberichte, 1997, ISBN 3–18–345602–8.

[9]   A. Sun, E. Kannatey-Asibu, et al.: *Sensor systems for real-time monitoring of laser weld quality. Jour. of Laser Applications.* 8 (1999) 4, p. 153–168.

[10]   N.N.: Lasag AG. Mittlere Strasse 52. CH-3600 Thun. Schweiz. *Company brochure 87.1561.* © Lasag AG JH 10.00 3000: 2001.

[11]   M. Aden: *Plasmadynamik beim laserinduzierten Verdampfungsprozeß einer ebenen Metalloberfläche.* Aachen, Verlag Shaker, 1994, ISBN 3–86111–834–3.

[12]   H. K. Tönshoff, et al.: *Laser micro welding of electronic components.* LASE high power laser and application, 19-25 January 2002, San Jose, California, USA.

Laser Droplet Weld - an innovative joining technology opens new application possibilities

Bernd Jahrsdörfer*[a], Gerd Eßer[b], Manfred Geiger[a], Edvard Govekar[c]

[a] University of Erlangen-Nuremberg, Chair of manufacturing technology, Egerlandstraße 11, D-91058 Erlangen Germany
[b] Bayerisches Laserzentrum gGmbH, Konrad-Zuse-Straße 4-6, D-91052 Erlangen Germany
[c] University of Ljubljana, Faculty of Mechanical Engineering, Askerceva 6, SI-1000 Ljubljana Slovenia

ABSTRACT

"Laser Droplet Welding" is an innovative joining technology. The welding is realised by a laser generated liquid metal droplet which is deposited onto the parts to be joined. The raw material is a metal wire. In conventional laser welding a gap between the parts worsens the quality of the laser welded joint substantially. Contrarily a droplet offers sufficient material to bridge gaps. Even different gap sizes can be bridged by a suitable selection of the droplet size. A further advantage is the controllable heat transfer, only given by the heat content of a single drop that is sufficient to produce a high-temperature weld. The droplet heating provides the opportunity to weld small devices, thin coatings and even heat sensitive components without negative influence on their mechanical and electrical function. It is also possible to interconnect different materials by the addition of material supplied in form of drops. With the Laser Droplet Weld it is furthermore possible to join high reflective materials. This article describes the process and the system technology as well as achieved results. It will mainly focus on the droplet detachment which influences the complete process, e. g. the heat quantity or weld splashes.

Keywords: Laser Droplet Weld, Welding Technology, Laser welding, Joining Technology, Drops

INDRODUCTION

The joining of two or more parts is a continuous task for mechanical and electrical components [1]. Conventional soldering and welding technologies are inapplicable for some joining applications. Therefore it requires innovative joining technologies which are able to solve the always new tasks of joining. The "Laser Droplet Weld" process offers the possibility to realize joining applications which can not be realized up to.

This paper describes the experimental set-up used for the investigation of the laser droplet welding process. The description of the experiments is followed by the presentation and discussion of the results. After the characterisation of the process phases welding results on blind welds and butt joints are described. Finally the main results are summarized.

EXPERIMENTAL

The main parts of the Laser Droplet Weld set-up (Figure 1) are a laser (pulsed Nd:YAG), a wire-feeder, a target-positioning system, a shielding gas supply and a mechanical positioning system for the laser optics [2]. With the used laser optics focus diameters between 280 μm and 400 μm are possible. Three laser beams are used to achieve homogeneous heating of the wire. The three laser optics are positioned around the wire in an angle of 120° and are fixed on micro positioning devices to achieve as many degrees of freedom as necessary. The mechanical set-up also allows to change the angle between laser beam and wire. A wire feed system moves the welding wire. Droplet creation occurs during a single laser pulse; thus the wire has to move in a controlled way while the laser is active. A synchronisation of the wire feeder and the laser is realised via controlled delay of the laser trigger signal, given by the wire feed system. An xyz-table is located underneath the set-up to ensure an exact positioning of the joining partners.

*b.jahrsdoerfer@lft.uni-erlangen.de; phone: +49/9131/97790-16; fax: +49/9131/97790-11; http://www.lft.uni-erlangen.de/
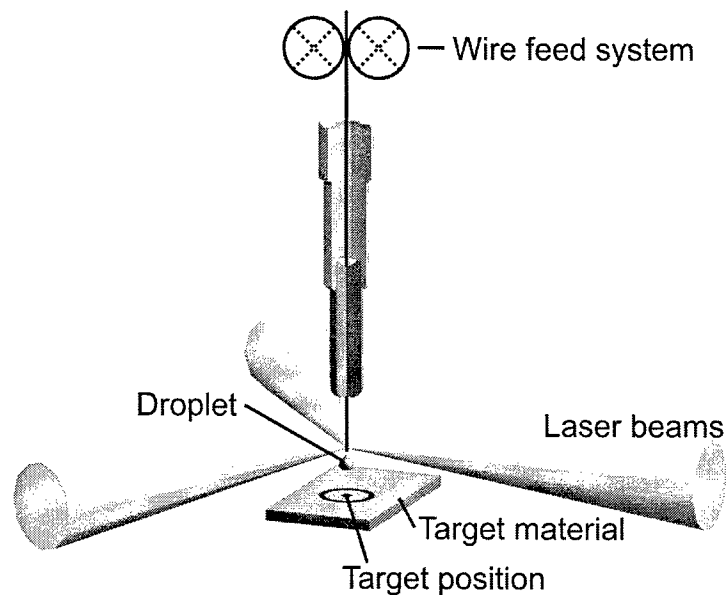
Figure 1:   schematic description of the laser droplet weld set-up

The laser pulse forms and the total pulse time are varied. All pulse forms show a characteristic profile which is illustrated in Figure 2: in a first time period (t1) the droplet is created and the laser power (P1) is chosen high enough to melt the wire. After that the laser power is reduced to a minimum (P2) and the wire is moved on for a time (t2) to position the droplet underneath the focus of the laser. The last step is to set a short laser peak (t3) of a comparatively high laser power (P3) to detach the droplet. If the detachment peak hits directly the molten material there are splashes visible on the substrate. Therefore it is necessary to move the wire for the time t2 with low laser power.
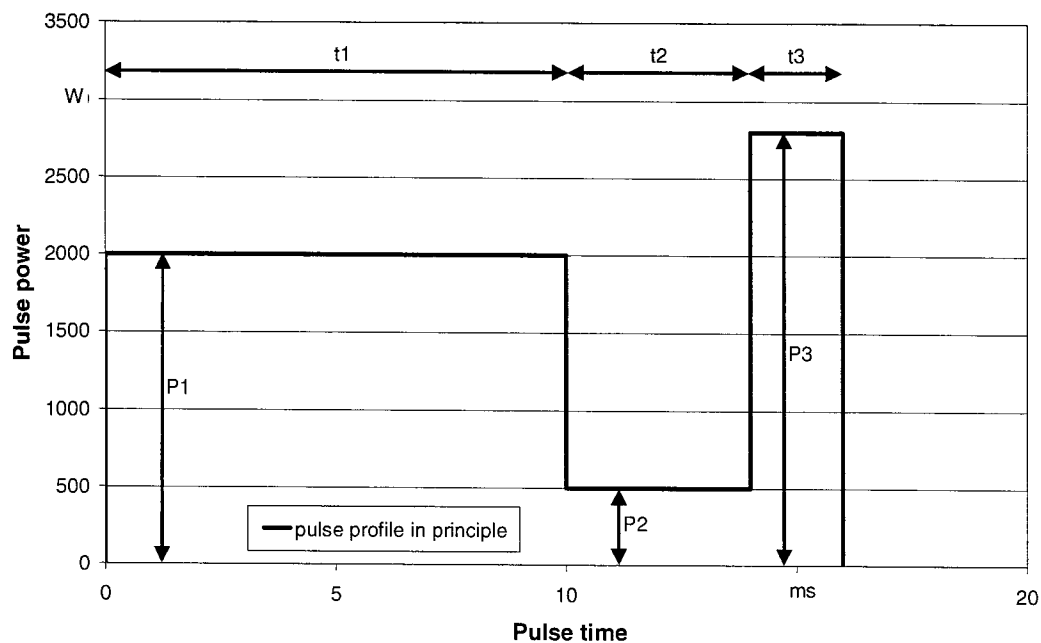

Figure 2:   Pulse profiles for 0,6 mm nickel wire (wire acceleration: $10 m/s^2$; wire velocity: 150 mm/s)

Welding results are evaluated based on the criteria represented in Figure 3. This allows to compare at least the welding results of blind welds. The diameter of the welded droplet (cap diameter), the droplet height (cap height) and the contact angle between droplet and joining partner are used for the characterisation of the blind welds. A further criteria is the position accuracy of the droplet that is measured as the distance between the target position and the real droplet position.
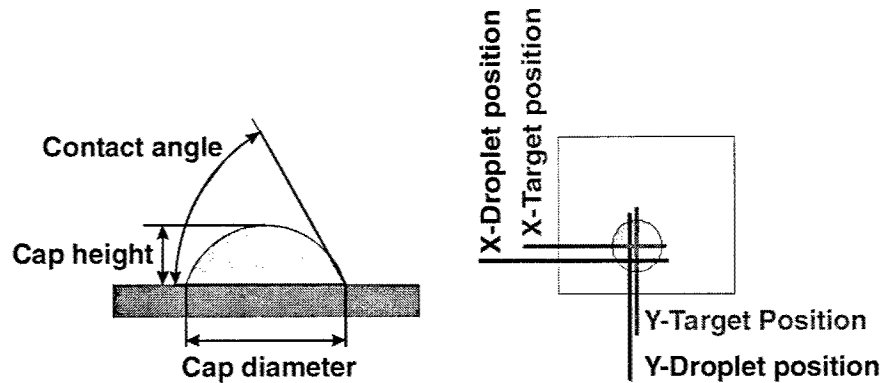

Figure 3:   Evaluation criteria for blind welds

RESULTS AND DISCUSSION

RESULTS ON THE PROCESS:

The complete Laser Droplet Weld Process can be split up into five phases: droplet creation, droplet detachment, droplet flight, droplet landing and droplet welding. All phases are part of an interconnected process and it is difficult to examine a single phase without looking at the other ones. Each phase influences at least the next phase and is dependent on the phase before.

During the first phase the droplet is created. A single laser pulse generates a droplet which is still connected to the wire. Figure 4 shows images of the droplet creation process. The solid-liquid transition line maintains nearly a constant position. That allows the conclusion that the temperature in the transition line is nearly constant for the correct adaptation of wire feeding speed and laser power. An approximate calculation of the droplet cooling shows that the droplet cooling is not important at least for the first 20 ms. During the droplet creation phase the droplet temperature increases and the temperature distribution inside the droplet gets homogenised.
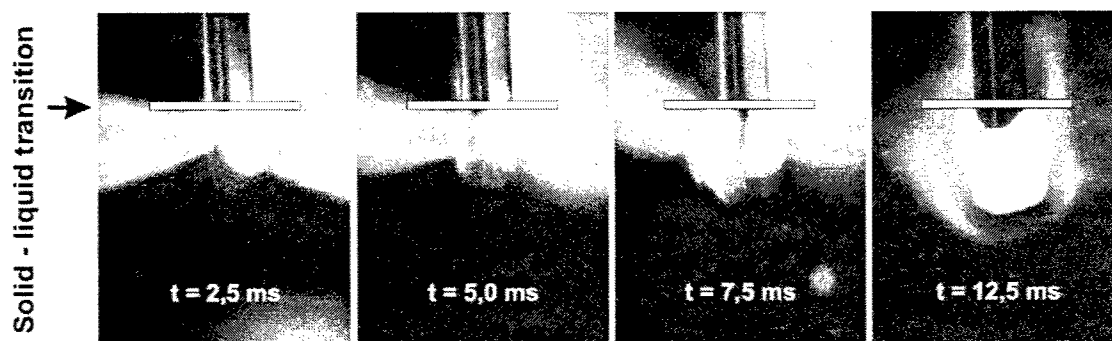

Figure 4:   Transition of solid and liquid material during droplet creation ($\varnothing$ 0,6 mm; wire acceleration: 10 m/s^2; wire velocity: 150 mm/s)

It turns out to be important with respect to the avoidance of melt splashes to separate the phase of droplet creation and droplet detachment. For the experiments reported here, the time of the wire movement is chosen equal to the pulse time and the wire velocity is adapted to the process. As an example the process window for a nickel wire (0,6 mm diameter), a wire velocity of 150 mm/s and an acceleration of 10 m/s^2 is shown in Figure 5. Looking at the process window for controlled droplet creation it is conspicuous that the boarders are running in a horizontal line. This is explainable by regarding the applied energy and the molten volume per time unit measured with respect to the solid-liquid transition line. After a time of 4 - 5 ms the curves increase approximately the same way and run nearly parallel. So the energy and the wire volume increase similar. Further information can be drawn from the process window calculating the energy per wire volume which is to melt. In the area "no droplet creation" the energy per volume is lower than 58 J/mm^3 and in the area "uncontrolled droplet creation" it is above 98 J/mm^3. Controlled droplet creation is possible in a range of 58 J/mm^3 to 94 J/mm^3. This explains the horizontal boarders of the process parameters.
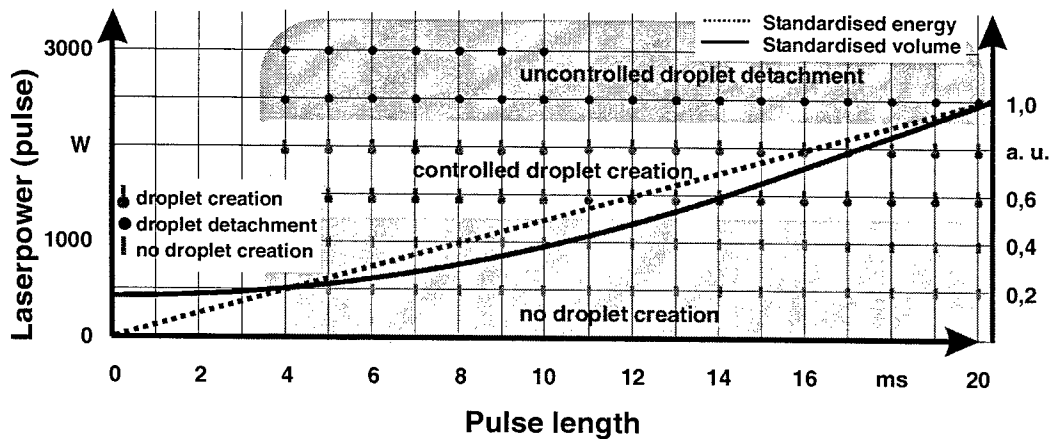

Figure 5: Process window for droplet generation with nickel wire (∅ 0,6 mm; wire acceleration: 10 m/s^2; wire velocity: 150 mm/s)

A controlled droplet detachment must be achieved in the second phase of the process. Three concepts to detach the droplets have been examined. An energy peak to detach the droplet turns out to be the best suited strategy for the laser droplet welding. To detach the droplets a short power peak at the end of the laser pulse is sufficient. In a number of experiments for a 0,6 mm nickel wire the length of the peak was optimised to 2,1 ms and a power of 2.800 W.

The droplet flight is the third phase of the process. The flight time of the droplet has been measured with an acoustic sensor. After the detachment the droplet has an initial speed of approximately 0,5 m/s. In order to determine the cooling of the droplet during the flight phase a mean droplet temperature slightly above the melting point is assumed. The droplet temperature of the falling droplet in a shielding gas atmosphere can be approximated by [4, 5]:

$$T_{droplet\,/\,shielding\,-\,gas}(t) = e^{-\dfrac{\alpha_{lam\,-\,gas}(t)\cdot A_{droplet}}{m_{droplet}\cdot c_{p\,-\,droplet}}\cdot t}\cdot(T_{droplet}(t=0)-T_{gas})+T_{gas}$$

The variables are defined in Table 1.

Variable	Unit	Annotation		Variable	Unit	Annotation
$T_{droplet\ /shielding\text{-}gas}$	K	Droplet temperature		$c_{p\text{-}droplet}$	J/gK	Heat capacity
$\alpha_{lam\text{-}gas}$	W/m²K	Heat transfer coefficient		$T_{droplet}$	K	Droplet temperature
$A_{droplet}$	m²	Droplet surface		T_{gas}	K	Gas temperature
$m_{droplet}$	kg	Droplet mass				

Table 1: Variables and constants for the heat calculation [4,5]

The temperature of the droplet during the flight is shown in Figure 6 for different droplet materials (nickel and copper) and with and without shielding gas. For a falling height of 3 mm the flight time is below 0,1 s and the temperature change during droplet flight does not exceed 30 K. This clearly shows that droplet cooling can be neglected.
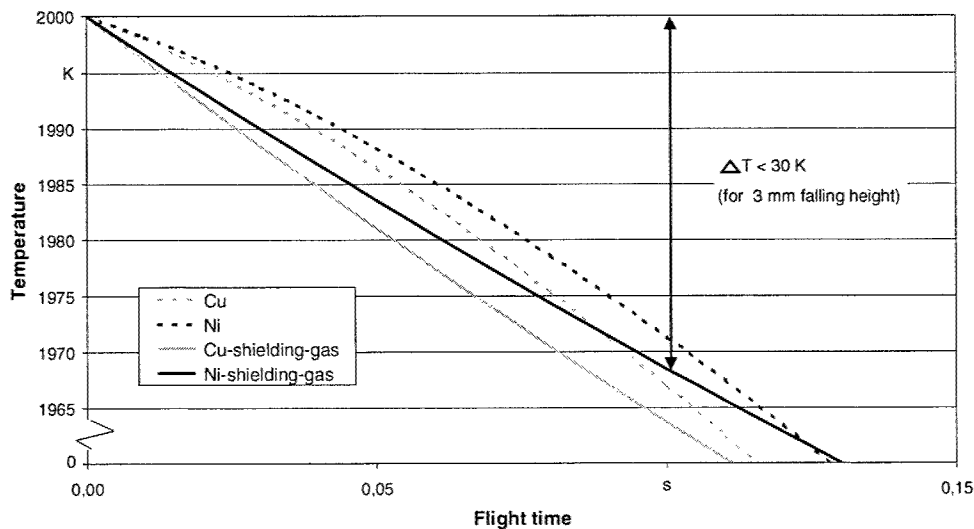

Figure 6:   Cooling of the droplet during the flight phase

The droplet landing is the forth phase of the laser droplet weld process. After landing the droplet contacts the joining partners but instantly no wetting occurs. This is shown by means of the wetting angle during this phase, which at the beginning of this phase is clearly over 90° and then slowly changes to under 90°. It is possible to estimate whether splashes develop within the impact or not by considering the surface energy and the kinetic energy of the drops [6, 7]. The surface energy calculates to

$$E_{sur} = \sigma \cdot A_{droplet} = 4 \cdot \pi \cdot \sigma \cdot r^2$$

and the kinetic energy to

$$E_{kin} = \frac{1}{2} \cdot m \cdot v^2 = \frac{2}{3} \cdot \rho \cdot \pi \cdot v^2 \cdot r^3 .$$

Thus the relation between kinetic energy and surface tension calculates with the following formula:

$$\frac{E_{kin}}{E_{sur}} = \frac{1}{6} \cdot \frac{\rho}{\sigma} \cdot v^2 \cdot r.$$

With a typical droplet mass of $\approx$ 4 mg, a droplet radius of $\approx$ 0,5 mm, a droplet velocity of 0,5 m/s and a material density of 8,9 g/cm^3, the surface tension is more than six times the kinetic energy. That means that the problem of splashes on the joining partners does not derive from the landing of the drops.

The last phase of the process is the welding phase. With the change from the landing phase to the welding phase the contact angle changes and shows a value clearly under 90°. During the landing phase the droplet heats the substrate and the substrate temperature exceeds in the welding phase the melting temperature, visible by a contact angle under 90°. Figure 7 shows highspeed camera pictures of the two phases landing and welding. The left image is the landing and the right image the welding phase. During the welding phase the droplet cools very fast what can be seen by the reduction of the brightness during this phase. The images are taken with a high speed camera working in the visible range. In the welding phase it should come to a material-conclusive connection between the drop material and the joining partners.
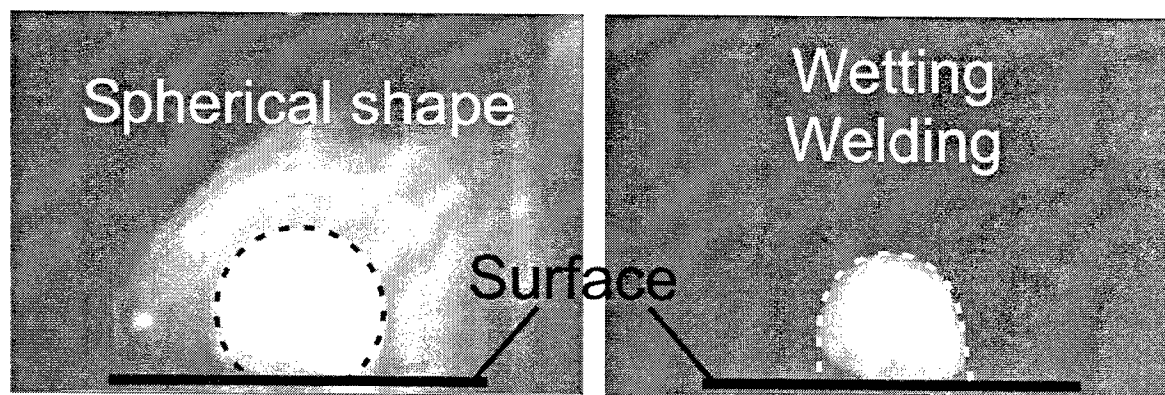

Figure 7:   Image of droplet landing (left) and droplet welding phase (right)

RESULTS ON THE PROCESS DIAGNOSTICS:

The use of Sensors in the Laser Droplet Weld technology can help to detect if the droplet detachment is successful or if the droplet remains on the wire. Tests with different acoustic sensors did not show any positive results because the wire movement causes too much noise. Good results are achieved using the reflected laser radiation that is detected by suitable photo diodes and then transformed in digital signals. For each laser beam such a sensor is used to detect the reflections. Using the standard profile there are just slight differences between the signal of a detached droplet and an un-detached one. This means that these signals do not provide enough information to monitor the process in a reliable way.

The use of a measurement laser pulse which has no influence on the wire melting offers the possibility to observe the droplet detachment (Figure 8). To achieve clear sensor signals the measurement laser peak is not placed directly after the detachment laser peak but after a certain waiting time.
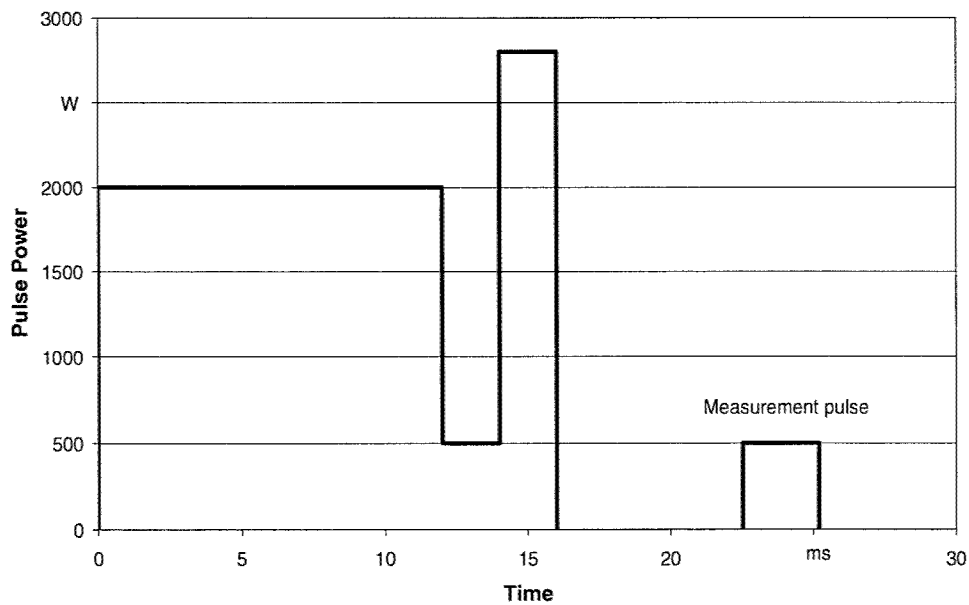
Figure 8:   Post-process measurement pulses with droplet generation pulse and wire feed profile for detection of the final state of laser generation process

Figure 9 shows the signals of the measurement laser pulse of the reflected light for detached and un-detached droplets. Low amplitude signals are typical for detached, high amplitude signals for un-detached droplets. For the characterisation of the process the sum of the three detected signals can be used (Figure 10). The experiments show that the sum of the sensor signals shows characteristic values for detachment. This sensing technique detects if the droplet detaches successfully and allows to monitor the important droplet detachment phase of the Laser Droplet Weld process.
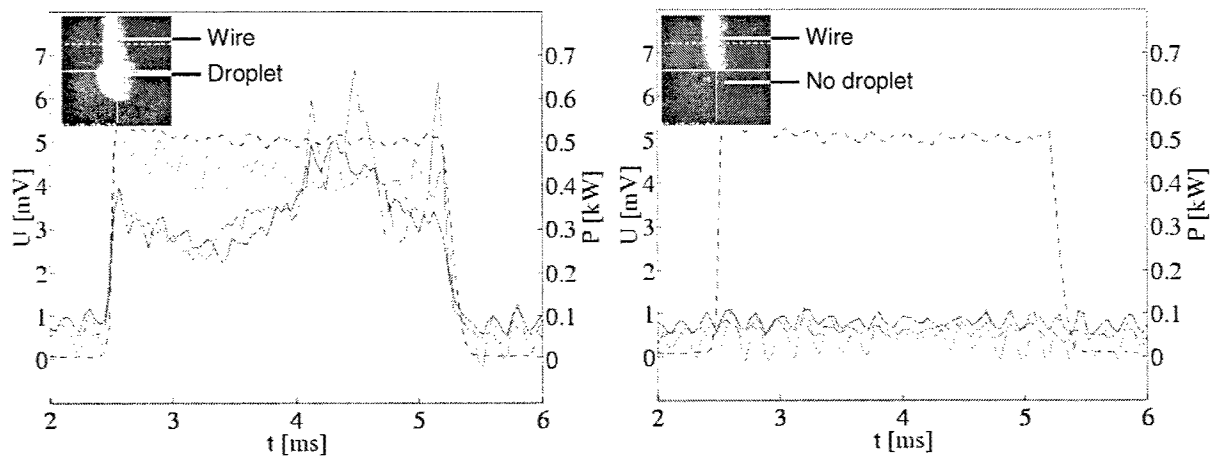

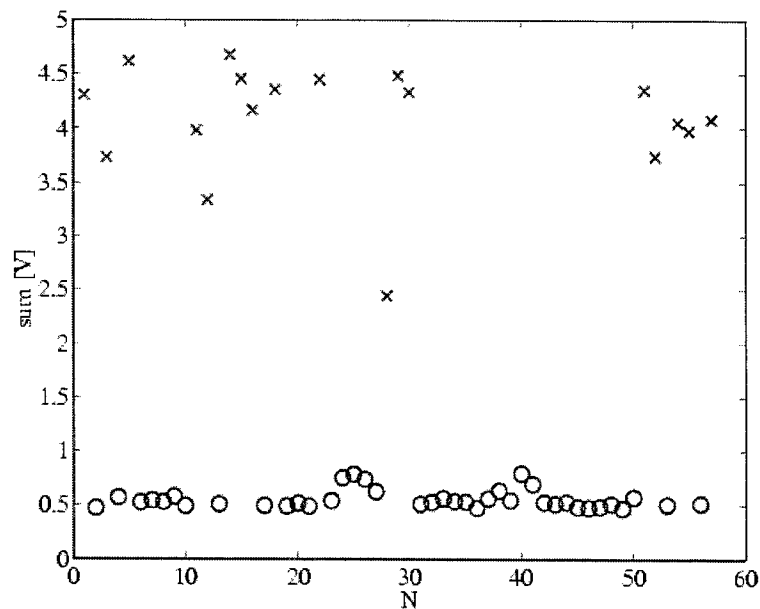Figure 9:   Measurement pulse and corresponding signals of reflected light; left: un-detached; right: detached

Figure 10:   Signal sum versus number of trials of droplet generation process; o: detached; x: un-detached

WELDING RESULTS ON BLIND WELDS

Blind welds help to analyse and characterize the achievable joining results. To analyse the joining quality, blind welds with stainless steel drops are done on alloy 42. The stainless steel contains 9 % nickel and the alloy 42 contains 42 % nickel. An element analysis for nickel shows that the concentration of nickel in the droplet is clearly over 9 %. In the cross section and the element analysis areas are visible, in which the materials are blended (Figure 11).
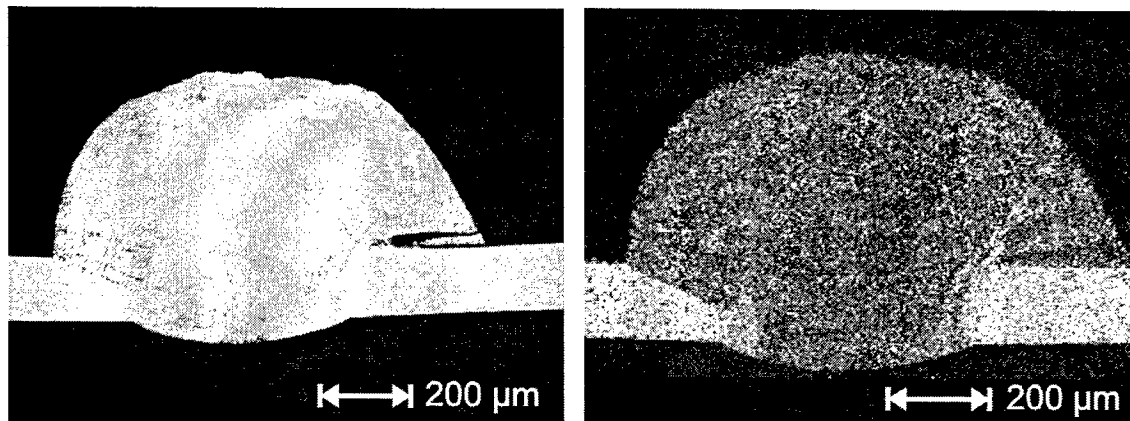

Figure 11:   Nickel droplet on alloy 42: cross section (left) and element analysis (right)

For a further characterization of the blind welds the values of droplet mass, droplet size, contact angle, cap height and droplet diameter are measured. With three different pulse profiles (Figure 2) and the nickel wire used ($\varnothing$ 0,6 mm) the average droplet mass is measured and calculated on the basis of the mass of the fed wire. The results are presented in Table 2 and prove that the droplet mass and also the droplet size are exactly adjustable. In a large number of experiments the droplet size and mass is for the same laser and wire parameters constant: no differences for one parameter combination are measurable. The small difference between the calculated and the measured weight (less than 3 % of the droplet weight) can be explained by small inaccuracies of the feeder, splashes and evaporated material.

Pulse profile	Measured weight per drop [mg]	Calculated weight per drop [mg]
Short	2,96	3,03
Standard	3,80	3,85
Long	4,70	4,75

Table 2: Definition of droplet mass for different pulse profiles

With the standard pulse profile investigations are executed concerning the positioning accuracy in dependency of the falling height. The experiments show positional variations of ± 0,5 mm independent of the falling height (1,3 mm – 4 mm). To reduce the influence of the shielding gas supply on the position accuracy a gas supply with an homogeneous gas flow is used.

Cap height, cap diameter and contact angle are measured for a single falling height of 3 mm. The droplet material is nickel and the substrate material is stainless steel with a thickness of 0,1 mm to 1 mm. The results are shown in Figure 12.
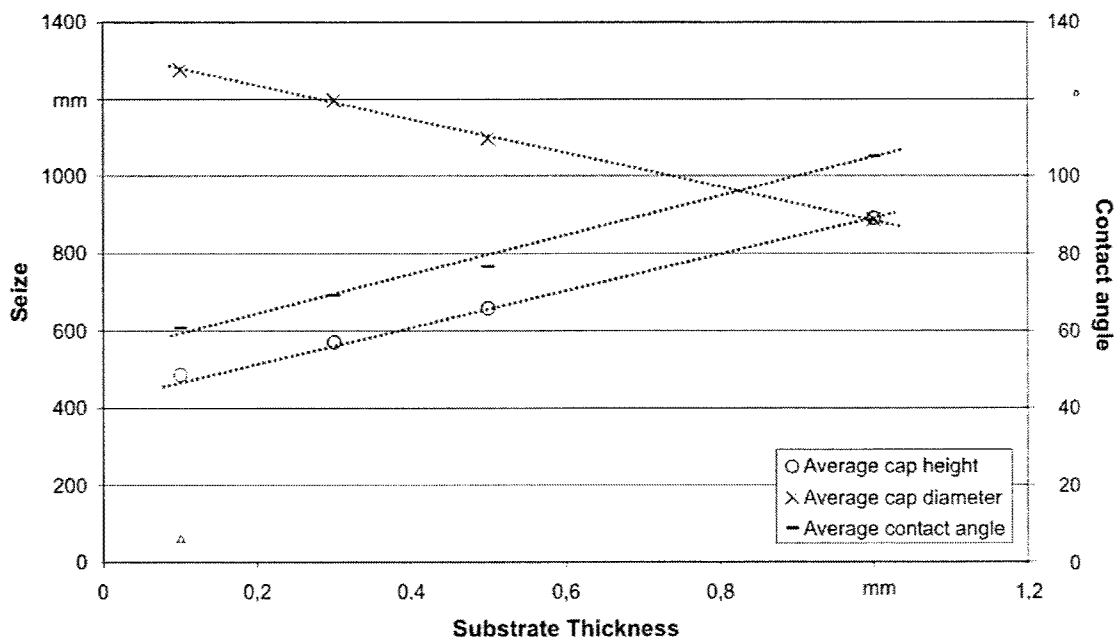

Figure 12: Droplet characterisation (standard pulse profile; ∅ 0,6 mm nickel wire; wire acceleration: 10 m/s^2; wire velocity: 150 mm/s)

Cap diameter decreases and the contact angle and cap height increases with an increasing substrate thickness. This is explained by a better heat dissipation in the thicker material. The heat content of the droplet is limited which results in a limitation of the thickness of weldable substrate material. Droplet Welding consequently is better suited for thin substrates with a low heat conductivity.

WELDING RESULTS ON BUTT JOINTS

In further investigations welding experiments are carried out with two stainless steel joining partners and nickel droplets. The joining partners are positioned as butt joints without a gap. With this arrangement the positioning problem of the droplets makes a reliable welding impossible because not every droplet hits the joining area. Attempts with butt

joints and a defined gap between the partners show better results. The droplets are exactly positioned between the two joining partners in the gap. In a large number of trials with different pulse profiles every drop is positioned exactly between the joining partners (Figure 13). For gaps with 50 μm up to 300 μm an exact positioning of the drops is observed nearly always. The exact positioning can be explained by two self alignment effects. One is a capillary effect where capillary forces bring the drops exactly between the joining partners in the gap. The second effect is that the gap prevents a tailback of the shielding gas which causes a gas cushion on the target. The sum of both effects leads to the exact positioning of the of the drops on the joining partners.
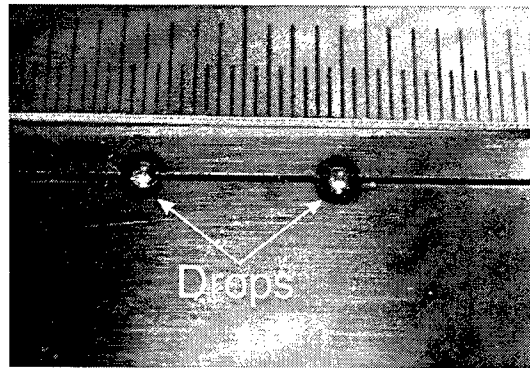

Figure 13:   Laser Droplet Weld (nickel droplet) of two plates (150 μm thick stainless steel) with a 200 μm gap

Welding tests for joining of two plates with two droplets are carried out with different pulse profiles and different thickness of joining partners. The tensile strength is measured to get quantitative results. The thickness of the plates is varied between 150 μm and 700 μm and the gaps from 50 μm to 300 μm. Figure 14 shows a cross section of such a laser droplet weld with a 200 μm gap and 200 μm thick plates. In the drop some inclusions can be seen which probably are caused by the shielding gas. The pictures show that the plates have a small heat affected zone but at the end of the plates the material is molten. A mixing of the materials occurs that is visible in the right image of Figure 14.
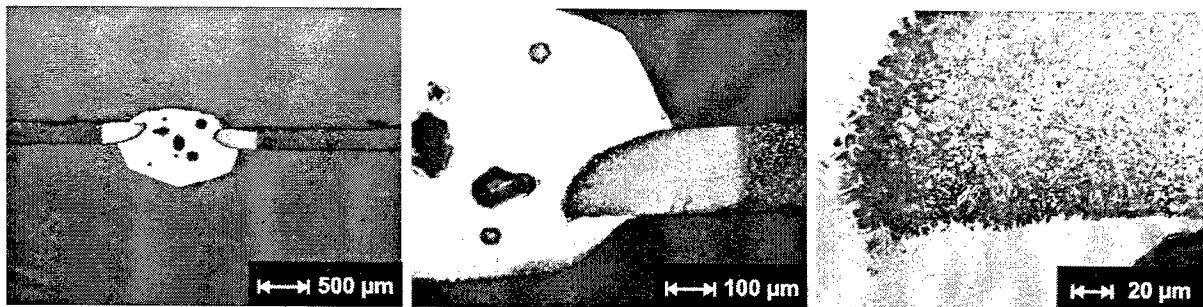

Figure 14:   Cross sections of a laser droplet weld (0,6 mm nickel wire, 200 μm plates, 200 μm gap)

"Laser Droplet Welding"-joints are realized by two nickel droplets on 150 μm thick plates with different gaps and pulse profiles. The results of the tensile tests are shown in Figure 15.
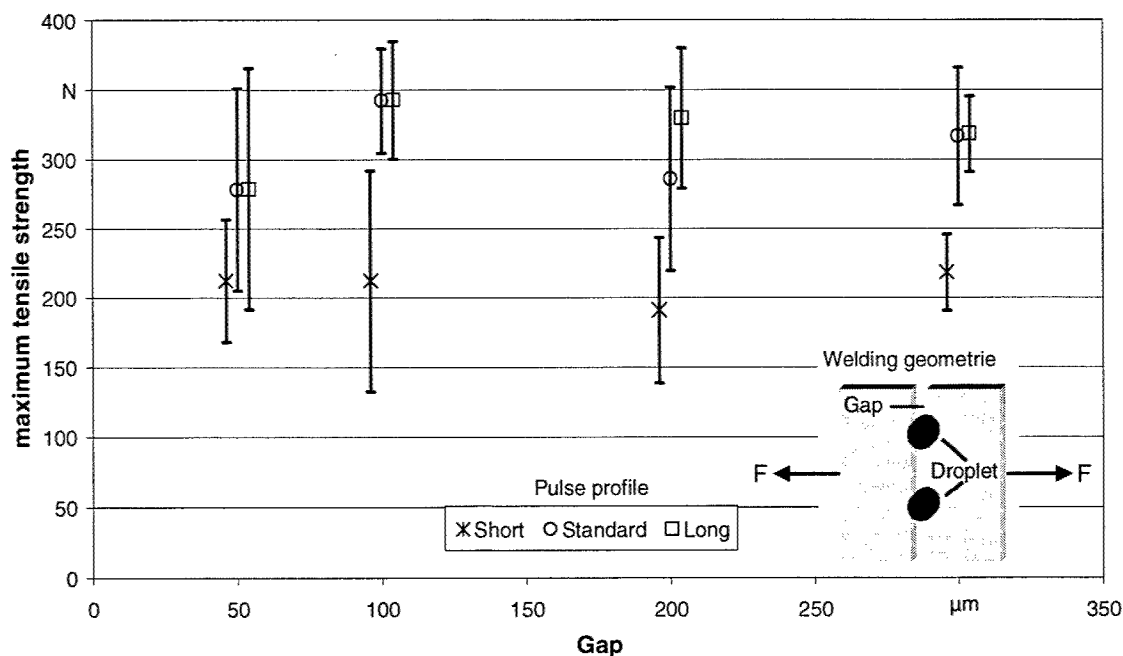
Figure 15: Maximum tensile load with 150 μm thick plates (∅ 0,6 mm nickel wire; wire acceleration: 10 m/s²; wire velocity: 150 mm/s)

The graphic shows that the tensile load achieved with the short pulse form results in the lowest strength. This is explained by the smaller amount of droplet material and heat energy which causes problems to melt sufficient material from the plates to achieve conclusive connections. The difference of the tensile load between the standard and the long pulse profile is quite low but different gaps influence the tensile force. The highest tensile loads are measured for 100 μm gaps. The 50 μm gaps do not provide higher mechanical strength caused by the fewer droplet material that moves between the plates and the smaller contact area of the welding material.

SUMMARY

Laser Droplet Welding is an innovative joining technology that will not replace soldering or conventional laser welding but it can be a complementation to these technologies. Material conclusive connections are realized by adding liquid metal droplets which are formed at the end of a metallic wire by means of laser radiation. The droplet detaches, wets the joining partners and produces material conclusive connections. The Laser Droplet Weld process can be split into five phases. The process parameters for droplet generation and detachment have been adapted for nickel wire (∅ 0,6 mm) and for silver wire (∅ 0,3 mm). The phases of droplet flight, landing and welding have been analysed on basis of blind welds. Joining results have been analysed for butt joints with and without gaps. For butt joints with only two welding droplets the achievable tensile loads exceed 100 N. In relation to conventional laser welding methods the "Laser Droplet Weld" process offers advantages, which make this process very interesting for some applications. A substantial advantage is the possibility to bridge gaps between the joining partners with the help of the droplet material, which makes the complex realization of a technical zero-gap unnecessary. Further advantages are the possibility to work with high reflective materials, the production of high temperature joints, the use of lead free materials and the possibility to join different materials. The process is particularly interesting for sensitive joining applications e.g. thin foils.

ACKNOWLEDGEMENTS

REFERENCES

1. Reichl, H.; Wolf, J.: Trends in der Aufbau- und Verbindungstechnik; In: Geiger, M.; Fleckenstein, M. (Editor): Tagungsband Laser in der Elektronikproduktion & Feinwerktechnik –LEF 2002; Bamberg: Meisenbach; 2002
2. Hoving, W.; Jahrsdörfer, B.: Laser Droplet Weld – Ein innovatives Fügeverfahren; In: Geiger, M.; Fleckenstein, M. (Editor): Tagungsband Laser in der Elektronikproduktion & Feinwerktechnik –LEF 2001; Bamberg: Meisenbach; 2001
3. Didzic, N.: Nonlinear Droplet Oscillations and Evaporation in an Ultrasonic Leviator. Dissertation Friedrich-Alexander-Universität Erlangen-Nürnberg. 1995
4. Baehr, H.-D.:Thermodynamik; Berlin: Springer; 2000
5. Cerbe, G.: Einführung in die Thermodynamik; München; Hanser; 1999
6. Huimin, L.: Science and Engineering of Droplets; New York: Noyes Publications; 2000
7. Clift, R.; Grace, J. R.; Weber, M. E.: Bubbles Drops and Particles; London: Academic Press, INC. LTD.; 1978

Application of melt ejection criterion
in simulation of micro-machining with laser

V. V. Semak[1], J. T. Schriempf[1], G. A. Knorovsky[2], and D. O. MacCallum[2]

Abstract

A theoretical criterion defining the threshold pulse energy and beam intensity required for melt ejection is proposed. The results of numerical simulation present dependencies of the threshold pulse energy and beam intensity as functions of laser pulse duration and beam radius. The experimental verification of the proposed criterion is described and the comparison of theoretical predictions and measurements is presented. The criterion is applied for simulation of laser drilling metal foil with thickness in the range 25 μm – 125 μm using a laser beam with 12 μm beam radius and pulse durations 10 ns and 100 ns. The computational results are used to interpret the results of an experimental study of laser drilling of 125 μm aluminum foil using a single mode beam of a XeCl laser performed at the Nederlands Centrum voor Laser Research (NCLR) and the University of Twente. Additional results on Nd:YAG spot welds in pure Ni are also presented.
Keywords: laser materials processing, laser welding, laser drilling, modeling, simulation

1. Introduction

The mechanism of material removal from the beam interaction zone is one of the most important research topics related to laser material processing. For almost fifteen years, since the invention of the laser, the common belief was that the material exposed to a laser beam is removed via evaporation [1]. In 1976 Dr. M. Von Almen proposed an alternative mechanism for material removal [2]. According to his revolutionary hypothesis, surface evaporation in the area exposed to a laser beam induces recoil pressure, which ejects molten material. The theory developed by Von Almen [2] allows order of magnitude estimation of drilling rates for microsecond and millisecond laser pulses which support the validity of the recoil pressure mechanism of material removal. Because an oversimplified method was used for computing the recoil pressure, the accuracy of this model is insufficient for practical application. Subsequent multiple attempts at modeling laser material interaction were based on even less adequate models for laser induced evaporation. However, an accurate sophisticated theory for laser evaporation was developed almost ten years earlier by Dr. S. Anisimov [3]. Shortly after, this theory was greatly improved with the contribution of Dr. B. Lukyanchuk (see refs in [4]). Perhaps, Anisimov's theory was disregard by material scientists and mechanical engineers representing the main core of laser processing modelers due to its apparent excessive complexity. It took almost 20 years to integrate Von Almen's concept of evaporation recoil pressure driven melt ejection and Anisimov's model of laser induced evaporation [5,6,7]. This integrated model [5,6,7] was developed in order to study laser keyhole welding. This developed approach is versatile and hence can be easily used in laser drilling modeling.

The proposed model of laser material processing [8], in particular, allows prediction of the thresholds for melt ejection and rates of drilling for different laser beam radii. The miniaturization trend dominating the electronics industry will require processing with beam diameters of 10 micrometers and less. The study presented in this article demonstrates that the melt hydrodynaimcs becomes very peculiar for such small spot sizes and, consequently, the experience gained in processing with spot sizes of several hundreds of microns becomes practically useless.

---

[1] Electro-Optics Center, ARL, The Pennsylvania State University, 77 Glade Dr., Kittanning PA 16201

2. Theory

2.1. Laser interaction simulation

The velocity of melt ejection by the evaporation recoil pressure can be calculated by integration of the equation for melt acceleration:

$$\frac{\partial v_m}{\partial t} + v_m \nabla v_m = \frac{\nabla p_r}{\rho},$$

(1)

where $\frac{\partial v_m}{\partial t}$ is the time derivative of melt velocity, p_r is the recoil pressure induced by evaporation and ρ is the melt density.

The recoil pressure, p_r, can be found utilizing Anisimov's theory [3]

$$p_r = 0.54 B_0 (T_s)^{-\frac{1}{2}} \exp\left(-\frac{U}{kT_s}\right),$$

(2)

where B_0 is the evaporation constant, T_s is the surface temperature, U is the latent heat of evaporation per atom and k is Boltzman's constant.

The surface temperature, T_s, can be determined as a function of laser beam intensity by numerically solving the heat transfer equation with boundary conditions taking into account the laser surface interaction utilizing standard techniques described in the literature [9]

$$\frac{\partial T}{\partial t} + v_m \nabla T = a \nabla^2 T,$$

(3)

where a is the heat diffusion coefficient.

Solving the system of equations (1-3) allows computation of melt velocity as a function of laser pulse energy, pulse duration and melt pool radius. The accurate calculation of melt velocity allows prediction of threshold beam intensities (beam intensity profiles) corresponding to establishing melt ejection and drilling rates for different laser pulse durations (pulse shapes) and different beam radii. Such a simulation requires intensive computations and, therefore is time consuming and costly. The numerical solution of the above system of differential equations can be performed with lesser accuracy but significantly faster if the averaged melt velocity values are computed. The work presented in this article demonstrates that computations using average values provides sufficient accuracy, which makes the simulation feasible for practical application.

2.2. Melt ejection criterion

In order for the melt to be ejected, the evaporation recoil pressure must accelerate a portion of the melt created at the beam center to a velocity sufficient for it to reach the edge of the melt pool during the portion of the laser pulse remaining after the surface melting has occurred. This assumes that the cooling is rapid, such that the time of melt existence after the end of laser pulse is negligible. Because of space limitations we will not discuss this assumption. However, this assumption holds at least for the conditions corresponding to the thresholds of melting and drilling. Thus, an approximate criterion for establishing laser drilling can be formulated:

$$t_{ej} = \frac{r_m}{<v_m>} \leq \tau - t_m,$$

(4)

where t_{ej} is the time for melt ejection from the melt puddle, r_m is the melt puddle radius, $<v_m>$ is the melt velocity averaged over the laser pulse, τ is the laser pulse duration and t_m is the surface melting time.

It is worth mentioning here that, if condition (4) is satisfied, then both keyhole welding and drilling can take place. The transition from keyhole welding to drilling requires application of another criterion, which describes whether surface tension at the melt edge is capable of retaining melt ejected from the beam irradiated area and forming a weld pool [8].

Solving the heat transfer equation (3) for the boundary condition when the surface temperature equals the melting temperature at the end of the pulse,

$$T_s\big|_{t=\tau} = T_m, \tag{5}$$

gives the threshold laser pulse energy (or beam intensity) corresponding to surface melting for a given beam radius and laser pulse duration.

The qualitative representation of the dependencies of ejection time and melting time as a function of pulse energy using equations (1-3), criterion (4) and boundary condition (5) is shown in Figure 1. Obviously, an increase of pulse energy results in a decrease of ejection time because, for a given pulse duration, higher pulse energy corresponds to higher beam intensity, higher surface temperature, higher evaporation recoil pressure and, consequently, higher melt ejection velocity. The dependence of ejection time, t_{ej} presented in Figure 1 is computed for all pulse energies under the assumption that melt always exists on the surface. Of course, for energies lower than the melting threshold, E_m, the part of the curve representing ejection time has no physical meaning and this part of the curve is represented by a dashed line. For pulse energies greater than the melting threshold the time when melt exists at the surface, τ-t_m, increases. The melt existence time increases from zero when the pulse energy equals to the threshold value, E_m, and asymptotically approaches pulse duration, τ. The laser pulse energy when the ejection time becomes equal to the melt existence time is denoted as the ejection threshold. E_{ej}.

Although this topic is beyond the present discussion, one can introduce the drilling threshold, E_{dr}, corresponding to a condition where the velocity of melt ejected from the melt zone is high enough that the dynamic pressure of the melt flow exceeds the surface tension pressure at the melt pool edge. For pulse energies exceeding E_{dr} drilling takes place. For pulse energies higher than the ejection threshold, E_{ej}, and less than the drilling threshold, E_{dr}, keyhole welding takes place, and for pulse energies between the melting threshold, E_m, and the ejection threshold, E_{ej}, so-called conduction limited welding takes place. By adopting such a classification, one can see the flaw of the widely accepted practice of labeling all shallow welds as conduction limited welds. Indeed, a shallow weld can correspond to a condition where melt ejection takes place but the keyhole growth rate is slow enough that during the laser pulse only a shallow weld is produced.

2.3. High aspect laser drilling

The proposed melt ejection criterion facilitates understanding and simulation of high aspect laser drilling when the drilling depth exceeds the diameter of the drilled cavity. For pulse energies exceeding the drilling threshold one can compute the amount of removed material by integrating the melt ejection velocity over the laser pulse. If the pulse energy is much higher than the drilling threshold, then the material is removed from the area with a radius equal to the melt pool radius. Thus, knowing the melting zone radius and the amount of material removed, the depth drilled per laser pulse can be computed. With the increase of the drilled depth the area of the surface exposed to the laser beam increases. When the melt zone becomes too large, such that the ejection criterion is not satisfied, drilling stops.

Two phenomena must be included in the modeling of high aspect laser drilling. First, the effect of multiple reflections and re-absorptions of the laser beam must be taken into account. A profile of absorbed beam intensity substantially narrows compared to the incident beam (Figure 2) with growth of the cavity depth. Note that the absorbed intensity profile is shown along the direction perpendicular to the beam axis and the substantial narrowing of the absorbed intensity profile results in a slower increase of the melt radius, r_m, measured along the material surface. Additionally, the maximum absorbed beam intensity increases above the maximum intensity absorbed at the flat surface (Figure 2) when the depth of the hole grows higher than the diameter of drilled hole (Figure 3). This slow growth of the radius of the melt zone and the increase of the maximum of absorbed intensity results in a faster drilling rate as compared to the simulation disregarding multiple reflections (Figure 3).

The second important phenomenon is the decrease of the melt radius starting when the hole depth exceeds approximately four hole diameters. Simulations show that for holes with depths higher than approximately four diameters the width of of the absorbed intensity profile does not change substantially and the maximum intensity starts decreasing. The decrease of the maximum absorbed intensity results in both a decreased melt zone radius and decreased melt ejection velocity. Decreased melt ejection velocity is generally accompanied by decreased drilling

rate. However, as the maximum intensity approaches the melting threshold the decrease of the melt zone radius can be so rapid that the ejection criterion remains satisfied. Additionally, the melt zone radius can decrease so fast that, even with still decreasing melt ejection velocity, the drilling rate can stop decreasing or, surprisingly, even slightly increase. Simulations and, in particular, the results of the drilling simulation presented below, confirm the possibility of such scenario.

3. Analysis of computational results

3.1. Thresholds of melting and melt ejection

The computed threshold pulse energies and beam intensities for melt ejection and surface melting are shown in Figures 4 and 5 as functions of the melt pool (laser beam radius) for the pulse durations 0.1ms and 1ms. In our computations, the beam intensity distribution is assumed to be uniform (tophat). The threshold pulse energies for melt ejection and melting decrease with the decrease of the beam radius. The threshold intensity for melt ejection first decreases and then increases with decreasing beam radius while the threshold intensity for surface melting first remains constant and then increases with decreasing beam radius. The increase of threshold intensities corresponding to the radius decrease is due to the three dimensionality of the heat transfer. For a given beam radius the threshold energies for melting and melt ejection are lower for shorter pulse duration (Figure 4). The threshold intensities for melting and for melt ejection are higher for shorter pulse duration (Figure 5).

This simulation data demonstrate behavior of a parameter very important for the practical application of micro welding, i.e. the behavior of the difference between the melting and melt ejection thresholds. The simulation predicts a smaller difference for a smaller beam radius. This means that the range of the beam intensities, or pulse energies, corresponding to welding without substantial melt displacement becomes narrower as the beam size decreases. In particular, for laser beam radii as small as 10 – 20 micrometers, the melt ejection threshold is practically the same as the melting threshold. This means that only keyhole welding is possible for micron size beams. Secondly, potentially, it will be difficult to achieve deep micro-welding because for the higher beam intensities needed for deeper penetration, drilling may occur.

These predictions are in agreement with the preliminary results of verification experiments which are in progress at Sandia National Laboratories. The experimental results obtained for interaction of a Nd:YAG laser beam with a target made of pure Ni are summarized in Table 1 for different laser pulse durations. The pulse duration values presented in the Table 1 correspond to the nominal width of the laser pulse. The conditions corresponding to initiation of melting are denoted in Table 1 with *italic* font, concave melt surfaces are denoted with normal font and the onset of drilling is denoted with **bold** font.

The measured surface melting threshold pulse energies are 7 mJ, 34 mJ and 74 mJ for 2 ms, 5 ms and 9.9 ms laser pulses respectively. The temporal profiles of the laser pulses for different power levels are presented in Figure 6. The melt ejection thresholds are 12 mJ, 48 mJ and 97 mJ for 2 ms, 5 ms and 9.9 ms laser pulses respectively. The appearance of the weld surface corresponding to flat melting, concave melting and drilling are shown in the Figure 7.

The approximate computations were performed assuming tophat beam intensity profile and rectangular laser pulse. The durations of the rectangular laser pulse were selected to be 1 ms, 3.5 ms and 7.6 ms, corresponding to the half width values of the experimental laser pulses (Figure 6). The computed threshold absorbed energies for the melt ejection were 3.05 mJ, 15.8 mJ and 34.3 mJ, correspondingly. Dividing the computed threshold by the experimentally measured values gives 0.25, 0.32 and 0.35 for pulses with duration 2 ms (1 ms half width), 5 ms (3.5 ms) and 9.9 ms (7.6 ms) respectively. The ratios of computed absorbed threshold energies and measured incident threshold energies are consistent with the absorptivity of the Ni surface at 1.06 μm wavelength.

Computations of the melting threshold provided values indistinguishable from the melt ejection threshold. Indeed, according to the simulation described above, for small beam (melt pool) radii, melt ejection takes place as soon as the surface melts. This discrepancy will be studied in future research. However, a possible explanation is that in the virtual experiments, the material surface was assumed to be ideally flat while in the real experiments the surface had some roughness. Obviously, the melting threshold for a rough surface is slightly lower than for an ideally flat one, and the melt produced on the rough surface is held in place by wetting forces until a certain depth of melt is produced.

In the conclusion of this subsection one important result of simulation has to be emphasized. The range of pulse energies where conduction limited welds exist is very small. Thus, for a 1 millisecond laser pulse and 500 micrometers beam radius surface melting occurs when the absorbed pulse energy is 540 mJ and melt ejection takes

Table 1 – Ni results. Grayed entries indicate a transition.

Peak Power (W):	2 ms	5 ms	9.9 ms
Power Setting: 6.5		6.4	8.1
7		9.1	11.2
7.5		12.6	14.3
8	4.4	17.3	18.5
8.5	6.8	24.5	23.5
9	10.9	36.0	32.0
9.5	16.7		40.0
10	26.6		

Energy/Pulse (mJ):	2 ms	5 ms	9.9 ms
Power Setting: 7		24	74
7.5		34	97
8	2	48	130
8.5	4	71	160
9	7	110	220
9.5	12		280
10	24		

Beam Radius (mm)	2 ms	5 ms	9.9 ms
Power Setting: 7		0.02	0.0235
7.5		0.0193	0.0238
8	0.018	0.021	0.026
8.5	0.019	0.0195	0.0338
9	0.019	0.019	.0238
9.5	0.025		.0265
10	0.024		

Intensity (kW/mm^2):	2 ms	5 ms	9.9 ms
Power Setting: 7		7.2	6.5
7.5		11	7.6
8	4.6	12.5	8.7
8.5	6.0	20.5	6.5
9	10	32	18
9.5	8.6		18
10	14		

Fusion Zone Dia. (mm): & Type: (*Italic:flat*, normal: concave, **bold: drilled**):	2 ms	5 ms	9.9 ms
Power Setting: 6.5		*0.013*	*0.014*
7		*0.015*	*0.022*
7.5		*0.0215*	0.021
8		0.0225	0.027
8.5	---	0.0275	0.044
9	*0.018*	**0.043**	0.046
9.5	0.022		**0.036**
10	**0.022**		**0.05**

place at an absorbed 700 mJ. For the above-mentioned conditions, the range of laser pulse energy where melt ejection does not occur is small; assuming a surface absorptivity of 0.3, only 0.5 J separates the incident pulse energy of 1.8 J when surface melting occurs and 2.3 J when the full melt ejection takes place. For the same pulse duration and smaller

beam radius of 200 μm this range is between an absorbed energy of 99.3 mJ and 113 mJ or between incident energies of 0.33 J and 0.37 J. This is only 0.04 J, which is comparable to the accuracy of the laser output control. In the case of longer pulse durations the range between melting and melt ejection threshold becomes even smaller. Thus, for a typical 1 ms – 10 ms laser pulse and 200 μm – 500 μm laser spot diameter conduction limited welding exists in a very narrow energy range. Thus, with great confidence it can be concluded that, practically all industrial laser welds are made in melt ejection (keyhole) regime. Therefore, numerous publications related to conduction limited laser welding (for example, [10-17]) based on a simple approach proposed in 1946 by D. Rosenthal [18] have very little academic value since the area of applicability is never discussed in these works and their results and conclusions have no practical value since they cannot be applied to industrially performed shallow welds.

3.2. Average depth removed per pulse during laser drilling of thin metal film

The dependencies of the average depth removed per pulse as a function of laser pulse energy, computed for two thickness of aluminum film 125 μm and 25μm, are shown in the Figures 8a and 8b. The computed dependence for 125 μm aluminum film is in agreement with the experimentally measured dependence [19]. Similar to experiment, the average depth removed per pulse was computed as a ratio of the film thickness and the number of laser pulses required for drilling through. Because the number of pulses is a whole number, for the pulse energies when penetration requires one or few pulses the dependence must exhibit "steps" when the average depth removed per pulse remains the same. The steps are not present in the experimental dependence, perhaps, because the intervals of the pulse energy change were too large in order to resolve fine features of the dependence.

The average depth removed per pulse decreases with the decrease of pulse energy. The simulation shows that the numerical results match the experimental dependence only if multiple reflections are included in the computations. In the case where only single absorption is included, the predicted drilling rate is smaller (Figure 3) and the simulation results significantly deviate from the experimental observations.

For relatively small pulse energies the average depth removed per pulse stops decreasing and remains constant while pulse energy decreases (Figure 8b). The dependence rapidly decreases in a threshold-like manner when the pulse energy decreases below a certain value. The reason for this counterintuitive behavior is described above, i.e. when the pulse energy approaches the melting threshold the melt radius rapidly decreases, resulting in the increase of the drilling rate. In this particular case, the increase of drilling rate occurs when the drilled depth reaches a value of approximately four hole diameters. The measurements of the hole diameters [19] support the proposed theoretical explanation.

The simulation results show that the dynamics of the drilling rate is rather complicated. The drilling rate changes substantially during one pulse if the pulse energy is large and the drilling rate also changes during the course of multiple pulse drilling with low pulse energy. Thus, describing the process with only the average depth drilled per pulse obscures a significant amount of information which is valuable for the application engineer. For example, the data obtained for 125 micrometer thick film are not directly applicable for other thicknesses (Figure 8). However, availability of an accurate model allows the design and control of the process using information unattainable via experimentation.

4. Conclusions

The first important practical conclusion is that in order to achieve micro welding short pulse durations should be used. In the case of pulse durations exceeding 5 ms the threshold for melt ejection practically coincides with the surface melting threshold.

Second, the range where melt ejection does not occur is relatively narrow except for the beam radii larger than 1mm, which has limited application for welding. For small radii the calculated ranges of pulse energy where melt ejection does not occur are typically narrower than the accuracy permitted by energy meters or the laser system energy controls. Additionally, the values of pulse energy required for welding without melt ejection for small beam radii can be less than the threshold of lasing. This means that the laser pulse must be attenuated and highly stable energy output is required. This represents substantial difficulties for the practical application of micro welding.

At this point an important comment should be presented. As was mentioned above, the melt ejection from the laser irradiated area does not necessarily correspond to the drilling regime. As analyzed in [8], the ejected melt can be decelerated and retained at the edge of the melt puddle by surface tension if the melt ejection velocity is not high

enough. According to the proposed classification [8], this regime corresponds to keyhole welding. For the higher beam intensities, when the recoil pressure generates faster melt flow and the surface tension can not stop the melt flow, the drilling regime takes place. In order to determine whether keyhole welding or drilling takes place for a particular interaction condition a comprehensive analysis including surface tension must be performed. However, at this point we can suggest with confidence that exceeding the computed melt ejection threshold for short pulse durations and small beam radii will result in either complete ejection, i.e. drilling, or in the formation of a depression with surrounding raised solidified melt rim. This is because the time required for the displaced melt to return to its initial position is expected to be more than the solidification time. Unlike for small radii and short pulses, in the case of larger beam radii and longer pulse durations the regime of keyhole welding exists for energies exceeding the melt ejection threshold and below the drilling threshold.

The third conclusion is that the range of energies where melt ejection can be neglected is so narrow that, speaking from the position of an application engineer, the regime of laser conduction welding simply does not exist.

Fourth, the numerical simulation of high aspect micro drilling demonstrated coincidence with the experimental measurements [19] and provided an in-depth understanding of the drilling dynamics.

Finally, the presented results demonstrate that, neither practical experience nor qualitative considerations can substitute for the numerical simulation. In the simple case of a rectangular temporal profile and uniform beam intensity distribution, numerical simulation can reduce the amount of experimentation needed for laser processing implementation. In cases which include different pulse shapes, beam intensity distributions and melt puddle sizes indirectly related to the beam sizes only simulation can provide a laser user with cost effective guidance in application development.

5. References

1. J.F. Ready, Effect of High Power Laser Radiation (Academic Press, London, 1971)
2. M. von Almen, Laser drilling velocity in metals, (1976) *J. Appl. Phys.*, v.47(12), pp.54-60-5463
3. S. I. Anisimov, (1968) *Sov. Phys. JETP* 27 p 168
4. S. I. Anisimov and V.A.Khokhlov, Instabilities in Laser - Matter Interaction, 1995 (CRC Press, Boca Raton, FL).
5. V. Semak and A. Matsunawa, The role of recoil pressure in energy balance during laser materials processing. (1997) *J. Phys. D: Appl. Phys.* 30(#18) pp. 2541-52.
6. A. Matsunawa and V. Semak, The simulation of front keyhole wall dynamics during laser welding. (1997) *J. Phys. D: Appl. Phys.* 30 pp. 798-809
7. V. V. Semak, W. D. Bragg, B. Damkroger, and S. Kempka, Transient model for keyhole welding, *J. Physics D: Applied Physics*, 32 (1999), pp. L61-L64
8. V. V. Semak, J. A. Hopkins, M. H. McCay, T. D. Mc Cay. A Concept for a Hydrodynamic Model of Keyhole Formation and Support During Laser Welding. *Proc. of ICALEO'94*, October 17-20, 1994, Orlando,FL, pp.641-650.
9. A. N. Tikhonov and A. A. Samarskii, Equations of Mathematical Physics, 1990 (Dover).
10. Dua J, Longobardi J, Latham WP, and Kar A, Weld strength and process controllability for laser welding of thin sheet metals, *J. Laser Applications* (2000)12 (6), pp. 239-244.
11. Wei PS, Ho CY, Shian MD, and Hu CL, Effects of mode structure on three-dimensional laser heating due to single or multiple rectangular laser beams, *Int. J. of Heat and Mass Transfer*, (1997) 40 (10), pp. 2283-2292.
12. Kar A, Scott JE, and Latham WP, Three-dimensional analytical temperature field and its application to solidification characteristics in high- or low-power-density-beam welding, *J. Appl. Phys.* (1996) 80 (2), pp. 667-674.
13. Manca O, Morrone B, and Naso V, Quasi-steady state 3-dimensional temperature distribution induced by a moving circular Gaussian heat-source in a finite depth solid, *Int. J. of Heat and Mass Transfer* (1995) 38 (7), pp. 1305-1315.
14. Gratzke U, Kapadia PD, and Dowden J, Heat conduction in high speed laser welding, *J. Phys. D: Appl. Phys.* (1991) 24 (12), pp. 2125-2134.
15. DebRoy T. and David S.A., Physical processes in fusion welding, *Review of Modern Physics*, (1995) 67(7), pp. 85-112.
16. Pitscheneder W., DebRoy, T., Mundra K., and Ebner R., Role of sulfur and processing variables on the temporal evolution of weld pool geometry in multikilowatt laser beam welding of steels, *Welding Journal*, (1996) 75(3), pp.S71 – S80.
17. Robert A. and DebRoy T., Geometry of laser welds from dimensionless numbers, *Metallurgical and Materials Trans. B- Process Metallurgy and Materials Processing Sci.* (2001) 32(5), pp. 941-947.
18. D. Rosenthal, The Theory of Moving Source of Heat and Its Application to Metal Treatments, *Transactions of ASME* (1946) v. 68, pp. 849-66.
19. A. Schoonderbeek, C. A. Biesheuvel, R.M. Hofstra, K. J. Boller and J. Meijer, High speed drilling of metals with a long pulse XeCl excimer laser, (2002) *Proc. SPIE 4760*, pp. 667-677.
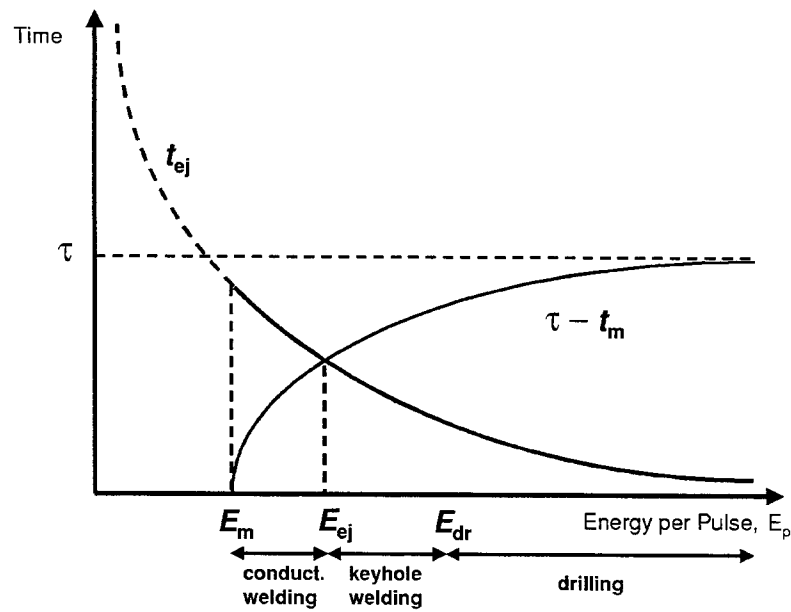
Figure 1: Melt ejection time, t_{ej}, and portion of laser pulse remaining after beginning of surface melting, τ-t_m, as function of pulse energy, E_p.
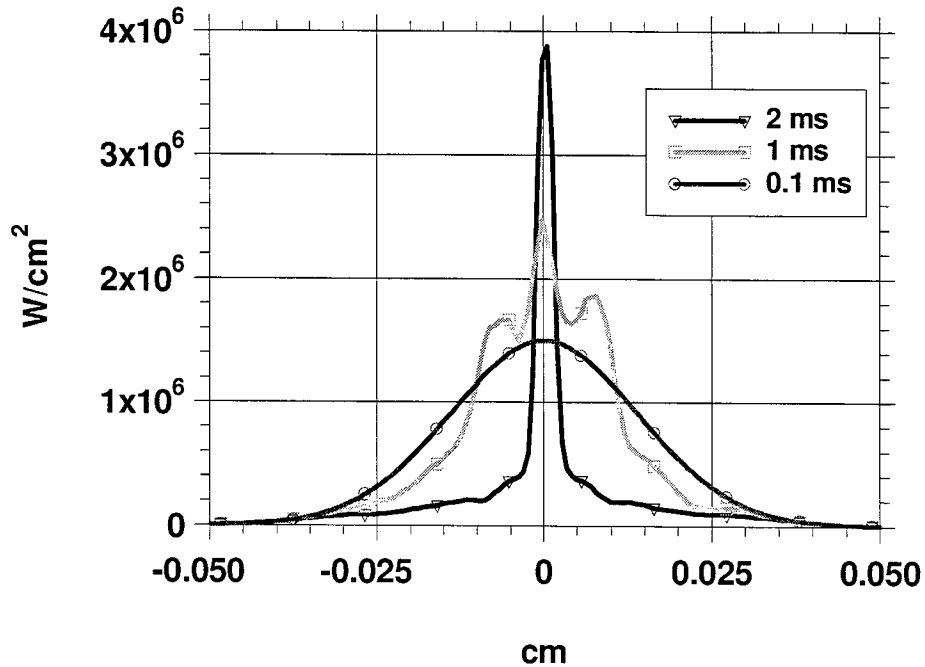

Figure 2: Laser intensity absorbed at the keyhole wall as a function of distance from the laser beam axis at different times during a pulse: case of multiple beam absorptions (3x) in the keyhole.
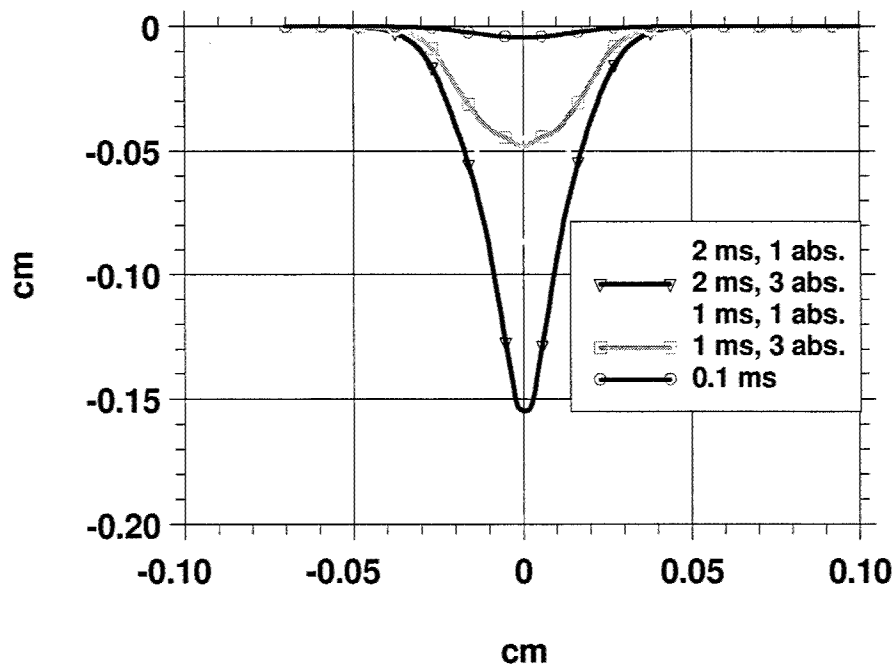
Figure 3: The evolution of keyhole shape for the cases corresponding to single and triple absorptions. The 0.1 ms case surface depression is so shallow that multiple absorptions do not occur.
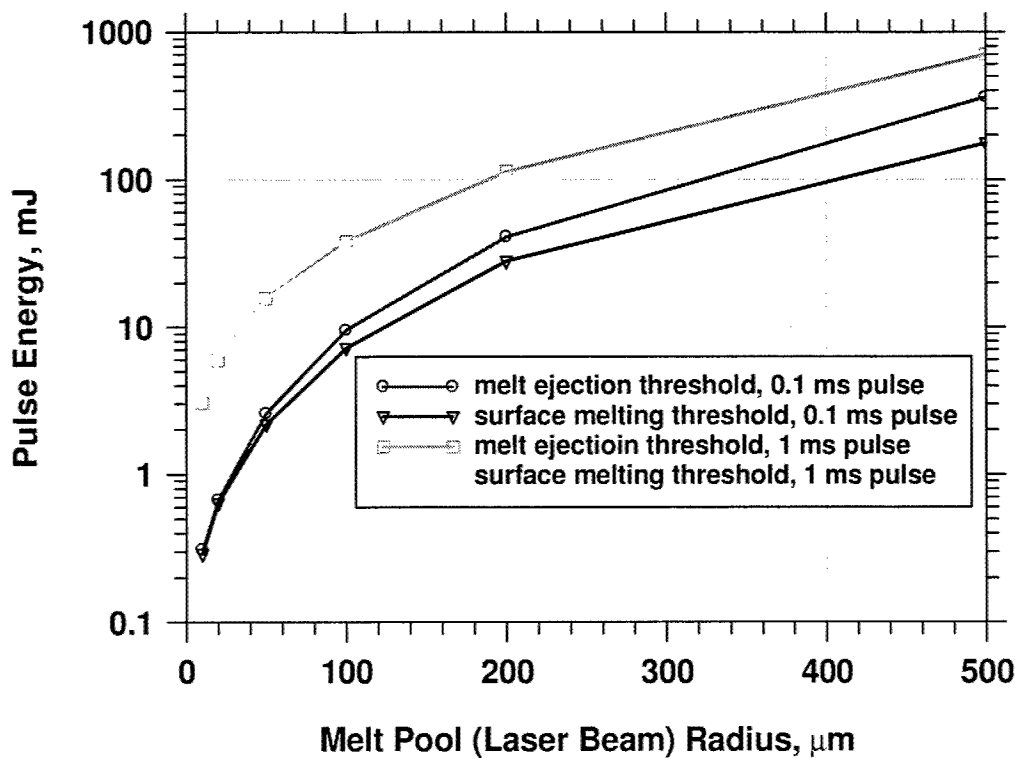
Figure 4: Calculated threshold pulse energies for melt ejection and surface melting as a function of the beam radius for pulse durations of 0.1 ms and 1 ms for pure Ni.
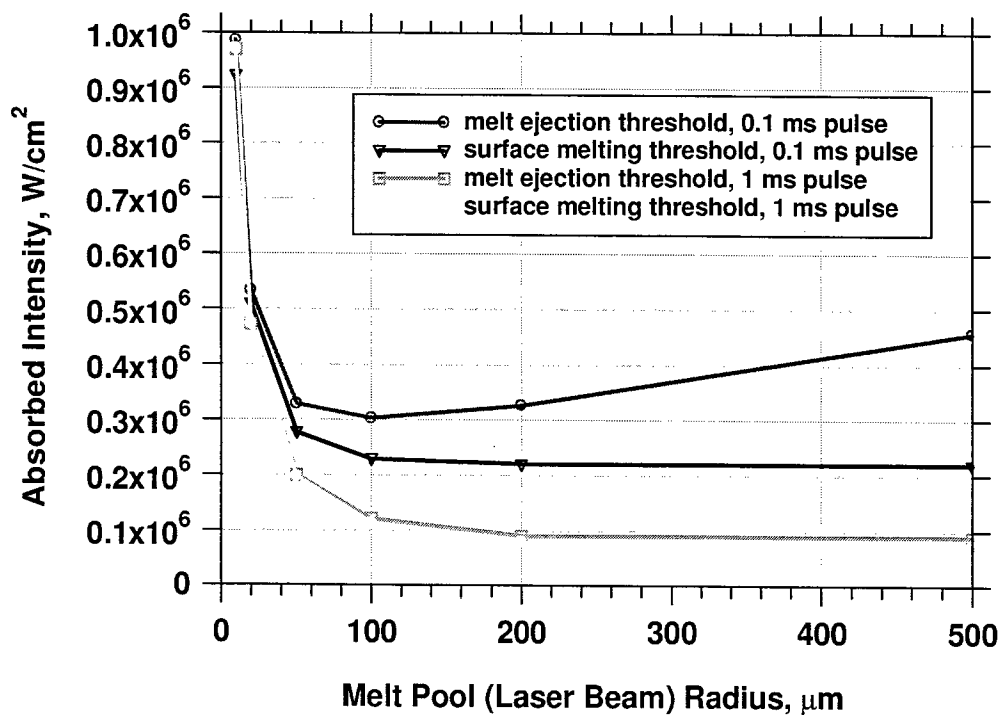
Figure 5: Calculated threshold beam intensities for melt ejection and surface melting as function of the beam radius for pulse durations of 0.1 ms and 1 ms for pure Ni.
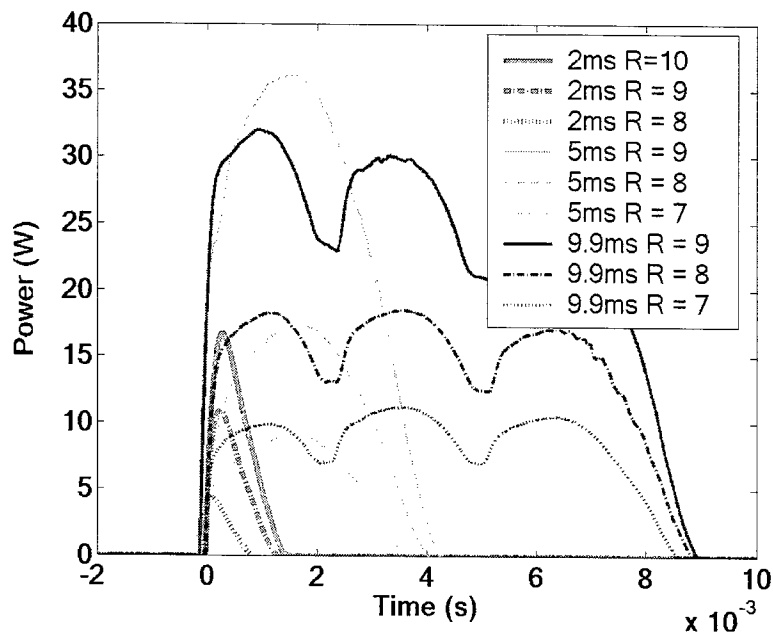
Figure 6: Power vs time, various pulse length & power settings.
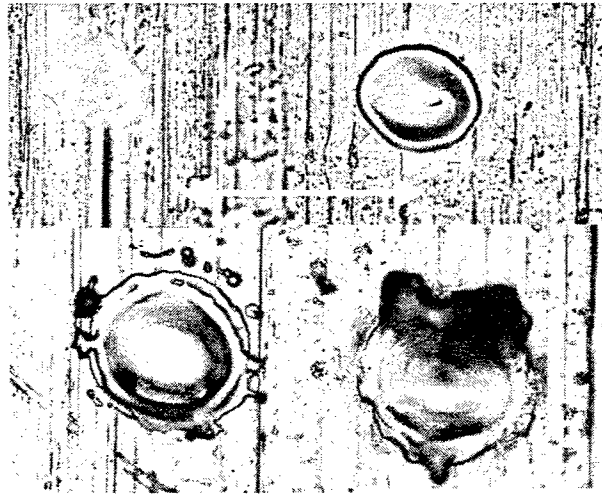
Figure 7: Optical metallography of 5 ms pulse fusion zones, at power settings showing transitions between flat @ 7, to concave @ 7.5, to drilled @ 8. Arrow is 50 microns long.
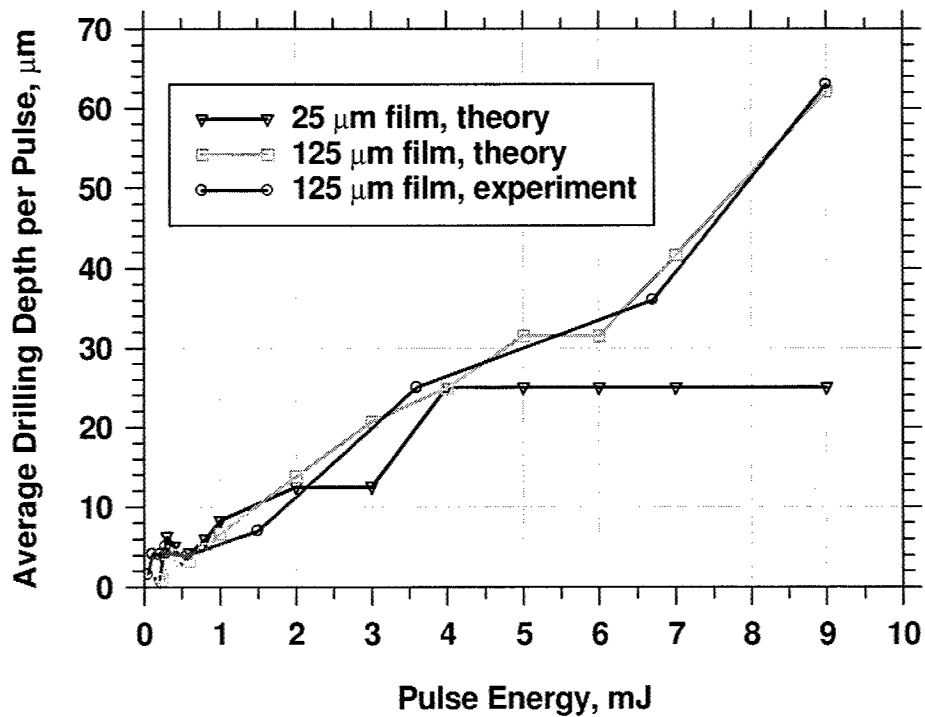
Figure 8.a: Average drilling depth per pulse as a function of pulse energy on Al film with 104 ns laser pulses from an excimer laser.
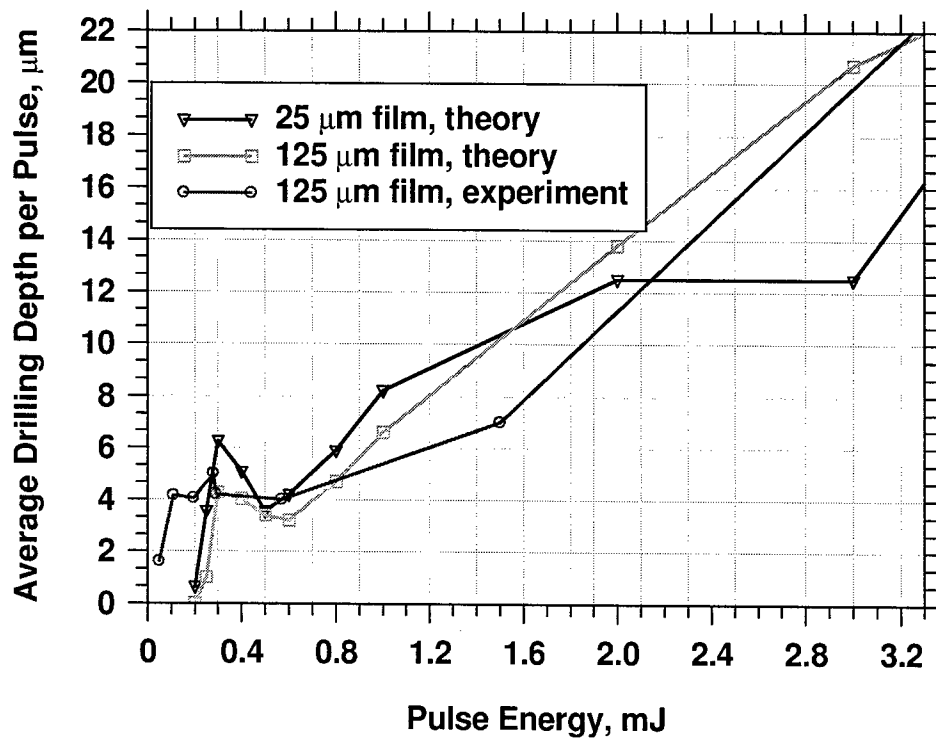
Figure 8.b: Expanded low energy part of Figure 8.b.

Laser processing of ceramic and crystalline wafer substrates for microelectronic applications

David Ashkenasi*, Alexander Binder, Houssam Jaber, Holger Kern,
Norbert Müller, Andreas Ziegert

Laser- und Medizin-Technologie GmbH Berlin (LMTB),
Department of Applied Laser Technologies, Berlin, Germany

ABSTRACT

Ceramic and crystalline wafer substrates are widely used in microelectronics. The individual choice is based on their thermal, optical and mechanical properties. For a variety of applications high quality laser micro processing of these materials, i.e. the generation of blind and through holes, grooves and even complex three dimensional micro structures, is gaining in importance. The department of applied laser technologies of the LMTB GmbH has conducted extensive studies on the versatility of q-switch Nd:YAG laser systems for the micro structuring of ceramic and crystalline wafer substrates that differ strongly in their optical and mechanical properties, such as Al_2O_3, AlN, sapphire, Si and SiC. This paper discusses the laser material micro machining results in respect to the laser parameters used to optimize the micro processing quality and speed for the different materials.

Keywords: laser material micro machining (LM^3), wafer substrates, semi-conductors, ceramics, transparent dielectrics.

1. INTRODUCTION

Laser material micro machining (LM^3) with solid state lasers is typically conducted in a direct writing alignment. The laser beam is focused down to the μm range to provide optimal spatial energy localization. Diffraction limited processing suggests a very good beam quality, i.e. TEM_{00} mode output. This can be easily provided with Nd:YAG laser systems at moderate average powers of 10 W. With the implementation of diode lasers pumping the solid state rods and driven by innovative resonator design, the average power for diffraction limited applications is constantly being shifted to higher levels. High average power at sufficient single pulse energy is an important factor for industrial applications, since it determines the processing speed and therefore the cost factor for any laser based batch production. However, many applications can be addressed at moderate laser average powers.[1]

For most LM^3 applications with metals and semi-conductors, the wavelength of 1.06 μm is adequate for micro structuring tasks, such as micro drilling. In the case of copper, for example, the processing at the 2. harmonic yielding a wavelength of 532 nm ensures an enhanced photon absorption and suggests a higher processing efficiency, even taking a 50 % conversion loss into account.[2] For the most dielectric materials, glass, crystals, polymers and ceramics, the linear absorption characteristics yield a fairly high penetration depth for laser light in the visible and infrared spectral range. Therefore, laser processing of these materials is usually performed using the third or fourth harmonic, 355 or 266 nm, to provide for higher excitation probabilities over linear and low order multi-photon absorption routes. A shift of the pulse width from ns to sub-ps laser pulses provides the potential of higher order multi-photon excitation. One expects a reduced wavelength dependence in LM^3 with ultra short laser pulses compared to applications using ns laser technology. This must not be true in all cases, since in multi-shot processes this depends also on the specific material reaction and ablation mechanisms, hence, forthcoming changes in the optical properties.[3]

Corresponding author: * d.ashkenasi@lmtb.de; phone: +49 30 67053-6; fax: +49 30 67053-500; http://www.lmtb.de; Schwarzschildstr. 8, D-12489 Berlin, Germany.

The increasing availability of ultra short laser pulses (sub-ps pulse width) has stimulated a growing interest in exploiting the enhanced flexibility of femtosecond technology for micro-machining.[4] However, there are a few important drawbacks to be considered presently, trying to implement ultra short pulse technology for wide spread LM^3, such as micro structuring or high aspect hole drilling. Presently, most laser systems capable of generating ultra short laser pulses are accompanied with certain disadvantages compared to industrial q-switch Nd:YAG lasers generating ns pulses: they usually do not allow "turn-key" operation (although this problem is being solved currently), they have a fairly complicated and costly design (especially during the proto-type stages), and, most importantly, a direct amplification of ultra short laser pulses is very difficult. The damage threshold limit of the optical elements for high peak intensities is a challenging task to overcome. Present commercially available ultra fast laser systems are typically limited to average powers of 1-5 W at a repetition rate of usually 1 kHz, leading to single pulse energy in the lower mJ range.

Basically, the choice of the laser parameters, e.g. wavelength, pulse width, average power and repetition rate, depends not only on the excitation state of the material, which is (peak) intensity related. An optimization of the relevant parameters depends also significantly on the desired material reaction. Access and control in the localization of the provided laser energy in the desired region of the material is the important factor in any successful LM^3. Fig. 1 outlines some of the most important contributions in laser-material interaction for laser-induced processing. In general, a division into three main mechanisms describes the interaction and forthcoming processes in different time domains. The lower axis relates the laser pulse width with the relevant dynamics in laser-material interaction. In addition, Fig. 1 also considers possible contributions in the repetition rate before and during material reaction.

Experiments on LM^3 have been carried out on various materials that are important base substrates for micro electronic applications and in many cases difficult to machine with conventional methods. Targeting on problems concerning devises with interlayer connections through circuit layer boards, substrates made of the ceramics Al_2O_3 and AlN were drilled using different solid state laser systems under varying ambient conditions. Sapphire, silicon and silicon-carbide wafer have been scribed to determine the maximum processing speed for precise consecutive dicing.
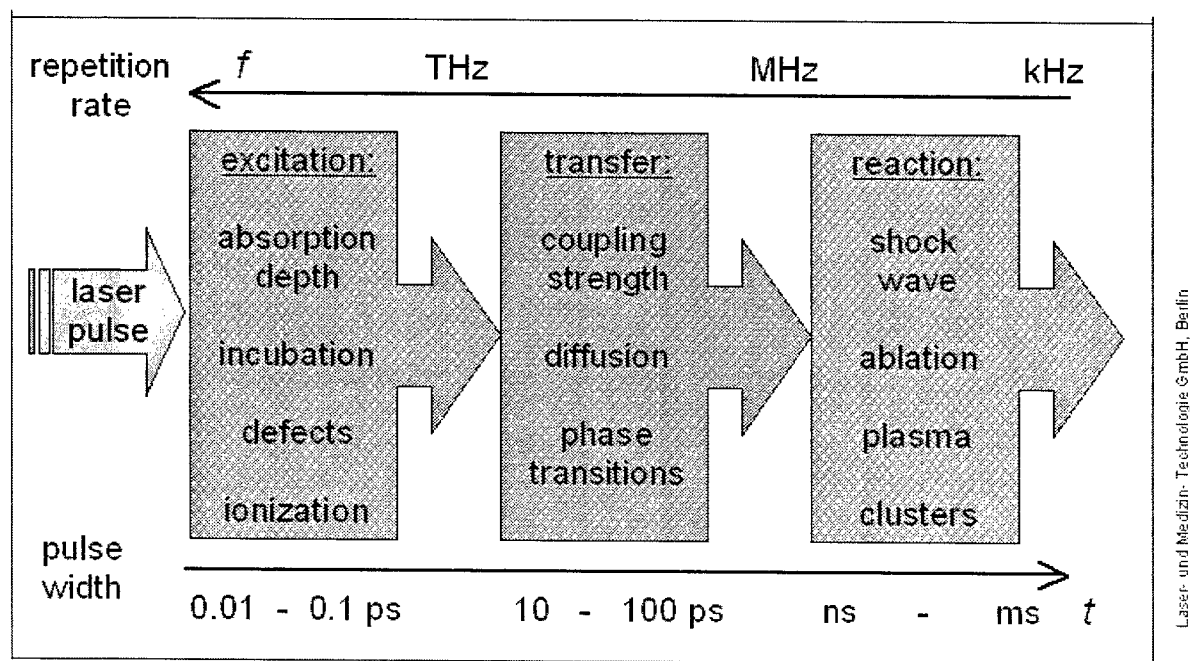

Fig. 1: Schematic illustration of the different mechanism involved in laser-material-interaction, electron excitation, energy transfer, and material reaction, separated by the expected dynamic response in respect to the possible influence of laser pulse width and laser repetition rate.

2. LASER SYSTEMS

The following section introduces five different q-switch Nd:YAG laser systems, the main working tools used in this study.

2.1 Diode-Pumped Nd:YAG-Laser (IB-Laser)

The commercial turn-key Nd:YAG laser system "DiNY cwQ"-series by IB-Laser, Berlin (www.IB-laser.com), provides 50 W average power in multimode and 8 W in TEM_{00} at a repetition rate up to 50 kHz and a pulse width around 30 ns. The system offers the opportunity to easily change the internal aperture straightforwardly, e.g. reducing the beam quality to enhance the average output power in cases where special energy localization is less crucial.

2.2 Arc Lamp-Pumped Nd:YAG-Laser (single-rod configuration, LMTB)

The single-rod arc lamp-pumped laser system is a non-commercial experimental setup designed at the applied laser technologies of the LMTB GmbH for research and comparative studies. The resonator design including AOM device, aperture and thin-film polarizor is very robust and easy to adjust. The crystal is pumped continuously by an arc lamp. The average output power reaches reliable 14 W at a beam quality of $M^2 = 1.3$. The pulse width varies between 50 and 80 ns, depending on the repetition rate which is typically set between 2 and 20 kHz.

2.3 Arc Lamp-Pumped Nd:YAG-Laser (double-rod configuration, LMTB)

The arc lamp-pumped system is another experimental setup designed at the LMTB-laboratories.[5] The resonator includes two cavities with a phase shift plate in-between to accomplish compensation of the thermal birefringence. The losses due to de-polarization in the resonator range around 5%. The average output power reaches a stable level of 30 W at a beam quality of $M^2 = 2.3$. Replacement of the high reflection mirror and aperture in the resonator provides average powers of 100 W at multimode operation in a $M^2 = 20$, see Fig. 2. Due to the longer resonator length the pulse width varies between 150 and 200 ns, depending on the repetition rate which is typically set between 6 and 20 kHz (in multimode from 1 to 20 kHz). Hence, in TEM_{00} or in multimode the maximum single pulse energy varies between 1 and 4 mJ or 5 and 100 mJ, respectively.
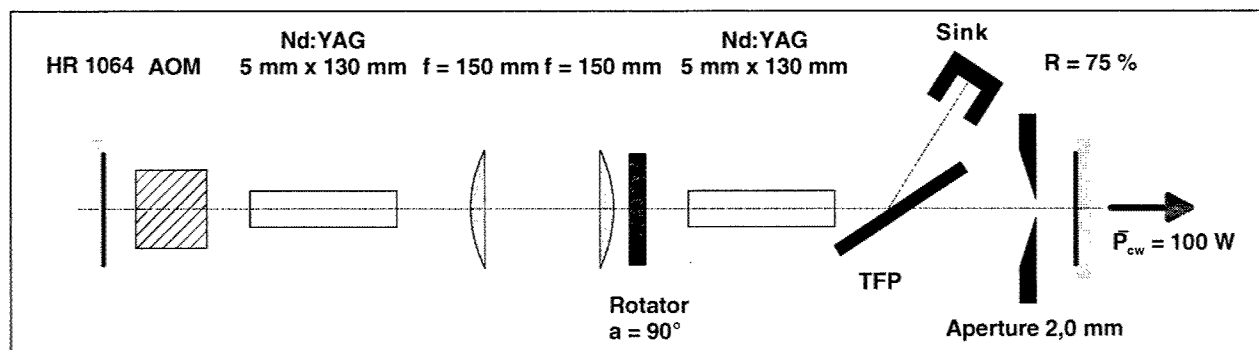

Fig. 2: Schematic set-up of the arc lamp-pumped double-rod Nd:YAG-system in multimode configuration.

2.4 Arc Lamp-Pumped Nd:YAG Master-Oscillator Power-Amplifier System (LMTB and TU-Berlin).

The setup of the master oscillator power amplifier (MOPA) system is sketched in Fig. 3.[6] The oscillator consists of a flash-lamp pumped single rod Nd:YAG resonator with AOM, very similar to the laser system described in section 2.2. With an internal aperture the beam quality results in $M^2 = 1.35$ at an average power of 10 W. The amplifier consists of two flash-lamp pumped cavities which are slightly tilted off the optical axis to prevent autonomous laser activity. In a single-pass set-up the amplifier is subjected to birefringence compensation which is obtained by mounting a quartz-rotator between the cavities, based on the experience in the double-rod design (section 2.3). The repetition rate varies from 100 Hz to 5 kHz leading to pulse width between 31 and 230 ns. The oscillator TEM_{00}-beam is amplified to > 100 W @ 1064 nm with $M^2 = 2.3$ and a single pulse energy up to 500 mJ @ 100 Hz. Based on the excellent beam quality first tests demonstrate high frequency conversion yielding 50 W @ 532 nm and 4.8 W @ 266 nm, respectively.
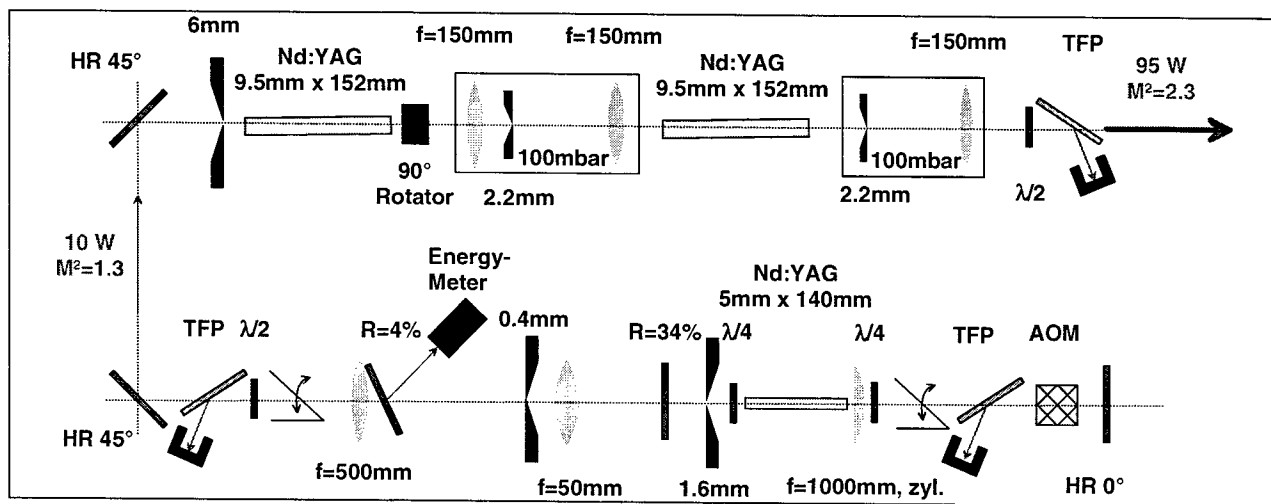
Fig. 3: Schematic set-up of the Nd:YAG MOPA system of the LMTB GmbH, Berlin, in cooperation with the Technical University Berlin.

2.5 Diode-Pumped Nd:YVO₄-Laser (Azura Laser)

The cw-diode pumped commercial $Nd:YVO_4$ laser system designed by Azura Laser, Berlin (www.azura.de) MESA AC UV-V-20 includes a third harmonic module providing laser pulses at $\lambda = 355$ nm at a maximum output power of 1 W @ 15 kHz. The repetition rate can be set between 1 Hz and 100 kHz. Due to the relatively compact resonator design the pulse width is less than 25 ns. Laser operation requires air-cooling only. The beam quality is better than $M^2 = 1.5$.

3. EXPERIMENT

The following section discusses examples of LM^3 with the in section 2 outlined laser systems, divided into different material classes. The AlN and Al_2O_3 samples were delivered by Anceram and Kerafol in Germany, respectively, single and poly crystalline silicon solar wafers were received by Solarc, Berlin, Germany, sapphire and SiC disks were send by MicroLaserTec, Meissen, Germany. The laser beam was expanded to above 15 mm diameter using telescope optics before being focused onto the sample surface. In some cases, laser processing (drilling) was conducted in a low pressure (< 100 mbar) environment.

3.1 Ceramic Aluminum-Oxide and Aluminum-Nitride

<u>multimode double-rod laser system</u>

Laser micro drilling of approx. 100 μm diameter holes focusing the laser beam of approx. 100 W power from the multimode the double-rod system with a lens of a focal length of 200 mm onto the sample surface resulted in a maximum depth of 8 mm into aluminum-oxide (Al_2O_3) and 6.6 mm in aluminum-nitride (AlN). Largest depth and best processing quality was obtained in a low pressure (< 100 mbar) environment. Fig. 4 illustrates two cross sections of laser drilling into AlN. The drilling made under a pressure of 1000 mbar has a distorted shape and a considerable Al_2O_3-debris around the hole. The low pressure drilling demonstrates a circular shape and an aluminized bore hole wall is observed. The illustration in Fig. 5 result from experiments with stacked specimen disks of 250 μm thickness. Comparing measurements with drillings into a single bulk Al_2O_3 and AlN work piece prove that the

Fig. 4: Microscope graphs of micro holes in 250 μm thick AlN, laser drilled under normal atmospheric conditions (left) and in low pressure environment (right).

geometrical shape of bore holes are identical, provided the stacked disks are pressed tightly together. Experiments on AlN demonstrates an enhanced quality of the bore hole at (slightly) reduced ambient pressure. Fig. 6 illustrates the different drilling depths and diameters obtained in the laser micro drilling experiments of Al_2O_3 and AlN.
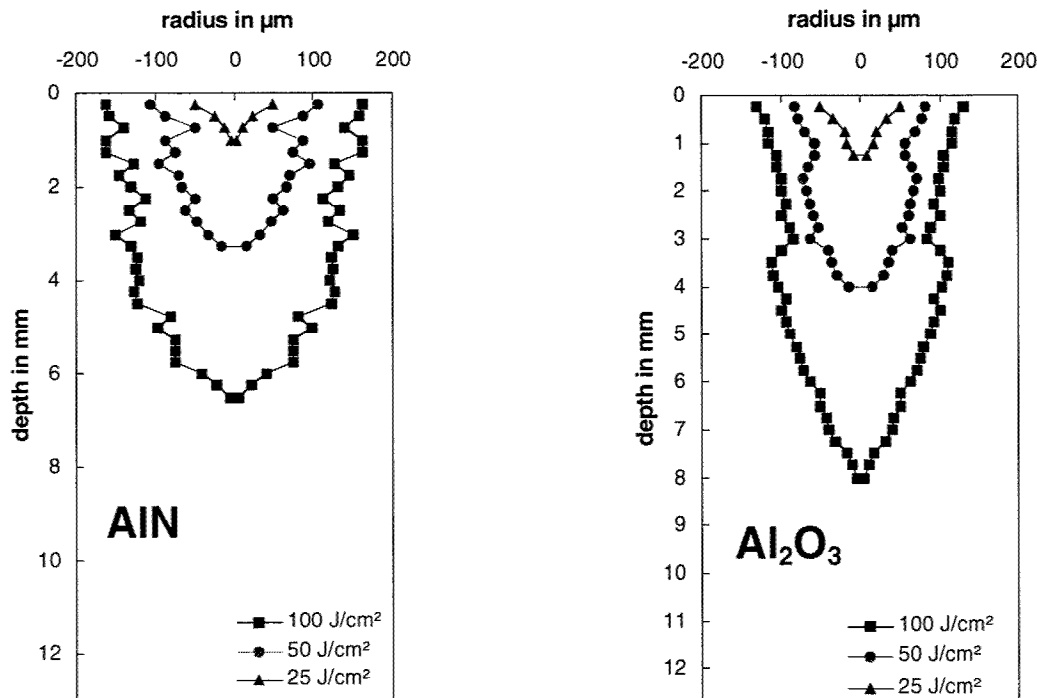
Fig. 5: Discrete progression of the bore-holes (in 250 μm steps), laser micro drilled in AlN (left) and Al_2O_3 ceramic at different fluence levels using the double-rod laser system in multimode configuration: (note the expansion for diameter in [μm] versus depth in [mm]). Laser parameters: repetition rate f_{REP} = 1.5 kHz; pulse duration τ_{PULSE} = 120 ns; average power P_L = 80 W; focus diameter = 200 μm; focal length: f = 200 mm; drilling time t = 200 s.
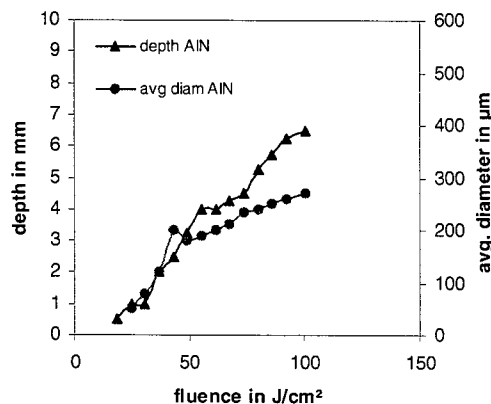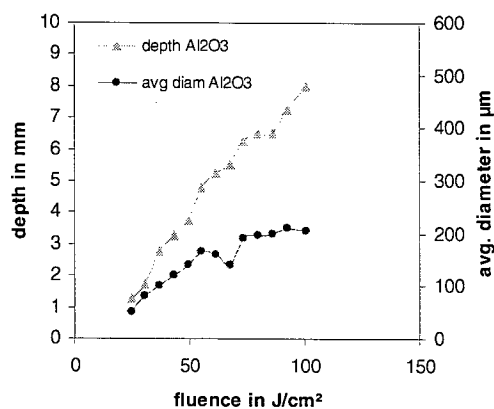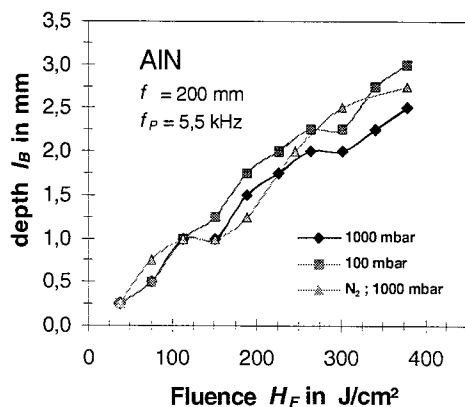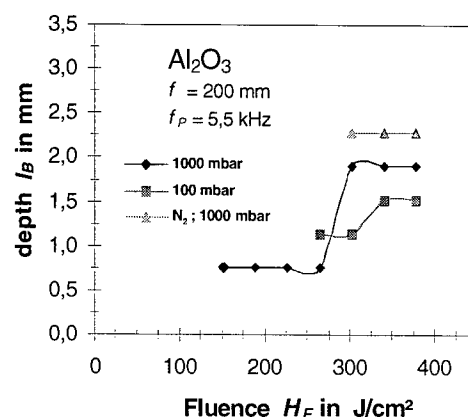
Fig. 6: Double-rod laser system at multimode configuration: laser micro drilling depth (left axis) and drilled average diameter (right axis) as a function of laser fluence. A) (left diagram) for AlN and B) Al_2O_3 (connecting line for eye guidance).

single-mode double-rod laser system

For comparison, laser micro drilling experiments on AlN and Al_2O_3 were also conducted using the double-rod laser system in single-mode alignment under different ambient conditions focusing the laser beam with the same lens of a focal length of 200 mm onto the sample surface. The focused beam had a measured diameter ($1/e^2$) of 60 μm on the surface of the ceramic samples. The achievable drilling depths were lower but an improved aspect ratio was obtained, since the hole diameter remained below 100 μm throughout the main part of the hole channel. In the low pressure arrangement (< 100 mbar air), a maximum drilling depth of 3 mm is obtained for AlN, whereas a maximum aspect ratio of 1:90 is reached at normal pressure in air. The deepest hole into Al_2O_3 (2.3 mm) is observed laser processing in a nitrogen atmosphere at normal pressure, at which aspect ratios of 1:70 is obtained. Fig. 7 compiles the depth results for the laser micro drilling studies in the two ceramic materials using the double-rod laser system in single-mode alignment in a fluence range up to 400 J/cm².

Fig. 7: Laser micro drilling into A) AlN and B) Al_2O_3 using the double-rod laser system in single-mode configuration: drilling depth versus laser fluence under different ambient conditions (air: <100 mbar, 1000 mbar and nitrogen: 1000 mbar).

The micrograph in Fig. 8 depict a set of micro-turbines in AlN (thickness: 250 µm) and a micro structure in Al_2O_3 (thickness 380 µm) for a biomedical application. The micro structure on the left image of Fig. 8 was laser cut using the double-rod laser system in single-mode alignment at an average power of 17 W, repetition rate of 7 kHz, and by applying 3 to 4 circulations with a feed rate of 1 mm/s. The micro structure made of Al_2O_3 was laser cut using the commercial DiNY cwQ laser system (IB laser) in single mode quality at average power around 10 W. A special cooling technique was developed to prevent the brittle ceramic material to crack during the LM^3 application with focused laser pulses.
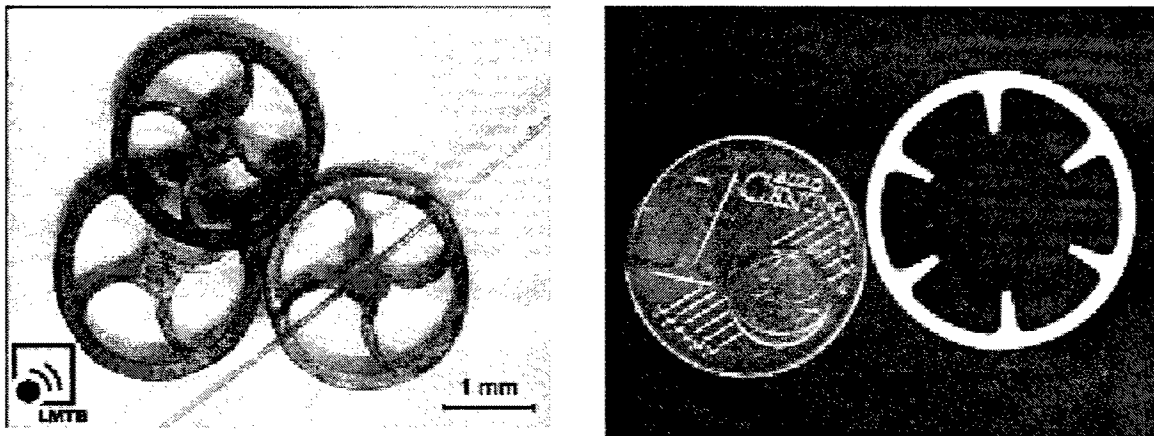
Fig. 8: Laser micro cut structures from ceramic materials: Left: image set of AlN micro-turbines (including a human hair for size comparison) laser cut using a double-rod Nd:YAG laser system (LMTB) in single mode configuration; right: image of an Al_2O_3 sieve-support laser cut using a diode pumped Nd:YAG system (DiNY cwQ, IB-Laser) in single mode configuration (European one cent coin for size comparison).

Nd:YAG-MOPA laser system

Outstanding aspect ratios for ceramic material is obtained using laser systems with high average power and good beam quality, as with the MOPA system.[7] Focusing the laser light with lens of a focal length of 250 mm, a maximum aspect ratio of 1:130 is observed in AlN and 1:120 in Al_2O_3. With an average hole diameter of 100 µm, the maximum drilling depth is 18 mm for Al_2O_3 and 15.5 mm for AlN, see Fig. 9. The experiments were carried out with an average power of 10 to 80 W (4 kHz, 130 ns). The focused beam had a measured diameter ($1/e^2$) of 145 µm on the surface of the ceramic samples. The average hole diameter increases with laser fluence, in our study from about 60 µm @ 20 J/cm^2 to 160 µm @ 120 J/cm^2.
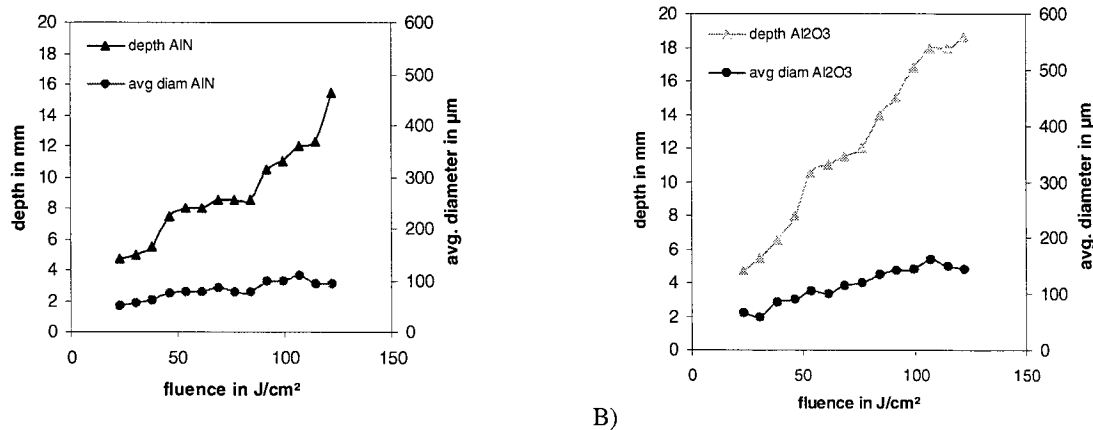
Fig. 9: YAG-MOPA-system: maximum depth and corresponding average diameter depending on the laser fluence on A) AlN and B) Al_2O_3. Laser parameters: repetition rate: f_{REP} = 4 kHz; pulse width : τ_{PULSE} = 130 ns; focal length: f = 250 mm, focus diameter on sample surface 145 μm;

Excimer laser (KrF 248 nm) projection processing

Studies in LM[3] using a commercial KrF excimer laser (LPX 325i, lambda physics) are conducted for comparative reasons. At the LMTB, excimer laser technology is not the prime tool of choice to generate high aspect ration micro holes in ceramic materials. Typically, laser micro drilling is conducted to a maximum depth of 500 μm. The excimer laser processing is performed by mask projection (1:14). The masks are laser cut utilizing the arc lamp pumped Nd:YAG-laser (single-rod configuration, LMTB). Projection mask with a aperture of 2 mm x 2 mm was used to determine the ablation rate for AlN and Al_2O_3 shown in Fig. 10. The ablation threshold for AlN is lower than for Al_2O_3. In addition, the ablation rate for AlN remains above of that for Al_2O_3.
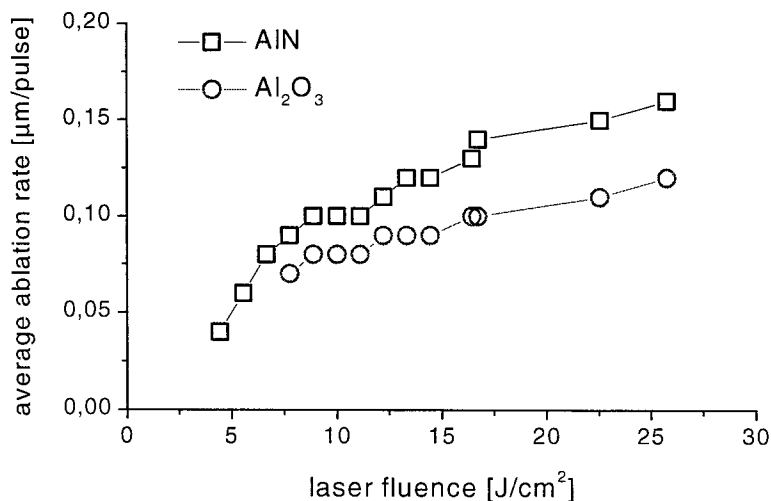

Fig. 10: Ablation rate of AlN and Al_2O_3 as a function of laser fluence (wavelength of 248 nm, KrF excimer laser, pulse width 20 ns). Laser irradiated area on the ceramic surface 143 μm x 143 μm. Sample was not moved during laser drilling.

A typical application in LM³, for which excimer laser is often utilized, is the generation of micro grooves, e.g. Fig. 11. The sample is moved at a certain processing velocity, defining the average number of shots per site taking the repetition rate and the irradiated area on the sample surface into account. The micro grooves in AlN and Al_2O_3, depicted in Fig. 11, were processed at identical fluence (19 J/cm²), repetition rate (150 Hz) and velocity (31.5 µm/s). However, the average number of laser shots N_{ave} differ strongly in the top and lower picture of Fig. 11, since different projection masks were used. The micro grooves in the top of Fig. 11 demonstrate an aspect ration of 1:1 at N_{ave} = 680 shots, and correspond in width with the irradiated area on the sample surface of 143 µm x 143 µm. The different depths in AlN and Al_2O_3 correspond to the relative differences in ablation rate, see Fig. 10. The surface irradiated in the lower example of Fig. 11 is 71 µm x 173 µm. Since the sample was moved parallel to the longer part of the rectangle, N_{ave} equals approximately 3400 shots, leading to larger groove depths of 270 µm (and to a higher processing efficiency). This is slightly lower than expected from the ablation rate per laser pulse data in Fig. 10. The reduced aperture of 71 µm perpendicular to the direction of translation yields a conical shape of the micro groove, clearly seen in the side view lower images of Fig. 11. This effect causes a reduction in the (average) ablation rate and demonstrates limitations in generation of micro grooves using excimer laser technology.
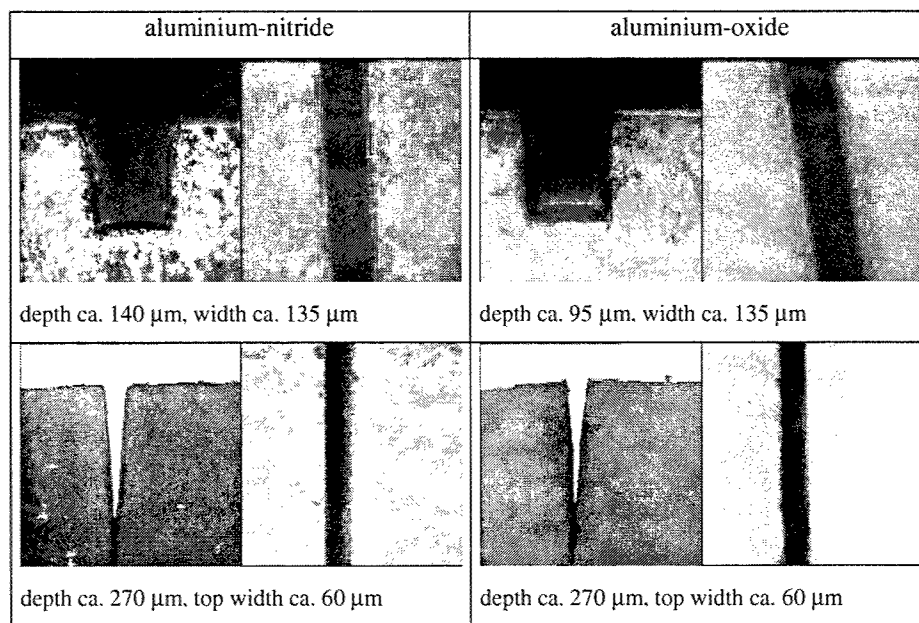

aluminium-nitride	aluminium-oxide
depth ca. 140 µm, width ca. 135 µm	depth ca. 95 µm, width ca. 135 µm
depth ca. 270 µm, top width ca. 60 µm	depth ca. 270 µm, top width ca. 60 µm

Fig 11: Side and top view micrograghs of micro grooves in aluminium-oxide (right) and aluminium-nitride (left), generated using excimer laser processing in projection technique at 248 nm and a fluence of 19 J/cm². The sample was moved at a processing speed v = 31.5 µm/s, the laser repetition rate was set at 150 Hz. Top: a square projection mask of 2 mm x 2 mm was used, yielding an UV irradiated area of ca. 143 µm x 143 µm on sample surface. Bottom: a square projection mask of 1 mm x 10 mm was used, leading a UV irradiated area of 71 µm x 713 µm on the sample surface. The sample was moved in direction of the longer side of the rectangle.

3.2 Silicon

Arc Lamp-Pumped Nd:YAG Laser (single-rod configuration)

Conventional separation methods (i.e. diamond saw) causes local short circuits (edge-shunts) at the p-n-transition, leading to a reduction in solar wafer efficiency down to 70 %. Applying the technique of laser scribing the rear side of the solar wafers and forthcoming mechanical separation the photo-voltage remains on highest level. The LMTB Nd:YAG laser in single-rod configuration running at a pulse duration around 100 ns proved to be a very suitable tool for scribing silicon wafers for various applications at processing speed in the multiple m/min range. To provide for a constant

scribing groove depth, long term average power stability is of key importance to avoid any undesired effects such as damage the p-n-boundary. The picture in Fig. 12 (left) depicts a snap shot during the laser micro scribing of a 4"-wafers. Also illustrated is the optics holder and the nitrogen supply to clean off any residuals during processing. Fig. 12 (right) illustrates a typical edge of a diced 400 μm thick poly-crystalline Si-wafer after laser scribing (top half) and mechanical separation. The average laser power remains stable at 10 W, running at a repetition rate of 5 kHz (2 mJ per pulse). The beam diameter on the surface of the wafer is focused to 20 μm (laser fluence ca. 600 J/cm^2). Processing speed for optimal laser scribing and precise mechanical separation of 300 to 400 μm thick wafer samples is set to 50 mm/s for poly-crystalline and 70 mm/s for mono-crystalline wafers, leading to an average number of shots per site of only $N_{ave} = 2$ and 1.5 respectively. The low N_{ave}, actually the high ablation rate per pulse in the range of 100 μm compared to the groove depth of 150 to 200 μm, accounts for the desired average laser power stability below 1 % in this application.
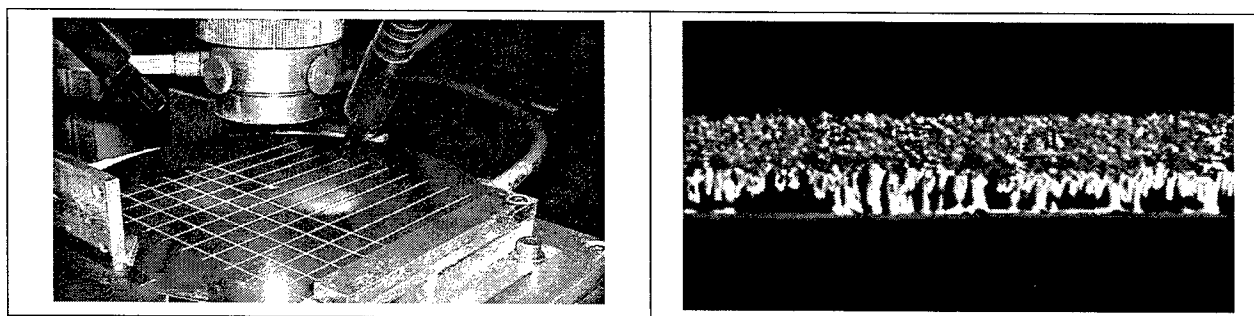
Fig. 12: Left: laser scribing of a 4" silicon wafer. Right: diced 400 μm thick poly-crystalline Si-wafer (upper region is laser scribed, bottom region illustrates the separated edge).

3.3 Silicon-Carbide and Sapphire

Diode-Pumped Nd:YAG Laser („DiNY" of IB-Laser)

Fig. 13 illustrates lengthwise sections of scribed SiC wafers at a wavelength of 1.06 μm using a diode pumped Nd:YAG laser (IB-Laser). The surfaces of the SiC samples were not polished and demonstrated strong scattering properties providing a strongly reduced optical penetration depth for the infra red laser light. The amorphously dark upper area is the image of laser scribed groove while the bright area below represents the region, where the specimen was mechanically separated. Best results are obtained at maximum beam quality, i.e. smallest aperture in the resonator. Larger aperture to obtain a higher average laser power lead to a notably stronger thermal load in the sample. Additionally, the grooves widened and more residuals are generated.
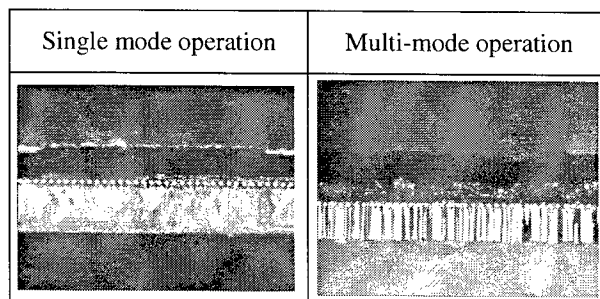
Single mode operation	Multi-mode operation

Fig. 13: Micrographs, lengthwise section of laser scribed SiC processed with different resonator apertures, hence, beam quality. Processing speed and focusing lens are identical in both cases. The dotted line indicates the boundary between laser scribing and breaking edge

single-mode double-rod laser system

Fig. 14 illustrates lengthwise sections of scribed SiC wafers at different processing velocities using the LMTB double-rod laser system in single-mode operation. Due to the higher laser power available (i.e. increased single pulse energy) at TEM_{00} beam quality and equal repetition rate, processing velocities could be increased. The desired 250 μm groove depth for straightforward mechanical separation is obtained at $v = 2$ mm/s with excellent consistency.

$v = 1$ mm/s	$v = 3$ mm/s
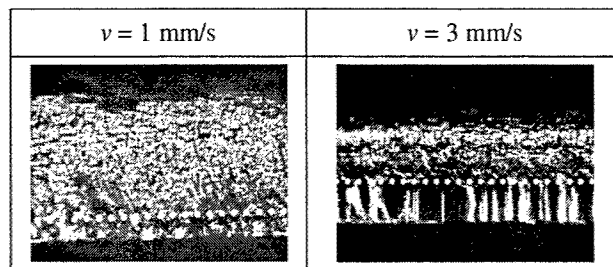
Fig. 14: Micrographs, lengthwise section of scribed SiC processed with different processing speed.

However, a considerable heat load of the SiC specimen has to be acknowledged in the laser micro scribing with above mentioned laser systems. The shape of the groove starts conically in a width of 70 μm from the surface until at a depth of 60 μm the width remains constant at 20 μm. A white debris of carbon (see Fig. 15) after laser scribing can be avoided with an efficient exhaust system, otherwise, post-processing (simple sonic bath or hand tissue cleaning) is required.
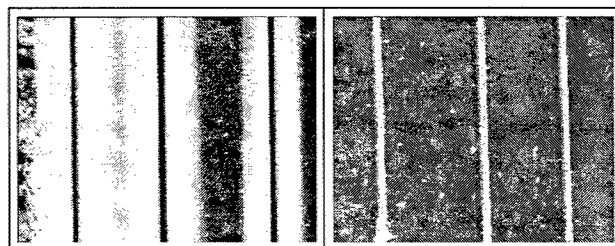

Fig. 15: Micrographs, surface view of scribed grooves into SiC before (left) and after cleaning (right).

Fig. 16 depicts the front entrance and rear exit of a micro hole in 1.2 mm thick sapphire wafer drilled with the LMTB double-rod laser system in single-mode operation at a wavelength of 1.06 μm. Here again, the top surface of the sapphire samples demonstrated strong scattering properties providing a strongly reduced optical penetration depth for the infra red laser light. The entrance hole diameter measures 75 mm, compared to a focus diameter of ca. 120 μm, while the exit hole is only 15 μm. Approx. 1 s percussion drilling time was necessary (less than 5000 laser pulses) to obtain structuring results as depicted in Fig. 16.
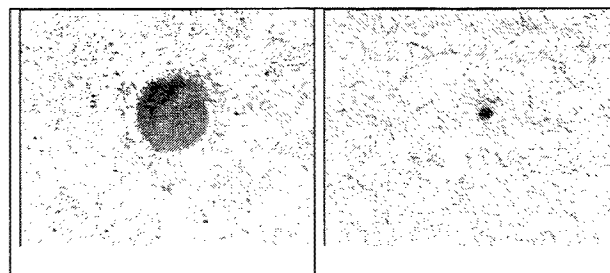

Fig. 16: Micrographs of laser micro drilled hole in sapphire substrate: left: entrance side, right: rear exit.

Diode-Pumped Nd:YVO₄-Laser (Azura Laser)

Fig. 17 depicts lengthwise and top view pictures of laser scribed sapphire wafer with a thickness of 700 μm, processed at a wavelength of 355 nm using the 1W diode pumped Nd:YVO₄ laser system (Azura Laser). Similar as in the laser scribing of silicon, the groove width for sapphire seems independent of the processing speed, however, more debris is observed at lower feed rates as more material is removed. Processing speed more than 5 mm/s resulted in a groove depth less than 1/3 of the wafer thickness at which reliable clean mechanical separation (dicing) becomes a difficult task. While sapphire shows a strong dependence of the processing speed, the micro scribing for SiC yield fairly constant groove depths of 100 μm in a processing speed range of 1 mm/s and 32 mm/s, to be seen in Fig. 18.
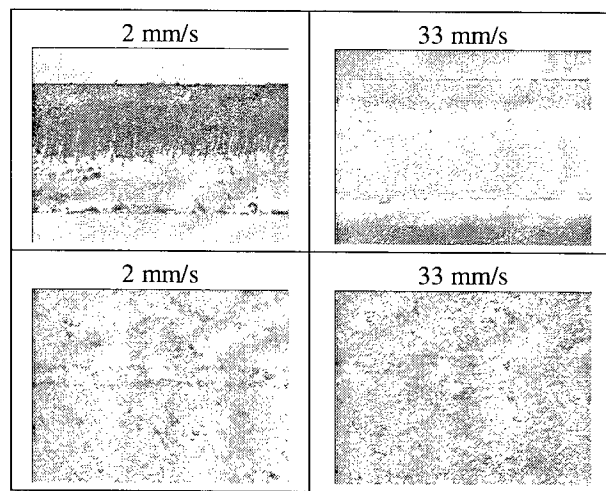
Fig. 17: Micrographs, lengthwise section (top) and surface view (bottom) of laser scribed sapphire wafers at different processing speeds.
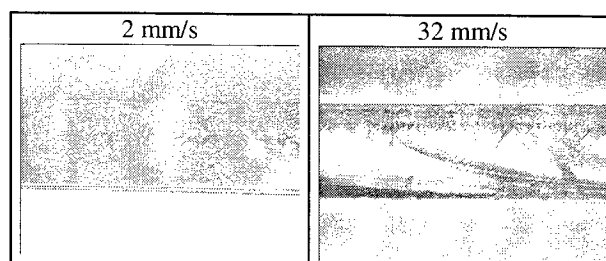

Fig. 18: Micrographs, lengthwise section of laser scribed SiC wafers at different processing speeds.

4. SUMMARY

Improved laser material micro machining (LM^3) for AlN, Al_2O_3, Si, c-Al_2O_3 and SiC is presented in this paper. The examples depicted for the micro drilling of AlN and Al_2O_3 and for the micro scribing of Si, c-Al_2O_3 and SiC demonstrate the strong importance of a good beam profile over high average power alone. A combination of both, good beam profile and high average power, as delivered by the Nd:YAG master-operator power amplifier (LMTB and TU-Berlin) with sufficient single pulse energies, e.g. > 10 mJ per pulse, provides the conditions necessary to micro drill holes with very high aspect ratio. This is demonstrated for AlN and Al_2O_3, where micro holes with an average diameter below 100 μm aspect ratio of 1:130 and 1:120, respectively, are achieved. Initial conditions as ambient pressure and surface roughness play an important role in LM^3. A reduced ambient pressure improves the processing quality and enhances the aspect ratio for laser processing of ceramics with ns laser pulses. The high scattering rate at the interface surface to bulk of the sapphire and SiC samples ensures sufficient absorption of ns laser pulses even at a wavelength of 1064 nm. With polished dielectrics at a band gap of 8 eV, certainly a shift to shorter wavelengths of the ns laser pulses is necessary to provide the linear and non-linear absorption conditions for a successful LM^3. This paper shows that micro scribing of several 100 μm thick solar cells and dielectric wafers at a moderate average laser power between 1 and 10 W can be performed at feed rates up to 100 mm/s and above 30 mm/s, respectively, for forthcoming mechanical separation.

ACKNOWLEDGEMENTS

REFERENCES

1) D. Ashkenasi, "The potential of ultra-short laser pulses (<10 ps) in future material processing: "mode-locked Ti:sapphire" vs. "q-switch Nd:YAG" applications", *SPIE 4637*, p. 378, 2002.

2) B. Smandek, B. Klimt, F. Maßmann, T. Metzger, D. Ashkenasi, Mikromaterialbearbeitung mit grünen Nd:YAG-Laser bei kurzen Pulsen", *LaserPraxis 2*, pp. 10-12, 2001.

3) D. Ashkenasi, A. Rosenfeld, "Processing of multi-layer systems using femtosecond, picosecond, and nanosecond laser pulses at different wavelengths", *SPIE 4637*, p. 169, 2002.

4) E.E.B. Campbell, D. Ashkenasi, A. Rosenfeld, *Lasers in Materials Science* (Trans Tech Publications, Switzerland, 1999), pp. 123-144, 1997.

5) N. Kugler, S. Dong, Q. Lü, and H. Weber, "Investigation of misalignment sensitivity of a birefringence-compensated two-rod Nd:YAG laser system", *Appl. Opt. 36*, pp. 9359-9366, 1997.

6) S. Seidel, A. Schirmacher, G. Mann, G. Nursiani; T. Riesbeck,: "Optimized resonators for high-average power high-brightness Nd:YAG lasers with birefringe compensation", *SPIE 3267*, 1998.

7) A. Binder, H. Kern, D. Ashkenasi, G. Müller, T. Riesbeck, H.-J. Eichler, „High quality micro laser drilling of metals and ceramics with maximum aspect ratio", *SPIE 4977*, in print, 2003

Precision-Drilling of Fused Silica with 157 nm Excimer Laser Radiation

Thorsten Temme*, Andreas Ostendorf, Christian Kulik, Klaus Meyer
Laser Zentrum Hannover e.V., Hollerithallee 8, 30419 Hannover, Germany

ABSTRACT

For drilling fused silica, mechanical techniques like with diamond drills, ultrasonic machining, sand blasting or water jet machining are used. Also chemical techniques like laser assisted wet etching or thermal drilling with CO_2 - lasers are established. As an extension of these technologies, the drilling of micro-holes in fused silica with VUV laser radiation is presented here. The high absorption of the 157 nm radiation emitted by the F_2 excimer laser and the short pulse duration lead to a material ablation with minimised impact on the surrounding material. Contrary to CO_2 – laser drilling, a molten and solidified phase around the bore can thus be avoided. The high photon energy of 7.9 eV requires either high purity nitrogen flushing or operation in vacuum, which also effects the processing results. Depending on the required precision, the laser can be used for percussion drilling as well as for excimer laser trepanning, by applying rotating masks. Rotating masks are especially used for high aspect ratio drilling with well defined edges and minimised debris. The technology is suitable particularly for holes with a diameter below 200 µm down to some microns in substrates with less than 200 µm thickness, that can not be achieved with mechanical methods. Drilling times in 200 µm fused silica substrates are in the range of ten seconds, which is sufficient to compete with conventional methods while providing similar or even better accuracy.

Keywords: Micro-machining, VUV Laser, precision drilling, fused silica, quartz glass, lab-on-chip

1. INTRODUCTION

Besides optical and telecom applications, fused silica or quartz glass is also a widespread material in chemical process technology and chemical analysis. Due to its high purity and high binding energy, this material is suitable to be used with reactive materials and hardly effected by reactive substances and thus often used in sensitive processes. With this background, quartz glass is also a promising material in applications which can be assorted to the emerging fields of life science, lab-on-chip, or genom analysis. Many applications in this field have in common a micro-fluidic system as a core element. These micro fluidics usually consist of channels, reservoirs, and transducers or drillings.

Several process technologies are available for drilling such transducers into fused silica; the most widespread techniques are diamond drills, supersonic machining, sand blasting or water jet machining. Additionally, laser assisted wet etching and thermal drilling with CO_2 lasers are carried out. Each of these techniques has its own advantages like high surface quality of the diamond drilling or the high processing speed for the CO_2 lasers, but often suffers some disadvantages like the low processing speed for the chemical processes or the limitations in the minimal achievable diameter for the mechanical techniques. It has been demonstrated, that the F_2 Excimer laser with an emitting wavelength of 157 nm is a promising production technology for single pulse ablation and surface structuring of fused silica, published e.g. in [1-3]. The short wavelength and thus high absorption in fused silica leads to an absorption of the laser energy in the upper few hundred nm below the surface. Combined with the nanosecond pulse duration a very high energy density is achieved in the irradiated volume and leads to an efficient evaporation of the glass material with a minor heat transfer into the base material. The short wavelength combined with the mask imaging technology allows lateral resolutions well below the one provided by the mechanical or CO_2 laser based techniques.

Contrary to the surface structuring, the drilling process usually aims to produce (micro) - holes with a high aspect ratio. Excimer laser drilling is usually carried out with the mask imaging technique, where a (circular) mask is irradiated by the laser raw beam and an image of the mask is then projected with an objective onto the work piece. Demagnification

factors vary with material and application, typical values are 5:1 to 50:1. The drilling of a hole by applying several laser pulses onto the same spot of the work piece is usually being referred to as percussion drilling. Excimer laser percussion drilling provides relatively high drilling speed and allows the manufacturing of manufacture micro holes of virtually any cross section (e.g. rectangular, triangular etc.) by using an appropriate mask. On the other hand, this technique shows some disadvantages in the processing result. Typical problems for drilling brittle materials are demonstrated in figure 1, where a 200 µm fused silica sample has been machined by 157 nm percussion drilling. On the beam entrance side rounding of the rim edge can be observed. This phenomenon is caused by wear from the ablated material, propagating in the form of plasma and material plume under high pressure (pmax = 500 MPa), speed (5 - 15 km/s) and temperature (Tmax = 50,000 K) out of the hole, as reported for the machining of ceramics in [4]. In some cases the wear results in a funnel shaped opening, which excels the diameter of the laser beam greatly. On the beam exit side the high pressure in the hole, combined with the brittle behaviour of the material, is bursting open the hole at the very end of the drilling process. This effect is producing a crater-shaped opening and sometimes cracks in the bulk material. Particularly for the percussion drilling of fused silica with 157 nm, it can be observed that the drilling diameter is reduced drastically below the diameter of the laser spot with increasing depth combined with a reduced ablation rate per laser pulse.

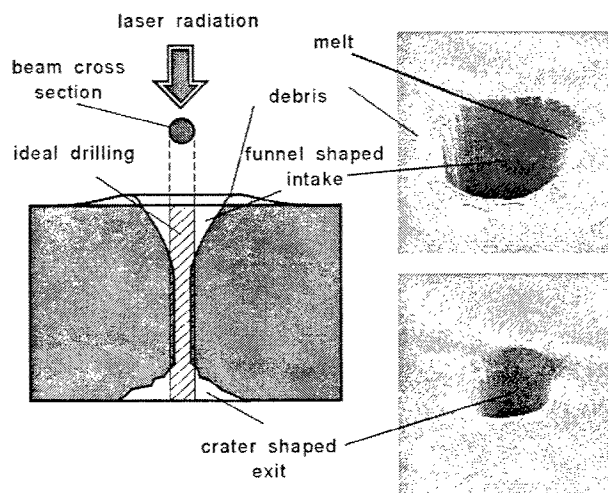| Material	Fused Silica, Suprasil 1, 200 µm thickness
Processing wavelength	$\lambda = 157$ nm
Mask geometry	Circular, 1,6 mm diameter
Energy density	H = 6 J/cm²
Image ratio	40 : 1
Number of pulses	n ~ 4000
Pulse repetition rate	$f_P = 200$ Hz
Hole diameter top	D = 60 µm
Hole diameter bottom	D = 25 µm

Figure 1: Drilling of 200 µm fused silica with 157 nm excimer laser by percussion drilling

Most of the above described aberrations from the ideal, cylindrical boring cause problems in lab-on-chip applications. The debris formation around the processing zone causes failures in following assembling processes, e.g. when a cover plate needs to be bonded on the machined plate. Additionally, the reproducibility of these borings in micro fluidic applications, where tolerances of 1..2 µm are often required, is limited. In this paper an approach is presented to reduce the above mentioned lacks regarding the drilling quality by applying rotating mask technology to the drilling of quartz glass.

2. EXPERIMENTAL SETUP

The principle set-up of the 157 nm machining tool used in the experiments here is given in figure 2. In order to prevent absorption by ambient oxygen due to the high photon energy, either vacuum environment or inert gas flushing, preferably nitrogen or helium is required. The set-up consists of two vacuum chambers: chamber I covers the beam shaping and beam preparation while chamber II includes the imaging optics, a high precision stage for the work piece positioning and cameras for alignment and monitoring. Two laser sources are available for the investigations, a Lambda Physik LPF 220 (30 mJ pulse energy, 200 Hz pulse repetition rate, 8 x 25 mm² beam profile, 25 ns pulse duration) and a TUI-Laser ExiStar S500 (1.5 mJ pulse energy, 500 Hz pulse repetition rate, 3 x 3 mm² beam profile, 10 ns pulse duration). With two elements, the optical set-up has been kept simple. A 1500 mm focal length field lens and an imaging lens with either 25, 40, 50 or 75 mm can be applied. Thus, an image ratio between 60:1 and 20:1 can be achieved and depending on the demagnification, energy densities up to 15 J/cm² can be achieved. The numerical aperture of this optical setup can be calculated to max. 0.5, depending on the imaging optics. The calculated optical resolution of this system is 500 nm; for material ablation on fused silica a lateral resolution of 1 µm has been achieved. The losses of laser power can be reduced to less than 5% for an ambient pressure below 5 Pa (5×10^{-2} mbar) or an oxygen concentration better than 10 ppm. With the installed oxygen sensor a concentration below 1 ppm can be detected, with Nitrogen purity 5.0 a minimum concentration of ~1 ppm has been measured in the chamber. A process gas nozzle is installed to apply a gas stream onto the processing zone. This allows e.g. to use helium as the process gas while the chambers are flushed with nitrogen.
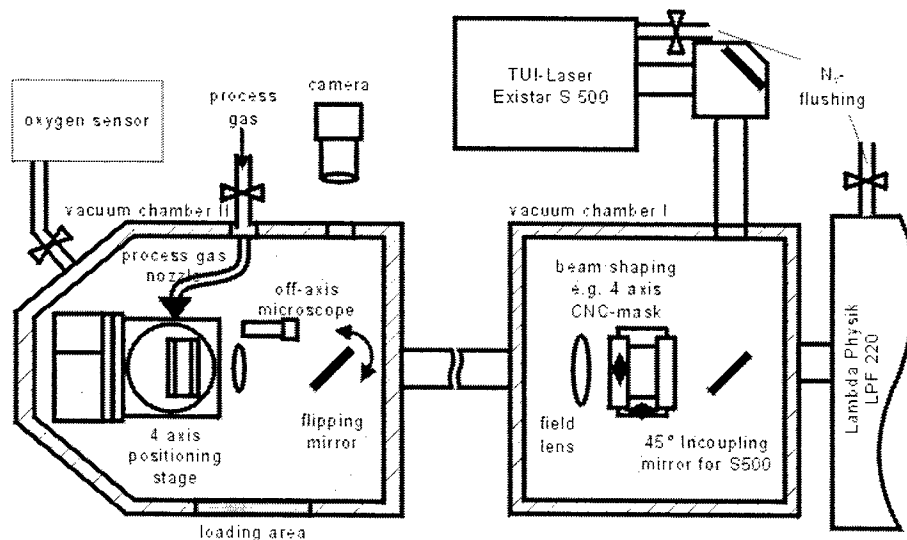

Figure 2: Principle set-up of 157 nm machining tool

The rotating mask technology as applied here is shown in figure 3. With the mask rotating the downscaled image of the mask also rotates on the work piece. While the laser emits at a constant repetition rate, the material is ablated in a cutting like process with many repetitions. According to [4], this drilling process can also be referred to as helical drilling.
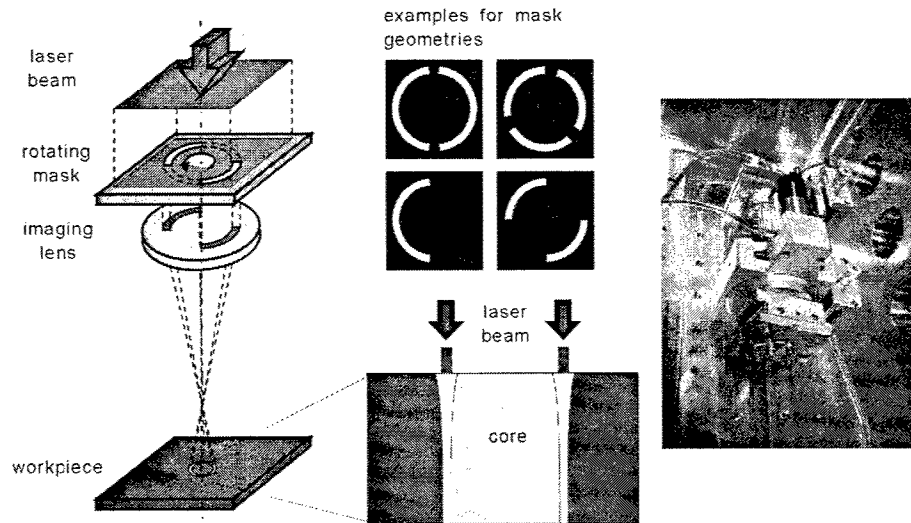
Figure 3: Excimer trepanning with rotating masks

3. EXCIMER LASER DRILLING WITH ROTATING MASKS

A sample result for the drilling of quartz glass with a rotating mask is given in figure 4 with the summarized processing parameters.

Material	Fused Silica, Suprasil 1, 200 μm thickness
Processing wavelength	$\lambda = 157$ nm
Mask geometry	2 * 90° segments, $D_{out} = 4$ mm, $D_{in} = 2,5$ mm
Energy density	$H = 6$ J/cm²
Image ratio	40 : 1
Number of pulses	$n \sim 2000$
Pulse repetition rate	$f_P = 200$ Hz
Hole diameter top	$D = 105$ μm
Hole diameter bottom	$D = 82$ μm
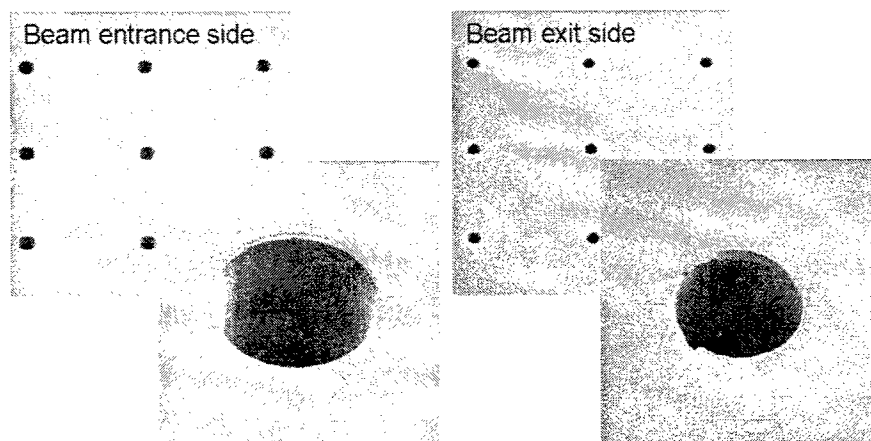
Figure 4 Fused silica, drilled with 157 nm excimer laser radiation rotating mask technique
Comparing the achieved micro-hole with the one given in figure 1, the following advantages can be seen:

- Well defined edges on both sides of the hole
- Minor formation of redeposites on the surface
- higher aspect ratio

For a better understanding and analysis of this result, the drilling process is split up into the primary mechanism of photothermal ablation and the secondary effect of abrasion by material evaporation.

The mask geometry gives an image of two circular segments on the work piece with an inner diameter of 75 µm and an outer diameter of 100 µm. The sample in figure 1 has been machined with a 1,6 mm mask and thus with a spot size of 40 µm on the work piece. The formation of the hole into the work piece is influenced by tunneling effects, which is shown in figure 5 for both techniques. Laser radiation that hits the side walls of the hole is only partly absorbed, there is also a portion being reflected and guided down into the work piece, figure 5. The wall angle and thus achievable aspect ratio, caused by these effects depends, besides wavelength and material, mainly on the energy density. In principle it can be stated that a higher energy density leads to steeper flanks.
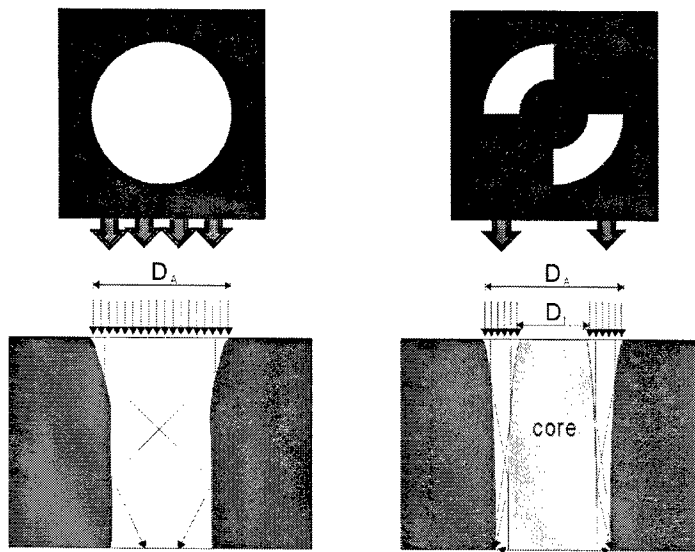

Figure 5 Bore formation for percussion drilling and trepanning due to tunneling effects and multiple reflection

Assuming that the laser spot directly only ablates material on a corresponding area on the work piece surface (in these examples $D_A = 40$ µm for percussion drilling and $D_A = 100$ µm for the trepanning, figure 5) and neglecting the abrasion, an ideal aspect ratio which only depends on the materials absorption characteristic and laser properties can be calculated. For the trepanning technique, the hole diameter is reduced by 18 µm, which is in the same magnitude of the aspect ratio achieved with percussion drilling (15 µm). With these numbers and a material thickness of 200 µm, the ideal flank angle can be calculated to 2.5° and 2,2°, respectively. Consequently, the flank angle or aspect ratio caused by the effects of photothermal ablation is only minor influenced by the applied drilling technique.

Due to the secondary effects of abrasion, the beam entrance side of the drill is given a funnel like shape. This abrasion widens the entrance diameter of the percussion drilling far more (+20 µm wider than the diameter of the laser spot diameter) than the trepanned one (+5 µm), mainly influenced by the intensity of the plasma plume. In figure 6, the time resolved formation of the plasma is shown for a percussion and a trepanning process. Due to limited access with the high speed camera to the processed material in the processing chamber, these experiments have been carried out for Al_2O_3 with 248 nm excimer laser radiation.

The interaction of pulsed UV laser radiation and dielectric materials like ceramics and glasses leading to a material ablation, can be split up into the steps absorption, bond breaking, heating, plasma and material plume formation. This

plume, the intensity of which depends on the applied energy density, drives the material out of the processing zone [6]. The concrete portion of the single steps to the entire ablation process depends on material properties and the laser fluence coupled into the work piece [7]. The formation of the plasma plume can also be classified into several groups depending on the applied fluence [7, 8]: Below a certain threshold there is no formation of a material plume. Besides a reflected and transmitted portion there is also absorption in the work piece, which heats up the material. Beyond a critical energy density on the work piece a material evaporation can be observed. The evaporated material and plasma expands and is being driven out of the processing zone. Typically, this formation of the plume starts 5 ns after the beginning of the laser pulse. With pulse lengths of excimer lasers between 10 and 30 ns, this means there is also an interaction between the plasma plume and the laser beam by absorption [9]. With the expansion of the plasma plume, there is a reduction of its density. The high speed of the plasma causes the ambient atmosphere to be compressed , which leads to a shock wave, the laser supported detonation (LSD).
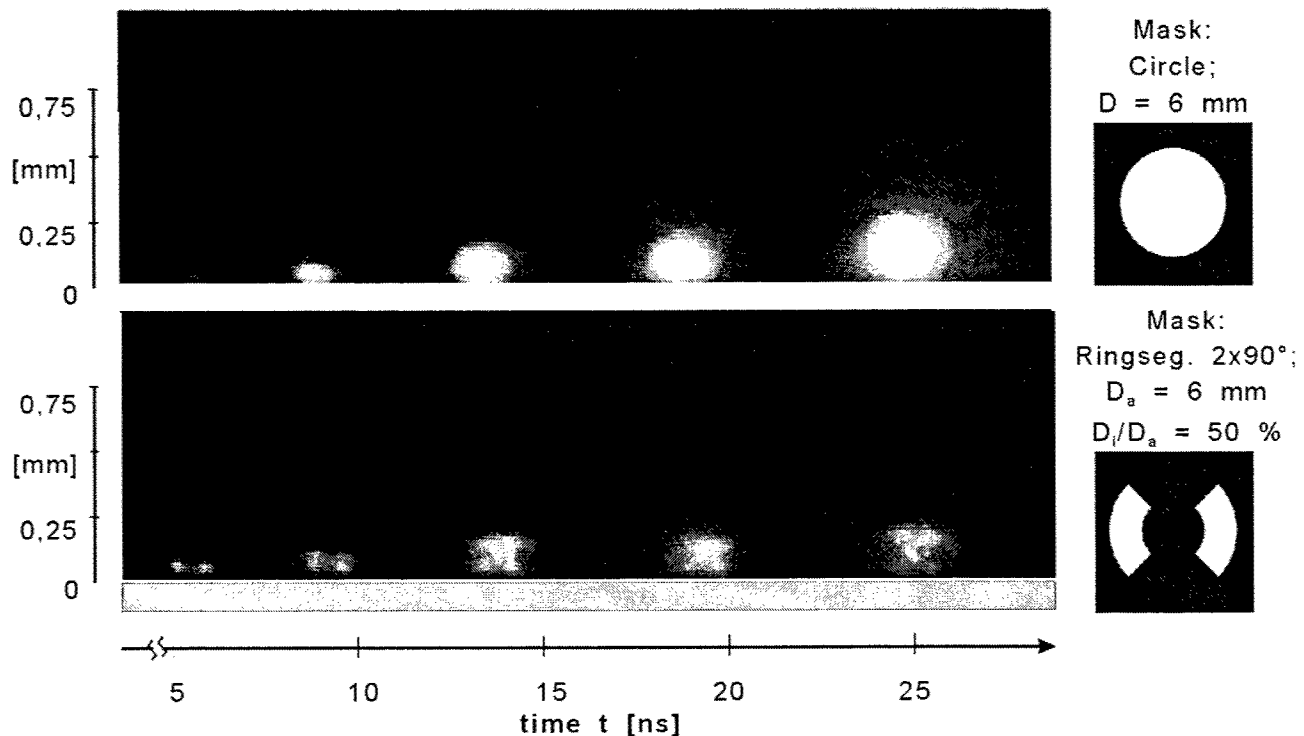

Figure 6: Formation of the plasma plume for percussion drilling and trepanning (KrF Excimer Laser / Al_2O_3)

Consequently, as seen in figure 6, there is a reduced intensity in the plasma plume when using the segmented ring mask and thus a reduced abrasion on the surface towards the laser beam [10]. With this background, figure 7 gives an overview on the achieved minimum flank angle depending on the mask diameter and the ratio D_i/D_a. The results have also been achieved with 248 nm excimer laser radiation and Al_2O_3.
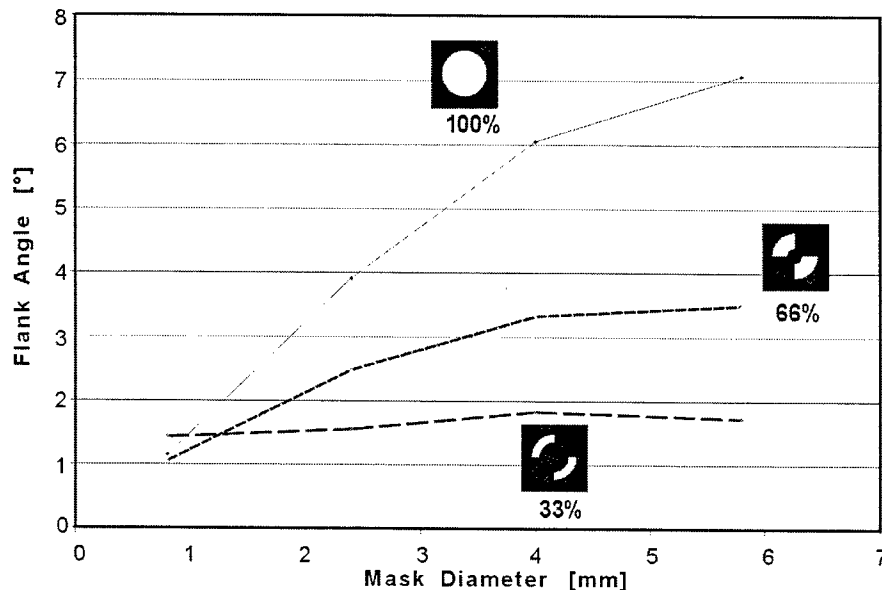
Figure 7: Flank angle depending on the mask geometry (KrF Excimer Laser / Al_2O_3)

Although the two segments of the mask cover only 50% of the outer circumference in the example of figure 6, this does not mean an increase of the required processing time [11]. The reduced plasma intensity also means a reduced interaction between the plasma and the incident laser beam. In [12] it has been demonstrated that the ablation rate drops with an increased ablation spot size caused by the higher plasma intensity. In the experiments here it has been observed that the processing time only slightly increases. A 100 μm hole in a 200 μm fused silica plate can be machined with both techniques in around 10 seconds.

4. CONCLUSION

It has been shown that the drilling of fused silica or quartz with 157 nm is a useful extension to the conventional technologies. For high quality drillings with high aspect ratio and minor debris on the surface, the rotating mask technique should be applied. Abrasion effects are reduced due to a less intense plasma formation. The drill time does not exceed drastically, although the effectively irradiated surface is reduced according to the used mask geometry. The achievable diameter of the holes depend on the raw beam of the excimer laser and the illumination optics. With the set-up used in this experiments, diameters up to 200 μm are possible in fused silica (8 mm mask, 40:1 image ratio). However, due to the high effort caused by the nature of the 157 nm radiation, this technique may be applicable for diameters below 100 μm, where competing technologies are less established.

5. ACKNOWLEDGEMENT

6. REFERENCES

1. A. Ostendorf, U. Stamm, T. Temme: Precision Machining of Innovative Materials Using 157 nm Excimer Laser Radiation; 2nd International Symposium on Laser Precision Microfabrication, Singapore; SPIE Vol. 4426, pp. 449-452 (2002).
2. H.K. Tönshoff, F. von Alvensleben, A. Ostendorf et al.: 3-D Microstructuring with F$_2$ Lasers; Micro-Opto-Mechanical Systems, Glasgow, SPIE Vol. 4075, pp. 159 – 166, (2000).
3. NN: Material Processing Using 157 nm Radiation; Lambda Highlights N° 55, Lambda Physik, (1999).
4. U. Sowada, P. Lokai, H.J. Kahlert, D. Basting, "Excimer Laser Processing of Ceramics -Results and Physical Processes", Laser und Optoelektronik 21(3)/1989.
5. H. Hügel, K. Schittenhelm, G. Jasper et al.: " Structuring with Excimer Lasers - Experimental and Theoretical Investigations on Quality and Efficiency"; Journal of Laser Applications; Vol. 10; S. 255; 6/1998.
6. H. Kappel: Oberflächenmodifikation technischer Keramik mit Excimer-Laserstrahlung. Dr.-Ing. Diss. University of Hannover, 1998.
7. J. Arnold : Abtragen metallischer und keramischer Werkstoffe mit Excimerlasern. Dr.-Ing. Diss. University of Stuttgart, 1994. Stuttgart: Teubner, 1994 – ISBN 3-519-06215-1.
8. R. Poprawe: Materialabtragung und Plasmawolkenformation im Strahlungsfeld von UV-Lasern. Dr.-Ing. Diss. University of Darmstadt, 1984.
9. M. Eyett, Bäuerle: Influence of the Beam Spot Size on Ablation Rates in Pulsed Laser Processing. Appl. Phys. Lett., 51 (1987) 24, S. 2054-2055.
10. H. K.Tönshoff, A. Ostendorf, K. Körber, K. Meyer: Comparison of machining strategies for ceramics using frequency converted Nd:YAG and excimer lasers. In: LPM2001, Proc. of 2nd Int. Symp. on Laser Precision Microfabrication; May 16th – 18th, Singapore, SPIE Vol. 4426. ISBN 0-8194-4137-6, pp. 408 – 411.
11. H. K.Tönshoff, A. Ostendorf, C. Kulik, K. Meyer: Improved Machining Strategy for the Micro Drilling of Ceramics using Excimer Lasers; LANE 2001, August 28. – 31. 2001, Erlangen, Germany.
12. M. Rinke: Glasbearbeitung mit ArF-Laserstrahlung. Dr.-Ing. Diss. University of Hannover, 2000.

High-speed singulation of electronic packages using a frequency doubled Nd:YAG laser in a water-jet and realization of a 200 W green laser

Frank R. Wagner[*a], Wentao Hu[**b], Akos Spiegel[***c], Nandor Vago[***c], Bernold Richerzhagen[*a]

[a]Synova Inc; [b]Quantronix Corp; [c]Dept. of Atomic Physics, Budapest Univ. of Techn. and Economics

ABSTRACT

Each electronic chip is packaged in order to connect the integrated circuit and the printed circuit board. In consequence high-speed singulation of packages is an important step in the manufacturing process of electronic devices. The widely used technique of abrasive sawing encounters problems due to the combination of different materials used in packages such as copper and mold compound. The sawing blade rapidly blunts because of the copper adhering to the saw blade and covering the diamonds. In fact, the abrasive saw, well adapted to silicon wafer sawing, has problems to adapt to package materials.

It has already been shown that the water jet guided laser can be used for efficient high quality singulation of leadframe based packages. In this technique a low-pressure water jet guides the laser beam like an optical fiber, providing efficient cooling of the cutting kerf at exactly the point that was heated during the laser pulse.

We present new cutting results using a frequency doubled Nd:YAG laser with 100 W average power, and the combination setup for generating a 200 W green laser beam. The timing between the two lasers can be precisely controlled.

Keywords: Laser cutting, electronic packages, copper, mold compound, 532nm, CSP, QFN, beam combination.

1. INTRODUCTION

Electronic packages are the interface between the printed circuit board and the silicon chip, containing the extremely miniaturized electrical elements. The chip is placed on a substrate that will be soldered to the final circuit board, the connection between the chip and the package substrate is realized by very thin gold wires or tiny solder balls (flip chip technology). The substrate itself is usually a copper lead frame or a thin glass fiber enhanced polymer circuit board with solder-balls. The whole assembly is protected, rigidified and isolated by mold compound. This material is normally a brittle, black polymer (epoxy, Bakelite) with different filler materials. These electronic packages are produced by numerous manufacturers and are referred to by different abbreviations. The most general designation is CSP (Chip Scale Package), which comprises the various types like such as BGA, QFN, and MLF[1]. Hereafter, they will be referred to simply as "electronic packages".

The biggest volume of mostly cheap components with relatively few in/out pins is packaged on copper leadframes. This type of package is often produced using a Matrix-Array Process, enhancing productivity roughly by a factor of 3[1]. If the packages are produced in this way, both materials, mold compound and copper, must be cut during the singulation process. Low-cost, high quality singulation of these packages is especially difficult because of the very different mechanical, thermal, optical and electrical properties of the materials involved. Nevertheless, the precise, burr free singulation of copper only, in the case of separately molded packages, is still a topic.

Today, mechanical sawing is primarily used to singulate these packages. The main problem with this method is the inherent softness of the copper, leading to important burr formation and rapid wear of the sawing blade due to smearing. The burr formation is a considerable disadvantage, because too big burrs limit the pitch of the packages, and, in the worst case, cause bad contact to the printed circuit board. Another approach for package singulation is conventional laser cutting, but it leads to poor cut quality, as the thermal and optical properties of the used materials are very different.

---

[*] wagner@synova.ch; phone +41 21 693 8371; fax +41 21 693 8370; http://www.synova.ch; Synova SA, PSE-A, CH-1015 Lausanne, Switzerland; [**] Whu@quantron.com; Quantronix Corporation, 41 Research Way, East Setauket, NY 11733, USA; [***] Spiegel@phy.bme.hu; Budapest University of Technology and Economics, Department of Atomic Physics, H-1111, Hungary

Therefore, we use since approximately one year an alternative method for package singulation[2]: the water-jet guided laser cutting[3]: With this unique laser cutting technique a free laminar water-jet is used as an optical wave guide in order to guide a high power laser onto the sample. The main advantages of this method compared to conventional laser cutting are: (i) parallel sidewalls (even in thick mold compound layers), (ii) low thermal load of the sample due to the cooling of the sample between the laser pulses exactly at the place where it was heated before, and (iii) an efficient expulsion of the melted copper due to the high momentum of the water-jet. Compared to sawing, burr free cuts of copper can be achieved and the mechanical force on the sample is much lower.

We report here on the advances we obtained during the last year where we mostly addressed the formerly still relatively low cutting speed by using a laser with higher average power and the development and realization of a combined laser source.

2. WATER-JET GUIDED LASER PROCESSING

The schematic of the used setup is shown in Figure 1. It differs from the setup used in reference[2] by the method to guide the light from the laser to the water-jet nozzle. In [2] we used simple direct focusing, here we opted for a fiber injection right after the laser and then we image the fiber exit onto the nozzle entry with a variable demagnification. This is more practical for placing laser and machine in the lab, and the intensity profile of the laser on the nozzle entry is more flat-top like resulting in a longer nozzle lifetime than observed with a Gaussian beam profile. The used lasers are multimode Q-switched lasers operating at 532 nm. We use pure de-ionized and filtered water at 50 to 500 bars for the water jet. The nozzles are made out of sapphire or diamond in order to generate a long stable water-jet. The laser beam is focused through a quartz window into the nozzle, very much like a usual fiber coupling and is thereafter reflected in the water-jet at the air-water interface due to the refractive index step (Figure 2).
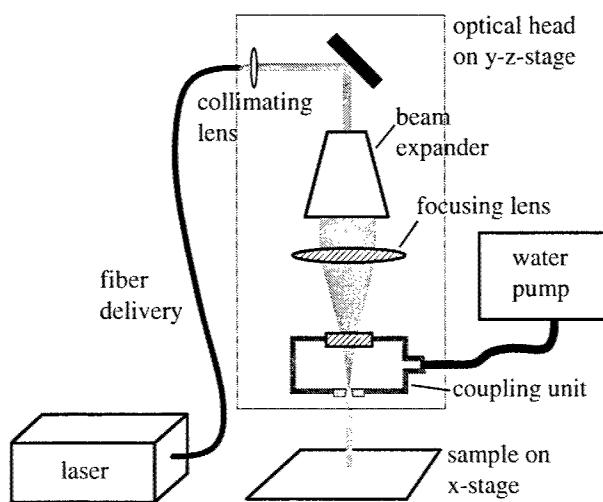

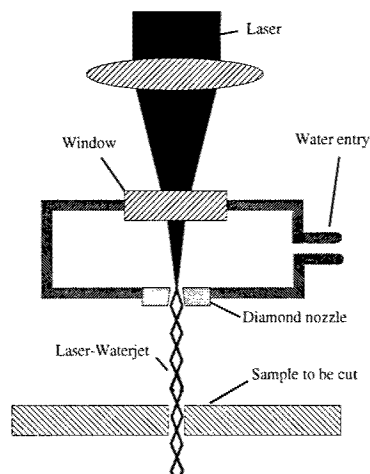Figure 1: Schematic of the water-jet guided laser setup

Figure 2: Detailed sketch of the coupling unit

The samples are clamped onto an x-stage, the optical setup is implemented in a "optics head" that is mounted on the y-stage. The z-variation of the stage is only necessary in order to adapt to the different working distances of differently sized nozzles at different water pressures[4] and is not used during the cutting procedure.

3. CUTTING RESULTS WITH THE 100 W LASER

The process of water-jet guided laser singulation of copper based electronic packages was already described elsewhere in detail[2]. Briefly, a two step process is applied: first the mold compound is cut with a 100 micron nozzle at low laser peak intensity, and in the second step the sample is flipped and the copper lead frame is cut with a 60 micron nozzle and higher laser peak intensity. At the time, we used a 70 W frequency-doubled diode pumped Nd:YVO$_4$ laser from Coherent Inc. (model Corona) and obtained approximately 20 mm/s cutting speed in the 0.9 mm thick mold compound, and 5 mm/s cutting speed in the 200 micron thick copper leadframe.

In a first step, in order to enhance the process speed, we used a laser with higher average power and choose the 100 W green laser from Quantronix (model: 532-CQE). This laser is a lamp pumped Nd:YAG laser with an intra-cavity frequency doubling and similar beam quality as the Corona, $M^2 = 35$. Average output powers and pulse peak powers of the 532-CQE are presented in Figure 3 at 10 kHz and 20 kHz pulse repetition rate.
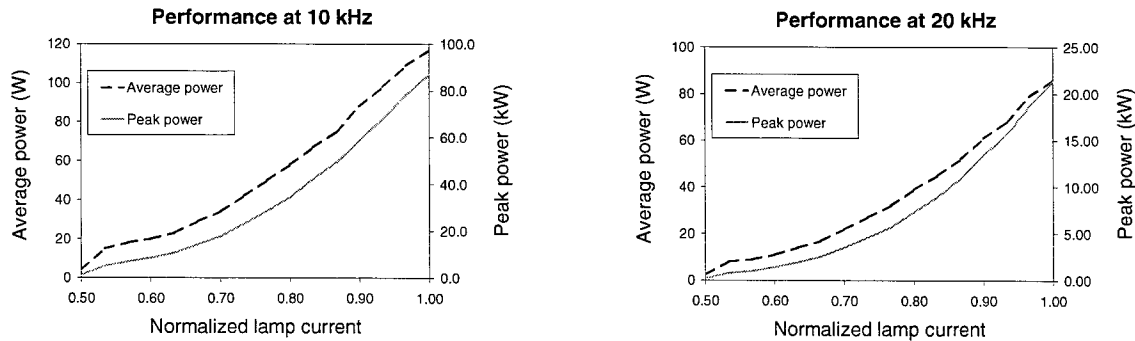

Figure 3: Laser performance at 10 kHz and 20 kHz pulse repetition rate (Quantronix, 532-CQE)

In spite of the lower pulse repetition rate and higher peak power, compared to the Nd:YVO$_4$ laser system, we could increase the cutting speed without decreasing the final edge quality. Cutting parameters and speeds for a package with a total thickness of 0.8 mm based on a 180 μm thick copper lead frame are presented in Table 1. Figure 4 shows microscope images of the obtained cutting quality.

Material	Cutting speed	I_{peak} (MW/cm^2)	v / (kHz)	τ (ns)	E_{pulse} (mJ)	P_{av} (W)	P_{wa} (bar)	D_{nozzle} (μm)
Mold compound 0.8 mm	80 mm/s, 2 passes = 40 mm/s	94	20	210	1.9	38	150	100
Copper 0.18 mm	50 mm/s, 6 passes = 8.3 mm/s	477	20	190	3.0	60.9	150	60

Table 1: Optimal processing parameters for copper and mold compound for a typical chip scale package. (I_{peak}: peak intensity, v: pulse repetition rate, τ: Full Width at Half Maximum (FWHM) pulse duration, E_{pulse}: energy per pulse, P_{av}: average laser power, P_{wa}: water pressure, D_{nozzle}: diameter of water-jet nozzle)
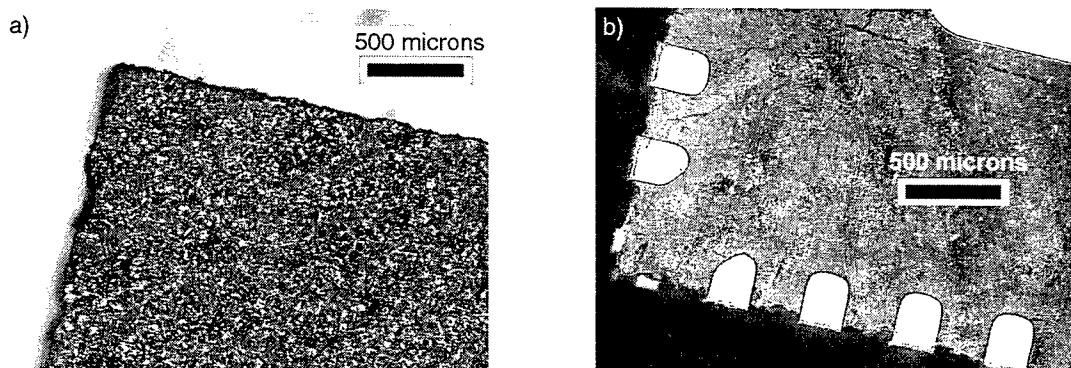

Figure 4: Optical microscope images of the edge quality obtained with the parameters given in Table 1. a) front side, b) backside. The higher peak intensities of the 100 W Nd:YAG laser, compared to the 70 W Nd:YVO$_4$ laser, did not alter the quality of the final cutting result. (c.f. reference[2])

The mold retraction, which has been discussed in [2], is shown to reduce if the cutting street of the package stripe does not contain copper at the surface (Figure 5). This is understandable reminding that the mold retraction has been shown to be caused by reflections of the light on the copper surfaces.
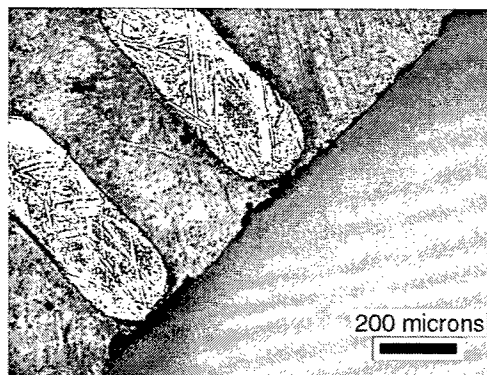

200 microns

Figure 5: Mold retraction is no longer observed if the street does not contain copper at its surface.

4. THE 200 W DOUBLE LASER

These good cutting results and the good experience with the higher pulse repetition rates of the YVO_4-laser encouraged us to realize a 200 W green laser source by combining two YAG-lasers with crossed polarizations. A sketch of the setup is shown in Figure 6 and a photograph of the combination optics is visible in Figure 7a.

Both lasers normally emit vertically linearly polarized light. We included a half wave plate in one of the systems in order to turn the polarization and combined both beams, after the same optical path length, with a thin film polarizer as polarization sensitive element. It is critical for the fiber-coupling that the beams are perfectly aligned to one another in near-field and far-field. The field lens, fl, together with the focusing objective generates the beam waist with the appropriate focus diameter and divergence for the fiber coupling.
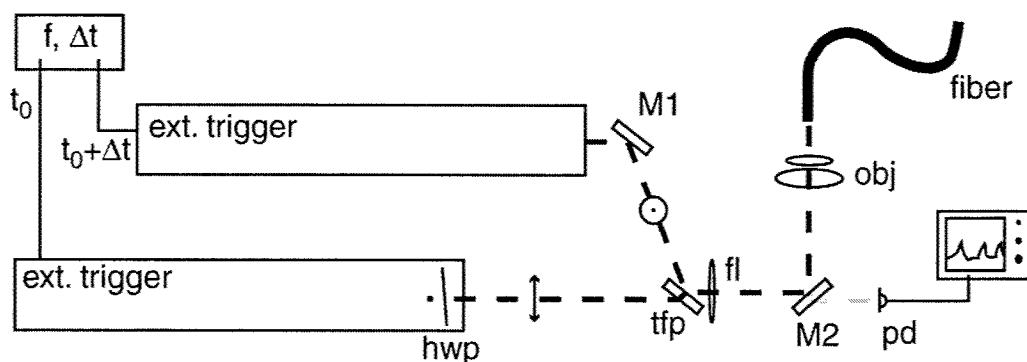

Figure 6: Schematic of the laser combination setup. Hwp: half wave plate, M1, M2: 90° edge mirrors, tfp: thin film polarizer. fl: field lens. obj: focusing objective for the fiber coupling.

Both lasers are triggered externally by a Stanford delay generator, allowing an adjustable delay time between both trigger signals. The effect of the chosen delay time is monitored using a fast photodiode and an oscilloscope.

Concerning the timing of the laser pulses and the power settings for each laser, we can distinguish 4 different cases which are interesting for laser material processing:

1. Same laser settings, equidistant spacing of the pulses: In this case we virtually double the pulse repetition rate of the system without changing peak power or pulse duration.
2. Same laser settings, simultaneous triggering: Here the peak power of the pulses is doubled, pulse repetition rate and pulse duration are not affected.
3. Same laser settings, pulses separated by one pulse length: The temporal pulse shape is influenced, the most important change will be the doubling of the pulse duration. Nevertheless peak power is also affected, because

of the typical slightly asymmetric temporal pulse shape of these lasers (Figure 7 b). The pulse repetition rate is not influenced.

4. Different laser settings, pulses separated by less than two pulse durations: This configuration allows to use a configuration where a pre-pulse prepares the material and the ablation pulse removes efficiently the material.

The setup was tested at 10 kHz pulse repetition rate and we obtained the expected 200 W average power of 532 nm output with 2% stability (Figure 7b).

Figure 7: a) Photo of the setup and b) photo of power meter and temporal pulse shape (right), both at maximum average output power.

We are still about to gain experience with the fiber coupling of this laser, but presumably it will be possible to use all settings up to maximum power for the fiber transmission, as long as the pulses are not superposed. An energy transmission of more than 85% has been obtained over the full range of presently tested settings.
Cutting results with the double laser will shortly be presented elsewhere.

5. FUTURE WORK

The first step to follow is the proof for the proportionality between pulse repetition rate and cutting speed in this particular application. As a matter of fact, the cutting speed can be limited either by the melt expulsion (performed by the water-jet) or by the laser pulse repetition rate. It is expected that increasing the laser repetition rate will increase significantly the cutting speed, but it is important to know to which extend the melt expulsion dynamic limits this increase. An hint that the melt expulsion is also an important point is the fact that the cutting speed in copper foils is slightly enhanced by the use of higher water jet pressure.

The next interesting topic will be the study of a pre-pulse influence on the mold retraction. The mold retraction was shown to be caused by light that is reflecting from the copper surfaces. Assuming that the copper reflectivity decreases with increasing temperature as it does at the fundamental Nd:YAG and CO_2-laser wavelength[5,6], it will be beneficial to use a pre-pulse of relatively low pulse energy. The pre-pulse will heat the copper surface and will thus increase the absorption of the following ablation pulse which removes the material efficiently.

6. CONCLUSIONS AND SUMMARY

Data on the cutting speed improvement due to the application of a lamp pumped 100W Nd:YAG based laser was given and compared to the data obtained with the diode pumped 70W Nd:YLF based laser. The cut quality improvement due to better package design was shortly mentioned. The combination of two high power lasers is presented and the potential of the system in micro machining is discussed. Finally, two precise projects for future work are presented. The realization of these studies will further enhance the package singulation capabilities of the water-jet guided laser technology.

7. ACKNOWLEDGEMENTS

8. REFERENCES

1. G. Kühnlein, "A Design and Manufacturing solution for high reliable non-leaded CSP's like QFN," Electronics Component and Technology Conference (ECTC), Orlando, Florida, 2001.
2. F.R. Wagner, A. Spiegel, N. Vago and B. Richerzhagen, "Water-jet guided laser: possibilities and potential for singulation of electronic packages," SPIE **4637** LASE 01, San Jose, CA, 2001.
3. B. Richerzhagen: Solid state technol., **44**, (2001), S25-S28.
4. A.M. Sterling and C.A. Sleicher: J. Fluid Mech., **68**, (1975), 477-495.
5. J. Xie, A. Kar, J.A. Rothenflue and W.P. Latham: J. of Laser App., **9**, (1997), 77-85.
6. B.S. Yilbas, K. Danisman and Z. Yilbas: Meas. Sci. Technol., **2**, (1991), 668-672.

Optical interconnections optimization based on a classical approach

V.P.Veiko[*1], N.B.Voznesensky[1], A.Petrov[1], V.F.Pashin[1], N.N.Voznesenskaya[1],
S.M.Metev[2], C.Wochnowski[2]

[1]St.Petersburg Federal Institute of Fine Mechanics and Optics (Technical University)
14 Sablinskaya str., St.Petersburg, 197101, Russia
[2]Bremen Institute of Applied Beam Technology, 2 Klagenfurter str., Bremen, D–28359, Germany

ABSTRACT

New branch in optoelectronics and photonics — integrated optical circuits as a part of hybrid optical devices and the problems of coupling efficiency in optical interconnections (OI) — is discussed. General approach to optical circuits analysis and adjustment based on classical optics is presented. The means to improve OI light efficiency in two regions — far–field (Fraunhofer diffraction zone) free space and near–field (Fresnel diffraction zone) vicinity of microoptical devices are proposed. New optical elements for OI — fiber–end mounted microlenses, their design, computer simulation and fabrication technique are considered.

Keywords: optical fibers, channel wave–guide, matching lens, Lagrange–Helmholtz invariance, laser technology.

1. INTRODUCTION

The latest progress in photonics shows that an important tendency in photonics devices is their miniaturization and integration. Miniaturization means diminution of size, weight and requested power of components. Integration — combining different functions on the same substrate. These two tendencies inevitably lead us to the concept of **photonics chips**. It is not a topic of this paper to go deeper in a discussion, which kind of a material will be better for first photonics chips — semiconductor $A_{III}B_V$, glass (quartz–glass) or optical polymers (PMMA or others).

The first photonics devices in our opinion are and will be a hybrid type in nearest future, because to combine all necessary functions in one material — it is a task not for 1–2 and even 5 years.

There are many examples of such kind of hybrid optical devices in optical information technique (especially in optical telecommunication), optical sensing, laser–based medical technique, near–field optics, material processing equipment, etc[1].

For any hybrid optical device the problem of **optical interconnections (OI)** — how to carry optical signal in some component and transfer it to other one is among the most important problems.

The usual way of realizing of OI (so–called physical contact) is bringing two optical components together as closely as possible and to fit them mechanically (or by gluing or welding)[2]. It needs rather complicated procedure and precise machines. This problem is especially complicated when it is necessary to connect geometrically very different components like semiconductor lasers, channel wave–guides etc with optical fibers.

So, evidently one needs a simpler and may be more efficient way to adjust different optical components.

Our idea for improvement of the coupling efficiency is based on a general approach for optical interconnection using specially designed optical elements as a part of an optical circuit to match the pair of optical components to be connected (Fig. 1). This approach could bring the higher optical efficiency and sometimes could drastically increase the field of available tolerances, which means more simple procedure and adjusting devices.
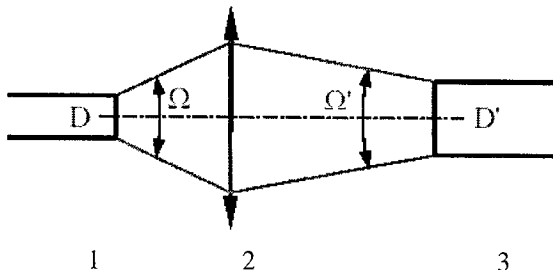

Fig. 1. Schematic of an optical matching component action: illustration of Lagrange–Helmholtz invariance. 1, 3 — functional components, 2 — matching component.

---

* Correspondence: e–mail: veiko@lastech.ifmo.ru; telephone/Fax: +7.812.2333406.

Such an OI could be a separate lens but from many other points of view the best way will be to form them on the ends of components, which should work together. One may hardly imagine lenses on the side of a channel wave–guide, as a part of integrated optical chip having many inputs and outputs.

But as for optical fiber–end lenses they could be easily performed by many techniques. Laser–based technique seems to be one of the best due to the good control ability and the many kinds of optical feed–backs which could be involved in the manufacturing process.

2. GENERAL APPROACH TO OI FUNCTIONS

We would like to show in this paper that physical contact is not always the best decision for OI and this problem needs more general approach.

Let us now involve in our consideration the following definitions:

1) **hybrid optical device** is an optical device consisting of different components as free optical components (lenses, prisms etc) working with optical beams in a free space, as guided components (optical fibers, channel wave–guides, integrated optical chips, etc) working with guided optical beams, including optical light sources (semiconductor lasers, etc) and detectors (photodiodes, CCD–cameras etc).

2) **optical circuit** is a part of hybrid optical device, including at least two functional components connected with optical fiber.

The criterion of optimization of OI is evident: energy losses minimization for non–imaging components, either minimization of information losses for imaging components.

In the most general case the optimized optical circuit should satisfy the energy conservation law and as one could say information conservation law. Both of them could be explained in a simple form of Lagrange–Helmholtz invariance J, applied to optical beams[3]

$$D\Omega = D'\Omega' = J = inv$$

where D is a beam diameter, Ω is a total divergence angle.

Values of J as well as D and Ω for some types of widely used components of hybrid optical circuits are given at the Table 1.

Table 1.

Type of component	Light beam diameter D, μm	Total divergence angle Ω, rad	Lagrange–Helmholtz invariance J, μm	Notes for $\lambda = 0.85$ μm
Single mode optical fiber	10	0.1	1	$J \sim \lambda$, equal to diffraction limit
Multimode optical fiber	200 400	0.2 0.2	40 80	$J \gg \lambda$, far from diffraction limit
Single mode channel wave–guide	$10/15$	$0.25/0.17$	$2.50/2.55$	$J \sim 2.5\lambda$, near to diffraction limit
Multimode channel wave–guide	$50/15$	$0.12/0.17$	$6.00/2.55$	$J > \lambda$, different for horizontal and vertical positions
Semiconductor lasers	$10/100$	$1.04/0.12$	$10.4/12$	$J \gg \lambda$, far from diffraction limit

As it is possible to see from the Table 1 for ideal Gaussian beam having only diffraction limited divergence — $J \sim \lambda$.

Thus a greater ratio J/λ means a greater difference for a beam from the diffraction–limited mode.

Note that Lagrange–Helmholtz invariance characterizes diffraction suitability (by pupils or numerical apertures) of components of an optical circuit.

From this point of view the physical contact as a way of matching optical components for guided light and integrated optics (planar wave–guide) is hardly to be optimized.

3. LENSLIKE MATCHING COMPONENTS FABRICATION

The general idea of fiber–end lens fabrication technique is a combination of a laser heating of a fiber–end with mechanical movements (e.g. pulling, rotation, stretching) and corresponding mechanical forces, mostly surface tension and centrifugal forces[4].

Using various treatment regimes for different fiber materials and sizes a number of tip microlenses with different optical and geometrical parameters has been made.

Photos of main fiber–end lenses types and their parameters are shown in Fig. 2.

Note, that two main types of lenses can be made: focusing and telescopic. Both types have a curvature center on the end plane of a fiber. The difference between them is in their tasks: the focusing lens is used for introducing the light into a fiber wave–guide and the telescopic (collimating) lens is used for collimating the light beam emerging from the fiber. Main parameters of lenses are pointed in Fig. 2. It is important to note that they could be controllably varied by combining different movements of the laser set–up.

$D = 125 - 600$ μm and more spherical focusing lenses, type 1

$D_L \sim (1-5)D$

$f \sim (0.5-1)D_L$

$d_0 \sim (1-2)D_c$

NA ~ 0.2–0.45
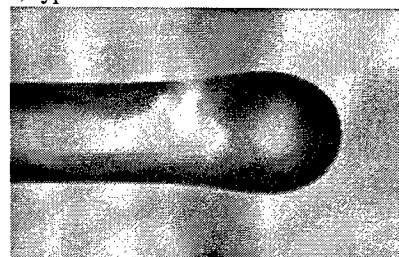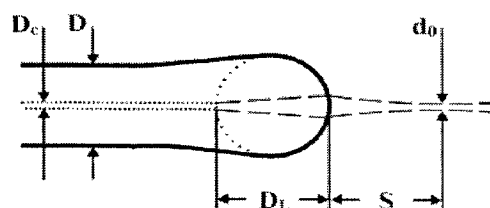
elliptical focusing lenses, type 2

$h_{L_S}/h_{L_B} \sim 1/2$

$h_{L_S} \sim (1.1-2)D$

$f \sim (0.1-1)h_{L_B}$

$d_0 \sim (0.5-2)D_c$

NA ~ 0.2–0.5
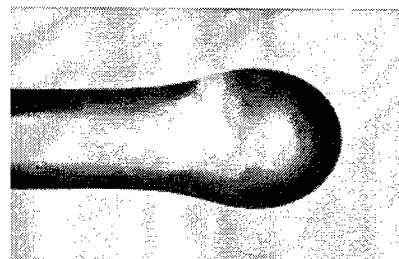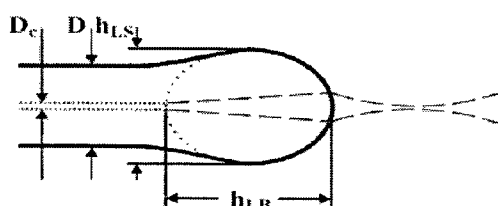
arc–like, telescopic lenses, type 3

$D_L \leq D$

$f = -h_L$
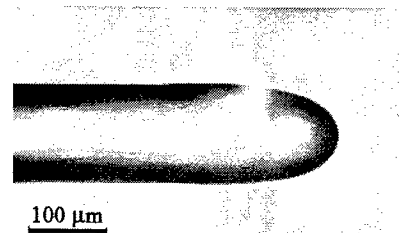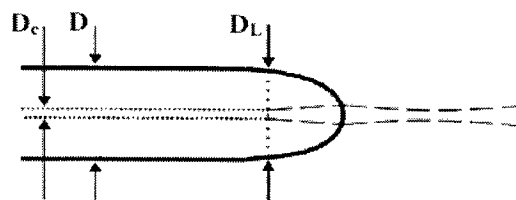
$d_0 \sim d_c$

NA ~ 0.55–0.65

100 μm

Fig. 2. Main types of fabricated fiber–end lenses (photos) and their parameters.

One very important feature of laser–based technique for lens fabrication is a possibility to use probe beam to check fiber–end lens parameters during processing.

According to the sense of matching optics for OI — lenses should be characterized by parameters responsible for delivery of energy. The most complete characteristic of this is NA — numerical aperture. In some cases the quality of lenses could be characterized by direct efficiency of energy transportation. Because of many specific features every task for different type of matching lenses fabrication needs the special testing procedure.
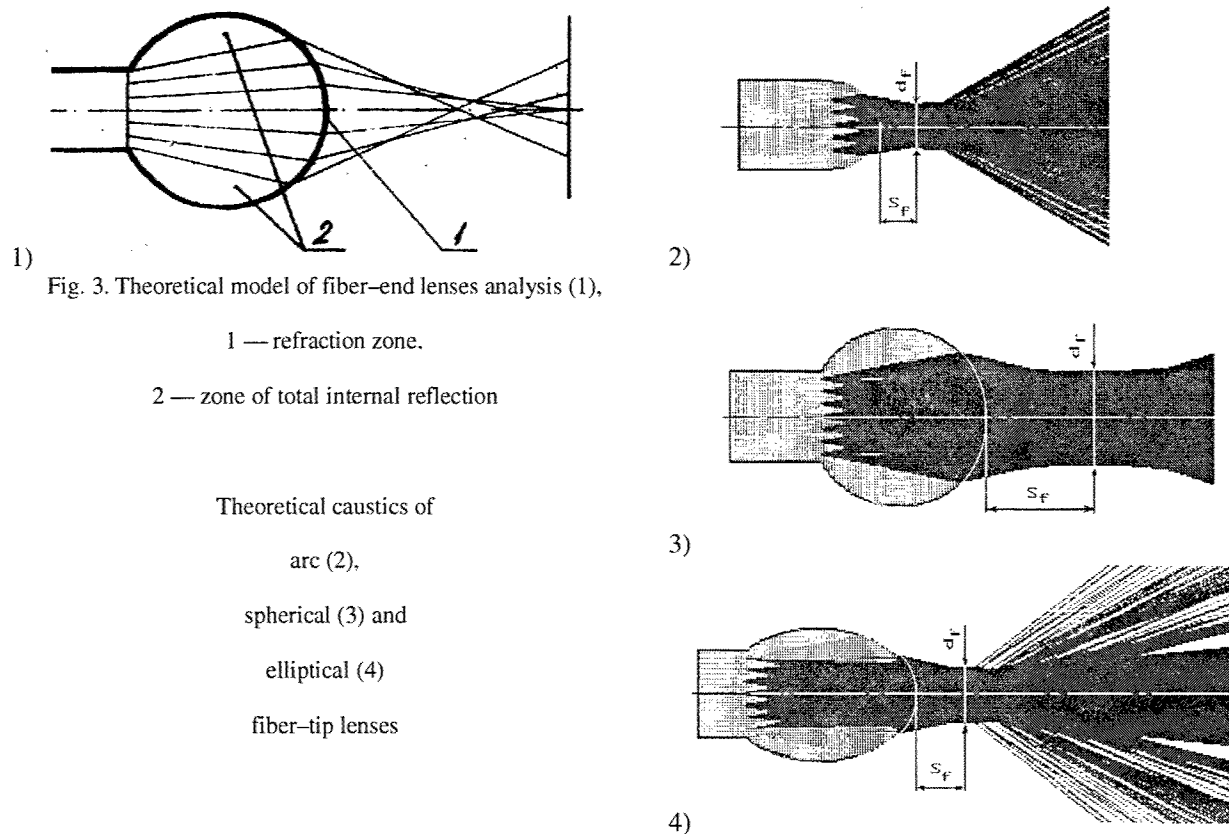
There were suggested and realized two diffrent approaches of matching lenses testing procedure[5]:

– **involving of NA measuring canal in a fabrication set–up** with precalculation of optical parameters of matching lenses (NA of microlenses),

– **measuring of coupling efficiency** during the microlense processing.

4. THEORETICAL BACKGROUND AND COMPUTER SIMULATION

The principles of OI action could be described in two ways — on the basis of ray tracing or wave–guide theory. Unfortunately both of these approaches are not sufficient for entire explanation of OI action: the ray tracing technique is valid only in far–field region which is corresponding to the condition that the wavelength is diminishing to zero and otherwise the wave–guide theory[6, 7] is well–constructed only for regular wave guides and does not offer solutions for connections of different elements with various shapes.

Ray tracing technique is based on common equations for rays refractions and reflections being used in various software systems for lens design (e.g. ZEMAX, SOLTSIS, Light Tools, etc.)[8]. In Fig. 3 there is given a ray tracing picture made based on IFMO software "Opal" which shows the spherically aberrated light beam emerging from a fiber–end microlenses and the Gaussian–like shape of the beam.

1)

Fig. 3. Theoretical model of fiber–end lenses analysis (1),

1 — refraction zone,

2 — zone of total internal reflection

Theoretical caustics of

arc (2),

spherical (3) and

elliptical (4)

fiber–tip lenses

2)

3)

4)

However this approach can be hardly applied to narrow laser beams propagation because of considerable interference effects described only in frames of the Hermit–Gaussian concept[6]. The main difference between ray tracing and Hermit–Gaussian solutions lies in the fact that in those parts of beams where rays pass very densely there occur specific light distributions being absolutely different from ray tracing predictions. These regions of beams are very important for OI analysis. Note that as it comes from the paraxial optics the Lagrange–Helmholtz invariance is an exact value only in frames of the ray tracing technique.

In order to suit reality better it is reasonable to use wave theory of light and try to extend the frames of the wave–guide upon the most actual OI cases. As it follows from the fundamentals of light diffraction[3] the Lagrange–Helmholtz invariance is an asymptotic far–field approximation of the transverse dimensions of a diffracted beam satisfying Fraunhofer conditions. Otherwise **the formalism of Gaussian beams treats either far– or near–field region, which is necessary for OI analysis. Unfortunately there are no analytical solutions for a general shape of a wave–guide**

end and moreover for various optical links. Therefore in this paper a plain domain technique[9] is used for numerical assessment of the light propagation through complicated shapes of micro sized optical elements.

The principle of the plain domain method is discretion of a structure in longitudinal (axial) direction by thin layers within which the light wave is treated on the basis of Fresnel diffraction approach. Besides each layer is regarded as consisting of homogeneous media. In this case the Fourier transform technique can be applied to calculation of plane waves expansion of complex field amplitude within each homogeneous domain. The plane waves are the set of Helmholtz equation solutions in general case and they give an easy opportunity for calculation of their propagation through a medium.

In Fig. 4 one can see an example of calculation of an intensity structure of a beam emerging from the channel wave-guide 50x25 μm and incoming into the focusing lens with diameter 124 μm, focal length 88 mcm mounted on the opposite fiber. The fiber with the lens is displaced by 24 μm from the axial position. The "capture" effect of light energy is shown. The results of calculations are presented in logarithmic scale in order to reveal the subtle details of the interference pattern.
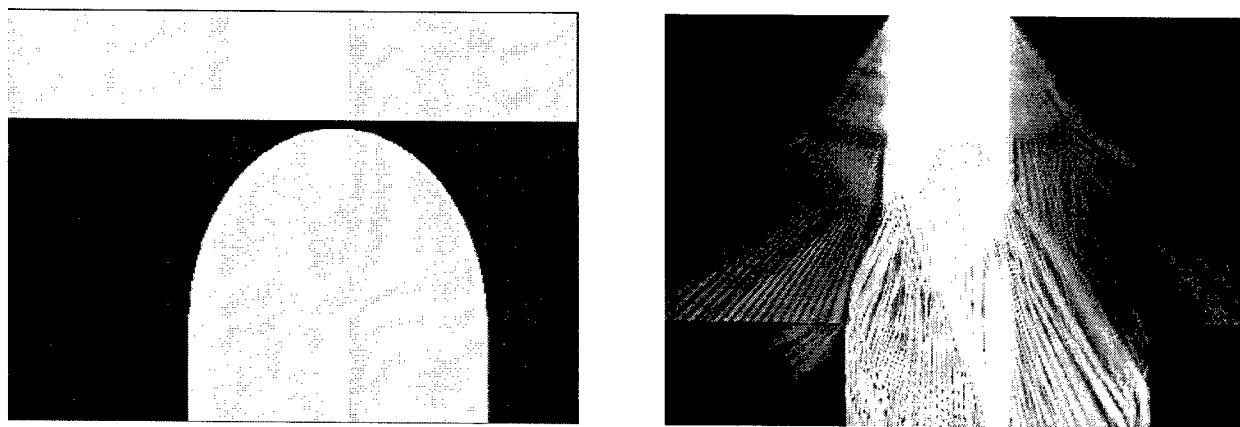
Fig. 4. The light emerges from the channel wave-guide 50x15 μm ($\lambda = 1$ μm) down to the focusing lens with diameter 124 μm and focal length 88 μm mounted on the opposite fiber end and displaced by 24 μm from the axial position. The light energy "capture" effect is well seen.

Some important OI examples have been taken to demonstrate the efficiency of the suggested approach.

5. APPLICATION EXAMPLES

Some important OI examples have been chosen to demonstrate efficiency of suggested approach.

5.1. Monomode fibers experiment

Generally connection of two single-mode optical fiber is a classical example where physical contact works well in a total accordance with the Lagrange–Helmholtz criterion. But **small transverse displacement ±6 μm can drastically decrease the efficiency of such a contact. At the same time a proper lens–equiped fibers can provide much wide range of tolerances** (Fig. 5).

The other large area for matching lens technique includes the free–beam devices (FBD): splitters, attenuators, demultiplexors, etc, which work with light beams in the free space. FBD are very popular structures but rather complicated and expensive.

For these devices telescopic fiber–end–lenses has been specially designed to collimate beams from single–mode fiber under condition $f = -h_L$.

Such kind of lenses has been fabricated and after that tested by CCD–camera. One can see in Fig. 6 cross–sections of a laser beam emerging from the lens at various distances, which is promising to suit standard realizations of FBD.
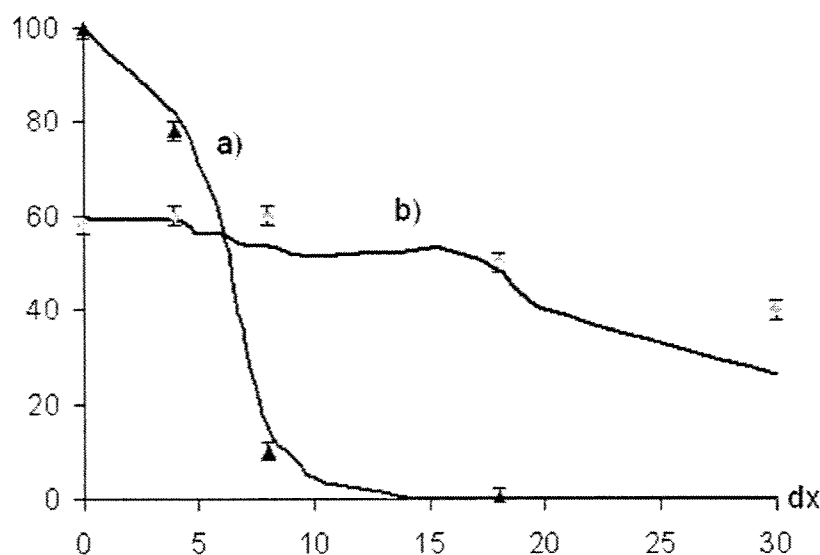
Fig. 5. Computer simulated (curves) and experimental (dots) efficiency of the optical contact of two monomode fibers: a) without collimating and focusing lens, b) with collimating and focusing lens. Note: the plain domain method shows the lower boundary of efficiency values which in reality may be higher.
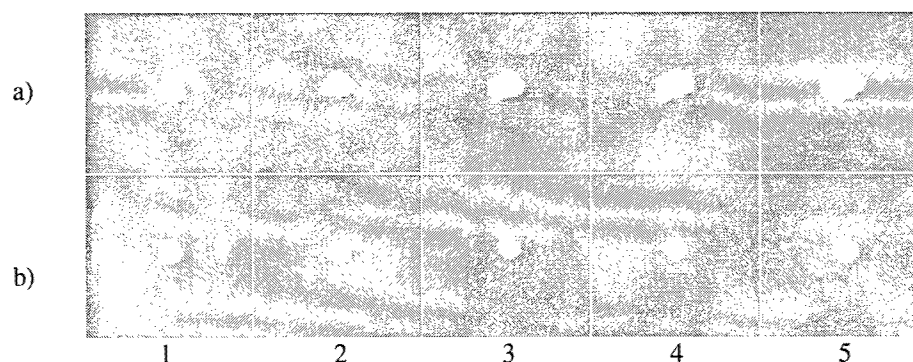

Fig. 6. Cross–sections of a light beam (pictures done by digital recording of the CCD–camera) after the standard single–mode optical fiber without a) and with end telescopic lens b) at various distances in micrometric scale: $1 - 0$; $2 - 40$; $3 - 80$; $4 - 120$; $5 - 160\mu m$.

5.2. Multimode fibers experiment

Standard for medical laser–optical equipment is the situation where an optical fiber of diameter 400 μm going from a laser source is connected with a distal end of diameter 200 μm handled by an operator (surgeon).

One can see that a **matching lens in this case can provide much higher efficiency of a contact (up to 65%) comparatively with a physical contact (theoretical maximum 25%), and much broader field of tolerances. And it is not surprising because** $J_1 > J_2$ **and efficient coupling is impossible without matching lens.**

Results of efficiency research were used for implementation in special units design.

Radiation of laser sources 3W Nd–YAG and 1mW He–Ne was delivered by a transporting flat-end fiber of diameter $D_1 = 400$ μm to a connector (Fig. 7). In the unit the transporting fiber was coupled with an applicator — optical fiber with diameter $D_2 = 200$ μm with a spherical–end lens.

Fig. 7. Optical scheme for calculation (a) and construction of some adjustment experimental modules (b).

Tip microlenses with various diameters D_L and shapes have been tested in order to find the maximum output efficiency and sensitivity to the displacements. Experimental results have verified calculation curves obtained by ray–tracing technique (Fig. 8). A spherical lens gives more than 5 times increasing effectiveness of coupling (63% with a matching lens against 12% for flat–ends physical contact coupling). End–lenses are also very useful for simplicity of adjustment.
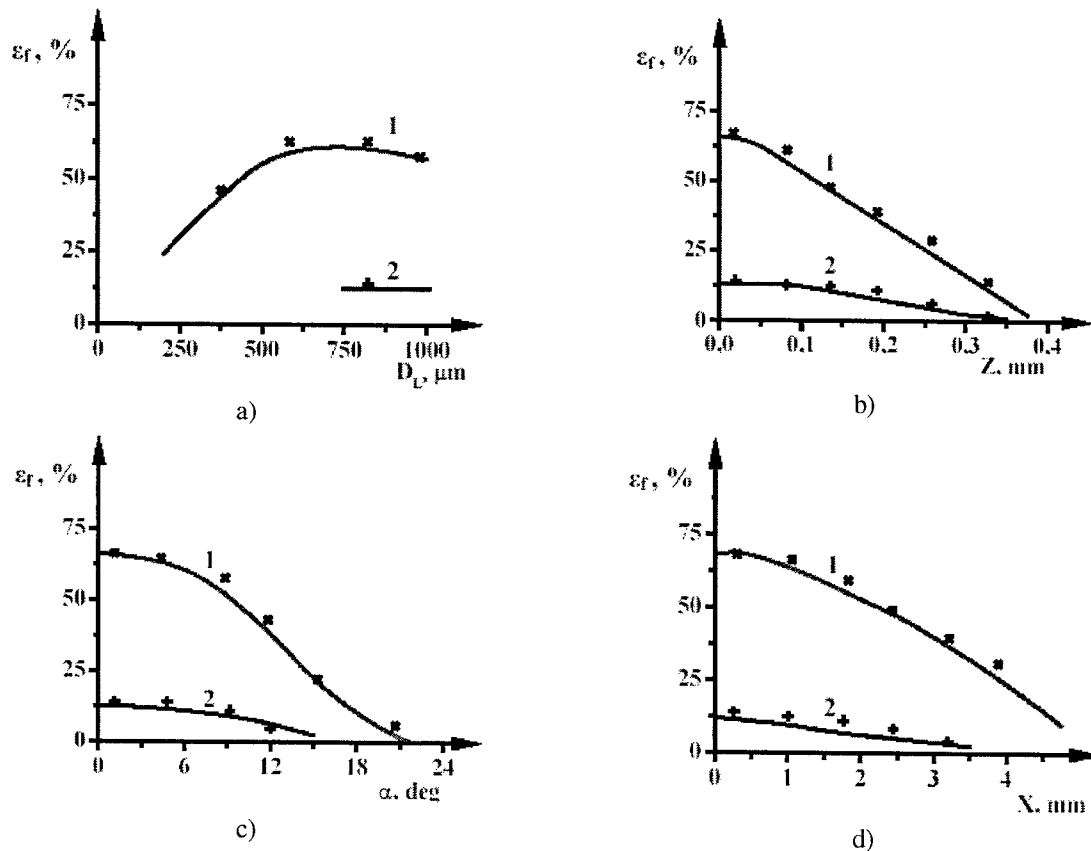
Fig. 8. Calculation curves and experimental points of effectiveness of 400 μm flat fiber–end and 200 μm lens–equiped fiber–end versus: a) lens diameter, b) transverse displacement, c) axial displacement, d) angle displacement.
1 — coupling with an optimal spherical lens with radius 360 μm, 2 — coupling with a flat end.

5.3. Channel wave–guide–optical fiber connection

This is especially hard task for effective optical contact. **The difference in the shape, size and modes structure of cylindrical and planar or channel wave–guides need a special solution for the optical connection in this case. The result highly depends on the size of wave–guide and direction of light propagation. The hardest case is when light goes from multimode channel wave–guide as a part of an integrated optical structure inside a polymer chip into a standard single–mode quartz–glass optical fiber. In this case** $D_1 > D_2$, $\Omega_2 > \Omega_1$ **and** $n_1 > n_2$ **(1 — polymer**

(PMMA) channel wave–guide, 2 — quartz–glass optical fiber). Calculation and experiments have been carried out for multimode wave–guide in PMMA with a transverse size 50 μm and effective deepness of 15 μm with a normalized refraction index after laser–assisted direct writing of the wave–guide $n = 1.5$ [10] (see Fig. 9B).
Experimental testing of the optical connection realized by physical contact of a plane fiber–end and by a matching spherical fiber–end lens are given in Fig. 9A.
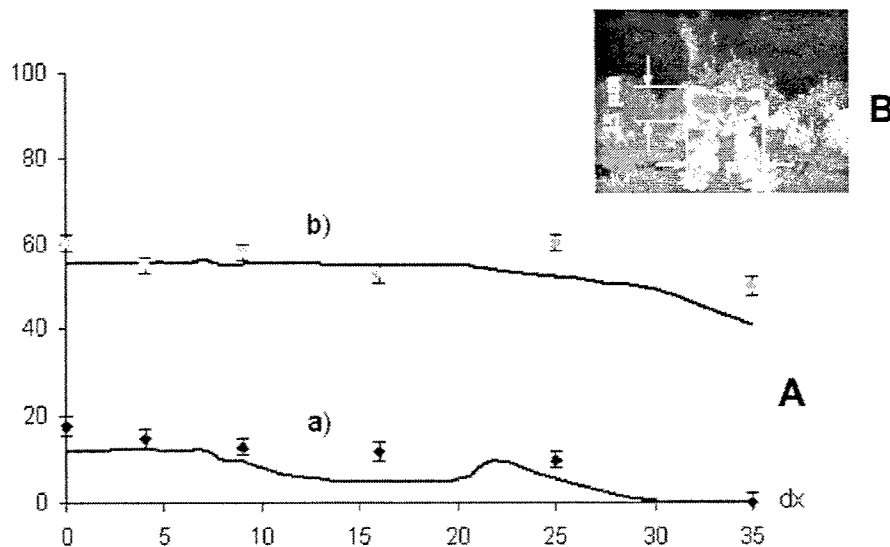

Fig. 9. A – Computer simulated (curves) and experimental (dots) efficiency of the optical contact of channel wave–guide 50x15 μm (exit) with a single–mode optical fiber versus cross displacement: a) plane end, b) lens–equipped end, lens diameter 124 μm. Note: the plain domain method shows the lower boundary of efficiency values which in reality may be higher.
B – mode propagation of a red light in a multimode wave–guide; cross–section picture done by digital recording of the CCD–camera.

One can see the great advantage of a matching lens in the efficiency and in the wider tolerance of the connection as well.

5.4. Semiconductor laser–monomode optical fiber connection
Semiconductor laser–monomode optical fiber connection is another hardest point in the entire OI field due to the great difference in J . Traditional way to solve this problem is the use of two cylindrical lenses in a different position according to astigmatism of the source. But effective adjusting matrices and even bars of them need a new approach. One of them could be adaptation of each lens from the lens raster by tiny laser ablation under an optical feed–back.

6. CONCLUSION
The above given considerations permit us to formulate **the laws of (passive) optical circuits for optical interconnections:**
1. **Lagrange–Helmholtz (J) invariances of the components with a highest J restrict energetic and informatics bandwidths of the transfer function of optical circuits.**
2. **Transfer of energy (and information) without losses can be realized only in a direction from the component with a smaller J to a components with a greater J , while in case of transfer signal in opposite direction energy and information losses are inevitable.**
Thus matching lenslike optical elements are necessary in general when components with different J values are working in one optical circuit (device), like semiconductor lasers, integrated optical chips (channel and planar wave–guides), multimode and monomode optical fibers.

7. REFERENCES

1. V.P.Veiko, N.B.Voznesensky, "Laser–light delivery microtools based on laser technology: design, fabrication, and applications", *Proceedings of SPIE*, **4274**, p.346–359, 2001.
2. S.Todoroki. A.Nukui, S.Inoue, "Formation of optical coupling structure between two ends of silica glass optical fibers by inserting tellurite glass melt", *J. Ceram. Soc. Jpn.*, **110**, no. 5, p.476–478, 2002.
3. J.W.Goodman, *Introduction to Fourier Optics*, McGraw–Hill, p.441, 1996.
4. V.P.Veiko, S.V.Kukhtin, M.P.Tokarev, V.A.Chuiko, "Microoptical fiber–tip components based on laser technology and its applications for medicine", *Proceedings SPIE*, **3573**, p.604–608, 1998.
5. V.P.Veiko, M.P.Tokarev, V.A.Chuiko, S.V.Kukhtin, "Control–in–time laser technique of optimal fiber–end microlenses fabrication", *Proceedings SPIE*, **2538**, p.219–229, 1995.
6. H.Kogelnik, "On the propagation of Gaussian beams of light through lenslike media including those with a loss and gain variation", *Appl. Opt.*, **4**, pp. 1562, 1965.
7. J.A.Arnaud, "Hamiltonian theory of beam mode propagation", *In Progress in Optics*, ed. E.Wolf, North Holland, Amsterdam, 1973.
8. *In SPIE's OE Magazine*, Sept., 2002.
9. N.B.Voznesensky, "Simulation model for light propagation through nanometer–sized structures", *Optical Memory and Neural Networks*, **9**, No.3, pp.175–183, 2000.
10. C.Wochnowski, S.M.Metev, G.Sepold, "UV–laser modification of the optical properties of polymethylmethacrylate", *Applied Surface Science 154–155*, p.706–711, 2000.

Laser Metallization for Microelectronics and Bio-applications

L. D. Laude, K. Kolev, Cl. Dicara and C. Dupas-Bruzek
Université de Mons-hainaut, Mons, Belgium

ABSTRACT

Excimer lasers were demonstrated to be effective tools in i) engraving ceramics and polymers, ii) changing irreversibly the surface chemistry of the irradiated material, and iii) restricting these effects to specific areas of interest. In so doing, excimer laser irradiation does open new routes to functionnalizing the surface of such diverse and difficult materials, allowing them to be utilized in given applications. In this paper, it is demonstrated how the above three potentialities of excimer laser surface irradiation may be put into practice in producing application-specific metallic tracks onto either sintered ceramics or polymeric materials. To this end, the accent is deliberately put here on the photochemical aspect of this irradiation process. The latter is responsible for modifying the surface stoichiometry and/or structure of irradiated ceramics and silicone rubbers and also, of some of the solid additives which combine to polymers to form so-called thermoplastics. An important consequence of this changing surface chemistry resides in the possibility for decorating the processed surfaces with metal via an electro less technique, thus establishing the ground for a novel metallization process that is presented and examplified.

Keywords: Excimer laser, sintered ceramics, polymeric composites, metallization.

1. INTRODUCTION

Changing state of matter is an ever-attracting challenge and light sources may provide the energy required for that challenge. Among light sources, excimer lasers have specific advantages that relate to i) their actual photon energy in the UV range, ii) the large number of these UV photons, and iii) the pulsed emission of these sources which deliver photons over a restricted period of time, typically 40 ns. These characteristics allow excimer laser sources to play a unique role in acting on dielectrics that may not be accessible to visible light photons. Since such materials are known to be particularly stable to adverse conditions, modifications that may be produced onto such inert materials being submitted to excimer laser irradiation are particularly important and worth investigating. They extend from irreversible structural effects, surface photochemical alteration to removal of matter (or ablation). Whatever these modifications, they may additionally be restricted to specific areas of interest, opening routes to application-specific processing.

In the packaging industry, products like hybrid circuits on sintered alumina plates or printed circuit boards (PCB's), enjoy world standards for more than twenty years. However, being so well established, their concepts have not much evolved since then though severe restrictions (e.g. environmental) have been introduced recently in their fabrication. New ways were explored and came to light in particular as molded interconnect devices (MID's) on polymeric substrates and with the so-called "direct copper bonded" technique (DCB) on ceramics. Given the limitations and specific difficulties of these techniques, the prospect of adhering metal onto a dielectric surface is still an opened challenge that calls for new proposals. Other challenges would be to produce such strongly adherent metal deposits i) onto high-definition restricted areas or tracks, and ii) via a *positive* technique, i.e. directly depositing the metal where and in quantity needed *without* "tailoring" such deposits by removal of metal. This presentation addresses these particular challenges in describing one single technique that exploits the full potential of excimer laser processing and allows developing application-specific metallic circuits onto either sintered ceramics or polymeric substrates.

2. THE MATERIALS

Materials concerned in this presentation are sintered ceramics and polymeric (plastic) composites at large. Though diverse as they are, they all have in common one very particular characteristic: they are *heterogeneous* in structure and composition. Basically, they consist of two types of ingredient: i) solid inorganic (oxide, in general) particles or *grains* that are maintained together within ii) a *matrix* (Fig.1).
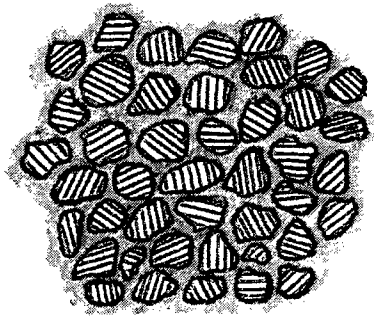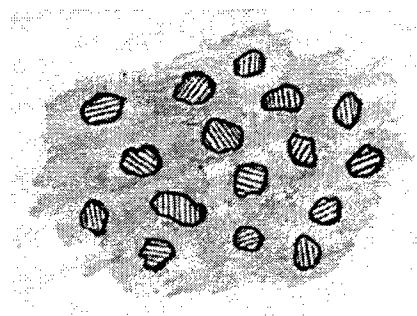
Figure 1: Heterogeneous structures (schematic) : a) sintered ceramic, b) polymeric composite.

In a sintered ceramic, the matrix is an inorganic cement that contains specific sintering agents. In a plastic composite, the matrix is an organic polymer and grains consist of oxides or poly-oxides. Though that heterogeneity may be varied widely until reaching qualification for a specific application, it is important to recognize that, in all instances, the physico-chemical properties of such heterogeneous materials are not monotonous at all, grains and matrix having (sometime drastically) different properties, in particular optical ones in the UV range. Whilst these material properties depend primarily on the intrinsic properties of the individual constituents, grains and matrix, a simple criterion in identifying the effective properties of such heterogeneous materials is the proportion of grains vs. matrix. That (massic) proportion exceeds 90% in ceramics and the characteristics of the grains (formulation, size distribution) dominate the ceramic properties. In polymeric composite materials, that (massic) proportion may vary in the range 3 to 60% and in such materials, those of one constituent no longer dominate properties; they may be additionally affected by the grain distribution within the material vs. its surface.

Another common characteristic to these materials is their particular inertness to the ambient. As dielectrics, they usually do not couple to light in the visible range and are electrical insulators. This latter property makes them excellent candidates for supporting electronic circuits. However, consisting of strongly (ionically or covalently) bonded atoms, their ability to interface with metal atoms is severely restricted. On a sintered alumina plate, formation of adherent metallic interconnects may be achieved via a combination of chemical processing and heat treatment (the DCB technique), however with much limited resolution and applicability (200μm thick tracks on strictly planar substrates only). On a plastic composite, metal deposits can be performed by either chemical means or evaporation, however with much too low adhesion and thickness for implementing possible interconnect applications.

3. THE METALLIZATION TECHNIQUE

Standard excimer sources deliver UV light pulses in the range 0.3 to 0.8 J, i.e. and most typically some 10^{18} photons of 5.0 eV energy (at 248 nm wavelength) over a period of 40ns at variable intervals (e.g. 0.1 s at 10 Hz repetition rate). Instant power is therefore extremely large (a few x10MW), a figure that may eventually be sufficient, in low thermal diffusivity dielectrics, for reducing thermal losses during pulse irradiation. As a consequence, and as long as optical absorption of the laser source photons is effective in terms of optically exciting valence electrons in the target material, either in *one or both* of its constituents, a light penetration depth may be defined over which energy transfer to the material is operative thus inducing, in the penetrated volume of matter, *irreversible* modifications of the atomic networks. As expected, the nature of these laser-induced modifications depends on the formulation of the material itself and on the amount of absorbed energy. They may concern one or both constituents. They may also either be structural, via a melt/quench procedure, or chemical, via surface decomposition and *non-congruent* emission of matter. As will be shown lately in this presentation, these modifications may affect directly the actual surface electronic structure of such materials and bring them to be electrically active. It is this electrical activation that is readily exploited in the metallization technique (1, 2) to be described in the following and examplified in the next sections.

In a first stage of the technique, the dielectric surface is irradiated with an excimer laser source. In this irradiation procedure, laser processing parameters (laser fluence, pulse repetition rate, beam scanning velocity onto the target surface) are varied and adjusted as to provide a relevant effective surface modification of the type mentioned above. These processing parameters being optimized for that particular modification, the latter is produced over the desired area of the material either by directly scanning the laser beam or by projecting it through a mask onto the material surface. In a second stage of the technique, the processed material is immerged in a standard (electroless) autocatalytic bath containing metal ions (e.g. Ni^{2+}, Cu^{2+} or Pt^{2+}). Such ions come then to sediment and neutralize onto the irradiated (and transformed) areas of the material, thus materializing the (restricted-area) metallization of the processed material, only on such areas that have been irradiated in the first stage. The time of immersion determines the actual metal thickness of the deposits. The material may be subsequently subjected to a thermal treatment in order to either, i) enhance metal adhesion by diffusion in the irradiated substrate, or ii) remove eventual volatile species that may be trapped in the metallized parts during immersion in the bath.

The nature of the metal adhesion to the irradiated surface is manyfold : i) *chemical* by forming ionic or covalent metal bonding to the surface atoms, ii) *mechanical* via the anchoring provided by the back face of the grains into the (unprocessed) volume material, and iii) *structural* by engraving via the eventual emission of matter that accompanies the irradiation process. The technique is fully adaptable to any sintered ceramic. Polymeric materials like thermoplastics that basically consist of polymers in which a number of inorganic additives are present are also nearly all metallizable through that technique, as well as silicone rubbers. For each type of dielectric, parameters of the technique need be optimized according to the desired metallization profile.

In the following, examples of the application of the technique are presented, pointing to the photochemical material surface alteration that, in each case, is responsible for the metal sedimentation.

4. SINTERED CERAMICS

4.1 α-alumina
Fine-grained (1-2μm grain size), α-alumina (0.6mm thick) plates are excimer-laser irradiated at 248nm. As produced, these materials do absorb 5eV photons (3), probably due to the actual electronic structures of the alumina grain surfaces as well as to the cement material itself. During irradiation, plates are mounted on a substrate holder in such a way as to favor or not heat diffusion (and cooling) during and after irradiation. At a fluence of 0.8 J cm^{-2}, 25 Hz pulse repetition rate and 0.5 mm s^{-1} laser beam scanning velocity, the alumina plate is brought to melt during irradiation over a depth of about 0.1μm (Fig.2).
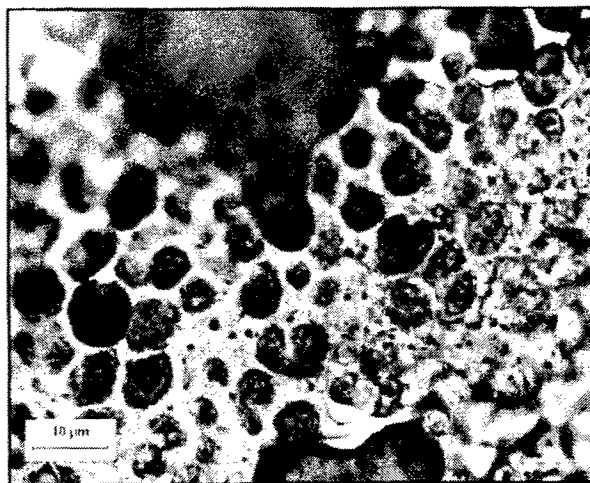

Figure 2: Transmission optical micrograph of a sintered alumina substrate after laser-induced melt/quench, showing transformed areas containing hemispherical islands surrounded by an homogeneous amorphous medium.

It resolidifies upon cooling immediately after interrupting irradiation. The structural characteristics of the quenched products depend on the actual cooling rates and, therefore, on the plate mounting (4). On slow-cooled plates ($\leq 10^8$ °K/s), diffusive *and* convective transports take place in the molten alumina (Fig.3) whilst only diffusive transport is operative on faster cooled plates ($\geq 10^9$ °K/s).
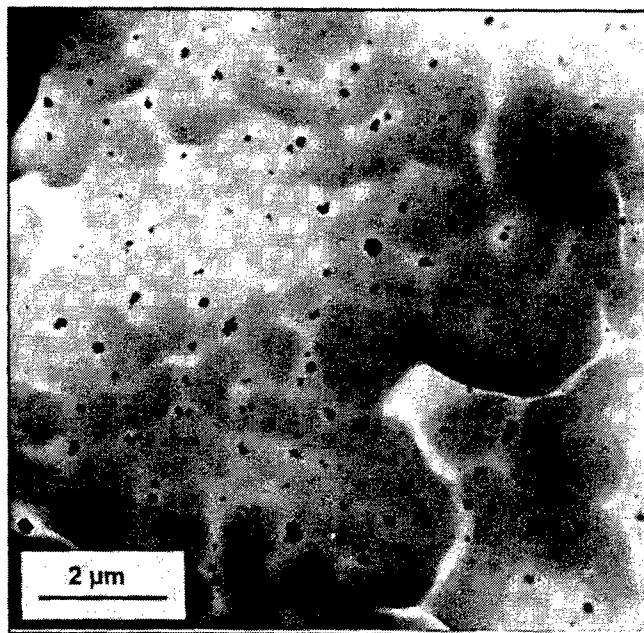

Figure 3: Transmission electron micrograph (TEM) of a slow-cooled irradiated and transformed alumina plate, showing convective structures in which (0.1 μm) crystalline structures are imbedded.

In fast cooled materials, transmission electron micrographs and diffraction reveal the presence of tiny (10 to 100 nm) spinel-type $CuAl_2O_4$ crystalline grains that are imbedded in an amorphous alumina matrix (Fig.4). Origin of these crystallites is to be found in the irradiation process itself as well as in the formulation of these α-alumina ceramics. After reaching melting and while being molten, alumina is still subjected to irradiation and starts decomposing following the reaction (3) : $Al_2O_3 \rightarrow 2AlO + 1/2O_2$, that materializes a *non-congruent* emission of matter. In effect, since AlO is volatile, this partial ablation induces an excess of atomic oxygen in the solidifying material. The latter would then transform locally into an O-enriched solid network that would crystallize into (Al-deficient) tiny γ-alumina grains containing all excess O atoms. These open structures do represent attractive centers for all impurity atoms that, being originally contained at alumina grain boundaries in the solid sintered alumina, diffuse widely in the molten material. In particular, Cu ones, that are present at concentrations of the order of 10^{20} cm^{-3} in sintered alumina, are driven to be selectively trapped into such γ-alumina grains and form the detected spinel structures (4).

Upon immersing such processed alumina plates into an electroless bath containing metal ions (e.g. Ni^{2+}), the latter are fixed onto these spinel particles, initiating full metallization of the irradiated surface upon bridging in between the spinel grains. After thermal treatment, adhesion of the resulting Ni layer on the alumina plate may be brought to exceed 40 Mpa (1). Standard 15-20 μm thick Ni layer can be produced after 1 hr immersion that are partially (5-10 μm) integrated into the alumina plate. Metallization being restricted to the irradiated areas, an excellent edge definition (± 5 μm) is achieved. Alumina being itself biocompatible, Pt metallization is performed to produce fully implantable Pt electrical circuits on alumina devices.
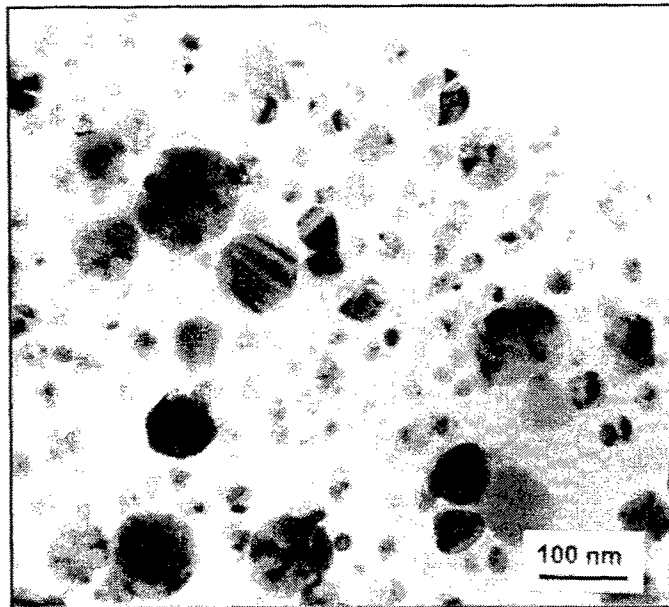
Figure 4: TEM micrograph of a fast–cooled alumina plate after irradiation and transformation, showing dispersed (10-50 nm) $CuAl_2O_4$ crystallites in an amorphous alumina medium.

4.2 Aluminum Nitride

AIN differs from sintered alumina having a much higher (x 20) heat diffusivity. Therefore, AIN may be an excellent alternative to α-alumina in producing medium-to-high power electrical circuits, would an appropriate way of metallizing it be at hand. None of the existing metallization technique does offer that possibility, contrary to the present one (1). In contrast with sintered alumina, AIN does not absorb 5 eV photons (5). However, sintering agents that are used with AIN grains imply Y_2O_3. Upon sintering, the latter is driven to react with AIN and form an Y-Al garnet (YAG) which forms the cement to sintered AIN. That oxide does absorb very effectively the excimer laser 5 eV photons (6). Upon irradiation, the garnet decomposes following the reaction : $Y_4Al_2O_9 \rightarrow 4YO + 2AlO + O_2 + 1/2 \ O_2$. All products of that decomposition are volatile, except atomic O that is brought to react to AIN with : $1/2 \ O_2 + \ AIN \rightarrow NO + Al$ (O affinity to N is larger than to Al). NO is volatile, therefore the outer surface of the sintered AIN grains is reduced to metallic Al. Though the latter does oxidize immediately in Al_2O_3, immersing the laser processed sintered plate into a high pH ionic bath induces dissolution of the Al oxide prior fixing metal ions on the oxide-free Al surface, hence the full metallization of the irradiated surface. Metallization may be carried out to extremely large thicknesses (200μm) and an additional heat treatment may bring adhesion to more than 20Mpa for such thick metal layers. 3-D metallization of that type has been demonstrated to achieve application-specific characteristics.

4.3 Zirconia

ZrO_2 does absorb 5 eV photons and a low fluence excimer irradiation may bring it to melt and quench, either being in the form of a film (7) or as sintered ceramic (8). The fast solidification that follows irradiation is observed to produce cubic zirconia with a metallic behavior. Immersing an irradiated (melt/quenched) zirconia target into an electroless metal bath induces again the selective metallization of the irradiated (cubic) zirconia.

5. POLYMERIC COMPOSITES

In polymeric composites, the matrix polymer is in general a carbon-based polymer or co-polymer. It may also be a silicon-based polymer or silicone. Inorganic additives are commonly oxides : minerals like talc, silica fiber and others in C-based composites, silica foam in silicone to form so-called silicone rubbers. One example of application of the metallization technique (2) to each of these polymeric composites is presented in the following.

5.1 C-based composites

Above a given laser energy threshold (usually between 0.2 and 0.8 Jcm^{-2}), excimer laser irradiation is known to decompose and ablate C-based polymers (9). After ablation, the processed C-polymer surface is quite similar to the virgin one, smooth and devoid of (structural or chemical) defects that could be decorated by metal ions upon immersing in an electroless bath. The presence of specific granular additives within the C-polymer matrix of a composite does not infere this behavior. However, as a result of the polymer ablation, these granular additives, being progressively liberated from their matrix, are themselves submitted to irradiation and develop their own reactivity to the laser photons. Contrary to their polymeric matrix, they are not ablated but rather, decompose like in a solid ceramic, along laser-induced photochemical reactions that tend in general to partially reduce these oxides. Being no longer stoichiometric, the actual irradiated surface of these oxide grains turns out to be partially ionized. Upon immersing such irradiated C-based composite into an electroless bath, metal ions from the bath fix onto the outer surface of these grains, bridge in between the grains and finally constitute a continuous metal layer all over the irradiated surface (Fig. 5).

In order to process the additive grains, and since these grains are usually not present at the composite surface but rather deeper in the material, polymer ablation (or engraving) needs be carried out at more than 10 μm. The consequence is that the above metal layer may be partially or totally imbedded into the composite. Therefore, adhesion of that layer is simultaneously chemical on the irradiated surface, mechanical via the metallized grain anchoring into the polymer matrix and structural due to the engraving. The effectiveness of the composite metallization process depends essentially on the additive content (formulation, grain size, concentration, actual didtribution near the surface of the composite). Standard metal thicknesses depend on the immersion time in the bath. Adhesion is further increased by heating the composite to near melting point.

5.2 Silicone rubbers

Silicone polymers are constituted of Si-O chains to which C-radicals are fixed via Si-C bonding. Such chains are further grafted onto a silica foam that helps maintaining the material in a controlable shape. In the bond hyerarchy (10), Si-C bonds are the weakest, followed by C-H bonds and finally, the strongest Si-O bonds. Upon excimer irradiation at 5 eV photon energy, optical absorption onto Si-C bond electrons prevails whichever the C-radicals (and silicone formulation). It induces decomposition of the silicone polymer into two parts : i) the inorganic Si-O back-bone chains and ii) the organic C-radicals that are emitted (Fig. 6). In the resulting irradiated chaotic silicone rubber, the grafted Si-O chains would tend to crosslink via Si-Si bonds, thus forming very imperfect random SiO networks that would remain largely non-stoichiometric at Si sites. Upon immersing the irradiated silicone rubber into an electroless bath, metal ions are driven to fix preferentially on dangling (Si) bonds, before forming thicker metal deposits in and on the irradiated silicone surfaces (Fig.7). The nature of this metallization is specific to silicone rubber that retains its flexibility after metallization. Narrow (100 μm wide) metallic tracks are produced that may form flexible metal circuits on thin (100 μm) two-sided silicone rubber foils. As on sintered alumina ceramics, Pt circuits are currently produced onto biocompatible silicone rubber substrates (Fig.8) to form implantable flexible, printed-circuit foils (11).

(a)   (b)

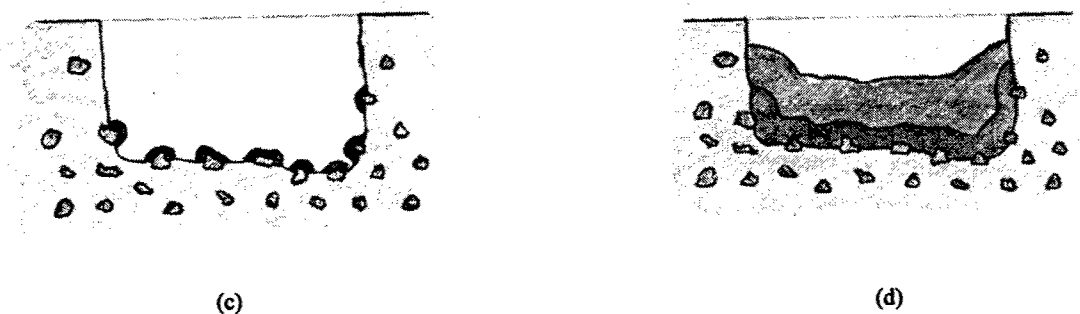(c)   (d)
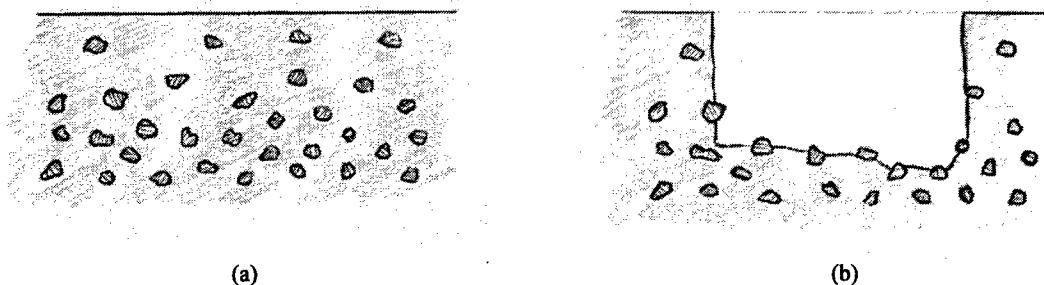
Figure 5: Schematic representation of laser processing and metallization of a polymer composite: a) section of polymer composite, b) polymer ablation + grain laser processing, c) metallization starts on processsed grains, d) metallization develops in processed area
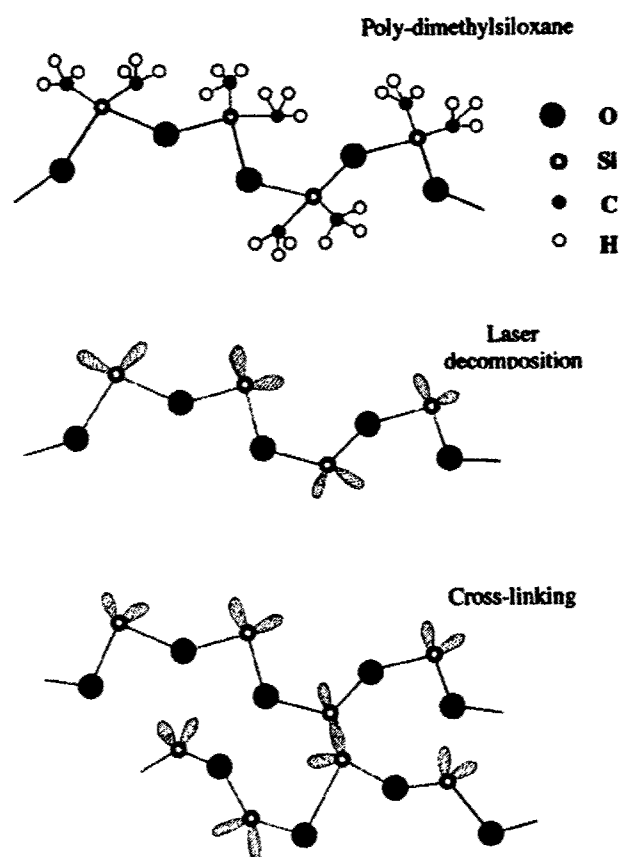

Poly-dimethylsiloxane

● O

◉ Si

● C

○ H

Laser decomposition

Cross-linking

Figure 6: Schematic excimer laser decomposition and cross-linking of (poly-dimethylsiloxane) silicone.

(a)   (b)
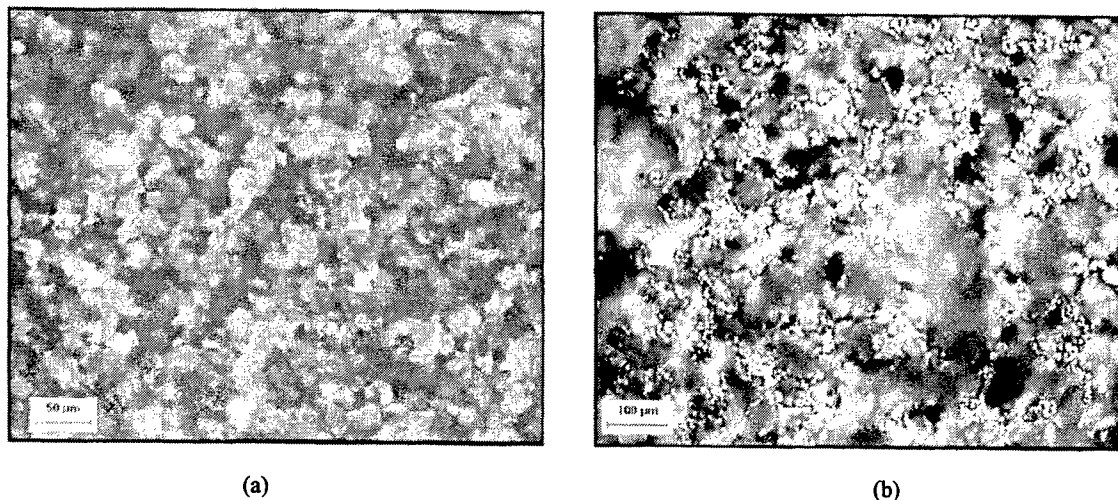
Figure 7 Optical micrograph of excimer laser processed silicone before (a) and after (b) Ni-metallization.
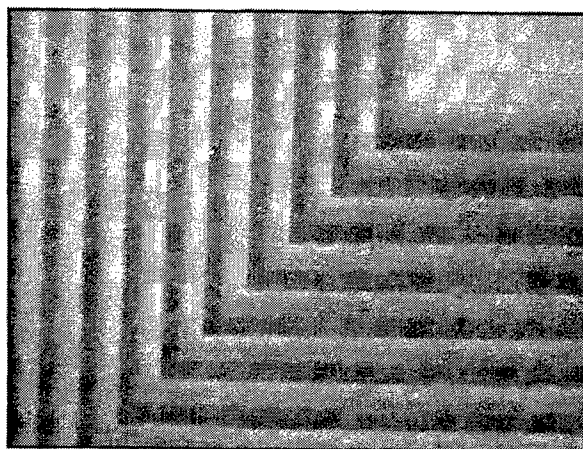
Figure 8 Network of (200 μm wide) Pt tracks performed on a thin (80 μm thick) biocompatible silicone rubber foil.

6. CONCLUSIONS

Directly metallizing a dielectric surface for effective metal interconnects is a complexe problem that had not received so far simple solutions. In this presentation, a positive technique is described that may provide substantially convincing means to achieve such objectives. The technique derives from the potential of excimer laser sources in acting on the various components of sintered ceramics and polymer composites. This action stems from laser-induced surface photochemical decompositions that may monitor the electrical activation of the irradiated surfaces and their further metallization in an electroless autocatalytic bath. The simplicity of the process implies a large degree of automaticity in production, and allows a wide range of adaptatability to a variety of applications, in particular in the demanding medical field.

REFERENCES

1. L.D. Laude, European Patents Nos. 0634502 and 0635585.
2. L.D. Laude, European Patent No. 0693138 ; US Patent No. 5,599,592.

3. L.D. Laude, K. Kolev, M. Brunel, M. Deleter, Appl. Surf. Sci. **86**, 368 (1995).
4. C. Dupas-Bruzek, L.D. Laude, F. Langenhorst, K. Kolev, J. of Appl. Phys. (in press).
5. G. Radhakrishnan, P.M. Adams, N. Marquez, MRS Symp. Proc, Vol. 397 (1996), p. 649-654.
6. N. Detournay et al., MRS Symp. Proc.., Vol . 397 (1996), p. 525-530.
7. K. Starbova et al. Appl. Surf. Sci. **173** (3-4) p. 177.
8. K. Kolev, C. Dupas-Bruzek, L.D. Laude (to be published).
9. M. Devalckenaere, A. Jadin, K. Kolev, L.D. Laude, Nucl. Instr. and Methods, B 151 (1999) 263-267.
10. T. Cottrell, "The strength of Chemical Bonds", Butterworth& Co Ltd., London, 1958, pp. 270-280.
11. Cl. Dicara et al., SPIE Proc. Adv. Laser Technologies Conf., 15-20 Sept. 2002, Adelboden, p. 98.

Excimer Laser Lift-off for Packaging and Integration of GaN-based Light-emitting Devices

Timothy D. Sands

School of Materials Engineering and School of Electrical and Computer Engineering
Purdue University, West Lafayette, Indiana

1 Abstract

The delamination of a thin film heterostructure by selective absorption of pulsed laser energy at a buried interface enables the transfer of the thin film heterostructure from its growth substrate to virtually any receptor substrate without significant heating of material outside the interaction zone. By combining this "laser lift-off" process with low-temperature bonding methods, disparate classes of materials can be intimately integrated without exceeding the thermal budget of the least robust of the materials to be integrated. Furthermore, heterostructures that can be grown by epitaxy on one substrate can be transferred intact, without significant deterioration in crystal quality, to a receptor substrate that enhances the performance or functionality of the heterostructure in a device or microsystem. In this paper, applications of laser lift-off in the packaging and integration of light-emitting GaN devices are highlighted. Transfer of these devices from their sapphire growth substrates to thermally and electrically conductive receptor substrates is shown to result in improved device performance through the reduction of thermal and electrical series resistances, and by the improvement in optical design enabled by access to both sides of the heterostructure. Continued development of laser lift-off packaging has the potential to reduce manufacturing costs and complexity as well through the elimination of the sapphire dicing step. Finally, the application of the LLO technique to the assembly of functionally-enhanced microsystems is illustrated with the example of an integrated fluorescence detection microsystem.

2 Introduction

2.1 Overview

Monolithic integration by sequential deposition, lithographic patterning, and etching of metal, dielectric and semiconductor thin films has been the dominant manufacturing scheme throughout the history of the integrated circuit. This manufacturing paradigm has been adapted to the fabrication of Micro-ElectroMechanical Systems (MEMS), active-matrix displays, read/write heads for disk drives, and optoelectronic devices. Although this single-substrate approach is scalable and inherently cost-effective, there are some materials systems, functionalities and device designs that cannot be realized in this manner. The ideal growth substrate for a specific thin-film heterostructure may not be the ideal substrate from the standpoint of heat extraction, mechanical properties, thermomechanical behavior, optical transparency, electrical conductivity or chemical compatibility. In these cases, the growth substrate must be removed, although it is not always practical to do so by mechanical or chemical means alone. In the longer term, it may be desirable - even necessary - to intimately integrate active thin-film heterostructures grown separately on several growth substrates onto a single chip-scale platform.

In this paper, the application of pulsed lasers to the separation of nitride heterostructures from their growth substrates is described. The basic process as illustrated in Figure 1 involves the irradiation of an interface between an absorbing film (e.g., GaN) and a transparent substrate (e.g., sapphire) using a short laser pulse, usually of nanosecond duration, directed through the transparent substrate. The absorption of laser energy induces localized heating of the interfacial material. At a critical fluence, the GaN decomposes to Ga metal and nitrogen gas. The thermochemical separation mechanism may be assisted by thermomechanical effects if the residual strain energy in the film is significant (>2-3 J/m^2). The laser wavelength must be chosen so that the photon energy is between the band gap energies of the substrate and interfacial thin film. This technique, often referred to as "Laser Lift-off" (LLO), was first demonstrated in the GaN/sapphire materials system by Kelly and coworkers (Kelly 1997) using the third harmonic of a Nd-YAG laser at a wavelength of 355 nm. Subsequent development of the technique with more powerful lasers at shorter wavelengths (e.g., KrF excimer lasers at 248 nm) revealed the utility of this method for the rapid separation and transfer of (In,Ga)N device heterostructures without sacrificing device performance (Wong et al. 1998, 1999A, 1999B, 1999C, 1999D, 2000A, 2000B); in some cases, the device performance was shown to be enhanced (Luo et al. 2002; Wong et al. 2001A). As unsupported thin-film membranes are generally not sufficiently robust to permit handling, the transfer of heterostructures from one substrate to another necessitates a bonding step prior to the separation process. This paper thus considers the entire "paste-and-cut" process.
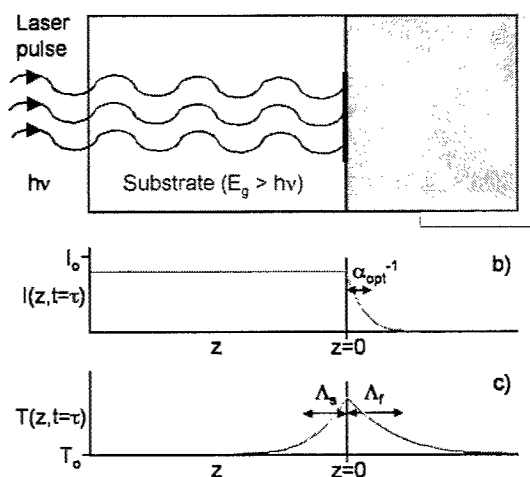
Fig. 1 Schematic illustration of the Laser Lift-off process. a) A single pulse from a nanosecond laser is directed through the transparent substrate. b) The laser energy is absorbed in the film with a characteristic length of $1/\alpha_{opt}$, where α_{opt} is the absorption coefficient in the film at the laser wavelength. c) The extent of heat conduction away from the interface is characterized by the thermal diffusion length, Λ, evaluated at the end of the laser pulse. Λ is greater than $1/\alpha_{opt}$ for uv nanosecond lasers interacting with most materials.

2.2 Layer Transfer and the Materials Integration Hierarchy

In combining two or more classes of active materials in a microsystem, there is generally a trade-off between the *degree of integration* and the *quality of the materials* as illustrated in Figure 2. At the lowest level of integration, one materials system may be interconnected to another via wire bonds between the two substrates, or by mounting the two substrates on a printed circuit board. In this case, the growth substrates may each be chosen to optimize the quality of the active device materials deposited upon them. At the other extreme, two classes of device materials may be intimately integrated at the nanoscale to provide functionality and scaling potential that could not be achieved by wire bonds or conventional lithographically-defined interconnects. In this latter case, though, it is essential that the two classes of functional materials be chemically, thermally and mechanically compatible. If the two classes of materials are not compatible, the quality of one or both of the materials will suffer.

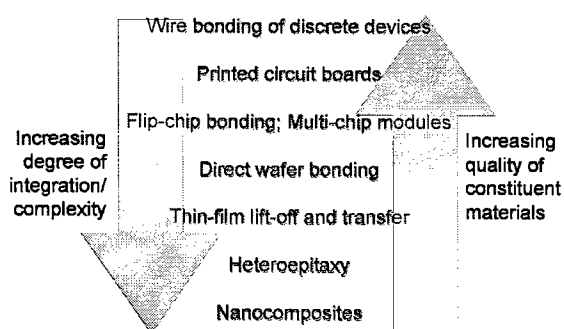## Approaches to Integration of Heterogeneous Epitaxial Materials and Devices

Wire bonding of discrete devices

Printed circuit boards

Flip-chip bonding; Multi-chip modules

Increasing degree of integration/ complexity

Direct wafer bonding

Increasing quality of constituent materials

Thin-film lift-off and transfer

Heteroepitaxy

Nanocomposites

Fig. 2 Hierarchy of heterogeneous integration methods illustrating the trade-off between materials quality and degree of integration.

Although the details differ from example to example, the basic trade-off between degree of integration (cost) and materials quality (performance of individual devices) is common to all examples of microsystems that necessitate the integration of disparate classes of active materials. Layer transfer is certainly not a substitute for conventional deposition, lithography and etching when it is possible to achieve the necessary device performance in this manner. However, layer transfer may prove to be an optimal compromise when a compact package is desirable, yet the materials systems cannot be integrated with sufficient quality by direct deposition onto a single substrate.

2.3 Layer Transfer for Device Packaging

An important subset of the spectrum of materials integration challenges are those in which the desired growth substrate hinders the performance of the device heterostructure grown upon it. For example, the new generation of bright amber and red LEDs are based on (Al,Ga,In)P heterostructures lattice-matched to GaAs substrates. The GaAs substrate absorbs the visible light, however, limiting the device efficiency. The solution has been to remove the GaAs substrate and bond the heterostructure to a transparent GaP wafer at high temperature and pressure (Kish et al. 1994). In another example, sapphire is the preferred growth substrate on the basis of cost and availability for GaN-based electronic and photonic devices. Attempts to grow GaN directly on silicon have met with some success (Guha and Bajarczuk 1998A; 1998B), although high-performance LEDs and diode lasers grown on silicon may be difficult to realize due to a high defect density. Silicon carbide is an attractive alternative, although substrate cost and dicing cost have inhibited progress with this substrate material. Despite the success with sapphire, it has poor thermal conductivity and is electrically insulating. Furthermore, sapphire is difficult to dice since it is hard and does not cleave easily. Hence, it is desirable, especially in the case of the highest performance devices (e.g., diode lasers or high-electron-mobility transistors), to remove the sapphire substrate and transfer the device heterostructure to a substrate with superior thermal, mechanical or electrical properties. Removal of the substrate also exposes the backside of the heterostructure, allowing for the implementation of "active packaging" schemes (Luryi 1994) including backside ohmic contacts to reduce series resistance and reflective surface coatings to enhance the external quantum efficiency of light-emitting devices (see Section 6). It is in this later example where the LLO layer transfer technique has proven to be an attractive alternative to mechanical grinding or chemical dissolution of the growth substrate.

2.4 Layer Transfer as a Materials Integration Tool for Enhanced Microsystem Functionality

Beyond packaging, layer transfer can, in principle, enable the assembly of microsystems with enhanced functionality through the intimate three-dimensional integration of thin-film materials. Although the most obvious benefit of such integration is in the fabrication of more compact, higher performance microsystems, it is conceivable that layer transfer could also lead to microsystem architectures with functionality that would not be possible with a lower level of integration. An example of integrated functionality enabled by layer transfer is the assembly of fluorescence-based detection systems by combining thin-film LEDs, thin-film optical filters and photodetectors on the same substrate. This example will be discussed in more detail in Section 6.3.

3 Thermal and Mechanical Behavior during Pulsed Laser Irradiation of a Buried Interface

3.1 Thermal Behavior

The temporal and spatial evolution of the temperature during irradiation of a buried interface at the nanosecond timescale can be modeled using the standard heat conduction equation. In the case of GaN/sapphire, the optical absorption length is substantially shorter than the thermal diffusion length evaluated at the end of the pulse; thus, the assumption that the heat source is located at the interface is justified. An example of a calculation of the temperature evolution in the vicinity of the interface between semi-infinite slabs of GaN and sapphire is shown in Figure 3. Note that the peak temperature is reached at the interface at the end of the simulated "square" laser pulse. The temperature decays rapidly after the end of the pulse, and in both directions during and after the pulse. A peak temperature rise of about 1000°C can thus be achieved without appreciable heating of the GaN material that is more than a few thermal diffusion lengths away from the interface.

Fig. 3 Calculated temperature distribution as a function of time and temperature during irradiation of a GaN/sapphire interface with a 38 ns pulse from a 248 nm laser at a fluence of 600 mJ/cm² incident on the sapphire entrance surface (after Wong et al. 1999D).
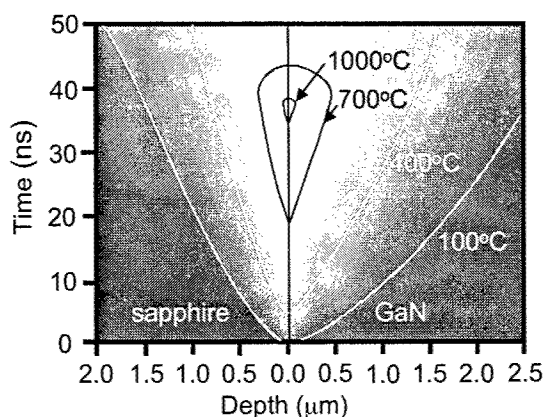
3.2 Thermomechanical Behavior

During the laser heating of a buried interface, biaxial compressive stresses are generated at the interface due to thermal expansion constrained by the bulk of the substrate, which is not appreciably heated, and by the unheated portion of the overlayer. This transient strain energy can, in principle, contribute to the delamination of the film from the substrate as discussed in Section 5.1. With knowledge of the elastic moduli (e.g., Young's modulus, Y, and the Poisson ratio, v, if assumed to be elastically isotropic) and the

thermal expansion coefficients, α_{CTE}, of the film or substrate, the peak stored transient elastic strain energy per unit area, $E_{transient}(\tau)$, in either the film or the substrate of thickness h can be estimated as

$$E_{transient}(\tau) = \frac{Y}{1-v}\frac{\alpha_{CTE}^2}{2}\int_0^h \left[\Delta T(z,\tau)\right]^2 dz, \qquad \text{(Eqn. 1)}$$

where $\Delta T(z,\tau) = T(z,\tau) - T_{ambient}$, and $T(z,\tau)$ is the temperature profile at the end of the square laser pulse. Numerical methods can be used to enhance the accuracy of the calculation if the temperature dependencies of the materials properties are known.

The transient thermoelastic strain energy is in addition to any strain energies associated with residual stress from film growth or cooling after growth. The residual strain should be added to the transient strain before calculating the total strain energy. However, the fact that the transient strain is localized and relatively large in magnitude justifies the approximation implicit in the direct addition of strain energies. This assumption will be employed in the development of a thermomechanical model for LLO (Section 5.1).

Much evidence suggests that the thermal decomposition process is nucleated heterogeneously, producing a penny-shaped delamination (Cho et al. 2003). The heated vapor produces a transient hydrostatic pressure on the internal walls of the delamination. If the peak crack-opening stress is sufficiently high to propagate the crack to a diameter comparable to or greater than the unsupported film thickness, then this mechanism alone may be responsible for film separation. The analysis of such a mechanism is complicated by the fact that the internal pressure should dissipate rapidly after the peak of the laser pulse, and as the crack volume grows. For the case of GaN decomposition at a GaN/sapphire interface during LLO, Wong estimated a relatively modest peak N_2 pressure of $\sim$ 85 MPa corresponding to a temperature of 1000°C (Wong 1999). A more detailed calculation indicates that the N_2 pressure can become significant at fluences that are significantly higher than the minimum necessary to induce decomposition (Tavernier and Clarke 2001). The impact of the decomposition pressure on the LLO mechanism depends on the mechanical constraints discussed in the following section.

3.3 Failure Mechanics

Presuming an unsupported film and a laser spot of finite diameter, the mechanics of failure can be described qualitatively by simple models (Wong 1999; Tavernier and Clarke 2001). If the film is under biaxial residual compressive stress σ_{res} prior to lift-off, the decomposition of the interface can be accompanied by film buckling if the diameter of the delaminated region exceeds d_{crit} as given below (Tavernier and Clarke 2001).

$$d_{crit} = 2.2h_{film}\sqrt{Y\big/(1-v)|\sigma_{res}|} \qquad \text{(Eqn. 2)}$$

For a residual stress of -250 MPa (Cho et al. 2003) and a biaxial modulus, $Y/(1-v)$, of 478 GPa (Polian et al. 1996) - values characteristic of GaN films - buckling is expected for delamination diameters exceeding $\sim$100 h_{film}.

Generation of vapor species at the interface can induce film bulging even in the absence of a compressive residual stress. Fracture of the film may result from crack deflection into the film at the perimeter of the delaminated area, or by blistering due to tensile failure at the center of a buckle or bulge. The details of these failure mechanisms as they pertain to LLO of GaN are discussed by Wong (Wong 1999) and Tavernier and Clarke (Tavernier and Clarke 2001). Any of these effects - buckling, significant bulging, blistering or crack deflection from the interface into the film - constitutes a failure mechanism for most applications of LLO.

From the considerations above, it is obvious that a stiffening layer will generally be required to prevent mechanical failure. Qualitatively, a stiffening layer has an effect equivalent to increasing the film thickness in Eqn. 2, provided that the adhesion between the film and stiffening layer is sufficient to prevent failure by delamination of the stiffening layer. Wong (Wong 1999) has used a relation similar to Eqn. 2 to establish "safe" stiffening layer thicknesses and stiffness regimes as a function of the delamination area. Tavernier and Clarke have developed detailed processing maps accounting for bulging, buckling and cracking for unsupported GaN films (Tavernier and Clarke 2001). These maps can be modified to account for stiffening layers, thus providing very useful tools for LLO process design.

4 Process Flows for Layer Transfer by Bonding and Laser Lift-off

4.1 Direct "Paste-and-Cut"

Application of LLO to heterogeneous integration requires the use of reasonably thin heterostructures that cannot be easily handled as free-standing films. It is therefore necessary to mechanically support the films throughout the film transfer process. Furthermore, the stiffening effect of the supporting substrate is often necessary to prevent failure due to blistering or crack deflection as described in Section 3.3. The simplest LLO integration scheme, direct "paste-and-cut," starts with the permanent bonding of the heterostructure to be transferred to the final substrate. Removal of the substrate by LLO completes the transfer, as illustrated in Figure 4. If the bonding material and substrate are relatively stiff and adhesion at the interfaces is strong, any residual stress in the film will remain after LLO.

Direct-Transfer Laser Lift-off Process
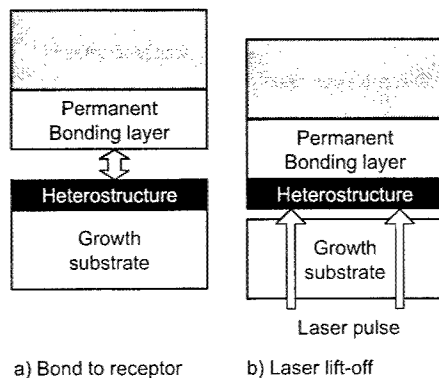
Fig. 4 Direct "Paste-and-Cut" transfer of a film or heterostructure by LLO

4.2 Double-Transfer "Paste-and-Cut"

The direct transfer process described above results in a heterostructure that is inverted relative to its orientation on the growth substrate. In some cases, it may be desirable to transfer a heterostructure in its original orientation. Such a process necessarily involves the temporary transfer of the heterostructure to a handle substrate, a subsequent permanent bonding of the transferred heterostructure to its final receptor substrate, and the release of the heterostructure from the handle substrate as in Figure 5. Double-transfer processes also offer potential advantages in the flexibility of the transfer process. For example, heterostructure "die" could be transferred first to a flexible tape, and then arranged as needed on the final substrate. The additional complexities associated with double transfer include the reduced mechanical stiffness associated with the temporary bonding material, which can lead to an increase in problems associated with blistering and crack deflection during LLO. Mechanical failure associated with film stress release can be mitigated by trench etching down to the growth substrate, thereby allowing some lateral relaxation of stress once the growth substrate is removed.
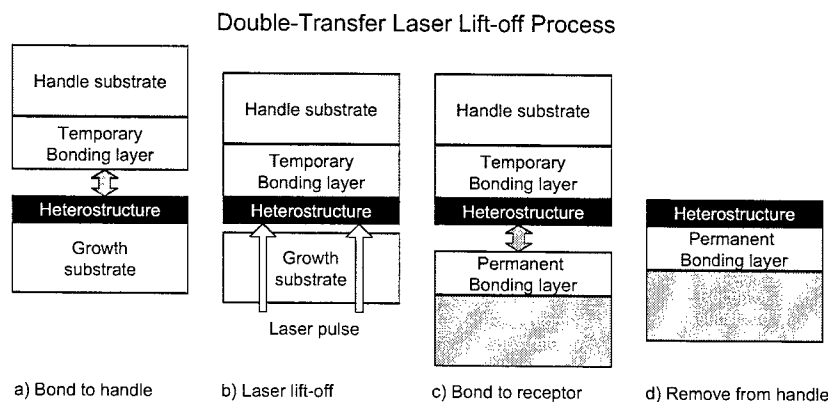
Fig. 5 Schematic process flow for double-transfer paste-and-cut LLO.

4.3 Bonding

The choice of bonding method depends on whether the bond is to be permanent or temporary, and electrically conductive or insulating. Furthermore, the properties of the materials involved will constrain the maximum temperature that may be employed for bonding. Although high-temperature direct bonding may be possible for some applications, the focus in this section is on bonding techniques of the broadest applicability that do not require temperatures above 200°C, and are thus compatible with some polymers and most metals, semiconductors and inorganic dielectric materials.

4.3.1 Permanent Metal Bonding by the Solid-Liquid Interdiffusion Method. Gold thermocompression bonding can be employed when a metal bond is required to make good electrical and thermal contact. If the Au bonding method is not mechanically or thermally compatible, a melt-based solder or indium bond can be used. Indium melts at 157°C, a temperature that is compatible with many polymers. If elemental

In remains in the bond, however, subsequent processing at temperatures above 157°C will induce undesirable remelting. To eliminate the elemental In, an additional metal layer that reacts to create a higher-melting-point intermetallic can be added to the bonding metallization. This approach is reminiscent of the Solid-Liquid Interdiffusion (SLID) bonding method developed in the 1960's for integrated circuit fabrication (Bernstein and Bartholomew 1966). For layer transfer applications, Wong and coworkers (Wong et al. 1999D, Cheung et al. 2002) developed a Pd/In SLID bonding metallization that melts initially at the In melting point. Continued heating at temperatures of about 200°C activates the interdiffusion necessary to form the intermetallic phase Pd_3In_7, a phase with a peritectic melting point of 664°C. To completely eliminate elemental indium, a Pd:In mole ratio of at least 3:7 is required. Note that the intermetallic phase, Pd_3In_7 was formerly identified as $PdIn_3$. A recent study by Häussermann and coworkers (Häussermann et al. 1998) has clarified the composition and crystal structure of this compound, the most In-rich of the Pd-In intermetallics.

It is also necessary to introduce a thin (nm scale) diffusion barrier between Pd and In to ensure that the reaction to form Pd_3In_7 does not go to completion prior to the melting of the indium that is necessary to form the bond. Details of the bonding process are described by Quitoriano et al. (Quitoriano et al. 2001). Figure 6 shows a GaN/Pd-In/Si heterostructure formed by Pd-In bonding and LLO. Several other bilayer metallizations are candidates for SLID bonding (Studnitzky and Schmid-Fetzer 2002), although Pd-In is the only one that has been investigated thus far for applications in layer transfer.

GaN (1ī00) facet

Pd_3In_7

Si {111} facet (inclined)   1μm
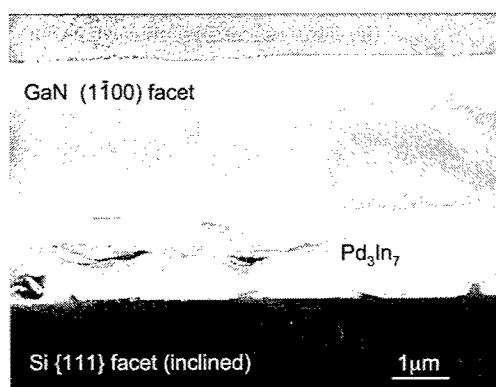
Fig. 6 SEM image of a GaN/Pd-In/Si heterostructure prepared by Pd-In SLID bonding and laser lift-off. The GaN prismatic cleavage plane was aligned with a <110> direction on the surface of the {111} Si wafer, so that cleavage of the Si resulted in the formation of a smooth cleavage facet in the GaN film (from Wong et al. 1999D).

4.3.2 Sacrificial Bonding for Double Transfer. Acetone soluble adhesives are the most convenient temporary bonding materials. Successful results have been achieved with the common household ethyl cyanoacrylates-based adhesives. Photoresist can also be used, although poor adhesion is a problem. Acetone-soluble thermoelastic materials are to be avoided, as they can be relatively brittle at ambient temperatures. These acetone soluble materials are generally not very thermally robust, and they are typically too compliant to restrain released films from buckling or cupping.

5. Laser Lift-off of GaN from Sapphire

The GaN/sapphire system is ideally suited to laser lift-off. Although GaN has a very high melting point of about 2500°C, the equilibrium partial pressure of nitrogen at the melting point is ~40 kbar (Perlin et al. 1995). At atmospheric pressure, GaN decomposes to liquid Ga metal and nitrogen gas at temperatures above approximately 890°C (Karpinski et al. 1984). A significant barrier to the reverse reaction ensures

that once N_2 is formed, GaN will not regrow during cooling after the laser pulse. The Ga metal that remains serves to provide a weak temporary bond between the released GaN film and the original sapphire substrate. This bond is easily overcome by application of a shearing force at a temperature above the Ga melting point.

From a technological perspective, the GaN/sapphire system is certainly one for which the advantages of substrate removal are clear. Although sapphire is of relatively low cost compared to alternative substrates, its only real virtue is its optical transparency in the context of flip-chip surface mounting for high-power LEDs (Wierer et al. 2001). In this configuration, the sapphire substrate may be used to improve coupling of light out of the GaN heterostructure. In view of the relatively low thermal conductivity, the electrically insulating behavior, and the poor cleavage and dicing properties, the ability to remove the sapphire presents an opportunity to address the problems of electrical series resistance, heat extraction from the active region, facet formation for edge-emitting lasers and dicing waste. Performing the removal process by mechanical means is not practical, thus defining a niche for laser lift-off.

5.1 Mechanism of GaN Laser Lift-off from Sapphire

The simplest model for GaN LLO is based on the thermochemical decomposition of GaN at the absorbing interface. One-dimensional calculations such as those described in Section 3.1 show that the temperature at the interface should reach approximately 1000°C for laser pulses at the observed threshold fluence for LLO. Considering only the factors that are dependent on the specific characteristics of the uv laser, the thermochemical LLO threshold fluence F_{tc} is roughly proportional to $\Delta T_{crit}\sqrt{\tau}$, where ΔT_{crit} is the temperature rise necessary to induce decomposition, and τ is the pulse length. The thermal decomposition model is also consistent with the observation of the metallization of the interface following a pulse of fluence above the LLO threshold. Since the GaN and sapphire are both transparent at visible wavelengths, the formation of Ga metal at the interface is readily revealed by casual inspection.

The thermochemical decomposition model for LLO proves to be insufficient for films greater than about 10 microns in thickness. Thicker films generally separate from the sapphire growth substrates at lower fluences and without visually apparent metallization of the interface. Thus, the separation for these thicker films occurs in a single step, without the advantage of the Ga interfacial layer that holds the film in place during LLO. Cho and coworkers (Cho et al. 2003) have studied the relationship between threshold fluence, film thickness and the residual stored strain energy in the GaN film. At lower stored strain energies, the mechanism is consistent with thermochemical decomposition at the predicted threshold fluence of about 560 mJ/cm² for a KrF excimer laser with a 38 ns pulse length. As the stored strain energy increases, the threshold decreases, and then saturates at approximately 400 mJ/cm². Cho et al. employed a simple thermomechanical model reminiscent of Griffith crack theory in brittle materials to explain these results. The model predicts that LLO will occur when the released strain energy per unit area, including both residual (static) and transient components (Eqn. 2), exceeds the work of adhesion, W_{adh}. The threshold fluence for LLO via this thermoelastic mechanism, F_{te}, has the form,

$$F_{te} = \left[B\left(W_{adh} - Ah_{film}\right)\right]^{1/2}$$
(Eqn. 3)

where W_{adh} has units of J/m², B is a combination of materials constants and the pulse length and has units of J/m², and A is the residual (static) strain energy stored in the film per unit volume. This relationship predicts that there will be a critical value of stored strain energy per unit film area for which the film is predicted to spontaneously delaminate upon cooling to room temperature after growth, without

the assistance of a laser pulse. The thermomechanical model is in qualitative agreement with the experimental data for residual strain energies per unit film area up to 2-3 J/m^2. The saturation of the experimental LLO threshold at 400 mJ/cm^2 suggests that either a critical flaw or a reduction in the work of adhesion is needed to induce brittle delamination by this mechanism. Cho and coworkers have found evidence for the formation of an Al-Ga-O-N quenched glassy layer at the interface after exposure to fluences above 400 mJ/cm^2, suggesting that the interface is weakened by eutectic melting.

6 Applications of Laser Lift-off to GaN-based Light-emitting Devices

6.1 (In,Ga)N Light Emitting Diodes

Many (In,Ga)N-based devices have been transferred from sapphire to another substrate. In the case of direct transfer, a combination of Pd-In SLID bonding and LLO has been used to fabricate inverted vertical LEDs on silicon (Wong et al. 1999B). Figure 7 shows the layer structure of an inverted LED and an image of the blue electroluminescence showing that the transferred device emits uniformly without evidence of cracking. In this structure, a reflective ohmic contact to the p-GaN and a vertical contact configuration (the ohmic contact to n-GaN was applied directly to the LLO-exposed surface rather than by etching through the p-GaN) represented departures from the conventional design of an (In,Ga)N LED on sapphire. The reduction in series resistance afforded by the vertical contact design was evaluated quantitatively in a study of LEDs on silicon fabricated by a double-transfer process (Luo et al. 2002). The combination of a reflective backside n-contact and the vertical contact configuration increased the light output (measured normal to the frontside exit surface) by 35% and reduced the series resistance from 22Ω on sapphire, to 4Ω on silicon with a vertical contact scheme. Figure 8 shows the electroluminescence spectra and I-V characteristics before and after LLO. The only internal changes in the emission characteristics are a slight broadening and red shift that are believed to have been introduced by relief of residual stress during the double-transfer process.
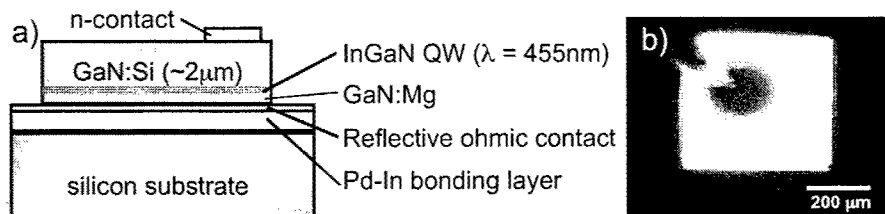
Fig 7 a) Schematic diagram of an inverted vertical LED on silicon fabricated by direct-transfer and Pd-In SLID bonding. b) photograph of the blue electroluminescence from a device of the type diagrammed in a). There is no evidence of cracking (after Wong et al. 2000B).

Fig 8 a) schematic of LED on sapphire b) schematic of LED after double-transfer to silicon, using a vertical contact scheme c) I-V characteristics of LEDs from the same growth substrate before double-transfer LLO, and after LLO with vertical contacts d) Electroluminscence spectra from an (In,Ga)N LED before and after double-transfer to a silicon wafer. (after Luo et al. 2002).
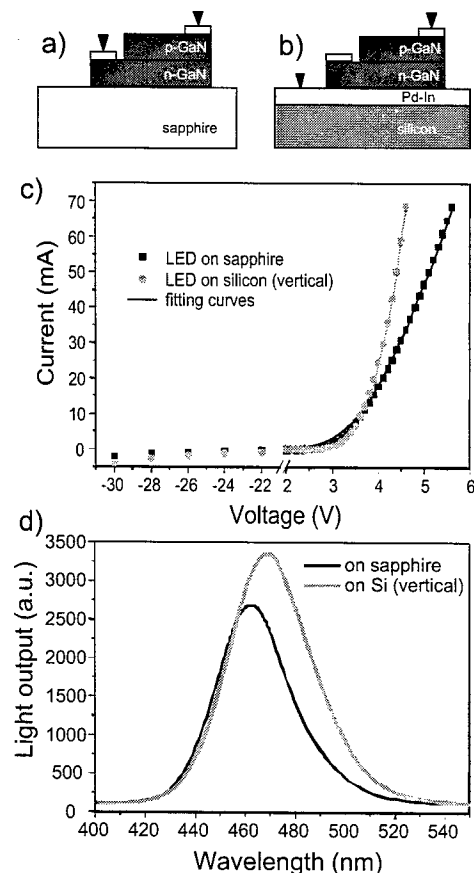
6.2 (In,Ga,Al)N Lasers

One of the most pressing problems in the fabrication of high-performance blue lasers is heat extraction from the active region of the heterostructure. Wong and coworkers (Wong et al. 2000A; Wong et al. 2001A) have employed LLO in the fabrication of (In,Ga,Al)N laser diodes that operate in continuous wave (*cw*) mode at room temperature. The double-transfer LLO process replaces the sapphire substrate with a copper heat sink, thereby improving heat extraction from the active region. The transferred lasers showed a 150% improvement in the maximum *cw* power output at room temperature compared to laser diodes from the same sapphire substrate before transfer (fig. 9).

Fig 9 Light output vs. current for an (In,Ga,Al)N laser diode on sapphire (circles) compared to a similar laser diode after LLO and bonding to a copper heat sink (adapted from Wong et al. 2001A)
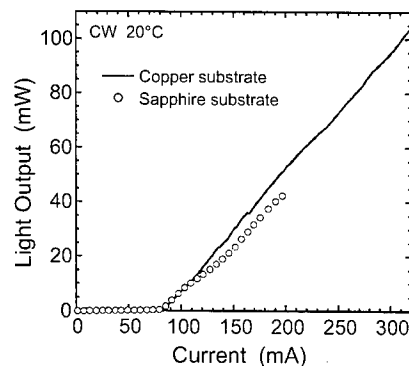
6.3 Assembly of Fluorescence-based Microfluidic Detection Systems

Early attempts to explore the potential of LLO for heterogeneous integration of active device components have been focused on the design and assembly of microsystems that serve the function of laser-induced fluorescence detection in DNA analysis and chemical detection. The present commercial technology utilizes macroscale discrete components for excitation, filtering and detection. It is possible in principle to achieve similar functionality in a chip-scale field-deployable unit by integrating blue-emitting LEDs with thin-film II-VI optical filters, Si-based photodetectors, and disposable polymer microfluidics. Such an integrated system has recently been proposed and a working prototype has been demonstrated (Chediak et al. 2003). Figure 10 is a schematic illustration of the device. A working prototype is shown in Figure 11, and the detection of fluorecein beads as a function of effective dye concentration is depicted in Figure 12. The addition of LED/filter combinations at different wavelengths along the same microfluidic channel would add functionality that cannot be realistically integrated by heteroepitaxy on a single growth substrate.
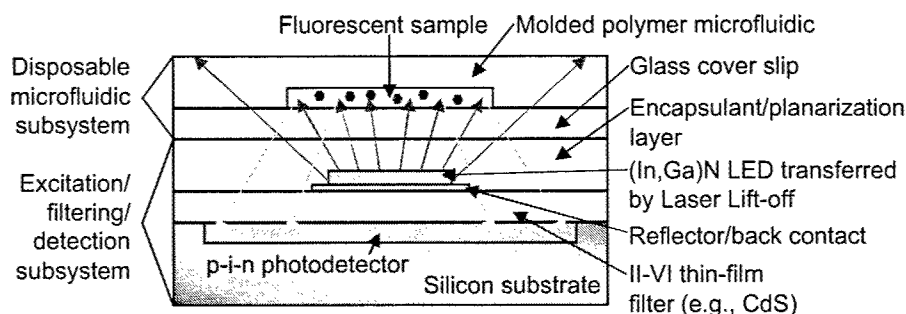
Fig. 10 Schematic diagram of integrated fluorescence detection device. The nondisposable subsystem includes a thin-film II-VI bandgap filter deposited onto a Si p-i-n photodetector. A thin-film (In,Ga)N LED is transferred by LLO and bonded to the CdS film. This subsystem is planarized, and then a disposable microfluidic subsystem (molded PDMS) is temporarily bonded to the excitation/filtering/detection subsystem. In the initial prototype, an LED emitting at 460 nm was bonded to a CdS filter (band edge at 504 nm) that transmitted only the fluorescence emission from the dye, centered at 510-530 nm (from Chediak et al. 2003).
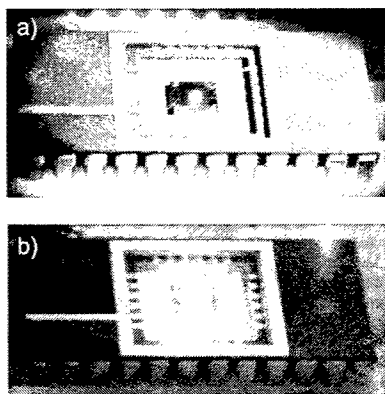
Fig. 11 Photographs of the fluorescence detection microsystem prototype illustrated schematically in Figure 10. a) The excitation/filtering/detection subsystem with the transferred LED emitting at 460 nm. The LED is 300 μm on a side and the photodetector is approximately 3 mm in diameter. b) The complete prototype in operation. The disposable microchannels are 2 mm wide and 100 μm deep and are molded from PDMS.
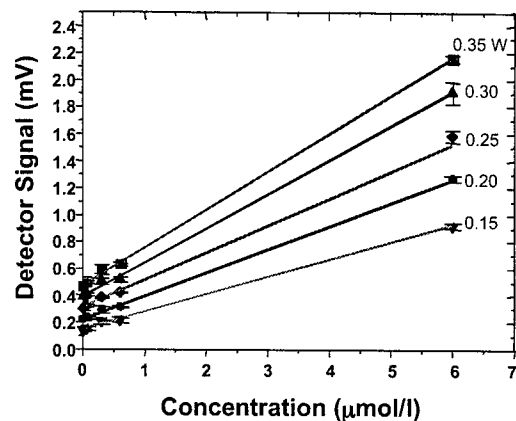
Fig. 12 Signal from the prototype as a function of effective dye concentration and LED power. The detection limit of this device is approximately 6×10^{-8} moles/liter (Chediak et al. 2003)

7 Prospects and Potential Impact of Laser Lift-off

Laser lift-off is now poised to impact die- and wafer-scale packaging of GaN-based LEDs and laser diodes. Further progress in these applications is dependent on the tailoring of processes for specific heterostructures, and then proving out these processes in pilot production. Significant room for improvement remains in the optimization of both metal and polymer bonding techniques. It is conceivable that large-area layer transfer could also provide hybrid microlaminated materials for three-dimensional heterogeneous integration. The power of the technique is in the ability to combine materials with very different properties – for example, nitride semiconductors, metallized CMOS and polymers. Exploitation of the full scope of heterogeneous integration by LLO awaits the development of methods for the transfer of single devices or die from a growth substrate to specific sites on a large substrate. It is likely that a combination of laser assisted bonding and LLO will be required to enable this new microsystem assembly paradigm.

Finally, much opportunity remains for the demonstration of LLO-based assembly of materials other than GaN. Preliminary results with PZT, ITO, ZnO and YBCO and SU-8 suggest that many complex oxides and polymers will also be amenable to this technique. The spectrum of potential materials is broadened further by allowing for the use of sacrificial LLO layers. Guha and coworkers have used LLO of GaN underlayers to transfer silicon thin films to virtually any substrate (Guha et al. 2000). Likewise, AlN-based materials grown on sapphire with GaN interlayers may be separated at laser wavelengths that are not absorbed by AlN. It is conceivable then, that it may be possible to design LLO-based microassembly tools that are capable of rapidly integrating an almost arbitrary range of functionality into complex microsystems while observing a thermal budget dictated by either the least robust of the materials to be integrated, or the largest thermal expansion mismatch between materials to be joined.

Acknowledgements

References

Bernstein L and Bartholomew H (1966) Application of Solid-Liquid Interdiffusion (SLID) Bonding in Integrated-Circuit Fabrication. Trans Metallurgical Soc of Amer 236: 405-12

Chediak JA, Luo ZS, Seo J, Cheung NC, Lee LP and Sands TD (2003) Hybrid Integration of CdS Filters with GaN LEDs for Biophotonic Chips. Proc. MEMS 2003, in press

Cheung NW, Sands TD and Wong WS (2002) U.S. Patent No. 6,335,263; Method of Forming a Low Temperature Metal Bond for Use in the Transfer of Bulk and Thin Film Materials, issued January 1st, 2002.

Cho Y, Schroeder JL, Sands T, Cheung NW and Stach E (2003) unpublished.

Guha S and Bajorczuk NA (1998A) Ultraviolet and Violet GaN Light Emitting Diodes on Silicon. Appl Phys Lett 72: 415-17

Guha S and Bajorczuk NA (1998B) Multicolored Light Emitters on Silicon Substrates. Appl Phys Lett 73: 1487-89

Guha S, Gupta A, Bajorczuk NA and Karasinski J (2000) Transplanted Si Films on Arbitrary Substrates Using GaN Underlayers. Appl Phys Lett 76: 1264-66.

Häussermann U, Elding-Pontén M, Svensson C and Lidin S (1998) Compounds with the Ir_3Ge_7 Structure Type: Interpenetrating Frameworks with Flexible Bonding Properties. Chem Eur J 4: 1007-15

Karpinski J, Jun J, and Porowski S (1984) Equilibrium Pressure of N_2 over GaN and High Pressure Solution Growth of GaN. J Cryst Growth 66: 1- 10

Kelly MK, Ambacher O, Dimitrov R, Handschuh R, and Stutzmann M (1997) Optical Process for Liftoff of Group III-nitride Films. phys stat sol(a) 159:R3-4

Kish FA, Steranka FM, DeFevere DC, Vanderwater DA, Park KG, Kuo CP, Osentowski TD, Peanasky MJ, Yu JG, Fletcher RM, Steigerwald DA, Craford MG, and Robbins VM (1994) Very high-efficiency semiconductor wafer-bonded transparent-substrate $(Al_xGa_{1-x})_{0.5}In_{0.5}P/GaP$ light-emitting diodes. Appl Phys Lett 64: 2839-41

Luo ZS, Cho Y, Loryuenyong V, Sands T, Cheung NW and Yoo MC (2002) Enhancement of (In,Ga)N Light-Emitting Diode Performance by Laser Lift-off and Transfer from Sapphire to Silicon. IEEE Photonics Technol Lett 14: 1400-02

Luryi S (1992) How to Make an Ideal HBT and Sell It Too. IEEE Trans Electron Devices 41. 2241-47

Perlin P, Suski T, Teissyre H, Leszczynski M, Crzegory I, Jun J, Porowski S, Boguslawski P, Bernholc J, Cherwin JC, Polian A and Moustakas TD (1995) Towards the Identification of the Dominant Donor in GaN. Phys Rev Lett 75: 296-99.

Polian A, Grimsditch M, Grzegory I (1996) Elastic Constants of Gallium Nitride. J Appl Phys 79: 3343-44

Quitoriano N, Wong WS, Tsakalakos L, Cho Y, and Sands T, (2001) Kinetics of the Pd/In Thin-film Bilayer Reaction: Implications for Transient-Liquid-Phase Wafer Bonding. J Electron Mater 30: 1471-5

Studnitzky T and Schmid-Fetzer R, (2002) Diffusion Soldering for Stable High-Temperature Thin-Film Bonds. JOM Dec 2002: 58-63

Tavernier PR and Clarke DR (2001) Mechanics of Laser-assisted Debonding of Films, J Appl Phys 89: 1527-36.

Wierer JJ, Steigerwald DA, Krames MR, O'Shea JJ, Ludowise MJ, Christenson G, Shen YC, Lowery C, Martin PS, Subramanya S, Götz W, Gardner NF, Kern RS, Stockman SA (2001) High-power AlGaInN Flip-chip Light-emitting Diodes. Appl Phys Lett 78: 3379-3381

Wong WS, Sands T, Cheung NC (1998) Damage-free Separation of GaN Thin Films from Sapphire Substrates. Appl Phys Lett 72: 599-601

Wong WS, Cho Y, Weber ER, Sands T, Yu KM, Wengrow AB, and Cheung NC (1999A) Structural and Optical Quality of GaN/metal/Si Heterostructures Fabricated by Excimer Laser Lift-off. Appl Phys Lett 75: 1887-89

Wong WS, Sands T, Cheung NC, Kneissl M, Bour DP, Mei P, Romano LT, Johnson NM (1999B) Fabrication of Thin-film InGaN Light-emitting Diode Membranes by Laser Lift-off. Appl Phys Lett 75: 1360-62.

Wong WS, Sands T, Cheung N, Kneissl M, Bour D, Mei P, Romano L, and Johnson N (1999C) Ubiquitous Blue LEDs: The Integration of GaN Thin Films with Dissimilar Substrate Materials by Wafer Bonding and Laser Lift-off. Compound Semi 5: 54-56

Wong WS, Wengrow AB, Cho Y, Salleo A, Quitoriano NJ, Cheung NC, and Sands T (1999D) Integration of GaN Thin Films with Dissimilar Substrate Materials by Pd-In Metal Bonding and Laser Lift-off. J Electron Mater 28: 1409-13

Wong WS, Kneissl M, Mei P, Treat DW, Teepe M, and Johnson NM (2000A) The Integration of $In_xGa_{1-x}N$ Multiple-quantum-well Laser Diodes with Copper Substrates by Laser Lift-off. Jpn J Appl Phys 39: L1203-05

Wong WS, Sands T, Cheung NW, Kneissl M, Bour DP, Mei P, Romano LT, and Johnson NM (2000B) $In_xGa_{1-x}N$ Light Emitting Diodes on Si Substrates Fabricated by Pd-In Metal Bonding and Laser Lift-off. Appl Phys Lett 77: 2822-24

Wong WS, Kneissl M, Mei P, Treat DW, Teepe M, and Johnson NM (2001A) Continuous-wave InGaN Multiple-quantum-well Laser Diodes on Copper Substrates. Appl Phys Lett 78: 1198-1200

Laser Direct-Write of Metal Patterns for Interconnects and Antennas

A. Piqué[*], C.B. Arnold, B. Pratap, R.C.Y. Auyeung, H.S. Kim and D.W. Weir

Naval Research Laboratory, Code 6370, Washington, DC 20375

ABSTRACT

The use of direct-write techniques in the design and manufacture of interconnects and antennas offers some unique advantages for the development of next generation commercial and defense microelectronic systems. Using a laser forward transfer technique, we have demonstrated the ability to rapidly prototype interconnects and various antenna designs. This laser direct-write process is compatible with a broad class of materials such as metals and electronic ceramics and its capable of depositing patterns of any of these materials over non-planar surfaces in a conformal manner. The laser direct-write process is computer controlled so as to allow any given design to be easily modified and adapted to a particular application. To illustrate the potential of this technique, examples of metal lines on laser micromachined polyimide substrates for interconnect applications, are discussed and evaluated. In addition, examples of simple planar and conformal antennas are provided to demonstrate how this technique can influence current and future microelectronic device applications.

Keywords: Laser Direct-Write, Laser Micromachining, Laser Forward Transfer, Conformal Antennas.

1. INTRODUCTION

Current trends for developing advanced electronic and sensor systems place great emphasis in achieving performance levels generally associated with integrated circuits. This requires further miniaturization, while enhancing the functionality and reliability of existing components. It also requires new strategies that can eliminate long lead times for fabricating prototypes and evaluating new materials and designs. These and other requirements have pushed traditional manufacturing techniques to their limits necessitating novel fabrication approaches for integrated microelectronic elements and systems.

The term direct-write refers to any technique or process capable of depositing, dispensing or processing different types of materials over various surfaces following a preset pattern or layout[1]. The ability to accomplish both pattern and material transfer processes simultaneously opens the door for the development and manufacturing of next generation commercial and defense microelectronic systems. The potential offered by direct-write techniques lie in their ability to transfer and/or process most materials over any surface with extreme precision, resulting in a functional structure or working device[2]. Direct-write technologies do not compete with photolithography for size and scale, but rather add a complementary tool for specific applications requiring rapid turnaround and/or pattern iteration, conformal patterning, or for modeling difficult circuits. Figure 1 provides a schematic comparing the steps required for generating a patterned structure onto a particular substrate for both traditional lithographic and direct-write processes.

During the past few years, our group at the Naval Research Laboratory has been developing a laser based direct-write process for both removal (laser micromachining) and addition of material (Matrix Assisted Pulsed Laser Evaporation Direct-Write or more recently Laser Direct-Write) for the fabrication of mesoscopic passive electronic devices[3,4],

---

[*] Correspondence: Email: pique@nrl.navy.mil; Telephone: (202) 767 5653; Fax: (202) 767 5301

miniature sensors[5,6] and micro-power sources[7,8]. In additive mode, our laser direct-write technique involves the forward transfer of materials from a UV transparent support to a receiving substrate. The transfers are performed by mixing the material to be deposited in liquid matrix to form an "ink". The ink is then applied to the UV-transparent support, forming the "ribbon". A focused UV laser pulse is directed through the backside of the ribbon so that the laser energy interacts with the ink at the support interface. Layers of matrix near the support interface evaporate due to localized heating from the laser-material interaction, which releases the remaining ink by gently and uniformly propelling it away from the support.

If instead, the processing requires the removal of material from the substrate, the laser direct-write system can be operated as a laser micromachining station by simply removing the ribbon and allowing the laser pulse to interact with the substrate. In this fashion, we are able to micromachine channels and through vias into polymer, semiconductor, and metal surfaces as well as trim deposited structures to meet design specifications. All micromachining and material transfer can be controlled by computer (CAD/CAM), which enables this tool to rapidly fabricate complex structures without the aid of masks or moulds. This technique, therefore, has the potential to fabricate complete prototype systems on a single substrate.

The fact that the source of material (the ribbon) and the source of energy (the laser) are decoupled from the substrate opens the possibility for the direct-write of materials over non-planar or conformal surfaces. The ability to deposit patterns of materials over conformal surfaces has always been a great challenge for lithographic process. In some cases,
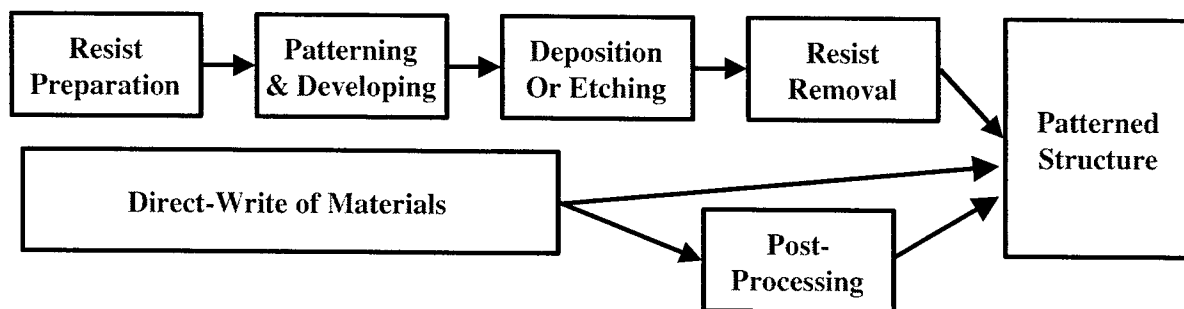
Figure 1. Schematic comparison between traditional photolithography and direct-write processes showing the steps required to generate a patterned coated surface. In some cases, the materials deposited by direct-write might require post-processing steps, indicated by the bottom path in the flowchart.

the conformal structure might just consist of a step or through hole on which material needs to be deposited, but in many other cases, conformal deposition might refer to a multi-curved, non-planar surface such as the housing of a cell phone. An example of an application for which the ability to generate a patterned conformal structure cannot be satisfied by lithographic techniques is in the fabrication of conformal antennas. Conformal antennas were originally developed for military applications where their aerodynamic and covert properties played key roles. The thin, unobtrusive nature of these antennas makes them ideally suited for relatively small platforms such as unmanned vehicles and portable or hand-held systems. However, the fabrication of antennas for such applications poses major challenges to currently available materials and manufacturing techniques. Direct-write processes, such as laser direct-write, circumvent these challenges, since they are capable of depositing patterns of materials over non-planar surfaces, which makes possible the fabrication of novel conformal antenna structures.

In this paper, the use of a laser direct-write process will be described for the deposition of silver metal patterns on various substrates (polyimide and glass) and examples of the various types of structures that can be generated over conformal surfaces will be presented. Finally, we will show how the laser direct-write technique can be used to fabricate novel conformal miniature antennas.

2. EXPERIMENTAL

The laser micromachining experimental setup is shown in Figure 2. The pulsed UV laser source for these experiments is a Nd:YVO$_4$ laser (Spectra Physics) operating at 355 nm with a frequency of 10 KHz and a pulse duration of 30 ns. The laser pulse passes through a series of focusing optics and a UV microscope objective before reaching the sample which is mounted on a vacuum chuck. The nominal laser spot size for micromachining in this setup is 25 μm in diameter. All the samples are irradiated at energies ranging from 3-30 μJ per pulse (~2-20 J/cm^2) with internal laser fluctuations of +/- 5% as measured by an energy-meter (Ophir Nova) monitoring the laser pulse energy during the experiment.

The spot-to-spot translation distance is controlled by an x-y motion control system (Aerotech D500) with a maximum x velocity of 115 mm/s and y velocity of 100 mm/s. An acousto-optic modulator (NEOS) is used to fix the dwell time between subsequent laser pulses. For all the experiments shown here, the time between pulses is 10 ms to allow for efficient stage operation and avoid cumulative heating effects. Inline video imagery enables sample alignment as well as real time monitoring of the micromachining process.

In the present study, polyimide (110 μm thick DuPont Kapton™ Type H) samples are irradiated at varying translation distances and laser energies. Substrates are cleaned with acetone and ethanol prior to laser micromachining. Trenches 1.25 cm long by 250 μm wide are machined at different translation distances in order to vary the depth. All experiments are performed at room temperature and ambient pressure where it has been shown that atmospheric conditions have no measurable influence on pulsed UV laser micromachining of polyimide[9].

The same apparatus is used to deposit conductive silver lines using a laser forward transfer direct-write technique described elsewhere[3,10]. A commercially available screen printing silver ink (Paralec Inc.) is spread in a 10 μm thick layer on a borosilicate blank that is then mounted above the machined substrate. The laser interacts with the ink and causes a forward transfer of material that lands on the waiting substrate 100 μm below. For deposition, the spot size is increased to 120 μm giving us a decreased laser fluence of ~0.1 J/cm^2. Conformal deposition over a variety of surface structures is easily obtained. Following deposition, the transferred ink is dried in an oven at 150 °C for 5 minutes.
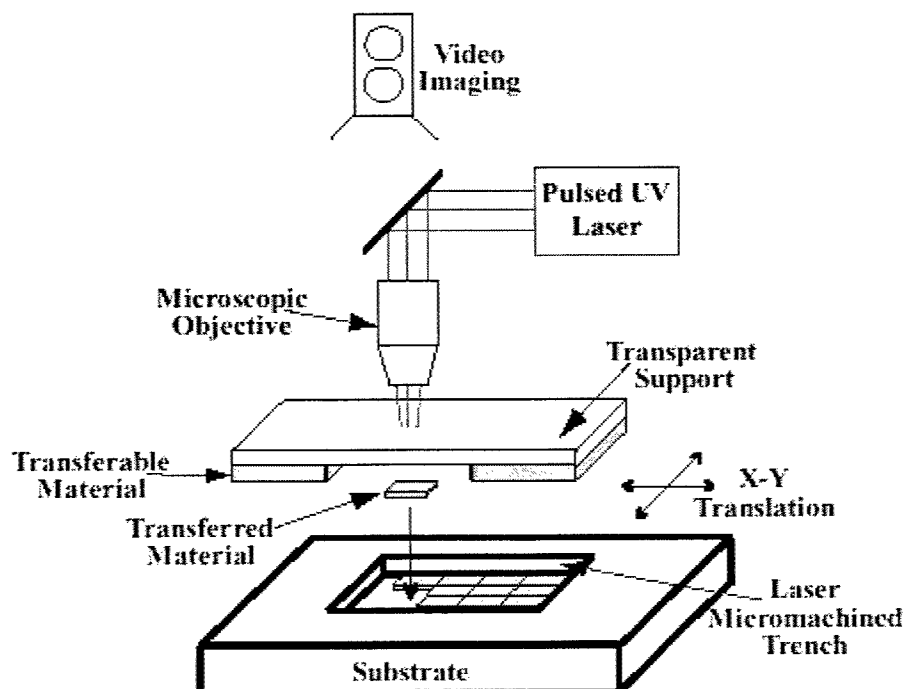
Figure 2. Schematic showing the components of a laser direct-write system capable of adding and subtracting material from a given substrate.

Surface characterization measurements are performed on samples after laser irradiation and after laser deposition without any additional substrate cleaning in order to preserve the surface structure. Depth and surface roughness measurements are performed using a stylus profilometer (Tencor Instruments P-10) with a 2 µm tip. Scanning electron microscopy (LEO 1550) is performed to further investigate surface features and morphology of the deposited patterns.

3. RESULTS AND DISCUSSION

3.1 Metal lines

Figure 3(a) shows an optical micrograph from a pair of silver lines that were deposited inside trenches with steps that had been generated by laser micromachining the polyimide substrate. The steps were carved by adjusting the translation distance at fixed laser energy of 30 µJ. Afterwards, using the laser direct-write process, we conformally deposited silver over the length of the trench and over the step, producing a layer that is on average 10 µm thick above the bottom laser machined trench. This can be seen from the profilometer scan results taken along the trench before and after the silver layer was deposited as shown in figure 3(b). As the scan shows, the silver deposited layer uniformly covers the step and the surface of the trench.
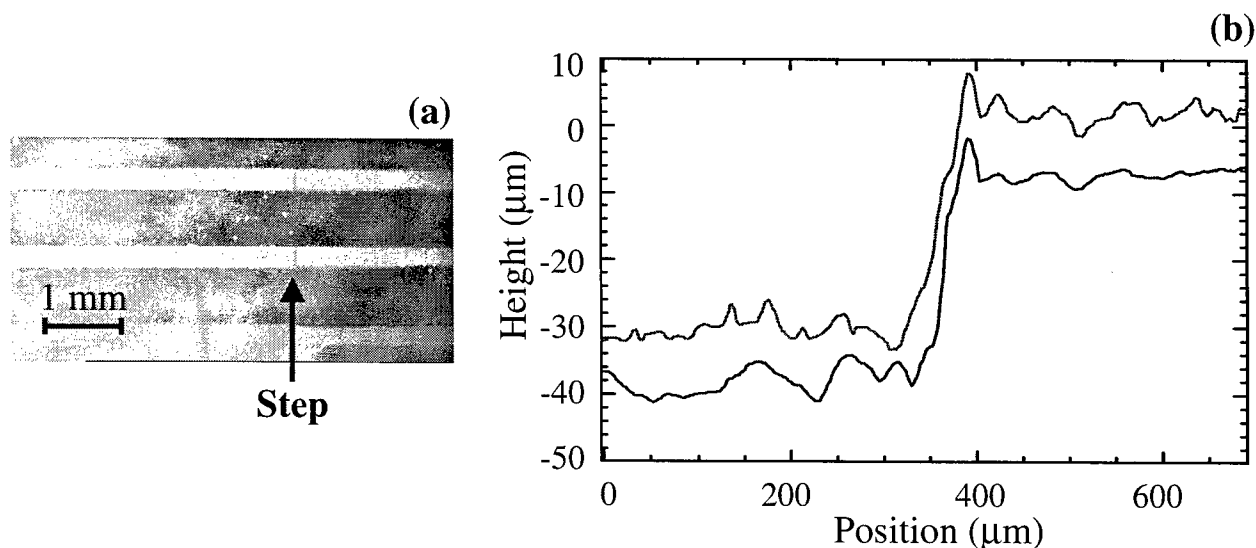
Figure 3. (a) Optical micrograph of silver lines deposited on trenches on polyimide substrates by laser direct-write. (b) Profilometer scan across the step before (lower trace) and after depositing the silver layer by laser direct-write (upper trace).

The adhesion of the silver metal lines was verified by subjecting the line to a scratch test using a #2 pencil and to the tape test using regular scotch tape. In both cases the silver lines survived without any noticeable signs of damage or metal loss. A four-point resistance measurement from one end of the silver line to the other showed that the laser-transferred films were electrically continuous, even across the step edges. Given the measured resistances, the length and average thickness of the silver lines we obtained a rough estimate for the resistivity of these silver lines to be about 40x that of bulk silver. Further characterization of these lines was performed by examining them under the SEM. Figure 4 shows an SEM micrograph of the region near the step in one of these lines. The image shows that pinholes are numerous in the laser transferred silver lines and are likely responsible for the high resistivities measured. In particular, this image shows that along the edge of the step, the density of pinholes is even higher.
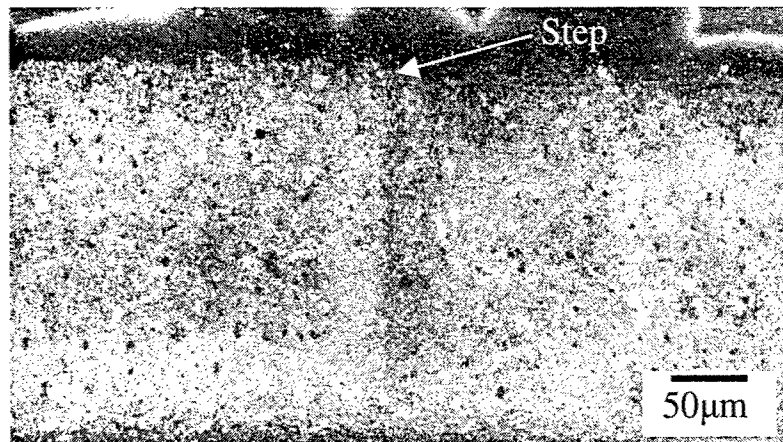
Figure 4. SEM micrograph of a silver line deposited by laser direct-write across a
step on a trench laser micromachined on a polyimide substrate.

It is worth noting that the resistivities calculated for the silver lines made by laser direct-write are of the same magnitude as the resistivities present on solder materials used for circuit boards. Furthermore, the laser direct-write process offers the unique ability to deposit the metal patterns over conformal surfaces with very uniform thickness, which becomes very important for making metal interconnects in 3D geometries typically found in vias, across layers and for connecting components to a circuit board.

3.2 Antennas

The ability to laser direct-write metal patterns can be used for the fabrication of antenna structures. Figure 5 shows optical micrographs of two simple planar antennas fabricated by depositing silver inks on glass substrates by laser direct-write. Figure 5(a) corresponds to a planar log-periodic spiral antenna, while Figure 5(b) shows a loaded half-wave dipole antenna. The dipole antenna was designed to resonate at a frequency of 4.7 GHz, which was in very good agreement with the measured resonant frequency of the sample antenna device shown in Figure 5(b).
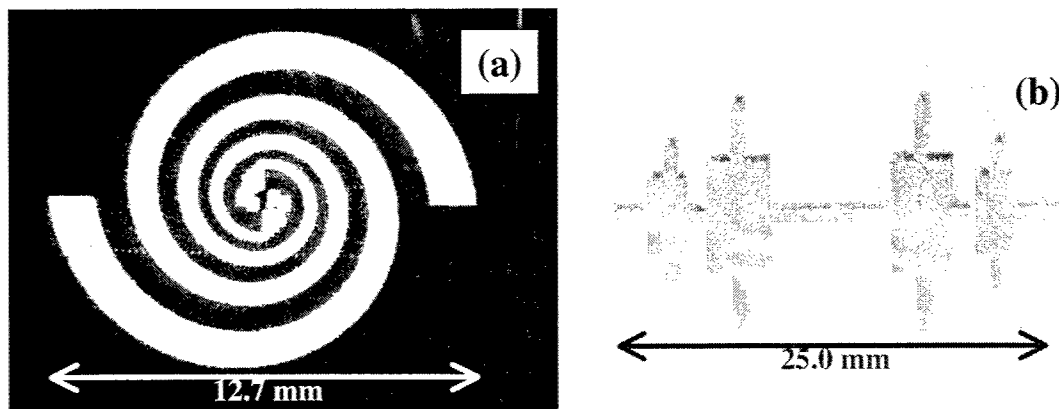
Figure 5. Sample planar antennas made by laser direct-write of silver on glass substrates: (a) log-periodic spiral and (b) loaded half-wave dipole.

To demonstrate the ability to deposit metal patterns over a conformal surface using the laser direct-write technique, we choose to deposit a simple spiral pattern over a plano-convex lens (f = 10 cm) as shown in Figure 6 (a). This simple pattern could be used as the radiating element for a spiral conformal antenna. This idea was taken a step further by depositing the spiral on a thin polyimide substrate and feeding the signal to the center of the spiral, resulting on a center-feed single arm spiral antenna operating in the 10-100 MHz range. The thin polyimide substrate was attached to the roof of a small toy car, thus conforming to the roof's non-planar surface, as shown in Figure 6(b). It should be pointed out

that our spiral antenna made by laser direct-write performed as well as the wire monopole antenna that is provided with the toy cars. However, the difference between both antennas becomes obvious when the low profile of the direct-write conformal antenna is contrasted with the wire antenna that protrudes 5 cm above the roof of the car.

4. SUMMARY

We have shown the use of a laser-based direct-write technique for generating patterns on various substrates by additive and subtractive direct-write processes. Laser micromachining was used to generate trenches and steps on polyimide substrates. Laser direct-write was used to deposit silver lines and patterns on polyimide and glass substrates. These lines are electrically conductive even over steps and curved surfaces. The versatility and CAD/CAM features of the laser direct-write technique can be used for the rapid prototyping and optimization of interconnects and vias, as well as conformal antennas.

5. ACKNOWLEDGEMENTS
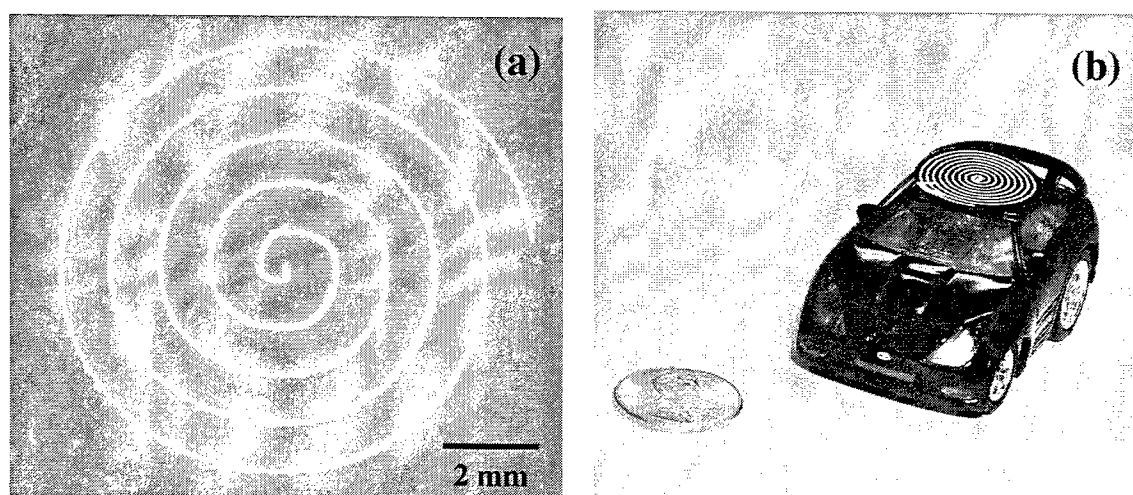
Figure 6. (a) Conformal spiral pattern made by laser direct-write of silver over a plano-convex lens with f = 10 cm. (b) Center-feed single arm spiral antenna used to operate toy car made by laser direct-write of silver onto a thin polyimide substrate.

6. REFERENCES

1. A. Piqué and D.B. Chrisey, editors, *Direct-Write Technologies for Rapid Prototyping Applications*, Academic, San Diego, 2001.
2. D.J. Nagel, "Technologies for Micrometer and Nanometer Pattern and Material Transfer", in *Direct-Write Technologies for Rapid Prototyping Applications*, edited by A. Piqué and D.B. Chrisey, p. 557, Academic, San Diego, 2001.
3. A. Piqué, D.B. Chrisey, R.C.Y. Auyeung, S. Lakeou, R. Chung, R.A. McGill, P.K. Wu, M. Duignan, J. Fitz-Gerald, and H. D. Wu, *SPIE Proceedings*, **3618**, 330, (1999).

4. A. Piqué, D.B. Chrisey, R.C.Y. Auyeung, J. Fitz-Gerald, H.D. Wu, R.A. McGill, S. Lakeou, P.K. Wu, V. Nguyen and M. Duignan, *Appl. Phys. A*, **69**, S279 (1999).

5. A. Piqué, D.B. Chrisey, J.M. Fitz-Gerald, R.A. McGill, R.C.Y. Auyeung, H.D. Wu, S. Lakeou, V. Nguyen, R. Chung and M. Duignan, *J. Mater. Res.*, **15**, 1872 (2000).

6. A. Piqué, D.W. Weir, P.K. Wu, B. Pratap, C.B. Arnold, B.R. Ringeisen, R.A. McGill, R.C.Y. Auyeung, R.A. Kant and D.B. Chrisey, *SPIE Proceedings*, **4637**, 361, (2002).

7. A. Piqué, K.E. Swider-Lyons, D.W. Weir, C.T. Love, R. Modi, *SPIE Proceedings*, **4274**, 317, (2001).

8. C.B. Arnold, R.C. Wartena, K.E. Swider-Lyons, and A. Piqué, *J. Electrochem. Soc.*, in press (2003).

9. J.H. Branon, J.R. Lankard, A.I. Baise, F. Burns, and J. Kaufman, *J. Appl. Phys, 58, 2036 (1985).*

10. D.B. Chrisey, A. Piqué, J.M. Fitz-Gerald, R.C.Y. Auyeung, R.A. McGill, H.D. Wu and M. Duignan, *Appl. Surf. Sci.*, **154**, 593 (2000).

Femtosecond laser ablation of gold in aqueous biocompatible solutions to produce colloidal gold nanoparticles

Andrei V. Kabashin[*], Michel Meunier
Laser Processing Laboratory, Department of Engineering Physics, Ecole Polytechnique de Montreal, Case Postale 6079, Succ. Centre-ville, Montreal, Quebec, Canada, H3C 3A7

John H.T. Luong
Biotechnology Research Institute, National Research Council Canada, Montreal, Quebec, Canada, H4P 2R2

ABSTRACT

Possibilities of the control of the size and size distribution of the colloidal gold particles produced by the 110-fs laser ablation from a gold plate in aqueous environment are studied. Compared to pure deionized water, significant reduction of the mean size and size dispersion of the produced particles was observed when the ablation was performed in aqueous solutions of cyclodextrins (CDs), while the efficiency of the size reduction depended on the concentration and type of the CD (α-CD, β-CD or γ-CD). In particular, ablation at 10 mM of β-CD led to a production of 2-2.4 nm particles with narrow size distribution of less than 1-1.5 FWHM, which were very stable under aerobic conditions without any protective agent present. In the UV-vis spectrum, the gold nanoparticles exhibited an absorption band at 520 nm due to the generation of plasmon resonances. The fabricated particles are of importance for biosensing applications.

Keywords: femtosecond laser ablation, gold nanoparticles, aqueous, cyclodextrins

1. INTRODUCTION

Having nanoscale size, gold colloidal particles possess several features that make them very attractive for intensive research in nanotechnology. In particular, 3-5 nm nanoparticles show a drastic decrease of the melting point[1,2] and display a highly selective catalytic activity for CO oxidation at -70 °C.[3] In addition, 1-500 nm nanoparticles exhibit a strong dependence of transmitted and reflected spectra on the nanoparticle size and a mean distance between them due to the generation of Mie resonances[4] and to quantum size effects (below 3 nm).[5] It is now actively discussed that gold nanoparticles can serve as efficient markers for selective biological interactions after an appropriate surface modification and linking with biological objects. In this case, the remarkable optical properties of gold colloids could give important sensing parameters to measure a biological interaction.

The gold colloids are generally fabricated by a chemical method, in which a diluted metal salt is reduced in aqueous solution with a reducing reagent.[6] This method enables to fabricate gold nanoparticles in the 10-20 nm diameter range with narrow size dispersion. However, the method is not free of contamination by-products, which complicate further stabilization and functionalization of the gold surface for biological immobilizations. Alternatively, laser-induced ablation from a solid target is known as an effective method to produce metal and semiconductor nanoparticles in a controllable, contamination-free environment. In particular, this method was successfully used for the deposition in inert gases of Si-based nanostructured films, whose photoluminescence properties were very attractive for Si-based optoelectronics applications[7-10]. On the other hand, ablating metals in a liquid environment, one can effectively produce colloidal metal nanoparticles in the liquid.[11,12] However, the size distribution of the nanoparticles in liquids tends to be broadened since the aggregation process of hot ablated atoms after the ablation process cannot be easily overcome.

---

[*]akabach@email.phys.polymtl.ca; phone 1-(514)340-4711 ext.4634 ; fax : 1-(514)340-3218

Therefore, several attempts have been made for the size control, including the ablation in liquid helium[13] and an additional irradiation of produced particles by a laser beam, of which wavelength is in the vicinity of the wavelength of the surface plasmon excitation of metal nanoparticles of interest (for gold nanoparticles λ = 520-530 nm).[14,15] In addition, aqueous solutions of surfactants such as sodium dodecyl sulfate (SDS) were used to control the particle growth, [16-20] which enabled to reduce the mean size of Au and Ag nanoparticles down to 4-8 nm and to minimize the particle size dispersion down to 5 nm. However, the fabrication of monodispersed gold nanoparticles in well-controlled, biologically friendly environment and appropriate termination of the gold surface is still under question.

In this paper, we adapted a femtosecond laser technique to ablate a gold target in aqueous solutions and study the possibilities of using important, biologically compatible materials to control the size and distribution of the produced colloidal particles. The test were performed with the use of neutrally charged cyclodextrins (α-CD, β-CD and γ-CD), torus-like macrocycles built up from glucose pyranose units, which are linked by α-1-4-linkages[21]. The femtosecond laser technique was employed with the anticipation to minimize the average particle size of ablated particles due to the absence of target heating effects.[22]

2. EXPERIMENTAL SETUP

The experiments were carried out with a Ti/Sapphire laser (Hurricane, Spectra Physics Lasers, Mountain View, CA), which provided 110 fs full width at half maximum (FWHM) pulses (wavelength 800 nm, maximum energy 1 mJ/pulse, repetition rate of 1 kHz). The radiation was focused by an objective with the focal distance of 7.5 cm onto a gold target, which was placed on the bottom of a 3-mL glass vessel filled with different aqueous solutions, as shown in Fig. 1. The thickness of the liquid layer above the rod was about 12 mm.

A gold rod (99.99%) from Alfa Aesar (Johnson Matthey Company, Ward Hill, MA) with the diameter of 6 mm and the height of 6 mm was used as a target in the experiments. The ablation experiments were carried out in pure deionized water and in aqueous solutions of α-cyclodextrin, β-CD, and γ-CD, which were obtained from Aldrich and used without further purification. All solutions were prepared from high-purity deionized water. CD solutions were prepared as stock solutions in appropriate buffers immediately prior to their use. The concentration of cyclodextrins was varied in different experiments: 0.01 M, 0.001 M and 0.0001 M.

A Transmission Electron Microscope (model Philips CM30, Philips Corp.) with 0.23 nm point-point resolution was used to take the electron images of the nanoparticles in the solution. A drop of a sample solution was placed on a carbon-coated copper grid. The drop was then dried at room temperature and the procedure was repeated 3 times. Normally, the diameters of 500-1000 particles were measured and the distribution of particle size (diameter) distribution was obtained. UV-Vis spectroscopic measurements were performed using a spectrophotometer (DU-640, Beckman) and room temperature in the range of 300-800 nm with a 1-cm optimal length cuvette.

110 fs. 800 nm
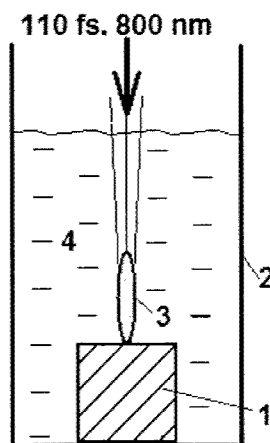
Fig. 1 Experimental setup: 1 – gold target, 2 –glass vessel, 3 – plasma plume, 4 – aqueous solution.

2. EXPERIMENTAL RESULTS

In our experiments, the ablation in liquids was accompanied by the presence of a plasma plume on the gold surface as easily observed by the naked eye. The plume intensity slightly decreased after several seconds of the ablation and then stabilized. The intensity decrease was probably related to certain absorption or scattering of the laser power by gold nanoparticles, which were formed and released to the bulk solution. However, no additional plume along the optical path due to the plasma ignition on separated gold particles was noticed. Besides, no plume was present on the water surface, suggesting that the fluence of the defocused laser beam on the surface was low enough to avoid the ignition of low threshold air optical breakdown.[23]

In pure deionized water, the ablation process led to visible changes of the solution color after several seconds into the ablation. The color was purple-red with some yellow tint. Figure 2 (a) shows a typical TEM micrograph and size distribution of gold nanoparticles obtained in deionized water at 0.8 mJ/pulse. Most of the particles had sizes of 40-70 nm, however, a rather broad size distribution ranging from 25 nm to 140 nm was noted. One can also reveal from the TEM micrograph that the periphery of larger particles was surrounded by small particles.
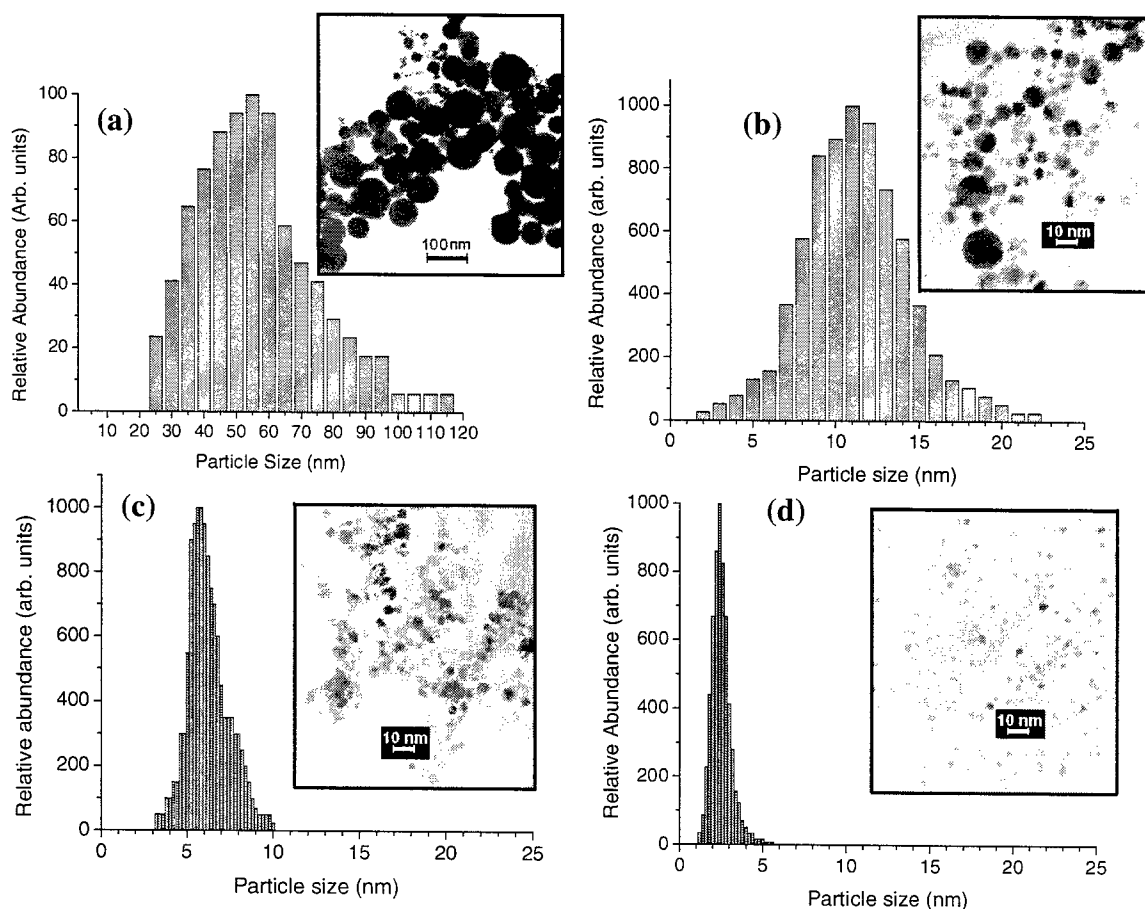
Fig. 2 TEM micrograph images and corresponding size distributions of gold particles prepared by the femtosecond laser ablation in deionized water (a) 0.0001 M β-CD (b), 0.001 M β-CD (c), 0.01 M β-CD (d). The laser energy was 0.8 mJ/pulse

However, the laser ablation in the presence of all three cyclodextrins led to quite different properties of the produced gold nanoparticles. At relatively low concentration of cyclodextrins, the process was accompanied by a deep red coloring of the solution. However, the increase of the CD concentration led to a certain decrease of the red color intensity. This was especially noticeable for 10 mM β-CD or γ-CD, which had only a pink color. An analysis of TEM micrographs clearly revealed that the presence of CDs in the solution led to a drastic decrease of the size of produced particles and their size dispersion, while the increase of the concentration of CDs reinforced the effect. As an example, Fig. 2 (b-d) demonstrates typical TEM micrographs of the produced particles and corresponding size distributions for different concentrations of β-CD. Moreover, the efficiency of size reduction depended on the type of CD. Our experiments showed β-CD provided the smallest particles with the narrowest particle size distribution, followed by γ-CD and α-CD, as one can see from Fig. 3. Ablation in 10 mM β-CD produced particles with the mean size of 2.1-2.3 nm (Figure 3 (a)) with a size dispersion less than 1 nm FWHM (Figure 3 (b)). For comparison, the laser ablation in the presence of 100 mM SDS led to much larger 4.6-8 nm particles with the dispersion of 5 nm FWHM.[16-19] Notice that chemical analysis performed in this study confirmed that not even traces of glucose, a major degradable products of CDs was present in the solution. In view of the very mild condition in laser ablation, it could be reasoned that CD molecules remained intact during the course of experiment.
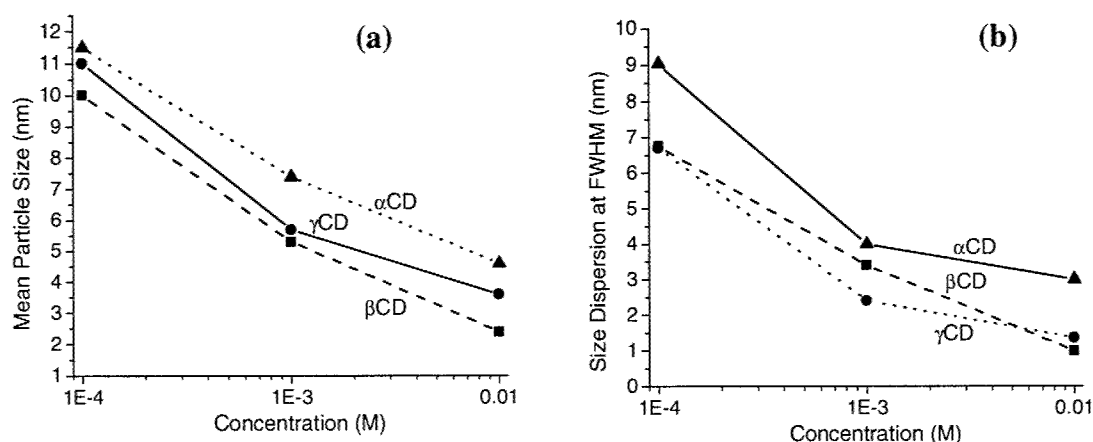
Fig. 3 Effect of the CD concentration on the resulting average particle size (a) and the size dispersion at FWHM (b).

In addition, optical absorption spectra of the samples were recorded. Just after the fabrication, gold colloids produced in deionized water and all cyclodextrins exhibited the characteristic peak of the surface plasmon resonance at 520-530 nm. In pure water, the absorbance measured at 520 nm retained only 7% of its original value after 5 days of aging in ambient conditions. Several precipitates were observed in the storage glass vial and the solution became dark blue, which confirmed that the nanoparticles continued to grow and/or aggregate with time in the solution. This behavior was due largely to the rapid increase in the attractive van der Waals force between nanoparticles as a function of their size. In contrast, gold colloids prepared in the presence of CDs exhibited good stability. In β-CD (0.1 to 10 mM in pure water), the 520 nm-peak height remained constant within this time window. The corresponding value for α-CD and γ-CD was 70% and 60%, respectively. Indeed, nanoclusters β-CD remained well dispersed in 10 mM β-CD for over 45 days with minimal loss of absorption intensity (5-7 %). This was very encouraging since all of the experiments were performed without any precaution taken, such as oxygen-free condition or under protective agents except for CDs.

3. DISCUSSION

It should be noted the mechanisms of the laser-induced ablation from a metal target and of a subsequent nanoparticle formation in aqueous environment are not yet clearly identified. However, some aspects of the phenomenon could be explained in terms of the dynamic formation mechanism suggested by Mafune and co-workers.[19] In brief, a dense cloud of gold atoms (plume) was accumulated in the laser spot of the gold target during the course of ablation. This core was made of a number of small gold atoms that were aggregated accidentally due to the density fluctuation to form embryonic nanoparticles. Even when the ablation process had been terminated, the aggregation continued at a

significantly slower growth rate until all atoms in the vicinity (~40 nm) of the embryonic nanoparticles were depleted.[19] As both ablated atoms and embryonic nanoparticles diffuse through the solution towards each other to form larger clusters, this consecutive nanoparticle growth was slow, random and could not be controlled. It has be proposed[19] that the presence of surfactants like SDS in the solution leads to a decrease of the concentration of free atoms or clusters due to the covering of their surfaces by the surfactant molecules. As a result, the growth of larger clusters decreases or stops.

A mechanism for the formation and/or stabilization of the gold nanoparticles by CDs is not yet clear. However, it was evident that CDs played a critical role in controlling the size as well as the stability of gold nanoparticles. The apolar cavity of the three CDs (internal diameter of 570, 780 and 950 pm, respectively) has been known to form inclusion complexes with various small hydrophobic molecules.[21] With such a dimension, it was very likely that a single gold atom (288 pm in diameter) could be enclosed in the CD cavity. In addition, CD molecules were also expected to bind to ablated atoms by chemisorption through multiple Au-O interactions, a mechanism similar to the binding of gold to resorcinarenes[24] to decrease the abundance of free ablated gold atoms in the plume. Embryonic nanoparticles formed in the plume became limited and had to compete with CD molecules for free ablated gold atoms in the vicinity of this region through diffusion. As CDs could form stable complexes with both free ablated atoms and embryonic nanoparticles, the consecutive particle growth due to the mutual coalescence between such objects was severely limited or terminated, particularly at high CD concentrations. This hypothesis was partly validated by the experimental data to confirm that the nanoparticle size and dispersion decreased with increasing CD concentrations. With the lowest aqueous solubility, β-CD should exhibit the strongest hydrophobic interaction with gold compared to both α- and γ-CD. Because both ablation and attachment of CD molecules to the surface of the developing Au particles took place almost simultaneously, the interplay between the kinetics of the two processes was likely the key factor that governed the average size diameter of the gold nanoparticles.

CONCLUSIONS

Femtosecond laser technique has been used to ablate a gold target in distilled deionized water and aqueous solutions of α-CD, β-CD or γ-CD in order to produce colloidal gold nanoparticles with no disturbing chemical impurities introduced. A drastic nanoparticle size reduction was recorded when the CDs were present in the solution. The gold nanoparticles demonstrated a good stability without an addition of any protective agent. To our knowledge, femtosecond laser and CDs have not been used for size control and stabilization of gold nanoparticles. This promising technique and can be extended for fabrication of other metal nanoparticles including multi-component ones with control of particle size distribution and particle morphology. The CD-modified gold nanospheres can also be used as multisite hosts for binding of hydrophobic guests in the solution.

ACKNOWLEDGEMENTS

REFERENCES

1. M. Takagi, *J. Phys. Soc. Jpn.* **9**, 359, 1954.
2. D. A. Buffat, J. P. Borel, *Phys. Rev. A* **13**, 2289, 1976.
3. M. Haruta, *Catalysis Today*, **36**, 153, 1997.
4. M. Kerker, The *scattering of light and other electromagnetic radiation*, Academic Press, New York, 1969.
5. U. Kreibig, M. Vollmer, *Optical Properties of Metal Clusters*, Springer-Verlag: Berlin, 1996.
6. M. A. Hyatt, Ed. *Colloidal Gold: Principles, Methods, and Applications*, Academic Press: New York, **3**, 1989.
7. I. A. Movtchan, R. W. Dreyfus, W. Marine, M. Sentis, M. Autric, G. Le Lay, N. Merk, *Thin Solid Films*, **255**, 286, 1995.
8. Y. Yamada, T. Orii, I. Umezu, S. Takeyama, T. Yoshida, *Jpn. J. Appl. Phys, Part 1*, **35**, 1361, 1996.
9. A. V. Kabashin, M. Meunier, R. Leonelli, *J. Vacuum Sci. Tech. B*, **19**, 2217, 2001.
10. A. V. Kabashin, J.-P. Sylvestre, S. Patskovsky, M. Meunier, *J. Appl. Phys.*, **91**, 3248, 2002.

11. A. Fojtik, A. Henglein, *Ber. Bunsen-Ges. Phys. Chem,* **97**, 252, 1993.
12. M. S. Sibbald, G. Chumanov, T. M. Cotton, *J. Phys. Chem.,* **100**, 4672, 1996.
13. J. L. Persson, Q. Hui, M. Nakamura, M. Takami, *Phys. Rev. A.,* **52**, 2011, 1995.
14. A. Takami, H. Yamada, K. Nakano, A. Koda, S. *Jpn. J. Appl. Phys.,* **35**, L781, 1996.
15. M. S. Yeh, Y. S. Yang, Y. P. Lee, H. F. Lee, Y. H. Yeh, S. S. Yeh, *J. Phys. Chem.,* **103**, 6851, 1999.
16. F. Mafune, J-Y. Kohno, Y. Takeda, T. Kondow, *J. Phys. Chem. B,* **106**, 8555, 2002.
17. F. Mafune, J-Y. Kohno, Y. Takeda, T. Kondow, H. Sawabe, *J. Phys. Chem., B,* **104**, 9111, 2000.
18. F. Mafune, J-Y. Kohno, Y. Takeda, T. Kondow, H. Sawabe. *J. Phys. Chem.,* **104**, 8333. 2000.
19. F. Mafune, J-Y. Kohno, Y. Takeda, T. Kondow, H. Sawabe *J. Phys. Chem. B.,* **105**, 5144, 2001.
20. Y.-H. Chen, C.-S. Yeh, *Colloids & Surfaces,* **197**, 133. 2002.
21. J. Szejtli, In *Comprehensive Supramolecular Chemistry,* Atwood, J.L., Davies, J.E.D., Macnicol, D.D., Vogtle, F., Eds.; Pergamon-Elsevier, New York, 1996; Vol. 3; pp. 5-40.
22. J. F. Ready, D. F. Farson, Eds.; *LIA Handbook of Laser Materials Processing,* Springer-Verlag and Heidelberg GmbH & Co., Berlin, 2001; pp. 499-508.
23. Y. P. Raizer, *Laser-Induced Discharge Phenomena,* Consultants Bureau, New York, 1977.
24. K. B. Stavens, S. V. Pusztay, S. Zou, R. P. Andres, A. Wei, *Langmuir,* **15**, 8337, 1999.

Fullerenes synthesis from carbon powder using CW-CO$_2$ laser

Seisuke Kano, Masamichi Kohno, Kaname Sakiyama, Shinya Sasaki, and Hirofumi Shimura
National Institute of Advanced Industrial Science and Technology (AIST)
Research Center for Advanced Manufacturing on Nanoscale Science and Engineering
Namiki 1-2-1, Tsukuba, Ibaragi 305-8564, JAPAN

ABSTRACT

A semi-continuous process for the synthesis of fullerenes is described. This novel process incorporated a carbon powder feed system in combination with a continuous-wave CO$_2$ laser irradiation source. The carbon powder contained no fullerenes but did contain graphite crystals and amorphous carbons of selected particle sizes (5, 10, or 20 μm), and selected irregular or spherical particle shapes. The method was successfully used to deposit C$_{60}$ and C$_{70}$ powders and films continuously. Laser irradiation of the carbon powder produced an observable laser plume. The experimental results and mechanism for the process are discussed.

Keywords: fullerene, carbon powder, CW-CO$_2$ laser, semi-continuous process, UV-Vis spectroscopy, Raman spectroscopy

1.   INTRODUCTION

Fullerene powders and films are produced industrially by many different methods. For example, synthesis can be achieved by an arc method [1] and laser irradiation method [2]. The production of fullerenes by these methods is usually a batch process. However, for industrial applications a continuous or semi-continuous process is considered to be an improvement because it enables the greatest possible process and production control. Of all the various possible techniques, laser processing methods have recently become popular because of the high energies obtained from the laser pulses. Usually, the fundamental or second harmonic of a nanosecond-pulsed Nd:YAG laser [3] is used to vaporize the graphite bulk. Some of the methods require an electronic-furnace to keep the laser-ablated carbon species at sufficiently high temperatures for a time period sufficient to produce deformation of the crystal structures [4]. CO$_2$ lasers have also been used to produce fullerenes [5], carbon nanotubes [6] and other forms of carbon [7] at room temperatures. Kasuya et al synthesized C$_{60}$ using 500 ms pulses from a CO$_2$ laser to vaporize a graphite bulk in an inert gas environment at room temperature [5]. Maser et al synthesized carbon nanotubes at room temperature using a CW-CO$_2$ laser to vaporize a graphite bulk [6]. Kokai et al also synthesized nanotubes using a millisecond-pulsed CO$_2$ laser ablation of a graphite bulk [8]. Almost all of the above experiments used pulsed lasers and solid graphite bulk targets. The disadvantage of the batch system is that it requires the target be exchanged periodically, and hence the system must be stopped for the period of the target replacement.

Furthermore, in the preparation of nanoparticles, such as fullerenes, it is important to keep the process conditions stable. We therefore have developed a semi-continuous process to synthesize fullerenes using a carbon powder feed system and CW- CO$_2$ laser irradiation system.

2. EXPERIMENTAL DETAILS

The semi-continuous synthesis of fullerenes using a carbon powder feed system and a continuous-wave CO_2 laser irradiation system are described below. The fullerene powders and films were prepared from carbon powder by means of irradiation with a high-power CO_2 laser (Mitsubishi ML-6050C). The laser power was fixed at 4.5 kW and the beam focused to a point. A schematic drawing of the experimental setup is presented in Figure 1. The carbon powder was carried through a stainless tube into a vacuum chamber and injected from the nozzle with the buffer gas into the vacuum chamber. The powder feeder was mechanically vibrated during the experiment to transport the powder smoothly. The inner diameter of the nozzle was 1.5 mm. After evacuating, the chamber was filled with buffer gas to a pressure of 30 or 200 Torr and maintained at this gas pressure using a vacuum pump system. A focused $CW-CO_2$ laser beam irradiated the carbon powder at room temperature. The laser beam produced a 3.0 mm diameter focal spot and the distance between the nozzle and the center of the beam was set to 2.0 mm.
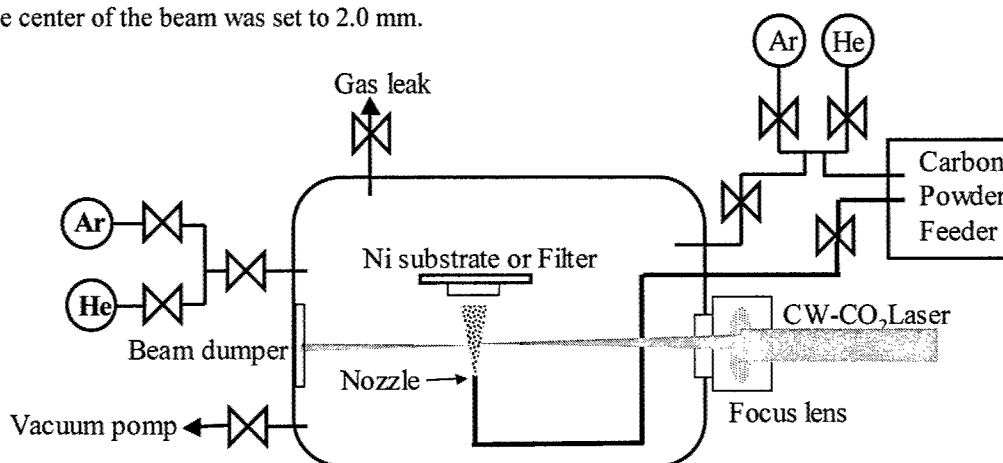
Figure 1 Schematic drawing of the system.

Carbon powders (Kojundo Chemical Laboratory and Japan Carbon) were used as the raw materials. The powders were selected and separated by their mean diameter into 5, 10, or 20 μm powders and their shapes were separated into irregularly shaped or spherically shaped particles. The powders were stored in a powder feeder with Ar-gas or He-gas and pressurized to 2 atmospheres.

Upon irradiation, the laser-irradiated powder collected on a piece of filter paper placed at the front of the nozzle using the middle-volume air sampling method. The collected laser-irradiated powder was dissolved in toluene and the absorption spectra for the powder measured in the UV-Vis (300 ~ 800nm) region. To synthesize a thin film, a Nickel substrate replaced the filter paper at the front of the nozzle. The distance between the substrate and the center of the focal spot was set to approximately 3.0mm. The laser-irradiated powder deposited on the substrate and formed a thin film. The thin films were analyzed using micro Raman spectroscopy in air at room temperature. The Ar ion laser beam (514.5nm) was carefully adjusted to sufficiently low powers (approximately 1 mW) to avoid changing the quality of the thin film.

3. RESULTS AND DISCUSSION

3.1 Starting materials

Fullerenes are easily obtained from fullerene containing carbons [9]. It is therefore necessary to determine the quantity of fullerenes in the carbon starting material. UV-Vis absorption spectroscopy and Raman spectroscopy are among the most commonly used analytical techniques for the detection of fullerenes. The UV-Vis absorption spectrum of the extracted

crude carbon powder in toluene solvent is shown in Figure 2. The absorption peaks distinctive for fullerenes were not observed in the crude carbon powder. We can therefore conclude that the concentration of fullerenes present in the powders was zero or so close to zero that it could not be detected. The Raman shifts of the crude carbon powders are shown in Figure 3. Only two significant peaks were observed, one at 1350 cm^{-1} corresponding to the "D-band" of the amorphous carbons and the other at 1590 cm^{-1} corresponding to the "G-band" of the graphite crystals. UV-Vis and Raman analysis indicated the irregularly shaped and spherically shaped carbons contained no fullerenes but did contain graphite crystals and amorphous carbons.
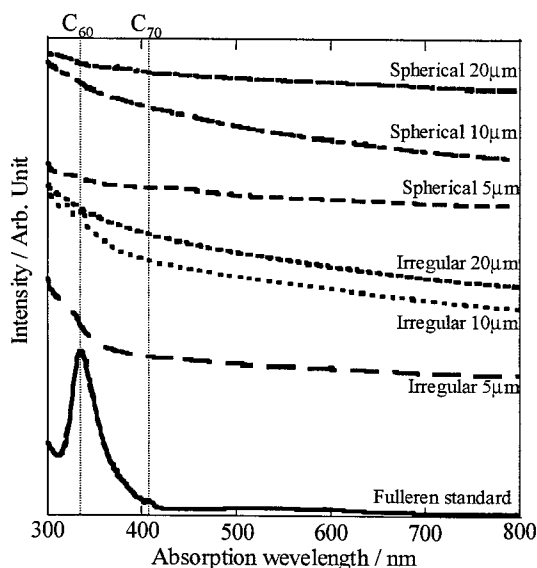
Figure 2 UV-Vis spectra of the crude carbon powders. Dotted lines show fullerenes absorption peaks.
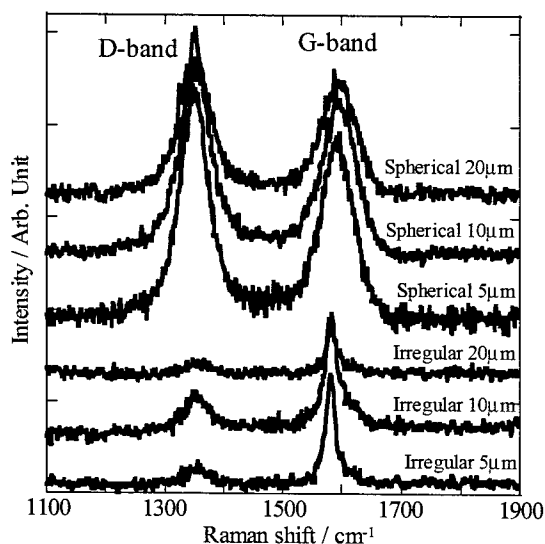
Figure 3 Raman spectra of the crude carbon powders.

3.2 Laser irradiated particles

The crude carbon powders were evaluated for graphite crystals and amorphous carbons. For a first comparison, the shape and size effects were investigated at a fixed laser powers and constant buffer gas conditions. The experiments were performed with the laser power fixed at 4.5 kW and the beam focused to a spot 3 mm in diameter. The chamber contained Ar buffer gas at 30 Torr. The laser irradiated powders were analyzed by UV-Vis absorption spectroscopy as shown in Figure 4. The UV-vis samples contained approximately the same concentration (30g/l) of the carbon powders in toluene. The absorption peak at 335 nm corresponded to the $\pi \rightarrow \pi^*$ transition of the C_{60} molecule [10, 11] and 378 nm peak corresponded to the C_{70} molecule [12]. The UV-Vis absorption spectra from the spherically shaped carbons showed smaller peaks at 335 nm than those from the irregularly shaped carbons.
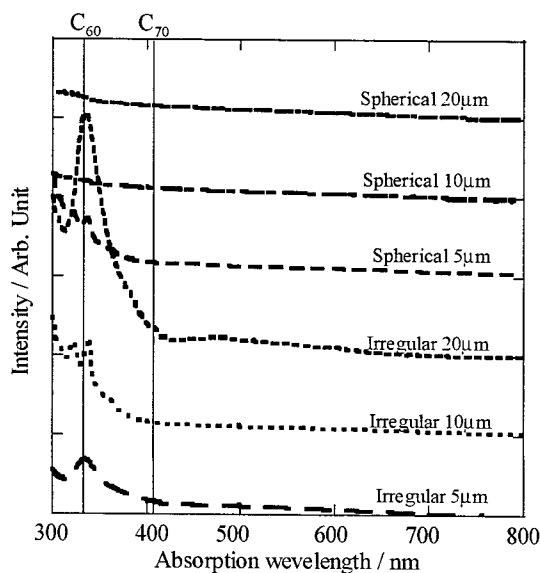
Figure 4 UV-Vis spectra of the laser irradiated carbon powders. Laser power at 4.5 kW and Ar buffer gas at 30 Torr.

The results indicate C_{60} molecules are formed much more easily from irradiation of irregular shaped carbon powders compared to the spherically shaped carbons powders under the specific process conditions described. For the irregular shaped powders the C_{60} absorption peak could be observed for even the smallest particle case (5 μm) which is half the size of the laser wavelength (10.6 μm). Hence, even small particles with particle sizes less than the laser wavelength were capable of absorbing the laser energy. The SEM images of the powder surfaces before and after laser irradiation are shown in Figure 5. For the spherically shaped carbons, laser irradiation resulted in no significant differences in the composition of the samples before and after irradiation. In contrast, the irregularly shaped carbons showed significant differences and the surface morphology of the samples changed upon laser irradiation for all sizes.

Further investigations were carried out into the effect of the atmospheric gas conditions on the properties of the shaped carbon samples. This investigation concentrated on the effect of the gas type and gas pressures using Ar-gas and He-gas at 30 Torr or 200 Torr for the irregularly shaped carbons of 5 μm diameter. The UV-Vis spectra of the laser irradiated powders at the following conditions; (a) Ar-gas at 30 Torr, (b) Ar-gas at 200 Torr, (c) He-gas at 30 Torr, and (d) He-gas at 200 Torr are shown in Figure 6. The experiments were performed at a fixed laser power of 4.5 kW and the beam focused to a 3 mm-diameter spot. For all four conditions, absorption peaks at 335 nm corresponding to C_{60} were observed.
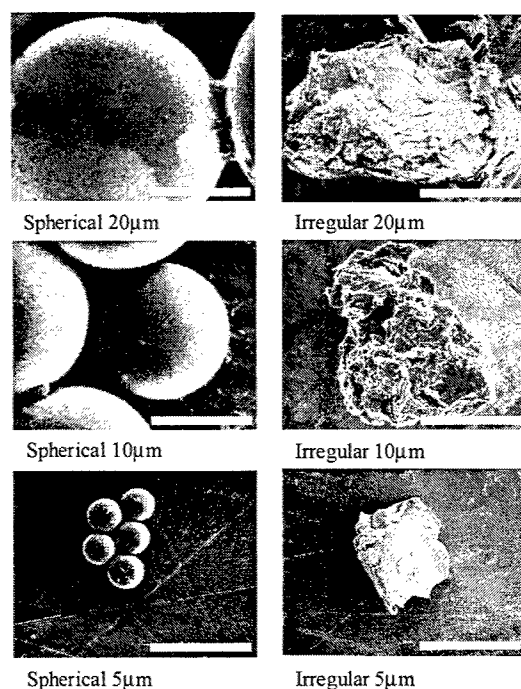
Figure 5 SEM images of laser irradiated carbon powders. Laser power at 4.5 kW and Ar buffer gas at 30 Torr. Scale bar shows 10 μm.
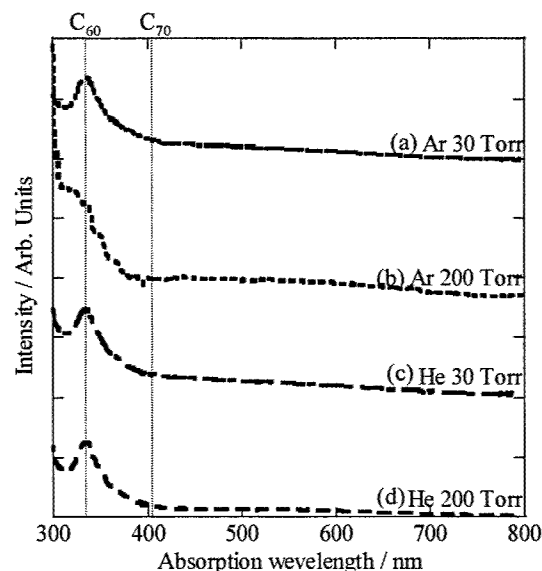
Figure 6 UV-Vis spectra of (a) Ar-gas at 30 Torr, (b) Ar-gas at 200 Torr, (c) He-gas at 30 Torr, and (d) He-gas at 200 Torr. Laser power at 4.5 kW and focused to 3 mm in diameter.

3.3 Film formation

The UV-Vis spectroscopy results are of interest because they act as a guide to understanding what type of powders and conditions are necessary for the successful synthesis of fullerene containing thin films, using the semi-continuous method. The analytical techniques of Raman spectroscopy and optical microscopy were used to analyze and observe the films.

A typical Raman spectrum of the synthesized film on the Ni-substrate at 30 and 200 Torr of Ar-gas and He-gas using the 5 μm irregularly shaped carbon powder is shown in Figure 7.

In addition to the D-band and G-band of the graphite (arrows), a peak at $1469 cm^{-1}$ (dotted line) can be clearly observed and assigned to the Ag-mode of C_{60} [13], indicating that the film contained C_{60}. The lower two Raman spectra were obtained from films that were laser-irradiated and deposited under He-gas conditions. In these spectra, the Ag-mode of C_{60} could be observed as a small peak between the D-band and G-band of the graphite. On the other hand, the upper two Raman spectra were obtained from films which were laser-irradiated and deposited under Ar-gas conditions. In these spectra, a sharp peak that correlated to the Ag-mode of C_{60} could be observed as a small peak between the D-band and G-band of the graphite. The results show that at low pressures the peaks due to graphite were still present while at the same time small peaks due to fullerenes appeared. At higher pressures the graphite peaks can be recognized as the shoulder of the peaks at $1335 cm^{-1}$ and $1568 cm^{-1}$. These peaks and other asterisk-marked peaks can be assigned to vibrational modes of C_{70} [14], and indicate the presence of C_{70} in the film.

Figure 7 Raman spectra of the synthesized thin film on the substrate at 30 and 200 Torr of Ar-gas and He-gas using irregularly shaped carbon powder as the crude material.

A comparison of the experiments under a Ar-gas atmosphere with those under a He-gas atmosphere revealed that the synthesis of the fullerene film is most successful in the Ar-gas atmosphere. The deposition of the fullerene film increased at higher pressures of Ar-gas (200 Torr pressure) compared to 30 Torr. Therefore, 200 Torr was the better operating pressure.

The film surface images and optical microscope images for the irregularly shaped laser irradiated powders (5 μm mean diameter) are presented in Figure 8, with the following experimental conditions; (a) Ar-gas at 30 Torr, (b) Ar-gas at 200 Torr, (c) He-gas at 30 Torr, and (d) He-gas at 200 Torr. The experiments were carried out at a constant laser power of 4.5 kW and the laser beam focused to a spot of 3 mm in diameter. In Figures 8(a) and 8(d), remarkable features were observed (see enclosed square and circle). In the square, black grains were observed and their shapes and morphologies were found to be very similar to that of the crude carbon powder. The Raman spectra from the black grains and those around them showed mostly graphite patterns. The grains were also observed in figures 8(a), 8(c), and 8(d). Figure 8(a) demonstrates that the grains were present, but occurred in smaller amounts and were diffused over a wide area.

Figure 8 Optical microscope images of the film surface under the following conditions: (a) Ar-gas at 30 Torr, (b) Ar-gas at 200 Torr, (c) He-gas at 30 Torr, and (d) He-gas at 200 Torr. The laser power was 4.5 kW and focused to 3 mm in diameter. Circles and square in (a) and (d) indicate remarkable shapes in the images.

In contrast, Figure 8(c) shows the substrate surface covered with black grains in a pattern that indicated the grains had aggregated together. In the circle, irregularly shaped particle thin films were observed which had a semi-transparent appearance. The Raman spectra of the semi-transparent thin films and their surrounding area included fullerene peaks. The films are shown in Figures 8(a), 8(b), and 8(c). Figure 8(a) shows that the semi-transparent films are observed and that a large part of the substrate surface had been covered with the films. Figure 8(b) shows the substrate surface covered with the semi-transparent films. The optical observations for the deposited films strongly support the results and conclusions obtained from the Raman spectra of the deposited films.

To understand the difference between the process conditions, the laser plumes were observed and their light emission spectra measured. Figure 9 shows the plumes observed under four conditions; (a) laser irradiation at 30 Torr in Ar-gas, (b) at 200 Torr in Ar-gas, (c) at 30 Torr in He-gas, and (d) at 200 Torr in He-gas. The configuration of the nozzle, carbon powder jet, and laser beam is shown in Figure 9 (left side). Higher pressures produced a brighter plume compared to the plume at lower pressures. The retention time of the laser-irradiated powder in the plume can be estimated from the length of the plume and the velocity of the jet. After considering the difference in the velocity of the buffer gases it can be determined that the laser-irradiated powder remained in the plume for longer times for Ar-gas compared to He-gas. The estimated time is of the order of hundreds of microseconds in both cases. The temperature of the plume could be determined from the light emission spectra of the plume and a simple calculation determined the temperature to be approximately 3500 °C. The time period and temperatures of the plumes determined in our experiments were in agreement with similar values previously found in C_{60} synthesis methods. Previous experiments and discussions by other research groups have suggested that it is important for the carbon vaporization by the laser to be kept at temperatures over 1000 °C for longer than a time of 400 microseconds [15, 16] to undergo the reformation into C_{60}.
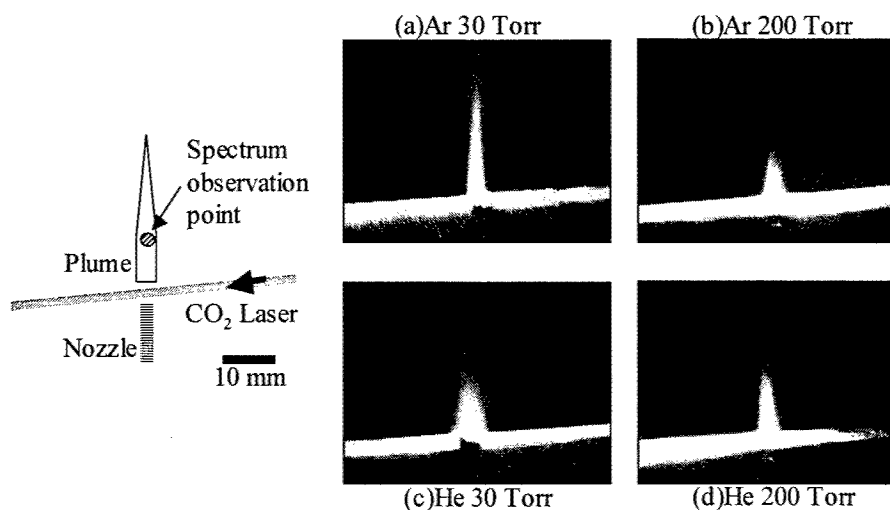
Figure 9 Plumes images of process. A schematic diagram of the measurement for plume is shown in left side. Spectrum of the plume was measured at 10 mm distance from the laser beam.

The process temperature of our experiments could be calculated from the light emission spectrum, which is mainly black body radiation. The process temperature is higher than the vaporization temperature of carbon. Therefore, the vaporized carbon would be carried with hot carbon powder in the plume above 1000 °C. The relative distance from the center of the laser beam to the deposition substrate is approximately 5 mm. If the carbon vaporized during the laser beam, it would take several tens of microseconds in order to move from the beam to the substrate surface. This time is shorter than the previous prediction, but the experimental results show that the carbon changed into fullerenes. The results

indicate that the time period of the experiment is shorter compared to many similar experiments previously reported by other groups but in compensation the temperatures in our experiments were higher.

In addition to temperature and time, the density of the vaporized carbon species is dependent on the type and pressure of the buffer gas and the extent of evaporation of the vaporized carbon species. If a large quantity of vaporized carbon species is produced, such as in the continuous arc discharge method [1], He-gas is the appropriate buffer gas. When only small quantities of the vaporized carbon species is produced, such as in nanosecond-pulsed Nd:YAG laser ablation [3] or millisecond-pulsed arc discharge methods [16], Ar-gas is the appropriate buffer gas. The SEM observation of the laser-irradiated carbon-powder showed that the surface morphology changed to be more smoother after irradiation but the grain size remained of the order of micrometers. This result suggested that the quantity of vaporized carbon was small. Therefore, in this study Ar-gas should be a better buffer gas than He-gas for the synthesis of fullerenes.

4. CONCLUSIONS

A new method for the semi-continuous synthesis of fullerenes is described using a CW-CO_2 laser and carbon powders. The fullerene products were identified by UV-Vis absorption and Raman spectroscopy. The C_{60} and C_{70} powders and films were successfully deposited using a novel semi-continuous process. Argon buffer gas environments were found to produce better results than Helium gas environments. The high pressure (200 Torr) increased fullerene formation, compared to the lower pressure (30 Torr). The formation of deposited films from the amorphous carbon and graphite powder for the irregularly shaped particles could be achieved at even the smallest particle size of 5 μm mean diameter, half the size of the wavelength of CW-CO_2 laser.

ACNOWLEDGEMENTS

REFERENCES

1.   R. E. Haufler, J. Conceicao, L. P. F. Chibante, Y. Chai, N. E. Byrne, S. Flanagan, M. M. Haley, S. C. O'Brien, C. Pan, Z. Xiao, W. E. Billups, M. A. Ciufolini, R. H. Hauge, J. L. Margrave, L. J. Wilson, R. F. Curl, and R. E. Smalley, "Efficient production of C_{60} (buckminsterfullerene), $C_{60}H_{36}$, and the solvated buckide ion" *J. Phys. Chem.* **94**, pp 8634-8636, 1990.

2.   L. Laska, J. Krasa, L. Hamplova and L. Soukup, "Fullerene production driven by long-pulses of near-infrared laser radiation", *Carbon* **34**, pp 363-368, 1996.

3.   R. E. Haufler, Y. Chai, L. P. F. Chibante, J. Conceicao, C. Jin, L. S. Wang, S. Maruyama, and R. E. Smalley, "Carbon arc generation of C_{60}", *Mat. Res. Soc. Symp. Proc.* **206**, pp 627-637, 1991.

4.   T. Wakabayashi, D. Kasuya, H. Shiromaru, S. Suzuki, K. Kikuchi, and Y. Achiba, "Towards the selective formation of specific isomers of fullerenes: T- and p-dependence in the yield of various isomers of fullerenes C_{60}-C_{84}", *Z. Phys.* **D40**, pp 414-417, 1997.

5. D. Kasuya, F. Kokai, K. Takahashi, M. Yudasaka, and S. Iijima, "Formation of C_{60} using CO_2 laser vaporization of graphite at room temperature", *Chem. Phys. Lett.*, **337**, pp 25-30, 2001.

6. W. K. Maser, E. Munoz, A. M. Benito, M. T. Martinez, G. F. de la Fuente, Y. Maniette, E. Anglaret, and J.-L. Sauvajol, "Production of high-density single-walled nanotube material by a simple laser-ablation method", *Chem. Phys. Lett.*, **292** , pp 587-593, 1998.

7. S. Iijima, M. Yudasaka, R. Yamada, S. Bandow, K. Suenaga, F. Kokai and K. Takahashi, "Nano-aggregates of single-walled graphitic carbon nano-horns", *Chem. Phys. Lett.* **309**, pp 165-170, 1999.

8. F. Kokai, K. Takahashi, M. Yudasaka, R. Yamada, T. Ichihashi, and S. Iijima, "Growth Dynamics of single-wall carbon nanotubes synthesized by CO_2 laser vaporization", *J. Phys. Chem.* **B103**, pp 4346-4351, 1999.

9. P. C. Eklund, A. M. Rao, Y. Wang, P. Zhou, K.A. Wang, J. M. Holden, M. S. Dresselhaus, and G. Dresselhaus, "Optical properties of C_{60}- and C_{70}-based solid films", *Thin Solid Films*, **257**, pp 211-232, 1995.

10. S. Leach, M. Vervloet, A. Despres, E. Breheret, J. P. Hare, T. J. Dennis, H. W. Kroto, R. Taylor, and D. R. M. Walton, "Electric spectra and transitions of the fullerene C_{60}", *Chem. Phys.* **160**, pp 451, 1992.

11. S. Kazaoui, R. Ross, N. Minami, "In situ photoconductivity behavior of C_{60} thin films: wavelength, temperature, oxygen effect", *Solid State Commun*, **90**, pp 623-628, 1994.

12. J. P. Hare, H. W. Kroto, and R. Taylor, "Preparation and UV/visible spectra of fullerenes C_{60} and C_{70}", *Chem. Phys.* **177**, pp 394-398, 1991.

13. A. M. Rao, P. Zhou, K.-A. Wang, G. T. Hager, J. M. Holden, Y. Wang, W.-T. Lee, X.-X. Bi, P. C. Eklund, D. S. Cornett, M. A. Duncan, and I. J. Amster, "Photoinduced polymerization of solid C_{60} films", *Science* **259**, pp 955-957, 1993.

14. D. S. Bethune, G. Meijer, W. C. Tang, and H. J. Rosen, "The vibrational Raman spectra of purified solid films of C_{60} and C_{70} ", *Chem. Phys. Lett.* **174**, pp 219-222, 1990.

15. R. Taylor, G. J. Langley, H. W. Kroto, and D. R. M. Walton, "Formation of C_{60} by pyrolysis of naphthalene", *Nature,* **366**, pp 728-731, 1993.

16. T. Sugai, H. Omote, and H. Shinohara, "Production of fullerenes by high-temperature pulsed arc discharge", *Eur. Phys. J.* **D9**, pp 369-372, 1999.

Optical patterning of individual organic/inorganic nanoparticles in solution at ambient temperature

Syoji Ito, Hiroyuki Yoshikawa, Hiroshi Masuhara

Dept. of Applied Physics and Handai Frontier Research Center, Osaka Univ., 2-1 Yamada-oka,

Suita, Osaka, Japan 565-0871

ABSTRACT

Laser manipulation technique was applied to patterning of single nanoparticles onto a substrate one by one in solution at room temperature. Individual polymer nanoparticles were optically manipulated to the surface of glass substrate in ethylene glycol solution of acrylamide, N,N'-methylenebis(acrylamide), and commercial radical photoinitiator. An ultra violet (UV) laser beam was focused to the nanoparticle, which led to generation of sub-μm sized acrylamide gel around the particle. The polymer nanoparticles were incorporated into the polymerized gel and fixed onto the substrate. A single gold nanoparticle was optically trapped and moved to the surface of the glass substrate in ethylene glycol. Additional irradiation of the UV laser light induced transient melting of the particle, resulting in its adhesion to the substrate. By the use of the present methods, arrangement of individual polymer and gold nanoparticles on any pattern was achieved.

Keywords: laser manipulation, fixation, nano-patterning, polymer nanoparticle, gold nanoparticle, photopolymerization, transient melting, laser ablation

1. INTRODUCTION

Since nanoparticles show specific and interesting properties originating from their intermediate size between single atoms/molecules and bulk, systematic studies on nanoparticles have been conducted extensively by many researchers. In many cases, however, measurements on nanoparticles have been performed for their ensemble, so that distributions in size, shape, defect, and so on cannot be analyzed directly. It is important, indispensable, and strongly required to manipulate, characterize, and fabricate individual nanoparticles, which makes it possible to understand properties of nanoparticles as functions of size, shape, microscopic environment, and so forth. In such a single-nanoparticle-experiment, manipulation and fixation of individual nanoparticles is considered one of key techniques. It is quite ordinary to apply scanning tunneling microscope and atomic force microscope (AFM) under vacuum at low temperature at the present stage of investigation, while manipulation, characterization, and fixation technique of individual nanoparticles in solution at room temperature is expected to be more fruitful.

It is well known that a fine particle dispersed in solution is trapped at the focal point when a tightly focused laser beam is irradiated to it. The technique was first demonstrated by Ashkin in 1986 [1,2], and now it is generally called laser trapping or optical tweezers. In the past decade, laser trapping has been further developed to a three-dimensional laser manipulation technique [3 - 5], which has been applied to chemistry, physics, biology and so on [6]. Laser manipulation is a very useful method to handle small objects in small domains. In the past few years, we have been extending the laser manipulation technique to handle nanoparticles and polymer chains in solution. Actually, we have already demonstrated that 10 ~ 20 nm sized entangled polymer chains could be trapped and assembled in solution at the focal point of a trapping beam [7 - 11]. Recently, we have shown that multiple nanoparticles in solution can be gathered and localized at the small area with the size of beam spot of a trapping laser beam, and also they can be aligned and fixed onto the substrate with the laser manipulation technique [12]. In addition, patterning of single metallic nanoparticles

was also achieved [13]. In this paper, we describe our recent results on laser patterning of individual organic (polymer) and metallic (gold) nanoparticles in solution at room temperature by means of local photoreaction induced by focusing UV laser pulse.

2. LASER TRAPPING OF NANOPARTICLES

When we consider interaction between a nanoparticle and near IR light, the nanoparticle can be regarded as a point dipole (Rayleigh approximation) and the photon force (F_{photo}) acting on it is given by eq.(1).

$$F_{photo} = F_{grad} + F_{scat} + F_{abs} \qquad (1)$$

Here, F_{grad}, F_{scat}, and F_{abs} are called gradient force, scattering force, and absorption force, respectively. The scattering force and absorption force are caused when the incident light is scattered and absorbed by the particle, respectively. Both push the particle toward the direction of light propagation. On the other hand, the gradient force is exerted when a particle is placed in a heterogeneous electric field of light. If the refractive index of a particle is higher than that of surrounding medium, the gradient force acts on the particle and push it toward the higher intensity region of the beam. In the case of laser trapping of nanoparticles, including metallic nanoparticles, the magnitude of gradient force is much larger than the scattering force and absorption force. Consequently, the particle is trapped at the focal point of the trapping laser beam where the beam intensity (electric field intensity) is maximum. The photon force is approximately expressed as follows [14].

$$F_{photo} \cong F_{grad} = \frac{1}{2} \varepsilon_m |\hat{a}| \, |\nabla \, E|^2 \quad , \qquad (2)$$

$$\hat{a} = 3V' \frac{\hat{e}_p - e_m}{\hat{e}_p + 2e_m} \quad , \qquad (3)$$

and

$$V' = 4\pi \int_0^R r^2 \exp\left(\frac{r-R}{\delta}\right) dr \quad , \qquad (4)$$

where E is the electric field of the light, $\hat{a}$ is the polarizability of the particle, $\hat{e}_p$ is the complex dielectric constant of the particle, e_m is the dielectric constant of medium, V' is the effective volume of the particle, R is the particle radius, and δ is the skin depth given by $\delta = \lambda_0 / 2\pi\kappa_p$ (λ_0: the wavelength in vacuum, κ_p is imaginary part of refractive index of the particle). Of course in trapping transparent dielectric nanoparticles such as polymer nanoparticles, we consider only the real part of dielectric constant and real particle volume.

3. EXPERIMENTAL

3.1 Samples

As a sample for fixation of polymer nanoparticles, polystyrene latex particles (PSt) with fluorescent dye (Polyscience, Fluoresbrite™ Yellow Green Carboxylate Microspheres, diameter ~ 220 nm) were dispersed in ethylene glycol containing acrylamide (AA) (Fluka), N,N'-methylene bis(acrylamide) (MBA) (Fluka), and Irgacure2959 (Ciba Specialty Chemicals) which are
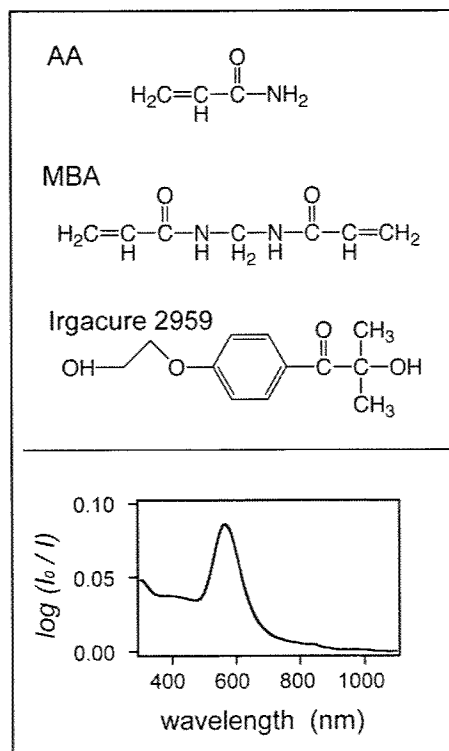
Figure 1. Chemical structures of acrylamide (AA), N,N'-methylene bis(acrylamide) (MBA), and Irgacure 2959. An extinction spectrum of 80-nm-gold nanoparticles (bottom).

polymerizable vinyl monomer, crosslinker, and radical photoinitiator, respectively. Concentrations of AA, MBA, and Irgacure2959 were adjusted to be 31, 2.2, and 3.3 wt%, respectively. Chemical structures of these compounds are shown in Figure 1. Concentration of polymer nanoparticles was adjusted $\sim 5.0 \times 10^{-4}$ vol%. In case of fixation of gold nanoparticles, gold colloid (British BioCell, EM.GC80, diameter $\sim$ 80 nm, 1.1×10^{10} particles/ml) were diluted five times ($\sim 2.2 \times 10^9$ particles/ml) with ethylene glycol. An extinction spectrum of the gold nanoparticles is also shown in Figure 1. The trapping laser beam (1064 nm) is little absorbed by the particles. On the other hand, the fixation laser pulse (355 nm) is efficiently absorbed by them. Concentration of the nanoparticles was adjusted to avoid the situation that more than two nanoparticles were trapped together during the fixation procedure.

3.2 Experimental setup

A schematic diagram of our experimental setup for optical manipulation and fixation of individual nanoparticles is shown in Figure 2. A TEM_{00} linearly polarized near infrared (IR) light from cw-Nd^{3+}:YAG laser (Spectron Laser Systems, SL-902T, wavelength $\sim$ 1064 nm) was introduced to an optical microscope (Nikon, Optiphoto2) through the external lenses (L1 and L2) and focused into the sample solution by an objective ($\times 100$, numerical aperture (NA) = 1.30). UV laser light from a Q-switched Nd^{3+}:YAG laser (Spectron Laser Systems SL-282G, wavelength $\sim$ 355 nm. pulse duration $\sim$ 6 ns, repetition rate $\sim$ 5 Hz) or a diode pumped UV pulsed laser (Nanolase, NV-0021x-100, pulse duration $\sim$ 0.5 ns, repetition rate $\sim$ 8 - 13 kHz, wavelength $\sim$ 355 nm) was combined coaxially with the near IR laser beam and introduced to the microscope. The near IR and UV laser beams were used for trapping and fixation of individual nanoparticles, respectively. The external lenses (L1 and L2) were used to determine the divergence of the beams and to adjust the location of the focal spots at the focal plane under the objective. Location of the beam spots (near IR and UV light) could be adjusted independently. A He-Ne laser (632.8 nm) was used for optical alignment and monitoring trapped nanoparticles by detecting back scattered red light from the particle. Experimental processes in a sample solution were observed by a charge coupled device (CCD) camera attached on the microscope. The microscope had an illumination unit (Nikon, EFD2) of super high-pressure mercury lamp so that fluorescence images could also be acquired.
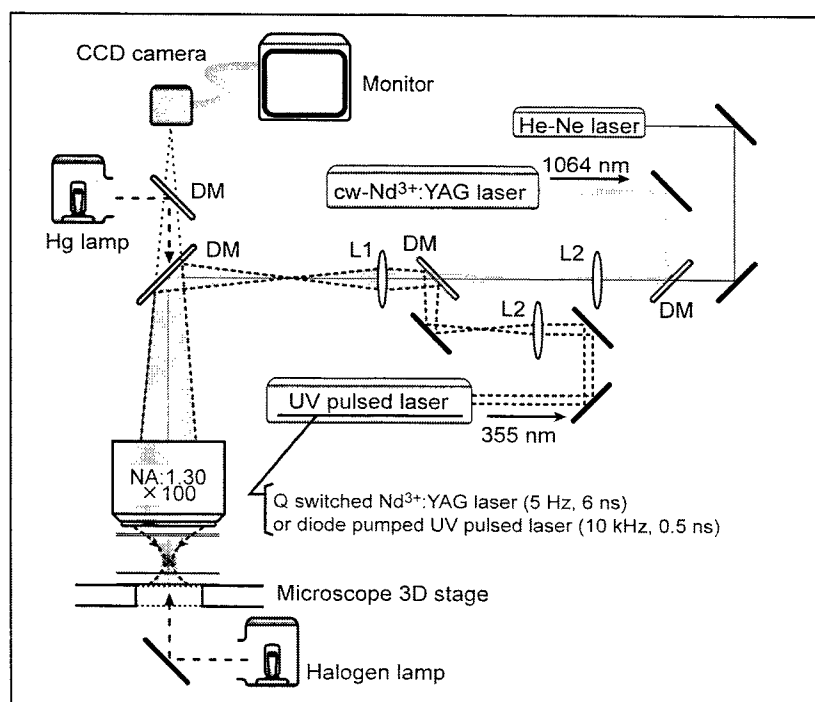
Figure 2. Experimental setup for laser manipulation and patterning of individual nanoparticles in solution.

4. PHOTOCHEMICAL FIXATION OF POLYMER NANOPARTICLES

When the sample solution was illuminated by blue light from the super high-pressure mercury lamp, individual polymer nanoparticles were observed as bright spots of yellow-green moving about randomly. Then the near IR laser beam was introduced into the solution. A polymer nanoparticle that accidentally entered the irradiated region was trapped at the focal point. The nanoparticle was moved to the certain point on the surface of glass substrate (Matsunami, micro slide glass, S-1111) by handling the microscope 3D stage. Additional irradiation of the UV laser pulse induced local photopolymerization just around the nanoparticle, resulting in generation of sub-μm sized acrylamide gel containing the nanoparticle on the substrate. After the fixation procedure, the substrate was washed with distilled water and fluorescence image of the acrylamide gel on the substrate in distilled water was acquired. Then the substrate was dried in the experimental room and topographic image of the gel was obtained by the atomic force microscope (AFM, Digital Instruments, Nanoscope 3).

Figure 3a is a fluorescence image of fixed polymer nanoparticles on the substrate in the sample solution for different irradiation time (20, 25, 30, and 35 s) of the UV pulse (~ 0.033 μJ/pulse) from the Q-switched Nd^{3+}:YAG laser. In case of ~ 15 s, no polymer nanoparticle could be fixed onto the substrate. AFM images of each acrylamide gel on the substrate are shown in Figure 3b. It was confirmed from the AFM images that individual nanoparticle fixation was achieved by the method and the size of the acrylamide gel increased with the UV pulse irradiation time. Multiple nanoparticles could also be fixed onto the substrate at a time with their number controlled in the same manner. Figure 4 shows AFM images of one, two, and three polymer nanoparticles fixed on the glass substrate. The laser nanomanipulation-fixation method enables us to pattern any number of polymer nanoparticles onto any point of substrate in solution.
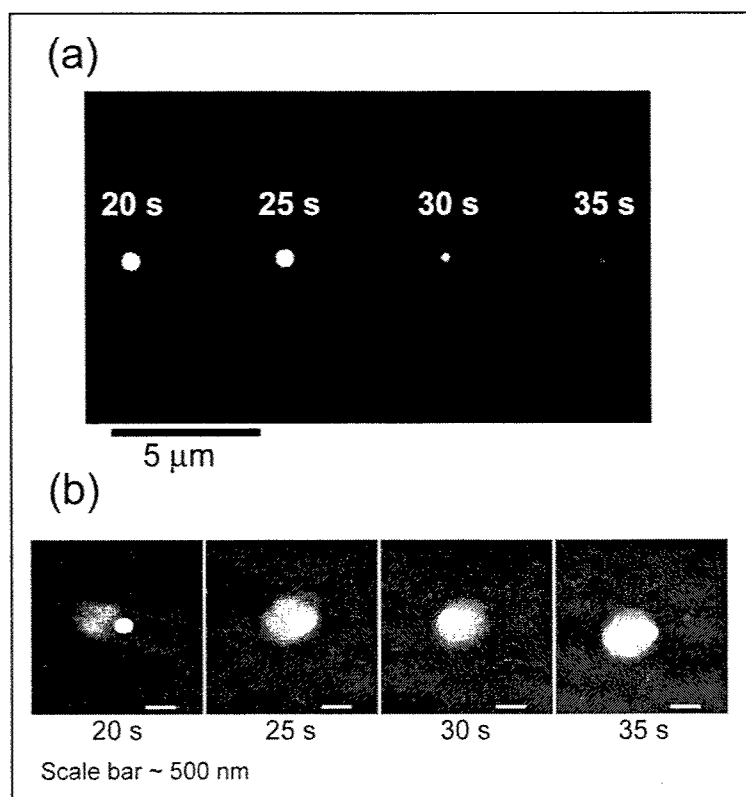
Figure 3. Fluorescence (a, in distilled water) and topographic (b, in the air) images of polymer nanoparticles included in produced acrylamide gel on the glass substrate. Repetition rate of the UV pulse ~ 5 Hz, pulse energy ~ 3.3× 10^{-2} μJ/pulse, laser pulse irradiation time ~ 20, 25, 30, and 35 s, and corresponding total photon energy 3.3, 4.1, 4.9, and 5.7 μJ, respectively.
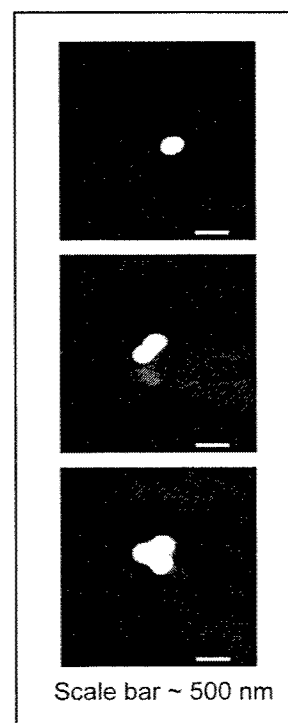
Figure 4. AFM images of fixed one (top), two (middle), and three (bottom) polystyrene nanoparticles on the glass substrate.

In addition to the condition of gel solidification, morphological damage of the particle itself or photochemical bleaching of fluorescent dye to the sample particle caused by laser pulse irradiation should also be considered in case of patterning individual nanoparticles of softmaterials without undermining their functions. Fluorescence from dyes in the polymer nanoparticle was quenched gradually with irradiation of the 5 Hz UV laser pulse as shown in Figure 3. At that time, no morphological change of the particles occurred. In order to investigate photodegradation of polymer nanoparticles caused by laser pulse, we used the diode pumped UV pulsed laser whose repetition rate is much higher than that of the Q-switched Nd^{3+}:YAG laser. No appreciable quenching of the dyes included in the particles was observed for different irradiation time (4 - 9 s) of the UV pulse from the diode pumped laser as shown in Figure 5a. In the fixation experiment using the Q-switched Nd^{3+}:YAG laser (Figure 3), averaged energy of a single pulse was $\sim 3.3 \times 10^{-2}$ μJ/pulse. On the other hand, when the diode pumped UV pulsed laser was used, that was $\sim 1.8 \times 10^{-5}$ μJ/pulse. It is considered that the dye molecules in the particles are degraded photochemically and/or photothermally due to the three orders higher pulse energy.
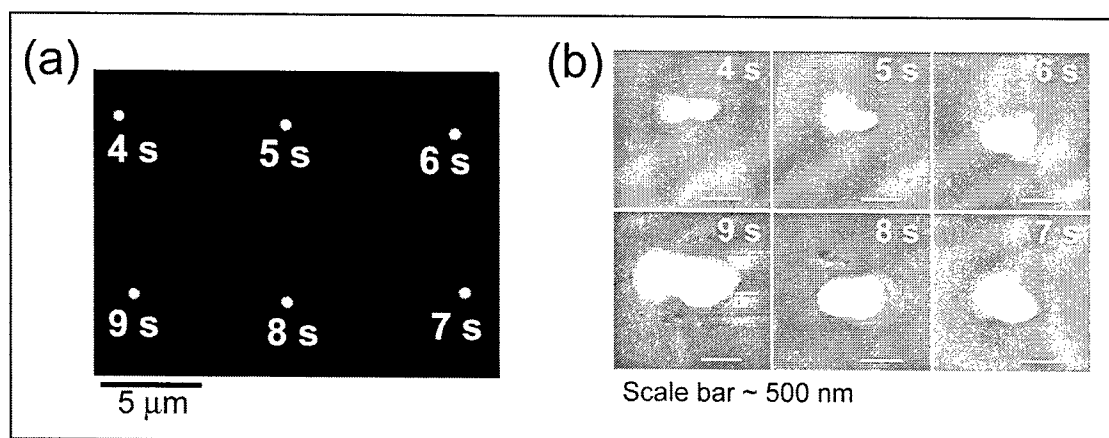
Figure 5. Fluorescence (a, in distilled water) and topographic (b, in the air) images of polymer nanoparticles included in acrylamide gel produced by irradiation of UV laser pulse with higher repetition rate. Repetition rate of the UV pulse ~ 10 kHz, pulse energy $\sim 1.8 \times 10^{-5}$ μJ/pulse, laser pulse irradiation time $\sim 4 - 9$ s, and corresponding total photon energy $\sim 0.70, 0.88, 1.1, 1.2, 1.4,$ and 1.6 μJ, respectively.

5. PHOTOTHERMAL FIXATION OF GOLD NANOPARTICLES

A single gold nanoparticles dispersed in the solution was optically manipulated to the surface of a glass substrate by handling the microscope 3D stage, and then the UV laser beam was additionally irradiated to it, which led to fixation of the particle to the substrate. The fixed particles were strongly adhered onto the substrate, resisting water flow. Typical AFM images of the fixed gold nanoparticles for averaged laser fluence of 46 and 160 mJ/cm^2 (5 Hz repetition, irradiation time ~ 5 s) are shown in Figure 6. At fluence of ~ 46 mJ/cm^2, gold nanoparticles were fixed on the substrate without morphological change and no damage was observed. On the other hand, figure 6(b) indicates that the gold nanoparticle was completely fragmented to smaller particles sized about 10 to 40 nm at the fluence of ~ 160 mJ/cm^2. The fragments were deposited on the substrate in the region of 200 – 300 nm square.

The present fixation mechanism can be explained by the transient temperature elevation of the gold nanoparticles. Interactions between gold nanoparticles and laser pulse have been well studied by El-Sayed et al. [15 - 17], Koda et al. [18, 19], Kondow et al. [20], and many other groups. Since electron-phonon relaxation time of gold nanoparticles is few ps order, which is much shorter than phonon-phonon (lattice-environment) relaxation time (few tens - 100 ps order), absorbed excitation energy is converted to heat efficiently in a

Figure 6. AFM images of a gold nanoparticle and its fragments remaining on the glass substrate in ambient air after fixation with fluence of 46 mJ/cm^2 (a) and 160 mJ/cm^2 (b).

gold nanoparticle during the ns-laser pulse, resulting in temperature elevation of the particle. In fact, it was mentioned in their reports that gold nanoparticles were melt (with lower fluence) and broken into several smaller particles with size of less than 20 nm (with higher fluence) when the laser pulse was irradiated to the particles. Especially, in the reports of El-Sayed et al. [16,17], which dealt with gold nanorods, it was shown that they were melt and their shapes were changed from rodlike to spherical by laser pulse irradiation. Although our results cannot be simply compared with their results because of the different experimental conditions (pulse wavelength, particle size, particle shape, and so forth), the laser-induced adhesion is considered due to transient melting.

One of the important characteristics of the present work is the spatial resolution of the fixation method under the present experimental condition. It is considered that the trapped gold nanoparticle is moving around the bottom of the optical potential well that becomes steeper with the near IR laser power. There, the near IR laser beam was fully expanded just in front of the objective so that the incident part of the beam into it had almost uniform distribution [21]. Therefore, the light intensity profile under the objective could be calculated by taking into account of Fraunhofer diffraction of plane wave.

The magnitude of positional fluctuation due to thermal motion was estimated by ~ 13 nm (FWHM) from numerical calculation under the condition (laser power ~ 30 mW, diameter of the gold nanoparticle ~ 80 nm, refractive index of the surrounding medium ~ 1.43). It is however expected that there are many factors to cause mechanical vibrations of the microscope stage in the actual experiment; vibration of water pump, wind from air conditioner, the photon force due to light scattering and absorption of the UV laser pulse, and so on. In order to determine actually spatial resolution of the fixation method, an experiment was carried out by moving a piezo electric 3D stage (Physik Instrumente, P-517.3CL). Five gold nanoparticles were successively fixed on the substrate on a line at intervals of 1000 nm (Figure 7). The dashed line in the Figure was fitted by the least squares method from the coordinate of each nanoparticle. From the result the accuracy was evaluated at ~ few tens of nm.
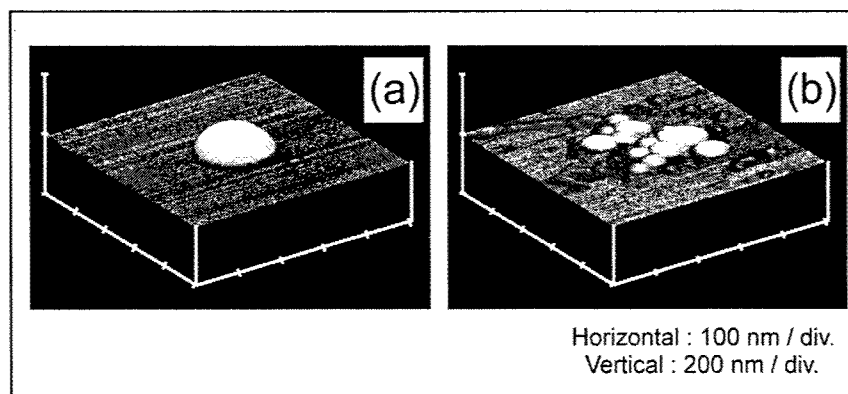
Scale bar ~ 500 nm
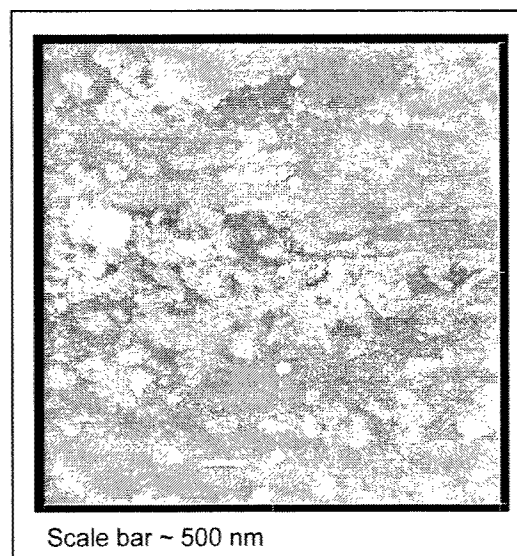
Figure 7. An AFM image of five gold nanoparticles successively patterned on a line at intervals of 1000 nm with fixation laser fluence of ~ 56 mJ/cm^2.

6. CONCLUSION

Thus we have succeeded for the first time in developing laser manipulation and adhesion methods for organic and metallic nanoparticles in solution. Individual polymer and gold nanoparticles were sequentially patterned on the substrate one by one by the use of local photopolymerization for polymer particles and transient temperature elevation for gold ones. Examples of well-controlled laser patterning of those are shown in Figure 8.

The significant importance of the laser manipulation-fixation technique is that we can trap, manipulate, and fix single and/or many nanoparticles in solution at room temperature, which is very difficult to achieve by other method such as scanning probe microscope and self organization of parrticles. The present technique is very powerful when we manipulate biological specimens such as living cells, subcellular organelles, and tissues under optical microscope. Actually, we have been applying the laser manipulation-fabrication method to bioengineering, e.g. cell-sorting [22], protein-chip fabrication [23], and so forth in the last few years.

In addition to handling micro/nanoparticles, we have been demonstrating that characteristic polymer aggregates can be formed by photon pressure of a focused near IR laser beam in various systems. At first, we applied the photon pressure to a closed system, i.e. polymer solution in a hermetically closed cell. In those experiment, polymer chains of 10 ~ 20 nm mean radius could be assembled and single microparticles are formed when the near IR laser beam was focused to the solutions [7 -11]. We have also revealed experimentally that polymer chains with chromophores, which have high polarizability, were preferentially attracted to the focal point. Recently, we have explored effect of the photon pressure upon drying process (dynamic system) of cast solution of wire-type dendrimers [24] and poly(fluorene) derivatives. Those conjugated polymers could be collected at the focal point of the near IR laser light in the drying process of their solution. Especially, in experiment of the poly(fluorene) derivatives, unique polymer aggregate was obtained on substrate after complete aridity of cast solution only when the near IR laser beam was irradiated to it. Fluorescence microspectroscopy suggested those optically collected molecules were oriented along the polarization direction of the near IR laser beam, and the molecular orientation was maintained after drying of the solution. Now, we are further investigating the effect of photon pressure upon such a dissipative structure in polymer solution and another dynamic systems, e.g. photochemical reactions. The laser trapping technique enables us to manipulate these various kinds of mesoscopic materials under the mild condition (in solution at room temperature). We foresee that the present nanomanipulation-fixation technique will be very useful to explore novel phenomena and to pioneer applications on further science and technology in nanospace.
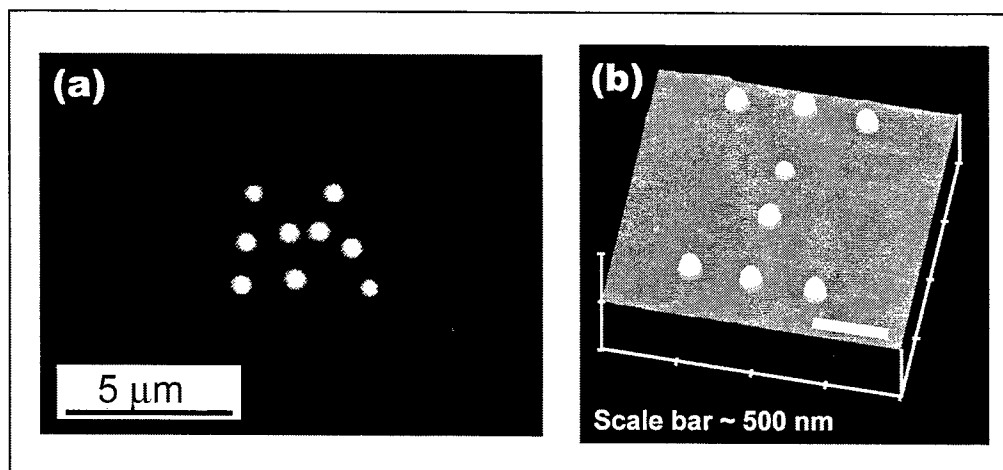
Figure 8. (a) A fluorescence image of polymer nanoparticles patterned on the glass substrate as a letter "M". (b) An AFM image of gold nanoparticles patterned on the glass substrate as a letter "I". The fluorescence and AFM images were acquired in distilled water and in air, respectively.

AKNOWLEDGEMENT

REFERENCES

1. A. Ashkin, J. M. Dziedzic, J. E. Bjorkholm, and S. Chu, "Observation of a single-beam gradient force optical trap for dielectric particles" *Opt. Lett.* **11**, 288 - 290, 1986.
2. A. Ashkin, J. M. Dziedzic, and T .Yamane, "Optical trapping and manipulation of single cells using infrared laser beams" *Nature,* **330**, 769 – 771, 1987.
3. K. Sasaki, M. Koshioka, H. Misawa, N. Kitamura, and H. Masuhara, "Laser-scanning micromanipulation and spatial patterning of fine particles" *Japanese Journal of Applied Physics*, **30**, L907 - L909, 1991.
4. K. Sasaki, M. Koshioka, H. Misawa, N. Kitamura, and H. Masuhara, "Optical trapping of a metal particle and a water droplet by a scanning laser beam" *Applied Physics Letters,* **60**, 807 - 809, 1992.
5. H. Misawa, K. Sasaki, M. Koshioka, N. Kitamura, and H. Masuhara, "Multibeam laser manipulation and fixation of microparticles" *Applied Physics Letters,* **60**, 310 - 312, 1992.
6. *Microchemistry: Spectroscopy and Chemistry in Small Domains*, edited by H. Masuhara, F. C. De Schryver, N. Kitamura, and T. Tamai, North Holland, Amsterdam, 1994.
7. J. Hofkens, J. Hotta, K. Sasaki, H. Masuhara, H. Faes, and F. De Schryver "Laser induced phase transition in aqueous solutions of hydrophobically modified poly(N-isopropylacrylamide)" *Molecular Crystals and Liquid Crystals,* **283**, 165–172, 1996.
8. J. Hofkens, J. Hotta, K. Sasaki, H. Masuhara, and K. Iwai "Molecular assembling by the radiation pressure of a focused laser beam: poly(N-isopropyl acrylamide) in aqueous solution" *Langmuir,* **13**, 414–419, 1997.
9. J. Hofkens, J. Hotta, K. Sasaki, H. Masuhara, T. Taniguchi, and T. Miyashita, "Molecular association by the radiation pressure of a focused laser beam: fluorescence characterization of pyrene-labeled PNIPAM" *Journal of the American Chemical Society,* **119**, 2741–2742, 1997.
10. P. Borowicz, J. Hotta, K. Sasaki, and H. Masuhara, "Laser-controlled association of poly(N-vinylcarbazole) in organic solvents: radiation pressure effect of a focused near-infrared laser beam" *The Journal of Physical Chemistry B,* **101**, 5900-5904, 1997.
11. T. A. Smith, J. Hotta, K. Sasaki, H. Masuhara, and Y. Itoh, "Photon pressure-induced association of nanometer-sized polymer chains in solution" *The Journal of Physical Chemistry B,* **103**, 1660-1663, 1999.
12. S. Ito, H. Yoshikawa, and H. Masuhara, "Optical patterning and photochemical fixation of polymer nanoparticles on glass substrates" *Applied Physics Letters,* **78**, 2566–2568, 2001.
13. S. Ito, H. Yoshikawa, and H. Masuhara, "Laser manipulation and fixation of single gold nanoparticles in solution at room temperature" *Applied Physics Letters,* **80**, 482–484, 2002.
14. K. Svoboda and M. Block, "Optical trapping of metallic Rayleigh particles" *Optics Letters,* **19**, 930–932, 1994.
15. S. Link, C. Burda, M. B. Mohamed, B. Nikoobakht, and M. A. El-Sayed, "Femtosecond transient-absorption dynamics of colloidal gold nanorods: shape independence of the electron-phonon relaxation time" *Physical Review B,* **61**, 6086-6090, 2000.
16. S. Link, C. Burda, B. Nikoobakht, and M. A. El-Sayed, "Laser-induced shape changes of colloidal gold nanorods using femtosecond and nanosecond laser pulse" *The Journal of Physical Chemistry B,* **104**, 6152-6163, 2000.
17. S. Link and M. A. El-Sayed, "Spectroscopic determination of the melting energy of a gold nanorod" *Journal of Chemical Physics,* **114**, 2362-2368, 2001.
18. H. Kurita, A. Takami, and S. Koda, "Size reduction of gold particles in aqueous solution by pulsed laser irradiation" *Applied Physics Letters,* **72**, 789-791, 1998.
19. A. Takami, H. Kurita, and S. Koda, "Laser-induced size reduction of noble metal particles" *The Journal of Physical Chemistry B,* **103**, 1226-1232, 1999.
20. F. Mafuné, J. Kohno, Y. Takeda, and T. Kondow, "Dissociation and aggregation of gold nanoparticles under laser irraidation" *The Journal of Physical Chemistry B,* **105**, 9050-9056, 2001.
21. H. Misawa, M. Koshioka, K. Sasaki, N. Kitamura, and H. Masuhara, "Three-dimensional optical trapping and laser ablation of a single polymer latex particle in water" *Journal of Applied Physics,* **70**, 3829-3836, 1991.

22. Y. Hosokawa, H. Masuhara, Y. Matsumoto, and S. Sato, "Dual-beam laser micromanipulation for sorting biological cells and its device application" *Proceeding of SPIE*, **4622**, 138-142, 2002.
23. Y. Hosokawa, S. Matsumura, H. Y. Yoshikawa, H. Masuhara, R. Nakamura, Y. Kanematsu, K. Ikeda, A. Shimo-oka, and H. Mori, "Fabrication and application of protein crystal microarrays" *Proceeding of MRS*, in press.
24. S. Masuo, H. Yoshikawa, T Asahi, and H. Masuhara, "Repetitive contraction and swelling behavior of gel-like wire-type dendrimer assembles in solution layer by photon pressure of a focused near-infrared laser beam" *The Journal of Physical Chemistry B*, **106**, 905-909, 2002.

Porous nanostructured layers on germanium produced by Laser optical breakdown processing

A. V. Kabashin[*], V-G. Pilon Marien, D.-Q. Yang, F. Magny, and M. Meunier

Laser Processing Laboratory, Ecole Polytechnique de Montréal, Case Postale 6079, Succ. Centre-ville, Montréal (Québec), Canada, H3C 3A7

ABSTRACT

Germanium wafer surface is modified by a technique of CO_2-laser induced air breakdown processing, which was recently introduced and used to produce photoluminescent Si-based nanostructured layers. Structural and optical properties of the Ge-based layers, formed under the irradiation spot as a result of the processing, are characterized by different techniques (SEM, XPS, FTIR, XRD, and PL). It has been found that the layers present a porous structure, containing nanoscale holes, and consist of Ge nanocrystals embedded into GeO_2 matrices. They exhibited strong photoluminescence (PL) in the green range (2.2 eV), which was attributed to defects in GeO_2 matrix due to the presence of Ge-O modes with some OH vibration in the FTIR spectra. The layers are of importance for local patterning of nanostructures on semiconductors.

Keywords: air optical breakdown, nanostructured Ge, visible photoluminescence, laser-assisted patterning

1. INTRODUCTION

Silicon and Germanium are group IV semiconductors, which are of vital importance for the microelectronics industry. However, having indirect and small band gaps (1.1 eV for Si and 0.6 eV for Ge), both materials do not emit visible light, which complicates their use for optoelectronics applications. Novel promises for these applications arose with the observation of visible photoluminescence (PL) from anodically etched porous Si[1] and nanostructured thin films prepared by different "dry" deposition techniques.[2-8] Similar effect was observed with chemically etched Ge[9,10] and Ge-based films[11-13]. Even if the origin of visible PL has not yet been clarified, applications of nanostructured semiconductors in photonics[14] and biosensing[15] are now extensively discussed.

By now there is a significant interest in the development of methods for local patterning of the nanostructured layers on a semiconductor wafer and, potentially, on an assembled integrated chip or optoelectronics device. One of the simplest vacuum-free and "dry" methods for the local nanostructuring is the processing of a semiconductor wafer by an electric spark[16-20]. The wafer is used as a cathode in a plasma-assisted process, in which unipolar discharges between two electrodes ionize the gaseous environment and accelerate the generated ions toward the semiconductor surface leading to its structural modifications. In the case of Si, the processed material exhibits PL with peaks in red (1.9 eV), green (2.36 eV) and UV/blue (3.22 eV) spectral ranges at room temperature[19]. In contrast, spark-processed germanium demonstrates a single PL peak at 2.2 eV.[20] Alternatively, we recently demonstrated another dry and vacuum-free method for local nanostructuring of semiconductors,[21,22] The method consists in the IR laser radiation-induced initiation of air breakdown on the semiconductor surface, while the target presence serves to decrease the threshold of the plasma initiation. The hot plasma of air optical breakdown causes a modification of target material, transforming it to a porous nanostructured layer. The method was successfully applied to treat silicon wafers and produce local nanostructured spots, exhibiting strong 1.9-2.0 PL.

[*] akabach@email.phys.polymtl.ca; phone 1-(514)340-4711 ext. 4634, Laser Processing Laboratory, Ecole Polytechnique de Montréal, Case Postale 6079, succ. Centre-ville, Montréal (Québec), Canada, H3C 3A7

In this paper, we apply the air optical breakdown technique to treat a germanium wafer and study properties of the layers formed on the wafer surface.

2. EXPERIMENTAL

In the experiments, the radiation from a pulsed TEA CO_2 laser (wavelength 10.6 μm, pulse energy 1 J, pulse length 1 μs FWHM, repetition rate 3 Hz), was focused by a Fresnel's lens (focal length of 5 cm) onto a Ge target. The radiation intensity was about 10^8 W/cm^2 at the focal plane. The experiment was carried out in atmospheric air (1 atm, 20° C, 40% humidity). Standard germanium wafers (n- and p-type, resistance 0.01- 10 Ohm·cm) with dimensions about 1×1 cm^2 were used as targets.

Scanning Electron Microscopy (Phillips XL20, Phillips Corp) was used to examine structural properties of the films. The crystalline structure of the films was examined by X-ray diffraction (XRD) spectroscopy (X'pert XRD system, Philips Corp). The surface analysis was performed at a base pressure below 10^{-10} Torr by the X-ray Spectroscopy (ESCALAB 3 Mark II, VG Scientific), using 1253.6 eV radiation from a Mg K$_\alpha$ X-ray source. High-resolution spectra were obtained at a perpendicular take-off angle, using 20 eV pass energy and 0.05 eV steps. Photoacoustic FTIR spectra were obtained using a He-purged MTEC 300 photoacoustic cell in a Bio-Rad FTS 3000 spectrometer[23]. The 2.5 kHz modulation frequency was used to probe the entire sample thickness. The PL spectra were measured at room temperature using a double spectrometer (model U100, Instruments SA) and a GaAs photomultiplier (Hamamatsu Photonics). The samples were illuminated by the radiation of a cw Ar$^+$ laser (model INNOVA 100) with the wavelength 488 nm.

3. RESULTS

3.1 Conditions of surface treatment

As in the case of silicon,[21,22] the breakdown initiation threshold on Ge depended on the efficiency of radiation absorption by the upper target surface layer. In particular, relatively high radiation powers were required to ignite the breakdown on a clean Ge wafer. However, the threshold was significantly lower when the radiation spot hit a dust on the wafer surface. After the breakdown ignition, the plasma intensity rose progressively with the number of laser shots on the same spot and stabilized only after 20-100 shots. The intensity gain was apparently related to the improvement of radiation absorption due to the formation of mechanical defects on the surface. In our experiments, the treatment was performed under near-threshold conditions to minimize possible deposition of material on the surrounding free target surface. After breakdown initiations by several laser pulses, a gray-tint area was formed under the focal spot on the silicon surface.

(a)   (b)
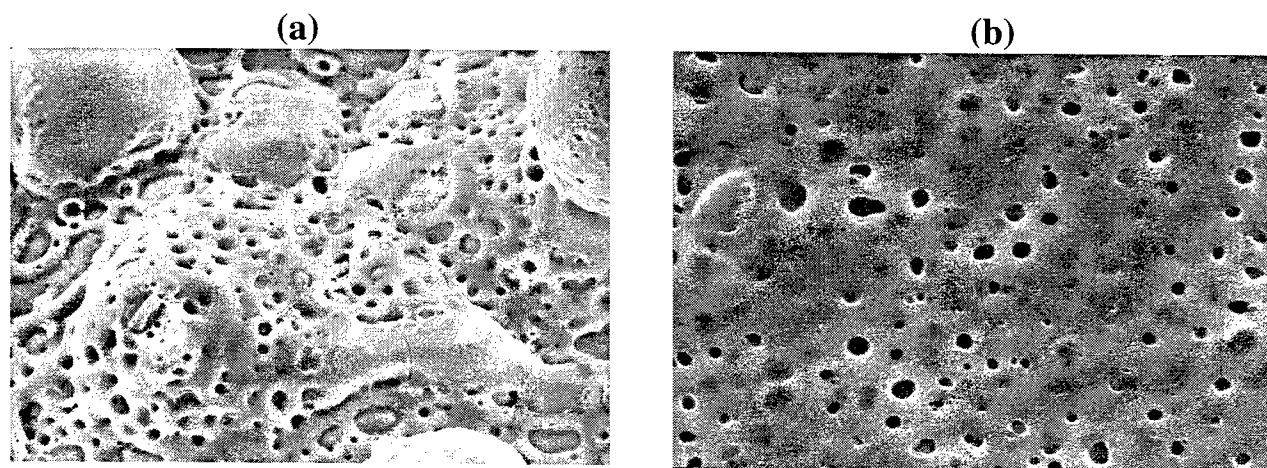
Fig. 1 SEM images of the treated Ge surface after 900 laser shots. (a) central region. 2000×. (b) peripheral region. 5000×

3.2 Surface morphology

It was found that the morphology of Ge surface after the laser irradiation was inhomogeneous. As one can see from SEM images depicted in Fig. 1, the processed layer was relatively non-uniform with casual formation of hill-like structures in the center of the irradiated spot, whereas in the peripheral part these structures were essentially absent. Nevertheless, the entire treated surface presented a highly porous material, containing nanoscale holes between 30 and 150 nm. It is worth mentioning that similar porous structures were observed after the air optical breakdown of silicon.

3.3 Surface chemical composition

We concluded from XPS spectra that only C, O and Ge were present in the surface modified layer of Ge. The peaks related to these elements can be clearly identified in the survey spectrum shown in Fig.2 (a). As follows from Fig. 2 (b), the high-resolution XPS spectrum of Ge samples before the treatment was characterized by peaks at 29 eV and 32.5 eV [Fig. 2 (b)], which are always assigned to the inoxidized Ge core and the natural GeO_2 oxide layer, respectively. Similar to the case of breakdown-treated $Si^{21,22}$, the treatment of Ge led to the disappearance of Ge-related peak, while the oxide-related peak became stronger, suggesting that the treatment led to a formation of germanium oxide shell (GeO_2). Thus, we can conclude that the upper treated layer mainly consisted of the germanium oxide.

(a)   **(b)**
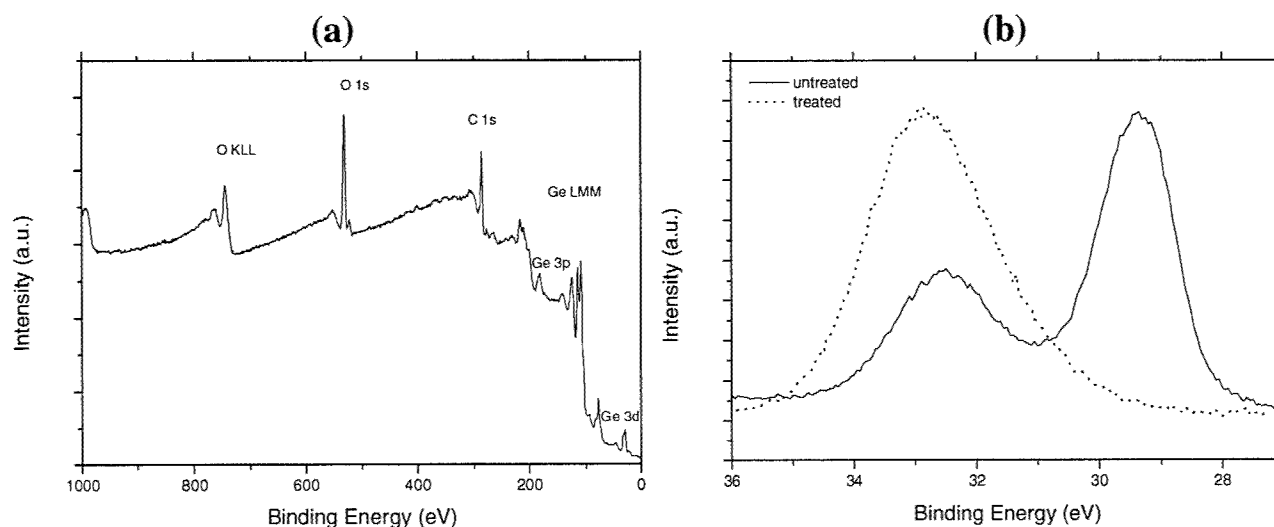
Fig. 2 XPS survey (a) and high-resolution (b) spectra from the breakdown-treated Ge surface after 900 pulses

Fig. 3 shows a typical photoacoustic FTIR spectrum from the treated surface. The major vibration features observed are the following: (a) The very strong and broad band, ~3500cm^{-1} , is assigned to bonded OH stretching vibration, while a sharp shoulder, appeared at ~3700 cm^{-1}, is usually assigned to the free absorbed OH; (b) ~2900 cm^{-1} band, which can be assigned to the C-H stretching mode associated with the CH$_m$ groups adjacent to the OH groups; (c) ~1050 cm^{-1}, which can be attributed to Ge-O stretching, the C-O stretching mode and Ge-OH, as well as Ge-O-C stretching is also located in this region. (d) the CH$_2$ chain-wagging mode progression at 1200-1350 cm^{-1}, (e) the C-H scissors deformation mode of the CH$_2$ group ~1500 cm^{-1}. Disregarding signals related to carbon contamination of samples, we may conclude from the photoacoustic study that two types of important chemical processes occur during the treatment. These are the oxidation and formation of hydroxyl groups related to Ge-O and Ge-OH stretching modes, respectively.
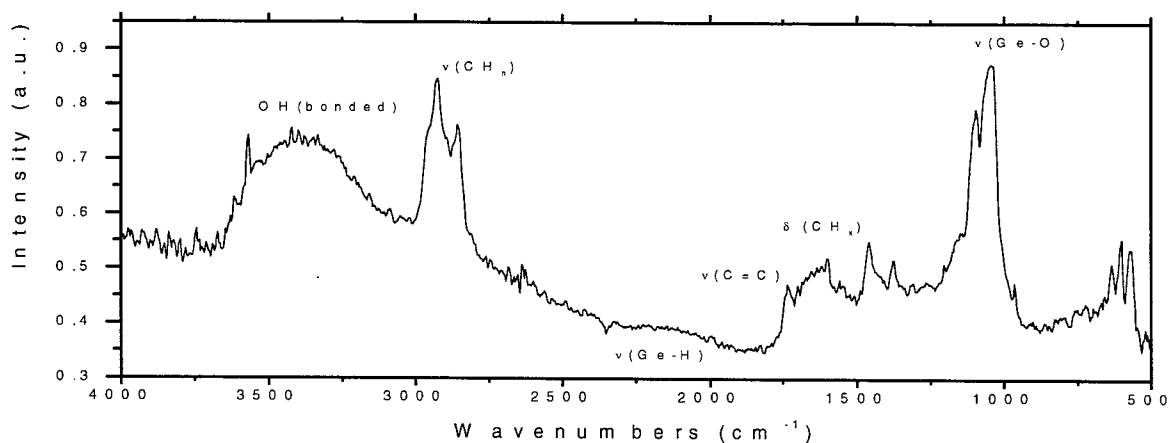
Fig. 3 Photoacoustic FTIR spectrum from the breakdown-processed Ge surface after 900 pulses.

3.4 XRD analysis

Nevertheless, XRD studies showed that Ge crystals are also present in the layer. Fig. 4 (a) shows typical spectra for a Ge target before and after the optical breakdown processing. One can see that the treatment led to the appearance of additional XRD peaks associated with different crystalline Ge states. This gives the evidence that the resulting layers consisted of Ge crystals embedded in GeO_2 matrix. It is known[24] that the broadness of XRD peaks is mainly determined by the smallest clusters in a deposit. As the instrumental noises are relatively low, this property could be used to roughly estimate the minimal size of crystals in the layer by the Debye-Scherrer formula[24]. Since the measured broadness of a typical Ge peak $\Delta(2\theta)/2$ is about 0.5 deg., the estimation gives the crystal size of the order of 20-30 nm. These values are similar to the nanocrystal size in the case of Si, obtained by the same method[21,22].

(a)   **(b)**
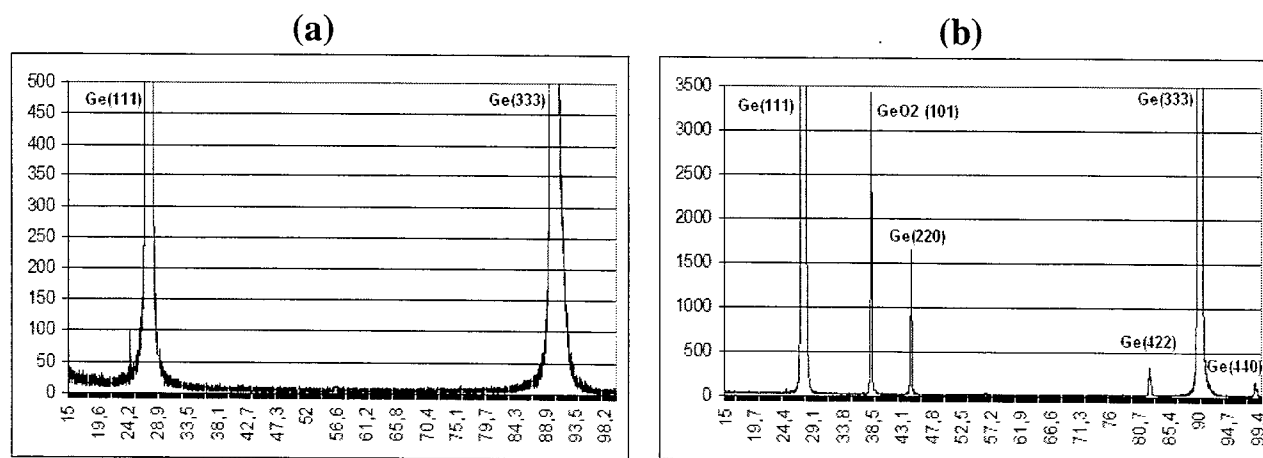
Fig. 4. Typical XRD spectra before (a) and after (b) the breakdown processing of a Ge wafer. To enhance XRD signal, a rectangular area with dimensions of 5×5 mm² was treated on the wafer by shifting the laser beam over the target.

3.5 PL studies

Similar to the case of Si, the breakdown-processed Ge surface shows strong visible PL in room temperature, which was visible by a naked eye. However, the maximum of PL emission was blue-shifted in comparison with Si (1.95 eV) and concentrated in the green range around 2.1-2.2 eV. As in the silicon case, the emission was uniform over the layer surface. It should be noted that similar PL signals were observed after the electric spark processing of germanium.[20]
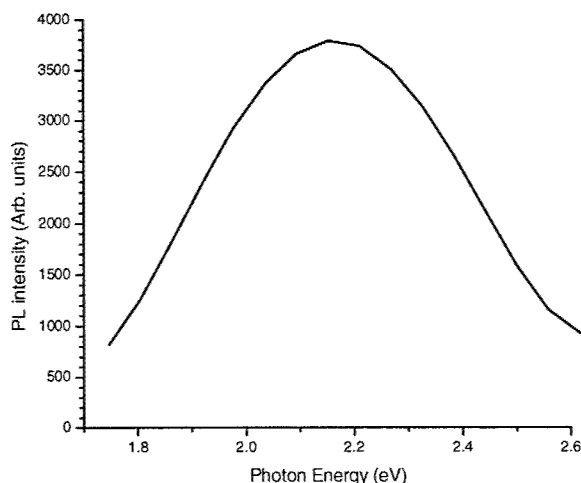
Fig. 5 Typical photoluminescence spectrum from the central part of Ge-based layer fabricated by the breakdown processing of a Ge wafer by 900 laser shots.

4. DISCUSSION

It is well known that the interaction of the CO_2 laser radiation with matter is characterized by a fast transition from a target-related to plasma-related radiation absorption[25]. The target generates initial electrons to ignite the gas discharge, which then develops in the cold gas toward the focusing lens, absorbing main IR radiation power and, as a consequence, getting heated up to high temperatures of more than 10^4 K.[25] The action of radiation probably causes a localized melting and even flash evaporation of the target material, leading to the appearance of pores on the target surface[22]. The laser-ablated material and the upper target layer are then heated by the hot CO_2 laser-induced breakdown plasma or its currents, leading to additional phase transformations and the initiation of chemical reactions. Since the radiation is pulsed, one can assume recrystallization or local vapor redeposition of the material during the off-times.

We believe that the mechanism of air optical breakdown processing is similar to the case of the electric spark processing[16-20]. Here, the modifications are attributed to pulsed ion bombardment of silicon surfaces, which led to a flash evaporation of the target material and its recrystallization during the off-times. Indeed, many properties of spark-processed and optical breakdown-processed semiconductors are similar. In particular, the spark-processed semiconductors also contained 10-500 nm holes and consisted of Si (Ge) nanocrystals embedded in SiO_2 (GeO_2) matrix[16,18,20]. Though PL properties of Si-based layers produced by these two methods could have certain differences, the Ge-based layers demonstrated similar properties with a strong peak at 2.1-2.2 eV. The generation of visible PL in the case of the spark-processed Ge was attributed to defects in GeO_2 structure rather than to the radiative recombination of excitons confined in nanocrystals[20]. In our opinion, this mechanism is also the most probable in the case of the optical breakdown processing. Indeed, plasma interaction with the Ge surface during the laser irradiation should form a large amount of defects in the oxidation layer and the interface. This is confirmed by the FTIR studies [Fig. 3], which gave a strong evidence for the OH absorption due the defect-related free radicals and dangling bonds. The quantum confinement effects are less probable in the case of Ge, but they can not be ruled out completely, taking into account that the nanocrystal size calculation by the Debye-Scherrer formula (in our case, 20-30 nm) is generally considered as a very rough estimation. In any case, more experimental data should be obtained for a clear identification of the PL origin. These studies are in progress.

5. CONCLUSION

Air optical breakdown has been produced on a Ge target to modify its surface. We showed that the breakdown production led to the formation of porous layer under the radiation spot, which consisted of Ge nanocrystals imbedded in GeO_2 matrix, while its surface was characterized by the presence of oxide and hydroxyl groups. The fabricated layers exhibited strong green PL, which is of importance for optoelectronics applications.

ACKNOWLEDGEMENTS

REFERENCES

1. L. T. Canham, "Silicon quantum wire array fabrication by electrochemical and chemical dissolution of wafers", *Appl. Phys. Lett.*, **57**, pp. 1046-1048, 1990.

2. H. Takagi, H. Ogawa, Y. Yamazaki, A. Ishizaki, and T. Nakagiri, "Quantum size effects on photoluminescence in ultrafine Si particles", *Appl. Phys. Lett.*, **56**, pp. 2379-2380, 1990.

3. Y. Kanemitsu, T. Ogawa, K. Shiraishi, and K. Takeda, Visible photoluminescence from oxidized Si nanometer-sized spheres: exciton confinement on a spherical shell", *Phys Rev. B*, **48**, pp. 4883-4886, 1993.

4. I. A. Movtchan, R. W. Dreyfus, W. Marine, M. Sentis, M. Autric, G. Le Lay and N. Merk, "Luminescence from a Si-SiO_x nanocluster-like structure prepared by laser ablation", *Thin Solid Films*, **255**, pp. 286-289, 1995.

5. Y. Yamada, T. Orii, I. Umezu, Sh. Takeyama, and T. Yoshida, "Optical properties of silicon nanocrystallites prepared by excimer laser ablation in inert gas", *Jpn. J. Appl. Phys., Part 1*, **35**, pp.1361-1365, 1996.

6. T. Makimura, Y. Kunii, and K. Murakami, "Light emission from nanometer-sized silicon particles fabricated by the laser ablation method", ", *Jpn. J. Appl. Phys., Part 1*, **35**, pp.4780-4784, 1996.

7. A.V. Kabashin, M. Meunier, and R. Leonelli, "Photoluminescence characterization of Si-based nanostructured films produced by laser ablation", *J. Vac. Sci. Tech. B*, **19**, pp. 2217-2222, 2001.

8. A. V. Kabashin, J.-P. Sylvestre, S. Patskovsky, M. Meunier, "Correlation between PL properties and morphology of of laser-ablated Si/SiO_x"*J. Appl. Phys.*, **91**, 3248, 2002.

9. M.Sendova-Vassileva, M.Tzenov, D.Dimova-Malinovska, M.Rosenbauer, M.Stutzmann, K.V.Josepovits, "Structural and luminescence studies of stain-etched and electrochemically etched germanium", *Thin Solid Films*, **255** (1995) 282

10. S.Miyazaki, K.Sakamoto, K.Shiba, M.Hirose, "Photoluminescence from anodized and thermally oxidized porous germanium ", *Thin Solid Films*, **255** (1995) 99

11. Y.Maeda, N.Tsukamoto, Y.Yazawa, Y.Kanemitsu, Y.Masumoto, "Visible photoluminescence of Ge microcrystals embedded in SiO_2 glassy matrices", *Appl.Phys.Lett.*, **59** (1991) 3168

12. L.Yue and Y.He, "Studies on room temperature characteristics and mechanism of visible luminescence of Ge-SiO_2 thin films", *J.Appl.Phys.*, **81** (1997) 2910

13. T.Kabayashi, T.Endoh, H.Fukada, S.Sakai, Y.Ueda, "Ge nanocrystals in SiO_2 films", *Appl.Phys.Lett.*, **71** (1997) 1195

14. L.Pavesi, L.Dal Negro, C.Mazzolenl, G.Franzo, and F.Priolo, "Optical gain in silicon nanocrystals ", *Nature*, **408** (2000) 440

15. V.S.-Y. Lin, K.Motesharei, K.P.S. Dancil, M.J.Sailor, and M.R.Ghadiri, "A porous silicon-based optical interferometric biosensor ", *Science*, **278** (1997) 840

16. R.E Hummel, S-S. Chang, "Novel technique for preparing porous silicon", *Appl. Phys. Lett.*, **61**, pp. 1965-1967, 1992.

17. E.F. Steigmeier, H. Auderset, B. Delley, and R. Morf, "Visible light emission from Si materials", *J. Luminescence*, **57**, pp. 9-12, 1993.

18. R.E. Hummel, A. Morrone, M. Ludwig, and S.-S. Chang, "On the origin of photoluminescence in spark-eroded (porous) silicon", *Appl. Phys. Lett.*, **63**, pp. 2771-2773, 1993.

19. M.H. Ludwig, A. Augustin, and R.E. Hummel, "Colour-switching effect of photoluminescent silicon after spark-processing in oxygen", *Semicond. Sci. Technol.*, **12**, pp. 981-986, 1997.

20. S.S.Chang, G.J.Choi, and R.E.Hummel, "Optical properties of spark-processed germanium", *Mat.Sci.Eng.*, **B 76** (2000) 237

21. A.V.Kabashin, M.Meunier, "Fabrication of photoluminescent Si-based layers by air optical breakdown near the silicon surface", *Appl.Surf.Sci.*, **186** (2002) 576.

22. A.V.Kabashin, M.Meunier, "Air optical breakdown on silicon as a novel method to fabricate photoluminescent Si-based nanostructures", *Proc. of SPIE*, **4636** (2002) 59.

23. S. Poulin, D.-Q. Yang, E. Sacher, C. Hyett, and T. H. Ellis, "The surface structure of Dow Cyclotene 3022, as determined by photoacoustic FTIR, confocal Raman and photoelectron spectroscopies", *Appl. Surf. Sci.*, **165** (2000) 24. B. D. Cullity, *Elements of X-ray diffraction* (Addison-Westley, Reading, MA, 1978).

25. Yu.P. Raizer *Laser-Induced Discharge Phenomena* (Consultants Bureau, New York, 1977).

Resonance energy of surface plasmon of nickel nanoparticles in silica glasses

H. Amekura[*], Y. Takeda, H. Kitazawa, N. Kishimoto

Nanomaterials Laboratory, National Institute for Materials Science (NIMS)

ABSTRACT

Absorption spectra of Ni nanoparticles in silica glass (SiO_2) fabricated by negative-ion implantation of 60 keV Ni to 4×10^{16} ions/cm^2 were determined from three sets of spectra, i.e., transmittance, reflectance of implanted-surface side and that of rear-surface side, of the same samples, to exclude incoherent multiple reflection (ICMR) due to substrates. Although the absorption spectrum of as-implanted state is smeared with defect absorption, two absorption bands at 3.3 and 6.0 eV due to Ni nanoparticles are observed after annealing at 800 °C in vacuum. However, a predicted peak energy from a criterion for surface plasmon resonance (SPR), $\varepsilon_m'(\omega) + 2\,\varepsilon_d'(\omega) = 0$, was in 2.8 eV, far away from the observed peaks. Another criterion, $(\varepsilon_m' + 2\varepsilon_d')^2 + (\varepsilon_m'')^2 = $ minimum, gives the peak energy of 5.9 eV. From decomposition of the dielectric constants into free- and bound-electron contributions, we conclude that the 3.3 eV peak is SPR-like, although the contribution of the bound-electrons to the 3.3 eV peak is not small. Size dependence also supports the assignment of the 3.3 eV peak. The large contribution of the bound electrons is due to a nature of the partially filled $3d$ orbitals of Ni. This is contrast to the closed $3d$ orbitals of Cu, and probably is the origin of the broad peak width.

Keywords: surface plasmon resonance, metal nanoparticle, incoherent multiple reflection, nickel, SiO_2, copper, Maxwell-Garnett theory, complex dielectric constants

1. INTRODUCTION

Metal nanoparticles dispersed in insulators draw much attention, because of applicability for optical switches[1] and single electron transistors,[2] etc. High-flux negative-ion implantation (HFNII) is one of the promising methods to fabricate metal nanoparticles in insulators, without heat treatment, with good controllability inherent in ion implantation and without surface charging.[3-6] Up to now, we have succeeded in fabricating of Cu nanoparticles in amorphous SiO_2 and some other insulators,[7,8] and in observing large optical nonlinearity,[9] ultrafast response,[10] and single electron transport.[11] The HFNII method is applicable not only to Cu but also to other metals including magnetic ones. To obtain better characteristics than the noble metals and/or additional functions, e.g., magnetic properties etc, various metallic nanoparticles have been under investigation. As for magneto-optical applications, magnetic metal nanoparticles, i.e., Fe, Co and Ni, are attractive. In fact, a small but certain amount of optical non-linearity was reported in Co nanoparticles in SiO_2.[12] However, as shown in Fig. 1 of Ref. 13, the absorption spectra of those nanoparticles in SiO_2 consist of much broader bands than the surface plasmon resonance (SPR) of noble metals. Assignment of the resonance energy and width of the surface plasmon (SP) in the magnetic nanoparticles are required. More generally, the proper estimation of SPR energy is required to design a nanoparticle composite with a large nonlinearity at a desired energy. The applicability of certain simple criteria for the SPR energy which were often used in literatures is one of the most fundamental issues, but has not been well understood. We have fabricated Ni nanoparticles in SiO_2, and have observed magnetic properties characteristic in nano-size,[13] i.e., the superparamagnetism. The next target is understandings of optical properties of Ni nanoparticles. However, the SPR criteria did not give a correct SPR energy. In this paper, the SPR energy of Ni nanoparticles and validity of the criteria will be discussed, in comparison with a well known system, Cu nanoparticles in SiO_2.

[*] AMEKURA.Hiroshi@nims.go.jp; phone +81-298-59-5060; fax +81-298-59-5010; http://www.nims.go.jp/heavyion/; Nanomaterials Laboratory, National Institute for Materials Science, 3-13 Sakura, Tsukuba, Ibaraki 305-0003, Japan.

2. EXPERIMENTAL

Optical-grade silica glasses (KU-1: OH- 820 ppm and other impurities 6.3 ppm) of 15 mm in diameter and 0.5 mm in thickness were mounted to a water-cooled copper block, and implanted with Ni negative ions of 60 keV from a Cs-assisted plasma-sputter type high-flux ion source.[5] The implanted area was 6 mmϕ in diameter. The ion fluxes and the doses ranged 1 - 100 μA/cm^2 and 3×10^{16} - 1×10^{17} ions/cm^2, respectively. The doses were confirmed by the Rutherford Backscattering Spectrometry (RBS) using 2.06 MeV He$^+$. In this paper, results of the samples implanted with the flux of 56 μA/cm^2 and the dose of 4×10^{16} ions/cm^2 are discussed. According to SRIM2000 code[14], the projectile range and the straggling of Ni ions of 60 keV are 47 nm and 16 nm in SiO$_2$, respectively.

The implanted samples show brownish color, but still transparent, i.e., suffer incoherent multiple reflection[9] (ICMR) due to substrates. To obtain ICMR-free spectra, three sets of spectra, i.e., transmittance $\Theta_T = I_T / I_0$, reflectance of the implanted surface side $\Theta_R = I_R / I_0$ and reflectance of the rear surface side $\Theta_R' = I_R' / I_0$, were measured on the same samples, where I_0, I_T, I_R and I_R' denote intensities of incident light, transmitted light, reflected light of the implanted surface incidence and reflected light of the rear surface incidence, respectively.[9] The ICMR-free transmittance of the implanted layer T and the ICMR-free reflectance of the implanted surface side R_1 are expressed as,

$$T = \frac{\Theta_T (R_0 - 1)}{\{R_0 (2 - \Theta_R') - 1\} \exp(-\alpha_S d_S)} \qquad (1)$$

$$R_1 = \Theta_R + \frac{R_0 \Theta_T^2}{R_0 (2 - \Theta_R') - 1} \qquad (2)$$

where d_S, R_0 and α_S denote substrate thickness, reflectance and absorption coefficient of unimplanted substrate, respectively.[9] We define optical density (OD) αd of the implanted layer as,

$$\alpha d = -\ln\left(\frac{T}{1 - R_1}\right) \qquad (3)$$

where α and d denote absorption coefficient and effective thickness of the implanted layer.

A dual-beam dispersive spectrometer with a resolution of 1 nm was used for measurements of the transmittance and the reflectance in the wavelength range of 190-1700 nm at room temperature. The incident angles were 0 degree for the transmission and 5 degrees for the reflection. The reference path of the dual-beam spectrometer was kept vacant.

Effects of the heat treatments on the absorption spectra were examined using a vacuum tube furnace at 400 - 1000 °C. Each of the treatment time was set in 1 hour. The base pressure was less than 1×10^{-5} Torr.

3. THEORETICAL BACKGROUND

Two different theories, Maxwell-Garnett (MG)[15] and Mie[16], are often used to describe optical responses of nanoparticle-dispersed composites. The MG theory regards the composite as a uniform medium with an effective complex dielectric constant ε_{eff},

$$\varepsilon_{eff} = \varepsilon_d \frac{1 + 2p(\varepsilon_m - \varepsilon_d)/(\varepsilon_m + 2\varepsilon_d)}{1 - p(\varepsilon_m - \varepsilon_d)/(\varepsilon_m + 2\varepsilon_d)} \qquad (4)$$

where ε_m, ε_d and p denote the complex dielectric constants of metal and of insulator, and volume fraction of the metal, respectively. The absorption coefficient α is obtained as $\alpha = 4\pi k/\lambda$, where k denotes imaginary part of complex refractive index. Theoretically, the MG theory is valid only for small volume fraction p. However, it is experimentally shown that the MG theory is applicable to nanoparticles in SiO$_2$ with even a few tens percents of p. On the other hand, the Mie theory regards the composite as a sum of single scattering centers. For nanoparticles with smaller diameters than 50 nm, the dipole approximation is applicable to the Mie theory. The extinction coefficient γ is described as,

$$\gamma = \frac{18\pi p\varepsilon_d{}^{3/2}}{\lambda_0} \frac{\varepsilon_m{}''}{|\varepsilon_m + 2\varepsilon_d|^2} \qquad (5)$$

where ε_m'' and λ_0 denote imaginary part of ε_m and wavelength of light in vacuum. Hereafter ' and '' denote real and imaginary parts, respectively. The extinction coefficient γ in Mie theory is identical to the absorption coefficient α in MG theory. The extinction consists of scattering and absorption. However, MG theory assumes a uniform effective medium, i.e., no scattering inside. For nanoparticles whose diameters are between ~2 nm and ~20 nm, both the theories give almost identical spectra. We mainly use MG theory in this paper.

Both the formulae, eqs. (4) and (5), include a factor of $(\varepsilon_m + 2\varepsilon_d)$ in the denominators. In the cases of non-absorbing substrates, ε_d is a real value, i.e., $\varepsilon_d'' = 0$, then $|\varepsilon_m + 2\varepsilon_d|^2 = (\varepsilon_m' + 2\varepsilon_d')^2 + (\varepsilon_m'')^2$. A criterion for SPR was believed as,

$$\varepsilon_m' + 2\,\varepsilon_d' = 0. \qquad (6)$$

4. RESULTS AND DISCUSSION

4.1 Optical spectra

Figure 1 shows absorption spectra of SiO_2 implanted with Ni negative ions of 60 keV with flux of 56 $\mu A/cm^2$ to a fluence of 4×10^{16} ions/cm^2. In as-implanted state, the optical density (OD) increases monotonically with increasing the photon energy, although a shoulder is visible around ~3 eV. With vacuum annealing up to 800 °C, another peak appears around ~6 eV. After peak separation using a computer, the spectrum is well-fitted by two Gaussians centered at 3.3 and 6.0 eV with broad FWHM of 2.2 and 2.8 eV, respectively.

The clear appearance of the 6.0 eV peak is a result of the ICMR-free spectroscopy. To our knowledge, this is the first *direct* observation of the 6.0 eV peak, although the peak has been theoretically predicted[17] and some attempts were done.[17,18]

Isobe et al.[17] reported optical absorption spectra from SiO_2 implanted with Ni positive-ions of 160 keV with flux of 3 $\mu A/cm^2$ to a fluence of 6×10^{16} ions/cm^2. They observed a monotonic increase around 6 eV even after annealing, probably due to the ICMR effect. They tried to obtain the peaks using a subtraction between an as-implanted spectrum and an annealed-in-air spectrum. They reported peaks at 3.6 and 5.7 eV. But their procedure was completely incorrect: The annealing in air oxidizes the Ni nanoparticles to Ni oxides. The as-implanted spectrum consists of defect absorption and Ni nanoparticle absorption. The annealed spectrum consists of Ni *oxide* absorption. The subtraction between them was meaningless.

Fig.1 Absorption spectra of SiO_2 implanted with Ni negative-ions of 60 keV with flux of 56 $\mu A/cm^2$ to fluence of 4×10^{16} ions/cm^2, after isochronal annealing at 400, 600 and 800 °C for 1 hr each, in vacuum. The incoherent multiple reflection due to the substrate is corrected.

Cíntora-González et al.[18] reported an OD spectrum from SiO_2 implanted with Ni positive-ions of 160 keV with a flux of 10 $\mu A/cm^2$ to a fluence of 1×10^{16} ions/cm^2. The OD monotonically increased with increasing photon energy. A small hump around 5 eV was identified to the neutral oxygen vacancy of SiO_2. Because the fluence was 4 times smaller than ours, the spectrum was dominated by defect absorption of SiO_2.

One of the advantages of our results is the ICMR-free spectroscopy, i.e., free from spurious absorptions. Features in the spectra are clearer than ordinary spectroscopy. Direct comparison with spectra and calculation is capable. To our knowledge, this work gives the first reliable absorption spectra of Ni nanoparticles in SiO_2.

4.2 Criteria for SPR energy

Using a sets of dielectric constants from a literature[19], the absorption spectra were calculated using both MG and Mie theories, and are shown in Fig. 2(a). Both the calculations relatively well reproduce the experimental result (after 800 °C annealing). Although origin of the small discrepancy between the experimental and the calculation is unknown, it is
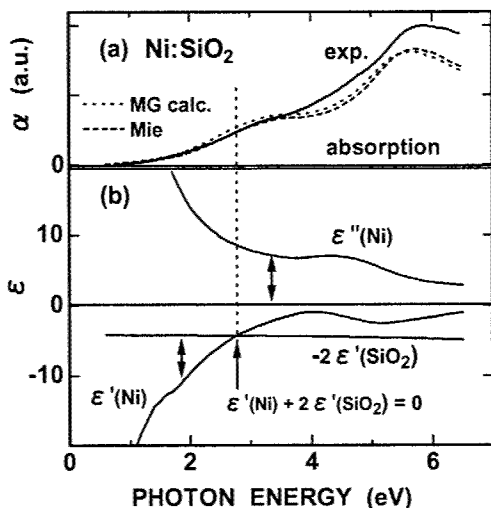
Fig. 2 (a) Comparison of absorption spectra: solid, dashed and broken lines indicate results of an experiment (after 800 °C annealing), results of Maxwell-Garnett and of Mie theories, respectively. (b) Energy dependence of real and imaginary parts of dielectric constants of Ni and SiO_2.
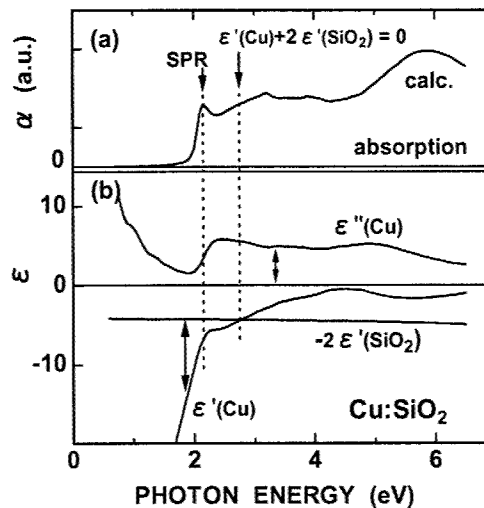
Fig. 3 (a) An absorption spectrum of Cu nanoparticles dispersed in SiO_2, calculated by Maxwell-Garnett theory. (b) Energy dependence of real and imaginary parts of dielectric constants of Cu and SiO_2.
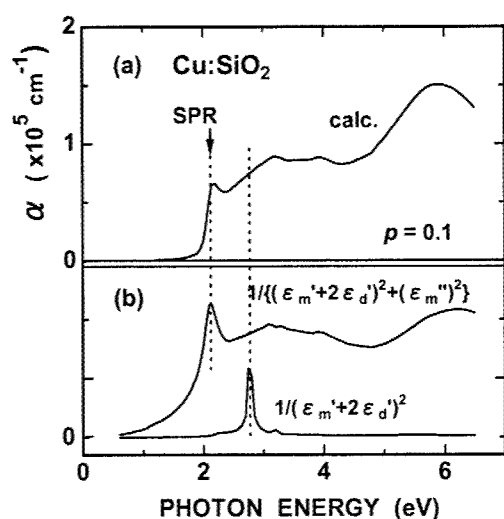
Fig. 4 (a) A calculated absorption spectrum of Ni nanoparticles dispersed in SiO_2. (b) Energy dependence of $(\varepsilon_m' + 2\ \varepsilon_d')^{-2}$ and $\{(\varepsilon_m' + 2\ \varepsilon_d')^2 + (\varepsilon_m'')^2\}^{-1}$ are plotted. The maxima correspond to the SPR criteria (6) and (7), respectively.
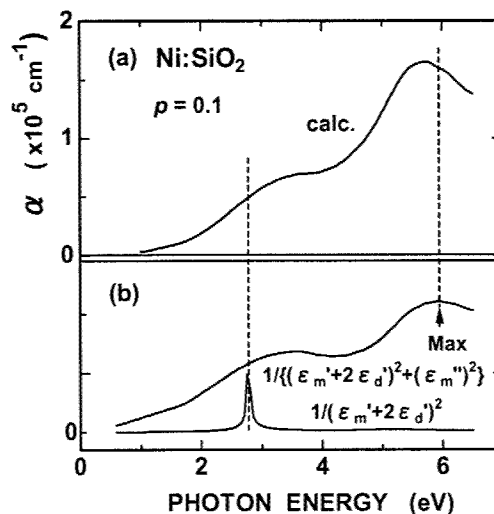
Fig. 5 (a) A calculated absorption spectrum of Cu nanoparticles dispersed in SiO_2. (b) Energy dependence of $(\varepsilon_m' + 2\ \varepsilon_d')^{-2}$ and $\{(\varepsilon_m' + 2\ \varepsilon_d')^2 + (\varepsilon_m'')^2\}^{-1}$ are plotted. The maxma correspond to the SPR criteria (6) and (7), respectively.

possibly due to residual defect absorption. It is noted that the size effect is not included in the calculations of this subsection, because the size effects on the absorption spectra are not large for Ni, as will be shown in subsection 4.4.

A next concern is identification of the SPR of Ni nanoparticles from the two peaks, 3.3 eV or 6.0 eV. Isobe et al.[17] assigned the 3.6 eV peak as SPR based on the criterion shown as eq. (6). However, an exact energy obtained from eq. (6) is in 2.8 eV. Similar procedures are shown in Fig. 2 with our data. The values of dielectric constants are after the same literature.[19] In Fig. 2(b), ε_m' and $-2\varepsilon_d$' are plotted against the photon energy, where ε_m' and ε_d' denote real parts of Ni and SiO_2, respectively. An intersection point between the two curves indicates ε_m' + $2\varepsilon_d$' = 0, i.e., the criterion (6). The criterion gives SPR energy of 2.8 eV, but the peak energy was 3.3 eV. The difference of ~0.5 eV is not negligible.

A similar plot for Cu nanoparticles in SiO_2 is shown in Fig. 3. The criterion (6) gives SPR energy of 2.8 eV, although the true SPR energy is 2.15 eV. A weak peak due to the band-to-band transition of Cu is visible around 3.2 eV. Only from the criterion, we cannot assign the SPR peak to either 2.15 eV or 3.2 eV. These facts indicate the criterion (6) is no longer reliable. The reason is probably due to neglecting ε_m''. The criterion (6) is valid only when ε_m'' is almost constant. However, as shown in Figs. 2 and 3, ε_m'' strongly changes with the photon energy. Next candidate criterion is

$$(\varepsilon_m' + 2\varepsilon_d')^2 + (\varepsilon_m'')^2 = \text{minimum.} \qquad (7)$$

To easily find minima of the criterion (7), the inverse of the left side of eq. (7) is shown in Figs. 4 and 5 with the absorption spectra. For comparison, the inverse of the criterion (6) is also shown. The peaks of the curves correspond to the candidate SPR energies. In $Cu:SiO_2$ shown in Fig. 4, the criterion (7) gives an energy of 2.1 eV close to the true SPR of 2.15 eV. However, in $Ni:SiO_2$ shown in Fig. 5, the criterion (7) gives an energy of 5.9 eV. From these results and the derivation, eq. (7) is the criterion for the absorption peak, but not only for SPR.

4.3 Dielectric constants of Cu and Ni

Dielectric constants of metals ε_m are described as a sum of free-electron contribution ε_f and bound-electron contribution ε_b,

$$\varepsilon_m = \varepsilon_f + \varepsilon_b \qquad (8)$$

The free-electron contribution ε_f is approximated by the Drude model,

$$\varepsilon_f = 1 - \frac{\omega_p^2}{\omega^2 + i\omega\omega_{tau}} \qquad (9)$$

where ω_p and ω_{tau} denote a bulk plasma frequency and a relaxation frequency. At low energy region but $\omega > \omega_{tau}$, real part and imaginary parts of ε_f are approximated as,

$$\varepsilon_f' \approx 1 - \frac{\omega_p^2}{\omega^2} \qquad (10)$$

$$\varepsilon_f'' \approx \frac{\omega_p^2 \omega_{tau}}{\omega^3} \qquad (11)$$

To obtain values of ω_p and ω_{tau}, the dielectric constant data were plotted in ε_f' vs. $1/\omega^2$ and $\omega\varepsilon_f$'' vs. $1/\omega^2$, as shown in Fig. 6 for Cu and Fig. 7 for Ni. The ω_{tau} value of Ni is 10 times larger than that of Cu. This is a reason of larger width of the Ni absorption peak comparing with the width of Cu SPR. Using the parameters ω_p and ω_{tau} determined, ε_f was plotted as solid lines in Fig. 8 for Cu and in Fig. 9 for Ni. The experimental data[19] of real and imaginary parts of the dielectric constants were shown as black dots. Difference between the Drude model (solid lines) and the experimental data (dots) is ascribed to the bound-electron contribution. In Cu, data below ~2 eV is well-fitted by the Drude model and the bound-electron contribution appears exceeding ~2 eV. As for Ni, in all the energy region shown in Fig. 9, a certain level of the bound-electron contribution cannot be neglected. The difference is interpreted as follows: Since Cu has closed d-bands, a certain amount of excitation energy, ~2 eV in this case, is required. Since Ni has partially-filled d-bands, lower energy excitation is possible. Since the dielectric constants of Cu are well-fitted by the Drude
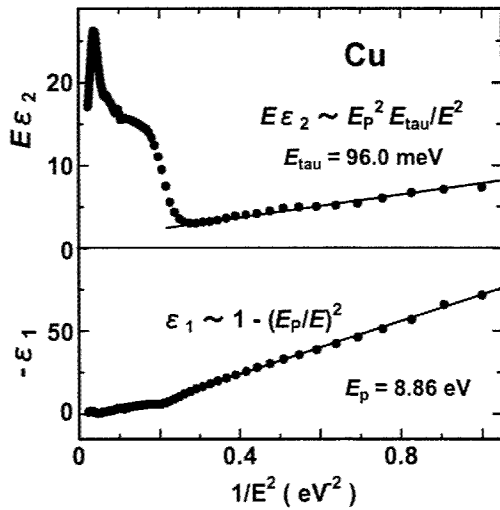
Fig. 6 Real and imaginary parts of dielectric constants of Cu are plotted as closed circles in $-\varepsilon'$ vs. E^{-2} and $E\varepsilon''$ vs. E^{-2}. From the slops, the (bulk) plasmon energy E_p and the relaxation energy E_{tau} are determined.
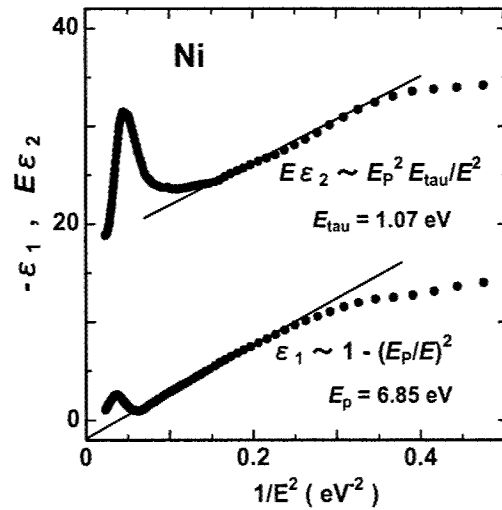
Fig. 7 Real and imaginary parts of dielectric constants of Ni are plotted as closed circles in $-\varepsilon'$ vs. E^{-2} and $E\varepsilon''$ vs. E^{-2}. From the slops, the (bulk) plasmon energy E_p and the relaxation energy E_{tau} are determined.
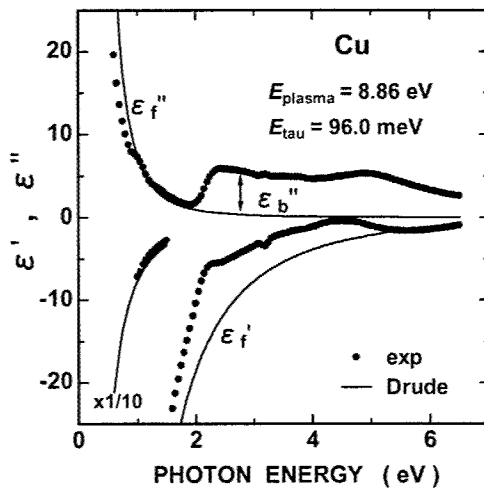
Fig. 8 Energy dependence of real and imaginary parts of dielectric constants of Cu. Closed circles and solid lines indicate literature data and free-electron contribution. Deviation between the circles and the lines corresponds to bound-electron contribution.
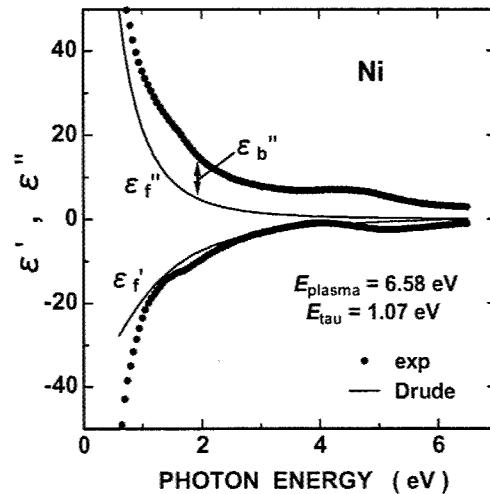
Fig. 9 Energy dependence of real and imaginary parts of dielectric constants of Ni. Closed circles and solid lines indicate literature data and free-electron contribution. Deviation between the circles and the lines corresponds to bound-electron contribution.

model below ~2 eV, i.e., free-electron like, the peak at 2.15 eV is ascribed to SPR. It should be reminded that the plasmon picture stands on the free-electron model. In the case of Ni, the dielectric constants, particularly in imaginary part, cannot be fitted with the Drude model in all the energy region. If we adapt a definition of SPR as an absorption band whose energy is close to an intersection between the free-electron like ε_m' which negatively diverges to zero energy, and substrate dielectric constant ε_d' multiply -2, the 3.3 eV peak is ascribed to SPR. However, the bound-electron contribution is also large to the 3.3 eV peak.

4.4 The mean-free-path confinement effect

The assignment of the 3.3 eV peak to SPR of Ni nanoparticles is also confirmed from calculated size effects. Mean-free-path of electrons in metal nanoparticles is limited by boundaries of the nanoparticles. This effect can be included in the calculation with modification of the relaxation energy ω_{tau}, as

$$\omega_{tau} = \omega_{tau,o} + \frac{2v_F}{d} \tag{11}$$

where $\omega_{tau,0}$ and v_F denote the relaxation energy of bulk and the Fermi velocity, respectively. Using the equation above with MG theory, size-dependent absorption spectra were calculated and are shown in Fig. 10 for Cu and Fig. 11 for Ni. According to an estimation[20], only Ni nanoparticles which includes more than 34 Ni atoms, i.e., ~0.9 nm of diameter, behave as metals. It may not be meaningful to simulate metal nanoparticles smaller than ~1 nm. However, since the estimation is rough, results down to 0.5 nm in diameter are shown in Figs. 10 and 11.

With decreasing the diameters of nanoparticles, absorption decreases for both Cu and Ni, although the volume fraction p is kept constant. In the case of Cu, below 20 nm of diameters, absorption lower than ~4.5 eV including SPR, decrease, although the 6 eV peak begins to decrease below 3 nm. This is why the 6 eV peak mainly consists of the bound-electron contribution. The 6 eV peak is less sensitive to nanoparticle size than the lower energy absorption including SPR. Below 5 nm, the SPR shifts to lower energy side and becomes broader. Finally, the SPR peak comes to ~1.6 eV at ~0.5 nm. At d ~0.5 nm, a new peak appears around 1.0 eV.

In the case of Ni, the size dependence is gentle. This is consistent with the fact the bound-electron contribution is not negligible in all the energy region shown, since the bound-electrons are less sensitive to the size. Below 3 nm, both the peaks at 3.3 and 6.0 eV begin to decrease, and absorption lower than 2 eV slightly increases. With decreasing the diameters, the 3.3 eV peak which is ascribed to SPR of Ni nanoparticles also shows a lower energy shift, similar to SPR of Cu nanoparticles. These shifts are mainly due to decrease of $\varepsilon_m' \sim - \omega_p^2/(\omega^2 + \omega_{au}^2)$, with decreasing d, i.e., increasing ω_{au}. The similar dependence of the 3.3 eV peak with the Cu SPR supports the assignment of the 3.3 eV to SPR.
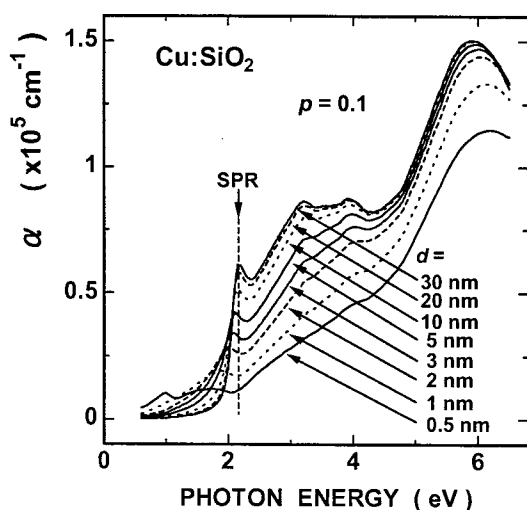
Fig. 10 Calculated diameter dependence of absorption spectra of Cu nanoparticles in SiO_2. The mean-free-path confinement effect is included. Volume fraction of Cu is kept as $p = 0.1$, irrespective of nanoparticle diameters d.
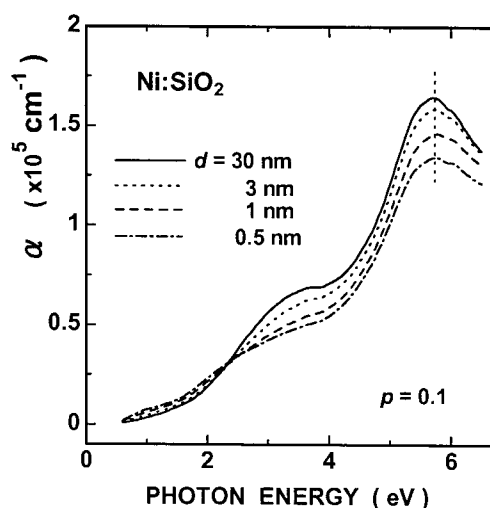
Fig. 11 Calculated diameter dependence of absorption spectra of Ni nanoparticles in SiO_2. The mean-free-path confinement effect is included. Volume fraction of Ni is kept as $p = 0.1$, irrespective of nanoparticle diameters d.

5. CONCLUSIONS

Absorption spectra of Ni nanoparticles in silica glass (SiO_2) fabricated by negative-ion implantation of 60 keV Ni to 4×10^{16} ions/cm^2 were evaluated as an example of magnetic metal nanoparticles which show much broad peaks than the SPR of noble metal nanoparticles. Three sets of spectra, i.e., transmittance, reflectance of implanted-surface side and that of rear-surface side, of the same samples were measured and processed to exclude effects of the ICMR due to substrates. Although the absorption spectrum of as-implanted state is smeared with defect absorption, two absorption bands at 3.3 and 6.0 eV due to Ni nanoparticles are clearly observed after annealing at 800 °C in vacuum. The clear appearance of the 6.0 eV peak results from the ICMR-free spectroscopy. To our knowledge, this is the first direct observation of the 6.0 eV peak, although the peak has been theoretically predicted and was indirectly observed.

A predicted energy from a criterion for SPR, $\varepsilon_m'(\omega) + 2\varepsilon_d'(\omega) = 0$, was in 2.8 eV, far away from the observed peaks. Another criterion, $(\varepsilon_m' + 2\varepsilon_d')^2 + (\varepsilon_m'')^2$ = minimum, gives a peak energy of 5.9 eV. From decomposition of the dielectric constants into free- and bound-electron contributions, we conclude that the 3.3 eV peak is SPR-like, although the bound-electron contribution to the 3.3 eV peak is not negligible. The calculated size dependence of the absorption spectra is also consistent with the assignment of the 3.3 eV peak. The large contribution of the bound-electrons is due to a nature of the partially filled $3d$ orbitals of Ni. This is contrast to the closed $3d$ orbitals of Cu, and probably the origin of the broad peak width. Similar broad peaks are also observed in Fe and Co nanoparticles, which are candidates of ferromagnetic species, in SiO_2. The ICMR corrections are important for measurements of such broad peaks.

ACKNOWLEDGMENTS

REFERENCES

1. R.F. Haglund, L. Yang, R.H. Magruder, C.W. White, R.A. Zhur, L. Yang, R. Dorsinville, R.R. Alfano, "Nonlinear optical properties of metal-quantum-dot composites synthesized by ion implantaition", *Nucl. Instr. and Meth.* **B91**, pp. 493-504, 1994.

2. A. Nakajima, H. Nakao, H. Ueno, T. Futatsugi, N. Yokoyama, "Coulomb blockade in Sb nanocrystals formed in thin, thermally grown SiO_2 layers by low-energy ion implantation", *Appl. Phys. Lett.* **73**, pp. 1071-1073, 1998.

3. Y. Mori, G.D. Alton, A. Takagi, A. Ueno, S. Fukumoto, "Further evaluation of the high intensity plasma sputter heavy negative ion source", *Nucl. Instr. and Meth.* **A273**, pp. 5-12, 1988.

4. J. Ishikawa, H. Tsuji, Y. Toyota, Y. Gotoh, K. Matsuda, M. Tanjyo, S. Sakaki, " Negative-ion implantation technique", *Nucl. Instr. and Meth.* **B96**, pp. 7-12, 1995.

5. N. Kishimoto, Y. Takeda, V.T. Gritsyna, E. Iwamoto, T. Saito, "A high-current negative-ion implanter and its application for nanocrystal fabrication in insulators", *IEEE Transactions from 1998 International Conference on Ion Implantation Technology Proceedings*, eds. J. Matsuo, G. Takaoka, I. Yamada, pp. 342-345, 1999.

6. N. Kishimoto, N. Umeda, Y. Takeda, V.T. Gritsyna, T.J. Renk, M.O. Thompson, "In-beam growth and rearrangement of nanoparticles in insulators induced by high-current negative copper ions", *Vacuum*, **58**, pp. 60-78, 2000.

7. N. Kishimoto, Y. Takeda, N. Umeda, V.T. Gritsyna, C.G. Lee, T. Saito, "Metal nanocrystal formation in magnesium aluminate spinel and silicon dioxide with high-flux Cu$^-$ ions," *Nucl. Instr. and Meth.* **B166-167**, pp. 840-844, 2000.

8. Y. Takeda, C.G. Lee, N. Kishimoto, "Nonlinear optical properties of Cu nanoparticle composites fabricated by 60 keV negative ion implantation," *Nucl. Instr. and Meth.* **B191**, pp. 422-427, 2002.

9. Y. Takeda, V.T Gritsyna, N. Umeda, C.G. Lee, N. Kishimoto, "Linear and nonlinear optical properties of Cu nanoparticles fabricated by high-current Cu⁻ implantation in silica glass," *Nucl. Instr. and Meth.* **B148**, pp. 1029-1033, 1999.

10. Y. Takeda, J.P. Zhao, C.G. Lee, V.T. Gritsyna, N. Kishimoto, "Nonlinear optical properties of Cu nanoparticles embedded in insulators by high-current Cu⁻ implantation," *Nucl. Instr. and Meth.* **B166-167**, pp. 877-881, 2000.

11. H. Amekura, N. Umeda, Y. Takeda, N. Kishimoto, H. Nejo, "Fabrication of Cu nanoparticles embedded in a-SiO₂ thin layer and observation of nonlinear transport," *Proceedings of the 5th International Symposium on Advanced Physical Fields (APF-5),* ed. K. Yoshihara, pp. 203-207, 2000.

12. E. Cattaruzza, F. Gonella, G. Mattei, P. Mazzoldi, D. Gatteschi, C. Sangregorio, M. Falconieri, G. Salvetti, G. Battaglin, "Cobalt nanoclusters in silica glass: Nonlinear optical and magnetic properties," *Appl. Phys. Lett.* **73**, pp. 1176-1178, 1998.

13. H. Amekura, H. Kitazawa, T. Mochiku, N. Umeda, Y. Takeda, N. Kishimoto, "Nickel nanoparticles dispersed in SiO₂ fabricated by high-flux negative-ion implantation of 60 keV," *Proc. SPIE* **Vol. 4936,** pp. 1 – 8, 2002.

14. J.F. Ziegler, J.P. Biersack, U. Littmark, *The Stopping and Range of Ions in Solids*, Chap.8, Pergamon Press, New York, 1985. http://www.srim.org/

15. J.C. Maxwell-Garnett, "Colours in metal glasses, in metallic films, and in metallic solutions.-II", *Philos. R. Soc. London* **205**, pp. 237-288, 1906.

16. For example, M. Born, E. Wolf, *Principles of Optics*, Chap.8, Pergamon, Oxford, 1959.

17. T. Isobe, S.Y. Park, R.A. Weeks, R.A. Zhur, "The optical and magnetic properties of Ni⁺-implanted silica," *J. Non-Cryst. Solids*, **189**, pp. 173-180, 1995.

18. O.Cíntora-González, C. Estournès, D. Muller, J. Guille, J.J. Grob, "Magnetic behavior of Ni⁺ implanted silica," *Nucl. Instr. and Meth.* **B147**, pp. 422-426, 1999.

19. E.D. Palik, *Handbook of Optical Constants of Solids, Vol. I, II, III*, Academic, San Diego, 1998.

20. J. Zhao, X. Chen, G. Wang, "Critical size for metal-nonmetal transition in transition-metal clusters," *Phys. Rev.* **B50**, pp. 15424-15426, 1994.

In situ optical absorption spectroscopy, incandencence, and light scattering characterization of single-wall carbon nanotube synthesis by the laser vaporization technique

Alex A. Puretzky[a], David B. Geohegan, Henrik Schittenhelm[b]

Oak Ridge National Laboratory, Oak Ridge, TN 37831
[a]Dept. of Materials Science and Engineering, University of Tennessee, Knoxville, TN 37996-2200
[b]Robert Bosch GmbH, Dept. of Physical Technologies, Gerlingen-Schillerhohe, Germany

ABSTRACT

In this paper we discuss three optical methods for in situ characterization of single wall carbon nanotube (SWNT) growth by laser vaporization at elevated temperatures: optical absorption spectroscopy, optical incandescence, and light scattering. Optical absorption spectroscopy was successfully used to estimate the size of carbon nanoparticles and to monitor the atomic metal catalyst in the propagating laser ablation plume. These measurements indicate that the aggregation rate of carbon nanoparticles increases rapidly at lower oven processing temperatures. The second method, incandescence, was applied to measure the particle temperature within the propagating plume at different times after ablation. The third approach, imaging of the plume using Rayleigh scattered light, was used to monitor the ejected material inside the hot furnace as well as to observe the plume when it exits the furnace, i.e., in the cold zone of a quartz tube reactor. We demonstrated that Rayleigh scattering imaging combined with TEM analysis of the produced material was very useful for controlling the length of SWNTs and estimation of the growth rates. A general picture of SWNT growth by laser vaporization based on in situ diagnostics of ejected material at different times after ablation is discussed.

Keywords: carbon nanotubes, laser plasmas, spectroscopy, in situ diagnostics, nanoparticles, hydrodynamics

1. INTRODUCTION

Single wall carbon nanotubes exhibit remarkable electronic and structural properties, which promise to revolutionize various application areas, from nanoscale electronics to ultra-lightweight structural materials [1]. Laser vaporization is one of the best methods to grow high-quality, high-purity SWNTs. As typically employed, each laser shot vaporizes a small amount of material ($\sim 10^{16}$ carbon atoms and $\sim 10^{14}$ metal catalyst atoms, e.g., ~ 1 at% Ni, Co, Fe, Y, etc.) inside an oven (~ 1200 C) into ~ 500 Torr of gently flowing inert gas [2,3]. On a single laser shot [4], the ejected material self-assembles to form a high volume fraction of SWNTs, which can be up to 10 microns in length [3, 5].

Since the first introduction of laser vaporization process in 1995 [2] researchers attempted optimization by manipulating numerous experimental parameters, e. g., laser parameters (energy fluence, peak power, repetition rate, cw vs. pulsed) [4, 6-9], target composition [10, 11], carrier gas flow rate and pressure [7, 12], ambient temperature [7, 13], etc.
These studies provided a reasonable optimization of the processs and created many speculations about the growth mechanism.

Unfortunately, the growth of SWNTs is not controlled or fully understood. Thus, their potential technological applications, which depend on the atomic-scale structure (chirality), growth rates and the possibility of large-scale production are affected by this lack of the fundamental understanding.

The first attempts to perform in situ spectroscopic studies during SWNT growth were based on the observation of the luminous laser plasma at early times after nanosecond Nd:YAG laser ablation (0-80 ms) [14] and after long-pulse CO_2-laser vaporization at 25-1200 C [15]. These measurements were limited to times while the ablated material is still quite hot.

Our approach to understanding the growth mechanism and optimizing the yield of SWNTs is to combine laser vaporization and in situ diagnostics [16-18]. Recently, we used laser-induced emission, gated intensified charge-coupled device (ICCD) imaging, and optical spectroscopy to probe the ablated material in a long time interval after ablation (from 0 to a few seconds) [16-18]. In this work the plume of ejected material was followed for several seconds after 8ns-Nd:YAG-laser ablation pulse using the combined imaging and spectroscopy of Co atoms, C_2, and C_3 molecules, and clusters. These spectroscopic

diagnostics showed that nanotube growth occurs within a vortex ring plume during the long periods of time (~1 s) when the atomic molecular vapor already condensed into clusters. The time for conversion of atomic and molecular species to clusters was estimated as ~200 ms for carbon and ~2 ms for cobalt at 1100 C. We concluded that SWNT grow by *condensed phase conversion* from feedstock of carbon and metal nanoparticles. This conclusion was confirmed by our recent work on ex situ high temperature (900-1200 C) annealing of the precursor material generated by time-restricted laser ablation and containing short SWNTs (<200 nm), amorphous carbon, and metal nanoparticles [19].

The main results of these studies were later confirmed by Kokai et al [20] who used similar time-resolved imaging and spectroscopy approach based on in situ measurements of laser plume emission and light scattering from the propagating plume.

In situ monitoring of catalyst Ni atoms by laser induced fluorescence near the target region (1-3 mm) was performed by De Boer et al [21], who concluded that Ni stays in atomic vapor phase for several milliseconds after ablation. This is consistent with our measurements on Co [16-18].

Prior to these diagnostic studies very little was known about where, when, and at what rate the growth occurred. Recently, despite diagnostic investigations, estimates for growth rates of SWNTs by laser vaporization inside the hot oven environment range over five orders of magnitude, from ~ 1 mm/s up to ~ 15 cm/s [22, 23].

In this paper detailed information on the growth environment of SWNTs during the early stages of their development is provided with new estimates of size and temperature of the aggregated nanomaterial which propagates inside the oven reactor a few milliseconds after laser vaporization. Optical absorption and emission spectroscopy techniques are described for these measurements. These measurements are correlated with oven temperature profiles and Rayleigh-scattering imaging of the propagating nanomaterial to restrict growth times available at known temperatures. Using length distributions of SWNTs produced under these well-defined conditions, the upper and lower limits of the growth rates of SWNTs were estimated as 0.6 and 5.1 mm/s for the typical nanosecond laser vaporization conditions used in this study.

In conclusion, a comprehensive picture of SWNT growth is presented which combines our spatial and temporal measurements of plume composition, temperature, and particle size. These new results further support our previous studies which indicate that SWNT grow over extended times (> 100 ms to seconds) by a condensed phase conversion process.

2. EXPERIMENTAL

The SWNT growth setup is similar to that described in Refs. [17, 18]. It consists of a quartz tube (2 in. diameter, 24 in. length) mounted inside a hinged tube furnace (12 in. length) that can operate at maximum temperature of 1200 C. The quartz tube was O-ring sealed to standard 4.5-in. conflat vacuum components. The ablation and probe laser beams entered the quartz tube through the same Suprasil window, which was mounted in a vacuum flange. A dichroic mirror was used to pass the ablation and probe laser beams coaxially. The furnace was equipped with a rectangular quartz window (10 in. length, 1 in. width, Suprasil 1) for spectroscopic diagnostics of ablated material inside the furnace. A temperature profile along the axis of the quartz tube was measured by introducing a thermocouple coaxially with the quartz tube. In this case the Suprasil laser-entry window was replaced with a mount for the thermocouple. The end of the thermocouple could be positioned at any point at the tube axis.

Argon gas was introduced around the quartz window and was controlled at 100 sccm to maintain a 500 Torr pressure. The gas was pumped out through a needle valve downstream of a brass water-cooled collector, which was inserted into the quartz tube and positioned just outside the furnace.

A 1-in. diameter graphite target containing 1 at % each of Ni (Alfa, 2.2-3.0 mm, 99.9%) and Co (Alfa, 1-6 mm, 99.8%) powders was prepared with carbon cement (Dylon GC). The target was screwed onto a 0.25 in. diameter graphite rod and was rotated during operation. This rod was mounted along the tube axis through a hole in the collector.

The ablation laser (1.06 mm Nd:YAG, 300 mJ, 8 ns FWHM pulse) beam was focused to a 4 mm-diameter, donut-shaped spot on the target. The energy density at the target was about 3 J/cm^2. A gated ICCD-camera system (Princeton Instruments, 5 ns minimum gate, 200-820 nm spectral range) was used to perform scattering imaging of the ablation plume using a defocused XeCl-laser pulse (308 nm, 30 ns FWHM, 6 mJ/cm^2) at different time delays. The 5 ns-ICCD gate was set to occur at the peak of the XeCl laser pulse.

A 1 in. diameter quartz window located near the center of the furnace at the opposite side of the rectangular window allowed absorption spectroscopy of the ejected material. In this case a collimated beam from a pulsed Xe-lamp (~1 ms FWHM) was passed through the plume and its extinction spectrum was measured at different times after ablation. The absorption spectra were recorded with a 0.3 m spectrometer (Acton VM-503) equipped with an intensified, gated diode array (Princeton Instruments IRY-700 RB).

3. IN SITU ABSORPTION SPECTROSCOPY OF CARBON NANOPARTICLES: ESTIMATING PARTICLES SIZE

To estimate the size of carbon nanoparticles in the plume we used absorption spectroscopy. In this case a beam from a pulsed Xe-lamp was passed through the plume and its extinction spectrum (scattering plus absorption) was measured (Fig. 1). The particle size was estimated from the shape of the extinction spectrum. It should be mentioned that such etimates could be done only in the case of a relatively large particle.

Really, for small particles ($2\pi a << \lambda$, Rayleigh criterion: $2\pi a < 0.3\lambda$) the absorption and scattering efficiency (cross-section/πa^2) are given by [24]

$$Q_{abs}=4(2\pi a/\lambda)Im[(m^2-1)/(m^2+2)], \quad Q_{sca}=(8/3)(2\pi a/\lambda)^4|(m^2-1)/(m^2+2)|, \quad (1)$$

where a is the particle radius, m is the complex index of refraction, m = n-ki. If m is only a weak function of λ over the measured wavelength range, than $Q_{abs} \sim 1/\lambda$, $Q_{sca} \sim 1/\lambda^4$, and there is no size information in the shape of the extinction spectra.

For larger particles ($a > 0.05\ \lambda$) the shape of the absorption/extinction spectrum is sensitive to the particle size. In this case the particle size can be estimated from the shape of the extinction spectra (absorption plus scattering) using Mie theory for spherical particles, the computer code given in Ref. [24] and the complex index of refraction, m(λ), for carbon soot particles given in Ref. [25]. Figures 2a, b show the example of these calculations for the carbon particle size in the range from 20 nm to 100 nm. The calculated absorption spectra (Fig. 2a) clearly show that for particle sizes > 40 nm there are pronounced maxima in the absorption spectra in the spectral range 300-500 nm, and the position of the maxima depends on the particle size. Unfortunately, one have to take into account losses due to probe light scattering which could be quite significant for a relatively large particle size. Figure 2b shows the calculated scattering spectra for the different particle sizes (20-100 nm). One can see that for a relatively small particle (< 20 nm) the scattering contribution to the extinction spectra is very small.

Fig. 1. Schematic of the experimental setup used for in situ absorption measurements.

Figures 3a, b show the extinction spectra of the laser generated plumes measured at two different ambient temperatures, 760 C and 1000 C, approximately 1 ms after ablation. The set of extinction spectra, calculated based on Mie theory for
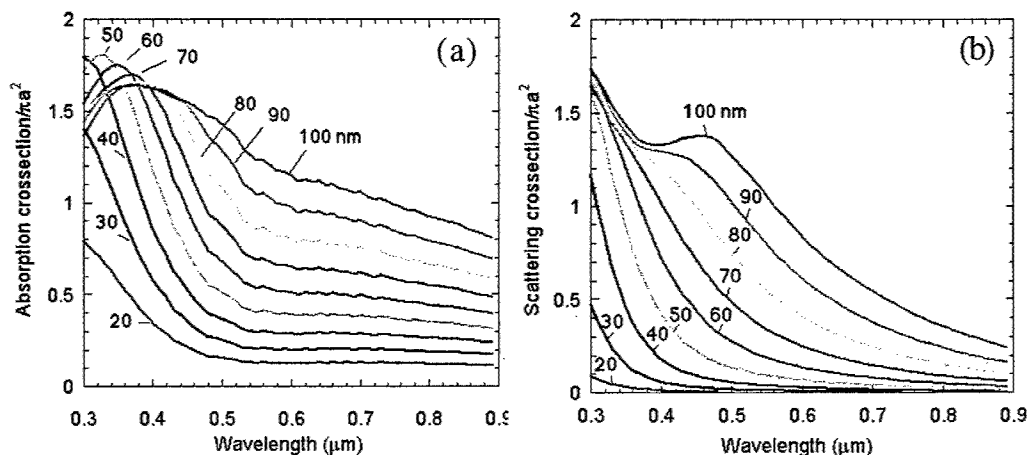
Fig. 2a, b. Calculated (a) absorption and (b) scattering spectra of spherical carbon nanoparticles for different particle sizes (20-100 nm).
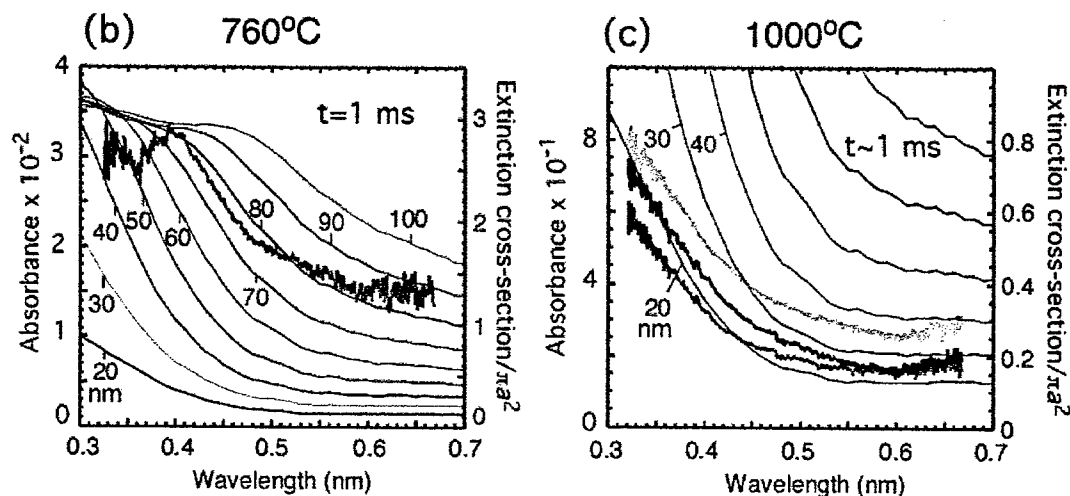
Fig. 3. *Experimental extinction spectrum (bold curve) and the set of extinction spectra calculated on the basis of Mie theory for spherical particles at t ~ 1 ms at (a) 760 C and (b) at 1000 C oven temperatures.*

spherical particles, having different radii is shown for comparison. One can see that at 760 C oven temperature the shape of the measured spectrum is approximately fitted by the curve calculated for $a = 80$ nm. This means that by 1 ms the clusters aggregated to form relatively large aggregates. The spectrum measured at 1100 C is fitted fairly well by the extinction spectum calculated for $a = 20$ nm. This particle size is close to obeying the Rayleigh criterion ($a\sim14$nm for $\lambda = 300$ nm) and one can conclude that in this case the size of the particles is smaller than 20 nm. The measured spectra have the same shape up to 4 ms after ablation. Summarizing the absorption measurements we can conclude that carbon nanoparticles aggregate much slower at higher ambient temperatures.

It should be mentioned that to deduce the particles size we used Mie theory for the spherical particles and the proper particle refractive index. In reality clusters form polydisperse fractal aggregates. The interpretation of absolute angular light scattering extinction measurements for such aggregates is given in Ref. [26], were it was shown that volume-equivalent single particle models (Rayleigh/Mie) overestimated the particle radius by a factor of ~3.

Using the absorption spectroscopy we can also monitor the atomic catalyst. Figure 4 shows the absorption spectrum measured at 600 ms after ablation at 1100 C.
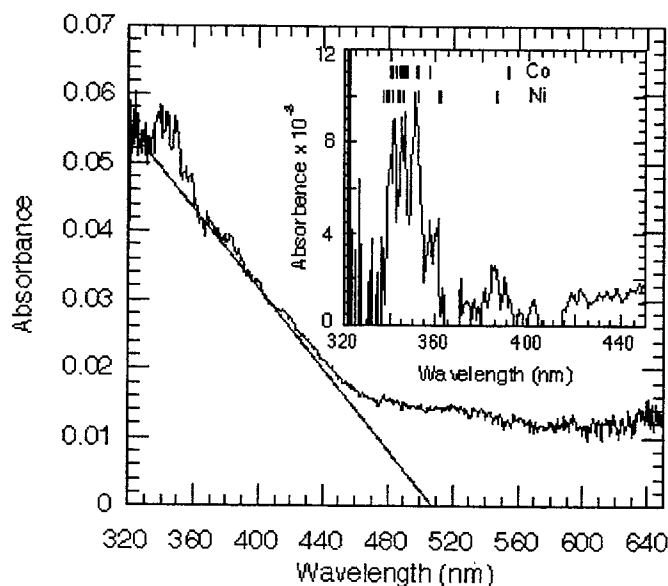
Fig. 4. *Absorption spectrum of C/Co/Ni plume measured at 0.6 ms after ablation. The inset shows the atomic Co, Ni spectrum obtained by subtraction of the continuous background spectrum from carbon nanoparticles. The set of the most intense atomic Co, Ni absorption lines is shown for the tentative assignment of the experimental peaks.*

The peaks near 350 nm can be assigned to atomic Co and Ni lines. Unfortunately, the low signal to noise level in this measurement did not allow us to make the exact assignment of these lines. These atomic lines are superimposed on the broad absorption spectrum from carbon clusters. The presence of the strong absorption continuum from carbon clusters at 600 ms after ablation is consistent with our previous studies based on laser induced fluorescence (LIF), which show that the atomic/molecular carbon converts to clusters very rapidly during the first 200 ms, but the catalyst metal stays in the atomic phase much longer and disappears approximately after 2 ms after ablation [17,18]. In addition to LIF spectroscopy and imaging to observe the metal catalyst atomic species, the absorption spectroscopy can be a useful tool to estimate an absolute concentration of metal catalyst atoms in the propagating C/Co/Ni plume.

4. IN SITU INCANDESCENCE: MEASUREMENTS OF PARTICLES TEMPERATURE INSIDE THE PROPAGATING VORTEX RING PLUME

It is important to know the temperature of the particles in the propagating plume and to correlate this temperature with the time after ablation. First, using this correlation we can estimate when SWNTs start to grow, since by this time the temperature should not exceed the eutectic temperature for carbon/metal catalyst nanoparticles. It was shown experimentally that the yield of SWNT drops rapidly at $T > T_{eut}$ (C/Co, C/Ni) [27]. Second, to limit the growth times and to estimate the growth rates of SWNTs it is necessary to determine how fast the species within the plume reach the ambient furnace temperature.

To estimate the temperature of carbon particles inside the propagating plume we measured their blackbody emission (incandescence) spectra at different times and positions in the furnace (Fig. 5a). The plume emission spectra were fitted with the Planck blackbody function. The intensity of the blackbody emission from a particle of radius a at a wavelength λ into interval $\Delta\lambda$ is given by

$$I(\lambda,a)=\varepsilon(\lambda,a)8\pi^2a^2c^2h\Delta\lambda/\lambda^5[\exp(hc/\lambda k_B T)-1], \qquad (2)$$

where $\varepsilon(\lambda, a)$ is the spectral emissivity and T is the absolute temperature of the particle. For small particles ($a < 0.3$ $\lambda/2\pi$) $\varepsilon(\lambda, a) \sim 1/\lambda$ and $I(\lambda, a) \sim 1/\lambda^6$. For larger particles we can assume that ε = const that gives, $I(\lambda, a) \sim 1/\lambda^5$. It should be mentioned that an ICCD detector counts photons, therefore the number of photons per unit time will be proportional to $1/\lambda^4$ in the case of the constant emissivity ε.

Fig. 5b shows an example of the blackbody fit of the emission spectrum of the carbon particles in the plume measured at t = 1ms after ablation assuming that ε = const. This fit gives the plume temperature of 1488 C. Figure 6a shows the temperature of the particles within the plume versus the time after ablation. The temperature of the plume approaches the ambient temperature (T_{abm}=750 C) after approximately 4 ms after ablation. For T_{amb} = 1100 C, a plateau is observed at T~2500 C in the time interval 0.3-0.7 ms (Fig. 6b). A similar plateau in the plume emission intensity was observed by Suzuki et al [28]. An exothermic process, probably formation of fullerene-like structures, keeps the plume temperature constant from 0.3 to 0.7 ms. In the case of higher ambient temperature (1100 C), it is also takes approximately 4 ms after ablation for the particles within the plume to cool down to the ambient temperature.
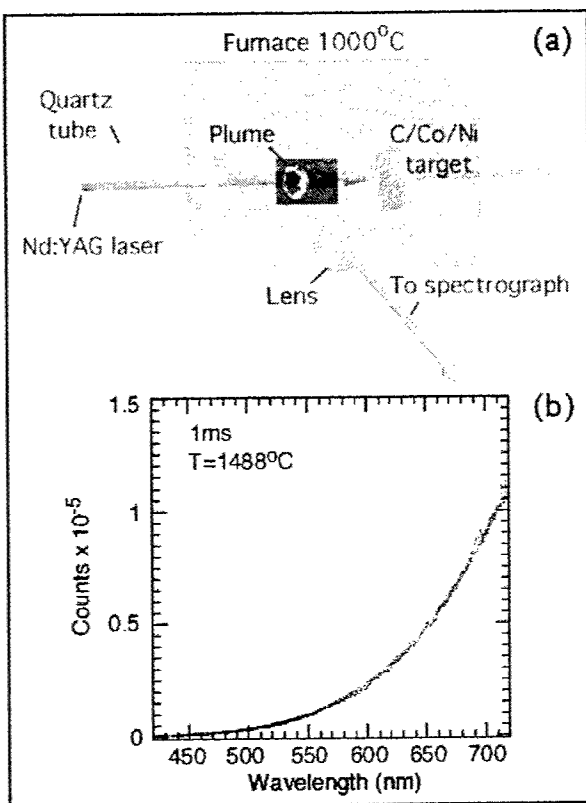
Fig. 5. *(a) Schematic of the temperature measurements of the particles inside the propagating plume. (b) Experimental blackbody emission spectrum of carbon nanoparticles within the plume measured at 1 ms after ablation (dark curve) and fit to Planck's Law yielding the temperature of 1488 C (light curve).*
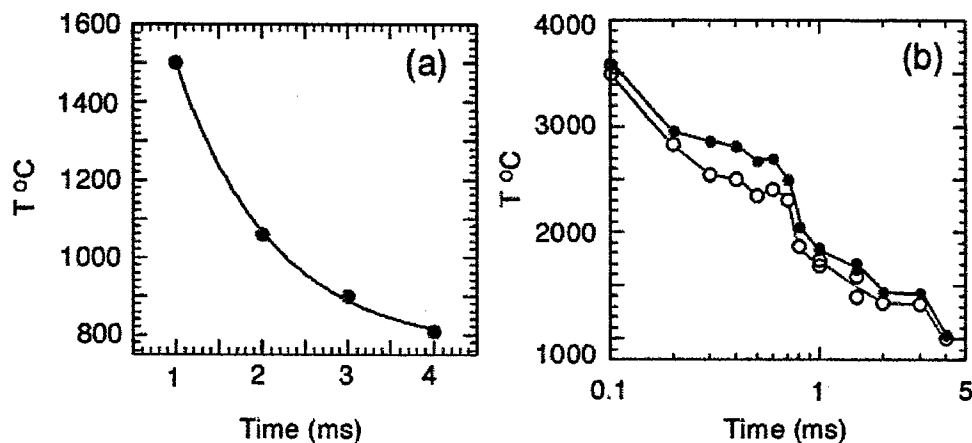
Fig. 6. Temperature of carbon particles inside the propagating plume versus time after ablation measured at different ambient temperatures: (a) 760 C, ε(λ, a) = const., and (b) 1100 C, ε(λ, a) = const. (solid circles), and ε(λ, a) ∝ 1/λ (open circles).

5. IMAGING OF SCATTERED LIGHT: GROWTH OF SHORT SWNTs

Growth rates of SWNTs were estimated by measuring the length distribution of SWNTs for known growth times. However, reliable estimates of SWNT lengths can only be performed for short nanotubes where the ends of the nanotubes can be clearly determined in TEM pictures. To limit the time available for nanotube growth, the target was located close to the front edge of the furnace (d = 10 cm) such that, after a known time spent at relatively uniform temperature, the plume would be thermophoretically drawn as rapidly as possible out the front of the oven to deposit upstream on the wall of the quartz tube. Of utmost importance, however, was to assure that the plume spent a guaranteed time (10-20 ms) in the uniform-temperature region of the oven before the rapid cooling at the oven edge. Rayleigh-scattering images of the plume (in association with the measured temperature profiles of the oven) were used to provide this known growth time at uniform temperature.

Figure 7 shows the oven temperature profiles measured at 780 C at the center of the furnace. The temperature distribution along the quartz tube axis is uniform near the center of the tube and drops rapidly at both ends. To define the uniform temperature zone we fitted the gradient region of the temperature profiles with a straight line and used a cross point to this line and the plateau to estimate the lower limit of the uniform temperature zone. The upper temperature was defined by the target position (see inset in Fig. 7).

Fig. 7. Temperature profiles along the furnace axis measured at 780 C at the center of the furnace. The inset at the bottom shows target and window edge positions relative to the oven edge at d = 0. The open circle separates steep gradient and uniform temperature zones.
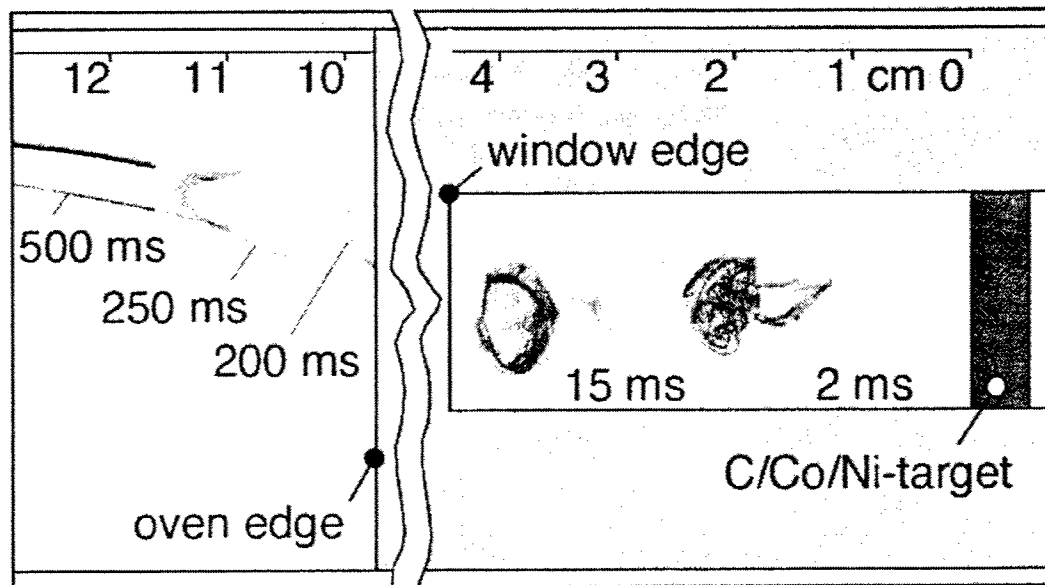
Fig. 8. *Images of Rayleigh-scattered light (308 nm XeCl-laser, 26 ns FWHM, 6 mJ/cm²) from C/Ni/Co plume during synthesis of short SWNTs at 2 and 15 ms after ablation inside the furnace and at 200, 250, and 500 ms when the plume exits the furnace. The temperature at the center of the furnace was 780 C. A Nd:YAG-laser vaporizes a C/Ni/Co target inside a 2-in. diameter quartz tube in 500 Torr Ar (flowing to the right at 100 sccm. Each image represents a different ablation event (5ns gate width, opened simultaneously with the probing XeCl-laser pulse).*

Using this procedure we defined a uniform temperature zone located approximately between 5 and 10 cm from the front oven edge. The temperature within this zone changes from 760 to 715 C ($\Delta T/T = 5.9\%$); 950-900 C ($\Delta T/T = 5.6\%$); and 1100-1050 C ($\Delta T/T = 4.6\%$) for three different temperatures used to grow short SWNTs. The gradient temperature zone located approximately between 0 and 5 cm (see Fig. 7) can be characterized by rapid temperature drop ~ 70 C/cm. This temperature zone was used to stop the growth of SWNTs.

To find the positions of the plume inside and outside the furnace we used Rayleigh scattering imaging. Figure 8 shows images of the plume at 2 and 15 ms after ablation inside the furnace and at 200, 250, and 500 ms when the plume exits the furnace. The detailed description of the plume dynamics during SWNT growth was given in Refs. [17, 18]. Initially the plume generates a strong shock front and traps itself between this shock front and the target. The forward propagating plume sets the surrounding background gas in motion in such a way that it flows around the plume and forms vortices. These vortices trap the ejected material at later times after ablation.

In the uniform temperature zone the shape of the vortex ring does not change much when it propagates forward. The diameter of the vortex ring usually increases slowly with time [17, 18]. When the vortex ring approaches the temperature gradient zone its plane tilts relative to the tube axis and the ring elongates along this axis [17, 18]. At 200 ms the plume exits the furnace in this tilted orientation to deposit onto the upper surface of the quartz tube. The ejected material spends approximately 10-20 ms at the uniform temperature and 100-200 ms in the steep gradient zone.

Using this approach we can grow short SWNTs. Figure 9a shows TEM images of short SWNTs synthesized at furnace temperature ~ 760 C. This image demonstrates that many short tubes sprout from catalyst nanoparticles represented by small black dots in Fig. 9a. In most cases we can easily see the ends of these short tubes and measure their length. The length distribution of short SWNTs was fitted with a logarithmic normal distribution (Fig. 9b). At higher furnace temperatures the maximum of the nanotube length distribution shifts to longer lengths and the width of the distribution increases. At 760 C the most probable value of length is 35 nm and 90% of all tubes are shorter than 90 nm. These values are 74 nm and 170 nm for 960 C; 77 nm and 240 nm for 1100 C.
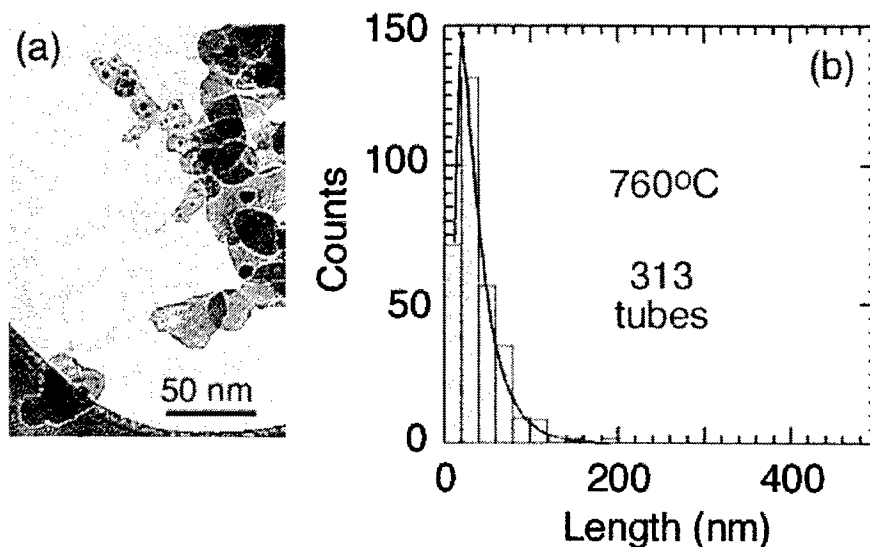
*Fig. 9. (a) TEM images of short SWNTs grown by laser vaporization at 760 C. Note that the tempera-
ture was measured inside the quartz tube at the target position. (b) Length distribution of short
SWNTs generated by the plume spending < 200 ms inside the furnace at 760 C. The curve represent
a logarithmic normal distribution fit.*

Using the measured values of the most probable length of SWNTs (Fig. 9b) and the times the ablated material spent in the uniform temperature zones, and taking into account the short time (~4 ms) required to cool the particles within the plume down to the ambient temperature we can estimate the growth rates of SWNTs.

We estimated the lower and the upper limits of the growth rates using two different criteria. The lower limit was estimated on the basis of the minimum temperature at which the SWNT can grow. Bandow et al [13] estimated that the yield of SWNT produced by nanosecond laser vaporization was about 3-5% at T = 780 C. They did not find any tubes at room tempera-ture. Sen et al [29] concluded that the lowest threshold temperature for nanotube growth in nanosecond laser ablation process is about 850 C. Our study shows that short SWNTs can be synthesized at 750 C. To estimate the lower limit of the growth rate we assumed that the minimum temperature for SWNT growth in nanosecond laser vaporization process is about 700 C, and estimated the times the ablated material spent at T > 700 C. The upper limit of the growth rate was estimated based on the time the vaporized material spent in the uniform temperature zone. Using these assumptions and assuming that the growth rate is constant we can estimate the growth rate of SWNTs as 1-5 μm/s.

6. CONCLUSIONS: THE SEQUENCE OF EVENTS IN LASER VAPORIZATION LEADING TO SWNT GROWTH

We can deduce a comprehensive picture of the events in laser ablation leading to SWNT growth by combining the results of the temperature and particle size measurements of the particles within the propagating plume with the results of our previous studies on plume dynamics and spectroscopy, described in references [17, 18].

Initially a Nd:YAG laser pulse produces atomic/molecular vapor containing ~ 5×10^{16} carbon and ~ 10^{14} Ni/Co atoms as estimated by weighing the C/Ni/Co target before and after laser ablation. The evaporated material stays in vapor phase until approximately 100 μs after ablation [17,18]. During the first 100 μs after ablation the laser plasma is very hot and emission from excited atoms and molecules dominate laser-induced emission from ground state species. The laser plasma cools down rapidly increasing population of the atomic and molecular ground states as indicated by LIF measurements.

To observe the plume of ejected material at t > 200 μs we used laser induced incandescence and Rayleigh scattering from clusters and nanoparticles. By that time the plume becomes substantially nonuniform as it can be seen from the Rayleigh scattering images demonstrating pronounced turbulent structure within the plumes. At later times (> 2ms) the plume aquires a characteristic vortex ring shape that still has a highly turbulent substructure.

Images of the plume and LIF spectra show that carbon condenses and forms clusters by t = 200 μs after ablation, while the metal catalyst atoms condense much later. The ground-state atomic Co population is maximum at t ~ 0.8 ms, and then ~ 90% of cobalt atoms condence into clusters by t ~ 2 ms [17, 18]. The absorption spectra measured at ~ 0.6 ms after ablation (Fig. 4) show that the atomic Ni, Co lines are superimposed on the strong background absorption from carbon nanoparticles. Thus, by ~ 2 ms the great majority of both carbon and metal vapor have condensed into clusters and nanoparicles a large fraction of which are somehow subsequently converted into SWNTs. The mobility of these nanoparticles clearly depends upon their size, hence the size and aggregation rate of these nanoparticles were measured during the crucial period between t=1-4 ms (see below).

The Mie theory interpretation of the extinction spectra (absorption plus scattering) shows that the size of the carbon particles within the plume at these times does not exceed 20 nm at ambient temperature of ~1100 C. However, at lower ambient temperatures (~760 C) a strong aggregation of carbon nanoparticles was observed and the size of these aggregates was estimated as ~ 80 nm using Mie theory for spherical particles. This rapid aggregation of carbon nanoparticles at lower processing temperatures results in a decrease in mobility and could be one of the reasons for the rapid decrease of SWNT yields at lower ambient temperatures.

The temperature measurements in this study permit an estimate for the onset of SWNT growth. At t = 2 ms the plume temperature is ~ 1400 C, just above the Ni/C and Co/C eutectic temperatures. Since it is well known that the yield of SWNTs drops rapidly at $T>T_{eut.}$ [7, 27], we can estimate the onset of SWNT growth as ~ 2ms for our experimental conditions. By this time, we have shown that the majority of the ejected vapor has already condenced into clusters and nanoparticulate aggregates, so SWNT nucleation appears to occur in this environment.

In order to confirm where the majority of SWNT growth occurs and estimate growth rates, plume imaging and steep temperature gradients near the end of the furnace were employed to restrict the growth times of SWNTs to about 15-20 ms. Very short SWNTs forming thin bundles consisting of a few tubes were found to have most probable lengths of 35-77 nm depending on the processing ambient temperature, 760-1100 C. This permits upper and lower limits for the growth rate of SWNTs to be estimated as ~ 0.6 and 5.1 μm/s, respectively. However, the main conclusions of these time-resolved growth studies are that the majority of SWNT growth occurs for times longer than 20 ms after laser vaporization, from a mixture of carbon and metal catalyst clusters and nanoparticles.

ACKNOWLEDGEMENTS

REFERENCES

1. B.T Yakobson and R.E. Smalley, *American Scientist*, **85** (1997) 324 .
2. T Guo, P. Nikolaev, A. Thess, D.T. Colbert, R.E. Smalley, *Chem. Phys. Lett.* **236** (1995) 419.
3. A. Thess, R. Lee, P. Nikolaev, H. Dai, P. Petit, J. Robert, C. Xu, Y.H. Lee, S.G. Kim, A.G. Rinzler, D.T. Colbert, G.E. Scuseria, D. Tomanek, J.E. Fisher, R.E. Smalley, *Science* **273** (1996) 483 .
4. M. Yudasaka, T. Ichihashi, T. Komatsu, S. Iijima, *Chem. Phys. Lett.* **299** (1999) 91.
5. A.G. Rinzler, J. Liu, H. Dai, P. Nikolaev, C.B. Huffman, F.J. Rodriguez-Macias, P.J. Boul, A.H. Lu, D. Heymann, D.T. Colbert, R.S. Lee, J.E. Fisher, A.M. Rao, P.C. Eklund, R.E. Smalley, *Appl. Phys. A* **67** (1998) 29.
6. M. Yudasaka, T. Ichihashi, S. Iijima, *J. Phys. Chem.* **B 102** (1998) 10201.
7. A.A. Gorbunov, R. Friedlein, O. Jost, M.S. Golden, J. Fink, W. Pompe, *Appl. Phys. A* **69** (1999) S593.
8. A.C. Dillon, P.A. Parilla, J.L. Alleman, J.D. Perkins, M.J. Heben, *Chem. Phys. Lett.* **316** (2000) 13.
9. A.C. Dillon, P.A. Parilla, K.M. Jones, G. Riker, M.J. Heben, *Mat. Res. Soc. Symp. Proc.* Vol. 256 (1998) 403.
10. M. Yudasaka, R. Yamada, N. Sensui, T. Wilkins, T. Ichihashi, S. Iijima, *J. Phys. Chem.* **B 103** (1999) 6224.
11. O. Jost, A.A. Gorbunov, J. Moller, W. Pompe, A. Graft, R. Friedlein, X. Liu, M.S. Golden, J. Fink, *Chem. Phys. Lett.* **339** (2001) 297.
12. M. Yudasaka, T. Komatsu, T. Ichihashi, Y. Achiba, S. Iijima, *J. Phys. Chem.* **B 102** (1998) 4892.
13. A.S. Bandow, S. Asaka, Y. Saito, A. M. Rao, L. Grigorian, E. Richter, P. C. Eklund, *Phys. Rev. Lett.* **80** (1998) 3779.
14. S. Arepalli, C.D. Scott, *Chem. Phys. Lett.* **302** (2001) 139.
15. F. Kokai, K. Takahashi, M. Yudasaka, R. Yamada, T. Ichihashi, and S. Iijima, *J. Phys. Chem. B* **103** (1999) 4346.
16. D.B. Geohegan, Talk presented at the Fifth International Conference on Laser Ablation, Goettingen, Germany, July 18-23, 1999.

17. A. Puretzky, D.B. Geohegan, X. Fan, S.J. Pennycook, *Appl. Phys. Lett.* **76** (2000) 182.

18. A.A. Puretzky, D.B. Geohegan, X. Fan, S.J. Pennycook, *Appl. Phys. A* **70** (2000) 153.

19. D.B. Geohegan, H. Schittenhelm, X. Fan, S.J. Pennycook, A.A. Puretzky, M.A. Guillom, D.A. Blom, D.C. Joy, *Appl. Phys. Lett.* 78 (2001) 3307.

20. F. Kokai, K. Takahashi, M. Yudasaka, and S. Iijima, *J. Phys. Chem. B* **104** (2000) 6777.

21. G. De Boer, S. Arepalli, W. Holmes, P. Nikolaev, C. Range, C. Scott, *J. Appl. Phys.* **89** (2001) 5760.

22. S. Arepalli, P. Nikolaev, W. Holmes, B.S. Files, *Appl. Phys. Lett.* **78** (2001) 1610.

23. C.D. Scott, S. Arepalli, P. Nikolaev, R.E. Smalley, *Appl. Phys. A* 72 (2001) 573.

24. C.F. Bohren, D.R. Huffman, *"Absorption and Scattering of Light by Small Particles"*, Wiley-Interscience, 1983, p.136.

25. E.A. Rohlfing, *J. Chem. Phys.* **89** (1988) 6103.

26. U.O. Koylu, *Combustion and Flame* **109** (1996) 488.

27. H. Kataura, Y. Kumazawa, Y. Maniwa, Y. Ohtsuka, R. Sen, S. Suzuki, Y. Achiba, *Carbon* 38 (2000) 1691.

28. S. Suzuki, R. Sen, H. Yamaguchi, T. Ishigaki, Y. Ohtsuka, Y. Achiba, H. Kataura, *"Time and space evolution of emitting carbon nanoparticles: correlation with the formation of fullerenes and carbon nanotubes"* (to be published).

29. R. Sen, Y Ohtsuka, T. Ishigaki, D. Kasuya, S. Suzuki, H. Kataura, y. Achiba, *Chem. Phys. Lett.* **332** (2000) 467.

Synthesis of Multifunctional Single Wall Carbon Nanotube - Amorphous Diamond Thin Film Composites

David B. Geohegan[a], C. Henrik Schittenhelm[b], Alex A. Puretzky[c], Michael J. Lance[a],
Gerald E. Jellison[a], Phillip F. Britt[a]

[a]Oak Ridge National Laboratory, Oak Ridge, TN 37831
[b]Robert Bosch GmbH, Corporate Research and Development, Stuttgart, Germany
[c]Dept. of Materials Science and Engineering, University of Tennessee

ABSTRACT

The first thin-film single-wall carbon nanotube (SWNT) composites synthesized by pulsed laser deposition (PLD) are reported. Ultrahard, transparent, pure-carbon, electrically-insulating, amorphous diamond thin films were deposited by PLD as scratch-resistant, encapsulating matrices for disperse, electrically conductive mats of SWNT bundles. In situ resistance measurements of the mats during PLD, as well as ex situ Raman spectroscopy, I-V measurements, spectroscopic ellipsometry, and field emission scanning electron microscopy, are used to understand the interaction between the SWNT and the highly energetic (~ 100 eV) carbon species responsible for the formation of the amorphous diamond thin film. The results indicate that a large fraction of SWNT within the bundles survive the energetic bombardment from the PLD plume, preserving the metallic behavior of the interconnected nanotube mat, although with higher resistance. Amorphous diamond film thicknesses of only 50 nm protect the SWNT against wear, providing scratch hardness up to 25 GPa in an optically transmissive, all-carbon thin film composite.

Keywords: carbon nanotubes, laser plasmas, spectroscopy, in situ diagnostics, nanoparticles, hydrodynamics

1. INTRODUCTION

Single wall carbon nanotubes (SWNTs) exhibit exceptional mechanical,[1-3] electronic,[4] thermal, and optical properties[5] which are envisioned for new generations of strong, lightweight, multifunctional composites. SWNT are currently being explored in bulk polymer and metal-matrix composites with key difficulties encountered in dispersing the nanotubes and forming strong bonds to the matrix material.[6-8] In this report, pulsed laser deposition (PLD, a versatile method for thin-film synthesis) is explored for the first time to encapsulate SWNT in a thin film composite. Purified SWNT were sprayed from solution and dried to form disperse, electrically-conductive interconnected mats on SiO_2 and Si substrates. Interconnected mats of SWNT exhibit pseudometallic behavior for a wide range of temperatures and applied fields[11], and might be used to lend electrical conductivity, electrostatic protection, and thermal dissipation paths in matrices of polymers and other materi-

Experimental setup
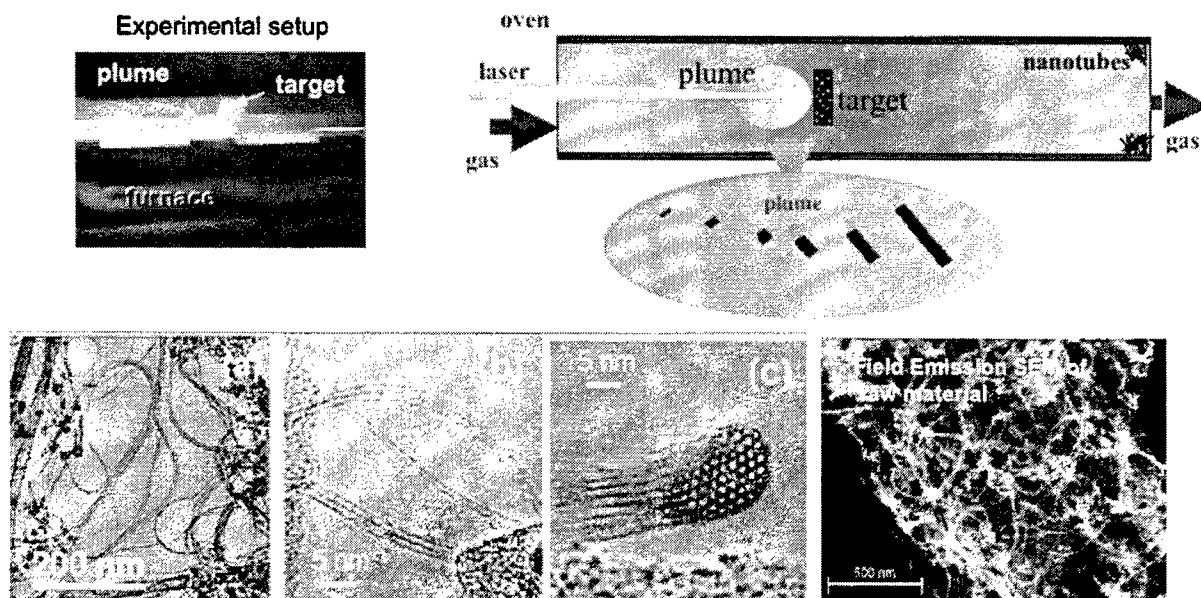
Fig. 1. Laser ablation of a carbon target (with 1 at.% each of Ni and Co as catalysts) in a tube furnace at 1150 C with 500 Torr Argon (flowing 100 sccm) was used to synthesis single wall carbon nanotubes (SWNT). The nanotubes form in the plume during its traversal through the furnace, and are collected outside the hot zone of the furnace.

als.

2. EXPERIMENTAL RESULTS

In this study, a matrix of amorphous diamond (tetrahedrally-coordinated amorphous carbon (ta-C))[9,10] was deposited by PLD to encapsulate the SWNT mats, forming a pure-carbon nanocomposite. The amorphous diamond film is intended to
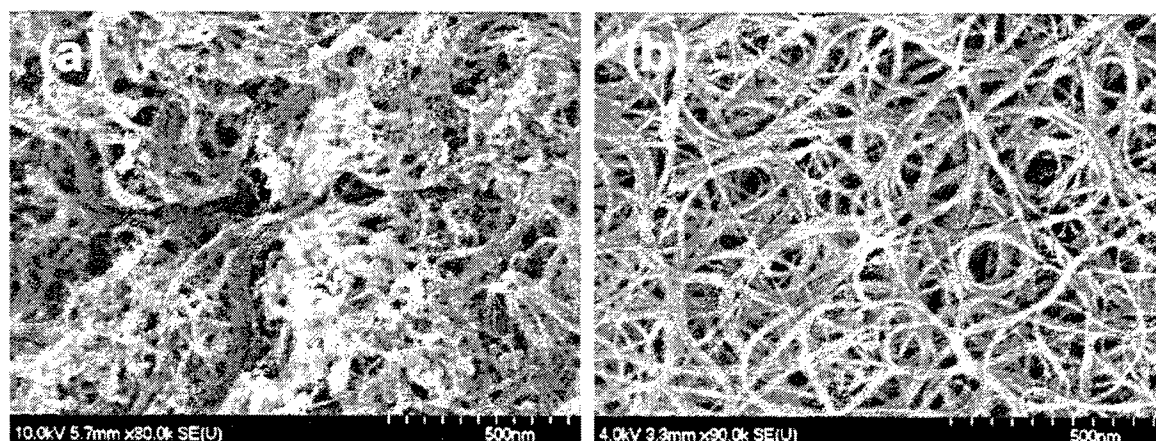
Fig. 2. Purification of single-wall carbon nanotubes utilized a combination of acid etching with 3M HNO_3 in H_2O, followed by rinsing, drying, and subsequent oxidation for ~ 30 minutes at 500°C in air. The acid etch dissolves the metal particles left in the raw nanotube material, whereas the subsequent oxidation burns away the amorphous carbon without significantly damaging the SWNT. (a) Raw SWNT Material. (b) Purified SWNT "Buckypaper"
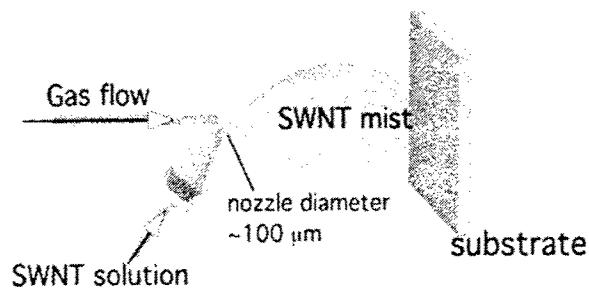
Fig. 3. Automated spraying of purified SWNT suspended in dicholoroethane (DCE) was performed with a commercial airbrush at various pressures onto Si and SiO$_2$ substrates. Dispersed SWNT mats of varying areal bundle densities and diameters could be achieved by applying different solvent concentrations and spraying strategies, resulting in interconnected nanotube mats with different resistivities.

provide a hard, scratch-resistant, transparent, and electrically insulating coating for the electrically-conductive, disperse mats of SWNTs and serve as an abrasion-resistant barrier to ambient gases and liquids, which have been observed to strongly influence the electronic properties of SWNT.[12,13]
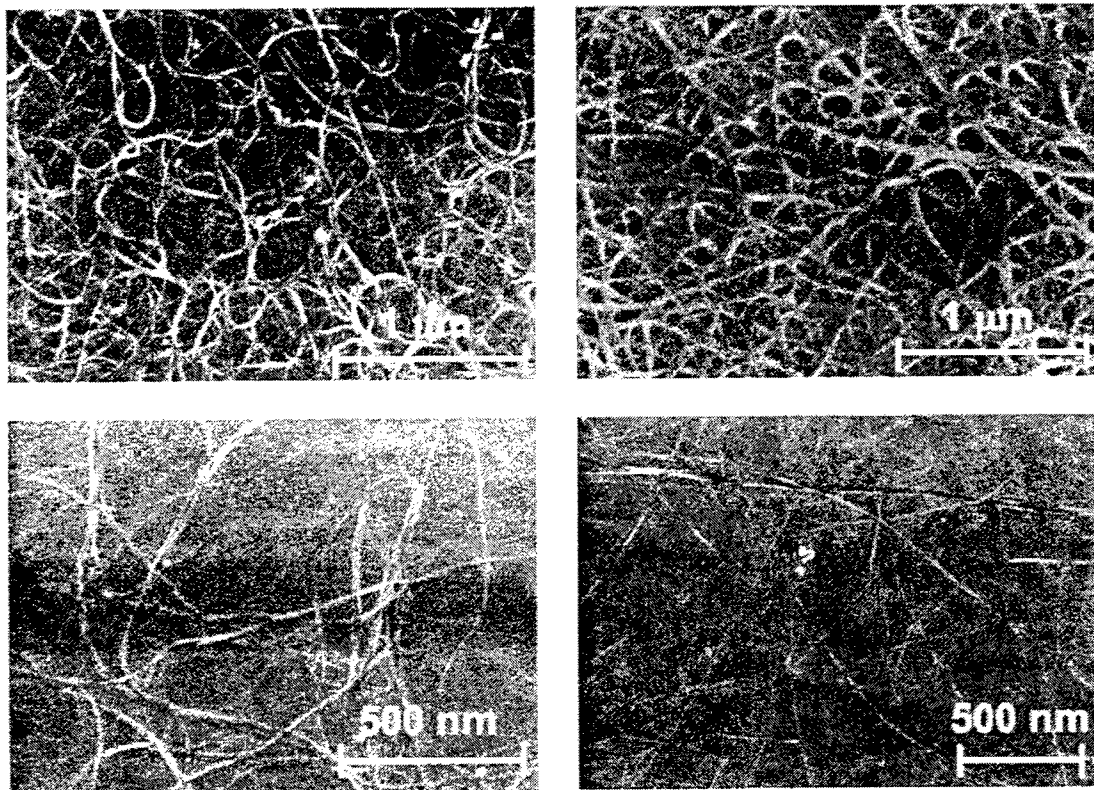
Fig. 4. SEM images of SWNT bundles on Si substrates deposited by solution spraying. By adjusting the spray duration, solvent concentration, nozzle pressure and spraying strategy the diameter of the bundles and the areal density of the interconnected SWNT mats can be controlled, thereby adjusting physical properties of the coating (e.g. resistivity). I-V curves of the interconnected mats showed metallic behavior, and resistances could be varied over several orders of magnitude.
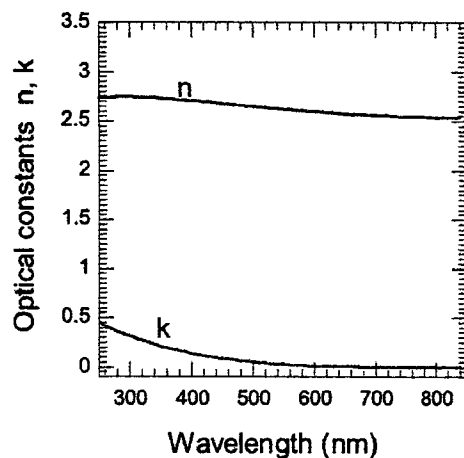
Fig. 5. Optical properties of the ta-C/SWNT/Si composite films. Spectroscopic ellipso-metry measurements of the *ta*-C films indicate an E_g = 1.84 eV. This corresponds to an sp³ content of ~ 70% and ~ 40 GPa hardness.

As shown in Figure 1, the SWNTs were synthesized by laser vaporization[14] of a Dylon® target (with 1 at.% of Ni and Co each as catalysts) in a tube furnace at 1150 C and 500 Torr Argon (flowing at 200 sccm). As shown in Figure 2, the SWNT were purified from amorphous carbon and metallic catalyst particles by a procedure which involves etching for 16 hours in 3M HNO_3 in H_2O, followed by rinsing, drying, and subsequent oxidation for up to 90 minutes at ~500 C.[15,16] Energy dispersive X-ray analysis and thermogravimetric analysis indicate that less than 0.5 weight % of residual metal catalyst particles remain in the purified SWNT.

The purified SWNT were dispersed in distilled dichlorethane (DCE) at concentrations of about 1mg/ml and spray-deposited onto Si and SiO_2 (Suprasil fused silica) substrates with a commercial airbrush apparatus (see Fig. 3). The SWNT/
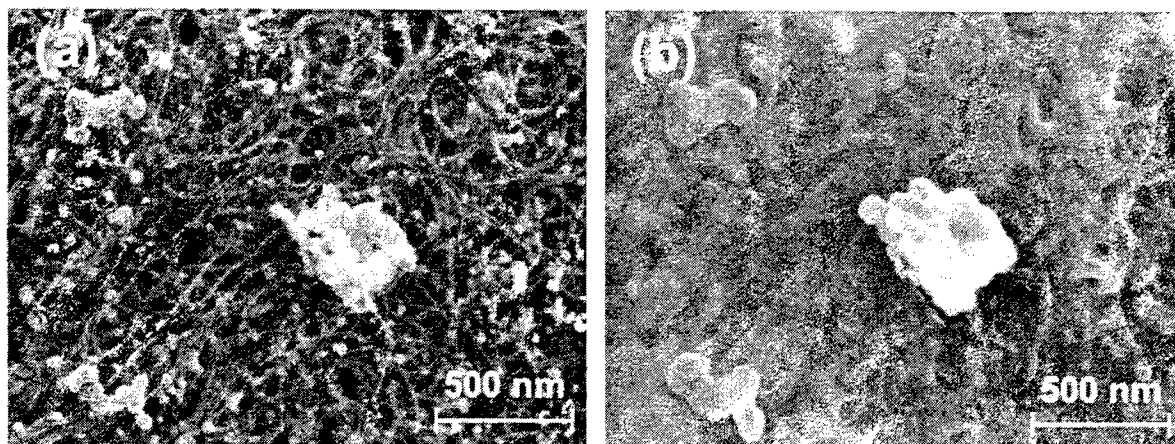
Fig. 6. FESEM imaging of a SWNT mat on a Si substrate before (left) and after (right) amorphous diamond thin film deposition.
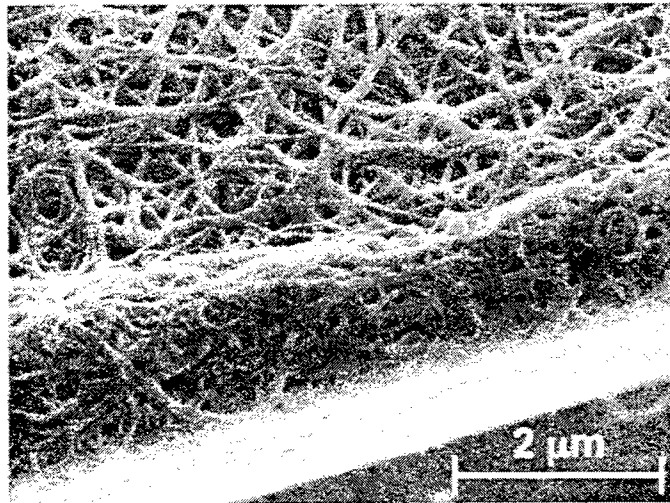
Fig. 7. FESEM image of a thick mat of SWNT bundles on a Si substrate covered with a thin film of amorphous diamond like carbon.

DCE solution was sonicated during the spraying process to inhibit SWNT aggregation while a motorized x-z stage was used to move the airbrush nozzle parallel to the substrate to obtain uniform SWNT dispersal on the substrates. By adjusting the spray duration, solvent concentration, nozzle pressure and spraying strategy the diameter of the bundles as well as the areal density of the interconnected SWNT mats could be controlled, thereby adjusting the resistance of the coating (Figure 4).

The nanotube laden substrates were then subjected to PLD conditions optimized for amorphous diamond film
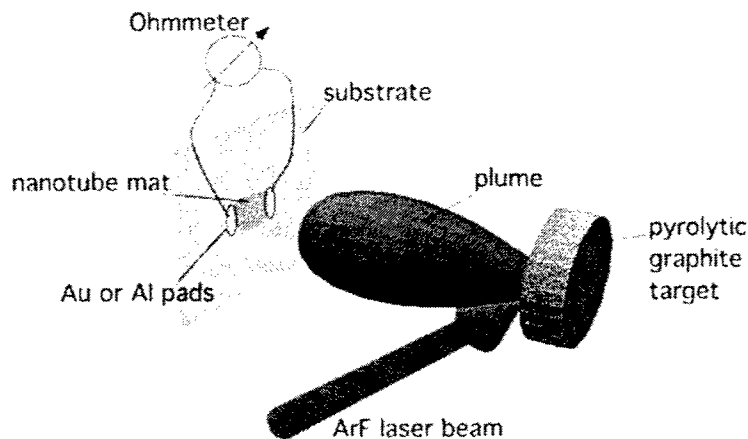
Fig. 8. Schematic of the pulsed laser deposition geometry with in situ resistivity measurements. A sprayed SWNT network was applied on an oxide-coated Si wafer with prepatterned gold or aluminum pads. The resistance of the SWNT network on the wafer was monitored via the two-point resistivity method during laser ablation of a pyrolytic graphite target in vacuum. The metal pads and electrode contacts were shielded from the plume during film deposition.
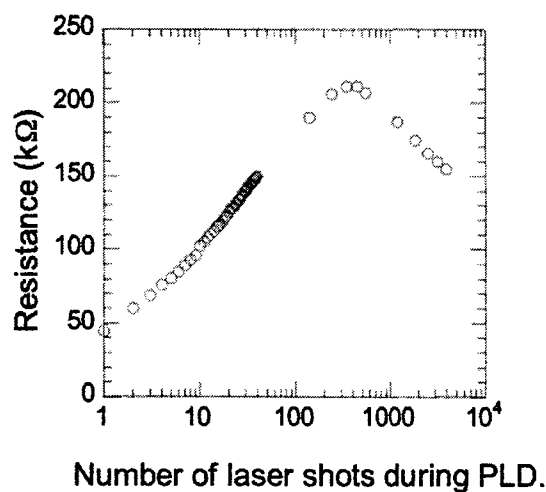
Fig. 8. Typical resistance of a SWNT mat vs. the number of laser shots during PLD of amorphous diamond coatings.   The rise of the resistivity during deposition correlates with the first few nm of *ta*-C film formation, which requires the creation of an interfacial layer and reordering of the sp² bonds. The subsequent drop in resistivity probably occurs due to improved intertube contact resulting from the compressive stress in the film.
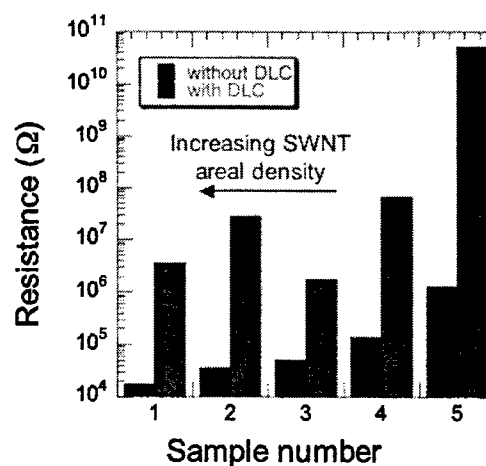
Fig. 9. Resistance before and after ta-C film deposition for thin SWNT films on Quartz substrates.

formation in vacuum.[17] An ArF-excimer laser irradiated (energy density F ~1.8 J/cm²) a pyrolytic graphite target in vacuum (~10^{-5} Torr), generating C^+ ions with most-probable kinetic energies ranging from 80-100 eV as measured with an ion probe.[18] These fast carbon ions and neutrals, along with slower C_2 and C_3 molecules, have sufficient kinetic energy to form amorphous diamond films on Si or SiO_2 substrates. However, it was unclear whether adherent films of amorphous diamond could be formed on webs of interconnected SWNT bundles which comprise up to 40% of the areal coverage (as shown in Fig. 4). After PLD in vacuum (at d = 7 cm), of film thicknesses between 10 nm and 50 nm (at rates of about 0.1 nm/s (0.01 nm/laser shot)), adherent films were found to conformally coat the SWNT in transparent, hard thin films as shown in Figures 6 and 7.

An HP 4156A Precision Semiconductor Parameter Analyzer was first used to measure the current-voltage characteristics of interconnected SWNT mats on SiO_2 substrates. Contact to the nanotube mat was made using evaporated Al pads on the SiO_2 which were deposited before nanotube spraying. All mats exhibited metallic behavior for applied voltages between -10V and +10V, however depending upon the areal density of the nanotubes forming the mat, resistances were varied between 15 kW and 1 MW over 1 cm distances. A Keithley 195 System digital multimeter monitored the resistance of the SWNT mat in situ during deposition of the *ta*-C film, while the Al pads and contact leads were shielded from the PLD plume. In each case, an initial rapid increase in the resistance was observed after each of the first 5-10 PLD pulses which was probably caused by the desorption or damage of some of the SWNTs by the impact of the energetic carbon ions and neutrals. The resistance continued to increase slowly over the first few nm of film thickness, and then stabilize or decrease with further

(a) $\lambda_{exc} = 633\ nm$

purified mat
10 shots
100 shots

Intensity (a.u.)
Wavenumber (cm⁻¹)
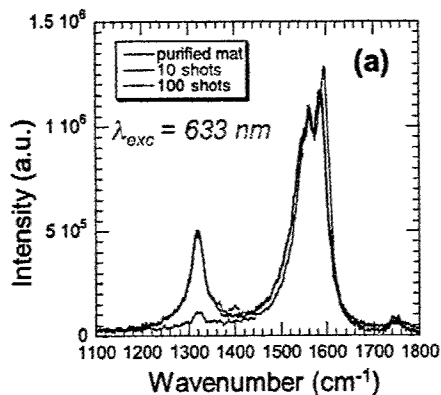
Raman signals for different ta-C film thicknesses on a pure SWNT mat

(b) $\lambda_{exc} = 633\ nm$

Intensity (a.u.)
DLC film growth time (s)
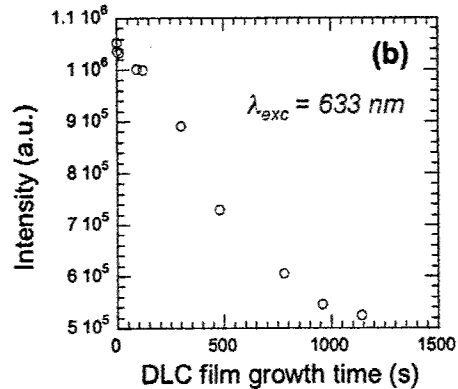
1562 cm⁻¹ SWNT Raman TM band intensity for different ta-C film thicknesses

(c) SWNT alone $\lambda_{exc} = 515\ nm$

With ta-C

Intensity (a.u.)
Wavenumber (cm⁻¹)
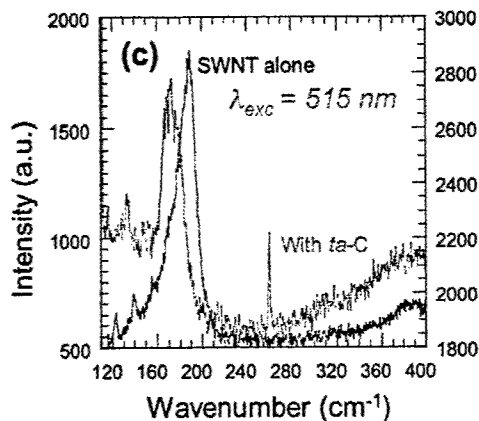
Raman spectra in the SWNT breathing mode region before and after ta-C deposition.

(d) SWNT alone $\lambda_{exc} = 515\ nm$

With ta-C

ta-C alone

Intensity (a.u.)
Wavenumber (cm⁻¹)
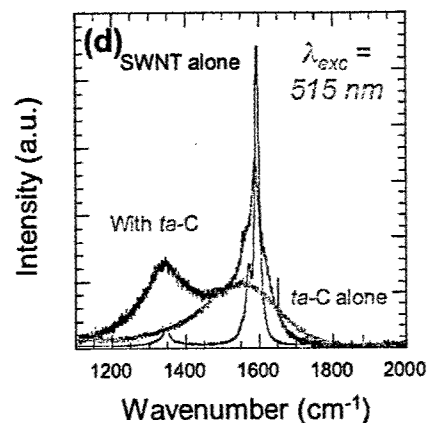
Raman spectra in the SWNT tangential mode region before and after ta-C deposition.

Fig. 10. Resonant Raman spectra from the SWNT before and after *ta*-C film deposition show that the characteristic SWNT tangential and breathing modes are still present, but decreased in magnitude, indicating that a large fraction of SWNT survive the energetic deposition process. The presence of amorphous carbon, most likely at the SWNT/ *ta*-C interface, is indicated by the broad bands at 1350 cm⁻¹ and 1580 cm⁻¹. Raman spectroscopy of the SWNT mat before and and after the deposition shows anincreasing D-band probably due to damage of the tubes by high energy C ions.

deposition. I-V curves were then remeasured ex-situ, and metallic behavior was again observed for the coated mats, however the resistance ranged from a factor of 3 to a factor of 10^4 higher after *ta*-C film deposition (resistances from 45 kW to 10^4 MW). By comparison, resistances for pure *ta*-C films were 6×10^5 MΩ over a distance of 1 cm. In general, mats consisting of high areal densities and thicker bundles of SWNT resulted in smaller increases in resistance after deposition. In each case, the metallic behavior of the SWNT mat was preserved.
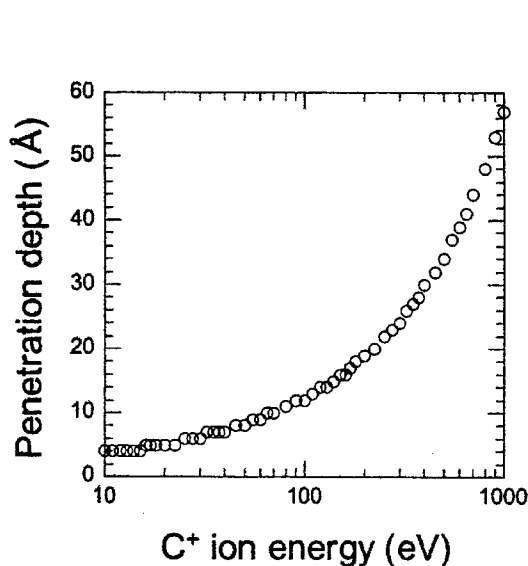
Fig. 11. Predicted penetration depth of carbon ions into SWNT bundles (density assumed 1.33 g/cm3).

Fig. 12. Physical model of the deposition process. Incident C[+] ions with kinetic energies around 100 eV cause damage to the upper layers of tubes in the SWNT bundles resulting in the increase of the Raman D-band. The penetration depth of these ions is around 1 nm and, therefore, defects should be located on the upper layers of a SWNT bundle. During the deposition of this layer, the resistance of the interconnected nanotube mat increases. The smaller the bundle diameter, the higher the fraction of damaged SWNTs which should be expected. Thin mats of SWNT with the smallest bundle diameters show the strongest increase in the resistance of the SWNT mat after ta-C deposition.

Spectroscopic ellipsometry measurements of a pure ta-C film and a representative ta-C/SWNT composite film (on Si substrates) are shown in Fig. 5, which assumes a Tauc-Lorentz model with variable surface void fraction to account for surface roughness.[19] First, the pure ta-C film is of high quality, with a high (n > 2.5) index of refraction and low absorption across the visible, corresponding to a bandgap of 1.84 eV and a hardness of ~ 40 GPa.[18] The effective medium comprised of ta-C with embedded SWNT exhibits a slightly lower refractive index and the expected higher absorptivity. However, good optical access to the embedded nanotubes is achieved since k = 0.19 at 500nm (close to 514 nm used for Raman probing) for the composite film, corresponding to an absorption coefficient of 48000 cm^{-1} and an 80% transmission through the 50 nm-thick film.

Resonant Raman spectra from the SWNT mats before and after ta-C film deposition are shown in Fig. 10. Although decreased in magnitude, the characteristic tangential (TM) and breathing (BM) modes are preserved indicating that a large fraction of SWNT survive the energetic deposition process. The Raman spectrum of the ta-C/SWNT composite in Figure 10 displays a combination of the SWNT TM and a broad "G-band" from the amorphous diamond coating. Depending on the areal density of the SWNTs before ta-C film deposition the TM mode feature in the composite film ranges from barely observable to very pronounced (as in Fig. 10). A slight red shift of both the Raman BM and TM signals from the SWNTs was

Fig. 13 SEM image of a crack in the *ta-C* coating revealing apparently intact SWNT bundles underneath the film. Raman spectroscopy confirms that the SWNTs are intact underneath the *ta-C* film and resistance measurements confirm that their electrical transport properties are preserved.
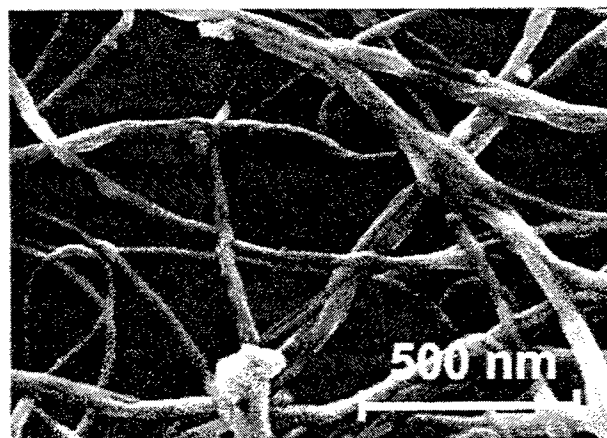
Fig. 14. SEM image of the resistive nanotube network of SWNT covered with a protective layer of *ta-C* (amorphous diamond). The *ta-C* coating forms an optically transparent, hard, scratch-resistant and chemically-protective coating to preserve the electronic properties of the interconnected nanotube network.

observed and is counterintuitive to the expected compressive strain of the SWNT from the *ta-C* film.

Figure 12 summarizes a model for *ta-C* /SWNT film formation consistent with the experimental results. High energy C^+ ions and neutrals during PLD introduce defects in the upper layers of the SWNT bundles, affecting interconnections between bundles in the mats, resulting in the increased mat resistance. Kinetic model simulations with a Monte Carlo TRIM code estimated a ~ 1-nm penetration depth for 100 eV C^+ ions into SWNT bundles (estimated 1.33 g/cm^3 density) as shown in Figure 11. Hence, defects should be located within a few upper layers of a SWNT bundle. After the first few nm of amorphous diamond film formation, which requires the creation of an interfacial layer and reordering of the sp^2 bonds, the SWNT bundles should be protected from further damage. Thinner bundles thereby experience a higher defect ratio than thicker bundles. High areal densities, where parts of some bundles are shielded by others on top of them, lead to a lower ratio of damaged nanotubes.

The synthesized composites were tested for wear resistance and scratch hardness. As schematically shown in Figure 15, a steel test ball (2g load, approximately 1.2×10^{-3} mm^2 contact area, load ~15 GPa) was moved across the SWNT mats on SiO$_2$ with and without protective amorphous diamond coatings while the resistance of the mats was monitored in-situ. As shown in Figure 16, the uncoated SWNT mats show a drastic increase in resistance after even one wear cycle. The resistance slowly saturates for more wear resistance lines (20 lines and more). Scanning electron microscopy (Figure 17) of the unprotected mat after wear testing showed that the thicker bundles were preferentially removed during the first few wear cycles, followed by the subsequent removal of thinner bundles. At the point of saturating resistance, only very thin bundles and single tubes were left on the surface to maintain conductivity of the mat. On the other hand, the *ta-C*/SWNT composite films showed high wear resistance compared to the uncoated mats. No increase in the resistance could be observed for up to 30 wear cycles. Scratch hardnesses of up to 25 Gpa were measured for the *ta-C*/SWNT composite films on Si using a diamond scratch tester with a spherical diamond tip of 75 mm and loads between 10 g and 100g.
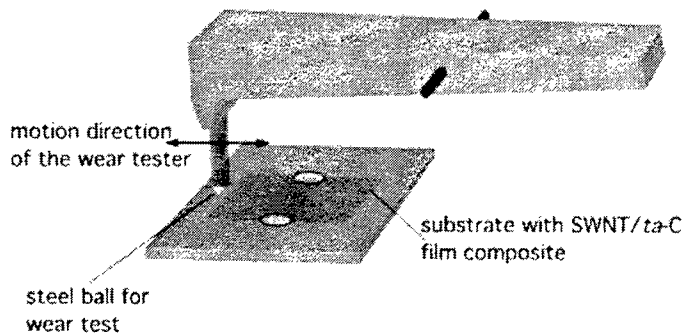
Fig. 15. The synthesized SNWT/*ta*-C film composites were tested for wear resistance. Schematic of the test procedure. A steel test ball (2g, 0.06 mm² contact area, ~100 GPa) was moved across the SWNT mats with and without protective *ta*-C coatings while the resistance of the mats was monitored.
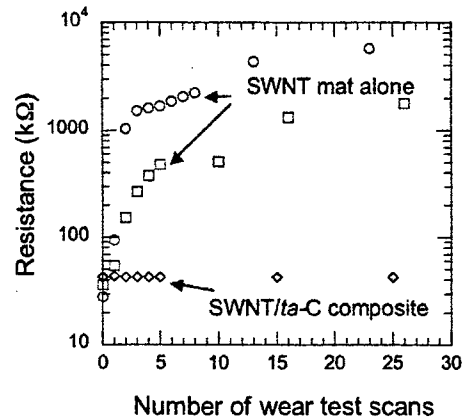
Fig. 16. The SWNT mat coated with a *ta*-C film shows high wear resistance compared to SWNT mats without the coating.

The results indicate that pulsed laser deposition (PLD) can be used to form ultrahard, transparent, pure-carbon amorphous diamond thin films as matrices to encapsulate and provide scratch-resistance for electrically conductive, disperse mats of SWNT. Moreover, PLD most often is performed in background gases where incident kinetic energies are far lower (< 1 eV). PLD therefore appears to provide a versatile method to incorporate SWNT or nanowires into thin films for the exploration of multifunctional thin film composites.

uncoated *SWNT mat*
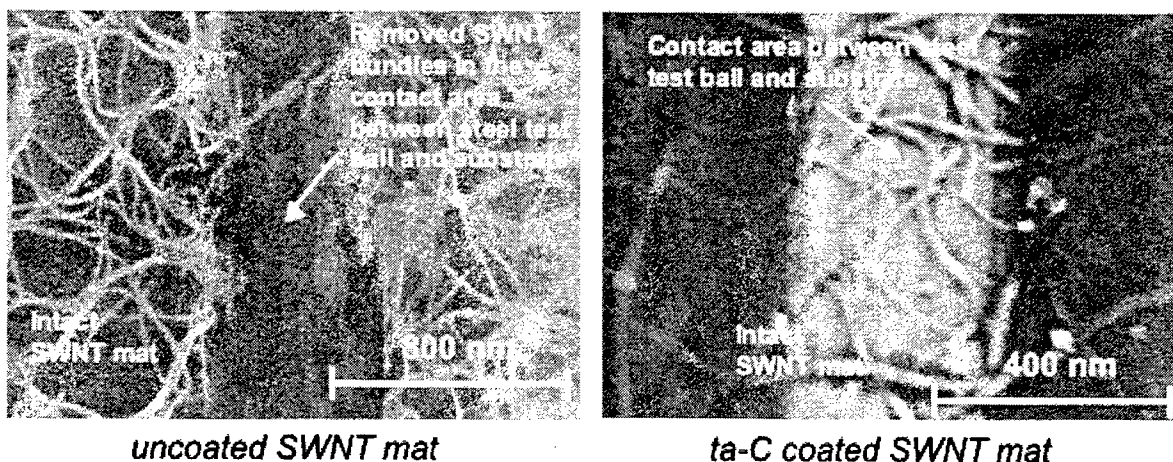
ta-C coated SWNT mat

Fig. 17. FESEM images of *ta*-C coated and uncoated SWNT mats after wear-testing show that the *ta*-C coating protects the SWNT against abrasion. Without the coating, (left) nanotubes are abraded within a few wear cycles. With the coating, (right) a wear mark is evident due to the different charging of the film in the SEM, however the intact nanotube network is visible in the image under the wear track.

3. CONCLUSIONS

In summary, a new all-carbon multifunctional nanocomposite was synthesized using laser-vaporization produced single-wall carbon nanotubes in conjunction with pulsed laser deposition of tetragonally-coordinated amorphous carbon (*ta-C*, amorphous diamond). First, a spray-deposition technique was developed to form coatings of disperse mats of purified single-wall carbon nanotube (SWNT) bundles on various substrates with varying resistance and metallic I-V behavior. Second, pulsed laser deposition (PLD) was utilized for the first time to encapsulate the interconnected SWNT into a thin-film composite with enhanced functionality.

The thin coatings of tetragonally-coordinated amorphous carbon (*ta-C*) were created by pulsed laser (193-nm) ablation of a pyrolytic graphite target in vacuum. High-energy (~100 eV) carbon ions were generated and were responsible for the high sp^3 content of the deposited films, as verified by spectroscopic ellipsometry. Simulations predict that the 100-eV C^+ ions generated in the PLD process necessary to produce the *ta-C* layer should penetrate ~ 1-nm into a SWNT bundle, and preserve most of the nanotubes in the bundle. In situ resistance measurements of the SWNT mats during PLD of the *ta-C* layer indicated initial damage or desorption of the mats, followed by densification and consolidation of the composite properties.

Resonant Raman spectra from the SWNT before and after *ta-C* film deposition show that the characteristic SWNT tangential and breathing modes are basically unchanged in shape, but decreased in magnitude, indicating that a large fraction of SWNT survive the energetic deposition process given a sufficient initial thickness of the SWNT layers. The presence of amorphous carbon, most likely at the SWNT/*ta*-C interface, is indicated by the broad bands at 1350 cm^{-1} and 1580 cm^{-1}.

Wear testing experiments of the coated and uncoated SWNT-film indicate that amorphous diamond thin films can be used as protective matrices for multifunctional SWNT composites. These films provide a wear-resistant coating to shield the SWNT against mechanical deformation and environmental exposure. In addition, amorphous diamond films are ultrahard, optically transparent, electrically insulating and preserve the metallic behavior of the interconnected SWNT mats.

This proof-of-principle experiment demonstrates that pulsed laser deposition can be used as a technique to encapsulate and lend additional functionality to assemblies of nanomaterials. Pulsed laser deposition usually involves the impingement of atoms and ions with far lower (~ 1 eV or below) kinetic energies. The encapsulation of single walled carbon nanotubes without destruction by carbon atoms and ions using high (~ 100 eV) kinetic energies implies that a wide range of other films may be used to form novel nanocomposite materials by pulsed laser deposition.

ACKNOWLEDGMENTS

REFERENCES

1. L. Vaccarini, C. Goze, L. Henrard, E. Hernandez, P. Bernier, and A. Rubio, *Carbon* **38**, 1681 (2000).

2. R. S. Ruoff and D. C. Lorents, *Carbon* **33**, 925 (1995).

3. Z. L. Wang, P. Poncharal, and W. A. de Heer, *J. Phys. Chem. Solids* **61**, 1025 (2000).

4. T. W. Tombler, C. Zhou, L. Alexseyev, J. Kong, H. Dai, L. Liu, C. S. Jayanthi, M. Tang, and S. Y. Wu, *Nature* **405**, 769 (2000).

5. N. Minami, S. Kazaoui, R. Jacquemin, H. Yamawaki, K. Aoki, H. Kataure, and Y. Achiba, *Synthetic Metals* **116**, 405 (2001).

6. R. Andrews, D. Jacques, A. M. Rao, T. Rantell, F. Derbyshire, Y. Chen, J. Chen, and R. C. Haddon, *Appl. Phys. Lett.* **75**, 1329 (1999).

7. R. Haggenmueller, H. H. Gommans, A. G. Rinzler, J. E. Fischer, and K. I. Winey, *Chem. Phys. Lett.* **330**, 219 (2000).

8. C. Stephan, T. P. Nguyen, M. L. de la Chapelle, S. Lefrant, C. Journet, and P. Bernier, *Synthetic Metals* **108**, 139 (2000).

9. F. L. Xiong, Y. Y. Wang, V. Leppert, and R. P. H. Chang, *J. Mat. Res.* **8**, 2265 (1993).

10. T. A. Friedmann, J. P. Sullivan, J. A. Knapp, D. R. Tallant, D. M. Follstaedt, D. L. Medlin, and P. B. Mirkarimi, *Appl. Phys. Lett.* **71**, 3820 (1999).

11. M. S. Fuhrer, W. Holmes, P. L. Richards, P. Delaney, S. G. Louie, A. Zettl, *Synthetic Materials* **103**, 2529 (1999).

12. A. Zahab, L. Spina, P. Poncharal, and C. Marliere, *Phys. Rev. B* **62**, 10000 (2000).

13. S. Kazaoui, N. Minami, H. Kataura, and Y. Achiba, *Synthetic Metals* **121**, 1201 (2001).

14. A. A. Puretzky, D. B. Geohegan, X. Fan, and S. J. Pennycook, *Appl. Phys A* **70**, 153 (2000).

15. P. F. Britt, H. Schittenhelm, D. B. Geohegan, A. A. Puretzky, to be published.

16. A. C. Dillon, T. Gennett, K. M. Jones, J. L. Alleman, P. A. Parilla, and M. J. Heben, *Advanced Materials* **11**, 1354 (1999).

17. A. A. Puretzky, D. B. Geohegan, G. E. Jellison, and M. M. McGibbon *Appl. Surf. Sci.* **96-8**, 859 (1996).

18. V. I. Merkulov, D. H. Lowndes, G. E. Jellison, A. A. Puretzky, and D. B. Geohegan, *Appl. Phys. Lett.* **73**, 2591 (1998).

19. G. E. Jellison, Jr., V. I. Merkulov, A. A. Puretzky, D. B. Geohegan, G. Eres, D. H. Lowndes, J. B. Caughman, *Thin Solid Films* **377-378**, 68 (2000).

20. H. Schittenhelm, D. B. Geohegan, G. E. Jellison, A. A. Puretzky, M. J. Lance, P. F. Britt *Appl. Phys. Lett.* **81**, 2097 (2002)

Iron-carbon nanocomposite obtained by laser induced gas-phase reactions

Dumitrache F.*[a], Morjan I.[a], Alexandrescu R.[a], Rand B.[b] Ciupina V.[c], Prodan G.[c], Voicu I.[a],
Sandu I.[a], Soare I.[a], Ploscaru M.[a], Fleaca C.[a], R. Brydson[b], E. Vasile[d]

[a]National Institute for Lasers, Plasma and Radiation Physics, P.O. Box MG-36, R-76900 Bucharest, Romania

[b]Institute for Materials Research, School of Process, Environmental and Materials Engineering, University of Leeds, Leeds FS2 9TT, United Kingdom

[c]"Ovidius" University of Constanta, Bd. Mamaia 124, Constanta, Romania

[d]S.C. METAV S.A., Str. Zapada Mieilor 16-18, Bucharest, Romania

ABSTRACT

Iron-carbon composite nanopowders have been synthesized by the CO_2 laser pyrolysis of gas-phase reactants. The experimental device allows for a very low reaction time and a rapid freezing that creates nanoscale-condensed particles. Iron pentacarbonyl and ethylene-acetylene mixtures were used as iron and carbon precursors. In a two-steps experiment, the reaction products may present themselves as iron-based nanoparticles dispersed in a carbon matrix. By a careful control of experimental parameters and radiation geometries we demonstrate the feasibility of an efficient and well-controlled, single-step technique for the production of iron-based nano-cores embedded in carbon layers. Highly dispersed nanoparticles, narrow size distributions and particles with about 4.5 – 6 nm mean diameters were obtained. Electron microscopy and Raman spectroscopy were used in order to analyze the structure and composition of the obtained nanopowders as well as their Soxhlet residue.

Keywords: nanopowder, composite, laser-induced pyrolysis, Fe/C

1. INTRODUCTION

The composite of metal nanoparticles dispersed in carbon matrix exhibit outstanding properties and can be widely used as electronic, electric, and magnetic materials, oxidation/reduction catalyst, adsorbents and antibacterial agents, etc. depending on the kind and structures of metals and carbons. Since the discovery of fullerene C_{60}, carbon nanocomposites and carbon-caged forms have received a wide interest from both scientific and technological point of view. Various forms of carbon-based materials have been synthesized such as onion-like structures, chemically modified fullerenes and more recently several types of carbon nanotubes and carbon nanocapsules .Carbon is a material, which is non-reactive at low temperatures and could produce a coating with desired properties..

As an example for a dispersed composite we may refer to the preparation of mesophase pitch from coal tar pitch using ferrocene as the catalyst [1]; however, the morphology and dispersed state of iron in carbon have not been investigated.

The embedding of metal-based nanoparticles in carbon layers has lately attracted much attention [2] since it allows confinement of nano-scale amounts of materials with novel physical properties as well as inertness and resistance to external detrimental conditions. Often, the introduction of metal particle in carbon coatings involves several steps of chemical procedures [3]

We report here preliminary results about the preparation of Fe-C nano-composite materials by using the CO_2 laser pyrolysis of gas-phase reactants [4,5]. Iron pentacarbonyl and ethylene-acetylene mixtures were used as iron and carbon

* fdumit@ifin.nipne.ro; phone: 0040 214574550 ext. 1879; fax: 0040214574243; [a]National Institute for Lasers, Plasma and Radiation Physics, P.O. Box MG-36, R-76900 Bucharest, Romania

precursors. In usual experimental conditions [6], the reaction products may present themselves as iron-based nanoparticles dispersed in a carbon matrix. By a careful control of experimental parameters and irradiation geometries we demonstrate the feasibility of an efficient and well-controlled technique for the production of iron-based nano-cores embedded in carbon layers. The structure and composition of the obtained nanopowders as well as their Soxhlet residue have been analyzed by electron microscopy and Raman spectroscopy

2. EXPERIMENTAL

The synthesis of Fe-C nanocomposites has been carried out in a flow reactor that has been described in detail earlier [7]. The focused continuous-wave (cw) CO_2 laser radiation (output power maximum 120 W, $\lambda = 10.6$ μm) was orthogonally crossed with the reactant gas stream that was admitted to the center of the reaction cell through a nozzle system. Two kinds of experiments were performed. In every case, the reactive flow gas was confined to the flow axis by a coaxial Ar stream.

First, in a two-steps experiment (labeled here-after RO), the reactant mixture was flowing through a single central nozzle (2.5 mm internal diameter) (Fig. 1). In the first step, the iron pentacarbonyl vapors carried by an ethylene flow (150 sccm) exits through the central nozzle and are pyrolysed by the laser beam (80 watt laser power). The freshly formed iron nanoparticles are collected by the filter. The outer Ar flow (1000 sccm) maintains the reaction towards the flow axis and prevents the freshly formed iron particles to spread outside the focused beam. In the second step, the flow of iron pentacarbonyl is stopped and a mixture of acetylene and SF_6 (SF_6: C_2H_2=1:4) is passing through the central nozzle (mixture flow rate: 250 sccm). The hot carbon fragments formed by the pyrolysis of acetylene are drawn away toward the filter (positioned in the vicinity of the induced reaction flame) where they cover the native iron already stored in-situ onto the filter. During the experiment, the pressure in the reactor was maintained at 400 mbar.
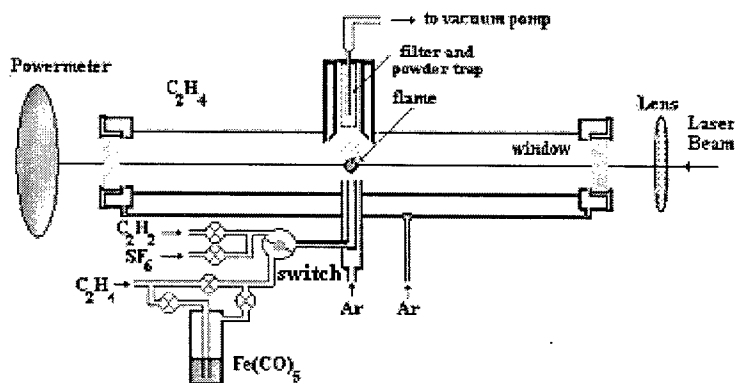
Figure 1: Experimental set-up for a two-steps experiment (RO)

Secondly, the Fe-C nanocomposite particles were prepared in a single-step experiment (labeled here-after CF), by the laser pyrolysis of the reactive flow partitioned between two concentric nozzles: $Fe(CO)_5$ vapors drawn away by C_2H_4 were admitted through the central inner tube while a hydrocarbon mixture including C_2H_2 and C_2H_4 emerged in the reaction cell through an outer concentric tube (Fig.2)

For the CF samples, the pressure in the reaction cell was maintained around 650-700 mbar. The CO_2 laser power was around 90 Watt. One of the most important parameters is the C_2H_4 carbonyl carrier flow. It was fixed at 100 sccm or 50 sccm for CF4 and CF5, respectively (the most representative samples of this work). The total hydrocarbon mixture flow was settled to around 150 sccm for sample CF4 (C_2H_4:C_2H_2=2:1) and to around 100 sccm for sample CF5 (C_2H_4:C_2H_2=1:2).
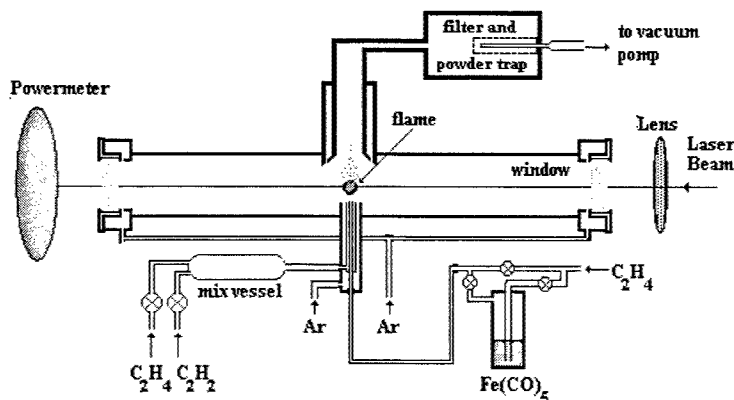
Figure 2: The experimental set-up for a single step laser synthesis of composite Fe-C system

In both experimental set-ups described above, ethylene and sulphur hexafloride play the role of sensitizers (which are excited by the absorption of the CO_2 laser radiation and then transfer the absorbed energy towards the other reaction partners by collision, thus finally increasing the temperature of the whole system). For producing iron nanoparticles iron pentacarbonyl precursor was used. Since the $Fe(CO)_5$ molecule does not absorb in the 10 μm region, C_2H_4 was used as sensitizer. Previous experiments have shown that $Fe(CO)_5$ decomposes and aggregates as iron clusters at relatively low temperatures (around 300 ^{0}C) for which ethylene remains stable For this purpose, the C_2H_4 gas was bubbled with different flow rates through the glass reservoir containing a sample of liquid $Fe(CO)_5$ (about 25 Torr vapor pressure at 20 C). The reactant gases were confined by a coaxial Ar flow (1100 sccm). In order to prevent the NaCl windows from being coated with powder they were continuously flushed with Ar (100 sccm). The interaction of reactant gas with the laser beam results in a yellow-white flame. The nucleated particles formed during reaction are entrained by the gas stream to the cell exit where they are collected in a trap, closed with a microporous filter in the direction of the rotary pump.

After synthesis, some of the as-prepared powders were toluene extracted using the Soxhlet method; this enables a separation from the carbonaceous residue of same other carbon compounds involved and their further identification as well as of the many polyaromatic hydrocarbons usually contained in the synthesized powder . The residue was dried and characterized.

The morphology and composition of Fe-C nanocomposites were characterized by medium and high-resolution transmission electron microscopy (TEM), selected area electron diffraction (SAED), energy depressive analysis (EDAX) and Raman spectroscopy.

3. RESULTS AND DISCUSSIONS

The Fe nanocomposite powders obtained are dark-brown to black in color and they flow easily in air. When the powder is approached with a magnet, the particles are instantaneously attracted to the magnet, thus indicating that the nanoparticles are magnetic at room temperature.

Studies of $Fe(CO)_5$ sequential decarbonylation by laser pyrolysis [8] revealed the fast removal of carbonyl ligands (first bond energy of 41.5 Kcal/mol), with the formation of metallic iron and CO:

$$Fe(CO)_5 \longrightarrow Fe(CO)x + (5-x)CO, \; x = 0 - 4 \qquad (1)$$
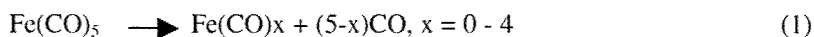
The formed metallic iron spontaneously burns in the atmosphere after withdrawal from the collection chamber. To avoid this process, iron particles should be covered by a protective shell (e.g. iron oxide or carbon-based coating).

In the two-step laser pyrolysis experiment, the high reactivity of freshly formed iron nanoparticles could promote chemisorption of hydrocarbon fragments (released by acetylene dissociation) onto the iron surface. On the other hand, SF_6 has a high absorption cross-section for the CO_2 laser radiation (absorption coefficient a=4.42x10^{-1} cm^{-1}* torr^{-1} at the 10P20 CO_2 emission line). Consequently, the use of SF_6 as sensitizer in the second step of the experiment, could speed up hydrocarbon decomposition.

The TEM examination of RO samples suggests that the iron nanoparticles formation occurred rather independently from carbon nucleation. The image in Fig 3 indicates complex powder morphology with different particle dimensions: the presence of small particles (about 5 nm mean diameter) as well as large ones (about 16 nm mean diameter) may be distinguished. The particle size distribution performed on this selected area (see insert in Fig.3) confirms the existence of the two before mentioned maxima, corresponding to either the small or to the large particles, respectively. According to the SAED analysis (insert in Fig.3), rings associated with bcc phase of iron could be identified (pattern 85-1410) which may be attributed to diffractions from small iron particles. Due to the setup of the SAED techniques, the image does not allow the determination of carbon that seems to be the structure of the large particles.
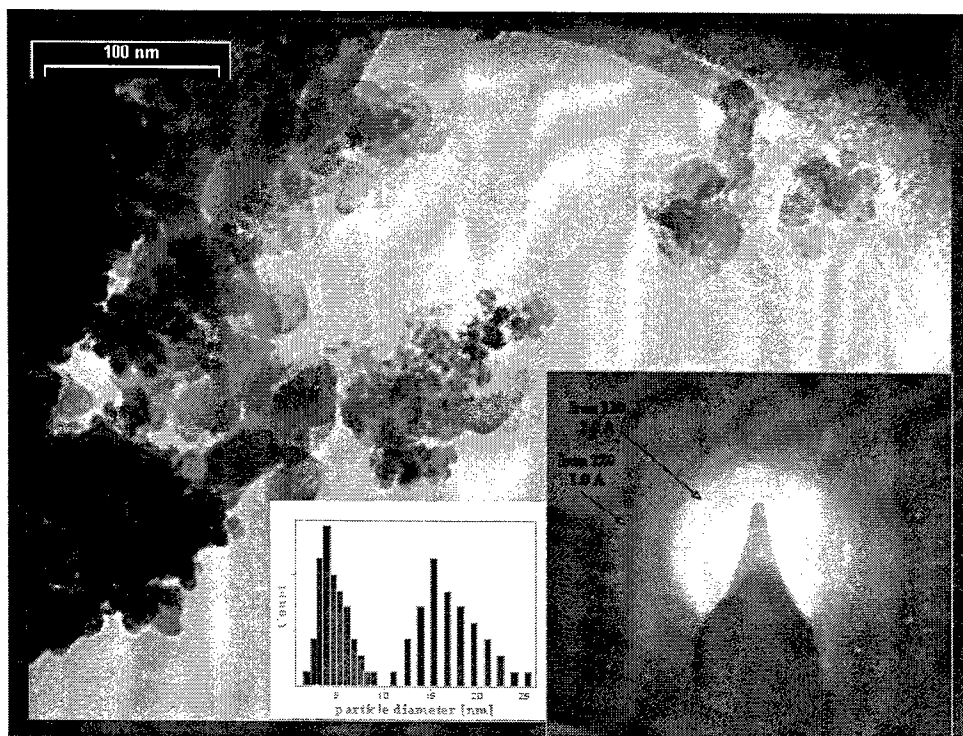
Figure 3: TEM investigations of carbon-iron clusters (sample labelled RO) obtained by two-step laser pyrolysis: the inserts show the SAED analysis with Fe (bcc) identification rings (pattern 85-1410) and the particle size distribution (exhibiting two maxima corresponding to small iron particles and to larger particles (probably carbon) distributions, respectively).

By the improved reactant flow geometries as well as by the appropriate choice of the iron and carbon donor flows, the single-step laser pyrolysis experiment could lead to the synthesis of a new Fe-C nanocomposite where iron cores are embedded in carbon sheets, inhibiting the homogeneous carbon nucleation. Indeed, we may suppose that the iron nanoparticles are the first to nucleate but during their consolidation their surface still remains hot. At the same time the excited hydrocarbon mixture may release carbon fragments due to the catalytic activity of the reactive iron surface. These fragments cover the iron aggregates, allowing for a specific structure composed by an iron core covered by carbon layers to be formed.
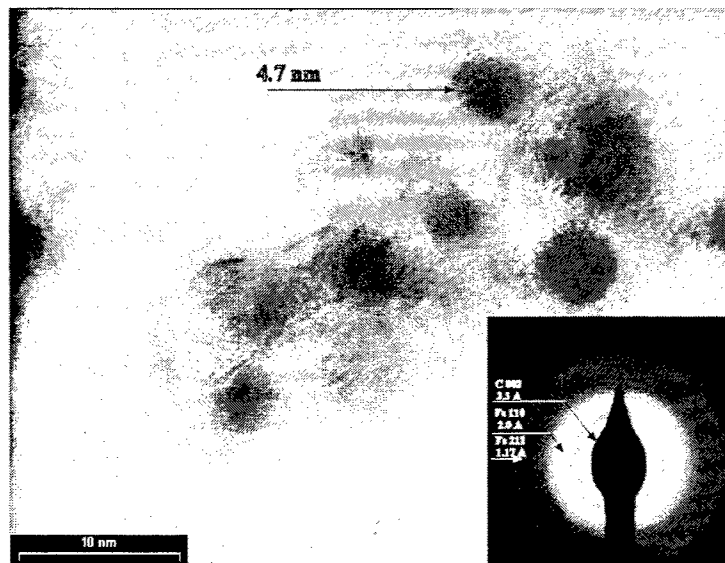
Figure 4: Medium-resolution TEM image of the as-prepared Fe-C nanocomposite, obtained in a single step laser pyrolysis experiment (sample CF4), and the corresponding SAED pattern (insert in the Figure).

The medium resolution TEM image (Fig.4) seems to indicate a rather even dispersion of Fe nanoparticles in a carbon matrix. Almost each particle presents a core (dark contrast) surrounded by a shell. The resolution of the image does not allow for an accurate evaluation of the thickness of the shell. The electron diffraction pattern obtained from a large area of particles shown in Fig. 4 seems to point the presence of bcc iron (as identified by the diffraction rings corresponding to the (110) and (211) hkl planes) as well as graphitic carbon (identified by the (002) hkl plane). The SAED diffraction features indicated low dimension ordering (lack spots and presence of diffuse diffraction rings).

A low resolution TEM image (Fig. 5) allows for the observation of a high number of nanoparticles, which show a uniform and well-dispersed distribution (sample CF5). The corresponding particle distribution of the carbon coated iron nanoparticles (insert in Fig. 5) is characterized by a mean size of about 6 nm, being spread from 3 nm to 9 nm.
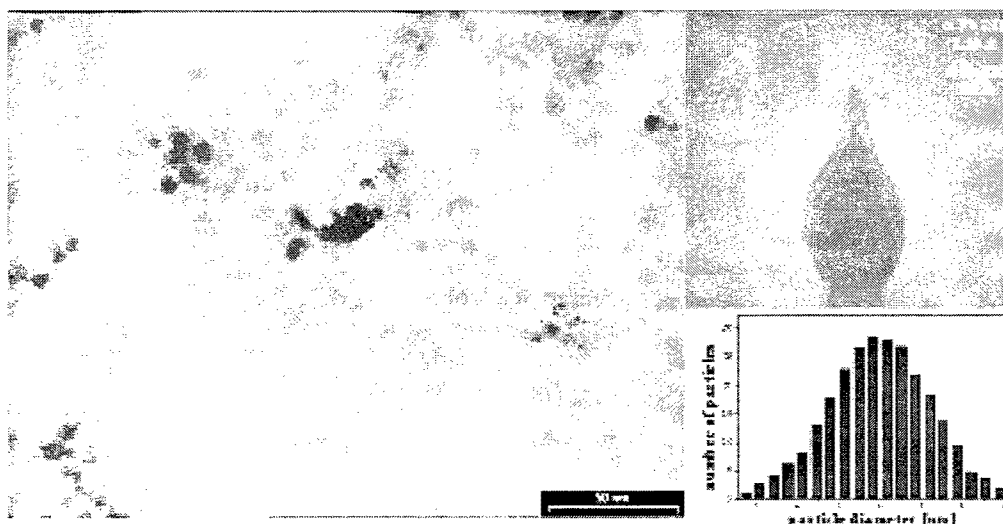
Figure 5: TEM image of the as-synthesized Fe-C nanocomposite, obtained in a single-step laser pyrolysis (sample CF5). The corresponding particle size distribution and the SAED analysis are shown in inserts.
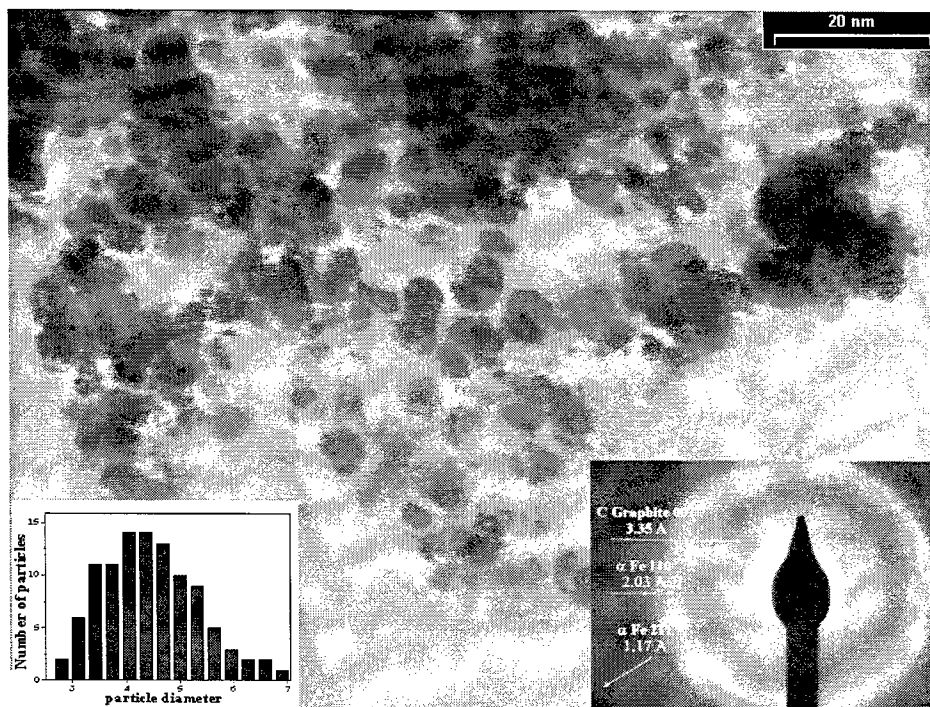
Figure 6: TEM image of the residue of Fe-C nanocomposite after Soxhlet toluene extract (sample FC 4 residue). The two inserts present the SAED analysis and the particle size distribution, respectively.

After synthesis the as-prepared powder was toluene extracted using the Soxhlet method. A TEM image of the composite material after extraction is presented in Fig. 6. The particles are characterized both by a low degree of agglomeration and low particle diameter spreading. The size distribution of the iron nanoparticles as evaluated from the TEM micrograph is presented in the insert of Fig.6. It is characterized by a mean size of about 4.5 nm.

Figure 7: HREM images (at two magnifications) of Fe-C nanocomposite residue (sample CF 4 residue).

The results of SAED analysis (insert in Fig.6) suggest the majoritary presence of Fe (bcc phase) identified by the characteristic rings, with corresponding (110), (211) hkl planes (pattern 85-1410).

For most nanoparticles of the Fe-C composite residue, investigated by high-resolution electron microscopy, a iron core surrounded by a carbon shell was observed. Figure 7 gives particularly nice examples showing almost spherical iron particles covered with few (3-4) carbon sheets. The almost perfect surrounding carbon coverage, which interferes with the metal core makes difficult the identification of the innermost crystalline network. However, lattice plane spacings could be measured toward the rim of the particle system (Fig. 7) and the results come close to d = 0.203 nm for the α iron core and to d = 0.345 nm for the carbon coating.

However, it should be stressed that the tabulated diffraction data were determined from macroscopic iron. For free iron nanoparticles, different lattice parameters could be expected, particularly when an outside shell could exert stresses on the lattice of the core.

The content in Fe of the nanocomposite residue is evidenced in Fig. 8 were the EDAX spectrum for the CF 4 sample is displayed.
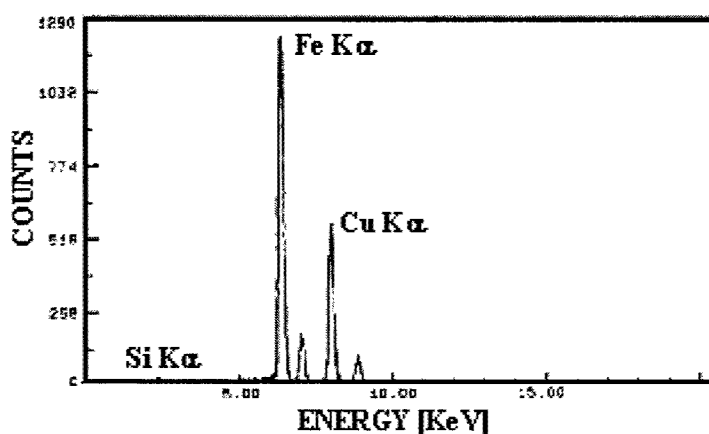
Figure 8: EDAX analysis of the Fe-C nanocomposite residue (after toluene extraction).

Fig. 9. Displays the carbon region of the Raman spectrum for the Fe – C nanocomposite synthesized in a single-step experiment (sample CF 5). The smooth curves in the plot represent the Gaussian fit for the D and G Raman-active bands (disorder and graphite, respectively). The position of the D band was found to center at 1302.3 cm^{-1}, with an average full width at half maximum (FWHM) intensity of 118.1 cm^{-1}. The position of the G band is centered at about 1590.7 cm^{-1}, with an average FWHM intensity of 77.5 cm^{-1}. The lower value for the position of the G and D band from that found in graphite (of small crystal size) is thought to provide information about the microstructure of the carbon layers. In pristine nanographite the two main peaks are found at 1352.9 and 1592.7 cm^{-1}, respectively [9].

It has been shown that the I_D/I_G ratio allows a quantitative characterization of the induced disorder in the sp^2 domains and that this ratio is inversely proportional to the effective crystallite size in the direction of the graphite plane [10] In this work, the I_D/I_G ratio is unusually high (I_D/I_G=8.47). An explanation for this behavior is not yet clear since an increased disorder or/and some short-range order in the sp^2 domains of the carbon coverage seems not to correspond to our results. A more plausible argument could be the effect of a few graphitic sheets with large curvature covering a metal core or/and the strength of the interaction between the metal particle and the carbon material [11]. It is worth to mention that for Fe-C samples labeled CF4 (obtained with higher carbon donor flow), I_D/I_G=1.21 i.e. much lower than in the previous case.
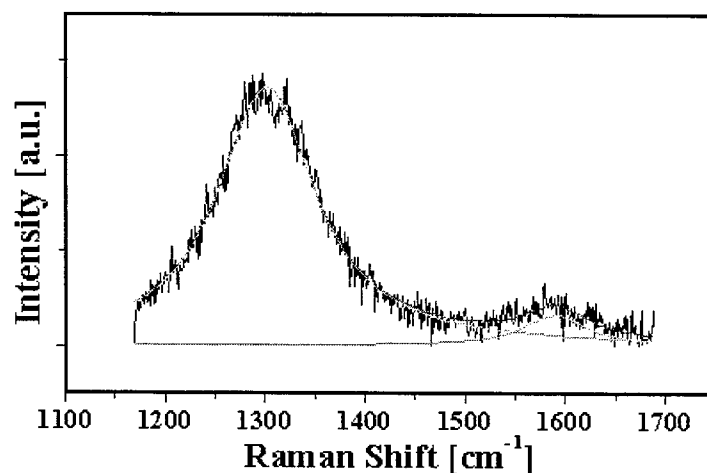
Figure 9: Raman spectra for CF5 sample

5. CONCLUSIONS

CO_2 laser pyrolysis of volatile iron and carbon precursors in a gas flow reactor was used in order to obtain Fe-C nanocomposites. The morphology and the particle composition depend on the preparation method. By a proper design of flow geometries, a single-step experiment is leading to the synthesis of iron nanoparticles (4.5-6 nm mean diameters) with a low degree of agglomeration, which are covered by carbon layers. HREM analysis of the Soxhlet toluene extracted powders indicates that the particles are well dispersed and seem to be embedded in a few graphitic sheets.

ACKNOWLEDGMENTS

REFERENCES

1. M. Bernhauer, M.Braun, K.L.Hutinger, *Carbon* **32,** pp. 1073-1078, 1994.

2. J. P. Hare, W. K. Hsu, H. W. Kroto, A. Lappas, K. Prassides, M. Terrones, . R. M. Walton, , "Nanoscale Encapsulation of Molybdenum Carbide in Carbon Clusters" *Chem. Mater.* **8,** pp.6-11, 1996.

3. W. Teunissen, F. M. F. de Groot, J. Geus, O. Stephan, M. Tence, C. Colliex, , "The Structure of Carbon Encapsulated NiFe Nanoparticles" *Journal of Catalysis* **204,** pp. 324-334, 2001.

4. J. S. Haggerty and W. R. Cannon "Laser Induced Chemical Processes", J. I. Steinfeld ed. pp. 165-241, Plenum. New York, 1981

5. E. Borsella, S. Botti, R. Fantoni, R. Alexandrescu, I. Morjan, C. Popescu, T. Dikonimos-Makris, R. Giorgi, S. Enzo, "Composite Si/C/N powder production by laser induced gas phase reactions" *J. Mater. Res.* **7,** pp. 2257-2265, 1992.

6. R. Alexandrescu, S. Cojocaru, A. Crunteanu, I. Morjan, I. Voicu, L. Diamandescu, F. Vasiliu, F. Huisken, B. Kohn, "Preparation of iron carbide and iron nanoparticles by laser induced gas phase pyrolysis*" J. Phys. IV France,* **9**, pp. Pr-8-537-544, 1999.

7. I. Morjan, R. Alexandrescu, I. Soare, F. Dumitrache, I. Sandu, I. Voicu, A. Crunteanu, E. Vasile, V. Ciupina, S. Martelli, "Nanoscale powders of different iron oxide phases prepared by continuous laser irradiation of iron pentacarbonyl-containing gas" *Materials Science and Engineering C* **1020,** pp.1-6, 2002.

8. K.E. Lewis, D.M. Golden, and G.P. Smith, *Journal of American Chemical Society* **106**, pp. 3905-3913, 1984.

9. B. L. V. Prasad, H. Sato, T. Enoki, Y. Hishiyama, Y. Kaburagi, A. M. Rao. G. U. Sumanasekera, P. C. Eklund, , "Intercalated nanographite: Structure and electronic properties" *Phys. Rev. B*, **64** pp. 235407-235417, 2001.

10. Ferrari A. C. and Robertson D., "Multi-wavelength Raman Spectroscopy of Carbon", *Phys. Rev. B*; **61**:pp. 14095-14099, 2000

11. Z. Zhong, B. Liu, L. Sun, J. Ding, J. Lin, K. Lee Tan, "Dispersing and coating of transition metals Co, Fe and Ni on carbon materials" *Chem Phys. Lett.* **362**, pp. 135-143, 2002.

Addendum

The following papers were announced for publication in these proceedings but have been withdrawn or are unavailable.

[4977-01] **Wavelength dependence of laser desorption from ionic single crystals**
J. T. Dickinson, L. Cramer, S. C. Langford, Washington State Univ. (USA)

[4977-04] **Interaction of 157-nm VUV F₂ laser radiation with fused silica: absorption and ablation characteristics**
C. D. Walton, P. E. Dyer, A.-M. Johnson, D. Sands, Univ. of Hull (United Kingdom); K. G. Snowdon, Nortel Networks (United Kingdom)

[4977-20] **Tailoring the size and shape of gold nanoparticles by nanosecond laser pulses**
F. Träger, C. Hendrich, T. Ziegler, F. Hubenthal, Univ. Kassel (Germany)

[4977-23] **Resonant-infrared pulsed laser deposition of organic thin films**
J. S. Horwitz, J. A. Callahan, E. J. Houser, R. A. McGill, Naval Research Lab. (USA); D. M. Bubb, Seton Hall Univ. (USA); R. F. Haglund, Jr., M. R. Papantonakis, Vanderbilt Univ. (USA)

[4977-24] **Laser ablation and PLD of a functional protein**
Y. Tsuboi, Hokkaido Univ. (Japan)

[4977-30] **Mechanisms involved in steam laser cleaning of submicron contaminants**
S. D. Allen, S. I. Kudryashov, S. Shukla, Florida State Univ. (USA)

[4977-32] **Buried diffractive phase elements: deep-ultraviolet laser writing**
A. H. Nejadmalayeri, P. R. Herman, J. Li, D. Coric, Univ. of Toronto (Canada)

[4977-36] **Laser processing of mesoscale energy storage systems**
C. B. Arnold, R. C. Wartena, K. E. Swider-Lyons, A. Piqué, Naval Research Lab. (USA)

[4977-37] **Femtosecond and nanosecond pulsed laser induced forward transfer of metals**
K. Komorita, T. Sano, H. Yamada, E. Ohmura, I. Miyamoto, Osaka Univ. (Japan)

[4977-41] **Laser micromachining of semiconductor and optoelectronic materials**
P. Subrahmanyan, Electro Scientific Industries, Inc. (USA)

[4977-50] **Laser processing of microelectronic materials including silicon**
T. Hannon, T. Hoult, Coherent Laser Div. (USA)

[4977-54] **Effects of a concentrated laser beam on some optical media**
C. Laurentiu, I. Viorel, H. Ilie, Univ. Lucian Blaga din Sibiu (Romania)

[4977-63] **Laser cleaning: a complex process**
J. Graf, M. Mosbacher, F. Lang, O. Dubbers, Z. Nadj, M. Sattel, P. Leiderer, Univ. Konstanz (Germany)

Author Index